Tomáš Březina
Ryszard Jabloński
Editors

Mechatronics 2013

RECENT TECHNOLOGICAL AND SCIENTIFIC ADVANCES

Springer

Mechatronics 2013

Tomáš Březina · Ryszard Jabloński
Editors

Mechatronics 2013

Recent Technological and Scientific Advances

Springer

Editors
Tomáš Březina
Faculty of Mechanical Engineering
Institute of Automation and Computer Science
Brno University of Technology
Brno
Czech Republic

Ryszard Jabloński
Institute of Metrology and Biomedical Engineering
Warszaw University of Technology
Warszaw
Poland

ISBN 978-3-319-02293-2 ISBN 978-3-319-02294-9 (eBook)
DOI 10.1007/978-3-319-02294-9
Springer Cham Heidelberg New York Dordrecht London

Library of Congress Control Number: 2013947579

Printed on acid-free paper

Springer is part of Springer Science+Business Media (www.springer.com)

Preface

This book is the fourth volume in series Recent Advances in Mechatronics, following the editions in 2007, 2009 and 2011. It comprises carefully selected contributions presented at the 10th International Conference Mechatronics 2013, organized by Brno University of Technology on October 7–9, 2013 in Brno, Czech Republic.

The selection of the contributions for this book was based on thorough reviews of full length papers, concentrating on originality and quality of the work. Finally 113 papers were selected for publishing in this book.

The book covers the areas design, modeling and simulation of mechatronic systems, in particular the r&d of mechatronic systems, model-based design, virtual prototyping, electrical machines, drives & power electronics, actuators and sensors, automotive and aerospace systems, measurement and diagnostics, signal processing, pattern recognition, wireless sensing, nanometrology, industrial and mobile robotics, microrobotics, unmanned vehicles, control and automation, industrial applications, vibration and noise control, the list of topics could go on and on.

We hope that the volume can serve as useful reference source in mechatronics not just among academics, but also in development departments in industry, as the mechatronics as a subject should be closely related with the rapid transfer of new ideas to products we can meet in our daily lives.

We would like to thank all authors for their contribution to this book.

Tomáš Březina
Conference Chairman
Brno University of Technology

Contents

Design, Modeling and Simulation of Mechatronic Systems

Electrical Machines, Drives and Power Electronics

Measurement and Diagnostics

Robotics

Control and Automation

Biomedical and Biomechanical Engineering

Mechatronic Education

Monitoring of Energy Flows in the Production Machines

J. Augste[1], M. Holub[1], R. Knoflíček[1], T. Novotný[1], and J. Vyroubal[2]

[1] Brno University of Technology, Faculty of Mechanical Engineering, Technická 2, 616 69, Brno, Czech Republic
y101686@stud.fme.vutbr.cz
[2] Research Center of Manufacturing Technology, Faculty of Mechanical Engineering, The Czech Technical University in Prague, Horská 3, 128 00, Prague, Czech Republic
J.Vyroubal@rcmt.cvut.cz

Abstract. The article deals with the development of software tools supporting visualization in order to assess the workload of electrical appliances installed in machine-tools. This enables us a considerably easier orientation and the control of energy consumption. The first part of the article is concerned with the application created for simulation of energy flows in the machine-tool with the help of advanced post-processing. That allows software to select to review only interesting data using peaks identifying algorithm. The second part deals with Sankey diagrams visualizations improvements. The tool developed for visualization was applied to the machine FUEQ 125 Efektiv company TOS Kuřim in cooperation with the Czech Technical University in Prague, Faculty of Mechanical Engineering, VCSVTT - Research Centre for Manufacturing Engineering and Technology.

1 Introduction

Energy reduction strategies are increasingly important with the constant increase in electricity costs and the rising environmental awareness of both manufacturers and customers [3]. A machine tool's replacement cycle, after installation, is up to 15–20 years; thus, it is critical to conserve energy on machines with methods that can be applied to both new and existing machines [10]. According to the publication of the European Union, "Ecodesign" aims at improving the environmental performance of products throughout their life-cycle (production, use, and end-of-life) by systematic integration of environmental aspects at the earliest stage of the product design. It is estimated that over 80% of all product related environmental impacts are determined during the design phase, and most of the costs involved are committed then. [11].

This description is very general; therefore, several analyses have to be used for evaluation. The method of "Lowest Life Cycle Cost" (LLCC) allows determining a total cost of ownership and operation of a particular product. LLCC is used to set a particular target minimum of these costs where the space between this minimum

T. Březina and R. Jabloński (eds.), *Mechatronics 2013*,
DOI: 10.1007/978-3-319-02294-9_1,

and the current state enables us to maintain a space for innovation (competition). To ensure the necessary innovation, the product is compared with the "Best Available Technologies" (BAT); in simple terms, using the best available technologies. These are technologies expected to be introduced into a standard product within a short time horizon. A comparison with the best non-available technologies (BNAT), i.e. with a top of the current state of the art in research and product development, indicates a possible market development in a longer time horizon.

Nevertheless, these analyzing tools are used only to determine the potential for improvement and the direction in which this improvement could occur. The energy-efficiency has to be evaluated [5] for a clear illustration of dependences of the individual variables. Due to complexity of energy flows in productions machines, it is convenient to use a graphical evaluation. That has to summarize data from all the energy-using components. Important points based on peaks and important intervals, for example coolant running, must be identified. Even on a single actuator it is a difficult task because these points could not be easily found without inspection of a smaller interval (Fig. 1).

Therefore, the essence of the proposal is to present improved visual decision-making platform for Ecodesign of machine tool previously described as ECO Design v1.0 [1].

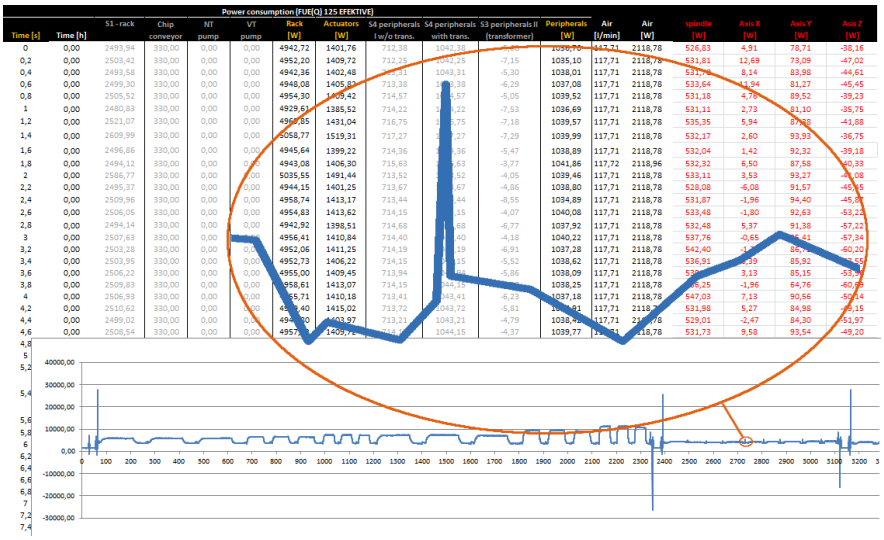

Fig. 1 Example of FU EFEKTIV measured data

2 State of Art

The application must allow a complete support for a product development with regard to energy efficiency [6]. For ECO Design v1.0 application testing data measured (Fig. 1) on floor type machining centre FU EFEKTIV (Fig. 2) were

used. Machine FUE (Q) 125 EFEKTIV is installed in TOS Kuřim. Based on testing results some of improvements were suggested by users.

The application itself enables making a straight and comfortable 3D visualization by Sankey diagrams [7] (Fig. 4) but in some cases 2D visualization with a precise value displayed could be more straightforward.

Because the data set sampling time is usually very short, little oscillation of Sankey represented by 3D body could occur. First version of application had implemented frame skip function to make visualizations smoother. Due to 2D diagrams and precise value support request it was necessary to choose different approach to suppress the phenomenon.

Fig. 2 Installed machine FUE(Q) 125 EFEKTIV in TOS Kuřim

3 Peak Analysis

One of typical step towards reducing energy consumption in machine tools is to analyze measured data over all actuators and find peaks and other critical time intervals.

There are several scenarios that have to be reviewed [8]:

- Reduce total energy use for the machine tool based on the usage during idle and non-value-added periods
- Identify disruptions in smooth part production based on anomalous power usage spikes
- Track maintenance state of the machine tool using historical power usage profiles
- Enable environmental reporting on a per-part basis by accurately accounting for the energy use of the part as it is being manufactured

– Notice emerging trends in the energy usage, such as increased total consumption for successive parts which may indicate process plan deviations and inconsistencies.

For peak analysis "window" approach is used. The input is a table of values equally spaced in time. Value in point *i* is local maximum on interval *k* when value of peak function *S* (1) there is bigger than a threshold. The threshold is calculated and a value bigger than zero is adaptively set on dataset. The value is written to matrix *p(i)* for next processing.

$$S(k,i,x_i,T)=\frac{\max\{x_i-x_{i-1},x_i-x_{i-2},...,x_i-x_{i-k}\}+\max\{x_i-x_{i+1},x_i-x_{i+2},...,x_i-x_{i+k}\}}{2} \quad (1)$$

After that local peaks are processed and compared in global context of data set. Point *i* could be global maximum *P(i)* for mean *m'*, standard deviation *s'* and constant *h.*

$$(a[i]-m')>(h*s') \quad (2)$$

Where constant *h* is:

$$1\le h\le 3 \quad (3)$$

Peaks close to each other must be removed. Every pair *(i, j)* is tested whenever they are closer than *k* on timeline. When this is true, then just one with larger value is a global maximum.

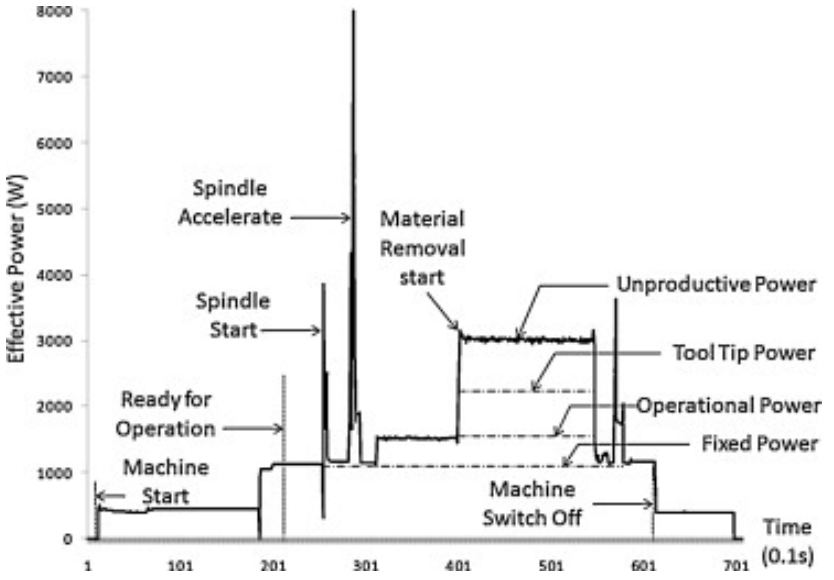

Fig. 3 Visualization of energy flows according to real measured data [2]

4 Sankey Diagrams

They are not visualized together with machine so it could by sometimes hard to understand them. We could also make them as a layer on picture of the machine but machines are usually too complex in the space to show just 2D picture and 3D modeling has been increasingly used for design. Making visualization in 3D enables to obtain a space for extension allowing an increase in the overall visual impression; e.g. by a complex kinematic simulation along with the simulation of energy flows.

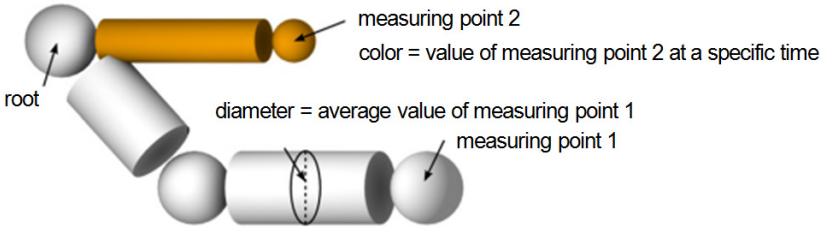

Fig. 4 Example of basic 3D Sankey diagrams [4]

4.1 2D Sankey Diagrams

Suitable design of 2D Sankey diagram for Ecodesign usage was publicized before [9]. It must involve a precise text value to allow users to read accurate value whenever it is needed. Diagrams are showed in separated window (Fig. 5) and were programmed in C# using OpenGL library as well as whole ECO Design application.

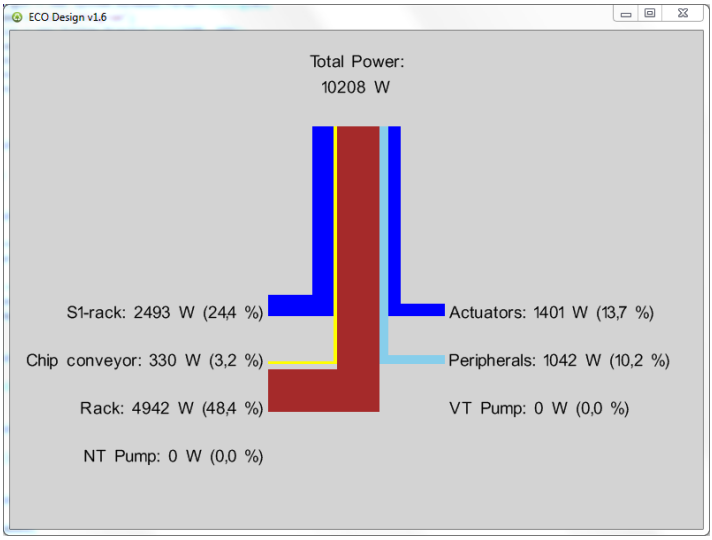

Fig. 5 2D Sankey diagram values according to measured data on FUE(Q) 125

4.2 3D Visualization

During practice testing used source style of 3D Sankey (Fig. 4) visualization was a little bit modified. Different visualization approach (Fig. 6) was designed to get better information value into visualization. There is a static basic color used for identification of object, combination of intensity of each color for indication of growth, transparency for average value and diameter for actual value. Indication of growth helps to predict peak states (Chapter 3) before they occur. Using transparency to visualize average value helps to highlight parts with significant energy consumptions compared to the other ones.

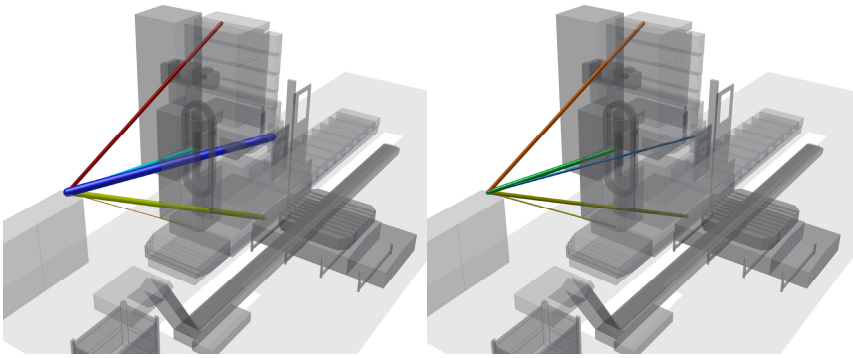

Fig. 6 Visualization of energy flows; values represented by diameter of bodies

5 Conclusions

The Eco Design v1.6 has been designed to provide energy flows post-processing to production machines designers. One of typical tasks realized in software is to analyze measured data over all actuators and find peaks and other critical time intervals. The main target is to find the peaks creation process. Thanks to implementation of 3D visualization, possible improvements of process could be suggested. On the other hand, 2D Sankey diagram enables precise value checking and, therefore adds the possibility to select from several variants. All of these functions and possibilities form a visual decision-making platform for Ecodesign.

Main possible future developments of the software are connections to virtual reality and augmented reality visualizations. Data review in CAVE using virtual reality for presentation of final results could show different states even on very complex machines and complexly solve Ecodesign study together with all other studies necessary to be done in design phase. On the other hand, augmented reality enables to changes overall impact to energy flows and consumption of the production machine.

Acknowledgments. This work has been supported by Brno University of Technology, Faculty of Mechanical Engineering, Czech Republic (Grant No. FSI-S-11-5). This project has been funded with support from the state budget through the Ministry of Industry and Trade of the Czech Republic (ID of project: FR-TI3/655 – ECODESIGN in tool machine construction) and by European Regional Development Fund in the framework of the research project NETME Centre under the Operational Programme Research and Development for Innovation. Reg. Nr. CZ.1.05/2.1.00/01.0002, id code: ED0002/01/01, project name: NETME Centre – New Technologies for Mechanical Engineering.

References

[1] Augste, J., Knoflíček, R., Holub, M., Novotný, T.: Tools for visualization of energy flows in the construction of machine- tools. MM Science Journal, 392–395 (March 2013) ISSN: 1803- 1269

[2] Duflou, J.R., et al.: Towards energy and resource efficient manufacturing: A processes and systems approach. CIRP Annals - Manufacturing Technology 61(2), 587–609 (2012) ISSN 0007-8506

[3] Behrendt, T., et al.: Development of an energy consumption monitoring procedure for machine tools. CIRP Annals - Manufacturing Technology 61(1), 43–46 (2012) ISSN 0007-8506

[4] Neugebauer, R., et al.: VR tools for the development of energy-efficient products. CIRP Journal of Manufacturing Science and Technology 4(2), 208–215 (2011) ISSN 1755-5817

[5] Götze, U., et al.: Integrated methodology for the evaluation of the energy- and cost-effectiveness of machine tools. CIRP Journal of Manufacturing Science and Technology 5(3), 151–163 (2012) ISSN 1755-5817

[6] Rünger, G., et al.: Development of energy-efficient products: Models, methods and IT support. CIRP Journal of Manufacturing Science and Technology 4(2), 216–224 (2011) ISSN 1755-5817

[7] Sankey, H.R.: The Thermal Efficiency of Steam-Engines. MPICE 134, 278–283 (1898)

[8] Vijayaraghavan, A., Dornfeld, D.: Automated energy monitoring of machine tools. CIRP Annals - Manufacturing Technology 59(1), 21–24 (2010) ISSN 0007-8506

[9] Behrendt, T., Zein, A., Min, S.: Development of an energy consumption monitoring procedure for machine tools. CIRP Annals - Manufacturing Technology 61(1), 43–46 (2012) ISSN 0007-8506

[10] Oda, Y., et al.: Study of optimal cutting condition for energy efficiency improvement in ball end milling with tool-workpiece inclination. CIRP Annals - Manufacturing Technology 61(1), 119–122 (2012) ISSN 0007-8506

[11] European Union. (2008) Draft Working Plan of the Ecodesign Directive (2009–2011), http://www.eup-network.de/fileadmin/user_upload/Produktgruppen/Arbeitsplan/DraftWorkingPlan_28Apr08.pdf

Off- Road Vehicle with Controlled Suspension in Soft Unprepared Terrain

A. Bílkovský[1] and Z. Šika[2]

[1] VUTS, a. s., Svarovska 619, 460 01, Liberec XI, Czech Republic
ales.bilkovsky@vuts.cz
[2] Czech Technical University in Prague, Faculty of Mechanical Engineering, Department of Mechanics, Biomechanics and Mechatronics, Technicka 4, 166 07, Praha, Czech Republic
zbynek.sika@fs.cvut.cz

Abstract. The paper deals with the investigation of the influence of the controlled suspension on the traction capability of the off-road vehicles, especially the agriculture tractors. The standard suspension of the tractor is realized by tires, the rear axle is firm. The controlled suspension is used to increase traction forces in the soft unprepared terrain. The models of wheel soil interaction describe the rigid and elastic models of wheel based on semi-empirical model.

1 Introduction

The prediction of the tractive and traction force is very important but it is very difficult. It depends on correct of models of terrain, the correct parameters of terrain and on model of the tire. The agricultural off-road vehicles are built with firm rear axle and the suspension of this vehicle is realized by tires. The suitable controlled suspension influences the motion of the vehicle in the terrain and the forces between the terrain and the wheel.

2 Modeling Elements

The basic model's elements for modeling of the vehicle in the terrain were used. The model describes the basic characteristic response of the real object. The model is consists of the vehicle model, the terrain and soil model and the wheel-soil interaction model. Each of models will be described below.

2.1 Vehicle Model

A 4-DOF half vehicle model is implemented to simulate the response of vehicle on different loading, terrain profile and to calculate the load on wheels.

T. Březina and R. Jabloński (eds.), *Mechatronics 2013*,
DOI: 10.1007/978-3-319-02294-9_2,

The four degrees of freedom of the vehicle are the heave, pitch and bounces of the two unsprung masses. The vehicle model (Fig. 1) is half car model and consists of body (sprung mass), two suspension systems and two wheels. Each of suspension system consists of linear spring and damper. The wheel is modeled as a linear spring too. The front suspension has stiffness k_f and damping b_f, the rear suspension has stiffness k_r and damping b_r.

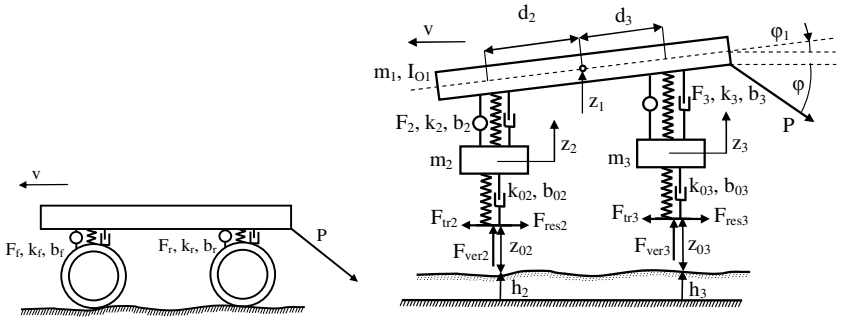

Fig. 1 Half car model

The set of ODE of vehicle model motion is obtained by Newton's method [6] as follows

$$\begin{aligned} m_1\ddot{z}_1 = &-k_2\left(z_1 - d_2\varphi_1 - z_2\right) - b_2\left(\dot{z}_1 - d_2\dot{\varphi}_1 - \dot{z}_2\right) - \\ &- k_3\left(z_1 + d_3\varphi_1 - z_3\right) - b_3\left(\dot{z}_1 - d_3\dot{\varphi}_1 - \dot{z}_3\right) - m_1 g - P\cos\varphi \end{aligned} \tag{1}$$

$$\begin{aligned} I_{01}\ddot{\varphi}_1 = &\, k_2\left(z_1 - d_2\varphi_1 - z_2\right)d_2 - b_2\left(\dot{z}_1 - d_2\dot{\varphi}_1 - \dot{z}_2\right)d_2 - \\ &- k_3\left(z_1 + d_3\varphi_1 - z_3\right)d_3 - b_3\left(\dot{z}_1 - d_3\dot{\varphi}_1 - \dot{z}_3\right)d_3 - M_P \end{aligned} \tag{2}$$

$$m_2\ddot{z}_2 = k_2\left(z_1 - d_2\varphi_1 - z_2\right) + b_2\left(\dot{z}_1 - d_2\dot{\varphi}_1 - \dot{z}_2\right) - m_2 g - F_{ver2} \tag{3}$$

$$m_3\ddot{z}_3 = k_3\left(z_1 + d_3\varphi_1 - z_3\right) + b_3\left(\dot{z}_1 + d_3\dot{\varphi}_1 - \dot{z}_3\right) - m_3 g - F_{ver3} \tag{4}$$

2.2 Terrain and Soil Model

In this study we used one type terrain profile to simulate the dynamic response of vehicle, illustrated in Fig. 2. The combination of loading of a pulled object and the terrain prepare the simulation conditions.

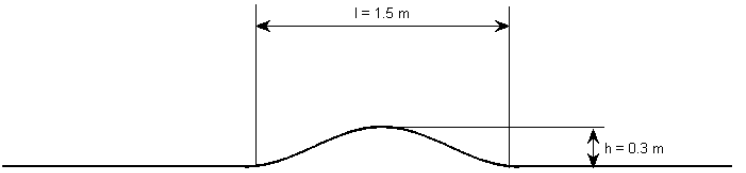

Fig. 2 Terrain profile

The mobility of wheel vehicle on soft terrain is determined by pressure sinkage relation and shear stress – shear displacement relation, which are established at the contact patch between the tire and the soil.

Typical parameters of the terrain are measured by the experimental method. The empirical and semi-empirical approaches is used to describe these relations as [1],[2] and [3]. The terrain is characterized by parameters, which are in Tab. 1. There are presented parameters for several types of the terrain.

Table 1 Parameters of terrains – taken from [2]

Terrain	n -	k_c (kN/m^{n+1})	k_ϕ (kN/m^{n+2})	c (kN/m^2)	ϕ (°)	K (m)
Grenville Loam	1.02	66.0	4486	3.1	29.8	0.038
Upland Sandy Loam (type 1)	1.1	74.6	2080	3.3	33.7	0.093
Upland Sandy Loam (type 2)	0.85	3.3	2529	2.5	28.2	0.041
Upland Sandy Loam (type 3)	1.74	259	1643	3.3	33.7	0.093

The most commonly used relations in terramechanics are Bekker's equation for pressure sinkage relation, shown in Eq. (5) and Janosi-Hanamoto equation for shear stress – shear displacement relation shown in Eq. (6).

$$p = \left(\frac{k_c}{b} + k_\phi \right) z^n \tag{5}$$

$$\tau = [c + p \tan \varphi] \ (1 - e^{(-j/K)}) \tag{6}$$

3 Models of Wheel

The wheel of the off-road vehicle is modeled as a rigid or an elastic wheel. It depends on critical pressure, which is compared with the average ground pressure. When the critical pressure is less than the average ground pressure, the tire is modeled as rigid. The average ground pressure is sum of tire inflation pressure and the terrain pressure due to carcass stiffness [1].

In other comparison of the rigid and the elastic wheel the depth of sinkage is used. When the depth of sinkage of rigid wheel and the depth of sinkage of elastic wheel are computed, these values are compared. When the sinkage of rigid wheel is higher then sinkage of elastic wheel, the wheel is modeled as the elastic. Otherwise, the wheel is modeled as rigid wheel.

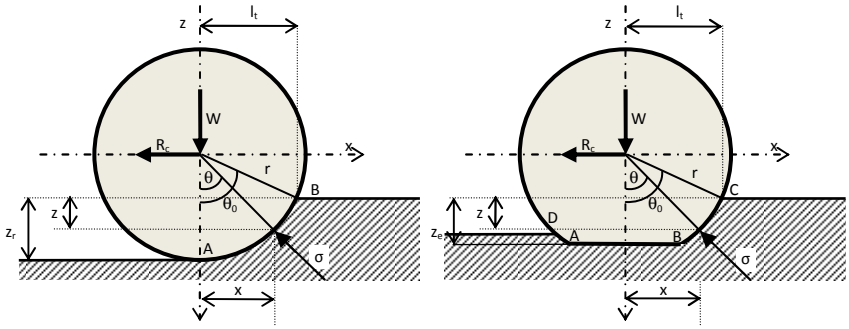

Fig. 3 Rigid and elastic model of the wheel

3.1 Rigid Wheel

When the wheel is modeled as rigid, the deformation of the terrain occurs. The wheel is not deformed. For the tire model, the sinkage is calculated by Eq. (7) and the shear displacement is calculated by Eq. (9) [2], [4].

$$z_r = r\left(1-\cos\theta_0\right) = \left[\frac{3W}{b\left(3-n\right)\left(k_c/b+k_\phi\right)\sqrt{2r}}\right]^{\frac{2}{2n+1}} \tag{7}$$

$$z_\theta = r\cos\theta - r + z_r \tag{8}$$

$$j = r\left[\left(\theta_0-\theta\right)-\left(1-i\right)\left(\sin\theta_0-\sin\theta\right)\right] \tag{9}$$

Substituting Eq. (5), Eq. (6) and Eq. (9) into the tractive force F (Eq.(10)), resistance force Rc (Eq.(11)) and drawbar pull force Fd (Eq.(12)) are calculated.

$$F = \int_0^{\theta_0} \tau\left(\theta\right)\cos\theta\cdot r\cdot b\cdot \mathrm{d}\theta \tag{10}$$

$$R_c = \int_0^{\theta_0} p\left(\theta\right)\sin\theta\cdot r\cdot b\cdot \mathrm{d}\theta \tag{11}$$

$$F_d = F - Rc \tag{12}$$

3.2 Flexible (elastic) Wheel

The elastic wheel model is used in case of deformation of the tire and the terrain. The circumference is divided into three parts as shown in Fig.3: input part BC, flat part AB and part or relaxing AD.

For the first section BC, the maximum sinkage and sinkage at any angle are Eq. (13) and Eq. (14).

$$z_e = \left(\frac{p_{agr}}{k_c / b + k_\phi} \right)^{1/n} \tag{13}$$

$$z_{BC} = r\left(\cos\theta - \cos\theta_0\right) \tag{14}$$

The shear displacement *j* developed along section BC can be determined in the same way as that earlier described for the rigid wheel [1], [2]. For the section AB the slip velocity is constant. The increase in shear displacement along section AB is proportional to the slip of tire and distance x between the points AB. The shear displacement along the section AD can be determined by the same way as that discussed previously.

4 Controlled Suspensions

The controlled suspension using in the model is based on Extended Ground Hook, called as "Skyhook". In Fig. 4 there is the representation of the theoretical approach and the realizing by the control law. This control is used with controllable damper. The characteristic of the controlled damper is shown in Fig. 4.

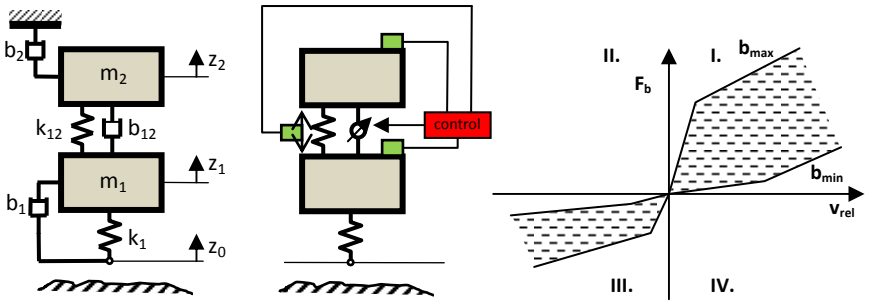

Fig. 4 Extended Ground Hook – theoretical, realization, characteristic of controlled damper

The control law [5] (Eq.(15)) is based on selection of parameters according to relative velocity between sprung and unsprung masses – as shown in Fig. 4.

$$F_b = b_{12}\,(\dot{z}_2 - \dot{z}_1) + b_2\,\dot{z}_2 - b_1(\dot{z}_1 - \dot{z}_0 + \dot{h}) \tag{15}$$

5 Numerical Results

To analyze of response of 4-DOF vehicle with the wheel – soil interaction the model runs the straight forward driving on Grenville loam. The vehicle runs over the hump (Fig. 2). The multi object parameter optimization of the controlled suspension was used. The optimized parameters were obtained. The next simulations were computed for obtained parameters for controlled suspension and then the results of response were compared with the vehicle with firm rear axle (usprung model) and with the rear suspension model (sprung model).

The vehicle runs straight forward with constant velocity 10 m/s, but real velocity of vehicle is lower, because during the running over the hump the slip increases. The wheel rotates with the constant velocity, but the vehicle is running slower (Fig. 5).

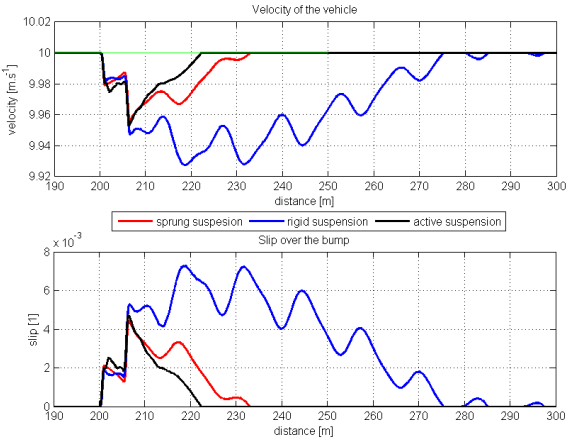

Fig. 5 Velocity of the vehicle running over the hump

The effect of the suspension and the tire stiffness uncertainty on the vehicle performance is shown in Fig 6. The heave of chassis is for unsprung model very uncomfortable, but for controlled suspension the heave is more comfortable. If the firm axle is used, the vehicle is not so inclined, but if the sprung axle is used, the vehicle is more inclined. This is results of sprung suspension; the construction changes can eliminate this fact.

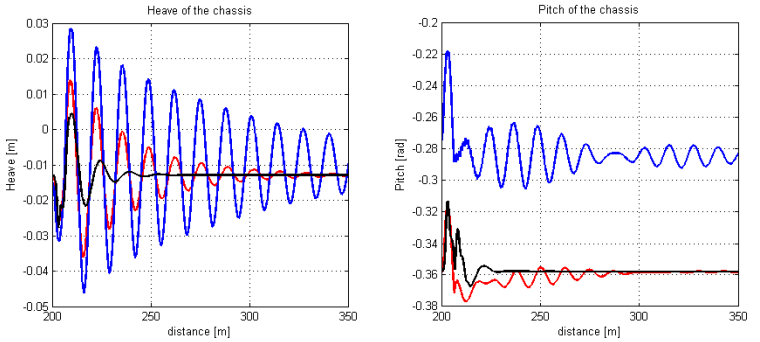

Fig. 6 Heave and pitch of the chassis

The effect of the suspension on the wheel – soil interaction forces is considerable. The tractive force and resistance force depend on soil parameters, on the geometry of the tire and on the vertical force operation on the wheel. The sinkage of the wheel increase, if the vertical force increases too. The resistance force depends on the sinkage and the force increase with the sinkage together. The results of tractive force minus resistance forces (depend on models, but buldozering effect, the deformation of tire are examples of resistance force) is drawbar pull (Fig. 7). This force represents the free capacity of wheel – soil interaction.

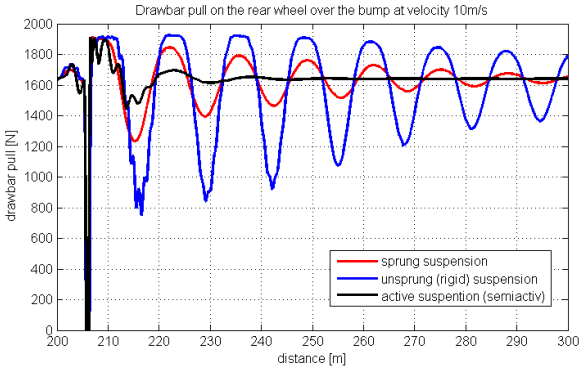

Fig. 7 Drawbar pull on the rear wheel over the hump at velocity 10m/s

6 Conclusions

This paper presents the influence of controlled suspension on the vehicle in the terrain. This is a way how to study the wheel – soil interaction and compare several models of vehicles. The prediction of mobility and performance of the off-road vehicle depend on realistic parameters, but the response of the simulation vehicle is similar. The results of simulation confirm that the controlled suspension increases the drawbar pull and enhances the comfort for the driver. The increase of mobility of the vehicle depends on the controlled suspension.

References

[1] Wong, J.Y.: Theory of Groung Vehicles. John Wiley, New York (2001)
[2] Wong, J.Y.: Terramechanics and Off-Road Vehicles. Elsevier Science Publisher, Amsterdam (1989)
[3] Muro, T., O'Brien, J.: Terramechanics: land locomotion mechanics. A.A. Balkema Publishers, Exton (2004)
[4] Li, L., Sandu, C.: On the impact of cargo weight, vehicle parameters, and terrain characteristics on the prediction of traction for off-road vehicles. Journal of Terramechanics 44(3), 221–238 (2007)
[5] Valášek, M., Novák, M., Šika, Z., Vaculín, O.: Extended Ground-Hook - New Concept of Semi-Active Control of Truck's Suspension. Vehicle System Dynamics 27(5-6), 289–303 (1997)
[6] Stejskal, V., Valášek, M.: Kinematics and dynamics of machinery. Marcel Dekker, New York (1996)

The Manipulator of the Passive Optoelectronic Rangefinder as a Controlled System of Servomechanisms

V. Cech and M. Cervenka

Oprox, Inc., Renneska 35, 639 00 Brno, Czech Republic
cech-vladimir@volny.cz, martin.cervenka@oprox.cz

Abstract. Passive Optoelectronic Rangefinder (POERF) is a measurement device as well as a mechatronic system. Design of the POERF manipulator, as a controlled system, creates potential which is used by servomechanisms of elevation and traverse. Thus creates presumptions for high quality target tracking by means of POERF cameras. Traditional design of the manipulator is ineffective. New solution was adopted with POERF model 2012, which has been patented. The aim of this article is to clarify reasons for this design and to explain the principle of the patented structure.

1 Introduction

Passive Optoelectronic Rangefinder (POERF) measures position of the moving target in spherical coordinate system (slant range D_T, elevation φ, traverse ψ) usually from 10 to 30 times per second. POERF transforms spherical coordinates of the target into UTM coordinates $(E, N, H)_T$ and uses them for extrapolation of the target trajectory. Acquired parameters of the target movement are sent with the stipulated frequency to clients (e.g. with a period of 1 second) via Internet/Intranet.

Main advantage of POERF is its passivity (does not emit any energy) and ability to function not only in on-line but also in off-line mode. General findings and history of POERF development were presented in a survey abstract [3]. Description of 2009 model (Fig. 1) is presented in [2]. The latest findings are published in [6] including links to other publications.

Principle of measurement is based on measuring stereoscopic disparity evaluated from frames of the master camera (reference image) and a slave camera (matching image) – Fig. 3. Continuous tracking of a target, which provides direction channel, whose servomechanisms of the elevation and traverse are the core of, forms a logical precondition. Controlled systems (objects) for these servomechanisms are elevation parts and traverse parts of the POERF – Fig. 2. We have patented a design of the elevation parts.

T. Březina and R. Jabloński (eds.), *Mechatronics 2013*,
DOI: 10.1007/978-3-319-02294-9_3,

Fig. 1 Photos of the Passive Optoelectronic Rangefinders (POERF) model 2009 and 2012

Sufficiently precise results can so far be acquired up to slant range D_{Tmax} = cc. (0,08 – 0,12)·D_{RF1}. Power constant D_{RF1} (Fig. 3) depends on a length of the POERF base b [m] – Fig. 2, 3, focal length of the lens f_a [m] and on characteristic dimension of the square pixels ρ [m]. On the basis of analysis [1] it can be presented that it is necessary to choose the length of the base b as long as possible. For example with 2009 model the base b = 860 mm and with 2012 model the base b = 1844 mm. Historical precursors of POERF – stereoscopic and coincidence rangefinders had a length of the base b up to 8 or 14 m.

At the same time, the crux of the problems, that has to be solved in a different way than with traditional camera manipulators (P&T device – Pan and Tilt device), lies in the necessity to use a long base b.

2 Principle of the Elevation Parts Design

If we require a constant flexural rigidity of the cameras beam, then the ratio moment of inertia of traverse parts J_ψ and elevation parts J_φ [kgm^2] is approximately constant. With common camera manipulators it does not differ a lot from one, whereas with POERF it is significant. For example for model 2012 it is 31,1 [-]. Mentioned ratio can be lowered by the modifications of a design but only in a limited way.

At the same time for moment of inertia of beams it applies

$$J = w \cdot b^5 \tag{1}$$

where w is empirical constant [kg/m^3] and b is base [m]. Empirical constant w is different for traverse parts and elevation parts. For example for model 2012 it is 1,63 or 0,0525 kg/m^3. Values are exactly in the ratio 31,1 and J_ψ = 34,73 kgm^2 and J_φ = 1,12 kgm^2.

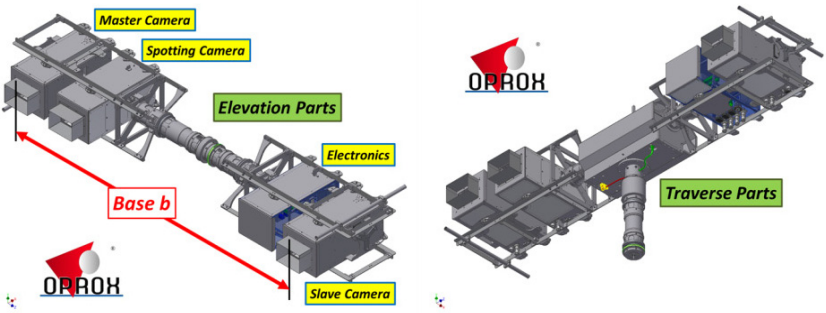

Fig. 2 Controlled Objects of the POERF model 2012. Elevations parts for the elevation motion ("tilting") and traverse parts for the traverse motion ("pan", "panning", "panoraming")

Without conducting any detailed analysis it is obvious that in situations when big angular accelerations of traverse motion are necessary, also big torques of the traverse motor are required.

Traditional camera manipulators have maximal/minimal elevation lower than ± 90°. Simultaneously they are usually required to have maximal traverse acceleration approximately twice higher than maximal elevation acceleration. If we applied the mentioned requirements on the design of traverse motor of the POERF, the designed motor would have an extreme rated torque.

At the same time we know that the maximal traverse acceleration is used with the traditional design of camera manipulators only in two situations that do not exceed 10% of operational time, but they still can not be neglected.

First situation appears while switching form the tracking of one target to tracking of another one. The highest requirements for maximal traverse acceleration arise when traverse angle between the two targets is just 180°. The maximal acceptable time for switch of aiming from one target to another is specified for such situation. For example it is specified that the switch of aiming must be shorter than 3 s or even only 1,5 s. Control proceeds in mode point-to-point with a given velocity-profile (ramp).

Next situation occurs for example while tracking of an aerial target with coming course. Tracking on approaching leg is terminated when maximal elevation is reached, then again traverse parts has to move into an angle of 180° (point-to-point control) and within minimal time. Only at that time it is possible to track on receding leg. Analysis of this situation is briefly presented in [4].

Mentioned problems can be eliminated or more precisely reduced in case the elevation is unrestricted. In practice, limits of elevation ±360° are sufficient. In this case special design of elevation parts needs to be used. One of the possible varieties has been patented by us [5] and used in a construction of model 2012 – Fig. 1, 2.

3 Design of POERF Elevation Parts

If the traverse motion is unrestricted, then the situations mentioned above are solved in the following way.

In the first situation the traverse angle does not change and the elevation angle changes within cc. 180° in accordance with angular height of the second target. By deeper analysis we ascertain that it is necessary to change the traverse angle maximally within ± 90°. I.e. in the given time for aiming to the second target we manage to work with the half value of maximal traverse acceleration.

In the second situation the target is tracked only in elevation with fluid pass over elevation +90°. Detailed analysis is presented in [4].

The very design of elevation parts with unrestricted elevation – Fig. 2. has to meet at least these three requirements:

1. protection of camera and lens in air-conditioned, dust and humidity-resistant space
2. sufficiently high flexural rigidity of the cameras beam
3. possibility to adjust cameras axes so that they will form a triangulation plane and a telemetric triangle in it – Fig. 3., i.e. the possibility to conduct cameras alignment (adjustment).

In order to meet the first requirement, box where the camera is placed has been used– Fig. 1, 2, 4.

For meeting the second requirement, cameras beam conception - (Pratt) truss has been utilized, whereas the function of web trusses (members) is fulfilled by sufficiently rigid and big camera boxes. As a result of this the elevation parts have a mass of only 57 kg.

Construction system enabling fulfilment of the third requirement was very complicated with 2009 model and working with it was very lengthy and not precise enough – Fig. 4 (in the left). Therefore for 2012 model different solution has been chosen – Fig. 4 (in the right).

Camera is mounted on its base – Fig. 4 (in the right). The base is adjustable, mounted by three adjustment screws in the box. The adjustment screw can be used

a) to set pixel rows of the CCD sensor of the camera parallel with the elevation axis. I.e. pixel rows of all cameras are parallel.

b) to set optical axis of each camera parallel with the triangulation plane in which the telemetric triangle lies – Fig. 3.

The box can be revolved around its vertical axis, so that

a) optical axes of master and spotting cameras are perpendicular to the elevation axis – Fig. 3, 4.

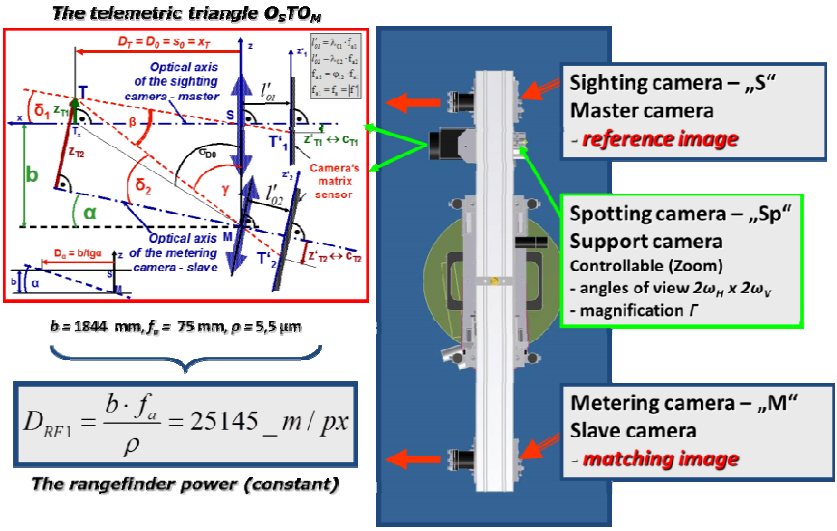

Fig. 3 Telemetric triangle a basis for the triangulation algorithms

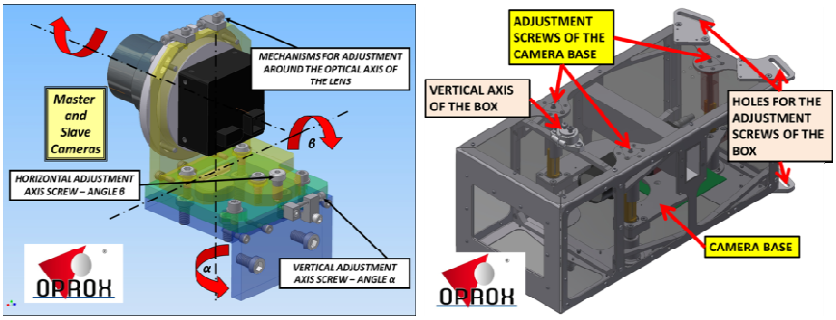

Fig. 4 Mechanisms for the adjustment of cameras to set the telemetric triangle

b) optical axis of the slave camera is deflected from its perpendicular position by a small angle of convergence α. This angle is cc. 1° for 2009 model and cc. 0,5° for 2012 model. Reasons are briefly clarified in [3].

All boxes are fixed in an adjusted position by adjustment screws – Fig. 4 (in the right).

4 Elevation and Traverse Servomechanisms

In Fig. 5 structure of elevation/traverse servomechanisms is illustrated. Considering the purpose of the article we will briefly deal only with requirements for characteristics of Controller 1, which result form the previous explanation in combination with limited stiffness of the transmission.

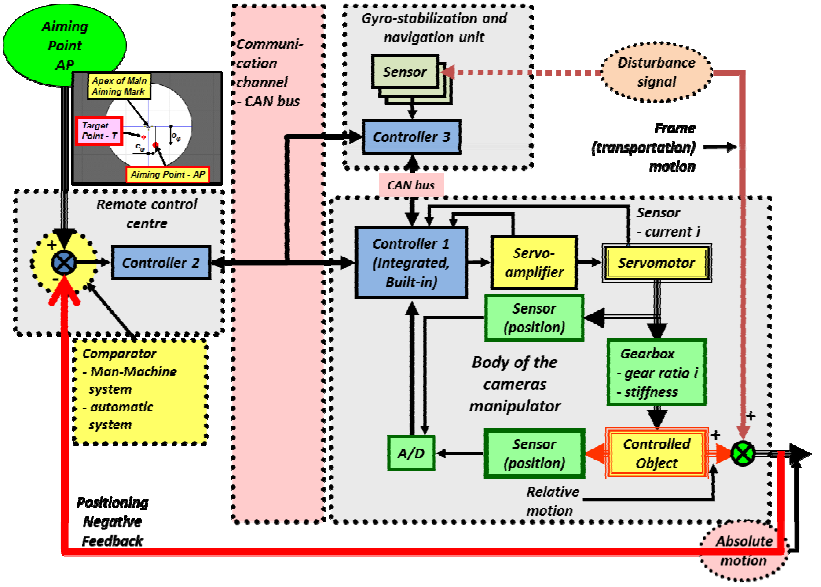

Fig. 5 Structure of the elevation/traverse servomechanisms

We have used DC motors by Maxon company namely for elevation or traverse servomechanism RE 35/90W or RE 65/250W.

We have chosen gear ratio 200. In the first stage there is a harmonic drive gearing (Harmonic Drive AG) with gear ratio 100 and in the second stage there is a belt drive (Gates Corp.) with indented belt and gear ratio 2.

In consequence of such choices relative values of the reduced moment of inertia on motor shaft for elevation or traverse servomechanisms are 5,8 or 7,8. Rated current for elevation or traverse motor is 0,92 A or 6,0 A, with corresponding rated demand electric power (U_R = 48 V) 44 W or 288 W. Next rated angular acceleration of controlled object is 14,0 or 3,6 rad/s^2 and rated angular velocity of controlled object 90°/s or 100°/s.

These data show that it seems we have managed to successfully solve the problems mentioned above. The reality is different though. Starting current for elevation or traverse motor is 4,16 A or 132,0 A, which starting demand electric power (U_R = 48 V) 200 W or 6340 W corresponds to.

Temporary current overload can be maximal cc. 5 times, therefore maximal current for elevation or traverse motor is limited to cc. 4,8 A or 30 A, which maximal demand electric power (U = 55 or 11 V) cc. 265 W or 330 W corresponds to. As it is obvious limitation of current basically applies only to traverse motor. Limiter of demand current has to form a part of SW controller 1.

POERF is a mobile system therefore its maximal demand electric power is strongly limited. Also 24 V electric sources are preferred. This leads to necessity to limit also the demand electric power. Overall demand electric power can be actually considered cc. 1 000 W; then division to cc. 250 W for elevation system

and cc. 750 W for traverse system is appropriate. The limiter of demand electric power thus has to be a part of controller 1 SW.

High demands on dynamic qualities of traverse system are due to high moment inertia and demands on point-to-point control while switching aiming from one target to another. They can not practically be achieved in demanded range considering the current and electric power limitation.

As stated in catalogues of harmonic and cycloid drive gearings, as well as of belt drives, these transmissions are known to have small torsion stiffness; therefore already with 2009 model two sensors of angular motion (position) were used. One sensor for motor shaft and the second for controlled object shaft. This enables measuring of torsion angle of transmission and sending particular feedback signal to controller 1. By the use of this sensor it is possible to eliminate the influence of friction of the transmission [7, 10] and influence of oscillation of the controlled object (Effects of flexible/elastic joints) [8, 9, 12].

Effects of flexible/elastic joints are extremely strong for the traverse system. I.e. according to the measurements made by I. Travnicek and V. Vaclavik (Oprox Inc.) on POERF model 2012 natural frequencies of the elevation or traverse controlled objects are 11,5 or 2,9 Hz and damping ratio is only cc. 0,02. Moreover according to measurement made on POERF model 2009 [11] also small torsion stiffness of the tripod is non-negligible.

As a result of the data presented above, model motor + transmission + controlled object used in controller 1 should have for elevation or traverse system 2 or 3 mechanical degrees of freedom (DOF).

5 Conclusions

We are currently working on further development of HW and SW of gyrostabilisation and navigation unit – Fig. 5 in cooperation with the Department of Measurement of the faculty of Electrical Engineering of CTU Prague and we are planning to newly design HW and SW controllers 1 including PWM amplifiers.

Acknowledgements. This work has originated under the support of financial means from the industrial research project of the Ministry of Industry and Trade of the Czech Republic – project code FR – TI 1/195: "Research and development of technologies for intelligent optical tracking systems" and financial means from the industrial research project of the Ministry of the Interior of the Czech Republic - project code VG20122015076: “Two survey points range-finding system utilization for perimeter security (screen)“.

References

[1] Balate, J.: Automatic Control, Praha, BEN, p. 664 (2004)

[2] Cech, V., Jevicky, J., Pancik, M.: Demonstration Model of Passive Optoelectronic Rangefinder. In: Brezina, T., Jablonski, R. (eds.) Proceedings of the 8th International Conference Mechatronics 2009 Recent Advances in Mechatronics 2008-2009, pp. 79–84. Springer, Heidelberg (2009)

[3] Cech, V., Jevicky, J.: Research and Development of the Passive Optoelectronic Rangefinder. In: Sergiyenko, O. (ed.) Optoelectronic Devices and Properties, ch. 16, pp. 323–348. InTech (2011), http://www.intech.org
[4] Cech, V., Jevicky, J.: Generator of Command Signals for Testing Servomechanisms of Pan and Tilt Devices. Engineering Mechanics – International Journal for Theoretical and Applied Mechanics 18(5/6), 331–340 (2011)
[5] Cech, V., Cervenka, M.: Patent CZ 3030559 B6. Passive Optoelectronic Rangefinder, Praha (Issued: October 24, 2012) (in Czech)
[6] Cech, V., Jevicky, J.: Effectiveness of Passive Optoelectronic and Laser Rangefinders. In: Wickert, M., Salk, M. (eds.) Proceedings of the 27th International Symposium on Ballistics, pp. 251–262 (2013)
[7] van Geffen, V.: A study of friction models and friction Compensation, DCT, 118 Technische Universiteit Eidhoven, p. 24 (2009)
[8] Moberg, S.: Modeling and Control of Flexible Manipulators, Dissertation No. 1349, p. 101. Linkoeping University (2010)
[9] Ozgoli, S., Taghirad, H.D.: A survey on the control of flexible joints robots. Asian J. of Control 8(4), 332–344 (2006)
[10] Virgala, I., Frankovsky, P., Kenderova, M.: Friction Effect Analysis of a DC Motor. Am. Journal of Mech. Eng. 1(1), 1–15 (2013)
[11] Vitek, R.: Measurement of the stereoscopic rangefinder beam angular velocity using the digital image processing method. In: 12th International Conference on Mathematical and Computational Methods in Science and Engineering (MACMESE 2010), pp. 230–235. WSEAS Press (2010)
[12] Zhang, Z., Hu, C.: Predictive Function Control of the Single-Link Manipulator with Flexible Joint. In: Altinay, M. (ed.) Application of Nonlinear Control, pp. 129–146. InTech (2012), http://www.intech.org

Energy Management System Algorithms for the Electric Vehicle Applications

J. Danko[1], L. Magdolen[1], M. Masaryk[1], J. Madaras[2], and M. Bugar[2]

[1] Slovak University of Technology, Faculty of Mechanical Engineering, Nam. Slobody 17, 812 31 Bratislava, Slovak Republic
jan.danko@stuba.sk
[2] Slovak University of Technology, Faculty of Electrical Engineering, Ilkovicova 3, 812 19 Bratislava, Slovak Republic
juraj.madaras@stuba.sk

Abstract. The paper presents methodology for design and application of energy management system for the hybrid energy system of the electric vehicle and its operational, critical states and processes. Energy control management of the electric vehicle's hybrid energy system is presented in introduction. Next chapter deals with mathematical analysis of the discharging and charging of the hybrid energy system. Simulation results for the proposed hybrid energy system are obtained using MATLAB/Simulink. Results confirm that the proposed control system of the energy management system is effective for the wide spectrum of the processes control in the electric vehicle application.

1 Introduction

The power management of the electric vehicle's hybrid energy system contains two main elements:

- First, when power is demanded from the energy storage system, the control strategy must determine how many power (current) can be delivered from the battery system and how many can be delivered from the supercapacitor system during the dynamic loading process.
- Second, the control strategy must determine when and how fast the traction system should charge the supercapacitor system.

2 Energy Control Management of the Electric Vehicle's Hybrid Energy System

A complete control strategy consists of a power flow management strategy and algorithms for battery system and the supercapacitor management strategy in terms of safety and dependability of the electric vehicle's traction system.

T. Březina and R. Jabloński (eds.), *Mechatronics 2013*,
DOI: 10.1007/978-3-319-02294-9_4,

To control the energy stored in supercapacitor system, it is needed that the voltage of the supercapacitor system should be controlled. If not, the upercapacitor voltage depends on the battery voltage, so there is no possibility to control the energy stored in supercapacitor system, [1].

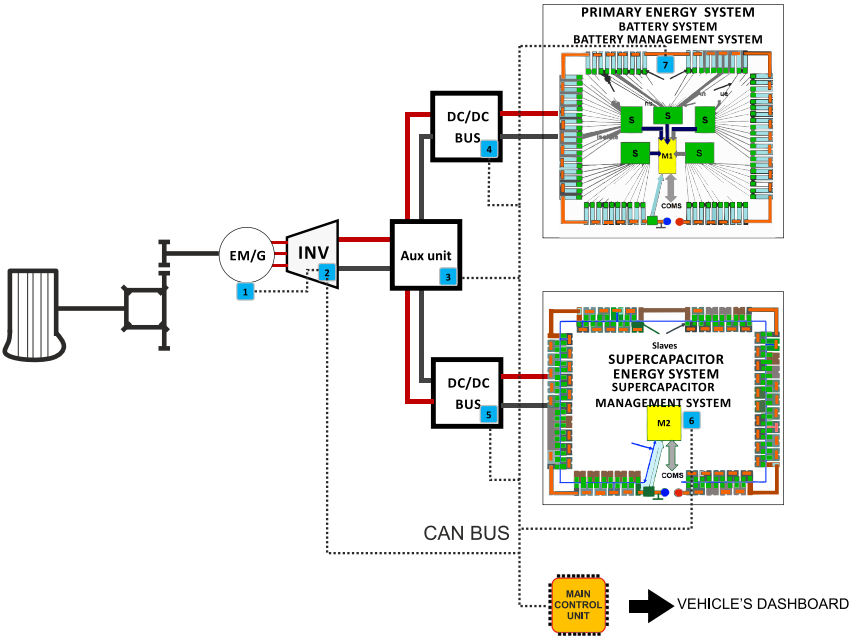

Fig. 1 Traction, hybrid energy, information and communication systems with sensor subsystem implemented to the electric vehicle

Bi-directional DC/DC converter is required for the voltage level regulation. Fig.1 shows the system configuration with battery system and supercapacitor system as hybrid energy storage also a control system and subsystem which controls the operational processes in electric vehicle system. Electric vehicle generally contain these main systems:

1. Traction system:
   - Traction electric motor/generator
   - Invertor (control power units)
   - Auxiliary unit (auxiliary unit with fuse box)
   - DC/DC Bus (power circuit with power relays)
2. Energy system:
   - Primary energy system (rechargeable battery system)
   - Secondary energy system (supercapacitor system)
3. Energy management system:
   - Embedded control system (battery management system - BMS and supercapacitor management system - SMS)
   - Main control system (Control unit processes data from embedded system and communicates with control systems of the electric vehicle)

3 Mathematical Analysis of the Discharging and Charging of the Hybrid Energy System

Part of the energy control management is based on the primary energy source that, a rechargeable battery system is. Rechargeable battery system provides a stable supply of energy and power during the dynamic movement of the electric vehicle. Supercapacitor system is a secondary electric source, which is designed to power supply the electric traction system.

The proposed control algorithm has implemented limit values of the control parameters. These parameters will be applied for the connecting of the each energy system (battery system, supercapacitor system) to the traction system, [4].

The energy requirement during dynamic loading is expressed by the equation:

$$E_{net} = \left[\int_{t=0}^{t=n} (P_{discharg\ batt} + P_{discharg\ sc})dt + \int_{t=0}^{t=n} (P_{charg\ batt} + + P_{charg\ sc})dt \right] \quad (1)$$

Where: E_{net} - energy required / generated by electric traction system, $P_{discharg\ batt}$ - required power from rechargeable battery systems for the traction system, $P_{discharg\ sc}$ - the required power from supercapacitor system for traction system, $P_{charg\ sc}$ - regenerative power, power delivering to the supercapacitor system from traction system during regenerative braking, $P_{charg\ batt}$ – regenerative power, power delivering to the rechargeable battery system from traction system during regenerative braking, t – time step, n-total time of the vehicle movement

Via equation (1), the main algorithm for hybrid energy sources management designed is. Main control algorithm of the hybrid energy sources task is to define, when the hybrid electric energy system will be used for demanded power (current) delivered into the electric traction propulsion system. Designed control algorithm of the hybrid energy management on the Fig. 2 shown is.

In the control algorithm the variable parameter (I_{limit}) implemented is. The variable parameter is the decision parameter for controlling the energy requirements and control energy delivering from specific energy source in the critical states.

This algorithm principle defines, that the required output current and the output power of the traction electric motor/generator for this case equivalent values is.

The proposed control algorithm with the control units is complex decision control system that manages the hybrid electric system. The control management is based on the conditions described by the equation (2) and equation (3) the control algorithm operates simultaneously with the equation (1). If the conditions are accepted, the power distribution system (DC/DC bus) will be connected to the supercapacitor system. If the conditions are not accepted, the power distribution system (DC/DC bus) will be connected to the rechargeable battery system.

$$I_{MOTOR}(A) > I_{LIMIT}(A) \quad (2)$$

$$E_{net}\ (P_{MOTOR})(kW) > P_{LIMIT}\ (kW) \tag{3}$$

Where: I_{MOTOR} - requirement of the current or generating of the current by electric power traction system, I_{LIMIT}- set the value of the limit parameter required for power distribution systems during discharging battery energy system, E_{net} – energy requirement (or generating) by electric power traction system, P_{motor} - Required (or generating) traction power, P_{lim} - limit value for required (or generating) power flow distribution performance of the energy system.

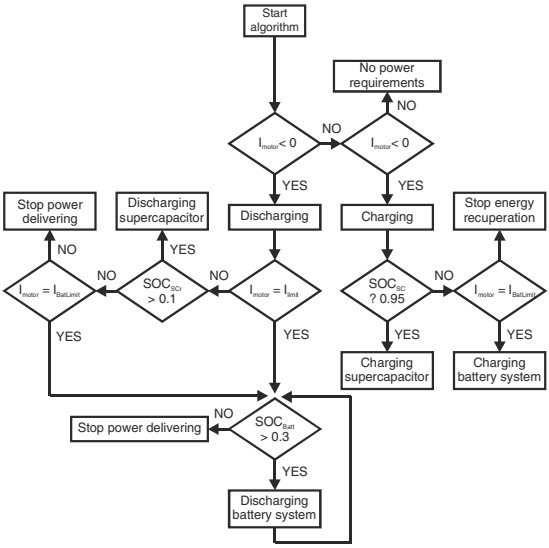

Fig. 2 Block diagram of the designed energy management system operational algorithm during discharging

For the dynamic simulation analysis of the electric vehicle, the value I_{lim} can be modified and set for next optimization options. By defining the parameters of the rechargeable battery system sufficient is. Supercapacitor system can be connected to the energy circuit and the traction system at the starting electric current requirement, until its falls to lower limit value of the state of charge.

3.1 Energy Management Control Algorithm Implemented for the Energy Management System of the Electric Vehicle Application

Energy management algorithm of the control unit for the current (power) control (redirecting), when electric motor /generator works in the electric motoring mode or the electric motor works in the generating mode [6].

```
function [Ich,Idis]= splitter1(Imot)
if Imot > 0
   Ich = Imot;
   Idis = 0;
elseif Imot < 0
   Ich = 0;
   Idis = Imot;
else
  Ich = 0;
  Idis = 0;
end
```

On the next can be seen an algorithm of the control unit for discharging current management between the battery system and supercapacitor system, with limit control management for discharging current of the battery system.

```
function [Isc,Ibatt]= splitter2(Idis,I_limit)
if abs(Idis) <= I_limit
   Iaku = Idis;
   Isc = 0;
else
   Ibatt= - I_limit;
   Isc = Idis + I_limit;
end
```

On the next can be seen an algorithm of the control unit for the management of the discharging current. When state of charge of the supercapacitor is 0% and then the battery system discharging is.

```
function [Iscout,Idisbatt] = splitter3(Isc,SOCsc)
if SOCsc > 0.10
  Iscout = Isc;
  Idisbatt = 0;
else
  Iscout = 0;
  Idisbatt= Isc;
end
```

On the next can be seen an algorithm of the control unit for control management of the regenerative current, which can be redirected to the rechargeable battery system if state of charge of the supercapacitor system, will be 95%.

```
function [Isccharingout,Ichargingbatt] = splitter4(Ich,SOCsc)
if SOCsc < 0.95
  Isccharingout = Ich;
  Ichargingbatt = 0;
else
   Isccharingout = 0;
   Ichargingbatt = Ich;
end
```

On the next can be seen an algorithm of the control unit for limit value of the battery charging current.

```
function Charging_current_batt = splitter(Ichargingbatt,Max_charge_batt)
if Ichargingbatt <= Max_charge_batt
        Charging_current_batt = Ichargingbatt;
else
        Charging_current_batt = Max_charge_batt;
end
```

4 Case Study and the Simulation Results

Simulation results for the proposed hybrid energy system are obtained using MATLAB/Simulink and SimPowerSystems based software packages by implementing the detailed mathematical and electrical models of the main components of the electric vehicle, [2], [3]. For simulating and searching operational and critical states of the hybrid energy system of the electric vehicle was chosen representative drive cycle, [5].

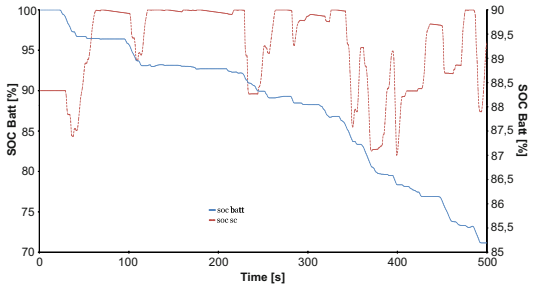

Fig. 3 Time response of the battery system and supercapacitor system state of charge

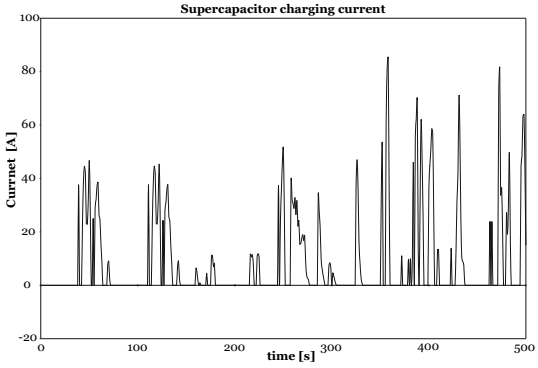

Fig. 4 Time response of the recuperated supercapacitor current of the electric motor/ generator during simulation

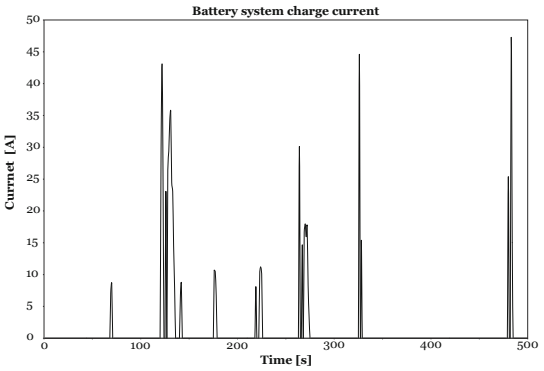

Fig. 5 Time response of the recuperated battery current of the electric motor/generator during simulation

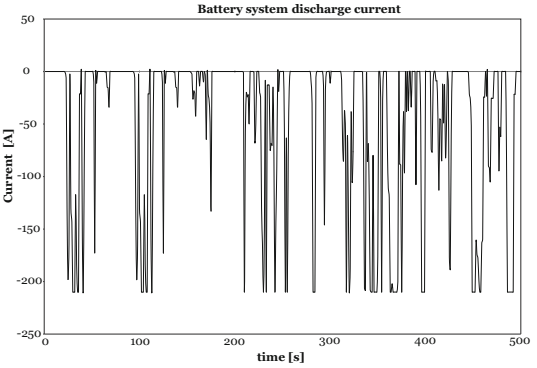

Fig. 6 Time response of the battery discharge current of the electric motor/generator during simulation

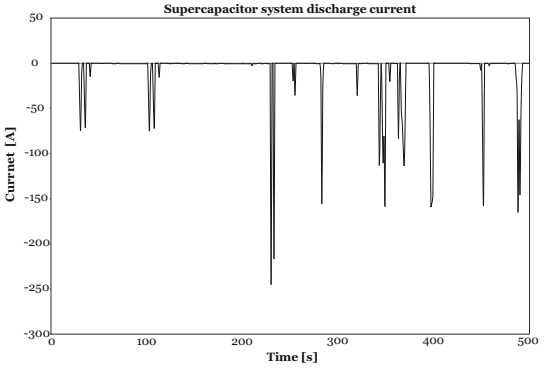

Fig. 7 Time response of the supercapacitor discharge current of the electric motor/generator during simulation

5 Conclusion

The electric vehicle contains systems that require electric energy. Electric energy requirements of the electric vehicle is a complex dynamic system with time-dynamic loads. Electric energy system of the electric vehicle should be providing power supplying during dynamic loading.

During the dynamic loads of the energy systems also occurring operation states, when these systems demanded an extreme value of the current (power). For this reason it is appropriate to apply a hybrid energy system that from a rechargeable battery system and supercapacitor system created is. These two systems are reversible energy sources. Based on the results of the simulations of hybrid energy system (Fig. 3 - 7) during the dynamic loads, the critical conditions during operation of electric vehicle detected are. Energy management system of the hybrid electric system has been designed, implemented and tested for electric vehicle by uses of computer simulations. Computer simulations of a electric vehicle hybrid energy system reveal reliable results of the proposed system in terms of energy saving and operational states. The proposed control algorithm and methodology allow an improvement of the function in a basic operational processes and states with decreasing of the performances of the propulsion system but increasing energy saving of the hybrid energy system.

The designed methodology and the case study results confirm that the proposed control system of the energy management system is effective for the wide spectrum of the processes control in the electric vehicle application.

Acknowledgments. This work was supported by the Scientific Grant Agency (VEGA) of Ministry of Education of Slovak Republic, grant no. 1/0178/12.

References

[1] Bijami, E., Askari, J., Hoseeinnia, S.: Power System Stabilization Using Model Predictive Control Based on Imperialist Competitive Algorithm. International Journal on Technical and Physical Problems of Engineering 3(4), 45–51 (2011)

[2] Jančo, R.: FEM in solution of beams and frames on elastic foudation, 1st edn. STU in Bratislava, Bratislava (2013)

[3] Écsi, L., Élesztös, P.: Moving toward a more realistic material model of a ductile material with failure mode transition. Materialwissenschaft und Werkstofftechnik 43(5), 379–387 (2012)

[4] Horvát, F., Hučko, B., Čekan, M., Šoltés, L.: Experimental Device for Determining Deviations in the Thoracolumbar Part of the Human Back. Scientific Proceedings Faculty of Mechanical Engineering STU Bratislava 20, 85–91 (2012)

[5] Tomoiagă, B., Chindriş, M., Sumper, A., Sudria-Andreu, A., Villafafila-Robles, R.: Pareto Optimal Reconfiguration of Power Distribution Systems Using a Genetic Algorithm Based on NSGA-II. Energies 6, 1439–1455 (2013)

[6] Janáková, H.: Creative management and innovation. Creative and Knowledge Society: International Scientific Journal 1, 95–112 (2012) ISSN 1338-4465

Virtual Commissioning of Mechatronic Systems with the Use of Simulation

J. Hloska[1] and M. Kubín[2]

[1] Brno University of Technology, Faculty of Mechanical Engineering, Technicka 2, 616 69, Brno, Czech Republic
yhlosk00@stud.fme.vutbr.cz
[2] Mendel University in Brno, Faculty of Agronomy, Zemedelska 1, 613 00, Brno, Czech Republic
martin.kubin@mendelu.cz

Abstract. This paper presents an approach by which it is possible to use standard software for simulation of a material flow for conducting tests of mechatronics, such as sensors, actors, PLCs or even a MFC. Applying simulation for testing responses of mechatronic systems, which might even be still under development, is also known as emulation and it is a modern way how to carry out virtual commissioning. First, current base of knowledge and related research is presented. Next, technological background of the presented solution is discussed together with its main logical and technical challenges. Finally, laboratory experiments conducted with an overhead crane interconnected with a simulation model are shown and direction of further research is outlined.

1 Introduction

Simulation can be generally understood as a part of a concept called digital factory. As such, simulation can be defined as „imitation of a dynamic process within a system with the use of a model that allows for experiments in order to gain information that can be transferred into a real system.“ [1] Simulation of a material flow is a specific part of general simulation which deals not only with flow of (countable/ discrete or continuous) material through a production, network or logistics system. Tools for material flow simulation enable more kinds of experiments to be carried out. In recent years, great emphasis has been put on virtual commissioning, especially in relation with its economic application. [2] Virtual commissioning is the way how to test and optimize products of mechanical engineering (mostly mechatronic components such as sensors, motors and other actors), control software (MFC or PLC) or logistic and transport systems [3] or even complex production systems (if certain standardization is implemented [4]) well in advance, i.e. before the real SOP (start of production) or start of operation.

1.1 Virtual Commissioning vs. Software Tests

It is important to stress that virtual commissioning cannot be seen as a substitute of or confused with software tests. Software tests are usually carried out by the

T. Březina and R. Jabloński (eds.), *Mechatronics 2013*,
DOI: 10.1007/978-3-319-02294-9_5,

same engineer who develops the software and therefore they tend to lead to badly structured programming codes which are not transparent for a third party due to various debugs and workarounds. This especially applies for software updates and extension of the functionality of the respective software. Moreover, during software tests it is not possible to incorporate the behaviour of the controlled system in relation to response time of the mechatronics and to reflect its stochastic nature, which in a real system is almost always to be count with. The most important advantages of virtual commissioning are listed below. [5]

- Shortening of the process of SOP.
- Possibility to carry out part of the SOP in more convenient environment (not necessarily on site) combined with the opportunity to use the emulation model for training of workers.
- Parallel development and optimization of mechanical parts, especially mechatronic mechanisms.
- Simultaneous programming and debugging of the control software (of MFC or individual PLCs).

1.2 Virtual Commissioning Using Material Flow Simulation

Very often virtual commissioning concerns a mechatronic system which is only a part of a more complex mechanical system (e.g. conveyor system, production line with robots, etc.). These mechanical systems which are designed to control and direct a flow of material (palettes, assembly parts, luggage...) are usually also tested and optimised by a simulation model. Therefore there is a potential to use an existing (valid) simulation model of the particular mechanical system not only for optimization of a material flow (and of utilisation of elements of the system – machines and stations) which are mostly the main objectives of the simulation, but also for virtual commissioning of its mechatronic parts or of the MFS and/or PLCs which should control its proper function. To sum this up, virtual commissioning is becoming an integral part of development and simulation of a MFC or PLCs and related mechatronic parts. Shortening of duration of planning and development of a (production) system as the main advantage of virtual commissioning (see the previous section) is depicted in more detail in Fig. 1.

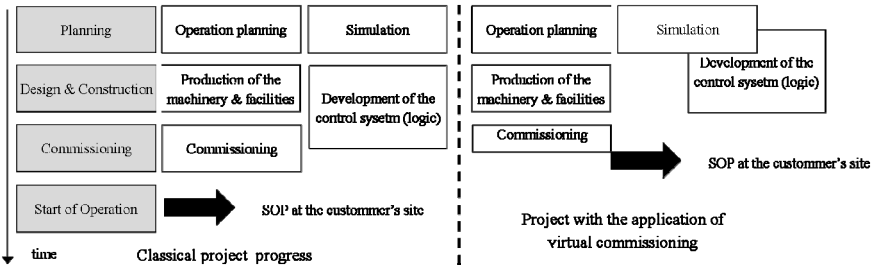

Fig. 1 Advantage of virtual commissioning with respect to project duration [5]

Using a simulation model, which, to certain extend, substitutes a real (control) system, in the sense that the simulation model receives and/or sends signals instead of that real (control) system, corresponds with the definition of emulation. Generally, emulation can be really defined as imitation of a system (here a MFC, PLC or other control system) by another system (in this case a simulation model), or more succinctly as "the process of exactly imitating a real system". [6]

Technical aspects which set conditions for the virtual commissioning by the use of a material flow simulation model are as follows [6, 7]:

- Synchronising of a real clock time between the PLC (and any other kind of physically existing control logic) and the simulation model, which is inherently discrete event oriented.
- Standardisation concerning the interface between the simulation software and the control logic (PLC). Generally, great simplification in this respect has been achieved thanks to OPC (OLE for Process Control). Currently, interfaces between the simulation software Plant Simulation and the Siemens protocols S5, S7 or PCS7 are applicable in praxis.
- Additional switch has to be implemented in the real (physically existing) control logic. This has to enable switching between the physical machine (sensor, actor) and the model.

Basically, three kinds of application of a simulation can be distinguished in dependence on the integration level of the simulation within the control software development and testing. This shows fig. 2 [5]

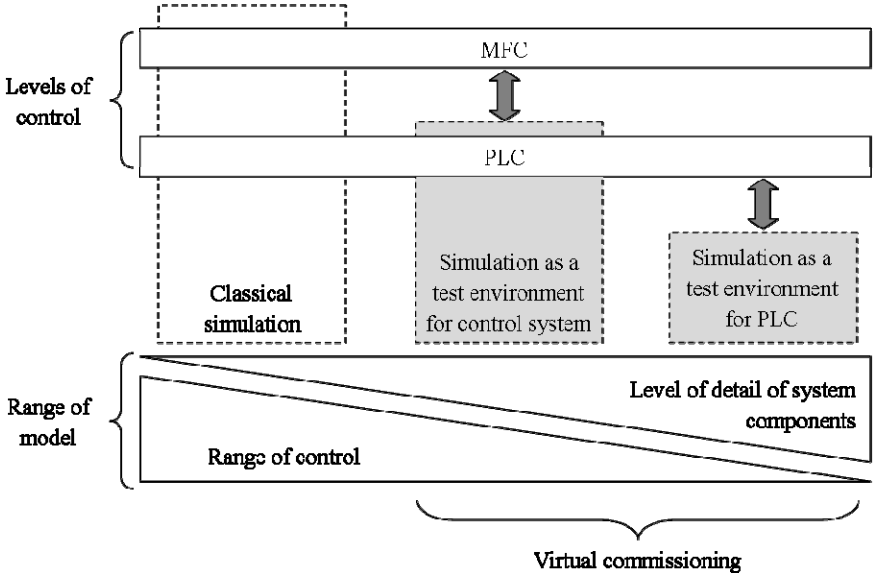

Fig. 2 Levels of integration between a simulation model and system control [5]

In case of a connection of the simulation model with a MFC the actions, which are attributed to the MFC, are also carried out by the MFC, i.e. the respective logic is not implemented in the simulation model. In this case, the simulation model merely sends and receives signals to or from the MFC. Technical problem to be solved here is to guarantee the correct communication via the industrial protocols.

Should the simulation model be used for tests of a PLC, it requires then a more detailed modelling. The reason is the necessity to transform all signals including single-bit signals (such as "on/off") into the simulation model and vice versa. The model also has to include elements which represent all the sensors and actors of the particular mechatronic system.

2 Proposed Methodology of Emulation

In this part a methodology of emulation which can be applied for the purpose of virtual commissioning in practice, is proposed. Several aspects had to be taken into account. With regard to the practical use of the proposed methodology, a major role played the choice of simulation software and communication interfaces. As in case of other similar studies, the possibility to model complex control structures with clear boundaries between the model itself and layers attributed to the PLC, and open architecture of the software, were decisive. [8]

As a subject of the simulation model a portal crane was chosen which was built within the project FRVŠ G1 3152/2011 – „Use of modern three-axes sensors and automatic control in the subject Applied Mechanics". The crane was equipped with capacitive accelerometers and angular velocity sensors 6D MEMS (three-axes accelerometer MEMS and three-axes gyroscope with integrated temperature sensor). All measurements carried out with the crane were registered in a format shown in fig. 3. The format of the data corresponds to with the two's complement, therefore the readings 0 and 255 both represent acceleration with an absolute value close to zero (0 m/s^2). The data could be also recorded on a microSD card. [8]

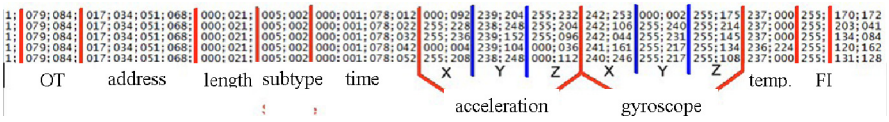

Fig. 3 Bit format of the recordings of the crane movements [9]

The crane was emulated by a simulation model where the movement of the cat of the crane is limited by a rectangular layout of scalable dimensions, while the lifting crane can also be arbitrarily adjustable. Apart from the part for communication between the simulation model and the physical control of the real crane the model has two other levels. The upper level contains event controller which enables the user to control the simulation run. Here the user can also observe the simulated movement of the crane (more precisely, the 2D movement of the cat across the x and y coordinates and numerical expression of the current z coordinate), together with

information concerning the action which is currently being carried out by the crane. This level, which can thus be seen as a control (quasi PLC) system of the crane, is shown in fig. 4.

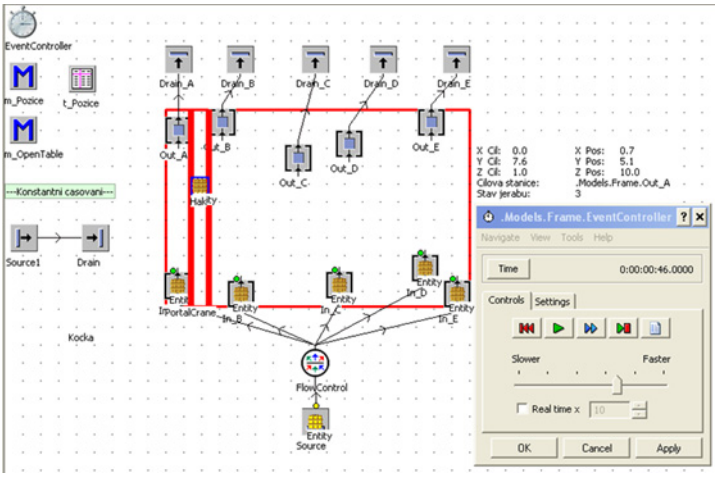

Fig. 4 Upper level of the simulation model of the crane

The lower level contains elements which simulate the actual movement of the crane and the transported material. In addition, range of the motion of the crane as well as dimensions in all three axes in a Cartesian coordinate system can be set here together with the size of acceleration and velocity vectors separately for loaded and free crane in x, y, and z direction. Next, positions (coordinates) of material supply points and targets can be adjusted. Finally a strategy can be chosen which determines the priority of serving the supply points and supplying the targets as well as the trajectory of the motion of the crane. The lower level is shown in fig. 5.

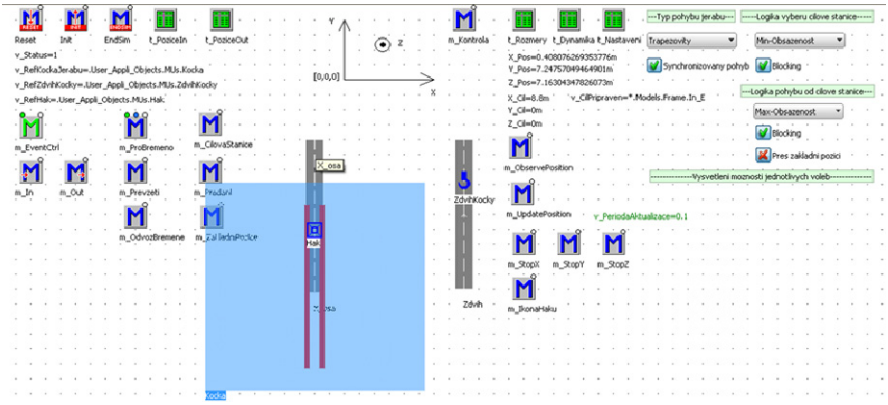

Fig. 5 Lower level of the simulation model of the crane with elements for model setting

As far as the communication between the simulation model and the control of the crane via industrial telegrams concerns, a solution similar to the one implemented in practice by the company iSILOG GmbH was applied. Also in this case the core is an adaptive definition of the communication protocols, both in MS Excel and in the simulation software Plant Simulation. In the individual tables the telegram system, headers of the telegrams and their definition had to be inserted.

Definition of the telegram system has to contain information whether the local application is server or client, IP-address of the server, port number of the connection and further information depending whether the telegrams are received or sent. Above all, time out has to be defined to alarm the user in case of interrupted communication (after the time out during which no signal was received the communication is considered disrupted).

Header of each telegram has to be defined, too. In the respective table name of each contained attribute, its data type and length (in bytes) have to be predefined. These tables together with the interface in the simulation model for defining and management of the protocol communication can be seen in fig. 6.

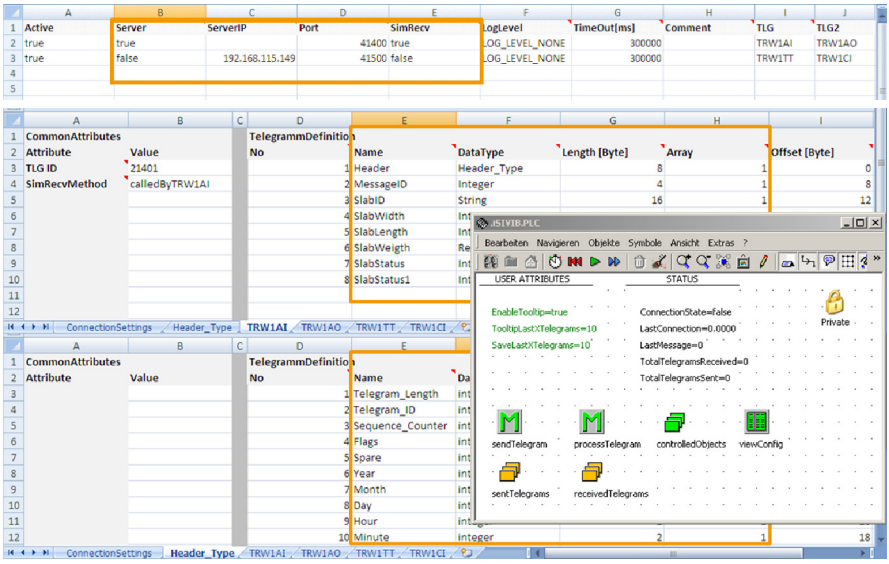

Fig. 6 Definition tables for protocol communication and interface in the simulation model

To the present time initial laboratory experiments were carried out. The purpose of these experiments was to check the function of all sensors and verification of the applicability of the MEMS technology in the field of crane technology. Example results are time dependences of accelerations in all three directions. Illustrative graphs are shown in fig. 6. Future research will be now focused on further measurements and comparison of their results with outputs of the simulation model.

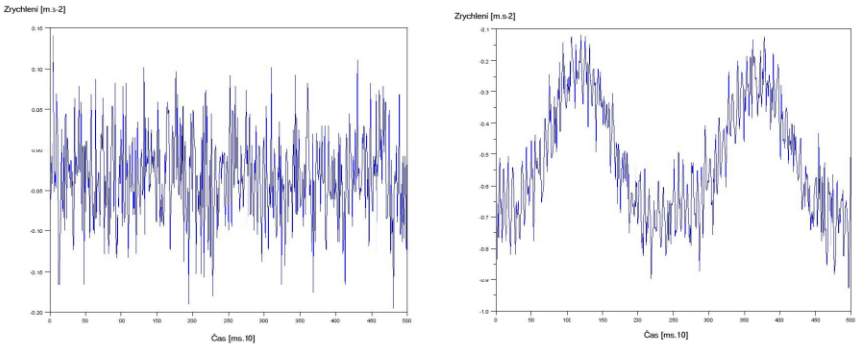

Fig. 7 Time dependence of x-axes acceleration (left) and z-axes acceleration (right)

3 Conclusions

Virtual commissioning is a modern way of conducting SOP test of various mechatronic systems. A vital part is played by simulation. A material flow simulation model can emulate a real system and part of its logic control. Virtual commissioning offers many advantages, thought there are still technical challenges to be resolved. These technical aspects are discussed in the paper.

Laboratory experiments were conducted in order to verify the suitability of interconnection of an overhead crane with a simulation model. The overhead crane was equipped with dynamic sensors and first measurements were carried out. Simultaneously a simulation model of the crane was built and interface for protocol communication between the model and the crane control was established.

Acknowledgments. The published results have been achieved with the help of the project No. FSI-J-13-2091 granted by specific university research of Brno University of Technology.

References

[1] VDI-Richtlinie 3633, Blatt 1 (2008)
[2] Reinhart, G., Wünsch, G.: Economic application of virtual commissioning to mechatronic production systems. Production Engineering, 371–379 (2007)
[3] Versteegt, C., Verbraeck, A.: The extended use of simulation in evaluating real-time control systems of AGVs and automated material handling systems. In: Proceedings of the 2002 SWC, pp. 1659–1666 (2002)
[4] Hoffmann, P., Maskoud, T.: Virtual commissioning of manufacturing systems: a review and new approaches for simplification. In: Proceedings of the 24th European Conference on Modeling and Simulation, pp. 175–181 (2010)
[5] Strigl, S.: Materialflusssimulation zur schnellen Inbetriebnahme realer Steuerungen. ZWF – Zeitschrift für wirtschlaftlichen Fabrikbetrieb 01-02, 76–80 (2009)

[6] Mayer, G., Burges, U.: Virtuelle Inbetriebnahme von Produktionssteuerungssystemen in der Automobilindustrie mittels Emulation. In: ASIM 2006 (2006)
[7] LeBaron, T., Thompson, K.: Emluation of a material delivery system. In: Proceedings of the 1998 WSC, pp. 1055–1060 (1998)
[8] Versteegt, C., Verbraeck, A.: The extended use of simulation in evaluating real-time control system of AVGS and automated material handling systems. In: Proceedings of the 2002 WSC, pp. 1659–1666 (2002)
[9] Kubín, M.: Laboratorní ověření dynamiky břemene mostového jeřábu. In: XXXVIII. mezinárodní konference dopravních, manipulačních, stavebních a zemědělských strojů. Plzeň: Západočeská univerzita v Plzni, pp. 107–110 (2012) ISBN 978-80-261-0141-3

Prediction of Machining Accuracy for Vertical Lathes

M. Holub[1], M. Michalíček[1], J. Vetiška[1], and J. Marek[2]

[1] Brno University of Technology, Faculty of Mechanical Engineering, Technicka 2, 616 69, Brno, Czech Republic
holub@fme.vutbr.cz
[2] TOSHULIN, a.s., Wolkerova 845, Hulín, 768 24, Czech Republic

Abstract. This article proposes the methodology allowing a prediction of geometric and working accuracy of large CNC machines tools (MT). The presented approach to behavior predicting is applied to kinematics of vertical lathe with an emphasis on different machining conditions. The resultant deflections of a tool and workpiece (WP) are described within the entire workspace of the machine tool with a simulation of different working conditions, whereby it is possible to effectively use the workspace in terms of working accuracy (WA). The results of the presented methodology can be used for selection of the appropriate type of machine tool and machining technology as early as in the tendering stage. This reduces the time required to select and submit a machine tool quotation. The proposed methodology for predicting the geometry and WA has been verified on a vertical lathe (VL) produced by the company TOSHULIN a.s.

1 Introduction

This article deals with the development of methodology allowing a prediction of geometric and working accuracy of vertical lathes, type SKIQ30, produced by TOSHULIN a.s. For prediction of behavior, a maximum amount of data obtained from the reception tests according to ISO standards should be primarily used; these tests are routinely performed in manufacturing companies. The tests concerned are essentially basic tests according to ISO 230-(2, 4), ISO 3655 P1 and P3, which are jointly carried out within the reception of vertical lathes. For kinematics of a vertical lathe, appropriate tools were selected to identify the geometric and working accuracy to the fullest possible extent of workspace. On the basis of the obtained data, a methodology for measuring and processing of data is proposed for a particular type of MT and its kinematics; this leads to the prediction of geometric and working accuracy of a MT.

Accuracy of MT is an important aspect for reliable and cost-effective production. With increasing requirements on production quality in aerospace, automotive and power industries, high demands are laid on the producers of MT. These requirements include both working and geometric accuracy of a MT. A check-up of

T. Březina and R. Jabloński (eds.), *Mechatronics 2013*,
DOI: 10.1007/978-3-319-02294-9_6,

the machine parameters is more and more often carried out according to customer's requirements, even with software compensations of the MT being turned off. Here, in principal extent, the occurrence can be traced of errors caused by inaccuracies in the production of individual parts, their assembly, and thermal dilatation; with large MT it is also the occurrence of elastic deformation resulting from moving parts. To verify the respective accuracy, tests are performed on all manufactured machines according to the standards ISO 230-(2, 4), ISO 3655 P1 and P3, and also on a particular piece given by the customer. Tests are carried out according to the standards with a given structure of record of measured values. These are coherent and easily controllable parameters that can further be effectively used as a feedback for a design office.

Increasing the geometric and working accuracy of MT is a challenging process involving changes in designing and manufacturing of individual components, their assembly and inspection of MT. The whole process is time-consuming and very costly, and therefore methodologies are sought to minimize time and financial demands while maintaining the trend of increasing the geometric and working accuracy.

Geometric errors are the main part of inaccuracies of MT [1], along with the error caused by the cutting forces they represent an increase in inaccuracy of the final WP. A classification of errors incurred on the MT is given by Ramesh et al. [2], where the individual components of error are described in greater detail. These components include geometric errors, kinematic errors, errors excited by heat influence, errors caused by instability of material, errors caused by cutting forces during machining, etc.

Based on the description of errors of three-axis and multi-axis machines, a number of compensation methods are built; these methods are based on different measurement strategies. One of the recent approaches to compensation is the use of so-called volumetric compensation enabled by the latest series of control systems. Measurement strategy for determining the parameters of volumetric compensation is dealt with in the publication by Aguado [3], where a measuring instrument called Laser Tracker was used. Other publications [4] are devoted to the calibration of multi-axis machine tools, where a measuring instrument Laser tracer was used to measure the volumetric accuracy of the MT. On the basis of the use of the above instruments, a methodology has been proposed to describe the errors in the workspace of the MT, which then lead to the prediction of geometric and working accuracy of VL type SKIQ.

2 Volumetric Error of Vertical Lathe

Vertical lathes are mainly used for machining of large cylindrical parts according to various requirements on both the machining technology and the resultant geometric accuracy of the WP. When considering all the errors involved in the final accuracy of WP, it is necessary to take into account that this is a very demanding

process of identification of the resultant deflection of the tool from the WP. A chart of vertical lathe SKIQ30 with the test WP according to ISO 3655 P1 is illustrated in Fig.1.

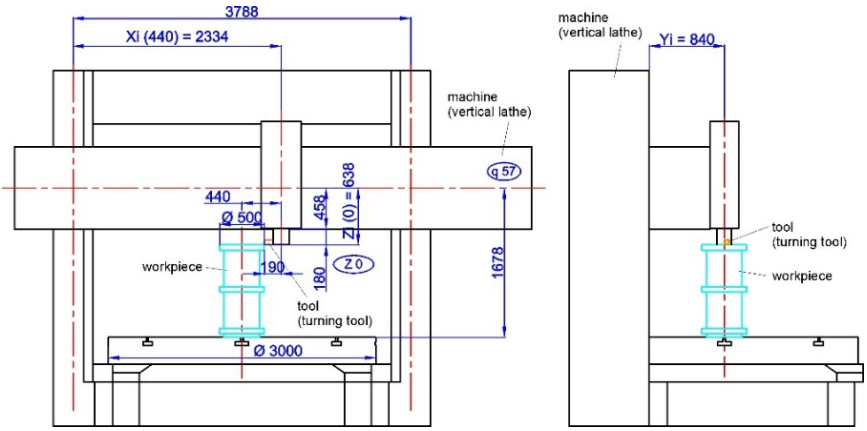

Fig. 1 Vertical lathe SKIQ30, TOSHULIN, a.s. with workpiece ISO 3655 P1

A total volumetric error is affected by a variety of factors shown in Fig.2. The main share of error in the resultant volumetric accuracy is due to the geometric error, thermal error, error caused by cutting forces and error resulting from WP clamping. With the machine SIKQ30, maximum load of clamping plates is 30,000 kg and maximum load of cutting forces is 40,000 N; this demonstrates a large range of machining conditions.

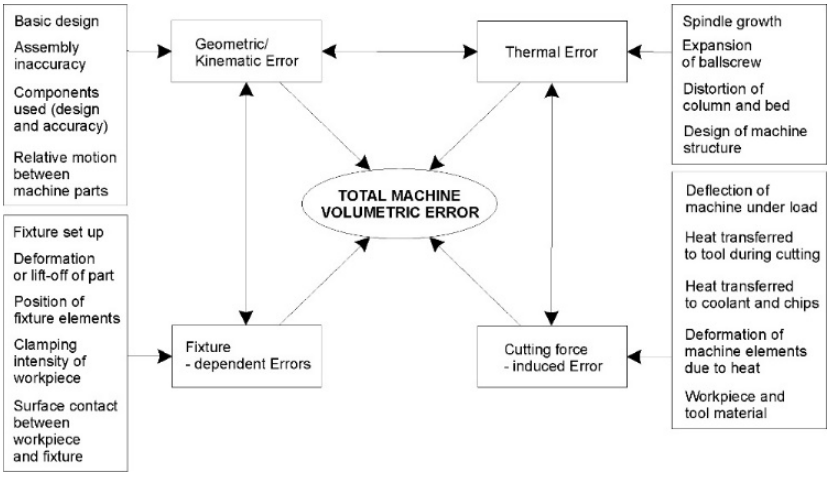

Fig. 2 Overview of the error budget in a machine tool and the factors affecting it [2]

2.1 *Identification of Geometric and Kinematic Errors on VL*

Standardized ongoing tests according to ISO enable us to identify errors e.g. EXX, EHR, EZX, XWZ, EZC, EXC, EYC, etc. In order to identify the necessary machine errors, the machine was divided into two parts. The first part identifies deflections of the tool from the ideal position for translational motion in the workspace. To determine the deflections in the respective working point of the machine DX, DY, DZ with defined travels of controlled axes OS X, Z, Z1, a measuring method was constructed as seen in Fig.3.

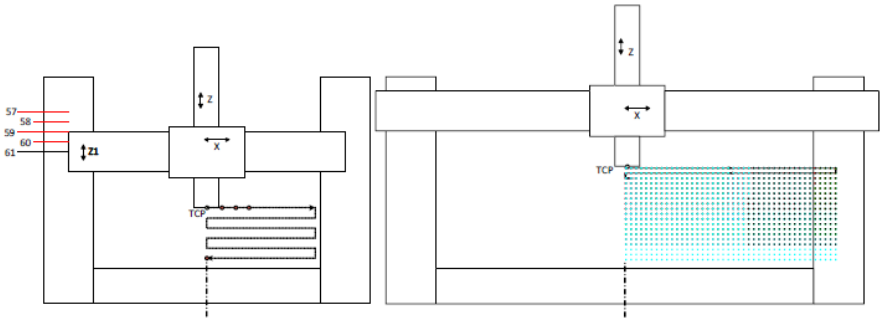

Fig. 3 Identification of errors caused by linear travels of VL

To measure the respective errors of machine translational axes, the following instruments were used: Laser Tracker, TRACEKR3, API and laser interferometer, Renishaw. Measurement results were processed according to the requirements on the individual deflections depending on the position in the workspace. A sample measurement and measured data are shown in Fig.4.

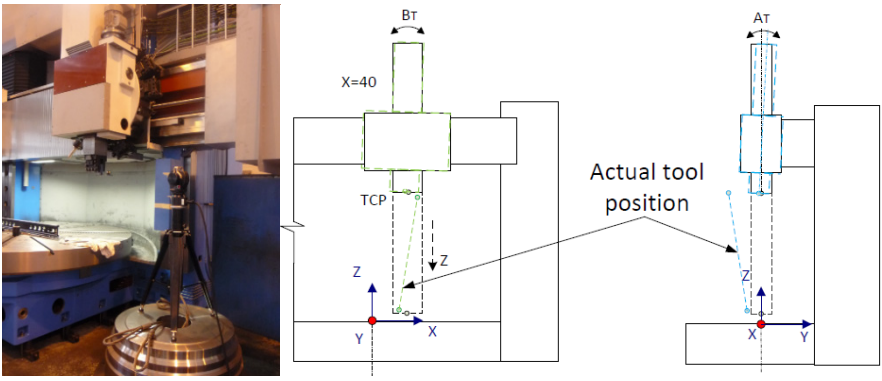

Fig. 4 Example of measurement of VL in company TOSHULIN. Real course of tool of VL

The second part of the volumetric error of vertical lathe is composed of errors occurring on the rotary plate. The principle of measuring and identifying the errors on the rotary plate has been presented in [5].

The resultant error V_{eg} is given by geometric and kinematic machine error induced by the rotation of the plate of vertical lathe M_r and translational motions of cutter head M_t. The errors resulting from the rotary plate also include the weight of future WP, which contributes to the total error. The equations 1 and 2 are described in greater detail in [6].

$$V_{eg(\Phi,x,z)} = M_{R(\Phi)} + M_{t(x,z)} \tag{1}$$

$$V_{eg(\Phi,x,z)} = \begin{pmatrix} \cos\delta_{\varphi y} & \sin\delta_{\varphi y}\cdot\sin\delta_{\varphi x} & \sin\delta_{\varphi y}\cdot\cos\delta_{\varphi x} \\ 0 & \cos\delta_{\varphi x} & -\sin\delta_{\varphi x} \\ -\sin\delta_{\varphi y} & \cos\delta_{\varphi y}\cdot\sin\delta_{\varphi x} & \cos\delta_{\varphi y}\cdot\cos\delta_{\varphi x} \end{pmatrix}_{\Phi} \begin{pmatrix} Xm \\ Ym \\ Zm \end{pmatrix} + \begin{pmatrix} \delta Rx \\ \delta Ry \\ \delta Rz \end{pmatrix}_{\Phi} + \begin{pmatrix} \delta X_T \\ \delta Y_T \\ \delta Z_T \end{pmatrix}_{x,z} \tag{2}$$

2.2 *Identification of Errors on a VL Induced by Cutting Forces*

The second part of the resultant error acting on the future WP, $V_{ec,}$ is focused on the load induced by the machining force. The following diagram shows the load of lathe cutter and the induction of moment at the cutter head of vertical lathe. The induction of deflections is shown in the following diagram in Fig. 5. The ideal position of the tool is given by the vector A_i. A_s (V_{eg}) shows a deflection from the ideal position caused by the positioning error (kinematics and geometry) calculated in relation to the cutter head, A_n is a deflection caused only by offset of the tool, A_o is a deflection caused by the component of machining forces.

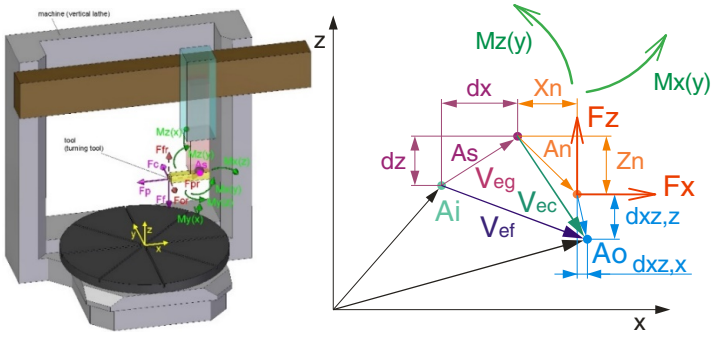

Fig. 5 Effects of machining forces on the structure of vertical lathe, analysis of deflections occurring on TCP

A total deflection caused by offset of the tool and machining deformation is marked as V_{ec} and is given by the equation 3.

$$V_{ec(F,K)} = A_n + A_{o(F,K)} \tag{3}$$

$$A_{o(F,K)} = \begin{bmatrix} d'_1 xz, x + d'_1 xy, x \\ d'_1 xy, y + d'_1 yz, y \\ d'_1 xz, z + d'_1 yz, z \end{bmatrix} = \frac{F}{K} \tag{4}$$

Deflection A_o is dependent on the size of machining forces F, machine stiffness at the given point $K_{(x,z)}$. The stiffness matrix has been obtained by experimental verification on a VL and only for the selected points in workspace of the MT. [7]

2.3 *Predicting Accuracy Behavior of Vertical Lathe*

Based on the above total deflection $V_{ef,}$ it is possible to set, depending on the weight of the WP and the position of the tool related to the WP, the resultant deflection dependent on the geometric behavior and cutting forces (Eq. 5).

This was verified on the test WP according to the standard ISO 3655 P1. The results show a proportion of the individual factors affecting the resultant error defined by Ramesh [2]. It is also possible to monitor the behavior of finishing and roughening operations, which affect the resultant geometric accuracy of the WP.

$$V_{ef(\Phi,x,z,F,K)} = V_{eg(\Phi,x,z)} + V_{ec(F,K)} \tag{5}$$

From the course of deflections shown in Fig. 6, it is evident that the greatest deflections occur in the direction of axis Y. In addition, it is obvious that the deflections due to the geometric error are greater than the deflections caused by machining forces. It is necessary to take into account that the computations are performed for machining which does not correspond to the finishing phase of machining and the forces acting on the tool are fourfold. In terms of finishing machining, geometric errors form the main part of the total error on the MT, which confirms the statement of Ramesh [2].

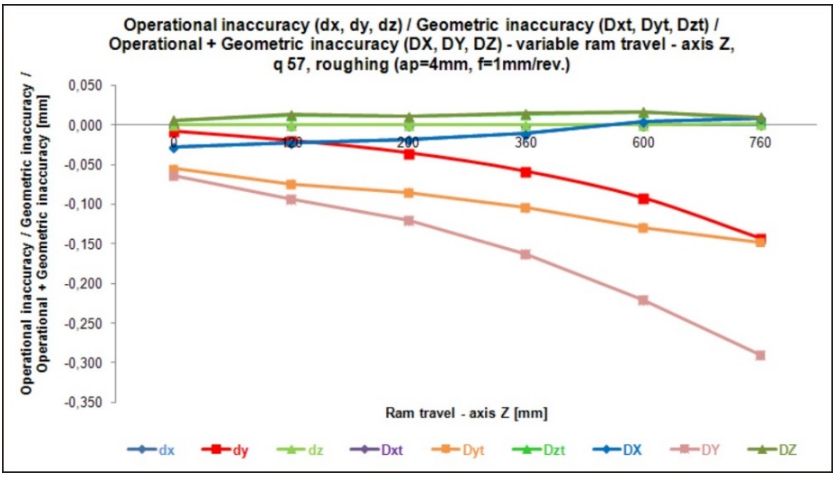

Fig. 6 Effects of machining forces on the structure, analysis of deflections on TCP

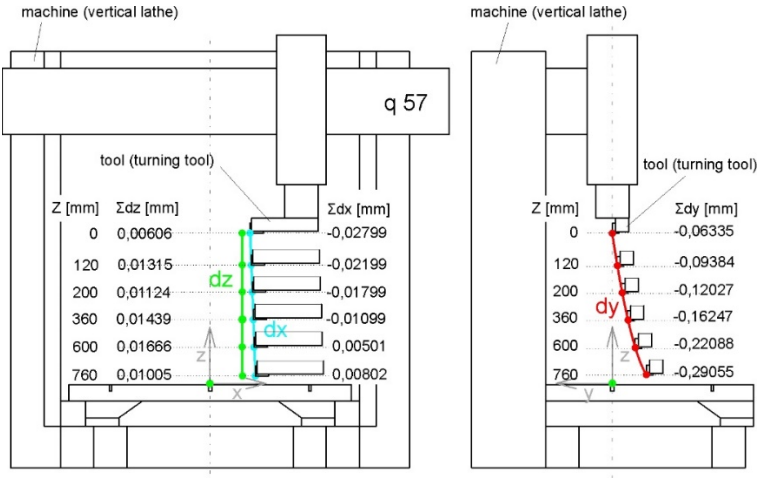

Fig. 7 Course of resulting deflection during machining of test WP - ISO 3655 P1

Fig. 7 shows the resultant deflections induced during machining of test WP. Based on the known parameters, it is possible to predict the resultant deflection on any diameter during machining of cylindrical surfaces. The observed deflection of circularity is in this case formed by errors dx and dy. Simultaneously, the error dy always has a much smaller share in the resultant error, whereby the largest deflection on the machine is at the position z = 760 mm and the smallest at the position z = 0 mm. The measured deflection of circularity on the WP was 0.015 mm at positions (z = 260-760 mm). The difference between the predicted and real value is induced by the remaining factors as described in [2].

3 Conclusions

The approach presented in this article enables to predict the geometric and working accuracy for kinematic structure of vertical lathe. This methodology was subsequently verified on a vertical lathe from the company TOSHULIN - SKIQ30. The entire methodology was designed with the aim to use the highest possible amount of information already available on the machine tool. Available sources of information primarily used were the measured data obtained from the reception tests; these were further supplemented by tests using the instrument Laser Tracker.

Processed results of both geometric and working accuracy will allow predicting the behavior of machines for finishing and roughening turning. A more detailed analysis is possible with the aim to further identify the share of geometric accuracy and working accuracy of vertical lathe and also to identify the "weak" points on the machine tool.

Acknowledgments. This work has been supported by Brno University of Technology, FME, Czech Republic (Grant No. FSI-S-11-5) and by European Regional Development Fund in the framework of the research project NETME Centre under the Operational Programme Research and Development for Innovation. Reg. Nr. CZ.1.05/2.1.00/01.0002, id code: ED0002/01/01, project name: NETME Centre – New Technologies for Mechanical Engineering.

References

[1] Du, Z., Zhang, S., Hong, M.: Development of a multi-step measuring method for motion accuracy of NC machine tools based on cross grid encoder. International Journal of Machine Tools and Manufacture 50(3), 270–280 (2010)
[2] Ramesh, R., Mannan, M.A., Poo, A.N.: Error compensation in machine tools — a review: Part I: geometric, cutting-force induced and fixture-dependent errors. International Journal of Machine Tools and Manufacture 40(9), 1235–1256 (2000)
[3] Aguado, S., Samper, D., Santolaria, J., Aguilar, J.J.: Identification strategy of error parameter in volumetric error compensation of machine tool based on laser tracker measurements. International Journal of Machine Tools and Manufacture 53(1), 160–169 (2012)
[4] Brecher, C., Flore, J., Haag, S., Wenzel, C.: High precision, fast and flexible calibration of robots and large multi-axis machine tools (2012)
[5] Holub, M., Pavlík, J., Opl, M., Blecha, P.: Identification of Geometric Errors of Rotary Axes in Machine Tools. In: MECHATRONICS: Recent Technological and Scientific Advances, pp. 213–217 (2011)
[6] Holub, M.: Effect of geometrical precision machining centers on the desired characteristics of the goods. Brno University of technology (2011)
[7] TOSHULIN a.s., Internal documents and test records

Towards to Haptic Keyboard: Modeling the Piano Action

P. Horváth

Széchenyi István University, Faculty of Engineering Sciences,
Egyetem tér 1, H-9026 Győr, Hungary
horvathp@sze.hu

Abstract. Keyboards of digital pianos have moderate dynamic performance compared to that of grand pianos. Real needs emerged to emulate haptic features of a piano action by a simple device. This paper deals with analytical and experimental investigation of check and repetition phase of touch. Finding out the relationship among initial velocity of hammer, duration and magnitude of impact impulse, key position, fly of time gives sound foundation for development of a haptic keyboard that offers the same sensation for pianist as the acoustic one. Parameters of governing expressions were determined by measurements.

1 Introduction

Digital pianos all have outstanding sound quality but poor touch sensation. This haptic feedback together with acoustic feedback is essential for pianist in interpreting classical piano music. Even the most sophisticated mechanical solutions (keyboards with hammer action) can partially replace inertial effects but miss escapement, check and repetition, the most significant haptic effects. The proposed solution replaces the mechanical action with an electronically controlled actuator [1, 2] (Fig.1). The paper concentrates only on the check and repetition phase of operation, because they are in close connection with each other.

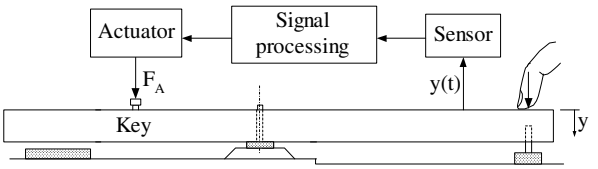

Fig. 1 Proposed haptic keyboard

The piano action can be studied in Fig. 2. The key is pressed down completely when hammer falls after striking the string. Repetition spring stores a portion of its kinetic energy and back check stops the hammer exerting an impulse to the key.

T. Březina and R. Jabloński (eds.), *Mechatronics 2013*,
DOI: 10.1007/978-3-319-02294-9_7,

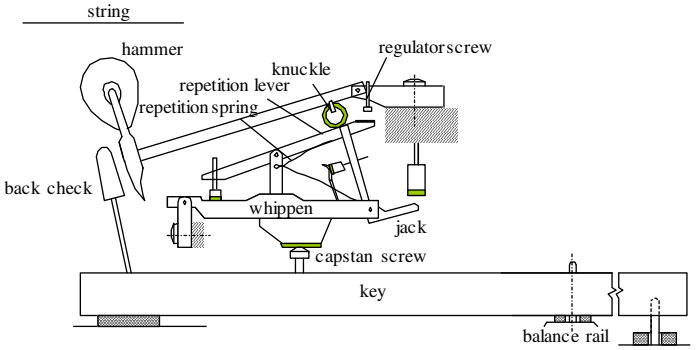

Fig. 2 Parts of grand piano action

When the player releases the key a bit (1-2 mm), contact between hammer tail and back check ceases and repetition lever lifts the hammer to be ready for another cycle. This process is called repetition. In the meantime repetition lever collides with the regulator screw that induces a second impulse that is transmitted to the key causing a "kick" perceived by the player.

2 Modeling the Piano Action

It is critical to accurately model piano operation because of the complexity of the system consisting of changing constraints and components with significant compliance, hysteresis and other non-linear properties. Even though the number of publications modeling piano action increases steadily [3, 4, 5, 6, 7], real breakthrough has not occurred so far. The philosophy of this paper differs a bit from that of above mentioned ones: it is to be determined only the net moment exerted by the action to the key, instead of modeling the motion of all action parts. In *a priory* knowledge of physical background one needs to determine only a few constants by measurements, instead of many parameters. As a consequence, simple expression will make it possible real time data processing.

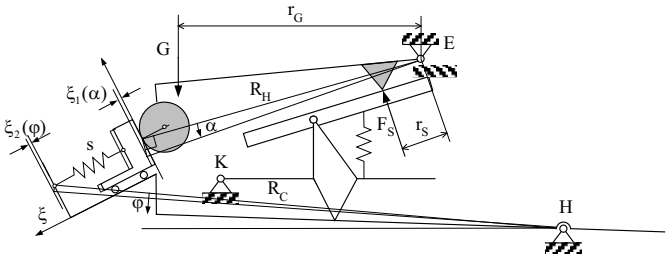

Fig. 3 Modeling back check with linear spring

After hitting the string, falling hammer is stopped by the back check that is modeled by a linear spring of stiffness *s* placed between the key and hammer tail (Fig. 3). Since geometric data change only slightly during check phase, the force arising in the back check spring can be calculated with linear expression:

$$N = s(c_1\alpha - c_2\varphi) \tag{1}$$

This expression is valid only for compression forces N>0. During check phase the key motion can be neglected, so the stored energy in back check spring is

$$U_b = \frac{1}{2} s c_1^2 \alpha^2 \tag{2}$$

During check phase frictional contact takes place between back check and hammer tail, the friction loss can be calculated as the work of friction force F_f:

$$W = \int_0^\alpha F_f \cdot R_H d\alpha = \int_0^\alpha \mu s c_1 \alpha R_H d\alpha = \frac{1}{2} \mu s c_1 R_H \alpha^2 \tag{3}$$

where the force arm R_H of the friction force can be regarded constant.

The repetition spring of very small stiffness is preloaded with force F_S, thus its change can be neglected. The potential energy stored in the repetition spring is approximately

$$U_r = F_S \cdot r_S \alpha \tag{4}$$

The energy balance of action during check phase can be calculated as follows:

$$\frac{1}{2} J\dot{\alpha}_0^2 + G r_G \alpha = \frac{1}{2} J\dot{\alpha}^2 + \frac{1}{2} s c_1^2 \alpha^2 + \frac{1}{2} \mu s c_1 R_H \cdot \alpha^2 + F_S \cdot r_S \alpha \tag{5}$$

where *J* is the mass moment of inertia of hammer, $\dot{\alpha}_0$ is the initial angular velocity of the hammer prior to checking, *G* is the force of gravity of the hammer, is the friction coefficient between back check and hammer tail. Introducing

$$A = \frac{2(Gr_G - F_S r_S)}{J} \quad ; \quad B = \frac{(sc_1^2 + \mu s c_1 R_H)}{J} \quad ; \quad D = \sqrt{\frac{A^2}{4B^2} + \frac{\dot{\alpha}_0^2}{B}}$$

new variables, and solving differential equation (5) for α with initial condition $\alpha(0)=0$ one obtains

$$\alpha(t) = D \sin(\sqrt{B}t - \arcsin \frac{A}{2BD}) + \frac{A}{2B} \tag{6}$$

Having a closer look at the parameters *A* and *B*, the relation A<<2B can be recognized. The solution of (6) then simplifies to

$$\alpha(t) \cong \underbrace{\frac{\dot{\alpha}_0}{\sqrt{B}}}_{\alpha_{max}} \sin \sqrt{B}t \tag{7}$$

It can be seen that the travel of hammer during check phase is approximately proportional to the initial velocity of hammer. Duration of check phase can be calculated from the $\dot{\alpha}(t_{stop}) = 0$ condition that results in a nearly constant value:

$$t_{stop} \cong \frac{\pi}{2\sqrt{B}} \tag{8}$$

It is to be noted that duration of check phase is independent of initial velocity of hammer. Until hammer moves, the contact force F_1 lies in the circumference of the friction cone. After stopping, the hammer may either rebound or remain in rest position latched depending on the equilibrium conditions of the hammer. Normally the moment of repetition spring force F_S about point E is higher then that of the gravity to be able to lift the hammer during repetition, but the back check can latch the hammer until releasing the key. As the magnitude of normal force N_{max} does not change shortly before and after stopping the hammer, the direction of contact force has to change in order to maintain the equilibrium of hammer. Fig. 4 shows the forces acting on the key at the end of check phase (F_1), during latching ($F_2 \approx N_{max}$) and shortly after ceasing latching (F_3). The change of force arm $r_1 \rightarrow r_2$ implies the reduction of force arm $k_1 \rightarrow k_2$ causing rapid drop of the moment $M_{max} \rightarrow M_{end}$ acting on the key and check phase has finished. These moments are

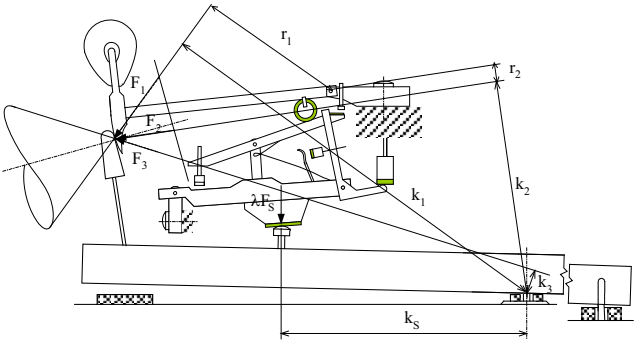

Fig. 4 Forces acting on the key before, during and after latching

$$M_{max} = k_1 s c_1 \dot{\alpha}_0 \sqrt{1+\mu^2} \Big/ \sqrt{B} + \lambda F_S k_S = K_1 \dot{\alpha}_0 + K_3 \tag{9}$$

$$M_{end} = k_2 s c_1 \dot{\alpha}_0 \Big/ \sqrt{B} + \lambda F_S k_S = K_2 \dot{\alpha}_0 + K_3 \tag{10}$$

respectively, where K_1, K_2, K_3 constants are to be determined by measurements.

Repetition phase begins when releasing the key steadily. In this case normal force of back check N lessens according to equation (1). In spite of this the hammer can remain latched for a good while, because increasing force arm r may sustain the equilibrium, while decreasing force arm k exerts smaller and smaller moment on the key. Finally contact ceases and no force acts between hammer and back check any more. The key is loaded only by moment $M_{min}=K_3$.

In the meantime repetition spring tosses up the repetition lever and hammer until repetition lever collides with the stationary regulator screw. As in general, impact impulse is proportional to the velocity of colliding point of repetition arm prior to impact that is near the same as that of the knuckle. First the velocity of knuckle v_k must be calculated at the instant of collision from the energy stored in repetition spring according to equation (4).

$$v_k = r_S\dot{\alpha}_c = r_S\sqrt{\frac{2(F_S R_S - GR_G)}{J\sqrt{B}}}\sqrt{\dot{\alpha}_0} = K_5\sqrt{\dot{\alpha}_0} \tag{11}$$

As mentioned before, impulse generating during impact is proportional to the velocity and a portion of this impulse is transmitted to the key by the whippen assembly. Thus the moment of impulse exerted to the key is also proportional to the square root of the initial velocity of the hammer:

$$\int M dt = K_4\sqrt{\dot{\alpha}_0} \tag{12}$$

where constant K_4 has to be determined by measurement. Unfortunately the shape of this momentum can not be calculated.

3 Measurements

In order to determine $K_1 \ldots K_4$ constants and duration of impulses, measurements have to be performed. Measurements were taken on a 1:1 model of the real piano action produced by Renner GmbH (Fig. 5).

In the first step the check phase was investigated. In practice key is already stationary when colliding with hammer. This fact allowed using a simple measuring procedure. The key was supported on a force sensor (Honeywell FSG 15N1A) and hammer was dropped with various velocities. Hammer velocity was measured by

Fig. 5 Piano action model

a transmission type optical sensor. The net moment acting on the key was proportional to the force measured. Moment versus time diagram during check phase with initial angular velocity $\dot{\alpha}_0 = 12\ \mathrm{rad/s}$ can be seen in Fig.6 where the analytically determined curve is also depicted. The similarity is apparent. It turned out to be from measurement that duration of check phase takes about 7-8ms.

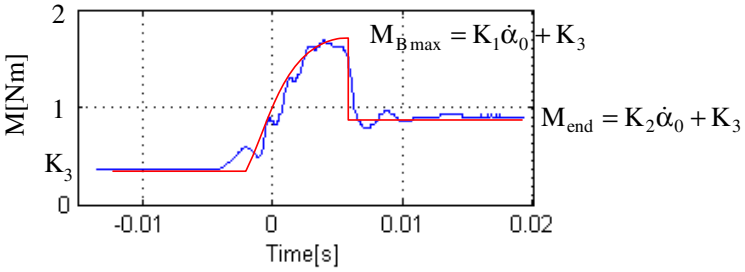

Fig. 6 Moment history of check phase

Calculating constants from measurement one obtains K_1=0,1125 Nms/rad, K_2=0,017 Nms/rad, K_3=0,4 Nm, respectively.

In the second step repetition phase was measured. The force sensor as a support was moved by a DC gear-motor driven micrometer screw allowing the key to release steadily. The moment history during repetition can be seen in Fig.7. At the beginning the decreasing contact force altogether with changing force arm cause decreasing moment. The moment falls from M_{end} to M_{min} approximately linearly as indicated "back check relief". The fly of time of hammer until collision can be neglected relative to the duration of impulse generating during impact of repetition lever and regulator screw. Duration of this triangle shaped impulse "kick" is about 60 ms because resilient whippen felt prolongs the contact time. From measurement constant K_4 can be calculated applying expression (12):

$$K_4 = \frac{\int \mathrm{M}dt}{\sqrt{\dot{\alpha}_0}} = \frac{0.06 \cdot 0.2}{2 \cdot \sqrt{12}} = 0.00173\ \mathrm{Nms}^{1,5}$$

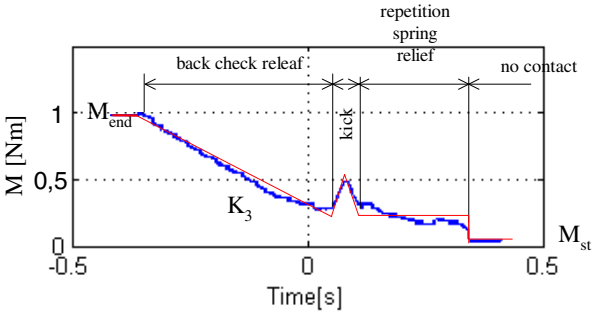

Fig. 7 Forces acting on the hammer before, during and after latching

Letting up the key further, repetition spring reliefs further but the moment remains approximately constant due to the small stiffness of repetition spring. At the end contact between repetition lever and regulator screw ceases and moment falls to its static value.

4 Conclusions

This paper dealt with modeling and measuring dynamic behavior of check and repetition phases of piano action in order to work out basic expressions for development of a haptic keyboard. Results of analytical investigation showed, that a) travel of hammer during check phase is approximately proportional to the initial velocity of hammer; b) duration of check phase is independent of initial velocity of hammer; c) shape of the moment history during check phase is sinusoidal; d) impulse during repetition exerted to the key is proportional to the square root of the initial velocity of the hammer. Simple analytical expressions worked out describe well haptic response of piano action with only a few parameters. These parameters were determined by measurements.

References

[1] Boccaletti, C., Duni, G., Elia, S.: Dynamic model of an electromechanical piano key by means of FEM techniques. In: Proc. of the Modelling and Simulation, Cancun, Mexico, pp. 308–313 (2005)
[2] Oboe, R.: A Multi-Instrumental, Force-Feedback Keyboard. Computer Music Journal 30(3), 38–52 (2006)
[3] Gillespie, B.: Dynamic Modeling of the Grand Piano Action. In: Proceedings of the International Computer Music Conference, San Hose, CA, pp. 77–80 (1992)
[4] Acker, A., Birkett, S.: Recent Research in Piano Key Action. In: Proc. of conference Haptics, Rochester, NY (2009)
[5] Gillespie, B.: Haptic Display of System with changing Kinematic Constraints. The Virtual Piano Action. PhD Thesis, Stanford University, CCRMA (1996)
[6] Hirschorn, M., Birkett, S., Mephee, J.: Kinematic Model of a Piano Action Mechanism. System Design Engineering, University of Waterloo, Ontario, Canada
[7] Horvath, P., Töröcsik, D.: Magnetic issues of a haptic keyboard. Przeglad Elektrotechniczny, pp. 61-63, R.89 NR 2b/2013

Gubanov Model for Vacuum Packed Particles

R. Zalewski and P. Chodkiewicz

Warsaw University of Technology, Institute of Machines Design Fundamentals,
Narbutta 84, 02-524 Warsaw, Poland

Abstract. The present work mainly focuses on modeling of the mechanical properties of the vacuum packed particles. Such structures are composed on the basis of loose granular materials encapsulated in a hermetic space. Initially granular system behaves like a classical plastic mass. When the internal pressure is pumped out of the system, what was baggy bulk transforms into solid (semisolid) state. Rheological Gubanov model is adopted to describe uniaxial compression loading experimental results of specially performed testing specimens. In the final part of the paper some numerical results are presented.

1 Introduction

Nowadays increased attention is observed in active and semi-active control devices field. The main advantages of semi-active vibration control techniques over active control systems are related to offering considerable effects without requiring the associated power sources. Typical examples of semi-active control devices are dampers or shock-absorbers designed on the basis of controllable fluids. Examples of “smart” fluids are electrorheological fluids (ER fluids) and magnetorheological fluids (MR fluids). Moreover, semi-active devices provide highly reliable operation.

In this paper author would like to present an innovative controllable structure, which appear to be an attractive alternative to "smart" fluids.

Vacuum packed particles systems are composed of a loose granular material encapsulated in a hermetic, soft plastomers envelope ([3]). When internal pressure is the same as surrounding atmospheric pressure, the system behaves similarly to a dense liquid ([6], [7]). When the structure is exposed to so called “underpressure” the essential characteristic of investigated systems transforms into viscoplastic solid ([8]). The underpressure is defined as a difference between an atmospheric an internal pressure.

Special granular structures (SGS) are in some aspects granular analogs of MR fluids. Loose grains can be compared to polarizable particles. Internal pressure is an equivalent of a carrier liquid. The impact of an electric or magnetic field is replaced by underpressure. Pumping out an air from the granular systems results in increasing “inter-granular” frictional forces acting between single grains. Also some grains displacements are observable for greater underpressure values. Described phenomenon

T. Březina and R. Jabloński (eds.), *Mechatronics 2013*,
DOI: 10.1007/978-3-319-02294-9_8,

is comparable to application of an electric or magnetic field to ER, MR fluids resulting in chains forming.

SGS under the impact of partial vacuum exhibit viscoplastic behavior.. Transition to rheological equilibrium can be achieved in a very short time, which is strictly depended on a vacuum pomp capacity and the volume of the system.

Moreover, SGS are not sensitive to impurities commonly encountered during manufacturing and usage. Another disadvantage of smart fluids in comparison to SGS is the impact of temperature. Although it is usually assumed that MR fluids can operate at temperatures from –40 to 150°C with only slight variations in the yield stress, it was revealed in [1] or [2] that this factor has much greater impact on operational properties.

Manufacturing process of vacuum packed particles systems is extremely uncomplicated and definitely less expensive. Only loose material and a hermetic wrap have to be provided. No more than a vacuum pomp is necessary for controlling physical properties of SGS. The grains applied in considered system can be absolutely optional.

2 Objectives

To evaluate the usefulness of vacuum packed particles systems for engineering applications, a testing specimen has been developed in Warsaw University of Technology, Institute of Machines Design Fundamentals.

The main objective of presented paper is to develop a suitable mathematical model to capture extraordinary features of SGS. Such task seems to be complex because the SGS are absolutely innovative. Like most semi-active control systems or novel structural materials ([9] or [10]) also SGS reveal highly nonlinear properties. To develop control algorithms which enables for maximum advantage of the extraordinary features of SGS, asuitable phenomenological model has to be developed.

A phenomenological Gubanov model was applied to capture nonlinear behavior of investigated structures. Previously mentioned model is numerically tractable and additionally efficiently represents the behavior of a SGS testing specimen.

In the final part of the paper the comparison of experimental and numerical data indicates that applied model is accurate.

3 Experiments

The experimental stand depicted in Fig. 1 was used in experiments carried out on cylindrical samples of vacuum packed particles. In this setup, the *MTS 809* universal tensile testing machine (Fig. 1a) was employed to drive a specimen. The vacuum pomp, made by *AGA Labor* (Fig. 1c), was used to control the internal

underpressure value. Using this experimental setup, different types of dynamic responses can be measured and recorded (Fig. 1b) for a wide range of excitation rules.

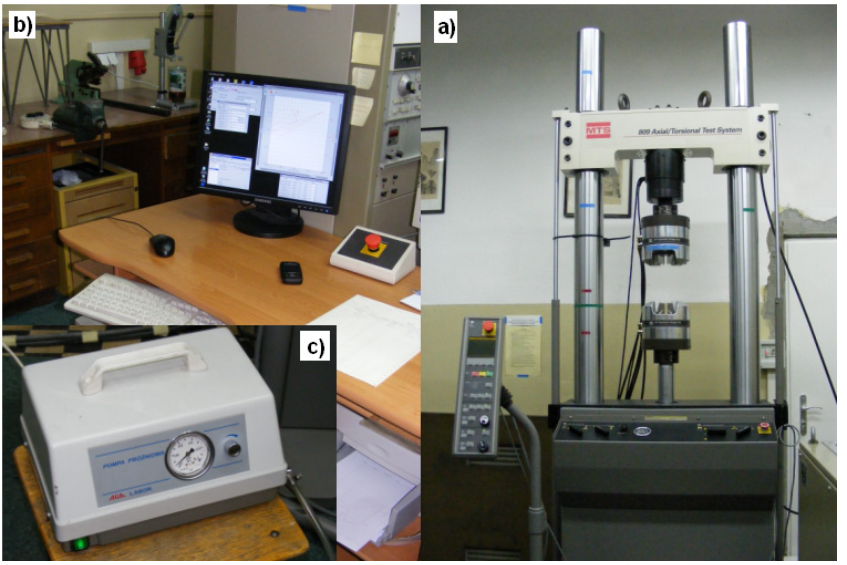

Fig. 1 Experimental stand: a) MTS 809 tensile testing machine, b) data acquisition system, c) vacuum pomp AGA Labor

The experimental testing specimen is shown in Fig. 2.

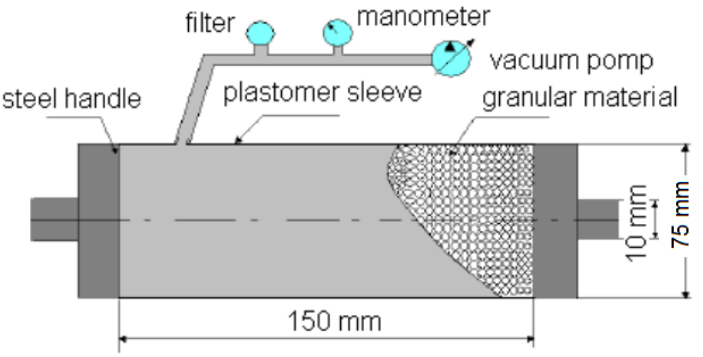

Fig. 2 SGS testing specimen

Investigated testing specimen consisted of a soft plastic cylinder filled with a polypropylene grains (PP). The shape of single grain was also cylindrical (1 [mm] diameter, 2 [mm] length). External wrap, due to a special valve, was connected to the vacuum pomp. Two specially performed steel discs made connection of the SGS sample into the MTS device possible. Dimensions of the sample have been depicted in Fig. 2.

A lot of additional problems have been encountered during experimental research of SGS structures. They have been discussed in details in ([3], [6] or [7]) and are consequently omitted in this paper.

Typical response of the SGS sample acquired in uniaxial compression tests is depicted in Fig. 3. Three various underpressure levels have been investigated: 0.08, 0.07 and 0.06 MPa.

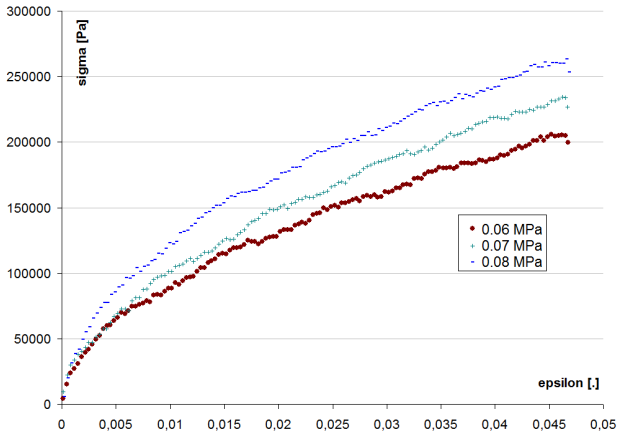

Fig. 3 SGS experimental hardening curves for various underpressure values

Data depicted in Fig. 3 reveals the strong impact of underpressure on experimentally acquired hardening curves. For higher underpressure values, the force required to yield the SGS specimen increase and produces behavior associated with a viscoplastic material.

In the next section the Gubanov model ([5]) is applied for predicting the response of the SGS specimen.

4 Rheological Model

Because granular structures are basically made of polymers, in this initial attempt to the modeling process a typical rheological model for such materials proposed in early Sixties by Gubanov is applied. Its mechanical scheme is depicted in Fig. 4.

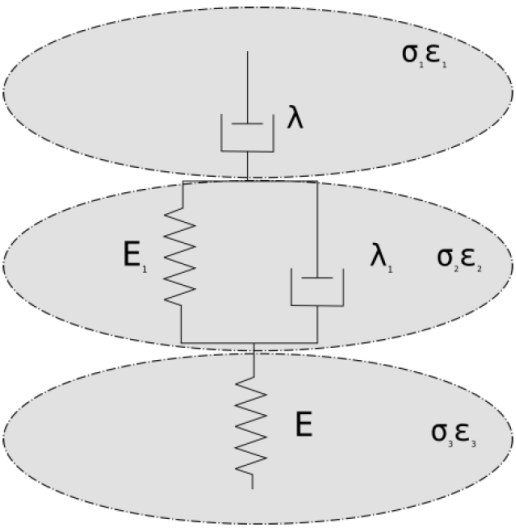

Fig. 4 Mechanical scheme of the Gubanov model

The model consists of a dashpot in series with a standard model of a linear solid ([4]). The governing equations for this model are given by

$$\sigma = \sigma_1 = \sigma_2 = \sigma_3 \tag{1}$$

$$\varepsilon = \varepsilon_1 + \varepsilon_2 + \varepsilon_3 \tag{2}$$

$$\sigma_3 = E\varepsilon_3 \tag{3}$$

$$\sigma_2 = E_1\varepsilon_2 + \lambda_1\dot{\varepsilon}_2 \tag{4}$$

$$\sigma_1 = \lambda\dot{\varepsilon}_1 \tag{5}$$

The final form of the Gubanov model taking advantage of the Laplace transform may be written in a following form

$$\sigma + \left(\frac{\lambda}{E} + \frac{\lambda + \lambda_1}{E_1}\right)\dot{\sigma} + \frac{\lambda\lambda_1}{EE_1}\ddot{\sigma} = \lambda\dot{\varepsilon} + \frac{\lambda\lambda_1}{E_1}\ddot{\varepsilon} \tag{6}$$

According to [5] it was assumed that the *E* parameter is a Young's modulus of the investigated system. In [3] author focused on determining the fundamental mechanical properties of discussed structure. In this paper this problem was neglected. Assumed Young's modulus values were in a following form

$$E(p) = 2.7*10^6 \exp(2.65p) \tag{7}$$

For numerical simulations following initial conditions were assumed:

$$\sigma(0) = 0; \dot{\sigma}(0) = at \tag{8}$$

where *a* parameter was calculated experimentally basing on direct experimental data.

Numerical simulations were carried out in the *Mathematica* environment. To solve a differential equation (6) the *NSolve* procedure was applied.

Numerical results - stress-time characteristics are depicted in Fig. 5.

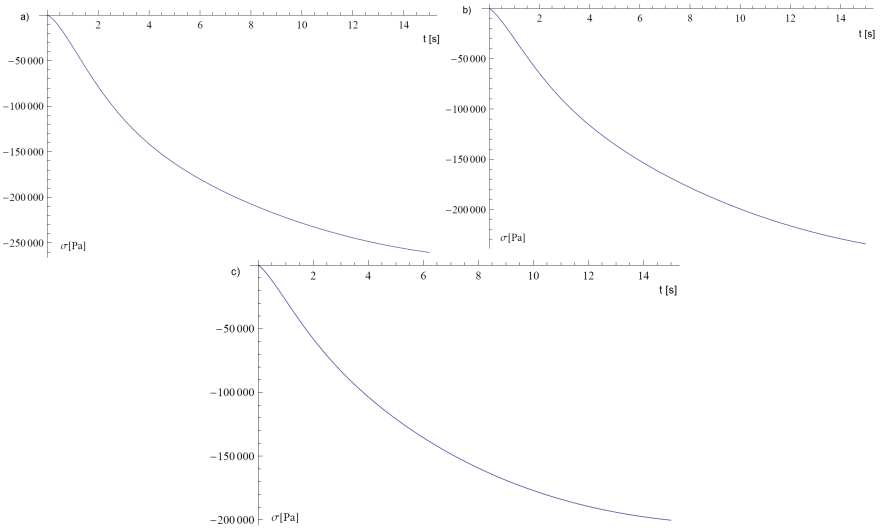

Fig. 5 Numerical results for various underpressure values: a) 0.08 MPa; b) 0.07 MPa; c) 0.06 MPa

In Fig. 6 Exemplary verification result of experimental and numerical data for compressed SGS under 0.08 MPa underpressure has been depicted in Fig. 6.

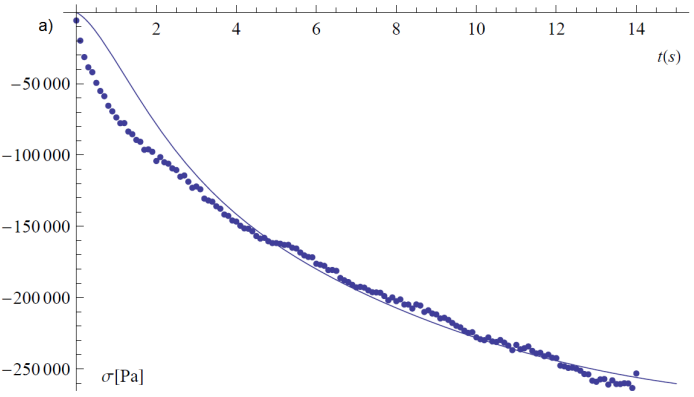

Fig. 6 Verification of experimental and numerical data

5 Conclusions

This paper introduces a new type of controllable structures. Special Granular Structures in some engineering applications (damping of vibrations, noise reduction screens) can compete with well commercialized devices working on the base of MR or ER fluids. The biggest advantage of SGS over the previously mentioned smart fluids is their price. From the economic point of view, easily accessible granular materials are much more attractive than MR or ER fluids.

The phenomenological behavior of SGS is more complex than intelligent fluids. Experimentally acquired cyclic loading loops for SGS are non-symmetric, which makes commonly used rheological models inadequate ([3]).

Gubanov rheological model has been used for description of the SGS behavior. Investigated model can capture the stress-strain behavior of compressed SGS with satisfactory accuracy.

Acknowledgments. This research received funding from the State Committee for Scientific Research: N N501 069638.

References

[1] Bajkowski, J., Jasiński, M., Mączak, J., Radkowski, S., Zalewski, R.: The active magnetorheological support as an element of damping of vibrations transferred from the ground to large-scale structure supports. Key Engineering Materials 518, 350–357 (2012)

[2] Makowski, M., Knap, L.: Reduction of wheel force variations with magnetorheological devices. Journal of Vibration and Control (2013), doi:10.1177/1077546312472916

[3] Pyrz, M., Zalewski, R.: Modeling of granular media submitted to internal underpressure. Mechanics Research Communications 37(2), 141–144 (2010)

[4] Shames, I.H., Cozzarelli, F.A.: Elastic and Inelastic Stress Analysis, pp. 120–122. Pentice Hall, Englewood Cliffs (1992)

[5] Wilczynski, A.: Mechanika polimerów w praktyce konstrukcyjnej, Warsaw (1984)

[6] Zalewski, R.: Constitutive model for special granular structures. Int. J. Non-Linear Mech. 45(3), 279–285 (2010)

[7] Zalewski, R., Pyrz, M.: Modeling and parameter identification of granular plastomer conglomerate submitted to internal underpressure. Engineering Structures 32(8), 2424–2431 (2010)

[8] Zalewski, R., Pyrz, M.: Experimental study and modeling of polymer granular structures submitted to internal underpressure. Mechanics of Materials 57, 75–85 (2013)

[9] Zalewski, R., Wolszakiewicz, T.: Analysis of uniaxial tensile tests for homogeneous solid propellants under various loading conditions. Central European Journal of Energetic Materials 8(4), 223–231 (2011)

[10] Zalewski, R., Pyrz, M., Wolszakiewicz, T.: Modeling of Solid Propellants Viscoplastic Behavior Using Evolutionary Algorithms. Central European Journal of Energetic Materials 7(4), 289–300 (2010)

Eco-design of Mechatronic Systems

M. Iskandirova, P. Blecha, M. Holub, and F. Bradáč

Brno University of Technology, Faculty of Mechanical Engineering,
Technická 2, 616 69, Brno, Czech Republic
blecha@fme.vutbr.cz

Abstract. In conformity with the Kyoto Protocol, by the year 2020 the European Union undertook to reduce CO_2 emission by at least 20%. The main sources of this greenhouse gas are transport, combustion of fossil fuels for power generation, and some industrial processes [1]. The most effective ways to protect environment are based on pollution prevention and on searching and elimination of its causes. Application of this strategy to manufacturing processes led to formation of "eco-design" concept. This paper deals with life cycle assessment of mechatronic systems, in our case CNC machine tool. It contains analysis of energy and material consumption during raw material extraction for machine tool production and actual machine tool production. Afterwards, impacts of these life cycle phases on the environment were evaluated according to chosen impact categories.

1 Introduction

What is eco-design? It is a process of design and development of a product focused on minimizing of its negative impacts on environment during its whole life cycle. To term "eco-design" another term "LCA" (Life Cycle Assessment) is closely related. It is a methodology for evaluating of the potential environmental impacts connected with product life cycle. LCA is used in analytical phase of eco-design. During this phase determining of the product environmental profile and formulation of the requirements to the final product properties are realizing. It is possible to use this analysis for life cycle assessment of the products, services, and technologies.

The efforts to evaluate environment impacts of product life cycle on the environment date back already to the beginning of the 1970s years. Mainly, these studies were focused on waste management and packaging [2]. Since then, LCA was applied to many other products, for example current transformers [3], mobile telefon [4], shopping bag [5], beverage packing [6], fossil fuels and bioethanol [7], batteries [8], renewable energy technologies [9], comparison landfilling versus incineration of mixed municipal waste [10], silicon photovoltaic panels [11], etc.

Nowadays, the Energy-related Products Directive 2009/125/EC regulates the sphere of ecodesign. This Directive concerns all energy-related products including the mechatronic systems that are largely involved in deteriorating state of the environment. Worldwide industrial production consumes approximately ¼ of all

T. Březina and R. Jabloński (eds.), *Mechatronics 2013*,
DOI: 10.1007/978-3-319-02294-9_9,

electrical energy, because the mechatronic systems can be used in any industry where precise and reliable work is required. However, experience with LCA implementation is not so big in this sphere. For example, there are studies described in publication [12-14]. Therefore, in this paper LCA methodology will be applied right on representative of the mechatronic systems – CNC machine tool.

Before the article focuses on the application of LCA to the chosen machine tool, the mechatronic systems and LCA methodology will be generally described.

2 Mechatronic Systems

The mechatronic systems are a complex of electromechanical linkages and relations between a working mechanism and an electromechanical system. It is a system consisting of different energy carriers controlled by the numerical, mostly distributed systems. The mechatronic systems are used to develop and manufacture products of high quality and the highest technological level.

The typical mechatronic system consists of a motor, a transmission mechanism, an actuator (frequency converter), a control system (microcomputer), a switching and an overload devices [15].

Scheme of the mechatronic system is shown in Figure 1.

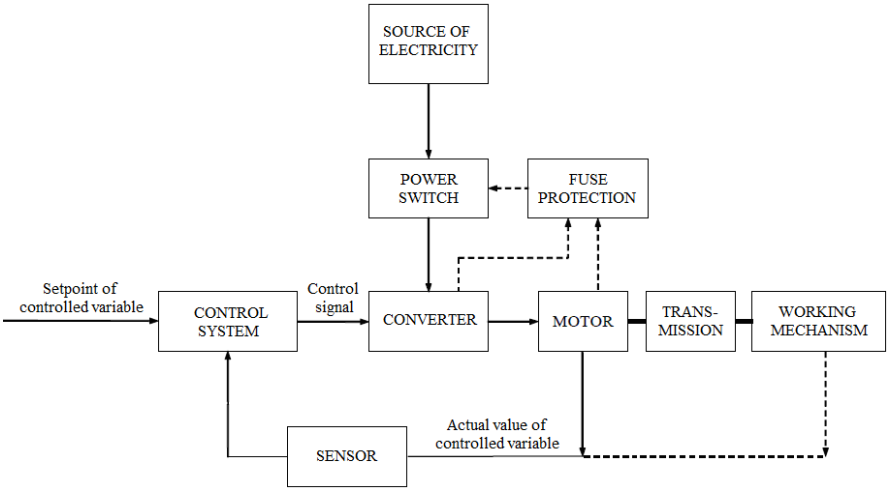

Fig. 1 Block diagram of the mechatronic system [15]

3 Life Cycle Assessment - LCA

As already mentioned in the introduction of this article, LCA is the methodology used for evaluating of potential product impact on the environment using the approach “from cradle to grave”. This approach takes into consideration all phases

of life cycle – from the raw material extraction to the disposal of waste. LCA is the only tool that assesses the environmental impacts of the product during its whole life cycle. Therefore, it can be used to identify opportunities for improvements of the assessed product in all life cycle phases [15].

Currently there are two standards specifying LCA: ISO 14040 defines the principles and framework of LCA, ISO 14044 clarifies the requirements for LCA and guidelines for LCA performance. LCA methodology has a fixed structure and it is performed in accordance with international standards of ISO 14040 series. For effective processing of LCA studies, commercially available databases of processes as well as material and energy flows are used. LCA is defined for whole life cycle of the observed product. Then, the life cycle can be divided into five phases shown in Figure 2 [15].

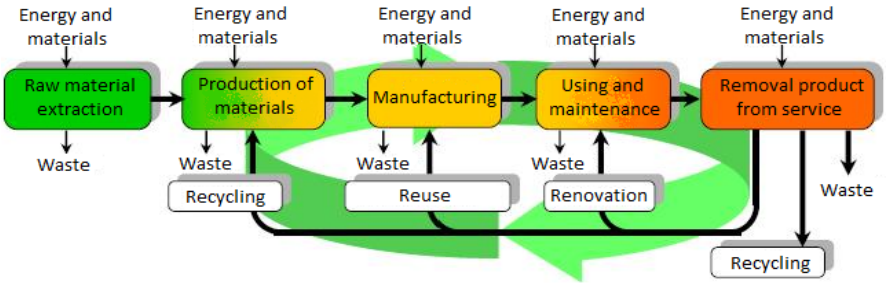

Fig. 2 Graphic representation of the product life cycle according to the ISO 14040 [15]

The study of the PE-International company and the LCA study have proved that phase of the machine using causes the biggest environmental burden, and energy consumption during machine operation has the biggest ecological impact [16]. For verification of this study, was suggested to use the principle described in publication [17]. It is possible to reduce energy consumption during machine operation already in the phases preceding its actual using. The paper deals with analysis and reducing of environmental burden during these phases.

For right LCA performance and determination of impacts on environment during whole life cycle, it is necessary to describe the assessed machine in detail.

4 Description of the Assessed Machine Tool

The LCA study was applied to the large CNC machine tool with horizontal headstock. This machine tool is used for to chip machining of material, also it can be used in such operations as milling, drilling, reaming and threading. It has modular design, which enables considerable variability of assembly. The machine tool consists of fixed sled, on which a stand moves in longitudinal direction. A console with laterally sliding horizontal headstock is placed vertically on the stand. Clamping space of workpiece is designed according to the customer requirements (clamping pates, rotary table, clamping squares, etc.) [15]. The block diagram of the assessed machine tool is shown in Figure 3.

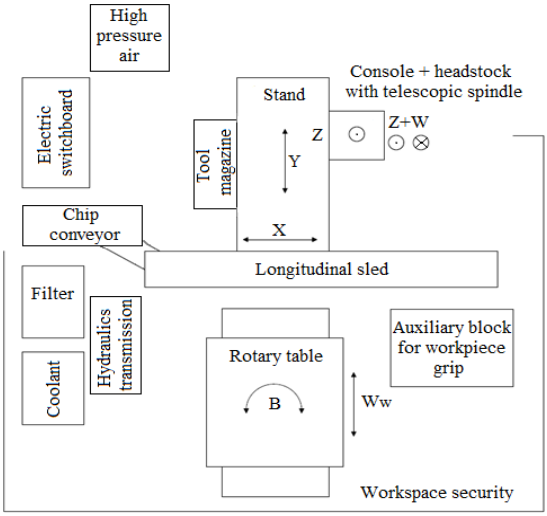

Fig. 3 The block diagram of assessed machine tool [15]

5 Realization of LCA Methodology on Assessed Machine Tool

Life cycle impact assessment of the machine tool was performed in the following order [15]:

1. During the first phase, aims and scope of study were determined. Also following impact category were chosen: global warming (kg CO_2 eq.), ozone layer depletion (kg CFC11 eq.), acidification (kg SO_2 eq.), photooxidants creation (kg C_2H_4 eq.), eutrophication (kg $PO_4$3-).
2. During the inventory analysis, data about ways of raw material obtaining, transportation, manufacturing, using of the assessed machine tool and its recykling were collected and processed. According to manufacturer's documentation, machine tool was laid out into structural units. Afterwards, material composition of each unit and the quantity of each material were described. From the above mentioned dividing for partial results for individual groups and total amount of consumed energy were determined. Results are presented in Figures 5 to 8.
3. In the third phase impact assessment of machine tool life cycle on environment was performed. To calculate the results of the inventory analysis LCA SW program Boustead Model was used. The results of the inventory analysis were converted into common units and the results were grouped within the impact categories. Afterwards, results of impact category indicator and partial results of ompact category indicator shown in Figures 9 to 13.

The results of performed study are presented in following charter.

6 Results of LCA Study

The results of performed study are shown graphically. Firstly, the results of inventory analysis are presented. They show total amount of consumed energy and energy consumed by partial machine tool components during the raw material extraction for their production and the actual production of these component [15].

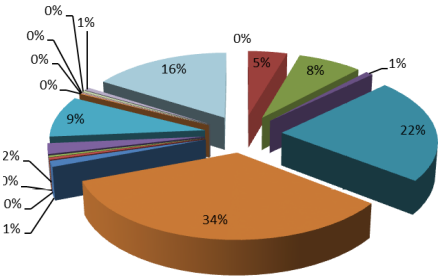

Fig. 4 Electric power consumption for particular machine tool components production

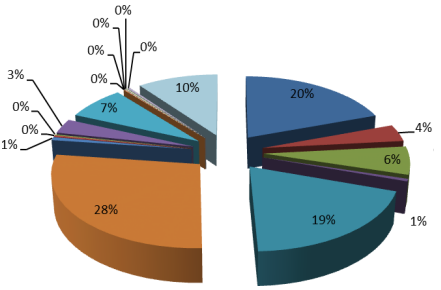

Fig. 5 Oil fuels consumption for particular machine tool components production

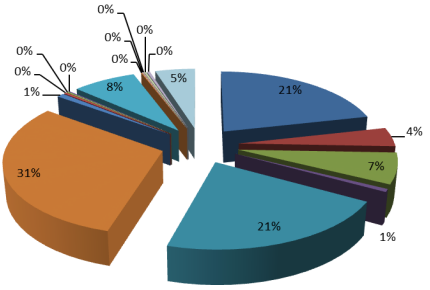

Fig. 6 Another fuels consumption for particular machine tool components production

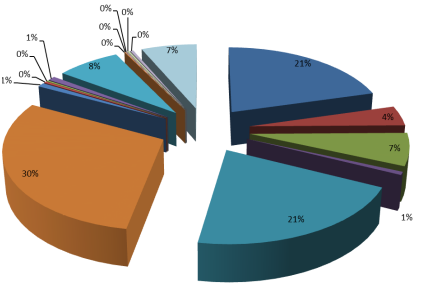

Fig. 7 Total energy consumption for particular machine tool components production

The grafs show that the following parts of machine tool consume the most of total energy: sled with revolving stand, sled and stand.

The results of the third LCA phase are shown in the form of partial graphs presenting environmental burden by particular machine tool components according to the chosen impact categories [15].

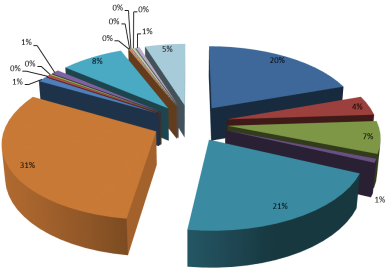

Fig. 8 Partial results of indicators for ozone layer depletion CO_2 eq.

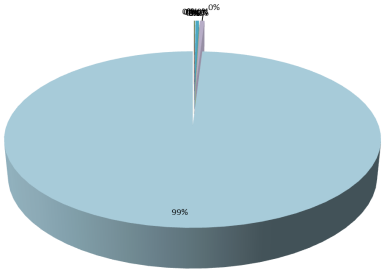

Fig. 9 Partial results of indicators for ozone layer depletion CFC-11 eq.

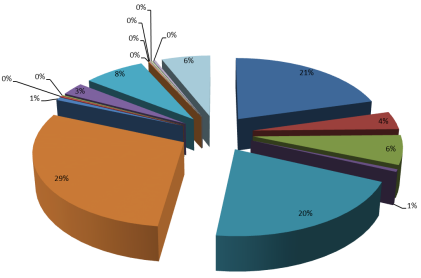

Fig. 10 Partial results of indicators for acidification SO_2 eq.

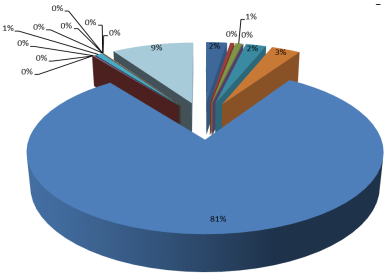

Fig. 11 Partial results of indicators for photooxidants creation C_2H_4 eq.

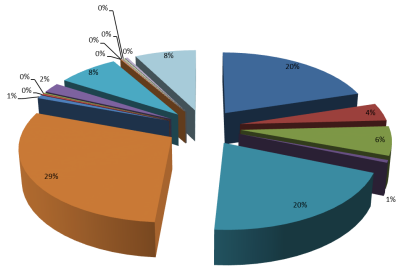

Fig. 12 Partial results of indicators for eutrophication PO_4^{3-} e

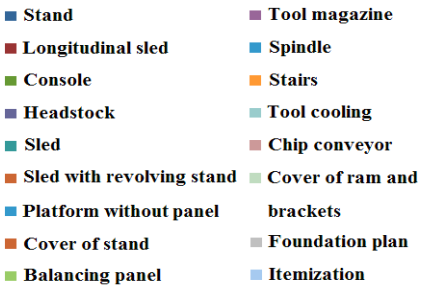

Fig. 13 Legend to Figures 5 to 13

According to the results of this phase, it is possible to make following conclusion about components the most burdening the environment in chosen impact categories: sled with revolving stand, sled and stand the most contribute to global warming and eutrophication; headstock the most contributes to ozone layer depletion; sled with revolving stand, sled, stand and headstock the most contribute to acidification; platform the most contributes to photooxidants creation.

Further, total amount of emissions in chosen impact categories produced during the raw material extraction and machine tool manufacture is presented (Table 1).

Table 1 Total amount of produced emissions [15]

Impact category	Amount	Unit
Global warming	3,81E+04	kg CO_2 eq.
Ozone layer depletion	1,85E-05	kg CFC11 eq.
Acidification	1,70E+02	kg SO_2 eq.
Photooxidants creation	3,73E+01	kg C_2H_4 eq.
Eutrophication	6,50E-05	kg $PO_4$3-

7 Conclusions

This article summarizes the results of LCA method application on mechatronics systems represented by machine tool. The main contribution of this paper is analysis of energy and material consumption of assessed CNC machine tool during raw material extraction for its production and actual machine tool production. Furthermore, the impact evaluation of the mentioned life cycle phases of machine tool on the environment.

As already mentioned, the phase of the machine tool using has the biggest impact on the environment. It is possible to influence this phase and following phases already in the preceding phases. The results of the performed study can be used to reduce the environmental burden and energy performance of machine tools. All of this can be realized by way of choosing of more environment-friendly materials, ways of their extraction, transportation, processing technologies, exchange of machine components for the more energy and material efficient components, etc.

Nevertheless, design of energy-efficient and safe machine requires comprehensive assessment of its whole life cycle, because the efforts to correct ecological impacts although lead to improvement in one area, but often lead to environmental deterioration elsewhere. Then it is necessary to consider if it is appropriate to take such corrective action at all.

Acknowledgments. This work has been supported by Brno University of Technology, Faculty of Mechanical Engineering, Czech Republic (Grant No. FSI-S-11-5), This project has been funded with support from the state budget through the Ministry of Industry and Trade of the Czech Republic (ID of project: FR-TI3/655 – Ecodesign in machine tool construction) and by European Regional Development Fund in the framework of the research project NETME Centre under the Operational Programme Research and Development for Innovation. Reg. Nr. CZ.1.05/2.1.00/01.0002, id code: ED0002/01/01, project name: NETME Centre – New Technologies for Mechanical Engineering.

References

[1] Herrmann, I.T., Hauschild, M.Z.: Effects of globalisation on carbon footprints of products. CIRP Annals - Manufacturing Technology 58(1), 13–16 (2009) ISSN 0007-8506, doi:10.1016/j.cirp.2009.03.078

[2] Kočí, V.: Vysoká škola chemicko-technologická v Praze. Příručka základních informací o posuzování životního cyklu. Praha (2010), http://www.lca.cz/download/13.pdf (retrieved)
[3] Karlson, L.: ABB corporate research. LCA study of current transformers, 17 (2004), http://www.dantes.info/Publications/Publication-doc/DANTES%20ABB%20LCA%20study%20of%20instrument%20transformers.pdf (retrieved)
[4] Pôle de compétence en environnement des industries electriques et electroniques. Analyse du Cycle de Vie d'un téléphone portable. Synthèse, Moirans (2008), http://www.ademe.fr/internet/telephone-portable/site-web/portable.pdf (cit. April 29, 2013) (retrieved)
[5] Ecobilan, P.W.C.: Évaluation des impacts environnementaux des sacs de caisse Carrefour: Analyse du cycle de vie de sacs de caisse en plastique, papier et matériau biodégradable (2004), http://www.ademe.fr/htdocs/actualite/rapport_carre-four_post_revue_critique_v4.pdf (cit. April 29, 2013) (retrieved)
[6] Tichá, M., Černík, B.: Porovnání environmentálnícii dopadů nápojových obalů v čr metodou LCA (2006), http://vskp.vsb.cz/document_root/soubory/lca-napojove-obaly.pdf (retrieved)
[7] Hromádko, J., Hromádko, J., Miler, P., Honig, V., Štěrba, P.: Life Cycle Assessment of Fossil Fuels and Bioethanol. LCaŘ 125 (November 2009), http://www.cukr-listy.cz/on_line/2009/pdf/320-323.pdf (retrieved)
[8] Leuenberger, M., Frischknecht, R.: Esu-services ltd. Life Cycle Assessment of Battery Electric Vehicles and Concept Cars. Uster (2010), http://www.esu-services.ch/fileadmin/download/leuenberger-2010-BatteryElectricVehicles.pdf (retrieved)
[9] Pehnt, M.: Dynamic life cycle assessment (LCA) of renewable energy technologies. Renewable Energy 31(1), 55–71 (2006), doi:10.1016/j.renene.2005.03.002
[10] Alsema, E.A., de Wild-Scholten, M.J.: Environmental life cycle assessment of advanced silicon solar cell technologies (2004)
[11] Paris, H., Museau, M.: Contribution to the environmental performance of the dry-vibratory drilling technology. CIRP Annals - Manufacturing Technology 61(1), 47–50 (2012), ISSN 0007-8506, doi:10.1016/j.cirp.2012.03.030
[12] Akbari, J., Oyamada, K., Saito, Y.: LCA of machine tools with regard to their secondary effects on quality of machined parts. Proceedings EcoDesign 2001: Second International Symposium on Environmentally Conscious Design and Inverse Manufacturing, 347–352 (2001), doi:10.1109/, 992379
[13] Duflou, J.R., Sutherland, J.W., Dornfeld, D., Herrmann, C., Jeswiet, J., Kara, S., Hauschild, M., et al.: Towards energy and resource efficient manufacturing: A processes and systems approach. CIRP Annals - Manufacturing Technology 61(2), 587–609 (2012), doi:10.1016/j.cirp.2012.05.002.
[14] Neborák, I., Báňská, V.Š.: Mechatronické systémy: pro kombinované a distanční studium, Ostrava (2009)
[15] Blecha, P., et al.: Průběžná zpráva za druhý rok řešení projektu FR-TI3/655 – Ecodesign ve stavbě obráběcích strojů na VUT v Brně, Brno p. 175 (2012)
[16] Houša, J.: Implementační akční plán oboru strojírenské výrobní techniky, Praha, p. 250 (2010)
[17] Blecha, P., et al.: Device for electric power measurement at machine tools. MM Science Journal 5 (2012) ISSN 1805-0476

Thick Film Polymer Composites with Graphene Nanoplatelets for Use in Printed Electronics

D. Janczak[1], M. Słoma[1,2], G. Wróblewski[1], A. Młożniak[2], and M. Jakubowska[1,2]

[1] Warsaw University of Technology, Faculty of Mechatronics,
8 sw. A. Boboli st., 02-525 Warsaw, Poland
dan.janczak@gmail.com
[2] Institute of Electronic Materials Technology, 133 Wolczynska st, 01-919 Warsaw, Poland
maljakub@mchtr.pw.edu.pl

Abstract. The paper presents the results of the investigation into layers based on graphene nanoplatelets in polymer resin. Several types of polymer composition with different amount of GNP's were prepared by modified mixing process used in thick film material preparation. The composite structure was observed under a scanning electron microscope and atomic force microscope. Electoral and mechanical properties of screen printed layers on flexible PET foil were checked. Banding tests show good adhesion to polymer substrate and proved that GNP's are good for reinforcing or as a conductive additive in composite materials.

1 Introduction

Graphene, a recently discovered two-dimensional allotropic form of carbon characterized by extraordinary properties, has focused the attention of scientists from all over the world. The high thermal and electrical conductivity [1] and incredibly high strength and flexibility [2] with an almost complete transparency of light in visible lengths [3,4] makes the graphene nanoplatelets an ideal functional phase material for polymer composites. The elimination of metal powders, graphite and carbon black composite with a low resistance to deformation enabled the formation of a new group of materials for use in flexible printed electronics. Low cost of implementation and high efficiency for the unit production and large series have given rise to ever-increasing demand for new types of conductive pastes and inks. Graphene layers are described in various applications like transparent electrodes [5], supercapacitors [6,7], FET transistors [8], photovoltaics [9,10], chemical and biochemical sensors [11-12].

2 Materials

Graphene nanoplatelets (GNP's), used in the present study as a reinforcing and conductive additive in composite with polymer carrier, were obtained by a chemical

T. Březina and R. Jabloński (eds.), *Mechatronics 2013*,
DOI: 10.1007/978-3-319-02294-9_10, © Springer International Publishing Switzerland 2014

method. Materials supplied by Cheap Tube Inc. have average thickness of 10nm, 100 m^2/g of surface area and average particle diameters of 15 µm, what shown on SEM photo.

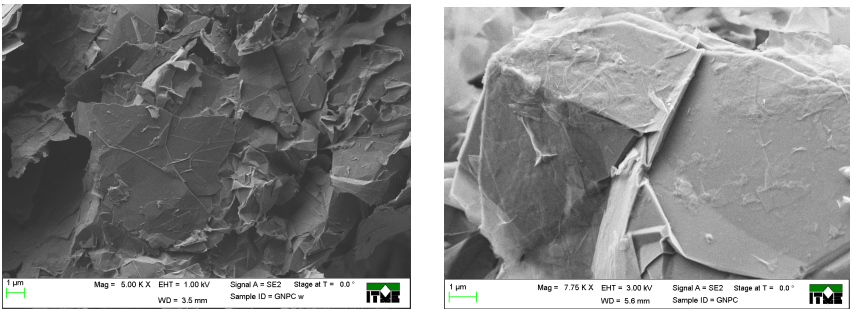

Fig. 1 SEM image of used Graphene Nanoplatelets GNP's material

As a fillers authors used 8 wt% Polymethylmethacrylate (PMMA) with butyl carbitol acetate solvent. Surfactants of NOF Corporation MALIALIM series were used to prepare well dispersed polymer-nanocarbon compositions.

2.1 Pasts Preparation Process

Nano carbon fillers with dispersants in toluene solution were sonicated for 120 min at room temperature (35 kHz, 300W). This method is more effective at dispersing particles into viscous systems than other techniques [13]. After evaporation of toluene graphene nanoplatelets with PMMA matrix were rolled twice on three roll mills with silicon carbide (SiC) roller. Samples prepared on screen printer AMI Presco typ 242 were cared at 120°C for one hour. On figure 2 shown SEM photo for the resulting thick films, a) 5 wt% content of GNP's and b) 10 wt% content of GNP's.

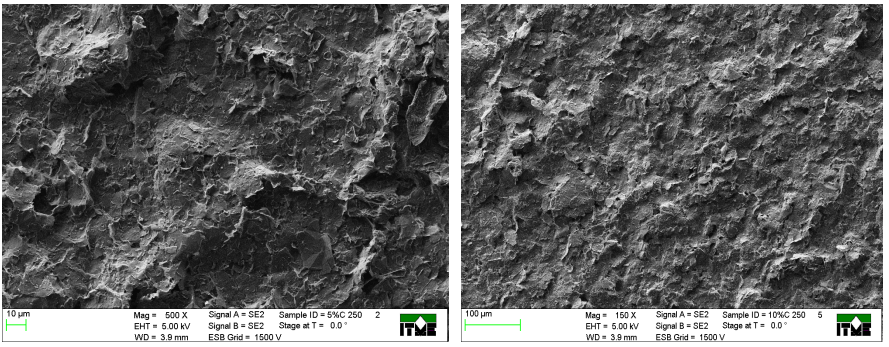

Fig. 2 SEM image of Graphene Nanoplatelets GNP's layers a) 5 wt% content of GNP's and b) 10 wt% content of GNP's

3 Results

Several types of polymer composition with different amount of GNP's were prepared. Sample for electrical and mechanical testes screen printed on polymer substrates. Test shape had ten paths of different length. Resistance of all paths was measured and results were divided by the length of paths' value to determined resistance per square of screen printed layers. Percolation threshold of polymer nanocomposites containing graphene nanoplatelets was observed for past 1,25 wt% GNP's.

Table 1 Results of resistance per square measurement

Composition	Resistance per square R/□ [kΩ]
1 wt% GNP's / 8 wt% PMMA	no measurable
1,25 wt% GNP's / 8 wt% PMMA	617,3
1,5 wt% GNP's / 8 wt% PMMA	23,4
2 wt% GNP's / 8 wt% PMMA	8,4
3 wt% GNP's / 8 wt% PMMA	0,734
5 wt% GNP's / 8 wt% PMMA	0,102
10 wt% GNP's / 8 wt% PMMA	0,086
13,5 wt% GNP's / 8 wt% PMMA	0,020

Resistance of the screen printed layer can be reduced in several ways. Firstly, higher cure temperature causes evaporation of the matrix and resistance decrease. Polymer substrate works to 230°C, polyamide withstands temperature up to 400°C, but adhesion disappears after hour in 350°C. Longer holding time also reduces the resistance but the most desirable is the addition of a dispersant. Some surfactants reduce resistance fivefold.

Results of stiffness measurements were made at Labsoft, Figure 3 shows the measurement of DMT module. Visible traces areas with high stiffness (about 20 GPa) - possibly reflecting the intense presence of the harder phase. On the figure4, a statistical distribution of stiffness of the visible area.

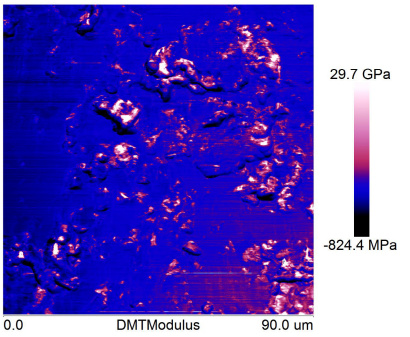

Fig. 3 Results of DTM Modules measurement

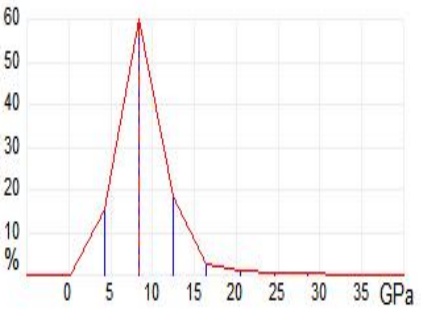

Fig. 4 Statistical distribution of stiffness of the visible area

AFM measurement results for GPN's layers shown figure 5, topography map was measured in Peak Force Tapping mode (50µm) with TAP525 blade (200 N / m), of the imaging speed 0.5 Hz. Measured RMS surface roughness was 363 nm.

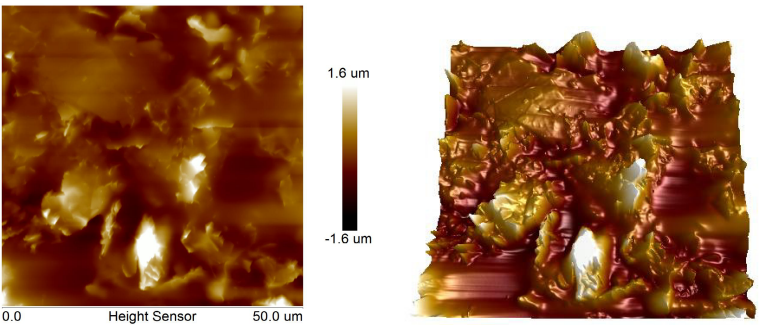

Fig. 5 AFM measurement results for GPN's layers

Authors compared different types of graphene-composites during the mechanical fatigue tests. Investigation proved that graphene layers have the same mechanical resistance as carbon nanotubes layers [14]. Mechanical fatigue tests verified the strength of the conductive layer and proved good adhesion to polymer surface after bending test. After nearly 50 000 cycles, the paths resistance of paste based on GNPs changed +/- 5%. Figure 6 shows the dependence of resistance changes during fatigue tests for graphene paths.

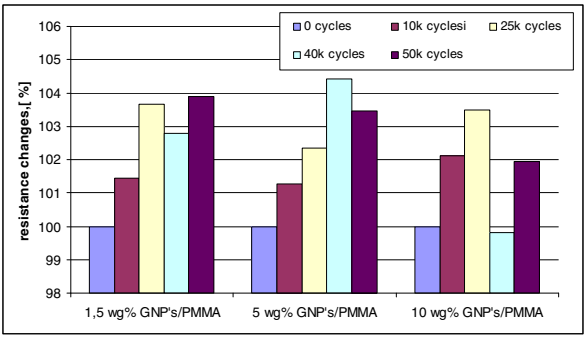

Fig. 6 Resistance changes during fatigue tests for graphene paths

4 Conclusions

Polymer composites containing graphene nanoplatelets were investigated. Percolation threshold of polymer nanocomposites was observed for samples with 1.25% GNP's, samples with 1,5 wt% GNP's content in composition with resistance per square 23,4 kΩ and transmissibility 20% were used like a transparent electrode for electroluminescent displays [15,16].

Fig. 7 Electroluminescent displays with screen printed transparent graphene composite electrode

Screen printed layers with GNP's can by used to detect pressure, authors used them as pressure-sensitive areas in sensors with comb electrodes [17]. Results of mechanical fatigue tests proved high durability of the sensors with almost unchanged resistance of the layers after 50'000 bending cycles. Good adhesion to the polyester foil substrate was also confirmed. Graphene nanoplatelets composites with polymer resin can by useful in many applications on flexible substrates like a conductive and resistive paths.

References

[1] Park, S., Ruoff, R.S.: Chemical methods for the production of graphenes. Nature Nanotechnology 4, 217 (2009)
[2] Lee, C., Wei, X., Kysar, J.W., et al.: Measurement of the Elastic Properties and Intrinsic Strength of Monolayer Graphene. Science 321(5887), 385–388 (2008)
[3] Nair, R.R., Blake, P., Grigorenko, A.N., et al.: Fine Structure Constant Defines Visual Transparency of Graphene. Science 320(5881), 1308 (2008)
[4] Supinda, W., Dmitriy, A.D., Sasha, S., Richard, P., Inhwa, J., Geoffrey, H.B.D., Guennadi, E., Shang-En, W., Shu-Fang, C., Chuan-Pu, L., SonBinh, T.N., Rodney, S.R.: Graphene–Silica Composite Thin Films as Transparent Conductors. Nano Letters 7, 1888–1892 (2007)
[5] Becerril, H.A., Mao, J., Liu, Z., Stoltenberg, R., Bao, M.Z., Chen, Y.: Evaluation of Solution-Processed Reduced Graphene Oxide Films as Transparent Conductors. ACS Nano 2, 463–470 (2008)
[6] Yan, W., Zhiqiang, S., Yi, H., Yanfeng, M., Chengyang, W., Mingming, C., Yongsheng, C.: Supercapacitor devices based on graphene materials. J. Phys. Chem. 113, 13103–13107 (2009)
[7] Stoller, M.D., Park, S.J., Zhu, Y.W., An, J.H., Ruoff, R.S.: Graphene-based ultracapacitors. Nano Lett. 8, 3498–3502 (2008)
[8] Kang, S.J., Kim, B., Kim, K.S., Zhao, Y., Chen, Z., Lee, G.H., Hone, J., Kim, P., Nuckolls, C.: Inking Elastomeric Stamps with Micro-Patterned; Single Layer Graphene to Create High-Performance OFETs. Advanced Materials (2011)
[9] Ding, J.N., Yu, C.T., Yuan, N.Y., Liu, Y.B., Fan, Y.: High-quality GS/TiO2 composite for the photoanode of the dye-sensitized solar cells. In: International Conference on Materials for Renewable Energy & Environment (ICMREE), pp. 90–94 (2011)

[10] Słoma, M., Wróblewski, G., Janczak, D., Młożniak, A., Jakubowska, M.: Conductive coatings based on nanomaterials deposited with spray coating technique. Microelectronic Materials and Technologies 1, 44–50, ISSN 0239 – 7129
[11] Bo, Y., Wang, W., Qi, J.: A DNA biosensor based on graphene paste electrode modified with Prussian blue and chitosan. ANALYST 136, 1946–1951 (2011)
[12] Parvin, M.H.: Graphene paste electrode for detection of chlorpromazine. Electrochemistry Communications 13, 366–369 (2011)
[13] Wang, Q., Xia, H.S., Zhang, C.H.: Preparation of polymer/inorganic nanoparticles composites through ultrasonic irradiation. J. Appl. Polym. Sci. 80(7-10), 1478–1488 (2000)
[14] Jakubowska, M., Słoma, M., Janczak, D., et al.: Printed transparent electrodes with graphene nanoplatelets. Elektronika rok 53(6), 97–99 (2012)
[15] Wróblewski, G., Janczak, D.: Screen printed, transparent and flexible electrodes based on graphene nanoplatelets pastes. In: Proceedings of the SPIE, vol. 8454
[16] Jakubowska, M., Słoma, M., Młożniak, A., Janczak, D., Wróblewski, G.: Investigation of screen printed thick film layers based on graphene nanoplatelets. ITR Progress in Eco-Electronics 2, 74–82
[17] Janczak, D., Wróblewski, G.: Screen printed resistive pressure sensors fabricated from polymer composites with graphene nanoplatelets. In: Proceedings of International PhD Workshop OWD 2012 - Conference archives PTETiS, vol. 31, pp. 171–175 (2012)

Safety Module for the System of Verticalization and Aiding Motion of the Disabled

D. Jasińska-Choromańska, B. Kabziński, M. Matyjewicz-Maciejewicz, and D. Kołodziej

Warsaw University of Technology, Faculty of Mechatronics,
Institute of Micromechanics and Photonics, ul. Boboli 8, 02-525, Warsaw, Poland
danuta@mchtr.pw.edu.pl

Abstract. Apart from mechanical problems in designing a System of Verticalization and Aiding Motion (SVAM), a development of a safety module is essential for its functionality and safety. This paper describes a decision process related to SVAM, and application of a Man-Technology-Environment model in creating a classification of risk estimation. The functional diagram of the safety module is described, and realization of a selected safety procedure regarding primary and secondary function is presented.

1 Introduction

The paper presents an analysis of a safety module for the System of Verticalization and Aiding Motion (SVAM) (Fig. 1), which is a first step in defining detailed technical requirements pertaining to the module.

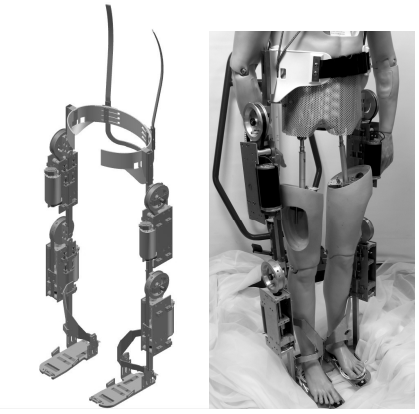

a) b)

Fig. 1 a) System of Verticalization and Aiding Motion (SVAM), b) SVAM installed on dummy

T. Březina and R. Jabloński (eds.), *Mechatronics 2013*,
DOI: 10.1007/978-3-319-02294-9_11, © Springer International Publishing Switzerland 2014

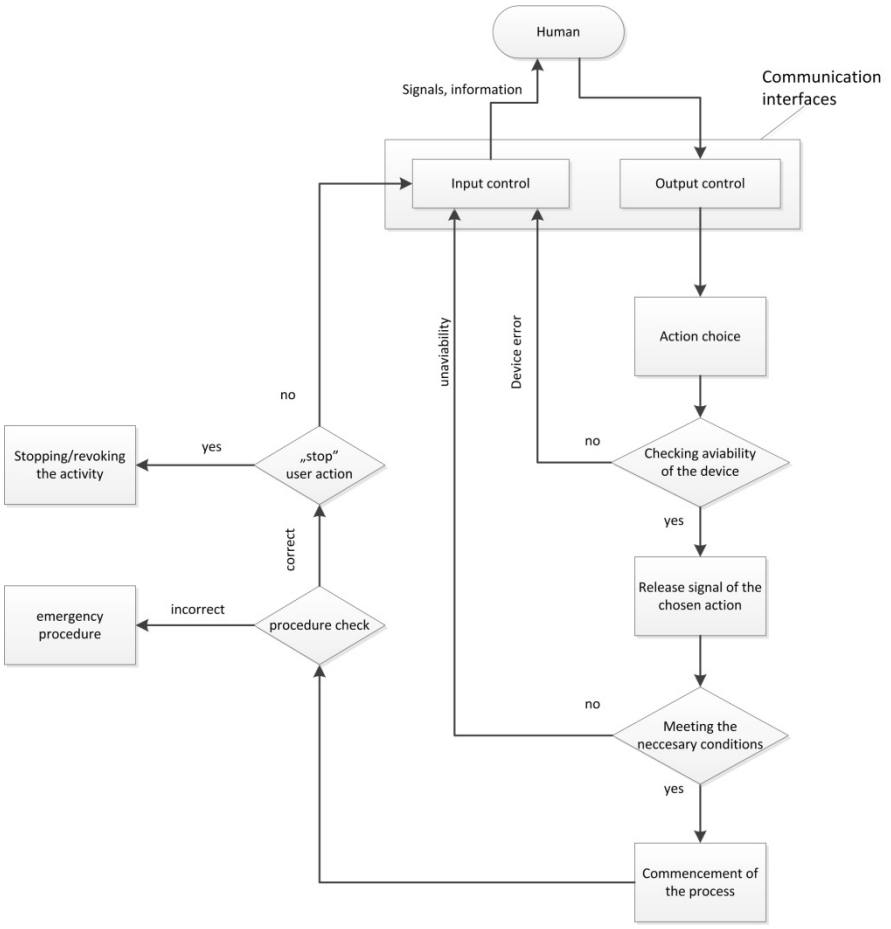

Fig. 2 Diagram of the decision process of the SVAM including emergency procedures

The System of Verticalization and Aiding Motion (SVAM) shown in Fig. 1 is an orthotic robot, i.e. a programmable mechanism aiding a handicapped function of the human organism – in this case the locomotor function. It has been elaborated within an ECO-Mobility project at the Faculty of Mechatronics, Warsaw University of Technology. Among its basic functions specified at the beginning of realization of the project is moving on flat surface, sitting down and rising as well as ascending and descending the stairs, with accordance to the diagram shown in Fig. 2. Similar schema of algorithm creating is used while creating movement algorithm of amphibian gait [6].

2 Functionality of the Safety Module

2.1 Introduction

Elaboration of a safety module requires to specify at the very beginning its range of operation, define the aim and function that it must realize as well as a method of realizing it. In order to do that, one has analyzed the risk [1] basing on a M-T-E model (Man-Technology-Environment) [2,7]. The result was a list, as exhaustive as possible, pertaining to the hazards along with a related qualitative and quantitative description. As a result of the analysis, the task of the safety module was limited to protection of the user of the system against a fall and its consequences.

According to [3], fall is generally a consequence of typical everyday activities, and is caused by events that are hard to foreseen, such as stumbling, slipping, or loosing one's balance (Fig. 3).

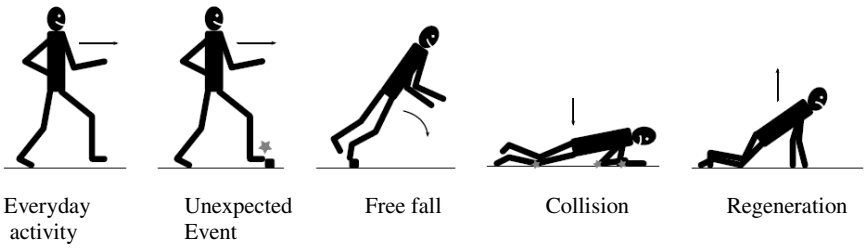

Fig. 3 Five phases of the fall, as in [3]

Should a hazardous situation occur, it is especially the number of points of support (activity, stage in the relevant cycle) and direction of the fall that are significant factors diversifying an indicator the hazard.

Realization of a task defined in such a way, can be carried out in many ways, i.e. by,

- preventing the causes of the fall,
- reducing the effects of the fall,
- counteracting the causes of the fall.

In order to realize protection of the user of SVAM against a fall and its consequences, the third method was accepted, i.e. counteracting the causes.

2.2 The Primary Function

Counteracting the causes of a fall are accepted as the primary function of the safety module, whereas activities aimed to obtain a contrary effect are regarded as counteracting an event.

In Table 1, there are presented methods regarded as the primary functions of the safety module.

Table 1 Methods of reacting to events resulting in a fall

Change of the area of support	Regaining the original area of support.
	Obtaining a new, stabile area of support.
	Shifting the center of gravity, so that it is found above a new area of support.
Shift of the center of gravity	Returning the center of gravity to a position above the area of support.
	Extending the area of support, so that it contains a new center of gravity.
Action of a constant force	Shifting the center of gravity, so that the resultant force is contained within the area of support.
	Extending the area of support, so that the resultant force is contained within it.
Combination of the above	

2.3 Auxiliary Function

Auxiliary functions of the safety module are all the functions, which are necessary to ensure execution of the primary function, as well as to meet the requirements related to the whole SVAM.

Additional auxiliary functions can be activities aimed at improving operation of the mechanism realizing the primary function. One of such activities that is realizable without changing the existing design of SVAM, based exclusively on control procedures, is bringing the system as well as the user to a low position.

It is a natural method of reducing effects of a fall, yet untypical as far as elimination of its causes is concerned. This activity increases the stability angle of the system as well as decreases the arm of the gravity force causing a fall (Fig. 4a and 4b, respectively).

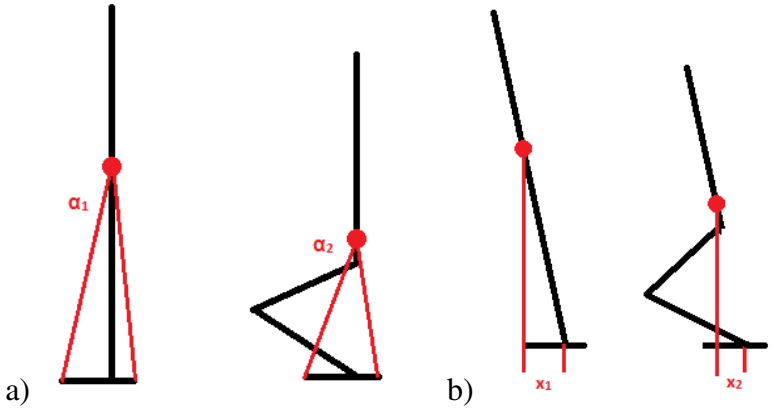

Fig. 4 Influence of the low position on, a) stability angle (α1<α2); b) arm of the force (x1>x2)

Realization of such operation can be based on following defined trajectories, elaborated especially for this purpose, or on making use of the fact that the mechanism is not self-locking – while the drives are left unpowered, SVAM may be allowed to freely fold due to the gravity force.

2.4 Functional Diagram of the Safety Module

Operation of the safety module is based on two algorithms: operational and preoperational.

Realization of the above algorithms as well as the primary function is possible while using a device equipped in the modules presented in the block diagram presented below (Fig. 5).

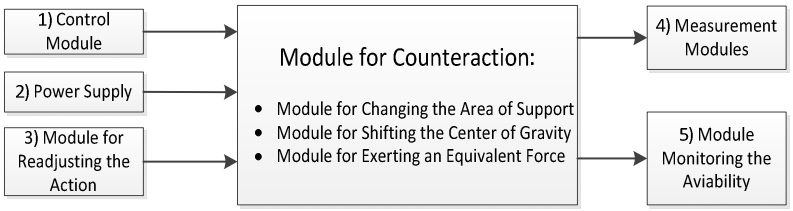

Fig. 5 Functional diagram of the safety module of SVAM

The safety module is activated at the moment, when a signal from the control module (1) has been received. It is a moment, when the aim of operation of the system is being changed from realization of the accepted trajectories and motion into protection of health and life of the user. Along with the signal indicating a dangerous situation, if need be, there are also sent all the necessary parameters.

Once the safety module gets activated, it receives energy from the power supply (2). Because of a short-time character of its operation – within long time intervals, yet very intensive, the energy must be supplied in pulses, within a short time. Once the necessary energy has been supplied, the power supply can remain inactive until the moment the safety module is prepared for another activation – whether by a service inspection, replacement of service parts, or hardware reset.

According to the related assumptions, SVAM is adaptable to individual characteristics of the user (weight, height, etc.). Because of this fact, a possibility of adjusting reaction of the safety module to analogous characteristics is foreseen, whether by means of mechanical or software operations. At the diagram in Fig. 6, this function is specified as the Module for Modifying the Parameters (3).

Mechatronic character of the safety module indicates application of the measurement modules (4). Such modules, first of all, are necessary for checking effectiveness of actuation of the mechanism, or realization of its control (provided such control is necessary). A particular measurement module specified in the diagram is the module monitoring the availability (5), necessary because of the fact that the safety module must operate faultlessly in moments that are impossible to foreseen, what requires its constant availability.

2.5 Realization of the Primary Function

The proposed solution consists in fixing to the system an actuator and a mass of high inertia, which in case of activating the safety program, would be accelerated by certain torque of a possibly high value. The torque, with accordance to the third law of motion, would also affect the system, with the result of making the fall much slower.

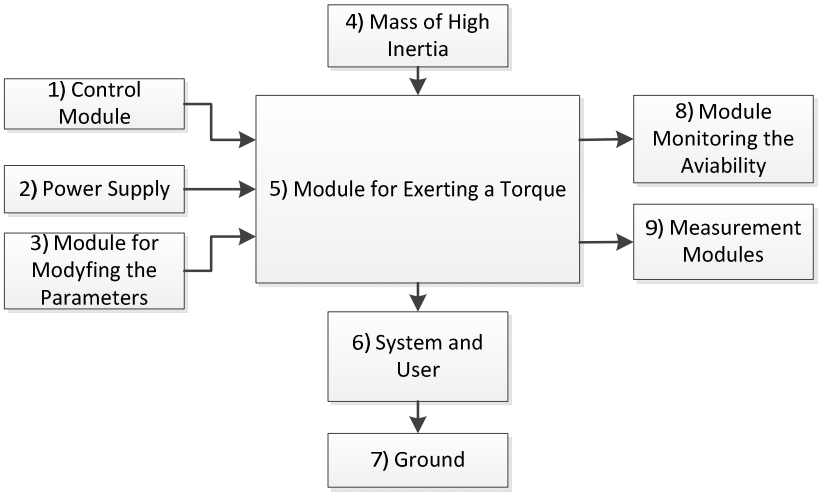

Fig. 6 Block diagram of the safety module based on exertion of an external torque

At the moment of receiving the signal indicating a dangerous situation from the control module (1), the module for exerting a torque (5) begins to accelerate the mass of high inertia (4), with the result of making the fall of the user equipped in the system (6) much slower. The module for modifying the parameters (3) should allow the maximal torque developed at the actuator (5) to be monitored, as well as direction in which it acts. As far as this version of the safety module is concerned, the module monitoring the availability (8) should be checking, among other things, availability of the power supply, or readiness of the actuator to perform a turn, and the measurement modules (9) should provide a feedback related to the effectiveness of suppressing the fall by means of this mechanism.

3 Discussion of the Accepted Solution

The torque mechanism presented in sec. 2.5 is, first of all, effective – an appropriately applied torque will always counteract a fall. However, because of limitations related to the mass and the power of the motor, it cannot completely stop a fall under a considerable tilt, and requires to foreseen direction of the fall (even though, theoretically, the mechanism is able not only to suppress the fall, but also

to revoke it). Therefore, it is foreseen to equip the safety module in a tilt sensor, most preferably based on application of MEMS accelerometers, as suggested e.g. in [4, 5].

It is worthwhile noticing that the mechanism operates on the basis of accumulating the energy in a flyweight, so once operation of the safety module is completed, while braking the flyweight, in a natural way, it would create a torque contrary to the one used when the safety program is activated.

4 Conclusions

Because of a wide range of problems related to the module, generally called the safety module, a functional structure of the module has been based on a thorough risk estimate, careful specification of the range of operation and a review, as exhaustive as possible, of the potential solutions at successive stages. As far as the project is concerned, one presented not only a proposition of the design solution, but also a whole nomenclature and a base of solutions and alternative functions rejected during a first analysis of the problem. The paper presents also chosen problems and solutions of the emergency safety module.

Acknowledgements. The presented works have been completed within the ECO-Mobility project, No. UDA-POIG.01.03.01-14-154/09-00, financed by the European Community.

References

[1] Duncan, W.R.: A guide of the project management body of knowledge. Appendix G; Project Management Institute (2000)
[2] Szopa, T.: Niezawodność i bezpieczeństwo, Oficyna Wydawnicza Politechniki Warszawskiej, Warsaw (2009) (in Polish)
[3] Abbate, S., Avvenuti, M., Corsini, P., Light, J., Vecchio, A.: Monitoring of Human Movements for Fall Detection and Activities Recognition in Elderly Care Using Wireless Sensor Network. A Survey, Wireless Sensor Networks: Application - Centric Design (2010)
[4] Łuczak, S.: Specific Measurements of Tilt with MEMS Accelerometers. In: Mechatronics. Recent Technological and Scientific Advances, pp. 705–711 (2011)
[5] Łuczak, S., Oleksiuk, W., Bodnicki, M.: Sensing Tilt with MEMS Accelerometers. IEEE Sensors J. 6(6), 1669–1675 (2006)
[6] Bodnicki, M., Sęklewski, M.: Design of Small-Outline Robot – Simulator of Gait of an Amphibian. In: Recent Advances in Mechatronics, pp. 77–81 (2007)
[7] Wierciak, J.: Improvement of Performance of Precision Drive Systems by Means of Additional Feedback Loop Employed. In: Recent Advances in Mechatronics, pp. 495–499 (2007)

Electromagnetic Coil Gun – Construction and Basic Simulation

B. Skala and V. Kindl

University of West Bohemia in Pilsen, Faculty of Electrical Engineering,
Univerzitni 26, 306 14, Plzen, Czech Republic
{skalab,vkindl}@kev.zcu.cz

Abstract. A single-stage, sensorless, coil gun was designed to demonstrate the capability to accelerate a ferromagnetic projectile to high velocity. This paper summarizes all important steps during coil gun design, such as physical laws of the coil gun, preliminary calculations, the testing device and the final product. The electromagnetic FEA model of the capacitor-driven inductance coil gun was constructed to be able to optimize the coil's dimensions. The driving circuit was implemented as a dynamic model for the simulation of current. The coil gun was not designed for really shooting applications, i.e. the projectile is accelerated to a relatively low speed.

1 Introduction

Electromagnetic accelerating systems are usually constructed as rail guns [1] or coil guns [2]. The rail gun is conceptually more simple then the coil gun, but has some inherent problems with plasma [3] during the projectile launches. That is why this conception is not used here.

On the other hand, the coil gun is much more suitable for common applications even though it needs some additional supporting facilities [4] such as energy accumulator, switcher and driver. Its main advantage lies in the elimination of almost all negative phenomena damaging the launch device.

Modern structures usually use single or multi-stage linear accelerator similar to a linear motor. The device typically consists of an electromagnetic coil, capacitor, switch, barrel and movable core - projectile. The coil can be wound as a solenoid electromagnet with a ferromagnetic projectile placed at one of its ends (starting position).

The launching process can be divided into three phases. The situation can be reflected in Fig.1.

In the first phase the energy needed for acceleration is stored in the capacitor [2] **C** using laboratory direct current source **U** (switch position 1). In the following phase, the energy must be transmitted to the projectile in the shortest time possible. The FET transistor working as a contactless switcher can be used for this purpose (switch position 2). This will provide a high-energy coil current peak creating a

T. Březina and R. Jabloński (eds.), *Mechatronics 2013*,
DOI: 10.1007/978-3-319-02294-9_12,

strong electromagnetic field. This field pulls the projectile inside the barrel with high acceleration. For the successful projectile launch the precise timing is necessary [5]. The current pulse must be switched off before the projectile passes the half of the coil length to prevent the projectile from becoming arrested at the centre of the electromagnet. In the final, third stage, the projectile leaves the coil and flies on its own momentum.

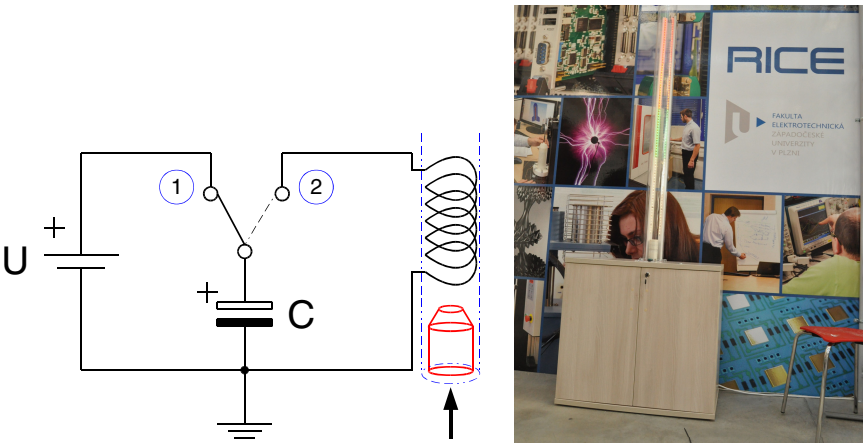

Fig. 1 The principle of launching process and final construction

Electromagnetic accelerating systems are usually constructed as rail guns [1] or coil guns [2]. The rail gun is conceptually more simple then the coil gun, but has some inherent problems with plasma [3] during the projectile launches. That is why this conception is not use here.

2 The Ejection Coil

The acceleration and speed characteristics of the projectile were computed. In order to get accurate results it was necessary to take into account electrical and mechanical properties in all calculations [5].

The mechanical properties are mainly defined by sizes of the muzzle of the coil gun. The muzzle has a relatively large diameter, hence the inner air can easily flow around the projectile and the damping air pressure is at relatively low level. Based on the same reason the coil must be designed with the suction hole placed in the bottom part of the coil frame.

Finally, the electrical properties are strongly defined by the coil's resistivity and inductivity affecting the time constant of transient response. The inductivity changes with the projectile position.

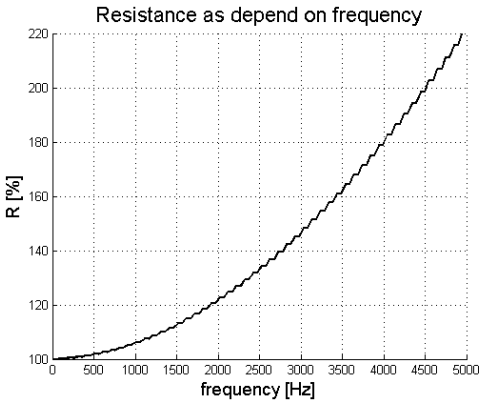

Fig. 2 The coil resistivity as depend on frequency

The resistivity is dependent on the frequency (skin and proximity effect) [6 - 7] of supplying current and cannot be therefore exactly computed by analytical equation. The curve computed by FEA can be seen in the Fig. 2. The magnetic force is dependent on both; the current and the position of the projectile with respect of the coil.

The electromagnetic field of the ejection coil was modelled by FEA (see Fig. 3). The coil has 5 wire layers with 21 turns per one layer which yields the inductivity of cca 12,5 mH (with no ferromagnetic materials). With consideration of the ferromagnetic projectile centre of the coil, the inductivity is more than 2 times higher, i.e. 30,8 mH. This effect causes a variation of time constant during the projectile launches.

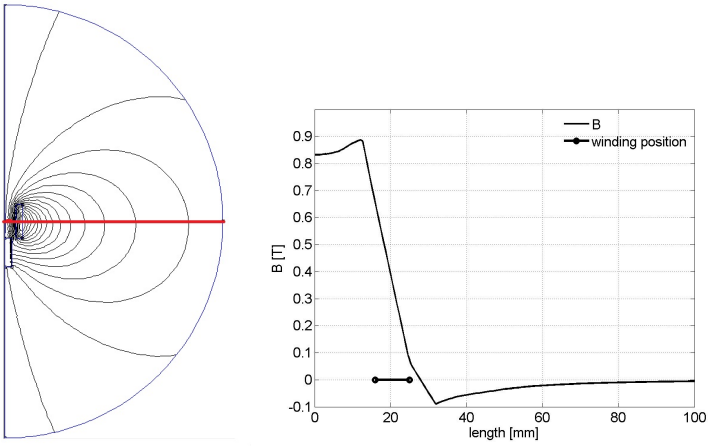

Fig. 3 The magnetic field of the ejection coil - starting position

The force acting on the projectile at its different positions can be seen in Fig. 4.

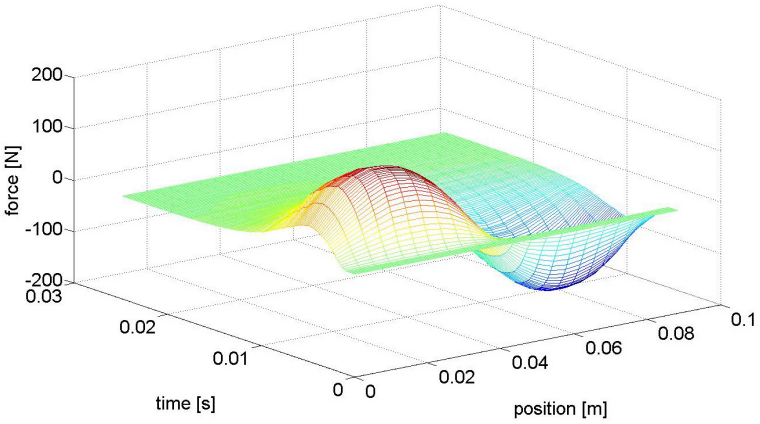

Fig. 4 The matrix of the current and force of the ejection coil

3 The Movement Simulation

The ejection coil has vertical orientation. Due to this fact the projectile movement consists of three phases: The first phase is the vertical uneven acceleration. This part of movement ends immediately when the centre of the projectile passes the centre of the coil. At this point it has a maximum velocity.

In the second phase the projectile decelerates. The phase ends when the projectile reaches the highest position of its trajectory.

The last phase is a free fall.

The projectile acceleration should be described by the equation

$$a = \frac{F}{m} \tag{1}$$

Where the F is the difference between the magnetic and the gravitation force and m is the weight of moving element. The speed can be calculated from

$$v = v_0 + at \tag{2}$$

and the vertical position for various times can be obtained from

$$y = v_0 t + \frac{1}{2} a t^2 . \tag{3}$$

The throw above is described by the relation for an instantaneous speed

$$v = v_0 - gt \tag{4}$$

where v_0 is the initial speed, t is time and g is gravity acceleration. The instantaneous vertical position should be calculated according to

$$y = v_0 t - \frac{1}{2} g t^2 \tag{5}$$

During the free fall downward, instantaneous speed can be calculated as

$$v = gt \tag{6}$$

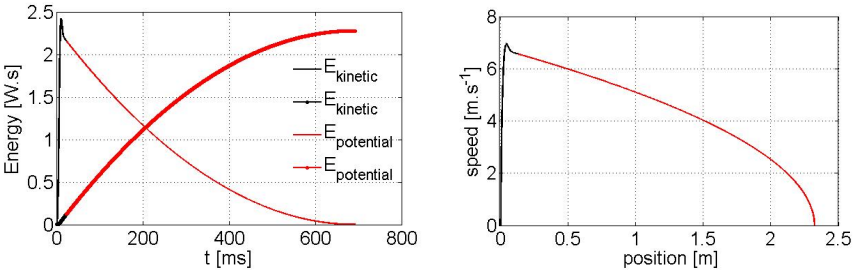

Fig. 5 The energy and the speed as depend on time and position

In the Fig. 5 you can see the energy as dependent on simulation time and the speed of projectile at the instantaneous vertical position.

4 The Electric Circuit Simulation and Measurement

The basic electric circuit was simulated via MATLAB/SIMULINK see Fig 6. At the first moment, the capacitor charges from the control voltage source through the switcher (IGBTD switched off). After the charging process the switcher disconnects and the coil gun is ready to launch. When the IGBTD switches on, the current flows from the capacitor into the launching coil.

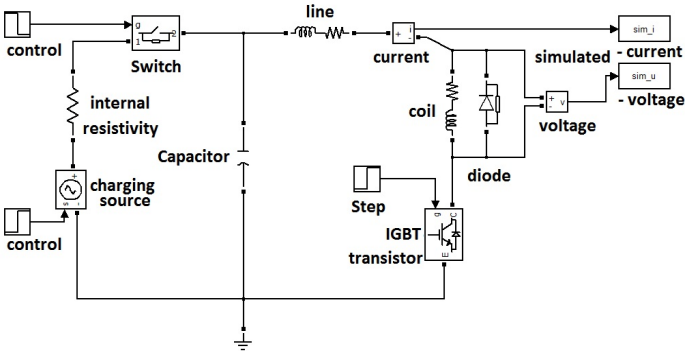

Fig. 6 The diagram of connection of power circuit

In the Fig 6 the component "line" represents the parameters of the supplying cable.

In the following picture 7 can be seen the simulated and the measured coil's current, in figure 8 the voltage.

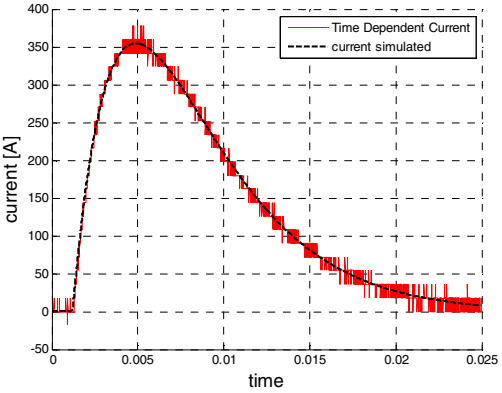

Fig. 7 The Measured and simulated coil's current

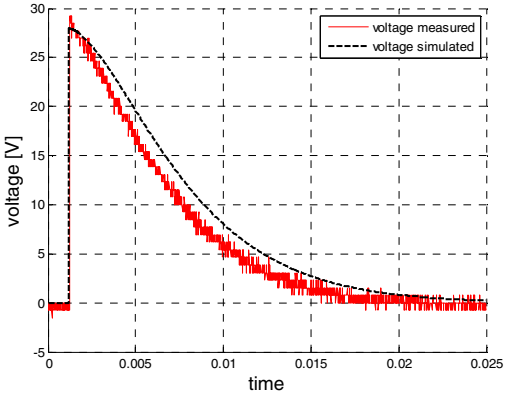

Fig. 8 Measured and simulated coil's voltage

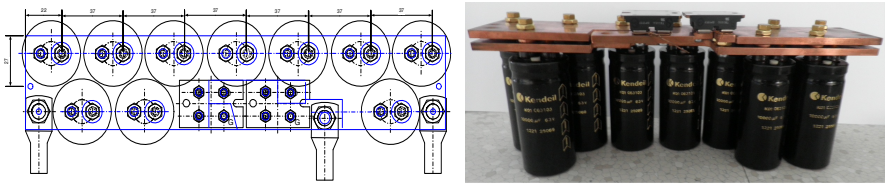

a) b)

Fig. 9 (a) The drawing of one layer of the sandwich (b) The construction of 2-layer sandwich

In Figure 9a can be seen the drawing of one layer of the "sandwich". It is necessary to use the sandwich construction for minimizing the parasite wires inductivity. In Figure 9b, in the top, you can see the diode and FET transistor. In case of large parasite inductivity the enormous current causes the overvoltage and destroys the semiconductors. In addition, both semiconductors are static sensitive device.

5 Conclusion

This paper has clearly shown the outline of a single-stage, sensorless, coil gun system. It has also demonstrated a few problems arising from the strong coupling between the electrical and mechanical properties of the coil.

The coil needs to be designed with respect to the varying time constant of transient response. This must be considered from the requested acceleration and output speed of the projectile (the current pulse must be down before the projectile passes the half of the coil length).

A high capacitor is needed for charging the energy. This capacitor must be implemented by special sandwich board (capacitors connected in parallel) because of the proper discharging current distribution.

Acknowledgments. This work was supported by project GA ČR No. 102/09/1164 and by European Regional Development Fund and the Ministry of Education, Youth and Sports of the Czech Republic under the Regional Innovation Centre for Electrical Engineering (RICE), project No. CZ.1.05/2.1.00/03.0094." and supported by the project SGS- 2012-071. This article was supported by an incentive system University of West Bohemia, part of the POSDOC.

References

[1] Keshtkar, A., Gharib, L., Abbasi, M.: Comparison between conventional railgun and two-turn railgun by 3D- FEM. In: 2012 16th International Symposium on Electromagnetic Launch Technology (EML), May 15-19, pp. 1–5 (2012)

[2] Guo, L., Guo, N., Wang, S., Qiu, J., Zhu, J.G., Guo, Y., Wang, Y.: Optimization for capacitor-driven coilgun based on equivalent circuit model and genetic algorithm. In: Energy Conversion Congress and Exposition, ECCE 2009, September 20-24, pp. 234–239. IEEE (2009)

[3] Yamori, A., Ono, Y., Sasaki, S.: Development of a plasma armature railgun with two distributed power supplies. In: 2004 12th Symposium on Electromagnetic Launch Technology, May 25-28, pp. 149–154 (2005)

[4] Kaye, R.J.: Operational requirements and issues for coilgun electromagnetic launchers. IEEE Transactions on Magnetics 41(1), 194–199 (2005)

[5] Bengui, Z., Yanjie, C., Jie, W., Huijin, W., Xuehui, C.: Magnetic-Structural Coupling Analysis of Armature in Induction Coilgun. IEEE Transactions on Plasma Science 39(1), 65–70 (2011)

[6] Dwight, H.B.: Proximity Effect in Wires and Thin Tubes. Transactions of the American Institute of Electrical Engineers XLII, 850–859 (1923)

[7] Dwight, H.B.: Electrical coils and conductors, their electrical characteristics and theory. McGraw-Hill book company, inc. (1945)

Generating Code Consistent with Simulink Simulation for Aperiodic Execution on a Target Hardware Powered by a Free RTOS

V. Lamberský[1], J. Križan[2], and A. Andreev[2]

[1] Mechlab, Brno University of Technology, Faculty of Mechanical Engineering, Technicka 2, 616 69, Brno, Czech Republic
ylambe00@stud.fme.vutbr.cz
www.mechlab.cz
[2] UNIS - Mechatronics and embedded systems, Jundrovská 33, 62400 Brno-Komín, Czech Republic
unis@unis.cz

Abstract. This paper presents concepts for implementing a variable step scheduled code on a low cost hardware using automatically generated code from Simulink running on a Free RTOS powered hardware. For models, which use a varying computing step, implementing variable step scheduler, instead of the default automatically generated fixed step scheduler, can improve algorithm performance. Concept and principles for creating Simulink model for code generation, which behaves the same way as generated code does, are explained in details. Previously described approach for automatically generated code from Simulink which implements variable step simulation is demonstrated using simple algorithm, running on a Cerebot MX7cK hardware.

1 Introduction

Today embedded applications in consumer and industrial applications are becoming more and more complex [1]. Compared to older generation, where embedded microcontrollers had a limited computing power, they were used only for simple tasks (e.g. simple control loop consisting of PID, state space or similar control algorithm). These algorithms are, almost without exception, using a constant computing step (with or without sub rates), implementing a rate monolithic scheduler, which requires only one periodic event for synchronization with real time (considering all computing steps are multiples of a base rate, which is a common requirement).

On the other hand, today systems usually implement advanced algorithms known from desktop-computer like environments (e.g. interfacing with user via display). This category of algorithms usually does not require strong real-time periodic execution. In some cases implementing aperiodic scheduling might help to save hardware resources and therefore making the system cheaper.

T. Březina and R. Jabloński (eds.), *Mechatronics 2013*,
DOI: 10.1007/978-3-319-02294-9_13,

The Matlab/Simulink software became a standard for developing control algorithms [2, 3]. It was only natural to introduce Embedded Coder toolbox which can generate efficient ("hand written like") C code [4, 5].

However, Simulink simulations were designed to use a constant step solver, where all rates are derived from base step size and the base step size remains constant for entire application lifespan. This would prevent introduce and simulate any asynchronous events (like interrupts), therefore additional mechanisms were introduced for creating concurrent simulations [6]. However, the standard Simulink tools for concurrent simulations only support the VxWorks operations system for code generation. This system might be not suitable as this OS is not very popular and does not have too many ports for different targets.

These restrictions lead to a need to develop another concept, which would enable development of dynamically scheduled applications in Simulink environment for embedded MCU easily ported to any RTOS (Real Time Operating System).

This paper presents a method based on a simulated scheduler to generate aperiodically executed code from Simulink. The Free RTOS [7] is used for aperiodic scheduling of automatically generated code on target hardware and modeled scheduler simulates the Free RTOS behavior in Simulink simulation. Thus, the same behavior of simulation and generated code was achieved.

2 Specific Properties of Generated Code and Simulation

Every bigger project consists of several separated modules. This is necessary as partitioning into independent modules allows parallel coding which enables shortening of the application development cycle [8]. The calling of prepared functions is done from main, timing module (usually some version of OS).

When following the V development cycle [9], it suggests developing a model, which is tested in consequent step.

Therefore, the desired state is to have a simulation which behaves the same way as the generated code does when executed. When simulating and generating code from Simulink targeted for embedded applications [10], as we have to consider:

- The scheduling method (hooking to a target specific scheduler)
- Interfacing with user defined functions
    - General C functions
    - Target specific C functions
        - Not required during simulation
        - Required during simulation

Since we can't simply modify the Matlab scheduler during simulation, we have to simulate the scheduler in Simulink simulation. E.g. each simulation step is an equivalent of "tick" event and the scheduler decides if a task should start and eventually calls a subsystem (which simulates activating a task).

The general C functions do not use target specific constructs and therefore, the same function can be used for code generation and simulation. On the other hand, target specific functions (interfacing with CPU peripherals) are different for

simulation and target hardware. Therefore, we need to provide different C functions for simulation and for code generation.

Some implemented functions do not have to be simulated (might be empty during simulation). For instance the *DispData(A)* function (described later) is empty for simulation, since we do not need to simulate the display procedure during simulation time.

Some functions have to have different functionality in simulation and for code generation. For instance the function *PeriodMult(n)* (mentioned in next sections), sets during the simulation a variable which is used by scheduler to enable or disable code for simulation and during the code generation process sets a variable for Free RTOS scheduler defining a period for executing the task generated from Simulink model.

3 Modeling Asynchronous Execution in Simulink Model Designed for Automatic Code Generation

This section explains and compares models targeted for a simple monolithic scheduler and our improved model, which is designed to generate code with a varying step size. The variable step implementation needs third party software (Free RTOS) when executed on target hardware. Various aspects of these implementations in Simulink model and generating code for target hardware are discussed.

3.1 The Description of Implemented Algorithm

To demonstrate the concept of scheduling with a variable computing step, we have created a model which plots measured values on display and changes its sampling frequency based on input signal characteristics. Particularly, if the difference

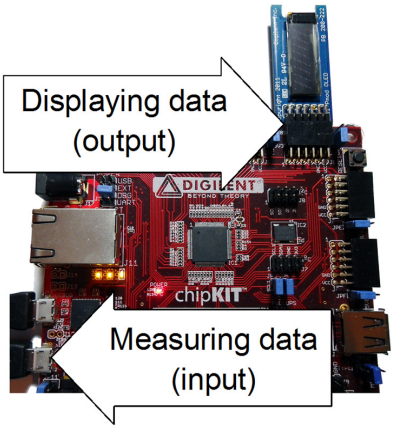

Fig. 1 Experimental hardware setup

between previously measured and actual value is greater than five, the computing loop works faster, if not, it is slowed down three times.

The Cerebot MX7cK hardware with display (PmodOLED) was chosen as a target for implementing this algorithm. Scheme of this platform is presented in Fig. 1. The input (representing a value from sensors) is generated from a separated computer and transmitted via UART interface.

3.2 Simulink Model

Previously described algorithm can be easily modeled using a Stateflow chart. Detecting high fluctuations in measured values will trigger a state transition.

Modeling this type of behavior using standard tools (automatically generated monolithic scheduler) can be done in many ways. For instance, using enabled subsystem or switching to idle states in Stateflow chart. The second option illustrates Fig. 3, left.

This strait forward approach generates waiting states, which waste resources. (The waiting state does nothing, but the simulation has to enter the Stateflow chart to update states).

It would seem more convenient to change execution speed (step size) instead switching to wait states. However, this can't be done directly as only fixed step size solver can be used when simulating model which supports code generation for embedded target. To overcome this limitation, we have chosen a third party scheduler (a Free RTOS) to call generated code. To achieve required consistency between simulation and generated code, a simple model of scheduler was created in Simulink model.

Using the Free RTOS scheduler and changing the step size instead introducing waiting states will generate code with the same functionality, but lower computation intensity (as the waiting states are eliminated), when executed on a target hardware. Described Simulink model which generates aperiodically executed code is illustrated below (Fig. 2.).

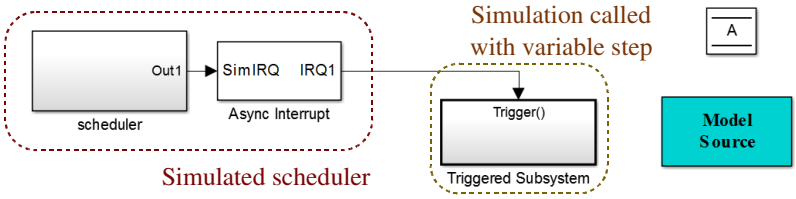

Fig. 2 Scheduler triggering model simulation an OS behavior

In this model, each rate is represented by one state. A Stateflow chart from this model is illustrated in Fig. 3, right. When entering the *LowRateState* state *periodMult(n)* is called. This function changes the "simulation step" by modifying a global variable used by scheduler function.

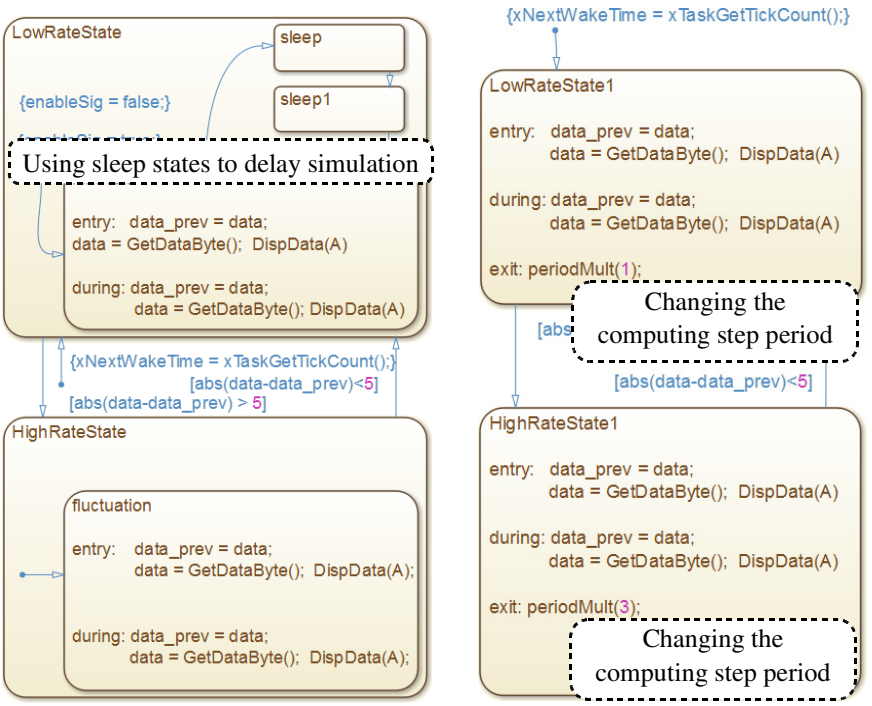

Fig. 3 Simulating the low rate execution speed by introducing sleep states (left) and changing computing step size with simulated scheduler (right).

Booth algorithms, presented in Fig. 3., perform basic sequence of placing measured value to end of a buffer and calling *DispData(A)* function to display data stored in buffer. The difference is in delay mechanism. The monolithic scheduling implementation uses sleep states. These states are not present in the model which uses varying step size for "creating" delay.

3.3 Integrating Generated Code into the Free RTOS

The Free RTOS has many ports, including official one for PIC33 MCU. This port can be imported to MPLAB X environment as is. During our experiments the Free RTOS was used only with one process and configured for cooperative multitasking mode.

As the Simulink coder does not support direct code generation for Free RTOS operating system, a few changes in code needs to be done manually. Particularly:

- Adding a blocking function at the end of generated code, to block code execution after each iteration. (*vTaskDelayUntil(&xNextWakeTime, var_waitMatlab);*).
- Wrapping the generated code into an infinite loop and place into task function.

4 Testing on Real Hardware

Each computing step consists of measuring value and updating the content of display. If the measured value fluctuates, the algorithm is executed every 0.1s, if the measured values become stable the loop is executed every 0.3s.

Following figure illustrates executing scheme of implemented algorithm, when the input value starts fluctuating (Fig. 4.).

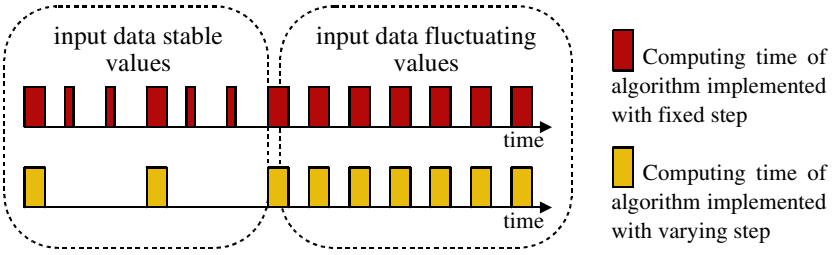

Fig. 4 The difference between computing times of the fixed step and variable step model

Measured execution times on a target hardware by reading synchronized digital out with simulation step are presented below:

Algorithm with fixed computing step (monolithic scheduling)

Computing state:	4,636 ms
Waiting state:	375 ns

Algorithm with varying computing step (varying step scheduling)

Computing state:	4,636 ms
Waiting state:	0 ns

5 Conclusions

We have presented a concept for simulating and generating code of algorithms using aperiodic function calls from Simulink. This concept was demonstrated and evaluated on a dsPIC33 hardware running the Free RTOS scheduler. When comparing execution times of models designed for monolithic and aperiodic scheduling, for active steps the computing times are almost the same, but time is saved during waiting states when implementing aperiodic simulation calls.

This implementation method should be considered for tasks where varying computing step is used (e.g. sequence for initialization, calibration etc.), as this concept will help save some computing resources.

Acknowledgments. This work was supported by the European Commission within the FP7 project Efficient Systems and Propulsion for Small Aircraft “ESPOSA”, contract No. ACP1-GA- 2011-284859-ESPOSA.

References

[1] Schlett, M.: Trends in embedded-microprocessor design. Computer 31(8), 44–49 (1998)

[2] Thate, J., Kagy, R., Jackey, R., Theyyunni, R., et al.: Methods for Interfacing Common Utility Services in Simulink Models Used for Production Code Generation. SAE Technical Paper 2009-01-0155 (2009), doi: 10.4271/2009-01-0155

[3] Vlachy, D., Zezula, P., Grepl, R.: Control unit architecture for biped robot. In: Recent Advances in Mechatronics, International Conference on Mechatronics (2007), doi:10.1007/978-3-540-73956-2_2, WOS:000251017700002

[4] MathWorks, Simulink Coder (2013), http://www.mathworks.com/products/simulink-coder/

[5] Thate, J., Kagy, R., Jackey, R., Theyyunni, R., et al.: Methods for Interfacing Common Utility Services in Simulink Models Used for Production Code Generation. SAE Technical Paper 2009-01-0155 (2009), doi: 10.4271/2009-01-0155

[6] Scaife, N., Caspi, P.: Integrating model-based design and preemptive scheduling in mixed time- and event-triggered systems. In: Proceedings of 16th Euromicro Conference on Real-Time Systems, ECRTS 2004, June 30-July 2, pp. 119–126 (2004), doi:10.1109/EMRTS.2004.1311013

[7] FreeRTOS - Market leading RTOS (Real Time Operating System) for embedded systems supporting 33 microcontroller architectures, http://www.freertos.org (accessed May 12, 2013)

[8] Vahid, F., Gajski, D.D.: Specification partitioning for system design. In: Proceedings of the 29th ACM/IEEE Design Automation Conference, Anaheim, California, United States, June 8-12, pp. 219–224 (1992)

[9] Dillaber, E., Kendrick, L., Jin, W., Reddy, V.: Pragmatic Strategies for Adopting Model-Based Design for Embedded Applications. SAE Technical Paper 2010-01-0935 (2010), doi: 10.4271/2010-01-0935

[10] Grepl, R., Lee, B.: Model Based Controller Design for Automotive Electronic Throttle. In: Recent Advances in Mechatronics: 2008-2009, 8th International Conference on Mechatronics, Luhacovice, Czech Republic (2009), WOS:000277076900036

A New Approximation of the Storage Efficiency for the Lean NOx Trap Model

B. Lee[1], R. Grepl[2], and M. Han[1]

[1] Dept. of Mechanical Engineering, Keimyung University, Daegu, Republic of Korea Zip 704-701
{mbhan2002,bslee}@kmu.ac.kr
[2] Mechlab, Faculty of Mechanical Engineering, Brno University of Technology, Faculty of Mechanical Engineering, Technicka 2, 616 69, Brno, Czech Republic
grepl@fme.vutbr.cz

Abstract. This paper presents a modelling of the lean NOx trap for the diesel engine. The experimental data was acquired using a bench flow reactor. The new model of storage efficiency of the LNT is developed based on system identification and its parameter estimation.

1 Introduction

Compared to the gasoline engine, a diesel engine has higher thermal efficiency and produces lower carbon dioxide (CO2) emission, while emitting relatively more particulate matter (PM) and nitrogen oxides (NOx) due to diffusion burning characteristics [1]. To mitigate those PM and NOx emissions simultaneously, recent research has been conducted to extend an ignition delay time and lower combustion flame temperature via an introduction of heavy exhaust gas recirculation (EGR), high injection pressure, optimized fuel injection timing and multiple injection shaping [2,3]. Those efforts contribute to form partially premixed fuel-air mixture before combustion and lower flame temperature, which enables simultaneous reduction of PM and NOx, commonly named low-temperature diesel combustion (LTC). This LTC strategy works at low-to-mid load under mid speed engine operating condition because the pressure rise rate is quite significant due to the premixed burning, and it should be limited to keep engine noise moderate.

To meet Euro-6 emission regulation in 2014, NOx emission should be reduced further by 45% of the current Euro-5. Thus it is inevitable to use an aftertreatment device to reduce NOx emission. Two types of NOx abatement aftertreatment draw attention: selective catalytic reduction (SCR)[4] and lean NOx trap (LNT)[5,6]. SCR technology uses urea solution to provide a reductant, ammonia (NH3) in the exhaust gas stream, which reacts with NOx and produces N2. To implement SCR technology in a passenger car, the system complexity and its cost are increased, adding a urea dosing injector, a mixer, and a urea tank. LNT technology enables to

T. Březina and R. Jabloński (eds.), *Mechatronics 2013*,
DOI: 10.1007/978-3-319-02294-9_14,

trap NOx in normal combustion mode while those stored NOx should be regenerated periodically by changing the mode to a rich combustion, i.e. regeneration, to provide enough reductants to the LNT when reaching a critical amount of NOx stored [7]. Regeneration of the LNT should be systematically and precisely operated.

For the successful implementation of LNT technology in a vehicle, it is important to determine when regeneration must be executed, while maintaining minimized fuel consumption and high reduction efficiency. To address those issues, a control-oriented LNT modelling should be developed [8-11]. LNT modelling mostly consists of a NOx storage model, a NOx reduction model, and a catalyst bed temperature model due to exothermic reactions of reductions with oxygen. Previous work [8-11] on instantaneous NOx storage efficiency was not fitted to our experimental work. Thus in this study we suggest a different form of the storage efficiency to catch LNT storage behaviour more precisely.

1.1 Experimental Setup and Measured Data

The experiment was conducted at the level of a bench flow reactor, which simulates engine-out exhaust gas by a simpler way, as shown in Fig.1. We use five mass flow controllers (MFC) to feed simulated gases such as N2, O2, NO, THC, CO into the oven where an LNT core sample is placed. The inlet temperature of that gas mixture is controlled by a thermo controller before the oven. LNT formulation is Pt/Ba/Al2O3 and its cell density is 62 cell/cm^2. The volume of the LNT core sample is 3.8cc with 22mm (diameter) × 10mm (length).

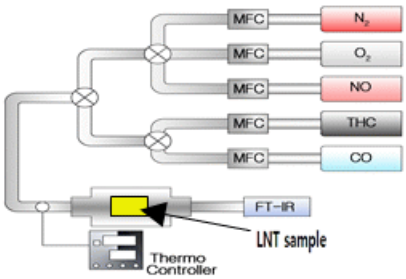

Fig. 1 Experimental setup

The experimental operating range was as follows: a space velocity (defined by total exhaust flow rate over the catalyst volume) of 50,000/hr and 80,000/hr with an LNT inlet gas mixture temperature from 473K to 773K with a 50K difference. The exhaust gases through the LNT are measured by a Fourier Transform Infrared Spectrometer(FT-IR) every 10 sec. The inlet gas composition during the LNT storage phase is composed of NO, O2, and N2 balanced, while CH4, C2H4, CO,

CO2, H2 and N2 balanced for the regeneration phase. Table 1 shows more detailed information of the inlet gas concentrations for the bench flow reactor test.

During the NOx storage phase, the NOx concentration on input u is constant and the NOx on output is measured. We consider this process as an input-output model as shown in Fig. 2. Based on [11], we define an instantaneous NOx storage efficiency as

$$\eta_S = \frac{u - y}{u} \tag{1}$$

Furthermore, normalized stored NOx (NOx storage fraction x) can be defined as

$$x = \frac{\int_0^t (u - y)\mathrm{d}t}{C_{LNT}} \tag{2}$$

Here, C_{LNT} is a NOx storage capacity as a main function of temperature. One example of NOx storage experimental data is shown in Fig. 3. As shown in Fig. 3 we can calculate storage efficiency η_S and storage fraction x.

Table 1 Inlet gas composition for the LNT catalyst bench flow test for storage and regeneration mode

Gas	Storage mode (lean)	Regeneration mode (rich)
NO	650 ppm (SV 50,000 /hr) 700 ppm (SV 80,000 /hr)	0 ppm
N2	balanced	balanced
O2	8%	0%
THC	0 ppm	CH4 1200 ppm
		C2H4 600 ppm
CO	0 ppm	3600 ppm
CO2	0 ppm	2670 ppm
H2	0 ppm	2450 ppm

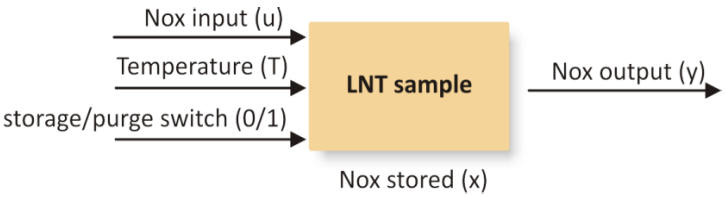

Fig. 2 Block schema of LNT model

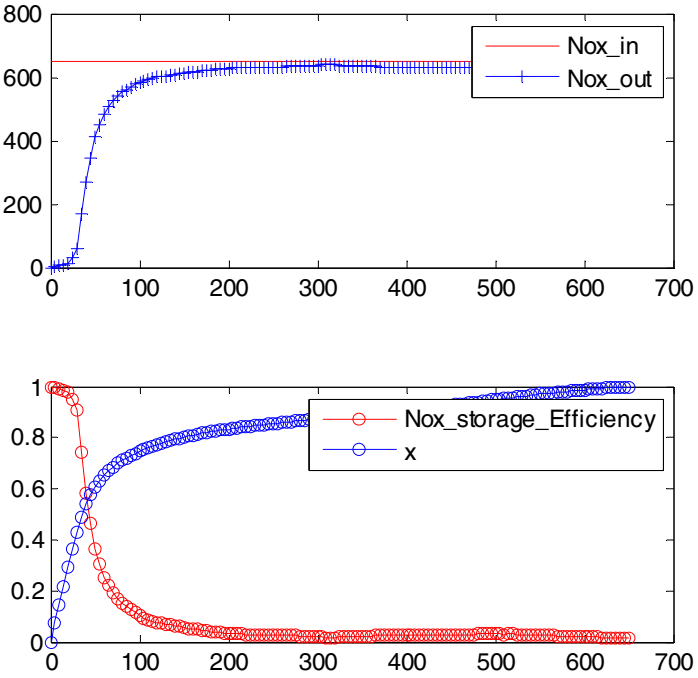

Fig. 3 Example of experimental data – storage phase (T = 473K)

2 LNT Model and Parameter Estimation

2.1 Parameter Estimation

The estimation of the parameters of the storage LNT model consists of the three following steps.

a) Data processing – The data processing was based on the cutting of the relevant part of experimental data, smoothing and resampling.
b) Selection of approximation function candidate – First, the validity of the approximations used in [11] was tested. Next, if not satisfactory, a search among the set of function candidates was performed programmatically.
c) Estimation of the parameters of the selected function – The Trust Region algorithm was used for the parameter fitting.

2.2 Modelling of Trap Capacity

The first step in the modelling of the storage process in LNT is the approximation of the trap capacity. It depends on the maximal capacity C_m and the temperature. We have successfully applied the model introduced in the [11]:

$$C_{LNT} = C_m e^{\left[-\left(\frac{T-T_m}{Ts}\right)^2\right]} \tag{3}$$

The Fig. 4 shows the fit of the model (3) as well as the estimated parameters.

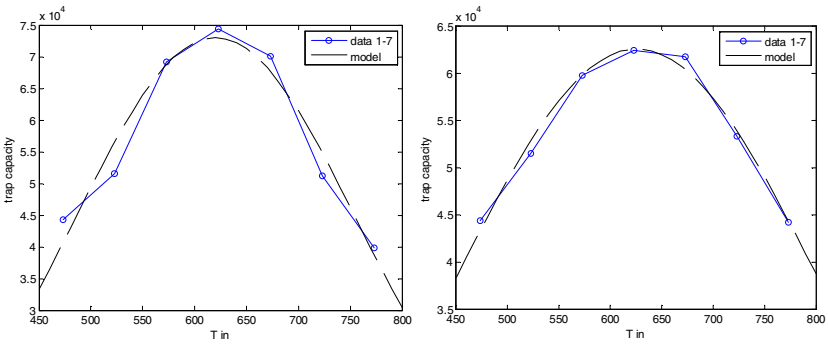

Fig. 4 Trap capacity depends on temperature (Left: data "Space Velocity = 50,000/hr, coefficients from regression: Cm = 7.3012e4, Tm= 620, Ts= 192 ; Right: data "Space Velocity = 80k, Cm = 6.2523e4, Tm= 626, Ts= 252)

2.3 Modeling of Storage Efficiency

The second step in the storage model derivation is the approximation of the storage efficiency. The [11] applied the following function:

$$\eta_S = \frac{e^{-\alpha x} - e^{-\alpha}}{1 - e^{-\alpha}} \tag{4}$$

However, our experimental data shows a very different relationship between the normalized stored NOx x and the efficiency η_S as is shown in Fig. 5. We proposed the new approximation in the form of

$$\eta_S = \frac{1}{1 + e^{-a_1(x-a_2)}} \tag{5}$$

The Fig. 6 presents the quality of the function fit on the data with a space velocity of 50,000/hr.

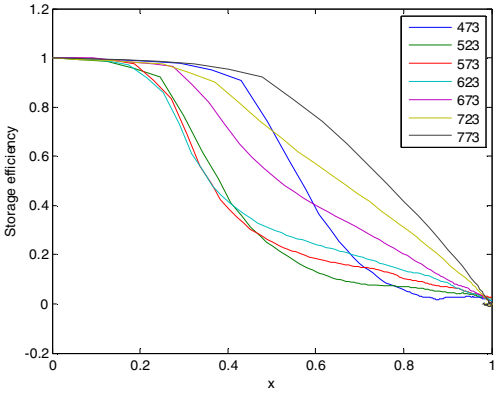

Fig. 5 Storage efficiency (data "Space Velocity = 50,000/hr)

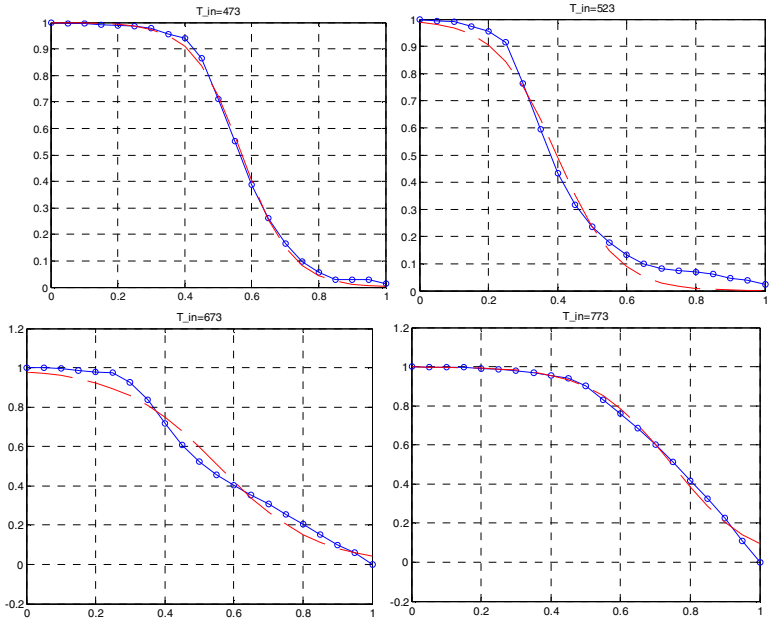

Fig. 6 Function of Storage efficiency relatively to "x". Approximation (5) is used. (data "Space Velocity = 50,000/hr)

3 Conclusions

The modelling of the storage process in the lean NOx trap was presented in this paper. Based on the experimental data acquired on the bench flow reactor, the trap capacity was found to be very similar to the function published in [11]. However, the storage efficiency does not correspond to [11], requiring a new approximation.

Based on the search among the several function candidates, the best model to fit our data has been found.

Although it follows the available data very well, for the practical implementation in real-time of an LNT controller, the look-up table approach can be also applied.

The future work will be focused on the modelling of the LNT using the data measured on the engine test stand.

Acknowledgments. The present work has been supported by European Regional Development Fund in the framework of the research project NETME Centre under the Operational Programme Research and Development for Innovation. Reg. Nr. CZ.1.05/2.1.00/01.0002, id code: ED0002/01/01, project name: NETME Centre –New Technologies for Mechanical Engineering).

References

[1] Heywood, J.B.: Internal Combustion Engine Fundamentals. McGraw Hill (1988)
[2] Akagawa, H., Miyamoto, T., Harada, A., Sasaki, S., Shimazaki, N., Hashizume, T.: Approaches to solve problems of the premixed lean diesel combustion, SAE Paper 1999-01-0183 (1999)
[3] Musculus, M.P.B., Lachaux, T., Pickett, L.M., Idicheria, C.A.: End-of-injection over-mixing and unburned hydrocarbon emissions in low-temperature-combustion diesel engines, SAE Paper 2007-01-0907 (2007)
[4] Koebel, M., Elsener, M., Kleemann, M.: Urea-SCR: a promising technique to reduce NOxemisssions from automotive diesel engines. Catalysis Today 59, 335–345 (2000)
[5] Hachisuka, I., Yoshida, T., Ueno, H., Takahashi, N., Suda, A., Sugiura, M.: Improvement of NOx Storage-Reduction Catalyst, SAE paper 2002-01-0732 (2002)
[6] Parks, J., West, B., Swartz, M., Huff, S.: Characterization of Lean NOx Trap Catalysts with In-Cylinder Regeneration Strategies, SAE paper 2008-01-0448 (2008)
[7] Koci, P., Schejbal, M., Trdlicka, J., Gregor, T., Kubicek, M., Marek, M.: Transient Behavior of Catalytic Monolith with NOx Storage Capacity. Catalysis Today 119, 64–72 (2007)
[8] Canova, M., Midlam-Mohler, S., Pisu, P., Soliman, A.: Model-based fault detection and isolation for a diesel lean NOx trap. Control Engineering Practice 18, 1307–1317 (2010)
[9] Midlam-Mohler, S.: Modeling, control and diagnosis of a diesel lean NOx trap catalyst, Doctoral dissertation, Ohio State University, Ohio, USA (2005)
[10] Nauta, K.M.: Model reduction of a lean NOx trap catalyst mdoel, Doctoral dissertation, Eindhoven University of Technology, Luxemburg, Netherland (2008)
[11] Sun, J., Kim, W.Y., Wang, L.: Aftertreatment control and adaptation for automotive lean burn engines with HEGO sensors. International Journal of Adaptive Control and Signal Processing 18, 145–166 (2004), doi:10.1002/acs.786

Overview of Computational Models Used for Mixed Lubrication

O. Maršálek, P. Novotný, P. Raffai, L. Drápal, and V. Píštěk

Brno University of Technology, Faculty of Mechanical Engineering,
Technická 2, 616 69, Brno, Czech Republic
{marsalek,novotny.pa,drapal,pistek.v}@fme.vutbr.cz,
raffai@iae.fme.vutbr.cz

Abstract. The ability to describe a mixed lubrication regime correctly has higher and higher importance along with the continued downsizing trend. Therefore, this paper deals with the application of different methods for determining the contact pressure in slide bearings, as well as the description of several strategies of 3D rough surfaces computer modelling. Furthermore, in this paper are shown result example of surface roughness generation and analysis results of slide bearing operated under different lubrication regimes.

1 Introduction

Slide bearings are still irreplaceable in many engineering applications, especially due to their properties, which include for example the ability to absorb shocks and vibrations; their simplicity and low cost; small sizes; light weight and others.

Along with the development of slide bearings (both in terms of materials and design) also computational methods and models are ought to be developed, which could ensure plausible description of the processes occurring in these bearings computationally.

One can say that only this path leads to the successful development not only in the field of slide bearings. Throughout history many computational models of mechanical friction losses were developed, which can be applied in the area of sliding bearings. It turns out that many of these computational models can only be successfully applied to surfaces with given specific properties, which include the distribution of asperities on the surface, their shapes, angle, curvature, etc. This means that the current state of knowledge in the field of computational modelling of mixed lubrication conditions will be able to choose the best computational algorithm for the given type of surface topography, as well as to determine the value of the mechanical friction losses.

2 Contact Models

Because the efficiency of the calculation it is very important, we need to take it into consideration during the design of contact analysis. In this section a very efficient

T. Březina and R. Jabloński (eds.), *Mechatronics 2013*,
DOI: 10.1007/978-3-319-02294-9_15,

computational model will be described for determining contact pressure. Furthermore a survey of more sophisticated computational models for the description of mixed lubrication conditions will be carried out.

2.1 Oil Film Height Equation

The most important step before calculating the contact pressure between the two surfaces is to determine the height of the lubricating gap. For this purpose were used a slightly modified approach, described in detail in [1]. The governing equation describing the behaviour of oil pressure can be written in the following form:

$$\frac{\partial}{\partial x}\left(h^3\frac{\partial p}{\partial x}\right)+\frac{\partial}{\partial z}\left(h^3\frac{\partial p}{\partial z}\right)=6\eta\left(U\frac{\partial h}{\partial x}+2\frac{\partial h}{\partial t}\right), \tag{1}$$

where p is the pressure, h is the oil film thickness, η is the dynamic viscosity of the oil and U is the effective velocity. The oil film gap is than defined as:

$$h = R - r + e\cos(\varphi), \tag{2}$$

where R is the shell's radius, r is the pin's radius, e is the pin's eccentricity and φ is the angle around the pin's axis.

The final definition of the dimensionless oil film gap depending on tilting angles is:

$$H = H(\varphi,\varepsilon,\gamma,\delta) = 1+\varepsilon\cos\varphi-\gamma Z\cos\varphi+\varepsilon\gamma Z\cos\varphi-\delta Z\sin\varphi, \tag{3}$$

where φ is the angle around the pin's axis, ε is the dimensionless eccentricity, γ is the dimensionless pin tilting angle at the narrowest oil film gap, δ is the dimensionless tilting angle in the plane perpendicular to the plane of the narrowest oil film gap.

2.2 Efficient Contact Pressure Computational Model

Computational model described in this chapter is based on the theory explained in details in [2].

The basic equation for the calculation of the contact pressure has the form:

$$p(d) = \frac{8\pi}{5}(\eta\beta\sigma)KF_{5/2}\left(\frac{d}{\sigma}\right), \tag{4}$$

where:

$$K = \frac{2\sqrt{2}}{3}(\eta\beta\sigma)E'\sqrt{\left(\frac{\sigma}{\beta}\right)}, \tag{5}$$

$$\sigma = \sqrt{Ra_1^2 + Ra_2^2}\ , \tag{6}$$

$$\frac{1}{E'} = \frac{1-\upsilon_1^2}{E_1} + \frac{1-\upsilon_2^2}{E_2}\ , \tag{7}$$

where η is the surface density of the roughness peaks [m^2], β is the radius of curvature [m], σ is the average roughness of surfaces [m], v is the Poisson constant of materials [-], Ra is the surface roughness [m], E' is the composite elastic modulus [Pa], E is the elastic modulus of materials [Pa] and $F_{5/2}$ is the roughness contact pressure function [-].

Then the total value of the pressure is given by the sum of the hydrodynamic pressure and the pressure, which is given by the contact between the asperities of the two surfaces. This can be expressed by the following equation.

$$P_{Total} = P_{Hydrodynamic} + P_{Contact}\ , \tag{8}$$

This fact should be closer studied, because these two different lubrication regimes are linked together (like describes Fig. 1.), and thus their separate calculation and subsequent sum of their values may bring some distortion into the final results.

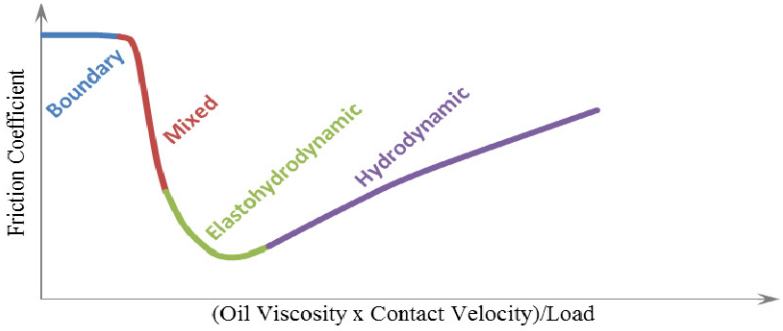

Fig. 1 Stribeck Curve

As it is described in the text above, this method is very effective, has been validated and is still in use. Despite these facts some types of tasks require a more sophisticated approach (as one of the reasons mentioned could be, that the asperity heights were assumed to follow a Gaussian distribution function). For this reason, there are some other approaches available, allowing the determination of the contact pressure between two rough surfaces.

For this purpose it is necessary to have the input data either directly from the surface roughness measurement, or they could be generated using different approaches. One of the possible generation methods could be the use of *random midpoint displacement*, or by many authors used generation of rough surfaces using fractal geometry, which will be described below.

2.3 Surface Roughness Generation

In 1998 for the purpose of generating a three-dimensional rough surface a modified two-variable Weierstrass-Mandelbrot function (WM function) was presented by authors Yan and Komvopulos (1998).

This function can be written as [3]:

$$z(x,y) = L\left(\frac{G}{L}\right)^{(D-2)}\left(\frac{\ln\gamma}{M}\right)^{1/2}\sum_{m=1}^{M}\sum_{n=0}^{n_{\max}}\gamma^{(D-3)n}\left\{\cos\phi_{m,n} - \right.$$
$$\left. -\cos\left[\frac{2\pi\gamma^n(x^2+y^2)^{1/2}}{L}\cos\left(\tan^{-1}\left(\frac{y}{x}\right)-\frac{\pi m}{M}\right)+\phi_{m,n}\right]\right\}, \tag{9}$$

where L is the sample length, G is the fractal roughness, D is the fractal dimension, γ is a scaling parameter, M is the number of superposed ridges used for construction of the profile of the surface, n is a frequency index and $\Phi_{m,n}$ is a random phase. The upper limit of the frequency index can be determined by the formula:

$$n_{\max} = \text{int}\left[\frac{\log\left(L/L_S\right)}{\log\gamma}\right], \tag{10}$$

where int[…] denotes the maximum integer value of the number in the brackets and L_S is the cut off length.

Example of the surface generated using this function is shown in the figure below.

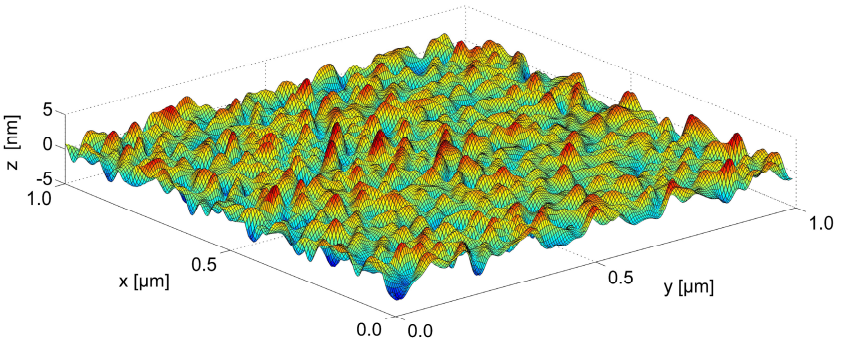

Fig. 2 Simulated three-dimensional fractal surface

As another mentioned method for contact pressure calculation an older approach to this problem should be described, which incorporates the Hertz theory.

2.4 Contact Modelling Using the Hertz Theory

In order to apply the Hertz theory to the problem of contact between three-dimensional fractal surfaces, it is necessary to take some simplifying assumptions. Bodies in the contact are assumed isotropic and elastic, perfectly smooth and the contact areas are taken flat and small relative to the radius of the undeformed bodies' curvature.

Then the contact between each surface peak (represented by a perfect sphere) and rigid flat plate is solved.

Final expressions for the contact area radius, maximum contact pressure and relative displacement of two spheres centres (caused due to local deformation contact at the interface), mentioned in [4] (such as other information from this chapter) can be written as shown below.

The contact area radius:

$$a = 0.88\left(\frac{2Pr}{E}\right)^{1/3}, \tag{11}$$

The maximum contact pressure:

$$\sigma_C = 0.62\left(\frac{PE^2}{4r^2}\right)^{1/3}, \tag{12}$$

and the relative displacement of two spheres centres:

$$\delta = 1.54\left(\frac{P^2}{2E^2 r}\right)^{1/3}. \tag{13}$$

Further a normal force is given by the formula:

$$P = 0.74|E|\left(\delta r^{1/3}\right)^{3/2}. \tag{14}$$

Then contact area between a sphere and a flat plate is:

$$A = \pi a^2. \tag{15}$$

3 Result Examples

Based on all of information mentioned above, the complex computational model was developed for detailed analysis of sliding bearings.

Result examples, which can be seen in the following figure, illustrate comparison of two different computational approaches used for crankshaft main bearing of naturally aspirated combustion engine analysis. As is evident from the figure caption, purely hydrodynamic and mixed lubrication regimes were considered.

Differences in the course of both curves clearly show that taking into account also mixed lubrication regime is practically necessary for the future of modern power units development.

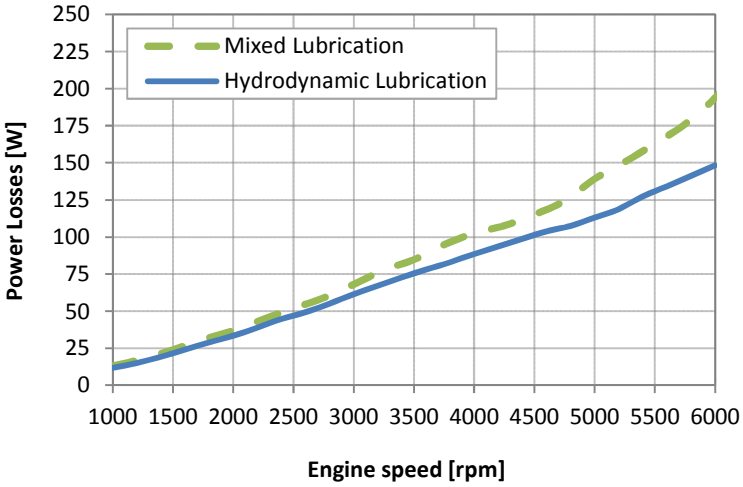

Fig. 3 Comparison of two different computational approaches

4 Conclusions

Contact mechanics is a frequently studied field. Many scientists around the world have been devoted large amounts of resources, effort and time to develop different methods of surface characteristics measurement. In literature mentioned are many modified approaches for determining the contact pressure ([3], [5], [6], [7], and others). Most of them are based on two approaches also mentioned in this paper.

Unfortunately it is almost always necessary to introduce certain simplifying assumptions in problem solving.

Car producers are still under bigger pressure of legislatures which directs to the reduction of frictional losses of power units and increasing their overall efficiency, leading to the CO_2 emissions reduction. The development of these advanced powertrains is than (from all of views) increasingly challenging.

In this paper described were two basic approaches for computational modeling of contact pressure, which should be well understood before studying other approaches. Further described has been one of the most used methods for generating random surfaces.

Although it may seem curious, it is still not common that combustion engines developers use so complex computational codes similar to this one. Therefore the main contributions of this paper are the developed comprehensive computational strategy for rigorous design of sliding bearings and the computational code, used for sliding bearing calculations.

Acknowledgments. The presented work has been supported by European Regional Development Fund in the framework of the research project NETME Centre – New Technologies for Mechanical Engineering, project reg. No. CZ.1.05/2.1.00/01.0002, under the Operational Programme Research and Development for Innovation and with the help of the project FSI-S-11-8 granted by specific university research of Brno University of Technology. This support is gratefully acknowledged.

References

[1] Novotný, P.: Virtual Engine – A Tool for Powertrain Development. Brno University of Technology, Brno (2009) Inaugural Dissertation
[2] Greenwood, J.A., Tripp, J.H.: The Contact of two Nominally Flat Rough Surfaces. Proc. Instn. Mech. Engrs. (1970)
[3] Yan, W., Komvopoulos, K.: Contact Analysis of Elastic-Plastic Fractal Surfaces. Journal of Applied Physics (1998)
[4] Shellock, M.R.: Contact analysis of nominally flat surfaces. Monterey, California, Master's Thesis. Naval Postgraduate School. Thesis Advisor: Young W. Kwon (2008)
[5] Pugliese, G., Tavares, S.M.O., Ciulli, E., Ferreira, L.A.: Rough contacts between actual engineering surfaces: Part II. Contact mechanics. Wear 264(11-12), 1116–1128 (2008)
[6] Hu, Y.-Z., Wang, H., Wang, W.-Z., Zhu, D.: A computer model of mixed lubrication in point contacts. Tribology International 34(1), 65–73 (2001)
[7] Bush, A.W., Gibson, R.D., Thomas, T.R.: The elastic contact of a rough surface. Wear 35(1), 87–111 (1975)
[8] Xian, L., Zheng, L.: A numerical model for the elastic contact of three-dimensional real rough surfaces. Wear 148(1), 91–100 (1991)

Heating of Mould in Manufacture of Artificial Leathers in Automotive Industry

J. Mlynek[1], T. Martinec[2], and R. Srb[2]

[1] Technical University of Liberec, Faculty of Sciences, Humanities and Education, Studentská 2, 461 17, Liberec, Czech Republic
jaroslav.mlynek@tul.cz
[2] Technical University of Liberec, Faculty of Mechatronics, Studentská 2, 461 17, Liberec, Czech Republic
{tomas.martinec,radek.srb}@tul.cz

Abstract. This article focuses on a model for the creation of artificial leather production in the automotive industry. Aluminium or nickel shell moulds are used in the production of leathers. The inner mould surface is sprinkled with a special PVC powder and the outer mould surface is warmed by infrared heaters located above the mould. This is an economically advantageous way to produce artificial leathers used in car interior equipment. The article includes a description of a model that allows us to calculate the heat radiation intensity across the mould surface for every location of heaters, and to optimize the location of the heaters by using a differential evolution algorithm. The process of experimentally measuring the heat radiation intensity in the surroundings of the infrared heater by using a robot is also described in the article. The calculations were performed using a Matlab code written by the authors. The article contains a practical example including graphical outputs.

1 Introduction

This article describes a procedure for the calculation of heat radiation intensity across the whole mould surface for fixed location of infrared heaters above the mould. It is necessary to ensure the same heat radiation intensity (within the specified tolerance) on the whole mould surface by finding suitable location of the heaters. In this way, the same colour and material structure of the artificial leather is assured. The process of heat radiation intensity optimization on the mould surface is rather complicated (moulds which are used, are often very ragged, during the process of optimization possible collisions between one heater and another as well as collisions between a heater and the mould surface must be avoided). The problem of optimization has many local extremes. Using gradient methods for finding the global minimum is therefore unsuitable, because there is a great likelihood of entrapment in a local extreme. This is the reason why a differential evolution algorithm is used. The manufacturer of artificial leathers needs to implement

T. Březina and R. Jabloński (eds.), *Mechatronics 2013*,
DOI: 10.1007/978-3-319-02294-9_16,

a procedure for optimization on the production line (after its verification in the Matlab system). Therefore we need to know the optimization process in every detail, and we do not use existing, commercially available, software tools.

The infrared heater manufacturer has not provided the distribution function of the heat radiation intensity in the heater surroundings. However, knowledge of this function is indispensable for our model and calculations. Therefore, we performed experimental measurements of heat radiation intensity in the surroundings of a heater which is described in the following chapter.

2 Automated Measurement System of Heat Radiation Intensity in the Heater Surroundings

The infrared heater has a tubular form and is equipped with a mirror located above the radiation tube which reflects heat radiation in a given direction. The length of the heaters can be between 15 and 25 cm. An experimental measurement of heat radiation intensity in the surroundings of the heater was automated by using an electromechanical KR 16 robot and a Hukseflux SBG01 heat flux sensor. A robot controlling unit was equipped to control both the robot and the additional external equipment (see Figure 1). We connected the heat flux sensor to the robot using the I/O system Wago.

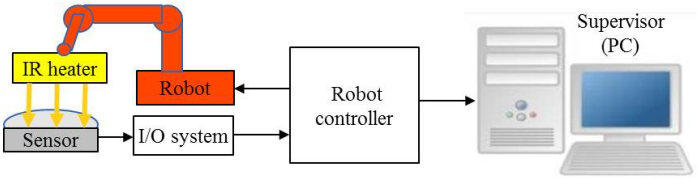

Fig. 1 Configuration of the automated measurement system

The sensor was fixed on the x_1x_2-plane (see Figure 2). A heater was mounted at the end of the robot arm. Due to the symmetry of the heat radiation intensity of the heater, we performed measurements only in part of the 3D space above the 1st quadrant of the Cartesian coordinate system of the x_1x_2-plane. The robot arm with heater moved in a few planes parallel to the x_1x_2-plane, and stopped at selected points in every plane for 100[ms]. Using the analog input values, heater positions together with heat radiation intensities at selected points were continuously transmitted through a KRC4 robot controller (KUKA Robot Controller version 4) to the supervising PC. The trajectory of the robot arm end with the mounted heater was programmed in the special programming language KRL (KUKA Robot Language). We recorded the measured values of the heat radiation intensity and actual heater positions using Cartesian coordinates in a text file. We performed experimental measurements for different deflections of the axis of the sensor (it corresponds to the different directions of the outer normal vector of the mould surface at given points).

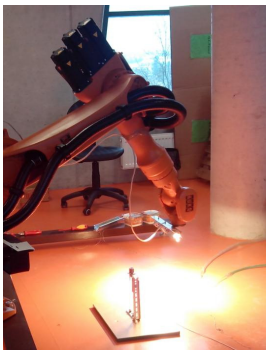

Fig. 2 Measurement of heat radiation intensity using a KR 16 robot and a Hukseflux SBG01 sensor

The working range of a used heat flux sensor is up to 200[kW/m^2] and its field of view is 180°. The sensor is passive and needs to be cooled with flowing water. The sensor was connected to the analog input of the Wago distributed I/O system. The whole Wago system was configured in the robot controller as an analog and digital I/O system.

The measured heat radiation intensity, and its interpolated values in 3 parallel planes with x_1x_2-plane are shown in colour in Figure 3 in the case of 0° deflection of the axis of the sensor (i.e., axis of the sensor is vertical).

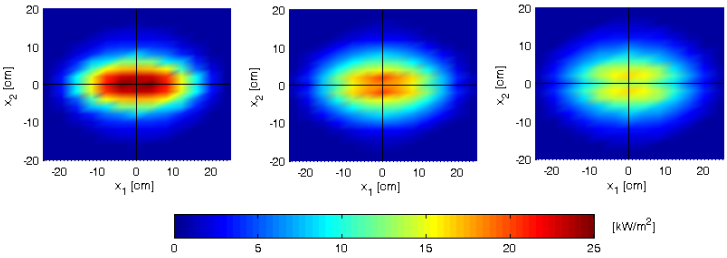

Fig. 3 Heat radiation intensity in the planes at distances 9, 11 and 13[cm] from the heater

3 Model of a Heat Radiation Intensity Calculation on a Mould Surface

In this chapter a model for the heating of the outer mould surface using infrared heaters located above the mould is briefly described (see Figure 5). The model is described in more detail in [2] and [3]. The heaters and the heated mould are represented in 3D Euclidean space E_3 using the Cartesian coordinate system (O, x_1, x_2, x_3) with base vectors $e_1 = (1, 0, 0)$, $e_2 = (0, 1, 0)$ and $e_3 = (0, 0, 1)$.

A heater is represented by a abscissa of length d. The location of every heater Z can be defined by the following 6 parameters

$$Z : (s_1, s_2, s_3, u_1, u_2, \varphi), \tag{1}$$

where s_1, s_2 and s_3 are coordinates of the heater centre S; u_1, u_2 are coordinates of the unit vector of the heat radiation direction u (the heater radiates "downward", i.e., $u_3 < 0$ and therefore u is defined by its first two coordinates); φ denotes the angle between the vertical projection of the vector r (determines direction of abscissa representing a heater in our model) onto the x_1x_2-plane and the positive part of the axis x_1 (vectors u and r are orthogonal, $0 \le \varphi \le \pi$).

The outer mould surface P is described by elementary surfaces p_j, where $1 \le j \le N$. It holds $P = \cup p_j$ and int $p_i \cap$ int $p_j = \emptyset$ for $i \ne j$. Every elementary surface p_j can be defined by the following 6 parameters

$$p_j : (t_1^j, t_2^j, t_3^j, v_1^j, v_2^j, c_j), \tag{2}$$

where t_1^j, t_2^j, t_3^j are coordinates of the centre of gravity T_j of p_j; v_1^j, v_2^j are coordinates of the unit outer normal vector v_j at the point T_j (we suppose v faces "upwards" and therefore is defined through its first two components); c_j is the area of p_j.

We are able to determine the heat radiation intensity of heater Z on the elementary mould surface p_j, which are in a general position. For this purpose we use the measured values of the heat intensity radiation in the surroundings of a heater, their linear interpolation and suitable transformation of the general position of heater Z and the elementary surface p_j to the position in the case of experimental measuring described in chapter 2 (see in detail [3]).

3.1 The Calculation of Total Heat Radiation Intensity

Now we will describe the numerical computation procedure for the total heat radiation intensity on the mould surface. We denote L_j the set of all heaters radiating on the jth elementary surface p_j ($1 \le j \le N$) for the fixed location of the heaters, and I_{jl} the heat radiation intensity of the lth heater on the p_j elementary surface. Then the total radiation intensity I_j on the elementary surface p_j is given by the following relation (see in more detail in [1])

$$I_j = \sum_{l \in L_j} I_{jl} \ . \tag{3}$$

The producer of artificial leathers recommends a constant value of heat radiation intensity across the whole outer mould surface. Let us denote this constant value as I_{rec}. We can define F, the aberration of the heat radiation intensity, using the relation

$$F = \frac{\sum_{j=1}^{N} \left| I_j - I_{rec} \right| c_j}{\sum_{j=1}^{N} c_j}. \tag{4}$$

We highlight that c_j denotes the area of the elementary surface p_j. We need to find the location of heaters so that the value of aberration F will be within a specified tolerance. Therefore, we will focus on the process of optimizing the location of heaters above the mould surface in the following chapter.

4 The Optimization Process of the Location of the Heaters

Function F, defined by (4), contains many local extremes. Using gradient methods for finding the minimum of function F is not appropriate. If we used a gradient method, there is a high likelihood that we would find only a local minimum of the function. Therefore, we use a differential evolution algorithm (denote DE, detailed in [4]), for finding a global minimum of function F (i.e., to optimize the location of the heaters). The disadvantages of a DE are its computational demand and slower convergence. The location of every heater is defined in accordance to the relation (1), using 6 parameters. Therefore, $6M$ parameters are necessary to define the location of all M heaters. One individual in the DE represents one possible location of all $6M$ heaters. In the algorithm we successively construct populations of individuals. Every population includes NP individuals, where every individual is a potential solution to our problem. We seek the individual $y_{\min} \in C$ satisfying the condition

$$F(y_{\min}) = \min\{F(y);\, y \in C\}, \tag{5}$$

where $C \subset E_{6M}$ is the set we are searching for. The identification of the individual $y_{\min}$ defined by (5) is not realistic in practice. However, we are able to determine an optimized solution y_{opt}. The generated individuals are saved in the matrix $\mathbf{B}_{NP\times(6M+1)}$ and every row of this matrix represents one individual y, and its value $F(y)$. Now we will describe schematically the particular steps of the DE named *DE/rand/1/bin* (for more detail see [4]) which is applied to our problem.

4.1 Differential Evolution Algorithm

Input: the initial individual y_1, population size *NP*, the number of used heaters *M* (dimension of the problem is 6*M*), crossover probability *CR*, mutation factor *f*, the specified accuracy of the calculation ε.

Internal computation:

1.create an initial generation (*G*=0) of *NP* individuals y_i^G, $1 \le i \le NP$,

2.a) evaluate all the individuals y_i^G of the generation *G* (calculate $F(y_i^G)$ for every individual y_i^G), b) store y_i^G and their evaluations $F(y_i^G)$ into the matrix **B**,

3. *repeat until* $\min\{F(y_i^G);\ y_i^G \in \mathbf{B}\} < \varepsilon$

a) *for i*:=1 *step to NP do*

(i) randomly select index $k_i \in \{1, 2, \ldots, 6M\}$,

(ii) randomly select indexes $r_1, r_2, r_3 \in \{1, 2, \ldots, NP\}$,

where $r_t \neq i$ for $1 \le t \le 3$ and $r_1 \neq r_2$, $r_1 \neq r_3$, $r_2 \neq r_3$;

(iii) *for j*:=1 *step* 1 *to* 6*M do*

$$\textit{if } (\text{rand}(0,1) \le \text{CR } \textit{or } j{=}k_i) \textit{ then } y_{i,j}^{trial} := y_{r_3,j}^G + f\left(y_{r_1,j}^G - y_{r_2,j}^G\right)$$

$$\textit{else } y_{i,j}^{trial} := y_{i,j}^G$$

end for (*j*)

(iv) *if* $F\left(y_i^{trial}\right) \le F\left(y_i^G\right)$ *then* $y_i^{G+1} := y_i^{trial}$ *else* $y_i^{G+1} := y_i^G$

end for (*i*)

b) store individuals y_i^{G+1} and their evolutions $F\left(y_i^{G+1}\right)$ $(1 \le i \le NP)$ of new generation *G*+1 into the matrix **B**; *G*:= *G*+1

end repeat.

Output: the row of matrix **B** that contains the corresponding value $\min\{F\left(y_i^G\right);\ y_i^G \in \mathbf{B}\}$ represents the best found individual y_{opt}.

Note that the function rand(0,1) randomly chooses a number from the interval $< 0, 1 >$. The denomination $y_{i,j}^G$ represents the *j*th component of an individual y_i^G in *G*th generation. The individual y_{opt} is the final solution and includes information about the location of every heater in the form (1).

5 Practical Example

Here we will describe a practical example of the heating of an aluminium mould. The volume of the mould is $0.8 \times 0.4 \times 0.15$ [m^3] (see Figure 5), the number of elementary surfaces, $N = 2{,}064$; the heat radiation intensity recommended by the producer of artificial leathers, $I_{rec} = 47$ [kW/m^2]. We use 16 infrared heaters (i.e., $M = 16$) of the same type (producer Philips, capacity 1,600 [W], length 15[cm], width 4[cm]).

The heaters of the initial location (corresponding to individual y_1) lie on the plane parallel to the x_1x_2-plane and at a distance of 10 [cm] from the centre of gravity T_j of the elementary surface p_j with the highest value $x_3^{T_j}$, where $1 \le j \le N$ (see left part of Figure 5). The aberration given by relation (4) for this location of heaters is $F(y_1) = 23.51$. We use the DE algorithm described in subsection 4.1 to optimize the location of the heaters. The parameters of the algorithm are as follows: population size NP =192 (dimension of the problem is $6M$ = 96), mutation factor f = 0.98 and crossover probability CR = 0.60. We obtain the optimized individual y_{opt} with a value of $F(y_{opt}) = 1.96$ after 6,000 generations of DE algorithm. The dependence of the aberration $F(y_{opt})$ on the number of generations is shown in Figure 4.

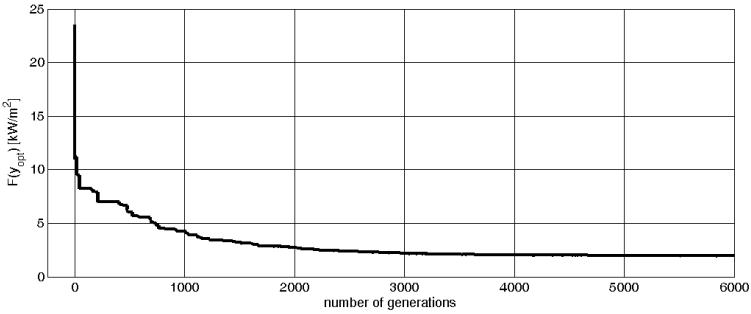

Fig. 4 Dependence of $F(y_{opt})$ on the number of generations

Figure 5 shows a graphical representation of heat radiation intensity on a mould surface, with the initial location of heaters y_1 in the left part, and the optimized location of the heaters y_{opt} in the right part of the figure.

The location of the heaters y_{tech}, determined on the basis of the experience of technicians, produces significantly worse results than ours (in this example $F(y_{tech}) = 11.21$) and is time consuming.

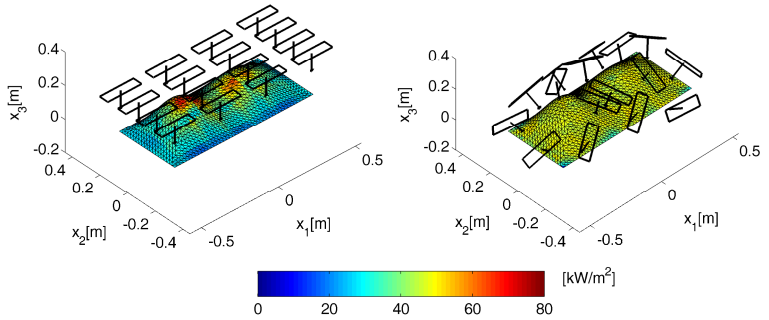

Fig. 5 Heat radiation intensity ([kW/m^2]) on the mould surface and the location of heaters corresponding to the individual y_1 (left part) and to the individual y_{opt} (right part)

6 Conclusions

On the basis of practical calculations, we get a sufficiently exact solution for the optimized location of heaters over the mould. We obtained more exact results using the DE algorithm than by using the genetic algorithm in numerical experiments (see [2], [3]). We are able to calculate the temperature on the mould surface during the warming by heaters on the basis of the solution of the parabolic evolutionary equation of heat conduction in the mould (e.g., using the software tool ANSYS, see [3]).

Acknowledgments. This work was supported by project OP VaVpI, No. CZ.1.05/2.1.00/01.0005 and by project TUL FM SGS 2013/78000.

References

[1] Cengel, Y.A.: Heat and Mass Transfer. McGraw-Hill, New York (2007)
[2] Mlynek, J., Srb, R.: Optimization of a Heat Radiation Intensity on a Mould Surface in the Car Industry. In: Jablonski, R., Brezina, T. (eds.) Proceedings of the 29th Mechatronics 2011 Conf., Faculty of Mechatronics, pp. 531–540. Warsaw University of Technology, Warsaw (2011)
[3] Mlynek, J., Srb, R.: The Process of an Optimized Heat Radiation Intensity Calculation on a Mould Surface. In: Troitzsch, K.G. (ed.) Proceedings of the 26th European Conf. on Modelling and Simulation, pp. 461–467. University Koblenz, Germany (2012)
[4] Price, K.V., Storn, R.M., Lampien, J.A.: Differential Evolution. Springer, Heidelberg (2005)

Influence of Underpressure on Acoustic Properties of Semi-intelligent Vacuum Packed Particles

M. Rutkowski

Institute of Aviation, Center of New Technologies, al. Krakowska 110/114,
02-256 Warsaw, Poland
michal.rutkowski@ilot.edu.pl

Abstract. This research is the next step in studying the properties of so called Special Granular Structures (vacuum packed particles). Started about ten years ago, the work has shown these materials to be a very interesting research subject (having controllable physical properties, depending on applied underpressure). The properties of investigated granular structures described in previous papers led author to believe, that also acoustic characteristics may change with applied underpressure. This work shows new potential possibilities of Special Granular Structures application (such as acoustic panels with controllable acoustic properties). Presented results prove, that acoustic properties of these materials can be controlled.

1 Introduction

Nowadays acoustics is becoming more and more important in the design process. Despite all kinds of actions aiming to decrease the level of noise emitted by machines, the problem is still present in various areas, from airfields and their influence on environment to the sounds produced by daily used equipment. There is a permanent increase of noise levels and a continuous increase in number of its sources, that humans and environment are exposed to. These facts are undoubtedly the result of development of our civilization. Along, there is a considerable growth of consciousness concerning noise and the dangers that it is related to, as well as means of limiting it. At the same time new policies are introduced, that aim to maintain noise at certain acceptable levels. To some extent the answer for higher demands in acoustics, are new more effective absorbing materials. The search for them brings often new ecological solutions, using e.g. recycled materials [3, 6, 7].

With respect to above facts, it is understandable, that researchers are looking for not only passive, but also active solutions. The most common would be probably systems known as ANC (Active Noise Control) used currently in headphones. The problem with ANC though, is that it is relatively expensive, very

T. Březina and R. Jabloński (eds.), *Mechatronics 2013*,
DOI: 10.1007/978-3-319-02294-9_17,

complex and suit only certain applications. Common usage of such systems is therefore a rather distant perspective.

Granular materials made from various plastics are widely used in absorption of acoustical waves ([1]), e.g. in construction industry in roofs. But they are never implemented with use of underpressure.

In this work, so called Special Granular Structures (SGS) were tested for absorption coefficient. That is the name for granules of plastics closed in an elastic container, in which a partly vacuum is created. The characteristics of described structure are controlled by a vacuum pump with a gauge.

The scientific work concerning analysis of possible applications of SGS and controlling their properties are being conducted for about a decade [8, 13]. Attempts were also made to model their behavior under applied partial vacuum [9, 10]. The main mechanisms, which influence changes of physical properties of investigated structures are: reduction of size (or disappearance) of air cavities and rapid increase of forces acting on edges of adjacent grains. This results in a major change of material structure. The possibility to control material mechanical properties inspired author to check for influence of underpressure on acoustic characteristics of SGS.

2 Scope of Work

The purpose of this work is to reveal selected part of acquired experimental results obtained during the whole research process. Discussing the all experimental data would end up with producing an extensive paper. The original research plan was aimed at finding impact of various factors on absorption coefficient of SGS. The factors investigated in this paper were:

a) level of underpressure generated inside the sample,
b) front material of the specimen (three kinds and three thicknesses were analyzed),
c) different kinds of granular materials (five types of plastics were tested: polypropylene, polypropylene talc, polystyrene, ABS (Fig. 1), poly(methyl methacrylate),
d) length of sample (130 mm and 200 mm).

The main purpose of present paper is to perform an analysis of the underpressure influence on chosen acoustic characteristics of SGS, composed of polypropylene (PP) particles. Secondly, author would like to analyze possibilities of using tested materials in acoustic barriers with controllable absorption.

Fig. 1 Typical granular materials investigated in this paper (ABS grains)

3 Methods of Measurement

The research was conducted in the Vibroacoustic Laboratory at the Faculty of Automotive and Construction Machinery Engineering, Warsaw University of Technology. The experimental setup (Fig. 2) consisted of B&K impedance tube (type 4206), two microphones (2670), generator (3160-A-04/2), amplifier (2716C), a vacuum pump with two gauges and a laptop with Pulse Lab Shop software.

Experiments were carried out according to EN ISO 10534-2 acoustic material testing standard [4]. Selected test stand limited investigated frequencies from 500 Hz up to 6400 Hz. Air conditioned room prevented from any impact of temperature or humidity changes on the results.

Fig. 2 Experimental setup

Because the test material and its use was specific in this type of testing, there were several issues that had to be resolved. The test sample was built of a delicate plastic material formed in a cylindrical shape, reinforced with a thin teflon ring in the front part. Since it was necessary to have a hermetic sample, also its face had to be sealed. Introduction of any material in the way of acoustic waves,

penetrating the test structure, produces obvious limitation to the SGS dissipation capabilities. Previously mentioned limitations are the only way to use vacuum packed particles having extraordinary features for semi-active noise damping. The underpressure was generated and controlled by a vacuum pump with gauge, connected to the back of the sample which was a steel disk of proper thickness, which also provided the proper rigidity behind the tested sample.

Dimensions of the specimen were: diameter 28.8 mm and length 200 mm. Its mass was 73.40 g, the mass of PP grains was 65.63g. Dimensions of used grains were: 2-3 mm (diameter) and 4-5 mm (length). The underpressure was generated from 0 to 0.09 MPa with step of 0.01MPa. The measurements were taken in three series.

4 Results and Discussion

Experimental results are shown in Figs 3-5 and additionally in Table 1. It can be easily observed, especially in Fig. 5, that the controlling parameter has a noticeable influence on acoustic properties of tested structures. Other tested plastics show similar response. In terms of absorption coefficient it is most obvious between 0 and 0.01 MPa. Depending on the material, some differences can be noticed also in two next ranges of generated underpressure, until a threshold limit approximately 0.03 MPa is reached.

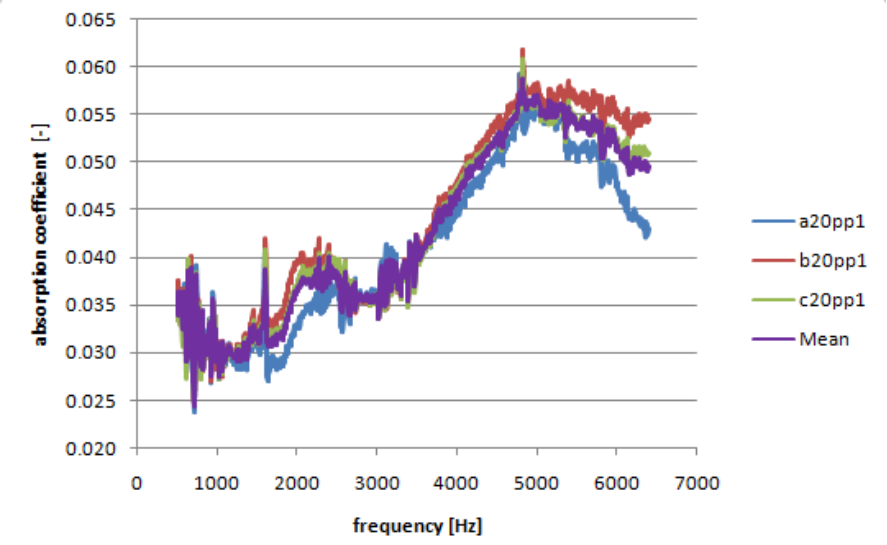

Fig. 3 Absorption coefficient for PP particles, underpressure 0.01 MPa

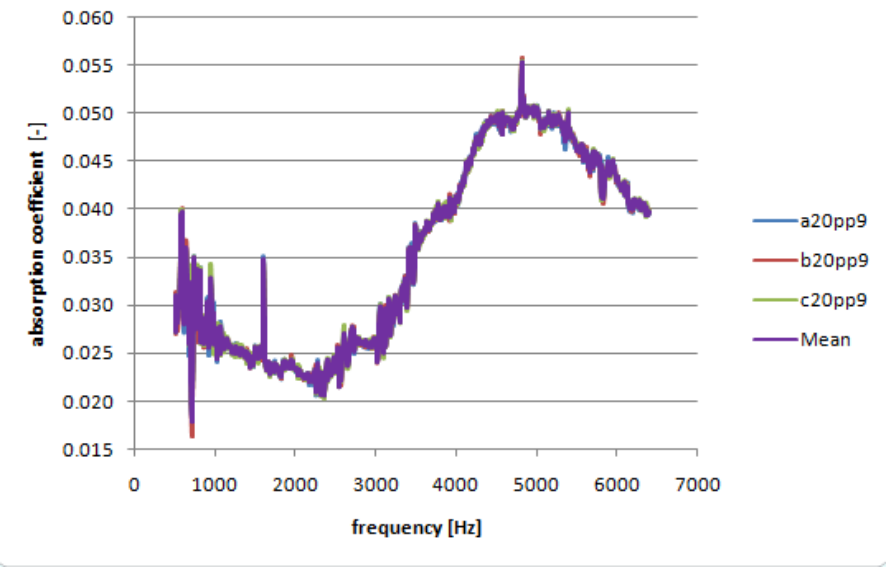

Fig. 4 Absorption coefficient for PP particles, underpressure 0.09 MPa

The absorption coefficient for 'loose' grains is at a level of about 0.6 for most of the tested frequency range. Author would like to emphasize, that results from research presented hereby may differ from 'similar' experiments concerning loose granular media of such kind. The cause is obviously the sample construction, described earlier.

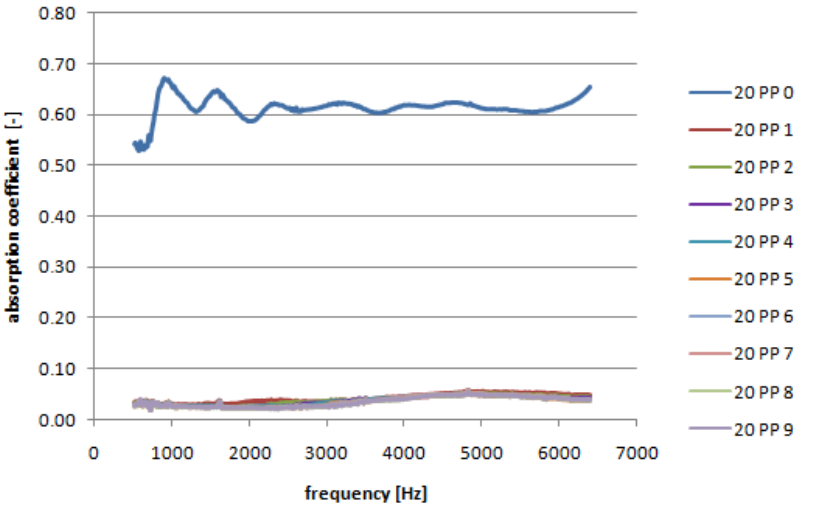

Fig. 5 Absorption coefficient for PP particles, underpressure levels 0-0.09 MPa

Table 1 Absorption coefficient for PP particles, underpressure levels 0-0.09 MPa

	Frequency [Hz]				
Underpressure [MPa]	500	1000	2000	4000	6400
0	0.543	0.651	0.587	0.619	0.615
0.01	0.034	0.031	0.036	0.047	0.052
0.02	0.032	0.029	0.028	0.043	0.046
0.03	0.028	0.028	0.026	0.043	0.044
0.04	0.028	0.028	0.024	0.043	0.042
0.05	0.028	0.028	0.023	0.044	0.042
0.06	0.027	0.028	0.023	0.044	0.042
0.07	0.027	0.027	0.023	0.043	0.043
0.08	0.027	0.027	0.023	0.041	0.043
0.09	0.027	0.027	0.023	0.041	0.043

5 Conclusions and Perspectives

Results obtained from experimental research carried out for Special Granular Structures revealed, that there is a considerable influence of the underpressure parameter on acoustic properties of Special Granular Structures. Such phenomenon results from structural changes previously described in Sec. 1. Because these changes are entirely reversible, it is possible to use SGS as a semi-intelligent absorbing layer - a part of a sound absorbing barrier.

In terms of acoustic characteristics of investigated granular systems, a lot of open questions still remain. The most interesting problem is the behavior of SGS between 0 and 0.01 MPa (most changes in properties take place in that range). Next one would concern the level of compaction of grains in a container. This parameter clearly determines the dimensions and shape of air cavities between single grains, that influence SGS properties [5, 11, 12]. Following are size and shape of particles, which may have similar effect on acoustic properties as previously mentioned. Another factor is the grains' material, which strongly influences its structure (in presented research the deformation of polypropylene particles was negligible).

Special Granular Structures reveal features, that are unique even for well commercialized smart materials. Their biggest advantage is common availability and price (they are very cheap compared to most popular smart materials, e.g. MR fluids [2]).

Former works concerning Special Granular Structures were aimed at investigations of their mechanical properties or realistic engineering applications. Current paper is devoted to a novel domain of absorbing materials and acoustics.

Generally material structures and physical systems have a characteristic response to any external excitations. To minimize complex and expensive laboratory research of innovative structures, which vacuum packed particles are typical example, a suitable mathematical model has to be developed. Although

such an approach is true for conventional structural materials, we can encounter a lot of unpredictable problems when dealing with nonclassical innovative structures [14] or [15] and complex systems. In such cases, the modeling process should be preceded by complex experimental research providing information about the extraordinary features of the investigated systems.

As a conclusion it is worth mentioning that for better understanding of the extraordinary acoustic properties of granular structures, more complex laboratory tests have to be carried out.

References

[1] Attenborough, K.: Acoustical characteristics of rigid fibrous absorbents and granular materials. J. Acoust. Soc. Am. 73, 785–799 (1983)
[2] Bajkowski, J., Jasiński, M., Mączak, J., Radkowski, S., Zalewski, R.: The active magnetor-heological support as an element of damping of vibrations transferred from the ground to large-scale structure supports. Key Engineering Materials 518, 350–357 (2012)
[3] Hong, Z., Bo, L., Guangsu, H., Jia, H.: A novel composite sound absorber with recycled rubber particles. Journal of Sound and Vibration 304(1-2), 400–406 (2007)
[4] EN ISO 10534-2
[5] Pyrz, M., Zalewski, R.: Modeling of granular media submitted to internal underpressure. Mechanics Research Communications 37(2), 141–144 (2010)
[6] Sikora, J., Turkiewicz, J.: Experimental determination of sound absorbing coefficient for se-lected granular materials. Mechanics 28(1), 26–29 (2009)
[7] Swift, M.J., Briš, P., Horoshenkov, K.V.: Acoustic absorption in re-cycled rubber granulate. Applied Accoustics 57, 203–212 (1999)
[8] Zalewski, R.: Rheological model proposition for granular structures in special conditions. Machine Dynamics Problems 32, 117–126 (2008)
[9] Zalewski, R.: Modeling of Rheological Properties of Special Granular Structures. Machine Dynamics Problems 32(1), 113–121 (2008)
[10] Zalewski, R.: Constitutive model for special granular structures. Int. J. Non-Linear Mech. 45(3), 279–285 (2010)
[11] Zalewski, R., Pyrz, M.: Modeling and parameter identification of granular plastomer conglomerate submitted to internal underpressure. Engineering Structures 32(8), 2424–2431 (2010)
[12] Zalewski, R., Pyrz, M.: Experimental study and modeling of polymer granular structures submitted to internal underpressure. Mechanics of Materials 57, 75–85 (2013)
[13] Zalewski, R., Rutkowski, M.: Wpływ objętości próbki badawczej na wyniki prób jednoosiowego rozciągania specjalnych struktur granulowanych. Mechanik 12 (2011)
[14] Zalewski, R., Wolszakiewicz, T.: Analysis of uniaxial tensile tests for homogeneous solid propellants under various loading conditions. Central European Journal of Energetic Materials 8(4), 223–231 (2011)
[15] Zalewski, R., Pyrz, M., Wolszakiewicz, T.: Modeling of Solid Propellants Viscoplastic Behavior Using Evolutionary Algorithms. Central European Journal of Energetic Materials 7(4), 289–300 (2010)

Hardware in the Loop Simulation Model of BLDC Motor Taking Advantage of FPGA and CPU Simultaneous Implementation

V. Sova and R. Grepl

Mechlab, Brno University of Technology, Faculty of Mechanical Engineering,
Technicka 2, 616 69, Brno, Czech Republic
y116063@stud.fme.vutbr.cz, grepl@fme.vutbr.cz
www.mechlab.cz

Abstract. This paper presents Hardware in the Loop (HIL) simulation of the BLDC motor used in aerospace applications. Due to a high frequency driving signals and a high dynamics of the electrical part of the BLDC motor, the utilization of FPGA is necessary. The algorithm is distributed between the CPU and the FPGA and targeted to dSPACE modular hardware.

1 Introduction

The popularity of the BLDC motor has continuously grown over recent years. This engine is used in such applications as automotive [1][2], aerospace [3][4], industry and home appliances. The advantages of this motor are easy control mechanism, cost and power density. BLDC motors are also suitable for critical safety applications e.g. in aerospace. To develop an ECU for this motor, especially for critical safety applications, there is a need to test the ECU in various operating conditions, simulate faults, etc.

A high frequency PWM signal is used for the electric motors' control, so the correct real-time (RT) simulation of electrics motors needs the implementation on the FPGA [5]. Not only does the electric part of the motors needs FPGA implementation, but also every RT simulation of the system with a high dynamic (small time constant or high frequency input signal) [6]. Today's processor based RCP and HIL HW allows computational steps up to 10 μs [7], that's the restriction for simulating high dynamic systems.

A similar problem, BLDC motor RT simulation, is described in [5]. But they simulate the BLDC motor on the level of power signals. Sometimes it's called Power HIL simulation [8]. In contrast, we simulate the behaviour of the BLDC motor and Power Inverter, and only the controller is under test (Fig. 1).

T. Březina and R. Jabloński (eds.), *Mechatronics 2013*,
DOI: 10.1007/978-3-319-02294-9_18,

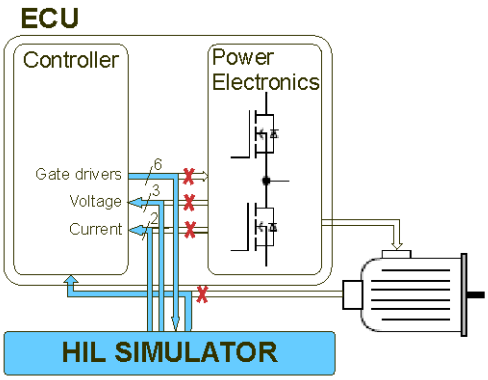

Fig. 1 BLDC motor HIL simulation scenario [9]

2 Simulation Model of BLDC Motor

A mathematical description is essential for offline and RT simulation. The model is derived on the following simplifying assumptions:

- The electric motor is symmetrical, three-phase star connected. Resistance and inductance of individual phases are equal.
- Inductance and mutual inductance are constant, independent of angular position.
- The magnetic circuit is unsaturated, leakage inductance and magnetic loss are ignored.
- Back Electro-Motive Force (BEMF) waveform is trapezoidal.
- Thermal influence is ignored.
- Only viscous friction is present.

The model is described by these equations [9]:

Electrical part

$$\begin{aligned} v_{as} &= Ri_a + L_s \frac{di_a}{dt} + e_a \\ v_{bs} &= Ri_b + L_s \frac{di_b}{dt} + e_b \\ v_{cs} &= Ri_c + L_s \frac{di_c}{dt} + e_c \\ i_a + i_b + i_c &= 0 \end{aligned} \tag{1}$$

Mechanical part

$$M_i = J\frac{d\omega_m}{dt} + B\omega_m + M_L \tag{2}$$

$$M_i = \frac{i_a e_a + i_b e_b + i_c e_c}{\omega_m}$$

$$\omega_m = \frac{1}{p}\frac{d\varphi_{el}}{dt},$$

where:

- v_{as}, v_{bs}, v_{cs} are phase voltages
- i_a, i_b, i_c are phase currents
- R is phase resistance
- L_s is substitional constant for inductance and mutual inductance
- e_{as}, e_{bs}, e_{cs} are BEMFs dependent on motor speed and angular position
- φ_{el} is electrical angular position of rotor
- ω_m is mechanical angular velocity of rotor
- B is viscous friction coefficient
- M_i is inner moment
- M_L is load moment
- J is moment of inertia
- p is number of pole pairs

Modeling of the BLDC motor according to these equations in a Matlab-Simulink environment seems an easy task. Sinusoidal (synchronous, induction) motors have at every moment accurately defined voltage at every terminal, and input to the model can be voltage. But the BLDC motor, in contrast of sinusoidal motors, needs a proper simulation model of the power inverter. During the commutation cycle of the BLDC motor, one phase is always unconnected, floating. A proper model of the power inverter has to be introduced.

3 Model of Power Inverter

Modeling the inverter with SimScape (physical system modeling library) under Simulink would be a simple task. But because we need to transform the model to FPGA with System Generator blocks, basic Simulink blocks have to be used.
One leg of the inverter (Fig. 2) has following behaviour:

- The top transistor is closed and the bottom is open, output is DC bus voltage (48 V).
- The bottom transistor is closed and the top is open, output is zero voltage (0 V).
- Both transistors are open and the current is positive, the current flows through the diode parallel to the bottom transistor, output is zero voltage minus voltage drop over diode (-0.6 V).

- Both transistors are open and the current is negative, the current flows through the diode parallel to the top transistor, output is DC bus voltage plus voltage drop over diode (48.6 V).
- Both transistors are open and the current is zero. Voltage according to (3) appears as if generated from a motor and keeps zero current during commutation phase.

For computational reasons the current is not compared to zero, but with a very low value close to zero. The algorithm is sensitive to zero-crossing detection settings because of the number of comparison blocks.

$$u_a = \frac{u_b + u_c + e_b - e_c + 2e_a}{2} \tag{3}$$

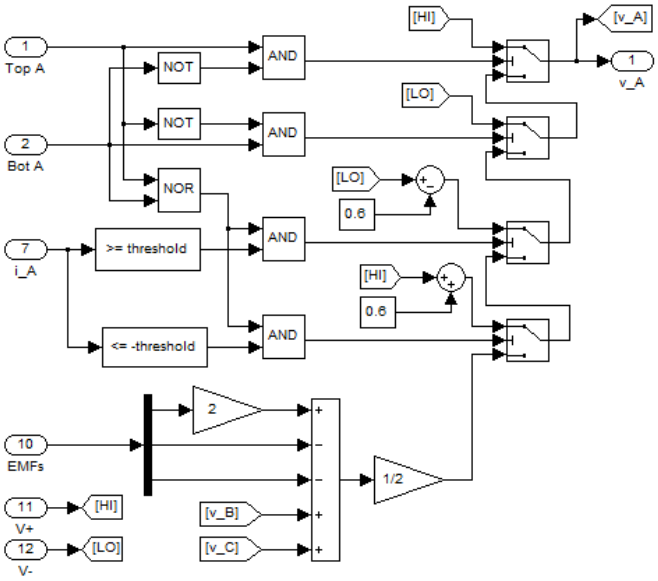

Fig. 2 Simulation model of one leg of power inverter [9]

4 Real-Time Model for HIL Simulation

This section deals with transformation of the simulation model, introduced in the previous section, in the model running in real-time. The RT model is targeted to modular dSPACE HW [10] with a DS1006 processor board and a DS5203 FPGA board [11]. The data can be shared between both boards via a fast PHS bus. So the model can be split between the FPGA and the processor. Parts of the model with high dynamic or high frequency driving signal (electrical part, power inverter) run on the FPGA and parts with low dynamics (mechanical part, hall signals and BEMFs generation) run on the processor.

Splitting the model between processor and FPGA also gets the advantage that parts targeting the processor are easily programmable, i.e. the model can be more complex. The distribution of the RT model and the testing scenario is in Fig. 3. The FPGA is running at 100 MHz so the resulting computational time step is 10 ns. The computational time step on the processor board is set to 20 µs.

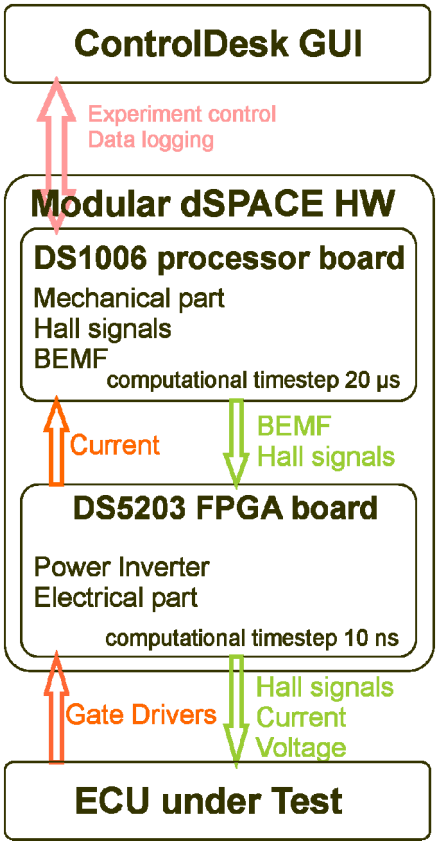

Fig. 3 BLDC motor HIL scenario and model division

The transition from the simulation model to the RT model was performed after the following steps passed. In the simulation model two computational time steps were set according to the FPGA and processor division and between these parts a communication traffic delay (model of communication delay between processor and FPGA board) was inserted. Continuous integration was replaced by discrete integration. After that the model behaves correctly. The next step was the replacement of floating-point data types for future FPGA parts with fixed-point data types. Common ranges of all signals were determined, and according to that the fixed-point range and resolution were set. After that the simulation was performed correctly and the transition could begin.

Mechanical parts of the simulation model of the BLDC motor targeting the processor board are easily portable with dSPACE RTI, and minimum work has to be done. Parts targeting the FPGA must be described with a Xilinx System Generator for DSP blocks (Fig. 4). In addition the FPGA timing constraint plays a role and lots of pipelining was used.

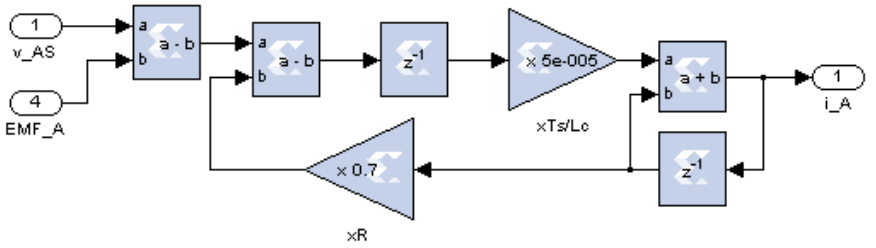

Fig. 4 Representation of one phase of BLDC motor according equation (1)

5 Experimental Results

RT simulation model was tested connected to the simulated controller. The simulated controller was just a simple six step commutation table and PWM control of the top transistors. RT simulation was stable and gives almost the same results as offline simulation describing the behaviour of the BLDC motor (Fig. 5). Resulting waveforms are consistent with the bahavior of real general purpose low-voltage BLDC motor.

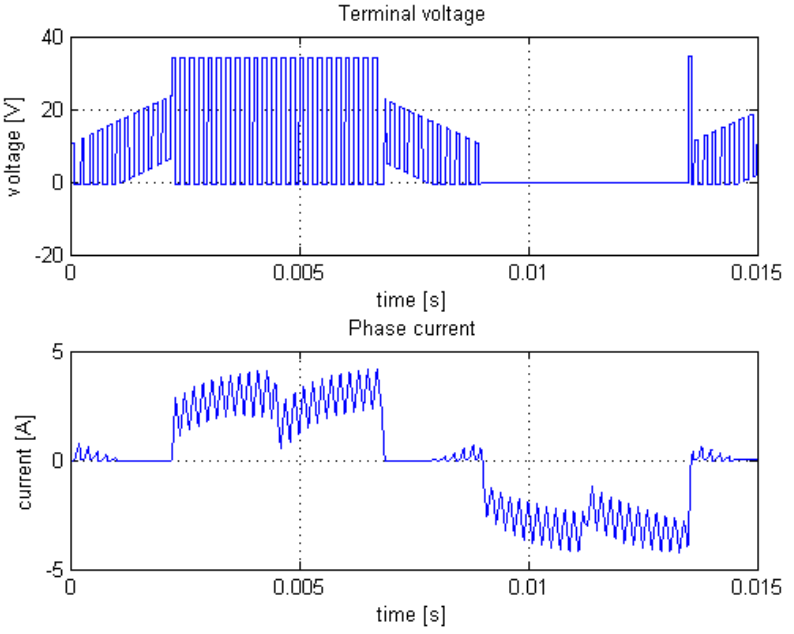

Fig. 5 Voltage and current waveform from RT simulation of BLDC motor [9]

The used simulation design is satisfactory to about 30000 electrical rotations per minute. Restrictions are mechanical parts computed on the processor with a relatively big time step. For higher velocities it is necessary to convert the mechanical part to FPGA.

6 Conclusion

In this paper a simulation model of the BLDC motor capable of real-time simulation on dSPACE modular HW was presented. This real-time model is suitable for HIL simulation and it was verified with a simulated controller. Due to high dynamics and high frequency driving signals, the electrical parts of the BLDC motor are computed on the FPGA.

All this work uses high-level programming/designing tools: Simulink and dSPACE RTI for the processor part, and Simulink, System Generator for DSP and dSPACE RTI FPGA for the FPGA. Creation and testing of the RT model was comfortable and relatively fast.

Acknowledgments. This work was supported by the European Commission within the FP7 project Efficient Systems and Propulsion for Small Aircraft "ESPOSA", contract No. ACP1-GA- 2011-284859-ESPOSA.

References

[1] Grepl, R., Lee, B.: Modeling, parameter estimation and nonlinear control of automotive electronic throttle using a Rapid-Control Prototyping technique. International Journal of Automotive Technology 11(4), 601–610, doi:10.1007/s12239-010-0072-7, WOS:000279216800018

[2] Grepl, R., Lee, B.: Model Based Controller Design for Automotive Electronic Throttle. In: 8th International Conference on Mechatronics Recent Advances in Mechatronics: 2008-2009, Luhacovice, Czech Republic (2009), WOS:000277076900036

[3] Toman, J., HubÍk, V., Singule, V.: Fuel metering pump development and modeling. In: ICINCO 2011, Proceedings of the 8th International Conference on Informatics in Control, Automation and Robotics, pp. 419–426. SciTePress, Portugal (2011) ISBN: 978-989-8425-74- 4

[4] Toman, J., HubÍk, V., Singule, V.: Development of the Control System for Electric Actuator with BLDC Motor. Engineering Mechanics 18(5/6), 289–296 (2012) ISBN: 978-989-8425-74- 4

[5] Schulte, T., Bracker, J.: Real-time simulation of BLDC motors for hardware-in-the-loop applications incorporating sensorless control. In: IEEE International Symposium on Industrial Electronics, ISIE 2008, June 30-July 2, pp. 2195–2200 (2008)

[6] Graf, C., Maas, J., Schulte, T., Weise-Emden, J.: Real-time HIL-simulation of power electronics. In: 34th Annual Conference of IEEE Industrial Electronics, IECON 2008, November 10-13, pp. 2829–2834 (2008)

[7] Abourida, S., Belanger, J., Dufour, C.: Real-time HIL simulation of a complete PMSM drive at 10 μS time step. In: 2005 European Conference on Power Electronics and Applications, p. 9 (2005)
[8] Wu, X., Lentijo, S., Deshmuk, A., Monti, A., Ponci, F.: Design and implementation of a power-hardware-in-the-loop interface: a nonlinear load case study. In: Twentieth Annual IEEE Applied Power Electronics Conference and Exposition, APEC 2005, March 6-10, vol. 2, pp. 1332–1338 (2005)
[9] Sova, V.: FPGA application for control and modelling of BLDC motor, Diploma thesis. Brno University of Technology, Faculty of Mechanical Engineering, Brno (2013)
[10] dSPACE Modular Hardware Overview, dSPACE GmbH (May 2013), http://www.dspace.com/en/pub/home/products/hw/modular_hardware_introduction.cfm
[11] DS5203 FPGA Board Overview, dSPACE GmbH (June 2013), http://www.dspace.com/en/pub/home/products/hw/modular_hardware_introduction/i_o_boards/ds5203_fpga_board.cfm

Using PSO Method for System Identification

M. Dub and A. Stefek

University of Defence, Faculty of Military Technology, Kounicova 65,
662 10, Brno, Czech Republic
{michal.dub,alexandr.stefek}@unob.cz

Abstract. The article deals with application of heuristic method in system identification process. Real measured data can be used for system identification. Usually real data has noisy component. For this reason sometimes the filtering is applied to original data and the result is used for identification. In this article the comparison of usage the original and prefiltered data is discussed. For identification the Particle swarm optimization method is used. Different approaches are also used to create initial agents' positions. Whole concept is tested using the MATLAB program.

1 Introduction

The optimization problem is common problem which we can meet everywhere. Nearly twenty years ago there were not enough powerful computers. For optimization the deterministic methods were used. When the computers become available it was possible to use stochastic methods. Many of stochastic methods are based on behaviour of real living creatures. There exist set of methods which are based on swarms, flocks, herds, ant hills etc. behaviour. One of first of them was Particle swarm optimization method [1][2].

The separately excited DC motor transfer function can be used as two or three-parameter system considering rotational speed response to armature voltage step. Such model can be more complicated considering passive friction torque and then four parameters must be used. System data are featured by input armature voltage and output rotational speed. The nominal voltage step function was used as a test input function. Rotational speed was measured by DC tachogenerator and thus voltage ripple and noise component at output can be found.

Particle Swarm Optimization (PSO) method has ability to explore the state space. The system introduced in previous paragraph can be described by 3-4 state variables. For this article the experiment will focus on problem with 3 state variables.

The initial estimates should be chosen according to PSO theory with uniformly distributed random vectors. Some modification of initial estimates based on previous study has been made to improve simulation of inexperienced operator effort. System data have also been used original as well as prefiltered to evaluate PSO ability to process noisy measured data [3].

T. Březina and R. Jabloński (eds.), *Mechatronics 2013*,
DOI: 10.1007/978-3-319-02294-9_19,

2 Particle Swarm Optimization Method

The PSO method uses set of agents which are moving across state space (set of feasible solutions) exploring it. In each step of moving the agent is evaluating fitness function. Each agent memories best personal position and "best in swarm" position. When agent finds new best position he informs all cooperating agents about this event so every agent has updated information about current stage of optimization process [1][2].

The model of agent moving is based on law of motion.

$$v(k+1) = c_1 v(k) + rc_2\left(x_p - x(k)\right) + rc_3\left(x_s - x(k)\right), \tag{1}$$

$$x(k+1) = x(k) + v(k+1), \tag{2}$$

where $x(k)$, $x(k+1)$ agent positions,
$v(k)$, $v(k+1)$ agent velocities,
x_p personal best positions,
x_s swarm best positions,
r random number (0;1),
c_1, c_2, c_3 PSO parameters;

Even if the PSO was widely discussed and many improvements were suggested, for this task the original algorithm was used. As proved before [3] the original algorithm offers good results so right now there is not any reason to use improvements which can complicate the implementation.

3 Experiment Description

It was decided to run two basic sets of experiments to evaluate PSO method as listed in Table 1. PSO coefficients $c_1 = 0.7$, $c_2 = 1.4$ and $c_3 = 1.4$ were used as basic PSO coefficients for all experiments. This decision considers another previous study [3].

Table 1 Performed experiments

Experiment	Number of agents	Number of PSO steps	Initial agents' positions
A	16	25	uniformly distributed random vectors
B	16	25	uniformly distributed random order of magnitudes

The quality of the identification process is evaluated by the integral fitness function J which is based on square differences between system output and its model output (Eq. 3a). For simulation purposes the discrete form of this function was used (Eq. 3b).

$$J = J(x) = \int_0^{tfinal} \left(\omega_{Mi} - \omega_{Si}\right)^2 dt\,, \tag{3a}$$

$$J = J(x) = \sum_{i=1}^{N} \left[\left(\omega_{Mi} - \omega_{Si}\right)^2 \Delta t\right], \tag{3b}$$

The model variables are motor gain coefficient K and motor time constants T_a and T_m which are stored in the vector of parameters $x = [K\ T_a\ T_m]$. It is possible to represent the search of the parameters as search of the J function minimum. The transfer function defined by this vector is introduced in Eq. 4.

$$F(s) = \frac{K}{T_a T_m s^2 + T_m s + 1}\,, \tag{4}$$

Just for clarification – for the identification there are another two models which can be used in this case (see Eq. 5a and 5b) but this paper will stick with model in Eq. 4.

$$F(s) = \frac{K}{(T_1 + s)(T_2 + s)}\,, \tag{5a}$$

$$F(s) = \frac{K}{as^2 + bs + 1}\,, \tag{5b}$$

4 Finding the Global Minimum

Rotational speed was measured by K6A1 DC tachogenerator. TiePie-HS4 oscilloscope with sampling frequency set to 20 kHz was used to measure and record the data. Measured tachogenerator voltage was converted to the rotational speed using MATLAB computation functions (original data). Noise fast changes of rotational speed were filtered off using low-pass filter with 0.003 sec time constant (prefiltered data).

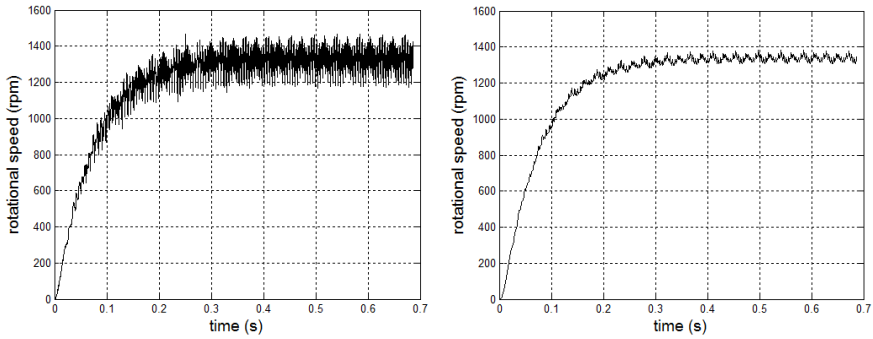

Fig. 1 System output (rotational speed): original (left) and prefiltered (right)

It is necessary to know global minimum of fitness function to evaluate PSO method. In this case Nelder-Mead simplex search method and knowledge based approach to get it was used. Experienced operator would set initial estimate x_0 of the searched parameters according to the system measured response. The motor gain (K) was set to 100 rpm/Volts, the electromagnetic time constant (T_a) was set to one millisecond and the electromechanical time constant (T_m) was set to ten milliseconds. The software support of the `fminsearch` function of the MATLAB program was used to find the minimum of a scalar function of several variables.

Table 2 Fitness function global minimum found by Nelder-Mead search

Data	x_0	x	J
noisy	1e+002	1.0655e+002	2.3432e+003
	1e-003	3.3478e-003	
	1e-002	6.5178e-002	
prefiltered	1e+002	1.0654e+002	1.5865e+002
	1e-003	6.0102e-003	
	1e-002	6.8055e-002	

5 Experiments Evaluation

Experiment A initial agents' positions were created according to PSO theory with uniformly distributed random vectors. Only positive numbers from particular interval given by its minimum and maximum were considered. Results of the simulations are listed in Table 4 and Table 5. Although a lot of simulations were calculated, only typical samples of results are presented because of paper limited space.

Random number generation was controlled to have ability to repeat simulation anytime in the future. Moreover, the routine is compiled that way the PSO method uses the same random number generator in both experiments. Seeds of the random number generator for all simulations are listed in Table 3. Tables 4-7 contain the results of simulations. The usage of seeds grants the same positions of agents at beginning of simulation – PSO optimization.

Routine was compiled in MATLAB R2009a release, so random number generator syntax should be updated if MATLAB R2011a or any modern release is used to repeat our simulations. Only part of MATLAB program is presented to show the ability to repeat simulation:

```
%% Data load
%% Optional prefiltering
%% Random number generator control
    idrnd=rand;
    rand('seed', idrnd)
%% Initial agents' positions: x0
    x0=max*rand(16,3);
%PSO algorithm
    rand('seed', idrnd)
    %% Choice of agent best position: xagent
    %% Choice of swarm: xswarm
    %% Computation of agents' velocities: v
    v=0.7*presentv(i,:)+
        1.4*rand(1)*(xagent(i,:)-presentx(i,:))+
        1.4*rand(1)*(xswarm-presentx(i,:));
    %% Computation of agents' positions: presentx
    %% Computation of agent position
    %% Evaluation of fitness function
%% Final results
```

Code 1 First part of MATLAB code (Experiment A)

Experiment B initial agents' positions are given by vectors of uniformly distributed random order of magnitudes (those two approach for generation of initial positions have same relation as Matlab commands `linspace` and `logspace`). Only positive numbers from the order of magnitudes interval I_B=[1e-003; 1e+004] were considered. Results of the simulations are listed in Table 4 and Table 5.

```
%% Initial agents' positions: x0
    RAD=[0.001 0.01 0.1 1 10 100 1000 10000];
    VRAD=ceil(8*rand(16,3));
         for R = 1:16
             for C = 1:3
                 x0(R,C) = RAD(VRAD(R,C))*rand(1);
             end
         end
```

Code 2 Variation of first part of MATLAB code (Experiment B)

Table 3 Seed of the random number generator

Seed of the random number generator				
323	6614	2795	8972	6909
3514	5764	4426	9924	4872
8551	600	1764	5942	5693
3708	7445	918	330	8957

Seeds in Table 3 were used for Experiment A-noisy, Experiment A-prefiltered, Experiment B-noisy, Experiment B-prefiltered and results of those simulations are at same position in Tables 4-7 as seed in Table 3.

Table 4 Experiment A results: original noisy data

Interval	Local fitness function minimum				
0	3.8232e+005	1.0323e+006	1.0332e+006	1.0259e+006	1.0312e+006
1e+004	6.6390e+005	9.6670e+005	1.0334e+006	3.8112e+005	8.0229e+005
	1.0319e+006	1.0037e+006	1.0244e+006	1.0273e+006	5.6869e+005
	9.2375e+005	1.0313e+006	8.7102e+005	1.0092e+006	1.0116e+006

Table 5 Experiment A results: prefiltered data

Interval	Local fitness function minimum				
0	3.7500e+005	1.0246e+006	1.0256e+006	1.0183e+006	1.0235e+006
1e+004	6.5634e+005	9.5903e+005	1.0257e+006	3.7405e+005	7.9468e+005
	1.0242e+006	9.9599e+005	1.0168e+006	1.0196e+006	5.6120e+005
	9.1610e+005	1.0236e+006	8.6339e+005	1.0015e+006	1.0039e+006

It must be noted that none of the local best identification processes of Experiments A reached such fitness function global minimum as listed in Table 2 (see shaded cells). Thus Experiment A was confirmed as unsuccessful.

Table 6 Experiment B results: original noisy data

Interval	Local fitness function minimum				
1e-003	1.5923e+005	1.5722e+005	2.6208e+003	1.6065e+005	7.6803e+003
1e+004	3.8150e+005	2.1174e+005	3.5194e+005	3.5725e+005	1.5871e+005
	1.5788e+005	1.3024e+004	1.2683e+005	1.2988e+005	1.5500e+005
	2.8867e+004	3.5544e+005	8.4793e+003	1.3546e+005	2.9960e+005

Table 7 Experiment B results: prefiltered data

Interval	Local fitness function minimum				
1e-003	1.5322e+005	1.5124e+005	2.6741e+002	1.5479e+005	4.3977e+003
1e+004	3.7419e+005	2.0482e+005	3.4472e+005	3.5002e+005	1.5265e+005
	1.5194e+005	1.0557e+004	1.2066e+005	1.2358e+005	1.4905e+005
	2.9589e+004	3.4808e+005	5.0180e+003	1.2968e+005	2.9233e+005

Note some of the local best identification processes of experiment B reached or were very close to fitness function global minimum as listed in Table 2 (see shaded cells). Thus Experiment B was evaluated as successful.

Table 8 Fitness function local minimum found by PSO method (experiment B)

Seed	Best swarm position based on noisy data	J_n	Best swarm position based on prefiltered data	J_p
2795	1.0587e+002	2.6208e+003	1.0617e+002	2.6741e+002
	1.0504e-002		1.0549e-002	
	6.2364e-002		6.6360e-002	
6909	1.0305e+002	7.6803e+003	1.0675e+002	4.3977e+003
	2.6080e-002		2.5053e-002	
	4.1584e-002		4.9888e-002	
918	1.0396e+002	8.4793e+003	1.0396e+002	5.0180e+003
	3.3850e-002		3.3850e-002	
	7.4989e-002		7.4989e-002	

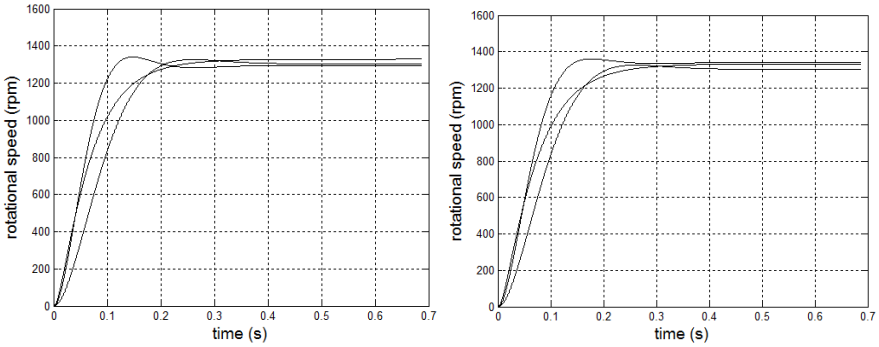

Fig. 2 Best PSO final estimates: noisy data (left) and prefiltered data (right)

6 Conclusion

Four basic experiments dealing with PSO method application to simple three-parameter model experimental identification were compiled and evaluated. Two of them were taken as a comparison [3] to new two experiments. New experiments used the original measured data with noisy component. In this study the general form of fitness function was defined and used for evaluation. One experiment uses the linear distribution while second uses the logarithmic distribution.

All experiments were fixed to predetermined random sequence. This approach allows the precious comparison of different configurations.

This study proved that logarithmic distribution of initial PSO particles positions will noticeable improve the results.

Acknowledgments. The work presented in this paper has been supported by the Ministry of Defence of the Czech Republic (K206 Department development program "Complex aviation electronic system for unmanned aerial systems").

References

[1] Kennedy, J., Eberhart, R.: Particle Swarm Optimization. In: Proc. IEEE International Conference on Neural Networks, Perth, Australia, pp. 1942–1948 (1995)

[2] Kennedy, J., Eberhart, R.: Swarm Intelligence. Morgan Kaufmann (2001) ISBN 1-55860-595-9

[3] Dub, M., Stefek, A.: Evaluation of PSO Method Application to DC Machine Experimental Identification. In: ICMT 2013 Conference, pp. 887–892 (2013) ISBN 978-80-7231-917-6

Damping of Machine Frame Vibrations by an Electro-magnetic Actuator

G.J. Stein and R. Chmúrny

Slovak Academy of Sciences, Institute of Materials and Machine Mechanics,
Račianska 75, SK-831 02, Bratislava, Slovakia
{stein,rudolf.chmurny}@savba.sk

Abstract. In the paper the use of permanent magnet with coil for transversal vibration control of a flexible slender beam is analysed. The magnetic flux is varied due to external harmonic excitation. The so induced alternating voltage drives alternating current through a closed electric circuit. The induced current driven through the coil generates magnetic force, which counteracts the excitation force and so damps the vibration. The internal losses in the coil influence the overall system's performance. A model of the system is derived in a simplified, linearised form. The extent of introduced damping is assessed.

1 Introduction

Many of the vibration control problems of rotating machinery are associated with various resonance phenomena in the machine frame. To avoid interaction of the dominant rotating frequencies with eigenfrequencies of the supporting structure following methods are used:

- Detuning of the frame eigenfrequencies from the operational frequencies,
- Introduction of additional damping to the structural damping of the frame.

Some innovative approaches have been explored recently using active and semi-active methods of vibration control. Piezoelectric, electro-dynamic and electro-magnetic actuators are widely used for such a control strategy, as presented e.g. in [1-3]. Some applications of vibration control of a cantilever beam using electromagnetic vibration controller were published, too [4-6].

The contribution, based on authors' previous work [7-9], analyses the use of a permanent magnet with a coil for similar purpose. It has been shown that the controller of interest is capable to introduce damping, as well as alter natural frequency of the oscillatory system. The dummy system mocks-up a rotating machine, situated on a frame.

2 Analysis of the Mechanical System

It is assumed that the particular machine frame can be approximated by a beam of length l, uniform cross-section of area A_b, moment of inertia of the beam

T. Březina and R. Jabloński (eds.), *Mechatronics 2013*,
DOI: 10.1007/978-3-319-02294-9_20,

cross-section I_b, made of material described the modulus of elasticity (Young's module) E_b. It is further assumed that the frame is rigidly fixed at both ends to a supporting structure. Approximately in the middle of the beam the rotating machine of mass M is located. Below the beam the yoke of the permanent magnet is located. Let us assume that the machine and the yoke could be represented as a concentrated mass, located at the beam mid-point.

During steady-state operation of the machine a harmonic force FE is generated at machine rotating frequency and its higher harmonics, due e.g. to small imbalance. The excitation force would induce transversal vibrations of the beam. Assuming, that the vibrations are of small magnitude and the beam is slender, the Euler-Bernoulli vibration theory of transversal beam vibrations can be applied. According to formulas given in [10], referring to [11], the fundamental angular eigenfrequency of the beam ωf, under stipulated conditions, is given by the formula:

$$\omega_f^2 = 192 \cdot \frac{E_b I_b}{l^3} \cdot \frac{1}{(M + \frac{13}{35} m)} = \frac{k_S}{M} \cdot \frac{1}{(1 + 0.3714 \frac{m}{M})} \quad . \tag{1}$$

If the load mass M is larger than the beam mass m, the fundamental eigenfrequency is essentially the same as the natural frequency of an single-degree of freedom (SDOF) oscillatory system with parameters M and k_S; however, slightly perturbed by the second term. There is an antinode at beam midpoint, hence vibrations at beam second eigenfrequency are not excited. Vibrations at higher eigenfrequencies are usually of very small amplitude and can be neglected [11]. So the most important resonance could occur at beam first eigenfrequency. Hence, the frame dynamics can be approximated by an equivalent SDOF oscillatory system.

The dynamics of the SDOF oscillatory system, subjected to a harmonic excitation force $F_E(t)$ with additional oscillatory magnetic force $F_M(t)$ is described by the governing equation:

$$M\ddot{w} + c_S \dot{w} + k_S w = F_E(t) - F_M(d_0, i(t)) \quad , \tag{2}$$

where: M is the mass of the yoke and mass of the machine, c_s is the damping coefficient, modelling the internal damping of the beam, k_s is the equivalent beam stiffness at its midpoint, w is midpoint displacement and d_0 is the distance between the upper plane of the core to the yoke in standstill.

Introducing the relative air gap width $\varepsilon(t) = w(t)/d_0$ and the natural frequency of the equivalent oscillatory system ω_0 ($\omega_0 = \sqrt{k_s/M}$), being beam first eigenfrequency:

$$\ddot{\varepsilon} + \left(\frac{c_S}{M}\right)\dot{\varepsilon} + \omega_0^2 \varepsilon = \frac{F_E(t)}{M d_0} - \frac{F_M(t)}{M d_0} \, . \tag{3}$$

The relative air gap width $\varepsilon(t)$ is in fact the relative dynamic displacement. It will be further assumed that $|w(t)| << d_0$, i.e. $|\varepsilon(t)| << 1$.

3 Derivation of the Magnetic Force Components

A pot type magnet is located below the ferromagnetic yoke, which is fixed in the middle of the machine frame. A static magnetic field is generated by the permanent magnet (PM), located in the centre of a coil. As the yoke vibrates due to the influence of the harmonic force FE(t), the air gap width d(t) varies with time. The variation of d(t) is responsible for time variation of the air gap reluctance and consequently for the primary magnetic flux time variations. According to Faraday's law, magnetic flux time variation induces alternating voltage u(t) in the coil. The induced voltage forces a current i(t) flowing in the closed electrical circuit. The direction of i(t) is such that so generated secondary magnetic field opposes the primary field of the PM (Lenz's law). The alternating magnetic force, due to the induced current counteracts the excitation force. The combination of the static magnetic force of the PM and the dynamic one influences the structure stiffness and thus the natural frequency. Moreover, the induced current i(t) influences the extent of damping [7-9].

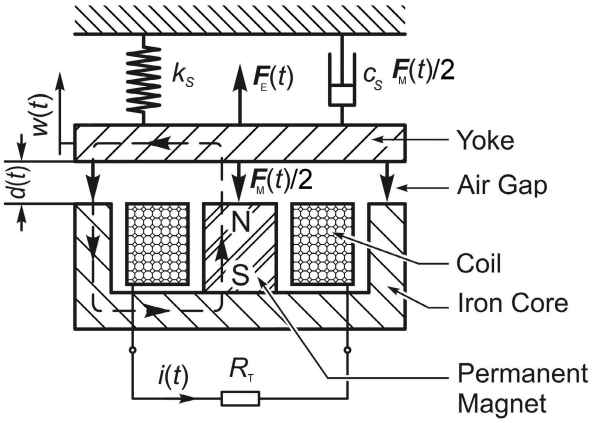

Fig. 1 Equivalent SDOF oscillatory system

The magnetic force for this particular case is in general given [9]:

$$F_M(t) = \frac{\mu_0 S_C}{4d_0^2} \frac{[M_m + i(t)N]^2}{[(1+\delta)+\varepsilon(t)]^2} = \frac{\mu_0 S_C}{4d_0^2} \frac{F_\Phi(t)^2}{[(1+\delta)+\varepsilon(t)]^2}, \quad (4)$$

where μ_0 is the permeability of air (vacuum), S_C is the core cross-section, N is the number of turns of the coil, M_m is the magnetisation of the PM, $i(t)$ is the induced current, $F_\Phi(t)$ is the so-called magnetomotive force [2] and d_0 is the distance between the yoke and the upper plane of the core.

The term $(1+\delta)$ accounts for the magnetic circuit properties in respect to air gap width d_0, as explained in more detail in [9]. The magnetic force is highly non-linear and some simplifications have to be made to allow the analytical treatment.

Because of $|\varepsilon| << 1$ the magnetic force F_M can be approximated by linearization in respect to the variable ε:

$$F_M(\varepsilon(t)) \cong \frac{\mu_0 S_C}{4d_0^2}\frac{\left[M_m + i(t)N\right]^2}{(1+\delta)^2} - \frac{\mu_0 S_C}{2d_0^2}\frac{\left[M_m + i(t)N\right]^2}{(1+\delta)^3}\varepsilon(t)\,. \tag{5}$$

The induced current $i(t)$ follows from application of the Faraday's and Lenz's laws for this particular configuration and is given by the formula [8, 9]:

$$i(t) = -\frac{NS_W}{R_T}\frac{dB(t)}{dt}\,, \tag{6}$$

where: R_T is the total circuit resistance and S_W is the cross section of the coil winding. It can be assumed that $S_W \cong S_C$. The total resistance R_T in the electric circuit is assumed to consist of the series combination of the external shunt resistance R_S, internal resistance of the coil R_C and the resistor R_L, which is used to model the frequency dependent losses in the magnetic material. The resistances R_C and R_L are connected in series with the coil inductance L_0:

$$R_T(\omega) = R_S + R_C + R_L(\omega)\,. \tag{7}$$

As expected, the induced current $i(t)$ is determined by the changes of the magnetic induction in the air gap dB/dt. As derived in [7] the time dependence of the variable magnetic induction $B(t)$ can be expressed as:

$$\frac{d^2B(t)}{dt^2}\left[\frac{\mu_0 N^2 S_W}{2d_0(1+\delta)}\right]\frac{1}{R_T} + \frac{dB(t)}{dt} = -\frac{B_0}{(1+\delta)}\dot{\varepsilon}\,. \tag{8}$$

The term in the square bracket is the self inductance L_0 of the coil at air gap d_0 and B_0 is the static magnetic induction in the air gap of width d_0.

In absence of vibration no current is flowing and just a static magnetic field of induction B_0 is present in the air gap due to PM magnetisation M_m:

$$B_0 = \frac{\mu_0}{2d_0}\frac{M_m}{(1+\delta)} = const(d_0)\,. \tag{9}$$

The static magnetic force F_{MS} is counteracted by the elastic spring force F_S. If F_{MS} were to overwhelm F_S, the yoke would be permanently attracted to the PM

and any oscillatory motion would cease. This situation has to be avoided. Hence, there is a limit on the distance d_0, as explained in more detail in [8, 9].

4 System Description for Harmonic Excitation

The response of the system is in further analyzed under steady state condition. It is assumed, that all transient phenomena (electric and mechanic) are extinct. The exciting harmonic force is $F_E(t) = F_0\sin(\omega t)$ of angular frequency ω is expressed, using the complex notation, as $F_E(t) = F_0\mathrm{Re}\{\exp(\mathrm{j}\omega t)\}$. Assuming, that the response will be harmonic too, the complex relative air gap width $\tilde{E}$ will be expressed as $\tilde{E}e^{\mathrm{j}\omega t} = \varepsilon_0 e^{\mathrm{j}\varphi_\varepsilon} e^{\mathrm{j}\omega t}$. Then:

$$\left[1 - \Omega^2 + 2\mathrm{j}\xi_S\Omega\right]\tilde{E}e^{\mathrm{j}\omega t} = \frac{\tilde{F}_E e^{\mathrm{j}\omega t}}{k_S d_0} - \frac{\tilde{F}_M}{k_S d_0}, \tag{10}$$

where $\Omega = \omega/\omega_0$ is the non-dimensional frequency ratio and $\xi_s = c_s/c_c$ is the damping ratio with $c_c = \sqrt{(k_S M)}$ being the critical damping coefficient.

The term in the square brackets on the left hand side is a linear second order operator, describing the behaviour of the SDOF oscillatory system without the influence of the PM magnetic field. The normalized displacement response of the uncontrolled mechanical SDOF oscillatory system $\tilde{E}_0$ can be evaluated for any external harmonic excitation force F_E by setting the magnetic force to zero.

The magnetic force phasor $\tilde{F}_M$ in linearised, approximate form can be expressed in the frequency domain as a series of components at multiples of the excitation angular frequency ω [7-9], as follows from Eq. (5):

$$\tilde{F}_M = \sum_{n=0}^{Q} \tilde{F}_{Mn} e^{\mathrm{j}n\omega t} = \frac{\mu_0 S_C}{4 d_0^{\,2}} \frac{(M_m + \tilde{I}N)^2}{(1+\delta)^2} - \frac{\mu_0 S_C}{2 d_0^{\,2}} \frac{(M_m + \tilde{I}N)^2 \cdot \tilde{E}e^{\mathrm{j}\omega t}}{(1+\delta)^3}. \tag{11}$$

Taking the Fourier transform of Eq. (6), the induced current phasor $\tilde{I} = I_0 e^{j\varphi_i}$ is described by the changes of magnetic induction phasor $\tilde{B} = B_0 e^{j\varphi_B}$:

$$\tilde{I} = -\mathrm{j}\omega \frac{N^2 S_W}{R_T} \tilde{B}. \tag{12}$$

The magnetic induction phasor $\tilde{B}$ is evaluated from Eq. (8) by applying Fourier transform. After some algebraic manipulation it follows:

$$\tilde{B} = -\frac{B_0 R_T}{(1+\delta)(R_T + \mathrm{j}\omega L_0)} \tilde{E}. \tag{13}$$

Further inserting B_0 from Eq. (9) the square of the magnetomotive force phasor $\tilde{F}_\Phi$ is expressed:

$$\left(\tilde{F}_{\Phi}\right)^2 = M_{\mathrm{m}}^{\,2} + \frac{2\mathrm{j}\,\omega L_0 M_{\mathrm{m}}^{\,2}\tilde{E}}{(1+\delta)(R_{\mathrm{T}} + \mathrm{j}\omega L_0)} - \left(\frac{\omega L_0 M_{\mathrm{m}}^{\,2}\tilde{E}}{(1+\delta)(R_{\mathrm{T}} + \mathrm{j}\omega L_0)}\right)^2 . \quad (14)$$

From Eqs. (11) and (14) it can be qualitatively seen, that after performing the prescribed multiplications and some algebraic re-arrangement following magnetic force components emerge [7-9]:

- *a static component for* $n = 0$, affecting the equilibrium position at d_0 and so the static magnetic induction B_0:

$$F_{\mathrm{MS}} = \frac{\mu_0 S_{\mathrm{C}} M_{\mathrm{m}}^{\,2}}{4d_0^2(1+\delta)^2} = \left[\frac{\mu_0 S_{\mathrm{C}} M_{\mathrm{m}}^{\,2}}{2d_0^3(1+\delta)^3}\right]\cdot\frac{d_0(1+\delta)}{2} , \quad (15)$$

- *a component at* $\omega(n = 1)$, contributing to the equation of motion:

$$\tilde{F}_{\mathrm{M1}} = \left[\frac{\mu_0 S_{\mathrm{C}} M_{\mathrm{m}}^{\,2}}{2d_0^3(1+\delta)^3}\right]\cdot\frac{\mathrm{j}\omega L_0}{R + \mathrm{j}\omega L_0}\cdot d_0\tilde{E} - \left[\frac{\mu_0 S_{\mathrm{C}} M_{\mathrm{m}}^{\,2}}{2d_0^3(1+\delta)^3}\right]\cdot d_0\tilde{E} . \quad (16)$$

Both terms give relation between the relative air gap phasor $\tilde{E}$ and the magnetic force component phasor $\tilde{F}_{M1}$.

- *a second harmonic component* at the angular frequency $2\times\omega$ ($n = 2$), which is well known to be associated with magnetic circuits [2, 12]. However, in the case of clamped-clamped beam excited at the midpoint, i.e. in the antinode, no mechanical effect could result. Hence, this component does not enter the analysis.
- *a third harmonic component* at the angular frequency $3\times\omega$ ($n = 3$). However, being of the order of $|\varepsilon|^3$ it can be assumed, for simplicity, that it does not markedly influence the system behaviour.

Note, that in Eq. (15) and (16) the same factor (highlighted in the square brackets), related to the magnetic circuit properties, occurs. This factor can be termed the equivalent, linearised magnetic field stiffness k_{M} for air gap width d_0. Then the Eq. (16) can be modified and introduced into Eq. (10), to arrive at the system behaviour at excitation frequency ω

$$\left[1 - \Omega^2 + 2\mathrm{j}\zeta_S\Omega\right]\cdot\tilde{E} = \frac{\tilde{F}_{\mathrm{E}}}{k_{\mathrm{S}}d_0} + \frac{k_{\mathrm{M}}}{k_{\mathrm{S}}d_0}\frac{(R_{\mathrm{T}}^2 - \mathrm{j}\omega L_0 R_{\mathrm{T}})}{R_{\mathrm{T}}^2 + \omega^2 L_0^2}\cdot\tilde{E} . \quad (17)$$

Introducing the stiffness ratio κ ($\kappa = k_{\mathrm{M}}/k_{\mathrm{S}}$) and the coil reactance X_0 at the mechanical system natural frequency ω_0: $X_0 = \omega_0 L_0$, Eq. (17) can be further modified to become:

$$\left[\left(1 - \kappa\frac{R_{\mathrm{T}}^2}{R_{\mathrm{T}}^2 + \Omega^2 X_0^2}\right) - \Omega^2 + 2\mathrm{j}\Omega\left(\zeta_{\mathrm{S}} + \frac{\kappa}{2}\frac{X_0 R_{\mathrm{T}}}{R_{\mathrm{T}}^2 + \Omega^2 X_0^2}\right)\right]\tilde{E} = \frac{\tilde{F}_{\mathrm{E}}}{d_0 k_{\mathrm{S}}} . \quad (18)$$

The displacement response of the system $\tilde{E}$, can be now evaluated from Eq. (18) and compared to the response of the uncontrolled mechanical system $\tilde{E}_0$. As discussed in more detail in [7], there is an optimal value of the total resistance R_T, equal to X_0, when the maximum of electromagnetic damping is attained.

5 Experimental Determination of the System Parameters

The equivalent beam stiffness for midpoint deflection k_s was measured using a rigid load of 6.925 kg situated at beam midpoint. The midpoint deflection was measured by a dial indicator as being 0.96 mm leading to $k_S = 7.08\times10^4$ N/m. The mass of the beam was 0.472 kg. According to Eq. (1) the first beam eigenfrequency under the given load is 97.8 rad/s, i.e. 15.6 Hz.

The static magnetic force F_{MS} dependence on air gap width d_0 is given by Eq. (15). However, not all variables in Eq. (15) are readily available. Hence, the dependence had to be established experimentally. For this purpose a test stand was made, enabling to move the PM in the vertical direction. The combination of the yoke weight and the magnetic force was measured by a force transducer, type LCM101, manufactured by Omega Engineering, Stamford, Con., USA; while the distance d_0 was determined by a set of plastic foils of thickness 0.22 mm. Because the force transducer was sensitive both to pull and to compression a somehow tricky adjustment was needed to arrive at the exerted force. From Eq. (15) follows:

$$\sqrt{\frac{\mu_0 S_C}{4F_{M0}}} = \frac{(d_0\delta)}{M_m} + \frac{d_0}{M_m} = \alpha + \beta d_0 , \tag{19}$$

wherefrom the unknown parameters $(\delta d_0) = d_m$ and magnetisation M_m can be identified by linear regression. The distance d_m represents the porperties of the magnetic circuit transformed into air [9]. Using a linear regression programme it was determined that $d_m = 0.50$ mm and $M_m = 900$ A. The regression coefficient was 0.996, indicating good linearity. Hence influence of stray magnetic field and magnetic material non-linearity [2, 12] is negligible. In comparison to PM used in [9] this one is much stronger.

The electric properties of the particular PM with coil, type GMPX 050 of the Magnet Schulz Company were measured for various air gap widths: 0.22 mm, 0.45 mm, 0.90 mm and 1.35 mm, using the automatic RLC meter of type Hioki IM 3570. For all air gap widths the DC coil resistance was $R_C = 17.0\ \Omega$. The core cross-section is, according to manufacturer's drawing, $S_c = 4.41\times10^{-4}$ m^2. It was observed, that the coil resistance, R_L, as well as coil reactance X_0 are frequency and air gap dependent [9]. From the said measurements the values of R_L and X_0 are interpolated.

6 Simulation Results for the Analysed Case

Eq. (18) was programmed in the Matlab® programming environment assuming the above chassis parameters, loaded by stipulated machine mass $M = 7$ kg at chassis midpoint. For the evaluated beam equivalent stiffness $k_S = 7.08 \times 10^4$ N/m the undamped natural frequency of the equivalent SDOF oscillatory system is some $\omega_0 \approx 100$ rad/s, i.e. 16 Hz. Let us assume mechanical damping ratio $\xi_S = 0.03$ and excitation force $F_E = 5$ N, due e.g. to machine imbalance.

For illustration the projection of the course of the FRF response modulus $\left|\tilde{E}\right|$, according to Eq. (18), for the air gap width $d_0 = 1.70$ mm and a set of shunt resistance R_S values is presented in Fig. 2. In Fig. 2 the thick gray curve depicts the course of the FRF modulus maximum, while the bold one represents the uncontrolled mechanical system FRF modulus of $\tilde{E}_0$. Note the increase in the controlled system FRF modulus in respect to increase of R_S, and, concurrently, decrease in the natural frequency. As noted above, from [7] follows, that the optimum damping is for $R_T = X_0 = 22\ \Omega$. Due to device internal losses this occurs for $R_S = 0$. As the R_S increases there is a departure from the optimum.

It can be concluded, that to obtain the most electro-dynamic damping out of the actuator the coil has to be short-circuited. The loss of mechanical energy is transformed into heat in the actuator and absorbed or radiated from the device.

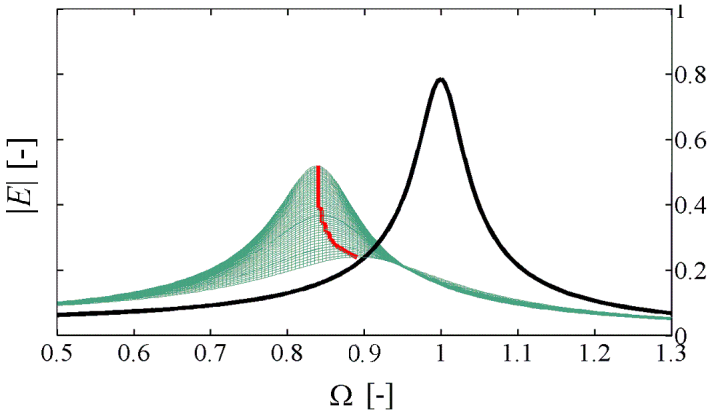

Fig. 2 Projection of the FRF modulus in respect to shunt resistance R_S ($R_S \in (0\ \Omega, 100\ \Omega)$)

Assuming a short-circuited coil, the only means of control is the air gap width d_0. From below the air gap width is limited by the limit when the static magnetic force would overwhelm the spring elastic, as explained in [9]. For the analysed case, given the magnetic circuit properties, the limit is at $d_{0L} \approx 1.00$ mm. The

dependence of the FRF response modulus $\left|\widetilde{E}\right|$ for selected air gap widths d_0 in comparison to the FRF modulus of uncontrolled system $\widetilde{E}_0$ is depicted in Fig. 3.

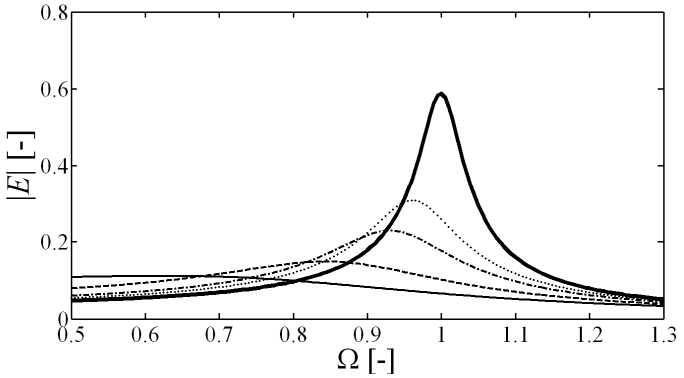

Fig. 3 The FRF modulus for $R_S = 0$ in respect to air gap width d_0 ($d_0 = 1.2$ mm, solid; $d_0 = 1.5$ mm, dashed; $d_0 = 2.0$ mm, dash--dotted; $d_0 = 2.5$ mm, dotted)

From Fig. 3 it is seen, that the best control is obtained for the smallest d_0, as expected. For the air gap width $d_0 = 1.2$ mm the improvement in respect to uncontrolled system is approximately 5.3-fold, i.e. by approx. 14 dB; decreasing as d_0 increases.

7 Conclusion

Based on the developed theory and some measured data for the particular permanent magnet with coil and a realistic machine chassis, the advantage of use of a permanent magnet with a coil as a vibration controller is exploited. It was found, that due to inherent electrical properties of the coil the best vibration attenuation is attained with a short-circuited coil. The original system natural frequency can be markedly lowered and up to five-fold vibration attenuation at the machine frame first eigenfrequency can be attained.

Acknowledgement. This contribution is a result of the project No. 2/0058/13 of the Slovak VEGA Grant Agency.

References

[1] Hagood, N., von Flotow, A.: Damping of structural vibration with piezoelectric materials and passive electrical networks. J. of Sound and Vibration 146(2), 243–268 (1991)
[2] Giurgiutiu, V., Lyshewski, S.E.: Micromechatronics: Modeling, Analysis and Design, 2nd edn. CRC Press, Boca Raton (2009)
[3] Preumont, A.: Vibration Control of Active Structures, 3rd edn. Springer, Berlin (2011)

[4] Gospodarič, B., Vončina, D., Bučar, B.: Active electromagnetic damping of laterally vi-brating ferromagnetic cantilever beam. Mechatronics 17(6), 291–298 (2007)
[5] Brezina, T., Vetiska, J., Hadas, Z., Brezina, L.: Simulation, Modelling and Control of Mechatronic Systems with Flexible Parts. In: Jablonski, R., Brezina, T. (eds.) Proc. 9th Int.Conf. Mechatronics 2011, pp. 569–578. Springer, Berlin (2011)
[6] Belhaq, M., Bichri, A., Der Hogapian, J., Mahfoud, J.: Effect of electromagnetic actua-tions on the dynamics of a harmonically excited cantilever beam. Intl. J. of Non-Linear Mechanics 46(6), 828–833 (2011)
[7] Stein, G.J., Darula, R., Sorokin, S.: Control of transversal vibrations of a clamped-clamped beam by a permanent magnet and a shunt circuit. In: Proc. of the 8th intl. Conference on Struc-tural Dynamics, pp. 1735–1741. Katholieke Universiteit Leuven (2011)
[8] Stein, G.J., Darula, R., Sorokin, S.: Control of forced vibrations of mechanical structures by an electromagnetic controller with a permanent magnet. In: Proc. Intl. Conference on Noise and Vibration Engineering (ISMA 2012). pp. 385–393. Katholieke Universiteit Leuven (2012)
[9] Stein, G.J., Chmurny, R.: Damping of beam transversal vibrations by a permanent magnet with coil. In: Proc. 19th Intl. Conference Engineering Mechanics 2013, Institute of Thermomechanics of CAS, Prague and Svratka (in press, 2013)
[10] Chai, G.B., Low, K.H.: On the natural frequencies of beams carrying a concentrated mass. J. of Sound and Vibration 160(1), 161–166 (1993)
[11] Timoshenko, S.: Vibration problems in engineering, 2nd edn. Van Nostrand, New York (1937)
[12] Mayer, D., Ulrych, B.: Elektromagneticke aktuatory BEN, Prague (2009) (in Czech)

Determination of Parameters of Second Order Integration Model for Weighing Scales

R. Ugodziński and R. Szewczyk

Warsaw University of Technology, Faculty of Mechatronics, św. A. Boboli 8,
02-525 Warsaw, Poland
rugodzinski@piap.pl

Abstract. Paper presents physical background of the second order integration model for laboratory weighing scales. Moreover, method of identification of the model's parameters is described. This method enables determination of parameters for both static and dynamic characteristics of the object. On the base of the determined model, the weighing scale control algorithm may be optimised. As a result, due to this optimisation, the weighing process may be significantly shortened, what is especially important from the point of view of the laboratory equipment's functional parameters.

1 Introduction

Laboratory weighing scales operate in a strictly controlled environment. This environmental control covers mainly the temperature, humidity and vibrations [1]. For this reason, running costs of the laboratory are significant. As a result, it is highly required to shorten the time of weight measurements in order to increase the efficiency of operation of the weighing laboratory.

Time of single mass measurement on laboratory weighing scale is connected with its dynamic characteristic. This characteristic is determined by the mechanical construction of the weighing scale as well as by its control algorithm. Whereas optimisation of the mechanical construction is problematic, due to stiffness and robustness requirements [2], the possibilities of optimisation of the weighing scale's control algorithm still seem to be significant.

For optimisation process oriented on the control of laboratory weighing scale, the most important issue is the proper determination of both static and dynamic transfer functions, as well as function's parameters. Moreover, especially in the case of high resolution weighing scales, nonlinearities of these characteristics can't be neglected. As a result, development of the mathematical model for dynamic of a weighing scale requires both detailed analyses of physical processes and careful identification of the model's parameters on the base of experiments.

T. Březina and R. Jabloński (eds.), *Mechatronics 2013*,
DOI: 10.1007/978-3-319-02294-9_21,

2 Description of the Object and the Control System

Schematic block diagram of the weighing scale is presented in figure 1.

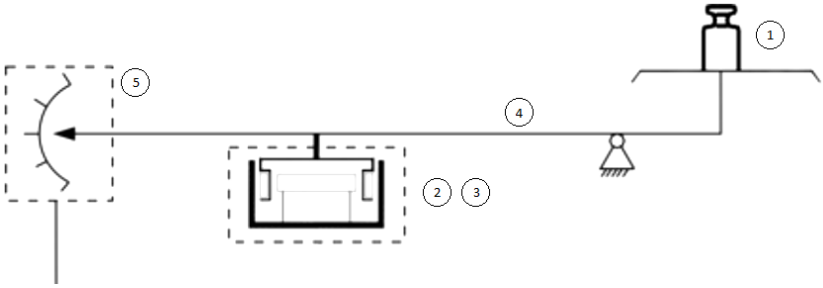

Fig. 1 Schematic block diagram of the laboratory weighing scale: 1 – measured mass *m*, 2 – magnetic coil, 3 – permanent magnet, 4 – arms, 5 – position indicator

In such weighing scale gravitation force of measured mass *m* (1) is balanced by the electromagnetic force generated by magnetic coil (2) together with permanent magnet (3) [3]. During this operation, the length of arms (4) has to be taken into consideration. Position of the pan with mass *m* is measured with the optoelectronic position detection module (5).

Position of the mass plate is the input signal for automated control system. This system tends to achieve the neutral position of the mass pan by changing the value of current *I* driving magnetic coil (2). Output value, nearly proportional to measured mass *m*, is the value of driving current *I* required for balancing the weighing scale.

3 Static Model of the Object and Identification of Its Parameters

For balanced weighing scale, the resultant moment of the test weight gravity force and the force derived from coil is given by equation (1):

$$\sum M = a * (m_0 + m) * g - b * B * I \tag{1}$$

where:

a (m) – length of the first arm,
b (m) – length of the second arm,
m_0 *(g)* – mass of measuring pan or zero mass,
m (g) – measured mass,
g (m/s^2) – gravitational acceleration,
B (N/A) – parameter describing the relationship between force and current *I* in the coil.

In a balanced state, the resultant moment $\sum M$ should be zero. As a result, the equation (1) can be rewritten:

$$I = \frac{ag}{bB}m + \frac{ag}{bB}m_0 = km + km_0 \tag{2}$$

where k is a static parameter. Equation (2) indicates that for constant value of B parameter, the static characteristic of the weighing scale should be linear. Result of the experimental identification of this characteristic is presented in figure 2.

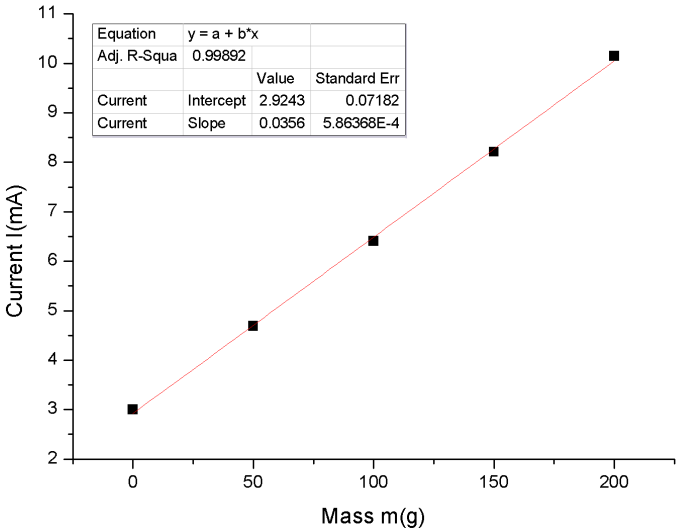

Fig. 2 Result of identification of the static characteristic of the weighing scale

From characteristic presented in figure 2, the static parameters were determined.

$$k = \frac{ag}{bB} = 0.0356\frac{mA}{g} \pm 0{,}0006\frac{mA}{g} \tag{3}$$

$$km_0 = 2.924mA \pm 0.072mA \tag{4}$$

$$m_0 = 82.1g \pm 6.7g \tag{5}$$

4 Model of Dynamic Behaviour and Its Parameters

As it was indicated in chapter 2, the output of control system is deflection of scale's arm measured by zero-position sensor. Therefore, resultant moment may be converted to deflection angle:

$$\sum M = \ddot{\varphi} * J \tag{6}$$

$$J = J_0 + m * a^2 \tag{7}$$

where:

J – moment of inertia of the system,
J_0 – moment of lever inertia,
a – length of the first arm,
m – measured weight,
φ – deflection of scale's arm

After substituting (6) to (1) and double integrating (without integral constants) equation (8) was achieved:

$$\varphi(t) = \frac{a(m_0+m)g}{J_0+m*a^2}\frac{t^2}{2} - \frac{bB}{J_0+m*a^2}\iint I(t)dt \tag{8}$$

This equation can be written as:

$$\varphi(t) = \frac{bB}{J_0+m*a^2}\iint \frac{ag(m_0+m)}{bB} - I(t)dt \tag{9}$$

$$\varphi(t) = C_2(m)\iint C_3(m) - I(t)dt \tag{10}$$

where:

$$C_2(m) = \frac{bB}{J_0+m*a^2} \tag{11}$$

$$C_3(m) = \frac{ag(m_0+m)}{bB} = \frac{ag}{bB}m + \frac{ag}{bB}m_0 \tag{12}$$

Accordingly to equation (1), the parameter $C_3(m)$ can be interpreted as current in coil to balance the scale.

On the other hand, to obtain the parameter $C_2(m)$ from real scales it must be done in point of weighing scale operation. After stabilisation step response must be added. Finally, the current $I(t)$ is given by equation (13):

$$I(t) = I_0 + \Delta I = \frac{ag(m_0+m)}{bB} + \Delta I \tag{13}$$

where I_0 is the operating point and ΔI is the step function. After substituting, equation (10) will reduce into form:

$$\varphi(t) = C_2(m)\iint \Delta I(t)dt \tag{14}$$

For $\Delta I(t)$ = *constant* system response will take the form of the function:

$$\varphi(t) = C_2(m) * \Delta I * \frac{t^2}{2} \tag{15}$$

$$C_2(m) = \frac{2\varphi(t)}{\Delta I*t^2} \tag{16}$$

By recording responses to ΔI for different value of mass dynamically provided on pan, value of parameter $C_2(m)$ as a function of mass m can be determined.

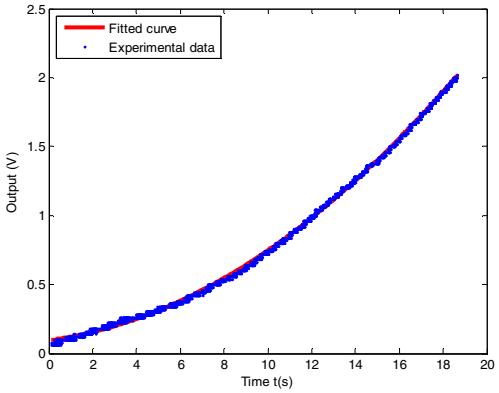

a)

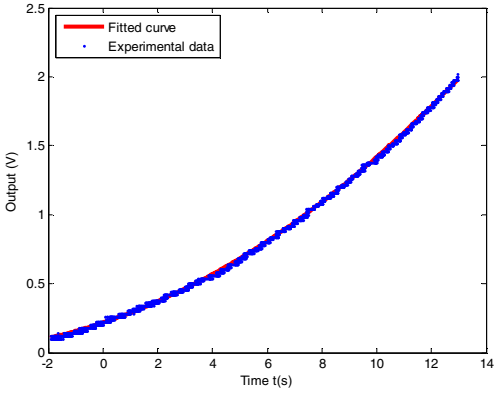

b)

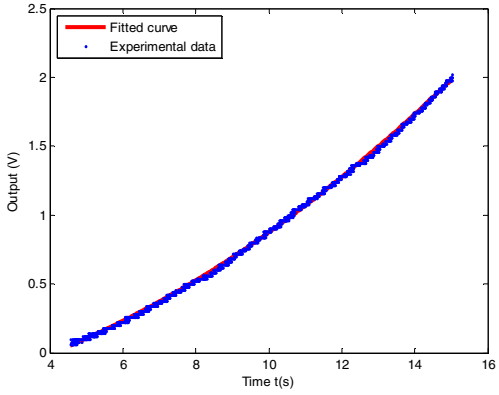

c)

Fig. 3 Dynamic response of the weighing scale presented as the output vs. time: a) the response to ΔI = 10μA and mass equal to 100g, b) the response to ΔI = 20μA and mass equal to 150g, c) the response to ΔI = 24μA and mass equal to 160g

5 Identification of Parameters for Dynamic Characteristics

Figure 3 presents the step responses obtained for different ΔI and mass. The results were averaged from set of five measurements.

Achieved experimental data were fitted to quadratic function [4]. As a result, the calculation of quadratic coefficient p_2 was calculated together with parameter C_2 for each value of m, given from equation (16).

Table 1 presents the results of fitting the quadratic function given by equation (15).

Table 1 Summary of measurements, fitting and calculating

Mass (g)	ΔI (μA)	Coefficient p_3	Constant C_2(m) (V/mA)
100	10	0.00440	0.440
120	8	0.00300	0.375
140	9,4	0.00300	0.320
150	20	0.00597	0.298
160	24	0.00661	0.275

On the base of these results, $C_2(m)$ can be fitted into parametric function (17):

$$C_2(m) = \frac{bB}{J_0 + m*a^2} = \frac{1}{\frac{J_0}{bB} + m*\frac{a^2}{bB}} = \frac{1}{p_1 + m*p_2} \tag{17}$$

As a result of this fitting p_1 equal 0.0631 and $p2$ equal 0.0220 was achieved.

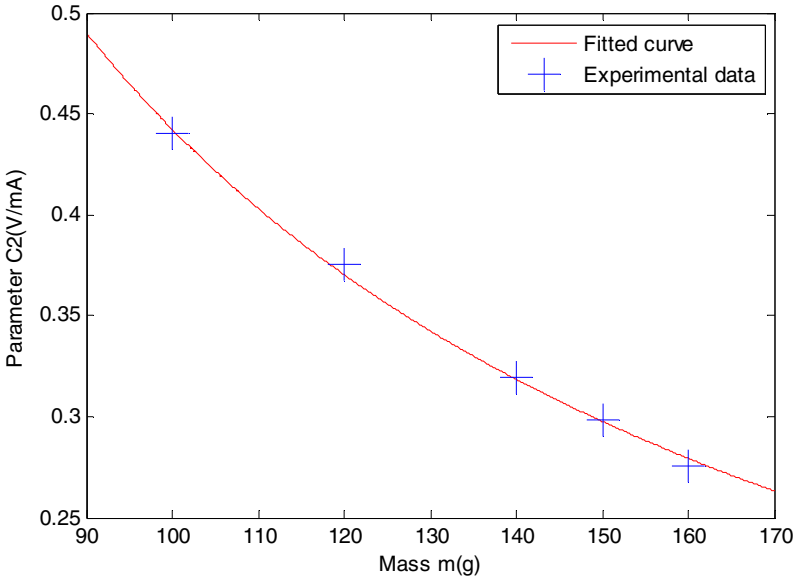

Fig. 4 Result of the $C_2(m)$ dependence determination achieved during the curve fitting

As it can be seen in figure 5, theoretical dependence given by equation (17) was confirmed by the experiment. As a result, even with limited number of experimental results, parameters of the $C_2(m)$ dependence can be achieved. As a result, the $C_2(m)$ dependence for all range of measured masses m can be predicted.

6 Conclusion

Physical dependences based model presented in the paper enables determination of both static and dynamic characteristic of a laboratory weighing scale. It was indicated, that static characteristic of the laboratory weighing scale with magnetic actuator is linear. However, the dynamic response of this weighing scale has quadratic character.

It should be indicated, that the presented experimental method of determination of parameters of both static and dynamic characteristics of the weighing scale was successfully validated. This method creates the possibility of parameters determination connected with specific weighing scale. Moreover, the character of experimentally achieved responses is in line with the presented models.

Presented models create new possibilities of effective tuning of algorithms for weighing scale control. It should be highlighted, that such algorithms are often non-linear as well as they have to operate on limited input data [5]. As a result, it is not possible to apply commonly known methods of on-line tuning of control algorithms [6]. However, the presented model enables the effective analyses of controlled system in modelling environments, such a s MATLAB-Simulink. In such case, the developed algorithms can be determined in general form and adjusted only for specific parameters of each weighing scale. With this method, the measuring time was shortened by about 20 percent versus old algorithm.

Acknowledgments. This work was partially supported by The National Centre of Research and Development (Poland) within grant no. PBS1/B3/8/2012.

Authors would like to express their gratitude to RADWAG (www.radwag.pl) for kind support during the experiments with the weighing scales.

References

[1] Gupta, S.V.: Mass metrology. Springer (2012)
[2] Jones, E.F.: Handbook of mass measurement. CRC (2002)
[3] Jiles, D.C.: Introduction to magnetism and magnetic materials. CRC (1998)
[4] Schwefel, H.P.: Numerical optimization of computer models. John Wiley & Sons (1981)
[5] Norden, K.E.: Electronic weighing - fundamentals and applications. Butterworth-Heinemann Ltd. (1993)
[6] Kurek, J.E., Szewczyk, R., Salach, J., Kłoda, R.: PI control of laboratory furnace for annealing of amorphous alloys cores. Journal of Automation, Mobile Robotics and Intelligent Systems 6(4), 13–15 (2012)

Feed-Rate Control along Multi-axis Toolpaths

P. Vavruska

Czech Technical University in Prague, Faculty of Mechanical Engineering,
Horská 3, 128 00, Prague 2, Czech Republic
p.vavruska@rcmt.cvut.cz

Abstract. This article focuses on options for feed-rate control in NC programs for multi-axis machining. In order to achieve adequate surface quality of machined parts, it is crucial for the production engineer to observe the programmed feed rate. Therefore the feed-rate characteristic along a toolpath has been measured first without the tool center point function in the CNC and next using the tool center point function. In the case that the tool center point function is not used, the algorithms for feed-rate prediction and correction are presented. Both of these algorithms are part of the postprocessor and can be used in generating the NC program.

1 Introduction

Production engineers cannot even imagine preparing NC programs for the production of complex parts without the use of CAD/CAM systems. The essential link is the postprocessor, which connects the CAM system and the control system of a machine with a particular kinematic configuration of axes. Using the post-processor, the NC program generation and thus the behavior of CNC machines for machining operations can be additionally affected. Milling technology is associated with a number of problems. At present, however, there is not sufficient evidence about technological conditions, particularly about feed-rate in multi-axis machining. The user must only rely on the information in the manuals for control systems and their functions.

A research work has been done on cutting forces prediction and required performance with regard to a tool in multi-axis machining. Long term research in this field has been conducted by authors of [4] and [8], where we can find a proposal of mathematical model for cutting forces prediction during the machining process. There is a case study of compressor wheel vane machining to show how to calculate cutting forces during finishing operation. The calculation is based on the tool geometry. The resulting graphs represent functions of cutting forces in each axis with relation to the measured values of cutting forces. Authors thus present achieving a certain correspondence of prediction and real test when small deviations are considered. This problem is also concerned by authors of [11], where the use of cutting forces prediction mathematical model for machining is

T. Březina and R. Jabloński (eds.), *Mechatronics 2013*,
DOI: 10.1007/978-3-319-02294-9_22,

also applied. The authors start with the CL data, which are obtained from CAM system and with a help of custom made SW they are able to predict the cutting forces. The result is the ability to optimize the feed-rate. Most of other proposed solutions aim to feed-rate generation with respect to the depth of cut (or rather the actual volume of material that is being cut). However the algorithms used for calculation of generated feed-rate are different. And more importantly the mathematical description of cutting tools is ever increasing. These topics are mentioned if the following references: [1], [3], [7], [2], [9], [10] and [13]. The cited articles show principles which the calculation methods for feed-rate computation are based on. It is not necessary to analyse these algorithms any further for the principle remains the same, however it is different from the principle that is of concern in this article which aims to feed-rate optimization with respect to the tool overhang length from the rotational axes.

2 Transformation of Coordinates in Multi-axis Machining

In terms of NC programs for multi-axis machining, it is becoming a fact of life that control systems are equipped with features that can compensate the tool overhang in multi-axis machining, allowing independence NC program on the kinematic configuration of the rotary axes of machine tools used. This function is usually called the Tool Center Point (TCP), or a Tool Tip Control. To use this function, it is imperative that the kinematics of the machine tool in the control system is defined, and also, TCP must be supported by the control system. The function ensures dynamic coordinate transformation in the performance of the NC program. The postprocessor used for CAD/CAM system must be equipped with an algorithm that generates activation of this function at the corresponding position of the NC program. The principle of TCP is that the machine moves linear axes so as to avoid undercuts on machined surfaces due to tool overhang and the position of the workpiece relative to the center of rotational axes (see lit. [6]). This feature has, however, one downside. The generation of coordinates is different than in the case when the function is not used. As a consequence, the machine operator has no idea about the subsequent movement of the tool reference point and the tool axis compared to the workpiece surface and thus may not be able to avoid potential collisions. This is, however, important for the operator, for example, when debugging the NC program, which is especially for prototype production - a very common way to test NC programs.

Some solution how to correct feed-rate in multi-axis machining without TCP function is presented in the lit. [5]. The feed-rate correction method is based on the proportion of toolpath increment in the CL-data, and toolpath increment in the NC program. A correction factor is calculated from these data and based on this, feed-rate in the NC program block is corrected. This results in certain machining time saving, but the real impact on the characteristic of feed-rate along the toolpath is not shown, so the suitability of this feature cannot be proven.

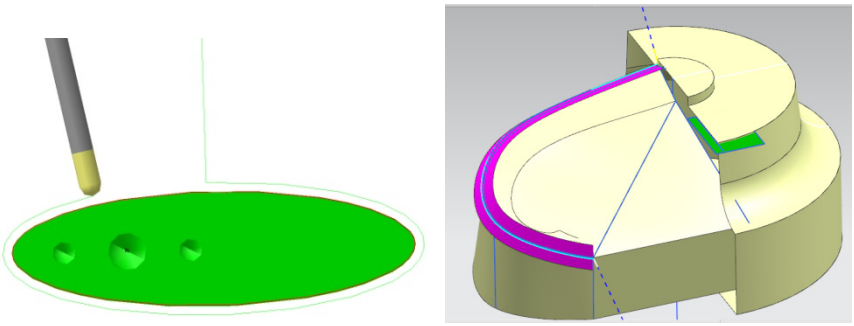

Fig. 1 Testing toolpaths for multi-axis machining (left – four-axis, right – five-axis)

For testing purposes 3D models for creating multi-axis toolpaths have been proposed. Fig. 1 (left) shows the toolpath for four-axis control and in Fig. 1 (right) shows the toolpath for five-axis control.

3 Feed-Rate Measurement

The characteristics of feed-rate were measured on five-axis machine tool. Fig. 2 shows the position of the device (the proposal mentioned in the lit. [12]) for measuring the feed-rate between the tool and the workpiece (left - four-axis control, right - the five-axis control).

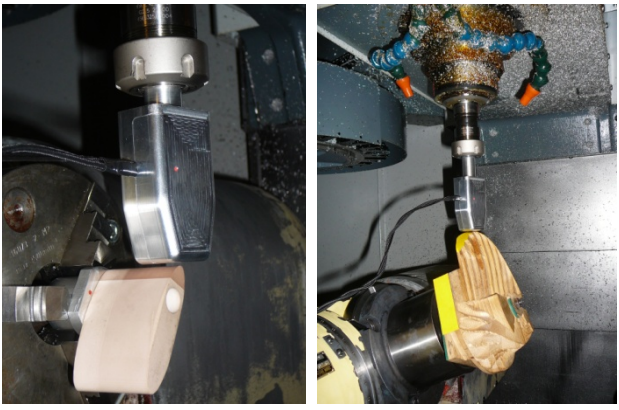

Fig. 2 Measuring of feed-rate on five-axis machine tool

Fig. 3 shows the actual characteristic of the feed-rate along the four-axis toolpath. Fig. 3 left captures the characteristic of feed-rate along the toolpath without using the TCP function, where it is clear that the feed-rate specified in the NC program (600 mm/min) has not been achieved and the decrease in feed-rate is

considerable. Constant feed-rate wasn't achieved even in the case of the toolpath using the TCP function (see Fig. 3 right), but it can be seen that the characteristic of feed-rate in this case is improved, and machining time is reduced.

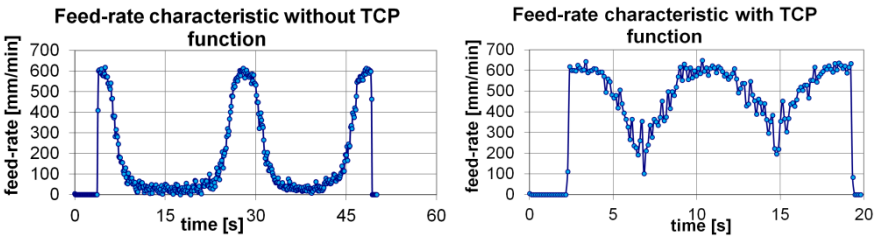

Fig. 3 Feed-rate characteristics measured along four-axis toolpath (left – without TCP, right – with TCP)

Fig. 4 shows real characteristics of feed-rate along the five-axis toolpath on the same five-axis machine tool, as in the case of four-axis toolpath mentioned above. In Fig. 4 left the captured characteristic of feed-rate along the toolpath without using the TCP function shows that the feed-rate specified in the NC program (600 mm/min) has not been achieved. First, the feed-rate along the toolpath increases above the programmed value. Next, there is a significant decrease in feed-rate. Constant feed-rate has not been achieved in the case of the toolpath with the use of the TCP either, which can be seen in Fig. 4 right. But it is evident that the characteristic of the feed-rate is in this case better and the machining time is minimized.

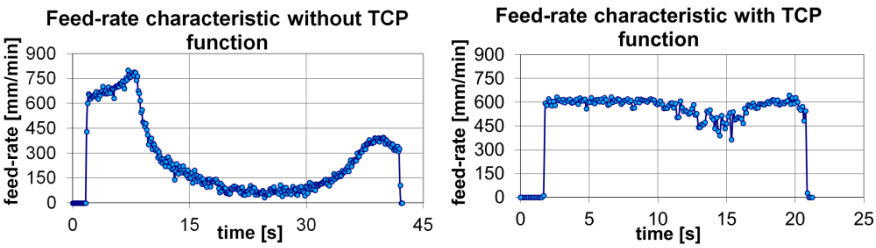

Fig. 4 Feed-rate characteristics measured along five-axis toolpath (left – without TCP, right – with TCP)

Testing the feed-rate characteristic using the Tool Center Point function is carried out here to demonstrate that the distribution of feed-rate may in certain circumstances be better than in the case without the TCP function. On some machines, this function is not available, and in some cases the production engineer and the operator of machine tool do not want to use this function, even if it is available. Therefore it is not meaningful to apply the prediction of feed-rate when the TCP function is used because maximum dispositions of the machine tool, its control system and the setup of drives are used to achieve the best characteristic of

feed-rate. In other cases, when the TCP function cannot be used, feed-rate prediction serves as a basis for further action - to correct the feed-rate the goal is to get close to the time savings when using the TCP function.

4 Algorithm for Feed-Rate Prediction

The algorithm calculates the time required for the execution of linear interpolation, which is chosen as the maximum value of the times required to move the particular machine tool axes. The algorithm also uses the NC block execution time, which is different for each control. Therefore the algorithm for feed-rate prediction will serve as a basis for an algorithm to correct the feed-rate.

The verification of the prediction algorithm of feed-rate is shown in Fig. 5. The orange characteristic of feed-rate is obtained using the algorithm in the postprocessor and the blue characteristics is obtained by measuring on a five-axis machine. Both characteristics in Fig. 5 (left) are for four-axis control when the programmed feed-rate was set to the value of 600 mm/min. Both characteristics in Fig. 5 (right) are for five-axis control when the programmed feed-rate was set to the value of 600 mm/min. It is clear that a very good agreement of prediction and measurement of feed-rate has been achieved.

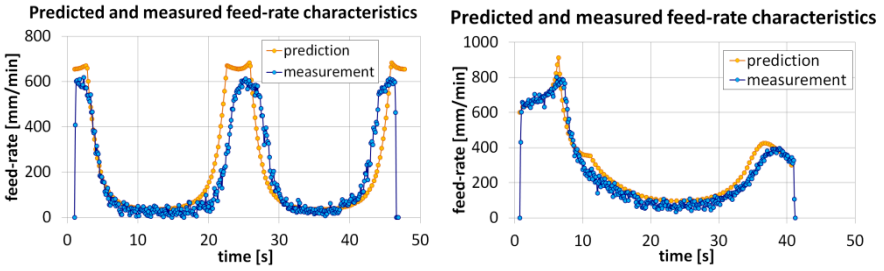

Fig. 5 Comparison of measured characteristics and predicted characteristics of feed-rate along four-axis toolpath (left) and five-axis toolpath (right)

To use the TCP it should be noted that the feed-rate is controlled by the control system so that the feed of rotary axes increases in compliance with the permitted value of the maximum feed-rate, which is set by the operator on the control system panel. Fig. 6 (left) captures the characteristic of feed-rate along the five-axis toolpath using the TCP function, but the control system has been configured to limit the maximum feed-rate to 2000 mm/min. Although this is a higher permitted value of feed-rate than the programmed feed-rate (600 mm/min), a big drop in feed-rate can be seen during the execution of instructions from the NC program. It is evident that in order to achieve the programmed feed-rate between the tool and the workpiece, the control system has to speed up some machine tool axes above the programmed value. The maximum feed-rate value affects the actual feed-rate when working with TCP.

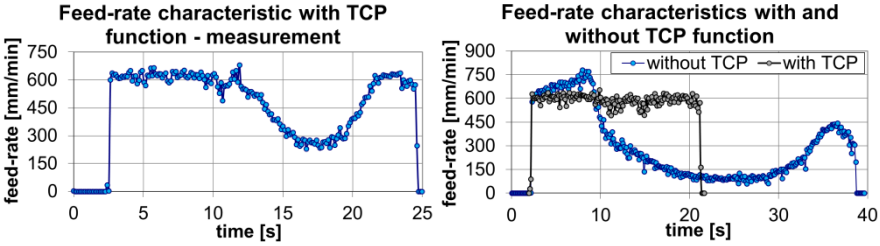

Fig. 6 Measured feed-rate characteristic along five-axis toolpath with TCP function and limited maximum feed-rate value (left) and comparison of measured characteristics of feed-rate along five-axis toolpath with and without TCP function (right)

Comparison of the measured feed-rate along the five-axis toolpath in the NC program using the TCP function and without the TCP function is shown in Fig. 6 (right). The characteristic of feed-rate without the use of TCP function is marked in blue and the characteristic of feed-rate with the TCP function is marked in black. It is obvious that the control system is able to keep the feed-rate at a constant value (except for two small fluctuations) when using TCP. The TCP function leads to a time saving of 17.4 s, which is 47.23% of the original machining time. It would therefore be desirable to be able to make the feed-rate correction as close as possible to this time saving.

5 Algorithm for Feed-Rate Correction

Two algorithms have been proposed to correct feed-rate. One (Alg. 1) is based on the same principle as the algorithm in the lit. [5] and the second (Alg. 2) is designed according to the prediction algorithm of feed-rate. Comparison of the measured feed-rate without the TCP function before the correction of feed-rate (blue characteristic) with the measured feed-rate corrected by Alg. 1 (purple characteristic) is shown in Fig. 7 left. It can be seen that by applying the correction of feed-rate using Alg. 1 we can achieve time saving, but the decrease in feed-rate along the toolpath is still considerable. Time saving achieved using the correction is 9.84 s, which is 26.7% of the original machining time. It is clear that applying the correction of feed-rate using Alg. 1 leads to time savings during operation, but compared to the time savings achieved when using TCP, there is a margin of about 43%.

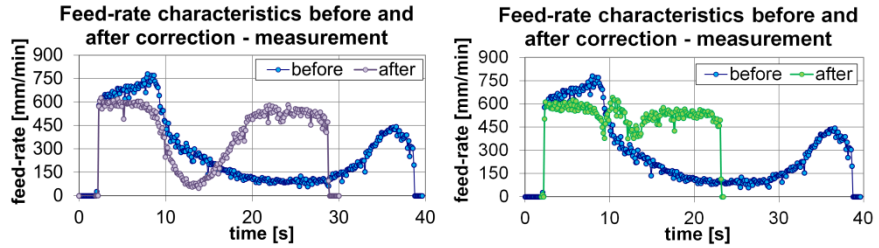

Fig. 7 Comparison of measured characteristics of feed-rate along five-axis toolpath (left – correction by Alg. 1, right – correction by Alg. 2)

Comparison of measured feed-rate without the use of the TCP function before correction (blue characteristic) and after correction of feed-rate using Alg. 2 (green characteristic) is shown in Fig. 7 right. By subtracting machining times we get a time saving of 15.48 s, which represents a saving of 42% of the original mach. time. From this it follows that using the correction of feed-rate by Alg. 2 significant time savings in machining can be achieved, comparable to the time savings achieved when using the TCP function of control system (see Tab. 1).

Table 1 Comparison of time savings

Programmed feed-rate [mm/min]	Machining time without feed-rate correction [s]	Machining time with TCP function [s]	Time savings with TCP function [%]	Machining time with feed-rate correction (alg. 1) [s]	Time savings with feed-rate correction (alg. 1) [%]	Machining time with feed-rate correction (alg. 2) [s]	Time savings with feed-rate correction (alg. 2) [%]
600	36,84	19,44	**47,2**	27	**26,7**	21,36	**42**

6 Conclusions

The algorithms for the prediction and correction of feed-rate have been designed in a very general way, so it is possible to apply them in various postprocessors for five-axis machines without using the Tool Center Point function in the control system of the machine tool. Verification of the proposed algorithm for the prediction of feed-rate in multi-axis machining was performed using measurements of feed-rate in multi-axis milling, and very good agreement has been achieved. With this algorithm production engineers have the ability to check the real characteristic of feed-rate along the multi-axis toolpath before the actual milling. The algorithm for feed-rate correction has been designed as an extension of the algorithm for prediction of feed-rate. By measuring the feed-rate it has been shown that without the TCP function in the control system of the machine it is not possible to achieve the programmed feed-rate in the NC program. The proposed algorithm differs from the algorithm proposed in the lit. [5], and after its application better characteristics of feed-rates along multi-axis toolpaths have been proven. Time savings of about 40% have been achieved compared to the original machining time, and the characteristic of feed-rate is more favourable in terms of uniform wear of the tool cutting edge, since the feed-rate along the toolpath requested by the production engineer was maintained as much as possible.

Acknowledgments. This article „ Feed-rate control along multi-axis toolpaths “ has been created with the financial support of **The Technology Agency of the Czech Republic**.

References

[1] Baek, D.K., Ko, T.J.: Feedrate scheduling for free-form surface using an NC verification model. International Journal of Machine Tools & Manufacture 48(2), 163–172 (2008)
[2] By Chen, J.-S., Huang, Y.-K., CHen, M.-S.: Feedrate optimization and tool profile modification for the high-efficiency ball-end milling process. International Journal of Machine Tools & Manufacture 49(9), 1070–1076 (2005)
[3] Feng, H.-Y., Su, N.: Integrated tool path and feed rate optimization for the finishing machining of 3D plane surfaces. International Journal of Machine Tools & Manufacture 40(11), 1557–1572 (2005)
[4] Ferry, W.B.S.: Virtual five-axis flank milling of jet engine impellers. Vancouver: The Univerzity of British Columbia. A thesis submitted in partial fulfillment of the requirements for the degree of doctor of philosophy (2008)
[5] Fornůsek, T., Rybín, J.: Optimalization of NC code. In: Proceedings of International Congress MATAR PRAHA 2008, Praha, pp. 137–141 (2008) ISBN 978–80–904077–0–1
[6] Heidenhain iTNC 530, User's manual – Heidenhain Conversational Format (June 2003)
[7] Hsu, Y.Y., Wang, S.S.: A new compensation method for geometry errors of five-axis machine tools. International Journal of Machine Tools & Manufacture 47(2), 352–360 (2007)
[8] Larue, A., Altintas, Y.: Simulation of flank milling processes. International Journal of Machine Tools & Manufacture 45(4-5), 549–559 (2005)
[9] Lee, H.U., Cho, D.-W.: An intelligent feedrate scheduling based on virtual machining. The International Journal of Advanced Manufacturing Technology 22(11-12), 873–882 (2003)
[10] Salami, R., Sadeghi, M.H., Motakef, B.: Feed rate optimization for 3-axis ball-end milling of sculptured surfaces. International Journal of Machine Tools & Manufacture 47(5), 760–767 (2007)
[11] Tunc, L.T., Budak, E.: Extraction of 5-axis milling conditions from CAM data process simulation. International Journal of Advanced Manufacturing Technology 43(5-6), 538–550 (2009)
[12] Vavruška, P., Konečný, P.: Measurement Method of Feed-Rate Between a Tool and a Workpiece. MM Science Journal, 21–27 (2011) ISSN 1803-1269
[13] Zhang, L., Feng, J., Wang, Y., Chen, M.: Feedrate scheduling strategy for free-form surface machining through an integrated geometric and mechanistic model. The International Journal of Advanced Manufacturing Technology 40(11-12), 1191–1201 (2009)

Model Based Design of Power HIL System for Aerospace Applications

J. Vejlupek, J. Chalupa, and R. Grepl

Mechlab, Brno University of Technology, Faculty of Mechanical Engineering,
Technicka 2, 616 69, Brno, Czech Republic
grepl@fme.vutbr.cz
www.mechlab.cz

Abstract. This article presents PHIL simulation of a DC motor with different approaches enabling testing control units with integrated power stage. Model also includes commutator induced current ripples, allowing the speed control based on spectral analysis of the current. In section 2, we present SimScape model of the complete PHIL simulation, and in section 3 experimental results are shown.

1 Introduction

Increasing system complexity of modern control units and requirements for the safety gives high requirements on testing. Hardware In the Loop (HIL) is well established method in the industry, and we can found this method throughout the industries. But as the most common HIL methods focuses on ECUs, there is also demand to test the complex control systems, which may already include power electronics coupled inseparably with the control unit. Traditional HIL would not be able to deal with the power electronics, as it usually has only ADC, DAC, DIO, communication channels and may be some additional electronics for signal level conversion and modulation. To fill in the need, lot of research and development is recently done regarding Power HIL (PHIL). PHIL is adding additional stages to cope with power electronics. Schematic connection is shown in Fig. 1. Demand for PHIL can be found in Automotive [1],[3], Aerospace [6] and Power generation and distribution Industries [4],[5]. Aim of this paper is PHIL for control units for brushed DC motor drives, where the feedback is either speed derived from the current ripples due to the commutation [7], or torque derived from the current through the motor itself. Typical connection scheme is presented in Fig. 2.

In this article we will present various options for brushed DC motor control unit PHIL, simulation model based on SimScape, experimental results, and further plans for PHIL.

T. Březina and R. Jabloński (eds.), *Mechatronics 2013*,
DOI: 10.1007/978-3-319-02294-9_23,

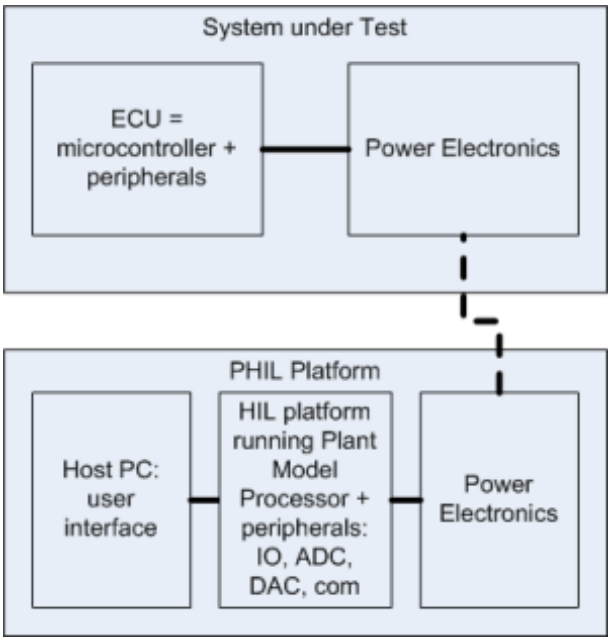

Fig. 1 PHIL schematic diagram

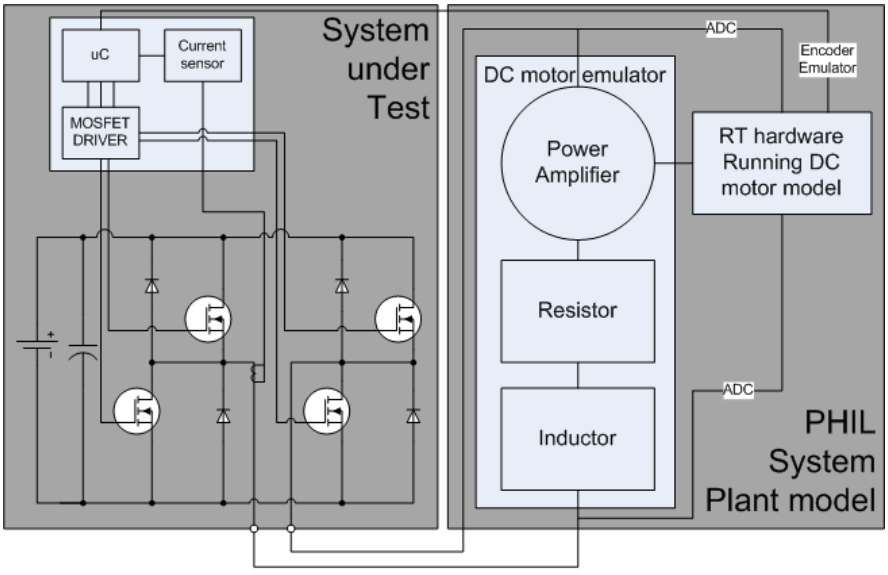

Fig. 2 PHIL schematics for 1-phase electrical system (DC motor)

2 Modeling of PHIL System

PHIL system for the brushed DC motor is presented in Fig. 2., DC motor is replaced with resistance, inductance and power amplifier. Resistance and inductance are chosen to match the parameters of the DC motor that would be actually connected. Power amplifier is used as a source of the voltage to emulate the voltage generated by the back electromagnetic force. This concept allows us to simulate the full brushed DC motor including the current ripples.

2.1 Mathematical Model

Mathematical model of the brushed DC motor is quite simple:

$$u = L\frac{\mathrm{d}i}{\mathrm{d}t} + Ri + k_{EMF}\omega \tag{1}$$

$$K_T \cdot i = I \cdot \frac{d\omega}{dt} + b \cdot \omega + M_{Load} \tag{2}$$

Where u is the voltage on the DC motor terminals, L is the windings inductance, R is the winding + terminal resistance, i is the current running through the motor, ω is the motor shaft rotational speed, k_{EMF} is the electromagnetic voltage constant, K_T is the motor torque constant, I is the rotor inertia, b is the viscous damping in bearings, and finally M_{Load} is the load torque.

This model is accurate enough to model a DC motor for a HIL simulation; however, it may require an additional model of an encoder or other position or speed sensor. In some cases, where the control unit is using current ripple for the information about speed, additional function should be added.

$$i_{ripple} = f(\omega) = g \cdot \sin(2 \cdot \pi \cdot c \cdot \omega \cdot t) \tag{3}$$

Where the c is the number of the commutator sections, and g will determine the amplitude of the current ripples. From our experiments, the amplitude g is almost linearly dependent on the current, and it is about 10% of its actual value.

2.2 PHIL Model

For the PHIL simulation, we have several options, how to set-up the system and that is what part of the system will be real, and which we will simulate. This also depends on the requirements for the tests. For example, if we do not need to model the changes in L and R, i.e.: due to the heat, we can use real components. From the electrical equation (1), we can see that the inductor and resistor could actually be real components and for the voltage induced by back electromagnetic force, we will need a voltage supply. So in this case, we have three options:

a) Full simulation according to equation (1).
b) Use real inductance and simulate the rest.
c) Use real inductance and resistor and simulate the rest.

First case is very demanding on precise and very fast timing, as there would be neither big resistance nor inductance in the circuit, which may lead to hardware damage due to inaccurate control.

The case b) simplifies the model, as the time constant on the inductor is about one order lower than the rest of the system, but the problem with precise timing still persists due to no resistance and the risk of shoot-through of the transistors. We will focus on the variant c), where the real components are used.

2.3 PHIL System SimScape Model

For the simulation of the complete PHIL system, SimScape blockset was used, enabling us to use physical modeling of the individual components. Simulation model is shown in Fig. 3 and it consists of the H-Bridge simulation model and the DC motor model. There are two options considered for the voltage supply: another H-Bridge, and Power Amplifier.

Parameters for the model were set accordingly to the components used in the experimental part. For the H-Bridge, we have used the H-Bridge described in [8], motor parameters are taken from the MY1035 motor. For the variant using power amplifier, two different audio-amplifiers are used: class A: LM4780 and class D TAS5631, both are manufactured by Texas Instruments. Class A audio amplifier works as amplifier, where as Class D is basically a h-bridge. Fig. 3 shows the model comparing the two methods of modeling the PHIL – H-bridge and power amplifier to the mathematical model. We have reached quite satisfactory results in the simulation, concluding that both methods are applicable.

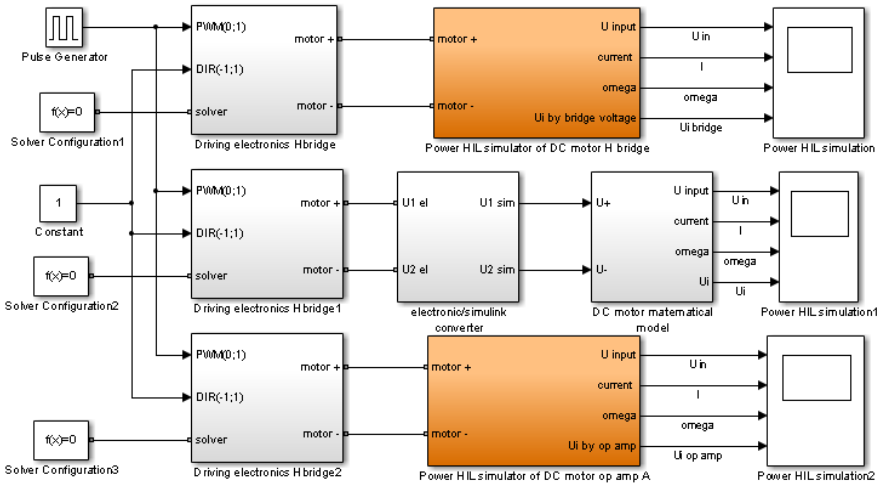

Fig. 3 PHIL simulation - SimScape complete system model

3 Experimental Verification

In this section, experimental results are presented showing the measurements from the real motor, and then the measurements from PHIL simulation using real motor with braked rotor as a real R+L and audio power amplifier as an emulator of the back electromagnetic force induced voltage.

3.1 Real Motor Data

In Fig. 4 we show the current ripple on the motor for five different voltages – speeds. Only the AC component is shown, as that is the source for the fft spectrum analysis, which gives us the frequency components. Frequency spectrum is shown in Fig.5; there are major peaks for each voltage, and if the frequency value peaks for each voltage are taken, and divided by 16, which is the number of commutator plates, we get the speed of the motor in revolutions per second.

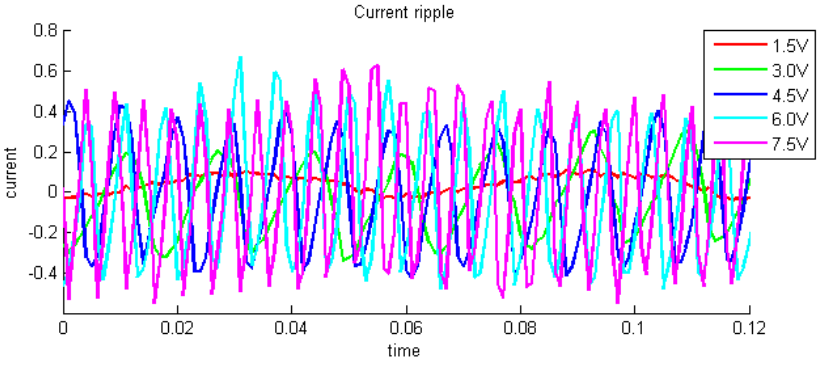

Fig. 4 Current ripple (AC component)

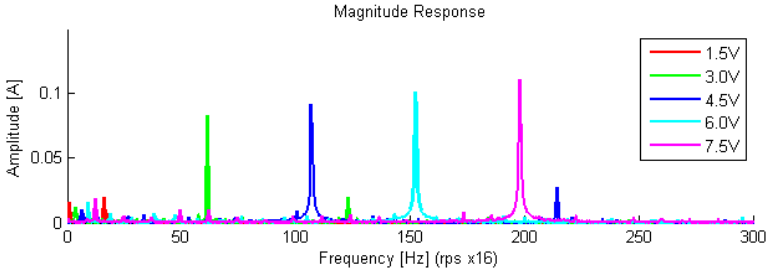

Fig. 5 Current ripple frequency spectrum

3.2 PHIL Simulated Motor

For the experimental verification, we have decided to use the class A audio amplifier connected in series with braked motor as an R+L load. Fig. 6 shows the

model running both, but independent simulation: In the top part, there is the PID controller interfaced through IO card MF624 with the H-bridge – subsystem includes the IO blocks for the MF624 card. This represents the tested control unit. In the bottom, there is a model which is getting the voltage as measured on the output of the tested H-bridge, and using mathematical model (1-3) to drive the audio amplifier.

Fig. 7 and 8 are showing measured current ripple from the PHIL simulation. These figures show that the PHIL simulation with inclusion of the commutation current ripple is quite accurate. Only difference is that there are almost no other frequencies in the current spectrum, but that is because we only included one frequency, which is the calculated frequency of current ripples. But it is quite straight forward to add any additional components to the model.

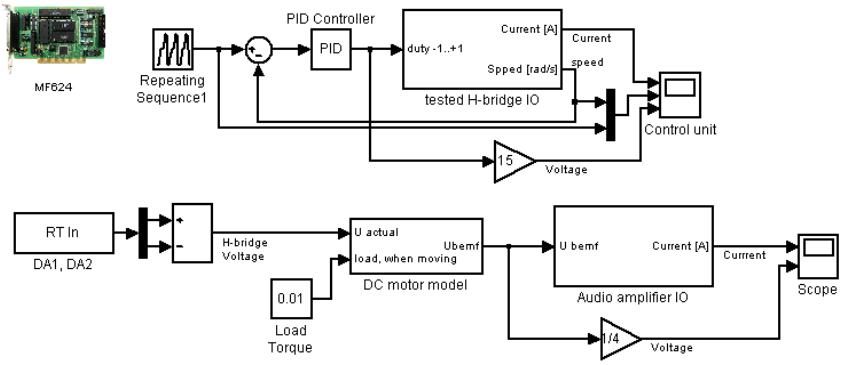

Fig. 6 Experimental control model

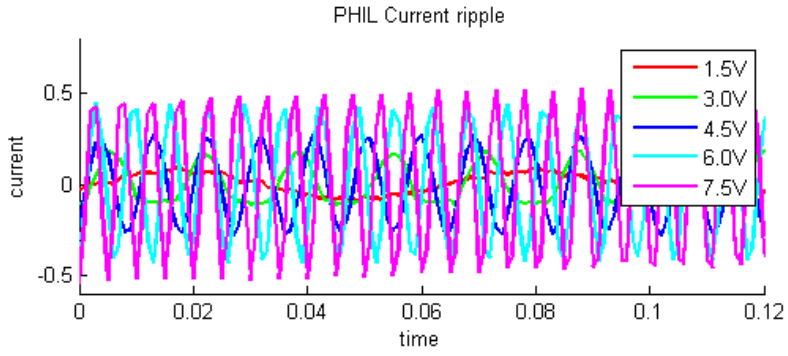

Fig. 7 Current ripple (AC component)

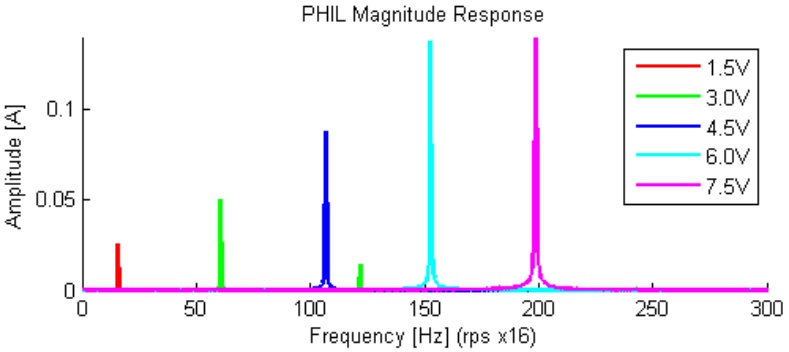

Fig. 8 Current ripple frequency spectrum - experimental data

4 Conclusion

The modeling of the PHIL simulation for the brushed DC motor control unit with integrated power stage was presented in this paper. Experimental verification concluded that the SimScape models presented in section 2 were quite accurate. Simulation model was extended with the current ripple simulation to include the commutator plate switching, which is in some control units used as a feedback for speed control.

Acknowledgments. This work was supported by the European Commission within the FP7 project Efficient Systems and Propulsion for Small Aircraft "ESPOSA", contract No. ACP1-GA- 2011-284859-ESPOSA.

References

[1] Choi, C., Lee, W.: Analysis and Compensation of Time Delay Effects in Hardware-in-the-Loop Simulation for Automotive PMSM Drive System. IEEE Transactions on Industrial Electronics 59(9), 3403–3410 (2012)

[2] Lu, B., Wu, X., Figueroa, H., Monti, A.: A Low-Cost Real-Time Hardware-in-the-Loop Testing Approach of Power Electronics Controls. IEEE Transactions on Industrial Electronics 54(2), 919–931 (2007)

[3] Baracos, P., Murere, G., Rabbath, C.A., Jin, W.: Enabling PC-based HIL simulation for automotive applications. In: IEEE International Electric Machines and Drives Conference, IEMDC 2001, pp. 721–729 (2001)

[4] Goyal, S.: Power network in the loop: System testing using a switching amplifier, PhD Thesis, Queensland University of Technology (2009)

[5] Jong, E., Graff, R., Vaessen, P., Crolla, P., Roscoe, A., Lehfus, F., Lauss, G., Kotsampopulos, P., Gafaro, F.: European White Book on Real-Time Powerhardware-in-the-Loop testing. DERlab (2011)

[6] Todd, R., Forsyth, A.J.: HIL emulation of all-electric UAV power systems. In: IEEE Energy Conversion Congress and Exposition, ECCE 2009, September 20-24, pp. 411–416 (2009)
[7] Grepl, R., Vejlupek, J., Matejasko, M., Zouhar, F.: Sensorless Detection of DC Motor Rotation Direction for Automotive Fuel Pump Fault Diagnosis, Recent Advances in Circuits, Communications and Signal Processing (2013)
[8] Vejlupek, J., Lamberský, V.: Multi-purpose mobile robot platform development. In: 9th International Conference Mechatronics, Warsaw (September 2011)

Visualization of Energy Flows Using a Particle System

I. Dudarev[1], V. Wittstok[1], F. Pürzel[1], and P. Blecha[2]

[1] Chemnitz University of Technology CUT, Institute for Machine Tools and Production Processes, Professorship for Machine Tools and Production Processes, Reichenhainer Str. 70, 09126 Chemnitz, Germany
{ivan.dudarev,volker.wittstock,
franziska.puerzel}@mb.tu-chemnitz.de
[2] Brno University of Technology, Faculty of Mechanical Engineering, Technicka 2, 616 69, Brno, Czech Republic
blecha@fme.vutbr.cz

Abstract. Nowadays simulation and visualization are used to a greater extent in real life. Needless to say, different kinds of visualization are widely applied in various spheres such as education, computer entertainment, economics and business, industrial sector, etc. New machine tools and industrial elements can be easily designed by means of visualization. Especially concerning research on energy efficiency, visualization is an important step for understanding. This paper describes a new method for energy visualization using a particle system.

1 Introduction

Data visualization and process simulation become more important in production development and management of enterprises. Correctly analyzed data can help to find more suitable solutions for existing problems. Most problems need to be solved in teams, involving people with different skills and knowledge with different approaches to define and solve these problems. Those teams include people that are experts for the specific problem and lay people. Therefore data visualization can be used to provide a common understanding and discussion platform. Data visualization should be simplified to be understandable for everyone.

Data will be easily understood by the means of transforming it to suitable diagrams, graphs or schemes. Different approaches are used for different types of data. One of the most applied ways for energy and power flow visualization is the Sankey diagram. Identification of inefficiencies and potentials for saving resources is a main task for the Sankey diagram. With this type of diagram it is possible to observe energy flows and energy waste in the best way. The intensity of energy flow is indicated by arrows and theirs width [1].

Within the recent work, a method was developed to use 3D-Sankey diagrams and virtual machine tools in a virtual reality (VR) environment to enhance the understandability of the visualized energy flow [2]. Afterwards different

T. Březina and R. Jabloński (eds.), *Mechatronics 2013*,
DOI: 10.1007/978-3-319-02294-9_24,

VR-based methods, including 3D-Sankey, were implemented and then tested regarding user acceptance and usability [3].

One of the results of that user test was that users would prefer dynamic visualizations that are well arranged and that transport a lot of information without being overloaded [3].

In addition to those user requirements, the proposed 3D-Sankey method has another drawback when using the dynamic adaption of the branch-thickness for visualization the current quantity of the energy. Especially when the intensity of the energy flow has a great variation, the thickest branches can cover the machine components and the thinnest branches are too small to be clearly visible [2].

Therefore this paper describes a new approach for energy visualization: particle system.

2 Particle Systems State of the Art

The term "Particle System" is well known computer graphics. Initially it was used by William T. Reeves to describe the "effect of a bomb explosion on the surface of a planet" [6]. This creation was realized in the movie Star Trek II: the Wrath of Khan. Natural phenomena, also called "fuzzy" phenomena as water, fire, rain, smoke or clouds have been a huge challenge for computer rendering at that time. These phenomena have undefined surfaces. The behavior of these objects is really complex and irregular. Reeves was searching for a realistic method of fire visualization. He understood that a behavior of such a surface is difficult to define. Therefore it would be better to set up dynamic rules for a huge amount of small points. For instance, a fire was represented by thousands of particles. [6].

Nowadays particle systems are mainly used for the simulation of complex objects and the movement of irregular objects. Liang realized a three-dimensional fountain simulation based on GPU. He simulated the movement of a fountain and rendered it. During the process of particle simulation, Liang considered all aspects from real life. The water fountain drops were affected by gravity, air resistance and wind power [4].

Zhou and Lu used the idea of particle systems for fire simulation as well. Their idea was implemented using VRML and was later used to develop a VR-based firefighting simulation. Thus the simulation was used to study and train people's reaction in a fire emergency situation without putting them at a risk [5].

This is one of the important tasks of a simulation: to understand how systems works and how it is possible to influence the system itself.

3 Particle Systems and Visualization of Energy

Basically, one particle it is a simple point or object in three-dimensional space, which has established attributes, boundaries of diffusion and is based on stochastic spreading functions, which are used to generate and control the huge amount of particles within a particle system [6].

Using the idea of particle system for the simulation of energy flows, the energy itself and the energy flows could also be rendered as complex objects consisting of many small particles. In parallel to the characteristics of electrical energy, it is possible to present energy flow or precisely electrical current like a movement of electrons in a conductor.

One of the main advantages of the particle systems compared to Sankey diagrams is that the movement (flow) of the particles clearly shows the source and consumer of the energy. This and other properties if the particle system can be effectively used to increase the understanding for energy flows, consumption and waste. Using other types of diagrams like bar charts, line diagrams or Sankey diagram is not sufficient to provide a clearly understandable visualization of the necessary data. The main disadvantage of those diagrams is their static character. Energy consumption is visualized by using branch thickness property and recoloring of branches. In case of scaling thin branches can disappear, which would mean losing information.

The particle system this is dynamic system. The attributes of particle systems and how they can be influenced to show energy flows is will be described below.

3.1 Particles Attribute

3.1.1 Color and Density

Particle systems have the following attributes:

- Particle opacity (transparency and intensity);
- Particle size;
- Particle color;
- Particle velocity (speed and direction);
- Particle initial position;
- Particle lifetime.

Each attribute can be adjusted. By adjusting the parameter of the particles it is possible to change the simulation.

The first idea to show different amount of energy is – following the Sankey method [2] – to change the color of the particles. Figure 1 shows a possible division of the color depending on the current energy consumption.

Up to 3kW	3kW-6kW	more than 10kW
Green	Yellow	Red

Fig. 1 Dividing energy consumption by color

In addition to the proposed method of just using color coding, the particles themselves can be used to give a clearer understanding about energy movement within the machine tool.

The energy consumption can be represented by changing densities of the particles over the time. Using particles for the visualization of the current energy consumption by letting them flow through the machine tools will help to increase understanding for the main consumers of energy and the behavior of energy within the machine tool.

Particles usually have a sphere shape. Each particle corresponds to certain quantity of power consumption. In case power consumption is low there are only a few particles in a system. If power consumption increases, the quantity of particles increases as well. Fig. 2 shows a combination of changing color and density of the particles to represent different energy consumption levels.

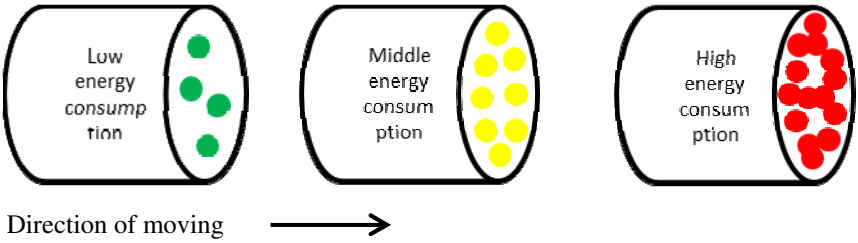

Fig. 2 Rendering energy consumption by changing density and color of the particles

In addition to color and density, the live span of the particles is another attribute that can be used to even better visualize energy flows.

3.1.2 Particles Lifespan

In principle the particle system has three stages: generation, dynamic changes and death.

A lifespan begins with the generation of the particles in an emitter. The emitter can be a single point or different types of surfaces (circle, rectangle, square, undefined surface). The emitter controls global settings of particles: number, speed, and direction in which they should be emitted. The particles are generated in an emitter and die, when lifetime reaches zero. In addition particles will die if they leave the set boundary of diffusion. In case a particle reaches a consumer (spindle, CNC controller, pumps, etc.) it will disappear.

In case of line losses (heat), there are no defined energy consumers in the machine tools. By using particles property to die when they are leaving the boundary of diffusion, it is possible to show this kind of energy losses.

It is complicate to show all energy consumers in a machine tool. For example, the chipping process requires only 14 % of the power at the main power supply, while 40 % of the power is needed at the servo unit drive [2]. Nevertheless it is necessary to simulate all energy consumers. Energy consumers which require a

little amount of energy but consist of different components will be present like one block with one branch (e.g. the control unit will be shown as one component, not separated into NC part, PLC part and HMI).

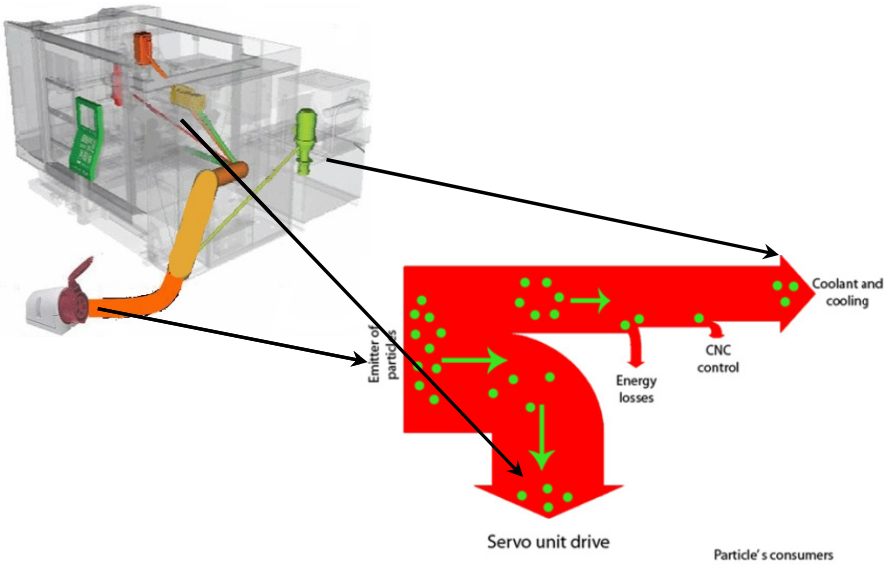

Fig. 3a Framework of machine tool and boundary of particle diffusion

Fig. 3b Schema of particles movement

Figure 3 shows the main energy consumers and the power supply unit. The power supply unit can be used as the emitter of the particle system. Coming from this emitter, one thick main branch represents all necessary energy needed by the machine tool. After entering the machine the main branch is devided to different smaller branches. Each branch should be connected to an energy consumer (e.g. spindle, axis, pump). The branches represent the boundaries for the particle system. The particles are moving through a machine from emitter to consumer simulating flowing energy. When particles reach the consumer they die and in the same time new ones appear from emitter.

The model of the energy flow is shown figure 3b, supposing, ten particles present the total energy consumption of the machine tool.

Where,

- 2 particles go to coolant;
- 1 particle goes to cooling;
- 1 particle goes to CNC control;
- 2 particles are energy losses.

The particle movement, including all divisions is represented by follow scheme (Fig. 4).

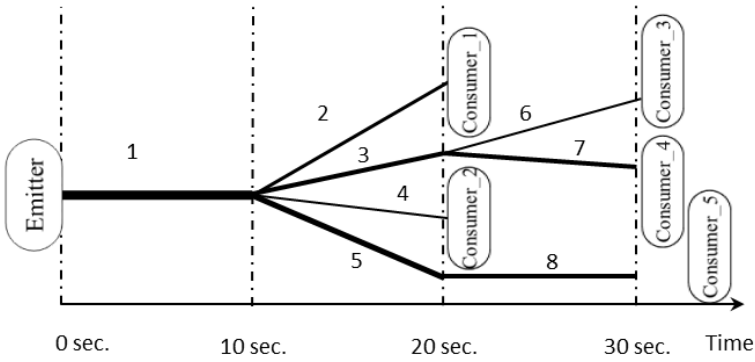

Fig. 4 Scheme of energy flow calculation

3.2 Mathematical Basis of Particle Movement

If the emitter of a particle system is not one single point, but a complex surface (rectangle, circle), the creation of the particles and their movement to the consumer can be represented by the following equations. The trajectory of particle movement is a simple line, which is described by vector-parametric equation line in space:

$$\vec{r} = \overrightarrow{r_0} + \vec{v}t \ , \tag{1}$$

where, $P_0(\overrightarrow{r_0}) = P_0(x_0; y_0; z_0)$ are the points in a line; $\vec{v}(l; m; n)$ is a direction vector of this line.

In the suggested system the direction of particle changes. For describing the behavior of all particles in a system, a set of equations depending on direction and time should be developed. In a scenario (energy flowing from emitter to consumer along branches 1- and 2) a particle changes direction one time. That means energy came from the power supply unit and then part of it went to one element (for instance X-axis). The description of particle way will be:

$$W_1(t)\begin{cases} P_1 + a_1(t)\vec{v}_1 & \begin{cases} t \in [0; 10] \\ t \in [10; 20] \end{cases} \\ P_2 + a_2(t)\vec{v}_2 \end{cases} \tag{2}$$

where, P_1 is an initial point of a system and P_2- the point, where particle changes the direction and t is a time.

The coefficient $a(t)$ should fulfill the followings condition:

$$a_i(t) = t - t_{io};\ t_i \in [t_{io}; t_{i1}] \tag{3}$$

The following equation represents scenario 1-3-8:

$$W_2(t)\begin{cases} P_1 + a_1(t)\vec{v}_1 & \begin{cases} t \in [0; 10] \\ t \in [10; 20] \\ t \in [20; 30] \end{cases} \\ P_3 + a_3(t)\vec{v}_3 \\ P_8 + a_8(t)\vec{v}_8 \end{cases} \tag{4}$$

The equation has to be adopted according to the current scenario. For example, according to [2] more than 40 % of the energy consumption goes to the servo drive unit (spindle, axis), whereas 19 % go to coolant, 13,8 % to cooling, 8, 6% to air cleaning, and 5, 2 % to CNC control.

4 Conclusions and Outlook

The primary idea of using particle systems is to show dynamic changes of energy consumption over the time. This paper shows a first approach to develop a more intuitive and understandable way for energy visualization.

In the next step the method will be evaluated at the machine model already used for the Sankey diagram. According to [3] a user evaluation is necessary to recognize the usability, clearness of getting information from the model and user understanding of the process of energy consumption.

Future research will be focused on the improvement of this system and the integration of this energy flow visualization in the whole factory. For more efficient work, visualization of energy consumption should be developed not only for expert, like energy engineers, but primarily for all employees in an enterprise. If employees from different division can realize, where energy is consumed, how it is flowing through a machine tool or a whole workshop or factory, everyone can propose different approaches to work more energy efficient and therefore save energy. By involving all employees in that process other ideas can be found, which might be hidden from expert energy-engineers.

Acknowledgments. The Cluster of Excellence "Energy-Efficient Product and Process Innovation in Production Engineering" (eniPROD©) is funded by the European Union (European Regional Development Fund) and Free State of Saxony.

References

[1] Schmidt, M.: The Sankey Diagram in Energy and Material Flow Management. Journal of Industrial Ecology 12(1) (2008)

[2] Neugebauer, R., Wittstock, V., Meyer, A., Glänzel, J., Pätzold, M., Schumann, M.: VR tools for the development of energy-efficient products. CIRP Journal of Manufacturing Science and Technology 4(2), 208–215 (2011)

[3] Wittstock, V., Klavina, E., Schütz, A., Pürzel, F.: Akzeptanz und Wirkung verschiedener Varianten der VR-Visualisierung von Energiekennwerten. In: Neugebauer, R., Götze, U., Drossel, W.-G. (Hrsg.) Energieorientierte Bilanzierung und Bewertung in der Produktionstechnik - Methoden und Anwendungsbeispiele. 2. Methoden Workshop der Querschnittsarbeitsgruppe "Energetisch-wirtschaftliche Bilanzierung" des Spitzentechnologieclusters eniPROD, pp. 91–98 (2012)
[4] Liang, Z., Zhou, H.: Three-dimension Fountain Simulation Based on GPU and Particle system. In: International Forum on Information Technology and Applications 2009, pp. 37–39 (2009)
[5] Zhou, S., Sun, Y., Lu, L., Chen, Z.: Fire model based on Particle system and its application in Virtual Reality. In: Processing of the 16th International Conference on Artificial Reality and Telexestence-Workshop (ICAT 2006) (2006)
[6] Reeves, W.T.: Particle system – A technique for modeling a class of fuzzy objects. ACM Transaction on Graphics 2(2), 91–108 (1983)
[7] Wittstock, V., Pätzold, M.: Data Analysis and Variants for VR-Visualization of Energy. In: Proceedings TechnischeUniverstät Chemnitz, Fraunhofer IWU, pp. 79–91 (2011)

Parameter Identification of Rheological Models Using Optimization Algorithms

V. Píštěk[1], P. Novotný[1], T. Mauder[2], and L. Klimeš[3]

[1] Brno University of Technology, Faculty of Mechanical Engineering, Institute of Automotive Engineering, Technická 2, 616 69, Brno, Czech Republic
{pistek.v,novotny.pa}@fme.vutbr.cz
[2] Brno University of Technology, Faculty of Mechanical Engineering, Heat Transfer and Fluid Flow Laboratory, Technická 2, 616 69, Brno, Czech Republic
mauder@fme.vubr.cz
[3] Brno University of Technology, Faculty of Mechanical Engineering, Energy Institute, Technická 2, 616 69, Brno, Czech Republic
klimes@fme.vutbr.cz

Abstract. The paper presents results of the application of optimization software GAMS and CONOPT solver for nonlinear optimization problems to identify multi-parameter elastomer rheological models. The solution is based on the experimentally set frequency-dependent dynamic stiffness of the elastomeric parts. Measured waveforms of dynamic stiffness are approximated using multi-parameter rheological models. The CONOPT solver has shown a significantly faster convergence and better accuracy of the calculation compared with the classical non-linear Gauss-Newton least square optimization technique.

1 Introduction

Many engineering mechanical structures are composed as linear structural components connected by elastomer parts. Examples include engine or tractor cab elastomeric mounts, rubber torsional vibration dampers of crankshafts, etc. These structures are usually analyzed using various finite element models. However, their computational efficiency is greatly dependent on interface modes. Mechanical properties of elastomeric components are usually highly dependent on the frequency, temperature and strain amplitude. Viscoelastic elastomer parts are difficult to model correctly by the finite element method due to their frequency-dependent mechanical properties. In most cases, a linear spring and a linear damper are used to model the elastomer. However, the simulation results may not match well with results of measurements in the time or frequency domain. Multi-parameter elastomer rheological models with a suitable structure can contribute to solving this problem.

T. Březina and R. Jabloński (eds.), *Mechatronics 2013*,
DOI: 10.1007/978-3-319-02294-9_25,

2 Computational Modeling of Elastomer Mechanical Properties

In the case of dynamic models with a viscous damping, the dissipated energy per period is given by

$$E_{\mathrm{dis}} = \pi\, k\, \omega \left|\bar{x}_0\right|^2 , \tag{1}$$

where k, ω and $\bar{x}_0$ represent the damping coefficient, angular frequency and amplitude of oscillation, respectively [1]. The amount of dissipated energy is therefore dependent on the frequency of oscillation.

Numerous experimental findings have shown that the hysteretic properties of many materials such as elastomers are frequency independent in the relatively large range of frequencies [2].

The viscoelastic mechanical properties of an elastomer component (see Fig. 1) are usually modeled using structural damping by assuming that the damping is proportional to stiffness. The governing equation of a single degree of freedom system for the hysteretic damping model has been formulated as

$$m\,\ddot{x} + \frac{h}{\omega}\,\dot{x} + c\,x = \bar{F}_0\, \mathrm{e}^{\,j\omega t} , \tag{2}$$

where m, h and c represent the mass, hysteretic damping coefficient and stiffness, respectively [2]. $\bar{F}_0$ and ω are the amplitude of the harmonic loading and the exciting frequency, respectively. Equation (2) is only valid for steady state harmonic solutions. In other words, the hysteretic damping can only be used for calculation of steady forced vibrations in the frequency domain.

In the case of dynamic models with a hysteretic damping the dissipated energy per period is given by

$$E_{\mathrm{dis}} = \pi\, h \left|\bar{x}_0\right|^2 \tag{3}$$

and is thus independent on frequency.

However, this approach does not take into account the frequency dependence of dynamic stiffness, which is a typical feature of silentblocks used in automotive technology.

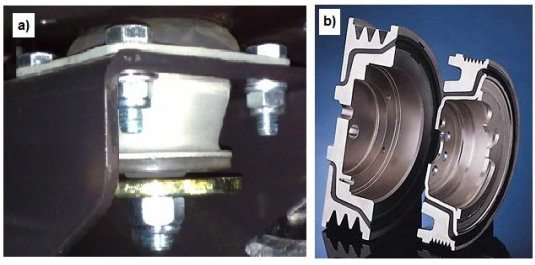

Fig. 1 Examples of a) rubber silentblock and b) rubber torsion dampers

Frequency dependence of the dynamic stiffness of an elastomer component can be modeled using multi-parameter rheological models with a suitably chosen structure arrangement of linear elastic and damping elements.

Basic elements of multi-parameter rheological models are simple two-parameter Kelvin and Maxwell model. Their configuration and the dynamic stiffness are illustrated in Fig. 2 a, b.

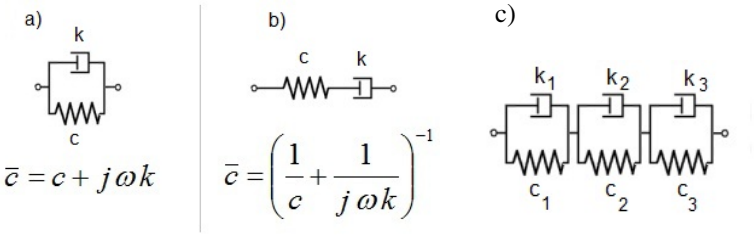

Fig. 2 Kelvin a) and Maxwell b) rheological models and the generalized three-element Kelvin model c)

Dynamic stiffness of more complex multi-parameter rheological models is set analogously to the two-parameter models in parallel or series arrangement. However, there is no developed finite element formulation to model dynamic behavior of silentblocks because of their frequency-dependent stiffness and damping properties. Technical measurements are used to create a sufficiently accurate computational model of elastomer components. Generalized three-element Kelvin model (see Fig. 2c) appears to be suitable for modeling the dynamic properties of automotive silentblocks [3].

3 Parameter Identification of Elastomer Rheological Model

Frequency dependence of the elastomer dynamic stiffness is determined experimentally on suitable test equipment. The elliptic force-displacement relationship is related to the dynamic stiffness of the system. The latter is defined by the ratio of input force $\bar{F}_0(\omega)$ to the response displacement $\bar{x}_0(\omega)$ in the frequency domain

$$\bar{c}(\omega) = \frac{\bar{F}_0(\omega)}{\bar{x}_0(\omega)} = c_R(\omega) + jc_I(\omega) \tag{4}$$

The elastomer component is the only flexible part of the test equipment, and therefore the dynamic stiffness $\bar{c}(\omega)$ provides the dynamic mechanical properties of the elastomer. The real part, $c_R(\omega)$, of the dynamic stiffness is called the storage modulus, and the imaginary part, $c_I(\omega)$, is called the loss modulus. Both the real and imaginary parts can be frequency-, temperature- and displacement-amplitude dependent.

Multi-parameter rheological model coefficients may be identified from the measured dynamic stiffness using the least square optimization method. To solve this optimization problem, for example the non-linear Gauss-Newton least square optimization technique was used [3], but its convergence is very slow. The optimization software GAMS and the CONOPT solver [4] for non-linear problems proved to be significantly more effective way to solve these problems.

The developed optimization program, which uses GAMS and CONOPT, allows the user to select the appropriate structure of the rheological model and to specify the initial values and limits for the searched coefficients (see Fig. 3). The measured frequency dependence of the dynamic stiffness of the elastomeric component is read from a simple data file.

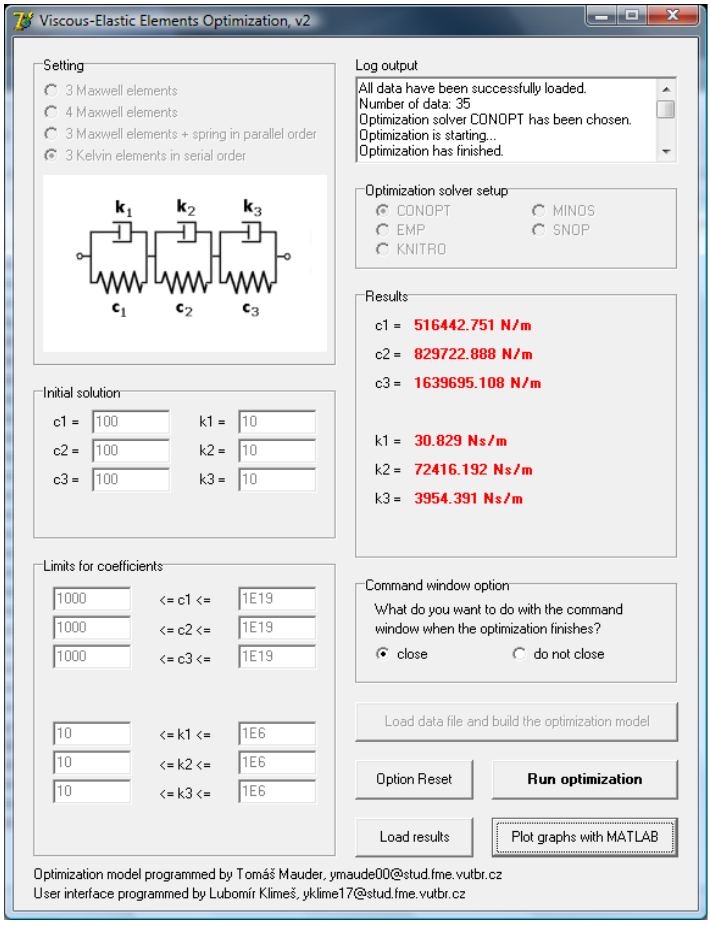

Fig. 3 View on graphical user interface of developed optimization program

4 Silentblock Dynamic Model for Automotive Use

The dynamic stiffness of the rubber silentblock was measured in the frequency range between 0 and 500 Hz at different temperatures and strain amplitudes. For modeling the dynamic stiffness generalized Kelvin model shown in Fig. 3 was chosen. Examples of measured values of the silentblock dynamic stiffness and the results for approximations using the generalized Kelvin model are shown in Fig. 4 and in Fig. 5.

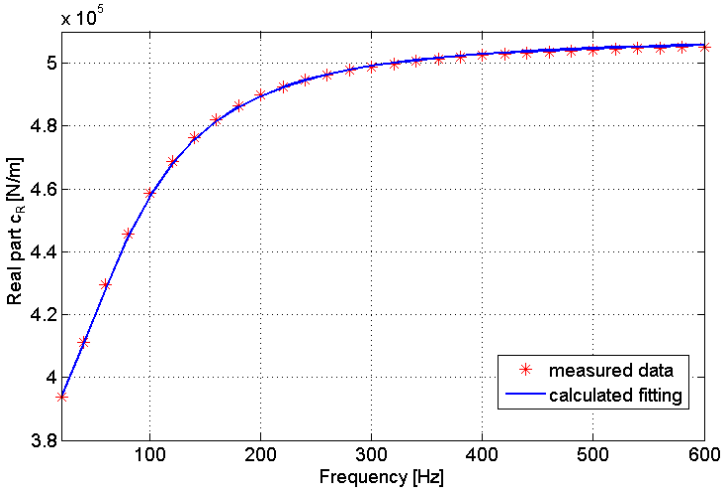

Fig. 4 Real part of the rubber silentblock dynamic stiffness

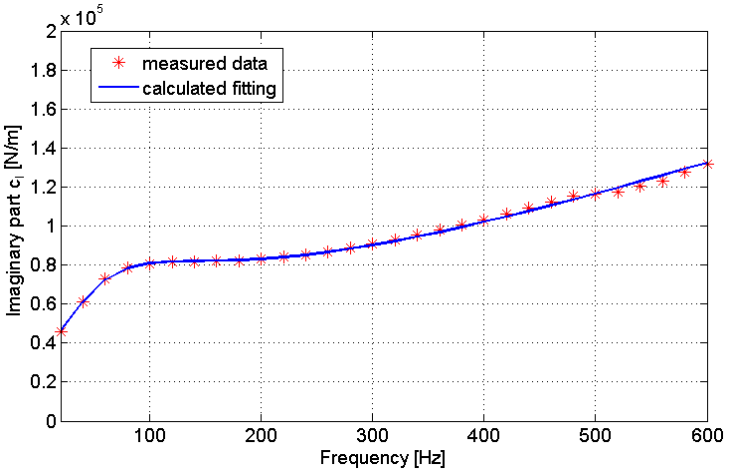

Fig. 5 Imaginary part of the rubber silentblock dynamic stiffness

5 Conclusions

The optimization software GAMS and the CONOPT solver are powerful tools for solving problems in the field of multi-parameter rheological models. As an example of successful application, the case of the rubber silentblock used in automotive technology was presented.

Optimization algorithms could also be applied in the identification of rheological models of high viscosity silicone fluids used in modern viscous type torsional vibration dampers of crankshafts. These silicone fluids exhibit under alternating stress not only the damping but also significant elastic properties. The dynamic stiffness can be well modeled using the generalized Maxwell model. In order to find the coefficients of the generalized Maxwell model, which consists of three or four parallel arranged two-parameter models shown in Fig. 2b, the software presented in Fig. 4 can also be used.

Acknowledgments. The presented work has been supported by European Regional Development Fund in the framework of the research project NETME Centre – New Technologies for Mechanical Engineering, project reg. No. CZ.1.05/2.1.00/01.0002, under the Operational Programme Research and Development for Innovation and with the help of the project FSI-S-11-8 granted by specific university research of Brno University of Technology. This support is gratefully acknowledged. The co-author, the holder of Brno PhD Talent Financial Aid sponsored by Brno City Municipality, also acknowledges for that financial support.

References

[1] Waller, H., Schmidt, R.: Schwingungslehre für Ingenieure. Wissenschaftsverlag, Mannheim (1989)
[2] Meirovitch, L.: Elements of Vibration Analysis. McGraw-Hill, New York (1986)
[3] Lin, H.: Dynamic Analysis of Structures with Elastomers using Substructuring with Non Matched Interfaces and Improved Modeling of Elastomer Properties. Dissertation, Oakland University (2009)
[4] Drud, A.: CONOPT – A GRG code for large sparse dynamic nonlinear optimization problems. Math. Program. 31, 153–191 (1985)

Cam Ring Force Simulation for Variable Roller Pump

P. Zavadinka and R. Grepl

Mechlab, Brno University of Technology, Faculty of Mechanical Engineering,
Technicka 2, 616 69, Brno, Czech Republic
yzavad02@stud.fme.vutbr.cz
www.mechlab.cz

Abstract. This paper deals with cam ring force simulation for variable roller pump. The goal of this article is to develop theory necessary for simulation model building. The measurements and simulations based on the developed theory show very good agreement. This theory provides next step for a variable roller pump model based design which finally has to results in more efficient hydraulic systems, higher performance and better durability. It extends state of art in the area of the variable roller pumps also.

1 Introduction

The hydraulic applications in mobile machinery market clearly indicate the increasing importance of fuel savings. Fuel costs and emissions rules of the engine have a big impact on each hydraulic system. New hydraulic systems have to be more efficient. The using of alternative components which can provide in the end higher energy savings in existing applications is one possible way how market demands can be fulfilled. The variable roller pump is one alternative component how to realize a variable pump for low pressure applications which displacement variability is the main added value of this pump. The variable roller pump could be used for example as an auxiliary pump or as a charge pump [1].

The typical configuration of a variable roller pump could be seen in Fig.1. The base parts of roller pump are the rotor (carrier) with roller slots, the rollers, the cam ring (stator), pivot, control spring and port plates which ensure connection of high pressure (HP - Outlet) and low pressure (LP – Inlet) to the chambers. The outer displacement chambers are located between rotor and cam ring. They are limited in the circumferential direction by the rollers. The inner displacement chambers are located between rollers in roller slots and rotor [1].

The rotor is placed eccentrically, the distance is called rotor eccentricity. The rollers can move radially in the slots and they are pressed against the cam ring due to the centrifugal force. The rollers are loaded by the pressure in the inner and outer chambers. For a correct pump function, it is necessary to ensure the sealing effect with the contact between cam ring and rollers. Due to the eccentricity of the

T. Březina and R. Jabloński (eds.), *Mechatronics 2013*,
DOI: 10.1007/978-3-319-02294-9_26,

rotor, the displacement of the outer and inner chambers increase during the first half rotor revolution, it means that the fluid is sucked (Inlet) and during the second part of the revolution, the displacement decrease and the fluid is delivered to the pump outlet **Chyba! Nenalezen zdroj odkazů.**.

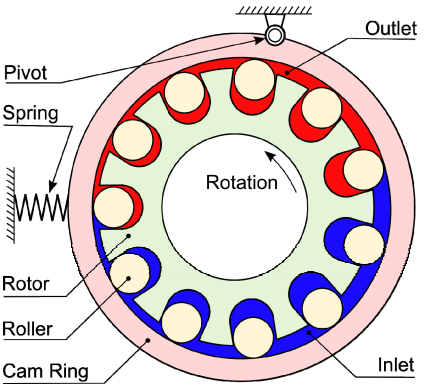

Fig. 1 Variable roller pump

The pump displacement control can be described in the following way: The pump displacement is proportionally depending on the rotor eccentricity, which changes with the cam ring motion around the pivot. At low outlet pressure the pump displacement is in maximum (maximum eccentricity) due to the spring force acting on the cam ring. An increase of outlet pressure increases the pressure force on the cam ring, which acts against the spring force and the pump displacement is reduced. The reduction of pump displacement results in decrease of outlet pressure because of the reduced flow. It means that a suitable spring design (spring preload, stiffness) can ensure a constant outlet pressure, which is often demanded in many applications.

1.1 Motivation and Goal

As described in the introduction, power savings of mobile hydraulic systems is the motivation for using a variable auxiliary pump like this. But using a variable pump in these mobile applications, we have to focus on durability, controllability and performance of the pump. All this must be simulated and simulation based optimized to fulfill the demands of these mechatronic application. The problem, that occurs now is the mostly unknown theory of the roller vane pump which is necessary for the model building: The literature search shows only one work focused on the kinematic and roller force study [4], another works focused numerical analyzes of a variable vane pump [5], [6] and some older works, dealing with control of vane pump with relatively simplified approach [7], but no complete derivation of the pressure, force and flow calculation.

As the flow and pressure calculation is already presented by the author of this paper [1], this paper is sequencing the previous publication with the derivation of the calculation of the resulting forces based on the flows and chamber pressures. Focus is hereby on the forces on the cam ring, as they are needed for the layout and dimensioning of a displacement control of the pump. The goal of this sequence is a simulation tool which is capable of a holistic pump simulation for optimization in regards to pump efficiency and controllability, so that on the one side an optimized design could be obtained and on the other side, in vehicle simulation models the performance and impact of the pump could be simulation-based tested.

2 Derivation of Force Calculation

The main forces acting on the cam ring can be identified according to the variable roller pump design (Fig. 1). They are: roller forces, pressure forces and spring force. The pivot friction was neglected. In the following chapters, the composition of the roller forces and pressure forces will be discussed.

2.1 Roller Forces

The Fig. 2 presents the forces acting on the roller: centrifugal force F_c , normal forces F_{ncam}, F_{nrot} and friction forces F_{fcam}, F_{frot} . In this case the Coriolis force was neglected; further information could be found in [1]. The outer chamber pressures p_{out} and inner chamber pressure p_{inn} act on the roller also.

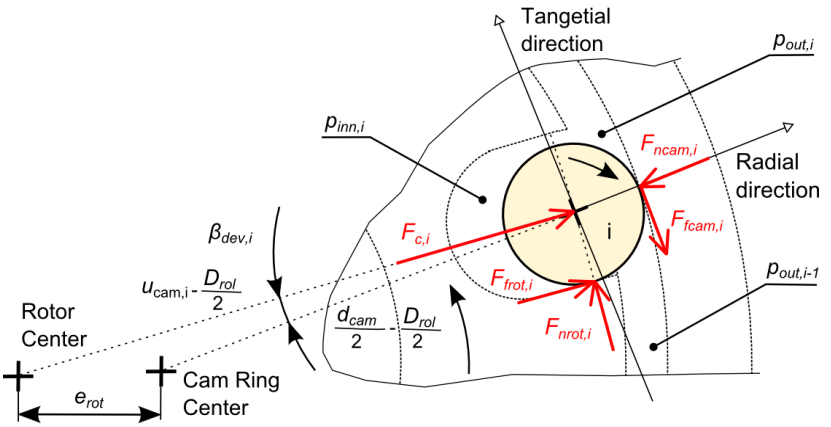

Fig. 2 Forces acting on the roller

The roller dynamics can be formulated according to Fig. 2. The Eq. (1) describes the roller dynamics in the radial direction where m_{rol} is the mass of the roller, x_{Rrol} is the roller stroke in radial direction, w_{rol} is the roller width, D_{rol} is the

roller diameter and β_{dev} is the deviation angle caused by the rotor eccentricity. The Eq. (2) presents the roller force balance in tangential direction where x_{Trol} is the roller stroke in tangential direction. The frictional forces were implemented into model as a Coulomb friction model.

$$m_{rol} \cdot \ddot{x}_{Rrol,i} = \left[F_{c,i} + F_{frot,i} + \left(p_{inn,i} - \frac{p_{out,i} + p_{out,i-1}}{2} \right) \cdot w_{rol} \cdot D_{rol} \right] \cdot \cdot \cos\left(\beta_{dev,i}\right) + \left[F_{nrot,i} - \left(\frac{p_{out,i} - p_{out,i-1}}{2} \right) \cdot w_{rol} \cdot D_{rol} \right] \cdot \sin\left(\beta_{dev,i}\right) - F_{ncam,i} \quad (1)$$

$$m_{rol} \cdot \ddot{x}_{Trol,i} = \left[-F_{c,i} - F_{frot,i} - \left(p_{inn,i} - \frac{p_{out,i} + p_{out,i-1}}{2} \right) \cdot w_{rol} \cdot D_{rol} \right] \cdot \cdot \sin\left(\beta_{dev,i}\right) - F_{fcam,i} + \left[F_{nrot,i} - \left(\frac{p_{out,i} - p_{out,i-1}}{2} \right) \cdot w_{rol} \cdot D_{rol} \right] \cdot \cos\left(\beta_{dev,i}\right) \quad (2)$$

The deviation angle β_{dev} ,caused by rotor eccentricity, could be derived from Cosin theorem in the following way.

$$\beta_{dev,i} = \cos^{-1}\left[\frac{-\left(e_{rot}^2 - \left(\frac{d_{cam} - D_{rol}}{2} \right)^2 - \left(u_{cam,i} - \frac{D_{rol}}{2} \right)^2 \right)}{2 \cdot \left(\frac{d_{cam} - D_{rol}}{2} \right) \cdot \left(u_{cam,i} - \frac{D_{rol}}{2} \right)} \right] \quad (3)$$

The Eq. (3) includes variable d_{cam} which represents the inner diameter of the cam ring. The next variable e_{rot} is the rotor eccentricity. The cam ring radius u_{cam} can be obtained from Eq. (4) where the angle φ represents the angular position of the demanded cam ring radius.

$$u_{cam}(\varphi) = e_{rot} \cdot \left(\cos\varphi + \frac{e_{rot}}{2 \cdot d_{cam}} \cdot \cos(2 \cdot \varphi) + \frac{d_{cam}}{2 \cdot e_{rot}} - \frac{e_{rot}}{2 \cdot d_{cam}} \right) \quad (4)$$

The centrifugal force F_c can be written as follows with the rotor speed ω_{rot}.

$$F_{c,i} = m_{rol} \cdot \left(u_{cam}(\varphi) - \frac{D_{rol}}{2} \right) \cdot \omega_{rot}^2 \quad (5)$$

2.2 Pressure Forces

The pressure force acting on the cam ring is the most important for the total spring force calculation and it is depending on the pressure profile in the outer chamber, which calculation was presented in the article [1]. The calculation of the chamber area which is loaded with the chamber pressure is shown in Fig. 3.

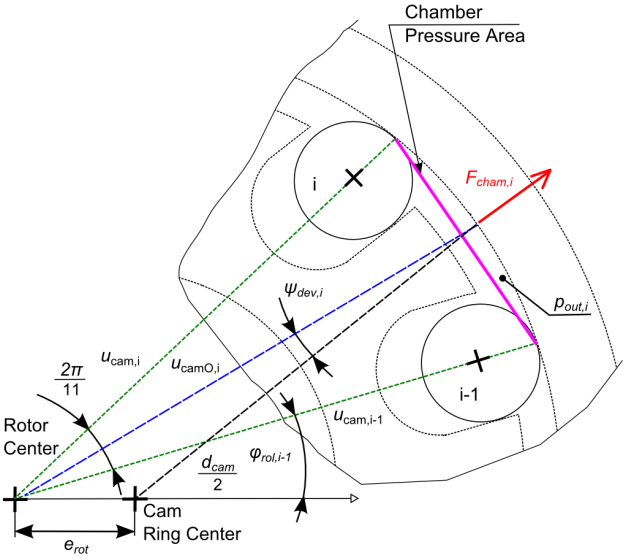

Fig. 3 Pressure force of outer chamber

The resultant outer pressure force acting on the cam ring area (magenta color) can be calculated also with the Cosine theorem, according to Eq. 6.

$$F_{cham,i} = p_{out,i} \cdot w_{rol} \cdot \sqrt{u_{cam,i}^2 + u_{cam,i-1}^2 - 2 \cdot u_{cam,i} \cdot u_{cam,i-1} \cdot \cos\frac{2 \cdot \pi}{11}} \tag{6}$$

2.3 Spring Force

The particular forces acting on the cam ring are presented in Fig. 4 where the direction and origin of each force is defined. Due to the rotor eccentricity it is necessary to determine the angles of the roller and chamber forces. The angles of the roller and chamber forces are known only for the coordinate system with the center in the rotor center, but for the resultant cam ring force calculation the origin in the cam ring center can significantly simplify whole calculation. The angle transformation equations are shown in Eq. 7 and Eq. 8 where ϑ_{rol} presents the angle of the roller force and ϑ_{cham} presents the angle of chamber pressure forces. The roller deviation angle β_{dev} can be obtained from Eq. 3 presented in previous chapter. In a similar way as β_{dev}, the chamber deviation angle ψ_{dev} can be derived also.

$$\vartheta_{rol,i} = \varphi_{rol,i} + \beta_{dev,i} \tag{7}$$

$$\vartheta_{cham,i} = \varphi_{cham,i} + \psi_{dev,i} \tag{8}$$

The spring force – force acting against the compression spring can be calculated as a sum of all forces acting on the cam ring.

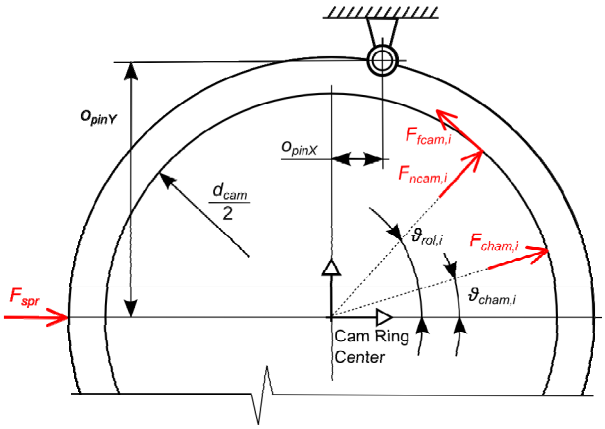

Fig. 4 Forces acting on the cam ring

In the case of steady state and with neglecting of pivot friction, final Eq. 9 for the spring force calculation is derived. The pivot horizontal offset o_{pinX} and vertical offset o_{pinY} are defined according to Fig. 4.

$$F_{spr} = -\frac{1}{o_{pinX}} \cdot \sum_{i=1}^{11} o_{pinY} \cdot \left(F_{cham,i} \cdot \cos \vartheta_{cham,i} + F_{rol,i} \cdot \cos \upsilon_{rol,i}\right) + o_{pinX} \cdot \left(F_{cham,i} \cdot \sin \vartheta_{cham,i} + F_{rol,i} \cdot \sin \vartheta_{rol,i}\right) + F_{cam,i} \cdot \frac{d_{cam}}{2} \tag{9}$$

3 Simulations and Measurements

The Previous equations were implemented into a Simulink model, which is also connected to a hydraulic (chamber pressure calculation) model, developed in [1]. Fig. 5 shows the shape of the spring force during one rotor revolution at full pump displacement. Eleven significant peaks can be seen which correspond to the eleven rollers. A more detail look into simulation results shows 22 peaks, which correspond to eleven rollers and two transition areas (Outlet →Inlet, Inlet →Outlet). This spring force oscillation is caused by the pressure profile in the chamber which is changing according to portplate timing. The big decrease of the spring force is repeating each approx. 33°, which is corresponding to the rollers (360°/11 roller), because each 33° of revolution the outer chamber is ported from low to high pressure, having a direct impact (reduction) on the spring force, down to the negative values. The porting from high to low pressure, visible in the smaller dips down to 35%, has because of the moment balance a smaller impact on the spring.

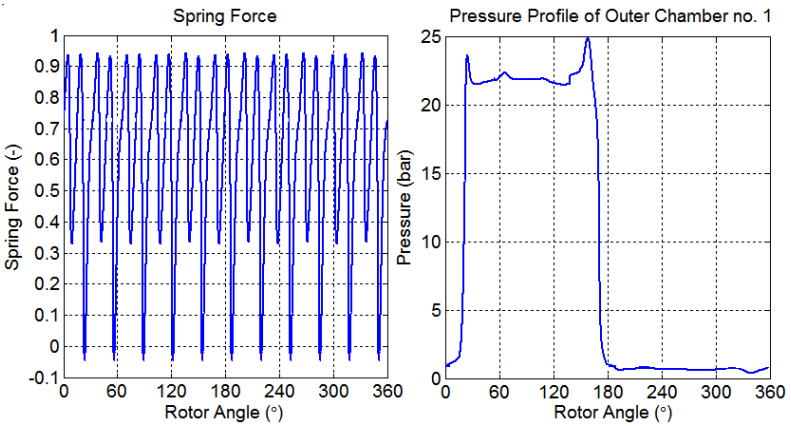

Fig. 5 Spring force (left) and chamber pressure (right) simulations at a pump speed of 2000 min-1 and Δp of 20 bar

The next figure (Fig. 6) presents a comparison between simulation and measurements for various speeds and different pressures at max displacement.

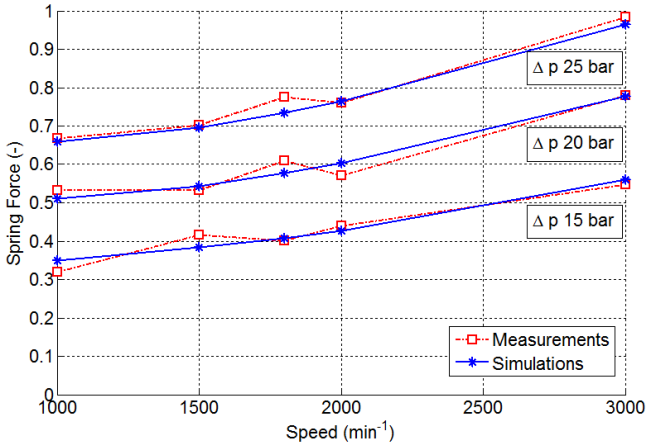

Fig. 6 Comparison between simulations and measurements in normalized scale in different operating conditions

This comparison confirms a good agreement between simulations and measurements. The biggest deviation (at 1800 min^{-1}) is probably caused by dynamic effects in the pressure profile simulation which are not included in hydraulic model.

4 Conclusions

The derivation of the forces on the cam ring of a variable roller pump was explained in this paper. For validation, the theory was confirmed by a comparison between simulations results and measurements.

This never before presented theory of a variable roller pump gives now a better understanding. The knowledge of the cam ring forces leads then to better designs of variable roller pump components, especially with focus on durability. A good example is the spring force, which has a very high excitation over a rotor revolution or wear of the cam ring/roller due to the contact forces.

If this theory is implemented in the existing calculation and optimization tool [1], it can then provide a holistic optimization of the pump and its efficiency.

Additionally, increased displacement control performance which can be achieved with application of suitable spring or more sophistic control as a hydraulic or electro hydraulic control have to result in higher efficiency of variable roller pump systems.

Acknowledgments. The present work has been supported by European Regional Development Fund in the framework of the research project NETME Centre under the Operational Programme Research and Development for Innovation. Reg. Nr. CZ.1.05/2.1.00/01.0002, id code: ED0002/01/01, project name: NETME Centre –New Technologies for Mechanical Engineering).

References

[1] Zavadinka, P., Grepl, R.: Simulation based optimization methodology of port plates for roller pumps, FPNI PhD Symposium on fluid power, Reggio Emilia (2012)
[2] Ivantysyn, J., Ivantysynova, M.: Hydrostatic Pumps and Motors, Principles, Design, Performance, Modeling, Analysis, Control and Testing. Academia Books International, New Delhi (2001) ISBN -81-85522-16-2
[3] Fitch, C.E., Hong, T.I.: Hydraulic System Modeling and Simulation. Bardyne, Stillwater (2001) ISBN 0-9705922-5-6
[4] Zhurba, N., Cleghorn, W.: Kinematic Solution and Force Layout of a Roller Pump with Internal Outlets. In: SAE 2000 World Congress Detroit (2000)
[5] Frendo, F., Novi, N., Squarcini, R.: Numerical and experimental analysis of variable displacement vane pumps. In: International Conference on Tribology, Parma (2006)
[6] Danardo, D., Kim, S.K., Roziboyev, E., Kim, U.C.: Design and optimization an LPG roller vane pump for suppression cavitation. International Journal of Automotive Technology (2010)
[7] Karmel, M.A.: Study of the Internal Forces in a Variable Displacement Vane Pump. General Motors Research Laboratories, Warren (1986)
[8] Kučík, P., Strážovec, I., Krišśák, P.: Hydraulický prenos energie. Mobilné Stroje, Edis (2000) ISBN 80-7100-725-0
[9] Tyler, B.L.: Design and control of a variable displacement vane pump for valveless hydraulic actuation. Dissertation, Vanderbilt University (2008)

Benefits of a Parallelization of a Stand-Alone Desktop .NET Application Threaded Instance Methods

I. Košťál

University of Economics in Bratislava, Faculty of Economic Informatics, Dolnozemská cesta 1, 852 35 Bratislava, Slovakia
igor.kostal@euba.sk

Abstract. The paper deals with a parallelization of a local object instance methods executed on the secondary threads of a stand-alone desktop .NET application in order to improve their execution effectiveness in comparison to serial methods of the same object. These serial and parallel instance methods compute the values of the definite integrals of two special functions by numerical approximation methods - Simpson's rule and the Left-Point rule because these functions do not have an elementary antiderivatives. Computed values of definite integrals then can be used, for example, in a computation of rotational kinetic energy of homogeneous solids of revolution created by the revolution of areas under curves of these functions within some intervals around the *x* axis. This may be an important dynamic parameter of mechanical components of the mechatronic system, which need to be determined the most effectively by the control software of the system. Then a stand-alone desktop .NET application can be an useful part of the control software of the mechatronic system.

1 Introduction

Quite often we need to create relatively simple, inexpensive, but effective control software of a mechatronic system. Such need appears when we develop such software for a more simple mechatronic system. It is not too desirable then to use a very sophisticated application architecture of a mechatronic system control software, such as, a distributed application architecture, because it could happen that the costs of developing and running such a sophisticated control software could significantly increase the acquisition costs of the entire mechatronic system. It may also happen that a more simple mechatronic system with a limited number of controlled activities cannot use all possibilities offered by such a sophisticated control system. In such cases, it is a good solution to create a more simple control software, with a less complicated application architecture, for example a stand-alone desktop .NET application, but with using modern programming approaches

T. Březina and R. Jabloński (eds.), *Mechatronics 2013*,
DOI: 10.1007/978-3-319-02294-9_27,

(threading instance methods, synchronizing access to shared resources) and with a focus on the most efficient operation of this application. This implies the use of some programming approaches improving the execution efficiency of a such application. That is for example, a parallelization of instance methods of a mechatronic system control application by the methods *Parallel.For* and *Parallel.ForEach* from the Task Parallel Library (TPL) and by data parallelism.

This paper deals with the creation of the stand-alone desktop .NET application with a maximum execution efficiency, using above presented programming approaches and techniques. This application could be a part of a mechatronic system control application. The task of the stand-alone desktop .NET application is to calculate definite integrals values of the functions $f_1(x) = \sqrt{1+x^4}$ and $f_2(x) = e^{-3x^2}/(1+4x^2)$ the most effectively and provide them into a control application of a mechatronic system. This control application can calculate using the values of the definite integrals of the functions $f_1(x)$ and $f_2(x)$ values of rotational kinetic energy of homogeneous solids of revolution created by the revolution of areas under curves of the functions $f_1(x)$ and $f_2(x)$ within given closed intervals around the x axis. By this calculation the control application determines an important dynamic parameter of mechanical components of the mechatronic system. Mechanical components can be just such or similar homogeneous solids of revolution performing rotational movement around the x axis.

However, the functions $f_1(x)$ and $f_2(x)$ are special functions. The antiderivatives of these functions exist but they cannot be expressed using any algebraic combinations of elementary functions, therefore, we cannot use the Newton-Leibniz formula to calculate definite integrals values of these functions on given intervals. One of possibilities to compute these values of definite integrals is the use of numerical approximation methods. Our stand-alone desktop .NET application calculates definite integrals values of these functions just in this way - using numerical approximation methods Simpson's and the Left-Point method.

2 Rotational Kinetic Energy of a Homogeneous Solid of Revolution

When we want to calculate rotational kinetic energy of homogeneous (of uniform density = ρ) solid of revolution created by the revolution of the area under the curve of a function $f(x)$ within an interval $\langle a, b \rangle$ around the x axis we have to compute the moment of inertia of this solid, first. From theoretical mechanics we know that the ***moment of inertia of*** *such* ***a homogeneous solid of revolution*** with respect to the axis of revolution is [1]

$$I = \frac{\pi\rho}{2}\int_a^b \left(f(x)\right)^4 dx \tag{1}$$

Then by means of the moment of inertia of a homogeneous solid of revolution we can compute the ***rotational kinetic energy of this solid*** using the formula (2)

$$KE_r = \frac{1}{2} I\omega^2 \tag{2}$$

where ω is the angular velocity of the solid revolving about the *x* axis. [1]

From the formula (1) it is clear that for the calculation of the moment of inertia value of a homogeneous solid of revolution is necessary to know the value of the definite integral. This can be efficiently calculated by numerical approximation methods - Simpson's rule or the Left-Point rule implemented in the stand-alone desktop .NET application.

3 Simpson's and the Left-Point Rule

As we know, finding the definite integral value of a function is equivalent to finding the area under the curve traced by that function.

Simpson's rule is a method for approximating a definite integral of the function *f(x)* on the interval <*a, b*> using quadratic polynomials (i.e., parabolic arcs instead of the line segments used in the trapezoidal rule). We have to divide the interval <*a, b*> into a set of *n* subintervals of equal width *h* to implement this rule. Simpson's rule requires that *n* be an even number. This is needed because the rule jointly approximates each pair of two consecutive areas and also because each parabola requires three points to specify it, so each parabola spans two intervals. [2]

Simpson's rule for numerical integration of the function *f(x)* over *n* subintervals in mathematics sometimes known as the composite Simpson's rule, can be expressed as the approximation

$$\int_a^b f(x)dx \approx \frac{h}{3}[f(x_0)+4f(x_1)+2f(x_2)+4f(x_3)+2f(x_4)+\cdots+4f(x_{n-1})+f(x_n)] \tag{3}$$

where $x_0=a$, $x_i=x_0+ih$ *(i=1, 2, …, n-1)*, $x_n=b$ and $h=(b-a)/n$ is the width of each subinterval, and *n* is the number of subintervals. [2]

The next way to approximate the area under the curve traced by the function *f(x)* is by dividing the area into rectangles and adding the rectangles together. The interval <*a*, *b*> is again divided into a set of *n* subintervals of equal width *h* to implement this rule. One of rectangle rules, the **left-point rule** sets the height of each rectangle to the leftmost value of *f(x)* in each subinterval, so that the approximation is

$$\int_a^b f(x)dx \approx h[f(x_0)+f(x_1)+f(x_2)+\cdots+f(x_{n-1})] \tag{4}$$

where $x_0=a$, $x_i=x_0+ih$ $(i=1, 2, \ldots, n-1)$ and $h=(b-a)/n$ is the width of each subinterval, and n is the number of subintervals. [2]

Our stand-alone desktop .NET application computes the definite integrals of the functions $f_1(x)$ and $f_2(x)$ by the formula (3) (*Simpson's rule*) and by the formula (4) (*the left-point rule*).

4 Parallel Programming in the .NET Framework and Data Parallelism

Nowadays, many personal computers and workstations have two, four or six cores (that is, CPUs) that enable multiple threads to be executed simultaneously. To take advantage of such hardware, we can parallelize our code to distribute work across multiple processors. The Microsoft Visual Studio 2012 development environment and the .NET Framework 4 support **parallel programming** by providing the Task Parallel Library and other tools.

The **Task Parallel Library** (TPL) is a set of public types and APIs (Application Programming interfaces) in the *System.Threading* and *System.Threading.Tasks* namespaces in the .NET Framework version 4. The purpose of the TPL is to make developers more productive by simplifying the process of adding parallelism and concurrency to applications. [3]

In parallel programming in the .NET Framework we know two kinds of a parallelism - data and task parallelism (we do not deal with task parallelism in this paper because we did not use this parallelism in a code of our application). **Data parallelism** refers to scenarios in which the same operation is performed concurrently (that is, in parallel) on elements in a source collection or array. Data parallelism with imperative syntax is supported by several overloads of the *For* and *ForEach* methods in the *System.Threading.Tasks.Parallel* class through which TPL supports this parallelism. In data parallel operations, the source collection is partitioned so that multiple threads can operate on different segments concurrently. We write the loop logic for a *ParallelFor* or *ParallelForEach* loop much as we would write a sequential loop. We do not have to create threads or queue work items. The TPL handles all the low-level work for us. When a parallel loop runs, the TPL partitions the data source so that the loop can operate on multiple parts concurrently. Behind the scenes, the *Task Scheduler* partitions the task based on system resources and workload. When possible, the scheduler redistributes work among multiple threads and processors if the workload becomes unbalanced. However, we can also supply our own custom partitioner or scheduler. [3] Data parallelism with the methods *Parallel.For* and *Parallel.ForEach* is used in a parallelized code of our stand-alone desktop .NET application.

5 Stand-Alone Desktop .NET Application

All parts of our stand-alone desktop .NET application were created and built in the Microsoft Visual Basic 2012 language and in the Microsoft Visual Studio 2012 development environment. The source code of this application is divided to two parts that are saved into files:

MyLocalType.vb - here is defined the *MyLocalType* class that includes 4 serial and 8 parallel member methods, that manage to compute the definite integrals values of the functions $f_1(x)$ and $f_2(x)$ by Simpson's or the Left-Point rule. From the *MyLocalType.vb* source file is built (.dll) library into the *MyLocalType.dll* file, that is the component of our stand-alone desktop .NET application.

StandAloneApplForm.vb - here is defined the *StandAloneApplForm* class that includes event handlers (member methods) of all controls of our stand-alone desktop .NET application. From the event handlers *Btn_CompDIBySimpsonM_Click* and *Btn_CompDIByLeftPM_Click* of two buttons this application calls serial or parallel instance methods of the local object, that compute by Simpson's or the Left-Point rule and return to the application text box the definite integrals values of the functions $f_1(x)$ or $f_2(x)$. The *StandAloneApplForm.vb* source file is built into the *StandAloneApplForm.exe* file. This *.exe* file refers to the *MyLocalType.dll* file, therefore this *.dll* file must be placed in the same directory as the executable file. The application *StandAloneApplForm.exe* is a Windows application.

Our stand-alone desktop .NET application works as a real threaded and parallelized application. When a user selects in the user interface of this application the function to integrate, switches to the parallel calculation of definite integrals values of the chosen function, inserts into the input text box of the application 13 correct inputs and starts the calculation, so in one period of time will be concurrently computed 11 definite integrals values of the selected function by 11 instance methods of the local object on 11 secondary threads of *StandAloneApplForm.exe*. Moreover, since it is switched to parallel calculation of definite integrals values, all cores (CPUs) of the computer on which running *StandAloneApplForm.exe* will in this period of time utilized at 100%, thus with a maximum efficiency.

Our stand-alone desktop .NET application is available upon request.

Fig. 1 shows the important part of the source code of the member method *GetDIBySimpsM4_PP* that computes parallel with the partitioner by Simpson's rule and returns the definite integral value of the function $f_2(x)=e^{-3x\wedge 2}/(1+4x^2)$) on the interval $<a, b>$ with n integration subintervals. This method, that is the member method of the class *MyLocalType*, calls the *Parallel.ForEach* method from TPL.

```
Public Class MyLocalType
                                                    . . .
  Public Function GetDIBySimpsM4_PP(ByVal a As Double, ByVal b As Double,
                                                    ByVal n As Long) As Double
    Dim DI_SM As Double = 0
    Dim x0 As Double = a
    Dim xn As Double = b
    Dim sum As Double = Math.Exp(-(3 * x0 ^ 2)) / (1 + 4 * x0 ^ 2) +
                        Math.Exp(-(3 * xn ^ 2)) / (1 + 4 * xn ^ 2)
    Dim h As Double = (xn - x0) / n
    Dim h_third As Double = (xn - x0) / (3.0 * n)

    Dim localMonitor = New Object()
    Dim startTimeCalcDI As DateTime = DateTime.Now
    Parallel.ForEach(Partitioner.Create(1, n), Function() 0.0,
                Function(range, state, localSum)
                  For i = range.Item1 To range.Item2 - 1
                    Dim x = x0 + (i * h)
                    If i Mod 2 <> 0 Then
                        localSum = localSum + 4 * Math.Exp(-(3 * x ^ 2)) / (1 + 4 * x ^ 2)
                    Else
                        localSum = localSum + 2 * Math.Exp(-(3 * x ^ 2)) / (1 + 4 * x ^ 2)
                    End If
                  Next
                  Return localSum
                End Function,
                Sub(localSum)
                  SyncLock (localMonitor)
                    sum += localSum
                  End SyncLock
                End Sub)
    DI_SM = h_third * sum
    Dim timeSpanCalcDI As TimeSpan = (New TimeSpan(DateTime.Now.Ticks –
                                                    startTimeCalcDI.Ticks))
    Dim string_timeSpanCalcDI As String = timeSpanCalcDI.ToString
    Dim msec_timeSpanCalcDI As Double = timeSpanCalcDI.TotalMilliseconds
                                                    . . .
    Return DI_SM
  End Function
                                                    . . .
End Class
```

Fig. 1 The part of the source code of the parallel member method *GetDIBySimpsM4_PP*

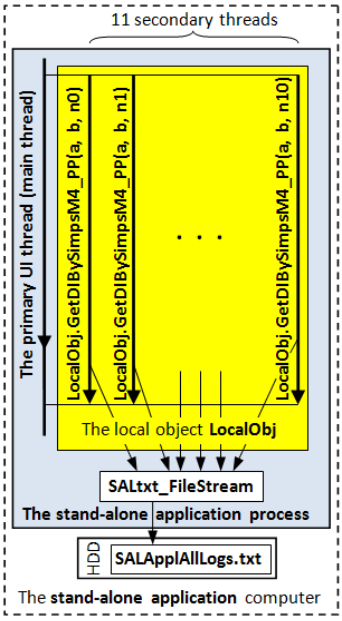

Fig. 2 Functioning of the stand-alone desktop. NET application during parallel computing with a partitioner of 11 definite integrals values of the functions $f_2(x)=e^{-3x^2}/(1+4x^2)$)

Fig. 2 shows the operation of the multithreaded stand-alone desktop. NET application, after its switching by the user on parallel computing with a partitioner the selected function definite integrals values. 11 local object parallel instance methods *LocalObj.GetDIBySimpsM4_PP* of this application, which calculate 11 definite integrals values of the function $f_2(x)$ at the same integration interval, but with 11 different numbers of integration subintervals, are executed on 11 secondary threads. During waiting for the end of asynchronous executing these 11 parallel instance methods it is executing 11 the *Do While* loops on the main thread of this application. These loops provide displaying the information about performed calculations by these instance methods to the graphical user interface of this application. Because these methods are parallel, the virtual machine for parallel processing distributes work of each of them among multiple virtual threads and processors (cores of CPU) that their workload becomes balanced and that these processors will utilized with a maximum efficiency (at 100%). These 11 parallel instance methods write information about their calculations through one shared data stream *SALtxt_FileStream* into the disk file *SALApplAllLogs.txt*. Therefore, access of these 11 parallel instance methods to one shared data stream *SALtxt_FileStream* is synchronized using methods *Monitor.Enter* (lock a data stream) and *Monitor.exe* (unlock a data stream).

6 Experiment and Its Results

We performed the experiment in order to measure the execution efficiency of parallelized instance methods of the local object of the stand-alone desktop .NET application compared to serial instance methods of the same local object. Serial and parallelized instance methods were computing by Simpson's or the Left-Point rule the definite integrals values of the functions $f_1(x)$ and $f_2(x)$. These instance methods were executed on secondary threads of this application.

Execution times of particular serial and parallel instance methods of the local object provides us stand-alone desktop .NET application itself, it also measures these times, saves them into the log file *SALApplAllLogs.txt* on the hard disc and displays them in the text box of this application. We used the measured execution times for calculations of speedups of parallel instance methods in opposite to serial instance methods.

Our stand-alone desktop .NET application was running on the computer with the hardware and software configuration displayed in Table 1.

Table 1 Overview of the basic hardware and software configuration of the computer of the stand-alone desktop .NET application

CPUs' configuration	Operating system	Microsoft .NET Framework
Intel Core i7-920 Processor (8MB Cache, 2.66 GHz, 4.80 GT/s Intel QPI, 4 Cores, 8 Threads)	Microsoft Windows 7 Enterprise Service Pack 1, 32 bit	Microsoft .NET Framework 4 Client Profile, Microsoft .NET Framework 4 Extend.

We used the following set of inputs for the function $f_1(x)$ to measure execution times of 2 serial and 4 parallel instance methods using Simpson's or the Left-Point rule

2,086;3,153;629486876;236897534;930568942;428567824;829657842;29658740;1029589236;329568740;728568952;128586368;530256872

We used the same set of inputs for the function $f_2(x)$ to measure execution times of 2 serial and 4 parallel instance methods using Simpson's or the Left-Point rule. This set differs only in the first two numbers 0,019; 0,728.

Each this set was entered into the relevant input text box of the stand-alone desktop .NET application. These sets contain the same numbers of integration subintervals up to 1,029589236 billion and different the endpoints of the integration intervals (the first 2 numbers in these sets).

We calculated the *speedups* of the particular parallel instance methods using p computing elements (CPUs) from measured execution times of serial and parallel instance methods by the following formula (5).

$$Speedup(p) = \frac{T_{serial}}{T_{parallel}(p)} \tag{5}$$

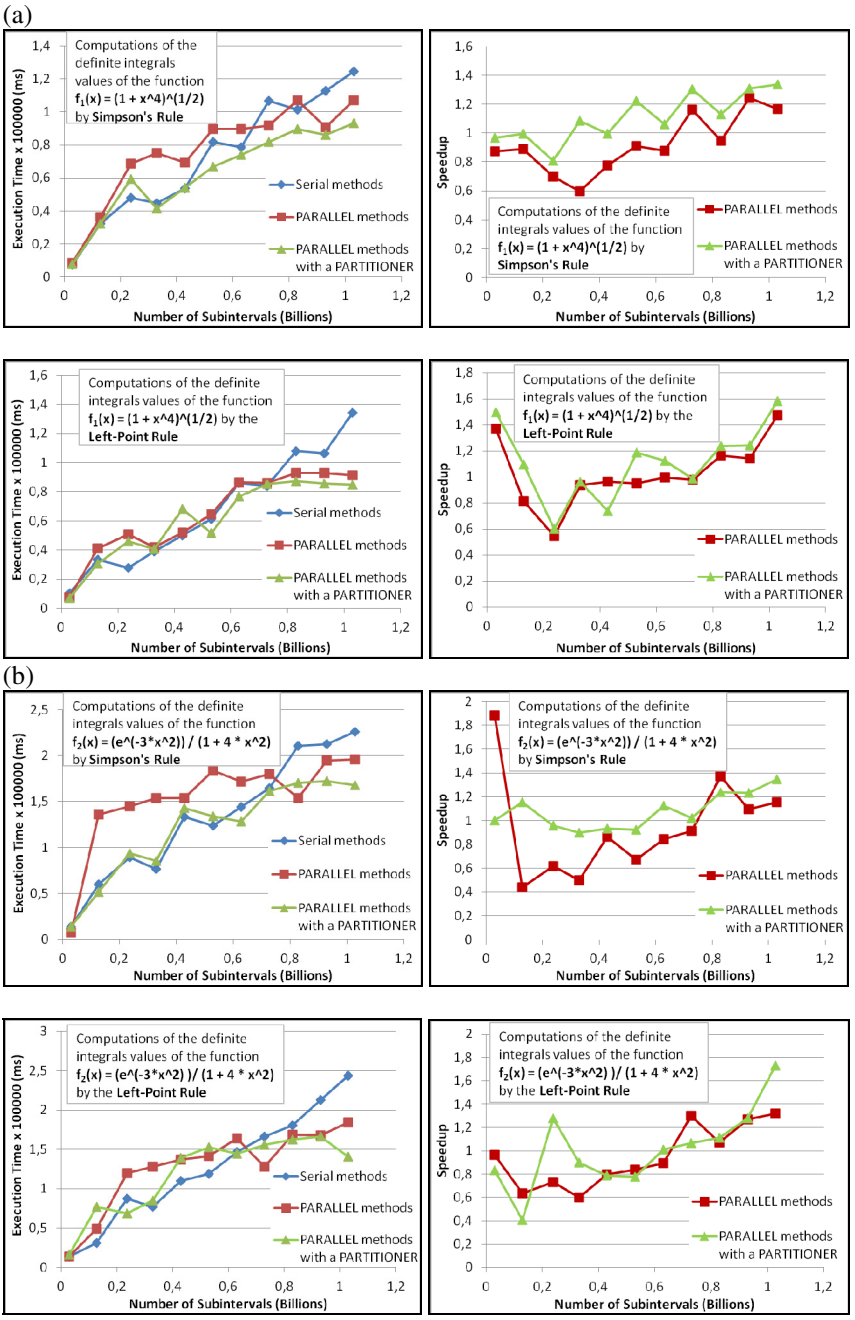

Fig. 3 Execution times of all instance methods and speedups of all parallel instance methods of the local object of the stand-alone desktop .NET application for both integrated functions and both rules ((a) $f_1(x)=(1+x^4)^{1/2}$, (b) $f_2(x)=e^{-3x^2}/(1+4x^2)$)

Measured execution times of all the instance methods and calculated speedups of all parallel instance methods of our stand-alone desktop .NET application calculating definite integrals values of the functions $f_1(x)$ and $f_2(x)$ are shown in the graphs in Fig. 3.

When we analyzed *the accuracy of the calculation of definite integrals values* of the functions $f_1(x)$ and $f_2(x)$ by instance methods of our application, we found that the instance methods using Simpson's rule have mathematically expected, significantly higher accuracy than instance methods using the Left-Point rule. This high precision of instance methods using Simpson's rule is in the used range of numbers of integration subintervals (from 29658740 to 1029589236) independent from them. It follows that these methods can achieve high accuracy in calculating the definite integral values of the functions $f_1(x)$ and $f_2(x)$ even at lower values of this range. In contrast, instance methods using the Left-Point rule achieve such high accuracy of the calculation only at the maximum values of the used range of numbers of integration subintervals. Based on this, we can say that instance methods of our stand-alone desktop .NET application using Simpson's rule to calculate the definite integral value of the given function achieve high accuracy of calculation of it at relatively small numbers of integration subintervals (29658740), when these methods have short execution times, thus they do not block the computing resources of the computer unnecessarily.

We used the definite integrals values of the functions $f_1(x)$ and $f_2(x)$ calculated by the MATLAB function *int* as reference values to measure the accuracy of the calculation of definite integrals values of these functions. Fig. 4 shows the definite integrals values of the functions $f_1(x)$ and $f_2(x)$ calculated using parallel instance methods with a partitioner of our stand-alone desktop. NET application.

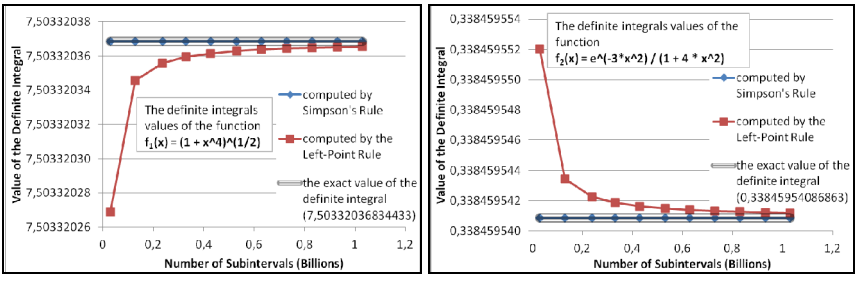

Fig. 4 Definite integrals values of the functions $f_1(x)=(1+x^4)^{1/2}$ (a) and $f_2(x)=e^{-3x^2}/(1+4x^2)$ (b) calculated using parallel instance methods with a partitioner of the stand-alone desktop .NET application

Brief results analysis. From the presented graphs showing execution times of all instance methods and speedups of all parallel methods our stand-alone desktop .NET application in dependency on the numbers of integration subintervals it is obvious that parallel methods have significantly shorter execution times on larger numbers of integration subintervals (greater than approximately 0,7 billion) compared to serial methods. The speedups of the parallel methods with a partitioner

are significantly greater than the speedups of the parallel methods without a partitioner on big numbers of integration subintervals (approximately 1 billion) compared to serial methods.

From the presented graphs showing the definite integrals values of the functions $f_1(x)$ and $f_2(x)$ calculated using parallel instance methods with a partitioner our stand-alone desktop. NET application it is clear that instance methods using Simpson's rule are more efficient and more accurate than instance methods using the Left-Point rule.

7 Conclusion

Parallel instance methods with the partitioner of the local object our stand-alone desktop .NET application show relatively large stable **speedups**, up to **1,72** for the function $f_2(x)$, on larger numbers of integration subintervals (greater than approximately 0,7 billion) compared to serial instance methods of the same local object. In addition, parallel instance methods with a partitioner using Simpson's rule achieve high accuracy of calculations of the definite integral values of the functions $f_1(x)$ and $f_2(x)$. This enables our stand-alone desktop .NET application to achieve very interesting execution efficiency and high accuracy of the calculations of definite integrals values of the functions $f_1(x)$ and $f_2(x)$ that do not have an elementary antiderivatives.

Using such calculated definite integrals values can be computed, for example rotational kinetic energy of homogeneous solids of revolution created by the revolution of curves of just such or similar functions around the x axis. This may be important dynamic parameter of mechatronic system components, which the control software of the system needs to determine the most effectively. Therefore our stand-alone desktop .NET application can be a useful part of this control software.

References

[1] Smith, P.F., Longley, W.R.: Theoretical Mechanics, pp. 7–30, 231–233. Ginn and Company, Boston (1910)
[2] Rouah, F.D., Vainberg, G.: Option Pricing Models and Volatility Using Excel-VBA, pp. 40–50. John Wiley & Sons, Inc., Hoboken (2007)
[3] Microsoft Corporation, MSDN Library (2013), `http://msdn.microsoft.com`
[4] Atkinson, K.E.: An Introduction to Numerical Analysis, 2nd edn., pp. 249–332. John Wiley & Sons, Inc., USA (1989)
[5] Davis, P.J., Rabinowitz, P.: Methods of Numerical Integration, 2nd edn., pp. 51–133. Dover Publications, Inc., New York (2007)
[6] Krylov, V.I.: Approximate Calculation of Integrals, pp. 65–132. Dover Publications, Inc., Mineola (2005)
[7] Schmidt, M.C., Samatova, N.F., Thomas, K., Park, B.-H.: A scalable, parallel algorithm for maximal clique enumeration. Journal of Parallel and Distributed Computing 69, 417–428 (2009)

[8] Overill, R.E., Wilson, S.: Performance of parallel algorithms for the evaluation of power series. Parallel Computing 20(8), 1205–1213 (1994)
[9] Lastovetsky, A., Reddy, R.: On performance analysis of heterogeneous parallel algorithms. Parallel Computing 30(11), 1195–1216 (2004)
[10] Mackie, R.I.: Design and deployment of distributed numerical applications using.NET and component oriented programming. Advances in Engineering Software 40(8), 665–674 (2009)
[11] Maghraoui, K.E., Desell, T.J., Szymanski, B.K., Varela, C.A.: Malleable iterative MPI applications. Concurrency and Computation: Practice and Experience 21(3), 393–413 (2009)

Morphing Structure with a Magnetorheological Material – Preliminary Approach

P. Skalski

Institute of Aviation, Centre of New Technologies, al. Krakowska 110/114,
02-256 Warsaw, Poland
pawel.skalski@ilot.edu.pl

Abstract. This paper shows new potential possibilities of a magnetorheological material (a smart skin) application such as morphing structures. Smart materials have properties that can be altered by temperature, moisture, electric or magnetic fields, pH, and stress. The morphing technology on aircraft has found increased interest over the last decade because it is likely to enhance performance and efficiency over a wider range of flight conditions. Conducted investigations in this work show magnetic properties of a smart skin for a morphing structure. Presented results prove, that magnetic properties of a magnetorheological skin can be controlled.

1 Introduction

In the past few decades, interest in morphing structures has increased due to the superior benefits they can provide. A structure that can change its geometric characteristics and tune its properties (stiffness and damping) to meet the mission's requirements or different load conditions is appealing. Since the shape of an aircraft strongly affects its performance and flight dynamics, morphing technologies have always been investigated by the Aerospace industry. The design of a morphing aircraft by means of smart materials is a problem that involves different disciplines. Morphing can be achieved by the use of motors or complex mechanism distributed through the wing [1].

Many "smart" materials were invented more than 30 years ago, but their development and improvement over the past three decades has led to new, more varied uses of these adaptable materials. Smart materials have properties that can be altered by temperature, moisture, electric or magnetic fields, pH, and stress. Control of vibration and flutter plays an important role in the satisfactory performance of many aero-mechanical systems such as aircraft wings, helicopter rotors, propellers of a turbo-prop engines, or compressor and rotors of jet engines. With advances in active materials, it has become possible to integrate sensing, actuation, and control of vibration and flutter intrinsically in the design of the structure [7].

T. Březina and R. Jabloński (eds.), *Mechatronics 2013*,
DOI: 10.1007/978-3-319-02294-9_28,

The current use of multiple aerodynamics devices (such as flaps and slats) represents a simplification of the general idea behind morphing. Traditional control systems (with fixed geometry and / or location) give high aerodynamic performance over a fixed range and for a limited set of flight conditions. Outside of this range, these traditional systems can be neutral or negatively influence the aerodynamics and hence often give lower efficiency. Conventional hinged mechanisms are effective in controlling the airflow, but they are not efficient, as the hinges and other junctions usually create discontinuities in the surface, resulting in unwanted fluid dynamics phenomena [3].

The intelligent structures are those which incorporate actuators and sensors that are highly integrated into the structure and have structural functionality as well as control logic, signal conditioning, and power amplification electronics. In an active (feedback) control, the strain developed in signal-conditioned and used for feedback control employing suitable control laws. The active control strategy for smart structure can be broadly classified as state-space control and distributed parameters control. A key challenge in developing a one dimensional morphing structure is the development of a useful morphing skin, defined here as a continuous layer of material that would stretch over the morphing structure and mechanism to form a smooth aerodynamics skin surface. Due to the large geometrical changes required for a span-morphing wingtip as envisioned here, metal or resin-matrix-composite skin material are suitable [7, 11].

In the field of a smart technology and control structures designed for airlines, which merged into a common system will form a novel structural element, designed to improve the functional characteristics of objects flying through the interaction with the centre, in which the movement takes place. The newly developed structural element, forming a structure analogous to mechatronics - a synergistic combination of control, innovative design solutions and materials, will use material and magneto-classical system is not the executive. The functional to be used as an element of the wing flaps, and its role may involve both an increase in the lift or reduce drag forces as well as influencing the active aerodynamics to reduce adverse effects such as flutter and excessive vibration and load structures, noise accompanying movement or mitigate the loss of energy necessary to move an aircraft [1, 3, 9].

2 Smart Materials

Smart materials are designed materials that have one or more properties that can be significantly changed in a controlled fashion by significantly stimuli, such as stress, temperature, moisture, electric or magnetic fields. There are a number of smart material, some of which are already common. Some examples are as following: piezoelectric materials, magnetorheological fluids, temperature-responsive polymers, or granular materials [2, 4, 7, 13]. The granular material enclosed in a

tight space enables an easy change of structural form and use of it as a kind of a plastic bulk filling the special encapsulation. The mechanical properties of such structures, obtained on the basis of a loose material, located in a tight space, are influenced by many factors. The most important factor is the underpressure value but the global material features depend also on the dimensions and the shape of a single grain, the type of granular material, surface roughness, filling ratio of the structure [6, 12, 13, 14].

For the envisaged shape changes, skin materials for morphing wings must have high recovery, strength and be flexible, elastic and resistant to the environmental conditions. Nowadays, alternatives to this end are: electroactive polymers (EAP), shape memory alloys (SMA), shape memory polymers (SMP), nanocomposites.

EAPs are suitable for morphing wing applications due to their responsive and tuneable properties. They can perform energy conversion between electrical and mechanical forms. Conductive polymers, ionic polymer metal composites, dielectric elastomers are examples of EAPs. Selection of these materials is generally based on actuation strain, speed, force, voltage and mechanical response entailed by application [8].

Shape memory polymers have attracted a great interest as promising morphing wing materials due to their shape recovery upon application of voltage. Therefore, they can be used as electroactive actuators. SMP can be thermoplastic or thermoset. These polymers consist of both hard and soft segments in their structure. The hard segments form physical or chemical crosslinks that is the main difference between these polymers. The ratio of the hard to soft segments and types of crosslinks determines the elastomeric nature of the polymer. Hard segments contribute crystallinity or crosslinking and give thermal and mechanical stability to the polymer in action, which is also known to be used in morphing air vehicle applications [5].

Combination of the superior properties of shape memory polymer (rubber, epoxy, thermoplastic elastomer, etc.) and nanofiller (carbon nanotube, zinc oxide, barium titanate, etc.) in composite structure are thought to be promising for the concept of morphing structure. In particular, reinforced shape memory polymers such as thermoplastic elastomer/ carbon nanotube composites have been investigated in terms of their shape recovery effect and actuation performance [5].

A magnetorheological fluid is a type of a smart fluid in a carrier fluid, usually a type of oil. When subjected to a magnetic field, the fluid greatly increases its apparent viscosity, to the point of becoming a viscoelastic solid. Typical magnetorheological fluids are the suspensions of micron sized, magnetisable particles (carbonyl iron, iron, reduced carbonyl iron, iron carbide, etc.).

The author of this paper proposes a new smart skin based on a rubber and a carbonyl iron powder.

3 Concept of Morphing Structures

The Merriam Webster dictionary defines “morph” as undergoing transformation to change the form of character of something. The NATO Research Technology Organization, and Applied Vehicle Technology Technical Team on Morphing Vehicles define morphing as a “real-time” adaptation to enable multi-point optimized performance. Morphing technology is born from the intent of making airplanes more efficient manoeuvrable and capable of multi-tasking missions. The first concept applied to morph the flight characteristics of an aircraft was based on a mechanism to vary the wing geometry. It was a mechanical system that, for the first time in aviation history, enabled an aircraft to change its aerodynamic wing characteristics in flight, such as the aspect ratio (AR) [10].

The design of a morphing aircraft by means of smart materials is a problem that involves different disciplines. In fact, the idea is to design a structure that is not only capable of withstanding prescribed loads, but also to change its shape in order to withstand different ones. Morphing can be achieved by the use of motors or complex mechanism distributed through the wing. Considering the weight of the actuators and the fact that changing the shape of a structure requires additional power to overcome its stiffness, using traditional actuators (electric or pneumatic) and complex mechanisms does not seem to bring the desired benefits that one should expect from a morphing concept. In order to reduce the complexity and hence increase the reliability, the actuation system, consisting of active materials, should be embedded in the structure. Ideally, there should not be a neat distinction between structure and actuation system, so that what is envisaged to produce and carry the loads, is also capable to change its own shape or a limited part of it. Apart from the benefits in terms of complexity, reliability, and production cost, such a concept would prove to be lighter. Fig. 1 indicates an approach to the design of a morphing concept [1, 3, 10].

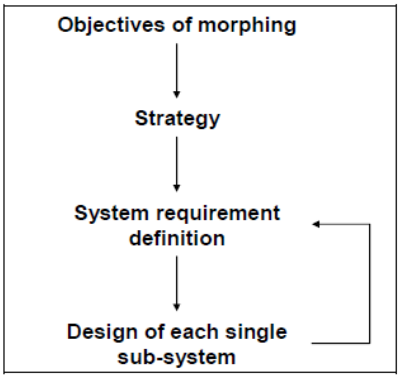

Fig. 1 Approach to the design of a morphing concept [10]

For flight control, the system should exhibit the following main characteristics:

-relatively fast dynamics in order to allow prompt response to inputs from the remote pilot or autonomous control system. In this way, the morphing system can also be used to counteract random disturbances: for instance gusts can be particularly severe flying between buildings or closed spaces;
-capability to operate over a wide range of flight conditions, like flight speed, air temperature, and wind;
-capability of high recoverable strains;
-capability of repetitive actuators;
-low power consumption;
-high reliability, since malfunctioning may cause the loss of the aircraft [10].

In order to meet the above requirements and to keep the design as simple as possible, avoiding the use of sophisticated kinematics, the smart material should respond quickly to the external stimuli, should be capable of large and recoverable free strains, ideally not affected by fatigue issues, and effective in transforming the input energy into mechanical energy. The ability to work under different conditions also implies that the morphing system has to be fully controllable: ideally all the positions, between the undeformed and the fully deflected, should be reachable in order to perform different maneuvers and to counteract random disturbances. The low power consumption requirement should take into account the fact that part of the structure needs to be deformed, and the contribution of the elastic energy may be considerable with respect to the aerodynamic work [1, 3, 10].

4 Smart Skin

A magnetorheological material (a smart skin) is a new development for morphing aircraft concepts. The primary phase of the morphing skin development a magnetorheological material was fabricated that would make up the skin or face sheet. Initially, a large number of rubber was tested for viability with a carbonyl iron powder (CIP). Fig. 2 shows a view of a new smart material. Elastomeric materials are ideal candidates for a smart skin. In morphing applications, where large shape changes are expected, the design of a suitable skin is a huge challenge and a key issue. The skin must be soft enough to allow shape changes but at the same time it must be stiff enough to withstand the aerodynamics loads and maintain the required shape/ profile. This requires thorough trade-off design studies between the required depends on the loading scenario and the desired change in shape (one-dimensional or multi-dimensional) [9].

Magnetic investigations of a magnetorheological smart skin were performed on the LAKESHORE vibrating sample magnetometer (www.lakeshore.com). The range of a magnetic field was between 0 – 1600 [kA/m] (2 [T]). Results of experiments were presented in Fig. 3. Presented results prove, that magnetic properties of a magnetorheological skin can be controlled.

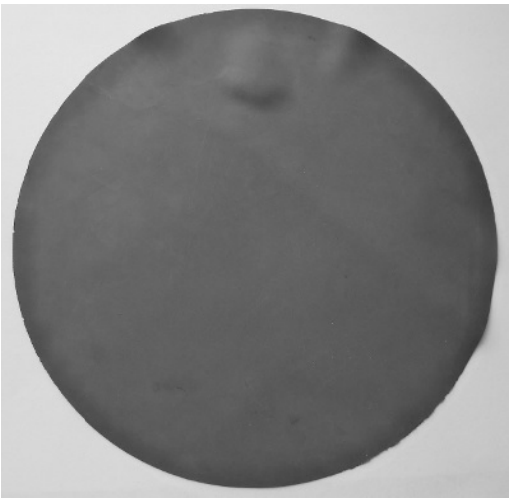

Fig. 2 View of a smart skin

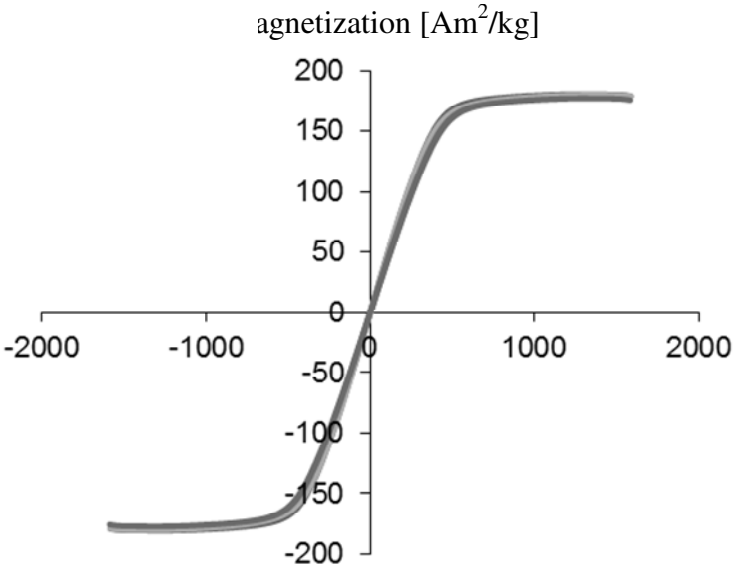

Fig. 3 Results of magnetic investigations of a smart skin

Results obtained from experimental research carried out for the magnetorheological material (smart skin) revealed, that there is a considerable influence of a magnetic field on properties of a smart skin. Because these changes are entirely reversible, it is possible to use a magnetorheological material as “intelligent” material - a part of a morphing structure.

5 Conclusions and Perspectives

The challenge in developing a morphing skin suitable as an aerodynamical surface is balancing the competing goals of low in-plane actuation requirements must be low enough that a reasonable actuation system within the aircraft can stretch the skin to the desired shape and hold it for the required morphing duration. At the same time, the skin must withstand typical aerodynamics loads without deforming excessively (e.g., rippling or bowing), which would result in degradation to the aerodynamics characteristics of the aerofoil surface.

The research in the area of smart materials and adaptive structures has huge potential to make substantial contributions in enhancing performance, reliability of aero-mechanical systems. Significant advances have been made in the field of magnetorheological materials, in formulating techniques for modelling, simulation, health monitoring, and control of complex systems.

Results obtained from experimental research carried out for the magnetorheological material (smart skin) revealed, that there is a considerable influence of a magnetic field on properties of a smart skin. Because these changes are entirely reversible, it is possible to use a magnetorheological material as “intelligent” material - a part of a morphing structure.

In terms of magnetic characteristics of investigated material, a lot of open questions still remain. The most interesting problem is the behaviour of a smart skin in a magnetic field between 0 and 2 [T] (most changes in properties take place in that range). Next one would concern the level of compaction of CIP in a rubber. This parameter clearly determines the dimensions, shape and properties of a smart material . Following are size and shape of particles, which may have similar effect on magnetic properties as previously mentioned. Another factor is the CIP’ material, which strongly influences its structure.

For better understanding of the magnetic behaviour of magnetic skin, the experiments will be continued.

Acknowledgments. The work reported in this paper was supported by the National Centre of Science, grant no. DEC-2011/01/D/ST8/07456.

References

[1] Baier, H., Datashvili, L.: Active and morphing aerospace structures – a synthesis between advanced materials, structures and mechanisms. Journal of Aeronautical & Space Science 12(3), 225–240 (2011)

[2] Bajkowski, J., Jasiński, M., Mączak, J., Radkowski, S., Zalewski, R.: The active magnetorheo logical support as an element of damping of vibrations transferred from the ground to large-scale structure supports. Key Engineering Materials 518, 350–357 (2012)

[3] Barbarino, S., Bilgen, O., Ajaj, R.M., Friswell, M.I., Inman, D.J.: A review of morphing air craft. Journal of Intelligent Material Systems and Structures 22, 823–877 (2011)

[4] Carlson, J.D., Weiss, K.D.: A growing attraction to magnetic fluids. Machine Design (9), 61–66 (1994)
[5] Cho, W.J., Kim, W.J., Jung, Y.C., Goo, N.S.: Electroactive shape memory polyurethane composites incorporating carbon nanotubes. Macromolecular Rapid Communications 26, 412–416 (2005)
[6] Pyrz, M., Zalewski, R.: Modeling of granular media submitted to internal underpressure. Mechanics Research Communications 37(2), 141–144 (2010)
[7] Schwartz, M.: "Smart materials," Book. CRC Press (2008)
[8] Schultz, M.R.: US Patent 7, 321, 185 (2008)
[9] Skalski, P., Parafiniak, M.: Application of a magnetorheological fluid to the aircraft wing. Acta Avionica XIV, 25, 93–95 (2012)
[10] Trapani, M.: Design & Modelling of a composite rudderless aeroelastic fin structure. PhD Thesis, CranfieldUniveristy (2010)
[11] Worden, K., Bullough, W.A., Haywood, J.: Smart technologies. World Scientific Publishing, University of Sheffield (2003)
[12] Zalewski, R.: Constitutive model for special granular structures. Int. J. Non-Linear Mech. 45(3), 279–285 (2010)
[13] Zalewski, R., Pyrz, M.: Modeling and parameter identification of granular plastomer conglomerate submitted to internal underpressure. Engineering Structures 32(8), 2424–2431 (2010)
[14] Zalewski, R., Pyrz, M.: Experimental study and modeling of polymer granular structures submitted to internal underpressure. Mechanics of Materials 57, 75–85 (2013)

Evaluation of Possibilities of Electroactive Polymers Application in Bio-inspired Adaptronic System

J. Kaleta, K. Kot, D. Lewandowski, K. Niemiec, and P. Wiewiorski

Wroclaw University of Technology, Institute of Materials Science and Applied Mechanics, Smoluchowskiego 25, 50-370, Wroclaw, Poland
katarzyna.niemiec@pwr.wroc.pl

Abstract. The paper presents an original design of 3-segments adaptronic analogue of units of mammal's vertebrae based on 8 actuators using dielectric electroactive polymer (*DEAP*). The way of preparation took into account the tendency of the *DEAP* material to local breakdowns, caused by degradation of the internal structure. The cross effects of phase response on a given electrical stimulus under high voltage were identified as well. The degrees of freedom of the analogue segments were determined, taking into account biological significance of vertebral endplates which a simplified form is included in the model. The work is to propose a bio-inspired techniques to build robots with many degrees of freedom using *DEAP* materials.

1 Introduction

Vertebral column is a multifunctional construction which, thanks to its central location, is an axis of the whole body. One of its most important features is the necessity of handling many complicated tasks that are required in the aspect of its correct operation. Its main functions include both protection of the spinal cord and soft organs as well as keeping the body straight. Vertebral column is also the one that plays the main role in the human musculoskeletal system and all the movement would be impossible without it. It has to be elastic and strong due to the fact that its role includes many complicated and complex tasks realised continuously. According to these reasons, it is also a very important element in designing of modern robots.

Nowadays, one of the most popular ways in designing innovative and advanced manipulators is the usage of bio-inspired methods together with different kinds of SMART materials. These materials enable designing of mechanical devices and robots without many heavy and relatively expensive parts, such as toothed wheels or bearings, making the whole structure lighter and simpler in production and operation.

T. Březina and R. Jabloński (eds.), *Mechatronics 2013*,
DOI: 10.1007/978-3-319-02294-9_29,

Because of the technological difficulties, it was not that long ago when, together with the raising popularity of the SMART materials, the possibilities of the bio-inspired methods usage in designing of modern robots expanded. That is why the amount of their programmable movements is still increasing. That allows creating devices with higher and higher level of technological complexity [5, 6]. One of the examples is focused on creation of the adaptronic analogue of mammal's vertebrae that, in the future, can be used as a part of a robot.

Anatomically, vertebral column is a vertical combination of repetitive segments separated by intervertebral discs that ease and cushion mechanical shocks. In its modular construction, it is possible to separate elemental, functional unit that consists of a pair of adjacent vertebrae's bodies together with an intervertebral disc and vertebral endplates that join two adjacent elements.

The intervertebral discs are relatively small elements (comparing to the vertebrae) that play important role in the vertebral column's correct functioning. One of the most important tasks realised by the intervertebral discs is shock absorption and cushioning of mechanical shocks that allow maintaining stabilization even when exposed to strong and sudden overloads.

Each vertebra is joined to the others by ligaments that stretch on the whole length of the vertebral column. Their basic function is maintaining the upright, natural position of the vertebral column. Ligaments do not allow any bones, discs or muscles movements but thanks to their flexibility and stretchiness allow the body movement.

The purpose of this work was the construction of 3-segments adaptronic analogue of mammal's vertebrae and the most efficient use of controlling that allows realization of a large variety of movements. For this purpose, the model consisting of 3 similar segments was built. Thanks to the usage of PolyPower actuators, each of them is controlled separately.

2 Material and Preparation

In the research, the PolyPower [7] thin layer was used as a SMART elastomer, together with additional applications such as sensors and actuators. Advantages of this choice were mainly little mass and a short reaction time [1].

A major limitation for the use of *DEAP* for actuator application is the high voltage required for operation [2]. The strain generated by the *DEAP* material is based on the electrostatic field created between the 2 electrodes of a capacitor. The dielectric layer is based on a soft silicone with a high relative permittivity and using metallic electrodes.

In this work, the properties of PolyPower membranes were presented together with preparation for a further research method. In the experiment, the electrostrictive properties of an electroactive polymer of the dielectric type (*DEAP*) were used. It allowed determination of the damping due to high voltage treatment characteristic U=f(l) (range of high voltage 2-5 kV). Firstly, membranes had to be prepared for a further research, because it was unable to run the tests on them in

the way they were delivered from the producer. It was important to cut alongside the *DEAP* roll they were on to prevent appearance of additional, unnecessary stresses (Fig. 1A).

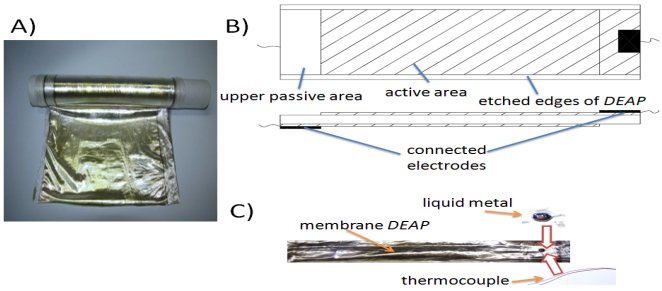

Fig. 1 PolyPower foil: A) On a roll, B). DEAP membrane preparation scheme together with connected wires. Active/passive areas marked, C) PolyPower membrane scheme together with the thermocouple-liquid metal connection spot.

Cutting the material perpendicularly to its waved structure orientation was also extremely important in order to prepare samples. It allowed to use the electric properties precisely. Moreover, careless moves might have caused irredeemable changes in the material's structure [3]. In some cases, had to be cut more material from the roll to make sure the structure of the sample would remain the same. Because of that, the selection of a cutting method and its parameters were a result of both material properties and a cutting way.

For a further research, rectangular (280 x 30 mm) elastomer samples were used. The material was cut alongside given texture directions delivered by the *DEAP* producer.

The second step was chemical etching of the 4 mm wide edges of previously prepared PolyPower membranes. Then, in order to prevent avalanche breakdown and "burning" of the *DEAP* membrane's edges, the conductive layers were removed using a dedicated gel-like preparation. Membrane preparation scheme, with active and passive areas and visible etched area is shown in the figure 1B.

Furthermore the electrodes had to be connected on the opposite sides of the previously prepared membranes in order to supply samples with a control voltage. The elastic and lightweight conductors, obtained from the T-type thermocouples (d= 0,08mm), were used as a wiring. For increasing the conductivity value of the membrane-wire connection, liquid metal drops (one of the Indium-Gallium alloys) were put in the contact spots. Then, the whole connection was covered with the cyanoacrylate adhesive (Fig. 1C).

3 Perpendicular PolyPower Membrane System

Specially prepared digesting method allowed the usage of previously prepared electroactive polymer membranes together with the attached wires as an active vibration damper. In this purpose, two PolyPower membranes were situated

(crossing each other) in the specially prepared testing frame (fig. 2). Membranes were pre-stretched so that the local small deformations would not be an obstacle in the further tests.

To obtain bending Δl results, the Keyence laser sensor was placed on the stand, in the characteristic "A" point (fig. 2).

Because the connection was located in the central parts of the membranes, non-conductive silicone film was put in the connection spot in order to prevent sparking.

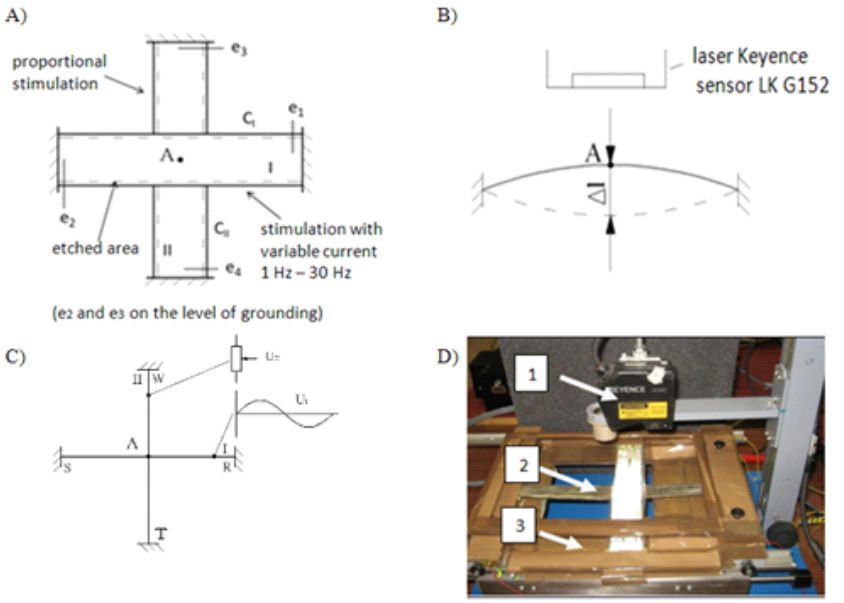

Fig. 2 The idea of two mechanically and electrically coupled *DEAP* membranes system: A) Mechanical system's scheme, B) Central point deflection measuring method, C) Scheme of the perpendicular membranes stimulation method, D) Stand view: 1 – laser sensor, 2 – tested *DEAP* membranes, 3 – laser measuring head's support stand.

One of the PolyPower membranes was activated with the sinusoidal voltage of programmable amplitude (500÷3000 V) and frequency (1÷30 Hz). As the consequence of this kind of stimulation, elongation of the membrane "I" and reduction of the prestress were observed. The only limitation of the membrane "I" relaxation was the perpendicular membrane "II" that was not stimulated with the alternating current but with the direct current of a programmable value. This kind of voltage on the membrane "II" had major impact on the self stretching of the membrane "I" because of the fact that membrane "II" worked as a damping system for the structure "I" in the non-potential conditions (without any extra electric field). On the other hand, when damping was at its highest value, the "II" membrane was allowing undamped cycle of stretching membrane "I", while having the maximal voltage on the *DEAP* "II".

The fig. 3 presents curves representing changes of the cyclic stimulation of the PolyPower "I" which was in the electrical and mechanical feedback with PolyPower

"II" for the frequency of 8 Hz. For these parameters, mechanical resonance of the investigated *DEAP* membrane set was observed. It was noticed as well that for the membrane "II" under the influence of voltage a cross effect characteristic with mechano-electrical features can be obtained. Because of the non-linear characteristic of the *DEAP* elastomeric membrane stretching process under the impact of a given voltage and gravity force, a lack of symmetry was visible in the obtained mechanical response. Determined loops change their shapes while the voltage value increases. Furthermore, increasing the voltage value delivered to the "II" membrane caused the enhancement of the possible deflection range of the tested system.

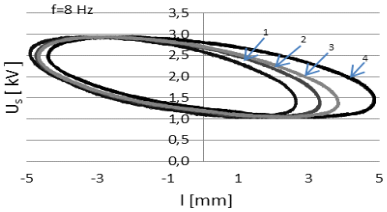

Fig. 3 Results of the damping level changes for the self-expanding membrane "I" due to the stimulation of the membrane "II" with certain DC voltage values: 1 – 0 V, 2 – 800 V, 3 – 1600 V, 4 – 2400 V

4 Bio-inspired Tail Based on PolyPower

The next area of the *DEAP* application was the 3-segments analogue model, controlled with a dedicated adaptronic system based on the mammal's vertebral column. Both, the vertebral column and its model, are based on the construction of rigid (vertebral body) and flexible (intervertebral disc and ligaments) parts. Because of that reason many different parts were used for the model's construction, such as spherical parts, electroactive *DEAP* polymer and others, responsible mainly for maintaining an upright base position of the model. The important element, that was joining all of the segments, was the PolyPower material. It also allowed well-controlled movement of the construction.

In the fig. 4A the real model is presented together with its visualization. Spherical elements represent the work of vertebral bodies, while the PolyPower simulates tendons' work. Moreover, inspired by the anatomical construction of the mammals' vertebral column model was designed taking into account a specific and complicated joining – intervertebral discs and vertebral endplates. Thanks to a special bushing, placed between the segments' borders, it can change its position easily. What is more, the whole structure was strengthened by elastic fibres which help maintaining the joint in a programmed position and preventing coming out of a central part during movement. Using the endplates and their movement kinematics helped in the smooth connection between particular analogue parts (Fig. 4A).

The 8 PolyPower actuators (280x30 mm) were prepared in this way (Fig. 4B). What is more, each of them was folded in two and secured by a thin non-conducting foil. In this way, the small packets were obtained what allowed the increase of the

processing efficiency. Before placing them on the spherical elements, each of them was pre-stretched by testing weights in order to eliminate deformations (local corrugations) that could cause damages to the *DEAP* bundles [4].

Electroactive elastomer works as the ligaments and allows smooth construction movements without causing any damage to itself. Moreover, thanks to the elastomer usage, other actuators are not the only ones carrying the whole construction mass. For example, to realize the process of leaning out the construction in one direction, one of the PolyPower packets stretches under the influence of the high-voltage, while the one on the other side of analogue shrinks which allows the well-controlled movement of the construction.

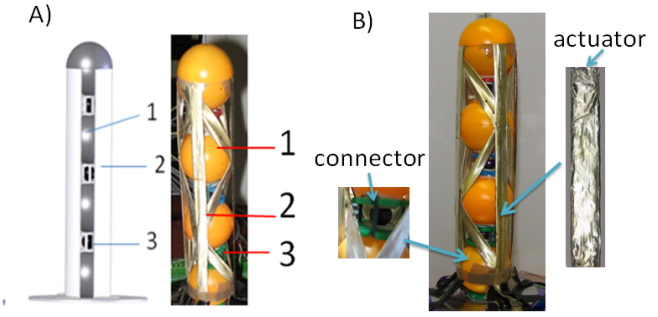

Fig. 4 A) Model's visualization in the CAD system, B) Real model; 1 – trunk, 2 – electroactive polymer, 3 – connector

Set of the 8 previously prepared actuators is the system with 6 DOFs (degrees of freedom) that allowed independent control of each of and that is why the model needed also slope and rotation registration in order to provide analysis of the whole system position. In the fig. 5A, different phases of the analogue's side-to-side movement were shown.

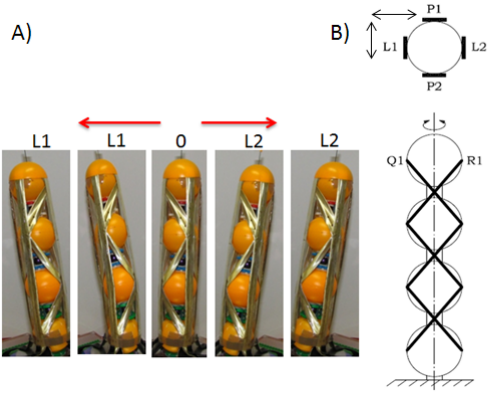

DIRECTION	L1	L2	P1	P2	Q1	R1
➡	10°	10°	0°	0°	0°	0°
⬅	10°	10°	0°	0°	0°	0°
⬇	0°	0°	10°	10°	0°	0°
⬆	0°	0°	10°	10°	0°	0°
↺	0°	0°	0°	0°	5°	5°
↻	0°	0°	0°	0°	5°	5°

Fig. 5 A) Succeeding side-to-side movement's phases of the 3-segments adaptronic analogue of mammal's vertebrae [°], B) Adaptronic analogue movements' visualization including directions and rotations [°].

The adaptronic analogue's movement visualisation in four different directions (left – L, right – R, forward and backward) and turns (left and right) is shown in the fig. 7A. The highest displacement values were obtained for L1, L2, R1 and R2 with a maximum of 10°. Displacement values for both rotations (Q1 and R1) were half as big (Fig. 5B).

Thanks to the microcontroller circuit, it was possible to control the movement of each part of the construction. Analog signal recorded by the microcontroller was transmitted to the high voltage converter. Moreover, it was supplied with a generator equipped with a high voltage transformer circuit and a rectifier that all together guaranteed stable voltage amplitude needed for the *DEAP* stimulation. In the Fig. 6 electrical analogue's controlling circuits schemes were presented.

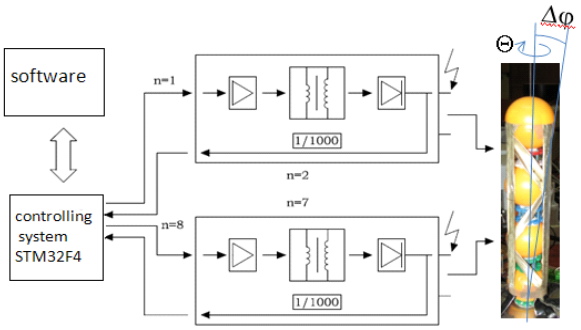

Fig. 6 Scheme of an electronic 3-segments adaptronic analogue of mammal's vertebrae control system

Each of the 8 actuators was independently controlled by the voltage of maximum 2,5 kV because exceeding this exact value caused local breakdowns and "burning" of the electrode-Polypower connection. Taking into account that the analogue can be controlled by the external stimulation such as vibrations and tilts of the model, it was necessary to provide a real-time controlling system. It was realized with the usage of ST Microelectronics Cortex M4 microprocessor system equipped with the SMT32F4-168MHz circuit. Computer software was used only for diagnostics and archivization.

5 Conclusions

The conclusions should summarize the essence of the paper, state the advantages compared to other methods, etc.

During the simulation process it was proven that there is a possibility of using *DEAP* for the bio-inspired constructions. Other important advantage of the method was the possibility of direct actuator control for the whole 3-segment construction. The designed software was a basis of the *DEAP* use for model controlling by the high voltage and dedicated microcontroller system.

Moreover, the constructed analogue allowed determination of the Polypore's properties as an actuator. The optimum preparation method of the *DEAP* elastomer was also described together with the range of possible steering voltage amplitudes. Besides, implementing moveable endplates appeared to be crucial step in the *DEAP*-based model designing.

In the base position, the built analogue is maintaining an upward position. The movement range of particular segments however, still needs additional focus so that much greater angular displacement values can be obtained.

In the future, each segment will be provided with the adequate MEMS sensor. It will allow precise positioning of a specific analogue's part with a focus on the powering method.

References

[1] Bar-Cohen, J., Sherrit, S., Lih, S.: Characterization of the electromechanical properties of EAP materials, Smart Structures and Materials (2001)
[2] Carpi, F., Chiarelli, P., Mazzoldi, A., De Rossi, D.: Electromechanical characterization of dielectric elastomer planar actuators, Sensors and Actuators (2003)
[3] Kaleta, J., Królewicz, M., Niemiec, K., Wiewiórski, P.: Cross effects in high voltage polymer membranes with a given texture. In: 7th International Symposium on Mechanics of Materials and Structures (2013) (in Polish)
[4] Kaleta, J., Kot, K., Niemiec, K., Wiewiorski, P.: Utilization of electroactive polymers actuators in a construction of 3-segments adaptronic analogue of mammal's vertebrae unit. In: 7th International Symposium on Mechanics of Materials and Structures (2013) (in Polish)
[5] Kim, K.J., Tadokoro, S.: Electroactive Polymers for Robotic Applications: Artificial Muscles and Sensors Springer-Verlag, London Limited (2007)
[6] Otake, M.: Electroactive Polymer Gel Robots: Modelling and Control of Artificial Muscles (2010)
[7] Danfoss (July 2012), `http://www.polypower.com/`

Transport Duty Cycle Simulation of Electro-hydro-mechanical Drive Unit for Mixing Drum

P. Krišš ák[1], J. Jakubovič[1], and P. Zavadinka[2]

[1] Sauer-Danfoss a.s., Kukučínova 2148, 017 01 Považská Bystrica, Slovak Republic
[2] Institute of Solid Mechanics, Mechatronics and Biomechanics Faculty of Mechanical Engineering, Brno University of Technology, Technicka 2896/2, 616 69 Brno, Czech Republic

Abstract. Presented paper related to a short description and simulation result of chosen parameter (drum speed) of drive unit for a mixing drum. The drive unit is disposed on a motor vehicle. Compared with prior art, the new system can exhibit further improvement to the efficiency of drive system of the mixing drum and truck mixer. The intention is to avoid unnecessary exhaust gas and noise emissions in transport duty cycle.

1 Introduction

Motor vehicles equipped for mixing and transporting concrete to building sites have been known for a long time. They have a rotary mixing drum disposed on a motor vehicle chassis and with large volume, rotation of which is usually effected by a hydraulic motor via a gearbox (see Fig. 1). The hydraulic motor is fed by a hydraulic displacement pump, which in turn is coupled to drive engine of the motor vehicle and is driven by mentioned pump [12]. During the transport of concrete to building sites, the mixing drum is generally being rotated at about 0.5 to 5 rpm, while during mixing and discharging it is being operated at substantially higher rotational speeds up to 15 rpm.

In such concrete mixing and transporting vehicles the problem appears, when drive engine of the motor vehicle is at standstill, a diesel engine in most cases and rotation of the mixing drum also necessarily comes to a standstill. This is disadvantageous when the drum is filled up; this can lead to de-mixing or to premature setting of the concrete, and that is undesired. Therefore, when the mixing drum is filled up, particularly during transport of concrete to the building site, mixing drum should rotate continuously. This results in the problem that, when the truck mixer is at a standstill, for example in traffic jams or during relatively long waiting times until discharge, the running drive engine of the truck mixer, in most cases a diesel engine, involuntarily causes exhaust gas and noise emissions that are damaging health, environmentally damaging and disruptive, particularly in enclosed spaces.

T. Březina and R. Jabloński (eds.), *Mechatronics 2013*,
DOI: 10.1007/978-3-319-02294-9_30,

The disadvantage of offered solutions described in known state of art [9], [11], [13] is that separate drive motor for the displacement pump has to be designed to be powerful to be capable to drive mixing drum even at the highest required rotational speed. A problem that occurs specifically in driving - the displacement pump of a hydraulic drive of mixing drum by the drive engine of the mixer vehicle also resides in fact that displacement pump connected to a power take-off of the drive engine is subjected to all the changes in rotational speed of drive engine. As a result of the automated gearbox and the abrupt accelerations and retardations of the latter, uniform loading of hydraulic drive cannot be guaranteed. In addition, power take-offs of the drive engine are loaded non-uniformly, which can disrupt gear changing operations. In addition, when the hydraulic drive is operated in the partial load range at about 5 kW, the efficiency is very low.

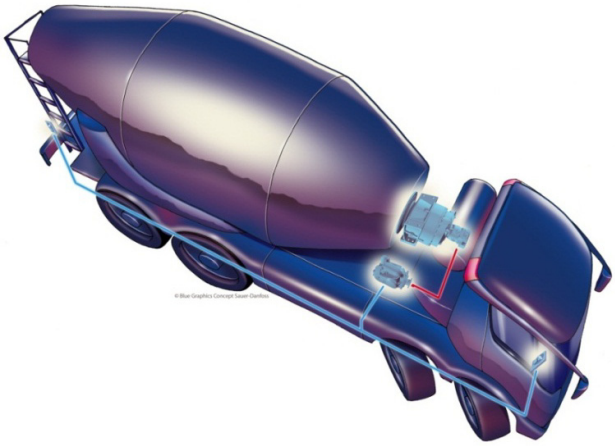

Fig. 1 Illustration of mixer vehicle example [12]

2 Description of Electro-hydro-mechanical Drive Unit

Drive unit for a mixing drum is disposed on a motor vehicle. Hydraulic drive comprising a displacement pump and a hydraulic motor are used to drive the mixing drum. The variable displacement pump is designed to convert a mechanical input power into hydraulic power. The input shaft, driven by the engine PTO, turns the pump cylinder block, which contains a ring of pistons. The pistons run against a tilted plate called swash plate. This causes those pistons to compress the hydraulic fluid, which imparts the input energy into hydraulic fluid. The high-pressure fluid is then ported out to provide the hydraulic pressure and flow to the fixed displacement motor. The swash plate angle can be varied by the actuating piston via the electrical proportional control valves depending on the current value

which is generated by the controller. The fixed displacement motor is designed to convert an input of hydraulic power into a mechanical torque and speed output power. The high-pressure hydraulic fluid enters through the input port. The fluid pressure builds behind the piston causing them to move down the swash plate. As the pistons returns up the swash plate again, the fluid is allowed to exit through the exit port. The spinning pistons are housed in a cylinder transit mixer. It is assembled to the mixer frame of base supports, which also transfer the torque force of the drive. The dynamic swivel angle of the output/drum flange will be compensating for the deflection of the truck frame mainly under off-road conditions.

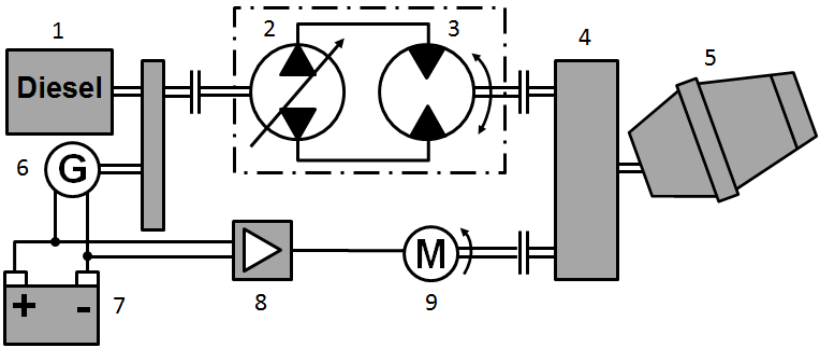

Fig. 2 The main components of a drive unit in a schematic illustration 1-Diesel engine, 2-Hydraulic pump, 3-Hydraulic motor, 4-Gearbox, 5-Drum, 6-Alternator, 7-Electric battery, 8-Inverter, 9-Electric motor

It is an aim to provide a drive unit for a mixing drum that is disposed on a motor vehicle which, as compared with the prior art, exhibits a further improvement to the efficiency of the drive system of the mixing drum and of the truck mixer, the intention is to avoid unnecessary exhaust gas and noise emissions. The drive engine, particularly the internal combustion engine of the truck mixer, should be capable of being shut down while the rotation of mixing drum is maintained. The drive system should be further capable of implementation inexpensively with little effort and robust and reliable in its execution. This object is achieved as a result of the fact that in addition to driving the mixing drum via a hydraulic drive train [11], the electric motor is or can be permanently connected to the truck mixer gearbox (see Fig. 2). The low-power electric motor is used to drive the mixing drum at low rotational speed during the transport journey of mixed concrete to building site, while the hydraulic drive drives the mixing drum at high rotational speed during loading, mixing and discharging. This way can be mixing drum driven solely by the electric motor with a relatively low power output, if is compared with the hydraulic drive power output.

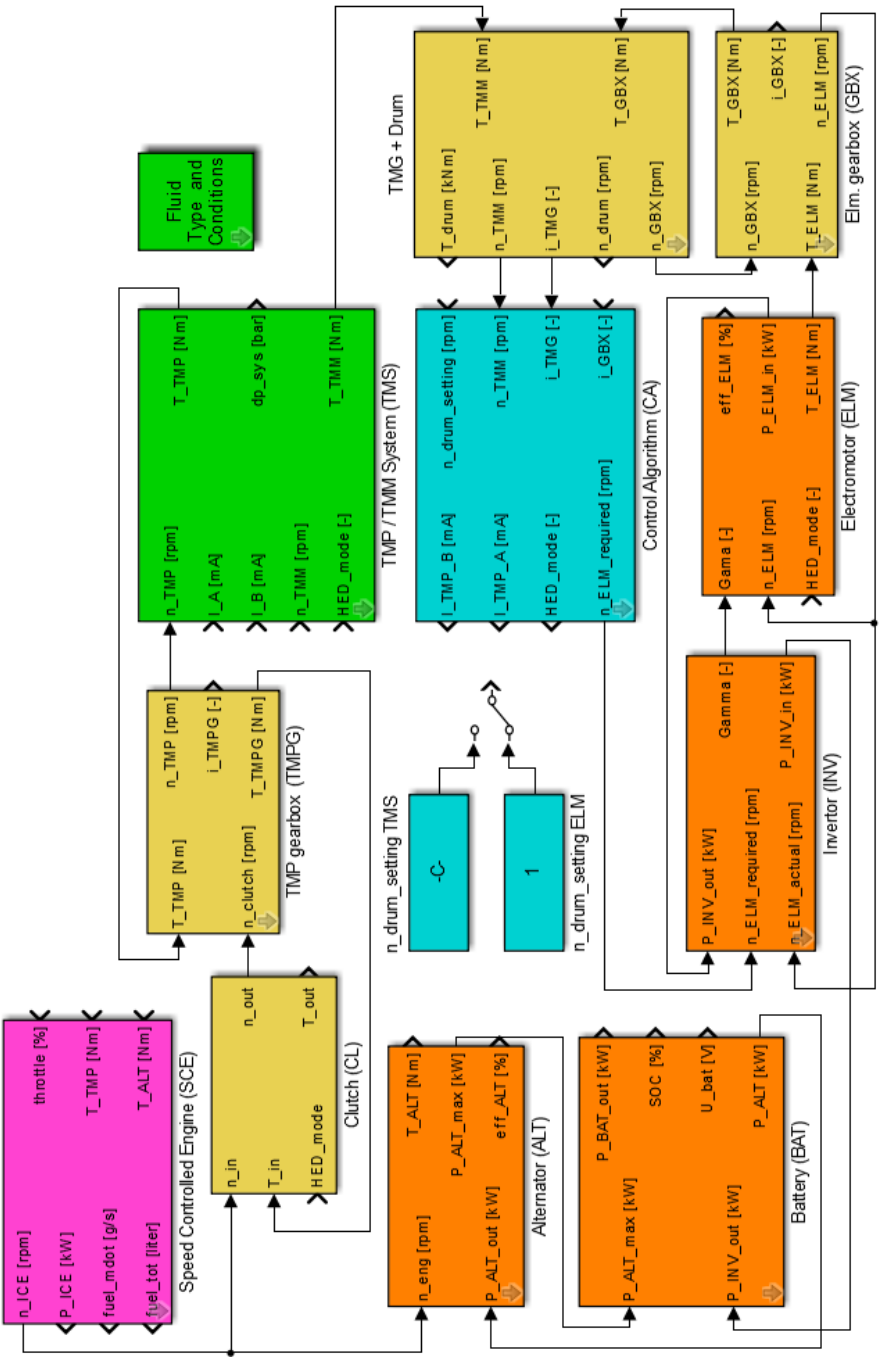

Fig. 3 The main structure of simulation model (extensive simplified)

3 Simulation Model

Drive line system consists of independent hydraulic and electric drive line. The main goal is to find parameters of given drive system configuration as output performance and final efficiency in transport and downtime working conditions.

Simulation model (see Fig. 3) is built as modular with possibility to change input parameters and monitoring operational parameters. Hydraulic drive line is assembled from subsystems Diesel engine - Hydraulic pump – Hydraulic motor - Gearbox - Drum. Electric drive line is assembled from subsystems Diesel engine - Alternator - Electric battery - Inverter - Electric motor - Gearbox - Drum. Used subsystems are mostly part of company simulation library. The mathematical background for model is described in [2], [4], [5], [8], [9]. From understandable commercial reason they cannot be described in more detail. Some parts of the simulation model are simplified in order to reduce number of states and thus increasing simulation speed [3], [14], [15]. Measurement data were used after testing of hydraulic and electric drive line as a part of input data for simulation model.

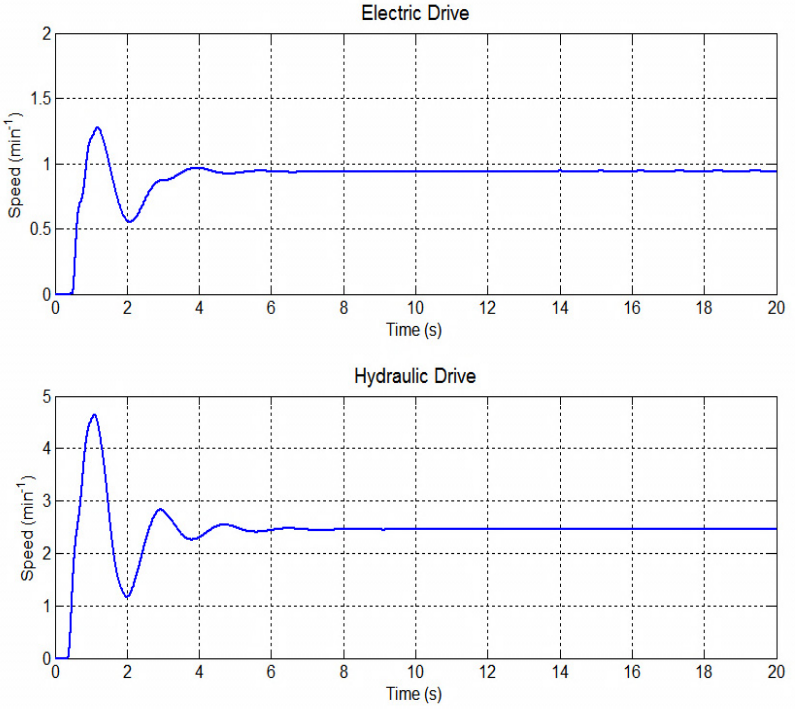

Fig. 4 Simulation results related to speed of drum driven by Electric and Hydraulic drive

4 Simulation Results of Transport Duty Cycle

Simulation of transport duty cycle should provide information in regards to the simulation of drive system for transit mixer application. Simulation model was verified with different testing modes of working conditions [1], [5], [6], [7], [15].

Fig. 4 shows chosen speed drum results compared from simulation and real test. Transit mixer in simulation model was driven in straight direction on flat road surface with the same of condition of drive for mechanic, hydraulic and electric drive line. Drum speed was set up for 8, 2.5, 1.2, 1 and 0.9 rpm. Minimum drum speed of real testing machine was for example adjusted at 1 rpm at low idle speed even through that the driver was adjusting (subjectively) the drum speed from 1 to 1.5 rpm at low idle speed. Based on this adjustment the average drum speed was around 2 rpm.

5 Conclusions

The one result of whole project is the new hybrid system with two independent drive units for the transit mixer. This means in background units design, mathematical description of behavior, building simulation model, design of control algorithm, testing solution in the field and solution optimization. In this paper are partly presented some basic information and chosen simulation results.

The hydraulic and electric drive lines were simulated in different working conditions. The simulation results were compared with measurements. The comparison shows a 5% difference in worst case in efficiency between simulation and prototype measurements and 3% difference between simulations and prototype measurements of speed. The electric drive line is more stable in drum speed as hydraulic one. All performed simulations show acceptable results, however in some cases (start, gear shift) it is necessary to consider physical and mathematical complexity of model's structure. During the simulation is important to know the relationships and principles behind the user interface of these blocks, otherwise the simulation results can be misinterpreted.

Acknowledgement. This paper has been supported by research project FSI-S-11-15 "Design, testing and implementation of control algorithms with use of nonlinear models of mechatronics systems".

References

[1] Carter, D.E., Alleyne, A.G.: Earthmoving vehicle powertrain controller design and evaluation. In: Proceedings of the 2004 American Control Conference, June 30-July 2, vol. 5, pp. 4455–4460 (2004)

[2] Fitch, C.E., Hong, T.I.: Hydraulic System Modeling and Simulation. Bardyne, Stillwater (2001) ISBN 0-9705922-5-6

[3] Grepl, R., Vejlupek, J., Lambersky, V., Jasansky, M., Vadlejch, F., Coupek, P.: Development of 4WS/4WD Experimental Vehicle: platform for research and education in mechatronics. In: IEEE International Conference on Mechatronics, ICM 2011, Istanbul, April 13-15 (2011)
[4] Ivantysyn, J., Ivantysynova, M.: Hydrostatic Pumps and Motors, Principles, Design, Performance, Modeling, Analysis, Control and Testing, Academia Books International, New Delhi (2001) ISBN -81-85522-16-2
[5] Kędzia, K.: Wyznacznik zmienności cyklu obciążenia jako kryterium stosowania wielośródłowego hydrostatycznego układu napędowego. Napędy i Sterowanie 12(1), 30–36 (2010)
[6] Kędzia, K., Chrostowski, H.: Self-locking phenomenon in hydrostatic motor working as reversible unit in multisources hydrostatic driving system. Hydraulika a Pneumatika, Žilina 8(3/4), 10–12 (2006) ISSN 1335-5171
[7] Kiencke, U., Nielsen, L.: Automotive Control Systems for Engine, Driveline and Vehicle, 2nd edn., vol. XVIII, p. 512 (2005) ISBN 978-3-540-23139-4
[8] Koreis, J.: Přenosové systémy dopravních prostředků, Univerzita Pardubice, p. 136 (1999) ISBN 80-7194-204-9
[9] Kučík, P., Strážovec, I., Kriššák, P.: Hydraulický prenos energie. Mobilné stroje, p. 384. EDIS, vydavateľstvo ŽU (2000) ISBN 80-7100-725-0
[10] Patent application DE 35 39 550 A1
[11] Patent application DE 10 2008 017 350 A1.
[12] Sauer-Danfoss: Series TM Transit Mixer Drive System, Catalogue 520L0482, Rev. BC (December 2010)
[13] Utility model DE 20 2009 001416 U1
[14] Zavadinka, P., Kriššák, P.: Modeling and simulation of mobile working machine powertrain. In: Technical Computing Prague 2009, Praha, Czech Republic, November 19, p. 118 (2009) ISBN 978-80-7080-733-0
[15] Zavadinka, P., Kriššák, P.: Simulation of vehicle working conditions with hydrostatic pump and motor control algorithm. JAMRIS, 40–46 (March 2012) ISSN 1897-8649, eISSN 2080-2145

Investigation on the Jump Phenomenon of Linear Compressor

H.M. Zou[1], M.S. Tang[1,2], Sh.Q. Shao[1], Ch.Q. Tian[1], and Y.Y. Yan[3]

[1] Technical Institute of Physics and Chemistry, Chinese Academy of Sciences, Beijing 100190, P.R. China
zouhuiming@mail.ipc.ac.cn
[2] University of Chinese Academy of Sciences, Beijing 100190, P.R. China
[3] Energy and Sustainability Research Division, Faculty of Engineering, University of Nottingham, Nottingham NG7 2RD, U.K.

Abstract. According to the experiments on the linear compressor operating in the refrigeration system, the occurrence conditions and regularity of jump phenomenon is investigated on different working conditions. When jump phenomenon happens, the current, input power, as well as piston stroke jumps upward abruptly. Under the same discharge pressure condition, the higher the power frequency is, the earlier the jump phenomenon will happen. When the power frequency decreases under a certain value, the jump phenomenon will disappear. The lower the discharge pressure is, the wider the power frequency range of jump phenomenon occurrence will be. Through the phase angle analysis, it is discovered that the jump phenomenon occurs not only on the status of mechanical resonance but also on the status of electromagnetic oscillation.

1 Introduction

Linear compressor has great application prospect due to its compact structure and high efficiency. However, the related research results show that because of its free piston structure, especially because of the existence of some nonlinear factors, such as gas force, motor coefficient et al., the performance of linear compressor is variable and sensitive with the working conditions. Minas [1] studied the non-linear dynamics of oil-less linear compressor by establishing a mathematical model and showed that the most efficient frequency of operation was determined for the piston stroke as well as the mass flow rates. Unger [2] developed and tested a linear compressor prototype under both freezer and fresh food conditions and enhanced performance and efficiency were observed compared to conventional compressor. Lamantia et al. [3] validated that linear compressor had high sensitivity to the driving frequency. Kim et al. [4] studied the coefficient of performance (COP) sensitivity of the linear compressor to the operating frequency in a refrigeration system with R600a refrigerant and it were

T. Březina and R. Jabloński (eds.), *Mechatronics 2013*,
DOI: 10.1007/978-3-319-02294-9_31,

found to vary within 3% according to the operating frequency of the system ranging from 48.5 to 51.5 Hz. Kim et al. [5, 6] presented a self-capacity modulated linear compressor without stroke controller by the designing the electrical parameters based on the sensitive characteristics of linear compressor. Bradshaw et al. [7, 8] established a comprehensive model for a linear compressor and the sensitivity studies conducted showed that the linear compressor is highly sensitive to changes in the leakage gap between the piston and cylinder as well as the spring eccentricity.

Furthermore, for linear compressor, jump phenomenon usually appears under certain conditions and may cause strong noise and mechanical damage when the piston stroke increases abruptly and bumps against the discharge valve. Walt and Unger [10] observed that the piston amplitude oscillated when the values of piston mass and spring stiffness were unsuitable. Oh and Kim [11] studied that the input power supply and the cooling capacity were both shaken by the operation instability of the piston. Choe and Kim [12, 13] established a two-degree freedom dynamic model with simplified gas force by Fourier transform and analyzed the effect of piston mass on jump phenomenon by the dynamic model. The previous investigation of present authors [14] on the jump phenomenon of the dual-cylinder opposed linear compressor showed that when the intrinsic frequency got close to the power frequency, the jump phenomenon was apt to occur and would cause discharge pressure fluctuation. Nevertheless, because the working condition of linear compressor is variational and the jump phenomenon is subject to occur occasionally, especially because the existence of nonlinear factors makes the numerical analysis very difficult, the present research still cannot know well about its occurrence mechanism.

To make sure that linear compressor can operate reliably, it is necessary for the control system to predict jump phenomenon precisely before it really happens. The primary objective of this paper is to study the occurrence conditions and occurrence regularity of jump phenomenon on different working conditions. The results based on the refrigeration experiments can offer a helpful proposal for the linear compressor control strategy design as well as structure design, so that the control system can predict and avoid the jump phenomenon according to the basic measurement of electrical parameters and simple calculation regardless of the working conditions.

2 Experimental System and Procedure

Fig.1 shows the schematic diagram of a linear compressor. The linear motor drives the piston to reciprocate around a central position. The piston displacement is expressed by $x = X \sin \omega t$, where X is the piston stroke and ω is angular velocity.

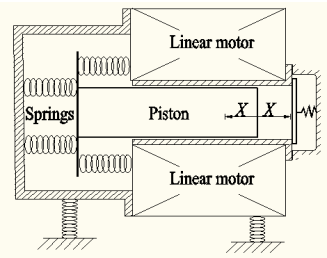

Fig. 1 Schematic diagram of a linear compressor

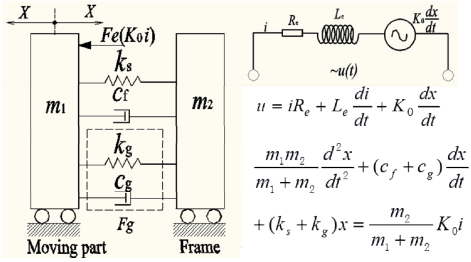

Fig. 2 Simplified theoretical model

Fig.2 shows simplified dynamic and electromagnetic models of linear compressor [2, 3]. In the dynamic model, m_1 is the moving part mass, m_2 is the frame mass, k_s is the stiffness coefficient of syntonic springs, c_f is the damping coefficient of friction, F_e is the electromagnetic force(expressed as $K_0 i$), and F_g is the gas force. The gas force can be linearized into equivalent stiffness k_g and equivalent damping cg by Fourier Transform [11]. In the electromagnetic model, u is the voltage (U is the effective voltage), i is the current (I is the effective current), K_0 is the electromagnetic force coefficient, R_e is the equivalent resistance and L_e is the equivalent inductance.

Piston stroke is an intuitional parameter to show the jump phenomenon as investigated by the previous research. However, in the actual application it is not practical to install a displacement sensor inside of the compressor shell for the sake of cost or space. The piston stroke is usually calculated based on electrical parameters equation. Thus measuring and analyzing the related electrical parameters directly is much more practical than analyzing the piston stroke calculated from the electrical parameters.

Fig.3 shows the vector diagrams of linear compressor according to the simplified theoretical model. The phase difference α between velocity dx/dt and current i, determined by the related parameters of elastic force, inertial force and damping force, represents the dynamic characteristics of linear compressor. The phase angle θ between voltage u and current i, determined by the voltage components of impendence, inductive reactance and induced electromotive force represents the electrical characteristics of the linear compressor.

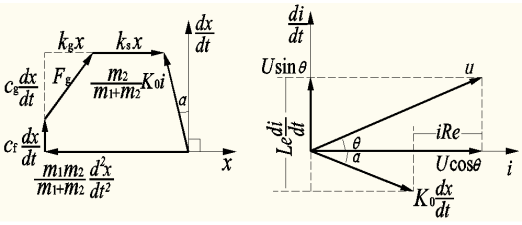

Fig. 3 Vector diagrams of the linear compressor

Fig. 4 Experimental devices diagram

Therefore in this paper the relationship between jump phenomenon and the phase angle α and θ are concerned and they can be calculated by measured voltage U, current I, angular frequency ω ($\omega=2\pi f$, where f is power frequency) and input power P_i:

$$\theta = \frac{180}{\pi} \arccos\left(\frac{P_i}{UI}\right) \tag{1}$$

$$\alpha = \frac{180}{\pi} \arctan\left(\frac{U \sin(\pi\theta/180) - \omega L_e I}{P_i / I - R_e I}\right) \tag{2}$$

Fig.4 shows the photo of the refrigeration experimental system with second refrigerant calorimeter according to the household refrigerator standard of ASHRAE23 for linear compressor. The constant temperature cooling water is supplied to the condenser and its temperature can be adjusted to change the discharge pressure of linear compressor. The electric heater installed in the calorimeter simulates the cooling load. The pressure gauges are installed in the suction pipe and discharge pipe. The stabilization power device has the function of adjusting the frequency f and effective voltage U independently and measuring the electricity parameters accordingly. The data acquisition connected to the computer collects the measurement parameters including discharge pressure, voltage, current and input power.

3 Experimental Results and Analysis

3.1 Features of Jump Phenomenon

When linear compressor is started under a certain working condition, jump phenomenon is searched by adjusting the voltage and frequency. Fig.5 shows the process of voltage adjustment with the jump phenomenon on 60Hz. The suction pressure is 0.06MPa and the discharge pressure is 0.4MPa. The current and input power jumped upward abruptly on a voltage value during the period of voltage increase and jumped downward abruptly on a lower voltage value during the period of voltage decrease. There is a hysteresis loop between the upward jump and downward jump.

Fig.5 (a) shows the current curves changed with the voltage. During the period of increasing voltage, the current decreased continuously till to an inflexion firstly, jumped upward abruptly from 1.12A to 1.446A at 100.2V shortly after the inflexion, and continued to decrease with the voltage increasing. During the period of decreasing voltage, the current increased continuously, jumped downward suddenly from 1.783A to 1.192A at 81.8V, and then continued to increase with the decreasing of voltage.

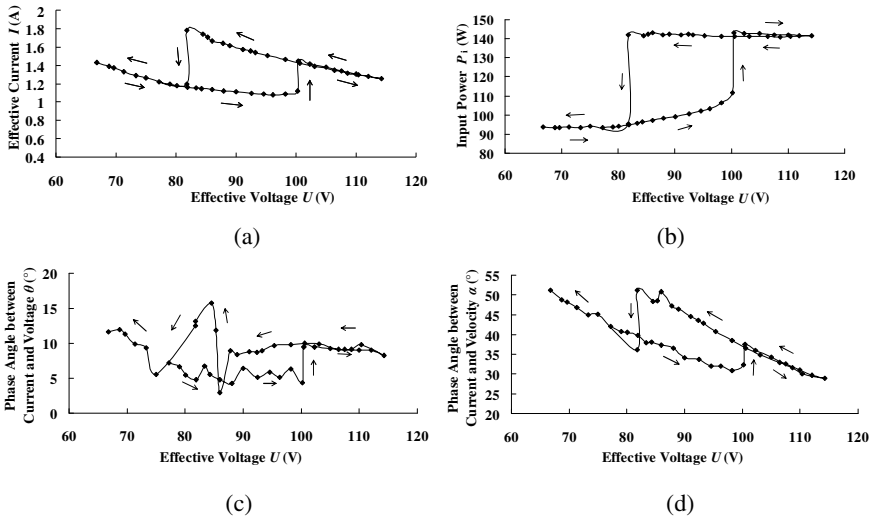

Fig. 5 Electrical parameters changed with the voltages: (a) current; (b) input power; (c) phase angle θ; (d) phase angle α

Fig.5 (b) shows the input power curves changed with the voltage. During the period of increasing voltage, the input power increased stably by jumping upward from 111.9W to 143.2W at 100.2V and then almost remained unchanged with the voltage increase. During the period of decreasing voltage, the input power changed very little at first till to jump downward suddenly from 140W to 98.2W at 81.8V and then continued to decrease with the voltage.

Fig.5 (c) shows the phase angle θ between the current and voltage changed with the voltage. During the period of increasing voltage, the phase angle θ fluctuated between 4° and 7° firstly before jumped upward from 4.4° to 9.5° and after then remained small change. During the period of decreasing voltage, the phase angle θ also changed very little firstly, then fluctuated acutely for a period of time, and finally continued to increase with the decreasing of voltage.

Fig.5 (d) shows the phase angle α between the current and velocity changed with the voltage. During the period of increasing voltage, the phase angle α decreased before jumped upward from 32.3° to 37.4°, after then continued to decrease with the increasing of voltage. During the period of decreasing voltage, the phase angle α increased continuously till to jump downward suddenly from 51.3° to 36.1°, and finally continued to increase with the decreasing of voltage.

It is worthy of note that under this working condition, the phase angle θ between the current and voltage is near 0°, while the phase angle α between the current and velocity is much greater than 0° when jump phenomenon occurs. This means that jump phenomenon happens under this condition is not for the reason of mechanical resonance as explained in the previous research.

3.2 *Occurrence Conditions and Regularity of Jump Phenomenon*

The experiment was carried out to seek jump phenomenon by changing the power voltage or frequency under different discharge pressure for discharge pressure is the major factor presenting the effect of working conditions. Fig.6 shows the voltage and piston stroke when the jump phenomena occurred under different discharge pressure on 60Hz. The voltage for upward jump was higher than that of downward jump under the same discharge pressure. Both the voltage and piston stroke increased with the increasing of discharge pressure.

Fig.7 shows the voltage when the jump phenomena occurred on different power frequency. Both the upward voltage and downward voltage decreased with the increasing of power frequency. The upward voltage was higher than the downward voltage over the same power frequency. The jump phenomenon occurred when the power frequency was no less than 58Hz at 0.45MPa and no less than 60Hz at 0.6MPa. When the power frequency was adjusted under the certain value, the jump phenomenon disappeared.

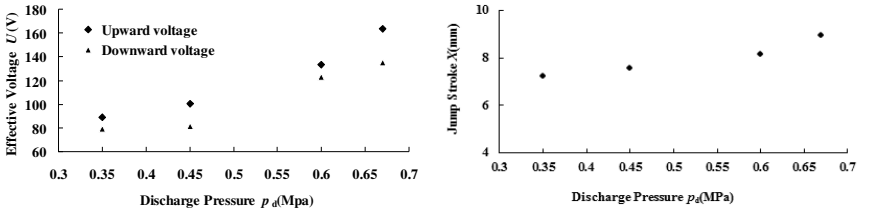

(a) (b)

Fig. 6 Voltage and piston stroke vs. different discharge pressure: 60Hz

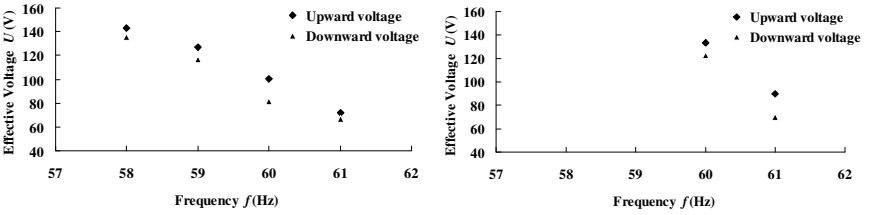

(a) (b)

Fig. 7 Voltage vs. different power frequency: (a) discharge pressure 0.45MPa; (b) discharge pressure 0.6MPa

Fig.8 shows the piston stroke before jump and after shrink on different frequency. These piston stroke values are calculated by equation (1). Under the same discharge pressure condition, the piston stroke values before jump and after shrink both decrease with the increasing of frequency. Under the same frequency condition, the jump point of piston stroke on the 0.6MPa discharge pressure is larger than that on 0.45MPa discharger pressure.

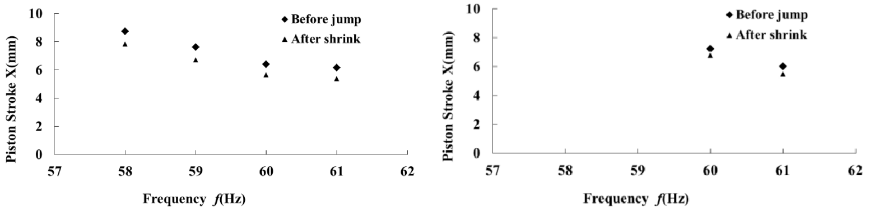

Fig. 8 Piston stroke vs. different power frequency: (a) discharge pressure 0.45MPa; (b) discharge pressure 0.6MPa

From the above experimental results, the occurrence conditions of jump phenomenon depend on the discharge pressure and power frequency. Under the same discharge pressure condition, the higher the power frequency is, the earlier the jump phenomenon will happen. The lower the discharge pressure is, the wider the power frequency range of jump phenomenon occurrence will be.

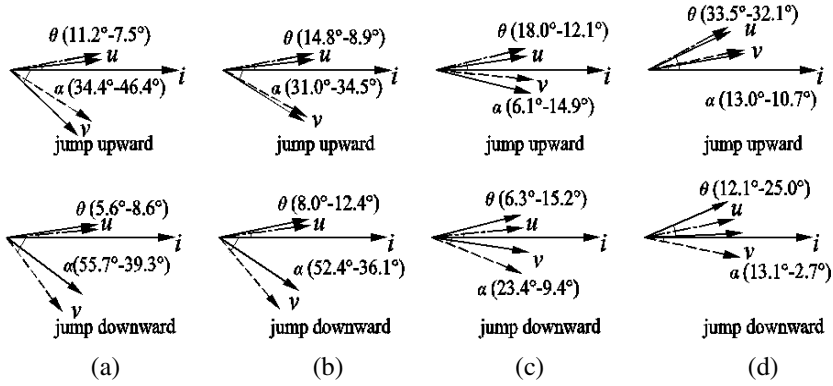

Fig. 9 Change of phase angle of α and θ on different discharge pressure:(a)0.35MPa; (b)0.45MPa;(c)0.6MPa;(d)0.67MPa

According to equations (1) and (2), the phase angle θ and α can be calculated when the jump phenomena occur. Fig.9 shows the change of phase angle θ and α from the dotted line to the solid line when the jump phenomena occurred under different discharge pressure. The phase angle θ increased from the degree near to 0° away with the increasing of discharge pressure. Different from the phase angle θ, the phase angle α decreased from the higher degree to 0° firstly and then increased to the reverse direction with the increasing of discharge pressure. When the discharge pressure was set on 0.35Mpa and 0.45MPa, the phase angle θ was near to 0°. When the discharge pressure was set on 0.6Mpa and 0.67Mpa, the phase angle α was near to 0°.

Fig.10 shows the change of phase angle θ and α from the dotted line to the solid line when the jump phenomena occurred on different power frequency. The phase angle θ and α both increased with the increase of power frequency. The phase angle α was near to 0° on 58Hz, 59Hz, 60Hz and 61Hz. The phase angle θ was near to 0° on 58Hz and much more than 0° on the higher power frequency.

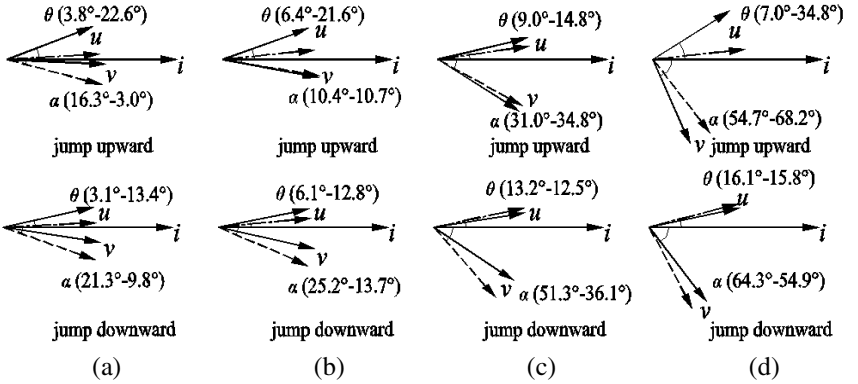

Fig. 10 Change of phase angle of α and θ on different power frequency:(a)58Hz; (b)59Hz; (c)60Hz;(d)61Hz

From the analysis on the phase angle, it is discovered that the jump phenomenon occurs when the phase angle α is near to 0°, or when the phase angle θ is near to 0°. When the phase angle α is near to 0°, the dynamic system of the linear compressor will be on the status of mechanical resonance and when the phase angle θ is near to 0°, the electrical system of the linear compressor will be on the status of electromagnetic oscillation. Therefore the jump phenomenon can be avoided based on this situation.

3.3 Prevention and Control Measures

Base on the above investigation results, jump phenomenon on the rated working conditions can be avoided in the stage of structure design. According to the above theoretical model of linear compressor, the relation between effective current I and displacement X can be expressed as:

$$I = \frac{\sqrt{2}X(m_1+m_2)}{2K_0 m_2}\sqrt{(\frac{m_1 m_2}{m_1+m_2}\omega^2 - k_g - k_s)^2 + (c_f + c_g)^2\omega^2} \tag{3}$$

$$\sin\alpha = (\frac{m_1 m_2}{m_1+m_2}\omega^2 - k_g - k_s)/\sqrt{(\frac{m_1 m_2}{m_1+m_2}\omega^2 - k_g - k_s)^2 + (c_f + c_g)^2\omega^2} \tag{4}$$

According to fig.3, when θ=0, $L_e I = \frac{\sqrt{2}}{2}K_0 X \sin\alpha$ (5)

From equations (3), (4) and (5), get the equation as follows:

$$L_e \frac{(m_1+m_2)}{m_2}\left[(\frac{m_1 m_2}{m_1+m_2}\omega^2 - k_g - k_s)^2 + (c_f + c_g)^2\omega^2\right] = K_0{}^2(\frac{m_1 m_2}{m_1+m_2}\omega^2 - k_g - k_s) \quad (6)$$

When $\alpha = 0$, $\frac{m_1 m_2}{m_1+m_2}\omega^2 = k_g + k_s$ (7)

Therefore, equations (6) and (7) can be used to avoid the jump phenomenon by configuring the relevant parameters in the period of structure design or adjusting the power frequency in the process of operating control.

Moreover, to make the linear compressor operate stably when the working conditions change with the circumstance factors, the control system can help to avoid jump phenomenon by adjusting the power voltage and frequency promptly based on the above investigation results. When the measured phase angle between current and voltage or that between current and velocity is close to 0°, the controller should decrease the power frequency little by little to make the phase angle depart from the nearby regions of 0° and then adjust the voltage to make the piston stroke meet the operating demand, so that the jump phenomenon can be avoided.

4 Conclusions

Since jump phenomenon could shorten the working life of linear compressor, it should be avoided by the control system during the operation process. The experimental results herein show that the current and input power will jump upward or downward abruptly when the jump phenomenon occurs. During the period of voltage regulation, there is a hysteresis loop between the upward point and downward point in the graph.

Under the same discharge pressure condition, the higher the power frequency is, the earlier the jump phenomenon will happen. The lower the discharge pressure is, the wider the power frequency range of jump phenomenon occurrence will be.The jump phenomenon will occur either when the phase angle between current and velocity, or the phase angle between current and voltage is close to 0°. When the power frequency decreases to a certain value, the jump phenomenon will disappear.

Through detection and comparision of phase angle between voltage, current and velocity, jump phenomenon can be predicted timely. By adjusting the supply power parameters to make the phase angle depart from the nearby regions of 0°, jump phenomenon can be avoided effectively.

Acknowledgment. This work was supported by a grant from the Natural Science foundation of China (Grand No. 51105355) and State Scholarship Found.

References

[1] Minas, C.: Nonlinear Dynamics of an Oilless Linear Drive Reciprocating Compressor. Journal of Vibration and Acoustics, ASME 116(1), 79–84 (1994)
[2] Unger, R.: Development and Testing of a Linear Compressor Sized for the European Market. In: Proceedings of International Appliance Technology Conference at Purdue, Purdue University, pp. 41–49 (1999)
[3] Lamantia, M., Contarini, A., Giovanni, S.: Numerical and Experimental Analysis of A Linear Compressor. In: Proceedings of International compressor Engineering Conference at Purdue, Purdue University, pp. 554–561 (2002)
[4] Kim, H., Roh, C., Kim, J., et al.: An Experimental and Numerical Study on Dynamic Characteristic of Linear Compressor in Refrigeration System. International Journal of Refrigeration 32, 1536–1542 (2009)
[5] Kim, J., Roh, C.G., et al.: An Experimental and Numerical Study on an Inherent Capacity Modulated Linear Compressor for Home Refrigeratiors. International Journal of Refrigeration 34, 1415–1423 (2011)
[6] Kim, J., Jeong, J.: Performance Characteristics of a Capacity Modulated Linear Compressor for Home Refrigerators. International Journal of Refrigeration 36, 776–785 (2013)
[7] Bradshaw, C.R., Groll, E.A., Garimella, S.V.: A Comprehensive Mode l of a Miniature-scale Linear Compressor for Electronics cooling. International Journal of Refrigeration 34, 63–73 (2011)
[8] Bradshaw, C.R., Groll, E.A., Garimella, S.V.: A Sensitivity Analysis of a Miniature-Scale Linear Compressor for Electronics Cooling. In: Proceedings of International Appliance Technology Conference at Purdue, Purdue University, p. 1113 (2012)
[9] Walt, N.R., Unger, R.: The Simulation and Design of a High Efficiency, Lubricant Free, Linear Compressor for a Domestic Refrigerator. In: Proceedings of International Appliance Technology Conference at Purdue, Purdue University, pp. 1–9 (1992)
[10] Oh, K.T., Kim, J.W.: Apparatus for Controlling Linear Compressor and Method Thereof. U.S. Patent (2001) 6289680B1
[11] Choe, G., Kim, K.: Analysis of Nonlinear Dynamics in a Linear Compressor. International Journal Series C of Japan Society of Mechanical Engineers 43(3), 545–552 (2000)
[12] Choe, G., Kim, K.: Theoretical and Experimental Analysis of Nonlinear Dynamics in a Linear Compressor. Journal of Vibration and Acoustics, ASME, 124 (2002)
[13] Zou, H., Zhang, L.: Experimental Envestigation and Performance Analysis of a Dual-cylinder Opposed Linear Compressor. Journal of Mechanical Science and Technology 25(8), 1–8 (2011)

Software Tool for Calibration of Hydraulic Models of Water-Supply Networks

J. Kovar[1] and J. Rucka[2]

[1] Brno University of Technology, Faculty of Mechanical Engineering, Technicka 2, 616 69, Brno, Czech Republic
kovar@fme.vutbr.cz
[2] Brno University of Technology, Faculty of Civil Engineering, Zizkova 17, Brno 602 00, The Czech Republic
rucka.j@fce.vutbr.cz

Abstract. Mathematical modeling and simulation techniques represent powerful tools for optimizing the operation of drinking water supply networks. The hydraulic model of the water supply network needs to be calibrated necessarily to provide reliable results. This article describes a very new software tool that is being developed to help water specialists to calibrate hydraulic models utilizing the hydraulic values measured on the water supply network in-situ. The measurement itself is realized by means of a specialized portable measuring device that enables continuous measurement of hydraulic values in the network. The technical tool for calibration of the network parameters is a newly developed software toolbox for application ADAM which is newly developed simulation software for hydraulic analysis of water supply networks.

1 Introduction

The mathematical model of water drinking water supply network, as a mechatronic system, is very complex system with many parameters [1], [2]. Even when the mathematical model of water supply system is based on manufacturing documentation, parameters of each modeled objects are often different from real object parameters. In order to find appropriate parameters, and thereby to obtain credible model of water supply network, it is appropriate to define correctly defined optimization problem [3], [4], [5], [6], [7]. Optimization process itself can be divided into three adjacent parts. Let's assume that we have model of water supply network. The first step is to measure significant physical properties of the transmitted medium in water supply network (pressure and flow). Second step is to link model o to measured data and finally the optimization technique to find appropriate parameters of models object can be utilized (grid calibration and detailed calibration).

T. Březina and R. Jabloński (eds.), *Mechatronics 2013*,
DOI: 10.1007/978-3-319-02294-9_32,

Basic principles of the hydraulic model calibration

The following text describes the process of modification of hydraulic model parameters so that the results of its simulations for different network scenarios correspond to the real in-situ measured hydraulic values – flow and pressure. It is important to highlight that the below described methodology distinguish between two different levels of calibration of the hydraulic model. The difference is as follows:

Grid calibration process is performed for routine daily regimes of the water-supply network that are defined with its characteristic water demands that forms the network flows in particular day-time periods. Neither extra demands exceeding the statistically evaluated network flows nor changes in network topology are simulated in the model. Typically the hydraulic model of a whole water-supply pressure zone is calibrated at the same time. Mainly fatal errors in the model are identified during the grid calibration, e.g. improper water tank elevation or some significant mistakes in the network topology, e.g. missing pipes, by mistake closed pipes, different position of pressure zone boundaries, etc.

Detailed calibration is a subsequent process that focuses in detail on smaller chosen parts of the network. Typically a continuous sequence of pipe sections of the total length 500 to 1000 m is calibrated at the same time. By means of specialized measuring apparatus (Fig. 1) an extra withdrawal is realized on the lower end of the calibrated part. That initiates the velocity highly exceeding commonly occurring velocities in the pipeline. The flow and hydrodynamic pressure are measured. Obtained data is used for calibration of the parameters of the corresponding pipe sections.

The essence of water supply hydraulic model calibration is to adjust hydraulic parameters of individual objects in order to obtain both the same values (measured and calculated) of hydraulic pressure in specific points. It is important to preserve the same initial and boundary conditions of the calculation. That means that e. g. water level in reservoir must be the same for mathematical model and real network. Denote this pressure difference as Δp [MPa]. Then

$$\Delta p = p_M - p_C \tag{1}$$

where p_M [MPa] is measured hydrodynamic pressure in the pipeline under the reference flow and p_C [MPa] is the calculated hydrodynamic pressure in the in the same node in the network under reference flow. Then model calibration is considered as satisfactory if a value of $\Delta p \leq 0{,}01$MPa is achieved. Higher accuracy is usually not necessary and often not technically achievable due to the inherit accuracy of pressure sensors, the fluctuation of water level in storage tanks and other uncertainty in the input data (e.g. water main bedding depth).

2 Hydraulic Values Measurement

The success of the entire calibration process of the hydraulic model is fundamentally in dependence on accuracy of the in-situ measurement of hydraulic values which are the hydrodynamic pressure in the pipeline and the flow [3],[4],[5]. The discharges from water supply tank to the network are measured by means of precise induction flow meter that is connected to the external data logger. The data is recorded based on pulse registration in the time. The volume corresponding to one pulse depends on expected magnitude of flows – usually 0,05 to 0,10 m^3. The calibration data is collected by extra withdrawal of a defined flow in several specific locations along the network (Fig. 1), typically underground fire hydrants, whilst monitoring the decrease in hydrodynamic pressure not only at the monitoring points, but also in a hydraulically connected part of the network (Fig 2).

Fig. 1 On-situ continuous measurement of flow and hydrodynamic pressure

Fig. 2 On-situ measurement of hydrodynamic pressure – underground hydrant

A very important factor impacting on the quality of the subsequent work and the results of the analysis is the accuracy of the procedures and the monitoring of the hydraulic characteristics.

At the current practice the accuracy of the in-situ measured values is shown in Table 1 (the accuracy of the instrument is satisfactory for the calibration of hydraulic models). Measured data are storage in datalogger. The calibration toolbox for ADAM application allows reading this type of data and links them to specified model object (data can be saved i.e. as CSV, TXT or MS Excel XLS(X) file etc).

Table 1 Accuracy of measurement apparatus

Flow measurement:	accuracy ± 0,1 $dcm^3 \cdot s^{-1}$, flow range 0,5 to 15,0 $dcm^3 \cdot s^{-1}$
Pressure measurement:	accuracy ± 0,0025 MPa, pressure range 0,0 to 1,0 MPa (limits may vary according to used pressure sensor)

3 Measured Data Preprocessing

Process of water supply network model calibration of is basically divided into two phases. First step is control of simulation results across for whole network (grid calibration). Second step is to calibration of individual network parts (detailed calibration).

Statistical processing of data used for grid calibration of routine daily regimes

In first phase of full-area network calibration under normal operational network states date representing measured flow can be used. First set of data are measured at tank outlet. Second data set is represented by measured flow and pressure at specific points of water supply network. For purpose of calibration is necessary to create statistic data analysis (data preprocessing). Results of analysis are minimal flow at night (Q_{min}), average flow (Q_p), maximal one hour flow (Q_h) and highest flow measured at 5 minutes interval (Q_{max}). All of these flow values can be obtained by using Calibration toolbox for ADAM software. Model of water supply network is verified by comparing hydrodynamic pressures (simulated and measured) at specific points of network under mentioned flow conditions. This type of calibration removes significant modeling mistakes.

Processing of deterministic data used for detailed calibration

Detail calibration of each network model sections follows successful grid calibration for entire pressure range. Purpose of detail calibration is to validate/set proper values of hydraulic parameters (inner diameter and hydraulic roughness) of individual continuous network sections. Measurement processing and data preprocessing is similar as in grid calibration phase. Model verification is finished when simulation results are satisfactory under new set of input data.

4 Calibration of the Hydraulic Model of the Water Supply Network – Toolbox for ADAM Software

Described methods of calibration, as well as some actions, described below can be partially described by set of pre-defined rules. Based on this rules the set of algorithm can be defined and used.

Grid calibration by Calibration toolbox for ADAM software

Let us assume that we have model of water supply network. Than simple rule can be defined as:

$$sgn(\Delta p_i) = 1 \Rightarrow \underline{\text{Increase water level in tank}} \tag{2}$$

and algorithm for pressure control under grid calibration conditions can be formulated as:

N1: [Network initialization; Start simulation]
N2: [Data initialization] // links measured data to points P1 to P5
N3: [Rule] If $p_M > p_C$ for every P then in *Tank* increase *water level*
N4: [End]

Another rule can be defined as:

$$sgn(\Delta p) = 1 \wedge q_M \approx 0 \Rightarrow \underline{\text{Pipe is closed}} \tag{3}$$

where q_M is measure flow in the end of pipe (at same point as pressures).

Note that results of these types of rules are in software presented as proposals. Calibration toolbox provides necessary statistical functions.

Detailed calibration by Calibration toolbox for ADAM software

I order to find calibrated mathematical model, in fact proper parameters of pipe model, has to be changed two parameters of each individual pipe of model network part.

Parameters of pipe model are length, elevation, hydraulic roughness and internal diameter (DN). But only a length and elevation of pipe does not change in time. So the parameters to modify are only diameter (more accurate inner profile) and hydraulic roughness.

Therefore detail calibration process can be defined as optimization problem for two variables. Based on experience, that first parameter to change is roughness (but not always), is defined optimization problem as:

$$\min(\Delta p) \ \underline{\text{by changing}} \ (k, D) \tag{4}$$

where k is hydraulic roughness of pipe and D inner diameter.

For purpose of parameters optimization Calibration toolbox for ADAM software contains implemented genetic algorithm and differential evolution algorithm, but also another types of optimization methods can be employed as well (e.g. neural networks etc.). Note that results of optimization are in software also presented as proposals.

5 Conclusions

The calibration of hydraulic models is subject of interest of many scientist and technicians all over the world. Many different methodologies have been described for the purpose. Some of the methods that have been implemented in commercial software are fully automated and utilizes the genetic algorithms optimization technologies. The above mentioned technique is based on several years of author's hands-on experience with mathematical modeling, field measurement and models

calibration. The presented two-step calibration methodology is based on grid calibration of the model in the first step that utilizes a sound statistical analysis of the discharge time series and precise in-situ measurement of the hydrodynamic pressure. The subsequent detailed calibration is performed for the chosen parts of the network and is based on measurement of hydraulic values in-situ during extra withdrawals that exceed common network flows. Both the grid and the detailed calibration process has been implemented in the newly developed toolbox that is part of ADAM software which is a specialized software application for hydraulic analysis of water supply networks.

Acknowledgments. This research work is funded by the Technology Agency of the Czech Republic in the frame of the research project titled "Tools for prevention of water discoloration in water mains" - registration number TA02020604. Additionally this work is supported by project European Regional Development Fund in the framework of the research project NETME Centre under the Operational Programme Research and Development for Innovation. Reg. Nr. CZ.1.05/2.1.00/01.0002, id code: ED0002/01/01, project name: NETME Centre –New Technologies for Mechanical Engineering.

References

[1] Riha, J.: Matematical modeling of hydrodynamical and dispersion phenomenons, Brno University of Technology (1997) (in Czech) ISBN 80-214-0827-8

[2] Hadas, Z., Vetiska, V., Singule, V., Andrs, O., Kovar, J., Vetiska, J.: Energy harvesting from Mechanical Shocks Using A Sensitive Vibration Energy Harvester. International Journal of Advanced Robotic Systems (2012) ISSN 1729-8806

[3] Tuhovcak, L., Rucka, J.: Hazard identification and risk analysis of water supply systems, Strategic Asset Management of Water Supply and Wastewater Infrastructures, pp. 287–298. IWA Publishing (2009) ISBN: 1-84339-186- 4

[4] Tuhovčák, L., Rucka, J.: Risk analysis concepts and methods - detailed methods. In: Proactive Crisis Management of Urban Infrastructure. 1, pp. 30–46. COST Office, SINTEF, Brusel (2008) ISBN: 978-82-536-1003- 0

[5] Votruba, L., Herman, J., et al.: Reliability of water system structures, pp. 80–209. Česká matice technická, Praha (1993) ISBN 80-209-0251-1 (in Czech)

[6] Brezina, T., Kovar, J., Hejc, T., Andrs, O.: Modeling and H-infinity Control of Centrifugal Pump with Pipeline, Mechatronics Recent Technological and Scientific Advances, pp. 523–530. Springer (2011) ISBN 978-3-642-23243-5

[7] Brezina, T., Hejc, T., Kovar, J., Huzlík, R.: Modeling and Control of Three-Phase Rectifier of Swirl Turbine, Mechatronics Recent Technological and Scientific Advances, pp. 285–291. Springer (2011) ISBN 978-3-642-23243-5

Practical Problems during Fuel Pump Development for Aerospace Industry

P. Axman, R. Král, V. Axman, and J. Berjak

UNIS, a.s., Jundrovská 33, 624 00, Brno, Czech Republic
{paxman,rkral,vaxman,jberjak}@unis.cz

Abstract. This paper introduces four problems that occurred during development process of the transport fuel pump for L410 airframe fuel system and one problem is detailed decribed. The fuel pump was developed with connection of three partners; Aircraft Industries, a.s. (AI, producer of L410), Jihostroj, a.s. (JSV, producer of transport fuel pump), UNIS, a.s. (Producer of control electronics FPC2).

1 Introduction

The development of new generation of transport fuel pump was invoked by requirements of aircraft producer (AI) for new design that implements "damage tolerance" maintenance philosophy which significantly increases the operation life of the aircraft. According to this fact the conception of the fuel pump powered with modern Brush Less Direct Current (BLDC) motor with control electronics was created.

2 Transport Fuel Pump Control Electronics for L410 Airframe Fuel System

The transport fuel pump (FP) is equipment intended for creating fuel pressure on the inlet of the turbine engine. The FP is driven by the BLDC motor and controlled and

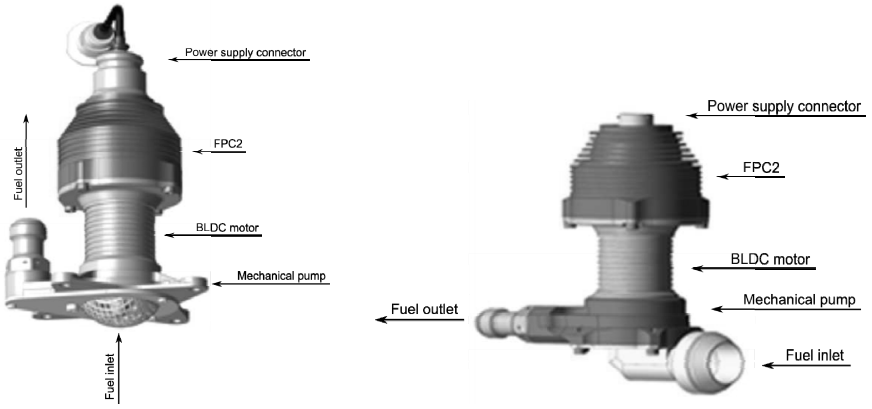

a) End tank FP b) Pipeline FP

Fig. 1 Developed variants of transport fuel pump

T. Březina and R. Jabloński (eds.), *Mechatronics 2013*,
DOI: 10.1007/978-3-319-02294-9_33, © Springer International Publishing Switzerland 2014

powered by control electronics (FPC2). Two variants of the FP are illustrated in figure 1.

The necessity of high quality of fuel pump and developed control electronics can be mainly shown on two requirements:

- Using inside aircraft fuel tank
- 30 years of lifetime

Both variants of FP are equipped with the same control electronics FPC2 shown in figure 2. Control electronics consists of two Printed Circuit Boards (PCBs); control board and power board. Control board contains all necessary components for ensuring control functionality (including Microprocessor Control Unit (MCU)), power board contains power components for connection of BLDC motor phases.

Fig. 2 Fuel pump control electronics (FPC2)

3 Solved Problems

During development process the following main problems were solved:

- System powering without using of high capacity capacitors **(described in this paper)**
- Energy saving after fuel is consumed
- Reliability of FPC2 for various environmental conditions
- Fuel pump maintainability according to the runtime information

3.1 System Powering

Power management problem occurred in connection with the requirement for storing runtime data even at the moment when the power voltage was turned off. This problem was solved as a combination of hardware (HW) and software (SW) parts with the following main restrictions:

- The size of the electronics was limited
- Environmental requirements had to meet requirements for using on aircraft fuel tank
- 30 years of lifetime

Combination of the input requirements (environmental temperature, vibrations and size) didn't allow using of high capacity capacitors (electrolytic and tantalum capacitors). HW problem was defined how to ensure enough energy for control electronics and prolong time for data storing process at the moment of power voltage off. SW problem was defined how to finish storing process in time when the control electronics power voltage is above defined minimal level.

Figure 3 shows the block diagram of the FPC2 connection to power supply voltage and BLDC motor. The red colour highlighted energy flow from power connector to two main parts; control electronics and power electronics.

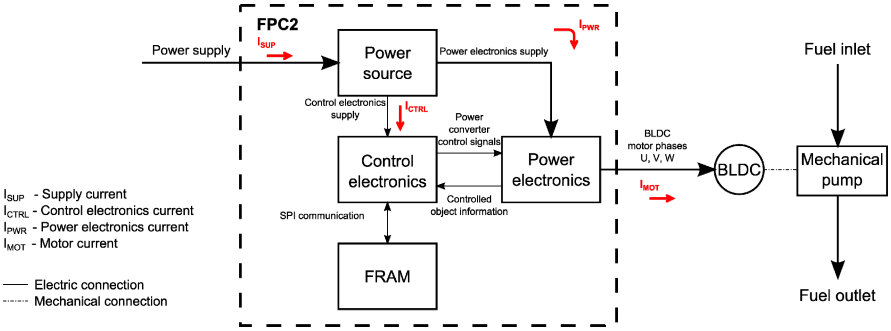

Fig. 3 FPC2 energy flow

3.1.1 HW Problem Solution

The problem could be normally solved by following ways:

- Using internal power source (battery, energy harvesting)
- Using external power source (backup low power source)
- Using BLDC motor as a generator
- Using residual energy of capacitors of all device part

Internal power source – internal power source like battery cannot be used for the 30 years lifetime without servicing and wide range of environmental temperatures from -50 to 125 °C. Energy harvesting cannot be used for the absence of required energy.

External power source – the input requirement is that the final device will be equipped by the single power connector with single power voltage. This variant is not applicable.

Using BLDC motor as a generator – for this variant of powering of the electronics is not enough required mechanical energy on the side of BLDC motor shaft (output shaft is equipped by centrifugal pump)

Using residual energy of capacitors of all device part – the functionality of the fuel pump must be guaranteed in a wide range of supply voltage from 10 to 50 V DC. There is useful energy in power board capacitors that can be used for powering of the control electronics digital part. Energy flow with using of residual energy is shown in figure 4.

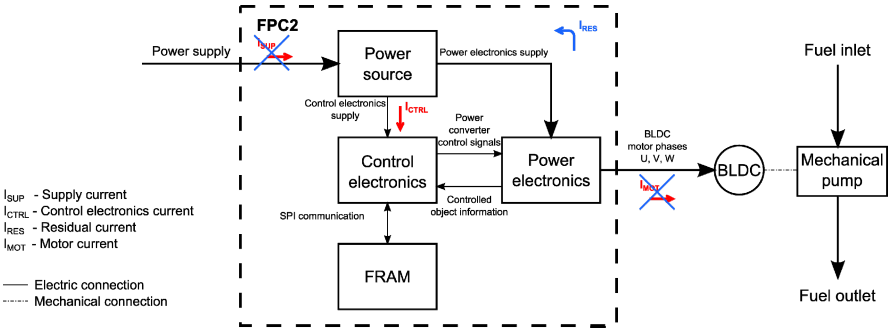

Fig. 4 Residual energy for powering digital electronics

Using of the residual energy is presented by the flow of the currents in the device. The diagram described the voltage levels in the FPC2 device is shown in figure 5.

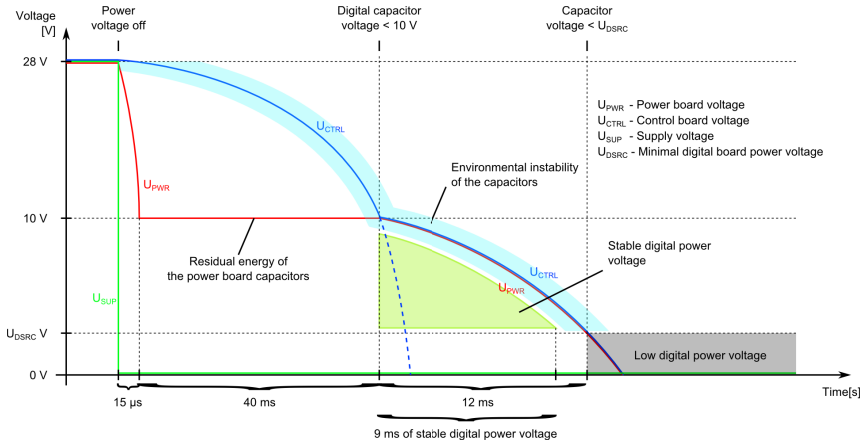

Fig. 5 Time diagram of the FPC2 voltage levels

As can be seen the maximal time for data processing and data storing into the integrated FLASH memory is approximately 52 ms for 28 V of supply voltage.

For minimal runtime voltage (10 V) the storing time is approximately 12 ms. If the environmental instability of the capacity is considered the maximal useful time for data processing is approximately 9 ms (green area on the figure 5). The time of the stable power voltage for the digital part is evaluated for defined power consumption of used components.

3.1.2 SW Problem Solution

During HW design the SW data processing was solved simultaneously. The analysis of the possible components was performed and according to this analysis the component base was defined. The main criterion for definition of the data storing component base was maximal time for necessary erase, write cycles. The timing for considered memory components is shown in table 1.

Table 1 Timing for considered memory components (typical values)

Memory type	erase cycle	write cycle	Number of write cycles
EEPROM	-	5 ms	10^6
FLASH	30 ms	3 µs	10^5
MCU internal FLASH	20 ms	20 µs	10^5
FRAM	-	300 ns	10^{12}

The values shown in the table 1 are acquired from producers' datasheets for chosen component. There should be differences between each component and producers. The FRAM memory type was chosen for the design of the fuel pump control electronics.

SW algorithm for data processing and data storing has to perform following operations for successful result:

- Stop motor
- Finish last FRAM operations
- Perform data evaluation
- Store data into FRAM memory
- Calculate memory checksum (CRC) – for service data area only
- Store CRC into FRAM memory
- Terminate program processing

All performed operations are necessary for future analysis during maintenance period. In this period the fuel pump lifetime is evaluated by the fuel pump producer according to damage tolerance maintenance philosophy.

4 Conclusions

The control electronics of the transport fuel pump is developed for using in L410 aircraft fuel system. There exist several requirements in aircraft industry which are

going against classical solution of common technical problems, e.g. 30 years lifetime, working temperature from -50 to 120°C, high reliability, long or no maintenance interval during lifetime, limited device size. According to these requirements careful selection of components has to be performed and some components cannot be used. It leads for usage of all available methods how to fulfil all input requirements as is shown in this paper for using all available energy after the supply voltage is turned off without common usable components in industry (battery, electrolytic capacitors, back-up power supply etc.).

Acknowledgments. This work was supported by the Ministry of Industry and Trade of Czech Republic, project MOSTA – Modernization of small transport aircraft to increase operation effectiveness and economy, contract No. FR-TI2/557.

References

[1] Reports of MOSTA project, UNIS, a. s. (2010, 2013)
[2] Annual reports of MOSTA project, Aircraft Industries, a. s. (2010, 2012)

Simulation Modelling of MEMS Thermoelectric Generators for Mechatronic Applications

L. Janak[1], Z. Ancik[2], and Z. Hadas[1]

[1] Brno University of Technology, Faculty of Mechanical Engineering, Technicka 2, 616 69, Brno, Czech Republic
ludek.janak@gmail.com, hadas@fme.vutbr.cz
[2] Unis, a.s., Mechatronic & embedded systems, Jundrovska 33, 624 00, Brno, Czech Republic
ancikzdenek@seznam.cz

Abstract. This paper deals with an introduction to the simulation modelling of transient behaviour of MEMS thermoelectric generators (TEGs) for mechatronic applications. Special emphasis is put on the simulation of recently commercially achievable modules. At first is given the overview of prospective mechatronic applications of MEMS TEGs and the existing commercially achievable MEMS TEG modules are listed in a short trade review. Afterwards, the main features of thermoelectric energy conversion are described together with the simple governing equations. In the main part of paper is presented the simulation model for investigations of transient behaviour of MEMS TEG module. Derived model is implemented in MATLAB/Simulink Simscape. Results given by dynamic model are compared with results obtained by other modelling approaches and transient behaviour of MEMS TEG is evaluated.

1 Introduction

Thermoelectric generators are one of the promising ways to produce the environmentally clean energy. Due to their relatively small efficiency are particularly considered their applications in the field of thermal energy harvesting – recovery of the small amounts of waste heat to the useful electric energy [1]. The main advantages for the use of TEGs in mechatronic applications are no movable parts which represent low demands on maintenance.

Promising area is the use of small amounts of locally harvested energy for powering the wireless applications, telemetry units, sensors, etc. This approach is particularly advantageous in the places where is difficult to trace wiring or where the battery replacement is challenging due to disassemble difficulties. Typical cases of this kind of application are the diagnostic systems in aerospace field [2, 3], portable medical devices [4], or autonomous measurement units in process control systems [5].

T. Březina and R. Jabloński (eds.), *Mechatronics 2013*,
DOI: 10.1007/978-3-319-02294-9_34,

Wider commercial use of the MEMS thermoelectric generators is in its infancy [6]. There are only a few existing commercial solutions in the field of MEMS TEGs and even fewer amount could be bought as a standalone solution. Standalone MEMS solutions have been developed by Micropelt GmbH [7], Nextreme Thermal Solutions, Inc. [8], Thermo Life Energy Corp., Inc. [9], Hi-Z Technology, Inc. [10] and Perpetua Power Source Technologies, Inc. [11]. Modules from the first two above-mentioned manufacturers – Nextreme and Micropelt – which are currently easily achievable through worldwide electronics components retailers are shown in Fig. 1.

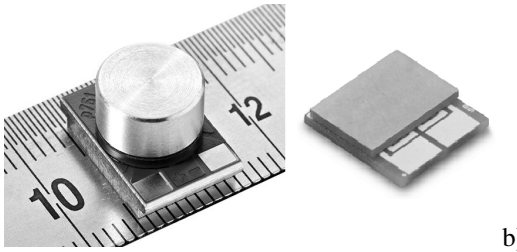

a) b)

Fig. 1 a) Micropelt TGP-751 in package [8], b) Nextreme eTEG HV56 [9]

In this paper is presented an approach to the modelling of MEMS TEG based on simulation model implemented in MATLAB/Simulink Simscape. The model is capable to carry out the dynamic simulations which give us the overview of transient behaviour and other time-domain properties of MEMS TEG. The model input data were set according to the specific case of Nextreme eTEG HV56 [12].

2 Basic Principles of Thermoelectricity

Physical nature of thermal energy harvesting - the Seebeck effect is based on the diffusion of electrons through the interface between two different materials – conductors or semiconductors. This diffusion is achieved by applying a heating at the junction of two materials which make a thermocouple. Heating causes the net changes in the materials and allows electrons to move from material where they have lower energy into material where the energy of electrons is higher. Because the electrical current is exactly a flow of electrons, this effect of passing electrons from one material to another makes an electromotive force (voltage) on the terminals of thermoelectric module [1, 13, 14]. Generated open circuit voltage is linearly dependant on the temperature difference between hot and cold sides of thermoelectric module:

$$U_{OC} = N.\alpha.(T_H - T_C) \tag{1}$$

where N is number of thermocouples, α is differential Seebeck coefficient (material constant), T_H is hot-side temperature and T_C is cold-side temperature [13].

In practical applications is TEG operated with electric load R_L (Fig. 2). TEG is, in fact, the temperature-controlled constant voltage source with internal resistance R_i. Thus the voltage U_L on load is:

$$U_L = \frac{R_L}{R_L + R_i} . U_{oc} \tag{2}$$

Current I_L in the TEG circuit can be easily calculated using Ohm's law. The maximum power point (MPP) is achieved when $R_i = R_L$. This mode of operation is called operation with matched load. Operation in the MPP mode with maximum electrical power on load P_L is desired in the most of applications [13].

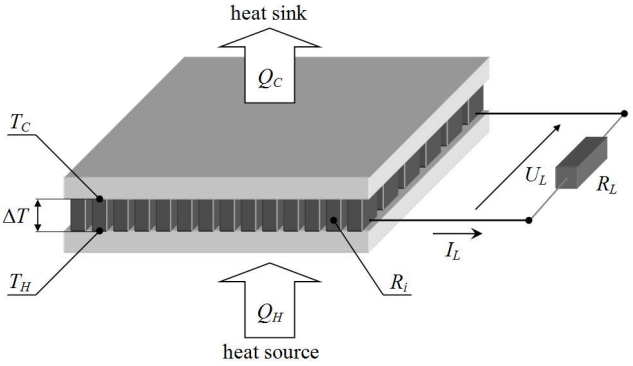

Fig. 2 Principle of operation of TEG into the load resistance R_L (current I_L, voltage U_L)

TEG is, in fact, a type of heat engine operating between two temperatures – T_H and T_C. Thus a theoretical efficiency of the thermoelectric energy conversion is limited by the Carnot's Theorem [1]. The efficiency of real TEG is exactly around 2 – 5 %. This reduction is caused by the materials- or design-related problems. Enhancement of efficiency and higher integration with surrounding systems are the tasks for MEMS and NEMS TEGs. [14]

3 Dynamic Model in MATLAB/Simulink Simscape

The considered dynamic model is an extension of steady-state Simscape model published in [15]. Parts of the model describing the transient behaviour of TEG are built-in according to the scheme of SPICE model described in [16]. Derived model was implemented in Simscape using the objects from Electrical and Thermal folders of Foundation Library. Overview of the model is shown in Fig. 3 – 5.

The whole simulation model consists of the thermal and electrical part and model of interconnections between these parts. The thermal part, shown in Fig. 3, is composed of thermal resistances and masses of wafer and thermocouples (R_{wafer},

C_{wafer}, R_{tcs}, C_{tcs}). Thermal materials properties are not directly offered by manufacturer and their estimation based on information from [12, 14] is necessary. Temperature dependences of the materials were neglected and their fixed values were estimated at the room temperature. Ideal heat flow sources Q_{joule}, Q_{pelC} and Q_{pelH} represent phenomena of the Peltier cooling and Joule heating which occur in TEG.

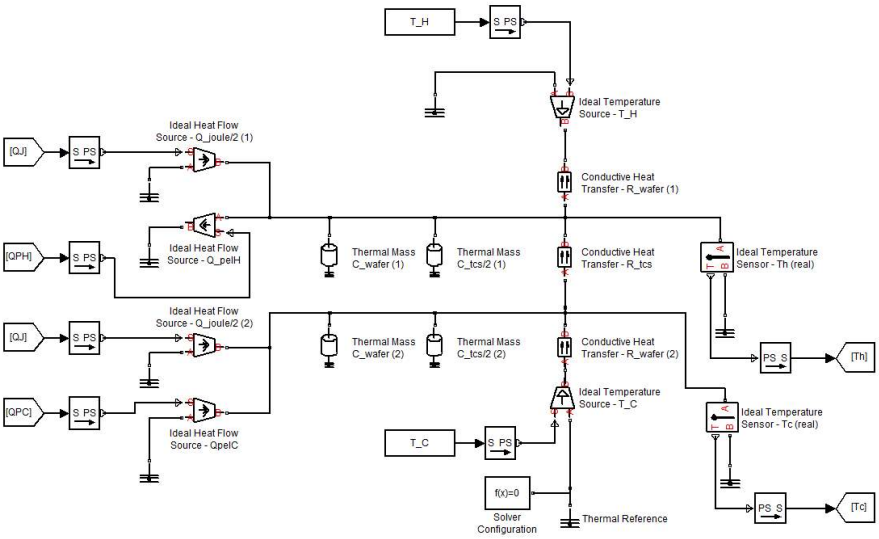

Fig. 3 Thermal Part of Model – Implemented in Simscape

Heat fluxes generated by heat flow sources are dependant on the current passing through the electrical part of TEG model. Thus the thermal and electrical parts are interacting together. Equations describing the implementation of multi-domain phenomena of Peltier cooling and Joule heating are shown in Fig. 4.

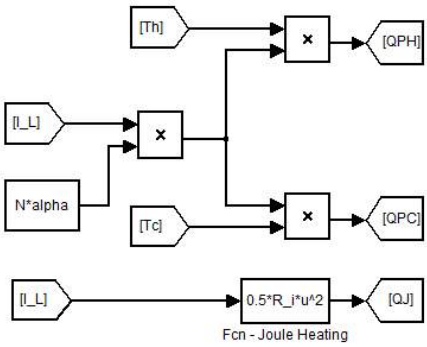

Fig. 4 Model of interconnections between thermal and electrical parts

Finally, the electrical part of TEG is built as the constant voltage source with internal resistance as described in the chapter 2. Output voltage is controlled by the real temperature difference on the thermocouples. Implementation of electrical part is shown in the Fig. 5.

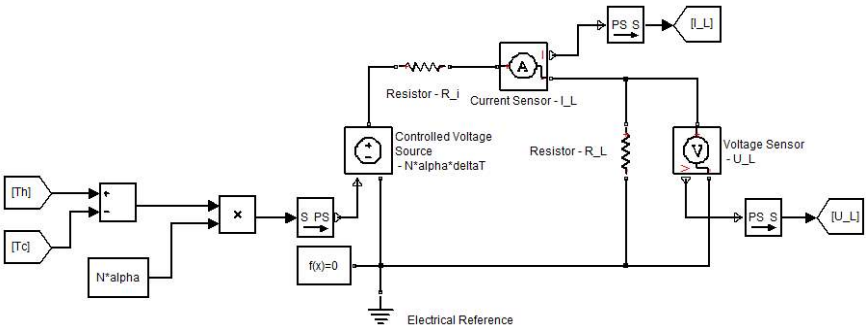

Fig. 5 Electrical Part of Model

Examined time-dependant output values from above-described simulation model include the voltage on load U_L, current through the circuit I_L and resulting electrical power P_L.

3.1 Comprehension of Results

Transient behaviour of MEMS TEG module was examined by applying the step function of hot-side temperature T_H. Input simulation parameters are set to the temperature difference of 50 °C and matched resistive load. Resulting step response of voltage U_L is shown in Fig. 6. As could be seen in Fig. 6, the occurring time constant is in the millisecond range. This rapidity is caused by the very small thermal masses appearing in the MEMS TEG module.

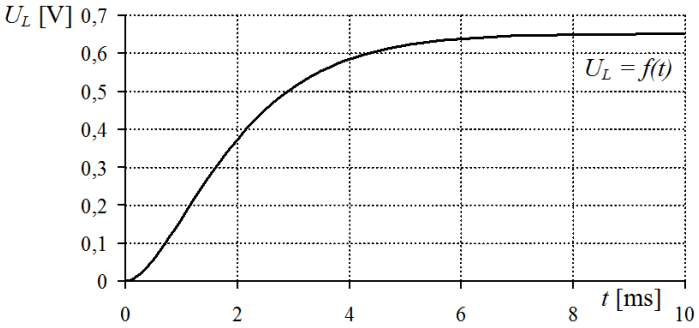

Fig. 6 Step response of dynamic Simscape model (MEMS eTEG HV56, conditions: ΔT_{out} = 50 °C, T_C = 25 °C, T_H = 75 °C, T_H applied at t = 0)

The steady-state value reached by the dynamic model was compared with results of other simulation modelling approaches. Steady-state values are listed and compared below in the Table 1. In the comparison are included results given by the simple modelling approach using (2) and Ohm's law, Analytic Model with Constant Resistances [14, 17] and FEM analyses [15]. Obtained output values are also compared with the datasheet values provided by manufacturer in [12].

Table 1 Comprehension of results (conditions: $\Delta T = 50$ °C, $T_C = 25$ °C, $T_H = 75$ °C, matched load)

Type of Model	Voltage on the matched load U_L [V]	Passing current I_L [mA]	Produced electric power P_L [mW]
Simscape dynamic	0,651	63,784	41,552
Voltage source with R_i	0,688	67,412	46,379
Analytic with contact res.	0,566	62,393	39,318
FEM (ANSYS)	0,688	-	-
Datasheet value	0,6	60	36

4 Conclusions

The above-described dynamic model of MEMS TEG was successfully implemented in Simscape and verified by application of the trivial input conditions – constant temperature difference and matched load. Very small time constant in the millisecond range was observed. The maximal observed difference between datasheet value and simulation was 15,4 % (P_L). In the comprehension with other simulation modelling approaches was observed the maximum difference of 15 % in the case of voltage U_L and analytic model with contact resistances. These inaccuracies could be reduced by identification of input parameters based on measurement. Better identification of input parameters and verification of models based on MEMS TEG module measurements are the tasks for future development.

The biggest challenges for the further work in energy harvesting area are the co-simulations with surrounding systems [18]. The Simscape model will be chiefly used for the co-simulations of MEMS TEG with surrounding power conditioning electronics.

Acknowledgments. This work has been funded by the European Commission within the FP7 project "Efficient Systems and Propulsion for Small Aircraft | ESPOSA", grant agreement No. ACP1-GA-2011-284859-ESPOSA. And this work has been additionally supported by the project "Complex Affordable Aircraft Engine Electronic Control (CAAEEC)" TA02010259 under The Technology Agency of the Czech Republic.

References

[1] Priya, S., Inman, D.J.: Energy Harvesting Technologies, pp. 325–336. Springer (2009)

[2] Featherston, C.A., Holford, K.M., Pullin, R., Lees, J., Eaton, M., Pearson, M.: An autonomous structural health monitoring solution. In: Proc. SPIE, vol. 8763, p. 876302 (2013)

[3] Becker, T., Kluge, M., Schalk, J., Tiplady, K., Paget, C., Hilleringmann, U., Otterpohl, T.: Autonomous Sensor Nodes for Aircraft Structural Health Monitoring. IEEE Sensors Journal 9(11), 1589–1595 (2009)

[4] Settaluri, K.T., Lo, H., Ram, R.J.: Thin Thermoelectric Generator System for Body Energy Harvesting. Journal of Electronic Materials 41(6), 984–988 (2012)

[5] Carstens, T.A., Corradini, M.L., Blanchard, J.P., Zhenqiang, M.: Thermoelectric Powered Wireless Sensors for Spent Fuel Monitoring. IEEE Transactions on Nuclear Science 59(4), 1408–1413 (2012)

[6] Natrop, P., Das, R.: Energy Harvesting and Storage for Electronic Devices 2010-2020. IDTechEx Ltd. (2010)

[7] Micropelt Thermoelectric Energy Harvesting Home, http://www.micropelt.com

[8] Nextreme Thermal Solutions – Microscale Thermal and Power Management, http://www.nextreme.com

[9] Powered by Thermo Life, http://www.poweredbythermolife.com

[10] Hi-Z Technology, Inc., http://www.hi-z.com

[11] Energy harvesting solutions for wireless sensors, http://www.perpetuapower.com

[12] eTEG HV56 Power Generator data sheet, http://www.nextreme.com/media/pdf/techspecs/Nextreme_eTEG_HV56_Data_Sheet.pdf

[13] Goldsmid, H.J.: Introduction to Thermoelectricity, pp. 1–15. Springer (2010)

[14] Rowe, D.M., et al.: Thermoelectrics handbook: macro to nano. Taylor & Francis Group (2006)

[15] Ancik, Z., Vlach, R., Janak, L., Kopecek, P., Hadas, Z.: Modeling, simulation and experimental testing of the MEMS thermoelectric generators in wide range of operational conditions. In: Proc. SPIE, vol. 8763, p. 87631 (2013)

[16] Dziurdzia, P.: Simulation Tool for Virtual Estimation of Harvested Thermoelectric Energy Supplying Wireless Sensor Nodes. In: 2nd International Conference on Software Technology and Engineering (ICSTE), pp. 414–418 (2010)

[17] Rowe, D.M., Min, G.: Design theory of thermoelectric modules for electrical power Generation. IEEE Proc. Sci. Meas. Technol. 143(6), 351–356 (1996)

[18] Hadas, Z., Singule, V.: Energy harvesting – opportunity for future remote applications. In: 17th International Conference on Engineering Mechanics, Svratka, Czech Republic, pp. 167–170 (2011)

Simulation Assessment of Suspension of Tool Vibrations during Machining

T. Březina[1], L. Březina[1], J. Marek[2], Z. Hadas[1], and J. Vetiška[1]

[1] Brno University of Technology, Faculty of Mechanical Engineering, Technická 2896/2, 616 69, Brno, Czech Republic
{brezina,brezina.l,hadas,vetiska}@fme.vutbr.cz
[2] TOSHULIN, a.s., Wolkerova 845, 768 24 Hulín, Czech Republic
jiri.marek@toshulin.cz

Abstract. Knowledge of an impact of a linked mass on a behavior of machine tools is a useful guide for their designers. This paper demonstrates a general approach which leads to a set of locally optimal parameters of mass, whose connection to the machine consequently suppresses vibrations during machining. The approach is based on simulation modeling of mechatronic systems with flexible bodies. Obtained parameters can be structurally interpreted e.g. as damper or absorber for the needs of the design already in preproduction stages.

1 Introduction

The main goal of industry companies is to fully satisfy requirements of a consumer. Such requirements naturally lead to the research of suitable design methods.

The basic inspiration for the designers is knowledge of an influence of a linked mass on the dynamic compliance of a machine tool. Such knowledge can be used as a base for the correction of the engineering design. The concept of simulation modeling of mechatronic systems is used to obtain the required knowledge and for the cheap experimenting with the machine dynamic compliance [1].

However, a solution of such problem is nontrivial because of: a) an integration of the mass is influencing the dynamics of all axes and improved behavior of one axis does not necessarily mean that the behavior is improved also in the other axis, b) a reliable model of the real machine has to contain flexible bodies which dramatically increase model order.

This paper demonstrates how to achieve locally optimal influence of the linked mass, which is flexibly joined with the tool holder, on vibration suppression of tool vibrations during a machining [2].

2 Task Formulations

An integration of the mass *A* is modeled by mechanical parameters - weight m_A linked to the mass center of a tool holder by an ideal damper with damping b_A and

T. Březina and R. Jabloński (eds.), *Mechatronics 2013*,
DOI: 10.1007/978-3-319-02294-9_35,

by an ideal spring with stiffness k_A. The mass is moving in φ_A, θ_A direction (Fig. 1), which represents geometric parameters (Fig. 1).

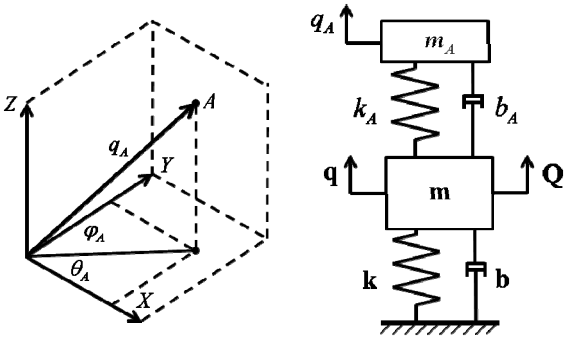

Fig. 1 Scheme of the integration of the mass *A* to the system

The dynamic compliance of the machine with integrated mass *A* describes equations (1)

$$\begin{aligned} \mathbf{m}\ddot{\mathbf{q}} + \mathbf{b}\dot{\mathbf{q}} + \mathbf{k}\mathbf{q} &= \mathbf{Q} - m_A\ddot{\mathbf{q}} + (\mathbf{h}m_A)\ddot{q}_A \\ m_A\ddot{q}_A + b_A\dot{q}_A + k_A q_A &= Q_A + (\mathbf{h}m_A)^T\ddot{\mathbf{q}} \end{aligned} \tag{1}$$

where $\mathbf{m}$, $\mathbf{b}$, $\mathbf{k}$ mean matrix of mass, matrix of damping, matrix of stiffness and $\mathbf{h} = \left[\cos(\varphi_A)\cos(\theta_A) \quad \cos(\varphi_A)\sin(\theta_A) \quad -\sin(\varphi_A)\right]^T$. The equations (1) can be equivalently expressed by a block model, Fig. 2.

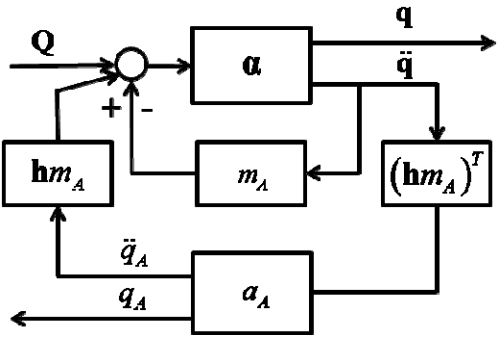

Fig. 2 Block model describing integration of the mass *A* to system according to (1), $\boldsymbol{\alpha}$ and a_A mean dynamic compliance model of the machine tool and of the integrated mass *A*

Improvement of the dynamic compliance of the machine tool by the integration of the mass *A* is formulated as a minimization of the objective function $g(\mathbf{p})$:

$$\begin{aligned}
\mathbf{p} &= \left[m_A \quad b_A \quad k_A \quad \varphi_A \quad \theta_A \right] \\
\Delta_{i,j}\left(\mathbf{p}\right) &= \frac{\max\limits_{\omega} \left| \boldsymbol{\alpha}^{A}_{i,j}\left(\omega,\mathbf{p}\right) \right|}{\max\limits_{\omega} \left| \boldsymbol{\alpha}_{i,j}\left(\omega,\mathbf{p}\right) \right|} - 1 \qquad , \; i,j = X,Y,Z \\
g\left(\mathbf{p}\right) &= \max_{i,j} \Delta_{i,j}\left(\mathbf{p}\right) \\
\mathbf{p}_{opt} &= \arg\min g\left(\mathbf{p}\right)
\end{aligned} \tag{2}$$

where $\max\limits_{\omega} \left| \boldsymbol{\alpha}^{A}_{i,j}\left(\omega,\mathbf{p}\right) \right|$ is a dominant amplitude – maximum of the amplitude characteristics of the dynamic compliance of the machine with integrated mass *A* and $\max\limits_{\omega} \left| \boldsymbol{\alpha}_{i,j}\left(\omega,\mathbf{p}\right) \right|$ means the same but without the integrated mass.

Following limitations are considered:

$$\begin{aligned}
&m_A, b_A, k_A, \varphi_A, \theta_A > \left(m_A\right)_{min}, \left(b_A\right)_{min}, \left(k_A\right)_{min}, 0, 0 \\
&m_A, b_A, k_A, \varphi_A, \theta_A \le \left(m_A\right)_{max}, \left(b_A\right)_{max}, \left(k_A\right)_{max}, 360, 360 \\
&\max_{i} \Delta_{i,i}\left(\mathbf{p}\right) < 0
\end{aligned} \tag{3}$$

The first two conditions represent limitations of the magnitude of the parameters values and the last condition is introducing requirement for the improvement of the dynamic compliance in particular axis. The dynamic compliances between the different axes can get worse but only as little as possible because the minimization of the objective function is considered.

It is necessary to dispose of low order model of the dynamic compliance to implement the minimization process [3].

3 Building and Verifying of Models Describing Dynamic Compliance of Machine

The important task to build a low order model of the machine dynamic compliance was solved for machine tool by TOSHULIN, a.s. producer. The model was built in axes X, Y, Z at the center of gravity of the tool holder for the excitation frequency range 0 - 280 Hz and asked correspondence with the real machine up to 10% at both time and frequency domain [4].

3.1 Modeled Machine Tool

A base of the machine center presents steel welded frame. Two stands fixed to the base of the machine are linked together by a crossbeam which guides the support carrying the slipper with the cutting tool, Fig. 3. The machine tool center makes possible to move the tool above the bed with the attached workpiece [5].

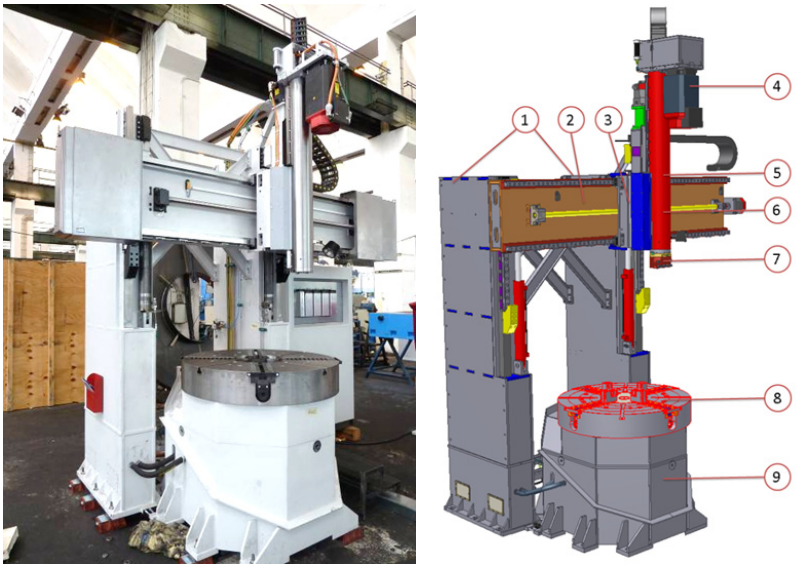

Fig. 3 a) Analyzed machine tool from TOSHULIN, a. s., b) CAD model analyzed machine tool from TOSHULIN, a. s (1 – stands, 2 – crossbeam, 3 – support, 4 – drive of the spindle, 5 – slipper, 6 – spindle, 7 – tool holder, 8 – clamping plate, 9 – bed)

3.2 Obtaining of Low Order Model via CAD, MKP and MBS Models

Obtaining the low order model is based on the mechatronic simulation modeling concept [6]. It is necessary to simplify CAD models of the machine and select the flexible and rigid parts first of all. Then the modal analysis of FEM models of flexible parts is performed [7]. The FEM models have the order around $10^5 - 10^6$ depending on their accuracy. Therefore the Graig-Bampton method [8] is used for reducing of the model orders at the given frequency range consequently. The reduced models of the order around $10^2 - 10^3$ are integrated to the complex multibody model with rigid bodies and complemented with mechatronic actuators [9]. The complete machine tool model has the order $10^2 - 10^3$. Finally the state-space LTI model $\boldsymbol{\alpha} \equiv (\mathbf{A}, \mathbf{B}, \mathbf{C}, \mathbf{D} = \mathbf{0})$ is exported and linearized around selected operation point. The approach is described in detail in [5].

Note that L-image of $\boldsymbol{\alpha}$ is for the zero initial conditions described as

$$\begin{aligned} s\mathbf{x}(s) &= \mathbf{A}\mathbf{x}(s) + \mathbf{B}\mathbf{Q}(s) \\ \mathbf{q}(s) &= \mathbf{C}\mathbf{x}(s) + \mathbf{D}\mathbf{Q}(s) \end{aligned} \tag{4}$$

where $\mathbf{x}(s)$, $\mathbf{Q}(s)$ and $\mathbf{q}(s)$ mean L-images of the vector of (inner) states, input vector of exciting force actions and output vector of corresponding displacements.

The dynamic compliance of machine tool or dynamic compliance only between axis j and i could be expressed by simple way as

$$\mathbf{q}(s) = \boldsymbol{\alpha}(s)\mathbf{Q}(s), \text{ or } q_i(s) = \boldsymbol{\alpha}_{i,j}(s)Q_j(s) \tag{5}$$

The order of the obtained model is 428. Its eigenfrequencies were compared with the measurements on the real machine - the accuracy was reached up to 10 % in the excitation frequency range 0 - 280 Hz. The accuracy of static stiffness in directions X and Y was up to 1 %.

3.3 Modification of LTI Model

It is suitable to transform the exported LTI model to the LTI with matrix $\mathbf{A}$ in a modified canonic modal form (6) for the next reduction of the order.

$$\mathbf{A} = diag\left(\mathbf{A}_1, \mathbf{A}_2, \ldots, \mathbf{A}_n\right) \tag{6}$$

All of matrices $\mathbf{A}_k$ are $2/2$ type and a couple of eigenvalues of LTI $\left(\delta \pm i\sqrt{\omega_0^2 - \delta^2}\right)_k$ or $\left(\delta \mp \sqrt{\delta^2 - \omega_0^2}\right)_k$ is projected as

$$\mathbf{A}_k = \begin{bmatrix} \delta & \sqrt{\omega_0^2 - \delta^2} \\ -\sqrt{\omega_0^2 - \delta^2} & \delta \end{bmatrix}_k, \text{ or } \mathbf{A}_k = \begin{bmatrix} \delta - \sqrt{\delta^2 - \omega_0^2} & \\ & \delta + \sqrt{\delta^2 - \omega_0^2} \end{bmatrix}_k \tag{7}$$

The symbol δ or expression $\delta \mp \sqrt{\delta^2 - \omega_0^2}$ means damping factors and ω_0 is the natural frequency of the couple.

The application of such LTI form has two principal consequences: the original model can be decomposed to a set of partial models $\boldsymbol{\alpha}_k \equiv \left(\mathbf{A}_k, \mathbf{B}_k, \mathbf{C}_k, \mathbf{D}_k = \mathbf{0}\right)$ of the second order, for which applies (8)

$$\begin{aligned} \mathbf{q}(s) &= \left(\sum_k \boldsymbol{\alpha}_k(s)\right)\mathbf{Q}(s) \\ &= \sum_k \mathbf{q}_k(s) \end{aligned} \tag{8}$$

see block model, Fig. 4a).

The second consequence results from the equivalent formulation of $\left(\boldsymbol{\alpha}_k\right)_{i,j}(s)$ by transfer function

$$\left(\boldsymbol{\alpha}_k\right)_{i,j}(s) = \left(\frac{\left(Q_j\right)_1 s + \left(Q_j\right)_0}{s^2 + 2\delta s + \omega_0^2}\right)_k \tag{9}$$

Regarding the denominator of the transfer function it is obvious that LTI model $\boldsymbol{\alpha}_k(s)$ describes the dynamic compliance of the (abstract) mass linked to the selected place of the machine tool by an ideal damper and ideal spring, see block model, Fig. 4b).

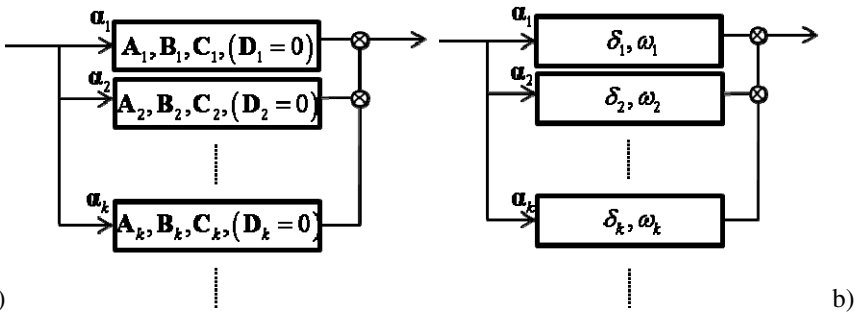

Fig. 4 Block model of the system a) according to (8), b) considering (9)

The modeled dynamic compliance $\boldsymbol{\alpha}(s)$ is according to (8) a sum of partial dynamic compliances $\boldsymbol{\alpha}_k(s)$, what can be utilized for the reduction of the LTI model $\boldsymbol{\alpha}(s)$ which respects the structure of the original model of the mechanical system. It is possible to perform the reduction of $\boldsymbol{\alpha}(s)$ by simple elimination of partial models $\boldsymbol{\alpha}_k(s)$ with no significant contribution to the original model.

The order 428 of LTI model was reduced to 80 with relative accuracy downgrade 7 % by this way.

4 Notes to the Minimization

The minimization according (2) (3) contains high number of local minima thus the computation must be performed by methods which are not designed to fast detection of the closest local minimum. Although these methods can find the local extreme but the time cost might be unacceptable. Therefore it is worked with sets of parameter values that correspond to the lowest achieved values of local extremes, i.e. with locally optimal solutions. There are consequently eliminated sets which would be difficult to implement as well as combinations of parameters with high impact on the objective function.

Minimizations are done on the reduced LTI of the order 80. The impact of its accuracy downgrade on the found parameters is eliminated by subsequent minimization on the full LTI of order 428. For that subsequent minimization, found parameter values are used as an initial estimation.

5 Example of the Locally Optimal Solution

An example of the dynamic compliance of the machine tool with the integrated mass *A* with locally optimal parameters summarizes Table 1. The dominant amplitude of the X axis is slightly decreased, of the Z axis is significantly decreased, Fig. 5. a), the axis Y remains practically without changes. The exception is represented by the dynamic compliance between axis X and Y (Fig. 5.b) where the dominant amplitude was increased. The rest of compliance dominant amplitudes show their decrease in tens of percent.

Table 1 Influence of the mass *A* with locally optimal parameters

$\Delta_{i,j}(\mathbf{p}_{opt})[\%]$	*X*	*Y*	*Z*
X	-0.1	**46.9**	-38.5
Y	**46.9**	0.0	-49.8
Z	-38.5	-49.8	**-72.0**

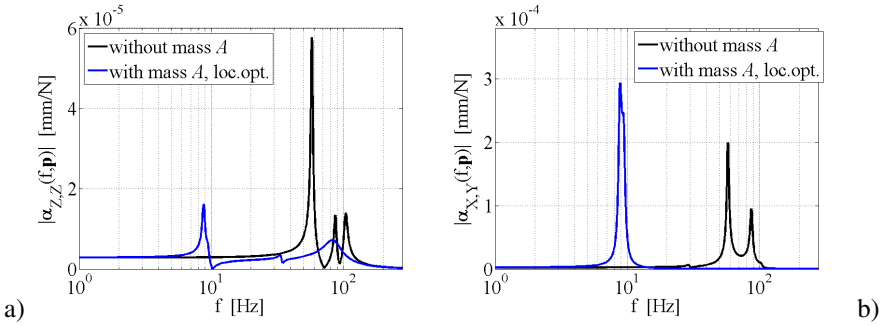

Fig. 5 The integration of the mass *A* with the locally optimal parameters a) The amplitude characteristics of the dynamic compliance of the machine in the Z axis (the best integration influence) b) The amplitude characteristics of the dynamic compliance of the machine between the X and Y axis (the worst integration influence)

The influence of the inaccuracy of the integrated mass *A* parameters on the machine dynamic compliance was evaluated through the worst behavior during the random changes of the optimal values of the individual parameters inside the prescribed range.

There was observed significant improvement of the amplitude characteristic during changes of all of parameters of the mass *A* in range ±2.5% (Table 2.), e.g. Fig. 6.a). The exception was again represented by the dynamic compliance between axis X and Y where the dominant amplitude got worse, Fig. 6.b).

Table 2 The influence of changes of mass *A* parameters, range **±2.5%**

$\Delta_{i,j}(\mathbf{p})[\%]$	*X*	*Y*	*Z*
X	-9.2	**77.6**	-39.3
Y	**77.6**	-13.7	-53.3
Z	-39.3	-53.3	**-72.2**

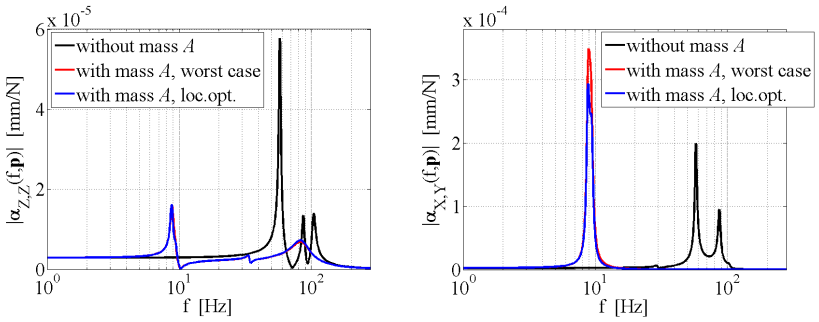

Fig. 6 Influence of the 2.5% random change of all of parameters of the mass *A* a) Amplitude characteristic of the dynamic compliance of the Z axis, b) Amplitude characteristic of the dynamic compliance between axis X and Y

The changes of the purely mechanical parameters in the range of ±10% caused in the worst case increasing of the dominant amplitude in the order of percent, Table 3, Table 1 and Fig. 7.

Table 3 Influence of the changes in mechanical parameters of the mass *A*, range **±10%**

$\Delta_{i,j}(\mathbf{p})[\%]$	*X*	*Y*	*Z*
X	3.9	**49.9**	-33.7
Y	**49.9**	-4.4	-53.1
Z	-33.7	-53.1	**-73.7**

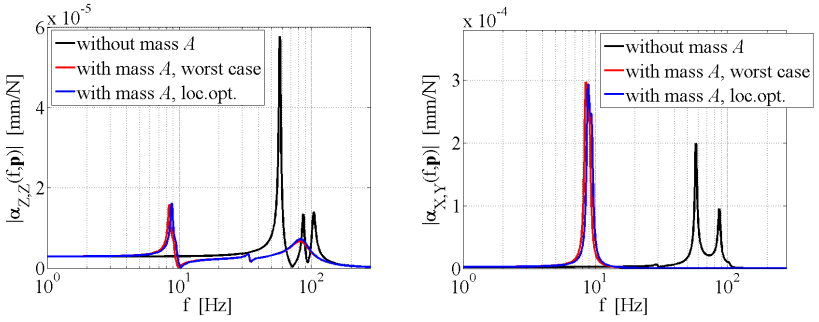

Fig. 7 Influence of 10% random change in mechanical parameters of integrated mass *A*, the worst case a) Amplitude characteristics of the Z axis, b) Amplitude characteristics of the transfer from the X axis to the Y axis

The all of demonstrated examples present almost complete suppress of the original dominant amplitudes in the frequency range 50-120 Hz. There is also observed new dominant amplitude at 9 Hz which is out of the typical work range of the analyzed machine tool.

The solution is more robust to the changes of the mechanical parameters compared to the changes of parameters which contain also geometric ones.

6 Conclusions

The proposed approach to the reduction makes possible to reduce the exported state LTI model order of the model to approximately 20%. The maximal difference between the eigenfrequencies is then typically up to 10%.

The higher robustness of the dynamic compliance against the changes of the purely mechanical parameters compared to the changes of geometrical parameters seems to be general characteristic for all of locally optimal solutions. This fact is positive because the practical achievement of the geometric parameters is easier than of the mechanical ones.

The results can be used for strategic decisions concerning their utilization at the engineering design phase. The implementation of the integrated mass A e.g. as damper or absorber is then modeled in the same way and it is evaluated whether the values of implementation parameters correspond with found locally optimal parameters. The model is then integrated to the model of the whole machine tool and the dynamical compliance is verified. The more detailed evaluation is consequently performed via co-simulations [10].

Acknowledgments. The present work has been supported by European Regional Development Fund in the framework of the research project NETME Centre under the Operational Programme Research and Development for Innovation. Reg. Nr. CZ.1.05/2.1.00/01.0002, id code: ED0002/01/01, project name: NETME Centre – New Technologies for Mechanical Engineering.

References

[1] Neugebauer, R., Denkena, B., Wegener, K.: Mechatronic Systems for Machine Tools. Annals of the CIRP 56(2), 657–686 (2007)

[2] Vetiška, J., Hadas, Z.: Using of Simulation Modelling for Developing of Active Damping System. In: International Symposium on Power Electronics, Electrical Drives, Automation and Motion, Sorrento, Italy, pp. 1199–1203 (2012)

[3] Banakh, L., Kempner, M.: Vibrations of mechanical systems with regular structure. Springer (2010)

[4] Brezina, T., Vetiska, J., Hadas, Z.: Simulation Modelling of Machine Tools with Flexible Parts as Mechatronic System. In: 6th Int. Conf. AIM, University of Defense, Brno, Czech Republic, pp. 99–104 (2011)

[5] Březina, T., Hadaš, Z., Vetiška, J.: Simulation Behavior of Machine Tool on the Base of Structural Analysis in Multi-Body System. In: Proc. 15th International Conference on Mechatronics, Mechatronika 2012, Praha, Czech Technical University in Prague, pp. 347–350 (2012)
[6] Brezina, T., Hadas, Z., Vetiska, J.: Using of Co-simulation ADAMS-SIMULINK for Development of Mechatronic Systems. In: Proc. 14th International Conference on Mechatronics, MECHATRONIKA 2011, Trenčín, TnUAD, Slovak Republic, pp. 59–63 (2011)
[7] Shabana, A.A.: Dynamics of Multibody Systems. Cambridge University Press (2005)
[8] Craig, R.R., Bampton, M.C.: Coupling of substructures for dynamics analyses. AIAA Journal 6(7), 1313–1319 (1968)
[9] Hadas, Z., Brezina, T., Andrs, O., Vetiska, J., Brezina, L.: Simulation Modeling of Mechatronic System with Flexible Parts. In: 15th International Power Electronics and Motion Control Conference and Exposition, EPE- PEMC 2012 ECCE Europe, LS2e.1/1-7 (2012)
[10] Brezina, T., Vetiska, J., Hadas, Z., Brezina, L.: Simulation, Modelling and Control of Mechatronic Systems with Flexible Parts. In: Jablonski, R., Brezina, T. (eds.) Proc. 9th Conf. Mechatronics 2011, pp. 569–578. Springer, Berlin (2011)

The Comparison of the Permanent Magnet Position in Synchronous Machine

P. Svetlik

University of West Bohemia in Pilsen, Faculty of Electrical Engineering,
Univerzitni 26, 306 14, Pilsen, Czech Republic
psvetlik@kev.zcu.cz

Abstract. This paper deals with positioning of permanent magnets in synchronous machine. The original electromagnetic design was calculated with permanent magnets mounted on the rotor surface. Using 2D finite element method modeling, the design results were reviewed and recalculated for different permanent magnet position. The possibility of ferrites instead of neodymium permanent magnets was also considered. However, the volume of these magnets must be several times higher than original neodymium ones.

1 Introduction

The permanent magnets are used in many different electrical machines nowadays. It is possible to find them in direct current, stepper, synchronous and many other machines. The strongest permanent magnet material is a well known compound of neodymium ($Nd_2Fe_{14}B$). The price of these magnets is higher in comparison with ferrite magnets.

Because of this, many scientists are trying to reduce the volume of rare-earth permanent magnets in general. One of the possible ways is lowering of rare-earth permanent magnets volume by suitable positioning. The other way is to use other types of magnets, ferrites for example. [2] [3]

The correct design of permanent magnets is a key matter in modern electrical machines. The influence of the magnet position itself could be very important in terms of the distribution of the magnetic flux density in the air gap. The focus of this paper is a comparison of three rotor geometries with a different position of permanent magnets and different types of permanent magnets. The fundamental harmonic component of air gap's magnetic flux density across all solutions is analyzed and compared.

2 The Finite Element Analysis

For further simulations an existing design of synchronous machine with permanent neodymium magnets with parameters listed below was used. For results' verification the fast Fourier analysis (FFA) was used [6].

T. Březina and R. Jabloński (eds.), *Mechatronics 2013*,
DOI: 10.1007/978-3-319-02294-9_36,

Table 1 Simulated motor parameters

parameter name	unit	value
Power	[kW]	45
Voltage	[V]	240
Nominal speed	[rpm]	400
Power factor	[-]	1,0
Air gap	[mm]	1.75
Air gap mag. flux density	[T]	0.95
Length of the armature	[mm]	185
Magnet width	[mm]	36
Magnet thickness	[mm]	8

2.1 The Original Solution

The original design was calculated for permanent magnets attached to the surface of the rotor. This mounting position is a very common solution used in full range of synchronous machines. The original design was modified for usage of higher type of permanent magnets, which affected obtained results [7] [10]. The fundamental harmonic component's magnitude results, according to accomplished fast Fourier analysis, near to 1.37 T (see fig. 2. and 3.) [6].

Table 2 Parameters of the neodymium magnet

magnet parameter	unit	value
Remanent mag. flux density	[T]	1.48
Coercive force	[kA/m]	891
Max. BH product	[kJ/m^3]	410

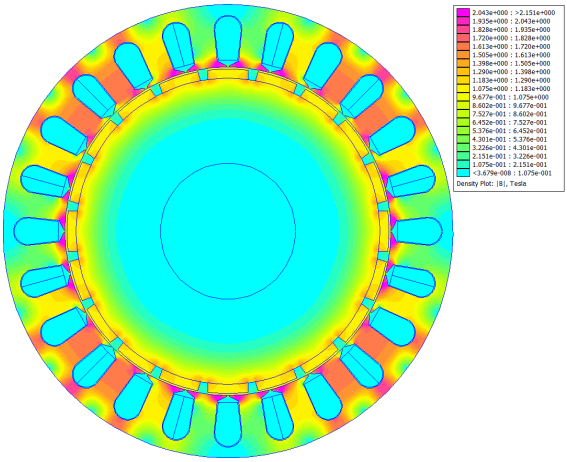

Fig. 1 The original solution with PM on the surface of the rotor

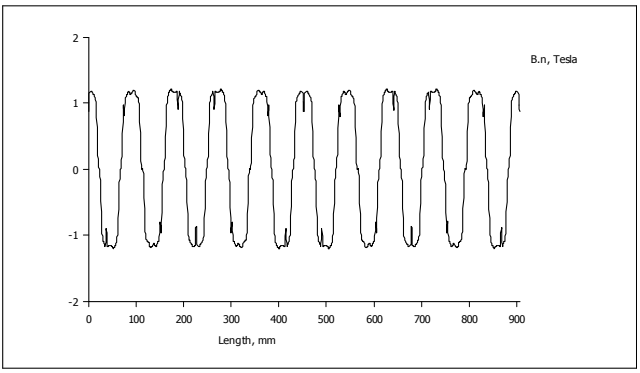

Fig. 2 The distribution of magnetic flux density in the air gap

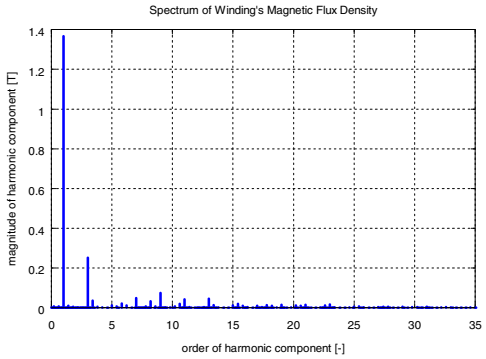

Fig. 3 The FFA of the original solution

2.2 The Usage of Interior Mounted Permanent Magnets

Another possibility is usage of the interior permanent magnet position. Several possibilities were tested with very promising results in comparison to original design [7][10]. The volume of originally calculated magnets was kept unchanged and magnets were put inside the rotor. Also the FFA [6] gives value of the fundamental harmonic component of the air gap magnetic flux density higher than 1.4 T.

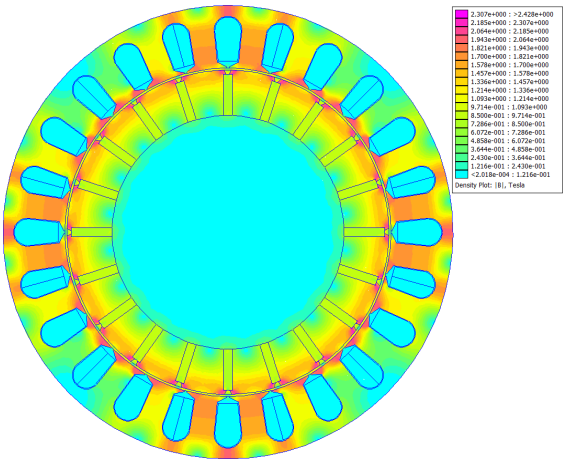

Fig. 4 The alternative solution with inner permanent magnets

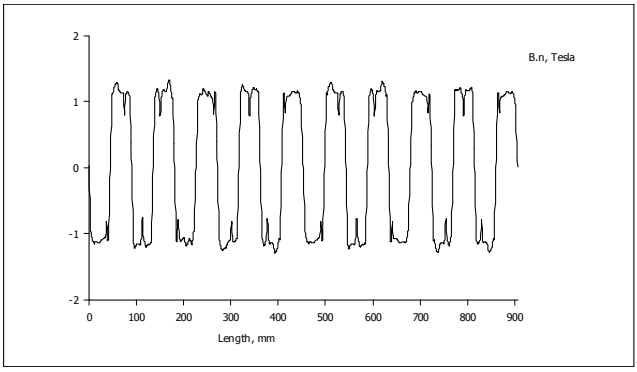

Fig. 5 The distribution of magnetic flux density in the air gap

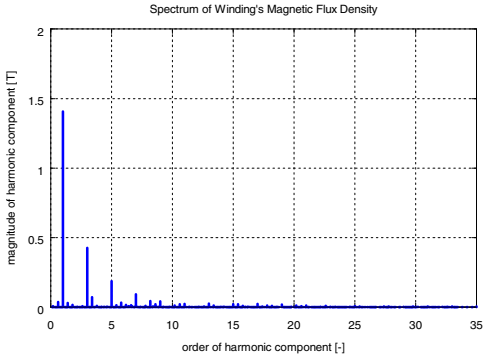

Fig. 6 The FFA of the alternative solution

This fact is caused by higher amount of power lines pervading the air gap and also by better distribution of power lines. Because of this higher value of magnetic flux density, it is possible to slightly reduce the volume of each magnet, which means lower cost of the machine. The comparison of the air gap magnetic flux density of these two solutions is shown in the fig.7.

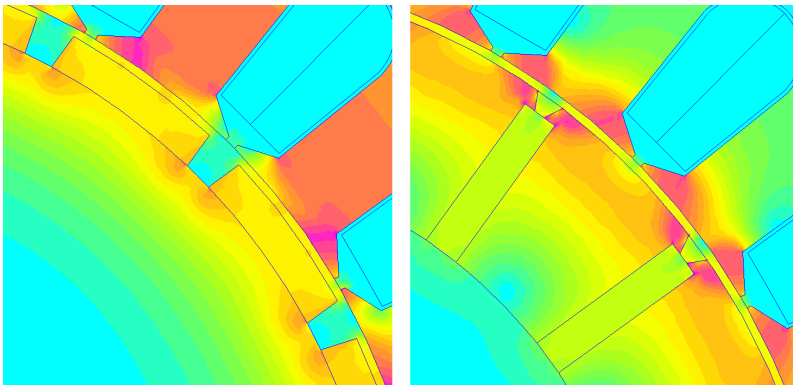

Fig. 7 The comparison of the distribution of magnetic field in the air gap and nearby elements

2.3 The Implementation of Ferrite Permanent Magnets

The usage of ferrite PM has many benefits. They are cheap, highly available and have higher work temperature in comparison to neodymium magnets. On the other hand, the remanent magnetic flux density of ferrite magnet is very low hence the volume of ferrite permanent magnets has to be several times higher than volume of rare-earth permanent magnets. According to calculations, the volume of this type of magnets would be bigger than the machine itself [5] [8]. For calculation the properties of ferrite permanent magnet type Y30BH were used.

Because of very high required volume of ferrite permanent magnets, the maximum possible volume of magnets was used for analysis of this solution. In this case the almost whole volume of the rotor is filled by permanent magnet material and only thin parts of rotor are used as rotor poles.

Table 3 Parameters of the ferrite magnet

magnet parameter	unit	value
Remanent mag. flux density	[T]	0.38
Coercive force	[kA/m]	238
Max. BH product	[kJ/m^3]	30

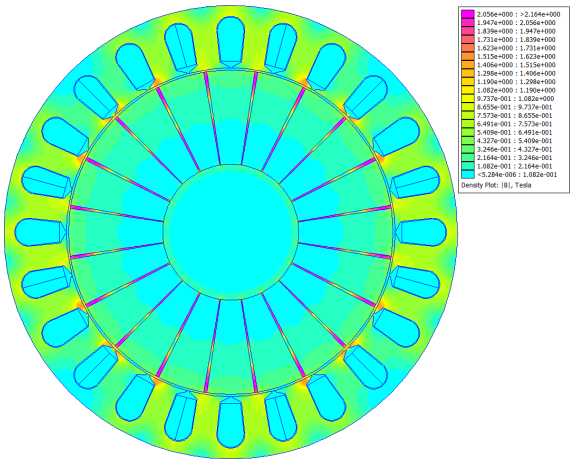

Fig. 8 Synchronous machine with ferrite magnets

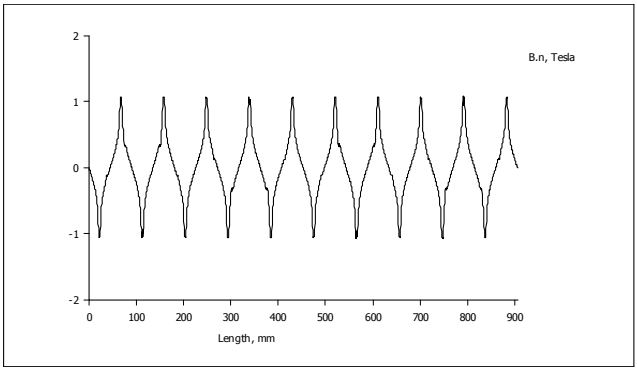

Fig. 9 The distribution of magnetic flux density in the air gap

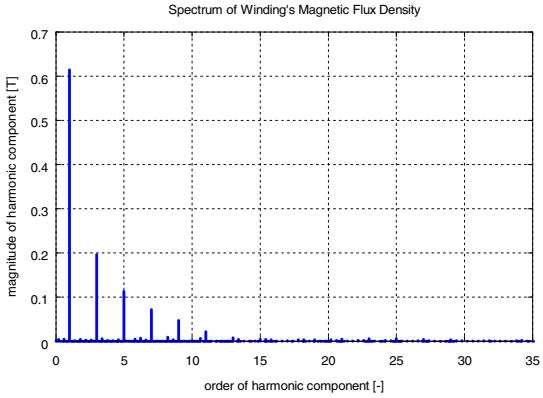

Fig. 10 The FFA of the ferrite solution

The maximum value of air gap magnetic flux density reaches values higher than 1T. However, these values could be found only in areas above the iron parts of rotor between magnets. The value of the fundamental harmonic component of magnetic flux density in the air gap is, according to FFA, slightly over 0.6 T only. The distribution of magnetic field is shown in the fig.11.

As seen from fig. 9, the magnetic flux density distribution along the air gap forms a row with triangular shape, which is not suitable for use in synchronous machines. This magnetic flux density dependence would cause unsuitable harmonic components in induced-back electromotive force resulting in problematic control of the machine. [1] [5] [11]

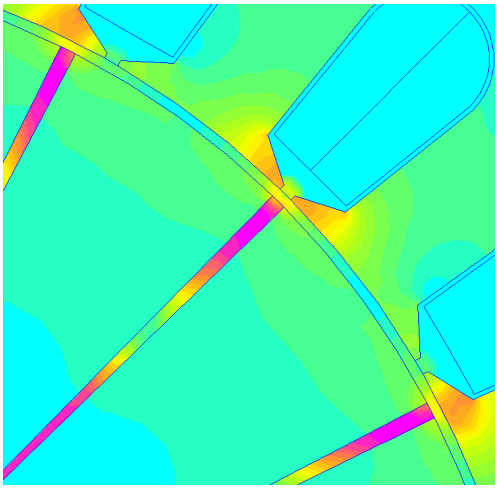

Fig. 11 The distribution of magnetic field in the air gap as provided by ferrite magnets

3 Conclusions

The solution of the permanent magnet synchronous motor, presented in this paper, shows that for machines with higher amount of poles with relatively small pole pitch are better to use inner storage of permanent magnets. It is caused by better cooperation of PM magnetic field. This leads to a higher value of the magnetic flux, which is able to pass through the air gap of the machine.

The usage of ferrite permanent magnets couldn't be recommended in this design, because of very low magnetic flux density provided by ferrite permanent magnets.

Acknowledgment. This paper was published with help of SGS project no.SGS-2012-071.

References

[1] Chunting, M., Filippa, M., Weiquo, L.: Analytical method for predicting the air gap flux of interior-tzpe permanent-magnet machine. IEEE Transactions on Magnetics 40(1), 50–58 (2004)
[2] Zhao, C., Wang, Y., Yan, Y.: The relation between pole pairs and air gap flux density, air gap flux respectively in IPM synchronous machine. IEEE Industrial Technology, 1325–1330 (2005) ISBN 0-7803-9484-4
[3] Petrov, I., Pyrhonen, J.: Performance of low-cost permanent magnet material in PM synchronous machine. IEEE Transaction on Industrial Electronics 60(6), 2131–2138 (2013)
[4] Bartoš, V.: Elektrické stroje, 2nd edn. University of West Bohemia, Pilsen (2004) ISBN 80-7043-332-9
[5] Hanselman, D.: Brushless Permanent Magnet Motor Design. Cranston, Rhode Island, The Writer's Collective (2003) ISBN 1 932133-63-1
[6] Eaton, J.W., et al.: GNU/Octave 3.6.2 (2012), `http://www.gnu.org/software/octave/`
[7] Meeker, D.C.: Finite element method magnetics, version 4.2 (October 11, 2010 Build) (2010), `http://www.femm.info`
[8] Hrabovcova, V., Jokinen, T., Pyrhonen, J.: Design of rotating electrical machines. Wiley, Great Britain (2008) ISBN 978-0-470-69516
[9] Kopylov, I.P., et al.: Design of electric machinery (Stavba elektrických strojů). SNTL, Prague (1988) ISBN 04-531-88
[10] Bianchi, N.: Electrical machine analysis using finite elements. Taylor & Francis, Boca Raton (2005) ISBN 0-8493-3399-7
[11] Di Barba, P., Savini, A., Wiak, S.: Field Models in Electricity and Magnetism. Springer, Berlin (2008) ISBN 978-1402068423

Air Gap Heat Transmission and Its Consideration in FEM Analyses

R. Pechanek, V. Kindl, and K. Hruska

University of West Bohemia, Faculty of Electrical Engineering, Regional Innovation Centre for Electrical Engineering, Univerzitni 26, 306 14, Pilsen, Czech Republic
{rpechane,vkindl,khruska}@rice.zcu.cz

Abstract. This article is aimed at thermal analysis of an induction machine, especially with focus on consideration of heat transmission in the air gap. Two modeling methods of heat transmission through the air gap are presented and compared to a measurement accomplished on a commonly produced induction machine available on the market.

1 Introduction

The design of an electric machine is inseparably bound with calculation of heat dissipation inside of the machine [1]. There are calculation methods, which more or less give results comparable to measured values, but in all case some simplifications have to be accepted [2-4].

The basic analytic calculation accomplished using thermal network [5] gives relatively good results for selected parts of the machine, but it is not suitable for general overview of heat dissipation. Such information may be obtained via finite element method [5]. Both methods – independently on calculation methodology – have to consider the transfer of heat the via air gap from the rotor to the stator packet [6]. The transfer of heat from the rotor to the stator is pursued by the air in the air gap. Since both machine's components do not have absolutely flat surfaces and they relatively move against themselves, the air forms turbulent motion (see Fig. 1), which is a very hard-to-analyze phenomenon [7].

The turbulent motion of the air [8] influences parameters important for successful calculation of the air gap heat transfer, above all the heat transfer coefficient and thermal conductivity of the air. These parameters are hard-to-consider in the finite element method analysis hence the conditions of the heat transmission through the air gap are in most cases simplified by using substitute conditions for heat transfer. This article compares two methods of substitution of air properties and compares their results with measured results.

T. Březina and R. Jabloński (eds.), *Mechatronics 2013*,
DOI: 10.1007/978-3-319-02294-9_37,

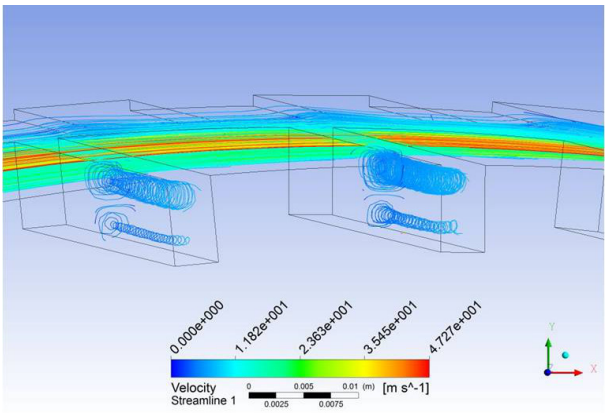

Fig. 1 Turbulent air flow in the air gap (result of CFD analysis)

2 Modeling of Air Gap Substituting Thermal Conductivity

The first method reduces consideration of three parameters – heat transfer coefficient, thermal conductivity and thermal capacity of the air – into one modified parameter without relation to real physical properties of the air. These properties are replaced by substitution thermal conductivity and the other physical properties are omitted. From physical point of view the resulting model considers air as a medium with absolute contact with both stator and rotor surfaces and infinite heat transfer coefficient between the air and the steel of the machine. The transfer of heat through the air gap is then influenced only by substitution thermal conductivity of the air [1].

The crucial parameter is in this case the substitution thermal conductivity of the air and its successful determination. In praxis this parameter is obtained by more-or-less empiric methods supplemented by measurements on manufactured machines. This method provides good results in steady state analyses, but it may lead to significant inaccuracies while analyzing a transient state of the machine, since it considers all parameters as invariant. These reasons do not make this method very suitable for virtual prototyping, but it provides sufficient results for machine's further analysis and optimization.

3 Air Gap Heat Transfer Modeling Using Averaged Temperature in the Air Gap

A different possibility is not to consider the thermal conductivity of the air at all. In this case the resulting FEM model does not need to have meshed air gap, since the air is modeled only by boundary conditions on surfaces of the stator and the rotor.

This approach calculates separately temperatures on stator and rotor, which are averaged and the resulting temperature is laid as boundary condition on the surfaces of both rotor and stator. Second boundary condition is the heat transfer coefficient which may be analytically pre-calculated. Since the relative speed of the air in the air gap is nearly equal in relation to stator and rotor, the heat transfer coefficient may be considered as equal on both surfaces. [1]

4 Theoretical Predictions and Measurement

4.1 Analytical Analyses of Induction Machine Temperature-Rise Test

The theoretical analysis of performed temperature-rise test is based on induction machine's equivalent in its Γ-form (see Fig. 2) [1]. Considering thermal dependencies of used material, both resistances of stator and rotor winding rise during the test. The rise of both stator and rotor resistances influences change of machine's working slip and consumption of input current. Using parameters of machine's equivalent circuit shown in Fig. 2 the machine's maximum torque slip moves to higher values mainly according to value of rotor temperature. These results offer a possibility of prediction of actual machine's working point.

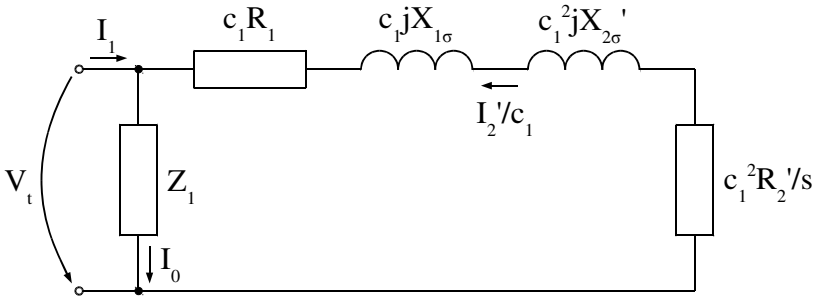

Fig. 2 Equivalent circuit of an induction machine in a Γ-form

Using thermal network method the temperatures of both stator and rotor resistances may be pre-calculated and using these values dependencies between machine's speed, current and temperature may be obtained (see Figs. 3 and 4). These results are also used as reference results for further accomplished finite element analyses and measurement.

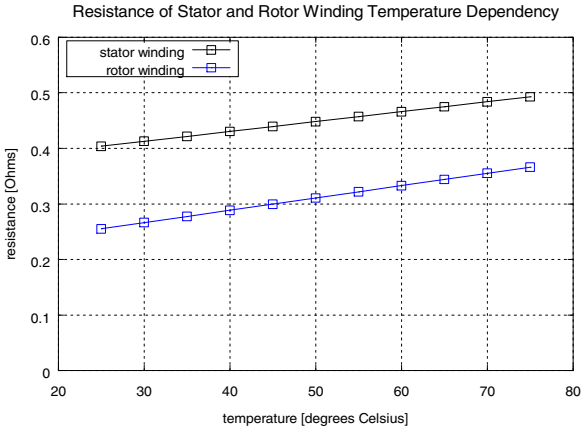

Fig. 3 Temperature dependencies of stator and rotor resistances

As seen from Figs. 3 and 4, together with rising temperature both values of stator and rotor resistances increase, which leads to slight lowering of machine's speed. The combination of both effects leads to relatively significant current drop and increase of machine's power factor. For the whole calculation machine's output torque is considered as constant.

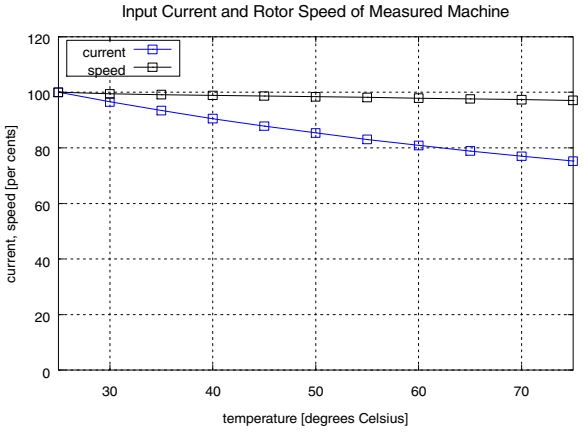

Fig. 4 Pre-calculated current and speed of selected induction machine

4.2 Coupled Electro-thermal Finite Element Analyses

Using results calculated in Section 4.1 two sets of coupled electro-thermal analyses have been prepared in ANSYS. These analyses themselves have been accomplished as weakly coupled [9-10], since both coupled tasks have ordinary different

values of time constants. From this point of view the electromagnetic parts have been considered as a series of harmonic analyses interleaved by transient thermal analyses performed according to a flow chart shown in Fig. 5. The result is then a time-dependency of temperatures in each part of the machine. A partial cross-section of designed FEM model is shown in Fig. 6.

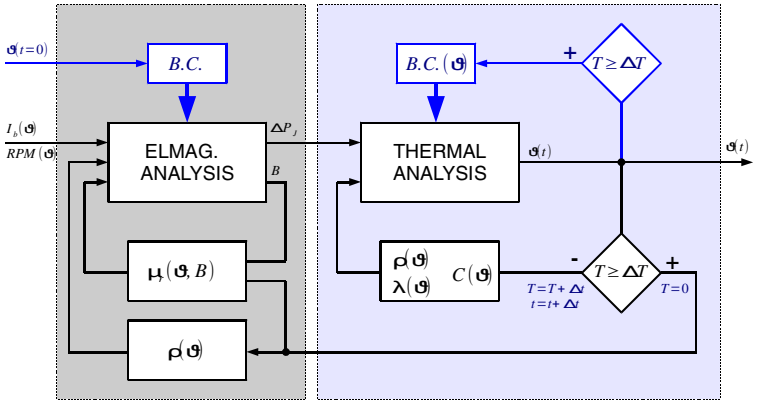

Fig. 5 Flow chart of performed coupled finite element analysis

For the purpose of comparison of results of both FEA methodologies mentioned in Sections 2 and 3 each set utilizes different definition of the air gap's air properties. Model set created according to methodology mentioned in Section 2 utilizes air defined by its thermal conductivity, which is constant during the whole thermal transient phenomena.

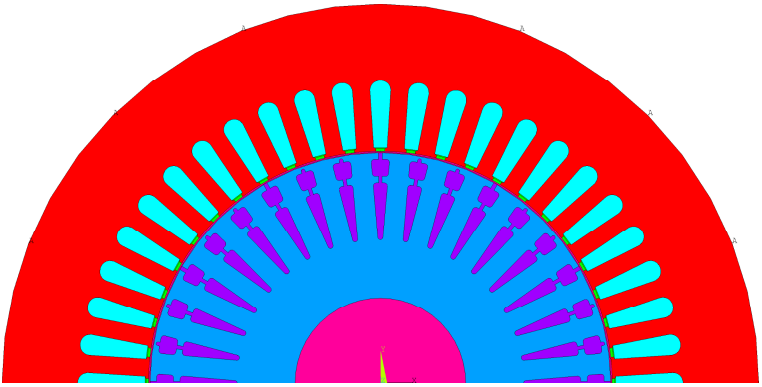

Fig. 6 Partial cross-section of designed finite element model

A model set created according to methodology mentioned in Section 3 lays on the surfaces of both stator and rotor a temperature averaged from the temperature conditions in stator and rotor respectively.

4.3 Measured Results

For the purpose of validation of obtained results a measurement stand has been set up consisting of studied induction machine SIEMENS 1LA7 163-4AA10 (11 kW output power) acting as motor and a direct current machine with external excitation acting as load (see Fig. 7). The temperature-rise test took circa 11 000 seconds long period, in which temperatures of aluminum cast frame and stator winding have been measured (shown in Fig. 8). Further measured values included currents and voltages in each phase, torque and speed of the machinery.

The measured induction machine has been supplied by a frequency inverter with sine filter [11] and slip compensation. These parameters avoid additional heating by higher order harmonic components generated by the inverter and ensure constant speed of the machine during the whole test. The torque produced by the DC machine (load torque) was not regulated during the test. Measured results and their comparison with theoretically predicted and modeled values are shown in Fig. 9.

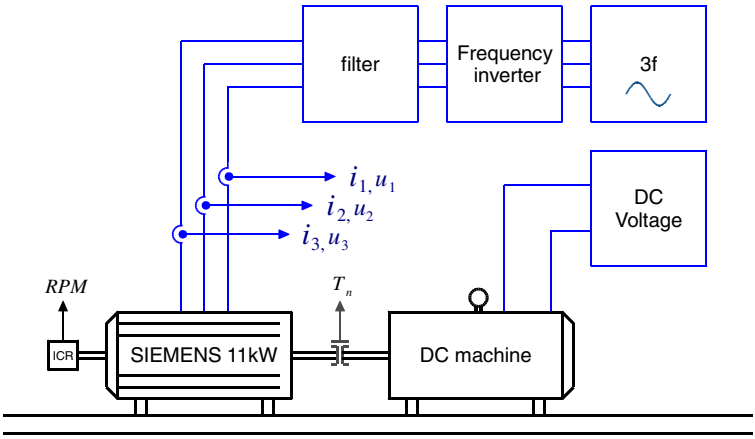

Fig. 7 Measured machinery arrangement

Measured results confirm long time constant of the whole warm-up test. After 10,200 seconds (circa 3 hours) the temperature of aluminum cast frame stabilized at 43.2 degrees Celsius, while the temperature of stator winding rose to nearly 74 degrees Celsius. As seen from Fig. 9, at the end of temperature-rise test in stabilized state both methodologies give similar results to measured values. During the transient part of the phenomena the traditional method shows temperature rise higher than measured values forming a slight overshoot. The results calculated using methodology described in Section 3 by contrast copies measured values.

The measurement of electrical values confirms significant drop of current of measured machine. The value of the current measured at the beginning of the temperature-rise test results 21.1 A and at the end of transient thermal phenomena it

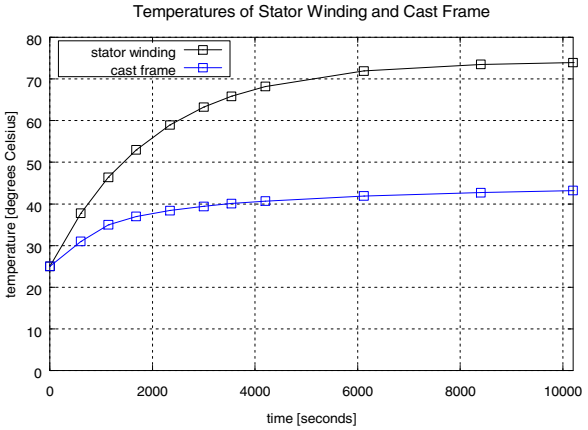

Fig. 8 Measured temperatures of stator winding and aluminum cast frame

stabilizes at 18 A, which means a drop to 85.3 per cents of original value. In comparison to predicted values, which give current drop from 21.5 A to 16.16 A, the current drop is slightly lower than really measured values and it furthermore influences results from finite element models. The differences between calculated and measured results are in this case mainly caused by slip compensation and high sensitivity of calculations in Section 4.1 on slip.

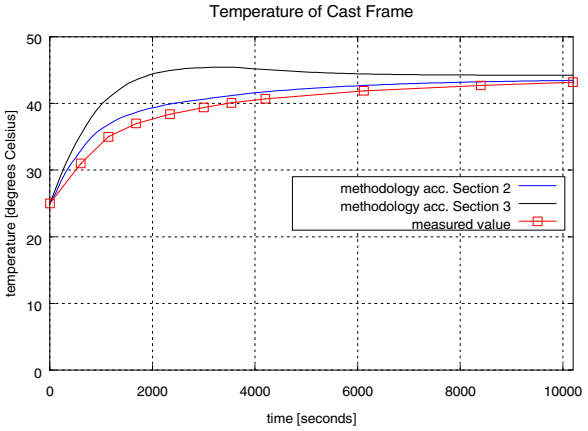

Fig. 9 Comparison of measured and calculated cast frame temperatures

5 Conclusions

The presented paper introduces a comparative study on modeling of air gap in the finite element method calculations and compares two available methods with

measured data. The comparison between both methods shows, that the methodology described in Section 3 does not produce overshoot in transient states and offers better correspondence with measured results. It also eliminates calculation error due to variability of used thermal conductivity of air. From the point of view of finite element method this methodology leads to reduction of elements of final model, since the air in the air gap is not meshed. This fact leads to reduction of model's element amount and therefore to decrease of computation time.

Acknowledgments. This research has been supported by the European Regional Development Fund and the Ministry of Education, Youth and Sports of the Czech Republic under the Regional Innovation Centre for Electrical Engineering (RICE), project no. CZ.1.05/2.1.00/03.0094, funding program SGS-2012-071 and UWB's Motivation system, component POSTDOC.

References

[1] Bolde, I., Nasar, S.A.: The Induction Machine Handbook. CRC Press (2001) ISBN: 978-0-8493-0004-2

[2] Vlach, R.: Thermal modelling of powerful traction battery charger. In: Mechatronics Recent Technogical and Scientific Advances, pp. 175–184 (2011) ISBN 978-3-642-23243-5

[3] Zhang, P., Du, Y., Habetler, T.G.: A Transfer-Function-Based Thermal Model Reduction Study for Induction Machine Thermal Overload Protective Relays. IEEE Transactions on Industry Applications 46(5), 1919–1926 (2010)

[4] Vlach, R.: Heating Prediction of Electric Machine Using Neural Network. In: MENDEL 2010 - 16th International Conference on Soft Computing. Brno, pp. 298–302 (2010) ISBN 978-80-214-4120-0

[5] Cannistra, G., Labini, M.S.: Thermal analysis in an induction machine using thermal network and finite element methods. In: Fifth International Conference on Electrical Machines and Drives (Conf. Publ. No. 341), September 11-13, pp. 300–304 (1991)

[6] Boglietti, A., Cavagnino, A., Staton, D.: Determination of Critical Parameters in Electrical Machine Thermal Models. IEEE Transactions on Industry Applications 44(4), 1150–1159 (2008)

[7] Li, W., Guan, C., Chen, Y.: Influence of Rotation on Rotor Fluid and Temperature Distribution in a Large Air-Cooled Hydrogenerator. IEEE Transactions on Energy Conversion 28(1), 117–124 (2013)

[8] Yan, H., Xiong, N.: Study on the gas-flow in the air-gap of evaporation cooling motor. In: Sixth International Conference on Electrical Machines and Systems, ICEMS 2003, November 9-11, vol. 2, pp. 907–910 (2003)

[9] Bastos, J.P.A., Sadowski, N.: Electromagnetic Modeling by Finite Element Method. Marcel Dekker (2001) ISBN: 0824742699, 9780824742690

[10] Tan, C.M., Li, W., Gan, Z., Hou, Y.: Applications of Finite Element Methods for Reliability Studies on ULSI Interconnections. Springer (2011) ISBN: ISBN 978-0-85729-310-7

[11] Cetin, N.O., Hava, A.M.: Compatibility Issues Between the Filter and PWM Unit in Three-Phase AC Motor Drives Utilizing the Pure Sine Filter Configuration. IEEE Transactions on Industry Applications 47(6), 2559–2569 (2011)

Problems of FEM Analysis of Magnetic Circuit

J. Roupec, M. Kubik, I. Mazůrek, and Z. Strecker

Brno University of Technology, Faculty of Mechanical Engineering,
Institute of Machine and Industrial Design, Technicka 2, 616 69, Brno, Czech Republic
roupec.j@fme.vutbr.cz

Abstract. This paper compares four different approaches to modeling of magnetic circuit in the ANSYS software. The approaches differ in various inputs of magnetic field source and varying levels of axial symmetry. The accuracy and the solution time were the main evaluation criteria. The analysis was performed on a simple magnetic circuit. The analysis results were compared with measurements on experimental device that was made for this purpose. The results show that planar solution in ANSYS Classic is the fastest and the highly accurate approach. The problem solution such as 3D axisymmetric task with the definition of magnetic field source with the stranded type is the most accurate, but more time-consuming.

1 Introduction

Analysis and synthesis of magnetic circuit were recently (1990) predominantly solved analytically or empirically. With the development of computer technology, the trend of computations has gradually shifted to the Finite Element Method (FEM). The solution of real magnetic circuits is time-consuming also for today's powerful computers, because most of the magnetic circuits are solved with material nonlinearity. Therefore, a simplified model of the solved magnetic circuit is created in Finite Element Analysis (FEA). As with any model, it is necessary to identify the impact of simplification on the accuracy of the results. Mei et al. approached to the solution of magnetic circuit using 2D axisymmetric geometry in FEM system ANSYS [1]. They used *quadrilateral* elements and applied the load by the current density on the cross-section of the loading coil. Cong et al. from Dalian University of Technology in China chose a similar approach [2]. The authors chose again the FEM system ANSYS and simplified a model using 2D axisymmetry. Lozada used the freely available FEM software FEMM Foster [3]. Approach to the solution of the model was the same as in the previous two cases using 2D axisymmetry. Yatchev et al. created the FEM model using Ansys Parametric Design Language (APDL) [4]. They created a fully parameterized 3D model of magnetic circuit with *tetrahedral* elements. The boundary condition was applied using a flux-parallel boundary. Ciocanel from Northern Arizona University used the FEM software Maxwell [5]. He used both 2D and 3D module of this program to model the magnetic circuit.

T. Březina and R. Jabloński (eds.), *Mechatronics 2013*,
DOI: 10.1007/978-3-319-02294-9_38,

In the well-known literature, no one has published a comparison of different, above mentioned approaches. This paper compares these approaches to FEM analysis of magnetic circuit in terms of solution time and accuracy.

2 Methods

Tasks are divided, depending on the geometry of the solved problem, into three main groups, namely the problems solved as planar (2D axisymmetry), three-dimensional with rotational symmetry (3D axisymmetry) and three-dimensional (fully 3D), see Fig.1. There is shown a *path*, for which results of magnetic flux density will be obtained.

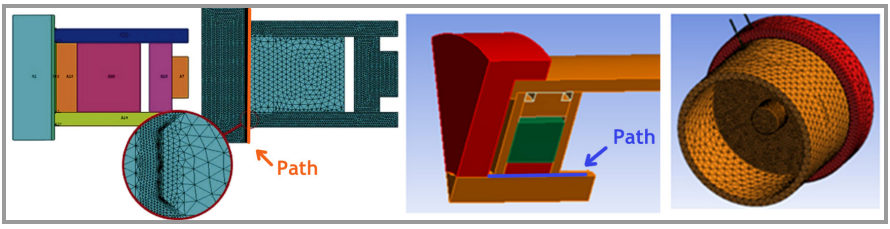

Fig. 1 (a) 2D axisymmetry; (b) 3D axisymmetry; (c) fully 3D

Models were created using finite element method in ANSYS Workbench 13. The analysis results were compared with experimental data to determine which model describes the distribution and size of the magnetic flux density in the working gap of the magnetic circuit best. For this purpose, a test magnetic circuit with a centering fixture was designed. It is a simple MR node that has air in the working gap. The groove for measuring sensor was manufactured in the shaft. The experiments were carried out with teslameter FW BELL TECTRA 5180 with an ultra-thin probe STD18-0404. When evaluating the accuracy of the model, the maximums of magnetic flux density in the measuring groove (*path*) were compared, because the magnetic flux density is measureable only in this one point of the circuit. The measured maximum of magnetic flux density was a default value (100%).

Nonlinear material of steel, described by the B-H curve (Fig. 2), was selected for the material of magnetic circuit. It is a steel AISI 1018, which is the most similar in material characteristics to used low-carbon steel ČSN 11 523 (Fig. 1 - orange color). In test device, aluminum alloy was also used (relative permeability 1 - red color) and the coil was wound from copper wire (green color). The entire model was surrounded by air using the tool *Enclosure*.

907,164 nodes and 673,883 elements with *tetrahedron* form were used on discretization. This number of elements is chosen as a computing limit for available PC with using of direct solver. This is particularly limiting for fully 3D model. SOLID117 element was used as the only possibility (assigned by SW). It is a 20 nodal element. The magnetic circuit had the elements of mesh with a size of 1 mm

and shaft geometry 1.2 mm. On the other part of the test device, element with a size of 3 mm was used. In the groove for sensor, the mesh was refined in a sphere area with a radius of 3 mm. Elements of refinement were 0.25 mm size. Methods *Aspect Ratio* (2.73) and the *Skewness* (0.28) were used to assess the quality of created mesh.

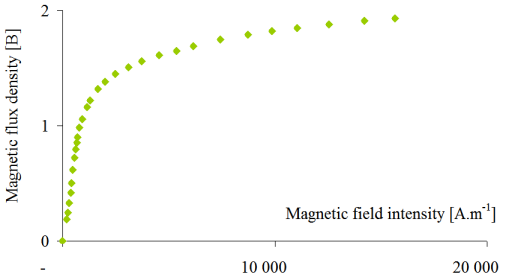

Fig. 2 B-H curve of AISI 1018

2.1 3D Axisymmetric Model – Stranded Source Conductor

The magnetic field applied to the model was specified using the option *conductor type - stranded*. This option represents the wound coil. This approach works with different distribution of current density in the coil section in accordance with the actual geometry. In ANSYS HELP, there is noted that the conductor still computes a current distribution according to the physics of a solid conductor, but in many cases the resulting current density distribution will not significantly affect the computed magnetic field results. Into the *source conductor* parameters, both the number of turns in the coil (118) and current (3.36 A) were assigned. It was also necessary to assign a parameter *Conducting area*. For an accurate calculation, it was assigned the cross section, which is filled by the winding in the tightest configuration of threads, and not cross section of the entire reserved space for the coil. Figure 3 shows the distribution and size of magnetic flux density throughout the entire model with the current 3.36 A.

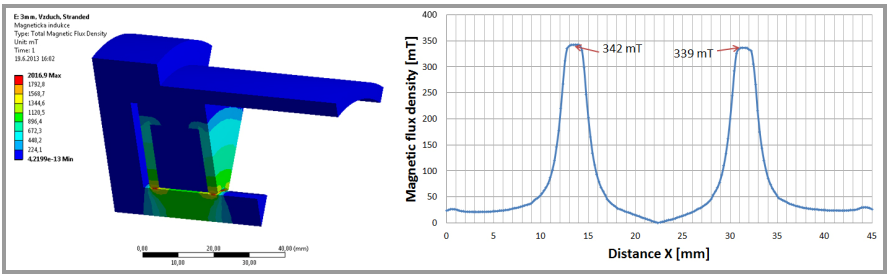

Fig. 3 Stranded coil – magnetic flux density distribution

2.2 3D Axisymmetric Model – Solid Source Conductor

The coil is in this model assigned as a *solid* body. Source of the magnetic field can be set in two ways: (i) by the voltage drop at two terminals of a conductor body, (ii) by grounding one end of a conductor (set voltage to zero) and applying the net current at the terminal's other end. The second option was chosen because the electric current was measured during the experiment more accurately than the resistance. Grounded zero potential (0 V) was set on one termination of conductor at symmetry plane of the coil and the exciting current (3.36 A) was set on the second termination. The number of turns is the same as in the case of *stranded coil* (118). In the case of the *solid* body it is allowed to specify the number of threads 1 (as is represented by the model geometry), but it is necessary to proportionally increase the load current according to formula $U_m = I.z$, where I is current, z is the number of threads and U_m is Magnetomotive voltage. Figure 4 shows the distribution and size of magnetic flux density throughout the entire model with the current 3.36 A.

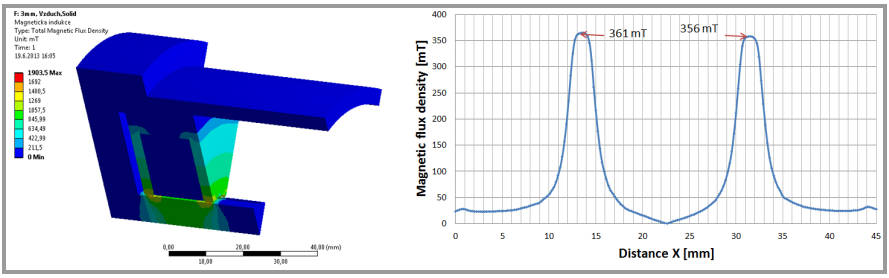

Fig. 4 Solid coil – magnetic flux density distribution

2.3 2D Axisymmetric Model – Current Density

This model was created using the APDL script in ANSYS. In this case the mesh is different to above mentioned models. Discretization was done using 8,759 nodes and 16,998 triangular elements. Planar, 4 nodal element PLANE13 was used. It is a linear element as SOLID117. Analysis was done with the element PLANE53, but the difference with the same number of elements was negligible (1mT). Loading of model was implemented through the current density. The value of the current density was calculated from the exciting current I, the number of turns in the coil N and the cross-section of coil S according to relation (1):

$$J = \frac{N \cdot I}{S} = \frac{118 \cdot 3{,}36}{224} = 1{,}77 \frac{A}{mm^2} \tag{1}$$

Source of the magnetic field specified by the current density is in principle the same as entering *Stranded source conductor body* in the Workbench environment. Figure 5 shows the distribution and size of magnetic flux density throughout the entire model with the current 3.36 A.

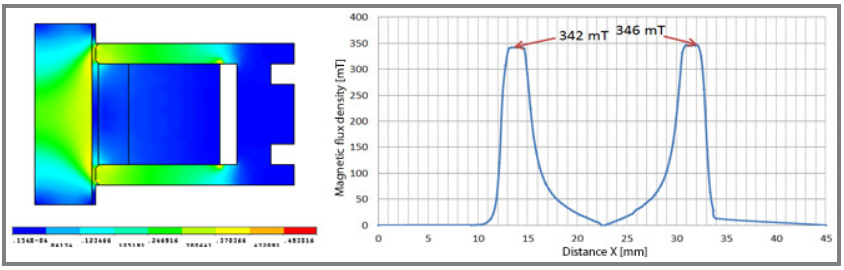

Fig. 5 2D axisymmetry – magnetic flux density distribution

2.4 Full 3D Model – Solid Source Conductor

This model was created with the full 3D geometry. The real geometry of the coil was replaced by the model coil. Model coil has 5 turns and it is modeled on the mean diameter of the real coil (Fig. 6). Model coil can be designed also as a single-thread, but in this case the distribution of current density is not too accurate. In the past, there were done several analyses that compared the model coils in different levels of simplification. Furthermore, it was found that the number of turns in the geometric model does not affect results if appropriate value of ampere-turns is specified.

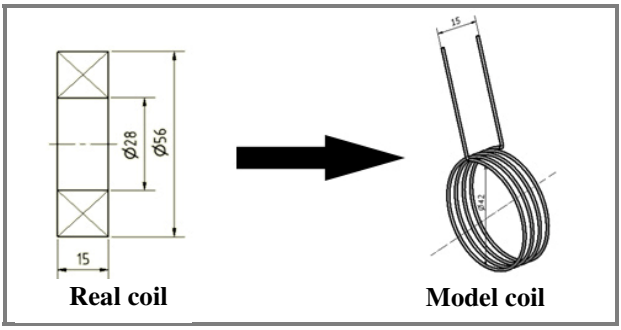

Fig. 6 Fully 3D model – replacing the real coil with the model coil

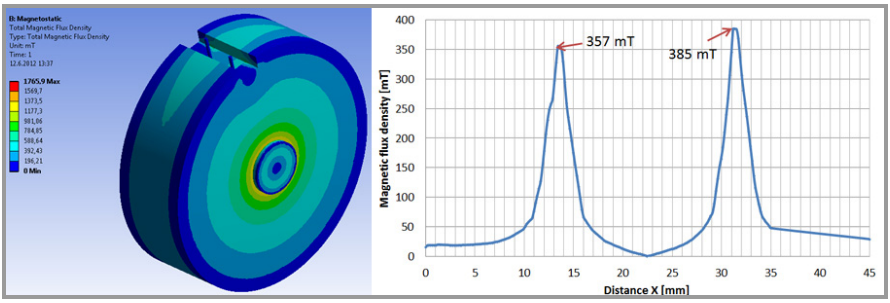

Fig. 7 Fully 3D model – magnetic flux density distribution

With the new fully 3D geometry, a new mesh was created. Discretization was done using 986,000 nodal points and 732,000 *tetrahedral* elements. Element SOLID117 was used. Source of magnetic field (source conductor) was set to a solid and defined by the zero potential (ground) and by the current on the both terminations of coil conductor. Proportionally to the lower number of turns (5) towards the real coil (118), it was necessary to adjust the amperage from 3.36 to 79 A. Figure 7 shows the distribution and size of magnetic flux density throughout the fully 3D model with the current 3.36 A.

3 Results

Table 1 compares the individual FE models with the measurement results according to the number of elements, solution time and maximal magnetic flux density. 3D axisymmetric models are marked as *stranded* and *solid* with the corresponding entering of the magnetic field source. All analyses show a higher magnetic flux density than what was actually measured. Magnetic flux density in the table is the maximum from the entire course of *path*. Models with setting of the magnetic field using current density (*Stranded* and *2D* models) are the closest to the measured values. The fully 3D model could be more accurate if the mesh was finer. But it was not possible due to the use of available PC.

Table 1 Compared the results of FEM analysis and experiment

	Stranded	Solid	2D	3D	Experiment
Number of elements	673 883	673 883	16 998	732 000	-
Solution time	20 min	21 min	15 sec	35 min	-
Max. flux density	342 mT	361 mT	348 mT	385 mT	328 mT
Difference	104%	110%	106%	117%	100%

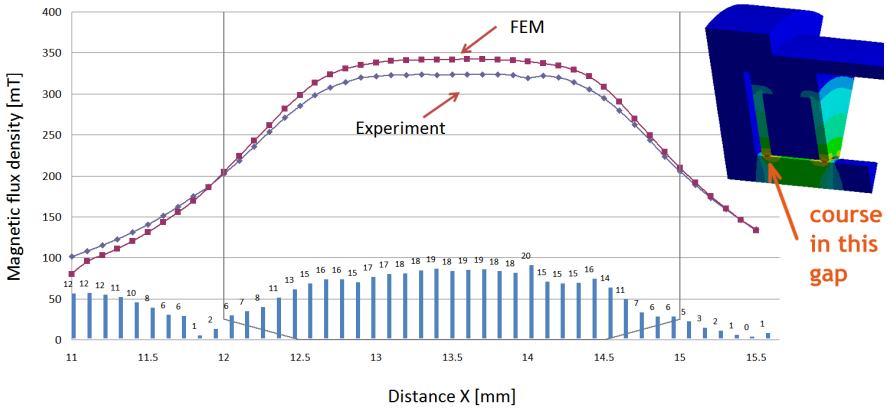

Fig. 8 Courses of magnetic flux density – FEM analysis (red); measurement (blue)

Figure 8 shows the measured flux density course and results of the analysis of model Stranded under the one edge of magnetic circuit. The courses are to some extent equal.

4 Conclusions

According to Table 1, s*tranded* FE model was evaluated as the most accurate. However, the 2D model is also very close to the measurement results and solution time is significantly shorter. Regarding to the possibility of assigning a various magnetic field source, it can be concluded that the most accurate results are achieved through precise definition of current density. In the process of designing of MR node, it is suitable for fast proposal of solution to use a 2D model in classic ANSYS. Also freely available software FEMM uses the same approach to solving and assignment of the magnetic field source. On the other side, for the final geometry optimization of MR node, it is preferred to use the ANSYS Workbench. This environment allows performing a sensitivity analysis of dimensions. Parametric input of any dimension of magnetic circuit using a table allows determining its effect on the resulting flux density. Thus more efficient circuit can be designed. Sensitivity analysis can be also used to define the tolerance of the individual dimensions. If the geometry of the magnetic circuit exhibits axis symmetry, it is suitable, in terms of accuracy of solution, to model a circuit as 3D axisymmetric and specify the magnetic field source as *Stranded coil*. Otherwise, it is necessary to select the 3D model. In any case, the solution time can be greatly decreased by the choice of a *direct* solver. It has, however, limitations in the number of elements, depending on the size of the memory of computer station.

Acknowledgments. This work was developed with the support of the grants ED0002/01/01, GAČR 13-31834P and CZ.1.07/2.3.00/30.0039.

References

[1] Mei, D., Kong, T., Shih, A.J., Chen, Z.: Magnetorheological fluid-controlled boring bar for chatter suppression. J. Mater. Process. Tech. 209(4), 1861–1870 (2009)
[2] Cong, M., Dai, P., Shi, H.: A Study on Wafer-Handling Robot with Coaxial Twin-Shaft Magnetic Fluid Seals. In: Xie, M., Xiong, Y., Xiong, C., Liu, H., Hu, Z. (eds.) ICIRA 2009. LNCS, vol. 5928, pp. 1123–1137. Springer, Heidelberg (2009)
[3] Lozada, J., Roselier, S., Periquet, F., Boutillon, X., Hafez, M.: Mechatronic Systems, Applications – ch. 12, pp. 187–212. InTech, India (2010)
[4] Yatchev, I., Ilieva, N., Hinov, K.: 3D Finite Element Modelling of a Permanent Magnet Linear Actuator. Serb. J. Electr. Eng. 5(1), 99–108 (2008)
[5] Ciocanel, C., Nguyen, T., Elahinia, M.: Design and modeling of a mixed mode magnetorheological (MR) fluid mount. In: Proc. SPIE, vol. 6928, p. 10 (2008)

FEM Model of Induction Machine's Air Gap Force Distribution

J. Sobra and V. Kindl

University of West Bohemia in Pilsen, Faculty of Electrical Engineering, Univerzitni 26, 306 14, Plzen, Czech Republic
{jsobra,vkindl}@kev.zcu.cz

Abstract. This paper deals with the forces acting in the air gap of an induction machine. The theoretical force distribution around the air gap is described. That is performed by the variable permeance of the magnetic circuit. Different permeance of both, the stator and the rotor slots and teeth is respected. An analytical calculation of Lorentz force acting on the rotor bars is presented. The 2D FEM model of squirrel cage induction machine is used for a calculation of the Maxwell force distribution in the air gap. That is realized by computing forces acting on the stator and the rotor teeth. The method used for the calculation is Maxwell Stress Tensor.

1 Introduction

The air gap force distribution [1, 2, 3] has a significant influence on the induction machines operation. That influence can be positive (making the torque) or negative as well [1]. For example, the forces acting in the air gap can excite the motor frame or the stator core vibrations [4, 5, 6]. There is also possibility of unbalanced magnetic pull, in case of eccentric or bent rotor.

The induction machine's air gap magnetic field is affected by many factors. These factors concern especially the slot harmonics caused by the stator and the rotor slotting and the harmonics of the magnetomotive force (MMF) of both windings [1].

A number of papers dealing with the air gap field calculation have been presented. Heller, Hamata [1] and Heller, Jokl [7] have calculated the air gap flux density as the product of permeance and the MMF. That calculation has considered MMF harmonics, rotor angular velocity, time and both; stator and rotor slotting.

However, the FEM model is valid for conditions defined below. For this reason, the equations presented in [1] and [7] are slightly simplified in this paper.

1.1 Flux Density in the Air Gap

The permeance value of the induction machine's magnetic circuit varies around the air gap circumference periodically. That is caused by different permeability in

T. Březina and R. Jabloński (eds.), *Mechatronics 2013*,
DOI: 10.1007/978-3-319-02294-9_39,

the stator and the rotor slots and teeth. Due to permeability, flux density in the air gap changes as well and it can be computed as a product of the MMF and permeance. In this calculation, the MMF harmonics, rotor angular velocity and stator radian frequency are neglected.

For a symmetrical three-phase stator winding the MMF fundamental is obtained by

$$F_1(x) = A_p \sin\left(px\right) \tag{1}$$

where A_p - maximum value of working wave, p - number of pole pairs and x - radian space location along the inner bore diameter of the stator.

Provided fixed position between the rotor and the stator; the air gap permeance including both the rotor and the stator slotting is given by

$$\Lambda(x) = c_0 + c_1^{'} \cos\left(Q_1 x\right) + c_1^{''} \cos\left(Q_2 x\right) \tag{2}$$

where

$$c_0 = \frac{1}{\delta k_{c1} k_{c2}}$$

$$c_1^{'} = \frac{1}{\delta k_{c2}} \beta\left(\frac{b_s}{\delta}\right) F_1\left(\frac{b_s}{t_s}\right)$$

$$c_1^{''} = \frac{1}{\delta k_{c1}} \beta\left(\frac{b_r}{\delta}\right) F_1\left(\frac{b_r}{t_r}\right)$$

and Q_1, Q_2 - number of stator/rotor slots, k_{c1}, k_{c2} - Carter coefficient of stator/rotor winding, δ - air gap length, b_s, b_r - width of stator/rotor slot opening, t_s, t_r - stator/rotor slot pitch and $\beta\left(\frac{b_s(b_r)}{\delta}\right), F_1\left(\frac{b_s(b_r)}{t_s(t_r)}\right)$ - coefficients given by characteristics in [7].

Finally, the flux density in the air gap caused by MMF fundamental and both stator and rotor slotting is obtained by

$$\begin{aligned} B(x) &= F(x)\Lambda(x) = A_p c_0 \sin\left(px\right) \\ &-\frac{1}{2} A_p c_1^{'} \left[\sin\left(\left(p - Q_1\right)x\right) + \sin\left(\left(p + Q_1\right)x\right)\right] \\ &-\frac{1}{2} A_p c_1^{''} \left[\sin\left(\left(p - Q_2\right)x\right) + \sin\left(\left(p + Q_2\right)x\right)\right] \end{aligned} \tag{3}$$

1.2 *Lorentz Force Calculation*

Based on the previous calculation, an analytical examination of Lorentz part of the force can be performed. The rotor current waveform is given by

$$I = I_m\left[\cos\left(Q_{2n}\xi+\varphi\right)+i\sin\left(Q_{2n}\xi+\varphi\right)\right] \tag{4}$$

where $$\xi = \frac{2\pi}{Q_2 p}$$

and I_m - rotor current amplitude, Q_{2n} - rotor bar number, φ - phase shift angle.

When the rotor current waveform is known, the Lorentz forces acting on the rotor bars can be determined [8]. In the Fig. 1, the Lorentz force distribution in the air gap and the force values acting on the rotor bars are shown. The values in the Fig. 1 correspond with the modeled machine.

It is obvious that the Lorentz force is negligible in comparison with the Maxwell one (Fig. 3 and Fig. 4). Considering the shape of the stator slots and the rotor bars, an exact analytical solution of the Maxwell force is impossible to derive. In the case of double squirrel cage especially. By this reason FE analysis is very useful way to determine the Maxwell force.

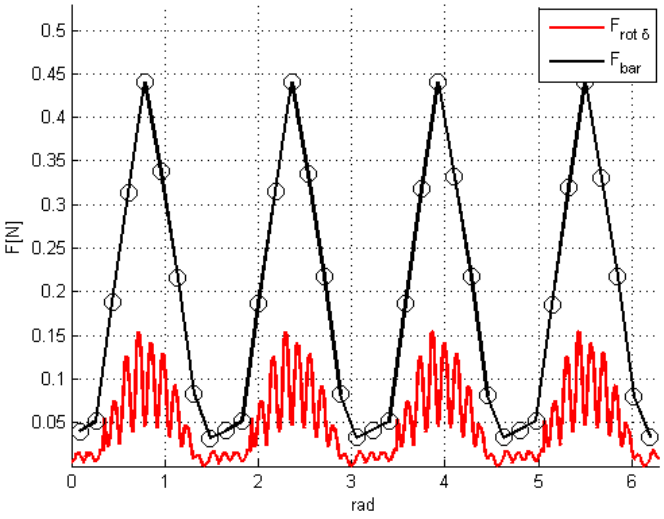

Fig. 1 Lorentz force in the air gap and force acting on the rotor bars

1.3 Model Description

For an accurate calculation of the air gap force distribution for specific machine geometry, the 2D FEM model of 4-pole, 11kW SIEMENS 1LA7 163-4AA10 induction machine is presented. The motor's power plate can be found in the Table 1. The model is valid for a steady nominal state and for fixed position between the rotor and the stator. Change of the rotor rotation angle for a new calculation is possible. The motor has 48 slots on the stator and 36 slots on the rotor. Geometry of the one motor's pole pitch is shown in the Fig. 2.

Table 1 Modeled motor's power plate

parameter name	unit	value
Power	[kW]	11
Voltage Δ / Y	[V]	230/400
Current Δ /Y	[A]	37.3/21.5
RPM	[min^{-1}]	1460
Number of poles	[-]	4
cos φ	[-]	0.84

Fig. 2 Model geometry

1.4 Air Gap Force Distribution

Forces acting in the air gap are calculated in the nodes of high permeance parts of the magnetic circuit, which are surrounded by the air. For the calculation,

Maxwell Stress Tensor method is used. That method is commonly used for a force calculation on the borderline of two materials with different permeability. For a 2D analysis of forces acting on the ferromagnetic material – air borderline, total force can be expressed by [9, 10]

$$F_m = \frac{1}{\mu_0}\int_S \left[\begin{pmatrix} B_x^2 - \frac{1}{2}|B|^2 & B_x B_y \\ B_x B_y & B_y^2 - \frac{1}{2}|B|^2 \end{pmatrix} \right] \begin{Bmatrix} n_x \\ n_y \end{Bmatrix} dS \tag{5}$$

where F_m - total force acting on the object, which surface is S, μ_0 - permeability of air, B_x, B_y - flux density components in the Cartesian coordinate system, $|B|$ - absolute value of flux density vector, n_x, n_y - components of the normal unit vector of the surface.

Directly on that borderline, relatively high flux density evaluation error can occur. By this reason, the air gap force is evaluated in the center of the air gap [11].

In the following figures, the force distribution in the modeled motor is presented. Forces acting on the stator (Fig. 3) and the rotor (Fig. 4) teeth are shown there. The forces are transformed to the cylindrical coordinate system. The fact that the stator forces act against the rotor ones is obvious.

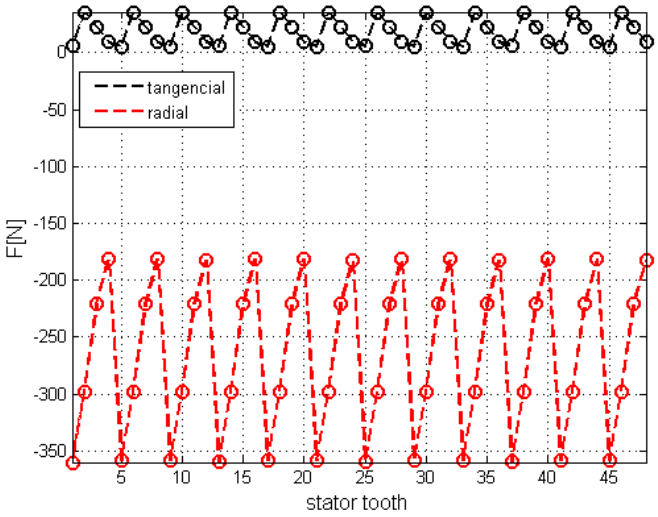

Fig. 3 Radial and tangential force components acting on the stator teeth

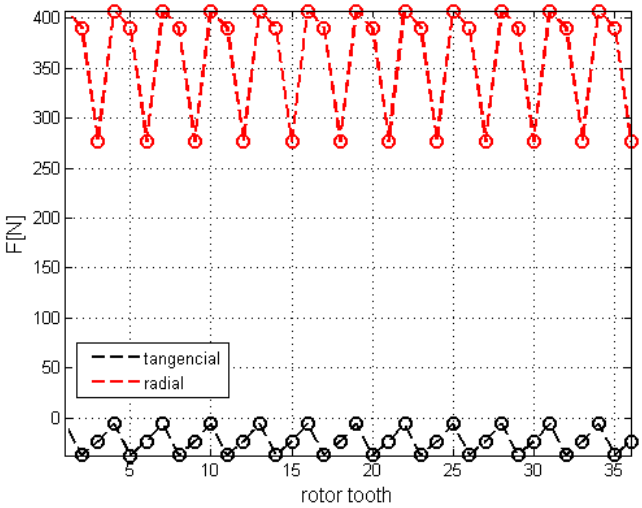

Fig. 4 Radial and tangential forces acting on the rotor teeth

2 Conclusions

The air gap field of induction machine for fixed position between the rotor and the stator is described in this paper. An analytical calculation of Lorentz force and a graphical representation of the Maxwell force distribution via FEM model are carried out.

Comparing Lorentz and Maxwell force, disregard of the Lorentz force can be concluded. The dominant force in the air gap is the Maxwell one. The FE analysis results can be used as an input values for a coupled electrical – mechanical problem [12]. The presented model is valid for simplified conditions than during operation occurs. The way to include these conditions and non-standard operational states modeling (eccentric rotor for example) are the subject of further research.

Acknowledgments. This paper was written with SGS-2012-071 project support.

References

[1] Heller, B., Hamata, V.: Additional fields, forces and losses in the induction machine. NCSAV, Praha (1961)

[2] Jimoh, A.A., Findlay, R.D.: Parasitic torques in saturated induction motors. IEEE Transactions on Energy Conversion 3(1), 157–163 (1988)

[3] Golebiowski, L., Mazur, D.: The effect of strong parasitic synchronous and asynchronous torques in induction machine with rotor eccentricity. In: 10th Mediterranean Electrotechnical Conference, MELECON 2000, May 29-31, vol. 3, pp. 982–985 (2000)

[4] Nau, S.L.: The influence of the skewed rotor slots on the magnetic noise of three-phase induction motors. In: 1997 Eighth International Conference on Electrical Machines and Drives (Conf. Publ. No. 444), September 1-3, pp. 396–399 (1997)
[5] Zhu, H., Zhou, G., Chen, J., Liu, H.: Analysis and Study of Skewed Slot Tooth Distance on Low Electromagnetic Noise of Three-Phase Induction Motor with Squirrel Cage Rotor. In: 2012 Sixth International Conference on Electromagnetic Field Problems and Applications (ICEF), June 19-21, pp. 1–4 (2012)
[6] Onodera, S., Yamasawa, K.: Electromagnetic vibration analysis of a squirrel-cage induction motor. IEEE Transactions on Magnetics 29(6), 2410–2412 (1993)
[7] Heller, B., Jokl, A.L.: Tangential Forces in Squirrel-Cage Induction Motors. IEEE Transactions on Power Apparatus and Systems PAS-88(4), 484–492 (1969)
[8] Griffiths, D.J.: Introduction to electrodynamics, 3rd edn. Prentice-Hall, Upper Saddle River (1999) ISBN 0-13-805326-X
[9] Mayer, D.: Aplikovany elektromagnetismus, KOPP, Ceske Budejovice (2012) ISBN 978-80-7232-436-1
[10] Promberger, M.: Anwendung von Matrizen und Tensoren in der theoretischen Elektrotechnik, pp. 126–128. Akad.-Verlag (1960)
[11] Dombrowsky, W.W., Khanin, M.D., Kuchinska, Z.M.: Common software for electromagnetic and heat field analysis of electrical machines including the force calculation. Advances in Engineering Software 22(3), 147–152 (1995)
[12] Lee, J.-H., Lee, Y.-H., Kim, D.-H., Lee, K.-S., Park, I.-H.: Dynamic vibration analysis of switched reluctance motor using magnetic charge force density and mechanical analysis. IEEE Transactions on Applied Superconductivity 12(1), 1511–1514 (2002)

Current-Voltage Characteristics and IR Imaging of Organic Light-Emitting Diodes

G. Koziol, J. Gromek, A. Arazna, K. Janeczek, K. Futera, and W. Steplewski

Tele and Radio Research Institute, Ratuszowa 11, 03-450 Warsaw, Poland
grazyna.koziol@itr.org.pl

Abstract. In this paper, a study of current-voltage characteristics and temperature distribution in the polymer organic light-emitting diodes are presented and discussed. The fabricated diodes consisted of ITO coated glass, PEDOT:PSS as a hole injection layer, one of eight different examined light-emitting compounds as an emissive layer, and aluminium cathode. The spectrum of light emitted by the fabricated OLEDs was also measured. Based on the results the most efficient.

1 Introduction

Organic Light Emitting Diodes (OLEDs) hold great promise for future use as a new generation of solid state light sources. In contrast to point source LED luminaries, OLEDs are dispersive light sources. Some of the many advantages are that OLEDs are "green" without hazardous material such as mercury, potentially energy efficient, and emit low intensity uniform light from an extremely thin flat surface [1].

There are two basic types of OLED systems: low molecular weight OLEDs and polymer OLEDs. Small molecule OLEDs are made via evaporation of materials under high vacuum. This method is so far mostly used for OLED lighting panels manufacturing. Polymer OLEDs are made of long chains of repeating structures and deposited from a solution. This solution processing bears the advantage of mass reproduction by e. g. gravure printing.

Today's OLEDs performance is already reaching market requirements for less demanding lighting applications, such as signage and signaling. Especially in monochrome colors, red and green, OLEDs perform already very well. The efficacies of 130 lm/W in green has already been achieved [2-7].

Worldwide research is ongoing to create high-brightness, highly efficient and long living OLEDs, especially manufactured using solution processable emitting layer. Tele- and Radio Research Institute has also undertaken studies on this area. In this paper, the electric response of the devices was evaluated based on the current-voltage characteristics. The evaluation of a working temperature of OLED operating under a changing DC voltage level were done used IR camera. The degradation at the cathode surface were evaluated through SEM (Scanning Electron

T. Březina and R. Jabloński (eds.), *Mechatronics 2013*,
DOI: 10.1007/978-3-319-02294-9_40,

Microscope). Based on the results demonstrators of OLEDs with the most efficient emission compound (achieved so far), were produced and evaluated.

2 Experimental

OLED devices were manufactured on the glass slides (the dimension of 25 x 25 x 1.1 mm) coated with ITO (film thickness of 15 - 30 nm, and sheet resistance of 70 - 100 Ω/□). In order to improve the hole injection, a highly conductive and transparent organic layer of Poly(3,4-ethylenedioxythiophene): poly(styrenesulfonate) (PEDOT:PSS) was used. Both glass substrates and HIL material (2% water solution) were purchased from Sigma-Aldrich Chemical.

Single-layer organic-light-emitting devices were fabricated by spin coating of polymeric solutions of emissive materials from American Dye Source: Poly[2-methoxy-5-(2-ethylhexyloxy)-1,4-phenylene-vinylene] – end capped with DMP (ADS1), Poly[2-methoxy-5-(2-ethylhexyloxy)-1,4-phenylene-vinylene] – end capped with Polysilsesquioxane (ADS2), Poly[2-methoxy-5-(3,7-dimethyloctyloxy)-1,4-phenylene-vinylene] – end capped with DMP (ADS3), Poly[2-(5-cyano-5-methylhexyloxy)-1,4-phenylene] – end capped with DMP (ADS4), Poly[(9,9-dioctylfluorenyl-2,7-diyl)-co-(1,4-benzo-{2,1',3}-thiadiazole)] 10% benzothiadiazole (y) (ADS5), Poly[(9,9-dihexylfluorenyl-2,7-diyl)-alt-co-(2-methoxy-5-{2-ethylhexyloxy}-1,4-phenylene)] (ADS7), and Poly[{9,9-dioctylfluorenyl-2,7-diyl}-co-{1,4-(2,5-dimethoxy)benzene}] (ADS8). All these emissive materials (EML) were dissolved in xylene (concentration 5 mg/ml).

The ITO coated glass substrates were first ultrasonically cleaned in acetone, and ethanol, for 5 minutes each. Such ITO treatment was considered as an effective method of ITO treatment for organic light-emitting devices in our previous work [8]. Next, the substrates were dried with compressed air and then on a hot plate PZ-28-2 (Harry Gestigkeit) in 80°C for 10 min. Then, two PEDOT:PSS layers were deposited on ITO with a modular spin processor WS-650-23NPP (Laurell Technologies Corporation) set to speed of 7500 rpm, acceleration of 6000 rpm/s and process time of 6 s. After deposition of each layer the sample was dried on a hot plate in 80°C for 10 min. EML layers were also spin coated with following settings: speed of 5500 rpm, acceleration of 4000 rpm/s and process time of 6s. Each layer was dried on a hot plate in 80C for 3 min. In the last step, the aluminum cathode was evaporated from aluminum slug (99.999% trace metals basis) at a base pressure of $\sim 10^{-3}$ mbar (Type Q150T ES, Quorum Technologies). All tested OLED devices were prepared in ambient conditions.

The structure of tested devices was ITO/PET/PEDOT:PSS 2x/ EM (ADS1-8) 3x/Al (100 nm). The device active area was 1 cm^2.

Current-voltage (I-V) characteristics of the prepared OLEDs were measured using a Hameg Instruments Company HMP 2020 Power Supply SourceMeter under ambient atmosphere at room temperature. The results given here represent the average of three measurements carried out for fresh manufactured devices

without encapsulation and every two weeks for OLEDs stored in ambient temperature (20 - 22°C) and constant and lower humidity (approx. 15%).

The operating voltage was defined as the voltage when emitting light is first detected.

Real-time measurements of the temperature of OLEDs operating under a changing DC voltage level were carried out using the measurement set-up shown in Figure 1. An OLED sample was placed at the focal point of the objective lens of the infrared imaging system. To calibrate the surface temperature of a sample, the emissivity of the sample and the ambient radiance was determined by measurements of the sample radiance at two given temperature levels.

The tested samples (at least five for each experiment) were connected to the power supply HMP2020 with DC voltage from 3 to 15 V and its temperature was measured with a thermographic camera FLIR A320.

The surface morphologies of OLEDs after thermal breakdown were studied using a scanning electron microscope (SEM), JEOL JSM 7600F.

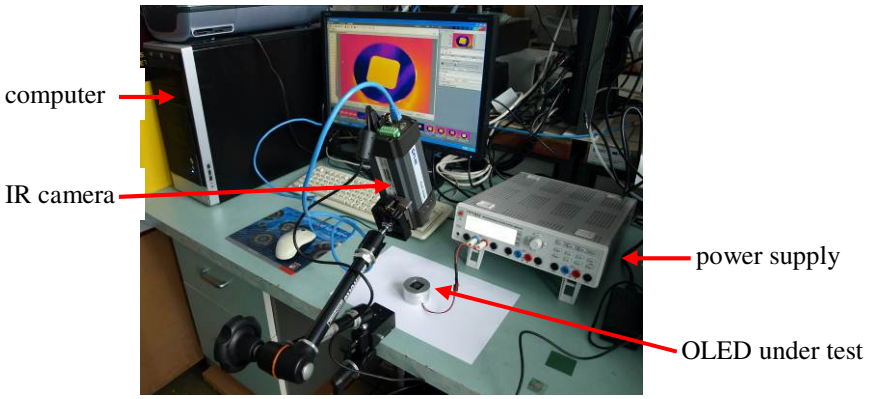

Fig. 1 A photo of the temperature measurement set-up

Electroluminescent (EL) spectra were obtained by Ocean Optics fiber optic spectrometer (SD2000). The characterisation was carried out at room temperature in ambient conditions.

3 Results and Discussion

The characteristics of current density (*J*) versus operating voltage measured for devices based on ADS1 - ADS8 (Fig. 2) showed a steeply increase in current density for most of the devices and almost flat curve for ADS4. OLEDs based on ADS2 and ADS4 exhibited the lowest current density and OLEDs on ADS1 and ADS6 the highest current density.

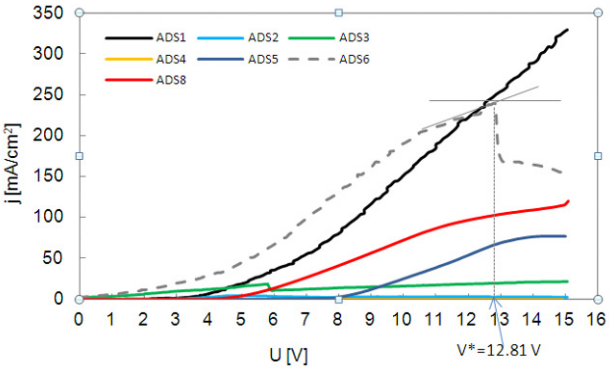

Fig. 2 The comparison of J-V characteristics of OLED samples based on different light emitting compounds

The voltage above which the value of current density increased (see Fig. 2) indicated the onset of light emission (the driving voltage). We can see that the device based on polymers ADS5 exhibited the highest driving voltage, and device ADS6 the lowest one. The "electrical failure voltage"- *V** can be defined using the J-V curve. For the OLED ADS6 the value of V* was 12.81 V.

The light emission was observed for OLEDs ADS5 and ADS8 by the naked eye in a natural daylight environment. The luminance of these devices was 110 cd/m^2 (Fig. 3), and 60 cd/m^2, respectively. Only small parts of OLEDs samples with ADS1 and ADS6 emitted light. The catastrophic failure was observed for samples based on ADS2, ADS3 and ADS4. The measured operating voltage for the devices ADS5 and ADS8 was 5.25 V and 8.35 V, respectively.

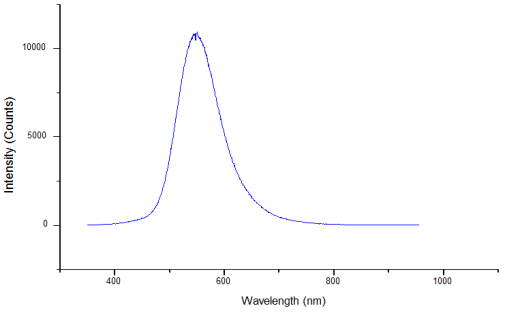

a)

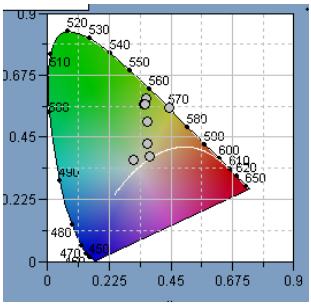

b)

Fig. 3 The OLED sample based on ADS5: a) the plot - intensity as a function of wavelength, b) an optical emission spectrum

The results of real-time measurement of the temperature of the OLEDs ADS5 and ADS8 operating under the voltage in the range of 0 - 20 V are presented in Fig. 4. A typical temperature image sequence of a working OLED ADS8 under the voltage values: 3, 6, 9, 12 and 15 V is demonstrated in Fig. 5.

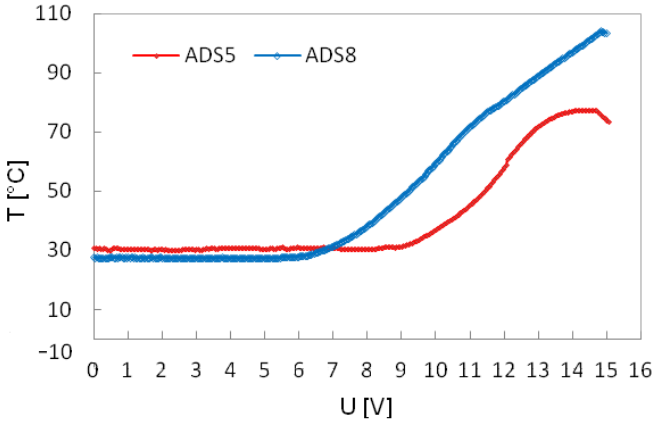

Fig. 4 Temperature of the OLED based on ADS5 against supply voltage

It was stated that the temperature of OLED ADS8 at the voltage over 7 V was higher than for the OLED ADS5. A steep rise in temperature in the device ADS5 may contribute to the accelerated thermal degradation. Especially when the temperature exceeds the glass transition temperature range of ADS5. In side of this temperatures, mechanical, electrical and optical properties of organics show dramatic and rapid changes [10].

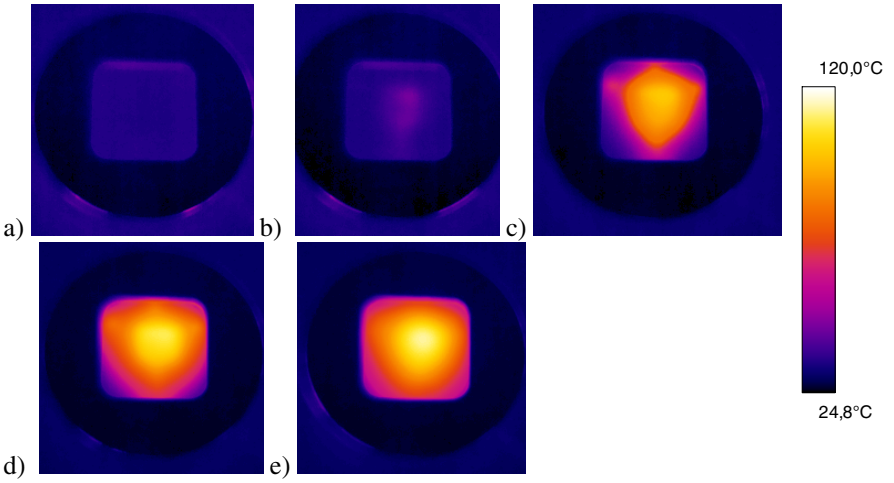

Fig. 5 Temperature image sequence of the working OLED ADS8 under the voltage values: a) 3 V, b) 6 V, c) 9 V, d) 12 V and e) 15 V

The analysis of the achieved results showed that all fresh OLED samples exhibited approx. comparable current density values, equal to about 90 mA/cm^2 for ADS5, about 100 mA/cm^2 for ADS8 for 15 V (Fig. 6).

The failure of the ADS8 diodes was observed after approx. 2690 hours and the current density at 15 V were lower by about 37% compared to the value of *J* for the fresh samples. The failure of the ADS5 diode was observed later than for the device ADS8 (after approx. 3000 h) and the current density at 15 V was lower by about 48% compared to the fresh samples.

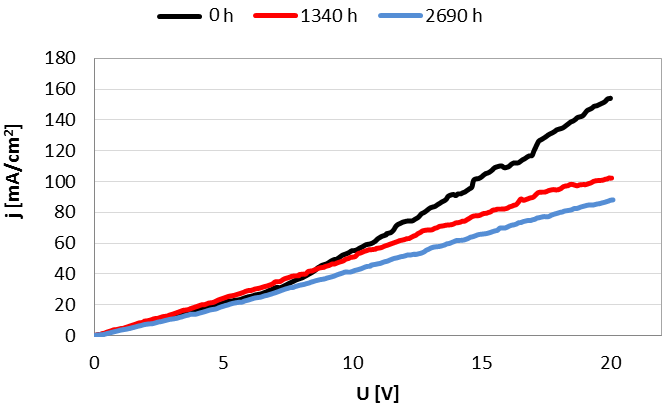

Fig. 6 J–V characteristics for the OLEDs ADS8. The results for: 0 – fresh sample, and after 1340 h, 2690 h of storage in a desiccator.

During the long-term storage in an atmosphere of oxygen (in air) functional properties of the organic layers were likely to be modified what contributed to reduction of the OLED sample's stability and the decrease in the value of current density [2, 3, 9].

Fig. 7 is an SEM image showing the morphology of the top Al electrode of the OLEDs after thermal beak-down.

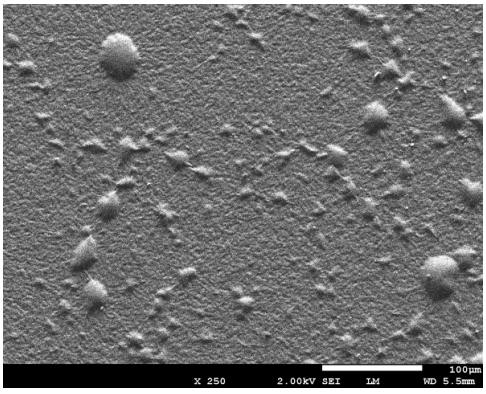

Fig. 7 Delamination of the cathode metal after thermal break-down

The Al film was likely to be blown up and this resulted in the delamination of the cathode metal. This phenomenon implied the presence of the areas which did not emit light and accelerated the degradation of OLEDs [2, 3, 7].

Based on the results of our studies some demonstrators of OLEDs were produced (Fig. 8).

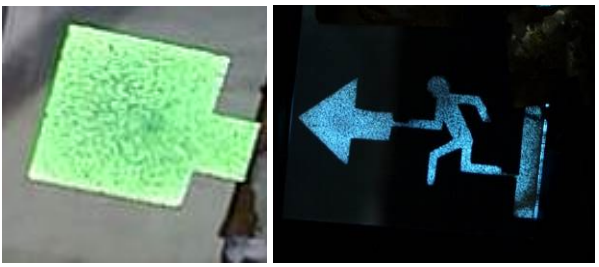

Fig. 8 Produced OLED demonstrators

4 Conclusions

Polymer-based organic light emitting diodes with the structure: ITO/PET/PEDOT:PSS 2x/ EM (ADS1-8) 3x/Al (100 nm) were manufactured by spin coating and the devices parameters were evaluated through their J-V characteristics and real-time measurements of the temperature of OLED working under a changing DC voltage. Their degradation during storage in a desiccator and delamination of the cathode metal after thermal break-down were observed through SEM. The best results were achieved for OLEDs based on ADS5 and ADS8 polymers. The luminance of these devices with an active area of 1 cm^2 was 110 cd/m^2 (Fig. 3), and 60 cd/m^2, respectively.

References

[1] Solid State Lighting OLED Manufacturing Roundtable Summary, http://www1.eere.energy.gov/buildings/ssl/techroadmaps.html

[2] Duan, L., Hou, L., Lee, T., Qiao, J., Zhang, D., Dong, G., Wang, L.: Solution processable small molecules for organic light-emitting diodes. Mater. Chem. 20, 6392–6407 (2010)

[3] Viser, P.: OLED technology: also the ultimate lighting solution?, http://www.optik-photonik.de

[4] Zhong, C., Duan, C., Huang, F., Wu, H., Cao, Y.: Materials and Devices toward Fully Solution Processable Organic Light-Emitting Diodes. Chem. Mater. 23, 326–340 (2011)

[5] AlSalhi, M.S., Alam, J., Dass, L.A., Raja, M.: Recent Advances in Conjugated Polymers for Light Emitting Devices. Int. J. Mol. Sci. 12, 2036–2054 (2011)

[6] Lussem, B., Reineke, S., Rosenow, T., Schwartz, G., Leo, K.: Novel concepts for OLED lighting. In: Proc. of SPIE, vol. 7617, p. 761712 (2010)
[7] Komoda, T.: Recent Progress and Future Trend of OLED Technologies for Lighting Application. In: Printed Electronics Europe 2012, Berlin (2012)
[8] Arazna, A., Kozioł, G., Janeczek, K., Futera, K., Steplewski, W.: Investigation of surface properties of treated ITO substrates for organic light-emitting devices. J. Mater. Sci.: Mater. Electron. 24, 267–271 (2013)
[9] Zhou, X., He, J., Liao, L.S., Lu, M., Ding, X.M., Hou, X.Y., Zhang, X.M., He, X.Q., Lee, S.T.: Real-Time observation of temperature rise and thermal breakdown processes in organic LEDs using an IR imaging and analysis system. Adv. Mater. 12(4), 265–268 (2000)
[10] Nenna, A., Flaminio, G., Fasolino, T., Minarini, C.: A study on thermal degradation of organic LEDs using IR. In: Macromol. Symp. 2007, vol. 247, pp. 326–332 (2007), http://www.ms-jornal.de

Complex Model of Asynchronous Machine as Traction Machine in Mining

R. Vlach

Brno University of Technology, Faculty of Mechanical Engineering,
Technicka 2, 616 69, Brno, Czech Republic
vlach.r@fme.vutbr.cz

Abstract. A complex approach to problem solving is demanded in all engineering fields today. This project is concerned with complex simulation of asynchronous machine heating during duty cycle. The asynchronous machine is used as traction machine in mining industry. The Complex model consists from electromagnetic model, ventilation model and thermal model. This paper shows the possibility for a new approach to the problem of cooling electrical machines in the engineering practice.

1 1 Introduction

The paper is concerned with complex computational modeling of traction machine heating during duty cycle. A new approach was used for solving this technical problem. Many authors have tried to complex modeling of electric machine as referenced in [9-13].

As the traction machine is used asynchronous machine with external ventilation. The machine is used in mining industry for carriage drive unit. The machine operates with variable load and revolution speed during duty cycle.

The design of the traction machine is currently based on nominal power and revolution speed of machine without respecting of load variation during duty cycle. The complex model of traction machine respect variation of all parameters, which influence of machine heating during duty cycle. One of the most important parameters is operating altitude, because it has fundamental influence on the heating during the course of machine operating.

The software Visual Basic for Excel was used for computational modeling. The program code in Visual Basic is easy interconnected to Microsoft Excel worksheet.

2 Complex Model of Traction Machine

The Complex model [1] consists from electromagnetic model, ventilation model and thermal model, where each influences others.

T. Březina and R. Jabloński (eds.), *Mechatronics 2013*,
DOI: 10.1007/978-3-319-02294-9_41,

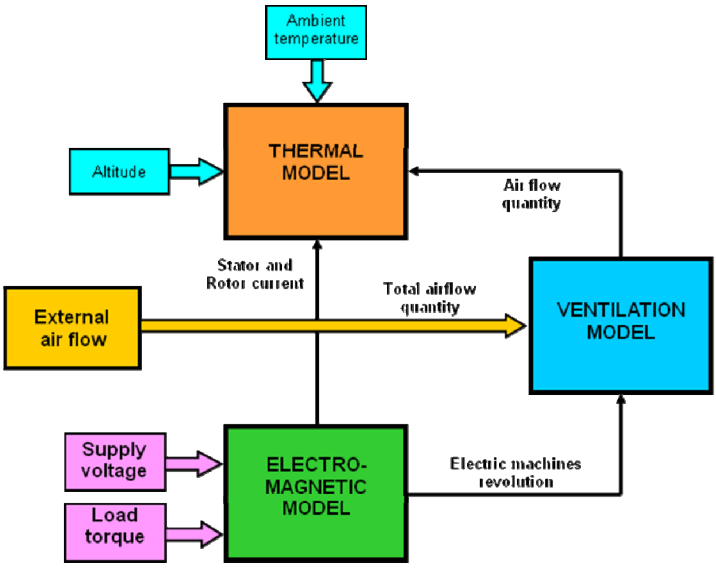

Fig. 1 Complex model of traction machine

2.1 Electromagnetic Model

The energy balance was used for description of electromagnetic model. Basic energy balance is given by:

$$\sqrt{3} \cdot U \cdot I \cdot \cos(\varphi) = \Delta P + T \cdot \varpi \ , \tag{1}$$

where T is torque on the shaft, ω is angular speed, U is supply voltage, I is stator winding current, cos(φ) is power factor and ΔP is total loss of machine.
Machine losses are given by:

$$\Delta P = P_{cu} + P_{fe} + P_{mech} + P_{add} \ , \tag{2}$$

where P_{cu} is heat loss in the winding, P_{fe} is iron loss, P_{mech} is mechanical loss and P_{add} is addition loss.

Heat losses in the winding depend on the winding resistance and current (Joule losses). Iron losses are losses in the teeth and core of stator and rotor packet owing to magnetic flux. The basic components of mechanical losses are losses in the bearings and ventilation losses of rotor. Using switching converter create addition losses in the machine iron.

All components of losses are changed to heat, which must be effectively removed from machine.

2.2 Ventilation Model

The ventilation network (Fig.2) was used for description of airflow in the machine. Ventilation network [2] describes airflow inside machine mainly division of airflow to stator and rotor axial channels in the iron packets. The knowledge of velocities in the machine individual parts is needed for determination of heat transfer coefficients, which is necessary for thermal model.

2.3 Thermal Model

The thermal network method [3],[4] was used for description of machine heating. Thermal network describes heating of machine individual parts mainly stator winding and rotor cage. Thermal networks (Fig.2) consist from forty-two nodes. Last four nodes (from 39 to 42) are used for description of cooling air heating [5]. Thermal model describes transient state, because machine operates with varying load.

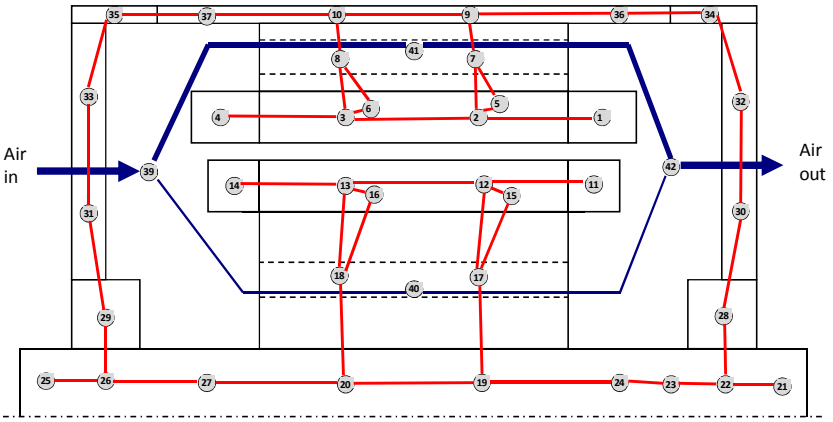

Fig. 2 Thermal network of traction machine

Thermal network is possible to be described by the system of differential equation:

$$C_i \frac{dT_i}{dt} + A \cdot T_i = b_i \,, \tag{3}$$

where C_i is thermal capacity concentrated in node i, A is matrix of thermal conductivities and b_i heat loss in node i and heat flux to ambient.

Temperatures of nodes describing heating of cooling air are given by [3],[7],[8]:

$$T_i\left(a_Q + \sum_j a_{ij}\right) - T_{(i-1)}\left(a_Q - \sum_j a_{(i-1)j}\right) - \sum_j T_{ij} a_{ij} - \sum_j T_{(i-1)j} a_{(i-1)j} = 0 \,, \tag{4}$$

where T_i is temperature of air node *i*, a_Q is thermal conductivity of flowing air, a_{ij} is thermal conductivity between nodes *i* (air node) and *j* (solid parts) and T_{ij} is temperature of solid parts, which is connected via conductivity a_{ij} to node T_i (temperature of air node).

Thermal model respects change of thermal properties of cooling air owing to altitude, because the machine sometimes operates at the top of hill.

3 Computational Simulation

The duty cycle is described by torque and revolution speed on the machine end shaft, which are required to carriage movement. The revolution speed is directly proportional to supply voltage, which is set by switching converter. The other influencing parameters are ambient temperature, altitude and total airflow quantity of cooling air.

Fig. 3 shows time behaviour of torque and revolution speed during one duty cycle of traction machine. The duty cycle consists from four intervals. The first interval describes haul of full carriage and the second interval describes dump and maneuver of carriage. The other interval describes return of empty carriage. The last interval describes wait to load and truck exchange.

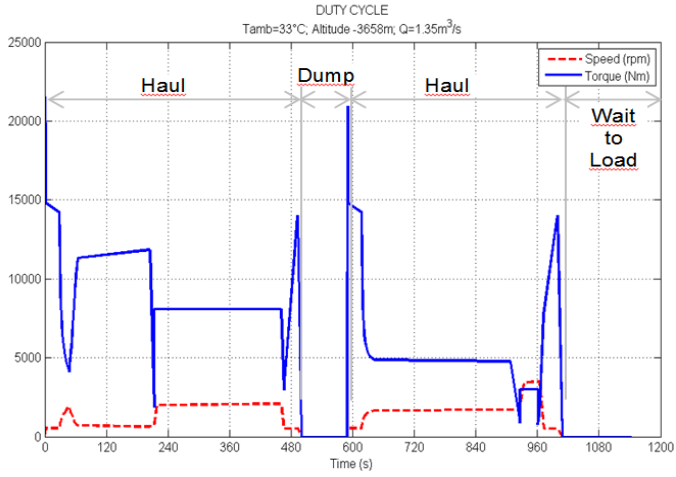

Fig. 3 Duty cycle of traction machine

The ambient temperature is commonly 33°C. The machine operates at altitude 3658m. Total air flow of external cooling air is $1.35 m^3 s^{-1}$ for nonzero speed. If speed is zero than air flow of cooling air is reduced to $0.765 m^3 s^{-1}$.

Fig. 4 shows heating of stator winding and rotor cage, which are the most important machine parts. Temperatures correspond with intervals of duty cycle. If the carriage moves than temperatures of machine parts increases. If the carriage wait to unload and load than temperatures of machine parts decreases.

The output air temperature is also shown on Fig. 4, because it is one of the main parameters. The output air temperature is used for basic balance of cooling efficiency.

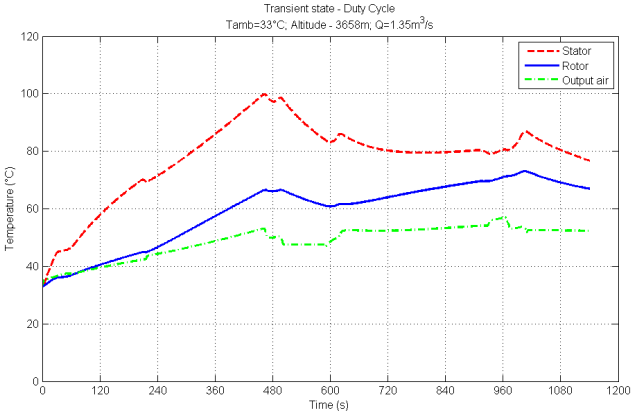

Fig. 4 Heating of traction machine during duty cycle

Heat losses of stator winding and rotor cage depend on actual temperature of these machine parts, so heat losses must be calculated for actual temperature in each time step. Heat transfer coefficients [4], [6] are also calculated in each time step.

The duty cycle (Fig. 3) is still repeated in operation, so temperatures of machine parts will increase. The traction machine has period of running for almost six hour. It corresponds eighteen duty cycles.

Fig. 5 shows heating of stator winding, rotor cage and output air for eighteen duty cycles respectively period of running. Individual peaks of temperature over time correspond with end of haul of full carriage in each duty cycle. Temperatures correspond with intervals of duty cycle. If the carriage moves than temperatures of machine parts increase. If the carriage waits to unload and load than temperatures of machine parts decrease.

The temperature peak is each time higher in the following duty cycle. Change the temperature peaks is almost negligible after approximately nine duty cycle. The heat is mainly absorbed to machine mass in the first half of period of running, so that temperatures are lower. After nine duty cycle temperature peaks are steady.

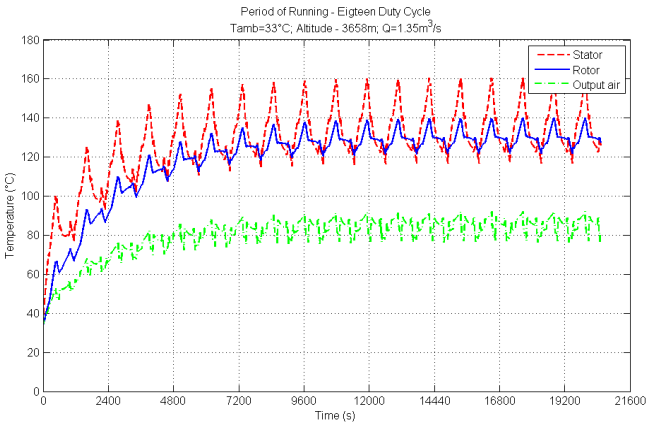

Fig. 5 Heating of traction machine during period of running

4 Conclusions

Paper describes example of using new approach to solving of cooling electrical machines in engineering practice. New method was used for asynchronous machine, which operates as traction machine in the mining industry.

The computational simulation shows using complex model of machine for solving of traction machine heating during period of running.

This new approach is applicable to any kind of traction machine or electric machines and devices operate with varying load.

Acknowledgment. This work was supported by Project FSI-S-11-15 "Design, testing, and implementation of control algorithms with use of nonlinear models of mechatronics systems."

References

[1] Vlach, R.: Control of Electric Machine Ventilation Using Artificial Intelligence. PhD Thesis, Brno, Czech Republic (2002)
[2] Idelchik, I.E.: Handbook of Hydraulic Resistance, 3rd edn. Jainco Publishing House, New York (2006)
[3] Ondruska, E., Malousek, A.: Ventilation and Cooling of Electric Machines. SNTL, Prague (1985)
[4] Hak, J., Oslejsek, O.: Computed of Cooling of Electric Machines. VUES Brno, Brno (1973)
[5] Hynst, R.: Solving of Thermal Network with Circulation of Coolant. Engineering of Electric Machines (1969)
[6] Yunus, A., Turner, H., Cimbala, J.M.: Fundamental of Thermal-Fluid Sciences, 3rd edn. McGraw Fill, Australia (2008)

[7] Ancik, Z., Toman, J., Vlach, R., Hubik, V.: Modeling of Thermal Phenomena in Liquid Cooling System for Aircraft Electric Unit. IEEE Transactions on Industrial Electronics 2011(99), 1–7 (2011) ISSN 0278-0046

[8] Vlach, R.: Thermal modelling of powerful traction battery charger. In: Mechatronics Recent Technogical and Scientific Advances, pp. 175–184 (2011) ISBN 978-3-642-23243-5

[9] Hruska, K., Kindl, V., Pechanek, R.: Design and FEM analyses of an electrically excited automotive synchronous motor. In: 2012 15th International Power Electronics and Motion Control Conference (EPE/PEMC), September 4-6, pp. LS2e.2-1–LS2e.2-7 (2012)

[10] Pechanek, R., Bouzek, L.: Analyzing of two types water cooling electric motors using computational fluid dynamics. In: 2012 15th International Power Electronics and Motion Control Conference (EPE/PEMC), September 4-6, pp.LS2e.4-1–LS2e.4-5 (2012)

[11] Hruska, K., Kindl, V., Pechanek, R.: Concept, design and coupled electro-thermal analysis of new hybrid drive vehicle for public transport. In: 2010 14th International Power Electronics and Motion Control Conference (EPE/PEMC), September 6-8, pp.S4-5–S4-8 (2010)

[12] Kindl, V., Pechanek, R., Bouzek, L.: Cooling of new designed machine. In: 2010 13th International Symposium on Mechatronika, June 2-4, pp. 95–98 (2010)

[13] Krasl, M., Pechanek, R., Vlk, R.: Traction Transformer 1 MV. A, Superconducting, Oil-immersed and Medium Frequency. In: Advances in Electrical and Electronic Engineering, vol. 7(1-2), pp. 191–194 (2011)

Energetic Properties of a New, Iron Powder Based Switched Reluctance Motor Drive

B. Fabianski

Poznan University of Technology, Faculty of Electrical Engineering,
Institute of Control and Information Engineering, Piotrowo 3a, 60-965 Poznan, Poland
bogdan.fabianski@put.poznan.pl

Abstract. The paper presents its origins as a derivative of a research grant in the topic of universal switched reluctance motor drive with powder magnetic circuit. The publication presents the results of comparison the energy performance of a prototype iron powder drive from the conventional one. The analysis of quantitative and qualitative parameters of the energy conversion process in the drive was presented. The global energy consumption statistics by electric drives to specify substance of the work of energy performance improvement was described. Introduction in power magnetic materials was done. An outline of the mechanical construction of the prototype of the engine and a dedicated control system was shown. An analysis of the compiled results, draws conclusions and proposes directions for further research were included in the end.

1 Introduction

The article genesis was the research grant named "Powder magnetic circuits in the universal electric drives", where the main goal was to made a new motors from iron powder material based on the conventional, commercial models for comparison. Because Switched reluctance motor (SRM) needs to be supply by power inverter [3] it was necessary to project and build a new, dedicated control system. The article presents a new SR iron-power based motor drive with the main concern about its energetic properties.

The two main reasons for the use of powder magnetic circuits are:

- ease of recycling and reuse
- improving energy efficiency

Research to improve the energy efficiency seem to be important and legitimate due to the high share of electric drives in the global energy consumption. Statistics relating to the problem was described in the next section.

1.1 Energy Consumption by Electric Drives

The global analysis of energy consumption in electric motor driven systems (EMDS) was presented in [7]. The vast majority of the electricity used by an

T. Březina and R. Jabloński (eds.), *Mechatronics 2013*,
DOI: 10.1007/978-3-319-02294-9_42,

EMSD is consumed by the electric motor itself. Only a very small amount is used to power control functions or other ancillary circuits. Electric motors and the systems they drive are the single largest electrical end-use, consuming more than twice as much as lighting, the next largest end-use. It is estimated that EMDS account for between 43 [%] and 46 [%] of all global electricity consumption, giving rise to about 6 040 [Mt] of CO2 emissions. End-users now spend USD 565 billion per year on electricity used in EDMS. By 2030, that could rise to almost USD 900 billion [7].

Table 1 shows aggregate of the energy consumed by an array of different types of motors operating within a wide set of applications in every sector of energy use, with opportunity for large savings in every sector.

Table 1 EDMS electricity consumption by sector

Sector	Electricity consumption [TWh/year]	% of all EMDS electricity	% of sector electricity
Industrial	4488	64	69
Commercial	1412	20	38
Residential	948	13	22
Transport and agriculture	260	3	39

1.2 Magnetic Materials

Soft magnetic materials are mainly used in electrical machines to transform electrical energy, its generation and conversion into mechanical energy (electric motors). Most are alloys of iron and silicon (a relatively cheap metal)/nickel (high initial permeability value)/cobalt (high value of the maximum magnetic permeability) [6].

The largest size of the domain – and thus the most inert – can be found in the iron sheets (conventional magnetic circuit). Although the properties depend on the specific chemical composition, thickness of the plate and the direction of the roll, you can define general characteristics of these materials: low operating frequency, high saturation flux density (of the level of 1.5 [T]), relatively high power losses caused by induced eddy currents and hysteresis loop, low price.

The second type of magnetic material used in the comparison is a powdered iron. Ground into small particles, mixed in some cases with *improvers* is treated with an organic filler, compacted under high pressure in an appropriate form. Form gives the material shape of the magnetic core. After the compression of such material between the iron particles are forming a so-called break gap occurring dispersed throughout the volume of the core. A core made of such a material has a non-linear magnetization as a function of the external magnetizing force, therefore, its specific properties are used for storing large amounts of energy. Conventional cores made of pure iron powder (material -26) are the cheapest and most common materials. The saturation flux density is 1.2 [T], and the maximum operating

frequency is about 80 [kHz]. A disadvantage of powder cores is susceptible to aging and is an irreversible process. It occurs at high temperature. It is recommended so the work of all iron powder cores at up to 363 [K] (90 °C) [6].

1.3 Switched Reluctance Motor with Iron-Powder Magnetic Circuit

It was proposed for increasing the energy efficiency ratio of switched reluctance motor by applying a magnetic circuit made of sintered metal powder as opposed to a solution based on a combination of the desired form stacking. Improving the energy performance through the introduction of powder materials was successfully obtained in pulse transformers. Assuming a similar nature excitations (pulse width modulation voltage) can presume analogous benefits for SRM.

Operating parameters of the engine used in the study were as follows: rated power P_N = 250 [W], maximum speed ω_{MAX}= 10000 [rpm], rated voltage U_N = 230 [V]. Topology of engine was 12/8. Standard model was came from Maytag Neptune washing machine.

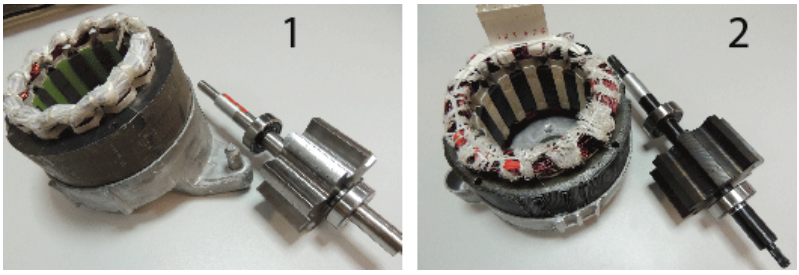

Fig. 1 Stator and rotor of SRM - the design of powder material (1) and metal sheet (2)

Figure 1 shows the conventional engine design (separately: a stator and a rotor with bearings) of rolled sheet metal (2), while the left side of the figure based on powder materials (1). Custom design of the converter was author's publications on the subject of systemic solutions in the asymmetric power bridge topology [5][2], complex SR motor control [1]. These articles give a picture of the work on the construction of the drive.

2 Energy Performance of Drive

2.1 Laboratory Stand

The main concern about custom laboratory stand construction project was: security, stability and low overall building costs. General structure of the drive system was presented on Figure 2. The drive project was an effect of compromised level of logic, galvanic and geometrical isolation blocks with potential source of electromagnetic interferences (EMI) from sensitive ones. As could be seen on the

corresponding draw there was achieved full separation the high voltage, high current parts side (Figure 2) from low current side.

The drive includes a power factor correction (PFC) block onboard (*HPWR PFC* – Figure 2). Standard drives with passive input filters gives large THD (Total Harmonic Distortion) and phase offset factor, what gives significant deformation of network supply voltage sinusoidal shape. To meet the EN61000-3-2 class D norm requirements, an embedded PFS729EG PFC controller was used. The chip was an continuous conduction mode boost power factor corrector with high efficiency. The results of PFS729EG usage will be presented with compare to the drive without PFC mechanism.

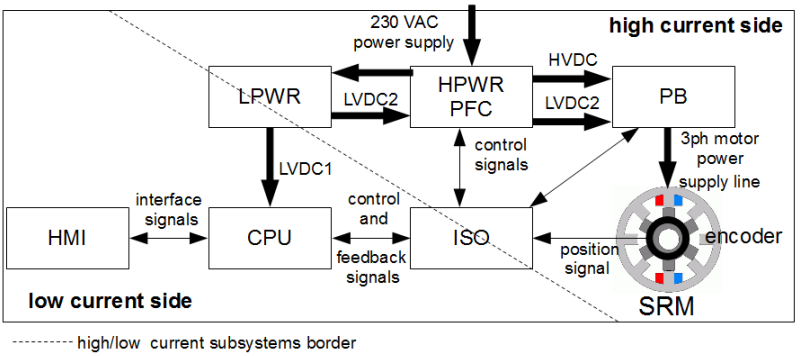

Fig. 2 SRM drive general structure

Figure 3 shows the image of the test bench. It consists of a PC enables the current shift parameters and monitoring of the microcontroller program. The position includes also two oscilloscopes: Tektronix DPO3014 and MSO3014 for trending respectively: signals specific to the SRM (phase currents, speed, load torque) and power supply (current, voltage, power). Next, applied auto-transformer to change the input voltage, the SRM inverter, input supply parameter measurement device (RMS current, voltage, power) and a shaft load torque measure device: MW2006-3S with MT-15 sensor. SRM motor is coupled to the torque measuring shaft through a clutch of eddy current.

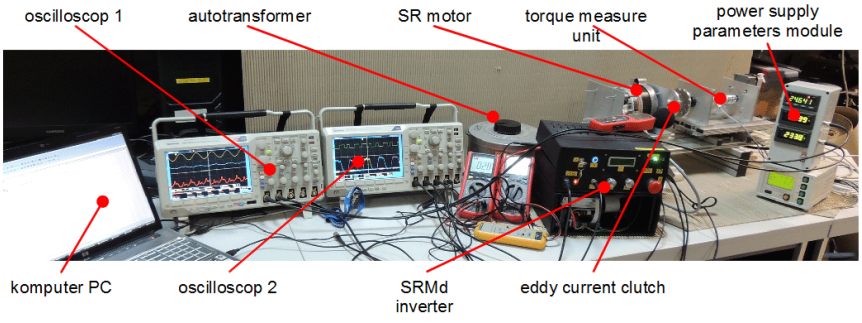

Fig. 3 Laboratory stand

2.2 *Power Quantity and Quality Analysis*

The primary determinant of the drive energy efficiency is the ratio of expended mechanical power and input power supply. The actual measurement of speed and load torque on the shaft allow direct determination of efficiency. As can be seen, in Figures 4-6 are plots of the dependence of the power consumption of the drive from the torque load at three speeds: 1000, 2500 and 5000 [rev/min]. The slope of the graph called p_c [W/Nm] (the power consumption per unit of load torque throughout the rev range) is a source of calculating energy efficiency. Summaries of p_c coefficients made in Table 2 as the energy efficiency from below equation:

$$\eta = \frac{\omega}{p_c} \tag{1}$$

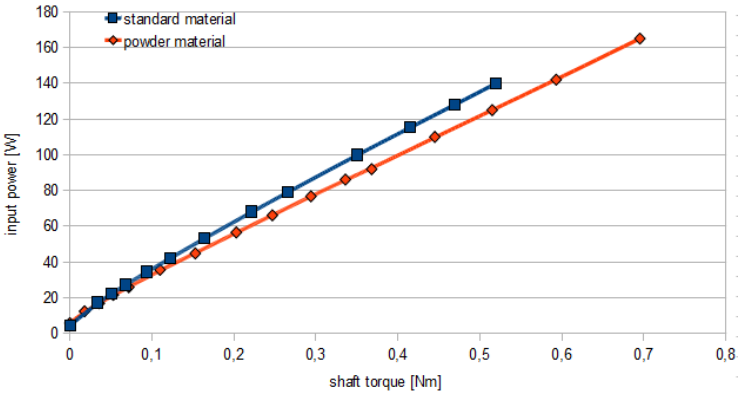

Fig. 4 Graph of the power consumption of resistive torque on shaft (P_i=f(T_r)) at constant speed 1000 [rpm]

In Figure 7.

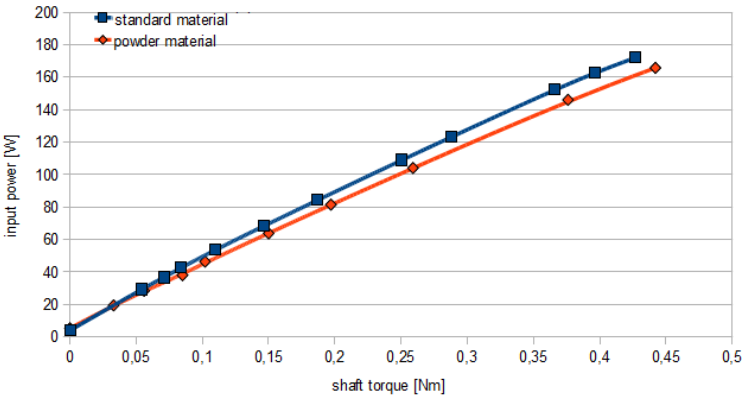

Fig. 5 Graph of the power consumption of resistive torque on shaft (P_i=f(T_r)) at constant speed 2500 [rpm]

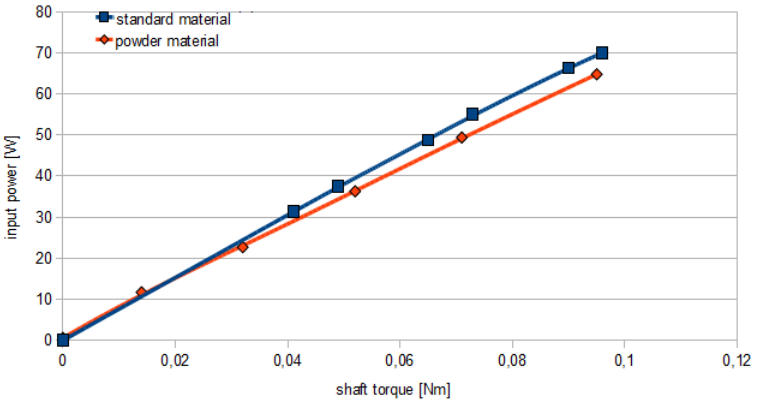

Fig. 6 Graph of the power consumption of resistive torque on shaft ($P_i=f(T_r)$) at constant speed 5000 [rpm]

Table 2 Power consumption coefficient (p_c) computation results

Speed [rpm]	standard material p_c [W/Nm]	powder material p_c [W/Nm]
1000	235,61	216,03
2500	406,28	363,12
5000	737,78	675,79

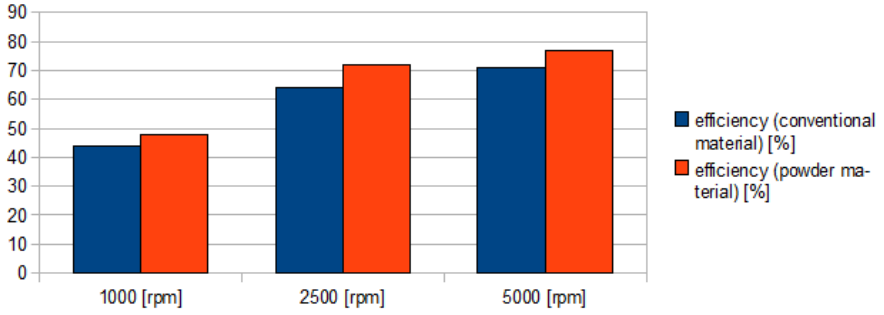

Fig. 7 Drive efficiency comparison at different speed level

Energy efficiency as a quantity index is not the only one. Power consumption from the grid should also be seen in terms of quality. Standard electric drive with the constant voltage level intermediate circuit is characterized by a high input current distortion. The operation of the power factor correction (PFC) module was determined by analyzing different THD values (THD-F – Total Harmonic Distortion in a comparison to fundamental and THD-R – in a comparison to signal's RMS value). Summary from figure 8 is a group of average values of drive measurements at 1000, 2500 and 5000 [rev/min] and with a power consumption of 50, 100, 150, 200 and 250 [W].

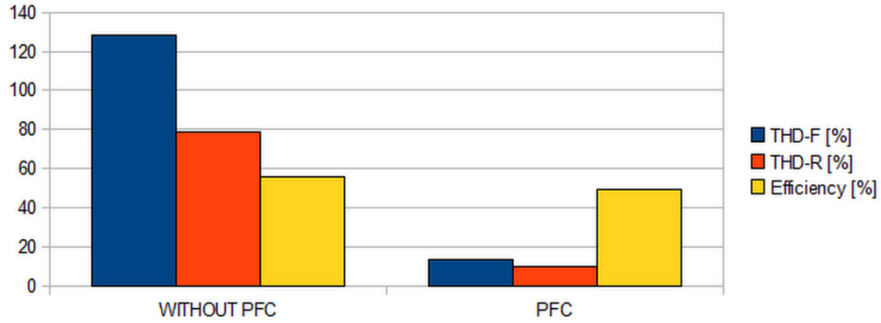

Fig. 8 Input current total harmonic distortion and drive overall efficiency with and without active power factor correction

3 Conclusions

It has been shown that the use of an active PFC based on boost topology allows for significant improvements in energy consumption quality from the grid. THD was reduced (on average 8 times) compared to the only passive input filter. The cost of PFC block usage in the drive was efficiency decrease of about 5 [%] at rated load and 40 [%] for low loads, what gives small absolute value.

Based on the results of the studies the use of powder material in the switched reluctance motor magnetic circuit increased the energy efficiency of the drive in comparison to a standard design composed of steel plates. The energy efficiency index increase by an average of about 10% for a wide range of speeds and load torques was shown. This allows to grounds further research into the way of modification of the powder composite and further efficiency improvement. The latest alternative to standard powder material cores are a *SMSS* (Super MSS^{TM}, improved *Sendust* material) , recognized today as the most valuable magnetic material [4]. It is possible to achieve: higher efficiency at high temperatures, high current carrying capacity, high energy storage capacity, low loss (10 times smaller in relation to the iron powder cores). These cores have been designed with the aim of replacing the powdered iron cores in systems operating in the frequency range 25-500 [kHz], while maintaining high performance stability during operation. All this makes them a high potential for use as building material SRM magnetic circuit in the future.

References

[1] Fabianski, B.: Phase synchronization of switched reluctance motor based on asymmetric feedback position signal. Studies from Automatics and Informatics (36), 15–26 (2011)

[2] Fabianski, B.: Switched reluctance motor drive inverter. In: SENE Conference Materials, Lodz (2011) CD ISBN: 978-83-7283-439-3

[3] Krishnan, R.: Switched reluctance motor drives. CRC Press (2001)
[4] Szycko, T.: Inductance. Practice Electronics 1, 96–99 (2005)
[5] Vukosavic, S., Stefanovic, V.R.: SRM inverter topologies: a comparative evaluation. In: Industry Applications Society Annual Meeting, vol. 2, pp. 946–958 (1990)
[6] Wac-Wlodarczyk, A.: Magnetic Materials – Modelling and Applications, pp. 16–17, 33–34. Lublin University of Technology Publishing (2012)
[7] Waide, P., Brunner, C.U.: Energy-Efficiency Policy Opportunities for Electric Motor-Driven Systems. International Energy Agency (2012)

Switched Reluctance Motor Drive Embedded Control System

B. Fabianski and K. Zawirski

Poznan University of Technology, Faculty of Electrical Engineering, Institute of Control and Information Engineering, Piotrowo 3a, 60-965 Poznan, Poland
{bogdan.fabianski,krzysztof.zawirski}@put.poznan.pl

Abstract. A new switched reluctance motor drive control system with real-time embedded system implementation example was presented in the paper. Genesis of the article, goals and motivation was shown. Construction of SRM with its advantages were described. Drive control system – hardware and software domain were introduced with the focus on low-resolution position feedback signal utilization in high speed drive problem. Details about phase synchronization and use of software phase locked loop were presented. Experimental results of embedded system implementation was shown to confirm the performance of introduced algorithms.

1 Introduction

The article genesis was the research grant named "Powder magnetic circuits in the universal electric drives", where the main goal was to made a new motors from iron-powder material based on the conventional, commercial models for comparison. As switched reluctance motor (SRM) needs to be supply by power inverter [5] it was necessary to project and build a new, dedicated control system. The article presents a new SRM drive control system operating with simple, single line binary rotor position feedback.

1.1 Switched Reluctance Motor

Switched Reluctance Motor Drive (SRMD) or just SRM was being of high interests from the industry because of its unique features. Monolithic, simple design of switched reluctance motor rotor results in resistance to centrifugal forces and the low probability of failure. This is about the potential for propulsion applications. The barrier of wideband use of SRM such as the need for complex control algorithms as a result of significant technological advances and declining chip prices was reversed. Given the high potential of SRM industry deployment, there are being intensive research in the field of control algorithms to improve the dynamics and quality of work SRM drives.

T. Březina and R. Jabloński (eds.), *Mechatronics 2013*,
DOI: 10.1007/978-3-319-02294-9_43,

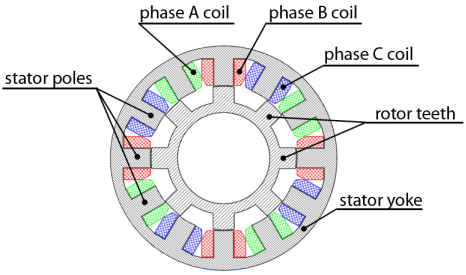

Fig. 1 Section of the SR motor

Operating parameters of the engine used in the study were as follows: rated power P_N = 250 [W], maximum speed ω_{MAX}= 10000 [rpm], rated voltage U_N = 230 [V]. Topology of engine was 12/8 (three-phase two pairs of stator poles and eight rotor teeth as shown in figure 1).

2 SRM Drive Control System

The main concern about custom laboratory stand construction project was: security, stability and low overall building costs. General structure of the drive system was presented on Figure 2. The drive project was an effect of compromised level of logic, galvanic and geometrical isolation blocks with potential source of electromagnetic interferences (EMI) from sensitive ones. As could be seen on the corresponding draw there was achieved full separation the high voltage part (Figure 3– HV) from low voltage (LV). More details about drive hardware construction details can be found in [3].

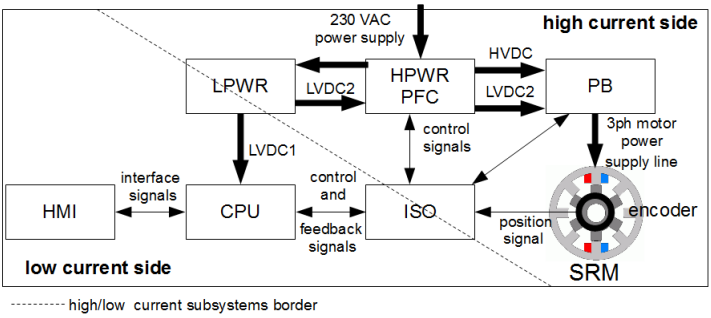

Fig. 2 SRM drive general structure

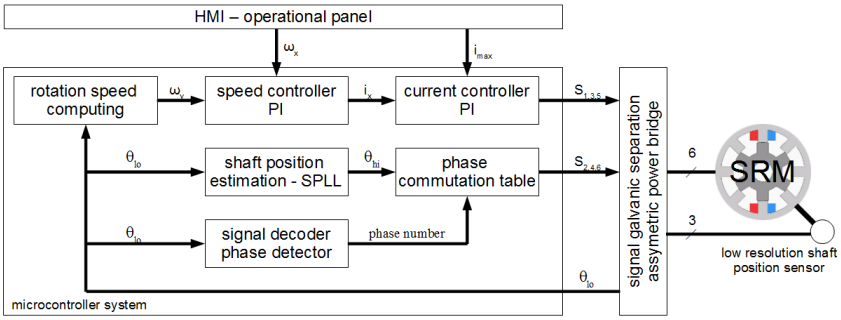

Fig. 3 SRM drive control system structure

Figure 3 shows a block diagram of the structure of the drive control SRM. The microprocessor system implemented algorithms:

- phase current controller with proportional-integrating structure (PI),
- drive speed controller (PI),
- determining the speed based on the feedback signal asymmetric return,
- determining the electronic commutation periods based on the actual value of the angle and phase synchronization signal,
- shaft position estimation algorithm based on phase-locked loop (PLL),
- detection of the sync point position of the rotor relative to the stator poles.

2.1 Active Phase Detection and PLL Control Algorithms

Figure 4 shows feedback signal shape. N (N corresponding to motor phase count) lines interface commonly used in electronic commutated motors (e.g. BLDC, SR motors with hall position sensors) was replaced there by single line binary code. Standard N lines interface binary combination directly gives information about motor active phase. Adequate solution for reduced, single line position feedback was introduced with utilization of its asymmetric nature (in the opposite to the incremental encoder). Signal could be decoded by its level and duration time. Four

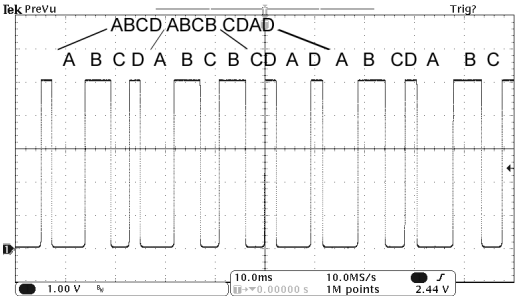

Fig. 4 Position feedback signal shape at constant speed

alphabet letters was taken into account to define signal shape (A, B, C, D – see Figure 4) that shown around in 12-elements cycles. Theoretically the alphabet was complex enough to detect the active phase (from all three motor phases) correlated to the rotor position.

It follows that the cycle of each phase of the electrical modulation corresponding to 4-element code, which should be determined in the numbering system. Selected, 4-piece set of characters of code is easy to record. Just two bits would be enough. The signal corresponds to the class A is coded as 00b, B - 01b, 10b is C, while D - 11b. For the interpretation of the single phase code modulation, 8bit variable is sufficient. Mechanism of signal assign in one of four classes requires its logic state detection and pulse duration. Classification is, however, difficult as pulse duration is dependent on the actual speed. Detection of logic state seems to be clear, the impetus for classification to a group of "long" or "short" would not. It was assumed therefore, that the repeated signal shape of twelve pulse has a width of 18 quanta. The signals of class A and B have a width of two, and C and D of one quantum. In this way, the classification set strict limits the pulse width in relation to the period:

$$g(L = 9, S = 18) = \frac{\frac{1}{L} + \frac{1}{S}}{2} = \frac{1}{12} \approx \frac{5}{64} \tag{1}$$

where: g-border classification, L-number of "long" pulses per period, S-number of "short" pulses per period. It could be seen, therefore, that the obvious method of classification derived from the same formula:

$$\omega = \frac{k}{q}, q = \frac{k}{\omega} \tag{2}$$

$$p = \frac{\delta}{q} = \frac{\delta\omega}{k} \tag{3}$$

where: ω - rotation speed, k - angle-velocity scaling factor (depending on the configuration of the digital system), q - number of units of time in which there was a pure-defined fixed rotation angle, p - absolute pulse width measured as the portion of the phase cycle, δ - the number of time units that defines the length of a single pulse. For such a defined problem, adopted solution of classification task will be simple:

- if (p <= g) signal belongs to class C or D (clarified of logic state reading),
- if (p > g) signal is a class A or B.

String of four pulses stored in the form of 8-bit number allows for a relatively simple interpretation of the classification results. For example, the string coded as CBCD corresponds to the value 0x9B, ADAB = 0x31, CDAB = 0xB1. As could be seen, there are only three allowed strings from 256 combinations. It follows that the probability of detecting a false point of the phase-locked (system error) when the pulse misclassification occurred was:

$$P(E) = \frac{3}{4^4} = \frac{3}{256} = 1{,}18\ [\%] \tag{4}$$

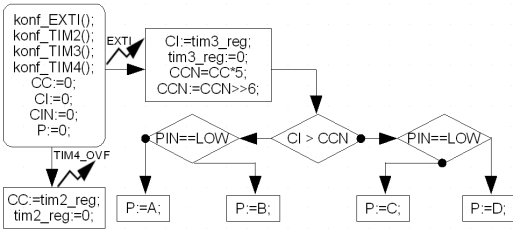

Fig. 5 Impulsator signal classification algorithm

The feedback pulse classification algorithm was approximated in the diagram of Figure 5 (details about microcontroller implementation could be found in [2]). Abbreviations used were: CC - encoder signal period, CI - pulse duration, CIN - normalized (to the CC) pulse width, TIM4_OVF - interruption after a period of the feedback signal, EXTI – interrupt after edge detection AI, P - the classification of the analyzed pulse. Note the step: *CCN = CC*5; CCN:= CCN>>6* (bit-shift operation), which corresponds to an optimized (which does not require time-consuming division) operation 1/12 – see equation (1).

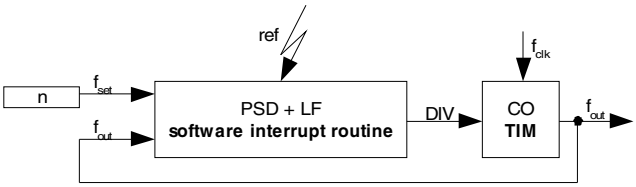

Fig. 6 Microcontroller implementation of PLL structure

In the proposed solution of feedback signal resolution increasing, the Phase Locked Loop (PLL) was used only as frequency multiplier of the reference signal. Very similar solution was described in [1], but presented system has four binary lines of the feedback system to use, which were not available in mechanical simplified system which the paper was about. Additionally it could be said that proposed in [1] solution becomes to DPLL (*Digital PLL*) class, fully hardware and digitally realized, where described implementation becomes to SPLL (*Software PLL*).

There was an idea of the optimization and implementation of Phase Locked Loop (PLL) in embedded system presented in Figure 6 based on general model. As the start point there was the presumption made that controlled oscillator role would be taken by built-in STM32F1 system timer (*TIM*) clocked by constant frequency with programmable division block (*DIV*) and the register *CNT*. Between the next reference signals with frequency (f_{ref}) proportional to the rotor speed there were synchronized with f_{ref} impulses counting from zero to the set count – n (which was multiplication factor). Achieved in this method CNT value was estimated angle position to direct use in control algorithms. The *DIV* value was computed in connected (in comparison to base model) blocks *PSD* and *LF,*

software realized in the system interrupt routine from external input signal – *ref*. As the time reference for phase shift there was the *TIM* register value taken. TIM register value with known *DIV* division factor and clock f_{clk} could be used for time measurement. The actual time period (T_{ACT}) of the loop outgoing signal (f_{out}) measured in the moment of *ref* interrupt routine handling (j – iteration) is equal to:

$$T_{ACT} = \frac{CNT_j \cdot DIV_j}{f_{clk}} \tag{5}$$

and the difference between the demanded time period and the real one (T_{DEL}) computed from the equation:

$$e_j = \mathrm{n} - \mathrm{CNT_j} \tag{6}$$

with the presumption of the error filtration for disturbances influence minimization on control loop as follows:

$$\Delta n_j = K_p e_j + K_I \sum_{i=0}^{j} e_i \tag{7}$$

is equal to:

$$T_{DES_j} = \frac{\Delta n_j \cdot DIV_j}{f_{clk}} \tag{8}$$

and:

$$T_{DEL_j} = T_{ACT_j} - T_{DES_j} = \frac{DIV_j\,(\mathrm{CNT_j} - \Delta n_j)}{f_{clk}} \tag{9}$$

To compute the new value DIVj+1 based on the current one equation (9) should be transformed and solved as shown:

$$\frac{DIV_j\,(\mathrm{CNT_j} - \Delta n_j)}{f_{clk}} = \frac{DIV_{j+1} \cdot \mathrm{n}}{f_{clk}}\,,\; DIV_{j+1} = \frac{DIV_j\,(\mathrm{CNT_j} - \Delta n_j)}{\mathrm{n}} \tag{10}$$

To optimize computing equation (10) and short division operation to one core clock the n value was set to 1024 to achieve enough resolution and reduce division by n to bit shift operation. There was used proportional-integral (PI) filter structure in the LF block with anti-windup algorithm of 2nd order. Appropriate gains: K_p and K_i values were set based on the article [4], where was proved that for the linear discrete model gains that gives stability and noise cancellation should be computed from the follow equations:

$$K_p + K_I = 1\,,\; K_I = K_p^2 \tag{11}$$

Finally $K_p = 0{,}62$ and $K_i = 0{,}38$ values were taken as the LF block gains.

When the PLL worked and the resolution of the position sensor was much improved it becomes possible to implement further algorithms for optimal turn-on and turn-off angles for the corresponding excited phase.

The implementation of the PLL and motor synchronization algorithms in a dedicated SRM drive allowed meaningful comparison of conventional construction and powder material based motor by compensating inaccuracies of sensor. Improper points of commutation would result drive dynamics and energy efficiency decrease. The development of algorithms based on the PLL loop resulted in the ability to control the advance angle of phase excitation and a significant enlargement of the drive achievable speeds and load torque.

2.2 *Experimental Results*

Figure 7 shows the real, recorded waveforms in sequence: 1 – PLL counter value, 2 – phase current correlated with PLL counter, 3 – primary signal of the low resolution encoder. Cursors: *a* and *b* marks software shift of the corresponding phase excitation moment. PLL counter value could be used to excitation offset as well as for turn-on angle advance what gives capability of wide range drive speed control at various load torque.

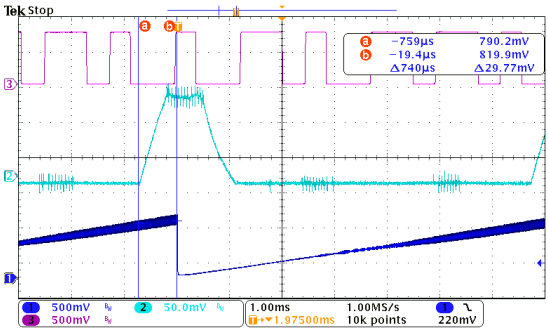

Fig. 7 Phase excitation advance angle based on PLL algorithm

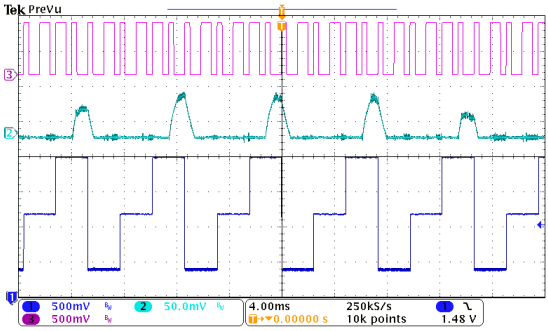

Fig. 8 Active phase detection algorithm visualization

Figure 8 shows the algorithm of the motor active phase detection based on the encoder signal. It presents the follows: 1 - active phase of the digitized signal decoded in the way of proposed algorithm (3 levels corresponding to the phases A, B and C), 2 - selected motor phase current, 3 – reference, low-resolution encoder signal. On the basis of previous experiments, there was no algorithm error detected.

3 Conclusions

There were presented a new switched reluctance motor drive control system with real-time embedded system implementation example in the article. Genesis of the article, goals and motivation was shown in the begin. Drive control system – hardware and software domain were introduced with the focus on low-resolution position feedback signal utilization in high speed drive. Details about phase synchronization and use of software phase locked loop were presented. Experimental results of embedded system implementation was shown to confirm the performance of introduced algorithms. Proposed structure of the control system made drive capable of wide range speed control at various load torque in relatively cheap and simple construction. Literature in the field of PLL usage in SRM drive was analyzed to confirm the original approach of presented work. The proposed solution would provide one of the starting points for the design of advanced expert system of SRM drive control for fault tolerant control.

References

[1] Deskur, J., Maciejuk, A.: Application of digital phase locked loop for control of SRM drive. In: 12th European Conference on Power Electronics and Applications (EPE), Aalborg (2007)
[2] Fabianski, B.: Phase synchronization of switched reluctance motor based on asymmetric feedback position signal. Studies from Automatics and Informatics (36), 15–26 (2011)
[3] Fabianski, B.: Switched reluctance motor drive inverter. In: SENE Conference Materials, Lodz (2011) CD ISBN: 978-83-7283-439-3
[4] Jin-Woo, A., Seok-Gyu, O., Sung-Young, P., Cheul-U, K., Young-Moon, H.: Digital PLL Technique for Precise Speed Control of SR Drive. In: Power Electronics Specialist Conference (PESC), vol. 2, pp. 815–819 (1999)
[5] Krishnan, R.: Switched reluctance motor drives. CRC Press (2001)

Design and Implementation of A Single-Stage Full-Bridge DC/DC Converter with ZVS Mode

A. Diker[1], D. Korkmaz[2], Ö.F. Alçin[2], U. Budak[1], and M. Gedikpınar[2]

[1] Bitlis Eren University, Faculty of Engineering and Arch., Bitlis, Turkey
aykutdiker@gmail.com
[2] Firat University, Faculty of Technical Education, Elazig, Turkey
mgedikpinar@firat.edu.tr

Abstract. In this paper, a single-stage full-bridge converter with auxiliary circuit elements which allow its main power circuit switches to operate with *ZVS* mode is presented. By creating dead time between power switches and working across, high frequencies which are the basis of the soft-switching are reached. Thus, more uniform output of system is obtained. In addition, it is observed that output rectifier diodes are exposed to parasitic oscillations. Experimental results obtained from the prototype with *DC 180V* input voltage, *DC 45V* output voltage and *50kHz* operation frequency are illustrated in the paper.

1 Introduction

The Switching techniques define the voltage and current conditions that are applied to the power switches in a switch mode full-bridge converter between conducting and non-conducting states. All power electronics applications include some switching methods. These methods are divided in two modes such as 'Hard-switching' and 'Soft-switching' [1]. However, the traditional hard-switching converters have high *dv/dt, di/dt* in their operation which causes extreme Electromagnetic Interference *(EMI).* If switching converter is not controlled sufficiently, these *EMI* noise negative affects the operation of other circuit components [2-7]. Moreover, at high frequency in switching mode, *EMI* and switching loses increase and high voltage and current stresses consist of power switches [7]. For correcting these problems, soft-switching techniques are used in these converters [5-13]. Soft-switching have a lot of advantages such as; simple control, analysis, high efficiency, better performance of power switches and low *EMI* [6-10]. Soft-switching methods are divided to four classes that are Zero Voltage Switching **(***ZVS***),** Zero Current Switching *(ZCS),* Zero Current Transition *(ZCT)* and Zero Voltage Transition (*ZVT)* [12-14]. Therefore, the switching losses, peak voltage and switch current are reduced, which lead to small interference. Besides, the resonant converters can operate at high frequencies, the size of circuit can be reduced and the power density can be raised. The resonant converter produces the damped resonant signals using the *LC* components with switch voltage or current waveform shaped as sinusoidal [12]. These conceptions include some disadvantages that are more complex control circuit and the effect of parasitic

T. Březina and R. Jabloński (eds.), *Mechatronics 2013*,
DOI: 10.1007/978-3-319-02294-9_44,

elements in the circuit performance. In order to overcome these disadvantages, various methods are derived [14-16]. The circuit can be operated at constant frequency so as to achieve better circuit performance. External capacitance can be used to turn-on and turn-off the switches with resonant inductance [12,16].

In this paper, the objective is to design and implementation a single-stage full-bridge converter with auxiliary circuit elements which allow its main power circuit switches to operate with *ZVS* mode.

The rest of this paper is organized as follows. In Section 2, the structure of a full-bridge soft-switching *DC/DC* converter and steady-state operations are detailed. Section 3 describes the equations and parameters of the designed system. The experimental results based on the prototype circuit are presented to verify the system performance in Section 4. Finally, conclusions are presented in Section 5.

2 Circuit Configuration and System Analysis

Driven with *IGBTs* (Q_A-Q_D), a full-bridge soft-switching *DC/DC* converter is shown in Fig. 1.

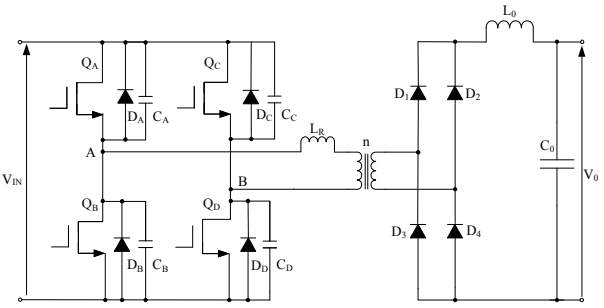

Fig. 1 Full-Bridge soft switching converter

Main transformer provides the electrical isolation and voltage level conversion and it comprises one primary windings and one secondary windings with n turns ratio. The inductor *Lr* represents the leakage inductance of the transformer. Under steady-state operation, four operating stages within one of the switching cycle are shown in Fig. 2. [12-13].

a) Stage 1 (t_0-t_1): Q_A, Q_D are turned on. The primary current linearly increases. The input power is transferred through the high frequency transformer from the DC voltage source V_{IN} [12-13].

b) Stage 2 (t_1-t_2): In this stage, Q_A is turned off and transformer primary current flows through C_A and C_B. At the same time, C_A charges from *0V* to V_{IN}. Transformer winding capacitance and C_B discharge. Voltage of Q_B and switch voltage V_{GE} is zero [12-13].

c) Stage 3 (t_2-t_3): When this stage begins, Q_B and Q_C are turned on, load current flows through D_2 and D_3. At this time, the *IGBT* terminal voltage approaches zero

voltage and the primary current is zero. At the same time, output filter inductance stores the energy [12-13].

d) Stage 4 (t_3-t_4): Primary voltage flows through C_C and C_D. Primary current is charged to C_D and discharged to C_C. When the end of stage C_D is charged to V_{IN}, C_C is discharged to zero [12-13].

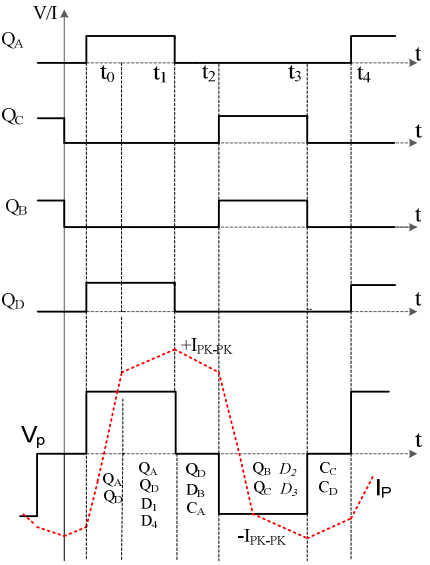

Fig. 2 Operation waveforms of full-bridge soft switching converter

Fig. 3. shows the equivalent circuits during a one period of steady-state operations.

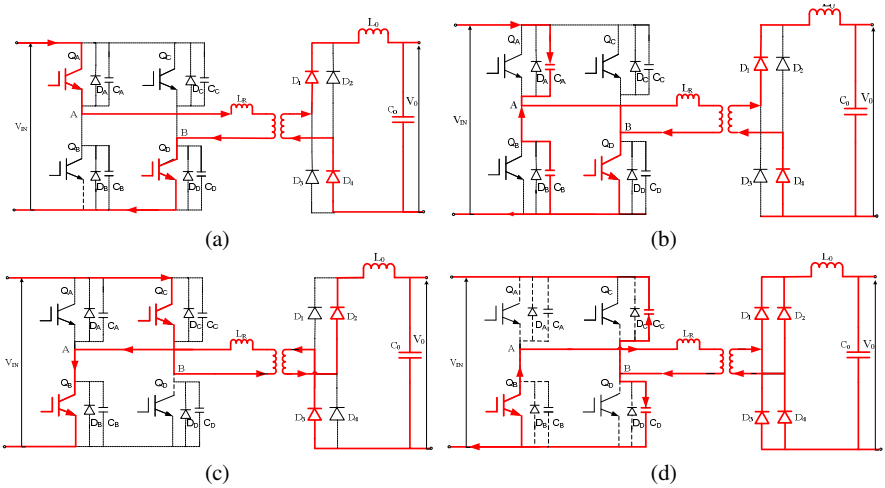

Fig. 3 Equivalent circuits during a one period of steady state operations: (a) Stage 1 (t0-t1). (b) Stage 2 (t1-t2). (c) Stage 3 (t2-t3). (d) Stage 4 (t3-t4)

3 Parameters and Equations of the Designed System

The equations of designed system are discussed in this chapter. The design parameters are listed as follow: *PWM* operation frequency is adjusted to *50kHz* to achieve a stable system; *DC* input voltage and *DC* output voltage are set to *180V*, *45V*, respectively and also, *ETD-44-N27* ferrit core power transformer turns ratio and primary turns ratio is set such as *n:4* and N_P*:32*, respectively, by using Equation (1) and (2). The design parameters of the transformer are expressed as [2,16]:

$$N_P=V_{IN}.t_{ON}.10^4(A_e.\Delta B) \tag{1}$$

$$n=N_{PRI}/N_{SEC} \quad and \quad V_O=V_{IN}/D \tag{2}$$

The resonant radian frequency (*Wr*) is related to the resonant components by the Equation (3):

$$Wr=1/(Lr/Cr)^2 \tag{3}$$

The inductance and capacitance of the output filter are given as:

$$L_o=V_o.t_{off}/\Delta I_0 \text{ and } C_0=\Delta I_0/(8.f_s.\Delta V_0) \tag{4}$$

The resonant inductance is obtained from the transformer leakage inductance and the resonant capacitance C_r is computed from the *IGBT* output capacitance C_{oes}. The transformer parasitic capacitor C_{xmfr} on the primary winding side is given as follow:

$$C_r=[8/3C_{oes}C_{xmfr}] \tag{5}$$

The delay time is set to one-quarter of the resonant period:

$$t_d=t_r/4=\pi(Lr/Cr)^2/2 \tag{6}$$

As detailed, the energy stored in the resonant inductor must be greater than the capacitive energy required for the transition to occur within the allocated transition time. The governing equations are summarized below:

$$0.5L_r(IP_{ri(min)})^2>0.5C_r(V_{in(max)})^2 \text{ or} \tag{7}$$

$$L_r(I_{Pri(min)})^2>C_r(V_{in(max)})^2$$

Cr and V_{IN} can be estimated for a given application, this term is a constant and *Lr* is quantified [2].

4 Experimental Results

Full-bridge, soft-switching *DC/DC* converter main circuit based on *DC 180V* input voltage and *DC 45V* output voltage is designed and implemented as seen in Fig. 4. Operation frequency is adjusted to *50kHz*. Also, switches of the bridge are driven at constant frequency and nearly *50%* duty ratios with *4.40usn* dead-times. Integrated *UC 3875* circuit is used for control of power switches with *PWM*

signals. The transformer turns ratio is *4*. Additionally, isolation system between control circuit and main circuit is provided by using *HCPL-3120* opto-coupler. *IRGP4PC50UD* is used for *IGBTs* power switches (Q_A-Q_D). Experimental results are obtained by using *DL OSC2CH100D* digital oscilloscope. In the system output, the resistive load is used.

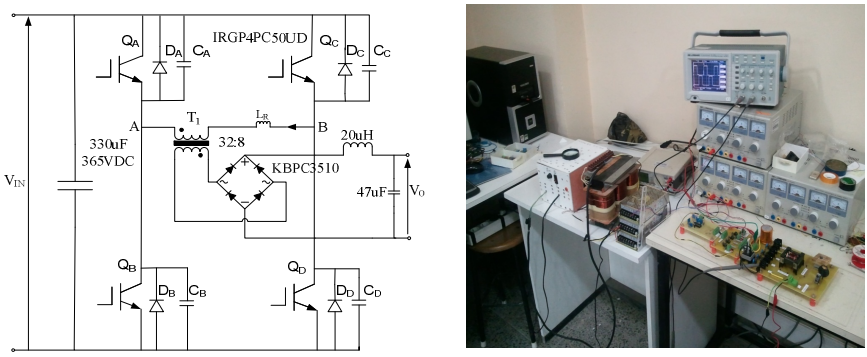

(a) (b)

Fig. 4 Experimental set-up: (a) Designed main circuit. (b) Experimental environment

Experimental results are presented in the form of photo images by using the interface program of the oscilloscope. Fig. 5 (a) shows gate-emitter *(V_{GE})* and collector-emitter *(V_{CE})* voltages of power switch Q_B obtained the experimental set-up. Transformer primary of the voltage *(Vp)* and current *(Ip)* are given in Fig. 5 (b). System output is given in Fig. 6 (a). Finally, *PWM* signals of the Q_A-Q_D and Q_B-Q_C are shown in Fig. 6 (b) in the form of captured photo image.

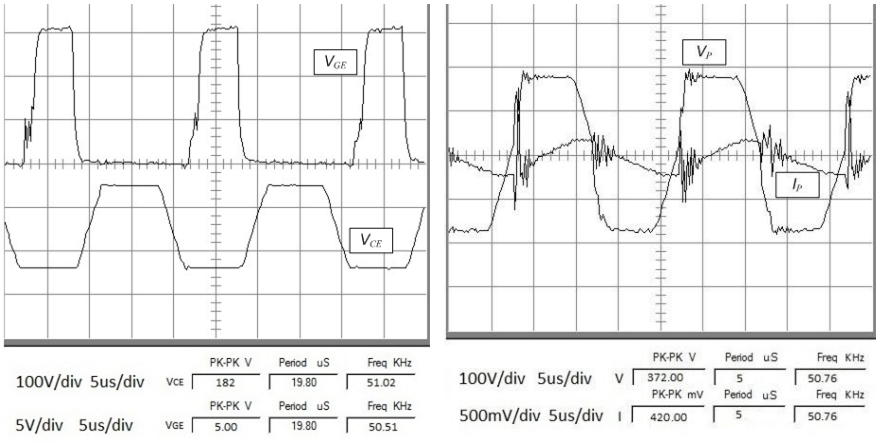

(a) (b)

Fig. 5 (a) V_{GE}-V_{CE} voltages of the Q_B. (b) Waveforms the transformer primary voltage (*Vp*) and current (*Ip*).

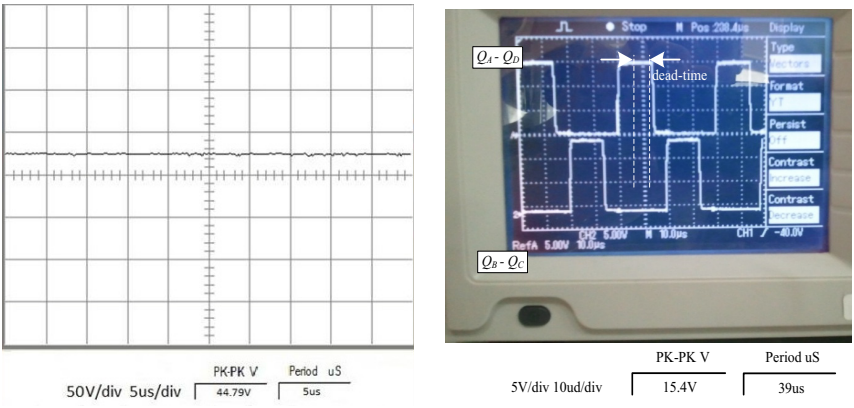

(a) (b)

Fig. 6 (a) System output of full-bridge soft-switching converter. (b) PWM signals Q_A-Q_D and Q_B-Q_C of the opto-coupler.

Obtained from the prototype at *DC 180V* input voltage and approximately *DC 45V* output voltage, V_{GE} and V_{CE} voltages of the power switches are reached to *15V* and *182V*, respectively. In the waveforms of experimental studies, by creating dead time between power switches and working across, high frequencies which are the basis of the soft-switching have been reached.

5 Conclusions

In this paper, a single-stage full-bridge converter with auxiliary circuit elements which allow its main power circuit switches to operate with *ZVS* is presented. The features of this converter include soft-switching mode for all switches and fixed frequency operation. The design guidelines of the converter and experimental results are given, respectively. The feasibility of the proposed converter is verified experimentally at *50kHz* operation frequency. The proposed converter is very suitable and has good performance for medium power and high efficiency *DC/DC* converter such as power supply. When the obtained experimental results are evaluated, it is considered for the control of *SMPS* that the effectiveness of the circuit can be increased by using microprocessor, microcontroller, *DSP*, etc.

Future research will focus on more robust circuit converter design for high power systems.

References

[1] Hutchings, B.: Introduction to SMPS Control Techniques. In: Product Marketing Manager, Digital Signal Controller Division, January 27, pp. 14–16 (2010)

[2] Ching, T.W., Chan, K.U.: Review of Soft-Switching Techniques for High-Frequency Switched-Mode Power Converters. In: IEEE Vehicle Power and Propulsion Conference, pp. 1–6 (September 2008)

[3] Hamada, S., Nakaoka, M.: Analysis and design of a saturable reactor assisted soft-Switching Full-Bridge DC-DC Converter. In: 22nd Annual IEEE Power Electronics Specialists Conference, PESC 1991 Record, pp. 155–162 (1991)
[4] Wu, X.H., Xu, M.D., Kong, J.H., Yang, C., Qian, Z.: High Power High Frequency Zero Current Transition Full Bridge DC/DC Converter. In: Proceedings of 1998 Thirteenth Annual Applied Power Electronics Conference and Exposition, APEC 1998, vol. 2, pp. 823–828 (1998)
[5] Wang, C.M., Wang, Y.N., Yang, C.H.: A New ZVS-PWM Full-Bridge Step-Up/Down Converter. In: The 30th Annual Conference of the IEEE Industrial Electronlcs Society, vol. 1, pp. 908–913 (November 2004)
[6] Redl, R., Sokal, N.O., Balogh, L.: A novel soft-switching full-bridge DC/DC converter: Analysis, design considerations, and experimental results at 1.5 kW, 100 kHz. In: Power Electronics Specialists Conference, PESC 1990, pp. 162–172 (1990)
[7] Martins, C.D., Barbi, I., Castaldo, F.C.: Application of the ZVS-PWM Commutation Cell to a Full-Bridge DC-DC Converter. In: 17th International Telecommunications Energy Conference, INTELEC 1995, pp. 558–564 (1995)
[8] Choo, H.-B., Kuk, L.-B., Yoo, S.-B., Hyun, D.-S.: A Novel Secondary Clamping Circuit Topology for Soft Switching Full-Bridge PWM DC/DC Converter. In: Proceedings of 1998 Thirteenth Annual Applied Power Electronics Conference and Exposition, APEC 1998, vol. 2, pp. 840–845 (1998)
[9] Moisseev, S., Sato, S., Hamada, S., Nakaoka, M.: Full bridge soft-switching phase-shifted PWM DC-DC converter using tapped inductor filter. In: 2003 IEEE 34th Annual Conference on Power Electronics Specialist, PESC 2003, vol. 4, pp. 1826–1831 (2003)
[10] Bhat, A.K.S., Luo, F.: A new gating scheme controlled soft-switching DC-to-DC bridge converter. In: The Fifth International Conference on Power Electronics and Drive Systems, PEDS 2003, vol. 1, pp. 8–15 (2003)
[11] Sato, S., Moisseev, S., Nakaoka, M.: A novel synchronous rectifiers based ZVS-PWM DC-DC power converter with extended soft-switching operation range. In: The 25th International Telecommunications Energy Conference, INTELEC 2003, pp. 268–273 (2003)
[12] Hsieh, G.C., Li, J.C., Liaw, M.H., Wang, J.P., Hung, T.F.: A Study on Full-Bridge Zero-Voltage-Switched PWM Converter: Design and Experimentation. In: IECON 1993, vol. 2, pp. 1281–1285 (1993)
[13] Diker, A.: Yumuşak Anahtarlamalı Tam Köprü Güç Kaynağı Tasarımı., Master Thesis, Fırat Universtiy, Institute of science, Elazig (2012)
[14] Hua, G., Lee, F.C.: Soft-Switching Techniques in PWM Converters. IEEE Transactions on Industrial Electronics 42, 595–603 (1995)
[15] Li, H., Jiang, Q.: Design of a FPGA Controller for Full Bridge Phase-Shifted Zero Voltage Switching DC/DC Power Converters. In: AUPEC 1999 (Australasian Universities Power Engineering Conference) (September 1999)
[16] Ahmed, N.A., Miyatake, M., Nishimura, K., Hyun, W.L., Nakaoka, M.: Novel High Frequency Planner Transformer Linked Soft Switching DC-DC Power Converter with Secondary Side-Phase Shifted PWM Active Rectifying Switches. In: International Conference on PEDS 2005, vol. 1, pp. 129–135 (2005)

Sensitivity Analysis of the Induction Machine Torque to the Substituting Circuit Elements

M. Patocka and R. Belousek

Brno University of Technology, Faculty of Electrical Engineering and Communication, Technicka 12, 616 00, Brno, Czech Republic
patocka@feec.vutbr.cz, xbelou01@stud.feec.vutbr.cz

Abstract. The paper deals with the theoretically derived sensitivity of the torque characteristics to individual substituting circuit parameters of the induction machine. It is considerably difficult to find the coincidence between the measured and calculated torque characteristics of the induction machine. It is caused by the implementation of several simplifying assumptions during the derivation of the torque characteristics. All of substituting circuit parameters are considered as constants when deriving characteristics. However, those assumptions don't meet with the real machine behavior. Particularly, skin-effect and temperature rise during measurement cause change of resistors values. Those changes afterwards lead to inaccuracy of characteristics comparison.

1 Introduction

It is known that attainment of the ideal coincidence between measured and calculated torque characteristics of the induction machine is considerably difficult. Deviations are caused by the change of the resistances due to skin-effect and especially due to temperature rise of windings during the measurement. It is also known that these torque deviations cannot be explained just only by the change of resistances. Articles [4], [5] deal with the measurement of the induction machine torque characteristics. Any problems and measurement results are discussed in article [3]. Article [2] deals with the identification of the substituting circuit parameters.

Therefore the sensitivity analysis of the torque characteristics to individual elements of induction motor substituting circuit was performed in this article. The analysis will be presented on the ordinary produced machine AOM 090L02-016, 2.2 kW, $2p = 2$, 3×400V, 50 Hz.

2 Substituting Circuit of the Induction Machine

The substituting circuit of the induction machine in the form of the Γ-network (see Fig. 1.) was chosen for the purpose of the sensitivity analysis. Purposely was not used T-network, because in [1] is shown that Γ-network is absolutely full-blown and equal when comparing it with T-network.

T. Březina and R. Jabloński (eds.), *Mechatronics 2013*,
DOI: 10.1007/978-3-319-02294-9_45,

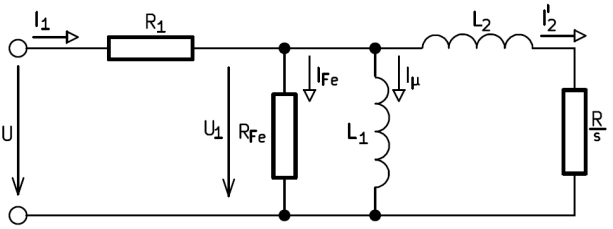

Fig. 1 Substituting circuit of the induction machine in the form of the Γ-network

The calculation of the sensitivity analysis will be based on the following torque characteristics equation of the induction motor which was derived for the Γ-network:

$$T = \frac{3U^2 Rp}{\omega s} \frac{1}{\left[\left(1+\frac{L_2}{L_1}\right)R_1 + \left(1+\frac{R_1}{R_{\mathrm{Fe}}}\right)\frac{R}{s}\right]^2 + \left[\left(1+\frac{R_1}{R_{\mathrm{Fe}}}\right)\omega L_2 - \frac{R_1}{\omega L_1}\frac{R}{s}\right]^2}. \quad (1)$$

In the displayed equation occur following parameters: rotor resistance R, stator winding resistance R_1, resistance R_{Fe} respecting iron losses, magnetizing inductance L_1 and leakage inductance L_2. All of these parameters have its significant influence on the final torque characteristics. The Table 1. shows values of these parameters for motor AOM 090L02-016, 2.2 kW, $2p = 2$.

Table 1 Substituting circuit parameters values

parameter name	unit	value
R	[Ω]	2.245
R_1	[Ω]	2.910
R_{Fe}	[Ω]	982
L_1	[H]	0.387
L_2	[H]	0.019

3 Sensitivity Analysis of the Torque Characteristics

Sensitivity of the torque characteristics to the chosen substituting circuit parameter is calculated as the partial differentiation (partial derivative) of the torque characteristics, i.e. (1), according to the selected parameter.

3.1 Sensitivity of the Characteristics to the Rotor Resistance R

It is appropriate to formally transform (1) into the following shape:

$$T = \frac{3U^2 ps}{\omega} \frac{R}{R^2\left[\left(1+\frac{R_1}{R_{Fe}}\right)^2 + \frac{R_1^2}{\omega^2 L_1^2}\right] + 2RR_1 s\left(1+\frac{R_1}{R_{Fe}}\right) + R_1^2 s^2\left(1+\frac{L_2}{L_1}\right)^2 + \omega^2 L_2^2 s^2\left(1+\frac{R_1}{R_{Fe}}\right)^2}. \quad (2)$$

Sensitivity to the change of the resistance R is determined as the derivative of (2) by the variable R:

$$\frac{\partial T}{\partial R} = \frac{3U^2 ps}{\omega} \frac{R_1^2 s^2\left(1+\frac{L_2}{L_1}\right)^2 + \omega^2 L_2^2 s^2\left(1+\frac{R_1}{R_{Fe}}\right)^2 - R^2\left[\left(1+\frac{R_1}{R_{Fe}}\right)^2 + \frac{R_1^2}{\omega^2 L_1^2}\right]}{\left[R^2\left[\left(1+\frac{R_1}{R_{Fe}}\right)^2 + \frac{R_1^2}{\omega^2 L_1^2}\right] + 2RR_1 s\left(1+\frac{R_1}{R_{Fe}}\right) + R_1^2 s^2\left(1+\frac{L_2}{L_1}\right)^2 + \omega^2 L_2^2 s^2\left(1+\frac{R_1}{R_{Fe}}\right)^2\right]^2}. \quad (3)$$

The term $(\partial T / \partial R)$ can be called as the *absolute* sensitivity. The *absolute* sensitivities to another parameters, e.g. $(\partial T / \partial R_1)$, $(\partial T / \partial L_1)$, can be determined by the similar way. However, the problem arises in the case when we want to compare the individual *absolute* sensitivities mutually. This is the reason why we are interested in the *relative* sensitivity $\partial T \Big/ \frac{\partial R}{R}$, i.e. the sensitivity to the *relative* change $(\partial R / R)$ of the resistance R. We can obtain this sensitivity by the modification of (3):

$$\frac{\partial T}{\partial R / R} = \frac{\partial T}{\partial R} R = \frac{3U^2 ps}{\omega} \frac{R_1^2 s^2\left(1+\frac{L_2}{L_1}\right)^2 + \omega^2 L_2^2 s^2\left(1+\frac{R_1}{R_{Fe}}\right)^2 - R^2\left[\left(1+\frac{R_1}{R_{Fe}}\right)^2 + \frac{R_1^2}{\omega^2 L_1^2}\right]}{\left[R^2\left[\left(1+\frac{R_1}{R_{Fe}}\right)^2 + \frac{R_1^2}{\omega^2 L_1^2}\right] + 2RR_1 s\left(1+\frac{R_1}{R_{Fe}}\right) + R_1^2 s^2\left(1+\frac{L_2}{L_1}\right)^2 + \omega^2 L_2^2 s^2\left(1+\frac{R_1}{R_{Fe}}\right)^2\right]^2} R \quad (4)$$

Equation (4) is graphically displayed in the Fig. 2. The figure shows that sensitivity is negative for the slip s = 0 to 0.34, i.e. to the critical torque. Therefore, in this area decreases torque if the rotor resistance increases.

In the following subchapters *3.2* to *3.5* are similarly derived and displayed sensitivities to the remaining parameters R_1, R_{Fe}, L_1, L_2. The Fig. 7. in the conclusion graphically summarizes performed sensitivity analysis of the torque characteristics.

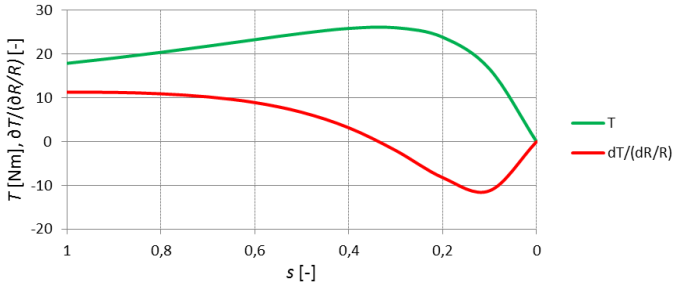

Fig. 2 Sensitivity of the torque characteristics to the relative change of the resistance R

3.2 Sensitivity of the Torque Characteristics to the Relative Change of the Rotor Resistance R_1

Sensitivity to the relative change of the resistance R_1:

$$\frac{\partial T}{\partial R_1} R_1 = -\frac{3U^2 Rsp}{\omega} \frac{2R_1 K_{1,R1} + 2R\left(s + \frac{R}{R_{Fe}}\right) + 2\omega^2 L_2^2 s^2 \frac{1}{R_{Fe}}}{\left[R_1^2 K_{1,R1} + R_1\left[2R\left(s + \frac{R}{R_{Fe}}\right) + 2\omega^2 L_2^2 s^2 \frac{1}{R_{Fe}}\right] + \omega^2 L_2^2 s^2 + R^2\right]^2} R_1, \quad (5)$$

where $K_{1,R1}$ is constant:

$$K_{1,R1} = \left\{\left[\left(1 + \frac{L_2}{L_1}\right)s + \frac{R}{R_{Fe}}\right]^2 + R\left(\frac{R}{\omega^2 L_1^2} - \frac{2s}{R_{Fe}}\frac{L_2}{L_1}\right) + \omega^2 L_2^2 s^2 \frac{1}{R_{Fe}^2}\right\}. \quad (6)$$

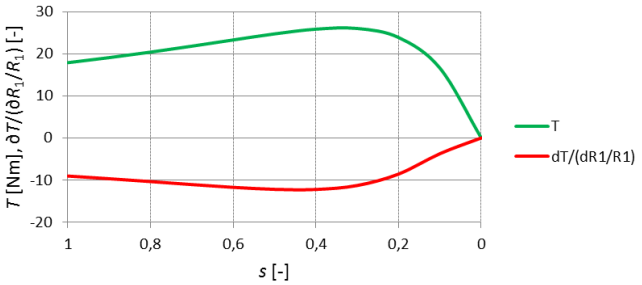

Fig. 3 Sensitivity of the torque characteristics to the relative change of the resistance R_1

Fig. 3. shows that machine torque decreases if the stator resistance increases (due to increasing temperature). This negative effect is observable in the whole range of the slip s.

3.3 Sensitivity of the Characteristics to the Resistance R_{Fe}

Sensitivity to the relative change of the resistance R_{Fe}:

$$\frac{\partial T}{\partial R_{Fe}} R_{Fe} = \frac{3U^2 Rsp}{\omega} \frac{R_{Fe}^2\left(2R_1 R(R_1 s + R) + 2\omega^2 L_2^2 R_1 s^2\right) + 2R_{Fe}\left(R_1^2 R^2 + \omega^2 L_2^2 R_1^2 s^2\right)}{\left[R_{Fe}^2 K_{1,RFe} + R_{Fe}\left(2R_1 R(R_1 s + R) + 2\omega^2 L_2^2 R_1 s^2\right) + R_1^2 R^2 + \omega^2 L_2^2 R_1^2 s^2\right]^2} R_{Fe}, \quad (7)$$

where $K_{1,RFe}$ is constant:

$$K_{1,RFe} = \left[R_1^2 s^2\left(1 + \frac{L_2}{L_1}\right)^2 + \omega^2 L_2^2 s^2 + R^2\left(1 + \frac{R_1^2}{\omega^2 L_1^2}\right) + 2R_1 Rs\right]. \quad (8)$$

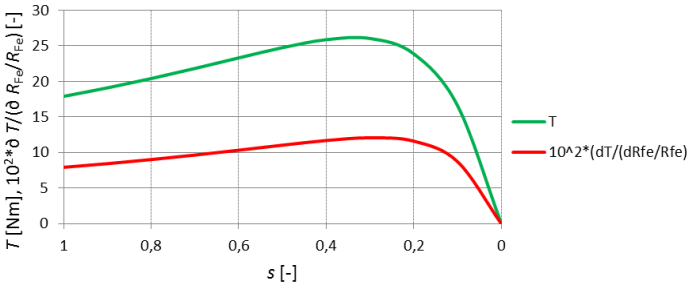

Fig. 4 Sensitivity of the torque characteristics to the relative change of the resistance R_{Fe}

Fig. 4. shows that sensitivity to the respecting iron losses resistance is positive in the whole range if the slip. This means that machine torque increases if the resistance R_{Fe} increases too. On the other hand it is obvious that sensitivity to the resistance R_{Fe} has no effect to the torque characteristics.

3.4 *Sensitivity of the Characteristics to the Magnetizing Inductance L_1*

Sensitivity to the relative change of the magnetizing inductance L_1:

$$\frac{\partial T}{\partial L_1}L_1 = \frac{3U^2 Rsp}{\omega}\frac{L_1^2 2R_1^2 L_2 s^2 + L_1 2\left[\dfrac{R_1^2 R^2}{\omega^2} + R_1^2 L_2^2 s^2\right]}{\left[L_1^2 K_{1,L1} + L_1 2R_1^2 L_2 s^2 + \dfrac{R_1^2 R^2}{\omega^2} + R_1^2 L_2^2 s^2\right]^2}L_1, \tag{9}$$

where $K_{1,L1}$ is constant:

$$K_{1,L1} = \left\{R_1^2 s^2 + \left(1+\frac{R_1}{R_{\mathrm{Fe}}}\right)\left[2R_1 Rs + \left(1+\frac{R_1}{R_{Fe}}\right)\left(R^2 + \omega^2 L_2^2 s^2\right)\right]\right\}. \tag{10}$$

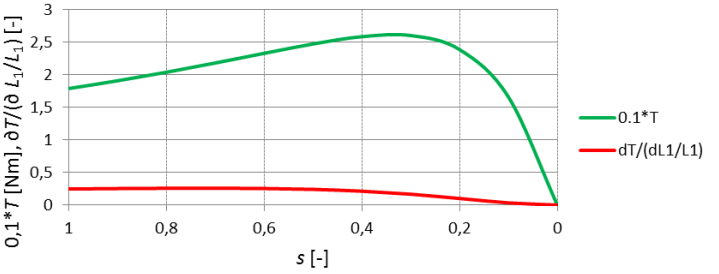

Fig. 5 Sensitivity of the torque characteristics to the relative change of the inductance L_1

Fig. 5. shows that inductance L_1 has insignificant effect to the torque characteristics. Sensitivity to the magnetizing inductance parameter is positive in the whole range of the slip s. The rise of the magnetizing inductance causes the growth of the torque. At same time this sensitivity is much smaller than sensitivity to the stator or rotor resistance.

3.5 *Sensitivity of the Characteristics to the Leakage Inductance L_2*

Sensitivity to the relative change of the leakage inductance L_2:

$$\frac{\partial T}{\partial L_2} L_2 = -\frac{3U^2 Rsp}{\omega} \frac{2L_2\left[\frac{R_1^2 s^2}{L_1^2} + \omega^2 s^2\left(1+\frac{R_1}{R_{Fe}}\right)^2\right] + \frac{2R_1^2 s^2}{L_1}}{\left[L_2^2\left[\frac{R_1^2 s^2}{L_1^2} + \omega^2 s^2\left(1+\frac{R_1}{R_{Fe}}\right)^2\right] + L_2 \frac{2R_1^2 s^2}{L_1} + K_{1,L2}\right]^2} L_2, \quad (11)$$

where $K_{1,L2}$ is constant:

$$K_{1,L2} = \left\{\left(1+\frac{R_1}{R_{Fe}}\right)\left[2R_1 Rs + R^2\left(1+\frac{R_1}{R_{Fe}}\right)\right] + R_1^2\left(s^2 + \frac{R^2}{\omega^2 L_1^2}\right)\right\}. \quad (12)$$

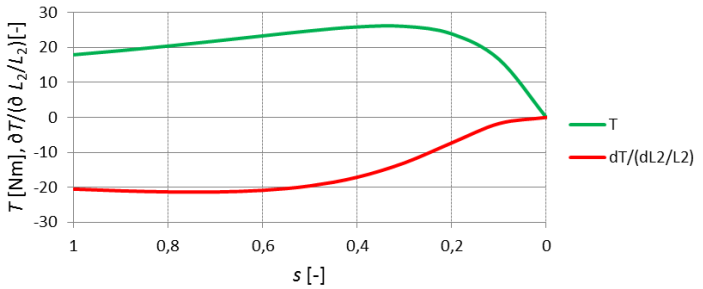

Fig. 6 Sensitivity of the torque characteristics to the relative change of the inductance L_2

Fig. 6. shows that sensitivity to the leakage inductance parameter is negative in the whole range of the slip s. At the same time it is obvious that sensitivity to the leakage inductance L_2 is the greatest of all.

4 Conclusions

In previous chapters were derived and displayed sensitivities to the parameters R, R_1, R_{Fe}, L_1, L_2 of the substituting circuit of the induction machine. The results are graphically summarized and compared in the Fig. 7.

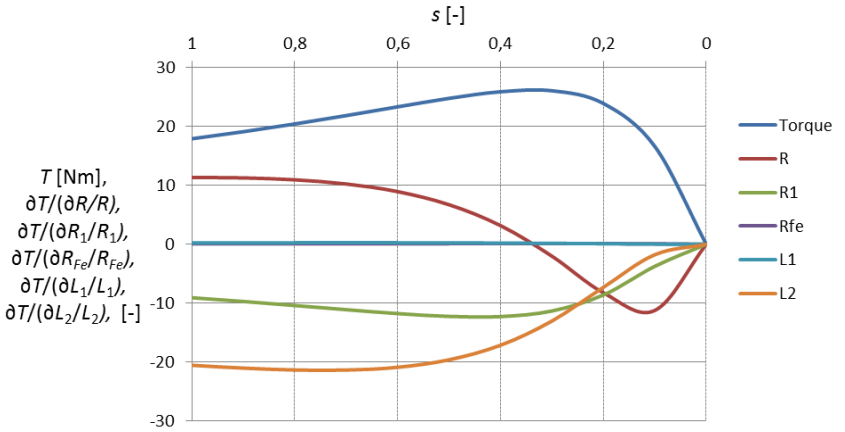

Fig. 7 Comparison of sensitivities of the torque characteristics to the relative changes of induction machine substituting circuit elements

It is well known that deviations between measured and calculated torque characteristics cannot be explained just only by the change of the stator and the rotor resistances. Presented analysis confirms the characteristics sensitivity to both resistances.

Additionally, it is very interesting that the torque characteristics is strongly dependent on the leakage inductance. Therefore, it is possible that the change of the leakage inductance can be responsible for the characteristics deviations. This possibility will be studied in the following experiments.

Acknowledgments. This work was supported by the European Regional Development Fund under project No. CZ.1.05/2.1.00/01.0014 and by the faculty project FEKT-S-11-14 "Utilization of new technologies in the power electronics".

References

[1] Novotny, D.W., Lipo, T.A.: Vector Control and Dynamics of AC Drives, p. 440. Oxford University Press, New York (1996) ISBN 0-19-856439-2

[2] Araujo, R.E., Leite, A.V., Freitas, D.S.: Estimation of Physical Parameters of an Induction Motor Using an Indirect Method. In: Proceedings of the 2002 IEEE International Symposium on Industrial Electronics, pp. 535–540 (2002) ISBN 0-7803-7369-3

[3] Cipín, R., Patočka, M.: New Infinitesimal Method for the Calculation of Self and Mutual Inductances of Arbitrary AC Windings. In: Proceedings of the 9th IEEE International Conference on Power Electronics and Drive Systems, pp. 717–722 (2011) ISBN 978-1-4577-0000-2

[4] Szabados, B., Dableh, J.H., Findlay, R.D., Obermeyer, G.M., Draper, R.E.: Measurement of the Torque-Speed Characteristics of Induction Motors Using an Improved New Digital Approach. IEEE Transactions on Energy Conversion, 565–571 (1990) ISSN 0885-8969

[5] Nelatury, S.R.: Uniqueness of Torque-Speed Characteristics of an Induction Motor. IEEE Transactions on Magnetics, 3431–3433 (2004) ISSN 0018-9464

Fractional-Order Model of DC Motor

R. Cipin, C. Ondrusek, and R. Huzlík

Brno University of Technology, Faculty of Electrical Engineering and Communication, Technicka 12, 616 00, Brno, Czech Republic
{cipin,ondrusek,huzlik}@feec.vutbr.cz

Abstract. This article deals with application of fractional calculus in a model of a DC motor. The basic assumption of fractional calculus is that the classical derivative can be generalized to non-integer one. The basic definitions of fractional calculus are presented. The fractional model of DC motor is simulated by a numerical scheme based on a Grünwald-Letnikov derivative. Possible usage of fractional calculus is shown for modeling a friction in electric machines.

1 Introduction

The simulations of DC motor with permanent magnets are well-known for almost everyone who deals with the control theory. Aim of this article is to explore the possibilities to apply the fractional calculus on generally known model of DC motor. The fractional calculus means, in brief, the substation of the classical integer derivative with the non-integer derivative. There is used its main feature to describe systems with a non-linear time dependencies, e.g. hysteresis.

The fractional calculus may be used for the description of memory and hereditary properties of various materials and process. In last decades, the fractional calculus was used in many scientific disciplines, for example: analysis of a projectile motion [1], analysis of an electrical skin effect [2], analysis of a fractional capacitor [3], control theory [4] and many more.

2 Fractional Calculus

The fractional calculus is a generalization of terms differential and integral and their unification. In fact, fractional calculus dealt with integrals and derivatives of arbitrary real order $q \in \mathbf{R}$, see [5, 6]. The continuous integro-differential operator is defined as:

$$ {}_{a}\mathrm{D}_{t}^{q} = \begin{cases} \dfrac{\mathrm{d}^{q}}{\mathrm{d}t^{q}} & q > 0 \\ 1 & q = 0 \\ \displaystyle\int_{a}^{t} (\mathrm{d}\tau)^{q} & q < 0 \end{cases} \tag{1} $$

where a and t are the bounds of the operation.

T. Březina and R. Jabloński (eds.), *Mechatronics 2013*,
DOI: 10.1007/978-3-319-02294-9_46,

The most used analytical definitions of fractional calculus are:

- Riemann-Liouvill definition

$$ {}^{\text{R-L}}_{a}\mathrm{D}_{t}^{q} f(t) = \frac{1}{\Gamma(n-q)} \left(\frac{\mathrm{d}}{\mathrm{d}\,t} \right)^{n} \int_{a}^{t} \frac{f(\tau)\mathrm{d}\,\tau}{(t-\tau)^{q-n+1}} \qquad n-1 < q < n \tag{2} $$

- Caputo definition

$$ {}^{\text{C}}_{a}\mathrm{D}_{t}^{q} f(t) = \frac{1}{\Gamma(q-n)} \int_{a}^{t} \frac{f^{(n)}(\tau)\mathrm{d}\,\tau}{(t-\tau)^{q+1-n}} \qquad n-1 < \alpha < n \tag{3} $$

Relation between Riemann- Liouvill derivative and Caputo derivative is:

$$ {}^{\text{R-L}}_{a}\mathrm{D}_{t}^{q} f(t) = {}^{\text{C}}_{a}\mathrm{D}_{t}^{q} f(t) - \sum_{k=0}^{n-1} \frac{(t-a)^{k-q}}{\Gamma(k-q+1)} f^{(k)}(a), \tag{4} $$

where $\Gamma(\cdot)$ is Euler's Gamma function [7].

The simulation of DC motor is done on base of numerical definition given by Grünwald-Letnikov derivative:

$$ {}_{a}\mathrm{D}_{t}^{q} f(t) = \lim_{h \to 0} \frac{1}{h^{q}} \sum_{j=0}^{\left\lfloor \frac{t-a}{h} \right\rfloor} (-1)^{j} \binom{q}{j} f(t - j \cdot h) \tag{5} $$

The Grünwald-Letnikov derivative coincides with the Riemann-Liouvill derivative in case that function $f(t)$ is $(n\text{-}1)$-times continuously differentiable on interval $[a, T]$ and that $f^{(n)}(t)$ is integrable on $[a, T]$ for $a < t < T$. These conditions are fulfilled for all quantities measured in DC motor (voltage, current, speed and so on).

General numerical solution of the fractional differential equation:

$$ \mathrm{D}_{t}^{q} y(t) = f[y(t), t] \tag{6} $$

can be expressed with help of (4) as:

$$ y(t_k) = f[t(t_k), t_k] h^{q} - \sum_{j=1}^{k} c_{j}^{(q)} y(t_{k-j}), \tag{7} $$

where $t_k = h \cdot k$ is discretized time, h is time step and $c_j^{(q)}$ are binomial coefficients:

$$ c_{0}^{(q)} = 1, \qquad c_{j}^{(q)} = \left(1 - \frac{1+q}{j} \right) c_{j-1}^{(q)} \tag{8} $$

It is important to note that in case of $q = 1, 2, \ldots$ the equation (7) represents simple numerical integration of differential equation (6). Above mentioned numerical scheme may be simple used even for system of differential equations.

Main draw-beck of (7) is caused by the second term on the right side. It is obvious that the computational demand of the binomial coefficient computation is very high for small step h ($k \approx 1/h$).

In further text, we assume the lower boundary $a = 0$ and the integro-differential operator is further written without the left subscript a.

3 Model of DC Motor with Permanent Magnets

Fig. 1 shows an equivalent circuit for DC motor with permanent magnets. Meaning of symbols: U_a is armature voltage, i_a is armature current, R_a is armature resistance, L_a is armature inductance, V_i is induced voltage, ω is angular velocity, T_i is electromagnetic torque, T_L is load torque, J is total moment of inertia.

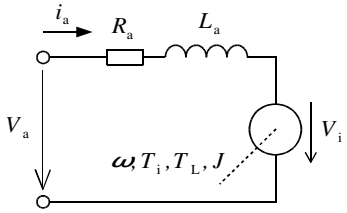

Fig. 1 Equivalent circuit for DC motor

Motor parameters are shown in Table 1. These parameters were identified for DC motor manufactured by Dynamo Sliven – model PIVT 6-25/3A 90W.

Table 1 Parameters of DC motor

parameter name	unit	value
R_a	[Ω]	2.13
L_a	[mH]	4.84
$c\phi$	[V.s]	68.3×10^{-3}
J	[kg.m^2]	114.8×10^{-6}
T_L	[N.m]	60.8×10^{-3}
U_a	[V]	14.0

The induced voltage can be calculated as:

$$V_i = c\phi \cdot \omega, \tag{9}$$

where $c\phi$ is motor constant.

The electromagnetic torque can be calculated as:

$$T_i = c\phi \cdot i_a \tag{10}$$

Differential voltage equation can be constructed according to Fig. 1:

$$V_a = R_a i_a(t) + L_a \frac{\mathrm{d}\, i_a(t)}{\mathrm{d}\, t} + \underbrace{c\phi \cdot \omega(t)}_{V_i} \tag{11}$$

Equation of motion has the form:

$$J\frac{\mathrm{d}\,\omega(t)}{\mathrm{d}\,t}=\underbrace{c\phi\cdot i_{\mathrm{a}}(t)}_{T_{\mathrm{i}}}-T_{\mathrm{L}} \tag{12}$$

Transition from integer order differentiate to non-integer order is done by simple change of used operator in (11) and (12). We get the fractional order model of DC motor:

$$\mathrm{D}_t^{q_1} i_{\mathrm{a}}(t)\equiv\frac{\mathrm{d}^{q_1} i_{\mathrm{a}}(t)}{\mathrm{d}\,t^{q_1}}=\frac{1}{L_{\mathrm{a}}}\left[V_{\mathrm{a}}-R_{\mathrm{a}} i_{\mathrm{a}}(t)-c\phi\cdot\omega(t)\right] \tag{13}$$

and

$$\mathrm{D}_t^{q_2}\omega(t)\equiv\frac{\mathrm{d}^{q_2}\,\omega(t)}{\mathrm{d}\,t^{q_2}}=\frac{1}{J}\left[c\phi\cdot i_{\mathrm{a}}(t)-T_{\mathrm{L}}\right] \tag{14}$$

These equations can be solved by numerical scheme according to (6) ÷ (8):

$$i_{\mathrm{a}}(t_k)=\frac{1}{L_{\mathrm{a}}}\left[V_{\mathrm{a}}-R_{\mathrm{a}} i_{\mathrm{a}}(t_{k-1})-c\phi\cdot\omega(t_{k-1})\right]h^{q_1}-\sum_{j=1}^{k} c_j^{(q_1)} i_{\mathrm{a}}(t_{k-j}) \tag{15}$$

and

$$\omega(t_k)=\frac{1}{J}\left[c\phi\cdot i_{\mathrm{a}}(t_k)-T_{\mathrm{L}}\right]h^{q_2}-\sum_{j=1}^{k} c_j^{(q_2)}\omega(t_{k-j}) \tag{16}$$

The simulations of system (13) and (14), resp. (15) and (16) are done for three different cases:

- q_1 is non-integer and q_2 is integer
- q_1 is integer and q_2 is non-integer
- q_1 and q_2 are non-integer

3.1 Model of DC Motor with Fractional Inductance

Model of DC motor with fractional inductance is simulated for $q_1 \in \{0.8, 0.9, 1, 1.1, 1.2\}$ and $q_2 = 1$.

Fig. 2 shows armature currents a motor speeds transition during motor plugging to power source 14 V. The armature current is about 0.89 A and motor speed is about 1662 rpm in steady-state. The steady-state parameters are almost equal for all simulation with different values of differential order q_1. These differences are mainly caused by numerical solution, i.e. time step h is too big; time steep was 0.0001 in our case. The simulations for non-integer q_2 have about the same curves

and therefore they are not shown. The simulation with fractional differentiation mainly influences the dynamics of DC motor.

Fig. 3 shows a detail transition during motor plugging with fractional inductance. The influence of fractional inductance is almost negligible in case of motor speed. On the other side, the armature current is highly influenced by change of differentiate order q_1. An increasing of the order q_1 causes an increasing of electrical time constant, i.e. ratio L_a/R_a.

3.2 Model of DC Motor with Fractional Torque

Model of DC motor with fractional torque is simulated for $q_1 = 1$ and $q_2 \in \{0.8, 0.9, 1, 1.1, 1.2\}$.

Fig. 4 shows a detail transition during motor plugging with fractional torque. A increasing of the differentiation order q_2 causes an increasing of mechanical time constant, i.e. ratio $L_a \cdot J/c\phi^2$. Practically it means that change of fractional order q_2 simulates some kind of friction in the machine. The mechanical time constant increase, i.e. motor start is slower and current waveforms correspond to this.

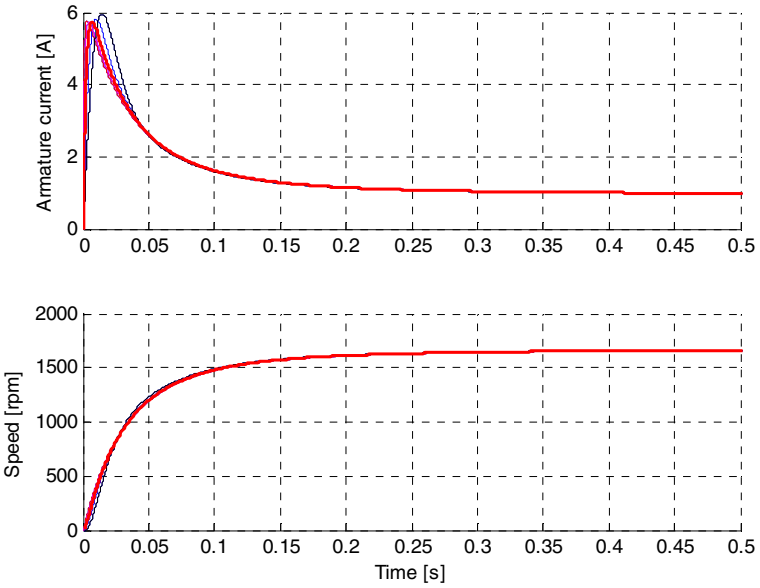

Fig. 2 Current and speed transition during plugging – fractional inductance

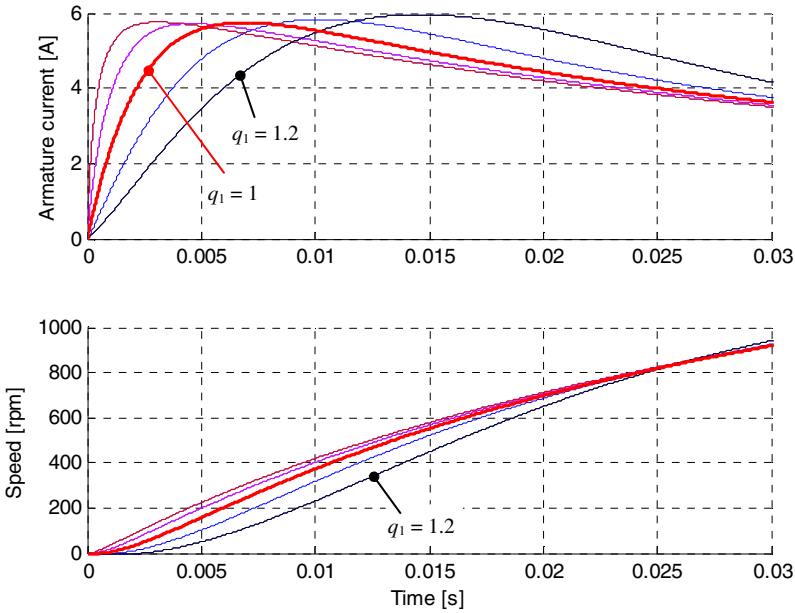

Fig. 3 Current and speed transition during plugging – fractional inductance – detail

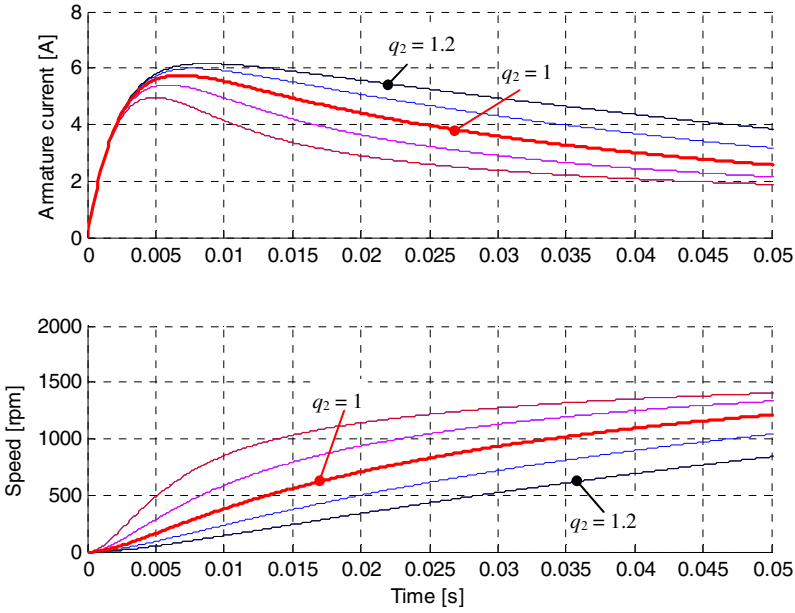

Fig. 4 Current and speed transition during plugging – fractional torque – detail

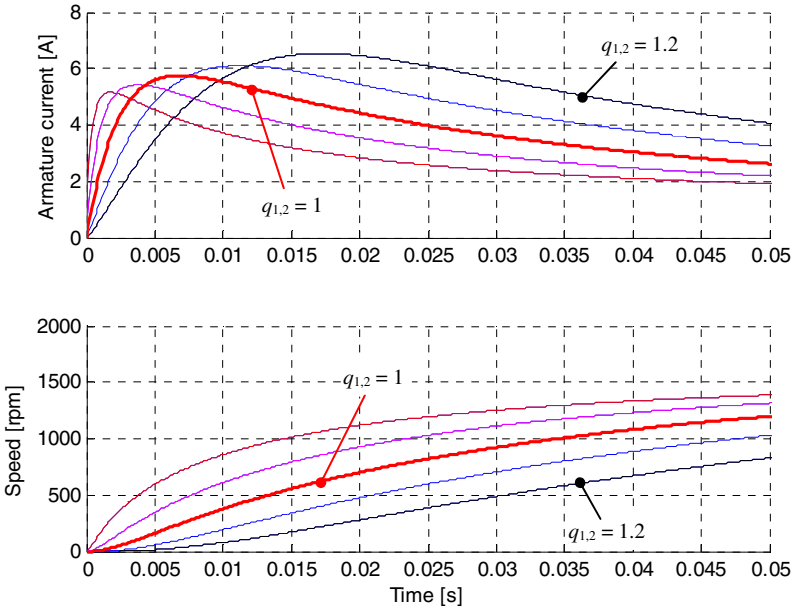

Fig. 5 Current and speed transition during plugging – fractional inductance and torque

3.3 Fractional Model of DC Motor

Model of DC motor with fractional torque is simulated for q_1 and $q_2 \in \{0.8, 0.9, 1, 1.1, 1.2\}$.

Fig. 5 shows a detail transition during motor plugging with fractional inductance and torque. Combination of both the above mentioned changes in DC motor model causes almost linear superposition of their influences, i.e. an increasing electrical and mechanical time constants.

4 Conclusions

The aim of this article led in a presentation of the fractional calculus for modeling a DC motor with permanent magnet.

There are studied three different models of DC motor:

- model of DC motor with the fractional inductance – Increasing of the fractional order causes an increasing of electrical time constant.
- model of DC motor with the fractional torque – Increasing of the fractional order causes an increasing of mechanical time constant.
- fractional model of DC motor

Further work may be aimed in modeling and identification of a friction by fractional calculus in rotational electric machines.

Acknowledgments. This work was solved in the frame of the faculty project FEKT-S-11-14; and the project No. CZ.1.07/2.3.00/30.005 funded by European Regional Development Fund.

References

[1] Abdelhalim, E.: Analysis of projectile motion in view of fractional calculus. Applied Mathematical Modelling (35), 1231–1239 (2011)
[2] Machado, J.A.T., Jesus, I.S., Galhano, A., Cunha, J.B., Tar, J.K.: Electrical Skin Phenomena: A Fractional Calculus Analysis. In: Advances in Fractional Calculus, pp. 323–332 (2007)
[3] Westerlund, S.: Capacitor theory. IEEE Transactions on Dielectrics and Electrical Insulation, 826–839 (1994)
[4] Tavazoei, M.S.: From Traditional to Fractional PI Control: A Key for Generalization. IEEE Industrial Electronics Magazine (6), 41–56 (2012)
[5] Petras, I.: Fractional-Order Nonlinear Systems: Modeling, Analysis and Simulation. Springer, Berlin (2011)
[6] Podlubny, I.: Fractional Differential Equations. Academic Press, San Diego (1998)
[7] Keith, B., Spanier, J.: The Fractional Calculus: Theory and Applications of Differentiation and Integration to Arbitrary Order. Academic Press, San Diego (1974)

FEM Model of Electro-magnetic Vibration Energy Harvester

Z. Hadas[1] and R. Huzlík[2]

[1] Brno University of Technology, Faculty of Mechanical Engineering, Technicka 2896/2, 616 69, Brno, Czech Republic
hadas@fme.vutbr.cz
[2] Brno University of Technology, Faculty of Electrical Engineering and Communication, Technicka 3058/10, 616 69, Brno, Czech Republic
huzlik@feec.vutbr.cz

Abstract. This paper deals with finite element method analyses, shortly FEM, of electro-magnetic vibration energy harvester in Ansys Maxwell environment. Development and simulation modeling of energy harvesting devices is presented long time by our mechatronic team and several successful harvesters were tested in industrial applications. The adequate simulation model is fundamental for development of a successful industrial application of the electro-magnetic vibration energy harvester due to complexity of this mechatronic system. The presented approach of simulation modeling is based on complex FEM analyses in Maxwell environment and it provides useful tool for precise simulation modeling of developed energy harvesting applications.

1 Introduction

The paper deals with finite element method analyses of electro-magnetic vibration energy harvester in Ansys Maxwell environment, shortly FEM. The electro-magnetic vibration energy harvester is mechatronic system [1] which harvests electrical energy from ambient mechanical vibrations [2]. The harvester consists of a spring-less resonance mechanism, magnetic circuit, self-bonded coil and power management electronics with powered electrical load and energy storage element [3]. The precise design of vibration energy harvester parameters is fundamental for correct operation due to resonance mode operation [4]. FEM analyses provide useful tools in development process of the electro-magnetic vibration energy harvester and the efficient energy harvesting device can be developed. There are analyses of magnetic stiffness in spring-less resonance mechanism, analysis of magnetic field through coil, induced voltage simulation and complex electro-magnetic model in ANSYS Simplorer can be solved. The used FEM analyses of this complex electro-magnetic device are presented in this paper.

T. Březina and R. Jabloński (eds.), *Mechatronics 2013*,
DOI: 10.1007/978-3-319-02294-9_47,

2 Electro-magnetic Vibration Energy Harvester

The developed electro-magnetic vibration energy harvester, Fig. 1, use ambient mechanical vibrations to harvesting of electrical energy in aeronautic applications [5]. This device is used as autonomous source of energy for wireless sensors. The harvester has operation frequency 17 Hz and maximal output power is 40 mW. Weight of this device is 125 grams in volume 80 cubic centimeters.

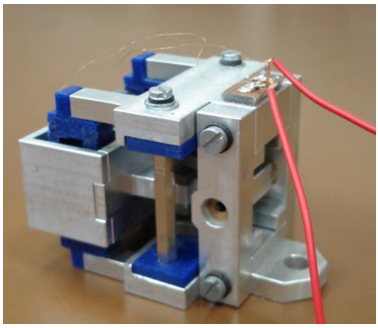

Fig. 1 Developed Electro-Magnetic Vibration Energy Harvester -17 Hz – 40 mW

Basic part of the vibration energy harvester, shown in Fig. 2 and presented in paper [6], is the resonance mechanism (seismic mass m suspended on magnetic spring k with damping b) with the suitable electro-magnetic converter (oscillating magnetic circuit against fixed coil L with inner resistance R_C) and the electronics (resistance of electrical load R_L). The simplified diagram of generator is shown in Fig. 2 a) schematic diagram of a simplified linear system is shown in Fig. 2 b).

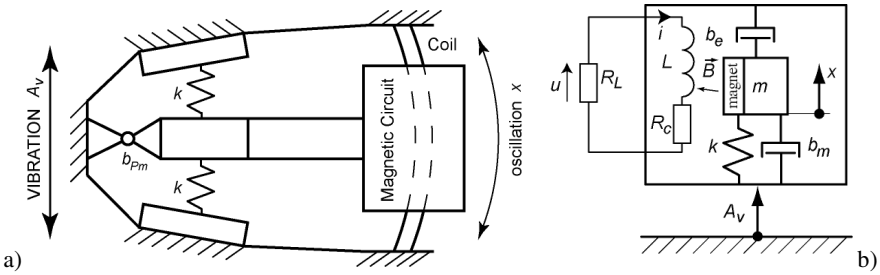

Fig. 2 a) Simplified diagram of harvester; b) Schematic diagram of physical model

During development process of this mechatronic device the simplified simulation model in Simulink [7] was used and harvester parameters were designed on the base of this Simulink model. There were several magnetic properties which were simulated as constant function and the simulation results were distorted [8]. Therefore the FEM model is used for correct predict of the magnetic model and appropriate model can be used for a future optimization study. This simulation modeling of the electro-magnetic energy harvester is presented in this paper.

3 Ansys Maxwell Model of Electro-magnetic Harvester

FEM model of the electro-magnetic vibration energy harvester was created, Fig.3, in Ansys Maxwell environment. This model consists of a moving seismic mass of harvester (arm with moving stiffness magnets and magnetic circuit), fixed stiffness magnets and fixed coil. The parameters and dimensions were used for the real harvester, Fig. 1, and rare earth magnets are used. On the base of FEM analyses the energy harvester model will be improved and consecutively the model will be used for precise optimization study.

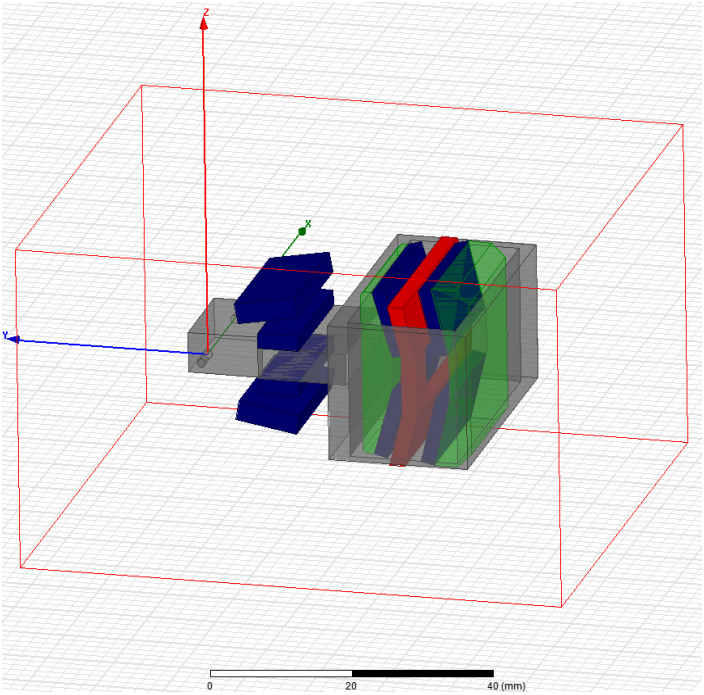

Fig. 3 Electro-magnetic Vibration Energy Harvester in Ansys Maxwell

3.1 Magnetic Flux Analysis of Magnetic Circuit

Magnetic flux in the FEM model was analyzed and results in cross-section are shown in Fig. 4. The results of this analysis in coil area can be used as precise input electro-mechanical model which simulates induced voltage due to Faraday's Law. Spread of magnetic flux through coil during moving of the arm with magnetic circuit affects amplitude and shape of induced voltage.

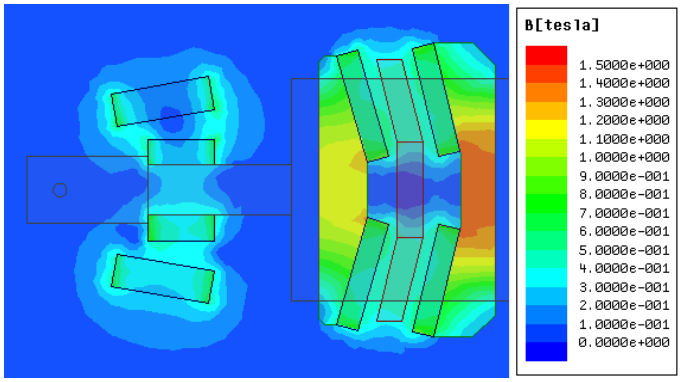

Fig. 4 Calculated Magnetic induction B in Harvester Cross-Section

3.2 Magnetic Stiffness Analysis

The fundamental issue of the vibration energy harvester is analysis of a stiffness characteristic. The stiffness and seismic mass ration determines operation resonance frequency of the harvester. This frequency is tuned up to dominant frequency in mechanical system, where our harvester generates useful electrical energy.

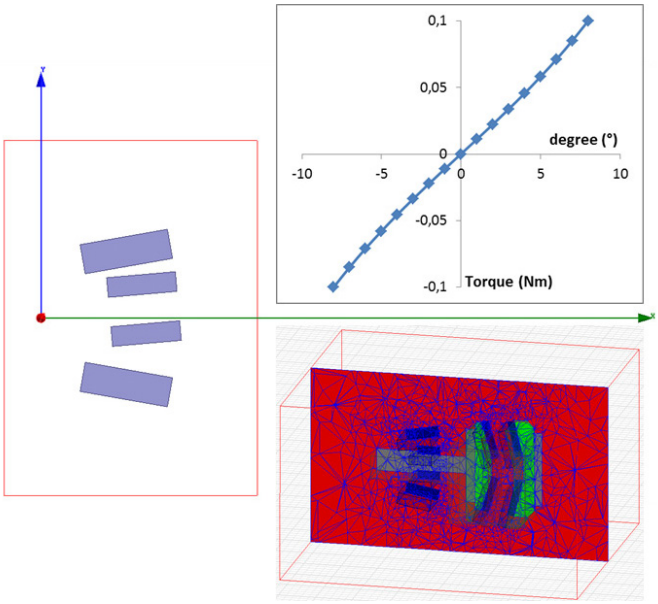

Fig. 5 a) Simple model of moving and fixed stiffness magnets and analyzed characteristic; b) Detail of Mesh Cross-Section of 3D Vibration Energy Harvester Model

The stiffness of this device is provided by set of repelled rare earth magnets, which are fixed and moving with seismic mass of the harvester arm. This set of magnets provides non-linear spring less stiffness and this stiffness characteristic can be analyzed in simple 2D model with fixed and moving magnets. It is shown in Fig. 5 a). The stiffness characteristic was usually used as a linear stiffness in previous Simulink models. This analysis can provide precise non-linear system behavior and the model of this non-linear resonance system can predict harvester behavior with shifting with frequency of input excited vibrations. It can affect excided movement and thereafter it affects harvesting of electrical energy.

There is way to use of the 3D FEM model for stiffness analyses. This model is shown in Fig. 5 b) and it can provide the similar stiffness characteristic but this model can be used in combination with another analysis, like analysis of oscillated arm moving, analysis of induced voltage, analysis of connected power electronics, etc.

3.3 Induced Voltage Analysis

Mechanical vibrations cause relative oscillation of seismic mass with magnetic circuit against coil and the induced voltage can be analyzed for different velocity in Ansys Maxwell. The 3D FEM model, which is shown in Fig. 5 b), can be used for this analyses and the effect of magnetic flux through coil can be observed for different amplitude and velocity of relative oscillating movement.

The velocity and amplitude of movement can be prescribed in simulation properties. However, the effect of connected electronics (resistance load) can be simulated in complex FEM model of the electro-magnetic vibration energy harvester. This model is schematically shown in Fig. 6 and the charts of induced voltage are shown there.

3.4 Complex Analysis of Electro-magnetic Vibration Energy Harvester in Ansys Simplorer

Ansys Simplorer is simulation tool which can be integrated in Ansys environment and this tool can connect results from individual analyses to one complex model with mutual feed-backs. The schematic diagram of the presented complex model of the electro-magnetic vibration energy harvester is shown in Fig. 6.

This model in Ansys Simplorer is excited by model of ambient mechanical vibrations and the resonance mechanism with calculated magnetic stiffness provides relative movement of the magnetic circuit against fixed coil. This movement of magnetic parts is connected with Ansys Maxwell model and induced voltage is solved in Ansys Maxwell environment due to Faraday's Law. Basic electric laws are calculated and the harvesting of electrical energy provides feed-back to model via electro-magnetic damping forces. This complex model provides useful tool for design of harvester parameters and development of a new harvesting devices.

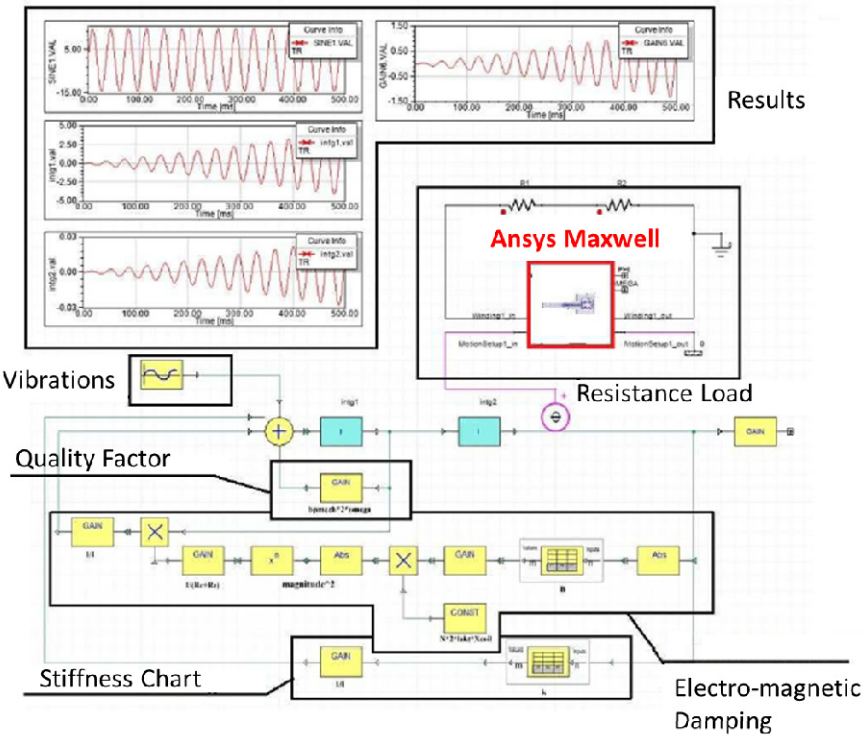

Fig. 6 Model of Electro-Magnetic Vibration Energy Harvester in Ansys Simplorer

4 Conclusions

The simulation modeling of the designed electro-magnetic vibration energy harvester is very important step in the development process, mainly in the field of energy harvesting. FEM model of this mechatronic device in Ansys Maxwell environment provides useful tool for development of energy harvesting systems.

The presented approach based on the FEM analyses of the developed harvester is very useful for developing of new electro-magnetic vibration energy harvesters. On the base of customer's requirements the FEM model of the electro-magnetic vibration energy harvester can be optimized [9]. There is very interesting opportunity to use this mechatronic device in aeronautic, automotive and heavy industry applications for energy harvesting from ubiquitous mechanical shocks [10].

Furthermore this approach can be used for precise simulation of electro-magnetic phenomena inside our harvester. It provides useful tool for simulation of electronics behavior, which dramatically affects harvested power. The presented simulation modeling of electro-magnetic vibration energy harvester could be very interesting with increasing of calculation power of present work stations.

Acknowledgments. This work has been funded by the European Commission within the FP7 project "Efficient Systems and Propulsion for Small Aircraft | ESPOSA", grant agreement No. ACP1-GA-2011-284859-ESPOSA. And additional support by European Regional Development Fund in the framework of the research project NETME Centre under the Operational Programme Research and Development for Innovation. Reg. Nr. CZ.1.05/2.1.00/01.0002, id code: ED0002/01/01, project name: NETME Centre – New Technologies for Mechanical Engineering.

References

[1] Hadas, Z., Singule, V.: Energy harvesting – opportunity for future remote applications. In: 17th International Conference on Engineering Mechanics, Svratka, Czech Republic, pp. 167–170 (2011)

[2] Mateu, L., Moll, F.: Review of Energy Harvesting Techniques and Applications for Microelectronics. In: Proceedings of the SPIE Microtechnologies for the New Millenium, vol. 5837, pp. 359–373 (2005)

[3] Hadas, Z., Kluge, M., Singule, V., Ondrusek, C.: Electromagnetic Vibration Power Generator. In: IEEE International Symposium on Diagnostics for Electric Machines, Power Electronics and Drives, Cracow, Poland, pp. 83–87 (2007)

[4] Hadas, Z., Singule, V., Ondrusek, C.: Optimal Design of Vibration Power Generator for Low Frequency. Solid State Phenomena, 147–149, 426–431 (2009)

[5] Hadas, Z., Ondrusek, C., Singule, V.: Power sensitivity of a vibration energy harvester. Microsystem Technologies 16(5), 691–702 (2010)

[6] Hadas, Z., Ondrusek, C., Kurfurst, J.: Optimization of Vibration Power Generator Parameters Using Self-Organizing Migrating Algorithm. In: Recent Advances in Mechatronics, pp. 245–250. Springer (2009)

[7] Hadas, Z., Singule, V., Ondrusek, C., Kluge, M.: Simulation of Vibration Power Generator. In: Recent Advances in Mechatronics, pp. 350–354. Springer (2007)

[8] Hadas, Z., Ondrusek, C., Kurfurst, J.: Optimization of Vibration Power Generator Parameters Using Self-Organizing Migrating Algorithm. In: Recent Advances in Mechatronics, pp. 245–250. Springer (2009)

[9] Hadas, Z., Kurfurst, J., Ondrusek, C., Singule, V.: Artificial intelligence based optimization for vibration energy harvesting applications. Microsystem Technologies 18(7-8), 1003–1014 (2012)

[10] Hadas, Z., Vetiska, V., Singule, V., Andrs, O., Kovar, J., Vetiska, J.: Energy Harvesting from Mechanical Shocks Using a Sensitive Vibration Energy Harvester. International Journal of Advanced Robotic Systems 9(225), 1–7 (2012)

Contribution to Determination of Target Angular Position by Single Visual Camera at Indoor Close Environs

R. Doskocil, V. Krivanek, and A. Stefek

University of Defence, Faculty of Military Technology, Kounicova 65,
612 00 Brno, Czech Republic
{radek.doskocil,krivanek,alexandr.stefek}@unob.cz

Abstract. This paper is a follow-up to issued results of the Research Intention at the Department of Air Defence Systems that were performed and published in period 2011 and 2013. The paper deals with practical experiments which have been performed in order to bring some evidences about possibilities estimating angular positions of the stationary target by using visual odometry. The single visual camera and the target have been used to estimate angular position and angle of rotation of the target in the laboratory conditions at short distances. Mainly the paper describes the results of performed experiments and possibilities reduction of errors caused by optical system of camera (e.g. field deflection).

1 Introduction

The Department of Air Defence Systems has an experience in construction of robot weapon systems and tried to develop one's potential all the time. The research and science tasks that have been solved here contain the individual parts from construction of chassis through sensor systems, intelligent control system etc., for more information see [5].

We want to acquire abilities to design the robot systems for military applications by means of our project RI-K208 [6]. We put stress on:

- the field of control of robots, i.e. from the direct and indirect (off-line) control up to online control when the robot adapts the changing outer conditions by means of sensors; the control of handling mechanism; navigation of robot in unfamiliar environment; autonomous motion in the unfamiliar space and cooperation of group of robots to fulfil the joint action;
- the field of sensor signal processing, i.e. use of simple and complex optical sensors, camera subsystems, ultraviolet or laser scanning; recognition of image, fusion of signal from sensors, location, obstacle detection, recognition of action etc.

With the last mentioned point we have arranged several experiments at the field of distance and angular measurement of stationary target by single visual camera

T. Březina and R. Jabloński (eds.), *Mechatronics 2013*,
DOI: 10.1007/978-3-319-02294-9_48,

in laboratory conditions. We wanted to estimate the distance and angular position of a target by using visual odometry. For these estimations we used a single camera and a reference target. Photos were taken to obtain the coordinates of reference points on the target surface. The coordinates obtained were used in optical equations to estimate position of the target in the space. For detail information see [2], [3] and [4]. These practical experiments establish a basis for the implementation of the positioning algorithm into navigation subsystem of swarm robots.

The important problem of velocities of objects and a robot is not solved in these papers because first of all, we focused on "simple" position problem only [7]. The research task will be continuing by solving this velocity problem in close future.

This paper follows the time-line described in the papers [2], [3] and [4] and published at the IEEE *15th International Conference Mechatronika 2012*, journal *Advance in Military Technology* and *3th International Conference of Military Technology 2013*. In the papers' conclusions [2], [3] and [4], the general experience and conclusions of the experiment are mentioned to enhance experiment results:

1) to find suitable parameters of camera or prime lens with the fixed focal length, i.e. focal length, F-number and light condition;
2) experimentally to find proper size of base *b,* sensor dimension and resolution;
3) to propose suitable algorithm for automatic photo processing of image, thereby to eliminate attitudinal error of observer-man that caused by evaluation of image base *b*';
4) to find appropriate filters of automatic evaluate software FORM1 for errorless recognition of reference points and errorless determination of different wrong points.

Now we can say that some described tasks we solved successfully [points 1) to 3)]. We have been working on improving software FORM1 characteristics in these days [points 4)].

This paper is focusing on measuring of angular position of target by single visual camera. We want to know the answer to following question: *"Is it possible to use single visual camera for angular position measurement of targets?" What the error measuring angular position of targets?*

It knows that there is some problem with optical measuring (especially range) when the line of sight of measuring device and referent surface of target is not perpendicular. *We have design some algorithm to reduce of mentioned influence*. It is very useful for automatic evaluation of target position, e.g. at swarm robots.

2 Experiment Background and Results

This section describes theoretical background of the realized experiments that try to find primary errors of angle measurement and secondarily the mathematical description measured distance variation that influenced by turning of reference target surface when the line of sight of measured device and referent surface of target is not perpendicular. So received mathematical description will be able to realize

regressive evaluation/correction of measured distance to real "right" distance. Our aim is to implement this algorithm to automatic swarm robot sensor system.

We used the same experiment basic optical scheme as in works [2], [3] and [4] for evaluation optical parameters. It means that we measure the distance by evaluation of a telemetric triangle with the base on object plane, so called stadimetric (reticular) rangefinder with fixed base in object plane. The principle layouts of realized main two experiments A and B are on the Fig l.

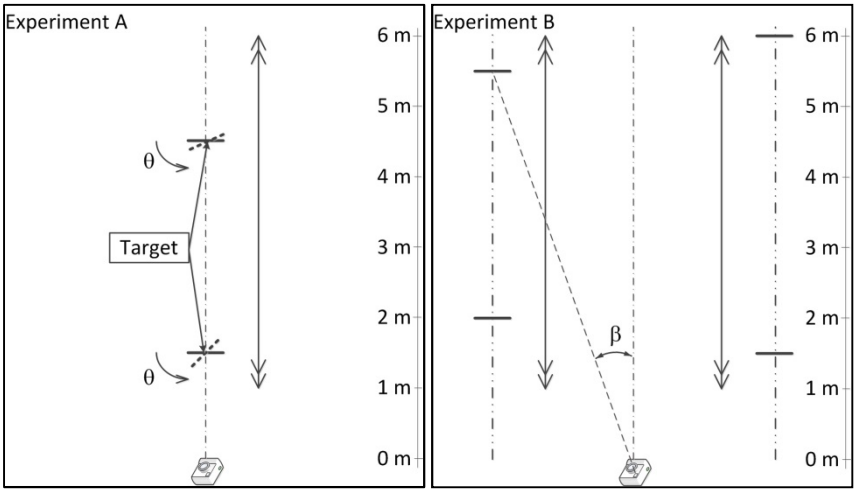

Fig. 1 Principle layout of experiment *A* and *B*

2.1 Description of Experiment A

Layout of experiment *A* is on the Fig. 1 (left side). The experiment was focused on algorithm of regressive evaluation/correction of measured distance. The values of quantities as known distance l and angle θ of rotation of model target were preconditions of the experiment *A*, see Table 1. We determined a rate between horizontal b' and vertical abscissa c', see Fig. 2, by Eq. (1). Constant value of the rate k for variable distance l is theoretical hypothesis this experiment.

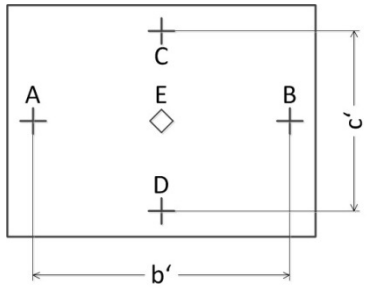

Fig. 2 Model of the target measured quantities

$$k = \frac{b'}{c'}. [-] \quad (1)$$

Table 1 Calculated values of the rate k for variables angle θ and distance l

		k [-]				
θ [°]	l [m]	1.00	2.00	3.00	4.00	5.00
0.00		1.66	1.66	1.66	1.66	1.66
14.05		1.62	1.61	1.61	1.61	1.61
26.51		1.51	1.49	1.49	1.49	1.48
44.96		1.20	1.18	1.16	1.17	1.17
56.26		0.95	0.92	0.93	0.91	0.92
63.39		0.77	0.74	0.74	0.75	0.74

From determined values of rate k is evident that our enter experiment hypothesis is fulfil. Values of the rate k are approximately constant for all change distances l and given constant value of angle θ. Shape of the curves we can see on Fig. 3.

Angle of rotation is possible calculate by theoretical function

$$\theta_t = arccos\left(\frac{b'}{c'} \cdot \frac{1}{k_o}\right) [\text{rad}] \quad (2)$$

where: b' is length of horizontal line in pixel, c' is length of vertical line in pixel and k_o is the rate between horizontal and vertical line for zero rotation. In this case k_o= 1.66.

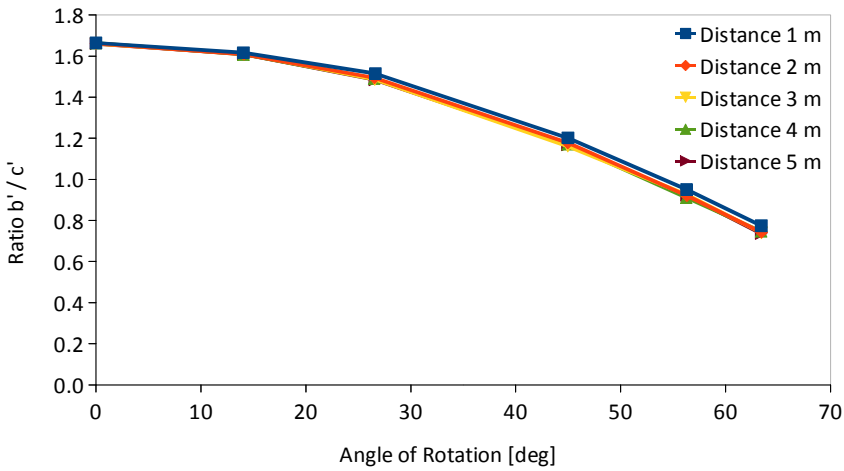

Fig. 3 Rate k = b' / c' as a function of angle of rotation θ and distance measurement l

The second way to calculate of this angle θ is e.g. by polynomial function

$$\theta_p = -141.01 \cdot k^5 + 545.84 \cdot k^4 - 682.42 \cdot k^3 + 190.03 \cdot k^2 + 139.88 \cdot k \quad \text{[rad]} \tag{3}$$

Calculated values of angles of rotation with using Eq. (2) and (3) are presented in the Table 2. Used measured distance was l = 4 m. We can see that method of approach by Eq. (2) is on the one hand simpler and as well as more exact than Eq. (3) one, especially for small angle of rotation θ (to about 30°). So, we decided to use Eq. (2) for implementation to regressive algorithm of evaluation/correction of measured distance to real "right" one.

Table 2 Values of angles θ_t and θ_p, and errors of approach algorithms by Eq. (2) and (3)

k [-]	1.66	1.61	1.49	1.17	0.91	0.75
θ_t [°]; Eq. (2)	0.00	14.10	26.15	45.19	56.76	63.14
$\delta\theta_t$ [°]; Eq. (2)	-	-0.34	0.50	-0.74	-1.01	0.31
θ_p [°]; Eq. (3)	0.83	12.34	27.60	44.43	56.64	63.24
$\delta\theta_p$ [%]; Eq. (3)	-	12.17	-4.14	1.16	-0.69	0,24

2.2 Description of Experiment B

An arrangement of experiment *B* is on the Fig. 1 (right side). The experiment was dedicated to evaluate ability measure the position angle of target by single camera. The target is moving on the left line (Line 1) and on right one (Line 3) outside the optical axes. The central line is Line 2. Target change the position between 3.5 and 6 meters. Angle β is established as relation between distance of target, and center of target and optical axes by equation

$$\beta = arctg \frac{b'[mm]}{f'}, \text{ [rad]} \tag{4}$$

where b' [mm] is given by Eq. (5), f' is focal length of camera lens (18 mm), CCD_x = 23.7 mm is a dimension of sensor in direction x, CCD_x = 3008 px is a resolution of sensor in direction x.

$$b'[mm] = b'[px] \cdot \frac{CCD_x\,[mm]}{CCD_x\,[px]} \tag{5}$$

Table 3 Values of the angles - θ_{real} real one and $\theta_{measured}$ measured one

Line 1						
l [m]	3.50	4.00	4.50	5.00	5.50	6.00
θ_{real} [°]	29.75	26.62	24.00	21.81	19.98	18.47
$\theta_{measured}$ [°]	29.65	26.58	24.04	21.86	20.13	18.60
$\delta\theta$ [%]	0.32	0.16	-0.18	-0.24	-0.75	-0.73
Line 3						
l [m]	3.50	4.00	4.50	5.00	5.50	6.00
θ_{real} [°]	29,74	26.54	23.43	21.79	19.97	18.40
$\theta_{measured}$ [°]	29.52	26.47	23.90	21.81	20.05	18.51
$\delta\theta$ [%]	0.72	0.26	-1.99	-0.08	-0.36	-0.62

Courses of error $\delta\theta$ are presented on the Fig. 4. Average value of error for the Line 1 is 0.34 % and for the Line 3 average value of error is 0.24 %. One value (1.99 %) from Line 3 is out of gotten range of accuracy. It was caused by accidental influences or subjective matter.

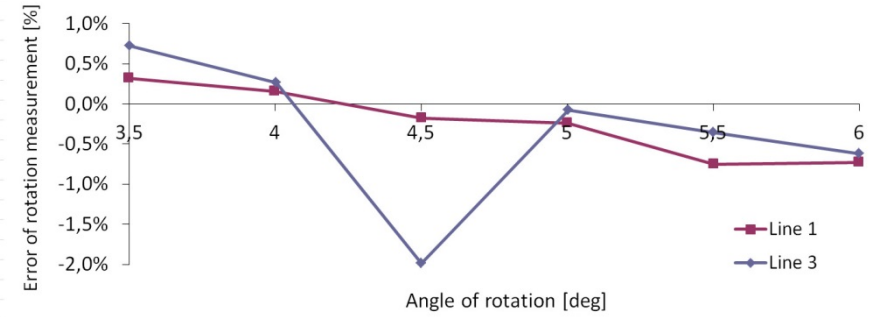

Fig. 4 The courses of error of angle measurement

3 Conclusions

The paper deals with the using of single camera to measurement of angles. The presented achievements are valid only for an exact type of camera in combination with a particular lens. Nevertheless, the conclusions are generally valid.

Our practical experience has proved that the optical angle measurement by single visual camera is possible and implementable for current course in robotics – swarm robotics. We are able to measure angle position of target(s) with appropriate accuracy.

We found out that arithmetic mean of error of measured angle is 0.34 % or 0.24 %. Next we found out the suitable regressive algorithm (Eq. 2) of evaluation/correction of measured distance to real "right" one for implementation to sensor subsystem of swarm robotics.

Finally, we can say that used method is suitable and sufficiently accurate for angle position measurement of objects and it gives of high quality results.

Acknowledgments. The work presented in this paper has been supported by the Ministry of Defence of the Czech Republic (project RI-K208 under the auspices of the "Institutional support of the research organization, 907 980 – Development of acquired operational abilities of the Czech Armed.

References

[1] Bergeron, Y.: Calculation of the distance covered by a robot thanks to image analysis with a two-robot team. In: Proceeding International Conference on Military Technologies 2011, pp. 849–854. University of Defence, Brno (2011) ISBN 978-80-7231-787-5

[2] Doskocil, R., Fischer, J., Krivanek, V., Stefek, A.: Measurement of Distance by Single Visual Camera at Robot Sensor Systems. In: Proceeding of the 15th International Conference of Mechatronika 2012, pp. 143–149. Czech Technical University in Prague, Praha (2012) ISBN 978-80-01-04985-3

[3] Bourdonnaye, A., Doskočil, R., Křivánek, V., Štefek, A.: Practical Experience with Distance Measurement Based on the Single Visual Camera. In: Advances in Military Technology, vol. 8(1) (2012) ISSN 1802-2308

[4] Doskočil, R., Křivánek, V., Štefek, A.: Effect of the Manual vs. Automatic Image Processing on the Measurement Accuracy of the Target Range. In: International Conference on Military Technologies 2013, pp. 1245–1254. University of Defence, Brno (2013) ISBN978-80-7231-917-6

[5] Defence University: Research K208, `http://www.unob.cz/fvt/k208/vyzkum.aspx` (cit. May 1, 2013)

[6] Research Intention at the Department of Air Defence Systems (RI-K208) - Development of Elements of Air Force with Respect to Simulation Technologies and Cybernetic Systems (Záměr pro rozvoj pracoviště Katedry systémů protivzdušné obrany - Rozvoj prvků vzdušných sil v návaznosti na simulační technologie a kybernetické systémy)

[7] Thrun, S., Burgard, W., Fox, D.: Probabilistic Robotics. Intelligent Robotics and Autonomous Agents series, p. 672. The Massachusetts Institute of Technology Press, USA (2005) ISBN 978-026-220-162-9

A Simple Acoustic Generator for Boiler Cleaning Applications

A. Jedrusyna and A. Noga

Wroclaw University of Technology, Wybrzeze Wyspianskiego 27,
Wroclaw, 50-370, Poland
{artur.jedrusyna,andrzej.noga}@pwr.wroc.pl

Abstract. One of the most important problems present in an industrial coal-fired heating devices is how to remove the soot and ash remains deposited inside the heating system. Traditional methods require the boiler to be switched off during the cleaning. An alternative is to remove such remains using high energy beam of acoustic energy. A simple acoustic generator with tubular resonator was built for the purpose. In the paper the control system for the generator was also described. The system used both accelerometer and microphone as a sound and vibration level sensors.

1 Introduction

Modern heating systems, especially coal-fired boilers very often have remarkable efficiency problems due to the ash and soot layers deposited on the internal heat transfer surfaces of the boiler. The tube bundle inside the boiler chamber could be an example of such structure. The soot layer can act as thermal insulator, reducing the heat transfer ratio between different parts of the boiler. As the result the hot flue gases temperature is increased and the amount of wasted heat is mounting up. The only cure is to remove this layers either manually or by appropriate machinery. The manual cleaning is very expensive, since it is only possible when the boiler is switched off and completely cooled down. Such a pause in operation is economically undesirable and should be avoided if possible. Therefore, an alternative method of cleaning that could be implemented during the normal operation of the boiler was necessary. The compressed steam jet could be used for the purpose, however its cleaning operation has only a very local effect. Notably better results have been obtained with high power beam of acoustic or sub-acoustic (infrasonic) waves [1].

1.1 Methods of Generation of High Power Acoustic Signals

Acoustic waves could be generated by different mechanical or electromechanical devices. Some constructions utilize modulated air stream which is controlled by a camshaft-operated mechanism [2]. Dynamic speakers could be also used for the

T. Březina and R. Jabloński (eds.), *Mechatronics 2013*,
DOI: 10.1007/978-3-319-02294-9_49,

purpose. A modulated stream of compressed gas is most often used for high power applications. However, a single point-type source usually cannot produce the desired level of acoustic pressure. Better results have been obtained with generator equipped with additional acoustic resonator. The most simple version of such a resonator was shown in Fig. 1.

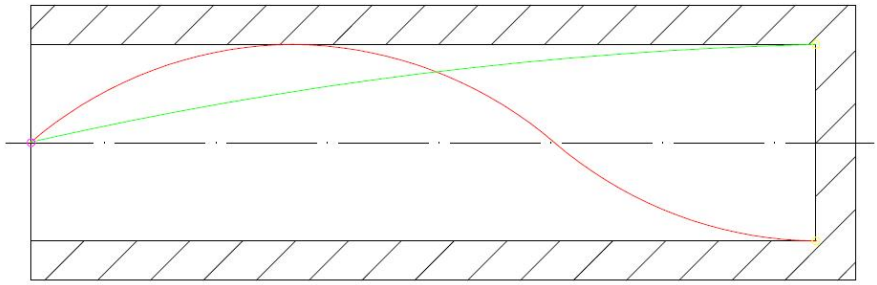

a)

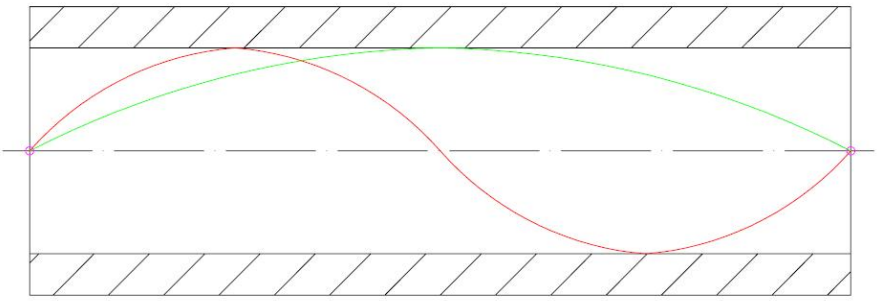

b)

Fig. 1 The first two modes of acoustic resonance in a cylindrical tube a) with closed end b) with open end. The source of acoustic waves is located on the left side.

The resonator consists of a rigid tube connected to the source of sound. The other end of the pipe can be open or closed. In practical applications open resonators are more often used. An open tube resonator resonates when the frequency f of the sound wave fulfills the equation:

$$f = \frac{n \cdot c}{2 \cdot L} \tag{1}$$

Where n is natural number, c is sound velocity in air and L is the length of resonator.

An open tube resonates at the fundamental frequency, for which the equation (1) is fulfilled. For the resonator with an open end the frequency of sound generator should be described by a condition:

$$L = n * \lambda / 2 \tag{2}$$

For the resonator with a closed end the resonance condition has a slightly different form:

$$L = n * \lambda / 4 \tag{3}$$

Where λ is wavelength of the operating frequency ($\lambda=c/f$) and n is natural number.

During the resonance, an antinode – a point of greatest vibration appears near the open end of the resonator. For such condition, the maximal amplitude of generated signal can be produced. However, the resonating frequency of a pipe resonator is not constant – it can be modified by changes in ambient temperature, humidity or by presence of chemical gases. During each cycle of operation the resonator should be tuned up in order to obtain maximal possible amplitude of acoustic wave at the open end of the tube. In order to do so, a feedback information about the current sound level is necessary. The sound intensity can be measured using microphone located inside the boiler chamber. However, such a solution bring notable problems related to overheating of the microphone and is very prone to malfunction. A more reliable measurement could be taken using an accelerometer located in the vicinity of the open end of the resonator. In this case the sound level is estimated by a structural vibration level of the open end of the resonator.

The acoustic wave produced by the generator located near the boiler chamber has the following effects:

- Produces intensive oscillations in a boiler chamber. As a result, the loose soot particles are unable to deposit and produce layers on heat transfer surfaces,
- The acoustic wave initiates fluidization of the deposited soot layers and then its removal,
- The acoustic wave brings also the internal structures of the boiler into oscillation, as a consequence the deposited ash layers are pulverized and removed.

The operation of high power, low frequency acoustic wave is omnidirectional, therefore the cleaning efficiency of complex structures inside boiler is very high. In practical applications the generator should be switched on for 1-2 minutes every hour. Such an amount of cleaning action prevents against the deposition of new soot layers. However, the efficiency of the cleaning decreases rapidly as the generator is tuned out of resonance. In order to maintain a good cleaning efficiency a re-tuning of generator is necessary before each cycle of operation.

It should be noted that an uncontrolled application of high power acoustic beam may have side effects related to the health of human personnel present in the vicinity of the sonic generator. In order to avoid any possible injury to the human auditory system, the generator should be mounted in such a way that the

generated acoustic beam cannot escape the boiler chamber. The sound pressure level necessary for proper cleaning action may well exceed 140 dB, which is usually above threshold of safety for an average person. However, the properly operated system can be regarded as entirely safe.

1.2 Test System Description

In order to test the viability of accelerometer utilization a simple test system was constructed. The diagram of the system was shown in Fig.2

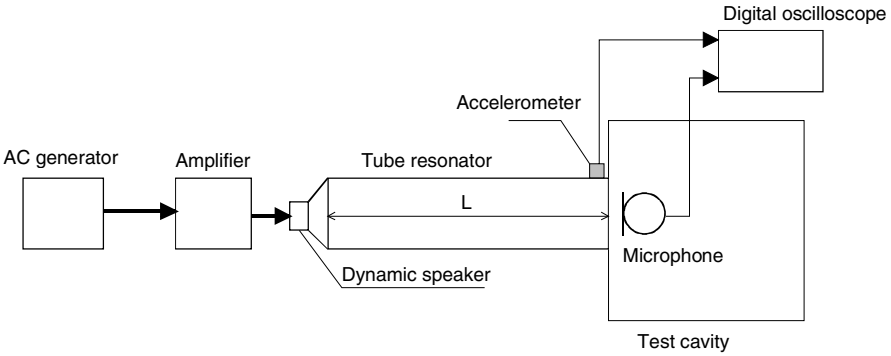

Fig. 2 Outline of experimental system

The system operating frequency is controlled by digital function generator, producing sinusoidal signal of variable frequency. This signal is amplified by power stage and then used for driving of the electropneumatic transducer. A dynamic speaker was used for this purpose. The generated sound wave is transferred into the resonance tube of length L=2,1 m. Inside the open end of the resonator a test microphone was located. The results of sound level measurements for different operating frequencies were shown in Fig.3.

In second version of the system, the length of the tube was increased to L=8m and the open end of the tube was mounted inside a resonance cavity with dimensions of 2x1,5x1m. The cavity has a damping effect and to the certain extent it can simulate the boiler chamber. The open end of the tube was additionally equipped with MEMS accelerometer with measurement range of 8g. The output signal from the accelerometer was measured with an oscilloscope.

1.3 Test Results

The results of measurements were shown in Fig.3.

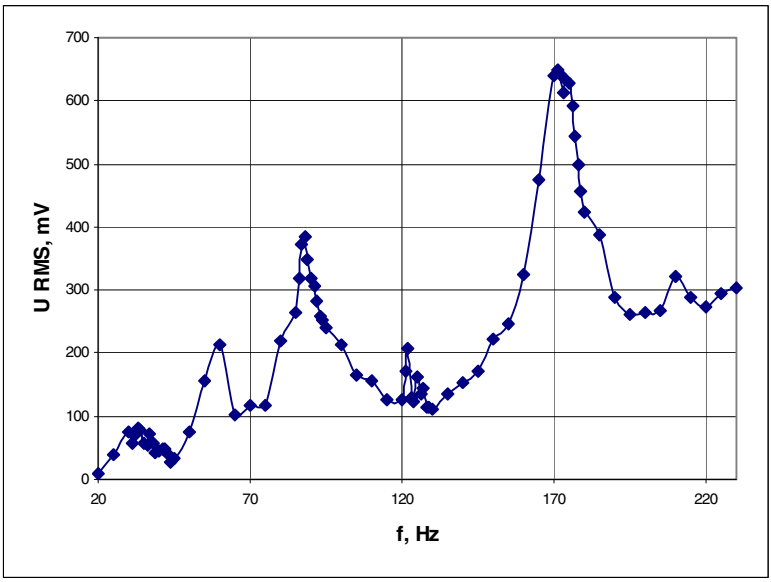

a)

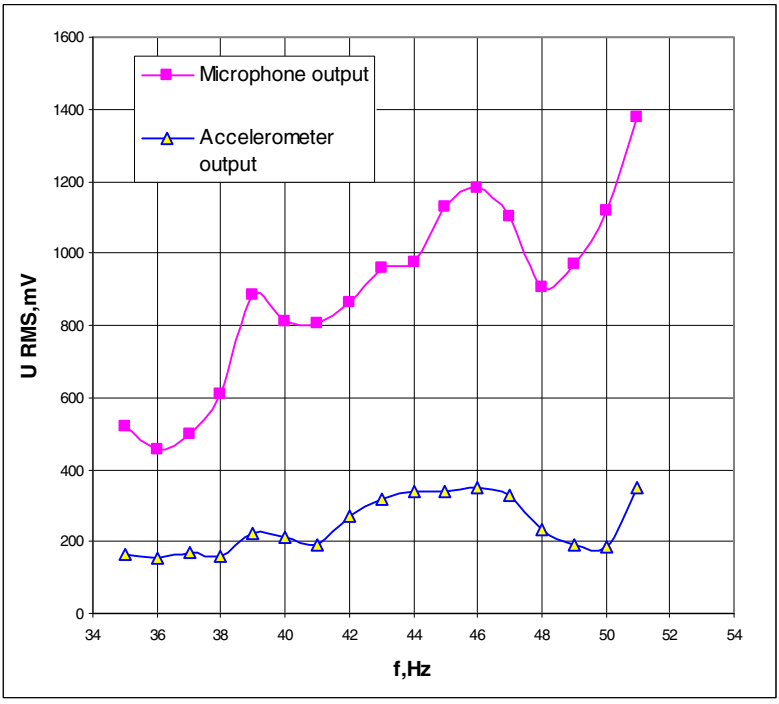

b)

Fig. 3 RMS signal amplitude for measurements for a) L=2100mm resonator with microphone, b) L=8000 mm resonator with additional cavity, equipped with both microphone and accelerometer

The RMS amplitude of voltage signals obtained from microphone and the accelerometer was measured with a digitizing oscilloscope.

The results of frequency sweeping for 2100 mm resonator visible in Fig. 3a) show clean peaks around 88 Hz (half-wave resonance) and 174 Hz (full-wave resonance). The similar test made for 8000 mm resonator show peak around 46 Hz (full-wave resonance). The signal from the accelerometer shows similar peak at 44-46 Hz. The damped shape of the accelerometer response may result from self-resonances in the construction of resonating pipe itself. It may suggest that further signal processing for accelerometer signal will be necessary.

2 Conclusions

During the experiment both methods of tuning the infrasonic generator to the optimal resonance produced comparable results. In the tuning process, the microphone sound level sensor is able to produce a more sharp resonance peaks. However, it is more prone to malfunction in difficult industrial environment. The output signal of the accelerometer is more damped, but and the resonance peaks are well visible. Therefore, the accelerometer signal can be used as equally good source of information. Such a configuration is more reliable since the vibration sensor is detached from an aggressive environment and is less prone to clogging and destruction by high temperature.

The device described in the paper was tested for low power operation and in near future it will be tested for higher level test signals. This version will be also using a lower operation frequency (below 20Hz). An additional increase in acoustic power level could be obtained by modifications of the shape of the open end of the resonator (application of horn antenna).

References

[1] Freund, M., Randy, V.: Acoustic Cleaning Combats PRB Ash Deposits on Regenerative Air Heaters. Power Engineering 106(9), 48–52 (2002)
[2] Infrafone AB website (April 2013), http://www.infrafone.se
[3] Kockum Sonics electronic guides on infrasonic cleaning (April 2013), http://www.kockumsonics.com/downloads/sonic_documents.htm
[4] Portable infrasonic duct cleaning system. Journal of Environmental Health 59(5), 32 (1996)
[5] Schimmoller, B.K.: Tuning in to acoustic cleaning. Power Engineering 103(7), 18–26 (1999)

Effects of Misalignments of MEMS Accelerometers in Tilt Measurements

S. Łuczak

Warsaw University of Technology, Faculty of Mechatronics,
Institute of Micromechanics and Photonics, ul. Boboli 8, 02-525, Warsaw, Poland
s.luczak@mchtr.pw.edu.pl

Abstract. The paper discusses effects of misalignments of the sensitive axes of MEMS accelerometers applied in tilt measurements. Possible ways of reducing the errors due to the misalignment are introduced and briefly discussed. Results of experimental and simulation studies are also presented, including values of the evaluated accuracy of measurements performed by means of a tilt sensor built of two commercial MEMS accelerometers. It was found out that the existing misalignment, being of ca. 0.9°, decreased accuracy of the measurements ca. 3 times, which in the case of aligned accelerometers was no worse than 0.35°. Designs of special precision instruments simplifying the aligning process are proposed.

1 Introduction

One of numerous applications of accelerometers are tilt measurements [1]. If the employed accelerometers are of small dimensions, e.g. their Micro Electro-Mechanical Systems (MEMS) versions, they can be applied for sensing tilt of various devices having large dimensions, like e.g. orthotic robots presented in [2], as well as featuring miniature size – mostly microrobots [3], e.g. a robot resembling an amphibian presented in [4] or a biped robot referred to in [5].

Low price, high reliability and high shock-survivability (up to 50,000 g) of MEMS accelerometers predestines them for various innovative applications, e.g. in safety systems of the mentioned orthotic robots [6], as there is a real risk of a fall of such device. It should be noted that even in applications where the size does not matter, miniature dimensions of MEMS sensors make it possible to realize almost non-invasive measurements, whose advantages can be compared to e.g. angular position transducer proposed in [7], which does not introduce any interference into the monitored system.

Generally, since introduction of additional sensor makes it possible to significantly improve performance of a device, like e.g. introduction of a force sensor into the control system for drives presented in [8], other numerous applications of MEMS tilt sensors can be easily envisaged.

If the foreseen tilt measurements are to be realized with an accuracy better than 1°, few issues related to operation of MEMS accelerometers must be dealt with.

T. Březina and R. Jabloński (eds.), *Mechatronics 2013*,
DOI: 10.1007/978-3-319-02294-9_50,

With respect to each sensitive axis, the following problems have to be taken care of: instability of the offset and the gain assigned to the output signal, application of appropriate mathematical formula for computing component tilt angles, misalignment of the axis. As far as the last is concerned, it can be divided into:

- misalignment of the silicon die with respect to the packaging of the chip,
- misalignment of the chip with respect to the PCB,
- misalignment of the PCB with respect to the casing of the tilt sensor,
- misalignment of the casing with respect to its seating in the final device (or the holder of the test rig used for experimental studies).

The first three kinds of misalignment are rather constant over time, and are reduced by minimizing the misalignment of the casing while seated in the final device. So, in most of the cases, it is the last kind that is the most crucial.

As it has been already mentioned, the alignment precision is one of the most crucial issues pertaining to application of MEMS accelerometers, especially with respect to their calibration accuracy [9]. It can be e.g. a source of apparent nonlinearity of the accelerometer [10]. Besides a physical alignment of the sensitive axes of MEMS accelerometers (resulting in a toilsome assembly of the accelerometer unit within the seating of the main device) there are other ways of dealing with the problem, usually by compensating for the misalignment angles (two angles in two perpendicular planes for each sensitive axis). Such approach requires to use complicated mathematical transformations (usually based on matrix analysis) while calculating the accelerations. The following concepts can be listed here:

- using empirical formulas, like in [11],
- using affine coordinate systems with experimentally determined angles between the axes [11]-[12],
- using an experimentally determined matrix with misalignment errors of each axis, like in [13]-[14],
- using sophisticated algorithms based on data fusion and quaternions [15].

As the misalignment (position of the PCB with the sensor-chip within the seating of the main device) may change over a long-term and with temperature or humidity variations, especially when certain elements are used in the construction of the mechanical casing of the sensor (e.g. rubber cushions), it is advantageous to apply systems that can be calibrated while operated (including corrections for the misalignment angles), like 3DM-GX3-25 by MicroStrain Inc. [16]. Then the related errors can be to some extent diminished. However, a decrease of the accuracy compare to a case of precise physical alignment under laboratory conditions must be taken into consideration. It is hard to provide strict numbers, however by analyzing the results reported in related papers, e.g. in [12], it may be stated that the accuracy corresponding to determination of tilt angles can be expected to be of ca 1° when the misalignment is experimentally evaluated, whereas a precise alignment ensures accuracy of at least 0.3° [17]. Even lower accuracy is usually obtained when the misalignment is evaluated using an autocalibration procedure,

with no test rig employed, like in [18]. So, the trade-off here is usually a decrease of the accuracy.

The physical alignment ensures the highest accuracy, however it is the most toilsome solution. In order to make it less laborious, few instruments for aligning and holding the tested sensors have been designed and used in experimental studies. They make it possible to align the PCB with the used single-chip accelerometer by adjusting its three angular degrees of freedom within a small range of ca. 3° with a high accuracy of ca. 0.02°. The instruments are presented in Fig. 1. The first (Fig. 1a) has a monolithic compliant structure with a necking, making it possible to apply angular displacements of the attached PCB with MEMS accelerometer.

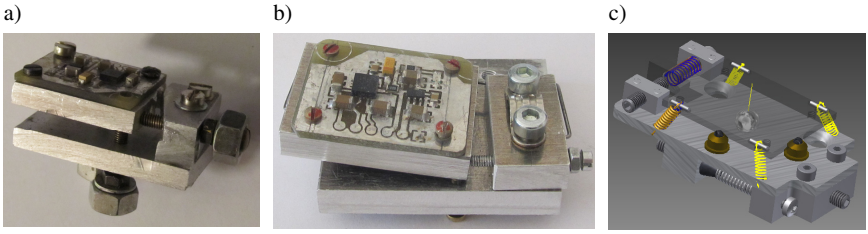

Fig. 1 Aligning instruments

The second instrument (Fig. 1b) employs a spring wire which by means of three screws can be bent (in two planes) or twisted, thus making it possible to align the PCB with MEMS accelerometer. The wire additionally eliminates all the plays. The third instrument (Fig. 1c) employs an idea of three-point support. Its screws with cone tips drive special pushers positioning the PCB holder supported on a ball (located right in the middle of the instrument) and two tips. Coil springs generate the necessary contact forces. In the case of all the three instruments, the aligning elements are self-retaining screws (M2 or M3) – standing out of the instrument outline.

It is worthwhile mentioning that if the highest accuracy of tilt measurements is searched for, the sensor built of MEMS accelerometers should employ three mono-axial accelerometers of high quality (e.g. manufactured by such companies as Colybris or Murata). Then, the presented aligning instruments would be much complicated as they should make it possible to adjust three angular degrees of freedom for three separate accelerometers.

2 Mathematical Relations

While using the analog outputs of MEMS accelerometers (what guarantees the highest accuracy of the measurements), whose sensitive axes are arranged into a Cartesian system, the generated voltage signals obtained while tilting the accelerometer within an appropriate vertical plane, can be represented by the following formulas [10]:

$$U_{x,z} = a_{x,z} + b_{x,z} \sin\left(\alpha + c_{x,z}\right) \tag{1}$$

and within a second vertical plane perpendicular to the first one:

$$U_{y,z} = a_{y,z} + b_{y,z} \sin\left(\beta + c_{y,z}\right) \tag{2}$$

where: $a_{x..z}$ – offset; $b_{x..z}$ – gain; $c_{x..z}$ – phase shift; α – pitch angle; β – roll angle.

The phase shifts $c_{x..z}$ represent misalignments of particular sensitive axis within the respective plane (i.e. plane of pitch or roll). As the component misalignments c_x and c_y are related to one plane only, it was taken care to diminish the other components as much as possible before starting the experimental studies, except for y axis, which was left misaligned purposefully (see Fig. 4). It should be noted that the phase shift c_z is of ca. 90° and has a value different for Eq. (1) and (2).

In order to simplify the further formulas, let us introduce the following equation (disregarding the phase shifts),

$$\frac{g_{x...z}}{g} = \frac{U_{x...z} - a_{x...z}}{b_{x...z}} = m_{x...z} \tag{3}$$

In order to demonstrate effects of the discussed misalignments, let us consider pitch angle only (analogous results can be obtained for the roll angle). Its value can be determined as follows [12],

$$\alpha = \arctan \frac{m_x}{\sqrt{m_y^2 + m_z^2}} \tag{4}$$

Value of the pitch α can be computed only when parameters $a_{x..z}$ and $b_{x..z}$ are known. While pursuing a high accuracy of tilt measurements, the parameters must be determined experimentally.

3 Experimental Results

In order to experimentally evaluate the influence of the discussed misalignments, appropriate tests were carried out. The test rig used for this purpose has been minutely described by the author in [19]. The tested tilt sensor was built of two dual-axis MEMS accelerometers ADXL 203 manufactured by Analog Devices Inc. [20]. Its structure is presented in Fig. 2. As can be seen, both accelerometers were aligned using a compliant mounting of their PCB, which employs 2 rubber cushions and 3 screws, each.

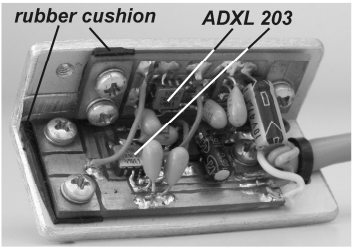

Fig. 2 The tested tilt sensor

The experimental verification consisted in applying successive tilt angles of the tested sensor by means of the test rig, and then recording the analog output signals of the sensor. Comparison of the pitch φ applied by means of the test rig and the pitch α calculated according to Eq. (4) on the basis of the sensor indications, made it possible to determine values of the measurement errors. The relevant error e has been defined as,

$$e = |\varphi - \alpha| \tag{5}$$

Its courses are presented in Fig. 3 for two various cases.

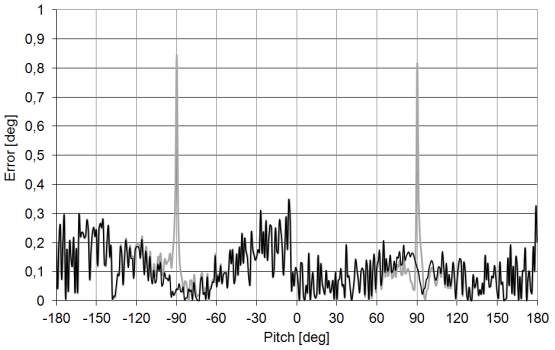

Fig. 3 Error of misaligned sensor

The gray course corresponds to the actual measurements realized with one sensitive axis (y axis) purposefully misaligned, whereas the black course corresponds to a perfect alignment of that axis, which was realized artificially, by means of a simulation. As can be seen, the misalignment of the sensitive axis y significantly increased the error of the tilt sensor (almost 3 times).

The effect of the misalignment is evident especially for pitch angles of -90° and 90°, and can be easily explained, observing variations of the output voltage U_y associated with the misaligned y axis, which should be almost invariable if the sensor were perfectly aligned and only pitched (keeping the roll angle β constant at 0°). The real variations of the voltage U_y are presented in Fig. 4.

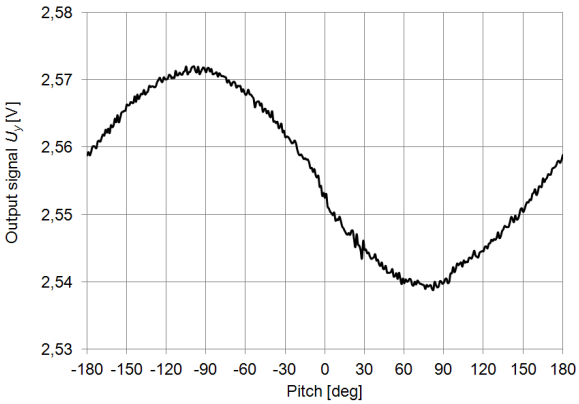

Fig. 4 Variations of the output signal due to the dominating misalignment (*y* sensitive axis)

On the basis of the presented course, magnitude of the misalignment can be evaluated at ca. 0.9°, by referring the amplitude of the variations (of ca. 0.017 V) to the gain b_y (in this case of ca. 1.026 V).

Simulation of the perfect alignment (related to the black course in Fig. 3) was realized in a very simple way. As the roll angle β was of 0° during the whole experiment, it was assumed, according to Eq. (2), that the variable m_y (see Eq. (3)) was of 0. This is a big simplification, because in this way the noise associated with *y* axis was eliminated as well (what is impossible in the real measurements). However, at the pitch angles where the effect of the misalignment is the most evident (i.e. ±90° in Fig. 3), value of the simulated error is very low, so even increasing it by the existing noise (of ca. 0.2°) does not disqualify the introduced simplification.

It is worthwhile mentioning that the course presented in Fig. 4 can have another character, as the misalignment can be resolved into two perpendicular component angles. So, the extreme values of the fluctuations may appear for other pitch angles than -90° and 90°, e.g. for -180°, 0°and 180°. The case presented in Fig. 4 is the worst possible, as referred to using Eq. (4).

4 Conclusions

While using MEMS accelerometers in relatively accurate measurements, the following three issues are the most crucial:

- determination of the offset voltage,
- determination of the gain,
- alignment of all the sensitive axes.

It can be stated that each of them has a significant effect on the accuracy of tilt measurements, and not only in terms of the accuracy of determining their standard value but also with respect to variations of the value (over temperature, time, etc.).

As reported in various sources, misalignment errors of MEMS accelerometers are usually of 2° [13], unless a special care is taken to align these sensors. If the misalignment errors are not compensated for (using various mathematical transformations), the misalignment angles, depending on their spatial orientation, may increase the errors of determining tilt angles up to their magnitude.

Except for using the arc tangent formula represented by Eq. (4), the component tilt angles (pitch and roll) can be determined using other types of mathematical equations, i.e.: arc sine [10]; arc cosine [11]; combination of arc sine and arc cosine (as proposed by the author et al in [17]), where each is used only in a limited range (i.e. 0–45° or 45–90°, respectively); weighted average (as proposed by the author et al in [21]).

Considerations pertaining to advantages and disadvantages of the listed equations have been presented by the author in [22]. For the purpose of the studied effects, the arc tangent equation was the best one, as it does not feature a significant nonlinearity, like the arc sine and arc cosine functions [17], increasing the maximal errors within the range of their strong nonlinearity. Analyzing the courses of the errors related to arc cosine and arc tangent formulas, analogous to the one presented in Fig. 3, it can be easily stated that for pitch angles of ca. ±90°, they are approximately the same. As the arc cosine function employs only the component accelerations in y and z axis [17], misalignment of the component acceleration in x axis can be thus disregarded. As the sensitive axis z was precisely aligned (with phase shifts c_z less than 0.01°), therefore in the case of the observed error peaks, the responsible factor was the signal related to sensitive axis y, being affected by the relevant misalignment.

To summarize, it can be stated that when accurate tilt measurements are striven for, where the accuracy should be no lower than ca. 0.3°, a precise alignment of the applied MEMS accelerometers is required. If this issue were neglected, the accuracy of the performed tilt measurements would be affected – a decrease by the magnitude of the misalignments should be taken into account.

Acknowledgments. The author would like to thank last year students of the Faculty of Mechatronics, Warsaw University of Technology – Mr. Łukasz Kozłowski, for designing and building a prototype of the aligning device presented in Fig. 1a, and Mr. Krzysztof Sikorski for designing the aligning device presented in Fig. 1c.

References

[1] Wilson, J.: Sensor Technology Handbook, Newnes, Burlington, pp. 396–399 (2005)
[2] Wierciak, J., Jasińska-Choromańska, D., Szykiedans, K.: Orthotic Robot as a Mechatronic System. In: Mechatronics. Recent Technological and Scientific Advances, pp. 579–588 (2011)
[3] Fatikow, S., Rembold, U.: Microsystem Technology and Microrobotics, p. 226. Springer, Heidelberg (1997)
[4] Bodnicki, M., Sęklewski, M.: Design of Small-Outline Robot – Simulator of Gait of an Amphibian. In: Recent Advances in Mechatronics, pp. 77–81 (2007)

[5] Zezula, P., Vlachy, D., Grepl, R.: Simulation modeling, optimalization and stabilisation of biped robot. In: Recent Advances in Mechatronics, pp. 120–125 (2007)
[6] Jasińska-Choromańska, D., Szykiedans, K., Wierciak, J., Bagiński, K., Bojarski, M., Kabziński, B., Kołodziej, D., Zaczyk, M., Credo, W., Lasecki, J., Rzeszotek, Ł., Semeniuk, J.: Mechatronic system for verticalization and aiding the motion of the disabled. Bull. Pol. Ac.: Tech. 61(2) (2013)
[7] Bodnicki, M., Hawłas, H.J.: Commutation Phenomena in DC Micromotor as Source Signal of Angular Position Transducer. In: Recent Advances in Mechatronics 2008-2009, pp. 263–268 (2009)
[8] Wierciak, J.: Improvement of Performance of Precision Drive Systems by Means of Additional Feedback Loop Employed. In: Recent Advances in Mechatronics, pp. 495–499 (2007)
[9] Syed, Z., Aggarwal, P., Goodall, C., Niu, X., El-Sheimy, N.: A new multi-position calibration method for MEMS inertial navigation systems. Meas. Sci. Technol. 18(7), 1897–1907 (2007)
[10] Low g Accelerometer Non-Linearity Measurement, #AN-00MX-014 Application Note n/r 5/12/03, MEMSIC Inc., North Andover (2005)
[11] Qian, J., Fang, B., Yang, W., Luan, X., Nan, H.: Accurate Tilt Sensing with Linear Model. IEEE Sensors J. 11(10), 2301–2309 (2011)
[12] Šipoš, M., Pačes, P., Roháč, J., Nováček, P.: Analyses of triaxial accelerometer calibration algorithms. IEEE Sensors J. 12(5), 1157–1165 (2012)
[13] Parsa, K., Lasky, T.A., Ravani, B.: Design and Implementation of a Mechatronic All-Accelerometer Inertial Measurement Unit. IEEE/ASME Trans. Mechatr. 12(6), 640–650 (2007)
[14] Ang, W.T., Khosla, P.K., Riviere, C.N.: Nonlinear regression model of a low-g MEMS accelerometer. IEEE Sensors J. 7(1), 81–88 (2007)
[15] Reinstein, M.: Evaluation of Fine Alignment Algorithm for inertial navigation. Przegląd Elektrotechniczny (Electr. Rev.) 87(7), 255–258 (2011)
[16] 3DM-GX3-25 Up and North Compensation, TN-I0029, MicroStrain Inc., Williston (2012)
[17] Łuczak, S., Oleksiuk, W., Bodnicki, M.: Sensing Tilt with MEMS Accelerometers. IEEE Sensors J. 6(6), 1669–1675 (2006)
[18] Frosio, I., Pedersini, F., Borghese, N.A.: Autocalibration of Triaxial MEMS Accelerometers With Automatic Sensor Model Selection. IEEE Sensors J. 12(6), 2100–2108 (2012)
[19] Łuczak, S.: Dual-Axis Test Rig for MEMS Tilt Sensors. Metrol. and Meas. Syst. (to be published)
[20] Precision ±1.7g Single/Dual Axis Accelerometer ADXL 103/ADXL 203, Analog Devices Inc., Norwood (2005)
[21] Łuczak, S., Oleksiuk, W.: Increasing Accuracy of Tilt Measurements. Eng. Mech. 14(3), 143–154 (2007)
[22] Łuczak, S.: Optimized Tilt Measurements Realized with MEMS Accelerometers. Int. J. Prec. Eng. Manuf. (to be published)

Method for Determining Direction, Velocity and Position of a Flying Ball

A. Nagy

Széchenyi University, Faculty of Engineering Science, Győr, Hungary
anagy@sze.hu

Abstract. This paper proposes an algorithm for an optical measuring system, which is capable of calculating the velocity and position components, the radius and the trajectory of a flying sphere-shape ball. The infrared light-emitting diodes and the IR sensors of the system are arranged in a single plane and create a lattice of infrared light beams. The FPGA based hardware of the system measures the points in time when the light beams are interrupted by the ball. The proposed algorithm uses the measured time-data with the associated positions of the interrupted light beams as input. The practical application such a systems can be measuring ball's velocity in several sports and games.

1 Introduction

There are several ball games where the velocity and the position of the ball in a particular moment can be interesting. A few methods such as a video image processing system with several cameras and, ultrasonic radar system have been developed to measure some of the outlined parameters. All existing methods, including ours have advantages, disadvantages and limitations. The methods based on high speed cameras are usually expensive, requires special cameras and powerful computers for image processing and the installation of such devices could be complicated. In other hand these systems could follow and measure the movement of the ball on the full court. The systems based on one Doppler radar are able to measure the actual speed only if the ball moves precisely to or from the radar. A quite different approach is placing the measurement device into the moving objects [4]. In this case the measurement devices must be not only highly durable but also lightweight in order to avoid the imbalance of the ball. Furthermore the installation of the device into a handball can be challenging.

The system based on interruptions of several infra light beams fitted into a single plane can be built into the frame of the goal and can be therefore a reasonable solution. In order to calculate the trajectory of the moving ball in three dimensions, it would be desirable to use light beams perpendicular to each other [1]. In almost all cases the perpendicular arrangement is not reasonable because the goal's frames have only three sides, the two vertical posts and the horizontal

T. Březina and R. Jabloński (eds.), *Mechatronics 2013*,
DOI: 10.1007/978-3-319-02294-9_51,

crossbar. For this reason our system uses only horizontal and slightly tilted light beams which deliver enough information to calculate all three dimensional parameters of the trajectory (Figure 1).

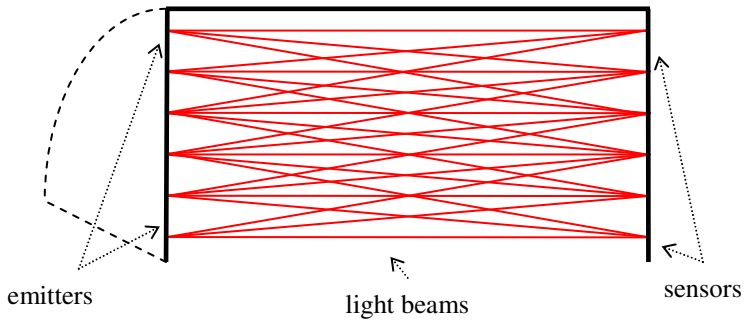

Fig. 1 Structure of the system (not to scale)

2 The Computation Algorithm [2]

Despite the fact that because of gravity a flying ball accelerates and does not move in a straight direction, the main part of the algorithm considers the movement as being uniformly in a straight line. This simplification of the computation is correct and causes no inaccuracy in case when the input parameters (vertical positions of the interrupted light beams) measured in a free falling coordinate system as function of time. The falling ball and the falling coordinate system move uniformly and linearly relative to one another. Of course our measurement system does not fall at all, only some computations are carried out in order to calculate the vertical positions of the system in function of time as it would fall.

2.1 Calculation from Parallel Light Beams

The first step of the proposed algorithm combines together only the events coming from the interruption of light beams which are parallel to each other. In the partial results provided by the first step, there is no information about the spatial and speed components that are parallel to the light beams used in the calculation. The silhouette of the ball in a perpendicular plane to the parallel light beams is a circle.

The calculation from interruption of light beams that are parallel to each other uses the following variables and symbols. The z direction is perpendicular to the plane of the light beams (same for each light beam). The y direction is in the plane of the light beams and perpendicular to the parallel light beams (depends on the slope of the light beams).

Symbols:

- R Radius of the flying ball
- A_z Distance between the plane of the light beams and the center point of the ball at t=0 time
- A_y Height of the center point at t=0 time in y direction
- v_z Speed component in z direction
- v_y Speed component in y direction
- t_i The time of the i-th interruption of the light beams
- y_i The spatial component of the beam of the i.-th interruption along the y direction
- tcross: The time when the center point of the ball crossing the plane of the light beams

Equations (1), (2) describe the two coordinates of the center point of the ball in function of time.

$$P_z(t) = A_z + v_z \cdot t \tag{1}$$

$$P_y(t) = A_y + v_y \cdot t \tag{2}$$

The number of the interrupted light beams depends on the radius of the ball and on the direction of the movement. In worst case minimum three parallel light beams must be interrupted by the ball. If the ball falls almost vertical then the number of the interruptions is the highest one.

At the $t=t_i$ time the distance between the center point of the ball and the interrupted light beam is R. That follows these points are on a perimeter of a circle. Because of the uncertain of the measuring and because of the over determination of the problem caused by variable number of points the algorithm applies the least square method to calculate the parameters of the circle.

$$f(R, A_z, v_z, A_y, v_y) = \sum \left[(A_z + v_z \cdot t_i)^2 + (A_y + v_y \cdot t_i - y_i)^2 - R^2 \right]^2 = Min \tag{3}$$

The partial derivations of equation (3) by all of the unknown variables give equitation (4-8).

$$\frac{\partial f}{\partial R} = \sum 2 \cdot Z \cdot (-2) \cdot R = 0 \tag{4}$$

$$\frac{\partial f}{\partial A_z} = \sum 2 \cdot Z \cdot 2 \cdot (A_z + v_z \cdot t_i) = 0 \tag{5}$$

$$\frac{\partial f}{\partial v_z} = \sum 2 \cdot Z \cdot 2 \cdot (A_z + v_z \cdot t_i) \cdot t_i = 0 \tag{6}$$

$$\frac{\partial f}{\partial A_y} = \sum 2 \cdot Z \cdot 2 \cdot (Ay + vy \cdot ti - yi) = 0 \tag{7}$$

$$\frac{\partial f}{\partial v_y} = \sum 2 \cdot Z \cdot 2 \cdot (A_y + v_y \cdot t_i - y_i) \cdot t_i = 0 \tag{8}$$

wherein:

$$Z := \left[(A_z + v_z \cdot t_i)^2 + (A_y + v_y \cdot t_i - y_i)^2 - R^2 \right] \tag{9}$$

Exploited the fact that R and v_z cannot be zero the equation (4-8) can be simplified.

$$\sum Z = 0 \tag{10}$$

$$\sum Z \cdot t_i = 0 \tag{11}$$

$$\sum Z \cdot t_i^2 = 0 \tag{12}$$

$$\sum Z \cdot y_i = 0 \tag{13}$$

$$\sum Z \cdot y_i \cdot t_i = 0 \tag{14}$$

Introducing some new variables into equation (9) we get equation (15).

$$Z = x_1 + x_2 \cdot t_i + x_3 \cdot t_i^2 + x_4 \cdot y_i + x_5 \cdot y_i \cdot t_i + y_i^2 \tag{15}$$

New variables are:

$$x_1 = A_z^2 + A_y^2 - R^2 \tag{16}$$

$$x_2 = 2 \cdot A_z \cdot v_z + 2 \cdot A_y \cdot v_y \tag{17}$$

$$x_3 = v_z^2 + v_y^2 \tag{18}$$

$$x_4 = -2 \cdot A_y \tag{19}$$

$$x_5 = -2 \cdot v_y \tag{20}$$

Using these variables the equations (10-14) form a linear system.

$$\sum \begin{bmatrix} 1 & t_i & t_i^2 & y_i & y_i \cdot t_i \\ t_i & t_i^2 & t_i^3 & y_i \cdot t_i & y_i \cdot t_i^2 \\ t_i^2 & t_i^3 & t_i^4 & y_i \cdot t_i^2 & y_i \cdot t_i^3 \\ y_i & t_i \cdot y_i & t_i^2 \cdot y_i & y_i^2 & t_i \cdot y_i^2 \\ y_i^2 & t_i^2 \cdot y_i & t_i^3 \cdot y_i & t_i \cdot y_i^2 & t_i^2 \cdot y_i^2 \end{bmatrix} \begin{bmatrix} x_1 \\ x_2 \\ x_3 \\ x_4 \\ x_5 \end{bmatrix} = \sum \begin{bmatrix} -y_i^2 \\ -y_i^2 \cdot t_i \\ -y_i^2 \cdot t_i^2 \\ -y_i^3 \\ -y_i^3 \cdot t_i \end{bmatrix} \tag{21}$$

From the solution of the linear system v_y, A_y, v_z, A_z and R parameters can be calculated.

$$v_y = \frac{-x_5}{2} \tag{22}$$

$$A_y = \frac{-x_4}{2} \tag{23}$$

$$v_z = \sqrt{x_3 - v_y^2} \tag{24}$$

$$A_z = x_2 - 2 \cdot A_y \cdot v_y \tag{25}$$

$$R = \sqrt{A_z^2 + A_y^2 - x_1} \tag{26}$$

The time when the center point of the ball crossing the plane of the light beams is:

$$A_z + v_z \cdot t_{cross} = 0 \Rightarrow t_{cross} = \frac{-A_z}{v_z} \tag{27}$$

Substituting t_{cross} back in equation (2) we get the height of the ball along the y direction.

$$h = A_y + v_y \left(\frac{-A_z}{v_z} \right) \tag{28}$$

2.2 Calculation of the Position of the Ball

The dashed lines in the Figure 2 depict the possible ball positions along different y directions calculated from two differently tilted light beams groups. The intersection of these lines determines the position of the ball at the point of time when the ball crosses the plane of the light beams (point C).

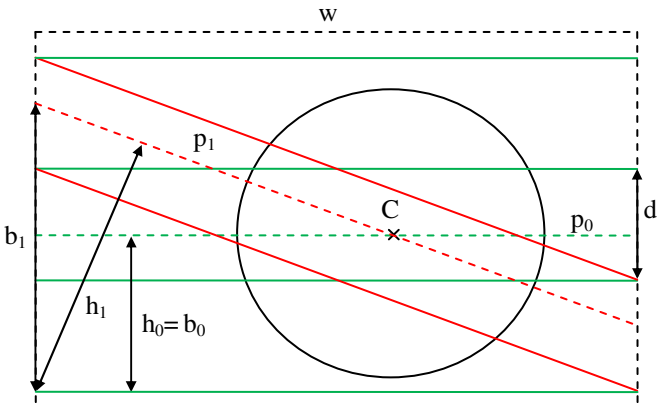

Fig. 2 Position of the ball

The equations of the dashed lines in the axis of the frame of the goal can be written in form:

$$y = m_k \cdot x + b_k \tag{29}$$

The slopes of lines depend on the width of the frame of the measuring system (w), on the vertical distances of the neighboring detectors (d) and on the differences in level between the emitter and sensor (k).

$$m_k = k \cdot \frac{d}{w}, \text{ where } k = -2,-1,0,1,2 \tag{30}$$

Because of the similarity between the triangle composed by b_k, h_k and the triangle composed by the horizontal line and a light beam with k slope:

$$b_k = h_k \cdot \frac{\sqrt{w^2 + (k \cdot d)^2}}{w} \tag{31}$$

Using equation (29) for two lines with different k value the intersection point C can be calculated. In order to decrease the uncertain of the measurement it is reasonable to choose lines whose slopes are differing as much as possible.

2.3 Calculation of the Speed Components of the Ball

The speed components in directions y and z (v_y, v_z) come directly from the calculation based on the measured time points of the interruptions of the parallel light beams. The calculation does not provide any information about the speed

component parallel with the light beams (v_x). The two dashed lines on Figure 3 depict the possible speed components calculated from two differently tilted light beams groups.

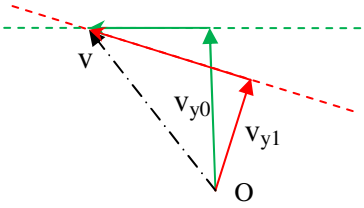

Fig. 3 Speed components of the ball in the plane of the light beams

The calculation of the speed components in the plane of the goal's frame (v) is almost the same as the calculation of the position discussed above. The forms of the equations of the dashes lines are the same as equation (29-30). The b_k parameters can be calculated from the equation (32).

$$b_k = v_{yk} \cdot \frac{\sqrt{w^2 + (k \cdot d)^2}}{w} \tag{32}$$

The v_z components are independent on the slope of the parallel light beams which were calculated from. The equality of these components can be used to check the result.

3 Conclusions

The performance of the proposed algorithm was tested in two different ways. At first step some simulations in Matlab environment were carried out [3]. These simulations allow one to determine how much the inaccuracies of the measured parameters affect the calculation. It turned out, that either the 10 μs long discrete time intervals of the measurement, or the thickness of the light beams does not influence significantly the results. After several simulations, the algorithm has been programmed in an embedded system built into a frame of a handball goal. The quantification of the accuracy of the whole system is difficult because of the lack of reference parameters. The radius of the flying ball was the only certainly known reference parameter. The radius calculated by the algorithm was compared to the actual radius of the ball. The differences between these values were highly independent from the speed of the ball and from the direction of the flying. Usually the differences were only in 0.3-0.5 mm range. Several circumstances can cause the inaccuracies of measurement. The author of this paper thinks that mainly the imperfectness of the ball's shape and the thickness of the light beams limiting the accuracy of the system. Even the high quality balls have no perfect sphere-shape.

For a 100 mm radius ball the variance in diameter could be more than 1 mm. The imperfect shape of ball does not allow one to determine precisely the accuracy of the measuring system. As regards the accuracy of the speed in z and vertical directions a conservative estimation based on the measurement of the radius of the ball could be +/-1 percent. In the x direction the accuracy of the measurement is probably worse and depends on the angle between the two parallel light beam groups used for the calculation.

At the final stage of the test period two handball goals were placed close one behind the other. One goal was lifted and shifted some centimeter relatively to the other. Neglecting the deceleration of the ball the two measured speed components in z and x direction expectedly are the same. The results of this test were in accordance with the accuracy estimation mentioned above.

References

[1] Boulware, J.L.: Apparatus for accurately determining a moving ball's position and speed. United States Patent US 5,602,638 (1997)

[2] Molnárka, G., Nagy, A., Sütő, I., Mórocz, T., Bozi, I., Varjasi, N.: Optical system and method for determining direction, velocity and position of a ball traversing a plane. EP 2 233 932, Belgium, Application number: E09462002.8 (2011)

[3] Stoyan, G., Gergó, L., Molnárka, G., Gyurkovics, É.: Matlab, Elte Typotex, Budapest (1999) (IInd edn. 2005)

[4] Marinelli, D.J.: Speed, spin rate and curve measuring devices using magnetic field sensors. United States Patent US 6,151,563 (2000)

Silicon PIN Photodiode-Based Radiation Detector for Mobile Robots

O. Petruk and R. Szewczyk

Warsaw University of Technology, Institute of Metrology and Biomedical Engineering, sw. A. Boboli 8, 02-525 Warsaw, Poland
szewczyk@mchtr.pw.edu.pl

Abstract. Paper presents the results of investigation on functional properties of a gamma detector with p-i-n photodiode. Research was carried out with S3590-08 p-i-n diode produced by Hamamatsu Photonics. Sensitivity of the diode was tested for three sources of gamma radiation: ^{22}Na, ^{137}Cs, ^{60}Co. The achieved results were compared with certified radiometer Polon Ekolab EKO-C.

1 Introduction

Certain level of gamma radiation is natural due to the naturally occurring radioisotopes as well as radiation from interactions with cosmic ray particles. However, the industrial accidents, terrorist acts or illegal transportation of radioactive materials may significantly increase this level to values that are dangerous for people and environment.

Unfortunately, animals or humans do not have the ability to sense the increase of gamma radiation and the effects of gamma radiation are irreversible for human health. For this reason, it is highly recommended to avoid exposition of people to gamma radiation whenever it is possible.

To minimise the exposition of people to gamma radiation, the mobile teleoperated robots may be used. Example of such robotic system is GRYF system developed by the Industrial Research Institute for Automation and Measurements PIAP [1]. These robots are commonly used by Police special forces for demining or for reconnaissance before the regular Police forces operation. In such a case, the knowledge about possible increase of gamma radiation level is critical.

It should be highlighted, during the development of gamma radiation sensor for mobile robot, the requirements to be considered are different, than during the development of portable system for manual operation.

First of all, a gamma detection system for mobile robots has to be resistant to a mechanical shock. During the transportation of a mobile robotic system, the gamma detector is subjected to high and low frequency vibrations, which shall not degrade the sensor's functional parameters. As a result, the commonly available Geiger-Mueller tubes [2] are not suitable for mobile robots applications. Moreover, the gamma detection system for mobile robotic application has to be able to

T. Březina and R. Jabloński (eds.), *Mechatronics 2013*,
DOI: 10.1007/978-3-319-02294-9_52,

be miniaturised. Another important problem is the power efficiency of the gamma detector for mobile robots.

To meet these strict requirements the semiconductor based gamma sensors should be applied. One of such sensors is the group of p-i-n photodiodes offered by Hamamatsu Photonics. This paper presents the results of functional tests of S3590-08 p-i-n diode produced by Hamamatsu Photonics as a gamma radiation sensor for mobile robotic applications.

2 Principles of Operation of p-i-n Photodiode as Gamma Radiation Sensor

P-i-n photodiodes are commonly used as optical detectors. The p-i-n diode consists of a semiconductor junction with acceptor layer *p*, the intrinsic region *i* and donor layer *n* [3]. A schematic diagram of the cross-section of a p-i-n photodiode is presented in figure 1.

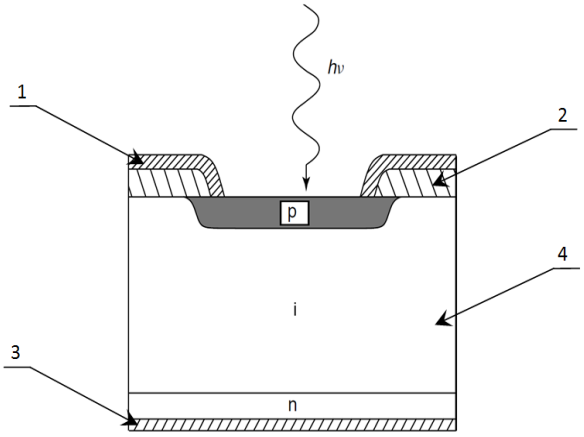

Fig. 1 Schematic diagram of the cross-section of a p-i-n photodiode [3]: 1 - metal contact, 2 - isolation SiO_2, 3 - metal layer contact and reflector, 4 - absorption layer

Interaction of gamma photon with the p-i-n diode structure generates a dark current in diode junction due to the charge carriers generation. This may be detected by electronic circuit as the dark current peaks.

Depending on the range of penetration of the semiconductor by a gamma ray, the charge carriers in the semiconductor may be generated in all three layers of the p-i-n diode.

Depending on the energy of the gamma photon, there are three possible modes of interaction between this particle and semiconducting structure:

- photoelectric effect,
- Compton effect,
- pair production.

The most commonly observed gamma radiation consists photons with energy ranging from 100 keV up to 1.2 MeV. For interaction of such photons with the semiconductor, mainly the Compton effect is observed. In such a case, the gamma photon transfers its energy to the semiconductor structure according to equation (1) [4]:

$$E = \frac{E_0}{1 + (E_0 / m_0 c^2)(1 - \cos\varphi)} \tag{1}$$

where: E – energy of dispersed gamma particle, E_0 – energy of gamma particle, φ – angle of dispersion, m_0 – mass of electron.

It should be stressed that from the technical point of view one of the most important parameters is the capacity of the p-i-n diode junction [5]. Large area p-i-n diodes exhibit a significant junction capacitance, what limits the possibility of observation of the dark current peaks, due to the presence of gamma particles. On the other hand, smaller values of p-i-n junction area limit the number of gamma particles counts.

3 Technical Solutions of p-i-n Diodes for Gamma Detection

There is a large number of producers offering the p-i-n photodiodes for gamma detection. However, two significant technical solutions have to be distinguished: the p-i-n photodiodes for large values of gamma radiation with continuous dark current measurements exhibiting large capacitance, as well as the p-i-n photodiodes with small capacitance, for detection of single gamma particles. This second kind of p-i-n photodiodes creates the possibility for measurements of energy given by gamma particle, by measurements of amplitude of the dark current peak.

Table 1 presents the selected p-i-n photodiodes developed by the most advanced producers. Due to the requirements for mobile robotic gamma detection, the list of p-i-n diodes was limited to diodes smaller than 40 mm^2, with capacity up to 300 pF.

Table 1 The most advanced p-i-n photodiodes [3]

Manufacturer	type	case	width (mm)	height (mm)
Hamamatsu	S3590-08	Ceramic	10	10
Hamamatsu	S3584-08	Ceramic	28	28
First Sensor	X100-7.2	Ceramic	10	10
Opto Diode Corporation	AXUV100	Ceramic	10	10

For the development of a gamma detector for the GRYF mobile robot, the Hamamatsu S3590-08 p-i-n photodiode [6] was selected. The diode is presented in figure 2, whereas the most important functional parameters of this diode are presented in table 2.

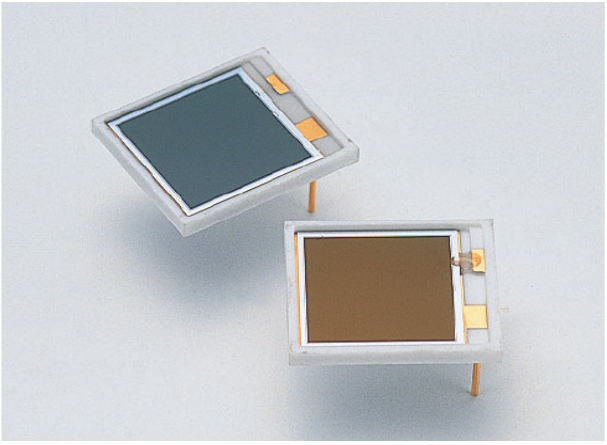

Fig. 2 View of p-i-n photodiode S3590-08 (Hamamatsu Photonics) [6]

Table 2 Properties of silicon p-i-n photodiode Hamamatsu S3590-08 [6]

parameter name	unit	value
Active area	($mm^{2)}$	100
Dark current	(nA)	2
Terminal capacitance (v_R=70V)	(pF)	40
NEP	(W/√Hz)	$3.8 \cdot 10^{-14}$

Verification of functional properties of the developed gamma radiation detector was performed with use of the certified radiometer Polon-Ekolab EKO-C with Geiger-Mueller sensor. The radiometer's parameters are given in table 3.

Table 3 Parameters of certified radiometer Polon-Ekolab EKO-C

parameter name	unit	value
Measuring range	(cps)	0.1 to 10^4
Energy of counted gamma particles	(keV)	50 to 1 500
Accuracy	(%)	±15
Sensor type	-	Geiger-Mueller sensor
Sensor area	(mm^2)	$5 \cdot 10^3$

4 Measuring Setup

Functional parameters of the developed gamma detector were verified for three different isotopes - gamma particles sources: ^{22}Na, ^{137}Cs, ^{60}Co. Energy of the gamma particles was: 662 keV, 1173 keV, 1274 keV and 1332 keV.

Electronic circuit for measurements of the dark current changes due to the presence of gamma particle is presented in figure 3. This circuit consist an fast operational amplifier in the current integrator configuration.

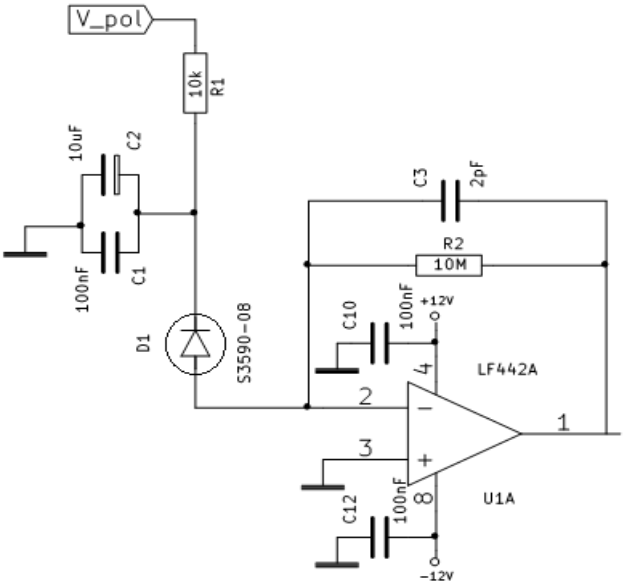

Fig. 3 Electronic circuit for p-i-n photodiode

During the measurements, the distance between gamma particles source and p-i-n photodiode was equal to 200 mm. The gamma sensor was exposed to the particles perpendicularly to its active area. There were two periods of measurements: 60 seconds and 600 seconds respectively. During the measurements the number of the dark current peaks due to gamma particle presence was counted by electronic circuit. A schematic diagram of the measuring system is presented in figure 4:

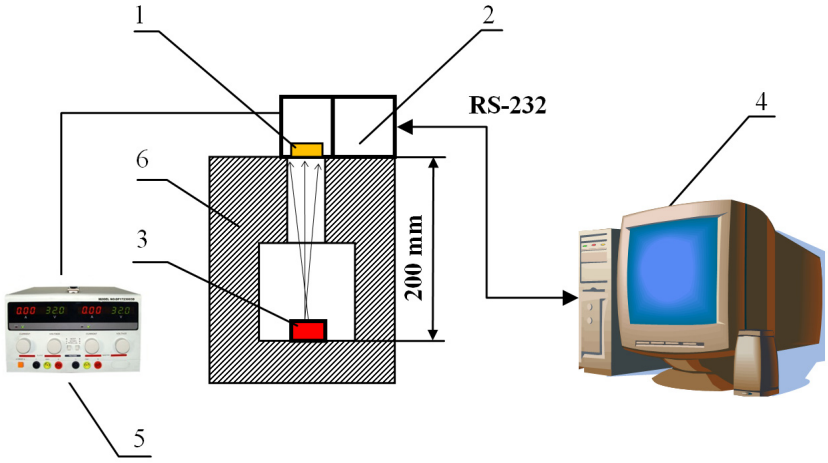

Fig. 4 Schematic diagram of the measuring system: 1- p-i-n photodiode, 2 – electronic circuit, 3 – gamma source, 4 – computer, 5 – power source, 6 - shielding

5 Results

Results of measurements carried out with the developed gamma detection system with p-i-n photodiode S3590-08 produced by Hamamatsu Photonics are presented in tables 4, 5 and 6. The difference between number of counts detected by p-i-n diode and EKO-C Ekolab Radiometer is caused by the different active sensing area of both devices. It should be indicated that this difference may be corrected by the multiplicative correction factor.

Table 4 Results of measurements for ^{22}Na isotope

device	unit	measuring time 60 [s]	measuring time 600 [s]
Radiometer EKO-C	(cps)	1 830	18 799
Developed gamma counter with photodiode S3590-08	(cps)	104	985

Table 5 Results of measurements for ^{137}Cs isotope

device	unit	measuring time 60[s]	measuring time 600[s]
Radiometer EKO-C	(cps)	1 269	12 702
Developed gamma counter with photodiode S3590-08	(cps)	63	573

Table 6 Results of measurements for ^{60}Co isotope

device	unit	measuring time 60[s]	measuring time 600[s]
Radiometer EKO-C	(cps)	2 200	20 361
Developed gamma counter with photodiode S3590-08	(cps)	144	1 206

Within presented results up to 12% of difference in correlation coefficients between tested sensors were observed. These differences are caused by random character of gamma radiation connected with difference in the sensing area of sensors. It should be highlighted, that EKO-C ECOLAB radiometer has sensing area about 50 times larger than S3590-08 p-i-n photodiode. However, expected uncertainty of gamma particles counting b EKO-C ECOLAB radiometer is about 15%.

During the measurements it was observed that the amplitude of output signal from electronic circuit with p-i-n photodiode S3590-08 is independent from the energy of the gamma particle. The typical output signal examples are presented in figure 5.

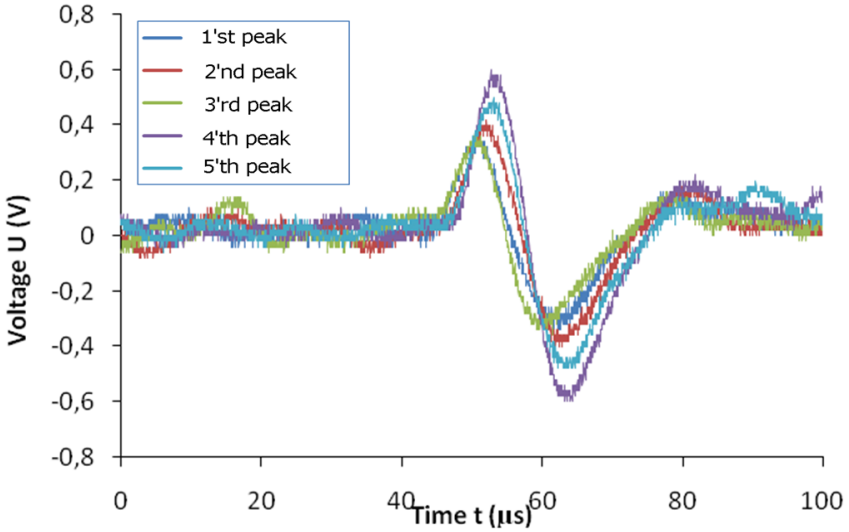

Fig. 5 Output signal from electronic circuit with p-i-n photodiode S3590-08

6 Conclusion

The p-i-n photodiodes may be used for development of gamma radiation sensors for mobile robotic applications due to its robustness, mechanical shocks and vibration resistance, reliability and limited power consumption. Moreover, the p-i-n photodiode based sensors may be miniaturised, what is especially important for mobile robots [8]. As a result, such p-i-n photodiode based sensors are more suitable for robotic applications than Geiger-Mueller tube based sensors.

Results of experiments indicated that the number of gamma particle counts of a p-i-n photodiode sensor was significantly smaller than the number of counts detected by Geiger-Mueller based radiometer. This phenomenon is caused by a smaller sensing area of p-i-n photodiode. Moreover, changes amplitude of the pulses during the gamma particle detection, due to the changes of gamma particle energy, may be neglected.

Acknowledgments. This work was partially supported by The National Center for Research and Development within grant no. O ROB 0015 01/ID15/1.

References

[1] http://www.antyterroryzm.com/product/pl/gryf
[2] Debertin, K., Helmer, R.G.: Gamma- and X-Ray Spectrometry with Semiconductor Detectors. North Holland (1988)
[3] Gåsvik, K.J.: Optical Metrology. John Wiley & Sons (2003)

[4] Taylor, J.R., Zafiratos, C.D., Dubson, M.A.: Modern Physics for Scientists and Engineers. Prentice Hall (2004)
[5] Gilmore, G.R.: Practical Gamma-Ray Spectrometry. John Wiley & Sons (2008)
[6] Hamamatsu Corporation, S3590-08/-09/-18/-19. Large active area Si PIN photodiode (2012)
[7] http://www.polon-ekolab.com.pl/ekoc/ekoc.htm
[8] Kasprzyczak, I., Trenczek, S., Cader, M.: Robot for Monitoring Hazardous Environments as a Mechatronic Product, Journal of Automation. Mobile Robotics and Intelligent 6, 57 (2012)

A Method for Measuring Size and Form Deviations of Rotary Components with Variable Curvature on FMM

M. Sieniło and S. Żebrowska-Łucyk

Warsaw University of Technology, Faculty of Mechatronics, św. Andrzeja Boboli 8, 02-525, Warsaw, Poland
m.sienilo@wp.pl, szl@mchtr.pw.edu.pl

Abstract. We present the method for expanding the measuring capabilities of form Measuring Machines (FMMs) commonly used for measuring object form, tilt, location and orientation deviations. We propose using a cylindrical standard with known diameter to also measure local radii lengths. We discuss manners of how the proposed method may be realized and suggest a choice amongst them. Technical and metrological requirements for the size standard are presented, along with its advantages, drawbacks, as well as applications of the proposed measurement method.

1 Introduction

One of the deciding factors in constant technological advance is the continuous rise of consumer expectations with regards to the quality, functionality and durability of manufactured goods. Further factors include legal and ecological standards as well as the pressure caused by the manufacturer's desire to reduce costs.

The durability, costs of use, comfort and safety of the device depend on the precision of its components. At many devices, mechanical parts with curvilinear surfaces perform a specific role; among other functions, they serve to transfer motion. The accuracy of such components is of great consequence taking into account their widespread applications, in particular in the automotive, aeronautical, machine and naval industries [1].

Most rotary surfaces are characterized by constant curvature. The methods of testing the geometrical accuracy of these components are already well mastered.

It is much more difficult, however, to check geometry of mechanical parts with varying curvatures, such as camshafts, the profiles of which are a combination of straight and curved segments with different radii. Components such as combustion engine pistons present a similar problem. The control of these elements requires linking consecutive measured local radii with the angle of rotation. This type of connection is ensured by coordinate measurement technique [2]. The appropriate

T. Březina and R. Jabloński (eds.), *Mechatronics 2013*,
DOI: 10.1007/978-3-319-02294-9_53,

uncertainty of measurement as well as sampling density is provided by some CMMs of highest accuracy such as UPMC 850 CARAT S-ACC by Zeiss [3], or LEGEX 300 by Mitutoyo [4]. These machines are, however, large and complicated, and critically also very expensive to operate as they require specific and difficult to preserve laboratory conditions. The costs of purchase and use of such machines is often difficult to bear for smaller manufacturers producing for the local market.

Therefore, the methods currently being applied for testing elements with variable curvature require the use of one or more specialized machines along with the relevant computer programming. The consequence of this is an increased cost of control and also the long time required to perform measurements.

2 Trend for Overlapping Application Areas of Different Measuring Machines

Prior to the invention of CMMs, measurement methods that allowed the linking of form deviation measurements with size measurements were an exception at this time. It was only the idea of the construction of CMM that gave rise to the possibility of simultaneously measuring multiple geometric features, including deviations in form, orientation, location and run-out. Coordinate measurement technology initiated and stimulated a process of enhancing and overlapping of individual measurement devices (Fig. 1).

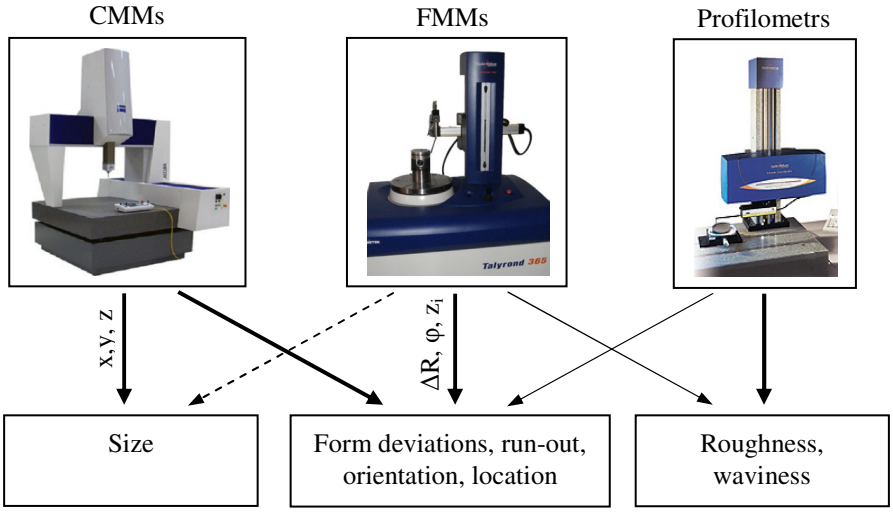

Fig. 1 Overlapping of applications of machines for texture, form and size measurement

This phenomenon applies both to profilometers as well as for Form Measuring Machines (FMM). In the case of the former, by increasing the range of the sensors

used (up to 2 mm or more), it is possible to measure not only roughness parameters but also certain form deviations. Some FMM, owing to their high-resolution transducers as well as regulated measurement speed, allow measurement of roughness besides of form deviations. Measurement devices have thus become more versatile. Still, their specificity remains; roughness measuring devices can be replaced only to a certain extent by FMM, while the same holds true for FMM and CMM.

In conventional FMMs, the gauge measures only the changes in the length of local radii ΔR_i as a function of the rotation angle φ. Vertical position of the gauge z_i is monitored as well. This set of source data is sufficient to determine the different types of geometric deviations and even to measure roughness, but does not allow the determination of the dimensions of the examined sections. Following the mentioned trends, is it technically possible to move a further step forward towards expanding the applications of FMM by measuring dimensions?

3 Extending the Applications of FMMs to Measuring Local Radii through Use of Size Standard

Some attempts to expand the measuring capabilities of FMM were undertaken at PTB and presented in [5, 6, 7, 8]. A Formtester MFU8 machine by Mahr was rebuilt and equipped with an interferometer which allowed the measurement of local dimensions. Certainly, this reconstruction of the FMM is expansive. Moreover, there is a large variety of the FMM types offered by various manufacturers (Taylor Hobson, Carl Zeiss, Mitutoyo, Mahr) and reconstruction should be adapted to each model separately [9, 10, 11].

For this reason, an attempt was made by authors of the paper to extend the scope of application of FMMs in a different way, only by use of a cylindrical standard with a known average diameter. This diameter can be measured previously using any relatively accurate method.

The general idea of the method is based on measuring the reference profile twice by FMM (at the beginning and end of the measurement cycle), as well as measuring the cross-sections of the examined piece. Next, the differences between the signals from the measurement of each cross-section and the average measurement value received for the reference profile are calculated. Taking into account the average diameter of the reference profile, it is possible to recover local radii for each cross-section and consequently identify size and shape deviations [12]. Two-time measurement of the reference cross-section ensures monitoring of the measurement cycle as well as information delivery, which can be used to numerically compensate for changes in the measurement conditions. A mathematical description of the method is provided [13].

The above measurement concept can be realized in two ways: by coupling the cylindrical standard with the examined element (Fig. 2a and 2b) or by setting the standard and the examined part on the FMM alternately (Fig. 2c).

In the experiments carried out by authors the first manner was chosen, as it allows for the rapid assembly of the master-specimen set, ease of fixing on the machine table, and also the leveling and centering. The eccentricity of the measured

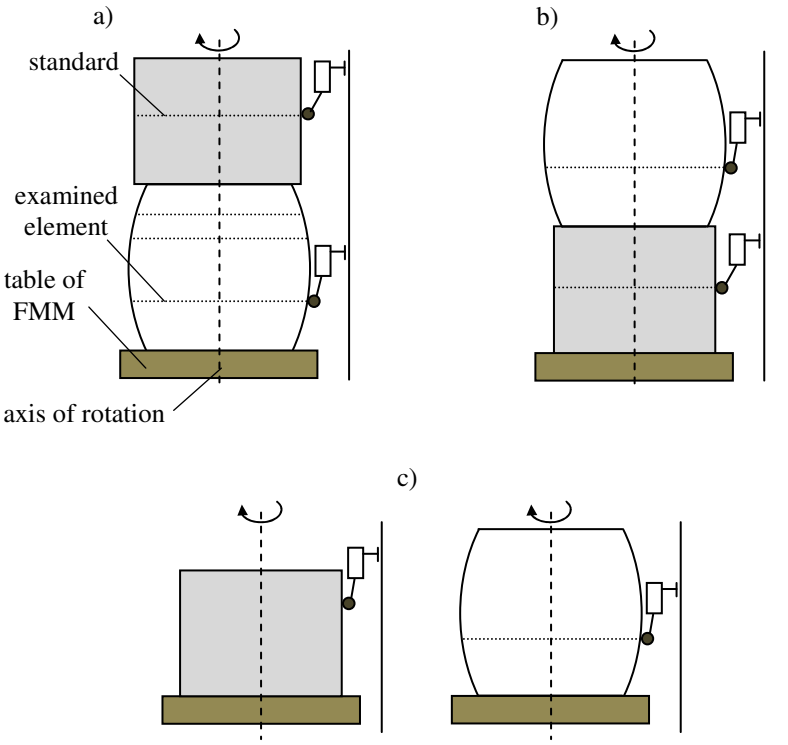

Fig. 2 Variants of measurement: a) mounting standard on the examined element, b) fixing the standard below the element, c) setting the examined element and standard alternately on the machine table

specimen with regards to the axis of rotation does not exceed a few dozen microns in this case. Furthermore, combination of the standard and tested element allows the simple performing of two measurements of the reference cross-section.

Considering the two variants of combining the master with the specimen to be measured - above the component (Fig. 2a), or as its base (Fig. 2b) - it was concluded to choose the second option as it ensures stable positioning of the set on the machine table regardless of the shape of the lower surface of the examined component.

An alternative method of measurement – putting the standard on the FMM table first followed by the examined element, cannot be recommended. This is due to the fact, that to ensure precise measurement the gauge should be located at the same distance from the axis of rotation at all times during the measurement cycle. So, the operator would have to be extremely skillful and take particular care to fix element of changing curvature in the same place on the machine table as the standard was without moving the gauge. This method can, however, be used in FMM equipped with the *Follow Mode* feature (horizontal arm of the machine follows variations of the gauge signal), but merely for the measurement of mechanical parts with dimensional tolerances of the order of a few dozen microns and larger.

4 Cylindrical Size Standard – Technical and Metrological Requirements

As the described method of measuring the size and form deviations on the FMM applies to rotating parts it is obvious that the reference element will be of a cylindrical nature. It was proved that the reference cross-section on the cylindrical standard doesn't have to be an ideal circle as just the average diameter of the reference profile is used to compute local radii of the examined sections. However, due to the need for the alignment of the standard on the machine, some requirements should be imposed on its accuracy. During one of the experiments performed by the authors it was assumed that the shape of the master should satisfy the condition CYLt < 2 µm. Fig. 3 illustrates the form deviations in the reference region of the standard which was applied.

In some cases, however, it could be more convenient to use a standard with cross-section profiles more similar to the profiles of the measured part. It should be noted, that the difference between the diameters of the examined element and the reference element should be relatively small, as all signals must be kept within the operating range of the gauge (using the standard length lever, this is typically 2 mm).

In the proposed measurement method, the cylindrical standard has several functions. The first of these is to reproduce a reference length as accurately as possible. This length is represented by the average diameter of an indicated cross-section on the standard. Applying the two-point method, it is recommended to estimate it on the base of a number of equally spaced local diameters. In such a way the impact of form deviations of the standard will be reduced.

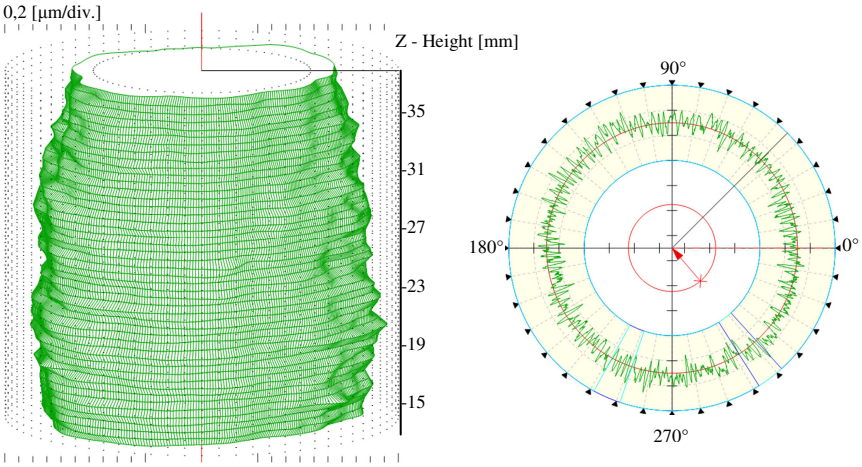

CYLt = 1,25 µm
(Gaussian filter 1-15 UPB)

RONt = 1,7 µm (without filtration)
RONt < 0,5 µm (Gaussian filter 1-15 UPR)

Fig. 3 Form deviations of the cylindrical master used for experiments: a) 3-D plot of cylindricity, b) cross-section profile

A second function of the standard is to guarantee stiff and fixed combination with the examined element, as well as its positioning (centering and leveling) on the FMM table. Both steps should be carried out effortlessly and quickly.

Further functions are to prevent gross errors and to compensate for thermal fluctuations. These tasks are accomplished by executing two measurements of the reference profile – the first at the beginning and the second at the end of each measurement series. On the basis of the arithmetic mean and the difference of the two reference signals, it is possible to monitor the effects of thermal fluctuations and detect possible excessive measurement errors, as caused by vibrations. To ensure the efficacy of this procedure it is strongly recommended to make the standard from the same material as the examined element, or from a material with a very similar thermal-expansion coefficient.

The fabrication of such a standard or even a few of them (taking wear into consideration), should not be a problem when using the proposed method for mass production.

5 Summary

This paper outlines the concept of a measurement method allowing an extension of the measurement capabilities of FMMs to include local radii. The proposed method is applicable to any FMM, provided there is access to source measurement signals registered during the profiles scanning. The only additional cost is associated with producing a suitably accurate standard which ensures rigid connection with the examined elements. The out of roundness of reference profile (RONt parameter) can amount to even a few micrometers, as its form deviations have no effect on the shape of observed profiles located on the examined surface, and only affect the mean values of the radii to a negligible extent.

The proposed method ensures a high sampling density, unlike specialized industrial devices, which are designed for measurement of a few distinct dimensions. Furthermore, as with the proposed method local radii are measured (not diameters), it allows for the detection of axial asymmetry of the tested cross-sections, for example a three-lobed effect can be revealed.

A limitation of the proposed method is the relatively small measuring range of the gauge, however in exchange the method provides a high resolution and accuracy of measurement.

The differential nature of the proposed measurement method allows compensation for the effect of changes in the temperature in the laboratory on the measurement results.

As the result of measurement is a large number of local radii values (typically hundreds or thousands of data points) for each examined profile, it allows for the detailed examination of local deviations with regards to the requirement given in technical specifications. For roundness profiles, commonly used parameters such as RONt, RONp, RONv, RONq can be obviously derived.

Several industrial and research laboratories apply FMMs for accurate measurement of geometrical deviations. The use of such devices to additionally measure local radii with uncertainty close to that obtained by CMMs, while maintaining

the high accuracy of form deviations characteristic to the radial method, corresponds to the needs of many manufacturers. It eliminates the costs associated with the purchase of new measuring devices and strongly reduces expenses related to air-conditioning at laboratory.

The method was designed to be used primarily in high-volume production, and in particular in the automotive and aerospace industries.

References

[1] Adamczak, S., Janecki, D.: Problems cencerning the measurement of form profiles of non-closed cylindrical surfaces of machine parts. Measurement Science Review 1(1) (2001)
[2] Ratajczyk E.: Coordinate Measuring Technique, Oficyna Wydawnicza Politechniki Warszawskiej, Warszawa (2005) (in polish)
[3] http://zeiss.com/
[4] Mitutoyo America Corporation, Bulletin No. 1740, USA (2004)
[5] Lüdicke, F., Jusko, O., Reimann, H.: Form and Length Measurements by Use of a Modified Commercial Form Measurement Instrument. In: ASPE Annual Meeting (2000)
[6] Sabuga, W., Priruenrom, T.: An approach to the evaluation of dimensional measurements on pressure-measuring piston-cylinder assemblies. In: IMEKO 20th TC3, Mexico (2007)
[7] Jusko, O., Neugebauer, M., Reimann, H.: Dimensional calibration techniques for pressure balances to be used in the new determination of the Boltzmann constant. In: INFOSIM, Brazil, pp. 14–23 (2009)
[8] Jusko, O., Bastam, M., Reimann, H.: Tactile and optical cylinder calibration with nanometer uncertainties. In: ASPE Annual Meeting (2009)
[9] http://www.taylor-hobson.com/
[10] http://www.mahr.com/
[11] http://ecatalog.mitutoyo.com/Roundtest-C1150.aspx
[12] Sieniło, M., Żebrowska-Łucyk, S.: Measurements of piston by radial method. Implementation of coordinate metrology, Bielsko-Biała, 26–35 (2012)
[13] Sieniło, M.: A method for measuring size and form deviations of rotating elements cross sections. PhD Thesis, Warsaw University of Technology, Warsaw (2012) (in polish)

Three-Dimensional Meshless Modelling of Functionally Graded Piezoelectric Sensor

P. Stanak[1], J. Sladek[1], V. Sladek[1], and A. Tadeu[2]

[1] Institute of Construction and Architecture, Slovak Academy of Sciences, Dubravska cesta 9, 845 03, Bratislava, Slovakia
peter.stanak@savba.sk
[2] ITeCons, University of Coimbra, Polo II, Rua Pedro Hispano, 3030-289, Coimbra, Portugal

Abstract. A meshless local Petrov-Galerkin (MLPG) method to analyse the electro-elastic response of functionally graded piezoelectric circular sensor is proposed. In this approach the analysed body is discretized using nodal points only, no finite element mesh is required. The moving least-squares (MLS) scheme is employed for the spatial approximation of unknown physical fields in terms of corresponding nodal quantities. Three-dimensional modelling enables asymmetric loading patterns to be used. The exponential gradation of material properties is proposed in the poling direction of the sensor. The effect of varying gradation coefficients on mechanical displacements and induced electric potential is investigated.

1 Introduction

Piezoelectric ceramics have recently been receiving significant attention as elementary components of various sensors and actuators. The coupling between mechanical and electrical behaviour in piezoelectric material allows the mechanical energy to be converted to electric energy and vice-versa, which is termed the direct and converse piezoelectric effect. Materials exhibiting a large direct or converse piezoelectric effect are required for effective practical applications.

Functionally graded materials (FGM) are multi-phase materials whose phase volume fractions vary gradually in space in a pre-determined profile [1]. These spatial gradients often cause FGMs to be superior to conventional composites. Piezoceramic materials can also be prepared as FGM composites, which results in continuously graded electric and mechanical properties at the macroscopic structure scale.

Since Tiersten's pioneering work [2], research on the behaviour of piezoelectric materials has encouraged the development of their numerical modelling. The finite element method (FEM) has been increasingly applied to solve piezoelectric problems [3, 4, 5]. The standard boundary element method (BEM) cannot be used for general anisotropic piezoelectricity because proper fundamental solutions are unavailable or difficult to obtain. In the last decade, special attention has been paid to mesh-free or meshless methods for numerical analysis. Of the wide range of such

T. Březina and R. Jabloński (eds.), *Mechatronics 2013*,
DOI: 10.1007/978-3-319-02294-9_54,

approaches the meshless local Petrov-Galerkin (MLPG) method [6] has received significant attention. The MLPG has recently been applied to the analysis of 2-D plane piezoelectricity [7] electroelastic plates [8] and laminated plates with piezoelectric layers [9, 10].

Recent progress in the development and research of FGMs has also heightened interest in the development of numerical methods for the solution of a number of problems, including continuously nonhomogeneous solids. FEM analysis of FGM materials may give rise to certain difficulties. The material coefficients in commercial FEM codes are assumed to be constant within an element, thus leading to the piecewise homogeneous conception of FGMs. The inherent nature of meshless methods, on the other hand, makes them perfectly suited for the analysis of continuously nonhomogeneous materials because no element mesh is required. Material properties are ascribed to each nodal point separately. The MLPG has recently been applied to continuously nonhomogeneous 2-D [11] and 3-D [12] elastodynamic problems. Analysis of piezoelectric FGM solids by the MLPG has focused only on 2-D and 3-D axisymmetric problems [13, 14, 15].

In this paper the MLPG formulation is developed for 3-D continuously nonhomogeneous piezoelectric solids. The material properties are deemed to vary in the vertical direction, for the FGM. The coupled electro-mechanical fields are described by constitutive relations and governing partial differential equations (PDEs). Nodal points are spread around the analysed domain without any restriction. A small local spherical subdomain is introduced around each nodal point. Local integral equations (LIEs) constructed from governing PDEs are defined over these spherical subdomains. The Heaviside unit step function is applied as a test function in each local subdomain which leads to a pure boundary integral formulation. The LIEs are non-singular and have a very simple form. If a simple form is chosen for the geometry of the local subdomains, numerical integrations can be easily performed on them. A moving least squares (MLS) approximation scheme [6, 16] is used to approximate the spatial variations of electric and mechanical fields in terms of specific nodal values. The essential boundary conditions on the global boundary are specified by the collocation of the MLS approximations for prescribed field quantities at the boundary nodes. Numerical examples demonstrate the applicability of the proposed method for the analysis of the piezoelectric sensor by considering different gradations of elastic and electric material properties. The electric response of the sensor is investigated for non-uniform static loading and the results are discussed.

2 MLPG Numerical Model for 3-D Piezoelectric Solids

The governing equations for 3-D piezoelectricity under quasi-electrostatic and elastostatic assumptions in continuously non-homogeneous solids are given by

the equation of motion and first Maxwell's equation for the vector of electric displacements $D_j(\mathbf{x})$ as

$$\sigma_{ij,j}(\mathbf{x}) + X_i(\mathbf{x}) = 0 \tag{1}$$

$$D_{j,j}(\mathbf{x}) + R(\mathbf{x}) = 0 \tag{2}$$

where $\sigma_{ij}(\mathbf{x})$, $X_i(\mathbf{x})$ and $R(\mathbf{x})$ are the stress tensor, vector of body forces and volume density of free electric charges, respectively. Cartesian coordinates are specified as $\mathbf{x} = (x_1, x_2, x_3)$.

The constitutive equations for the continuously non-homogeneous piezoelectric material poled in the x_3-direction are given as

$$\sigma_{ij}(\mathbf{x}) = C_{ijkl}(\mathbf{x})\varepsilon_{kl}(\mathbf{x}) - e_{kij}(\mathbf{x})E_k(\mathbf{x}) \tag{3}$$

$$D_i(\mathbf{x}) = e_{ikl}(\mathbf{x})\varepsilon_{kl}(\mathbf{x}) + h_{ik}(\mathbf{x})E_k(\mathbf{x}) \tag{4}$$

where $C_{ijkl}(\mathbf{x})$, $e_{kij}(\mathbf{x})$ and $h_{ik}(\mathbf{x})$ are respectively the elastic, piezoelectric and dielectric material tensors. The strain tensor $\varepsilon_{ij}(\mathbf{x})$ and electric field vector $E_k(\mathbf{x})$ are related to mechanical displacements u_i and electric potential ψ as

$$\varepsilon_{ij}(\mathbf{x}) = \frac{1}{2}\left(u_{i,j}(\mathbf{x}) + u_{j,i}(\mathbf{x})\right), \quad E_k(\mathbf{x}) = -\psi_{,k}(\mathbf{x}) \tag{5}$$

On the global boundary Γ of the assumed 3-D body Ω, the essential boundary conditions for the displacements $\tilde{u}_i$ and electric potentials $\tilde{\psi}$, as well as the natural boundary conditions for the surface tractions $\tilde{T}_i = \sigma_{ij}n_j$ and surface density of electric induction field flux $\tilde{Q} = D_i n_i$, are defined. n_i is the unit normal vector.

2.1 Local Integral Equations

Instead of writing the global weak form of the governing equations, the MLPG method uses the local weak form over local subdomains Ω_s defined for each node in the global domain Ω [6]. No restriction is placed on the shape of local subdomains; in our formulation the spherical shape is considered.

The local weak forms of governing equations (1) and (2) are then

$$\int_{\Omega_S} \sigma_{ij,j}(\mathbf{x},t)\, w^*(\mathbf{x})\, d\Omega = -\int_{\Omega_S} X_i(\mathbf{x},t)\, w^*(\mathbf{x})\, d\Omega \tag{6}$$

$$\int_{\Omega_S} D_{j,j}(\mathbf{x},t)\, p^*(\mathbf{x})\, d\Omega = -\int_{\Omega_S} R(\mathbf{x},t)\, p^*(\mathbf{x})\, d\Omega \tag{7}$$

Heaviside unit step functions $w^*(\mathbf{x})$ and $p^*(\mathbf{x})$ are chosen as test functions in each subdomain Ω_s [6, 9]. Applying the Gauss divergence theorem to the domain integrals on the left-hand side of equations (6), (7) and assuming that both the volume forces and volume density of free charges vanish, we get the following local integral equations, written in component form as

$$\int_{\partial\Omega_S} \sigma_{ij}(\mathbf{x})\, n_j(\mathbf{x})\, d\Gamma = 0\,, \quad \int_{\partial\Omega_S} D_i(\mathbf{x})\, n_i(\mathbf{x})\, d\Gamma = 0 \tag{8}$$

where $\partial\Omega_S$ is the boundary of the local subdomain Ω_s.

Note that LIEs (8) do not contain any domain integrals, thus pure boundary integral formulation is obtained. In the MLPG method the test functions and trial functions are not necessarily from the same functional space [6]. In this paper we have chosen the trial functions as the moving least-squares (MLS) approximations for the field unknowns specified over a set of nodal points.

Using the MLS scheme, the approximation of mechanical displacements u_i and electric potential ψ by approximants $u_i^h(\mathbf{x})$, $\psi^h(\mathbf{x})$ is given by

$$u_i(\mathbf{x}) \cong u_i^h(\mathbf{x}) = \sum_{a=1}^{n} \phi^a(\mathbf{x})\hat{u}_i^a \quad , \; \psi(\mathbf{x}) \cong \psi^h(\mathbf{x}) = \sum_{a=1}^{n} \phi^a(\mathbf{x})\hat{\psi}^a \tag{9}$$

where the nodal values $\hat{u}_i^a$ and $\hat{\psi}^a$ are regarded as fictitious parameters for the mechanical displacements and electric potential, respectively. MLS shape function $\phi^a(\mathbf{x})$ is defined over a set of n nodes located in the support domain Ω_x [6]. The spatial derivatives are approximated with use of the shape function derivative [6] and same fictitious parameters as

$$u_{i,j}(\mathbf{x}) \cong u_{i,j}^h(\mathbf{x}) = \sum_{a=1}^{n} \phi_{,j}^a(\mathbf{x})\hat{u}_i^a \quad , \; \psi_{,j}(\mathbf{x}) \cong \psi_{,j}^h(\mathbf{x}) = \sum_{a=1}^{n} \phi_{,j}^a(\mathbf{x})\hat{\psi}^a \tag{10}$$

Discretization of local integral equations (8) is performed by inserting the MLS approximations (9, 10) into constitutive equations (3), (4). Essential boundary conditions on the global boundary are specified by the collocation of the MLS approximations (9) for the prescribed field quantities at the boundary nodes. Natural boundary conditions are specified using corresponding LIEs (8) [6]. Collecting all the discretized local equations together with the discretized boundary conditions gives the complete system of algebraic equations that is solved for the fictitious nodal values $\hat{u}_i^a$ and $\hat{\psi}^a$. The resulting values of the mechanical displacements and electric potential are finally retrieved by inserting fictitious values into the MLS approximations (9).

3 Numerical Example

Numerical analyses are performed for the piezoelectric FGM solid representing a sensor of cylindrical shape with radius $r = 0.015\text{m}$ and thickness $h = 0.003\text{m}$. An exponential gradation rule in the x_3-direction is considered for the piezoelectric properties as

$$P\left(x_3\right) = P^{(0)} e^{\delta x_3 / h} \tag{11}$$

and for the mechanical properties as

$$P\left(x_3\right) = P^{(0)} \left(d - e^{\gamma x_3 / h}\right) \tag{12}$$

where symbol $P\left(\mathbf{x}\right)$ is used for the particular material property, $P^{(0)}$ is the reference material property, δ, γ and d are the grading constants, which differ for electric and mechanical properties. The reference material considered is PZT-4 piezoelectric ceramics [9].

The geometry of the piezoelectric solid is discretized using 1005 nodal points. The sensor is loaded at the top with the asymmetric linearly varying load $f\left(x_1, x_2, x_3 = h\right) = 1e^6 + 5e^7 x_1 \ \left[\text{Pa}\right]$. The displacements and electric potential at the bottom vanish.

The numerical results for $\delta = 0,\ \gamma = 0$ and $d = 2$ are evaluated first, which represents a homogeneous material distribution (pure PZT-4). Fig. 1(a) shows the variation of induced electrical potential ψ at the top of the sensor.

Numerical results for $\delta = 135.155,\ \gamma = -231.05$ and $d = 1.5$ are evaluated next, which represents a 1.5-times increase in the piezoelectric properties at the top of the sensor, while the mechanical ones are lowered to one half of the

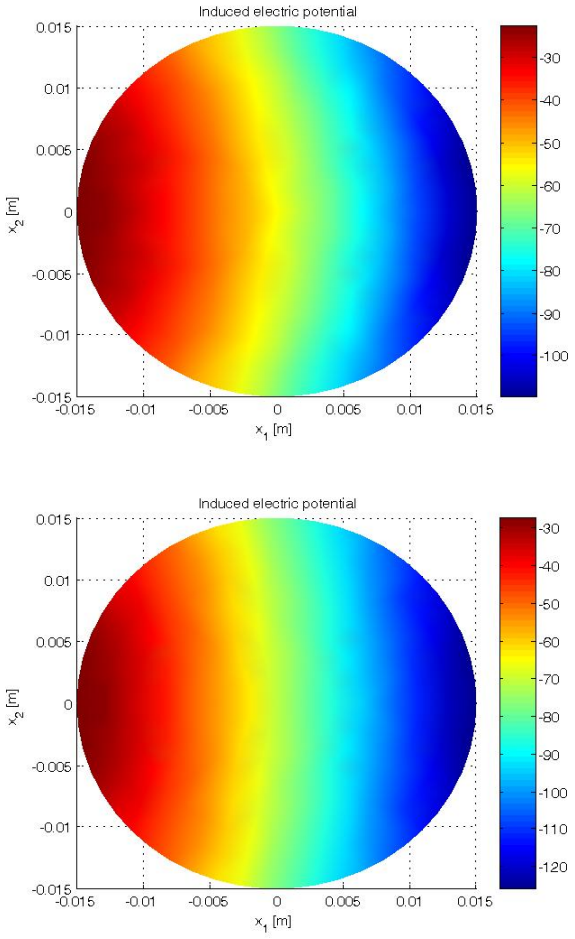

Fig. 1 Induced electric potential at the top $(x_3 = h)$ of piezosensor: (a) with homogeneous properties; (b) with functionally graded material properties

reference value in the opposite direction. The results for induced electrical potential ψ at the top of the graded sensor are shown in Fig. 1(b). Compared with the case of homogeneous material, higher values of potentials are induced. Further change in the gradation parameters may change the response in another way. The desired electric output of the sensor can thus be obtained. The deformed shape of the non-homogeneous piezosensor is shown in Fig. 2 in terms of nodal positions at the boundary. Nodal displacements are multiplied by magnification factor $m = 5e^4$. The effect of applying the asymmetric load can be clearly seen in the resulting deformation of the sensor.

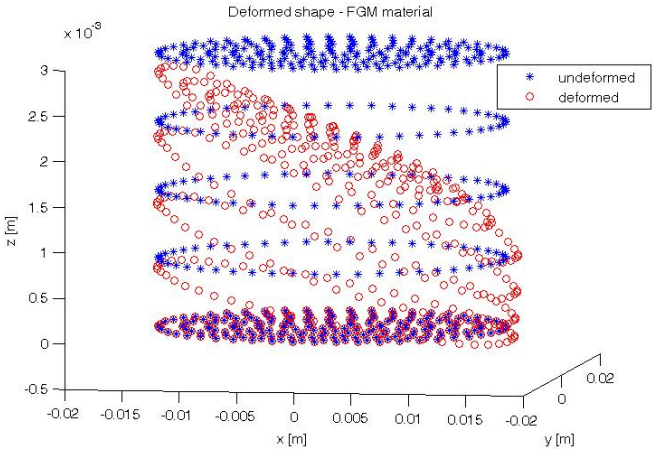

Fig. 2 Deformed shape of the FGM piezosensor in terms of nodal position (magnified)

4 Conclusions

A meshless numerical model based on the MLPG approach has been presented for the 3-D analysis of functionally graded piezoelectric solids. The electric response of the piezosensor is changed by the effect of material gradation. Thus the response can be tuned to desired way for certain practical applications.

The use of a meshless method can be advantageous for a medium with spatially varying properties. Spatial variation of physical fields has been approximated by the MLS scheme in terms of nodal values only. Where there is uniform or symmetric loading the axisymmetric analysis may decrease the computational effort required.

Acknowledgments. This research has been supported by the Slovak Science and Technology Assistance Agency through the scientific grant registered under number APVV-0014-10. The financial support is gratefully acknowledged. The support from ITeCons is also appreciated.

References

[1] Suresh, S., Mortensen, A.: Fundamentals of Functionally Graded Materials. Institute of Materials, London (1998)
[2] Tiersten, H.F.: Linear Piezoelectric plate vibrations. Plenum Press, New York (1969)
[3] Allik, H., Hughes, T.J.R.: Finite element method for piezoelectric vibration. International Journal for Numerical Methods in Engineering 2, 151–157 (1970)
[4] Hwang, W., Parkt, H.: Finite element modeling of piezoelectric sensors and actuators. Sens. Actuators A 5, 930–937 (1993)

[5] Benjeddou, A.: Advances in piezoelectric finite element modeling of adaptive structural elements: a survey. Computers and Structures 76, 347–363 (2000)
[6] Atluri, S.N.: The meshless method (MLPG) for domain & BIE discretizations. Tech Science Press, Forsyth (2004)
[7] Sladek, J., Sladek, V., Zhang, C., Garcia-Sanchez, F., Wunsche, M.: Meshless Local Petrov-Galerkin Method for Plane Piezoelectricity. CMC: Computers, Materials & Continua 4(2), 109–117 (2006)
[8] Sladek, J., Sladek, V., Stanak, P., Pan, E.: The MLPG for bending of electroelastic plates. CMES – Computer Modeling in Engineering & Sciences 64, 267–298 (2010)
[9] Stanak, P., Sladek, J., Sladek, V., Krahulec, S.: Composite circular plate analyzed as a 3-D axisymmetric piezoelectric solid. Building Research Journal 59(3-4), 125–140 (2011)
[10] Sladek, J., Sladek, V., Stanak, P., Wen, P.H., Atluri, S.N.: Laminated elastic plates with piezoelectric sensors and actuators. CMES – Computer Modeling in Engineering and Sciences 85, 543–572 (2012)
[11] Sladek, J., Sladek, V., Zhang, C.: Stress analysis in anisotropic functionally graded materials by the MLPG method. Eng. Anal. Bound. Elem. 29, 597–609 (2005)
[12] Sladek, J., Sladek, V., Solek, P.: Elastic analysis in 3D anisotropic functionally graded solids by the MLPG. CMES – Computer Modeling in Engineering & Sciences 43(3), 223–251 (2009)
[13] Sladek, J., Sladek, V., Solek, P., Saez, A.: Dynamic 3D axisymmetric problems in continuously nonhomogeneous piezoelectric solids. Int. J. Sol. Struct. 45, 4523–4542 (2008)
[14] Sladek, J., Sladek, V., Stanak, P., Zhang, C., Wunsche, M.: Analysis of the bending of circular piezoelectric plates with functionally graded material properties by a MLPG method. Engineering Structures 47, 81–89 (2012)
[15] Stanak, P., Sladek, J., Sladek, V., Krahulec, S.: Bending of functionally graded circular plates wih piezoelectric layer by the MLPG method. In: Proc. Engineering Mechanics 2012, CD-rom (2012)
[16] Lancaster, P., Salkauskas, T.: Surfaces generated by moving least-square methods. Math. Comput. 37, 141–158 (1981)

Diagnostics of Mechatronic Systems on the Basis of Neural Networks with High-Performance Data Collection

P. Stepanov[1] and Yu. Nikitin[2]

[1] Novouralsk Technological Institute, Department of Mechanical Engineering, Lenin str.85, 624130, Novouralsk, Russia
push-tet@mail.ru
[2] Izhevsk State Technical University, Faculty of Quality Management, Studencheskaya str.7, 426069, Izhevsk, Russia
nikitin@istu.ru

Abstract. The paper presents diagnostics of mechatronic systems on the basis of AI-based techniques. The paper gives an analysis of diagnosis methods. Development of neural network for diagnosis of mechatronic systems are discussed. Diagnostics system software functions are determined. The input layer is used as the data acquisition unit on base National Instruments devices with LabView software. AI-based techniques for diagnostics are discussed. For diagnosis of CNC machines, a neural network can be applied, consisting of modules, which correspond to each CNC machines units. Each module processes the obtained information according to its diagnostic parameters.

1 Introduction

Modern machines become more and more intelligent. To implement the assigned purpose, such machines must have information on their state, that is, a diagnosis system must be available, which is actively interacting with an adaptive control system.

A great attention, paid to diagnosis, is explained by the following factors. Its implementation allows: to control the current technical state of machines, to determine the time and contents of repair works, to control the quality of their execution, to decrease costs of machine maintenance, to extend the overhaul period and lifetime of equipment, to escape sudden breakdowns of machines and production stops.

Nowadays a "revolution" takes place in systems of machines diagnosis, which is determined by development of a wide spectrum of smart sensors with wireless data transfer, high-performance computational systems and computational intelligence.

The progressive mathematical apparatus for creation of systems of automatic diagnosis of machine units is application of neural networks. They possess the

T. Březina and R. Jabloński (eds.), *Mechatronics 2013*,
DOI: 10.1007/978-3-319-02294-9_55,

following advantages: quick training algorithms, possibility to operate in the presence of undesired signals, possibility to operate with various data and possibility to solve several tasks simultaneously.

Increase of intensity of investigating the methods and means of diagnosis system is caused by a number of reasons.

1 Cost increase of complex automated production systems results in great financial losses in case of their breakage. It is reasonable to perform repair works depending on the state of a machine, rather than according to plan.

2 Microminiaturization of microprocessor means, sensors, reduction of their power consumption and development of wireless techniques of data transfer allow to build them into any objects of diagnosis, right up to bearings.

3 Development of mathematical apparatus on basis of artificial intelligence methods of machine fault detection allows to increase the accuracy of diagnosis statement.

4 Application of new programming methods allows to perform diagnosis in real time, transferring data on the object condition to an adaptive control system.

5 Cost reduction of microprocessor means with increase of their computational power and functional capabilities allow to implement complex diagnosis algorithms.

6 Application of modularity principle facilitates the design of diagnosis means, which must be developed at the stage of designing the diagnosis object.

Diagnostics of machinery and mechatronic systems are considered in papers [1-11]. Issues of reliability, planning, maintenance and repair considered in paper [12].

2 Analysis of Diagnosis Methods

Mechatronic systems demand to provide a high quality level of functioning and reliability. This requirement becomes especially actual, when the system operation influences the fulfillment of the assigned task, connected with the hazard of human life loss or considerable financial investments. Reserve of reliability increase is the changeover from a scheduled maintenance and repair to the maintenance and repair according to the actual technical state. Application of this strategy requires a wide adoption of means and methods of diagnosis.

One of the most important advantages of neural networks is their ability to represent nonlinear transformations. Therefore, neural networks are capable to generate a very precise approximation for nonlinear functions of any degree of complexity.

Neural networks are the alternative version of design of estimating devices. The important property of neural networks is that they study dynamics of a system during the training process, consisting of several training cycles with training data, either coming from the previous cycle, or consisting of real signals. After every cycle a neural network learns more and more about the object dynamics. One of

the most important properties of neural networks is their ability to study dynamics of nonlinear systems performance automatically, in case if architecture of neural networks contains at least three layers.

Advantages of a classifier, created on basis of neural networks over conventional estimating methods are such factors as: independence on noise, self-training, possibility of parallel processing and so on.

For diagnosis of a mechanical subsystem, means of diagnostics are applied, based on measurement of vibration parameters of elements, heat radiation, resistance of oil film, analysis of particles in oil.

For diagnosis of electro-mechanical, electrical and electronic subsystems, means of diagnostics are applied, based on measurement of electrical parameters: current, resistance, analysis of digital signals.

Nowadays a new progressive possibility appeared to diagnose the electron drive apparatus – watt-metry.

Program software of a diagnostics system must have the following functions:

1 Availability of database, allowing to store information about the controlled equipment over rather long period.

2 Availability of function of estimating the current technical state and residual life of equipment.

3 Availability of adaptive functions, describing variation of parameters in the course of time.

4 Availability of a built-in expert system. Conclusions of such system are additional to calculations of periods of repair works. In ideal case the diagnostics system must “hand” the optimal period of repair works with the list of defects to be remedied.

5 Availability of a system or even just elements of parametrical diagnostics of equipment condition.

6 Planning of periods of repair works. It is one of the most important functions of a diagnostics system, since the main expenses for equipment maintenance appear during repair works.

7 Estimation of quality of performed repair works. This function is used to evaluate the quality of repair services, which is especially actual when changing over maintenance service by independent contractors.

3 Development of Neural Network for Diagnosis of Mechatronic Systems

For diagnosis of mechatronic systems, a neural network can be applied, consisting of modules, which correspond to each mechatronic subsystem. Each module processes the obtained information according to its diagnostic parameters.

Neural network consists of layers: input layer, where diagnostic information from sensors and information on operation modes is received; hidden layer, where data is processed and weight factors are assigned during the training process; output layer.

Signals from sensors and information about operation modes of a mechatronic system come to the input layer. In this layer a number of neurons is determined by a number of diagnostic parameters in each module. In the hidden layer a number of neurons is equal, as a rule, to the number of neurons in the previous layer or can be defined. Each module with its own input layer doesn't have any connections with other modules.

4 The Implementation of the Input Layer as the Data Acquisition Unit

To collect information from a large number of diagnostic sensors developed system should include a set of high-performance hardware, with the ability to quickly reconfigure a necessary equipment. This is achieved through the use of universal devices with programmable them under the required tasks.

One of the most successful means to set goals is the equipment of National Instruments, in particular devices NI PXI. The main advantage of such devices is the modularity, which allows devices to come by building an optimal and universal problem-solving diagnostics. In his composition, the device has a built in controller, managed by software LabVIEW.

Information acquisition unit with diagnostic sensors is represented as a universal high-speed 16-bit DAQ NI PXI-6254.

In the developed diagnostic system uses the following sensors: vibration, acoustic emission, current (restated power consumption engine), temperature (the difference with the environment, the time of the engine and estimated heating).

Are processing the following information: waveform, spectrum, trends.

Consider the example of building data collection block the system for vibration monitoring of ball bearings.

On the fig. 1 shown structural scheme of data collection block.

To determine the changing parameters for vibration diagnostics the bearing inner ring rolling was introduced defect of the "pit" (fig. 2).

On the fig. 3 shown the spectrum of the signal received by the module NI PXI and the software LabView for serviceable single-row radial ball bearing, inner ring diameter of 78 mm. Rotational speed 1,900 rpm.

Test stand worked 6 hours, in order to determine how to change the level of a trend over a long period of time. Fig. 4 shown a graph of the trend of vibration (vibration moving).

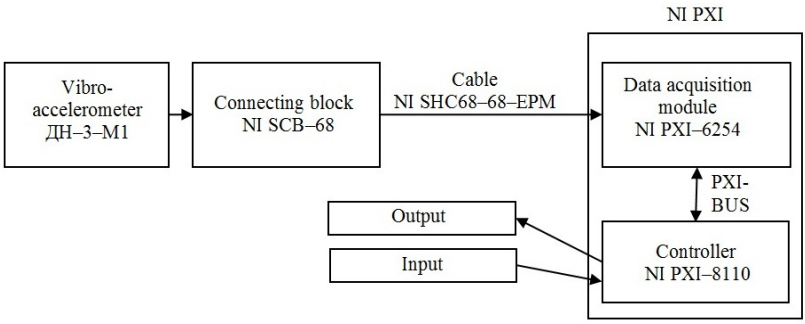

Fig. 1 Structural scheme of data collection block

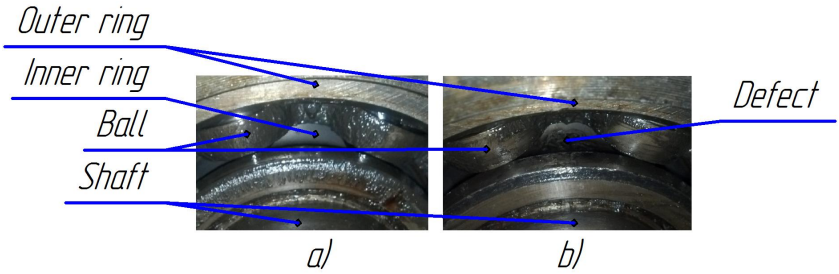

Fig. 2 a) Bearing without defect; b) Bearing with defect

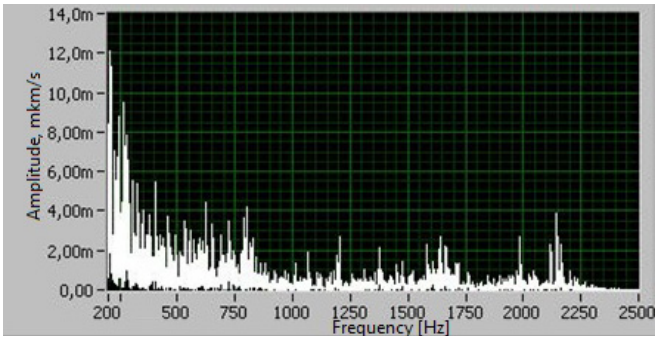

Fig. 3 The spectrum of vibration of bearing without defect

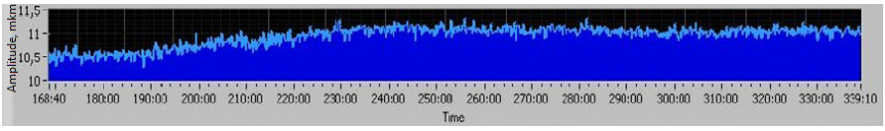

Fig. 4 Trend of vibration of bearing without defect

After making the defect following results were obtained (fig. 5, 6)

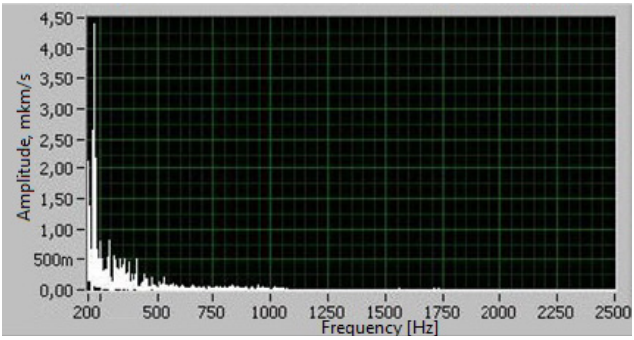

Fig. 5 The spectrum of vibration of bearing with defect

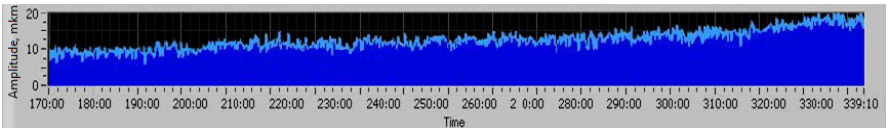

Fig. 6 Trend of vibration of bearing with defect

These data indicate that introduction of a defect in the rolling bearing significantly affects both the vibration spectrum (especially in the low frequency component: increasing the amplitude of nearly 200 times), and the trend of vibration (a significant increase in the signal level and the rate of change).

The information in this block can be transmitted to the input layer of the neural network, where there is a further detection of defects appropriate unit. This approach allows us to more fully examine the current state of the equipment.

5 AI-Based Techniques for Diagnostics

There are many types of AI-based techniques for diagnostics. Some of these use expert systems, artificial neural networks (ANNs), fuzzy logic, fuzzy-ANNs, genetic algorithms (GAs), etc. The essence of an expert system is the ability to manage knowledge-based production rules that model the physical system, while it is a main feature of ANNs that they are general nonlinear function approximators. This function approximation is achieved by using an appropriate network built up from artificial neurons, which are connected by appropriate weights. However, the exact architecture of a ANN is not known in advance. It is usually obtained after a trial-and-error procedure. Fuzzy logic systems are expert, rule-based systems, but they can also be considered to be general nonlinear function approximators. In contrast to ANNs, they give a very clear physical description of how the function

approximation is performed (since the rules show clearly the function approximation mechanism). On the other hand, fuzzy-ANNs are basically ANNs with fuzzy features, and it is one main advantage over "pure" ANNs that their architecture is well defined. Finally, GAs are not general function approximators, but they are stochastic optimization techniques. However, they can be used together with neural or fuzzy-NNs, e.g., to obtain optimal weights in a "pure" ANN, or to obtain the membership functions in fuzzy logic systems, etc.

There is a great variety of neural networks and algorithms of their training. The choice of type and structure of the neural network determined by the specific task. The Rosenblatt network was chosen, which had the algorithm of back propagation of error. This algorithm represents an iterative gradient algorithm of minimization of mean square deviation of value of output from desired values (error minimization) in multilayer neural networks. Training of a neural network is performed with the assistance of a tutor. Availability of an associative memory is not required, since it is insignificant, if the network memorizes connections between neurons or not, the necessary result can be achieved by means of a "black box" model. The neuron activation function chosen exponential sigmoid.

For diagnosis of CNC machines, a neural network can be applied, consisting of modules, which correspond to each CNC machines units. Each module processes the obtained information according to its diagnostic parameters.

First, errors are calculated in the last layer – layer A (on basis of output and calibration signals), then in the next to last layer – layer S and then in the input layer – layer X. Initial values of weights are chosen in a random manner and, as a rule, are assigned close to zero.

The number of examples must be not less than the number of input data. The more examples will be, the more ambiguous data will be, the deviation will be normal up to a certain value, and after that it will go outside the limits of required values. Errors of data processing also influence the deviation.

6 Conclusions

Diagnostics system software functions are determined. The input layer is used as the data acquisition unit on base National Instruments devices with LabView software. For diagnosis of CNC machines, a neural network can be applied, consisting of modules, which correspond to each CNC machines units. Each module processes the obtained information according to its diagnostic parameters. The accuracy can be assigned as 0.01%, but more time will be needed to process data and the network can cycle. In order to make the network provide the required accuracy, it is necessary to base on requirements to output parameters. In this case, the deviation from training output parameters can vary within the insignificant range up to 5%. Three layers of a neural network are recommended to be assigned: 1 input, 1 output and 1 hidden layer.

References

[1] Rafajdus, P., Peniak, A., Brandt, M.: Parametrical Model of Power Transformers Used for Diagnostics Systems. In: Proceedings of 15th International Conference on Mechatronics, Prague, December 5-7, pp. 42–48 (2012)

[2] Karaduman, G., Karakose, M., Akin, E.: Experimental Fuzzy Diagnosis Algorithm Based on Image Processing for Rail Profile Measurement. In: Proceedings of 15th International Conference on Mechatronics, Prague, December 5-7, pp. 86–91 (2012)

[3] Aydin, I., Karakose, M., Akin, E.: A New Contactless Fault Diagnosis Approach for Pantograph-Catenary System. In: Proceedings of 15-th International Conference on Mechatronics, Prague, December 5-7, pp. 92–97 (2012)

[4] Zhang, Y., Bingham, C., Yang, Z., Gallimore, M., Stewart, P.: Applied Sensor Fault Detection and Identification Using Hierarchical Clustering and SOMNNs, with Faulted-Signal Reconstruction. In: Proceedings of 15th International Conference on Mechatronics, Prague, December 5-7, pp. 107–113 (2012)

[5] Zhang, Y., Bingham, C., Gallimore, M., Yang, Z., Stewart, J.: Based on Y-indices and Residual Errors. In: Proceedings of 15th International Conference on Mechatronics, Prague, December 5-7, pp. 119–127 (2012)

[6] Lafata, P., Bakala, B.: Designing and Realization of Free-space Optical Link and Its Diagnostic. In: Proceedings of 15th International Conference on Mechatronics, Prague, December 5-7, pp. 182–186 (2012)

[7] Nikitin, Y.: Diagnostics of mechatronic systems on the basis of neural networks. In: State-of-the-Art in Mechatronics, vol. 2, pp. 167–188. Simulation Research Press, Alphen aan den Rijn (2010)

[8] Nikitin, Y.R., Abramov, I.V.: CNC machines diagnostics. In: Proceedings 13th International Simposium on Mechatronics, Trencinske Teplice, June 2-4, pp. 89–91 (2010)

[9] Nikitin, Y., Abramov, I.: Mechatronic modules diagnosis by use of fuzzy sets. In: Proceedings of 14th International Conference on Mechatronics, Trencinske Teplice, June 1-3, pp. 109–111 (2011)

[10] Štollmann, V., Ilčík, Š.: Assessment of the current theory for projecting cableway routes in terms of the risk level in overloading. Research in Agricultural Engineering 55(1), 35–38 (2009)

[11] Stollmann, V., Bozek, P., Barborak, O., Nascak, L., Walekova, G.: Virtual technologies for specialized robotic workplaces. In: Annals of DAAAM for 2008 & Proceedings of the 19th International DAAAM Symposium Intelligent Manufacturing & Automation: Focus on Next Generation of Intelligent Systems and Solutions, Vienna, vol. 19(1), pp. 1319–1320 (2008)

[12] Yu, T., Maga, D., Faitova, N.: Building of a Flexible (Adaptive) Structure for Mechatronic System's Repair Cycle. In: Proceedings 13th International Simposium on Mechatronics "Mechatronika 2010", Trencinske Teplice, Slovakia, June 2-4, pp. 112–114 (2010)

Signal Processing in DiaSter System for Simulation and Diagnostic Purposes

M. Syfert[1] and P. Wnuk[2]

[1] Institute of Automatic Control and Robotics, Faculty of Mechatronics, Św. Andrzeja Boboli 8, 02-525, Warsaw, Poland
m.syfert@mchtr.pw.edu.pl
[2] Prague Technical University, Faculty of Mechatronics, Dolni 255, 111 50, Praha, Czech Republic
norton@cvut.cz

Abstract. This paper is focused on mechanisms and possibilities of signal processing in DiaSter system, with special attention on diagnostics. First short description of the system is given, then two main libraries: signals and communication are presented. Those libraries are the core of data exchange mechanism. Signals library allows to manipulate system variables in uniform way, communication library is designed to exchange different type of signals and data between system modules. Next part is focused on data exchange between system modules, and in particular in calculation module PExSim. Paper ends with presentation of DiaSter possibility in area of mechatronic system simulation and technical diagnostic.

1 Introduction

A growing demand for the use of increasingly sophisticated algorithms responsible for implementing functions such as advanced monitoring and diagnostics, advanced control, optimization or process modelling can be observed in recent years [1]. The use of such algorithms in industrial applications typically requires an access to advanced environment processing variables that describe the analysed process. On the other hand, the growing computational power of computers, availability of more powerful development tools (as well as development environments) and growing users demands influence a strong development of a new generation of process monitoring and control systems. The applications of complex computational algorithms, developed on the basis of information technology, automation, diagnostics and knowledge engineering are enabled due to those modern solutions. This type of software has a form of special software modules, that are the components of automatic control system or expert systems integrated with it. One of the packages allowing the implementation of advanced variables processing algorithms developed in recent years is a software platform of advanced control and diagnostics system DiaSter [1]. It is a continuation of

T. Březina and R. Jabloński (eds.), *Mechatronics 2013*,
DOI: 10.1007/978-3-319-02294-9_56,

advanced monitoring and diagnostic system AMandD [2]. It was created within the cooperation of research teams from Warsaw University of Technology, Silesian University of Technology, Rzeszów University of Technology and the University of Zielona Góra under a development grant "Intelligent diagnostic and automatic control support system for industrial processes DiaSter".

The DiaSter system is a configurable, multi-modules system that can operate in decentralised structure. Each module can communicate with other modules via native communications mechanisms based on TCP/IP network, or using a common database. The main modules of the system (processing of archival data, the current process data processing and visualization) are additionally equipped with plug-in mechanisms enabling easy extension of their functionality.

The purpose of this paper is to present the capabilities of the software platform of the DiaSter system in the scope of rules, limitations and possibilities of processing process variables with particular emphasis on the implementation of diagnostic functions. The comparison of described solution with other ones available on the market is not an aim of this paper, however, the distinguishing features of the DiaSter system are emphasized.

2 Signal and Communication System Libraries

Today, commercial automatic control systems utilize mainly simple data types.

The information required for current process control can be coded only as simple data types as Boolean, integer or floating-point. For a long time the use of only such simple types of data covered the needs of the implemented algorithms.
However, with the introduction of modern techniques of monitoring / control, and the development of information technology, it can be concluded that such a restriction, in some applications, is a strong limitation or, at least, is inconvenient. For example, the transmission of measured value and the uncertainty of its designation requires the creation of two classic signals, even though it is logically one signal. Moreover, some data cannot be transferred in this way, e.g. fuzzy values. Thus, the modified types of values are introduced in DiaSter system. Generally, it is assumed, that each value processed by the system is characterized by several features:

- The status is always related with value. It is a carrier of additional information, such as: an error that occurred during its calculation, the lack of measurement, exceeding limit values, etc. The status is assigned to a value by its generator (source element) and can be modified by each following, processing element.
- The second element that always occurred with the value is a time stamp. The system assumes that the time stamp is attributed by the signal value generator. The resolution of time stamp in the DiaSter is 1.0E-6. It allows to process high-frequency vibration signals.

- The values in the system can be serialized. From the information theory point of view it means that each type of value may be stored, at any time, as a sequence of bytes, and then sent over the network or stored in non-volatile media. Later, it can be restored for further use.

It may be noticed, that there is no "value" among mentioned signal properties. It means, that the system processes all types of values in the same way, without taking into account, at low level, their characteristic properties. Whether the value can be transferred between the modules of the system, processed inside the module, archived or reproduced from the archives, does not depend on its type. In practice, this approach allowed to create flexible system, devoid of the disadvantages of typical automatic control systems.

The technical realisation of processing of any value type by the DiaSter system is based on the concept of **abstract value interface**, called **ICValue**. The interface together with its basic implementation include the mechanisms supporting time stamps, statuses and values serialization and deserialization. All the values processed by the system are the types derived from ICValue. The following types are delivered with the system platform: Boolean, integer, float, char, string and vector of any kind of sub-types. The above list is not final. The user can add to the system his own type of variables by creating derived type of ICValue and registering it in central configuration database. In this way, it is possible to implement simple data types, e.g. 12-bits numbers corresponding to typical resolution of AC converters, as well as more sophisticated.

Fuzzy variables developed at the Institute of Automatic Control and Robotics are an example of the implementation of advanced data type. Such variables are characterised by interesting properties. Each fuzzy value is inextricably connected with corresponding definition of its fuzzyfication - the definition of fuzzy sets and its membership functions. The access to the value of fuzzy signal as well as to the definitions of its fuzzyfication is needed for complete signal restoration, e.g. for visualization purpose. Sending the definitions of fuzzy regions with each processed value is extremely ineffective, especially that the configuration of fuzzyfication changes relatively rarely. In the described system, the problem of efficient transmission of the variables is solved due to the possibility of flexible definition of user data types. There are introduced two types of fuzzy variables. Depending on the needs, there is transmitted only basic one (the values of membership functions) or the complete one (all the parameters describing fuzzyfication) signal. Sending only the function values allows efficient operation and saves bandwidth.

Flexible approach described above allows to avoid most of the problems arising during the implementation of new types of information processing in the previous generation of automatic control systems.

3 Communication between System Modules

DiaSter has a modular structure, wherein each module is independent executable possible to be run on a separate machine. In such case there is a need to provide

elastic way to exchange information between modules, keeping the most simple configuration and minimizing network usage.

To provide such features there is provided native communication system called MRIaS, designed with a set of protocols allowing direct and broadcast communication, and remote procedures call. More advanced tasks can be realized through CORBA based object sharing across system modules, or via system database.

3.1 Online Data Exchange

The basic data exchange mode in the DiaSter platform is based on the transmission of messages between modules in two modes: direct and broadcast. Direct mode means that every message sent includes information about the recipient, in the form of a unique module name defined in the system configuration phase. In case of problems with the immediate delivery of the message to the recipient, it will be placed in FIFO queue, until it overflows.

More Interesting mode of communication is broadcast. In this case, the sender of the message does not specify the recipient, but the topic. On the topic can be subscribed any number of recipients. Each message sent to the topic will be resent to all modules who are subscribed to it. Implementation of the described mechanism in the DiaSter system requires no additional configuration. Topics that do not exist are created when somebody subscribe to it, or when a new message to given topic is sent.

All kind of messages are always sent through MRIaS server (a part of DiaSter platform). MRIaS is used always as a routing, stateless server. Current implementation uses TCP/IP as a transport layer, no matter if communicating modules are working on same PC, or on several PC's connected with network. Described mechanism is used mainly to send / receive fast (high-frequency) data, e.g. process variables, calculation results, etc. Communication subsystem allows to send any type of data known to the system (integers, floating point numbers, binary signals, text, fuzzy values, etc.).

3.2 Remote Procedure Call

In case of transmitting acyclic information, or request to execute specific procedure, DiaSter provides Remote Procedure Call (RPC) mechanism.

RPC mechanism in the system is the native solution, with the emphasis on minimizing the amount of data in the network. To use RPC comfortable APIs with full implementation in the form of DLL is provided. DiaSter supports remote procedure call with any number of input and output parameters, limiting the type of parameters. The system supports only simple parameters and all types of system variables described in Chapter 2.

From the external software modules, or internal from system module, by sending a message with standardized format, one can call remote procedures specific function blocks in PExSim module, or defined procedures for other modules. In

case of PExSim module, the received RPC message is decoded and passed to a particular function block. The corresponding block is searched through a unique identifier. The function block must have implemented a particular RPC. An example use of this mechanism may be the implementation of the control unit, where the settings can be changed remotely or one can remotely start the auto-tuning procedure.

3.3 CORBA

More sophisticated mechanisms for communication provides some of the modules operating on-line. Applied interfaces with CORBA-compliant implementation provide access to properties and methods of each object embedded in the PExSim environment, with no restrictions on the type and number of parameters. Additionally, one can remote control the simulation process. Similar mechanism is implemented in visualization module, what allows the transfer of complicated and rarely changing information to / from distributed objects in the system.

4 Signal Propagation in Calculation Module PExSim

One of the main modules of the DiaSter system is the calculation / simulation module called PExSim [3, 4]. Processing algorithms implemented in the PExSim are built in the form of block diagrams, so called processing paths, from the user point of view similar to Matlab/Simulink. Module can process multiple paths simultaneously. Paths can be independent or dependent (if exist data exchange between them). Each path consists of a number of function blocks implementing various operations on processed signals. Blocks are connected via inputs and outputs connectors, what gives adequate flow of signals. Proposed mechanism for creating connections is a standard solution: Each output can be connected to several inputs, and to one input can be connected to only one output signal. Due to the possibility of processing of various types of signals (including user-defined types), PExSim checks signal types when user tries to connect input to output, and allows only to connect compatible signals. Function blocks can be designed to allow the connection of different types of input signals. In the path can also be embedded subsystem (subpath) executed as a part of parent path. In this way, the algorithm can be arranged in a hierarchical structure of information processing.

4.1 Internal Signals Transmission and Calculations Triggering

Each data type that derivatives after ICValue can be transmitted in the calculation paths, wherein always a copy of the data (not reference) is sent. But the transmission of the signal is not the main problem. In systems enabling flexible folding processing paths usually there is a problem how to determine calling sequence of

calculations for each block. In PExSim module, due to the possibility of joining the inputs / outputs of each block, and create loops, the problem was recognized as an important issue.

The solution proposed and implemented in PExSim is based on the information propagation and calculation triggering in order determined by signals flow defined by blocks connections. This way of processing is schematically shown in Fig. 1. The main idea is to separate a special type of blocks, named sources, who are responsible for generating signals. For each root-level path, the simulation mechanism in the first stage trigger sources (step 1) in the order defined by the order of their creation. Triggered source block calculates the value of their output signals and shall forward the results of their calculations to the next block. Signals appearing at the inputs of the standard block (Step 1.1, 2.1 and 3.1) make its initial activation, during which it is verified that the values were determined for all inputs to the block. When all inputs are available, the block is triggered and calculates its own output values (step 2, 3 and 4), resulting in activation of the next block in the structure of processing.

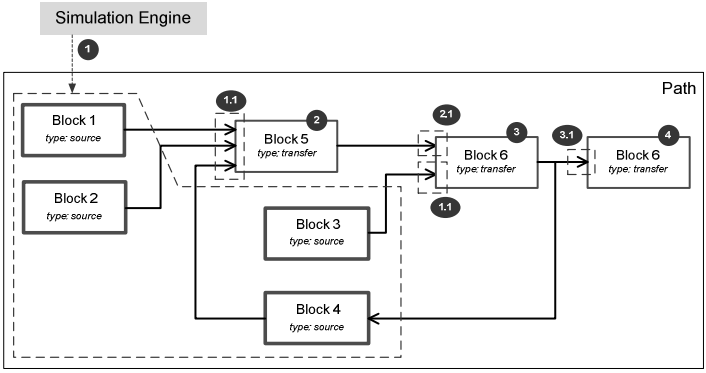

Fig. 1 Calculations triggering inside single path

4.2 Data Exchange with Other Modules in the System

Described in the previous section mechanism allows to work as a stand-alone unit. When PExSim works as a module of a distributed system, there is need for additional support for external events handling. This amounts to trigger the calculation by the incoming new data packages (messages). The process of receiving external data, their synchronization (including eg time stamps determination for a new step in the simulation), and eventually trigger a path is controlled by special input buffers (Fig. 2).

Similar mechanism is used also to send signals between paths not belonging to the same sub-tree. In this case one can use so called internal variables. These are simple buffers that store the output values of the specified paths and allows to read

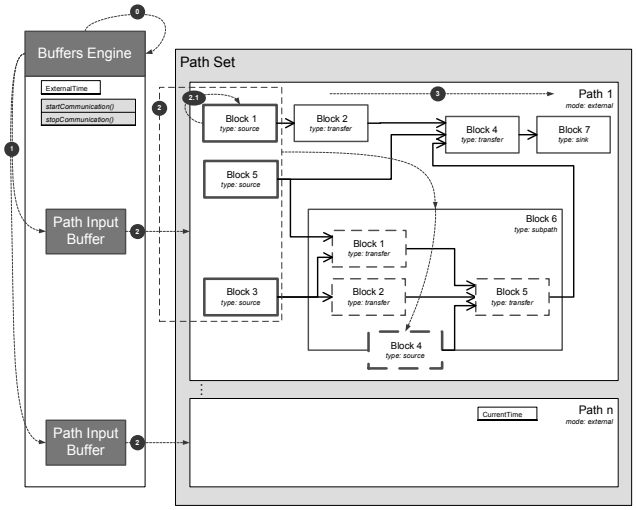

Fig. 2 Calculation triggering through external events

them through special sources "Internal Variable". Such mechanism of synchronization does not ensure proper sequence of calculations, if the buffer do not add any delay. In such case, the responsibility for proper execution of the calculations rests with the algorithm designer.

4.3 Synchronous and Asynchronous Processing of Paths

PExSim paths can have defined triggering mode as synchronous or asynchronous. Synchronous paths are triggered by simulation kernel. Its role is to measure current simulation time (according to a preset simulation interval) and trigger the calculations for subsequent processing paths at a certain sampling period. Paths are triggered in the predefined order. In addition, each processing path can have specified its own simulation ratio. It is an integer that multiplies core sample time for given path, resulting with less frequently calculations.

Asynchronous mode is not controlled by simulation kernel. Each occurrence of an external event causes with start the mechanism described in section 4.1 in order to check input data availability. If calculations cannot be continued due to missing input values, they are suspended. If all input signals are set – path is calculated, and after that all inputs for all blocks in given path are reset.

5 Conclusion

The paper presents the general principles of signal processing and data exchange modules used by the DiaSter system, both in terms of internal processing and communication with external systems. In the description, in particular, highlighted the

innovative elements that distinguish described processing methods from conventional automation systems or simulation software. Summary description is quite general in nature, taking into account the capabilities of the system. It allows to get an idea of its capabilities. Potential use of the described system include both classic application of automation systems (balance calculations, the conversion of units), as well as advanced, distributed simulation of the mechatronic systems, on-line simulators, diagnostics and optimization. Due to the high flexibility of the described technique it is possible to easily implement any new monitoring or control algorithm, and to test it with simulated as well as real device. In practice system in current version was tested as a tool for modelling artificial heart devices, a diagnostic system for laboratory installations, or as a platform for brewery simulator.

References

[1] Korbicz, J., Kościelny, J.M.: Modeling, Diagnostics and Process Control. Implementation in the DiaSter System. Springer, Heidelberg (2010)
[2] Kościelny, J.M., Syfert, M., Wnuk, P.: Advanced monitoring and diagnostic system for industrial processes AMandD. Control Engineering Polska 2(45), 40–44 (2008) (in Polish)
[3] Kościelny, J.M., Syfert, M., Wnuk, P.: Introduction to the DiaSter system. W pracy zbiorowej pod redakcją. In: Korbicz, J., Kościelny, J.M. (eds.) Modeling, Diagnostics and Process Control. Implementation in the DiaSter System, p. 42. Springer (2010)
[4] Janiszowski, K., Wnuk, P.: PExSim – a novel approach to problem of investigation of complex dynamic systems in industrial environment, Problemy Eksploatacji – Maintenance Problems, No 4 (2006)
[5] Syfert, M., Wnuk, P.: Signal processing in PExSim package: rules, techniques, possibilities. Pomiary-Automatyka-Robotyka PAR (11), 84–89 (2010) (in Polish)
[6] Wnuk, P., Syfert, M., Kościelny, J.M.: Intelligent system for diagnostics and control support of industrial processes DIASTER. In: Kowalczuka, Z. (ed.) Systemy wykrywające, analizujące i tolerujące usterki, pp. 57–64. PWNT, Gdańsk (2009)

System for Multipoint Measurements of Slowly Varying Magnetic Fields

M. Szumilas, E. Ślubowska, and K. Lewenstein

Warsaw University of Technology, Faculty of Mechatronics, ul. św. Andrzeja Boboli 8, 02-525, Warsaw, Poland
m.szumilas@mchtr.pw.edu.pl

Abstract. The paper summarises a design of a system capable of measuring slowly varying magnetic field in many points simultaneously. System has a centralised structure consisting of a single main module and multiple slave modules. The main module collects data from the slave modules (up to five), which in turn measure the magnetic field vector. For measuring the magnetic field Hall sensors are used. There are measured three components of the magnetic field vector in range: ±3 T, with resolution: 6 mT, and sampling rate: 50 Hz. Discussed in paper accuracy of the system equals ±14%. The future development of the system will probably comprise modification of the sensor probe and reduction of the modules' dimensions, which are intended to increase accuracy of measurements and to improve portability of the device.

1 Introduction

Magnetic resonance (MR) systems are widely used for imaging purposes in medical diagnostics. Since the strength of a static magnetic field generated in an MR apparatus interior and its surroundings is about 10,000 times higher than the strength of Earth's field, such an environment is not common for a human. Medical consequences of such exposure are not fully known so we decided to carry out research on a portable data logger capable of monitoring exposure of the MR scanner staff [1]. This design was focused on low frequency (less than 10 Hz) components of magnetic field. We wanted to observe selectively the static field generated by the super-conducting electromagnets of an imaging system, not the gradient and radio frequency fields that are present only during patient examination. The static field is always turned on and when the workers move around the scanner while attending patients, the field vector's magnitude and direction change relatively to them. It is due to the fact that the MR apparatus stray field is not homogenous and also is a consequence of workers' rotation (when the vector magnitude remains constant, but its direction changes).

T. Březina and R. Jabloński (eds.), *Mechatronics 2013*,
DOI: 10.1007/978-3-319-02294-9_57,

The data logger, designed and built during the research mentioned above, has proven its functionality in measurements conducted around the MR systems with magnet strengths 1.5 T and 3 T. However, as they were all single-point measurements, the possible analysis was limited. Therefore, we decided to develop a new system, capable of measuring the magnetic induction in many points simultaneously. We presume that this will extend the range of exposure analysis. Moreover, the acquired data may serve as an input for modelling the time-varying spatial field distribution in human tissues which enables a calculation of induced electric fields, e.g. as it has been shown in [2].

The case of the MR staff should be considered specific and there are legal issues related to specifying the exposure limits for this occupational area. In 2004, directive 2004/40/EC, on the minimum health and safety requirements regarding the exposure of workers to the risks arising from electromagnetic fields, was adopted and should have been implemented in the European Union countries. However, the implementation has been postponed twice because the medical community claimed that the exposure limits laid down therein would significantly hinder the use of MR techniques in medical imaging. Other industrial sectors were also concerned about the impact of the directive on their activities. In consequence, a new directive [3] was proposed and it will supersede the directive 2004/40/WE. The new directive exempts the medical MR sector from the exposure limits but it states that appropriate protection methods must be worked out. In such circumstances, results of our research may be useful for developing these methods.

2 System Structure

The designed multipoint measurement system has a centralised structure consisting of a single main module and multiple slave modules. The main module collects data from the slave modules, which in turn measure the magnetic field vector. Up to five slave modules may be connected to the master module at the same time.

The main module consists of following blocks (Fig. 1): a user interface, a data storage block (with a Flash card) and a power supply (which includes an energy measurement unit and an on-board battery charger). The slave module consists of a signal processing chain and a power supply block (which includes a reference voltage source and a sensor's power supply). Downloading measured data and charging a battery takes place through the main module's USB interface. Each module has its own control unit, the 8-bit megaAVR microcontroller.

The main module communicates with the slave modules in a synchronous mode. A physical connection between modules is made with shielded signal cables fitted with RJ12 and RJ45 connectors.

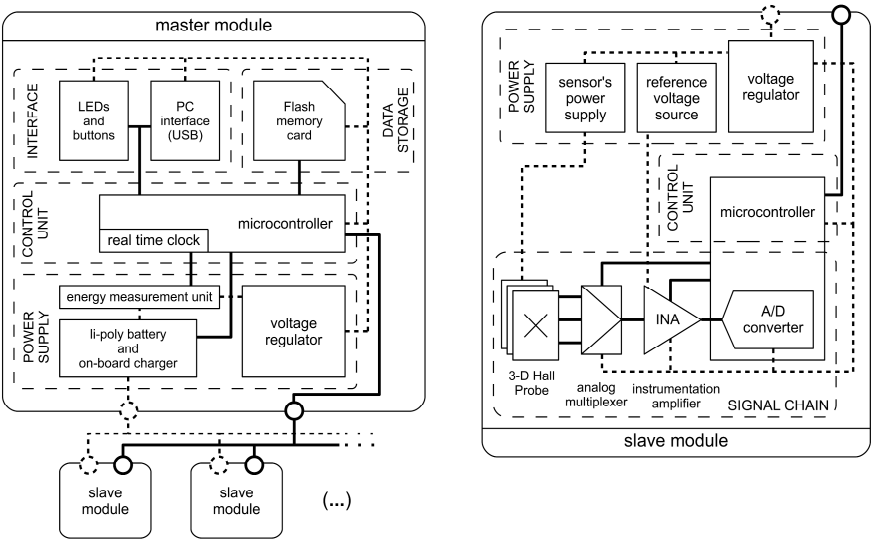

Fig. 1 The block diagrams of the system modules, solid lines resemble signal connections and dashed lines resemble power connections

The system uses Hall sensors to measure the magnetic field. Measuring the field vector is possible with specially made three axis sensor probes (Fig 2.).

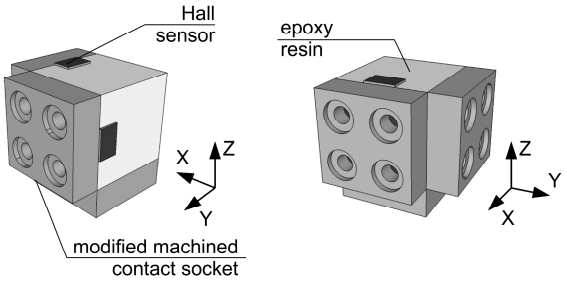

Fig. 2 3-D model of the three-axis Hall sensor probe

Each probe is set up from three individual CYSJ166A Hall sensors in SMD packages which are oriented perpendicularly. The sensors' biasing inputs are connected in parallel what enables powering them with two leads only. The sensors' input and output connectors are made from modified machined contact sockets. The probes are resin-coated to protect them against a mechanical damage. They fit into a cube of an edge length 12 mm, what makes possible calibrating the probes inside a relatively narrow gap of strong magnetic field sources, e.g. laboratory electromagnets.

The signal chain consists of a sensor probe, a differential analog multiplexer, an instrumentation amplifier and an analog-to-digital (A/D) converter. The bias current is provided to the probe from a current source with thermal compensation of the Hall sensor's temperature-related change of sensitivity (for applied sensors it equals -0.06%/°C). The voltage signals from each individual sensor in the probe are multiplexed in pairs (the Hall sensor's output is differential) into the instrumentation amplifier (INA). The INA's output signal is measured by the 10-bit A/D converter, which is a part of the module's microcontroller. The sampling frequency equals 50 Hz and the delay between subsequent samples is about 100 µs (it is time of completing a single A/D conversion). In frequency spectrum of the measured magnetic field, all components with the magnitude exceeding the system resolution come from the static field source of a MR apparatus. Therefore, due to the fact that the field changes are related only to workers' moves, an aliasing does not occur and a low-pass analog filter is not required.

3 Features of the System

The most important features of the presented system:

- master module:
  - maximum number of slave modules operating together: 5
  - output data rate: approx. 36 kB / minute (for each slave module)
  - data is stored on a Flash memory card; storage is limited by the maximum file size (4 GB) and a capacity of the card
  - USB interface (data transfer rate up to 50 kB/s)
  - battery capacity: 650 mAh
  - power consumption: < 1.3 mA in sleep mode, 5 mA in other modes
  - dimensions: 89 mm / 61 mm / 20 mm
- slave module (measuring module):
  - measures three components of the magnetic field vector
  - measuring range: ±3 T
  - resolution: 6 mT
  - sampling rate: 50 Hz
  - accuracy: ±(14% of the measured value + 28 mT) (temp. range: 10 ÷ 40ºC)
  - power consumption: < 0.13 mA in sleep mode, 7 mA in measuring mode
  - dimensions: 40 mm / 40 mm / 20 mm

Signal chains of the modules must be calibrated in order to achieve the given accuracy. This is since the Hall sensor's sensitivity was specified inexactly by its manufacturer. During the calibration, the sensor probe is placed inside a magnetic field reference source and the sensor's sensitivity is determined on the basis of acquired data. As can be seen in Table 1, the sensitivity error of sensor probe has

the most significant impact on the measurement's relative error. Other important source of the result uncertainty is non-perpendicular orientation of the individual sensors in the probe, so the measured vector components are derived from the skewed coordinate system. Nonetheless, the vector components are considered to be orthogonal because the angles between particular axes are not known. In a consequence, the angles are only estimated. During the future development of the device it may be advantageous to substitute the probe made from individual sensors with an integrated 3-D sensor, such as the one presented in [4], manufactured in the CMOS technology.

Table 1 Error budget analysis of the analog signal chain (temp. range: 10ºC to 40ºC)

Components of Absolute Error		Components of Relative Error	
Error Source	RTO [mT]	Error Source	RTO [%]
Instrumentation Amplifier Offset	12.1	3D Hall Probe Sensitivity Error	5.14
A/D Converter Error	9.9	Non-perpendicular Sensing Axes in 3D Hall Probe	4.67
Reference Voltage Error	3.5	Instrumentation Amplifier Gain Error	2.06
		3D Hall Probe Current Supply Error	1.12
Other Error Sources	2.3	Other Error Sources	0.45
TOTAL:	27.8	TOTAL:	13.44

RTO referred to output value.

4 Algorithm and Computer Application

The main function of the master module is to acquire data from the slave modules and to store it in a non-volatile memory.

The device has three operating modes: sleep, idle and measurement. After entering the measurement mode (Fig. 3), connections with all slave modules are established and their addresses are received. The addresses are necessary for matching data with appropriate modules. Afterwards, the measuring modules are checked for new data every 10 ms. If the data is available, it is sent in packets to the main module and each event of data loss or corruption is recorded. To improve readability of a data file, and for additional validation of data completeness, a timestamp is stored in the file in a one-second period. The data file is updated as soon as a data buffer contained in the RAM memory of the microcontroller reaches its capacity. Data files are managed on the memory card with FatFs, which is a FAT file system module licensed as free software.

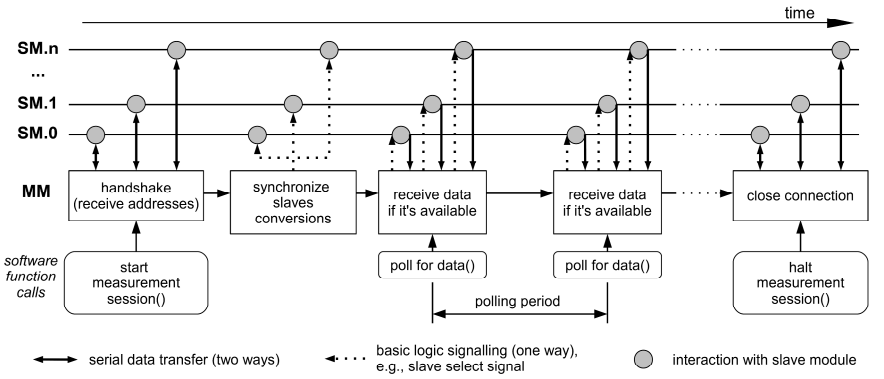

Fig. 3 Program execution in the measurement mode: SM.n - the nth Slave Module, MM - the Master Module

In order to increase the system energy efficiency, low-power operating modes are implemented in modules. In the main module a sleep mode involves: disconnecting power from the slave modules and memory card and also putting the microcontroller into a power-save mode. The microcontroller wakes up only to measure energy consumption and track current time. When the main module is in an idle mode (e.g. when communicating with a computer) the slave modules remain in a sleep mode which involves: disconnecting power from the signal chain and putting the microcontroller into a power-down mode. The slave modules wake up when the system is entering a conversion mode.

An application for Windows was made to enable communication between the master module and a computer. The application allows a user to: read the system status, set up the master-slave transmission parameters, manage data files and convert binary data to the ASCII format. Basic data processing functions are also available: converting raw data to the magnetic field values on the basis of modules' calibration parameters, calculating the magnetic field vector's magnitude and its changes in time, low-pass digital filtering of the acquired signal. The converted data can be analysed in each application that reads tab-separated text files.

5 Testing

The measuring system in a configuration with three slave modules is presented in Fig. 4a. A specially made carrying vest (Fig. 4b) consists of an abdominal belt with mounting stripes and braces. The modules may be mounted on the braces or on the belt. In order to enable the system to operate in strong magnetic fields the modules are made mainly from non-magnetic materials and are closed in plastic casings.

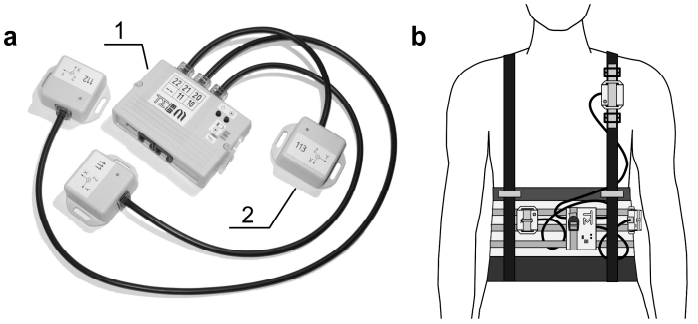

Fig. 4 a The data logger system: 1 - master module, 2 - slave module; **b** An example configuration of our system, the modules are mounted on the specially made vest

Each data record consists of three components of a magnetic field vector. From the vector's components following values are calculated: the magnitude of a field vector $|\boldsymbol{B}|$, the derivative of a field vector $|\boldsymbol{dB/dt}|$, the derivative of a field magnitude $d|\boldsymbol{B}|/dt$ and the product of the vector's magnitude and its angular velocity $|\boldsymbol{B}|\omega_B$. The angular velocity of a magnetic field vector is a time derivative of an angle between subsequent measured vectors, where the angle is calculated from their scalar product. The derivatives are approximated with a central difference quotient. The $d|\boldsymbol{B}|/dt$ and $|\boldsymbol{B}|\omega_B$ values are used to determine whether the vector's magnitude change or its rotation contributes more to the overall vector's change. As can be seen in Eq. 1, with a sufficiently small time step, square root of this parameters' sum of squares converges to a time derivative of a field vector $|\boldsymbol{dB/dt}|$.

$$dt \ll 1/\omega_B \quad \Rightarrow \quad \sqrt{\left(\frac{d\left|\vec{B}\right|}{dt}\right)^2 + \left(\left|\vec{B}\right|\omega_B\right)^2} \rightarrow \left|\frac{\overrightarrow{dB}}{dt}\right| \tag{1}$$

In Fig. 5 we present the example data acquired during the system's tests around the 1.5 T MR apparatus.

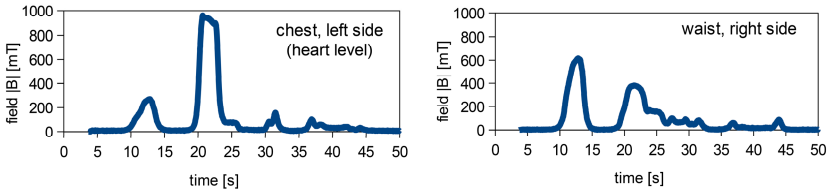

Fig. 5 The data acquired during trial measurements of the magnetic field around the 1.5 T MR apparatus; the data logger configuration was similar to the one from Fig. 4b, two out of three available data series are presented

6 Conclusions

The presented multipoint measurement system should be considered fully functional. The data acquired during its tests is applicable for further analyses. Since the implemented structure with interchangeable slave modules has the advantage of being versatile, the system can be easily extended with new modules. They can, for example, monitor the worker's health parameters or measure the magnetic field from other frequency ranges, with a different resolution. The future development of our system will probably comprise modification of the sensor probe and reduction of the modules' dimensions, which are intended to increase accuracy of measurements and to improve portability of the device.

Acknowledgments. This work was supported by the Dean of the Faculty of Mechatronics, Warsaw University of Technology [grant number 504M/1142-0414 000].

References

[1] Szumilas, M., Ślubowska, E., Lewenstein, K.: Osobisty rejestrator wolnozmiennych pól magnetycznych. Elektronika – Konstrukcje, Technologie, Zastosowania 3, 46–49 (2012)

[2] Laakso, I., Kännälä, S., Jokela, K.: Computational dosimetry of induced electric fields during realistic movements in the vicinity of a 3 T MRI scanner. Phys. Med. Biol. 58, 2625–2640 (2013)

[3] Proposal 2011/0152(COD) for a Directive of the European Parliament and of the Council on the minimum health and safety requirements regarding the exposure of workers to the risks arising from physical agents (electromagnetic fields) (2011)

[4] Pascal, J., Hébrard, L., Frick, V., Blondé, J.-P.: 3D Hall probe integrated in 0.35μm CMOS technology for magnetic field pulses measurements. In: Proc. of the IEEE NEWCAS-TAISA 2008 Conference, Montréal, Canada, pp. 97–100 (2008)

X Band Power Generator

R. Krizan and L. Drazan

Dept. of Radar Technology, Faculty of Military Technology, University of Defence,
Kounicova 65, 662 10 Brno, Czech Republic
{rene.krizan,libor.drazan}@unob.cz

Abstract. This article describes one part of a dual microwave pulse generator which is X band high-power generator. The generator uses a high-frequency valve (magnetron) – as used in boat radars. This generator can be used for verifying and setting standards appropriate for measuring and mapping high-frequency electromagnetic fields, or may be applied for running electromagnetic pulse resistance and electromagnetic compatibility tests.

1 Introduction

Research at the University of Defence focuses, among other things, on high-power electromagnetic weapons. It is necessary to know their effects, features and methods of protection against their misuse. For this reason several high-power generators were constructed and used for measuring and testing purposes. One of them is the X band high-power electromagnetic generators described below.

2 X Band Power Generator

This generator works in the X band and uses magnetron 9M31, profusely used in boat radars. The magnetron was selected because it is cheap and widely available. Also because it is so easy to get parts it is very unlikely to be the target of terrorist groups or those wanting to destroy electromagnetic devices working in this band. This generator can be divided into blocks as shown in Fig.1.

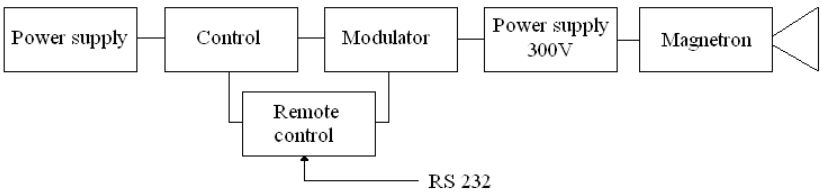

Fig. 1 Block diagram of high-power microwave impulse generator

T. Březina and R. Jabloński (eds.), *Mechatronics 2013*,
DOI: 10.1007/978-3-319-02294-9_58, © Springer International Publishing Switzerland 2014

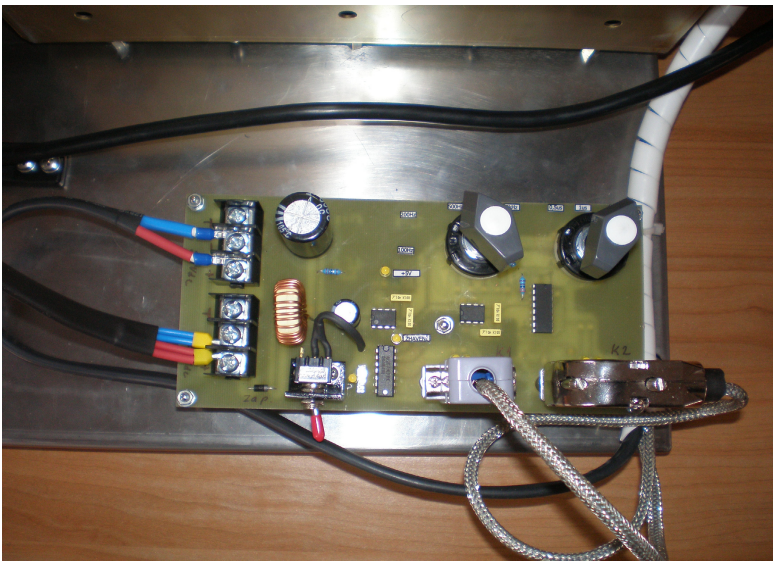

Fig. 2 Control and Remote control

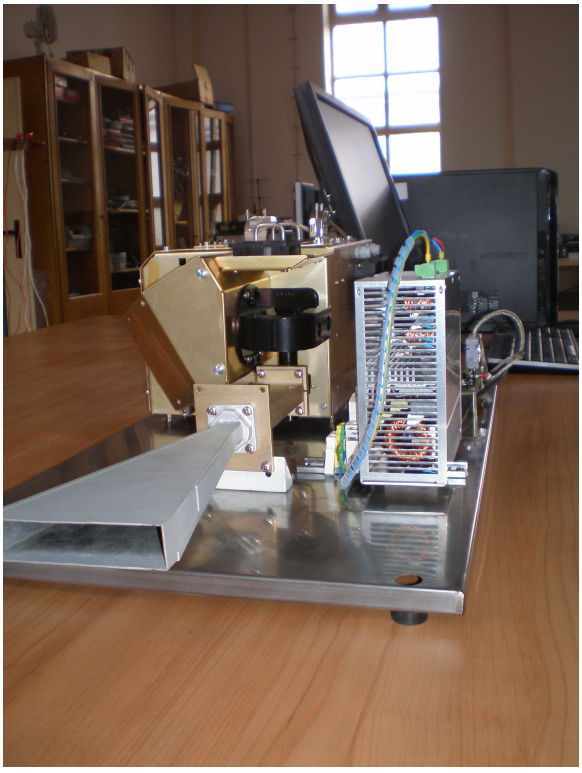

Fig. 3 Magnetron and Horn antenna

The generator is powered by mains 230V 50Hz. This voltage is run through a surge protector to a rectifier and stabilizer block. The next block is supplied with ± 24V DC. The main control circuit can run independently using preset control switches or can be run by a control computer via an RS 232 interface (fig. 2). The high-voltage source creates a voltage of 300V for powering the magnetron.

A modulator modulates the voltage on the magnetron according to the required values from the control circuit. The modulated voltage is then applied to the magnetron creating high-power impulses according to the control circuit settings or also according to the parameters inputted into the PC and transferred to the control circuit via the RS 232 interface.

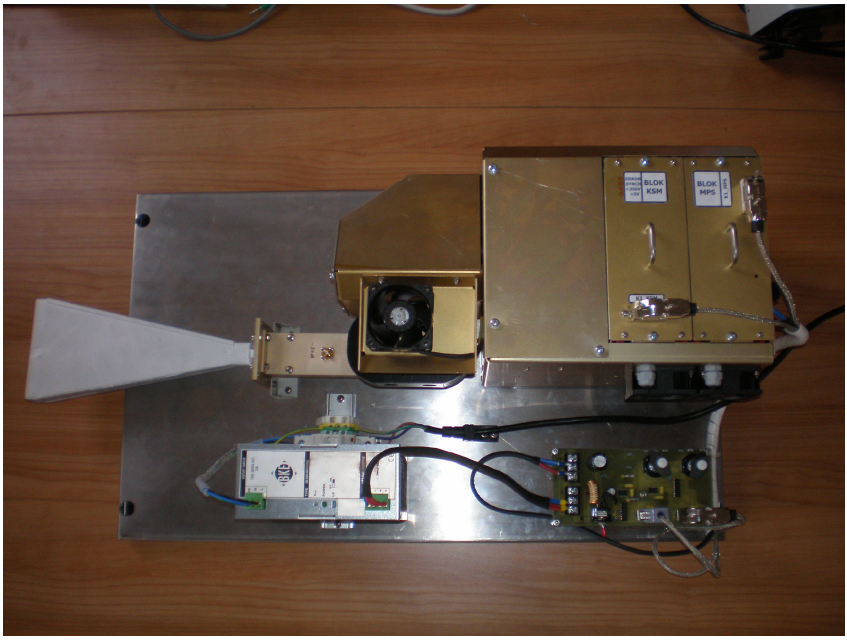

Fig. 4 X band generator

Table 1 Channel X Electrical Characteristics

parameter name	unit	value
Channel	[ ]	X
Frequency	[GHz]	9.4
Pulse width	[µs]	0.5 to 2
Pulse duty factor	[ ]	0.001
Peak power of pulses	[kW]	40
Waveguide	[ ]	R100

The high-frequency energy is then transferred from the magnetron by standardised waveguide R100 into the output funnel antenna and from there to the open space. An integral part of this generator is also a fan system used to cool down individual generator components and the magnetron itself.

The impulse width and the pulse duty factor can be set within the range as shown in Tab. 1.

3 Design Problems

In the process of designing the generator, it was necessary to solve not only issues with controlling and regulating the generator by a PC placed outside the measuring point, but also the issue of protection of individual components, as they were retroactively affected by the generated high-frequency energy.

The solution to this problem was to enclose the constructed generator in a metal case. Another problem occurred with the high-voltage transformer. When used for a long time, an electric discharge occurred between the secondary transformer winding and the metal shielding cover of the generator. Enclosing the high-voltage transformer in a dielectric case solved this problem.

4 The First Test

After solving design problems is now performed the first experiments on the generator. The test focuses on the functionality of the generator. One of the tests is

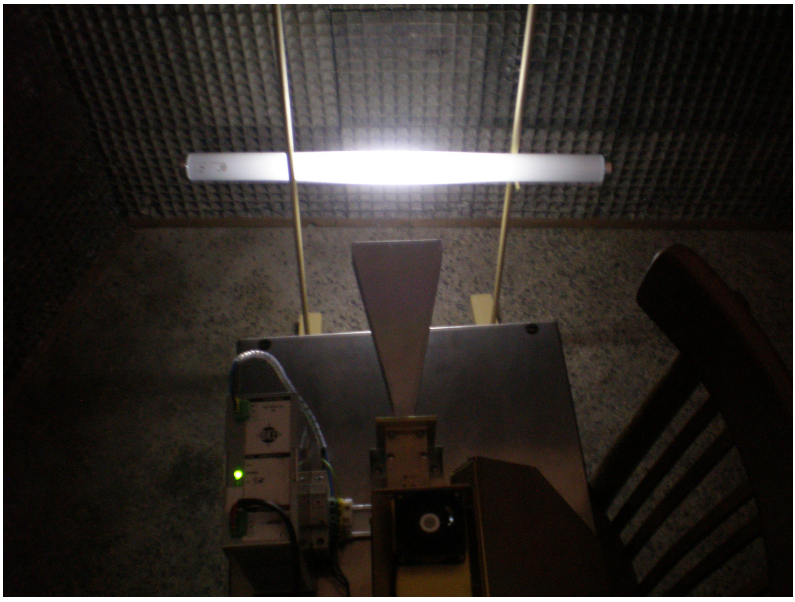

Fig. 5 X band generator – functionality test

shown in figure 5. There is clearly visible effect HF energy transmitted from the generator energy to the lamp. It is placed on the stand without any contact.

The test was focused on the change pulse width and power of pulses. The figure shows the influence of directivity horn antenna. Further tests will follow in the autumn.

5 Conclusions

This generator will be used for developing, verifying and setting standards that are appropriate for measuring and mapping high-frequency electromagnetic fields of high power, such as calorimeter. It can also be used as the source of a high-frequency electromagnetic field of high power imitating interferences in the X channels. At the same time it may be used for running EMP resistance and EMC (electromagnetic compatibility) tests.

References

[1] Palisek, L.: Zbrane s rizenou energii. VTUPV Vyskov (2002)
[2] Drazan, L.: Vybrane problemy konstrukce elektromagnetickech zbrani pracujicích v pasmu radiovych vln a mikrovln, VA Brno (2007)
[3] Drazan, L., Vrana, R.: Axial Vircator for Electronic Warfare Applications. Radioengineering 18(4) (December 2009)
[4] Krogager, E., et al.: Lecture Series SCI-249: Phenomenology and Basic Theory of Electromagnetic Fields. In: Radio Frequency Directed Energy Weapons, Liptovsky Mikulas, Academy of the Armed Forces, Slovakia (2012)
[5] Roemer, B., et al.: Lecture Series SCI-249: Electromagnetic Field Generation (Sources). In: Radio Frequency Directed Energy Weapons, Liptovsky Mikulas, Academy of the Armed Forces, Slovakia (2012)
[6] Roemer, B., et al.: Lecture Series SCI-249: Attack Detection & Modeling and Simulation of EM Field Interaction with Targets. In: Radio Frequency Directed Energy Weapons, Liptovsky Mikulas, Academy of the Armed Forces, Slovakia (2012)
[7] Chevalier, B., et al.: Lecture Series SCI-249: Electromagnetic Pulses. In: Radio Frequency Directed Energy Weapons, Liptovsky Mikulas, Academy of the Armed Forces, Slovakia (2012)
[8] Chevalier, B., et al.: Lecture Series SCI-249: Methodology and Test Facilities. In: Radio Frequency Directed Energy Weapons, Liptovsky Mikulas, Academy of the Armed Forces, Slovakia (2012)
[9] Arnesen, O.H., et al.: Lecture Series SCI-249: Protection Against EM Threats. In: Radio Frequency Directed Energy Weapons, Liptovsky Mikulas, Academy of the Armed Forces, Slovakia (2012)
[10] Peterkin, F., et al.: Lecture Series SCI-249: High Power Microwave Applications. In: Radio Frequency Directed Energy Weapons, Liptovsky Mikulas, Academy of the Armed Forces, Slovakia (2012)
[11] Peterkin, F., et al.: Lecture Series SCI-249: RF DEW Scenarios and Threat Analysis. In: Radio Frequency Directed Energy Weapons, Liptovsky Mikulas, Academy of the Armed Forces, Slovakia (2012)

A New Approach to the Uncertainty in Diameter Measurement Using Laser Scanning Instrument

Ryszard Jablonski[1] and Pawel Fotowicz[2]

[1] Warsaw University of Technology, Faculty of Mechatronics, Sw. A. Boboli 8, 02-525, Warsaw, Poland
yabu@mchtr.pw.edu.pl
[2] Central Office of Measures, Elektoralna 2, 00-139, Warsaw, Poland
uncert@gum.gov.pl

Abstract. Coverage interval is a new concept for expressing the uncertainty in metrology. The computation of measurement uncertainty of diameter is presented basing on analytical method for calculating the coverage interval. In measurement a laser measurement scanner was used and a change in the position of an object was considered as the source of a systematic error (which is treated probabilistically as a component of the coverage interval).

1 Introduction

At present, the traditional approach to evaluation of measurement data, based on statistical analysis is replaced by probabilistic determination of uncertainty sources connected with the measurand. The conception of probabilistic evaluation of measurement result is promoted by the international document [1]. The new approach equally treats the information derived from different sources, especially outside the measurement utilizing the credible analysis connected with measurement process. This information is converted by the random quantities and further computations are made in accordance with the rules of probability calculus. In the present document [2] the propagation of distributions through the mathematical model of the measurand is recommended. The method is based on reporting the results in the form of probability density functions by the simulation of Monte Carlo method.

For below described experiments, a classical electromagnetic laser scanner was chosen and it was applied for contactless measurement of optical fibres during manufacturing process (measuring range up to 200 μm, resolution 0.5 μm).

2 Analytical Method

The coverage interval is defined as the shortest interval between two quantiles of distribution for the output quantity values corresponding to 95 % coverage

T. Březina and R. Jabloński (eds.), *Mechatronics 2013*,
DOI: 10.1007/978-3-319-02294-9_59,

probability [2]. In the case of symmetrical distribution, there is only one interval symmetrical about its expectation:

$$I_p = [y_{\text{low}}, y_{\text{high}}] \tag{1}$$

where: $y_{\text{low}} = G^{-1}(\alpha)$, $y_{\text{high}} = G^{-1}(\alpha+p)$.

$G^{-1}(\alpha)$ is an α-quantile and $G^{-1}(\alpha+p)$ is an $(\alpha+p)$-quantile of the distribution function $G(\eta)$. It was adopted that $\alpha = 2.5$ %, and $p = 95$ %. With reference to the classic notation of expanded uncertainty, the coverage interval can be defined as:

$$I_p = [y - U,\ y + U] \tag{2}$$

For linear model of measurand, practically for direct measurement, the propagation of distributions can be realized by applying an operation of their mathematical convolution, when all input quantities can be treated as independent random variable.

The analytical method depends on the approximation of the result of convolution of standard distributions for input quantities [3]. These standard distributions are: Student's, normal, rectangular, triangular or trapezoidal. The multiple convolutions of the normal and rectangular distributions can be approximated by R∗N distribution, which is a convolution of rectangular and normal distributions. The probability density function of R∗N distribution depends on parameter r (ratio of the standard deviation of the rectangular distribution to the standard distribution of the normal distribution):

$$g_{\text{RN}}(\eta) = \frac{1}{2\sqrt{6\pi}\cdot r}\int_{\eta-\sqrt{3}\cdot r}^{\eta+\sqrt{3}\cdot r} \exp\left[-\frac{\xi^2}{2}\right] \mathrm{d}\xi \tag{3}$$

The parameter r can be approximated by an uncertainty ratio:

$$r_u = \frac{|u_i(y)|}{\sqrt{u_{\text{c}}^2(y) - u_i^2(y)}} \tag{4}$$

where $u_i(y)=c_i\cdot u(x_i)$ is the largest contribution of the input quantity having a rectangular distribution, c_i is a sensitivity coefficient and $u(x_i)$ is standard uncertainty. The expanded uncertainty can be calculated from:

$$U = k_{\text{RN}}\sqrt{\sum_{i=1}^{N}\left(\frac{t(v)}{k_{\text{N}}}u_i(y)\right)^2} \tag{5}$$

where k_{RN} is a coverage factor for R∗N distribution. The coverage factor k_{RN} values corresponding to 95 % confidence level are presented in [3]. For normal, rectangular, triangular and trapezoidal distributions $t(v) = k_{\text{N}}$ should be assumed ($k_{\text{N}} = 1.96$ for $p = 95$ %).

3 Laser Measuring Scanner

Elementary units of laser measuring scanner (LMS) are presented on Fig.1. When transverse scanning is applied, an object to be measured is placed in the measuring area and the detector with collecting lens further behind. The detector output signal is in the form of shadow of an object (Fig.2) and is usually measured in reference to time. At the assumption of extremely small uncertainty of time measurement ($1 \cdot 10^{-5}$), the measurement uncertainty is a result of transformation uncertainty of a scanning lens (usually f-θ lens), instability of rotational velocity of a drive (discussed in [4]), deflector introduced uncertainty and detector signal uncertainty.

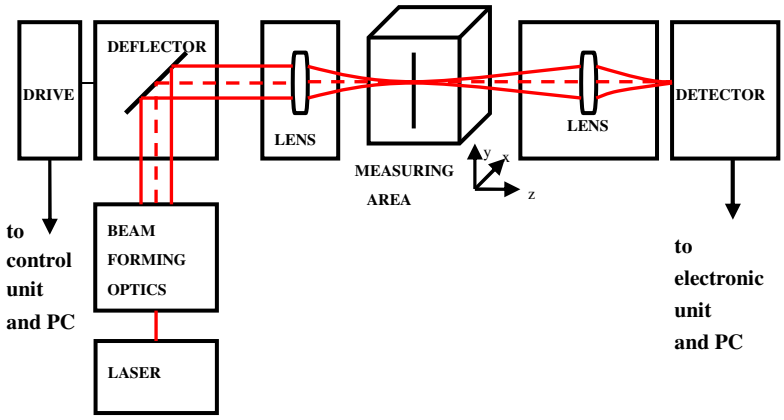

Fig. 1 Elementary units of laser measuring scanner

The transformation of a laser beam, when passing through the optical system is well defined and can be calculated from formula:

$$2w = 2w_0 \sqrt{1 + \left(\frac{z\lambda}{\pi w_0^2} \right)^2} \tag{6}$$

where: $2w_0$ is minimum spot size (beam waist); $2w$ is the beam diameter at distance z from the beam waist.

An ideal signal shape (determined by the diameter of an object and laser spot size) is trapezoidal and assuming constant scan velocity, the shadow time Δt is the measure of the size of an object (usually determined in the middle between max. and min. signal, $(V_{max}-V_{min})/2$, Fig.2). This value vary depending on the detecting angle, but also because in addition to the ideal output detector signal, the interfering signals occur.

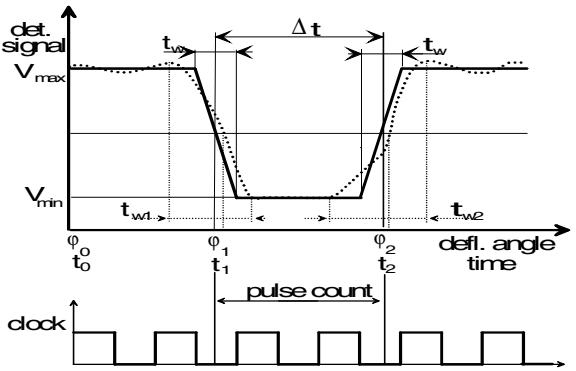

Fig. 2 Real and ideal (trapezoidal) signal shape of laser beam diffracted on cylindrical object

The interfering signals result in the intensity distribution collected by detector, and are due to superimposition of diffracted, reflected, scattered, incident, transmitted light. The proportions between above mentioned components vary in time and also the total intensity distribution changes; consequently an ideal trapezoidal pulse is much distorted (Fig.2).

All the above mentioned errors have been discussed in [5] and for the certain LMS configuration can be considered as well defined. For the needs of presented work the measurement model contains only: resolution, systematic error and uncertainty of reference standard. The systematic error is caused by a change in the position of an object within the measuring area and is treated probabilistically as a component of the coverage interval. Its maximum value is estimated with the use of mathematical analysis based on known dependences in laser optics.

4 Measurement Equation of Outer Diameter by Scanner

In order to determinate the metrological properties of LMS the diameter of reference standards was measured. The obtained nominal values, applying laser diffraction method, are: d = 52,8 µm, 75,1 µm, 99,4 µm, 125,2 µm, 151,7 µm.

$$d = d_{\mathrm{m}} + \delta d_{\mathrm{m}} + \delta d_{\mathrm{s}} + \delta d_{\mathrm{st}} \tag{7}$$

where: d_{m} – measured diameter, δd_{m} – instrument resolution, δd_{s} – systematic effect, δd_{st} – standard accuracy.

First component of measurement equation is input quantity, with uncertainty determined by A-method (statistical method based on observation series). Its estimator is mean value from observation series and standard uncertainty measure is experimental standard deviation of average.

Other components are input quantities, which are centered random variables with uncertainties determined by B-method, based on scientific analysis and available information sources. Resolution and randomized systematic effect have

rectangular distributions. The measure of standard accuracy is in general extended uncertainty given with coverage factor $k = 2$ for probability $p = 95$ %. Therefore this value can be assigned with normal distribution.

Theoretical values of systematic error were calculated for optimal constructional parameters of measuring stand, which were used at projecting stage of LMS. The obtained laser beam waist $2w_0 = 47$ μm. It was acquired for scan lens of focal length $f = 50$ mm. The systematic error of measurement $e(d_s) = e(d_w)$ is determined from:

$$e(d_w) = d_w - d = d\left\langle 1 - w\left\{ \sqrt{\frac{2}{\pi}} \int_{-d/2}^{d/2} \exp\left[-2\left(\frac{x}{w} \right)^2 \right] dx \right\}^{-1} \right\rangle \tag{8}$$

The error occurs at moving the object (standard) along optical axis (see coordinates XYZ on Fig.1). Systematic error $e(d_s) = e(d_h)$, appearing at moving the measured object transversely to axis of optical setup, may be calculated from:

$$e(d_h) = d_h - d = d\left(\frac{\Delta\psi_h}{\Delta\psi} - 1 \right) \tag{9}$$

where $\Delta\psi_h$ is a scanning measurement angle of object diameter for a distance h from the optical axis, and $\Delta\psi$ is a scanning angle when the object is on the optical axis.

On the basis of obtained measurement results the bias was calculated as difference between mean value form observation series and value represented by standard:

$$e(d) = \bar{d} - d_{\mathrm{st}} \tag{10}$$

where: $\bar{d}$ – average of series of observations, d_{st} – standard diameter.

The measuring standards were moved along and transversely to optical axis from the middle of measuring area of instrument with increment 1 mm. The values of bias for standard diameter movement along optical axis of instrument and for standard diameter movement transverse to optical axis of instrument were determined. In the paper, only the results for standard diameter moving along axis are presented (see tables); the procedure for transverse movement is analogous.

5 Coverage Interval for Measurement of Diameter by Scanner

Coverage intervals for measured diameters are calculated by analytical method, on the basis of measurement equation:

$$U = k_{\mathrm{RN}} \sqrt{\left(\frac{t(\nu)}{k_{\mathrm{N}}} u(d_{\mathrm{m}})\right)^2 + u^2(\delta d_{\mathrm{m}}) + u^2(\delta d_{\mathrm{s}}) + u^2(\delta d_{\mathrm{st}})} \tag{11}$$

Standard uncertainty of the first component is determined by means of observation series. In each measuring point $n = 10$ series of readings are done. For mean value (which is estimator of measurement results) is assumed Student's distribution with number of degrees of freedom $\nu = 9$. The measure of uncertainty of this component is experimental standard deviation of mean value.

Standard uncertainty of second component is determined on the basis of scanner resolution, which was used for measurement, assuming its rectangular distribution. This uncertainty is invariable for each reading.

Standard uncertainty of third component is calculated regarding to the boundary values, which are representing theoretical systematic errors $e(d_w)$ and $e(d_h)$ with rectangular distribution. Measured object is within measuring area; its location is random with equal probability within the measurement area (Fig.1).

The measured standard uncertainty of fourth component is in a good agreement with data obtained from scientific literature [6]. The data concern comparisons of outer diameter standards in range from 0.05 mm to 1 mm with estimated uncertainty: $U = 0.15$ µm, $k = 2$. This component can be assigned with normal distribution.

Results of calculations and measurements are shown in Tab.1. They are represented by centered boundaries of coverage interval $I(d)$. The boundaries of these intervals round estimators of measured diameters are: $I(d) = \pm U$. In all points of measuring area, in which measurements and calculations were done, systematic errors are enclosed in coverage intervals and did not cross boundary values of those intervals.

Table 1 Coverage interval and bias for measurement result of standard diameter moving along optical axis

z (mm)	d = 52,8 µm		d = 75,1 µm		d = 99,4 µm		d = 125,2 µm		d = 151,7 µm	
	I(d) (µm)	e(d) (µm)	I(d) (µm)	e(d) (µm)	I(d) (µm)	e(d) (µm)	I(d) (µm)	e(d) (µm)	I(d) (µm)	e(d) (µm)
-5	±17,46	-15,3	±10,01	-9,4	±4,50	-4,1	±1,74	-1,5	±0,77	-0,6
-4	±11,17	-10,3	±5,50	-5,1	±2,05	-1,8	±0,84	-0,5	±0,65	-0,4
-3	±6,07	-5,1	±2,50	-2,3	±0,92	-0,7	±0,68	-0,3	±0,65	-0,3
-2	±2,60	-2,2	±1,06	-0,7	±0,65	-0,4	±0,63	-0,2	±0,66	-0,2
-1	±0,90	-0,6	±0,59	-0,2	±0,61	-0,2	±0,57	-0,1	±0,66	-0,2
0	±0,64	-0,1	±0,63	-0,1	±0,65	0	±0,61	0	±0,66	-0,2
1	±0,92	-0,5	±0,63	-0,3	±0,64	-0,1	±0,63	-0,2	±0,66	-0,2
2	±2,60	-2,1	±1,06	-0,6	±0,58	-0,3	±0,57	-0,3	±0,65	-0,3
3	±6,07	-5,3	±2,48	-2,2	±0,90	-0,6	±0,62	-0,4	±0,65	-0,3
4	±11,17	-10,5	±5,49	-5,2	±2,05	-1,7	±0,85	-0,6	±0,65	-0,4
5	±17,46	-15,5	±10,01	-9,6	±4,50	-4,0	±1,72	-1,4	±0,82	-0,7

Table 2 Coverage interval calculated using a Monte Carlo method for measurement result of standard diameter moving along optical axis

z (mm)	d = 52,8 µm		d = 75,1 µm		d = 99,4 µm		d = 125,2 µm		d = 151,7 µm	
	$I(d)$(µm)	δ (%)	$I(d)$(µm)	δI(%)	$I(d)$(µm)	δI(%)	$I(d)$(µm)	δI(%)	$I(d)$(µm)	δI(%)
-5	**±17,40**	0,35	**±9,98**	0,26	**±4,51**	-0,15	**±1,75**	-0,92	**±0,77**	0,47
-4	**±11,13**	0,40	**±5,51**	-0,20	**±2,06**	-0,54	**±0,84**	0,82	**±0,65**	0,16
-3	**±6,07**	-0,12	**±2,52**	-0,75	**±0,91**	0,60	**±0,68**	0,33	**±0,66**	-0,44
-2	**±2,62**	-0,60	**±1,05**	0,36	**±0,65**	-0,29	**±0,63**	0,02	**±0,66**	-0,24
-1	**±0,90**	0,46	**±0,59**	-0,32	**±0,61**	-0,28	**±0,57**	-0,03	**±0,65**	0,36
0	**±0,64**	-0,20	**±0,63**	-0,07	**±0,66**	-0,50	**±0,61**	-0,10	**±0,66**	-0,32
1	**±0,91**	0,37	**±0,63**	0,22	**±0,64**	0,09	**±0,63**	-0,21	**±0,66**	-0,30
2	**±2,62**	-0,59	**±1,06**	0,18	**±0,59**	-0,37	**±0,57**	-0,11	**±0,65**	-0,21
3	**±6,07**	-0,10	**±2,50**	-0,96	**±0,90**	0,72	**±0,62**	-0,28	**±0,66**	-0,66
4	**±11,14**	0,27	**±5,50**	-0,10	**±2,06**	-0,63	**±0,85**	0,69	**±0,65**	-0,11
5	**±17,44**	0,13	**±9,98**	0,28	**±4,51**	-0,10	**±1,73**	-0,78	**±0,81**	0,77

6 Calculations Using a Monte Carlo Method

Coverage intervals were also calculated with recommended Monte Carlo Method, for trials number M = 10000, on the basis of measurement equation and in accordance with numeric algorithm presented in document [2]. Results of calculations are shown in Tab. 2. They also contain relative differences between results of calculations by analytical method and Monte Carlo method:

$$\delta I = \frac{I(d) - I(d)_{\mathrm{MC}}}{I(d)_{\mathrm{MC}}} \tag{12}$$

where $I(d)$ is coverage interval determined by analytical method, $I(d)_{\mathrm{MC}}$ is coverage interval determined by Monte Carlo method. The differences δI do not exceed 1%, which is in agreement with [2].

The results obtained with analytical method are in grey columns in Tab. 1 and results obtained with Monte Carlo method are also in grey columns in Tab. 2.

7 Conclusion

The paper presents practical application of analytical method for elaboration of measurement result given by coverage interval. It is done in accordance with definitions proposed in newest international metrological documents concerning analysis of measuring data. The method is alternative for recommended numeric reference method with linear or linearized measurement model. There is no necessity to use advanced, special computer programs and its computational accuracy is comparable with reference method in form of Monte Carlo simulation.

The main subjects of metrological analysis were results obtained by measuring outer diameter with use of laser scanner. The main source of systematic errors is a displacement of measured object within measuring area (it commonly happens during in-process control of the diameter of optical fibers or wires). And because there is no reason to distinguish any privileged position of measured object within this area, we can assume equal probability for any position.

Analytical method of coverage interval calculation can be used in any practical elaboration of result of direct measurement, especially when significant and variable systematic errors occur. Result of such calculations shows, that systematic error can be dominant and variable component (random component) of measurement uncertainty budget provides slight part in resultant uncertainty.

References

[1] Evaluation to measurement data – GUM. JCGM 100 (2008)
[2] Evaluation to measurement data – Supplement 1 to the Guide – Propagation of distributions using a Monte Carlo method. JCGM 101 (2008)
[3] Fotowicz, P.: An analytical method for calculating a coverage interval. Metrologia 43, 42–45 (2006)
[4] Jabłoński, R., Fotowicz, P.: New generation of lasermikes. In: Int. Symp. "Laser Metrology 1999". Proceedings of the SPIE, vol. 4420, pp. 91–98 (2001)
[5] Jabłoński, R., Kretkowski, M., Fotowicz, P.: Simple lasermike for measurement of dimension, form and position of cylindrical elements. Engineering Mechanics 12, 299–305 (2005)
[6] Lipinski, G., Priel, M., Vailleau, G.P.: European comparison of external diameter measurements of metallic wires. Metrologia 34, 235–240 (1997)

Real-Time Edge Detection Using Dynamic Structuring Element

M. Kawecki and B. Putz

Warsaw University of Technology, Faculty of Mechatronics, ul. św. Andrzeja Boboli 8, 02-525 Warszawa, Poland
mariusz.kawecki@neostrada.pl, bputz@mchtr.pw.edu.pl

Abstract. The morphological gradient is the classical, useful tool in image edge enhancement, but it can be insufficient in real-time applications due its complexity, as are different modifications of this method proposed in literature to obtain clearer edge information. In this paper a novel, simple and fast morphological edge detector is presented. It is based on the definition of a non-flat, dynamic structuring element and on the new definition of a simple morphology operation, useful as a generalisation of many image processing operations. The several results of the algorithm's application are presented, as along with the results of its implementation in a real-time IR and TV image fusion hardware system.

1 Introduction

Image edge detection is an important basis of analysing images and feature extraction [1]. Among classical differential methods we have simple linear filters, which are less or more noise sensitive, such as Prewitt and Sobel operators, and Canny edge detector which is reckoned to be the best, but with significant complexity. Mathematical morphology [2], developed from the set theory, offers less conventional methods based on nonlinear transformations and constitutes an important area of research in image processing.

In greyscale morphology [3] two basic operations for 2D image are used – erosion defined as operation minimum and dilation defined as maximum:

$$L_E(x, y) = \min_{m,n \in SE} L(m,n) \qquad L_D(x, y) = \max_{m,n \in SE} L(m,n) \tag{1}$$

where $L(x, y)$ is the greyscale intensity of pixel (x, y) and SE denotes the structuring element, that is the small two-dimensional set of points enclosing the area of image analysis, with an anchor point (the origin) coinciding with the analysed pixel (x, y). For example – to perform erosion operation – if the structuring element (SE) moves over the image, the minimum intensity of pixels covered by SE replaces the value of image pixel under the anchor point.

To detect the edges of the image, the classical morphological gradient [4] is used, defined as the difference between dilation and erosion:

T. Březina and R. Jabloński (eds.), *Mechatronics 2013*,
DOI: 10.1007/978-3-319-02294-9_60,

$$G(x, y) = L_D(x,y) - L_E(x,y). \quad (2)$$

This defined gradient represents the maximum variation of the greyscale intensities within the elementary neighbourhood. It requires the determination of two extreme intensities in the neighbourhood of every image pixel. The internal and external morphological gradients are also defined analogously. Some additional operations are usually necessary after dilation and erosion computing.

The shape and size of SE plays a crucial role in morphological operations. Thus different modifications of morphological gradient are proposed to obtain more abundant, pinpointed edge information and/or better noise restraining.

Some of these methods are based on multi-structure elements, for example in [5] eight different directional structure elements are constructed in the same square window to calculate the final weighted edge. Other methods use an adaptive structuring element, which changes during image scanning. In [6] the adaptive SE is defined by two fuzzy parameters: the degree of resemblance and degree of membership, to locate the pixels on the same feature with a central pixel and construct the optimal shape SE. Another adaptive SE is proposed in [7]. Here the shape of the SE is constant, but its size depends on the local image area: in the non-edge region (the methods of looking for it are defined) the SE is reduced to suppress blurring of the edge, otherwise SE is enlarged to enhance the edge details.

In the solution presented in [8] the values of pixels covered by SE are sorted to calculate the new values of pixels using differences between the maximum and minimum in pairs of values; the mean and standard deviation is then calculated to realize a non-edge suppression and edge enhancement. Another new approach, also based on dilation and erosion operations, is presented in [9–10]. The proposed multi-scale methods employ additional opening-closing morphology operators and can get clearer edges. The weighted fusion of multi-structure and multi-scale morphology constitutes the solution presented in [11]. Yet another kind of morphology edge detector is proposed in [12] in the form of a soft morphological method which can attain a single-pixel-wide edge. However it uses additional hard-core elements and loop performing, so its time consuming nature makes it impractical in real-time requirements.

In contradiction to the above methods, this paper presents a novel fast edge detection algorithm based on a dynamic structuring element and dedicated to real-time applications. In section 2 the definition of the simple morphological operation is proposed as a generalisation of morphological and other image processing operations. The idea of edge detection using a non-flat dynamic structuring element is presented in section 3. The results and applications are discussed in section 4 and conclusions are given in section 5.

2 Simple Morphological Operation

The minimum and maximum operations (1) used for erosion and dilation performing do not fill the morphological approach to greyscale images. To the minimum

and maximum operations upgrade in a natural way, we propose generalisation of the SE definition as well as generalisation of the morphological operation.

In section 1 different structuring elements have been mentioned; standard and adaptive. It was assumed traditionally that SE is a *flat* structuring element, defined only by the set of points composing its 2D shape. Non-flat SEs [3] have greyscale values that vary over their domain of definition, thus more general definitions of erosion and dilation are known [1].

The non-flat SE will be used also in our considerations. Let us introduce the following definition.

Definition 1
Non-flat dynamic structuring element denotes an SE whose greyscale values can vary over their domain of definition as SE is scanning the image.

On this basis we propose a generalised morphological operation.

Definition 2
A *simple morphological operation* denotes an image transformation in which every pixel (*x, y*) is related to the intensity value *L*(*x, y)* defined in greyscale according to the formula (3)

$$L(x, y) = f\left(L(m, n) \circ SE\right) \tag{3}$$

where:

- f – function defining simple morphology operation, determined for every image pixel.
- SE – any type, in general: non-flat dynamic structuring element.
- $L(m, n)$ – the intensity of image pixel (m, n) covered by SE, i.e. the structuring element anchored at (x, y) encloses the domain of function f to the pixels covered (indicated) by SE.
- „$\circ$” – any two-argument operation defined by the intensity values of pixels covered by SE (first argument) and values of points of SE (second argument).

In particular, the "$\circ$" operation can be empty, which means that values of SE points are not significant. On the other hand, the "$\circ$" operation can be defined as a matrix product or a matrix convolution, where the first matrix is defined by the image area covered by SE and the second matrix is composed of SE values.

This defined simple morphological operation is a very catch-all idea. It incorporates classical, well-known morphological operations and operations not identified with morphology, such as different types of linear filters. We can construct

non-flat SEs for contrast enhancement with others used as edge detectors. The last one is considered below as the topic of the paper.

3 Edge Detection by Simple Morphological Operation

A morphological gradient is used to emphasise image edges as boundaries between regions with different intensity. To highlight sharp greyscale transition within the neighbourhood of the analysed pixel we propose a generalisation of the morphological gradient. The idea is the use of a non-flat dynamic structuring element and a simple morphological operation.

To do it, let us take a non-flat SE filled by values of absolute differences between the intensity of the analysed pixel and the intensities of pixels covered by SE. For example, the neighbourhood of the image pixel of intensity value 117 (Fig. 1a) produces a SE with greyscale values as in Fig. 1b.

a)

141	152	106
74	117	151
39	58	114

b) **SE** =

24	35	11
43	0	34
78	59	3

Fig. 1 a) Analysed image pixel (117) and its neighbourhood covered by SE; b) the values calculated for non-flat SE

Thus for every pixel (m,n) of the image the values of non-flat SE are computed according to (4):

$$\{x = m-1, m, m+1;\ y = n-1, n, n+1:\ SE(x,y) = \left|L(x,y) - L(m,n)\right|\} \tag{4}$$

So the SE values vary as SE scans across the image. Thus, according to Definition 1, we can say that it is a non-flat dynamic structuring element.

To enhance the image edge, the "$\circ$" operation and function *f* used in formula (3) must also be defined:

- The idea of the "$\circ$" operation is to replace image pixel intensity with the value of the corresponding point of SE.
- The *f* function can be calculated as a maximum value of SE points or a mean value of SE points or a sum of the values of SE points.

As a result, we propose the following three definitions (5)-(7).

$$L_{K\max}(x,y) = \max_{m,n} SE(m,n) \tag{5}$$

$$L_{Ksum}(x, y) = \sum_{m,n} SE(m, n) \tag{6}$$

$$L_{Ksr}(x, y) = \frac{\sum_{m,n} SE(m, n)}{m + n} \tag{7}$$

The idea of formulas (5)–(7) is common: the analysed pixel is related to the difference between its intensity and intensity of its neighbourhood covered by SE – calculated in some way. A bigger intensity difference results in a clearer edge at the pixel of interest. We say that formulas (5)–(7) define the property of the biggest intensity difference characteristic for image edges. Additionally, the sum of intensities obtained during the workings of the algorithm may be used – in comparing with analogous sums for neighbour pixels – to check to what degree the analysed pixel belongs to the edge. It should be noted that the mean value in formula (7) needs to be calculated without the value of middle element, because this value is by definition equal to zero.

4 Results and Applications

The results of the new algorithm for the "pepper" image and "cameraman" image are presented in Fig. 2 and Fig. 3, with the different cases of formulas used. Clear and subtle edges can be obtained with formula (5), which indicates the direction of the maximum intensity gradient, and thus directly points to the edge. Although different in nature, good results were also obtained by simply calculating the sum or mean intensity of neighbours (formulas 6–7) with the necessary scaling of the results to enhance the differences between pixel intensities. The experiments have proved that, alternatively, with better effects, we can square the mean value and cut the result if it exceeds the maximum intensity value (what happens very rarely for typical, real images). To speed up the algorithm, we can use 4-neighbourhood instead of 8-neighbourhood in formulas (6–7), which does not significantly reduce the edge quality.

It is worth comparing our results with those presented in other papers. We can find the results of edge detection for "cameraman" image in [5], [8] and [11] (together with poor results for standard simple edge detectors, which are not therefore replicated in this paper). We can find the results of edge detection for "pepper" image in [10] and [12]. We can notice, however due to cursory observation, that our results are at least not inferior to most results in cited papers, despite our method being very simple and fast.

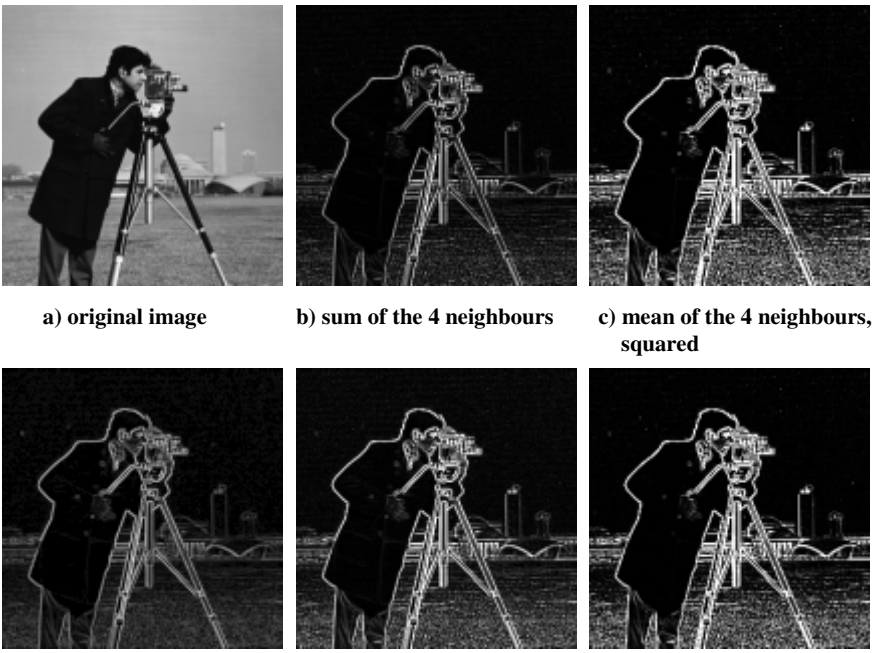

a) original image **b) sum of the 4 neighbours** **c) mean of the 4 neighbours, squared**

d) maximum of the 8 neighbours **e) sum of the 8 neighbours** **f) mean of the 8 neighbours, squared**

Fig. 2 The original "cameraman" image and results of edge detection with different formulas of the new algorithm

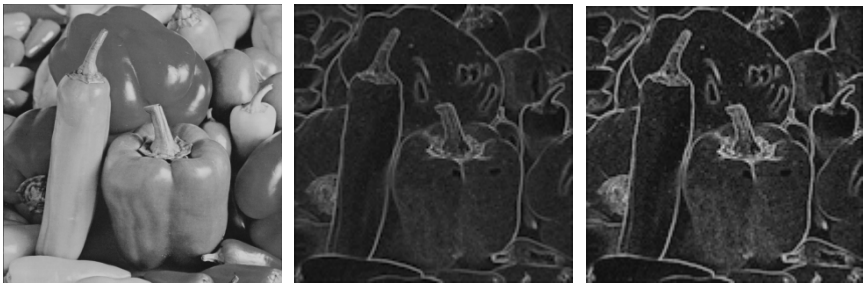

a) original image **b) sum of the 4 neighbours** **c) mean of the 8 neighbours, squared**

Fig. 3 The original "pepper" image and results of edge detection with different formulas of the new algorithm

The presented algorithm has been used in a real-time IR and TV image-fusion monitoring system, which has been built as a prototype and consists of a hardware solution based on a single FPGA chip and the designed software [13]. Edge extraction before image registration turned out to be necessary because it was shown to improve the result of the image-alignment process.

The several edge detectors (Harris detector, simplified Canny algorithm, different modifications of morphological gradients) have been accommodated and tested, and applied to both infrared and visible images. We have got unexpectedly good results of the simple algorithm presented in this paper, with successful edge enhancement both in TV and IR images and, consequently, image alignment (Fig. 4). After many experiments, the squared and truncated mean of the 8-neighbours has been used. To speed up the calculations, the mean value of intensities has been checked – if it is greater than 15, the final value is equal to 255, otherwise the mean value is multiplied by itself (assuming 8-bit greyscale images).

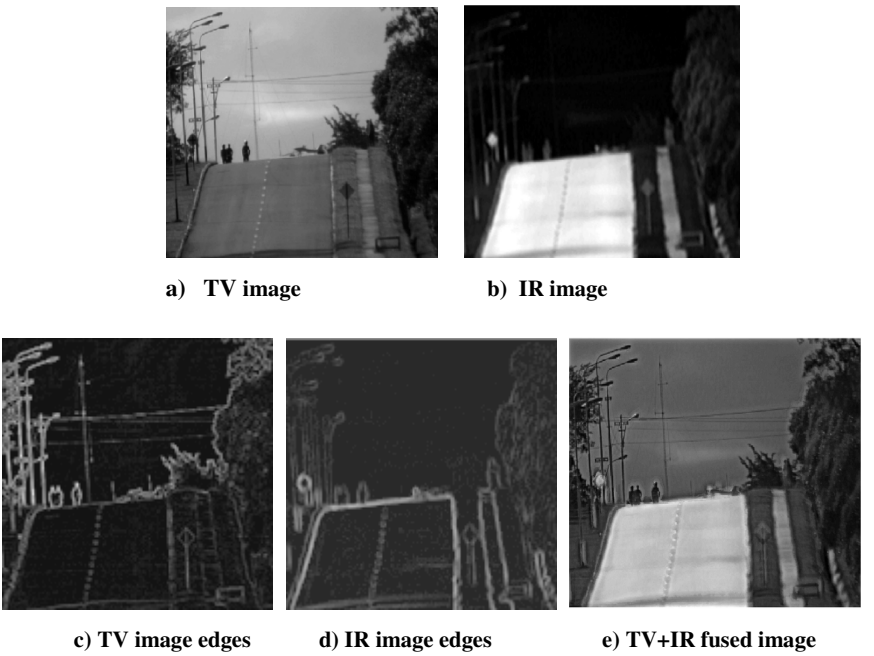

a) TV image **b) IR image**

c) TV image edges **d) IR image edges** **e) TV+IR fused image**

Fig. 4 The results of edge extraction by the new algorithm (using mean of the 8 neighbours, squared) for the visible and infrared images and the final result of fusion

5 Conclusions

In contradiction to the morphological gradient, the edge detection algorithm presented in this paper does not need to use the dilation and erosion operation. Thus the search for maximum and minimum intensity values, which must be done for every image pixel in the area covered by SE, is not necessary with our algorithm, assuming the use of formulas (6)–(7), which only need to sum several little values (in other known algorithms such a summing operation is performed as a supplement to the erosion and dilation operations necessary for every pixel). Thus the

algorithm is very fast indeed. It has been proved to be very useful in real-time applications and very simple in FPGA implementation.

References

[1] Gonzales, R.C., Woods, R.E.: Digital Image Processing, 3rd edn (2008)
[2] Serra, J.: Image Analysis Using Mathematical Morphology. Academic Press, London (1982)
[3] Sternberg, S.: Grayscale morphology. Computer Vision, Graphics and Image Processing, 333–355 (1986)
[4] Rivest, J.F., Soille, P., Beucher, S.: Morphological gradients. J. Electronic Imaging 2(4), 326–336 (1993)
[5] Zhao, Y., Gui, W.: Edge Detection Based on Multi-Structure Elements Morphology. In: Proceedings of the 6th World Congress on Intelligent Control and Automation, pp. 9795–9798 (2006)
[6] Lü, Z., Wang, F., Chang, Y., Liu, Y.: Edge Detection Based on Adaptive Structure Element Morphology. In: Proceedings of the IEEE International Conference On Automation and Logistics, pp. 254–257 (2007)
[7] Xiuli, W.: Image Edge Detection Based on Adaptive Selection the Value of Structure Element of Mathematical Morphology. In: 2009 International Conference on Electronics Computer Technology, pp. 197–199 (2009)
[8] Xiao-Qiang, Y., Rang-Ding, W., Ji-Long, B., De-Chun, Z.: A New Edge Detector Based On Morphology. In: 2010 International Conference on Multimedia Technology, pp. 787–790 (2010)
[9] Xia, P., Gong, G., Liu, X., Xiang, X.: Image Edge Detection Based on Multi-scale Morphological Operator. In: World Automation Congress, pp. 27–30 (2010)
[10] Tao, W., Na, W.: Multi-scale Mathematical Morphology based Image edge detection. In: 2012 International Conference on Intelligent Systems and Engineering Applications, pp. 1060–1062 (2012)
[11] Li, C., Zhao, L., Sun, S.: An Adaptive Morphological Edge Detection Algorithm Based on Image Fusion. In: 2010 3rd International Congress on Image and Signal Processing, pp. 1072–1076 (2010)
[12] Junna, S., Feng, J.: An Algorithm of Edge Detection Based on Soft Morphology. In: 2012 IEEE 11th International Conference on Signal Processing, pp. 166–169 (2012)
[13] Bartyś, M., Putz, B., Antoniewicz, A., Zbrzeżny, Ł.: Real-time Single FPGA-Based Multimodal Image Fusion System. In: 2012 IEEE International Conference on Imaging Systems and Techniques, pp. 460–465 (2012)

Investigation Method for the Magnetoelastic Characteristics of Construction Steels in Nondestructive Testing

D. Jackiewicz, R. Szewczyk, J. Salach, A. Bieńkowski, and K. Wolski

Warsaw University of Technology, Faculty of Mechatronics, św. A. Boboli 8,
02-525 Warsaw, Poland
d.jackiewicz@mchtr.pw.edu.pl

Abstract. Paper presents new, reliable method of testing the magnetoelastic properties of construction steels. In this method frame-shaped samples are used. Moreover, due to special, force reversing mechanism, tensile stresses may be generated in the sample with use of compressive force produced by the oil hydraulic press. Paper presents also the result of analyze of flux density and stress distribution in frame-shaped sample during the tests. Moreover, developed method was validated during the investigation of magnetoelastic properties of C45 construction steel. As a result it was confirmed, that presented method may be applied for magnetoelastic characterization of construction steels for nondestructive testing.

1 Introduction

For the first time, the magnetoelastic effect in steel was reported by Villari in 1865 [1]. Since this time, this effect is intensively investigated, both from theoretical and application point of view.

Magnetoelastic effect is important from theoretical point of view, due to the lack of holistic, quantitative model of interaction of magnetic and mechanical processes [2]. This model is especially important for development of novel, functional materials, such as amorphous [3] or nanocrystalline [4] magnetic materials. On the other hand, practical applications of magnetoelastic effect covers development of robust stress and force sensors [5] and stress assessment in the base of changes of magnetic properties of steel [6].

Due to possibility of this stress assessment, magnetoelastic effect opens very promising ways of development of non-destructive testing methods. It should be indicated, that changes of flux density B as the function of applied stresses σ are often monotonous. As a result it is possible to estimate the value of stresses in the material on the base of measurements of its magnetic characteristic. In addition such measurements are relatively simple and nondamaging for the sample.

T. Březina and R. Jabloński (eds.), *Mechatronics 2013*,
DOI: 10.1007/978-3-319-02294-9_61,

On the other hand, significant barrier in industrial application of magnetoelastic effect is lack of information about magnetoelastic characteristics of different types of construction steels. To create the database covering wide variety of steels, the unified method of testing the steel samples has to be developed. Frame-shaped samples based methodology presented in the paper fills this gap in knowledge.

2 Tested Samples

Figure 1 presents the general view of frame-shaped sample suitable for magnetoelastic characteristics investigation. This sample is 200 mm long and 2 mm thick. Magnetizing and sensing windings are wound on columns of the sample. The length of the windings is 60 mm. It should be stressed, that both magnetizing and sensing windings have to be wound on each column of the sample. Moreover, it is highly recommended to place sensing winding under the magnetizing winding. Number of turns of magnetizing windings is connected with expected coercive field H_c of the tested steel. Typically it varies from 300 to 700 turns for each column. Number of turns of sensing winding is determined by saturation flux density B_s of the steel and typically should be 200 turns for each sample's column.

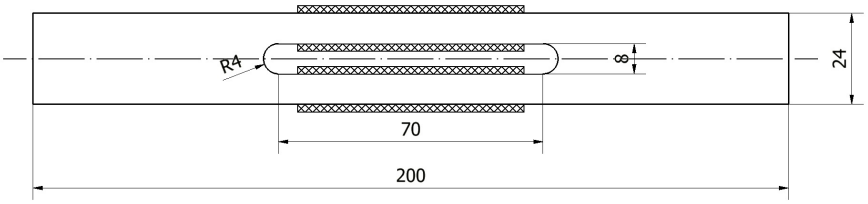

Fig. 1 Frame-shaped sample for magnetoelastic tests of construction steels

3 Mechanical Setup

Mechanical force reversing system is presented in figure 2a, whereas the oil hydraulic press based system providing the compressive force F is presented in figure 2.b.

Force reversing system is made of non-magnetic materials, mostly duralumin. Moreover, special grooves are made in the surface of lockers (2) to prevent sliding of tested sample (1). The main screw (4) in oil press system gives possibility of adjustment of experimental setup accordingly to the length of tested sample. Value of generated force F is measured by high accuracy strain-gauge sensor (5).

Developed oil press system may provide compressive force up to 100 kN. Such force can generate stresses up to 3000 MPa in the columns of the sample presented in figure 1. Such range of stresses is sufficient to test for many kinds of steels.

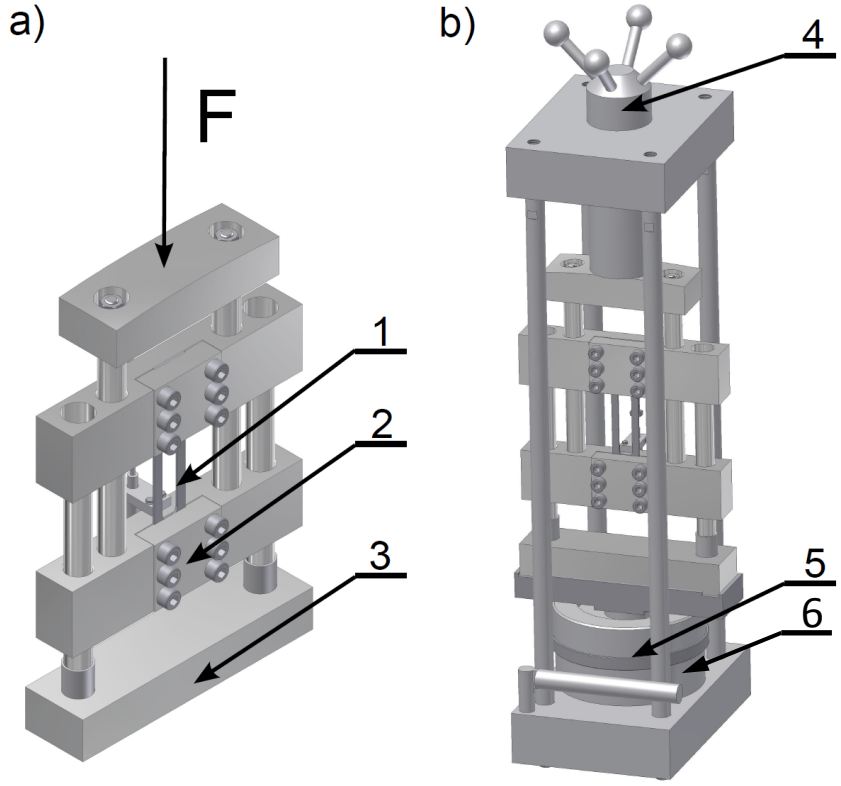

Fig. 2 Mechanical system for magnetoelastic investigation: a) force reversing system, b) oil hydraulic press based system providing the compressive force F, (1) tested frame-shaped sample, (2) locker, (3) nonmagnetic base, (4) main screw, (5) strain-gauge based force sensor, (6) piston oil hydraulic press

4 Results of Modeling

From the point of view of magnetoelastic effect analysis, providing the uniform distribution of both flux density B as well as stresses σ in the sample under investigation is the most important task. To verify this uniformity, the Finite Element Method based simulations were done using the Matlab software.

Figure 3 presents the results of simulation of flux density B distribution in frame-shaped sample with constant magnetic amplitude permeability μ_a=1000.

During this simulation it was assumed, that both columns of the frame-shaped sample are magnetized by magnetizing winding with 60 mm length.

Results of finite elements method based simulations of distribution of stresses in frame-shaped sample subjected to tensile force F is presented in figure 4. In this figure both parallel *y* and perpendicular *x* component of stresses σ is presented.

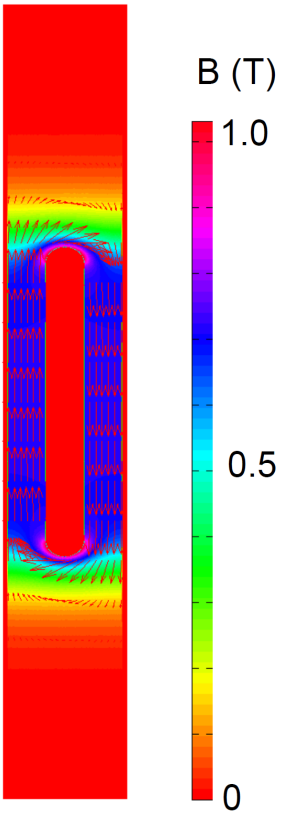

Fig. 3 Results of finite elements method based simulations of flux density B distribution in frame-shaped sample with constant magnetic amplitude permeability

The results presented in figure 3 indicated, that highly uniform distribution of flux density B is achieved in both columns of the sample. Some nonuniformities occur in columns junctions. These nonuniformities have to be considered during calculation of the magnetic path length. Preferably "Calculation of the effective parameters of magnetic piece parts" standards [7] have to be used for this calculations.

Results of mechanical simulations indicated in figure 4 confirms, that only tensile stresses occur in columns of the frame-shaped core. However, some nonuniformities in columns measured in x direction occurs. These nonuniformities don't exceed 10%. As a result value of tensile stresses in the column may be averaged. In addition it should by indicated, that stress distribution in column's junction is highly nonuniform. However, the length of junctions is significantly smaller than the column's length. As a result, the stress nonuniformities in column's junctions can be neglected.

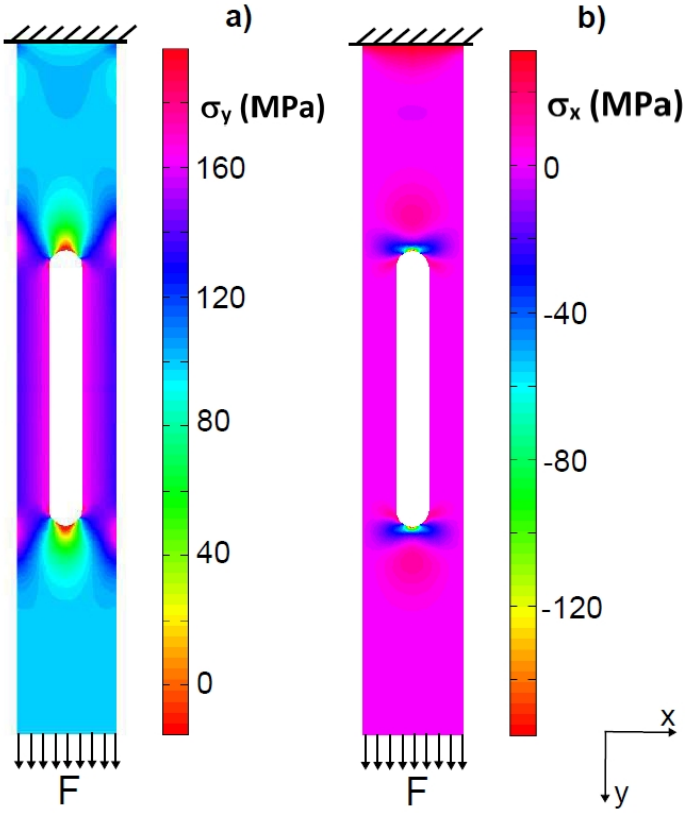

Fig. 4 Results of finite element method based simulations of distribution of stresses in frame-shaped sample subjected to tensile force F = 5 kN: a) normal y component of stresses σ, b) perpendicular x component of stresses σ

5 Experimental Results

For experimental validation of developed method of testing the magnetoelastic properties of steels, measurements of changes of magnetic properties of frame-shaped sample made of C45 construction steel subjected to tensile stresses were carried out. These measurements were performed with use of KEPCO BOP36-6 voltage-current converter and Lakeshore 480 fluxmeter. Whole system was controlled by data acquisition card produced by National Instruments. Moreover, hysteresis graph software was developed with use of LabView. Voltage sine wave generated by the data acquisition card drives voltage/current converted Kepco BOP 36, with current output connected to the magnetizing winding of the investigated core. Measuring winding is connected with Laleshore 480 fluxmeter, which measure flux density B in the sample. Voltage output of the fluxmeter is connected to the data acquisition card.

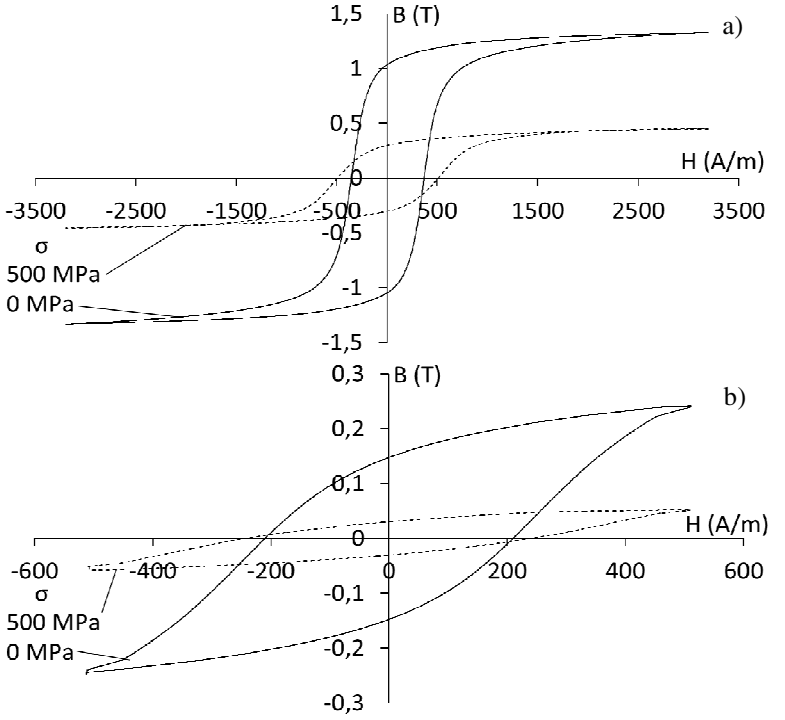

Fig. 5 The influence of tensile stresses σ up to 500 MPa on the shape of B(H) hysteresis loop of frame-shaped sample made of construction steel C45: a) for the amplitude of magnetizing field H_m = 3450 A/m, b) for the amplitude of magnetizing field H_m = 510 A/m

The influence of tensile stresses σ on the shape of B(H) hysteresis loop of frame-shaped sample made of construction steel C45 is presented in figure 5. It may be observed, that under the tensile stresses σ up to 500 MPa, shape of the magnetic hysteresis loop changes significantly. For amplitude of magnetizing field H_m = 3450 A/m, as it is presented in figure 5a, the flux density B under such stresses decreases about 65%, whereas 38% increase of coercive force H_c was observed. On the other hand, for lower values of amplitude of magnetizing field H_m, the flux density B under stresses decreases more, whereas coercive force H_c is nearly constant. Results presenting this phenomenon for the amplitude of magnetizing field H_m = 510 A/m are presented in figure 5b.

Figure 6 presents $B(\sigma)_{Hm}$ characteristics of frame-shaped sample made of construction steel C45. On these characteristic the maximum *B* may be observed. This maximum, called the Villari reversal point [8] is connected with minimal value of total free energy of sample subjected to both mechanical stresses and magnetizing field. It should be stressed, that $B(\sigma)_{Hm}$ characteristics may be treated as a standard of presentation of magnetoelastic properties of construction steels. Such standard would be especially useful from the point of view of mechanical stress assessment during non-destructive testing of construction elements.

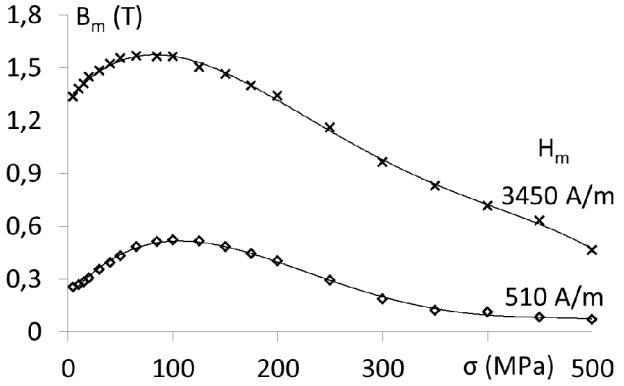

Fig. 6 Magnetoelastic $B(\sigma)_{Hm}$ characteristics of frame-shaped sample made of construction steel C45

6 Conclusions

Method of magnetoelastic investigation presented in the paper creates novel possibility of description of stress dependences of magnetic characteristics of construction steels. Moreover, due to special mechanical reversing system, tensile stresses in the frame-shaped samples may be generated with use of compressive forces from the oil hydraulic press.

Results of simulation made with use of finite elements method confirms uniform distribution of flux density B in the columns of frame-shaped sample used for magnetoelastic tests. Moreover, simulations confirmed the lack of perpendicular stresses in the core under stresses. On the other hand, some nonuniformities in stress distribution in the core were detected. However, these nonuniformities may be effectively averaged.

Results of experimental tests of the magnetoelastic properties of C45 construction steel validated proposed methodology of magnetoelastic investigation. It was observed, that under the tensile stresses σ up to 510 MPa, for amplitude of magnetizing field H_m = 3450 A/m, the flux density B under such stresses decreases about 65%. However the coercive force H_c increases 38%.

Presented frame-shaped samples based methodology opens the possibility of filling the gap of knowledge about magnetoelastic characteristics of different types of construction steels. As a result, the database covering wide variety of steels may be developed and used in non-destructive tests of construction elements.

Acknowledgments. This work was partially supported by The National Centre of Research and Development (Poland) within grant no. PBS1/B4/6/2012. Calculations for the modelling were made in the Interdisciplinary Centre for Mathematical and Computational Modelling of Warsaw University, within grant G36-10.

References

[1] Bozorth, R.M.: Ferromagnetism. D. Van Nostrood Company, New York (1956)
[2] Jiles, D.C.: Introduction to Magnetism and Magnetic Materials. Chapman & Hall, London (1998)
[3] Stokłosa, Z., Rasek, J., Kwapuliński, P., Badura, G., Haneczok, G., Pająk, L., Lelątko, J., Kolano-Burian, A.: Magnetic, electrical and plastic properties of $Fe_{76}Nb_2Si_{13}B_9$, $Fe_{75}Ag_1Nb_2Si_{13}B_9$ and $Fe_{75}Cu_1Nb_2Si_{13}B_9$ amorphous alloys. Journal of Alloys and Compounds 509(37), 9050–9054 (2011)
[4] Bieńkowski, A., Szewczyk, R., Kulik, T., Ferenc, J., Salach, J.: Magnetoelastic properties of HITPERM-type $Fe_{41.5}Co_{41.5}Cu_1Nb_3B_{13}$ nanocrystalline alloy. Journal of Magnetism and Magnetic Materials 304(2), e624–e626 (2006)
[5] Bieńkowski, A., Szewczyk, R., Salach, J.: Industrial Application of Magnetoelastic Force and Torque Sensors. Acta Physica Polonica A 118, 1008–1009 (2010)
[6] Atherton, D.L., Coathup, L., Jiles, D.C., Longo, L., Welbourn, C., Teitsma, A.: Stress induced magnetization changes of steel pipes-Laboratory tests. IEEE Transactions on Magnetics 19(4), 1564–1568 (1983)
[7] International Electrotechnical Commision (affiliated to the International Organization for Standardization - ISO), Calculation of the effective parameters of magnetic piece parts, Publication 205, Geneve, Suisse 1st edn. (1966)
[8] Bieńkowski, A.: Magnetoelastic Villari effect in Mn–Zn ferrites. Journal of Magnetism and Magnetic Materials 215-216, 231–233 (2000)

Testing of Automotive Park Assistant Control Unit by HIL Simulation

P. Krejci

Brno University of Technology, Faculty of Mechanical Engineering,
Institute of Solid Mechanics, Mechatronics and Biomechanics, Technicka 2896/2,
616 69, Brno, Czech Republic
krejci.p@fme.vutbr.cz

Abstract. The paper deals with Hardware in the Loop (HIL) testing of automotive park assistant control unit (PDC). In case of long-term control unit testing it is impractical to use real ultrasonic sensor and manual positioning of the obstacle. Therefore the project is focused on replacement of ultrasonic parking sensors with simulations of their behavior and virtual obstacle simulation with positioning of the obstacle behind the virtual vehicle. In the project four ultrasonic parking sensors of PDC are substitute with HIL simulation which communicates with control unit identically to real sensor during positioning of virtual (simulated) obstacle. The HIL solution was tuned on the project of car Fabia Facelift. Based on the verification of the functionality the HIL simulator is included in the standard test of the vehicle components.

1 Introduction

Development of electronics devices is accompanied by the need to test the functionality of the product during the development phase and during operational implementation (see ref. [2] and ref. [4]). Especially, development of electronic control units (ECU) for the automotive industry requires time-consuming functional testing in all possible operating and faulty modes of vehicle. It is often impossible to test ECU on the real vehicles in real traffic. Therefore, during the development and testing of ECU not only in the automotive industry, HIL simulation method (see ref. [3]) can be used to verify the real behavior of the control unit without risk of damage or destruction of the controlled system by unexpected or faulty behavior of the control unit. The real control unit in form of the physical hardware is connected to the computer (instead of real controlled system) where the controlled system is simulated using various techniques. Inputs and outputs of the control unit are usually signals from sensors and actuators. These signals are generated and processed by plant simulation model in case of HIL testing. For the correct behavior of HIL simulation it is necessary to provide the same I/O signals in terms of type and level with real sensors and actuators.

T. Březina and R. Jabloński (eds.), *Mechatronics 2013*,
DOI: 10.1007/978-3-319-02294-9_62,

In case of HIL testing of PDC it is necessary to convert digital serial communication from TTL logic on the side of the computer to the digital level typical for automotive application of 10V on the side of PDC control unit.

2 HIL Test of PDC

Signal processing and communication with the sensors is performed for all simulated sensors simultaneously. Therefore, hardware performing HIL testing of PDC should allow parallel processing of control (or communication) signals transmitted between the control unit and ultrasonic sensors. For this reason it was decided to use the hardware with FPGA technology allows parallel execution of code on hardware level.

The Compact RIO hardware from National Instruments has been chosen as HIL simulator for ultrasonic parking sensors. The Compact RIO is embedded hardware with real-time operating system and its chasse contains FPGA chip that can be defined by LabView software (see ref. [1]). The structure of HIL simulator is shown on Fig. 1.

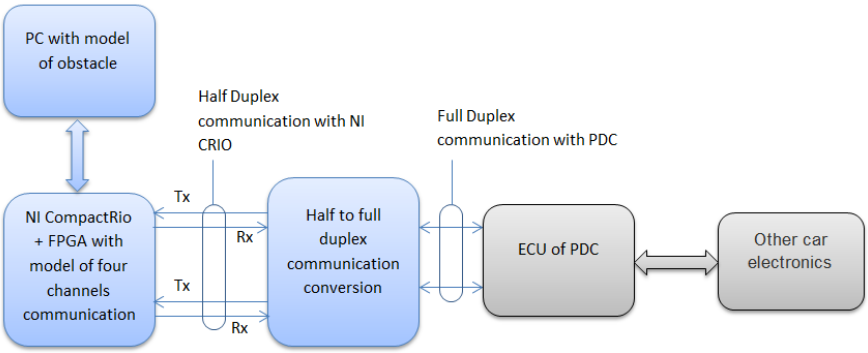

Fig. 1 PDC HIL simulation scheme

Ultrasonic sensors communicate with PDC digitally using one-wire bidirectional digital lines. In one direction, the ECU sends commands to the sensors. In opposite direction sensors send to the PDC digitized echo which corresponding to reflected signal from obstacles. Digital communication occurs at a voltage level of 10V. To work with the CompactRIO I/O module it is preferable to divide bidirectional communication to the two-wire with separate section for receiving and transmitting information to and from the sensor. To adjust the voltage levels to TTL and the transfer of one-wire to two-wire communication the custom electronic module has been made and was placed in front of the I/O module of CompactRIO.

The model of the virtual obstacle is prepared on the PC. The model calculates time of reflection of ultrasonic signal from virtual obstacle for each sensor. Those times are transferred to CompactRio Real-time processor via Ethernet communication and via PCI bus to FPGA where the communication model is programed.

The model of the communication receiving digital commands from ECU, generate response for commands and based on received times generate echo for each sensor line.

2.1 Model of Digital Communication between PDC and Sensor

The communication scheme is unknown and is copyrighted by PDC ECU producers; therefore the communication between sensor and PDC was recorded for real obstacles positioned behind the vehicle. As it was mentioned before the communication between sensor and PDC ECU is leads on one wire. Based on the measurement results it is very difficult to recognize the ECU and the sensor part of communication at it seems to be an essential part of the project. Example of communication is shown on Fig. 2 for sequence recognized as initialization and on Fig. 3 for sequence recognized as reset of the sensor.

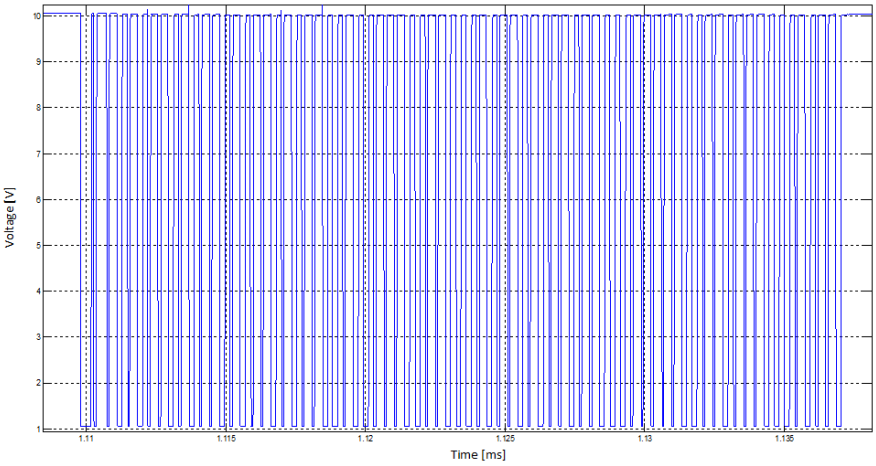

Fig. 2 Communication between PDC and ultrasonic sensor – Inicialization

Communication, that was recognized between the sensor and the control unit includes the initialization phase of communication, reset the sensor, active mode when sensor transmit the ultrasonic signal and wait for its receiving and passive mode when the sensor does not transmit any signal, just waiting for the reflected one from other sensors.

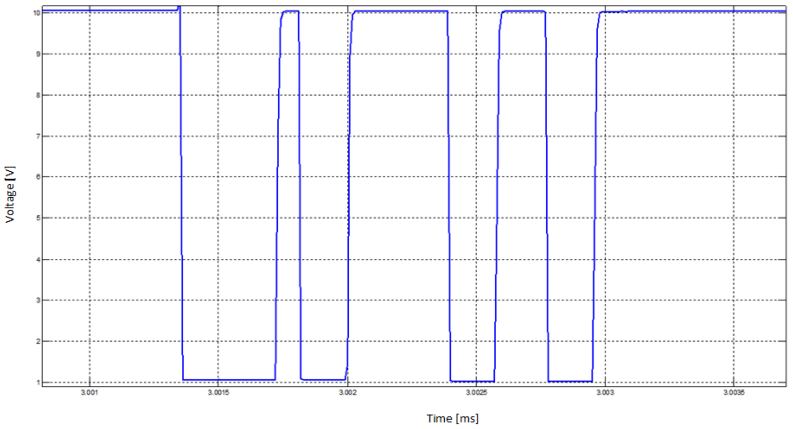

Fig. 3 Communication between PDC and ultrasonic sensor – Reset of the sensor

All four sensors communicated at the same time and it is necessary to simulate them on the hardware which allows parallel processing. The FPGA of the CompactRIO chassis allows parallel simulations in real time on hardware level. Each channel is simulated as state machine performing the specific action of simulated sensor for each recognized ECU command. Each state machine also receiving information about obstacle distance from the model of the virtual obstacle. The distance corresponds to time required to signal reflection. Schema of the state machine of one channel is shown on Fig. 4.

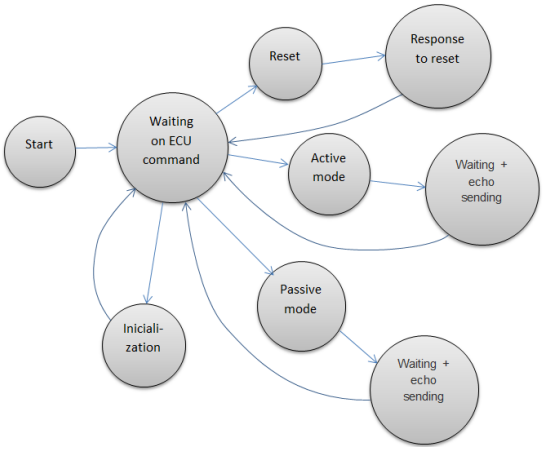

Fig. 4 Schema of one channel state machine

2.2 *Virtual Obstacle Model*

Model of the obstacle calculates for each simulated sensor the time in which the reflected echo will be received. The whole model is designed to respect the physical behavior of ultrasonic sensors, and can be divided into three parts:

- Calculation of the angle under which sensor "sees" the edges of the obstacle (see Fig. 5 for more details)

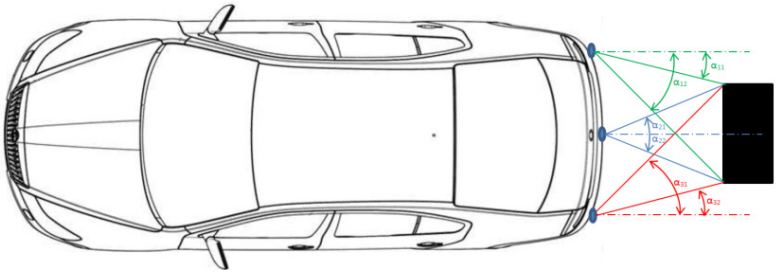

Fig. 5 Angle calculation

- Calculation of the impact area of the reflected signal. The reflected signal depends on directional characteristic of used sensors. The beam angle of ±60 degrees was used as simplification characteristic of the sensor.

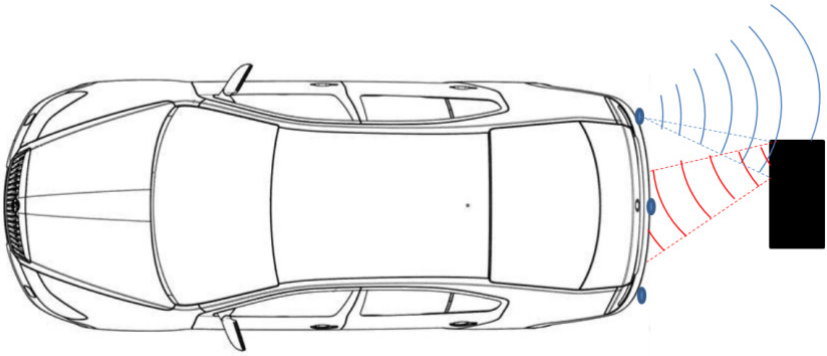

Fig. 6 Calculation of impact area

- Calculation of the distance between the sensor receiving the reflected ultrasonic signal and an obstacle. The distance is than recalculated to time corresponding to flight time of ultrasonic beam. This time corresponds to delay between PDC command and returned echo described above.

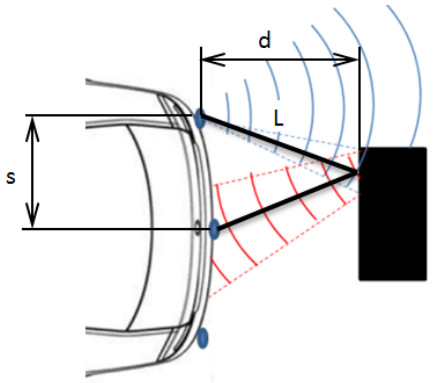

Fig. 7 Calculation of distance

The HIL simulator is shown on Fig. 8.

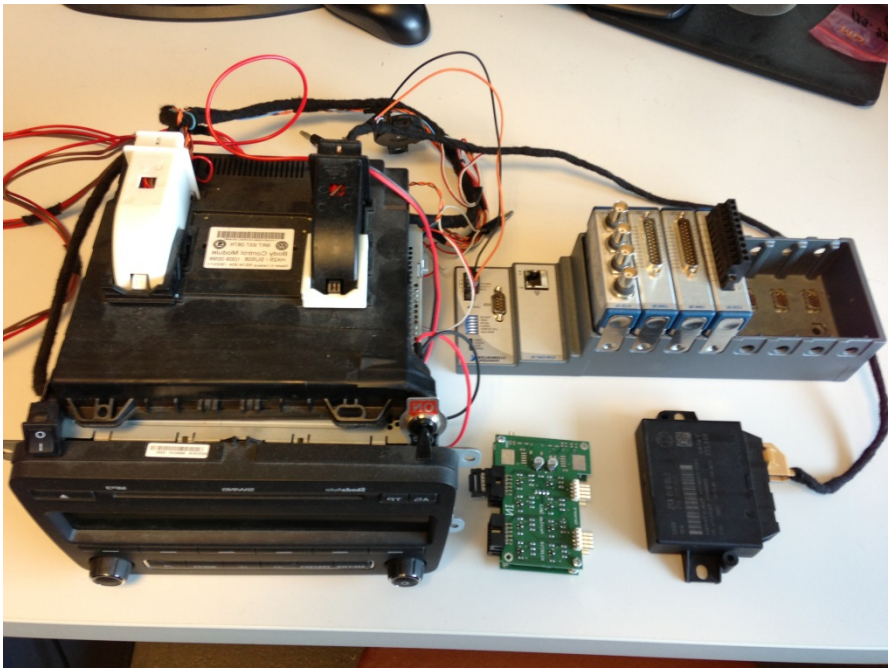

Fig. 8 PDC HIL simulator

3 Conclusions

The paper presents solution for long time testing of automotive control unit for park assistant. The solution presents substitution of four ultrasonic sensors with HIL simulation of sensor function. The HIL simulator allows defining the virtual obstacle and its position and distance behind the vehicle. The simulation has been tested on real car control unit and based on the result, the HIL simulator of automotive parking sensor will be used during test procedures of new developed cars. Based on the car equipment the solution can be easily modified for arbitrary number of parking assistant channels.

Acknowledgments. Published results were acquired with the support of the NETME Centre - New Technologies for Mechanical Engineering project no. CZ.1.05/2.1.00/01.0002.

References

[1] Krejci, P., Bradac, M.: Using LabVIEW for Developing of Mechatronic System Control Unit. In: 9th International Conference on Mechatronics Mechatronics: Recent Technological And Scientific Advances, Warsaw, Poland (2011) WOS:000309670600038

[2] Grepl, R., Lee, B.: Modeling, parameter estimation and nonlinear control of automotive electronic throttle using a Rapid-Control Prototyping technique. International Journal of Automotive Technology 11(4), 601–610, doi:10.1007/s12239-010-0072-7, WOS:000279216800018

[3] Isermann, R.: Mechatronic systems - Innovative products with embedded control. Control Engineering Practice 16, 14–29 (2008)

[4] Grepl, R., Lee, B.: Model Based Controller Design for Automotive Electronic Throttle. In: 8th International Conference on Mechatronics Recent Advances in Mechatronics: 2008-2009, Luhacovice, Czech Republic (2009) WOS:000277076900036

Coupled Thermal-Structural Transient Analysis of Pressure Sensors

R. Vlach

Brno University of Technology, Faculty of Mechanical Engineering, Technicka 2, 616 69, Brno, Czech Republic
vlach.r@fme.vutbr.cz

Abstract. This paper describes computational simulation of coupled analysis of pressure sensors during passage through the furnace. This analysis should show residual stress that is the problem for the next operation as pressure sensor. The software ANSYS/Workbanch was used for coupled thermal-stress analyses. The goal of the project is determination if the residual stress cause by temperature rise in the furnace has a significant impact on pressure sensor accuracy.

1 Introduction

A minimize of parasitic effect is in term of accuracy, linearity and repeatability of measuring crucial for final using. Hence, it would be appropriate to star research of mathematical modeling of accurate differential pressure sensors.

The software Ansys/Workbench [1], [2] is regarded as the appropriate tool in relation to the specified requirements. The software Ansys/Workbench is based on finite elements method (FEM) and can be used for modeling of various physical processes. The one possibility is coupled transient thermal-structural analysis. In the first step, transient thermal calculation is done. In the second step, results of thermal analysis are automatically converted to transient structural analysis as inputs. The advantage is that the same finite elements method model is used in both calculation steps. After whole calculation, the mechanical stress in dependence on time can be analyzed.

The mathematical model can be used for the analysis of temperature influence on ceramic joining of pressure sensors parts. The pressure sensors consist from two ceramic parts that are joined using glass film as is shown in figure 1. A glass film is applied on the basic ceramic body and has a thickness about 0.03 mm. A circular membrane of thickness from 0.18 to 0.62mm is placed on the ceramic body and is separated by the glass film. This assembly is inserted into the furnace. Two ceramic parts are joined by influence of high temperature in the furnace, where the glass film is melted. Thereafter, the glass film solidifies during cooling outside the furnace.

T. Březina and R. Jabloński (eds.), *Mechatronics 2013*,
DOI: 10.1007/978-3-319-02294-9_63,

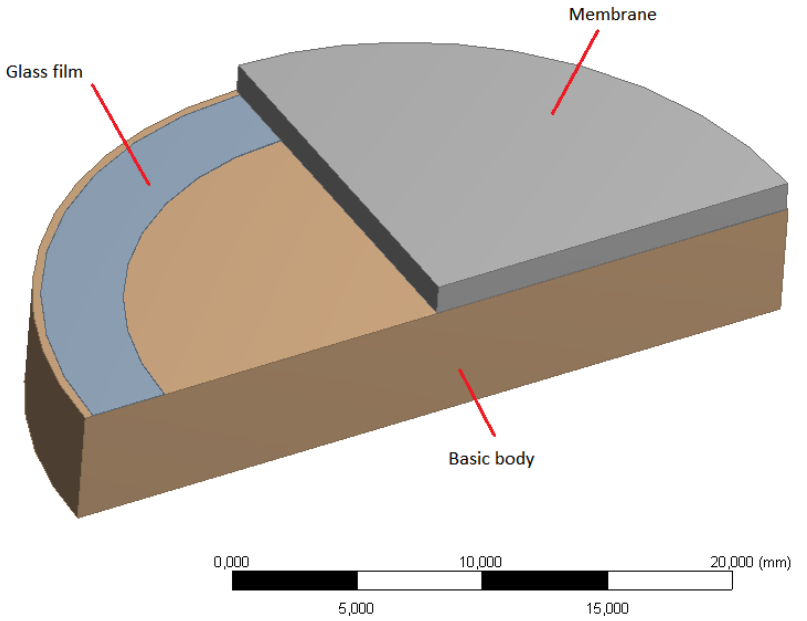

Fig. 1 Scheme of pressure sensor configuration

The problem with residual stress is cause by different material properties of the individual parts of pressure sensor mainly coefficients of thermal expansion. The residual stress can cause membrane curvature as shown by test samples of pressure sensors.

2 Computational Model

The computational model assumes symmetry of geometry and loads. Therefore, the pressure sensor computational model is modeled as axisymmetric. This will result in a shorter computing time.

The model geometry has to be filled by mesh of finite elements before calculation. A mapped mesh was used for basic ceramic body and membrane and six or eight elements were set across membrane thickness in dependence on its thickness. The problem was only with mesh of the glass film, because minimum of two elements across thickness is required for better accuracy. Elements used have mid nodes on the element edge for better calculation accuracy. The figure 2 shows the final mesh with pressure sensor assembly. The total elements number is from 9000 to 10000 in dependence on membrane thickness. It is with regard to the problem of adequate.

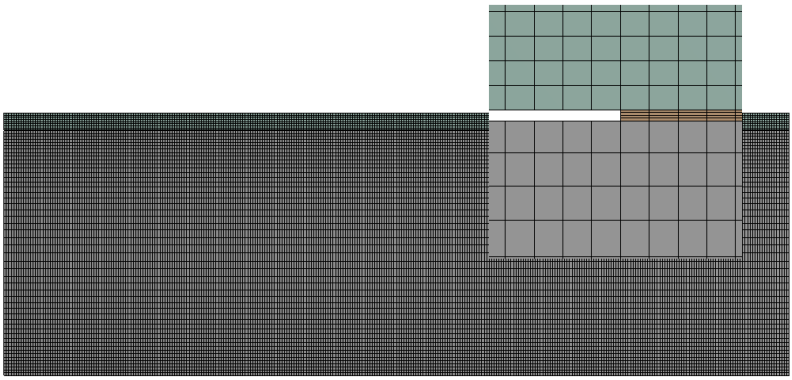

Fig. 2 Finite elements method model a pressure sensor assembly

Boundary conditions and material properties of individual parts are one of the most important aspects influencing the credibility of a mathematical model. In the case coupled thermal-structural analysis, we need to know both thermal and mechanical material properties of individual pressure sensor parts. Material properties used are summarized in the Table 1.

Table 1 List of material properties

Part/material	Thermal properties	Mechanical properties
membrane - Al2O3 sensor body - Al2O3	conductivity – 30,3 $Wm^{-1}K^{-1}$ specific heat - 900 $Jkg^{-1}K^{-1}$ density - 3880 kgm^{-3}	Elastic modulus - 300000Mpa Poison ratio - 0,3 Thermal expansion - 8,1e-6K^{-1}
glass	conductivity – 1,14 $Wm^{-1}K^{-1}$ specific heat - 750 $Jkg^{-1}K^{-1}$ density - 2200 kgm^{-3}	Elastic modulus – viz. graf Poison ratio - 0,25 Thermal expansion - 10e-6K^{-1}

Whereas the glass changes its physical state around temperature of 850°C and initial temperature after removal from the oven is 850°C, there is necessary to set the dependence of elastic modulus on temperature as is shown in figure 3. It is the simplest material model of phase change, which should include the real behavior of the glass material depending on temperature.

Boundary conditions are necessary part of setting a finite elements model. Boundary conditions for both thermal and mechanical analysis to be set, because it is coupled analysis.

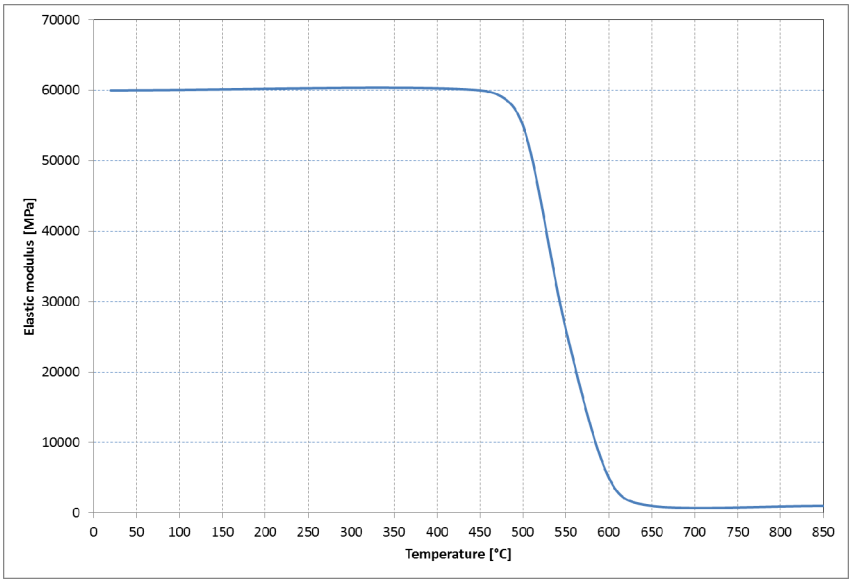

Fig. 3 Glass elastic modulus dependence on temperature

Boundary conditions for thermal part of analysis were:

- Simulation time 7500 seconds
- Heat transfer by radiation from all external surfaces
- Heat transfer by natural convection from all external surfaces.

A thermal contact between appropriate parts in the contact is necessary to be set for thermal analysis.

Boundary conditions for structural analysis are more complicated mainly contact setting. Importing of thermal analysis results as a boundary condition in structural analysis is relatively simple. The boundary condition displacement between the basic body and the support that is not included in the model, it is also easy to set.

As mentioned above, the mechanical contact between the glass film and the membrane is changed during coupled process in the furnace. Therefore, two types of contacts had to be set. First contact between the membrane and the glass film is a type of frictional that is active during the first nine substeps. The second contact is the type of bonded that is active from the tenth to the last substep. The activation and deactivation of contacts between the membrane and the glass film is realized using macro where is created or killed contact elements. The activation and deactivation of contacts between the membrane and the glass film is realized by macros where are contact elements created or killed. The deactivation of friction contact and the activation of bonded contact is corresponds the time when the glass film is melted and begins to solidify.

3 Computational Simulation

The whole calculation process is divided into three phases, which directly follow each other. In the first, the ambient temperature is set on the all parts of pressure sensor assembly. In the second, the heating in the oven to temperature 850°C is simulated. Finally, the cooling after removal from the oven is simulated. The time for heating and cooling was set five minutes and two hours respectively. It has proved sufficient.

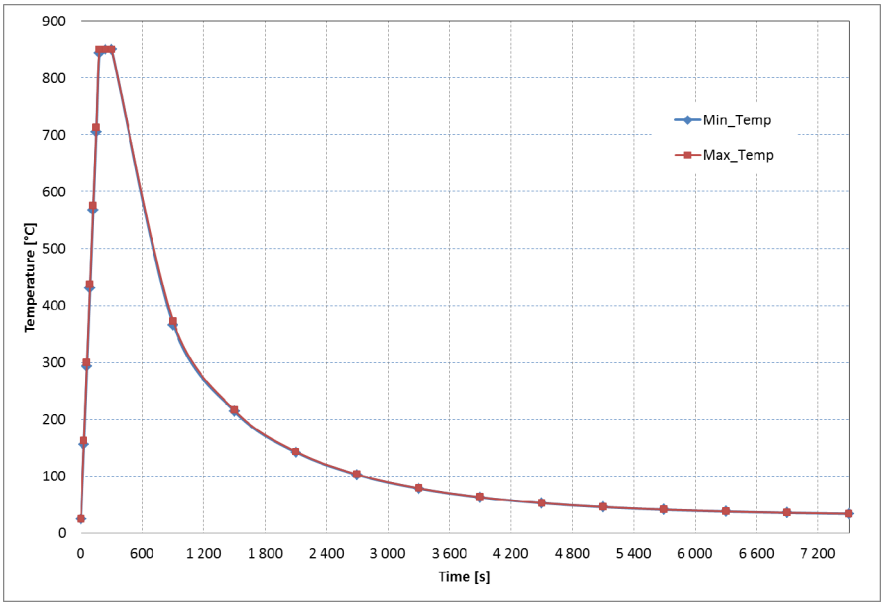

Fig. 4 Maximal and minimal temperature in time

As mentioned above, the first step of simulation is the thermal calculation. The calculation result is pressure sensor individual parts temperature in time. Figure 4 shows the timing of maximum and minimum temperatures, which were reached during the simulation. The temperatures in time correspond to the theoretical assumptions. The heating is linear, because it is an isolated system after inserting pressure sensors components to the oven. In contrast, the cooling process is exponential progress as expected. Differences between minimal and maximal temperature are very small. It indicates that the pressure sensor has almost homogenous temperature at each time. This is caused by small size and relatively high thermal conductivity of the materials used in comparison with cooling conditions.

The result of structural analysis calculation is deformation and stress distribution in pressure sensor individual parts in time. The deformation and stress are caused by changes in temperature and different thermal expansion of used

material. The maximal stress in the pressure sensor during heating and cooling is shown for main parts in the figure 5.

The stress value is relatively small for ceramic parts as shown in figure 5. The maximal stress is circa 90 MPa at time about 600 seconds. The residual stress in the membrane and basic body after cooling to ambient temperature is 41 MPa and 24 MPa respectively.

In contrast, the glass film is more stressed as shown figure 5. The maximal stress is at the same time as the case ceramic parts. It corresponds to the time of glass solidification. The residual stress in the glass film after cooling to ambient temperature is 78 MPa. This implies the possibility of cracking by comparison with glass-strength film.

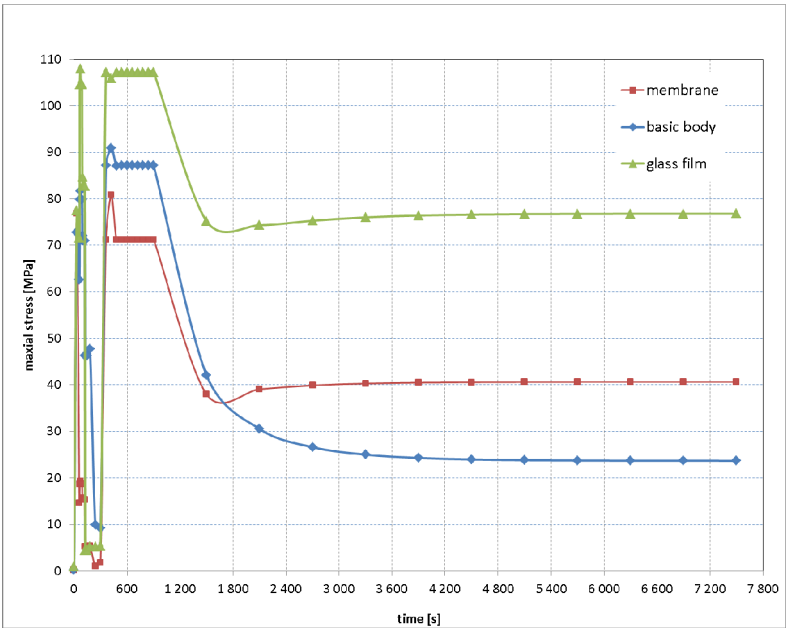

Fig. 5 Maximal stress in time of transient structural analysis

4 Conclusions

The result of coupled thermal-structural analysis shows the effect of technological process of pressure sensors manufacture, which is based on the passage furnace.

On the one hand, the simulation results indicate low stress and deformation to make pressure sensor with initial deflection of membrane. The effect of thickness of membrane should be tested in the following simulations.

On the other hands, the glass film is near to strength limit of used material. It indicated the possibility of glass film cracking during technological process

mainly after cooling to ambient temperature. This hypothesis is confirmed by many experiments.

The detailed model of glass solidification and influence of thermal contact parameters should be tested. However the essential change in the results should not occur.

Acknowledgment. This work was supported by Project FSI-S-11-15 "Design, testing, and implementation of control algorithms with use of nonlinear models of mechatronics systems." and FR-TI3/017 "Research of sensors for sensing low pressure and pressure in vacuum with digital interface for remote configuration and diagnostics".

References

[1] Vlach, R., Kadlec, J.: Design of Capsule Pressure Sensors Thermal Compensation. In: Recent Advance in Mechatronics, pp. 103–108. Springer, Heidelberg (2009) ISBN 978-3-642-05021-3

[2] Kadlec, J., Helán, R., Urban, F., Vlach, R., Vrba, R.: Temperature calibrated design of the optical pressure sensor capsule. In: Proceedings of the EDS 2008 Conference, Brno, Ing. Zdeněk Novotný CSc, pp. 1–6 (2008) ISBN 978-80-214-3717-3

[3] Kadirvel, K., Taylor, R., Horowitz, S., Hunt, L., Sheplak, M., Nishida, T.: Design and Characterization of MEMS Optical Microphone for Aeroacoustic Measurement. In: 42nd Aerospace Sciences Meeting & Exhibit, Reno, January 5-8 (2004)

[4] Švéda, M., Vrba, R., Beneš, P.: A System Architecture of Networked Pressure Sensors. In: Proceedings of the 5th WSES/IEEE World Conference on Systems (CSCC2001), WSES/IEEE, Rethymno, Greece, pp. 3541–3546 (2001) ISBN 960-8052-33-5

[5] Senthil, S., Batra, R.C.: Three-dimensional analysis of transient thermal stressesin functionally graded plates. International Journal of Solids and Structures 40, 7181–7196 (2003)

[6] Ying, A., Narula, M., Zhang, H., Abdou, M.: Coupled transient thermo-fluid/thermal-stress analysis approach in a VTBM setting. Fusion Engineering and Design 83, 1807–1812 (2008)

Device for Measuring of Active Power and Energy at Machine Tools

R. Huzlík, P. Blecha, A. Vašíček, P. Houška, and M. Holub

Brno University of Technology, Faculty of Mechanical Engineering, NETME Centre, Brno, Czech Republic, Technicka 2, 616 69, Brno, Czech Republic
huzlik@feec.vutbr.cz, {blecha,houska.p,holub}@fme.vutbr.cz, vasicek@phd.feec.vutbr.cz

Abstract. This article describes developing of device for measuring active power and energy at machine tools. Demands on measuring of electric energy flow in machine tools are more often with requirement to increasing of efficiency. This problematic is very complicated, because there are some types of electric power supply. Machine tools have main supply with harmonic supply with disturbance, direct current supply with high-frequency disturbance and power supply with PWM modulation. This device primary serves for measuring of AC power between inverter and motor, but also is able measure at other places. Developing consist from developing of electronics and algorithm. Both these part are describes in article.

1 Introduction

Active power and consumption energy is one of main indicator of efficiency of utilization of machine tools today. Ecodesign is one of actual theme in construction of machine tools. Increasing of efficiency is one of way, how can be decrease impact of machine tools on environment. Following the upcoming ISO standard "ISO 14955 - Environmental evaluation of machine tools", extensive research has been established concerning various aspects of Ecodesign in machine tool construction. It is not only about an attitude to access the impact of machine tools on the environment but also other issues are involved; e.g. measuring apparatus design, acquired data processing and visualization. How to mutually access the energy efficiency of machine tools is described by a variety of authors in the following contributions [1], [2], [3], [4]. In their works they define a division of operation modes for a subsequent assessment. This work is followed by authors [2], where criteria for scaling of machine tools are defined with respect to machine tools. An important and integral part is evaluating the energy consumption in the machining process and various suggestions of a testing sample have been currently made (e.g. by JSA).

T. Březina and R. Jabloński (eds.), *Mechatronics 2013*,
DOI: 10.1007/978-3-319-02294-9_64,

1.1 Measuring of Power at Machine Tools

Active power can be defined as mean value of product of voltage and current during one period (1).

$$P = \frac{1}{T} \int_0^T u(t) \cdot i(t) dt \tag{1}$$

In terms of machine tools, the power measurement can be divided into three types based on measuring places.

Measurement of devices operated directly from the mains supply is the first type of measurement. We can be assumed that it is supplied by a harmonic voltage and time course of taken current is also harmonic or very close to harmonic. For this kind of measurement, measuring instruments intended for 50/60 Hz can be used. A big problem of this measuring method can be the deformation of harmonic voltage caused by a non-linear appliance (e.g. a frequency inverter) that takes non-linear current if connected to the same voltage line. In this case, a drop of voltage occurs within incoming conductors that superpose the supply voltage resulting in a possible deformation of the supply voltage itself (Fig. 1).

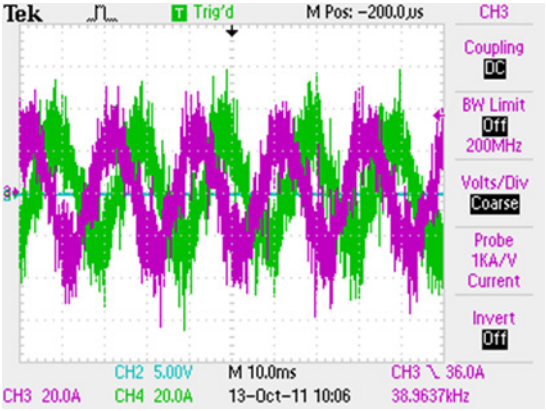

Fig. 1 Disturbance at power supply at machine tool

Measurement on motors (servo drives) supplied by inverters is the third type of measurement. It is necessary determine required characteristic voltage value that is modulated in the sinusoidal PWM with a precisely defined switching frequency. For this type of measurement it is required to use instruments for measuring in a larger frequency range. The sampling frequency of the instrument needs to be at least ten times greater than the switching frequency of inverter transistors that can be about 5 kHz.

Measurement on the common direct link circuit is the last and three type of measurement. In this case, the voltage is direct and its mean value remains almost

the same. The voltage change is only caused by the energy recuperation from one of the drive back to the direct link circuit. Expected time course of current within the link circuit can be characterized as a series of pulses of a high repetition frequency and since it is necessary to use proper measuring instruments with a high frequency width.

2 Device for Measuring

2.1 Demands on Measuring Device

Generally properties of device were described in [5].

Some demands for design of measuring device was determine:

- supply voltage : 24 V,
- communication via RS-485,
- operation temperature range: 10-60°C,
- operation in switchgear with inverters,
- measured maximal voltage: 850V Amplitude
- measured maximal current: 25 A RMS,
- inner diagnostic of device (temperature etc.).
- ability measure between inverter and servo-motor

Development of device started on the base of these demands.

Measuring device consists from several parts:

- voltage sensors
- current sensors
- control part with measuring algorithm

Developing running in two separate tasks, which is connected on the end to developing complete device. Developing of voltage and current sensors is the first task. Developing of control algorithm is the second task.

2.2 Process of Device Development

Some types of commercial voltage and current sensors were test in the first step. DAQP-HV module from Dewetron and NI-9225 module from National Instruments was choosing as example of commercial voltage modules or sensors. DAQP-HV is module, which is able convert voltage with maximal level 1kV to equal signal with maximal level ±5V with maximal frequency bandwidth 300 kHz. NI-9225 is 300V RMS module to CompactRIO platform with sampling frequency 50kS/s. A main disadvantage of DAQP-HV is the cost. Main disadvantages of NI 9225 are platform dependence and low voltage. Way of own voltage sensors development was be choose.

LAH 25-NP from LEM, ACS712-30B from Allegro MicroSystems and NI-9227 module from National Instruments was choosing as example of commercial current modules or sensors. LAH25-NP and ACS712-30B is current sensors.

NI-9227 is 5A RMS module to CompactRIO platform with sampling frequency 50kS/s. Main disadvantages of NI 9227 are platform dependence and low current. A main disadvantage of ACS712-30B is worse accuracy then LAH25-NP. LAH-25 needed symmetrical supply voltage ±15V, but this disadvantage was determined as a negligible and this sensor was choosing to use in the device.

Design of measuring device was inspirited by tested commercial modules. Device consists from voltage and current sensors, which have own A/D converters. These converters communicated via SPI buses with control part. NI sbRIO-9606 was choosing as control part.

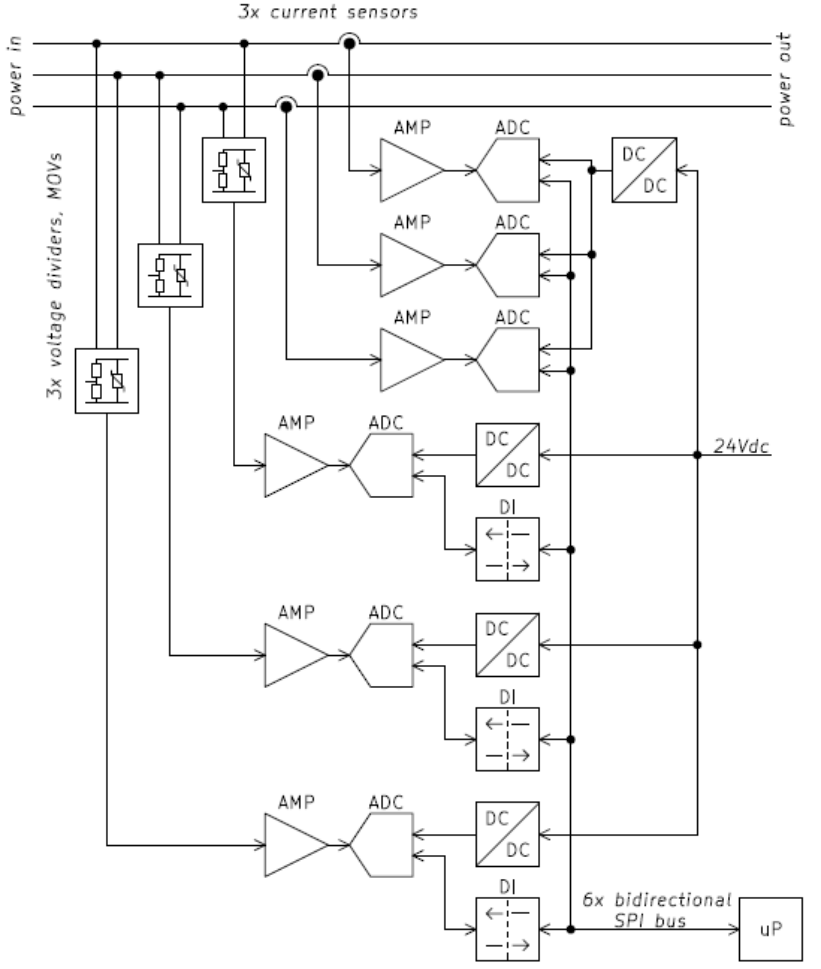

Fig. 2 Diagram of measuring device

Measuring power accurately in all three phases requires isolating associated circuitry not only between phases, but also (due to noise susceptibility) from the digital controller part. The voltage between phases can reach amplitude of up to 850V and still there should be enough of security margin. Therefore the isolation between the phases has to withstand at least 1kV common mode voltage. At current measurement channels, this is ensured by using fast and accurate isolated LEM current measuring sensors. Voltage measurement channels are powered using isolated DC/DC converters and all the communication lines of SPI buses are isolated using digital signal isolator. The block diagram of the power measurement board is on the Fig. 2.

For the phase currents to be accurately measured, they are fed through the LEM current sensors with declared accuracy of ±0.3%. Their frequency bandwidth is limited to 200kHz. As such high frequency signals are mostly noise related, the corner frequency of subsequent active filters is set to around 70kHz. They act as an antialiasing filters and level shifters ensuring proper biasing of the analog-digital converters.

The phase-to-phase voltages are measured using resistor divider networks. The corner frequency of subsequent active filters (see previous paragraph for more details) is again set to around 70 kHz.

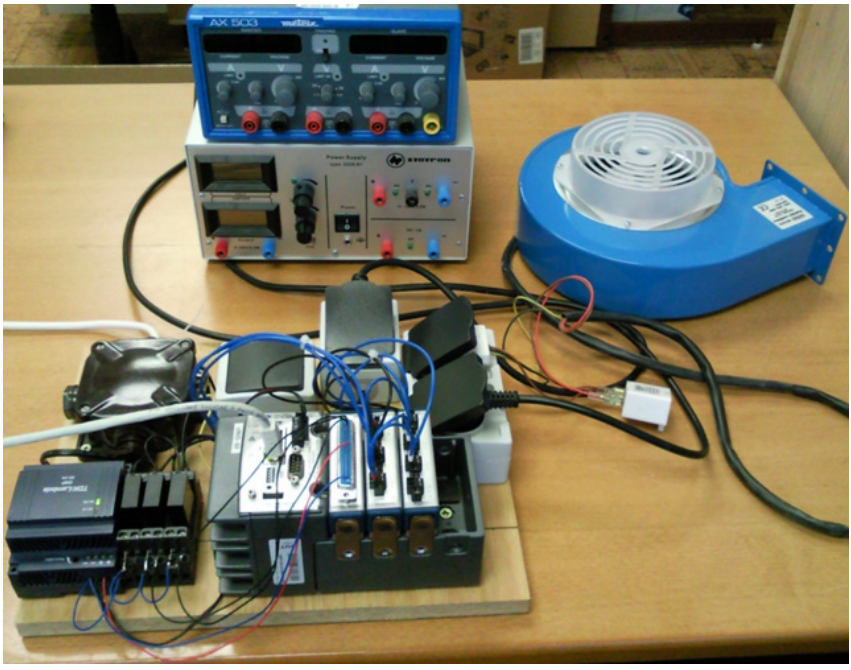

Fig. 3 Test-stand for development of algorithm

The converters used are 16-bit 500kSPS SAR type low power parts, one per channel. The reference voltage is provided using precision monolithic references REF5050, which ensures good temperature and long term stability. Each of the six measurement channels is output via the separate SPI bus to the single board embedded computer to compute actual power.

Test-stand (Fig 3.) was built to developing of measuring algorithm.

Test-stand consists from CompactRIO platform with NI-9225 and NI-9227 modules. These modules are connecting via plug to measured device.

LabVIEW was choosing for developing of measuring algorithm. Measuring algorithm is very simple and operates on the base of (1).

3 Conclusions

Measuring of electric power is very complicated problem and in the area of machine tools is more important with request to increasing of machine tools efficiency. Many producers offering commercial measuring devices (wattmeter or energy meter), but these devices haven't requested parameters or are much expensive.

Developing of device for measuring active power and energy at machine tools was described in this article. This device primary serves for measuring of AC power between inverter and motor. Developing consist from developing of electronics and algorithm. Both these part are describes in article. Some types of voltage and current sensors and modules were tested during of developing. The device was design made on the base of acknowledgement obtain during testing of modules.

Acknowledgments. This project has been funded with support from the state budget through the Ministry of Industry and Trade of the Czech Republic (ID of project: FR-TI3/655 – Ecodesign in machine tool construction) and by European Regional Development Fund in the framework of the research project NETME Centre under the Operational Programme Research and Development for Innovation. Reg. Nr. CZ.1.05/2.1.00/01.0002, id code: ED0002/01/01, project name: NETME Centre – New Technologies for Mechanical Engineering.

References

[1] Dahmus, J.B., Gutowski, T.G.: An Environmental Analysis of Machining. In: Proceedings of 2004 ASME International Mechanical Engineering Congress and RD&D Expo. Paper IMECE2004-62600 (2004)

[2] Behrendt, T., Zein, A., Min, S.: Development of an energy consumption monitoring procedure for machine tools. In: CIRP Annals - Manufacturing Technology (2012) (Article in Press) ISSN 00078506

[3] Duflou, J.R., et al.: Critical comparison of methods to determine the energy input for discrete manufacturing processes. In: CIRP Annals - Manufacturing Technology (2012) (Article in Press) ISSN 00078506
[4] Duflou, J.R., et al.: Towards an Eco label for Machine Tools: A Methodological Basis and Implementation Considerations. In: Neugebauer, R. (ed.) Proceedings of the ICMC 2012, Chemnitz, pp. 461–484 (2012) ISBN: 9783942267403
[5] Blecha, P., Huzlík, R., Houška, P., Holub, M.: Device for electric power measurement at machine tools. MM Scinece Journal (1-6) (2012) ISSN: 1805- 0476

Effect of Gear Ratio on Energy Consumption of Actuators Used in Orthotic Robot

K. Bagiński and J. Wierciak

Warsaw University of Technology, Faculty of Mechatronics, 8 Św. A. Boboli St.,
02-525 Warsaw, Poland
{k.baginski,j.wierciak}@mchtr.pw.edu.pl

Abstract. During works upon system for verticalization and enforcing movement of people with paraplegia designers faced a problem of selecting drive units which would have low energy consumption during the gait cycle. It is very important criterion due to the fact that actuators are powered by a portable electric energy source. Authors have focused on the effect of gear ratio on energy consumption. Simulation experiments of an actuator for driving the hip articulation were done. The results of simulation aid designers to make proper selection of technical solutions with respect to minimal energy consumption of the system and accuracy of required movements.

1 Introduction

At present, orthotic robots constitute the most sophisticated, with regard to the technology, group of devices applied for aiding or replacing lost motor functions of man [12, 13]. Such robots are not only equipped in advanced actuators but also various sensors, e.g. miniature tilt sensors discussed in [9, 10]. According to the guidelines proposed in the relevant bibliography, important criteria for evaluating actuators are: fidelity of reconstructing the accepted motion profiles within the user's joints, as well as a low actuators power demand, which results in using the portable energy source sparingly. As long as the first criterion is related to effectiveness of the device, the second represents its energetic efficiency. It is easy to prove that the higher the power of the applied drive modules the bigger the actuators ability to realize the desired movements. In the case of electric drives, this is strictly connected with an increase of their weight, especially when they are expected to develop considerable torques. An increase of the weight of the drive modules, that are mechanically coupled with the driven fragments of the user's limbs, results in an increase of the dynamic torques, and thus increase the demand of the system for the energy. The actuators will then consume more energy from the supply, what results in its faster run-down. Therefore, an additional criterion for selection of drive modules should be their possibly small weight.

By design, the methods of selecting the drives proposed by the manufacturers of electric machines, can refer only to relatively simple cases of using the motors;

T. Březina and R. Jabloński (eds.), *Mechatronics 2013*,
DOI: 10.1007/978-3-319-02294-9_65,

in particular, they assume a constant values of the relevant loads [6, 11]. The mechanical structure of the orthotic robot is subjected to significantly variable loads generated by the driven body members of the user [2]. In such case, selection of drive modules usually consists in evaluating the maximal required torque and designing a module that is able to develop this torque at certain velocity of the driven members. Such module meets the basic functional requirements, however does not ensure to satisfy the aforementioned additional criteria, important with regard to the discussed application, such as possibly low energy consumption. The drive module to be applied in a technical model of the robot has been created just in this way. The next section contains a description pertaining to the design of the module.

2 Drive System

Drive units used for running robot articulations are built as shown in Fig. 1. The DC motor 1 drives screw gear of ball type 3 through synchronic belt transmission 2. Rotation of screw is transferred to linear movement of nut with attached tie 4. The tie is wrapped around and fixed to a roll 5 so that its linear displacement makes articulation turn. The actual position of the articulation is measured by means of either linear or rotational potentiometer. In future some contactless methods will be considered, e.g. using electrical signals from the driving motor [4].

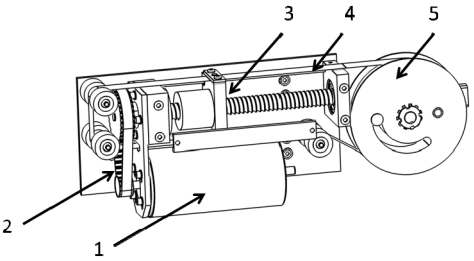

Fig. 1 Mechanical structure of the drive unit that has been designed [7]

3 Performance Analysis

One carried out a simulation experiment that consisted in reconstructing by the robot movements of the user's limbs during a gait. The gait cycle was accepted of 3 s – as long as the standard operation of the robot is expected to take. One recorded time responses of the torque, angular velocity and instantaneous power P_w in the hip and knee articulations of the robot. For further studies, one selected the actuator driving the hip articulation. In Fig. 2, there is presented a course of the torque loading the articulation of the hip joint, obtained by means of simulation.

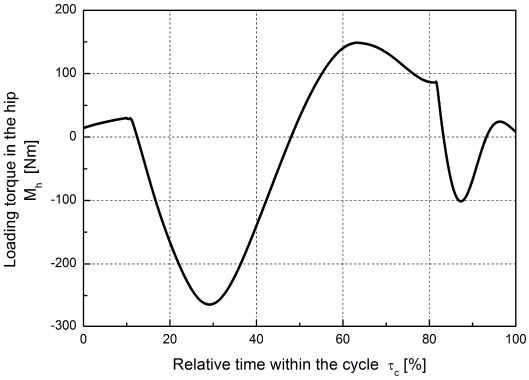

Fig. 2 Graph of the torque M_h transmitted by the hip articulation within the whole gait cycle obtained by means of simulation

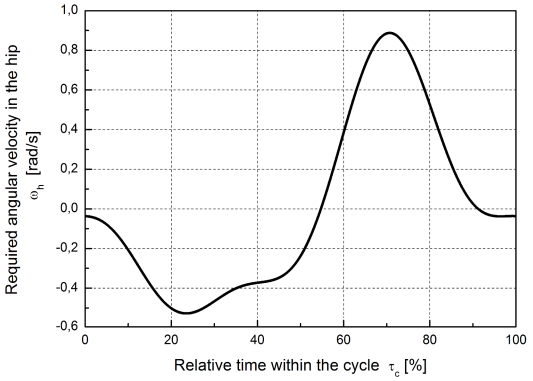

Fig. 3 Graph of the required angular velocity ω_h in the hip articulation within the whole gait cycle

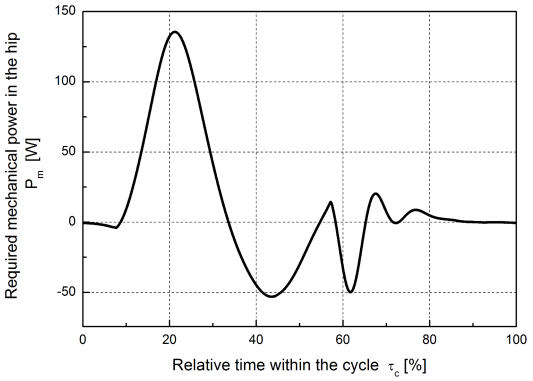

Fig. 4 Graph of the required mechanical power P_m in the hip articulation within the whole gait cycle obtained by means of simulation

Course of the angular velocity in this articulation is shown in Fig. 3, and the related instantaneous mechanical power are presented in Fig. 4.

Characteristic of the mechanical power in function of the relative time within the full gait cycle (Fig. 4) indicates that in some phases of the robot motion the driving motor operates as a motor, whereas in other phases – as a generator.

4 Model

The modelled drive units are expected to reconstruct reference movement profiles in user's joints. These profiles are used by control system as input signals for drive units. Drive units make robot elements move. Mechanical structure of robot is coupled with parts of human lower limbs in such way that together they constitute a parallel mechanism. Due to that movements of robot entail rotation in user's joints. On the other hand drive units have to overcome loads resulting from weights and mass moments of inertia of parts of human body as well as elements of robot itself. The described idea of model was realized by creating models of the following subsystems (Fig. 5): user's body, mechanical structure of orthotic robot, drive units and control system [1].

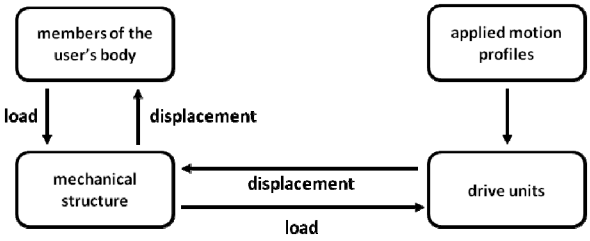

Fig. 5 Schematic of the simulation model [1]

The human body was divided into sixteen parts (Fig. 6), and each of them has its own mass, length, mass moment of inertia with respect to the three axes of the coordinate system and position of the center of gravity. The mentioned values were determined on the basis of the data provided in the related literature [3]. For the sake of simplicity, it was accepted that the upper limbs are immobile, body parts are represented by rigid solids and connections between successive body segments at the hip joint, knee joint and ankle joint are provided by single-axis articulations.

The model of the robot includes a backpack mounted on the user's trunk which imitates a portable power supply (Fig. 6). Each leg of the robot consists of three couplers of the joints which are the main elements of the mechanical structure of the robot. The couplers make it possible to fix to them the drive units, to connect them with the user's body and to transmit motion from the drives to the man. The couplers are fastened to articulations located in the axis of the natural joints.

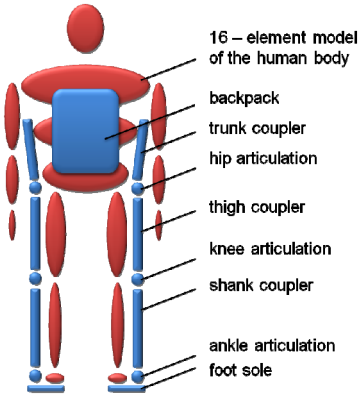

Fig. 6 Mechanical models of the human body and the orthotic robot accepted for the simulation tests

A model of the drive unit was created using classic relationships describing the following subassemblies: flexible connector drive with rollers, screw gear converting the rotational motion into linear, synchronous belt drive, DC motor [8] and classical PID controller of the motor. It is also possible to apply more sophisticated controller using friction compensator. An example of such control of DC motor is presented in [5].

The desired values used in the control loop of the actuators were obtained owing to examinations of the gait function in the case of healthy persons. The obtained experimental data were approximated with mathematic functions, using a fast Fourier transform (FFT), which made it possible to convert the experimental data in a form of time series into in a form of a cosine series:

$$f(t) = A_0 + \sum_{n=1}^{m} A_n \cos(2\pi n f_0 t + \varphi_n) \,, \tag{1}$$

where: n – harmonic number, m – total number of harmonics, f_0 – basic frequency, T_0 – period of the motion, A_0 – amplitude of the constant component, t – time, A_n – amplitude of the n-th harmonic, φ_n – phase shift of the n-th harmonic.

5 Experiments

Simulation experiments were carried out, which consisted in forcing a gait of the patient having predetermined mass and height, by the studied system. There was studied an influence of the gear ratio and DC motor selection on the energy consumption and accuracy of reconstruction the motion profile for the hip. The energy was calculated by integrating the instantaneous electric power

$$E_h = \int_0^{Tc} u_h i_h \, \mathrm{d}t \,, \tag{2}$$

where: E_h – energy consumed by the drive unit for the hip articulation, i_h, – instantaneous input current of the drive, u_h, – instantaneous voltages controlling the drive, T_c – gait cycle length. Instantaneous errors of reconstructing the desired motion profiles of the patient's joints were calculated as follows

$$\Delta\alpha_{\max}(i) = \max\left|(\alpha_{calc} - \alpha_{set})\right| , \tag{3}$$

where: α_{calc} – calculated rotation angle of hip joint, α_{set} – preset rotation angle.

In the experiments one used parameters of the Dunkermotoren GR 63Sx55 and Maxon EC 4-pole 30 motors (Table 1).

Table 1 Parameters of DC motors used in experiments [6, 11]

Parameter name	Unit	Dunkermotoren GR 63x55 130 W	Maxon EC 4-pole 30 200 W
Nominal voltage	V	24	24
Torque constant	Nm/A	$63.79 \cdot 10^{-3}$	$13.6 \cdot 10^{-3}$
Terminal resistance	Ω	0.45	0.102
Friction torque	Nm	0.02	0.009
Back-EMF constant	V/rad/s	$63.79 \cdot 10^{-3}$	$13.6 \cdot 10^{-3}$
Rotor inertia	kgm^2	$750 \cdot 10^{-7}$	$33.3 \cdot 10^{-7}$
Terminal inductance	H	$1.67 \cdot 10^{-3}$	$0.0163 \cdot 10^{-3}$
Weight	kg	1.7	0.3

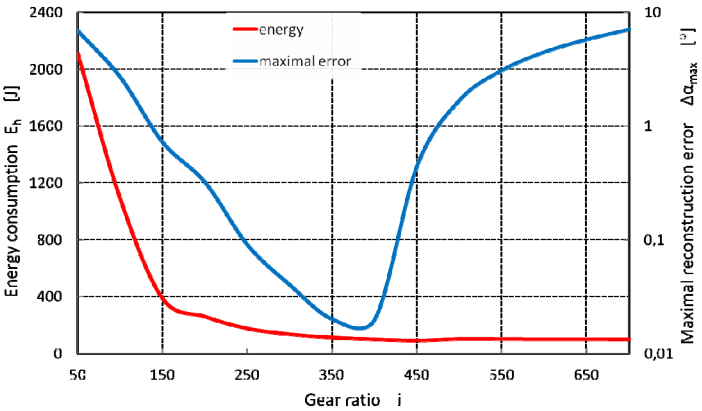

Fig. 7 Graph of the energy consumption and maximal reconstruction error in function of gear ratio for drive unit using Dunkermotoren DC motor

The studies have been planned in such a way, as to make it possible on their basis to evaluate the usefulness of the proposed method, as well as to draw conclusions related directly to the designed drive modules. The results are presented in a form of a dependency of the energy required for realization of a single gait

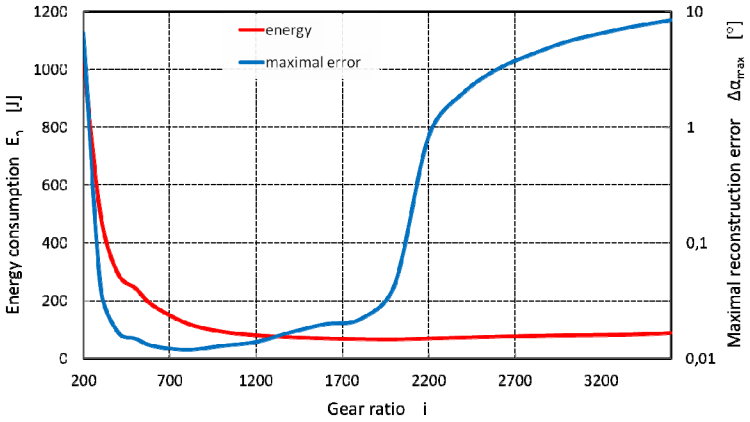

Fig. 8 Graph of the energy consumption and maximal reconstruction error in function of gear ratio for drive unit using Maxon DC motor

cycle and maximal error of reconstruction standard motion profile on the gear ratio (Fig. 7, 8).

Simulation results indicate the strong dependency of energy consumption and accuracy of reconstructing the motion profile on the gear ratio. After rejection of results that didn't fulfill functional requirement, e.g motion profile reconstruction error exceeded 1°, one receives a set of gear ratios providing the lowest energy consumption for a concerned DC motor.

6 Conclusions

The proposed algorithm of selecting drive modules for a robot (or in general, for other devices operating under a considerably variable static and dynamic load) assumes that one will carry out some studies referring to a limited set of motors and gears that feature parameters provided in the relevant catalogs. The presented works prove that simulation studies make possible defining a range of gear ratios which provides the lowest energy consumption. It is very valuable information for designers of drive units for a robot, but it should by emphasized that it's only one of many criteria which must be considered when selecting actuators.

Acknowledgments. The presented works have been financed within a UE Research Project "**ECO-Mobilność**" No. UDA-POIG.01.03.01-14-154/09-00.

References

[1] Bagiński, K., Wierciak, J., Jasińska – Choromańska, D.: Simulation model of actuators of an orthotic robot. PAK 57(6), 583–586 (2011) (in Polish)

[2] Bagiński, K., Wierciak, J.: Selection of drives for orthotic robot based on simulation studies. Machine Dynamics Research 36(1), 5–14 (2012)

[3] Bober, T., Zawadzki, J.: Biomechanics of the Human Motion System. BK Publishing House, Wrocław (2006) (in Polish)
[4] Bodnicki, M., Hawłas, H.J.: Commutation Phenomena in DC Micromotor as Source Signal of Angular Position Transducer. In: Recent Advances in Mechatronics 2008-2009, pp. 263–268 (2009)
[5] Grepl, R.: Composite Controller for Electronic Automotive Throttle with Self-tuning Friction Compensator. In: Mechatronics. Recent Technological and Scientific Advances, pp. 73–78 (2011)
[6] High precision drives and systems, Catalogue, MAXON, (2012)
[7] Jasińska – Choromańska, D., Credo, W., Szykiedans, K.: Making use of anthropometric data while designing drive units of an orthotic robot. Machine Dynamics Research 36(1), 90–98 (2012)
[8] Kenjo, T., Nagamori, S.: Permanent magnet and brushless DC motors. Clarendon Press, Oxford (1985)
[9] Łuczak, S.: Specific Measurements of Tilt with MEMS Accelerometers. In: Mechatronics. Recent Technological and Scientific Advances, pp. 705–711 (2011)
[10] Łuczak, S., Oleksiuk, W., Bodnicki, M.: Sensing Tilt with MEMS Accelerometers. IEEE Sensors J. 6(6), 1669–1675 (2006)
[11] Permanent magnet DC motors, Catalogue, Dunkermotoren (2011)
[12] Pons, J.L.: Wearable Robots: Biomechatronic Exoskeletons. John Wiley & Sons, Chichester (2008)
[13] Wierciak, J., Jasińska-Choromańska, D., Szykiedans, K.: Orthotic Robot as a Mechatronic System. In: Mechatronics. Recent Technological and Scientific Advances, pp. 579–588 (2011)

Precise Model of Multicopter for Development of Algorithms for Autonomous Flight

R. Baranek and F. Solc

Brno University of Technology, Faculty of Electrical Engineering and Communication, Technicka 12, 616 00, Brno, Czech Republic
xbaran10@stud.feec.vutbr.cz, solc@feec.vutbr.cz

Abstract. This article describes precise mathematical model of multicopter. The model can be easily implemented in various simulation environments like Simulink®, Xcos etc. The advantage of using mathematical models for development of navigational, control and attitude estimation algorithms lies in the impossibility to damage the real platform and in the knowledge of all state variables. The model is based on classical free rigid body dynamics driven by forces and moments. The quaternions are used for attitude representation for nonsingular operation. This rigid body dynamics are extended by precise models of inertial and magnetic sensors, by motors thrusts to forces and torques relations and by precise model of aerodynamic drag forces and torques.

1 Introduction

Multicopters are very popular robotic platform nowadays. The multicopter is a mechanically very simple flying robot which consists of even number of fixed propellers connected to motors. The movement of such a robot is controlled solely by changing the speed of individual motors and which leads to mechanical simplicity. The typical scheme of multicopter is depicted on Fig. 1. Due to usual small size and weight (less than 1 m and 1 kg) the dynamics is so quick that direct control of motor speed by teleoperator is impossible. Even for non-autonomous operations there is a need for stabilization.

Every test of algorithm for multicopter is challenging when testing directly on real platform. Usually such a test ends with damaged platform because of the algorithm bug or wrong parameters setup (usually in control algorithms). The use of mathematical model for algorithm testing and development is much more comfortable. However the design of precise mathematical model is often difficult and the precision of the model significantly increases the probability of good operation of developed algorithms after implementing on real platform.

There are many papers dealing with mathematical models of multicopters. The papers are usually concerned with control algorithms for which the mathematical model is needed for development [1], [2] and [3]. In [4], there are along with

T. Březina and R. Jabloński (eds.), *Mechatronics 2013*,
DOI: 10.1007/978-3-319-02294-9_66,

modeling and control also information about estimation of attitude. In [5] the precise effects of drag forces induced by propellers are described. The main contribution of this paper is the collection of the best modeling approaches from available literature. Also the precise models of sensors are mentioned, which are important for development of attitude estimation algorithms.

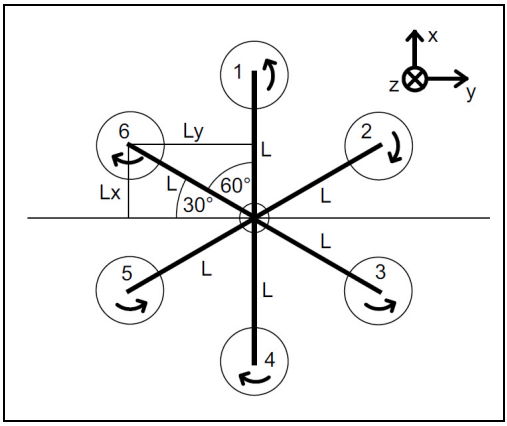

Fig. 1 Scheme of multicopter with 6 propellers so-called Hexacopter

2 Rigid Body Dynamics and Kinematics

The core of the mathematical model is the set of equations describing the rigid body dynamics and kinematics. This set of equation is present in any model and it varies only in attitude representation. In some models there is a simplified assumption for inertia matrix. Here no simplifications for inertia matrix are considered.

2.1 Kinematic Equations

The most inner part of the multicopter model consists of kinematic equation for position and attitude (orientation). Here quaternion attitude representation is used. The kinematics of position is driven by acceleration vector $\mathbf{a}_{\mathrm{I}}$ expressed in inertial (reference) frame and attitude kinematics is driven by angular acceleration vector $\boldsymbol{\varepsilon}_{\mathrm{B}}$. The position vector $\mathbf{p}$ follows equation:

$$\mathbf{p}(t) = \mathbf{p}(t_0) + \int_{\tau=t_0}^{t} \mathbf{v}_I(\tau) \cdot d\tau \tag{1}$$

where

$$\mathbf{v}_I(t) = \mathbf{v}_I(t_0) + \int_{\tau=t_0}^{t} \mathbf{a}_I(\tau) \cdot d\tau \tag{2}$$

is speed expressed in inertial frame. The quaternion representing attitude follows equation:

$$\dot{\mathbf{q}} = \begin{bmatrix} \dot{q}_1 \\ \dot{q}_2 \\ \dot{q}_3 \\ \dot{q}_4 \end{bmatrix} = 0.5 \begin{bmatrix} q_1 & -q_2 & -q_3 & -q_4 \\ q_2 & q_1 & -q_4 & q_3 \\ q_3 & q_4 & q_1 & -q_2 \\ q_4 & -q_3 & q_2 & q_1 \end{bmatrix} \begin{bmatrix} 0 \\ \omega_x \\ \omega_y \\ \omega_z \end{bmatrix} \tag{3}$$

where angular rate vector $\boldsymbol{\omega}$ is defined by:

$$\boldsymbol{\omega}(t) = \boldsymbol{\omega}(t_0) + \int_{\tau=t_0}^{t} \boldsymbol{\varepsilon}_B(\tau) \cdot d\tau \tag{4}$$

In all these equations no parameter of multicopter is present, but this property is inherent for kinematic equations.

2.2 Dynamics Equations

Dynamics equations determine acceleration and angular acceleration vectors from all forces and consequent torques acting on the robot. The acceleration vector is determined by the sum of all forces:

$$\mathbf{a}_I = \mathbf{g} + \frac{\sum_k \mathbf{F}_I^k + \mathbf{R} \sum_l \mathbf{F}_B^l}{m} \tag{5}$$

where $\mathbf{g}$ is gravitational acceleration, $\mathbf{R}$ rotational matrix which converts quantities from body to inertial frame, $\mathbf{F}_I$ are those forces expressed in inertial frame, $\mathbf{F}_B$ are those forces expressed in body frame and m is the mass of rigid body. The relation for angular acceleration vector is similarly determined by the sum of all torques and gyroscopic effect:

$$\boldsymbol{\varepsilon}_B = \left[\left(\sum_k \mathbf{M}_B^k + \mathbf{R}^T \sum_l \mathbf{M}_I^l \right) - \left(\boldsymbol{\omega}_B \times \mathbf{I}_B \boldsymbol{\omega}_B \right) \right] \cdot \mathbf{I}_B^{-1} \tag{6}$$

where $\mathbf{M}_I$ are those torques expressed in inertial frame, $\mathbf{M}_B$ are those torques expressed in body frame, $\boldsymbol{\omega}_B$ is angular rate vector expressed in body frame and $\mathbf{I}_B$ is inertia matrix of rigid body expressed in body frame.

The equations (1) to (6) form the general case for the movement of rigid body with 6 degree of freedom driven by forces and moments and with mass m and inertia matrix $\mathbf{I}$ as only parameters. The next step is to determine the individual forces and torques (drag, propellers, etc.).

3 Multicopter Forces and Torques

As was mentioned in the introduction the multicopter have only motors with propellers which are the only controllable elements and the only active contributors to forces and torques.

3.1 Model of Motor with Propeller

In some simplified models of multicopter the dynamic properties of the motor with propeller are neglected, but model this system as a first order system is more precise approach. Motor is usually controlled by input value which is related to speed of the motor. The changes are not infinitesimally fast, but they almost match the behavior of first order systems:

$$\dot{\omega}_P = k_1 S - k_2 \omega_P \tag{7}$$

Where ω_P is the angular speed of the propeller, S is the input value and k_1 and k_2=1/τ are the parameters of the system. The thrust to speed relation is modeled by the relation [4]:

$$T = c_T \cdot \omega^2 \tag{8}$$

where T is the thrust produced by the propeller spinning at angular speed ω and c_T is the constant parameter including the parameters of the propeller, drag ratio etc. From the principle of action and reaction, the motors are producing reactive torque which has opposite direction than the propeller:

$$M_R = c_R \cdot T \tag{9}$$

where M_R is the reactive torque and c_R is the constant parameter. This model which mathematically describes the dynamics and static behavior should be used for each motor with propeller present on the modeled multicopter.

3.2 Thrust to Forces and Torques Relation

The individual propellers on the multicopter produce thrusts and reactive torques. These thrusts and reactive torques produce total force vector and total torque vector. If we consider for instance hexacopter (multicopter with six motors) depicted on Fig. 1 with length of the arm L then the relation is:

$$\begin{bmatrix} F_z \\ M_x \\ M_y \\ M_z \end{bmatrix} = \begin{bmatrix} -1 & -1 & -1 & -1 & -1 & -1 \\ 0 & -L\frac{\sqrt{3}}{2} & -L\frac{\sqrt{3}}{2} & 0 & L\frac{\sqrt{3}}{2} & L\frac{\sqrt{3}}{2} \\ L & \frac{L}{2} & -\frac{L}{2} & -L & -\frac{L}{2} & \frac{L}{2} \\ c_R & -c_R & c_R & -c_R & c_R & -c_R \end{bmatrix} \begin{bmatrix} T_1 \\ T_2 \\ T_3 \\ T_4 \\ T_5 \\ T_6 \end{bmatrix} \tag{10}$$

where the thrust are considered positive when producing thrust for hover and the z axis points down (Fig. 1). The forces and torques are expressed in body frame. This relation changes with the different number of propellers but it can be derived easily using simple mechanics.

The equations (7) to (10) describe the dynamics characteristics of the multicopter propulsion system and also describe the relation for computing the forces and torques. Now, roughly speaking, we have all equation needed for simulating multicopter, but important characteristics are not modeled yet which are very important for precise match of behavior of real multicopter and for possible transfer of algorithms developed using model to real platform. These are mainly the aerodynamic drag and noise and bias characteristics of sensors.

4 Aerodynamic Drag and Sensor Model

Including the aerodynamic drag and sensor model into the simulation has high importance when focusing to development of algorithm for attitude estimation.

4.1 Aerodynamic Drag

Aerodynamic drag force of a moving object in air is usually modeled as a proportional to square of the speed with respect to air:

$$\mathbf{F}_D = -c_D \mathbf{v} \cdot \|\mathbf{v}\| \tag{11}$$

where c_D is the constant parameter and $\mathbf{v}$ is the speed vector of the multicopter with respect to the air. The minus sign reflects the fact that the drag force has opposite direction than the velocity vector.

When the multicopter or generally rigid body is rotating only (no movement of the center of mass) the individual parts is also experiencing local drag forces which produces aerodynamic drag torque. The drag torque can be modeled in the same way as the drag force:

$$\mathbf{M}_D = -c_T \boldsymbol{\omega} \cdot \|\boldsymbol{\omega}\| \tag{12}$$

where again the c_T is a constant parameter. This drag force and torque cause that even if permanent imbalance in individual thrusts is present the velocity

vector and angular rate vector will settle to some equilibrium value. This phenomenon is to some extent observed also on a real multicopter.

4.2 Sensor Model

The typical sensors used on multicopters are gyroscopes, accelerometers and magnetometers, these sensors are in some defined way related to the state variables of the multicopter namely to angular rate for gyroscope, to non-gravitational acceleration for accelerometers and to attitude for magnetometers. These sensors are usually used for attitude estimation which is of high importance for autonomous operation of multicopter. Thus the precise modeling is very valuable when the model is used for development of such an algorithm for attitude estimation.

Each sensor outputs three-dimensional vector so each sensor can be modeled in the same way but with different parameters to get the similar signal characteristics like with the real sensor. The relation for the modeled sensor output is:

$$\mathbf{a}_{OUT} = (\mathbf{M} + \mathbf{S})\mathbf{a}_{TRUE} + \mathbf{b} + \mathbf{n} \tag{13}$$

$$\mathbf{M} = \begin{pmatrix} 0 & m_{xy} & m_{xz} \\ m_{yx} & 0 & m_{yz} \\ m_{zx} & m_{zy} & 0 \end{pmatrix} \tag{14}$$

$$\mathbf{S} = \begin{pmatrix} S_x & 0 & 0 \\ 0 & S_y & 0 \\ 0 & 0 & S_z \end{pmatrix} \tag{15}$$

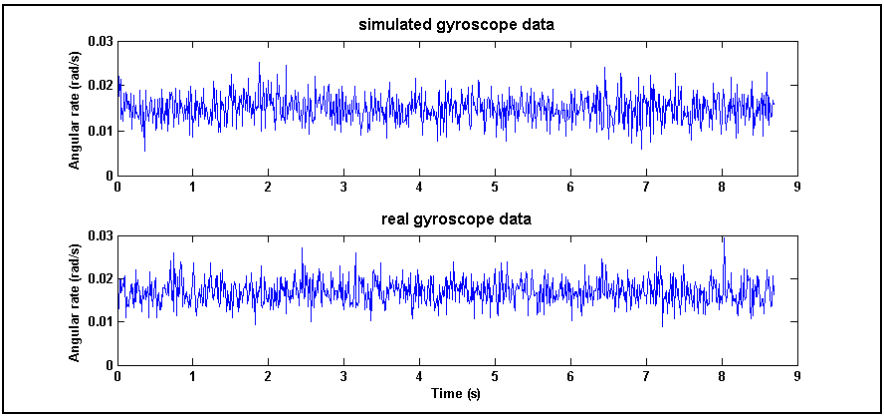

Fig. 2 Simulated and real gyroscope data comparison

where **M** is a so-called misalignment matrix, **S** is scaling factor matrix and **b** is a constant bias vector and **n** is a Gaussian white noise vector. By finding the appropriate parameters the modeled sensor output can be very similar to the real one. The Fig. 2 shows the steady state behavior of gyroscope output for one axis for simulated and for the real sensor.

5 Conclusion

This paper presents the mathematical model of multicopter flying robot. At first the rigid body dynamics with no constrains driven by forces and torques is mentioned (eq. (1) - (6)). Then the propulsion multicopter system is described which inputs are the signals to motors and the output are total thrust and total torque (eq. (7) – (10)). Finally the models for aerodynamic drag forces and torques (eq. (11) and (12)) and for simulated sensor output (eq. (13) – (15)) are showed. All equations mentioned here form the complete model of multicopter (specifically hexacopter with relation (10)). These equations can be easily implemented to some simulated environment and used for development for various algorithms for autonomous flight of such a multicopter.

Acknowledgments. This work was supported by grant "(Supporting) Research of Modern Methods and Approaches in Automation" from the Internal Grant Agency of Brno University of Technology (grant No. FEKT-S-11-6).

References

[1] McKerrow, P.: Modelling the Draganflyer four-rotor helicopter. In: Proc. of International Conference on Robotics & Automation, pp. 3596–3601 (2004)
[2] Bouabdallah, S., Murrieri, P., Siegwart, R.: Design and Control of an Indoor Micro Quadrotor. In: Proc. of International Conference on Robotics & Automation, pp. 4393–4398 (2004)
[3] Solc, F.: Modelling and Control of a Quadrocopter. Advances in Military Technology 5(2), 29–38 (2010)
[4] Mahony, R., Kumar, V., Corke, P.: Multirotor Aerial Vehicles - Modeling, Estimation, and Control of Quadrotor. IEEE Robotics & Automation Magazine 9(3), 20–32 (2012)
[5] Martin, P., Salaun, E.: The true role of accelerometer feedback in quadrotor control. In: Proc. of 2010 IEEE International Conference on Robotics and Automation (ICRA), pp. 1623–1629 (2010)

In-pipe Microrobot Driven by SMA Elements

M. Bodnicki[1] and D. Kamiński[2]

[1] Institute of Micromechanics and Photonics, Faculty of Mechatronics,
Warsaw University of Technology, 8 Sw. Andrzeja Boboli Str., Warsaw, 02-525, Poland
m.bodnicki@mchtr.pw.edu.pl
[2] Graduate of Faculty of Mechatronics, Warsaw University of Technology,
8 Sw. Andrzeja Boboli Str., Warsaw, 02-525, Poland

Abstract. The paper presents a microrobot designed for moving inside of pipelines, whose actuator is based on a strand made of Shape Memory Alloy (SMA). According to the accepted assumptions, a device of a simple structure has been elaborated; it consists of a possibly small number of members and employs a simple control system and power supply. Simplicity of the control system and the power supply was achieved owing to heating the SMA strand by means of an impulse DC supply. Movement within the pipeline is realized by a sequence of displacements of two members of the frame, and the resultant position is kept automatically due to interactions of the flat springs with the internal wall of the pipeline. A demonstrator of the robot was built and experimentally tested, mainly in order to determine its ability to transfer loads. Limitations pertaining to the realized concept are indicated, and solutions improving dynamics of operation of such robot are put forward.

1 Introduction

Classification of the robots moving inside of pipelines includes [1,7],

- PIG robots – moving due to a thrust exerted onto their surface by a medium flowing through the pipeline. In this case, the biggest shortcoming is a lack of control over the rotary movements with respect to their central axis.
- Crawler or wheeled robots – advantage of this design is an easy control over the velocity and direction of motion of the robot, yet they can be vulnerable to an overturn or can easily get stuck in the pipeline.
- Robots with elastic elements – they adjust to the dimension of the inside diameter of the pipeline; the elastic elements can be a fragment of the drive, at the same time.
- Walking robots – supported on legs inside the pipeline; the legs can be driven in various ways.
- Earthworm-like robots – design used most often in the case of pipelines of a small diameter. Their motion is based on imitating movements of the earthworm.

T. Březina and R. Jabloński (eds.), *Mechatronics 2013*,
DOI: 10.1007/978-3-319-02294-9_67,

- Helical robots – moving within the pipelines owing to rotations along a spiral/helical trajectory.

Crawling robot design can be much simpler than walking solutions requiring advanced control algorithms [1, 11].

Shape Memory Alloys (SMA) are characterized by the fact that they are able to remember their initial shape, to which they can return under appropriate external conditions, i.e. temperature. One of such materials is nitinol [12].

The temperature can be changed by:

- heating with an external source of heat,
- heating due to heat dissipation within a conductor.

After the heating, return to the martensitic phase can be speeded up by,

- cooling with an airflow,
- cooling with a surface (e.g. realized by miniature heat pumps – Peltier cells),
- mechanically, by introducing an additional load,
  - gravitational,
  - anti-parallel, realized by a second SMA element,
  - realized by other type of actuator.

The SMA actuators are recommended as elements of mechatronic systems [8]. They give the designer possibility of directly realization of linear movement, without transmission converting rotational to linear movement. The SMA elements are open used in biomechanical devices as construction elements or actuators (e.g. in prosthetics) [4,10].

Methods of testing as well as original test equipment dedicated for SMA wires are presented in [5].

2 Design of a New Robot

The applied solution based on fixing the SMA strand at both ends within one positioning module only, whereas the bight of the wire thus created wraps a guide pin mounted within the second positioning module. Such solution decreases half the size the employed change of the strand length (i.e. the step), yet is advantageous because of design reasons.

Both positioning modules constitute the frame of the robot; it is but necessary to connect them in such a way, as to make it possible to change their position with respect to one another within the range of the operational motion of the SMA element.

Two ways were considered: a sliding interconnection of the modules (a guide featuring one degree of freedom), or an elastic interconnection (function of restoring the frame to its initial length, merged with a function of integrating the frame) – see visualization presented on Fig 1.

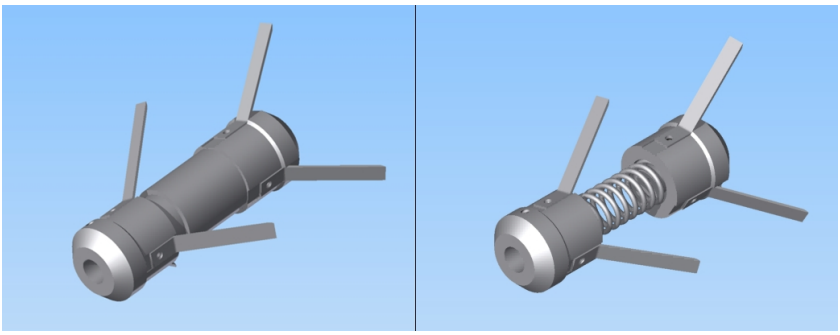

Fig. 1 Visualization of two module in-pipe microrobot
Left – modules connected by tubular guide, right – modules connected by coil spring

As far as the presented design of the demonstrator is concerned, the first option has been accepted, where the returning function is realized by an additional compression spring. Design diagram of this solution is presented in Fig. 2.

The microrobot is put into the pipeline by the user. The control system realizes a sequence of an impulse voltage supply featuring the assumed pulse-width. The time of supplying the SMA element (1), as long as 2.5 s, was experimentally matched. At this stage, a contraction of the strand takes place. The flat springs (3) mounted within the rear module (5) deflect due to the acting force, whereas the flat springs of the frontal module (4) seize against the wall of the pipeline, thus making it possible to realize an advance motion. When the power supply is cut off, a relief of the SMA actuator takes place and is speeded up by the contraction spring (2). As a result, the frontal module (4), responsible for keeping a stable position within the pipeline, shifts. Experimental and numerical analysis of in-pipe microrobot element – passive smart bristles and description of forward and backward motion is presented in paper [2].

Phases of the motion of the robot are presented in Fig. 3.

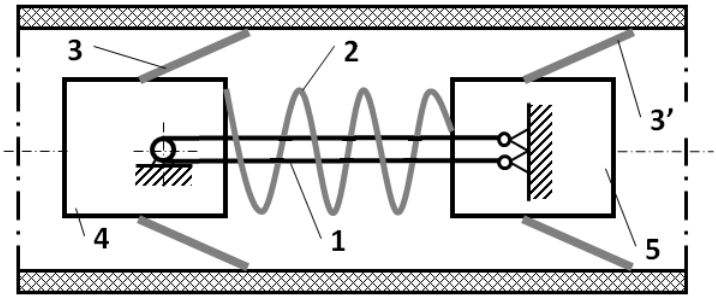

Fig. 2 Structure of the robot
1 – SMA element (wire), 2 – contraction spring, 3 – flat springs, 4 – frontal module, 5 – rear module

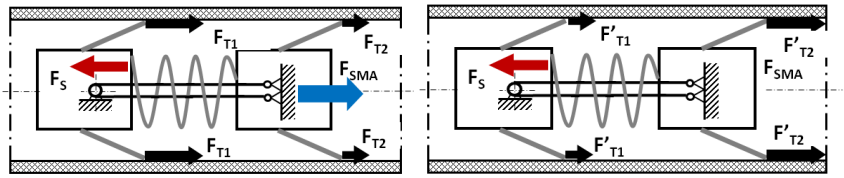

Fig. 3 Phases of the motion of the robot
F_S – force of return spring, F_{SMA} – force of SMA wire, F_{T1}, F'_{T1} – friction forces in frontal module, F_{T2}, F'_{T2} – friction forces in rear module
Left – SMA wire is activated and F_{SMA} drives the rear module, right – phase of the relief of SMA and F_S drives the rear module

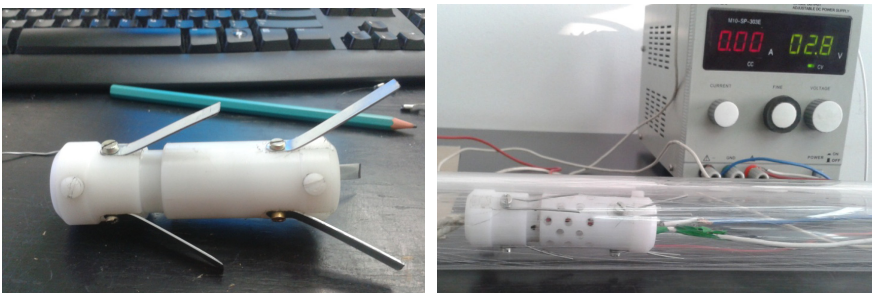

Fig. 4 Demonstrator
Left – microrobot without ventilation holes, right – microrobot with ventilation holes inside pipe during laboratory tests

A set of ventilating holes, arranged along the circumference, was machined in the frame in order to make it easier to remove the heat from the SMA element. Both modules with tubular guide are made from Teflon and flat springs from welding wire. Demonstrator of technology is presented in Fig. 4.

Ultimately, the device can be equipped with a microcamera and sensors (e.g. temperature). Such system should be equipped with a tilt measurement unit, realizing most preferably the measurement case discussed in [6].

3 Experiments

Experimental research was carried out in three stages. First, the SMS wire was tested, also for revision of the catalogue data (e.g. force of contraction 20 N). The results of the dynamic parameters research included measurement on time of action and relaxation as a function of the current in the wire. Results of such experiments are presented in Fig. 5. In effect, current in supply unit has been restricted to 2 A in a cycle consisted of 2.5 seconds supply and 14.5 seconds of pause. Temperature of supply wire was less than 303 K.

Then there were experimentally chosen the parameters of the flat springs (elements no 3 on Fig. 1) and the return spring force equal to 10 N (driven force during power interruption) by the working movement of 3 mm and force of the SMA equal 20 N.

Another study focused on the robot's movement inside the tube made from PMMA. The device worked properly with different pipes tilt relative to the ground (in the range 0-90 degrees). Experimental studies are done in lift force. When moving in a horizontal position he is able to move the weight 6 kg. In the vertical position moves upwards moving mass of 2 kg.Due to idea of movement and frequency of cycle of supply unit the average speed was relative small – 10 mm/min.

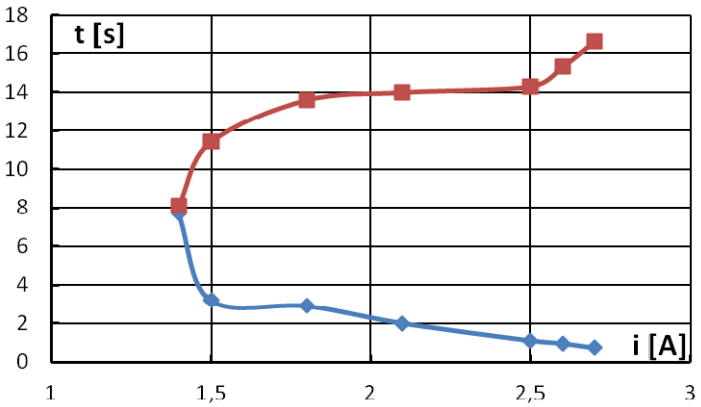

Fig. 5 Time of SMA contraction (bottom/blue curve) and relaxation (top/red curve) versus current in the wire

4 Summary and Conclusions

While realizing the project, the accepted assumptions have been successfully observed. The created device is characterized by a very simple mechanical structure as well as a simple control and power supply. One made use of a simple and inexpensive SMA element, in the form of a wire (strand).

The experiments related to application of the built demonstrator proved effectiveness of moving inside the pipelines. By the way, the applied way of displacing the movable element by means of a sequence of micro-displacements and frictional immobilization of one of the modules, can be also used as an interesting concept of driving a pusher of a micro-actuator.

The experimental studies performed on the demonstrator indicted that also low-quality (as far as the generated forces are concerned) SMA wires can be applied in the microrobot design, and these are yet characterized by a faster relief process (of ca. 6 s). That increases in a simple way the average velocity of the motion. Here, a significant modification will be application of a higher number of SMA actuators,

appropriately arranged and sequentially controlled in such a way that after operation of one actuator, another one would be activated and so on, until the idle time of operation, resulting from the cooling process, is completely eliminated. There is possible to use algorithms of "intelligent drives", adaptive to load conditions (such idea par linear stepping actuators was presented in [9].

The applied way of changing the temperature of the SMA, as a result of passing the current sequentially, considerably simplified the problems related to controlling and supplying the robot.

At the moment, the robot is used to demonstrate the new drive technology for information meetings, picnics and festivals of science. In the near future the robot drive unit will be used station to study the mechanical characteristics of miniature linear actuators - as a reference force applying module.

Owing to the experience gained while designing the device, one has started to build a series of types of miniature positioners with SMA strands. In these devices, it is taken into consideration to employ a forced cooling of the strand. Such solutions (e.g. employing miniature Peltier cells) will ensure repeatability of the operational movements, as well as increase frequency of the deformations.

References

[1] Choi, H.R., Roh, S.: In-pipe Robot with Active Steering Capability for Moving Inside of Pipelines. In: Habib, M.K. (ed.) Bioinspiration and Robotics Walking and Climbing Robots. I-Tech Education and Publishing, Vienna (2007)

[2] Dovica, M., Gorzás, M., Kaťuch, P., Kováč, J., Ondočko, Š.: Mechatronic aspects of wired in-pipe passive smart bristle micromachine design. In: Proceedings of 5th International Conference Mechatronics 2004, pp. 167–170 (2004)

[3] Grepl, R.: Extended kinematics for control of quadruped robot. In: Recent Advances in Mechatronics, International Conference on Mechatronics, Warsaw, Poland, pp. 126–130 (2007)

[4] Jasińska-Choromańska, D., Szykiedans, K., Wierciak, J., Bagiński, K., Bojarski, M., Kabziń-ski, B., Kołodziej, D., Zaczyk, M., Credo, W., Lasecki, J., Rzeszotek, Ł., Semeniuk, J.: Mechatronic system for verticalization and aiding the motion of the disabled. Biuletyn PAN 61(2) (2013)

[5] Kłapyta, G., Kciuk, M.: Experimental measurements of shape memory alloys wires. Archives of Electrical Engineering 61(2), 129–138 (2012)

[6] Łuczak, S.: Specific Measurements of Tilt with MEMS Accelerometers. In: Mechatronics Recent Technological and Scientific Advances, pp. 705–711 (2011)

[7] Mateos, L.A., Vincze, M.: DeWaLoP-Monolithic Multi-module In-Pipe Robot System. In: Jeschke, S., Liu, H., Schilberg, D. (eds.) ICIRA 2011, Part I. LNCS, vol. 7101, pp. 406–415. Springer, Heidelberg (2011)

[8] Sapińsko-Wcisło, A.: Mechatroniczne człony wykonawcze z zastosowaniem materiałów inteligentnych, Akademia Górniczo-Hutnicza, Kraków (2006)

[9] Wierciak, J.: Improvement of Performance of Precision Drive Systems by Means of Additional Feedback Loop Employed. In: Recent Advances in Mechatronics, pp. 495–499 (2007)

[10] Wierciak, J., Jasińska-Choromańska, D., Szykiedans, K.: Orthotic Robot as a Mechatronic System. In: Mechatronics Recent Technological and Scientific Advances, pp. 579–588 (2011)
[11] Zezula, P., Vlachy, D., Grepl, R.: Simulation modeling, optimalization and stabilisation of biped robot. In: Recent Advances in Mechatronics, International Conference on Mechatronics, Warsaw, Poland, pp. 120–125 (2007)
[12] Ziółkowki, A.: Pseudosprężystość stopów z pamięcią kształtu. Badanie doświadczalne i opis teoretyczny. Instytut Podstawowych Problemów Technicznych Polskiej Akademii Nauk, Warszawa (2006)

Adaptive Cruise Control for a Robotic Vehicle Using Fuzzy Logic

A. Hassan and G. Collier

School of Mechanical and Automotive Engineering, Kingston University London, UK
ali.ab.hassan@gmail.com, Gordana.Collier@kingston.ac.uk

Abstract. This paper presents the modelling, simulation, and implementation of an ACC system for a robotic vehicle using Fuzzy Logic control strategy. Implementation has been carried out using the graphical programming environment of LabVIEW and a robotic vehicle based on a real-time single board computer. The paper demonstrates control design process including the implementation of the fuzzy logic design rules, showing a good correlation between simulation behaviour and real-life implementation. The work is a part of a larger research informed teaching project for teaching engineering at Kingston University London.

1 Introduction

Kingston University London has been conducting substantial research related to teaching methods for engineering subjects and is presently developing teaching materials using industrial standard technology. The aim is to engage students in the learning process and prepare them for work in industry. One of the areas addressed in this body of research is Control Theory. A real-life example with a hands-on approach is expected to be beneficial when adopting this concept. Furthermore, adaptive cruise control (ACC) is becoming a standard in modern automotive vehicles and is thus an ideal application that can be implemented using a range of different control strategies.

This paper presents one of the three experiments in the series related to the design of an ACC system for a robotic vehicle used in teaching at both undergraduate and postgraduate level. The three experiments are based on the same ACC strategy implemented in a rapid electronic prototyping platform (robotic vehicle), demonstrating the performance dependant on strategy only, namely: classical (PID) [5], model predictive and Fuzzy Logic control, which is described in this paper.

The scenario is based on ACC implemented in a robotic vehicle (referred to as the 'Follower'), tasked to maintain velocity/distance from the vehicle in the front (referred to as the 'Leader'). The two identical robotic vehicles (DaNI2 robots) are equipped with real-time, single board computers (sbRIO) from National Instruments (NI) using the NI graphical programming environment, Lab View.

T. Březina and R. Jabloński (eds.), *Mechatronics 2013*,
DOI: 10.1007/978-3-319-02294-9_68,

The motor controllers output Pulse Width Modulated signal to drive the two 12V DC motors on the DaNI2 robot, and the braking is applied by simply reducing the voltage to the motors.

The paper is laid out to first describe the system identification, thus obtain and verify the transfer function of the DaNI2 robot in a Laplace domain followed by definition of the proposed ACC control concept. Controller design using the extracted transfer function, based on fuzzy logic rules, is described in Section 2. Section 3 deals with the robotic vehicle simulation for controller tuning. Real robotic vehicle implementation, results and discussion are presented in Section 4, with the brief evaluation of the tools and the experiment being presented in Section 5.

2 Controller Design

2.1 System Identification and Validation

The system identification process was carried out based on a single input-single output (SISO) model that represents the output speed to input speed in the Laplace domain. LabVIEW code used for system identification and validation. The same stimulus signal (sinusoidal input) that was used for both, the system identification and the validation process.

2.2 Adaptive Cruise Control Switching Rules

ACC is an extension of the conventional cruise control system, with the added feature that when closing the gap with a slower moving car ahead, it automatically slows down to keep a desired distance between the two cars. Once the road is clear again, the ACC accelerates to the original set speed [3]. The headway desired distance between two vehicles that share the same deceleration rate can be calculated using (2):

$$d_{des} = l + d_s + hv \tag{1}$$

Where l represents the vehicle length, d_s is the safety distance between two vehicles, v is the speed in m/s, and h is the constant-time headway in seconds [1].

In this paper, the actual gap between the two robots is calculated by taking the integral of their relative velocities using the simple formula:

$$d = \int_0^t (v_h - v_l)dt \tag{2}$$

Where v_h and v_l are the follower and leader velocities, respectively. The switching between ACC and CC has been done in accordance switching methodology by Shakouri et al. [6], shown on Table 1.

Table 1 ACC/CC switching method

	$v_h < v_{des}$	$v_h \geq v_{des}$
$d < d_{des}$	ACC	CC
$d \geq d_{des}$	CC	CC

d actual distance (m)
v_h follower vehicle speed (m/s)
d_{des} desired distance in meters (m)
v_{des} follower vehicle desired speed (m/s)

Thus ACC system control consists of two control loops. The inside loop which does the cruise control CC. This controller performs velocity tracking, whilst the other loop performs distance tracking. In a fully comprehensive ACC system, the CC controller does the manipulation of both brake and throttle in order to follow the reference speed, according to Shakouri et al. [4].

2.3 Fuzzy Logic Rules

Fuzzy logic concepts are not new - the procedure for the data-driven generation of fuzzy rules used to assist a driver in vehicle speed and distance control, was presented as far back as 1996 [1]. In his survey from 2006, Swain [7] reported on the significant use of fuzzy logic in intelligent transportation systems, including ACC. However the approach has not been utilised to its full potential, possibly due to the difficulties in tuning and the demand for computing power. The availability of significant computer power in recent years allied with the use of the graphical programming environment toolkit may result wider implementation of this powerful control method.

Fuzzy Logic is a rule-based method of decision making, which can be very effective when dealing with subjective, linguistic, and descriptive processes. A fuzzy controller uses a knowledge base of rules to produce a control signal to achieve a desired output based on the values of the input variables. The Mamdani controller as described by Zimmerman [8], and used in this paper, processes its states by means of linguistic variables, used as inputs, taking into account all the rules in a single stage without any chaining. The input and output membership functions for the follower vehicle controller described in this paper are shown on Table 2.

Table 2 Input and output functions

Name	Type	Range	Number of membership functions
Error	Input	-1 to 1	3
Rate	Input	-1 to 1	3
Integral	Input	-1 to 1	3
Speed	Output	-1 to 1	5

The rules are composed from linguistic terms and the membership functions translate them into numerical values as the degree of membership of each linguistic variable within its linguistic term as shown in Table 3:

Table 3 ACC rules

CC Rules
1. IF 'error' IS 'desired<<<actual' AND 'rate' IS 'nochange' THEN 'speed' IS 'DecFast'
2. IF 'error' IS 'desired>>>actual' AND 'rate' IS 'nochange' THEN 'speed' IS 'ACCFast'
3. IF 'error' IS 'desired=actual' AND 'rate' IS 'accelerating' THEN 'speed' IS 'DecNormal'
4. IF 'error' IS 'desired=actual' AND 'rate' IS 'decelerating' THEN 'speed' IS 'AccNormal'
5.IF 'error' IS 'desired=actual' AND 'rate' IS 'nochange' AND 'Integral' IS 'zero' THEN 'speed' IS 'Nothing'
6. IF 'error' IS 'desired=actual' AND 'rate' IS 'nochange' AND 'Integral' IS 'negative' THEN 'speed' IS 'DecNormal'
7.IF 'error' IS 'desired=actual' AND 'rate' IS 'nochange' AND 'Integral' IS 'positive' THEN 'speed' IS 'AccNormal'
connective: AND (Minimum) ; implication: Minimum ; degree of support: 1.00

The defuzzification process is implemented by the aggregation of all consequences using logical operators such as “Max”. The defuzzification method used is the "Centre of Area". The shape of the membership function is decided based on the application. For the purpose of the ACC application, a smooth transition in terms of the input is needed, hence a Gaussian shape is chosen. The output

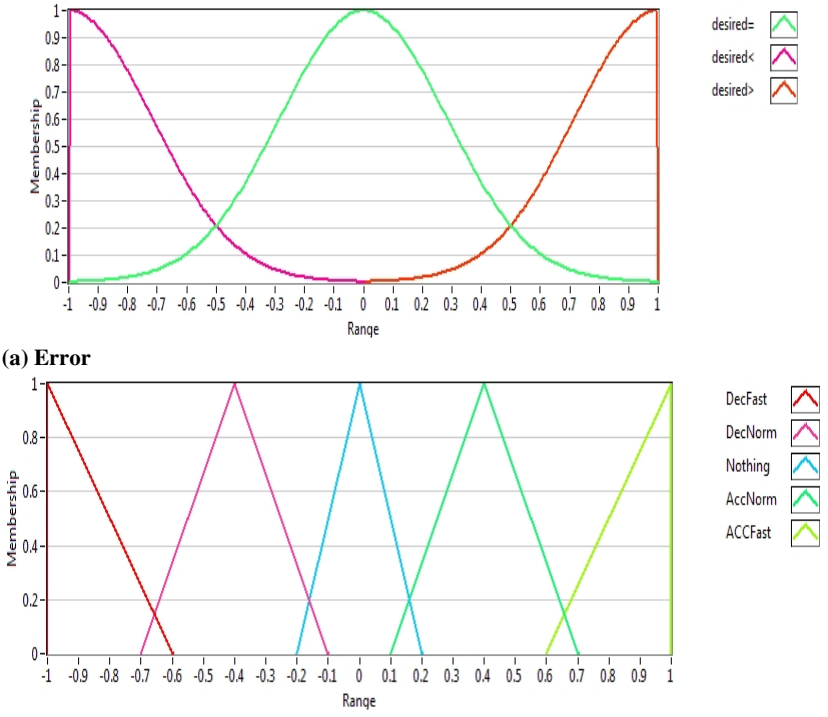

Fig. 1 Graphic representation of input (a) and output (b) functions

(membership) needed to be a single crisp value of the speed in both controllers. Thus triangular output membership functions have been chosen as shown on Fig. 1.

3 Robotic System CC and ACC Simulation and Real System Implementation

The simulated operation of the follower robot in order to perform the initial tuning of the system is based on the extracted transfer function of the robot, as a result of system identification, described in section 2.1 and the fuzzy controller designed in section 2.3. The desired gap calculation between the two vehicles is based on (1), which relates the instantaneous velocity of the follower robot, the time headway and the safety distance. The actual gap is calculated by taking the integral of the relative velocities of the two robots. The ACC loop performs distance tracking by

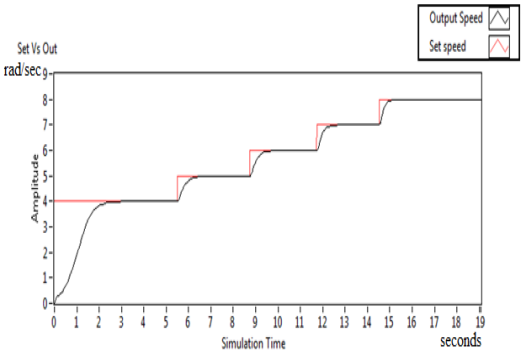

(a) Set speed and output speed

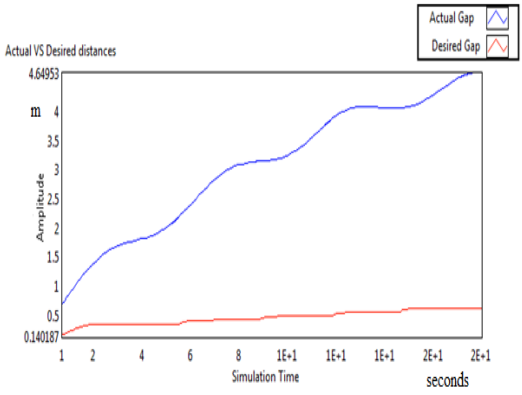

(b) Actual and desired distance

Fig. 2 CC operation: (a) speed and (b) distance tracking

converting the difference between the desired and actual distance into a new reference speed output. If the calculated gap is greater than the safety distance, CC control is applied.

As per the graph in Fig. 2, CC is in operation as long as the actual gap is greater than the desired one, and with a set speed increase from 4 rad/sec to 8 rad/sec the output speed follows smoothly and rapidly. However the gap between the two vehicles is still greater than the safety gap, as the follower vehicle speed is not sufficient to reduce the gap between the two vehicles below the safe distance, remaining in CC mode.

Fig. 3 shows the switchover to ACC mode. The front vehicle has a sinusoidal stimulus with a varying speed (6 rad/s to 14 rad/s). As the follower vehicle speed increases, the gap between the two vehicles decreases and ACC takes over from CC changing over from speed to the distance tracking mode at t=33s.

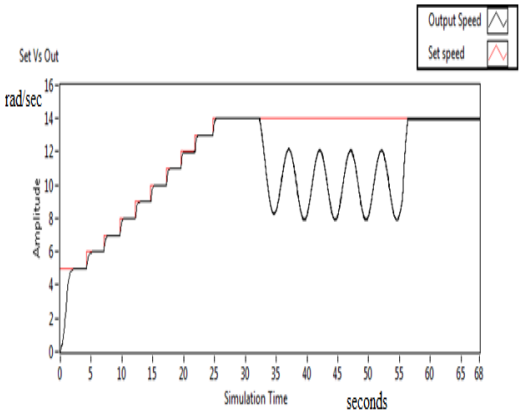

(a) Set speed and output speed

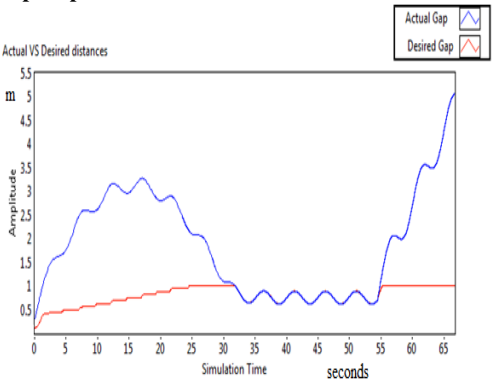

(b) Actual and desired distance

Fig. 3 ACC operation: Switching between CC and ACC mode (a) speed and (b) distance

At t=60s, the front vehicle speed reaches a range of 14-28 rad/sec and the gap becomes greater than the desired one, causing CC to take over and bring the follower vehicle back to the original set speed. Fig. 3(b) shows the distance between the two vehicles. In the first 30 second of the simulation, the actual gap was greater than the desired one, thus CC is on. After 30 seconds, the follower vehicle speed becomes high enough to catch up with the front vehicle. At this instance, the actual gap falls just below the desired one, switching on ACC.

As ACC takes over, velocity tracking becomes distance tracking, in which the actual gap is maintained just at the desired value. After 55 seconds, the font vehicle speeds up (due to stimulus), causing the gap between the two cars to become greater than the desired one, allowing for CC to take over and bring the speed of the follower car to the original set speed, thus accurately executing the adaptive switching control strategy described in 2.2.

Following on from simulation, the programme was implemented in real environment, using two DaNI2 robots, the leader and the follower, as described in the introduction. The follower robot was equipped with an ACC controller and an ultrasonic sensor that measures the distance to an obstacle up to 3 metres ahead. The front robot travelled in a sinusoidal manner. The follower robot was programmed to perform the ACC. The scenario sets the CC system to drive the follower robot to maintain a predefined speed, set in the code. The LabVIEW codes have been written using the robotics and real-time toolkits with the control loop frequency of 1kHz. The encoders measuring the speed of the motors showed a noisy reading. Although filtered, this noisy output from the encoders affected the performance, as it is used to calculate the desired distance. Furthermore, the ultrasonic sensor also showed noisy readings, introducing a jerk while ACC is engaged. This noise was reduced by filtering and decreasing the sampling ratio; however a compromise between noise elimination and sufficient sampling ratios had to be made.

4 Conclusions

An ACC system for a robotic vehicle, DaNI2 using Fuzzy Logic control strategy showed good results in both simulation and real-time implementation. The LabVIEW system identification toolkit was found to be an excellent tool for system identification. Furthermore LabVIEW allows manipulation of the control parameters, while the simulation or implementation is running, assisting the tuning process. The ACC fuzzy controller reached the desired speed quickly and smoothly, maintaining the desired gap between the two vehicles, thus the CC section of the controller, designed and tuned in simulation was not used in the real implementation.

References

[1] Gerdes, J.C., Hedrick, J.K.: Vehicle speed and spacing control via coordinated throttle and brake actuation. Control Engineering Practice 5(11), 1607–1614 (1997)

[2] Holve, R., Protzel, P., Naab, K.: Generating fuzzy rules for the acceleration control of an adaptive cruise control system. In: 1996 Biennial Conference of the North American IEEE Fuzzy Information Processing Society, NAFIPS (1996)

[3] Martinez, J., Canudas-de-Wit, C.: A Safe Longitudinal control for adaptive cruise control and stop-and-go scenarios. IEEE Transactions on Control Systems Technology 15(2), 246–258 (2007)
[4] National Instruments Fuzzy Logic Manual (2009), http://www.ni.com/pdf/manuals/372192d.pdf (retrieved May 12, 2013)
[5] Shakouri, P., Collier, G., Ordys, A.: Teaching control using NI starter kit robot. In: Proc. IEEE UKACC (2012)
[6] Shakouri, P., Ordys, A., Laila, D.S., Askari, M.R.: Adaptive Cruise Control System: Comparing Gain-Scheduling PI and LQ Controllers. In: 18th IFAC Proc. Elsevier (2011)
[7] Swain, N.K.: A survey of application of fuzzy logic in intelligent transportation systems (ITS) and rural ITS. In: Proc. IEEE SoutheastCon (2006)
[8] Zimmerman, H.-J.: Fuzzy Set Theory and Its Application. Kluwer Academic Publishers, Dordrecht (2001)

Robot with Adjustable Undercarriage – The Design and the Simulation

M. Dovica, T. Kelemenová, M. Kelemen, and T. Lukac

Technical University of Košice, Faculty of Mechanical Engineering, Letna 9, 042 00, Košice, Slovak Republic
{miroslav.dovica,tatiana.kelemenova,michal.kelemen}@tuke.sk

Abstract. The paper deals with the design of four wheeled robot that is able to adjust its undercarriage according to the roughness of the terrain. Movement of the robot is based on the differentially operated undercarriage. The aim of this paper is to design a universal robot, a robot for rough terrain and also for limited area.

1 Introduction

The service robots are often used for various special tasks such as an inspection of car undercarriages, a firefighter works, a tactical fight robot, a bomb finder or a bomb remover. There exist several tasks (Figure 1) for special robots with low clearance of their undercarriage or for robots with big wheels and with high clearance of the undercarriage [1-5].

Practice points out a need of more flexible robots that would adjust to the changes in the environmental conditions. The aim of this work is to design a robot with adjustable clearance of its undercarriage and automatic setting according to the roughness of the terrain [6-10].

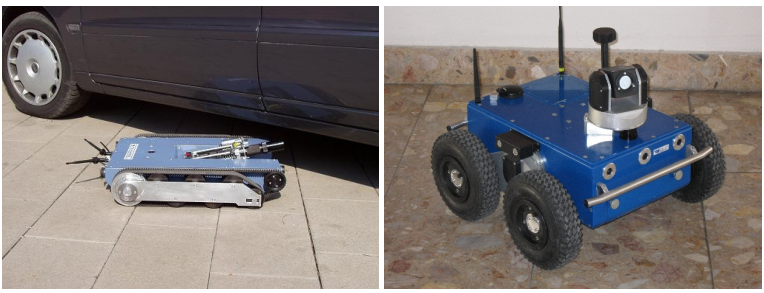

Fig. 1 Mobile miniteleoperator SCORPIO and four wheeled robot MRVK-01. [1-5]

T. Březina and R. Jabloński (eds.), *Mechatronics 2013*,
DOI: 10.1007/978-3-319-02294-9_69,

2 Concept of the Robot Undercarriage

Concept of the undercarriage comes from the lever mechanism shown in the Figure 2. Thanks to the proposed design, the robot changes the clearance of its undercarriage to the wider extent which is important when crossing very rough terrain. For minimizing the transmission mechanisms, there are the driving motors inside the wheels. This arrangement also ensures the partial protection against possible damage. (Figure 3) [10].

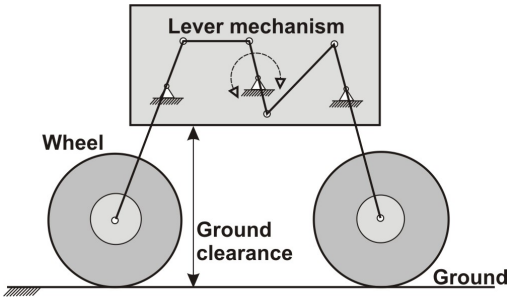

Fig. 2 Concept of the robot undercarriage

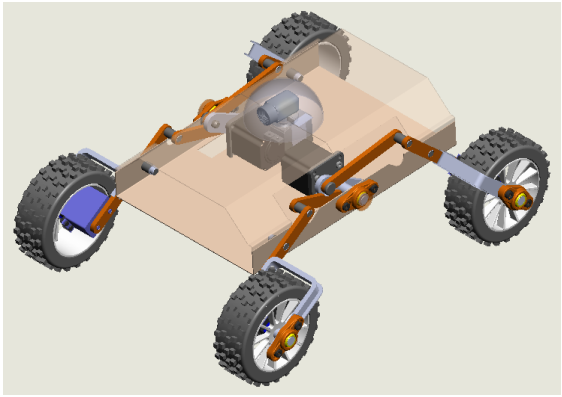

Fig. 3 Design of the robot

The undercarriage also contains three sensors, i.e. inductive, capacitance and optical, which are used to measure the distance. (Figure 4) Afterwards, this information is used for automatic setting of desired value capturing the distance between the undercarriage and the road. The other possibility how to adjust the clearance of the undercarriage is to use the teleoperator.

3 Sensing the Clearance of the Undercarriage and the Obstacle Sensing

Ultrasonic sensors together with the infrared optical triangulation sensors are used for the obstacle sensing (Figure 5). Furthermore, data fusion and data collected by these sensors are consequently used for obstacle avoidance. If there is a higher obstacle, the controller sends a command to lift the clearance of the undercarriage. Also, if any dimensional constraint occurs from the upper side, then the carriage adjusts by pushing itself downwards.

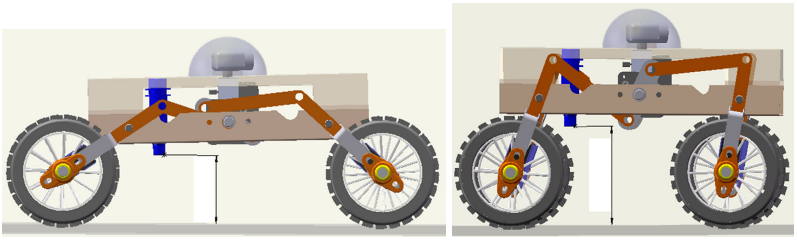

Fig. 4 Sensing the clearance of the undercarriage

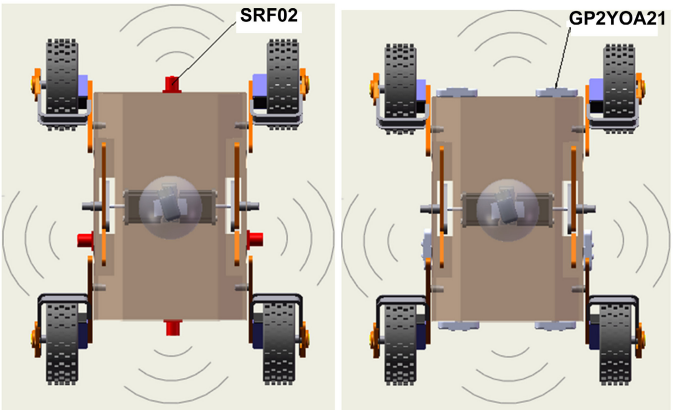

Fig. 5 Obstacle sensing and the placement of sensors

4 Design of the Robot Carriage and Its Simulation

CAD model of the robot was designed using Solid Works Environment. To simulate the behavior of the robot, we used Matlab, Solid Works and Cosmos Works. We ran the analysis of the static load, carriage lifting and forward movement of the robot [10-12].

Lever mechanism (Figure 6) ensures the lifting of the robot undercarriage. Thanks to the static analysis, we are able to study the critical state of the lever mechanism.

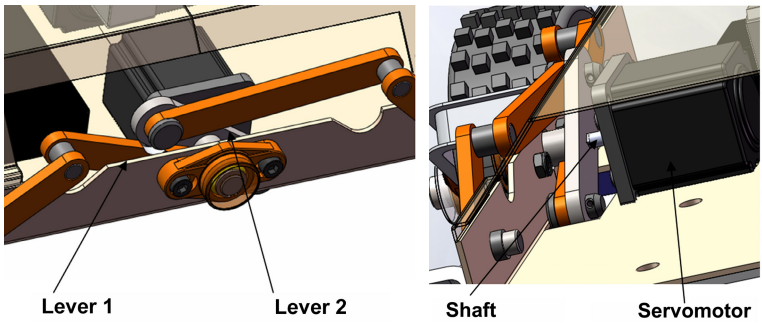

Fig. 6 The lever mechanism and the drive

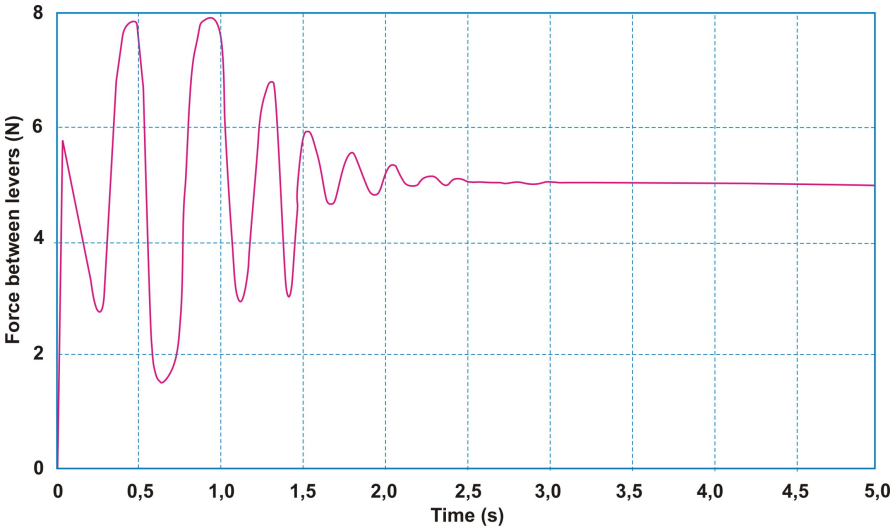

Fig. 7 Static analysis of the lever mechanism

The simulation takes 5 s. Maximum load was applied in the form of a jump and the Figure 7 shows the response to this jump with maximum contact force of F = 8,308 N between the levers (Figure 6) which occured in time 0,96 s (Figure 7).

Moreover, we simulated the undercarriage lifting. (Figure 6) Duration of this simulation was 5 s. The aim of this simulation (Figure 8) was to identify the maximum torque value on the shaft, which is necessary for undercarriage lifting. The maximum torque value was M_k = 769,846 N.mm (7,69 kg.cm) in time 0,01s. The motor has to start at this point in time. It means that the velocity of rotation increases from zero to maximum value (Figure 8). This obtained value of the maximum torque can be used for the first selection of drive.

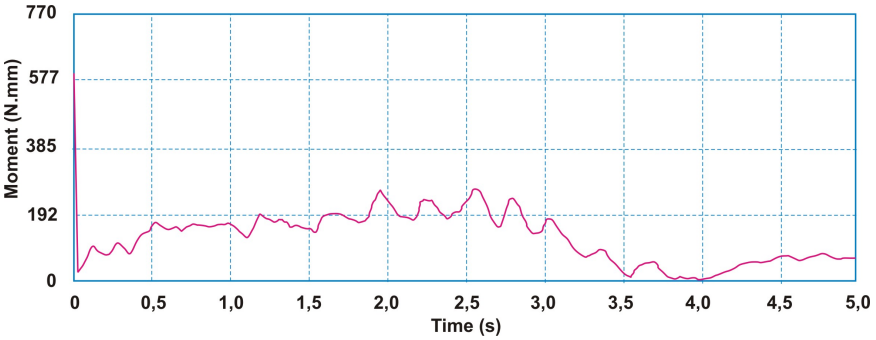

Fig. 8 Analysis of torque on the drive shaft

Furthermore, we ran the analysis of the forward movement on the traction unit (Figure 9). The aim was to find the maximum torque value for a drive used for the movement. The maximum torque value (Figure 10) was M_k = 1602,042 N.mm (16,02 kg.cm) in time 0,105 s. The obtained dependence of the torque has been used for the drive selection. The large torque value is caused by the starten of the drive from zero to maximum velocity.

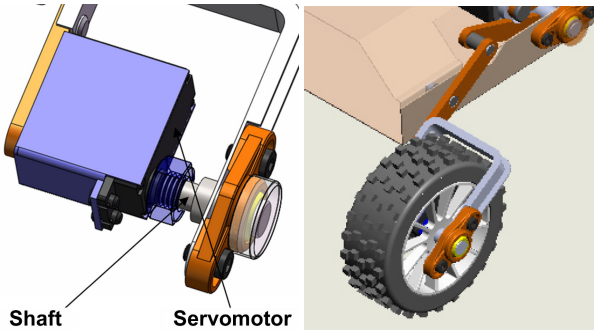

Fig. 9 Drive of the wheels

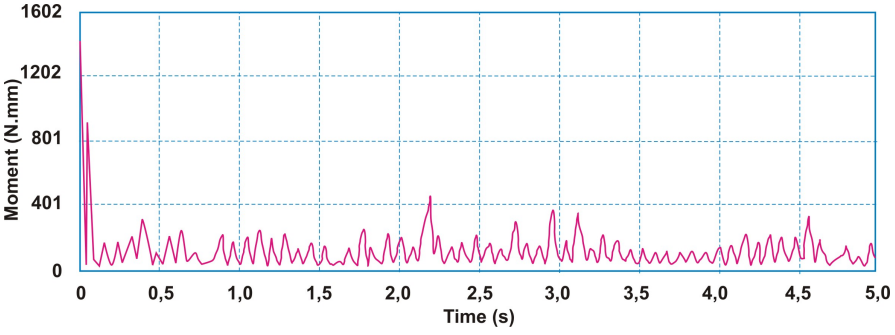

Fig. 10 Movement simulation of the drive of wheels

The chosen drive has been used for the simulation of other parts via FEM (finite element method) (Figure 11).

Upper position of undercarriage has to be fixed, because the mechanism is not self locking. The weight of the robot may lead to the fall of the lower part of the undercarriage. For this purpose, the locking mechanism was designed. (Figure 12) This mechanism consists of servomechanism that moves the pin into the locking position. This solution is also suitable from the energy point of view.

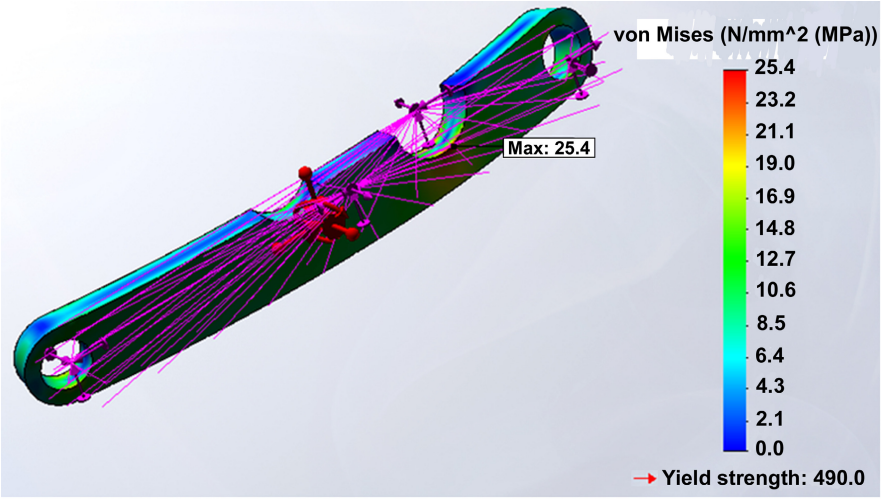

Fig. 11 FEM analysis of the lever inside the lifting mechanism

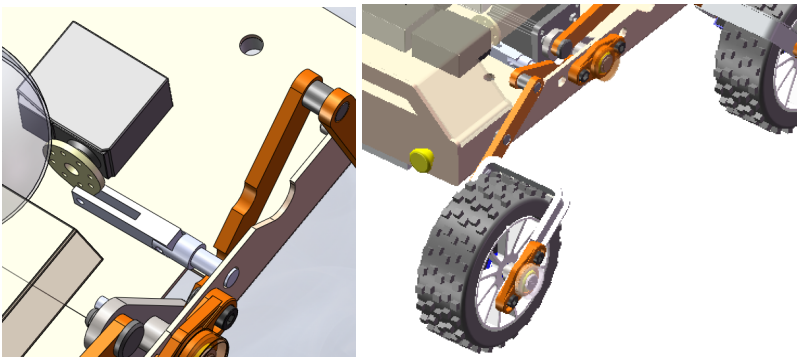

Fig. 12 3D model of the locking mechanisms

5 Final Design of the Robot

Final design of the robot is shown in the Figure 13. The overall dimensions are 280 x 351 x 175 mm and its weight is 3,3 kg. Clearance of the undercarriage is

adjustable from 120mm to 150mm. Calculated maximum velocity on the surface without any obstacle and roughs is 0,47 m/s.

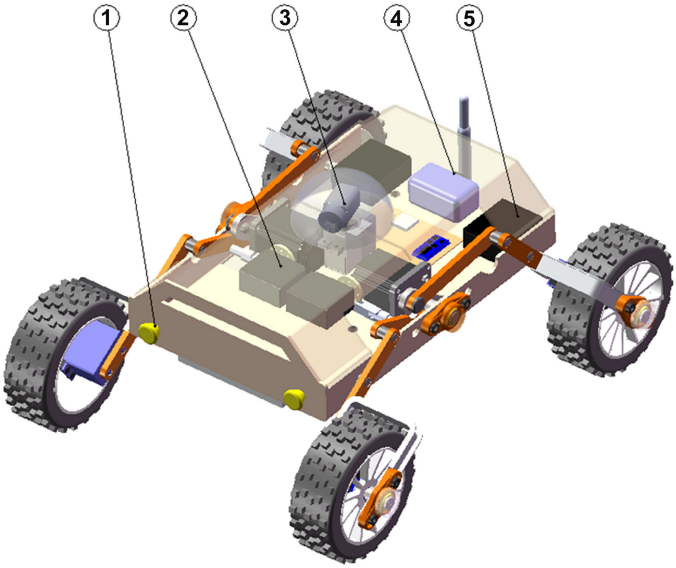

Fig. 13 3D CAD model of the final designed robot (1-lights, 2-locking mechanism, 3-CCD camera, 4-receiver, transmitter, 5-power supply

6 Conclusions

Due to the ability of the robot to adjust to the roughness of the terrain, the proposed mobile robot is unique. Position of the centre of gravity changes and it also helps to obtain better stability of robot on inclined roads. Robots are now under construction. Although, the robot will be operated as teleoperator system, there are several tasks that will be executed autonomously. One of these tasks is the adaptability to the roughness of the terrain or adaptability to any dimensional limits from upper side [10-13].

Acknowledgments. The authors would like to thank to Slovak Grant Agency – project VEGA 1/0085/12, VEGA 1/1205/12 and project KEGA No. 005STU-4/2012 2012. This contribution is also the result of the project implementation: Research of modules for intelligent robotic systems (ITMS: 26220220141) supported by the Research & Development Operational Programme funded by the ERDF.

References

[1] Jezný, J., Paulik, J., Holcer, R.: Remote controlled robots for inspection, pyrotechnical and special tasks. In: Proceeding of 3rd Int. Conf. Safe Slovakia and European Union, VŠBM 2009, Košice, November, 12-13, pp. 109–112 (2009) ISBN 978-80-89282-33-3

[2] Jezný, J.: Manipulators and teleoperators. Acta Mechanica Slovaca 2(3), 353–360 (2008) ISSN 1335-2393
[3] Jezny, J., Paulik, J., Holcer, R.: Robots for Inspection and Pyrotechnical Tasks. In: ICMT 2011: Int. Conf. on Military Technologies, Brno, May 10-11, pp. 901–905 (2011) ISBN: 978-80-7231-787-5
[4] Jurisica, L., Duchon, F., Kastan, D., Babinec, A.: High Precision GNSS Guidance for Field Mobile Robots. International Journal of Advanced Robotic Systems 9, 169–178 (2012) ISSN 1729-8806
[5] Duchon, F., Jurisica, L., Klucik, M.: Service Robots. ATP Journal PLUS Č. 1, 53–56 (2011) ISBN: 1336-5010
[6] Auchter, J., Moore, C.A., Ghosal, A.: A novel kinematic model for rough terrain robots. In: Ao, S.-I., Rieger, B., Chen, S.-S. (eds.) Advances in Computational Algorithms and Data Analysis. LNEE, vol. 14, pp. 215–234. Springer, Heidelberg (2009)
[7] Iagnemma, K., Golda, D., Spenko, M., Dubowsky, S.: Experimental Study of Highspeed Rough-terrain Mobile Robot Models for Reactive Behaviors. Tr. Adv. Robot 5, 654–663 (2003)
[8] Tai, M.: Modeling of Wheeled Mobile Robot on Rough Terrain. In: Proc. IMECE 2003 (2003)
[9] Jarrault, P., Grand, C., Bidaud, P.: Robust obstacle crossing of a wheel-legged mobile robot using minimax force distribution and self-reconfiguration. In: 2011 IEEE/RSJ Int. Conf. on Intelligent Robots and Systems. IEEE International Conference on Intelligent Robots and Systems, pp. 2753–2758 (2011)
[10] Lukac, T.: The mobile robot for the motion in the rough terrain. Technical University of Kosice, Faculty of Mechanical Engineering. Ms Thesis, 96 pages (2009)
[11] Ostertagova, E.: Computer aided learning of math at FEI TU Kosice. In: Int. Conf. on Inovation Process in e-learning, Bratislava, March 10, pp. 1–5. Ekonom, Bratislava (2011) ISBN 978-80-225-3112-2
[12] Ostertagova, E.: Time series modeling. In: Prceeding of the 4th Int. Conf. Modelling of Mechanical and Mechatronical Systems MMaMS 2011, Herlany, Slovakia, September 20-22, pp. 366–373. Technical University, Kosice (2011) ISBN 978-80-553-0731-2
[13] Pásztó, P., Hubinský, P.: Mobile Robot Navigation Based on Circle Recognition. Journal of Electrical Engineering 64(2), 84–91 (2013) ISSN 1335-3632

Project of Autonomous Control System in HUSAR Lunar Mining Rover

P. Węclewski[1], G. Bujko[1], P. Etz[1], Ł. Godziejewski[1], J. Kaplińska[1], P. Kicman[2], and M. Wiśniowski[1]

[1] Warsaw University of Technology, Faculty of Mechatronics, Św. Andrzeja Boboli 8, 02-525, Warszawa, Poland
[2] Warsaw University of Technology, Faculty of Power and Aeronautical Engineering, Nowowiejska 24, 00-665, Warszawa, Poland

Abstract. In near future, autonomous space rovers operating on near-Earth objects will become widely used. HUSAR lunar mining rover is prototype construction designed to participate in NASA Lunabotics Mining Competiton. In this paper the concept of high-level autonomous control, low-level PLC-based operations and communication between working rover and ground station manned by human operator/supervisor is presented and discussed.

1 Introduction

NASA's Fourth Annual Lunabotics Mining Competition is a world-wide competition of 50 university-level teams. The main challenge for participating teams is to design and build a lunar excavator (Lunabot) capable of mining and depositing a minimum of 10 kg of lunar regolith stimulant BP-1 [7] from special arena (LunA-rena) within 10 minutes of competition time. In rover performance scoring several factors are considered important, including: amount of excavated material, Luna-bot mass limitations, remote teleoperation or autonomous control, dust tolerance, power consumption and communication efficiency. The technological solutions used in rovers were constrained – no contraptions that wouldn't work in lunar environment. Moreover, only wireless Wi-Fi communication is allowed.

NASA's main interest from the competition is encouraging the development of innovative projects which could be applied in future devices. Autonomous control is deemed one of vital concepts for near-Earth robotic missions. The reason behind such importance stems from the fact of great distances between celestial bodies causing delays in communication with Earth-based command center, for example 7-minute delay for Mars Science Laboratory mission [2]. Under such circumstances teleoperation control alone is considered highly inefficient.

The main purpose of proposed project is to provide an effective autonomous control system in HUSAR lunar rover. Mechanical design was considered of sec-ondary priority and thus simplified. The control system has four parts: low-level

T. Březina and R. Jabloński (eds.), *Mechatronics 2013*,
DOI: 10.1007/978-3-319-02294-9_70,

control, communication, control center (ground station - GS), and navigation, including obstacle avoidance, driving algorithm and state machine based autonomous control.

2 Mechanical Design

The mechanical design for HUSAR rover (figure 1) consists of three subsystems: bucket wheel (1), arms (2.1) and platform (3.1). The platform is main part of the rover, housing the electric system box (3.2) and gondola (3.4) for batteries. Four-wheel differential drive (3.3) is implemented for driving the rover. The bucket wheel is used for excavating and storing lunar regolith. Arms (2.1) with tie system (2.2) are responsible for lowering and lifting the bucket wheel. There are four predefined positions for wheel, determined by proximity sensors.

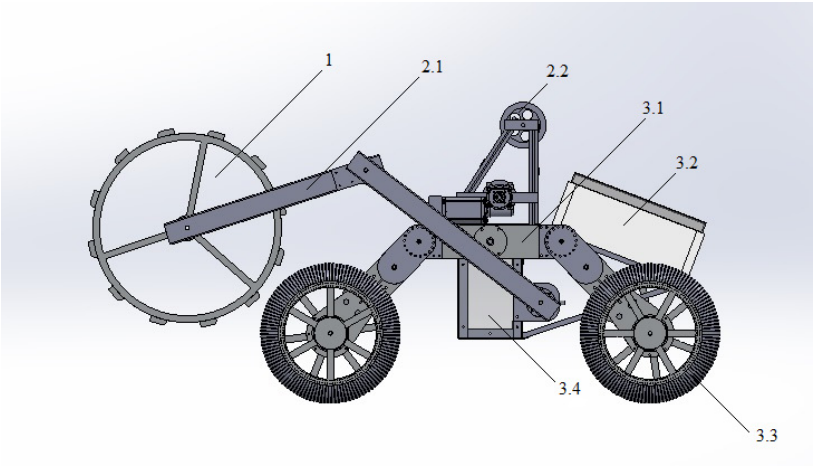

Fig. 1 CAD model of HUSAR lunar rover

3 Control System

According to competition requirements the rover should be controlled in autonomous mode or teleoperation mode in case of failure. Low-level functionality is executed on an industrial PLC controller. For autonomous control, on-board PC placed in electronic box is used. The computer runs custom software based on Petri net. The robot can be remotely controlled from ground station. On-board PC or GS can both issue low-level commands to PLC through Ethernet network (with access point in case of teleoperation mode).

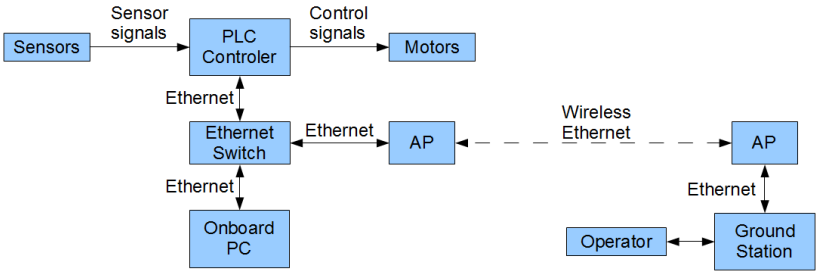

Fig. 2 HUSAR system structure

3.1 Low-Level PLC Control

For low-level control, Siemens S7 1200 PLC was recognized as the best option considering reliability, cost and implementation time. PLC commands are grouped in several categories: basic instructions, safety commands, drive commands and semi-autonomous procedures.

Basic instructions are simple orders to rover actuators: two drive motors, arm elevation motor, bucket wheel motor, electromagnet (bucket wheel lock - for dumping regolith), or check on sensor states: four position proximity sensors, bucket wheel orientation and electromagnetic lock, power parameters module and force sensors used to calculate excavated mass. Drive commands utilize basic instructions to achieve rover movement with desired speed. Three commands were developed: forward movement, driving along an arc and rover rotation. Safety commands are orders used to stop one or all motors in case of undesired behavior. Switching off autonomy and activating teleoperation mode can be also achieved by appropriate safety command. These are considered with the highest priority compared with other functions – when safety command is issued, current order will be interrupted, stopping motors immediately.

Semi-autonomous procedures are order lists of basic instructions designed to be executed with only one command in order to minimize bandwidth when in teleoperation mode. These procedures include routine actions of rover, like excavating regolith or emptying bucket wheel.

3.2 Ground Station

The main purpose of GS is to provide an user-friendly and full-featured system for supervisory control of HUSAR rover operations. To keep communication well-maintained the connection between PLC and on-board computer is separated in order to avoid breaking the transfer in case of on-board PC failure. The framework chosen for GS implementation is QT4 because of overall efficiency and esthetic interface.

For GS two widgets were developed: diagnostic windows and operator panel, both of these are available in either autonomous or teleoperation mode. In autonomous mode the requests sent by operator (except security functions) are ignored, but preview of the rover is still available by supervisory control window.

GS consists of three classes: Robot, MainWindow and SCADA (*Supervisory Control And Data Acquisition*) for robot state graphical presentation. The architecture of the application is shown in Figure 3.

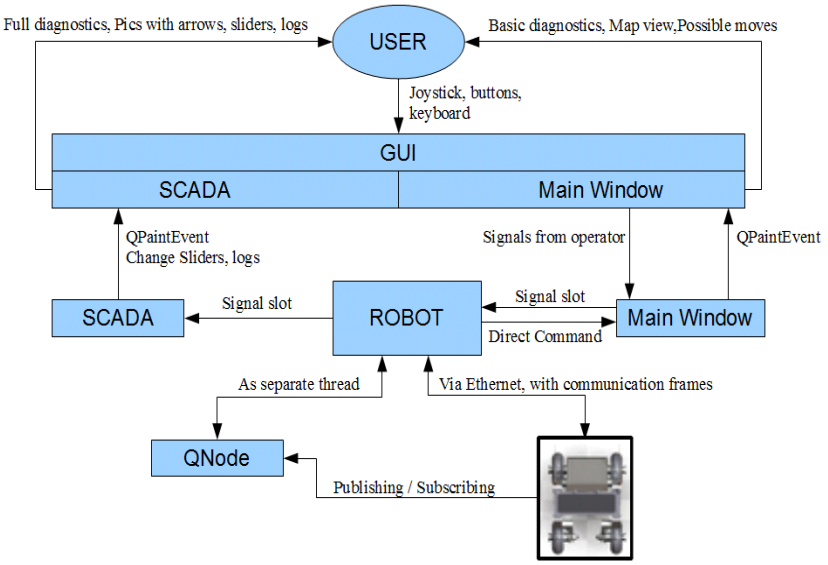

Fig. 3 GS architecture

Class Robot communicates with HUSAR using communication frames and stores its state. What is more, Robot has a separate thread – QNode- to use ROS (Robot Operating System) [4] to retrieve rover's position. The main advantage of this solution is independent and parallel communication via ROS with on-board PC and PLC. Used ROS package – qt_ros – provides easy integration of QT and ROS.

SCADA provides the diagnostic panel. It displays low-level information such as speed, current and voltage on each motor, bucket sensor information, mass of excavated material, arm position and current position on the Petri graph. This system improves responding to fault states such as overcurrent and overload.

The operator panel, implemented in MainWindow class, contains all commands eligible for PLC, which can be called by joystick or keyboard. Semi-autonomous procedures are grouped into subordinate functions, making the manual activation of subsequent procedure steps possible if necessary.

3.3 High-Level Control

The robot activities can be divided into four distinct phases: Initialization, journey to and from mining spot, mining, dumping the regolith into bin.

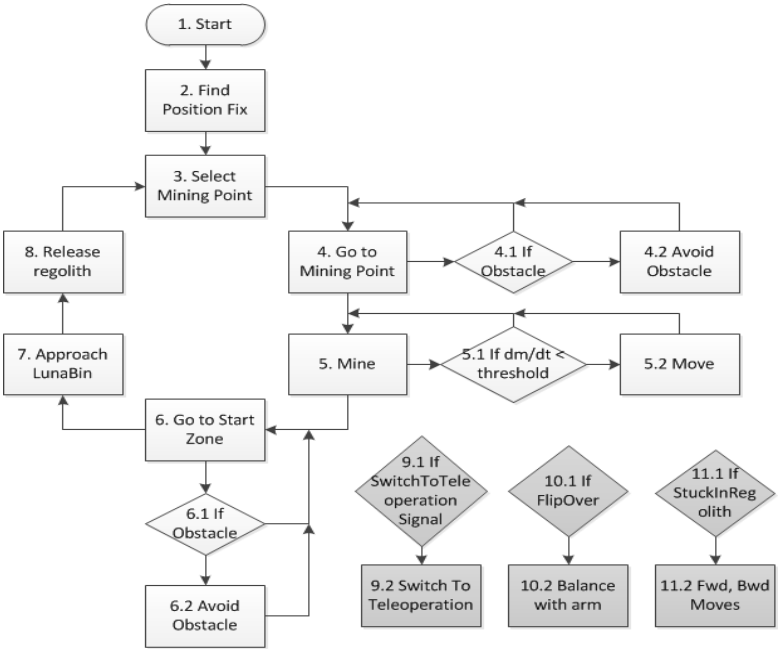

Fig. 4 State Machine graph

Basic high-level behavior diagram is presented in Figure 4. Few emergency conditions are also highlighted.

The algorithm shall be repeated several times during one run. In the robots' representation LunArena is represented as 3x3 grid: Start Zone, Obstacle Zone and Mining Zone subdivided into three parts each. In each zone robot's behavior is different. This ensures that robot will comply to the competition rules, i.e. will not start mining in Obstacle Zone. Using specification provided in previous chapters the Petri net [6] was developed, describing high-level control of the rover. Automata based on this class of algorithms provides easy to implement and highly reliable tool, which also allows for monitoring of robot states.

Petri nets have been widely used for control of mobile robots, e.g. tour guide robot presented in [8], as well as in many other applications. In our design, partially presented in Figure 5, places of the Petri net are states in which robot can operate. Transitions between the nodes are usually associated with appropriate sensory reading (e.g. obstacle detection, desired localization reached) or operator command (in emergency situations).

3.4 Localization

NASA Lunabotics Mining Competition imposes very strict rules regarding navigation systems used on the rover. In short, electromagnetic based equipment can only be used, with limits as not to interfere with other team's devices. However, it is possible to place markers on the walls in order to simplify the navigation.

For HUSAR rover, IFM O3D201 PMD[1] camera is used [3]. The area in which the rover operates is contained in a 7.38x3.88m sandbox filled with BP-1 regolith.[5]

Place	Description
P2	Autonomous driving towards selected goal
P3	Obstacle avoidance
P4	Finding position fix
P5	Ready position (arm up, mining zone)
Trans.	**Description**
T2	Obstacle detected
T3	No obstacles in front of the robot
T4	Reached the goal at mining zone, Stop.
T5	Lost position fix
T6	Position fix found
T9	Bucket full, set driving goal for starting zone

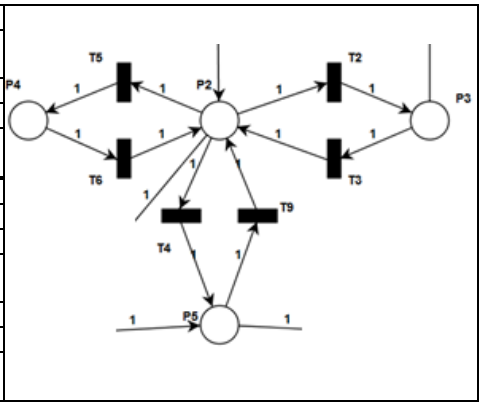

Fig. 5 Part of Petri Net used for autonomous driving of the robot

The camera outputs a 2D depth image, which is converted by our driver into a 3D PointCloud image. The algorithm we use converts the middle section of the 3D image into a 2D laserscan-like image.

The rover's position is calculated from the distance to the detected corners and orientation is calculated by comparing the previous orientation with a normal vector of the flat projection of detected wall. In order to simplify autonomy operations, position will be approximated to one of nine cells in a 3x3 grid map. This method of localization was chosen because of its relative simplicity and computational effectiveness.

Corner detection is achieved by comparing the normal vectors. A corner is assumed if the absolute difference between two neighboring vectors' yaw value is higher than a predefined threshold. In order to avoid not detecting a corner due to a curvature(which can result from imaging inaccuracy), there is also a redundancy check, which compares the current vector's yaw with a temporary variable, which assumes the value of the first yaw of the current wall. If a corner is detected, the temporary yaw variable assumes the value of the first yaw of the new wall.

[1] http://www.ifm.com/

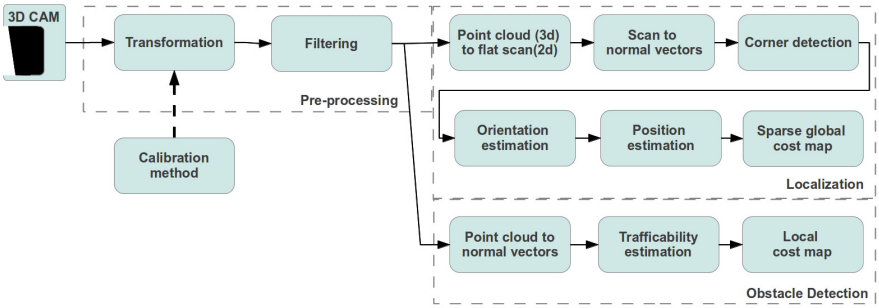

Fig. 6 3D data processing pipeline

The localization process is divided into two stages. In first stage the rover rotates until it finds a predefined corner and then aligns itself perpendicular to the wall to the left from the corner, which is still in the field of view. After aligning itself, the algorithm starts the second stage, where the current orientation is defined on the basis of the detected wall normal vector and converted to the actual orientation – added or subtracted by a fixed value, which depends on the number of corners that have passed in the rover's field of view. If more than one wall is in the rover's field of view, the algorithm takes into account the larger wall.

On the basis of the calculated position, position in the grid matrix is approximated. The grid matrix is filled with zeroes except the field the rover is currently in.

The obstacle detection algorithm consists of three main stages. Normal vector coordinates for each point of the whole PointCloud are calculated. In the second stage, each vector is converted to a unique RGB value [1], in order to use efficient image processing algorithms. In the last stage the gradient of the image is checked and in case its value is above a threshold, an obstacle flag is raised. The obstacle local position is calculated by getting its position from Point Cloud coordinates.

4 Conclusions

The autonomous operation system outlined in this paper provides basic framework for operating HUSAR lunar mining rover in LunArena environment. As several system tests had shown, the adopted solution is simple, yet efficient and cost-effective. This approach will be further developed and tested in order to be used in 2014 Lunabotics Mining Competition.

References

[1] Borkowski, A., Siemiatkowska, B., Szklarski, J.: Towards semantic navigation in mobile robotics. In: Engels, G., Lewerentz, C., Schäfer, W., Schürr, A., Westfechtel, B. (eds.) Nagl Festschrift. LNCS, vol. 5765, pp. 719–748. Springer, Heidelberg (2010)

[2] Makovsky, A., Ilott, P., Taylor, J.: Mars Science Laboratory Telecommunication System Design. Jet Propulsion Laboratory, California Institute of Technology (2009)
[3] Prusak, A., Melnychuk, O., Roth, H., Schiller, I., Koch, R.: Pose Estimation and Map Building with a PMD-Camera for Robot Navigation. In: Proceedings of Dyn3D Workshop DAGM, Heidelberg, Germany (2007)
[4] Quigley, M., Conley, K., Gerkey, B., Faust, J., Foote, T., Leibs, J., Ng, A.Y.: ROS: an open-source Robot Operating System. In: ICRA Workshop on Open Source Software, vol. 3(3.2) (2009)
[5] Rahmatian, L.A., Metzger, P.T.: Soil Test Apparatus for Lunar Surfaces. NASA (2010)
[6] Reisig, W.: Petri nets: an introduction. Springer, New York (1985)
[7] Stoeser, D.B., Wilson, S., Rickman, D.L.: Preliminary Geological Findings on the BP-1 Simulant. NASA (2010)
[8] Tsai, C., Shish, S., Huang, H., Wang, M., Lee, C.C.: Autonomous Navigation of an Indoor Tour Guide Robot. Advanced robotics and Its Social Impacts (2008)

Object Classification Using Dempster–Shafer Theory

B. Harasymowicz-Boggio and B. Siemiątkowska

Warsaw University of Technology, Faculty of Mechatronics, Warsaw, Poland
rrg.wut@gmail.com

Abstract. This paper presents a new method of complex object recognition and classification by a mobile robot. Through applying Dempster-Shafer theory, our algorithm allows to make use not only of object features, but also of information about sensor uncertainty, possible occlusions and can handle contradictory evidence in an integral way. The proposed method has been implemented and tested with complex objects from a real indoor environment, showing that it can be efficiently applied for cluttered data and also make correct decisions even when whole parts of the objects are occluded and the visible parts lack unique features.

1 Introduction

The ability to navigate is the most important competence of an indoor mobile robot. This task is a combination of three elements: mapping, localization and path planning. The mapping problem is one of the most active areas in robotics. Most of the navigation systems use a global metric map [1,2,3]: an occupancy grid or feature-based representation [3]. Some authors have also proposed topological-metric representations [4], which are usually designed as a graph. The nodes of the graph correspond to particular elements of the building.

A modern navigation system requires efficient human-robot interaction. This kind of interaction is impossible when the user has to indicate the goal for the robot using non-intuitive metric information. We want the robot to perform a task which is described in natural language - for example, we want the robot to go to the kitchen without having to specify the exact (x,y,z) coordinates.

A solution proposed in our previous work is the use of a BIM-based (building information modeling) representation of the environment (BIMR) [5]. In BIMR the components of a building are described as a hierarchy of objects which have attributes and application rules. This kind of representation is more suitable for human-robot interaction, but requires semantic analysis of the data obtained from the robot sensors.

There are many known methods of object recognition and classification [6,7,8,9,10] but they are always subject to the limitations of the robot sensors. When a camera is used, classification is performed based on color and texture [11,12], but images are very sensitive to the changes of the camera position and to

T. Březina and R. Jabloński (eds.), *Mechatronics 2013*,
DOI: 10.1007/978-3-319-02294-9_71,

lighting and texture variations. In the case of metric sensors (laser scanners) the density of point clouds depends on the distance between the sensor and the object which is observed [13,14]. The same applies to RGB-D devices which are based on triangulation. Even though sensors such as the Kinect are often used in indoor environments [15,16], the distance to the object has a great impact on data precision.

In this article we present a method of handling input data based on Dempster-Shafer theory which allows to take into consideration the limitations of the sensor used for object recognition and combine multiple sources of information (e.g. observed segments) to make more reliable decisions.

2 Hardware

In our research project the "Kurier" mobile robot is used. The robot was built in the Warsaw University of Technology as an experimental platform. Beside low-level sensors which allow to detect obstacles, the platform is equipped with a laser range finder and a 3D Kinect sensor. This sensor is based on software technology developed by Microsoft Game Studios and PrimeSense range camera technology.

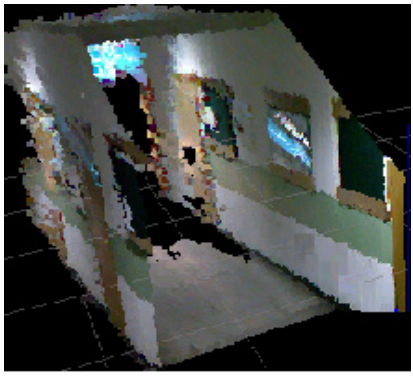

Fig. 1 Point cloud obtained by a Kinect sensor

The Kinect consists of an infrared laser projector and a monochrome CMOS sensor. Structural light emitted from the projector allows to capture video data in 3D under any indoor lighting conditions. The device is additionally equipped with an RGB camera, which gives images that are superposed to the point cloud but play no role in depth measurements. The Kinect outputs video at a frame rate of 30 Hz. The RGB video stream uses 8-bit VGA resolution (640×480 pixels). The monochrome depth sensing video stream is in VGA with 11-bit depth. The angular field of view of the sensor is 57 degrees horizontally and 43 degrees vertically. This high level sensor is the primary source of data for object classification. Fig. 1 presents the consistent point clouds obtained by the sensor.

3 Dempster–Shafer Theory

In artificial intelligence, classification is the problem of identifying to which class an object belongs on the basis of an observation. Individual observations are analyzed and described with a set of quantifiable properties, known as explanatory variables, or *features*. Bayesian methods can calculate the probability of each classification hypothesis based on the given data to make a prediction [17].

When data is obtained in a real environment, we deal with two kinds of uncertainties [18]:

- aleatory (stochastic) uncertainty which results from the fact that the system behaves in a random way,
- epistemic (subjective) uncertainty which results from lack of knowledge.

Usually the conventional probabilistic theory is used in both types of uncertainties, but it requires an adaptivity assumption and information about probabilities of all events, so it is not capable of capturing epistemic uncertainty.

Dempster-Shafer theory [19] (DST) is designed to deal with distinction between uncertainty and ignorance. DST is a mathematical theory of evidence which can be regarded as a generalization of the Bayesian theory. It is often used as a method of sensor fusion.

DST consists of two ideas:

- obtaining degrees of belief for a hypothesis based on facts,
- applying Dempster's rule for combining degrees of belief when they are based on independent facts.

A degree of belief (a mass) is represented as a belief function (not a probability distribution). Masses are assigned to *sets* of possibilities and not to single events.

Each fact has a degree of support between 0 and 1 and a degree of negation. In comparison to the Bayesian theory belief in a hypothesis and its negation need not to sum to 1 and both values can even be equal 0, which would mean that there is no evidence for or against the theory.

When we have two sources of information about a certain hypothesis described by the belief functions m_1 and m_2,they can be combined according to the following formulas:

$$m(h)=\frac{m_1(h)m_2(h)+m_1(uh)m_2(h)+m_2(uh)m_1(h)}{1-m_1(h)m_2(nh)+m_1(nh)m_2(h)} \tag{1}$$

$$m(nh)=\frac{m_1(nh)m_2(nh)+m_1(uh)m_2(nh)+m_2(uh)m_1(nh)}{1-m_1(h)m_2(nh)+m_1(nh)m_2(h)} \tag{2}$$

$$m(uh)=1-m(h)-m(nh) \tag{3}$$

where: h – the hypothesis, nh – negation of the hypothesis h, uh – uncertainty of the hypothesis.

4 Data Classification

The object classification method proposed by the authors of this paper consists of the following stages:

- Initial scene segmentation into smooth patches, which are interpreted as object parts (or whole objects in the case of simple objects);
- Features extraction, for which the CAT [20] (convexity, anisotropy of convexity and polar angle "theta") surface features are applied;
- Estimation of the influence of each segment on the object hypotheses. This influence consists of belief (h), negation (nh) and uncertainty (uh) and is calculated based on the part's histogram of CAT features, the percentage of visible part area, the distance to the sensor and the confirmation the segment provides for concurrent object hypotheses.
- Dempster-Shafer data combination and finding the best hypothesis (i.e. the hypothesis with the highest belief value). This step is performed according to the diagram presented in Fig. 2. using the formulas 1, 2 and 3 for data combination for each object hypothesis.

The system has been implemented and tested with real complex objects for different cases of occlusion. The results are presented in the next section.

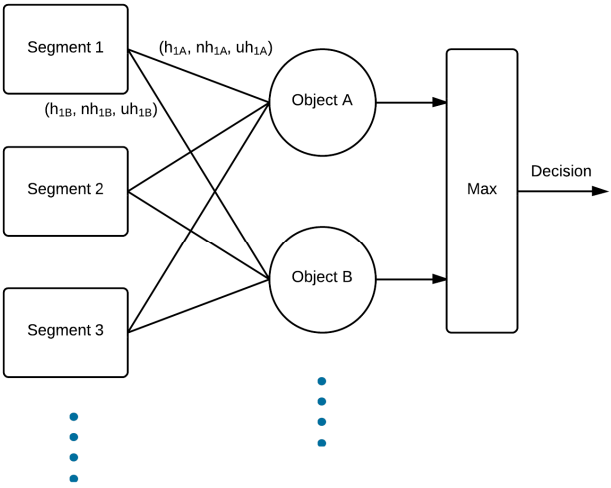

Fig. 2 Flow diagram of the classification system

5 Experimental Results

The described object classification system has been tested using scenes captured by the Kinect sensor with a realistic degree of cluttering. The test objects were: a

book, a juice carton and a lamp (Fig. 3.). The vertical and horizontal object parts (such as book-1, lamp-1 and carton-1) are especially difficult to differentiate based on segment features, as they are rife flat surfaces.

Different cases of whole part occlusions have been tested for each object, comparing the resulting belief degrees of each hypothesis (Table 1). In all the cases the correct object hypothesis achieved the highest belief degree (among other hypotheses) when at least 2 parts were visible.

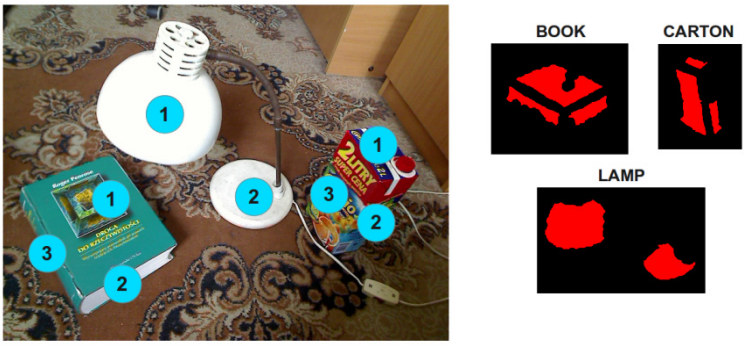

Fig. 3 Part labels of the test objects (a) and their cluttered views used in the experiment (b)

Table 1 Belief of the object hypotheses after Dempster-Shafer data combination. The tested cases are: only part 1 is visible (1), parts 1 and 2 are visible (1+2) and all parts are visible (1+2+3)

Visible:	1	1+2	1+2+3
Book	**0.50**	**0.67**	**0.91**
Carton	0.00	0.31	0.31
Lamp	0.50	0.50	0.50
Book	0.00	0.40	0.40
Carton	**0.47**	**0.55**	**0.82**
Lamp	0.05	0.05	0.05
Book	0.00	0.33	-
Carton	0.00	0.00	-
Lamp	**0.86**	**0.91**	-

6 Conclusions

In this work we described a new approach to classification of complex objects present in the environment of a mobile robot. This approach consists on applying the Dempster-Shafer theory to make use of uncertainty of the data and handle contradictory evidence. The proposed method has been tested in an experiment

with real-world objects and shown to be effective in cases where features alone are insufficient to distinguish objects.

Acknowledgments. This work has been partially supported by the National Science Center (grant 2011/01/B/ST6/07385).

References

[1] Elfes, A.: Sonar-based real-world mapping and navigation. IEEE Journal of Robotics and Automation 3, 249–265 (1987)
[2] Moravec, H., Elfes, A.: High resolution maps from wide angle sonar. In: Proc. IEEE International Conference on Robotics and Automation, pp. 116–121 (1985)
[3] Thrun, S., Burgard, W., Fox, D.: Probabilistic Robotics (Intelligent Robotics and Autonomous Agents). The MIT Press (2005)
[4] Remolina, E., Kuipers, B.: Towards a general theory of topological maps. Articial Intelligence 152(1), 47–104 (2004)
[5] Siemiątkowska, B., Harasymowicz-Boggio, B., Przybylski, M., Różańska-Walczuk, M., Wiśniowski, M., Kowalski, M.: BIM Based Indoor Navigation System of Hermes Mobile Robot. In: Proceedings of the 19th Romansy, pp. 378–381 (2012)
[6] Anguelov, D., Biswas, R., Koller, D., Limketkai, B., Sanner, S., Thrun, S.: Learning hierarchical object maps of non-stationary environments with mobile robots. In: Proceedings of the 17th Annual Conference on Uncertainty in AI (UAI), Edmonton, Canada (2002)
[7] Anguelov, D., Koller, D., Parker, E., Thrun, S.: Detecting and modeling doors with mobile robots. In: Proceedings of the IEEE International Conference on Robotics and Automation, ICRA (2004)
[8] Mozos, M.O., Chollet, F., Murakami, K., Morooka, K., Tsuji, T., Kurazume, R., Hasegawa, T.: Tracing commodities in indoor environments for service robotics. In: Proc. of the 10th IFAC Symposium on Robot Control, Dubrovnik, Croatia, vol. 10, pp. 71–76 (September 2012)
[9] Lai, K., Bo, L., Ren, X., Fox, D.: Detection-based object labeling in 3D scenes. In: IEEE International Conference on on Robotics and Automation (2012)
[10] Mozos, O.M., Mizutani, H., Kurazume, R., Hasegawa, T.: Categorization of indoor places using the kinect sensor 12(5), 669–671 (2012)
[11] Ziegler, A., Christiansen, E., Kriegman, D., Belongie, S.: Locally uniform comparison image descriptor. In: Bartlett, P., Pereira, F., Burges, C., Bottou, L., Weinberger, K. (eds.) Advances in Neural Information Processing Systems 25, pp. 1–9 (2012)
[12] Vedaldi, A., Zisserman, A.: Efficient additive kernels via explicit feature mapsin. In: Proceedings of the IEEE Conf. on Computer Vision and Pattern Recognition, CVPR (2010)
[13] Zhang, C., Wang, L., Yang, R.: Semantic segmentation of urban scenes using dense depth maps. In: Daniilidis, K., Maragos, P., Paragios, N. (eds.) ECCV 2010, Part IV. LNCS, vol. 6314, pp. 708–721. Springer, Heidelberg (2010)
[14] Krainin, M., Konolige, K., Fox, D.: Exploiting segmentation for robust 3D object matching. In: Proc. of the IEEE International Conference on Robotics & Automation, ICRA (2012)

[15] Siemiątkowska, B., Szklarski, J., Gnatowski, M.: Mobile robot navigation with the use of semantic map constructed from 3D laser range scans. Control and Cybernetics 40(2), 437–453 (2011)
[16] Lai, K., Bo, L., Ren, X., Fox, D.: RGB-D object recognition: Features, algorithms, and a large scale benchmark. In: Consumer Depth Cameras for Computer Vision: Research Topics and Applications, pp. 167–192. Springer (2013)
[17] Russell, S.J., Norvig, P.: Artificial Intelligence: A Modern Approach. Pearson Education (2003)
[18] Helton, J.C.: Uncertainty and Sensitivity Analysis in the Presence of Stochastic and Subjective Uncertainty. Journal of Statistical Computation and Simulation 57(1-4), 3–76 (1997)
[19] Pearl, J.: Reasoning with Belief Functions: An Analysis of Compatibility. The International Journal of Approximate Reasoning 4(5/6), 363–389 (1990)
[20] Harasymowicz-Boggio, B.: 3D object detection and reconstruction based on CAT featurespatch backprojection and hidden Markov models (Submitted for publication 2013)

A Novel Indoor Localization Scheme by Integrating Wiimote Sensing and a Controllable IR-LED Array

Y.T. Fu and K.S. Chen

National Cheng-Kung University, Department of Mechanical Engineering,
1 University Rd. Tainan, Taiwan, 70101, R.O.C.
zj4m42k6@hotmail.com, kschen@mail.ncku.edu.tw

Abstract. In this work, a novel wiimote localization scheme is proposed based on kinematics and coordinate transformation. By integrating the scheme with a controllable IR-LED array, it is possible to interpret the absolute coordinate and orientation of mobile carriers even under the influence of passing through possible shelters such as furniture. The scheme is experimentally verified by using a servomotor. Finally, the scheme is applied on an omni-wheel mobile robot for trajectory control to demonstrate the possible application of this wiimote localization scheme in indoor living space applications.

1 Introduction

Trajectory control of indoor mobile robot is important for subsequent intelligent life applications such as medical care or movement assistance [1]. In order to achieve the above mentioned goals, an accurate and reliable motion sensing system is essential. With accurate positioning information, important tasks in navigation, feedback control, coordinated motion, and trajectory planning can be realized. However, due to restrictions in positioning resolution, system dynamic responses, available sensing range, and compromising with various complicated indoor environments, a flawless positioning technique has not yet been achieved. Various solutions currently exist for indoor positioning, navigation, and communications such as GPS localization and inertial navigation system (INS)[2], have been developed. These techniques have their own strengths and weaknesses.

IR localization is another possible choice [3,4]. In particular, IR-LED based wiimotes have been proposed for many other applications beyond its original TV game design. Recently, due to simple relationship between the displayed pixel and the sensing distance, it has been used as an alternative choice for indoor localization sensors. It has been demonstrated that the milimeter sensing resolution can be achieved [5]. With such a sensor resolution and a bandwidth approximately 107 Hz, it is possible to integrate wiimote with other indoor applications such as mobile service robots manipulations in intelligent living technology.

T. Březina and R. Jabloński (eds.), *Mechatronics 2013*,
DOI: 10.1007/978-3-319-02294-9_72,

The wiimote sensing zone is based on the pixel location of the IRLED in the viewing area, which contains 1024 x 768 pixels. The actual pixel length is proportional to the sensing distance. Therefore, there is a trade-off between sensing zone and the spatial resolution. For a typical sensing distance (i.e., distance between ceiling and the floor) of 2.5 m, the spatial resolution is approximately 5 mm and the viewing area is 60 x 80 cm. The resolution is sufficient but the area is obviously too small. In our previous study, Chen et al [5] has proposed a multi-zone scheme to extend the sensing area of wiimote to virtually entire indoor space. However, it is only valid with pure translational motion. Gu et al further extended Chen's work to cover this main drawback by simultaneously monitoring the position of two IR-LEDs[6]. By such an approach, both the location and orientation can be precisely determined and the scheme has been served as the feedback sensor for position control of mobile robots.

Although Gu's work[6] has demonstrated the applicability of wiimote as an accurate and reliable position sensor for indoor environment, its position sensed is actually the relative position at a particular zone and the initial location must specified before the scheme can be applied. The inability to identify the individual zone presents the major drawback of wiimote in comparison with other similar systems such as Stargazer. One major consequence of Gu's scheme is that the mobile carrier must be continuously monitored[6]. That is, once a carrier passes under a shelter such that the wiimote temporally loses the tracking, the position information calculated by wiimote will be resumed back to the starting location once the carrier leaves the shelter and is re-contacted by the wiimote. This flaw presents a remained obstacle for realizing the wiimote-based indoor localization.

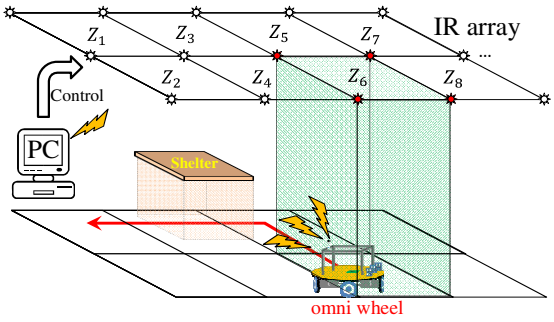

Fig. 1 Schematically plot of the proposed wiimote localization system

In this work, as schematically shown in Fig. 1, we proposed a novel scheme by integrating wiimote with a controllable IR-LED array. By the controlled input of the IR-LED array, it is possible to interpret the absolute coordinate and orientation of mobile carriers. The scheme is robust even the carrier continuously moves in and out of a shelter. In addition, it is also possible to guide the motion of mobile robot by means of lighting sequence. We believe that this should present significant contribution in indoor localization for related applications.

2 Wiimote Fundamentals

As shown in Fig. 2, wiimote contains a built-in "wiimote camera" to detect up to four IR LEDs with visual angles of approximately 45 (X) and 35 (Y) to form a sensing zone with a resolution of 1024×768 pixels. Since 2008, there have been many investigations on exploring wiimote's applications beyond its original design, particular in multi-media [7], object tracking and small area localization. In this work, we are mainly interesting on its localization ability and the potential for using it as an indoor global position/orientation sensor. For a fixed sensing distance, a relative lateral motion will be sensed by the IR camera and the position of the IR LED can be reported to LabView after being lumped into a point fitted into the sensing zone. The position is linearly proportional to the image pixel location and the sensing distance. Our previous experimental investigation [5] indicated that the resolution is around 2 mm for typical indoor space and the bandwidth was 107 Hz. These results imply that wiimote could play as a fast and accurate position sensor in a living space.

The above features form the fundamentals of wiimote localization. In a typical living space application, the sensing area must be expanded, the orientation of the associated mobile carrier must be detectable, and the influence of possible shelters (e.g., moves under a table) must be considered. Through the efforts of our previous works, the first and the second concerns have been solved and the indoor localization of mobile robots in a large open area can be successfully monitored. In this work, a modified scheme is further proposed to solve the last issue. By the method presented in this work, the positioning of mobile units in a large indoor space containing IR shelters such as furniture could be achieved and this scenario should very close to the real situation to be encountered.

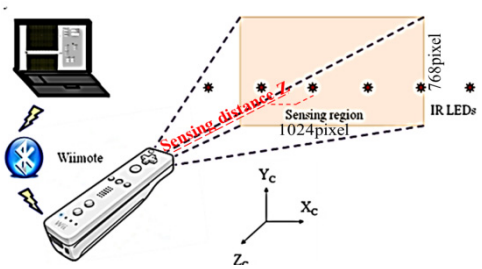

Fig. 2 Schematic plot of wiimote for IR LED location sensing

3 Proposed Wiimote Localization Scheme

As already shown in Fig.1, consider an indoor space with an IR LED array on the ceiling where the coordinates of all IR-LEDs are pre-determined, a mobile robot with a wiimote mounted on moves in a 2D manner. The wiimote is mounted on the exact center of rotation. At the very beginning, the IR-LEDs in the array are

sequentially turned on and off to make interaction with the wiimote mounted on the robot. Once the contact is established, the zone where the robot is located is known. The remaining work is to find the location of the robot at this zone by using the information of the true coordinates and the wiimote readouts of these IR-LEDS by developing a coordinate transformation relation. By such a transformation, both the robot location and orientation can be found.

As shown in Fig. 3, there are three possible types of contact between a wiimote and IR-LEDs. A reference point R_c must be pre-established based on the detected IR-LED positions. Based on the number of IR-LEDs contacted, the manner to find R_c is slightly deferent. For example, if four IR-LEDs are observed, the reference point R_c is determined as the geometric center of the four LEDs.

Taking the situation shown in Fig. 3(a) as the example, the relationship between the reference point R_c and the locations of two key-IR-LEDs p_{c1} and p_{c4} can be expressed as

$$\begin{bmatrix} x_{cr} \\ y_{cr} \end{bmatrix} = \frac{1}{2}\begin{bmatrix} x_{c1} + x_{c4} \\ y_{c1} + y_{c4} \end{bmatrix}, \tag{1}$$

From the true coordinates and the wiimote readouts of p_{c1}, p_{c4}, and R_c, it is possible to calculate two rotating angles θ and ϕ for determine the robot orientation. That is, by referring to Fig. 4(a), it can be seen that

$$\theta = \tan^{-1}\frac{(x_{c1} - x_{c2})}{(y_{c1} - y_{c2})}, \tag{2}$$

$$\phi = \tan^{-1}\frac{y_{cr}}{x_{cr}} \tag{3}$$

Finally, the location and orientation of wiimote (or the robot) relative to R_c can be found as $(-x_{cr}, y_{cr}, -(\theta+\phi))$. Once this information can be determined, the robot location and orientation at the entire living space can be found by adding the above quantity with the absolute coordinate of R_c.

The flowchart of the proposed method is schematically shown in Fig. 4(b) and is briefly stated below.

1. Layout an IR-LED array to pre-determine the coordinates of all IR-LEDs. The IR-LEDs are controlled to turn on/off sequentially. Once the wiimote detects IR-LEDs, it is possible to know the zone where the robot is located.
2. Using the coordinates and the wiimote readout of these contacted IR-LEDs to determine the coordinate of the reference point R_c.
3. Calculate the rotation angle θ and the angle ϕ using R_c and wiimote readout of the contacted IR-LEDs.
4. Compute the absolute position and orientation of the robot by adding the information of zone number and the relative position inside a zone.

5. For next time increment, return to step 2 and repeat the process until the motion stops.

It is worth to compare the proposed scheme and our previous approach [6] here. Previously, the IR-LEDs are not controlled and are always turned on. As a result, it is required to pre-determine the starting location of the robot. It then uses the wiimote readout of the sensed IR-LEDs to determine the rotation angle and perform coordinate transformation to calculate the position increment of the robot. The new position is obtained by adding the increment to the previous location.

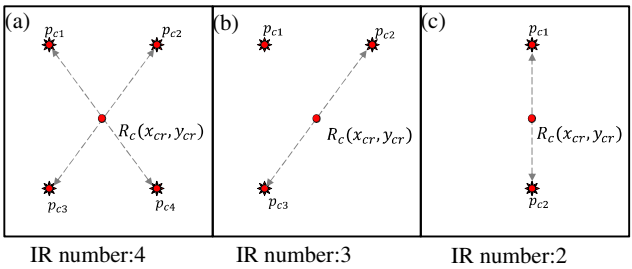

Fig. 3 Three possible patterns of IR-LEDs observed by wiimote and the definition of the associated reference point Rc

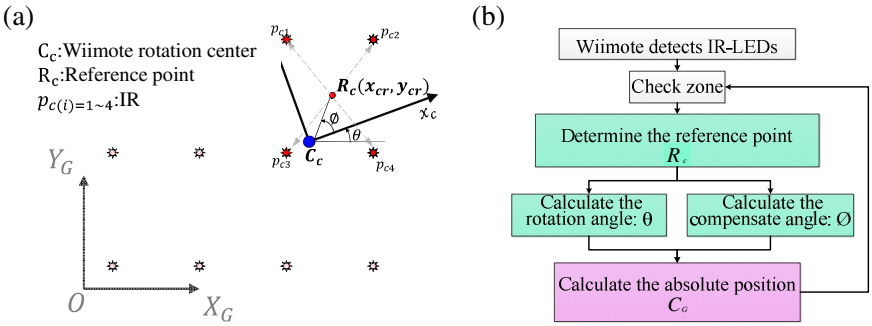

Fig. 4 (a) schematics of the coordinate transformation and (b) the brief flowchart of the localization scheme

Conversely, the current approach uses known IR-LEDs position to find the reference point and the required rotation information. The robot location and orientations are then obtained. For each time increment, the robot location is recalculated and is not relied on the previous robot location. Therefore, the positioning error is not accumulated. Nevertheless, perhaps the most important difference occurs at robot passes under a shelter. When robot moves under the shelter, it is out of monitoring. As it eventually moves out of the shelter and re-contacted by wiimote, its location must be reported correctly. However, in our previous

approach [6], the determination of this position relies on the previous step's information, which is the position right before entering the shelter and thus the calculation will result in an incorrect answer. On the other hand, in the present approach, the determination of current location does not rely on the moving history and can be obtained solely by the current observed IR-LEDs. This feature implies that the proposed localization scheme could be suitable for more complicated indoor living space where many shelters resulted from furniture is expected.

4 Experimental Results

A 3×5 IR LED array is constructed for validating the proposed scheme. A wiimote is mounted on a two-axis linear servomotor. A shelter is placed between the wiimote and the IR-LED array to mimic the scenario of robot moving through a table. The results are shown in Fig. 5, it can be seen that before entering the shielding area, the robot position can be monitored by wiimote well. When the robot is in the shielding area, it is temporally losing contact. However, once it travels out of the shielding zone, the wiimote immediately re-captures the position and orientation of the robot. Although this result may be easy to be achieved by other type sensors (which suffer from other problems), it is not trivial for wiimote localization. As mentioned in Section 1, with the problem being solved, one should be able to use wiimote localization in general indoor living space.

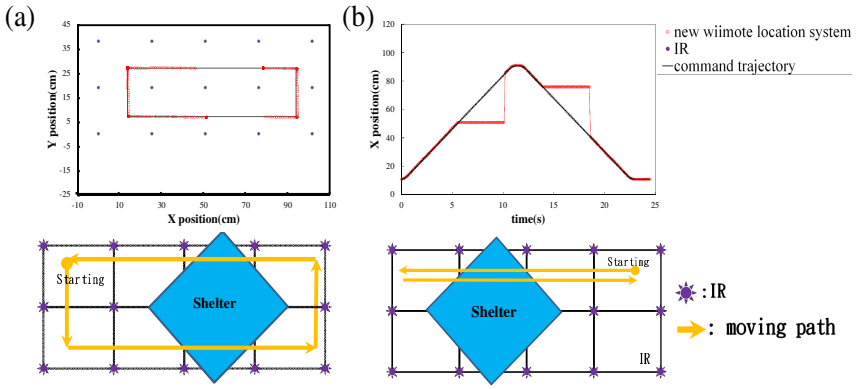

Fig. 5 Wiimote moves passing under a shelter. (a) comparison between the command and the actual reported location, (b) the x-position history

The localization scheme is finally integrated with an omni-wheel mobile robot to demonstrate its ability on monitoring and controlling indoor robot. As shown in Fig. 6, the robot is commanded to travel a rectangular path and is forced to pass under a shelter. The wiimote system successfully monitors the trajectory of the robot before it enters the shielding zone and quickly re-contacts the robot once it leaves the shelter.

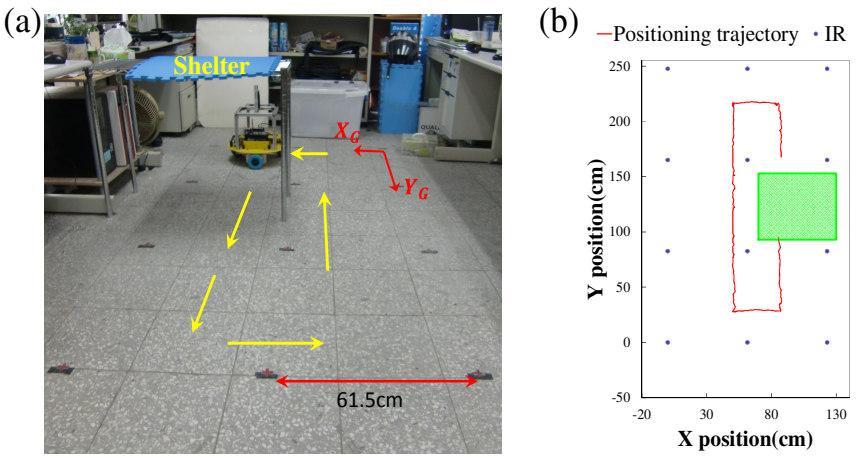

Fig. 6 The experimental demonstration setup and the localization result

5 Discussion

In this work, a modified 2D multi-zone localization scheme based on wiimote is proposed. Both translation and rotation motions can be accurately monitored and the location of carriers can be determined even the motion contains self-rotation and traveling passing under shelters. The scheme provides a reliable global position sensing for monitoring indoor moving robots and the global position control over the entire living space can be achieved, which is critical since the embedded sensors in a robot cannot evaluate the external disturbances such as slipping.

However, it is important to point out that in order to fully monitor and control mobile robots in a typical living space, an auxiliary self-contained localization scheme such as INS should also be incorporated, which is merely used when a robot is lost contact with wiimote. Furthermore, additional autonomous navigations such as obstacle avoidance should also be included. Currently, we are integrating the presented wiimote localization scheme with a group mobile robot to form group control of mobile units for smart building related applications [8].

6 Summary and Conclusion

Indoor localization of mobile units is critical for subsequent task of intelligent living technology. In this work, a novel wiimote localization scheme is proposed and validated. By operating IR-LEDs in a controlled manner, it can detect the specific zone where the robot is located. In addition, by the positions of interacted IR-LEDs and the readout of wiimote, it is possible to compute the location and orientation of the robot in this zone and consequently the absolute coordinate of the robot inside the living space can be determined. The scheme is experimentally

verified by using a servomotor. Finally, the scheme is applied on an omni-wheel mobile robot for trajectory control to demonstrate the possible application of this localization scheme in indoor living space applications.

Acknowledgments. This work is supported by National Science Council of Taiwan under contract number 100-2628-E-006-020-MY3.

References

[1] Fox, D., Burgard, W., Thrun, S.: Markov Localization for Mobile Robots in Dynamic Environments. J. Artificial Intelligence Research 11, 391–427 (1999)

[2] Barshan, B., Durrant-Whyte, H.: Inertial navigation systems for mobile robots. IEEE Transactions on Robotics and Automation 11, 328–342 (1995)

[3] Krejsa, J., Vechet, S.: Infrared Beacons based Localization of Mobile Robot. Elektronika Ir Elektrotechnika 1, 17–22 (2012), doi:10.5755/j01.eee.117.1.1046. WOS:000300026100004

[4] Vechet, S., Krejsa, J., Houska, P.: The enhancement of PCSM method by motion history analysis. Recent Advances in Mechatronics, 107–110 (2007), doi:10.1007/978-3-540-73956-2_22. WOS:000251017700022

[5] Chen, P.W., Ou, K.S., Chen, K.S.: IR indoor localization and wireless transmission for motion control in smart building applications based on Wiimote technology. In: Proc. SICE 2010, 49th Annual Conf. of the Society of Instrument and Control Engineers of Japan, pp. 1781–1785 (2010)

[6] Gu, D., Fu, Y.T., Ou, K.S., Chen, K.S.: Design of wiimote indoor localization technology for omnidirectional vehicle trajectory control. In: 2012 IEEE International Conference on Computer Science and Automation Engineering (CSAE 2012), Zhangjia-jie, China, May 25-27 (2012)

[7] Lee, J.C.: Hacking the nintendo wii remote. IEEE Pervasive Computing 7, 39–45 (2008)

[8] Chen, M.H., Gu, D., Fu, Y.D., Pi, C.H., Ou, K.S., Chen, K.S.: Wireless group manipulation of autonomously guided mobile robots for smart living space applications. In: Proc. SICE 2011, 50th Annual Conf. of the Society of Instrument and Control Engineers of Japan, Tokyo, Japan (September 2011)

Hybrid Navigation Method for Dynamic Indoor Environment Based on Mixed Potential Fields

S. Vechet[1], K.S. Chen[2], and J. Krejsa[1]

[1] Brno University of Technology, Faculty of Mechanical Engineering, Technicka 2, 616 69, Brno, Czech Republic
vechet.s@fme.vutbr.cz, krejsa@fme.vutbr.cz
[2] National Cheng Kung University, Department of Mechanical Engineering, No.1, Ta-Hsueh Road, Tainan 701, Taiwan
kschen@mail.ncku.edu.tw

Abstract. Navigation task for highly populated indoor environment belongs to the most difficult issues in mobile robotics. Presented paper deals with a hybrid approach which combines three methods: potential fields, Voronoi diagrams and rule based path planner. Such combination takes the best of all mentioned methods to create reliable navigation system with maximum emphasis on safety. The method was verified using real mobile robot in common environment with dynamic obstacles.

1 Introduction

Potential field method belongs to the popular ways of path planning in discrete space. Typical applications are usually from the field of robot soccer [1] or in indoor navigation of small robots [2]. Operation in continuous spaces is not required in these types of application, and the time of calculation can be defined by resolution of the state space.

Another method which can be successfully used for navigation is based on Voronoi diagrams [3]. This method can be used in continuous space as well as in discrete one. Typical applications are path planning in offices filled with obstacles [4].

Both mentioned path planning methods are primarily suitable for usage in static environment, but on the other hand taking into account known limitations of those methods, the use in dynamic environment with limited number of dynamic obstacles is possible. In these cases the high speed computation unit is required, to generate the navigation path dynamically when the configuration of environment changes due to the presence of dynamic obstacles.

In this paper we present a method for dynamic motion planning based on combination of path planning methods mentioned above with a rule based planner [5]. The combination of all three algorithms reduces the computational cost and increases the robustness of navigation.

The main idea of further described approach is based on following principle: First we consider the robot to be placed in static environment represented by e.g. walls and/or pieces of furniture. The static environment is used for path planning with a

T. Březina and R. Jabloński (eds.), *Mechatronics 2013*,
DOI: 10.1007/978-3-319-02294-9_73,

global goal [6]. Dynamic obstacles are usually represented by moving people. The problem of moving people avoidance is solved locally by the rule based path planner. The static approach to the environment is used to generate a static potential field combined with Voronoi diagram, giving the static obstacles free path, while the rule based path planner simultaneously effects the real path to avoid dynamic obstacles in order to reach the pre-calculated free path. The computation cost is reduced as the potential field is generated only in the case that the goal has changed.

The paper is organized as follows. Next two chapters present the potential field and Voronoi diagram methods. The fourth chapter briefly describes the rule based path planner. The key chapter 5 shows how to combine these three methods together for navigation task. The final chapter discusses the utilization of presented method in real world application and future work.

2 Potential Field

Potential field is popular method for path planning on the grid. The implementation is simple and straightforward. A typical application is path planning in static environment. There are many different implementations which are appropriate for various environments.

The main principle of the method is in creating a discrete field over the environment, where each cell of the field represents a potential with a relation to the goal. The cell value (with respect to the values of surrounding cells) is then used to determine the movement direction of the robot. The simplest method for evaluation of the potential field is calculation of the value for the cell as a Euclid distance to the goal. This method is simple but usable just for convex obstacles. When the environment contains obstacles with more complex shapes this method fails.

To avoid problems with obstacles of various shapes the flood-fill method is used. The minimum value of the potential field is set to the goal and the algorithm starts from this point until all possible cells are searched. The algorithm of flood-fill method is shown in table 1.

Table 1 Pseudo code of Flood-fill algorithm for potential field evaluation

```
FloodFill()
  goal.value = 1
  fifo_push(goal)
  while fifo_pop(cell):
    if cell == robot_position:
      return True
    else:
      for x in all_neighborhoods_of(cell):
        if x not visited:
          x.value = cell.value + 1
          fifo_push(x)
  return False
```

The typical potential field generated via the flood-fill method is shown on figure 1.

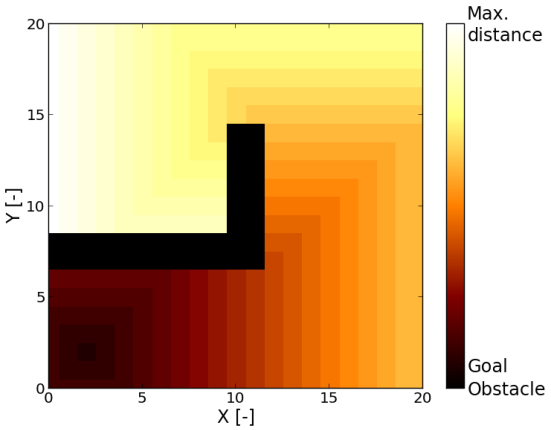

Fig. 1 Potential fields generated via the flood-fill method

3 Voronoi Diagrams

Voronoi diagrams belong to the group of method for planning in continuous space. In contrast with the potential field method, the Voronoi diagrams are used for path planning with maximum clearance, not the shortest path. The method is applied when the essential task of the robot is to move in safe distance from obstacles (furniture, stairs ...), such as indoor environments of offices or shopping malls. The algorithm for creating a discrete Voronoi diagram is shown in table 2 and example of corresponding diagram is shown in Fig. 2.

Table 2 Pseudo code of discrete Voronoi diagram

```
Voronoi()
  for cell in grid
    if cell == is_near_obstacle:
      cell.value = 1
      fifo_push(cell)
    while fifo_pop(cell):
      for x in all_neighborhoods_of(cell):
        if x not visited and x not obstacle:
          x.value = cell.value + 1
          fifo_push(x)
```

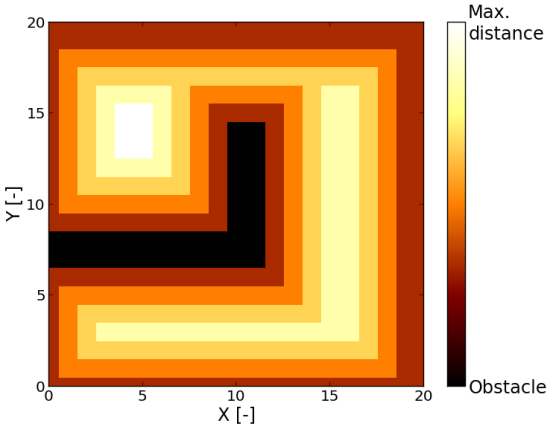

Fig. 2 Discrete Voronoi diagram algorithm result

4 Rule Based Path Planning

Rule based path planner is based on predefined rules which describe the behavior of the robot in dynamic environment, see [7]. The main advantage of this method is safety, reliability and robustness. All mentioned aspects are crucial for movement in dynamic environment full of moving people, because of the safety restrictions.

The rule based path planning method works as Mealy state-machine which is a kind of finite state-machine, where outputs are based on both inputs and current state. The key advantage of such state-machine is that the output can change even when there are changes in inputs only and no change in the state occurs.

The Mealy machine is defined as a set of six parameters $(S,S_0,\Sigma,\Lambda,T,G)$, where:

S set of possible states
S_0 initial state
Σ input alphabet $(x_0,\ldots,x_n)$; x_i are possible input values
Λ output alphabet $(z_0,\ldots,z_n)$; z_i are possible output values
T transition function; $T{:}S\times\Sigma\rightarrow S$
G transition function; $G{:}S\times\Sigma\rightarrow\Lambda$

Such a finite state-machine can be used for path planning through unknown environment full of dynamic obstacles. Sensor measurements are transformed to the input alphabet Σ. Output alphabet Λ is used afterwards for motion planning. An example of finite state-machine used in robot Advee [8] with particular content of the state and alphabet is defined as follows:

Possible states $S=\{s_0,s_1,s_2,s_3\}$; where $s_0=Forward$, $s_1=Backward$, $s_2=Pause$, $s_3=Stop$

Initial state $S_0=s_2=Pause$

Input alphabet $\Sigma=\{-1,0,1\}$ is defined with respect to the robots detection areas

Λ output alphabet $\Delta=\{z_0,\ldots,z_8\}$; where $z_0=Follow\_a\_goal$, $z_1=Turn\_right\_sharply$, $z_2=Turn\_left\_sharply$, $z_3=Turn\_right$, $z_4=Turn\_left$, $z_5=Follow\_a\_corridor$, $z_6=Backward$, $z_7=Back\_right$, $z_8=Back\_left$,

Transition functions T and G are joined into one transition function $T:S\times\Sigma\rightarrow S\times\Lambda$.

Each sensor has its detection range divided into the three discrete zones, which are used as inputs. The discretization is accomplished via the definition (1).

$$F(d)=\begin{Bmatrix} 1 & d>0.6 \\ 0 & d=[0.2,0.6] \\ -1 & d<0.2 \end{Bmatrix}, \tag{1}$$

where d is the measured distance.

5 Hybrid Solution of Navigation Method

All three presented methods are combined into one simple and robust hybrid method, which enables the robot to move safely in highly populated indoor environment.

The combination of potential field with Voronoi diagram creates a field with one global minimum which simplifies the path planning with the respect of maximum clearance. Therefore the path is not optimal in its length but in its safety. The final mixed potential field is defined by equation 2.

$$h_{x,y}=\left(\max V-v_{x,y}\right)+p_{x,y} \tag{2}$$

Where x,y are the coordinates in 2D potential field, V is complete set of values for potential field generated as discrete Voronoi diagram, $v_{x,y}$ represents single value with given coordinates from the discrete Voronoi diagram, $p_{x,y}$ represents single value from potential field and $h_{x,y}$ is the value of resulted mixed potential field.

The final product of this operation in form of mixed potential field is shown on figure 3 and 4.

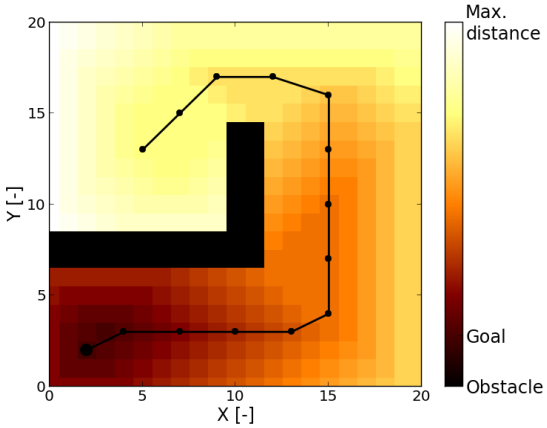

Fig. 3 Fussion of potential field and Voronoi diagram

The key idea of this hybrid solution is that the global goal path is always defined by the mixed potential field. However, whenever the dynamic obstacle is detected by the proximity sensors, the rule based path planner handles the obstacle avoidance, and when completed, it returns to the global path found previously. This method ensures that the robot will always move in the sufficient distance from static obstacles on the path to the goal, while safely avoiding unexpected dynamic ones.

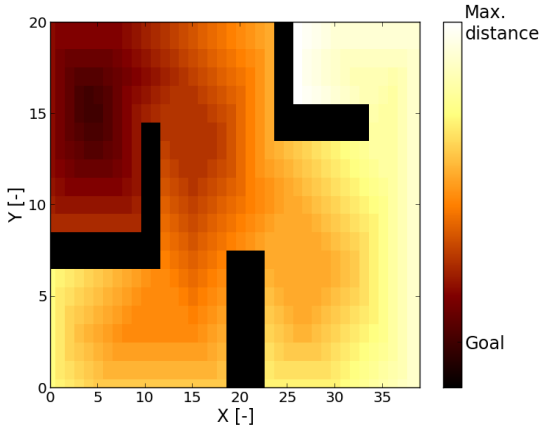

Fig. 4 An example of mixed potential field for more complex environment

The method was extensively tested in a number of simulations that verified the expected behavior. Figure 5 shows graphical output of simulation environment: the robot is represented by green sensor beams; detected landmarks are represented by orange circles and dynamic obstacles by blue ones; the goal is marked as a white cross. The moving speed of dynamics obstacles were 0.3 m/s

and diameter was chosen randomly in range $\langle 0.2,0.8 \rangle$. The number and size of obstacles were estimated from typical real-world environment represented as a shopping mall, which is the main environment, the robot Advee [8] was designed for. The localization method used in this simulation is based on particle filters [9].

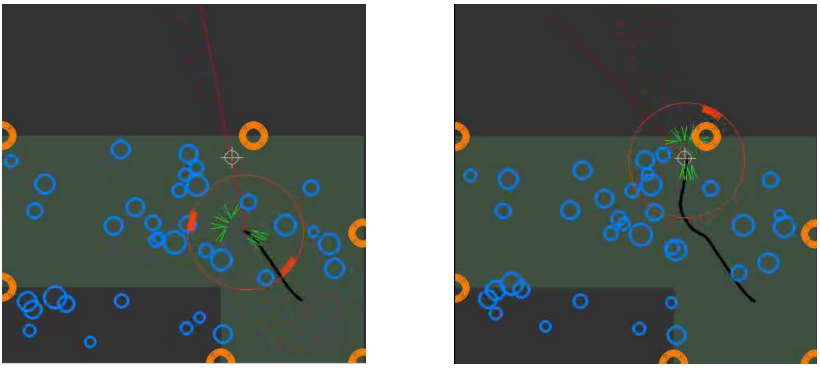

Fig. 5 Dynamic environment simulation (dimensions 14x14m); finding path (left) to the goal (right) through the overcrowded space

The real world tests were performed on non-holonomous Ackerman chassis [10] based presentation robot Advee. During the tests the total path of over 10 km in crowded environment full of unaware bystanders, with no incident occurring.

6 Conclusions

Presented hybrid navigation method was successfully used in various dynamics real-world environments. The hybrid approach is not optimal in its performance but in the robustness and with a respect to the safety of both the robot and surrounding walking people. Operation safety is crucial for working in public environments as shopping malls or exhibition centers, where service robots are intended to operate.

Future work will be focused on more precise navigation in large spaces with the possibilities to drive to the specific location.

Acknowledgments. The present work has been supported by European Regional Development Fund in the framework of the research project NETME Centre under the Operational Programme Research and Development for Innovation. Reg. Nr. CZ.1.05/2.1.00/01.0002, id code: ED0002/01/01, project name: NETME Centre – New Technologies for Mechanical Engineering and by National Science Council of Taiwan under contract number NSC-100-2628-E-006-020-MY3.

References

[1] Vail, D., Veloso, M.: Multi-Robot Dynamic Role Assignment and Coordination Through Shared Potential Fields. In: Schultz, A., Parker, L., Schneider, F. (eds.) Multi-Robot Systems. Kluwer (2003)
[2] Li, G.-H., Chang, C.-F., Fu, L.-C.: Navigation of a wheeled mobile robot in indoor environment by potential field based-fuzzy logic method. IEEE Workshop Advanced robotics and Its Social Impacts 1(6), 23–25 (2008)
[3] Shojaeipour, S., Haris, S.M., Khalili, K., Shojaeipour, A.: Motion planning for mobile robot navigation using combine Quad-Tree Decomposition and Voronoi Diagrams. In: The 2nd International Conference on Computer and Automation Engineering (ICCAE), February 26-28, vol. 1, pp. 90, 93 (2010)
[4] Sakahara, H., Masutani, Y., Miyazaki, F.: Safe Navigation in Unknown Dynamic Environments with Voronoi Based StRRT. In: 2008 IEEE/SICE International Symposium on System Integration, pp. 60, 65, 4–4 (2008)
[5] Vechet, S.: The Rule Based Path Planner for Autonomous Mobile Robot. In: 17th International Conference of Soft Computing, MENDEL 2011, pp. 546–551 (2011)
[6] LaValle, S.M.: Planning Algorithms. Cambridge University Press (2006)
[7] Vechet, S., Ondrousek, V.: Motion Planning of Autonomous Mobile Robot in Highly Populated Dynamic Environment. In: Jabloński, R., Březina, T. (eds.) Mechatronics, vol. 86, pp. 453–461. Springer, Heidelberg (2011)
[8] Krejsa, J., Vechet, S., Hrbacek, J., Ripel, T., Ondroušek, V., Hrbacek, R., Schreiber, P.: Presentation Robot Advee. Engineering Mechanics 18(5-6), 307–322 (2012)
[9] Thrun, S., Burgard, W., Fox, D.: Probabilistic Robotics. MIT Press, Cambridge (2005)
[10] Choset, H., Lynch, K.M., Hutchinson, S., Kantor, G., Burgard, W., Kavraki, L.E., Thrun, S.: Principles of Robot Motion: Theory, Algorithms, and Implementations. MIT Press, Cambridge (2005)

Human-Machine Interface for Mobile Robot Based on Natural Language Processing

P. Mašek and M. Růžička

Brno University of Technology, Faculty of Mechanical Engineering, Technicka 2,
616 69, Brno, Czech Republic
{y70232,y110384}@stud.fme.vutbr.cz

Abstract. This paper deals with the design of the communication interface for autonomous mobile robot which is able to interact with human operator. The communication interface is based on natural language processing with support of voice synthesis and speech recognition. Presented paper describes the core of the communication interface based on mobile platform for Android operating system.

1 Introduction

At the present time, a typical human-machine interface for mobile robot is usually limited to a few simple commands to ensure the basic communication with the human operator. Such simple interface can be easily realized by alphanumeric displays or binary switches. These basic peripherals enable to get some information about the device status (display) and enter simple commands (switches, buttons).

With increasing availability of service robots of various purposes, more mobile robots are used for closer interaction with human operators, so more natural communication interface is demanded.

Currently the most sophisticated example of such a system is the communication interface designed for supercomputer Watson from IBM. It is an extensive expert system with learning abilities, which is processing and interpreting the natural language [1].

Many robotic competitions exist with the main objective to develop such a human-machine interface suitable for mid-sized mobile robots [2], e.g. RoboCup@Home league section deals with development of human-machine interface for robotics assistance systems [3]. These systems are presented in RoboCup competition every year.

This paper is organized as follows. Section 2 deals with the used methods, section 3 describes the human-machine interface and section 4 presents accomplished voice recognition experiments. The last section is reserved to conclusions and future work.

T. Březina and R. Jabloński (eds.), *Mechatronics 2013*,
DOI: 10.1007/978-3-319-02294-9_74,

2 Materials and Methods

The communication interface with the limited ability of processing and interpretation of natural language can be based on various methods. The commonly known solutions are Google Assistant and Siri [4].

Presented system will be tested on an Advee mobile robot platform. Advee is advertising mobile robot with advance communication interface and uses an indoor navigation system based on infrared beacons[5], odometry sensors, cam, touch screen and speech output [6].

For the speech recognition and voice synthesis the Google Application Programming Interface (Google API) available methods will be used [7]. These APIs are included in Android operating system Software Development Kit. This is Text to speech (TTS) APIs functions. Both of them are easy to use for this task solution.

Speech recognition APIs can be used in offline mode (without internet connection) for latest Android operating system versions. It means for versions 4.1 and higher. These API needs internet connection for earlier versions of Android operating system. The offline mode supports the English language only in the case of speech recognition task. Text to speech (TTS) API for free use supports English, German, French and Chinese languages.

3 Human-Machine Communication Interface

Described human-machine interface is suitable mainly for robots which are able to connect to the devices running Android operating systems since the communication interface is primarily designed for mobile platforms. These platforms are low power consumption and easily integrated into the mobile robots.

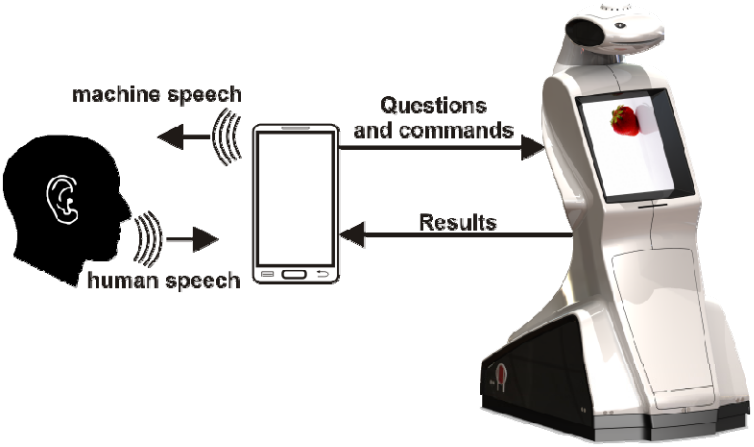

Fig. 1 Human-machine interface

This system is an open source and therefore it can be used for any mobile platform. The communication interface is divided into two independent modules: client and server.

The client section includes software routines for voice recording and speech synthesis while the server section includes the voice recognition as well as the syntax and database module. The overall communication work-flow is shown on Figure 1.

3.1 Client

The client part contains a module for recognition and speech synthesis. The client is in the form of an application for the device running Android operating system. Client application communicates with the user by the limited form of natural language, which is realized by the voice recognition and voice synthesis (TTS). These are realized by internal module of Android operating system. The voice recognition is based on Google recognition API and the speech synthesis is realized by text to speech software module, which is included in Android SDK. The client is able to communicate with the server section on robot side using a wireless networks assistance packets, which are transmitted in both directions in the form of text strings. The client block diagram is shown in figure 2.

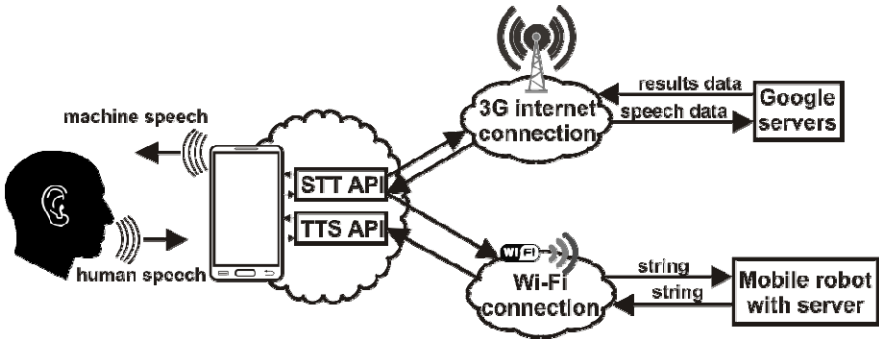

Fig. 2 Client block diagram

3.2 Server

The server is an application for the Android operating system, which runs on the robot`s main computer. The server processes the queries in form of string formatted requests and communicates with the syntax and context modules.

The results are posted to the output database module, where the result is translated to the string format in the simple string form (e.g. “battery level is 20 %”). The output database module post-processes this string to a correct sentence: “The battery level is 20 percent“. Such a formatted sentence is served to the client. The block diagram is shown on figure 3.

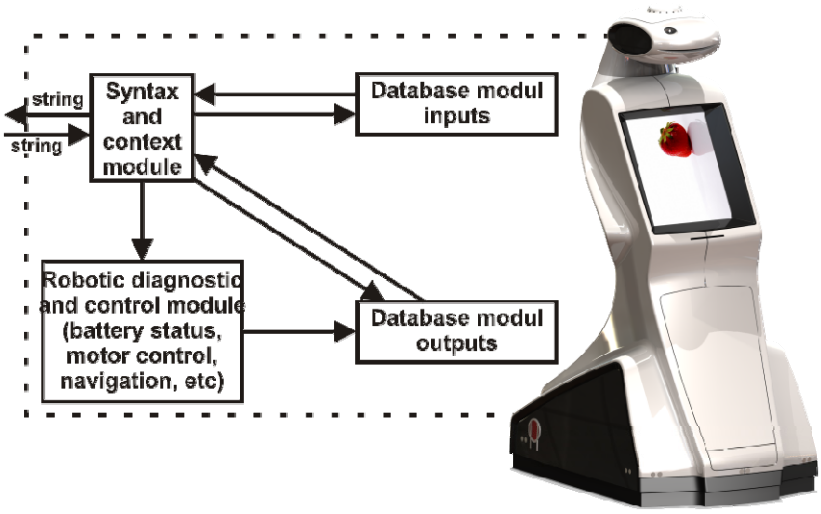

Fig. 3 The server communication work-flow

4 STT API Experiments

The proof of concept experiments were performed in three different kinds of environments: without noise, with noise and noisy. The environment without noise was represented by enclosed room; the second (with noise) was represented by open space (e.g. on the street); the noisy environment was typical shopping mall.

Table 1 Experiment results with single channel microphone

Voice command	Number of measurements	Without noise	With noise	To noisy
"stop"	50	49	42/50	15/50
"start"	50	47	40/50	13/50
"turn left"	50	48	39/50	18/50
"turn right"	50	49	41/50	19/50
"Turn off engines"	50	45	37/50	14/50
"find docking station"	50	43	39/50	9/50
"Are sensors ready to use"	50	35	18/50	10/50
"Activate autonomous mode"	50	25	21/50	6/50
"Activate manual mode"	50	21	16/50	8/50
"Get me battery status"	50	41	22/50	18/50
"Battery status"	50	48	32/50	22/50

There were 50 measurements for each environment. The commands used in presented experiments are listed in Tables 1 and 2 with results included. The number of correct positive recognitions was used as an evaluation criterion.

The results depend on used device, because some devices have dual channel microphone, which can reduce noise. This means the devices with single channel microphone has less accurate results, than dual channel microphone devices. Results presented in table 1 were performed by device with single channel microphone. Table 2 shows results for dual channel microphone.

Table 2 Experiment results with dual channel microphone

Voice commands	Number of measurements	Without noise	With noise	To noisy
"stop"	50	50/50	46/50	28/50
"start"	50	48/50	45/50	25/50
"turn left"	50	47/50	46/50	27/50
"turn right"	50	49/50	47/50	30/50
"Turn off engines"	50	46/50	45/50	21/50
"find docking station"	50	42/50	40/50	23/50
"Are sensors ready to use"	50	33/50	26/50	13/50
"Activate autonomous mode"	50	24/50	24/50	14/50
"Activate manual mode"	50	23/50	20/50	9/50
"Get me battery status"	50	42/50	33/50	20/50
"Battery status"	50	48/50	45/50	29/50

Presented results clearly shown, that the dual channel microphone has more significant impact to experiments performed in noisy environment.

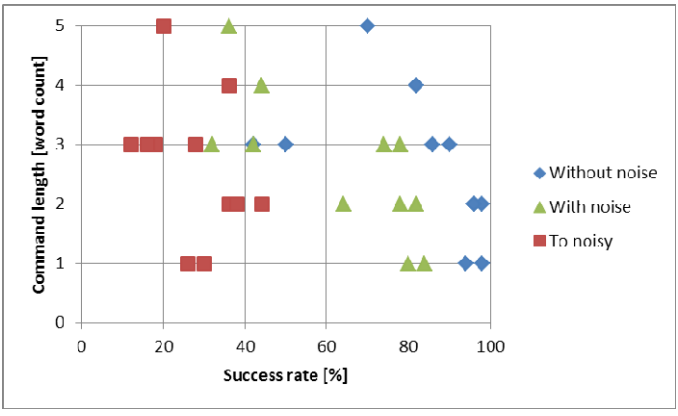

Fig. 4 Success rate in experiments with single channel microphone

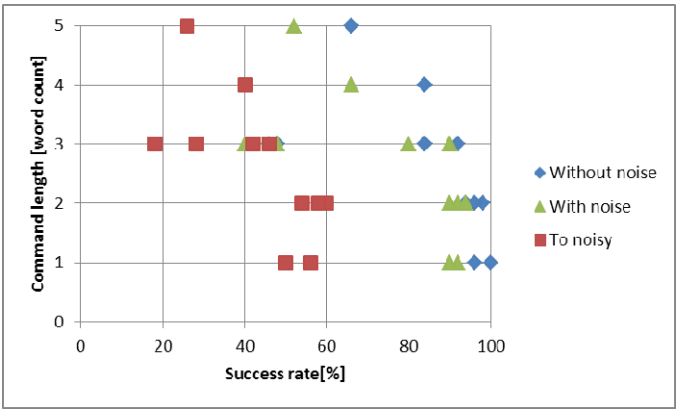

Fig. 5 Success rate in experiments with dual channel microphone

The difference between single and dual channel microphone become apparent in noisy environments where the success rate rises up to 50 percent. This is still not enough to use this recognition engine in such a noisy environment, but it shows that better microphones can be a passive solution for noisy environments. In case that just better microphone is not enough the software signal filtration must be included in the data processing.

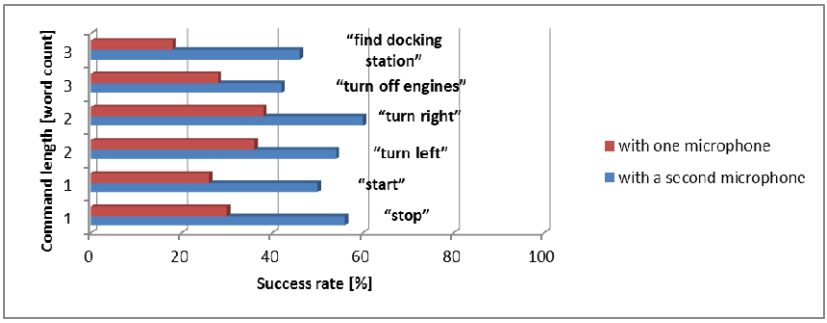

Fig. 6 Success rate of selected commands performed with dual channel microphone

Figures 6 and 7 show the comparison of success rate for selected voice commands in the different environments. There are results for without noise and to noisy environments to show the difference.

Presented experiments also shows that the success rate of used voice recognition engine also depends on engine language settings, where better results were acquired with *English (UK)* settings than with *English (US)*.

Another issue for future experiments is based on the definition of success rate, due to the fact that in some experiments the sentence was marked as false, despite the fact that some of the significant words in the sentence were recognized correctly. Typical example is voice command e.g. “Get me the battery status” which

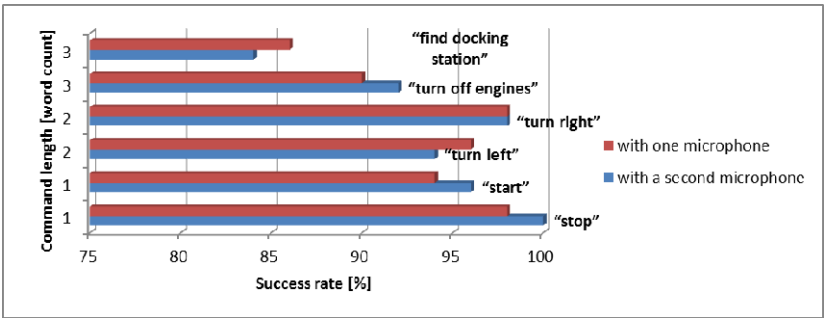

Fig. 7 Success rate of selected commands performed with dual channel microphone

returns false ("- - - battery status") because the engine doesn't recognizes the words "get" and "me", but there is still enough information to recognize the requested command "battery" and "status". This issue can be solved by the probabilistic approach in consequent work.

5 Conclusions and Future Work

The core of the human-machine interface was described. The speech recognition API was tested successfully in different environments with respect to the noise level. The robot communicates with the user through the Text to Speech (TTS) API. The module separation into the two independent parts: client and server sections enables to reach small demands on the main computer. The client runs on an external mobile device that communicates with the server via wireless network. This ensures that the robots main computer can simultaneously process other more demanding tasks, such as image processing, navigation, path planning etc.

In further developments the system will be tested on devices with dual channel microphone to reach more accurate results and expand the utilization of developed human-machine interface.

Acknowledgment. This work was supported by the project FSI-S-11-23.

References

[1] Wagle, K.: IBM Watson: Revolutionizing Healthcare? Young Scientists Journal 6(13), 17–19 (2013)

[2] Grepl, R.: Extended kinematics for control of quadruped robot. In: Recent Advanced Mechatronics, International Conference on Mechatronics, Warsaw (2007) DOI 10.1007/978-3-540-73956-2_26, WOS:000251017700026

[3] Vlachy, D., Zezula, P., Grepl, R.: Control unit architecture for biped robot. In: Recent Advanced Mechatronics, International Conference on Mechatronics, Warsaw (2007) doi:10.1007/978-3-540-73956-2_2, WOS:000251017700002

[4] Weaver, J.: Siri is my client: A First Look at Artificial Intelligence and Legal Is-sues. New Hampshire Bar Journal 52(4), 6–10 (2012)
[5] Krejsa, J., Vechet, S.: Infrared Beacons based Localization of Mobile Robot. Elektronika Ir Elektrotechnika (1), 17–22 (2012) doi:10.5755/j01.eee.117.1.1046, WOS:000300026100004
[6] Vechet, S., Krejsa, J., Houska, P.: The enhancement of PCSM method by motion history analysis. Recent Advances in Mechatronics, 107–110 (2007) doi:10.1007/978-3-540-73956-2_22, WOS:000251017700022
[7] International Business, "Exclusive: Google Voice Assistance for Android Tablets Coming Soon", International Business Times, Regional Business News,T 0005 (October 2012)

Real Time Object Tracking Based on Computer Vision

M. Růžička and P. Mašek

Brno University of Technology, Faculty of Mechanical Engineering, Technicka 2, 616 69, Brno, Czech Republic
{y110384,y70232}@stud.fme.vutbr.cz

Abstract. This paper deals with the design of a software module for real time object tracking based on computer vision. An autonomous convoy task is the main purpose of the tracking system module. Each convoy unit/car must follow the trajectory of previous unit with respect of local neighborhood, which may include the dynamic obstacles. The presented paper is focused on the detection of previous unit position only. The nVidia Tegra 3 was used as a main computer vision platform, which can be applied in low power systems onboard of small autonomous robots.

1 Introduction

Computer vision is an approach to solve many tasks as detection of cars, faces or various features, contours, etc. This paper deals with the design of software module for real time tracking based on computer vision. The computer vision software module is focused on a semiautonomous convoy task [1]. The semiautonomous convoy slave unit must precisely follow the trajectory of leading unit. Software module design is focused on low cost power devices, especially on the nVidia Tegra 3 platform, which can be easily implemented to small mobile robots.

The main software module realizes the object detection task and the results are used as an input to the control unit, which controls the engines. The major part of this module is the detection method, which can have many different solutions [2], but the most effective way how to detect the known object is to use Haar like features [3] or Local Binary Patterns (LBP) [4] cascade classifiers.

This approach is commonly used for human face detection with excellent results and enables us to detect complex objects. This method complements color blob detection method to detect markers, which are attached to the detected object.

In this paper only the main tracking method is described. This paper is organized as follows. Section 2 deals with problem description. Section 3 is focused on the main tracking method and the evaluation unit description. Section 4 contains performance results of the main tracking method. The last section is reserved to conclusions and future works.

T. Březina and R. Jabloński (eds.), *Mechatronics 2013*,
DOI: 10.1007/978-3-319-02294-9_75,

2 Problem Description

The convoy contains a few mobile units with two level cascade control system to maintain the control task.

The first part of the control system contains the main control unit [7], based on the nVidia Tegra 3 platform. This computer provides image processing, engines control, wireless communication between all units and USART communication with low level module which forms the second part of the system [8].

The low level system controls the engines, steering, reads the sensor information [6] and encapsulates the information to correct format for the high level control system.

The image processing part of the high level system contains the object tracking software module, which is the crucial module for the convoy unit [4] to follow the leader car. The object tracking software module is described in the next section.

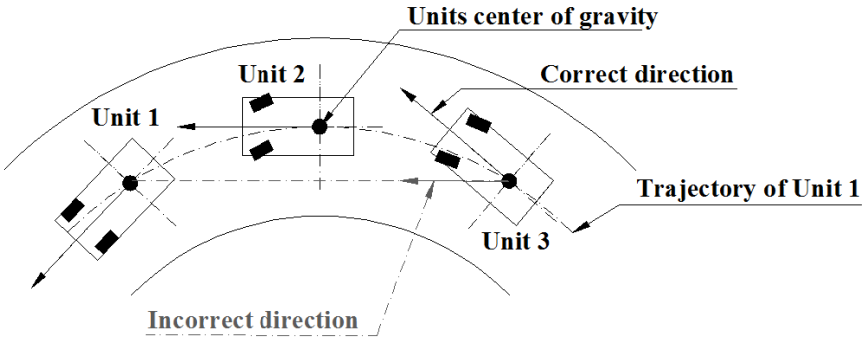

Fig. 1 Convoy units sample

3 Object Tracking Method Description

The object tracking system contains two detection methods. First method solves the complex object detection. The second method complements main method and solves object markers detection, which are attached to the back side of the object. Object to be detected is the convoy unit. For the both image processing methods the OpenCV software development kit for Android operating system in a Java language was used.

3.1 Tracking Method

Main tracking method was designed to detect an object as a whole. Detection of the entire object is not trivial, because each object may have similar shapes and

various colors. The detected object represents a convoy unit. The approach chosen to solve this problem is commonly used to human face detection and is based on Viola-John's method, which combines four key concepts:

- Rectangular features
- An integral image
- AdaBoost machine learning method
- A cascaded classifier to combine many features efficiently

Viola-John's based methods are commonly used for human face detection with excellent results [1].

OpenCV SDK supports two kinds of cascade classifiers: Haar Like Features and Local Binary Patterns. The cascade classifiers based on Haar Like Features are more precise than Local Binary Patterns for detection, but more demanding on computational cost, because of the usage of floating point data structures. In comparison, the Cascade classifiers based on Local Binary Patterns are less accurate but faster due to the usage of integer data structures.

Lower accuracy in not dramatically lowered against Haar Like Features cascade classifiers. Local Binary Patterns are more suitable for mobile platforms, which are less efficient than desktop platforms.

3.1.1 Local Binary Patterns

Camera frame forms a bitmap in grayscale color space. Grayscale image is represented by pixel matrix. Each pixel is value in interval <0, 255>, where 0 is black color and 255 is white color. Local Binary Patterns (LBP) method uses primitive operators to image description. Grayscale image description can be represented as 256 binary values histogram. The matrix of 3x3 pixels represents the operator, where center pixel value is thresholded with each neighborhood pixel value. This procedure is described on figure 2.

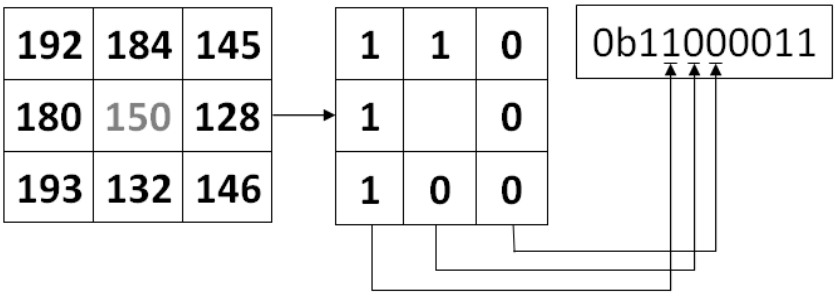

Fig. 2 Example of LBP calculation

The operator application result is binary number, which represents pattern type. Pattern types are shown on figure 3.

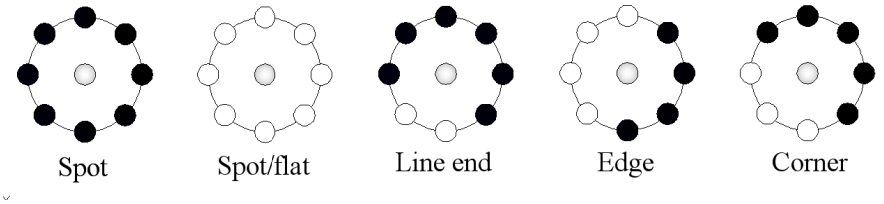

Fig. 3 Example of LBP patterns types

Operators are used over the image and they create histogram to image description. Image calculation is not performed from single one, but from many histograms. The image is divided to few non overlapping regions ordinarily 24x24 pixels. Each region with their histograms illustration is shown on figure 4. Searching of object is based on histograms values.

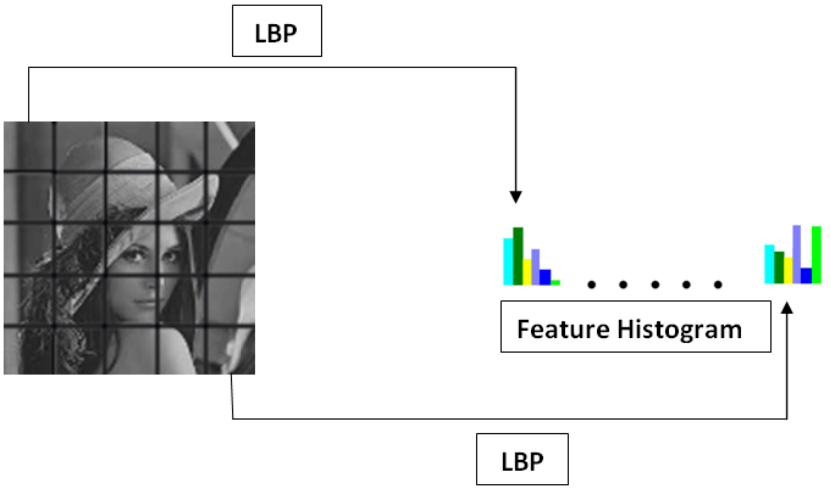

Fig. 4 Example of regions histograms

3.1.2 Learning Method

Main advantage of this method is the opportunity to learn to detect specific entity. Gentle AdaBoost [3] [9] is progressive method to create classifier for simple histogram. Gentle AdaBoost algorithm is described in table 1.

Table 1 Gentle AdaBoost algorithm

Gentle AdaBoost algorithm	
1.	Start with weights $w_i = \frac{1}{N}\ i = 1,2,\ldots,N, F(x) = 0.$
	for(i = 0; i <= M; i++)
	{
(a)	Estimate $f_m(x)$ by weighted a fit of y and x.
(b)	Update $F(x) \leftarrow F(x) + f_m(x)$.
(c)	Update $w_i \leftarrow w_i e^{-y_i f_m(x_i)}$ and renormalize.
	}
2.	
3.	Output the classifier $sign[F(x)] = sign[\sum_{m=1}^{M} f_m(x)]$

Positive and negative samples are used for the learning process. An image, which contains object to be detected, is the positive sample while the image that does not contain the object to be detected is a negative sample. For the learning process a few thousands positive and negative image samples must be used. This process is too long and computationally intensive, but results enable detect object as a whole.

Classifiers output is True (positive result), or False (negative result). Each histogram is classified by weak classifier, and strong classifier used for object detection, is composed from the weak classifiers. Cascade classifier can be created by OpenCV tools [3] [9]. Strong classifier is formed as the cascade of weak ones. This is shown on figure 5.

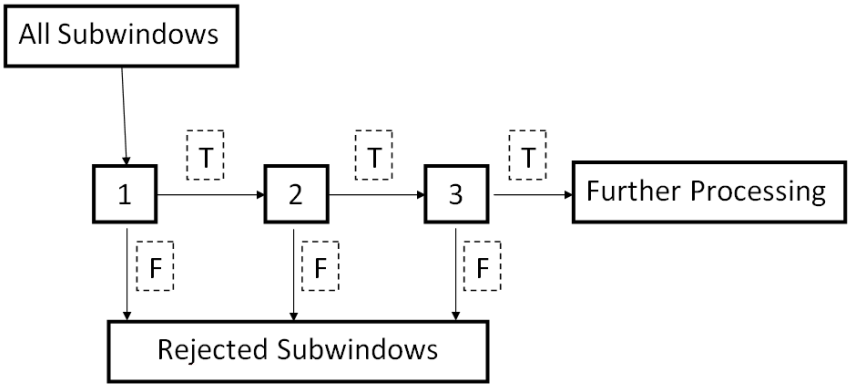

Fig. 5 Example of weak classifiers cascade

If the weak classifier result is false for specific region, then the sub window is not considered to global result. If the result is true, then this sub window is considered to global strong classifier result. Image regions, which were considered to

the global result do create region, where the probability of occurrence of object to be detected is high. Specific cascade classifier must be created for each object to be detected. Center of detected object area forms an input to evaluation unit to compute the deviation from image center.

3.2 Evaluation Unit

The output of the evaluation unit is a single point, which represents the center of the detected object. We premise that the axis of the camera is the same as axis of convoy unit in x dimension and detected object center is the same as leads convoy unit axis. It means that the center of image frame holds the axis of convoy unit. Output of this evaluation unit is vector, which is created from the center of image frame and detected object center. This vector determines the value of deviation leads convoy unit axis and own axis in x dimension. Sample output is shown in figure 6. Deviation vector is assign by blue color.

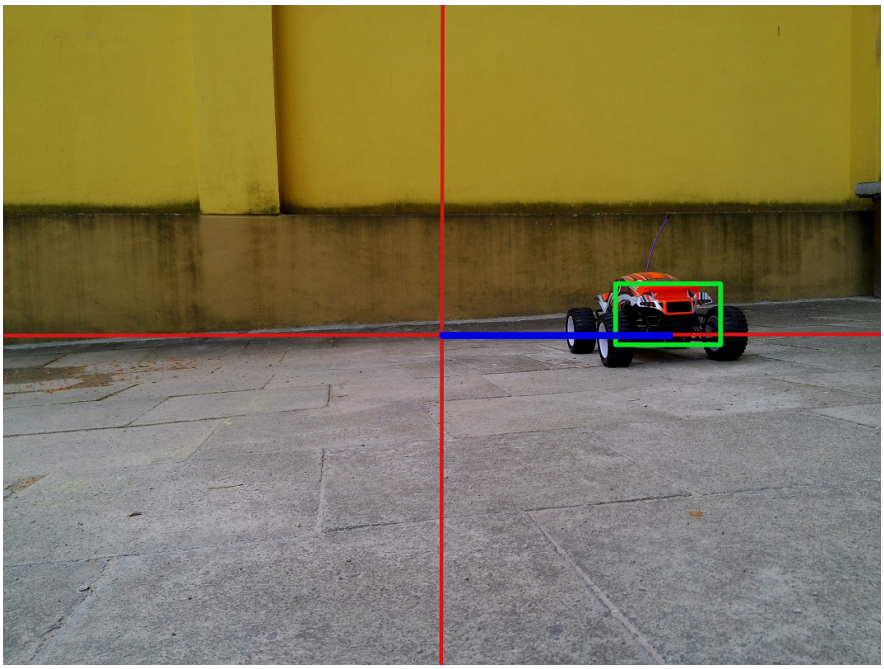

Fig. 6 Example of deviation vector

4 Experimental Results

Presented method was tested on nVidia Tegra 3 platform in multiple camera frame resolutions. Each frame was processed by detection method. Camera frame rate is only 16 frames per second without image processing on Tegra 3. This small

frame rate is due to the slow OpenCV interface to camera hardware on android devices. The method performance is shown in table 2 for a multiple camera output resolutions.

Table 2 Results

Results/resolution	Unit	320x240	640x480	800x600	1280x720
Frame rate	[frame per second]	8.3	5.2	3.6	1.1

5 Conclusions and Future Works

In this paper we described the software module for real time object tracking based on computer vision. The module contains two tracking methods. The main tracking method was designed for leading convoy unit detection as a whole and it is based on Local Binary Patterns cascade classifier. The second method was designed for detection of led light markers on the back side of the leading convoy unit. In this paper we described the main tracking method only, together with the description of tracking method evaluation unit of slave to convoy unit control. The module was primary focused on semiautonomous convoy task and on low cost power devices especially on nVidia Tegra 3 platform. Tracking method has good performance results on Tegra platform.

This work will be extended by the application of Kinect camera, which allows the use the Kinect depth sensor for obstacles detection. In the future we plan to use nVidia Tegra 5 and Tegra 6 platforms as main computer unit to increase compute performance, which enable use both tracking methods to run parallel in real time.

Acknowledgment. This work was supported by the project FSI-S-11-23.

References

[1] Davis, J., Animashaun, A., Schoenherr, E., McDowell, K.: Evaluation of semi-autonomous convoy driving. Journal of Field Robotics, 880–897 (2008)
[2] Ferrari, V., Tuytelaars, T., Van Gool, L.: Object detection by contour segment networks. In: Leonardis, A., Bischof, H., Pinz, A. (eds.) ECCV 2006. LNCS, vol. 3953, pp. 14–28. Springer, Heidelberg (2006)
[3] Viola, P., Jones, M.: Rapid object detection using a boosted cascade of simple features. In: Conference on Computer Vision and Pattern Recognition, pp. 511–518 (2001)
[4] Chang-yeon, J.: Face Detection using LBP features, CS 229 Final Project Report (2008)
[5] Vechet, S., Krejsa, J., Houska, P.: The enhancement of PCSM method by motion history analysis. Recent Advances in Mechatronics, 107–110 (2007) doi:10.1007/978-3-540-73956-2_22, WOS:000251017700022

[6] Krejsa, J., Vechet, S.: Infrared Beacons based Localization of Mobile Robot. Elektronika Ir Elektrotechnika (1), 17–22 (2012) doi:10.5755/j01.eee.117.1.1046, WOS:000300026100004
[7] Grepl, R., Lee, B.: Model Based Controller Design for Automotive Electronic Throttle. Recent Advances in Mechatronics, Luhacovice (2009) WOS:000277076900036
[8] Vlachy, D., Zezula, P., Grepl, R.: Control unit architecture for biped robot. Recent Advances in Mechatronics (2007) doi:10.1007/978-3-540-73956-2_2, WOS:000251017700002
[9] Liao, S., Zhu, X., Zhen, L., Zhang, L., Li, S.: Learning Multi-scale Block Local Binary Patterns for Face Recognition. In: Internacional Conference on Biometrics (ICB), pp. 828–837 (2007)

Searching for Features in Laser Rangefinder Scan via Combination of Local Curvature Scale and Human Obstacles Detection

J. Krejsa and S. Vechet

Institute of Thermomechanics ASCR, v.v.i., Academy of Sciences of the Czech Republic, Technicka 2, 616 69, Brno, Czech Republic
{krejsa,vechet.s}@fme.vutbr.cz

Abstract. Detection of reliable features in sensor data is the base for most localization and SLAM algorithms. The paper presents a combination of local curvature scale that enables to easily find environment features such as corners and edges in laser rangefinder scan data with human obstacles detection, used to extract such dynamic obstacles reading from the scan thus improving the robustness of feature detection.

1 Introduction

Finding reliable features in surrounding environment is the basic task in mobile robotics navigation, as most of the localization methods and subsequently path planning algorithms rely on such information. Features detection can be based on vision processing [1],[2], that is particularly useful in outdoor unstructured environment; in structured environment proximity sensors based feature detection and subsequent navigation is commonly used, such as 2D laser scanner, sonars, etc, see e.g. [3]. Contrary to use of artificial landmarks, both active and passive, natural landmarks detection in spite the fact that it is generally more difficult can reach results similar to the artificial ones, while reducing substantially the preparation time and cost when mobile robot has to operate in new and previously unseen environment.

2D laser rangefinders lately became affordable for the whole range of service robotic applications. It produces consistent low-noise data, distance range can be selected to cover most of indoor environments and apart from special cases such as glass surfaces the readings precision exceeds localization methods requirements. Thus 2D laser rangefinder scan or a series of scans provides a good base for feature extraction.

There is a number of methods for feature extraction, typically the line features with Hough transform [4] or fuzzy clustering [5]; corners are another representative, found using the extracted lines processing or independent algorithm, such as RANSAC [6]. Recently a new family of digital boundary descriptors was studied,

T. Březina and R. Jabloński (eds.), *Mechatronics 2013*,
DOI: 10.1007/978-3-319-02294-9_76,

coming from the idea, that objects appearance depends on the scale of observation, thus fine scale features are sensitive to noise, contrary to coarse scale ones. Such descriptors can be used globally or locally, however, the global approach usually requires extensive calculation of complete scale space map. Fortunately, Rueda et. al. [7] published a nice new concept of local curvature scale (or C-scale), together with the shape descriptor based on C-scale. This concept can be easily adopted for landmarks extraction from 2D rangefinders data.

In common environment the major disturbance of digital boundary is caused by dynamic obstacles, typically the bystanders. Such disturbance, however, can easily be detected in most cases, when subsequent scans are used, it can even provide the data for bystander behaviour estimation model.

This paper presents the use of detected bystander in the data in order to enhance the C-scale based feature detection. The paper is organized as follows. First the C-scale is quickly revised, then the human detection method is presented. Chapter 4 contains the core of the paper - the way the methods are combined and features detected, while final chapter concludes the paper.

2 Local Curvature Scale

Local curvature scale (C-scale) is a method of curvature estimation applicable to digital boundaries, such as the 2D laser rangefinder scan. The basic idea (seeing [7] is recommended) is to analyze the local curvature for each member of digital boundary set by determining the longest possible set of symmetrical boundary member neighbors that meet following criterion: all the points within local boundary are not further from the straight line formed by connection of local boundary limits than certain value. More formally, let us define discrete boundary $B = \{b_i \,|\, i = 1..., K\}$, where b_i is a boundary element. Each boundary element has associated C-scale segment $C(b_i)$, that is evaluated as:

$$C(b_i) = \left\{ b_{i-t}, ..., b_i, ..., b_{i+t} \,\middle|\, t = \sup\left(d_i^n < d_{\max}\right) : n \in \left[1, ..., \left\lfloor \frac{K-1}{2} \right\rfloor\right] \right\} \tag{1}$$

where d_i^n represents the distance of b_i to the chord of associated C-scale segment $C(b_i)$. The segment is the straight line from the edges (end points) of local digital boundary b_{i-t} and b_{i+t}. The maximum value of the distance is given by threshold $d_{\max}$, so for implementation one simply starts with the immediate neighbors and increases the size of C-scale up to the point when the distance from the chord for arbitrary boundary elements exceeds the threshold. The length of the chord corresponding to the C-scale is denoted as C-scale value $C_c(b_i)$ and corresponding arc length can be determined, for details see [7], [8].

An example of the C-scale values course along the digital boundary, represented by the 2D laser rangefinder scan is shown on Fig. 1. The method assumes that the distances between the neighbors are roughly the same, which might not be the case for the scan. In [8] Liu suggested modified C-scale, however, according to our experiences the improvement does not justify the increase in computational cost.

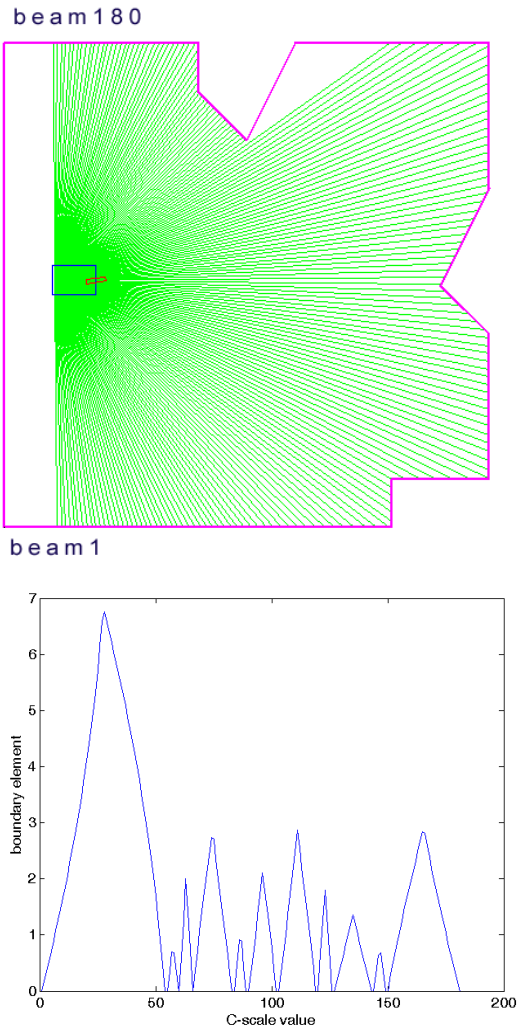

Fig. 1 Example of digital boundary reading and corresponding C-scale values course

As shown on Fig. 1. the end points of the scan, corresponding to the straight line form a peak in C-scale value course, with valleys corresponding to corners and edges. As some parts of the real boundary can be hidden in shadow, the data

must be segmented first and C-svale value determined on each segment separately. Whenever the human being, or any other dynamic obstacle appears in the scanned area, the scanned boundary is corrupted and would be segmented. The idea of this paper is to remove the corrupted boundary elements prior to segmentation and calculate the C-scale value course afterwards.

3 Human Detection

Bystanders represent most of the dynamic obstacles in real-world indoor environment. Detection methods depend on used sensors and processing algorithm, methods that are based on 2D laser rangefinder scan are divided to methods that use single scan or multiple consecutive scans. Single scan processing methods come from simple local minima search through combination of scan data with other sensors and probability based methods to inscribe angle variance method [9-11]. Multiple scans based methods compare the differences between scans incorporating the motion of the robot, with possible tracking of humans detected [12-13].

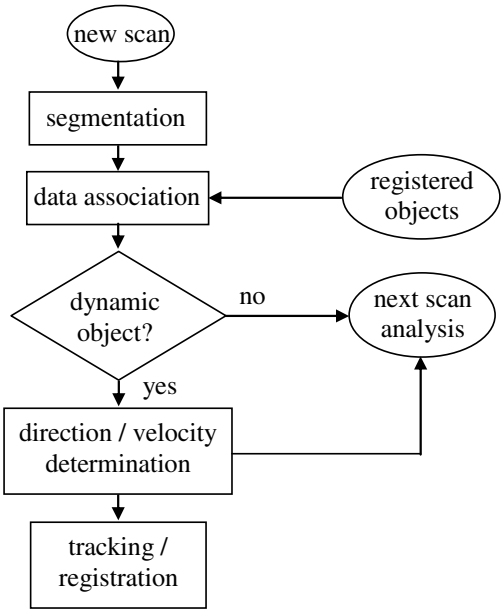

Fig. 2 Laser rangefinder scans based human detection algorithm data flow

Method based on consecutive scans with no additional sensors information fusion was chosen and implemented, with the algorithm shown in Fig. 2. New scan is first segmented and portions geometrically similar to humans are detected, compared with possible positions from previous scan and registered, with estimation of object(s) velocity and direction being the output.

Segmentation filtering is based on geometry and possible positions of legs in the scan (legs apart, forward straddle, behind each other - single leg). Object edges are detected with output segment being the left-right edges combination of the object, depending on the leg position, e.g. LRLR for legs apart, LRR or LLR for forward straddle or LR for single leg. Depending on configuration a series of filters is applied to edges to verify the object correspond to the human leg(s), e.g. distance between edges can not be higher than given limit size of the leg, recalculated for the distance from the sensor, etc. This way the elements of the scan that correspond to the human bystanders can be detected, and further used as described in next chapter.

4 Feature Detection

Feature detection combines two above described methods in the following way:

1. The human legs are detected in the scan according to the method described above.
2. Corresponding scan elements are removed, with the original scan stored for further use in human legs detection.
3. Breakpoints in digital boundary are detected. Breakpoints are discontinuities that appear in the scan. The discontinuity caused by the human legs removal is ignored.
4. Detected breakpoints are used to create several portions of the scan, each starting and ending with an edge, except the start of first and end of last portions, that correspond to the first and last reading of the scanner. As limited angle range is assumed (commonly 0-180 degrees), those exceptions correspond to the readings limits and have no connection to the environment features.
5. Portions smaller than threshold t_p are discarded. The threshold depends on the inverse of the average reading distance, as closer objects cover larger number of readings.
6. On each portion of the scan, C-scale value course is found, using formula (1). The choice of threshold $d_{\max}$ is crucial for the proper course determination, however it depends mainly on the noise in readings which for laser rangefinders is distance-independent.
7. Detection of valleys in the C-scale value course is used for further segmentation, with each segment corresponding to straight line or curved line. Local minima therefore correspond to edges or corners.

Breakpoints detection in step 3 is performed according to commonly known adaptive formula, applied for each reading r_i

$$\left\| r_{i+1} - r_i \right\| > r_i \frac{\sin \Delta\varphi}{\sin\left(\chi - \Delta\varphi\right)} + 3\sigma \tag{2}$$

where $\Delta\varphi$ is the angular resolution of the scan, χ represents the worst incidence angle (usually up to 10°) and σ is residual variance.

Whenever the discontinuity coming from the human obstacle is recorded, the above test is ignored for the first element of the scan following the discontinuity.

Further processing, such as detection of virtual corners, calculation of curve segments centers, etc. is possible, however, in most environments unnecessary. Detected features can then be used for localization, SLAM, and general navigation of mobile robot.

The methods were implemented in Matlab for verification in simulation process. To compare the ability of the method with and without the human detection, a series of simulations was performed, in the following way. Simulated robot was moving in indoor environment on predefined trajectory, taking scan each second. Various number of human obstacles was present in the view, moving in random directions with random speed. Environment features were detected by C-scale value based method both with and without human detection enhancement. As the experiment was performed on simulation, the real position of the features is known and can be compared with the features detected. This way the percentage of detectable features (features that are in view of the scanner and are not hidden by dynamic obstacle) can be determined, serving as a measure of method performance.

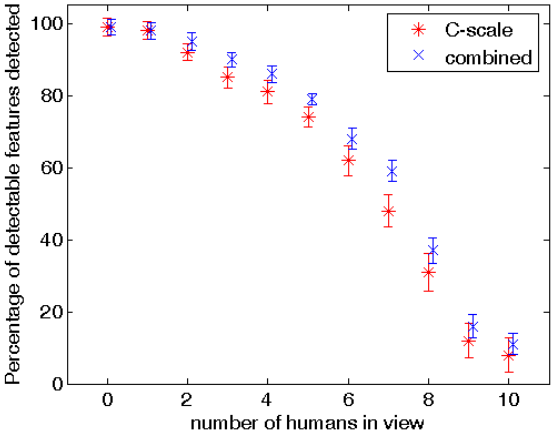

Fig. 3 Comparison of C-scale value based feature detection with and without human detection, showing the percentage of detectable features detected depending on the number of humans in view

The results are shown on Fig. 3. It is clear that C-scale value based detection combined with the human obstacles detection improves the C-scale alone. The improvement is larger for the few people, when the view of the scanner is disrupted too much, both methods ability to detect the features degrades, as there is simply not enough data to extract the features from.

5 Conclusions

Presented combination of C-scale value based feature detection with human detection shows performance enhancement over the non-modified detection method. The improvement is the best for a certain number of humans in view, with most of the view field disrupted, the efficiency drops, as expected. The enhancement is not dramatic, however, the additional computation, required to detect human obstacles, can be used for further navigation tasks, such as path planning or human-machine communication use, and therefore in our opinion does pay off.

Future work will be focused on improving the position of the features, as currently the features are represented directly by boundary element. For larger distances of the feature from the scanner, the position error might be quite large, this problem we believe could be resolved by further processing of locally found curves.

Acknowledgement. Published results were acquired with the support of the Academy of Sciences of the Czech Republic with institutional support RVO:61388998.

References

[1] Zhou, C., Wei, Y., Tan, T.: Mobile robot self-localization based on global visual appearance features, Robotics and Automation. In: Proceedings of the IEEE International Conference on Robotics and Automation, ICRA 2003, pp. 1271–1276 (2003)

[2] Se, S., Lowe, D., Little, J.: Mobile Robot Localization and Mapping with Uncertainty using Scale-Invariant Visual Landmarks. The International Journal of Robotics Research 21(8), 735–758 (2002)

[3] Lingemann, K., Nuchter, A., Hertzberg, J., Surmann, H.: High-speed laser localization for mobile robots. Robotics and Autonomous Systems 51(4), 275–296 (2005)

[4] Iocchi, L., Nardi, D.: Hough localization for mobile robots in polygonal environments. Robotics and Autonomous Systems 40(1), 43–58 (2002)

[5] Borges, G.A., Aldon, M.: Line extraction in 2D range images for mobile robotics. Journal of Intelligent and Robotic Systems 40(3), 267–297 (2004)

[6] Chum, O., Matas, J.: Optimal Randomized RANSAC. IEEE Transactions on Pattern Analysis and Machine Intelligence 30(8), 1472–1482 (2008)

[7] Rueda, S., Udupa, J.K., Bai, L.: Local curvature scale: A new concept of shape description. In: Medical Imaging 2008: Image Processing. Proceedings of SPIE, vol. 6914, SPIE, Bellingham (2008)

[8] Liu, M., Lei, X., Zhang, S., Mu, B.: Natural Landmark Extraction in 2D Laser Data based on Local Curvature Scale for Mobile Robot Navigation. In: Proceedings of the 2010 IEEE International Conference on Robotics and Biomimetics, Tianjin, China, December 14-18, pp. 525–530 (2010)

[9] Bellotto, N., Hu, H.: Multisensor-Based Human Detection and Tracking for Mobile Service Robots. IEEE Transaction of Systems, Man and Cybernetics-Part B: Cybernetics 39(1) (2009)

[10] Dong-Hyung, K., Youngmyung, L.: Detection, Motion Planning and Control of Human Tracking Mobile Robots. In: 8th International Conference on Ubiquitous Robots and Ambient Intelligence (2011)
[11] Zivkovic, Z., Krose, B.: Part based people detection using 2D range data and images. In: IEEE/RSJ International Conference on Intelligent Robots and Systems (2007)
[12] Chen Tun, C., Jiun-Yi, L.: Multi-robot Cooperation Based Human Tracking System Using Laser Range Finder. IEEE International Conference on Robotics and Automation (2011)
[13] Polychronis, K., Baltzakis, H., Trabanias, P.: Learning Moving Objects in a Multi-Target Tracking Scenario for Mobile Robots that use Laser Range Measurements. In: IEEE/RSJ International Conference on Intelligent Robots and Systems (2009)

Orthotic Robot as a Self Optimizing System

J. Wierciak, K. Bagiński, D. Jasińska-Choromańska, and T. Strojnowski

Warsaw University of Technology, Faculty of Mechatronics, Św. A. Boboli 8,
02-525, Warszawa, Poland
{j.wierciak,k.baginski,danuta,t.strojnowski}@mchtr.pw.edu.pl

Abstract. One of the crucial development trends in building of mechatronic devices is designing and realising self optimizing systems, i.e. systems that are capable of changing the objective of their operation due to variable conditions under which they operate. An example of such system is an orthotic robot – a device restoring to individuals with paralysed legs a capability of taking on a vertical position and performing basic motor activities. As far as operation of such device is concerned, it is important that it does not pose any threat of injuring the user, and what is more – that it would be capable of minimizing the results of possible hazardous situations. The paper presents selected activities that have been undertaken by a team building an orthotic robot, in order to ensure its self optimization.

1 Introduction

Development of mechatronic systems made it possible to solve on a technological basis many problems that have been deemed too difficult to overcome till recently. One of such fields, in which mechatronic concept pertaining to the structure of the devices made it possible to address new design and research problems, is biomechanics. In numerous scientific centres all over the world there are undertaken studies on replacing the lost motor functions of humans by special devices [3, 4, 5, 15, 16, 19] known by the name of orthotic robots (Fig. 1). A crucial issue that must be solved while designing an orthotic robot is to ensure a safety of the user,

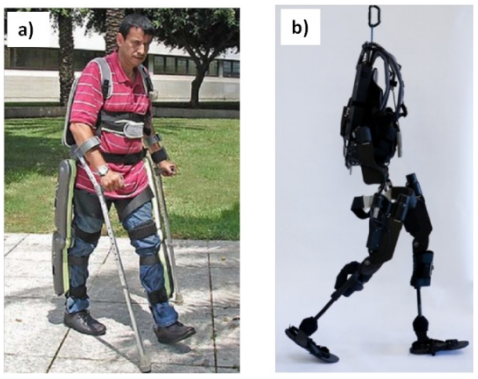

Fig. 1 Exemplary orthotic robots: a) ReWalk [3], b) e-Legs [17]

T. Březina and R. Jabloński (eds.), *Mechatronics 2013*,
DOI: 10.1007/978-3-319-02294-9_77,

i.e. a disabled person, which often has already been a victim of an accident that happened in the past. Analysis of such problems yields advanced systems solutions defined as self optimization. The authors, having been engaged in a design of an orthotic robot, carried out a comparison of their own approach, applied while designing the device, with the methodology of building self optimising systems as proposed by the authors originating from the University of Paderborn [6, 7].

2 Design of Mechatronic Systems

There exist many ideas of describing the design process of mechatronic systems [8, 10, 18]. With regard to their basic principles, these descriptions are coincident with each other, as they result from similar experiences gained while realising various design projects. One can always find in them a stage of developing a concept of a device or a system, a stage of designing actuators and sensors, and a stage of integrating the subsystems. A commonly accepted model of the mechatronic design is a so-called V-model elaborated by VDI and published within the guidelines of this organization [18]. This model is referred to by authors formulating design methodology of self optimising systems discussed in [6, 7]. A conceptual design proposed by these authors can be comprised of the following stages:

- planning and clarifying the design task
- conceptual design at the system level
- conceptual design at the module level
- integration of concepts.

A concept of the system elaborated in this way is described by a set of partial models, which represent the system in certain aspects. These are: environment, application scenarios, requirements, system of the objectives, functions of the system, active structure, shape and the system behaviour.

While working on the orthotic robot, the authors used their own methodology of designing devices, including the following six characteristic stages:

- determination of needs related to technical and operational issues (foredesign),
- analysis of the main function,
- development of actuators and sensors,
- development of subsystems,
- control over manufacturing of a technical model,
- launching the system and its tests.

At the following sections, there are presented activities that were undertaken at particular stages of the design in order to obtain a self optimizing character of the device that has been built.

3 Foredesign

At that stage of designing, one formulated the basic requirements regarding the robot that has been built. They include description of functions that are foreseen to be realised by the system, as well as a list of necessary interfaces: to the user, to the physical and technical environment, and also to regulations.

3.1 Functions of the System

The main functions of the system include: walking on a flat surface, sitting down and getting up from a chair, as well as ascending and descending the stairs. Besides, one proposed original ideas for auxiliary functions, including a turnaround and a gait by the way of sidesteps. It was accepted that the safety function of the user of the system is superior to the listed motor functions.

The main functions of the system are described by algorithms created on the basis of experimentally determined motion profiles of particular parts of human limbs (Fig. 2).

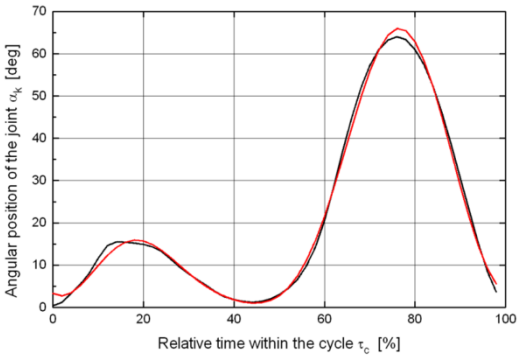

Fig. 2 Exemplary course of the bending angle at the knee articulation within a single gait cycle [1]: black line – measurement data, red line – approximation for control needs

Functions connected with the safety result from an analysis of potential hazardous situations. They may be caused by an improper behaviour of the user, failure of the device (Fig. 3) or external impacts.

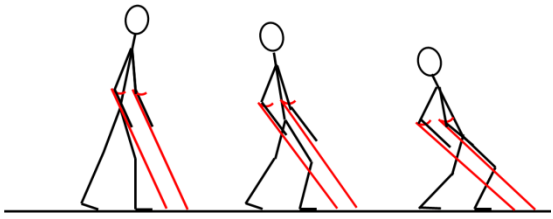

Fig. 3 Possible course of an event due to a decay of the power supply of the robot drives

3.2 The User

Potential users of the systems for verticalization and aiding the motion (i.e. orthotic robots) are persons suffering from paralysis of the lower limbs, yet having the upper part of the trunk able and strong enough to keep one's balance by means of crutches or a walking frame. These persons do care for a possibly high self-reliance.

3.3 The Environment

While elaborating the brief foredesign related to technical and operational issues, one characterized first of all a foreseen environment in which the device that has been designed operates. Both interiors of buildings as well as their surroundings were considered, using descriptions of selected elements of the environment, i.e. stairs, included in related regulations [20].

4 Objectives of the System

Analysis of the foredesign related to technical and operational issues makes it possible to create a system of objectives, which will be referred to in the future by the control algorithms of the device. The objectives resulting from requirements of the users concern, among other things, comfort of and safety of using the device. The objectives the designers must face, are safe operation of the device with respect to the user and the environment, a correct realisation of the motor functions as well as high energetic efficiency.

While designing the robot, one accepted a hierarchic structure of the objectives (Fig. 4). A superior objective of the system is to ensure safety of the user. Provided this objective is met, other subordinate objectives can be realised, including a precise reconstruction of the accepted motion profiles of the legs. An important objective is minimization of the energy consumed by the system while operated. Internal objectives i.e. objectives which are persecuted by the system when performing an optimization are generated from the external and inherent objectives (Fig. 5).

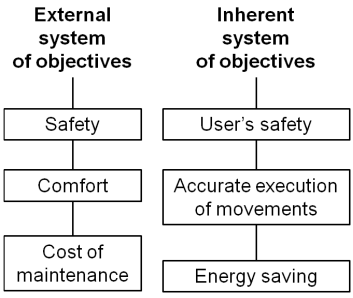

Fig. 4 Hierarchy of the external and inherent objectives of the orthotic robot

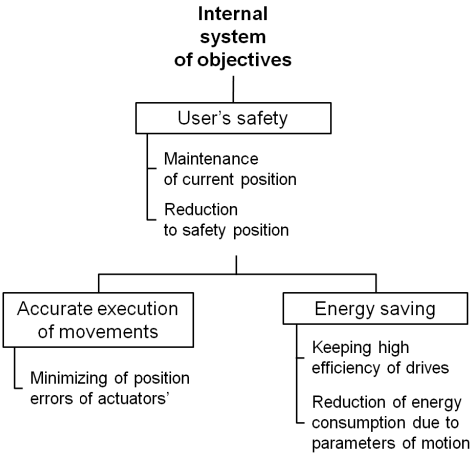

Fig. 5 Structure of internal objectives of the robot

5 Analysis of the Function

At this stage of the design, one elaborated operation algorithms of the device, both while realising its primary functions as well as functions related to the safety. Analysis of these algorithms allows one to create a list of actuators and sensors of the robot that comprise its functional structure (Fig. 6) along with technical requirements set for such elements. As it usually takes place in present machines, modules for realization of main functions are tightly integrated with safety system [12].

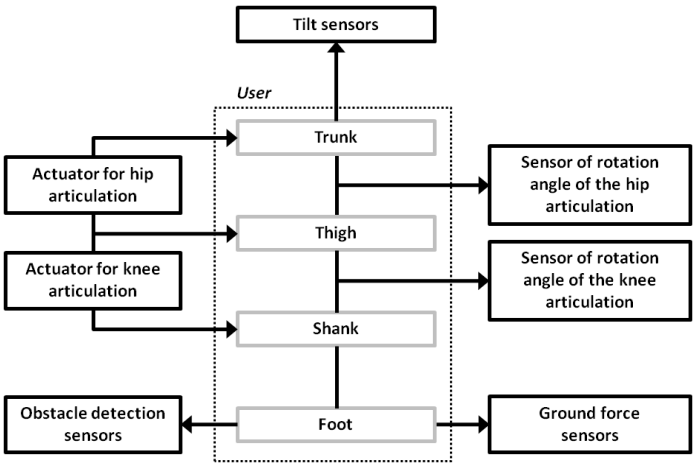

Fig. 6 Functional block diagram of the robot

It can be noted that the specified sensors are used first of all to realise the functions related to the safety of the user, whereas the other, not included in the diagram, are integral part of the actuators, such as described in [2]. The control system employs a tilt sensor, based on MEMS accelerometers as suggested in [14], which determines the axial tilt according to one of the ways proposed in [13].

6 Elaboration of the Functional Modules

The stage of developing the functional modules is important, among other things, because of a possibility of achieving synergic effects, owing to which the structure of the device gets simplified. In the case of the orthotic robot, in one of the variants of the actuator forcing the motion of the limbs (Fig. 7a) one has foreseen an electromagnetic brake release that makes it possible to realise selected safety algorithms, e.g. to maintain a standing position of the user in the case when the power supply of the drives decays. In the made-up technical model of the robot different version of actuator was employed (Fig. 7b). It uses screw gear of ball type and converts linear movement of the nut to rotational movement of articulation by a tie mechanism.

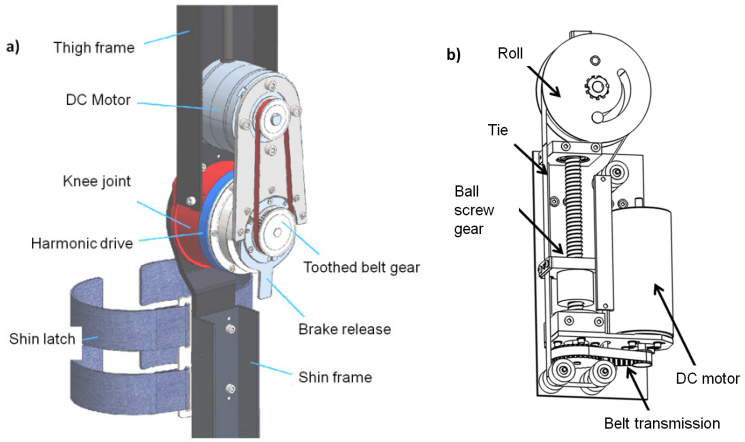

Fig. 7 Mechanical structures of the actuator of the knee joint: a) with a brake release, b) version without brake applied in the prototype of robot

7 Elaboration of the Subsystems

At this stage of the works, designers and information scientists integrate elements and units within particular subsystems: mechanical, electronic and software. Depending on the solutions that were proposed before, the self optimization can be realised by parametric or structural adaptation [7]. As far as the presented example is concerned, the change of the objective of the device operation from a precise

reconstruction of the movements into a minimization of power consumption will consists in prolonging the gait cycle within a certain range of its length [16], so in a modification of one of the considered parameters of motion. This can be achieved by means of the control software or by changing presets of the hardware [9]. En example of structural adaptation will be a change of the way of using the brakes in the drive modules, so a change within the mechanical structure aimed to realise the algorithms of the safety system.

8 Summary

Comparison of the selected parts of the works, presented in the paper, pertaining to the system aiding motion of the disabled, with the description of an innovative project of a system of autonomic shuttles [6, 7] prove that the scopes of activities undertaken in order to built a self optimizing system are very similar. Some differences are evident only in the ways of describing the partial models and the software tools applied while building them.

References

[1] Bagiński, K., Wierciak, J.: Selection of drives for orthotic robot based on simulation studies. Machine Dynamics Research 36(1), 5–14 (2012)
[2] Bodnicki, M., Hawłas, H.J.: Commutation Phenomena in DC Micromotor as Source Signal of Angular Position Transducer. Recent Advances in Mechatronics 2008-2009, 263–268 (2009)
[3] Bogue, R.: Exoskeletons and robotic prosthetics: a review of recent developments. Industrial Robot: An International Journal 36(5), 421–427 (2009)
[4] Dollar, A.M.: Lower Extremity Exoskeletons and Active Orthoses: Challenges and State-of-the-Art. IEEE Trans. Robotics 24(1), 144–158 (2008)
[5] Farris, R.J., Quintero, H.A., Goldfarb, M.: Preliminary Evaluation of a Powered Lower Limb Orthosis to Aid Walking in Paraplegic Individuals. IEEE Transactions on Neural Systems and Rehabilitation Engineering 19(6), 652–659 (2011)
[6] Gausemeier, J., Donoth, J., Pook, S.: Conceptual Design of Self-Optimizing Mechatronic Systems. Self-optimizing Mechatronic Systems. Design the Future, HNI-Verlagsschriftenreihe 223, 36–51 (2008)
[7] Gausemeier, J., Kahl, S., Pook, S.: From Mechatronics to Self-Optimizing Systems. Self-optimizing Mechatronic Systems. Design the Future, HNI-Verlagsschriftenreihe 223, 3–32 (2008)
[8] Gawrysiak, M.: Mechatronics and mechatronic designing. Białystok University of Technology, Scientific Works 44 (1997) (in Polish)
[9] Grepl, R.: Composite Controller for Electronic Automotive Throttle with Self-tuning Friction Compensator. Mechatronics Recent Technological and Scientific Advances, 73–78 (2011)
[10] Isermann, R.: Mechatronic Systems - Fundamentals. Springer, London (2005)
[11] Jasińska – Choromańska, D., Credo, W., Szykiedans, K.: Making use of anthropometric data while designing drive units of an orthotic robot. Machine Dynamics Research 36(1), 90–98 (2012)

[12] Kiel, E. (ed.): Drive solutions. Mechatronics for Production and Logistics. Springer, Berlin (2008)
[13] Łuczak, S.: Specific Measurements of Tilt with MEMS Accelerometers. Mechatronics Recent Technological and Scientific Advances, 705–711 (2011)
[14] Łuczak, S., Oleksiuk, W., Bodnicki, M.: Sensing Tilt with MEMS Accelerometers. IEEE Sensors J. 6(6), 1669–1675 (2006)
[15] Mohammed, S., Amirat, Y.: Towards Intelligent Lower Limb Wearable Robots: Challenges and Perspectives – State of the Art. In: Proc. IEEE Int. Conf. ROBIO 2008, pp. 312–317 (2009)
[16] Pons, J.L.: Wearable Robots: Biomechatronic Exoskeletons. John Wiley & Sons, Chichester (2008)
[17] Strausser, K.A., Kazerooni, H.: The Development and Testing of a Human Machine Interface for a Mobile Medical Exoskeleton. In: IEEE/RSJ International Conference on Intelligent Robots and Systems, pp. 4911–4916 (2011)
[18] VereinDeutscherIngenieure (VDI), Design methodology for mechatronic systems. Beuth-Verlag, Berlin (2004)
[19] Wierciak, J., Jasińska-Choromańska, D., Szykiedans, K.: Orthotic Robot as a Mechatronic System. Mechatronics Recent Technological and Scientific Advances, 579–588 (2011)
[20] Executive regulation of Minister of Infrastructure from 22.04.2002 with regard to technical conditions buildings and their location have to fulfill, Dz. U. 2002 nr 75 poz. 690 (2002) (in Polish)

Trajectory Generation for Autonomous Vehicles

Vu Trieu Minh

Tallinn University of Technology, Department of Mechatronics, 19086 Tallinn, Estonia
trieu.vu@ttu.ee

Abstract. This paper presents the problem of trajectory generation for autonomous vehicles with three different techniques in flatness, polynomial and symmetric polynomial equations subject to constraints. Kinematic model for each technique is built subject to constraints including position, body angle, steer angle and their velocities. Simulations for each technique are conducted and compared. Findings in this paper can be used to develop a real-time controller for auto-driving and auto-parking systems.

1 Introduction

This paper studies problem related to trajectory generation for autonomous vehicles moving from a start point to any destination point subject to constraints. Study of this paper can be used to develop a real-time control system for autonomous ground vehicles which can track exactly on any feasible paths from the global positioning system (GPS) maps or/and from unmanned aerial vehicle (UAV) images. This system can be also applied to autonomous unmanned ground vehicles (on road or off road), and auto-parking, auto-driving systems.

Basic studies on the flatness, nonholonomic, and nonlinear systems can be read from the book of Levine J. in [1] where the fundamental motion planning of a vehicle is presented. The flatness and controllability conditions for this nonlinear system are also well investigated and defined. Parking simulation of a two-trailer vehicle is also demonstrated but without the constraint of steer angle and steer angular velocity.

The problem of trajectory generation for nonholonomic system is also presented by Dong W and Guo Y in [2] where two trajectory generation methods are proposed. The control inputs are the second order polynomial equations. By integrating those control inputs, coefficients for those second order polynomial equations are found. However this paper is lacking constraint analysis on the vehicle velocity and the steer angle.

Optimal control based on cell mapping techniques for a car-like robot is studied by Gomez, M. in [3] subject to the energy-optimal constraint and based on bang-bang control theory. This paper shows a simulation of a wheeled mobile robot moving on a path with the steering angle velocity control. However the paper does not mention on the algorithms for generating the vehicle trajectory. Several other

T. Březina and R. Jabloński (eds.), *Mechatronics 2013*,
DOI: 10.1007/978-3-319-02294-9_78,

research papers on optimal trajectories and control of autonomous vehicles can be read in [4], [5], [6], and [7], however most of those studies are based on the real traffic flow roads and the control algorithms are to perform the maneuver tasks such as lane-changing, merging, distance-keeping, velocity-keeping, stopping, and collision avoidance, etc.

This paper, therefore, focuses on the applicable algorithms to generate feasible trajectories from a start point to any destination point subject to vehicle constraints. This paper is the continuation of the previous paper on vehicle sideslip model and estimation by Minh V in [8]. The nonlinear computational schemes for the nonlinear systems are referred to in Minh V and Nitin A. in [9] and [10]. The outline of this paper is as follows: Section 2 describes the kinematic model; Section 3 presents the flatness method; Section 4 presents the polynomial method; Section 5 introduces the symmetric polynomial method and the performance of the three methods; finally, conclusion is drawn in section 6.

2 Kinematic Model of a Vehicle

A kinematic model of a vehicle can be drawn in figure 1:

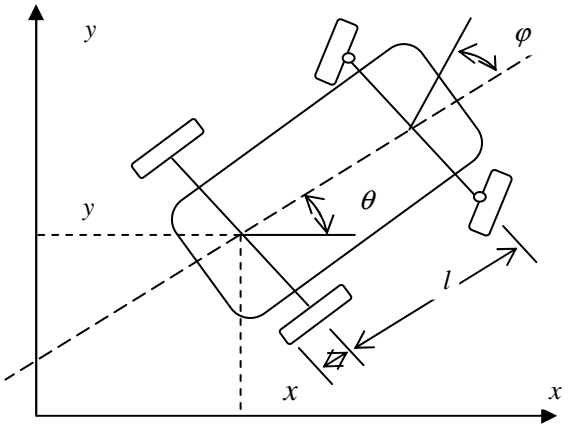

Fig. 1 A simplified vehicle model

The kinematic model of a forward rear-wheel driving vehicle can be written as:

$$\begin{bmatrix} \dot{x} \\ \dot{y} \\ \dot{\theta} \\ \dot{\varphi} \end{bmatrix} = \begin{bmatrix} \cos\theta \\ \sin\theta \\ \dfrac{\tan\varphi}{l} \\ 0 \end{bmatrix} rv_1 + \begin{bmatrix} 0 \\ 0 \\ 0 \\ 1 \end{bmatrix} v_2 \tag{1}$$

where $X = [x, y, \theta, \varphi]'$ is the system state variables, (x , y) are the Cartesian coordinates of the middle point of the rear wheel axis, θ is the angle of the vehicle

body to the *x*-axis, φ is the steering angle, l is the vehicle wheel base, r is the wheel radius, v_1 is the angular velocity of the rear wheel, and v_2 is the angular steering velocity. Given the initial state $X(0)=[x_0, y_0, \theta_0, \varphi_0]'$ at time $t=0$ and the final state $X(T)=[x_T, y_T, \theta_T, \varphi_T]'$ at time $t=T$, the paper generates a feasible trajectory for this vehicle.

Similarly, the model for a forward front-wheel driving vehicle is presented as:

$$\begin{bmatrix} \dot{x} \\ \dot{y} \\ \dot{\theta} \\ \dot{\varphi} \end{bmatrix} = \begin{bmatrix} \cos\theta\cos\varphi \\ \sin\theta\cos\varphi \\ \dfrac{\tan\varphi}{l} \\ 0 \end{bmatrix} rv_1 + \begin{bmatrix} 0 \\ 0 \\ 0 \\ 1 \end{bmatrix} v_2 \tag{2}$$

For a vehicle moving in a reverse direction (backing), the velocity, v_1, of this vehicle is assigned in a minus value:

$$\begin{bmatrix} \dot{x} \\ \dot{y} \\ \dot{\theta} \\ \dot{\varphi} \end{bmatrix} = -\begin{bmatrix} \cos\theta \\ \sin\theta \\ \dfrac{\tan\varphi}{l} \\ 0 \end{bmatrix} rv_1 + \begin{bmatrix} 0 \\ 0 \\ 0 \\ 1 \end{bmatrix} v_2 \tag{3}$$

From the above kinematic models, flatness equations for the vehicle trajectory generation are presented in the next section.

3 Vehicle Flatness Trajectory Generations

From figure 1, the vehicle angular velocity can be calculated as:

$$v_1 = \frac{\sqrt{\dot{x}^2 + \dot{y}^2}}{r} \tag{4}$$

Transformation from equation (1), the vehicle body angle is:

$$\theta = \arctan\left(\frac{\dot{y}}{\dot{x}}\right) \tag{5}$$

From the derivative of the above trigonometric, θ, the body angular velocity, $\dot{\theta}$, is achieved:

$$\dot{\theta} = \frac{\ddot{y}\dot{x} - \ddot{x}\dot{y}}{\dot{x}^2} \frac{1}{\left(\dfrac{\dot{y}}{\dot{x}}\right)^2 + 1} = \frac{\ddot{y}\dot{x} - \ddot{x}\dot{y}}{\dot{x}^2 + \dot{y}^2} = \frac{\tan\varphi}{l} rv_1 \tag{6}$$

Therefore, θ and φ can be directly calculated from variables: $\dot{x}$, $\ddot{x}$, and $\dot{y}$, $\ddot{y}$. And it means that the above system is flat [1]. Thus, all state and input variables can be presented by the flat outputs *x* and *y*.

The boundary conditions for the outputs *x* and *y* are:

$$\frac{\partial^2 y}{\partial x^2} = \frac{\tan\varphi}{l\cos^3\theta} \tag{7}$$

The initial state at time, $t = 0$, to the final state at time, $t = T$ for $x(t)$:

$$x(0) = x_0, \text{ and } x(T) = x_T \tag{8}$$

The initial state for $y(t) = y(0)$ and the final state for $y(t) = y(T)$:

$$y(0) = y_0 = \tan\theta_0 \Rightarrow \frac{\partial^2 y}{\partial x^2}\Big|_{t=0} = \frac{\tan\varphi_0}{l\cos^3\theta_0} \tag{9}$$

$$y(T) = y_T = \tan\theta_T \Rightarrow \frac{\partial^2 y}{\partial x^2}\Big|_{t=T} = \frac{\tan\varphi_T}{l\cos^3\theta_T} \tag{10}$$

From the initial state $(x_0, y_0, \theta_0, \varphi_0)$ at the time $t = 0$ to the final state $(x_T, y_T, \theta_T, \varphi_T)$, under a real condition that $|\dot{x}(t)| \geq \varepsilon > 0$. If it is assumed that, $\varepsilon = \frac{|x_T - x_0|}{2T} > 0$, the trajectory of $x(t)$ can be written freely as:

$$x(t) = \left(\frac{T-t}{T}\right)x_0 + \frac{t}{T}x_T + |x_T - x_0|\frac{t(t-T)}{2T^2} \tag{11}$$

And the trajectory of $y(t)$ can be selected as:

$$y(t) = y_0 + t\alpha_1\tan\theta_0 + t^2\frac{\alpha_2\tan\varphi_0}{2l\cos^3\theta_0} + t^3b_1 + t^4b_2 + t^5b_3 \tag{12}$$

where $\alpha_1 = \frac{2(x_T - x_0) - |x_T - x_0|}{2T}$, $\alpha_2 = \frac{|x_T - x_0|}{T^2}$, and $\alpha_3 = \frac{2(x_T - x_0) + |x_T - x_0|}{2T}$;

and $b = [b_1, b_2, b_3]^* = A^{-1}c$ with $A = \begin{bmatrix} T^3 & T^4 & T^5 \\ 3T^2 & 4T^3 & 5T^4 \\ 6T & 12T^2 & 20T^3 \end{bmatrix}$ and

$$c = \begin{bmatrix} y_T - y_0 - T\alpha_1\tan\theta_0 - T^2\dfrac{\alpha_2\tan\varphi_0}{2l\cos^3\theta_0} \\ \alpha_3\tan\theta_T - \alpha_1\tan\theta_0 - T\dfrac{\alpha_2\tan\varphi_0}{l\cos^3\theta_0} \\ \dfrac{\alpha_2\tan\varphi_T}{l\cos^3\theta_T} - \dfrac{\alpha_2\tan\varphi_0}{l\cos^3\theta_0} \end{bmatrix}.$$

From equation (10),

$$\theta = \arctan\left(\frac{2T^2\left(\alpha_1 \tan\theta_0 + \dfrac{\alpha_2 \tan\varphi_0}{l\cos^3\theta_0} t + 3b_1 t^2 + 4b_2 t^3 + 5b_3 t^4 \right)}{\left(2T(x_T - x_0) - T\left|x_T - x_0\right| + 2\left|x_T - x_0\right| t\right)} \right) \tag{13}$$

and from equation (5),

$$\varphi = \arctan\left(\frac{\left(\dfrac{\alpha_2 \tan\varphi_0}{l\cos^3\theta_0} + 6b_1 t + 12b_2 t^2 + 20b_3 t^3 \right)\left(2T^2\right)^2 l\cos^3\theta}{\left(2T(x_T - x_0) - T\left|x_T - x_0\right| + 2\left|x_T - x_0\right| t\right)^2} \right) \tag{14}$$

The angular velocity of the vehicle in equation (1) can be calculated from (13) and (14).

$$\dot{y}(t) = \left(\alpha_1 \tan\theta_0 + \frac{\alpha_2 \tan\varphi_0}{l\cos^3\theta_0} t + 3b_1 t^2 + 4b_2 t^3 + 5b_3 t^4 \right) \tag{15}$$

$$\ddot{y}(t) = \left(\frac{\alpha_2 \tan\varphi_0}{l\cos^3\theta_0} + 6b_1 t + 12b_2 t^2 + 20b_3 t^3 \right) \tag{16}$$

$$\dot{x}(t) = \left(\frac{\left(2T(x_T - x_0) - T\left|x_T - x_0\right| + 2\left|x_T - x_0\right| t\right)}{2T^2} \right) \tag{17}$$

$$\ddot{x}(t) = \left(\frac{\left|x_T - x_0\right|}{T^2} \right) \tag{18}$$

The absolute vehicle velocity can be calculated from equations (15) to (18) with:

$$v_1(t) = \frac{\sqrt{\dot{x}^2 + \dot{y}^2}}{r} \tag{19}$$

$$\dot{\theta} = \frac{\ddot{y}\dot{x} - \ddot{x}\dot{y}}{\dot{x}^2 + \dot{y}^2} = \frac{\tan\varphi}{l} r v_1 \tag{20}$$

Simulation for this flatness technique is conducted with $l = 2m$, $r = 0.25m$, $x(0) = \left[0,0,0,0\right]'$, $x(T) = \left[10,10,0,\frac{\pi}{6}\right]'$, and $T = 100$. Figure 2 shows the trajectory and the velocity. Figure 3 shows the vehicle body angle, θ, and the steering angle, φ, corresponding to their angular velocities, $\dot{\theta}$, and, $\dot{\varphi}$.

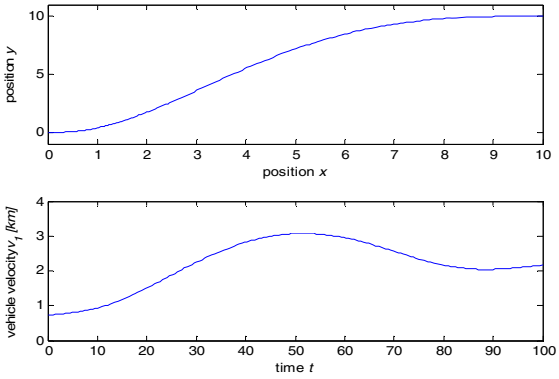

Fig. 2 Trajectory and velocity

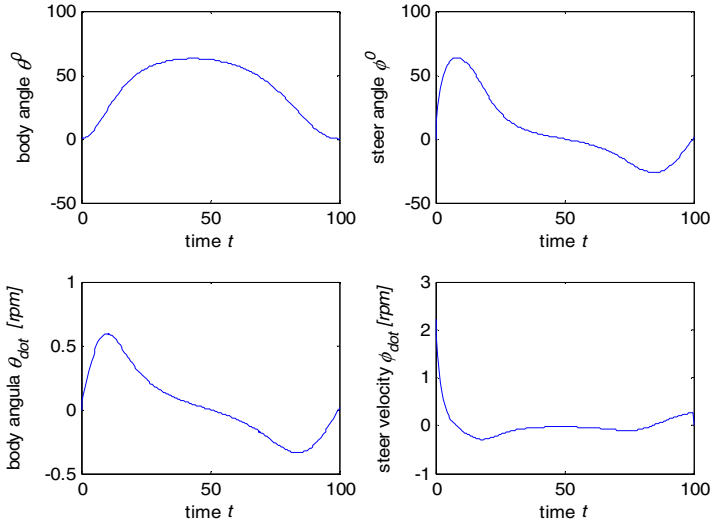

Fig. 3 Body and steering angle

Due to the size of this paper, the sideslip of the vehicle model is ignored. In reality, the sideslip of a vehicle depends on the tire stiffness and the cornering velocity. Then the trajectory generation in this study does not depend on the vehicle velocity. Next part, a new vehicle trajectory generation based on polynomial equations is investigated.

4 Polynomial Trajectory Generations

For faster generation of a feasible vehicle tracking, a second order polynomial for trajectory generation is presented. The equation (1) is separated into the following forms:

$$z_1 = x\,,\ z_2 = \frac{\tan\varphi}{l\cos^3\theta}\,,\ z_3 = \tan\theta\,,\ \text{and}\ \ z_4 = y \tag{21}$$

$$\dot{z}_1 = \dot{x} \tag{22}$$

$$\dot{z}_2 = \frac{v_2 l\cos^2\theta + 3rv_1\cos\theta\sin\theta\sin^2\varphi}{l^2\cos^5\theta\cos^2\varphi} \tag{23}$$

$$\dot{z}_3 = \frac{\tan\varphi}{l\cos^2\theta} rv_1 \tag{24}$$

$$\dot{z}_4 = \dot{y} = \sin\theta rv_1 \tag{25}$$

The vehicle will move from the initial state $(x_0, y_0, \theta_0, \varphi_0)$ at time $t = 0$ to the final state $(x_T, y_T, \theta_T, \varphi_T)$ at time $t = T$ corresponding from the initial state at $(z_{1.0}, z_{2.0}, z_{3.0}, z_{4.0})$ to the final state at $(z_{1.T}, z_{2.T}, z_{3.T}, z_{4.T})$.

For $0 \le t \le T$, the calculation of $[z_1(t), z_2(t), z_3(t), z_4(t)]$ will be:

$$z_1(t) = z_{1.0} + gt \tag{26}$$

$$z_2(t) = z_{2.0} + h_1 t + \frac{1}{2}h_2 t^2 + \frac{1}{3}h_3 t^3 \tag{27}$$

$$z_3(t) = z_{3.0} + gz_{2.0}t + \frac{1}{2}gh_1 t^2 + \frac{1}{6}gh_2 t^3 + \frac{1}{12}gh_3 t^4 \tag{28}$$

$$z_4(t) = z_{4.0} + gz_{3.0}t + \frac{1}{2}g^2 z_{2.0}t^2 + \frac{1}{6}g^2 h_1 t^3 + \frac{1}{24}g^2 h_2 t^4 + \frac{1}{60}g^2 h_3 t^5 \tag{29}$$

with $g = \frac{z_{1.T} - z_{1.0}}{T}$, $[h_1, h_2, h_3]' = D^{-1}e$,

$$D = \begin{bmatrix} T & \frac{1}{2}T^2 & \frac{1}{3}T^3 \\ \frac{1}{2}gT^2 & \frac{1}{6}gT^3 & \frac{1}{12}gT^4 \\ \frac{1}{6}g^2T^3 & \frac{1}{24}g^2T^4 & \frac{1}{60}g^2T^5 \end{bmatrix} \text{ and } e = \begin{bmatrix} z_{2.T} - z_{2.0} \\ z_{3.T} - z_{3.0} - gz_{2.0}T \\ z_{4.T} - z_{4.0} - gz_{3.0}T - \frac{1}{2}g^2 z_{2.0}T^2 \end{bmatrix}.$$

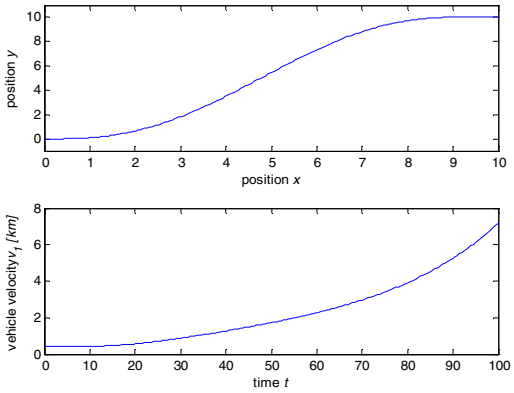

Fig. 4 Trajectory and velocity

Simulation of this method is conducted with the same parameters in section 2 and shown in figure 4 and figure 5.

Figure 4 shows the trajectory for the vehicle from initial point to the final point, and the velocity of the vehicle.

Figure 5 shows the vehicle body angle, θ and the steering angle, φ corresponding to the angular velocity, $\dot{\theta}$ and, $\dot{\varphi}$ of the vehicle.

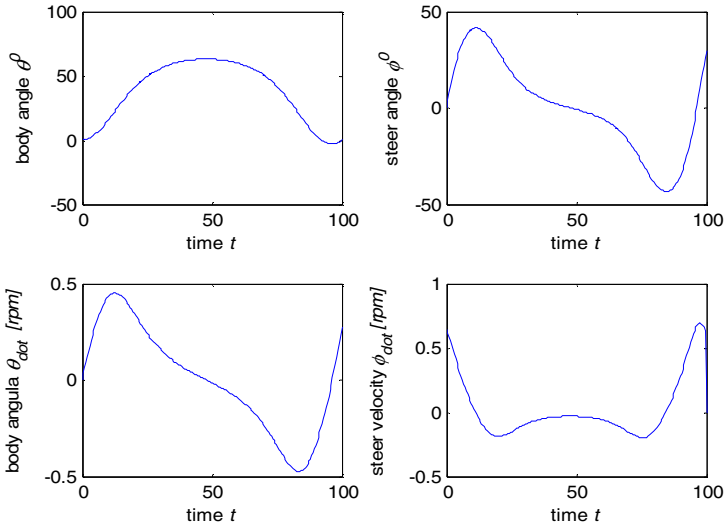

Fig. 5 Body and steering angle

From figure 4, it is really not realistic when the vehicle speed is increasing exponentially. It is expected that, when a vehicle is moving from one point to another point, the speed will increase gradually at the starting point and decrease gradually to the destination point. Therefore in next part, new symmetric polynomial equations in third order are investigated.

5 Symmetric Polynomial Trajectory Generations

Since the system is flatness and each flat output can be parameterized by a sufficiently smooth polynomials. Symmetric third order polynomial equations are tried for this trajectory generation. Because the sideslip is ignored and then, the vehicle trajectory doesn't depend on its speed, v_1, and on the travelling time, T. A new time variable, therefore, for this system is applied with a ratio of $\frac{t}{T}$ for $t = 0 \div T$:

$$x(t) = -(\frac{t}{T} - 1)^3 x_0 + \left(\frac{t}{T}\right)^3 x_T + a_x \left(\frac{t}{T}\right)^2 (\frac{t}{T} - 1) + b_x \frac{t}{T} (\frac{t}{T} - 1)^2 \qquad (30)$$

$$y(t) = -(\frac{t}{T}-1)^3 y_0 + \left(\frac{t}{T}\right)^3 x_T + a_y \left(\frac{t}{T}\right)^2 (\frac{t}{T}-1) + b_y \frac{t}{T}(\frac{t}{T}-1)^2 \quad (31)$$

$$\dot{x}(t) = -3(\frac{t}{T}-1)^2 x_0 + 3\left(\frac{t}{T}\right)^2 x_T + a_x 2\frac{t}{T}(\frac{t}{T}-1) + a_x\left(\frac{t}{T}\right)^2 + b_x(\frac{t}{T}-1)^2 + b_x 2\frac{t}{T}(\frac{t}{T}-1) \quad (32)$$

$$\dot{y}(t) = -3(\frac{t}{T}-1)^2 y_0 + 3\left(\frac{t}{T}\right)^2 y_T + a_y 2\frac{t}{T}(\frac{t}{T}-1) + a_y\left(\frac{t}{T}\right)^2 + b_y(\frac{t}{T}-1)^2 + b_y 2\frac{t}{T}(\frac{t}{T}-1) \quad (33)$$

Then,

$$\ddot{x}(t) = -6(\frac{t}{T}-1)x_0 + 6\frac{t}{T}x_T + a_x 2(2\frac{t}{T}-1) + a_x 2\frac{t}{T} + b_x 2(\frac{t}{T}-1) + b_x 2(2\frac{t}{T}-1) \quad (34)$$

$$\ddot{y}(t) = -6(\frac{t}{T}-1)y_0 + 6\frac{t}{T}y_T + a_y 2(2\frac{t}{T}-1) + a_y 2\frac{t}{T} + b_y 2(\frac{t}{T}-1) + b_y 2(2\frac{t}{T}-1) \quad (35)$$

The constraint on speed:

$$rv_1 = \frac{\dot{x}}{\cos\theta} = \frac{\dot{y}}{\sin\theta} \quad (36)$$

The constraint at starting point $t = 0$:

$$\dot{x}(0) = k_0 \cos\theta_0 \text{ , and } \dot{y}(0) = k_0 \sin\theta_0 \quad (37)$$

The constraint at destination point $t = T$:

$$\dot{x}(T) = k_T \cos\theta_T \text{ , and } \dot{y}(T) = k_T \sin\theta_T \quad (38)$$

From equation (36) and (38), for the calculation simplicity, it is assumed that the speed coefficients at the start and destination point, $k_0 = k_T = k$, then,

$$a_x = k\cos\theta_T - 3x_T \text{ , and } b_x = k\cos\theta_0 - 3x_0 \quad (39)$$

$$a_y = k\sin\theta_T - 3y_T \text{ , and } b_y = k\sin\theta_0 - 3y_0 \quad (40)$$

Simulation is conducted with the same parameters and shown in figure 6 and figure 7.

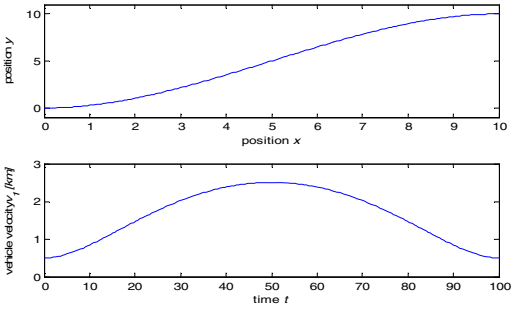

Fig. 6 Trajectory and velocity

It can be seen from figure 6 that the trajectory of this symmetric polynomial is more realistic because the velocity increases from the starting point and decreases in the destination point as per the expectation.

The maximum steering angle for the symmetric polynomial method is $\varphi = 41.1622^0$ and satisfied the constraint, $-45^0 \le \varphi \le 45^0$. This steer angle is smaller than the steer angle in the second order polynomial method.

Comparison performances of the three methods on the trajectory generation and the vehicle velocity are shown in figure 8 and figure 9.

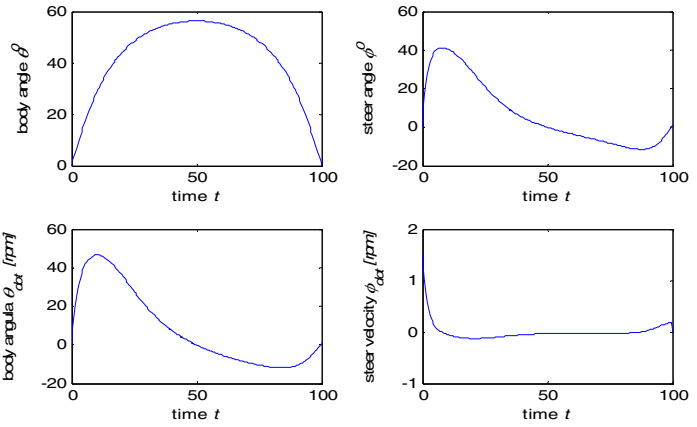

Fig. 7 Body and steering angle

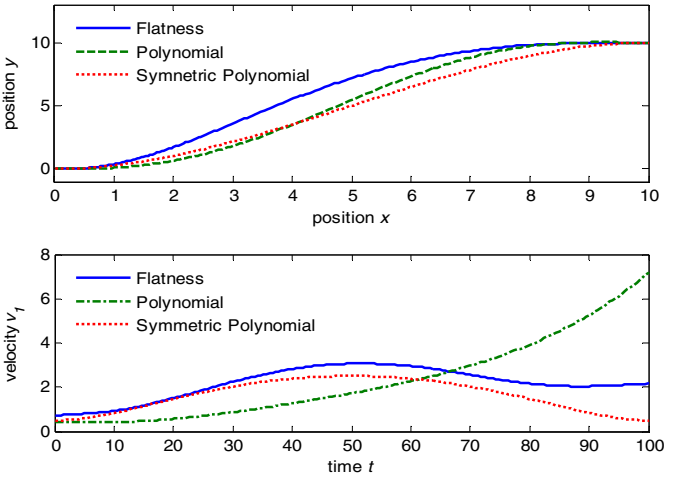

Fig. 8 Comparison of trajectory and velocity

It can be seen that the symmetric polynomial generation can produce a more realistic speed and a smoother trajectory since it allows the vehicle gradually increasing the speed at the start point and reducing the speed to the destination point.

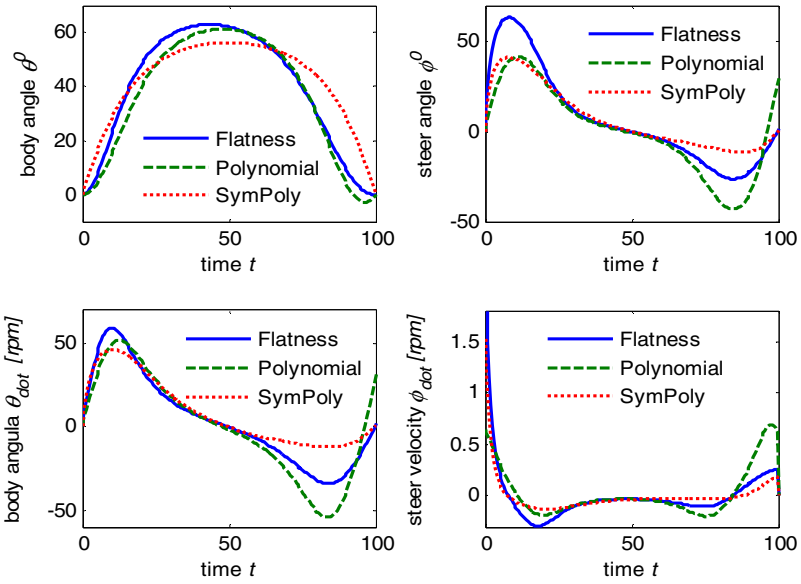

Fig. 9 Comparison of body and steering angle

Figure 9 shows that the symmetric polynomial method providing the lowest body angle, $\theta(t)$, the body angle velocity, $\dot{\theta}(t)$; the steering angle, $\varphi(t)$, and the steering angle velocity, $\dot{\varphi}(t)$. Therefore, this method is recommended for the development of an automatic control of tracking vehicles.

6 Conclusions

The paper has presented three methods of trajectory generation for autonomous vehicles subject to constraints. Regarding to the real vehicle speed development, the third order symmetric polynomial trajectory is recommended. Simulations and analyses are also conducted for vehicle moving in forward and in reverse speeds. Results from this study can be used to develop a real-time control system for auto-driving and auto-parking vehicles. The limitation of this study is the ignorance of the vehicle sideslip due to the cornering velocity. However this error can be eliminated with the feedback control loop and some offset margin of the steer angle constraint.

Acknowledgments. The author would like to thank the Estonian Ministry of Education and Research (Project SF0140113Bs08) for financial support of this study.

References

[1] Levine, J.: Analysis and Control of Nonlinear System, a Flatness-based Approach, 1st edn., pp. 319–328. Springer (2009)
[2] Dong, W., Guo, Y.: New Trajectory Generation for Nonholonomic Mobile Robots. In: Proc. International Symposium on Collaborative Technologies and Systems, pp. 353–358 (2005)
[3] Gomez, M.: Optimal control for Wheeled Mobile Vehicles based on Cell Mapping Techniques. In: Intelligent Vehicles Symposium, pp. 1009–1014 (2008)
[4] Wang, J., Lu, Z., Chen, W., Wu, X.: An Adaptive Trajectory Tracking Control of Wheeled Mobile Robots. In: 6th Proc. on Industrial Electronics and Applications, pp. 1156–1160 (2011)
[5] Werling, M., Kammel, S., Ziegler, J., Groll, L.: Optimal Trajectories for Time-critical Street Scenarios Using Discretized Terminal Manifolds. International Journal of Robotics Research 31(3), 346–359 (2011)
[6] Kanjanawanishkul, K., Hofmeister, M., Zell, A.: Smooth Reference Tracking of a Mobile Robot using Nonlinear Model Predictive Control. In: Proc. of 4th European Conference on Mobile Robots, pp. 161–166 (2009)
[7] Klancar, G.: Tracking-error Model-based Predictive Control for Mobile Robots in real time. Robotics and Autonomous Systems 55(6), 460–469 (2007)
[8] Minh, V.T.: Vehicle Steering Dynamic Calculation and Simulation. In: Proc of 23rd Symp DAAAM International Vienna, pp. 237–242 (2012)
[9] Minh, V.T., Nitin, A.: A Comparative Study on Computational Schemes for Nonlinear Model Predictive Control. Asian Journal of Control 8(4), 324–331 (2006)
[10] Minh, V.T.: Fuzzy logic and slip controller of clutch and vibration for hybrid vehicle. International Journal of Control, Automation and Systems 11(3), 526–532 (2013)

Robotnic Underwater Vehicle Steered by a Gyroscope – Model of Navigation and Dynamics

E. Ładyżyńska-Kozdraś

Warsaw University of Technology, Faculty of Mechatronics, ul. A.Boboli 8,
02-525 Warszawa, Poland
e.ladyzynska@mchtr.pw.edu.pl

Abstract. This paper presents mathematical model of navigation for a underwater vehicle equipped with a gyroscope being an executive element of the system scanning the seabed's surface and following the detected target. In such kinds of underwater vehicles, tracking objects detected by them, the main element is a self-guiding head, which is operated by a steered gyroscope. The dynamics and the method of steering such a vehicle [3] has been here supplemented with dynamics of the gyroscope during the process of scanning and following the detected object were subject to analysis.

1 Introduction

People's interest in the space between the surface and the bottom of seas, oceans and lakes dates back several thousands of years. Submarine vehicles, however, emerged much later. The first deep-sea unmanned vehicle was a torpedo, which was designed by the Austrian navy captain, Giovanni Luppis, in 1864 and built two years later in eng. Robert Whitehead's mechanical plant. This event can be treated as the moment when mankind entered the period of technological development of remotely controlled underwater vehicles, one of the links of which was a torpedo weapon.

In this paper has been performed modelling of the movement dynamics of a robotic underwater vehicle steered by a gyroscope .

This study is a continuation and generalization of the article published in the "Solid State Phenomena" [3], where was proposed an algorithm of modelling of the movement dynamics of a robotic underwater vehicle including non-holonomic constraints.

The use of mathematical model for algorithm testing and development is comfortable. However the design of precise mathematical model is often difficult and the precision of the model significantly increases the probability of good operation of developed algorithms after implementing on real platform.

There are papers dealing with models of underwater vehicles, however the papers are usually concerned with control algorithms for which the mathematical model is needed for development [1], [2].

T. Březina and R. Jabloński (eds.), *Mechatronics 2013*,
DOI: 10.1007/978-3-319-02294-9_79,

This paper presents the modelling of the dynamics of a self-guided underwater vehicle steered using a gyroscope. In such kinds of objects the main element is a self-guiding head, which is operated by a steered gyroscope [4]. The paper presents the dynamics and the method of steering such a underwater vehicle, that has been supplemented with dynamics of the gyroscope during the process of scanning and following the detected object were subject to analysis.

2 The Parameters of Navigation and Dynamics Vehicle

Underwater vehicle has been treated as a non-deformable block – rigid, with six degrees of flexibility, completely immersed in water.

Reference systems, linear and angular coordinates underwater vehicle together with installed gyroscope have been shown in Fig. 1. The axis of the gyroscope is rigidly associated with the rotor.

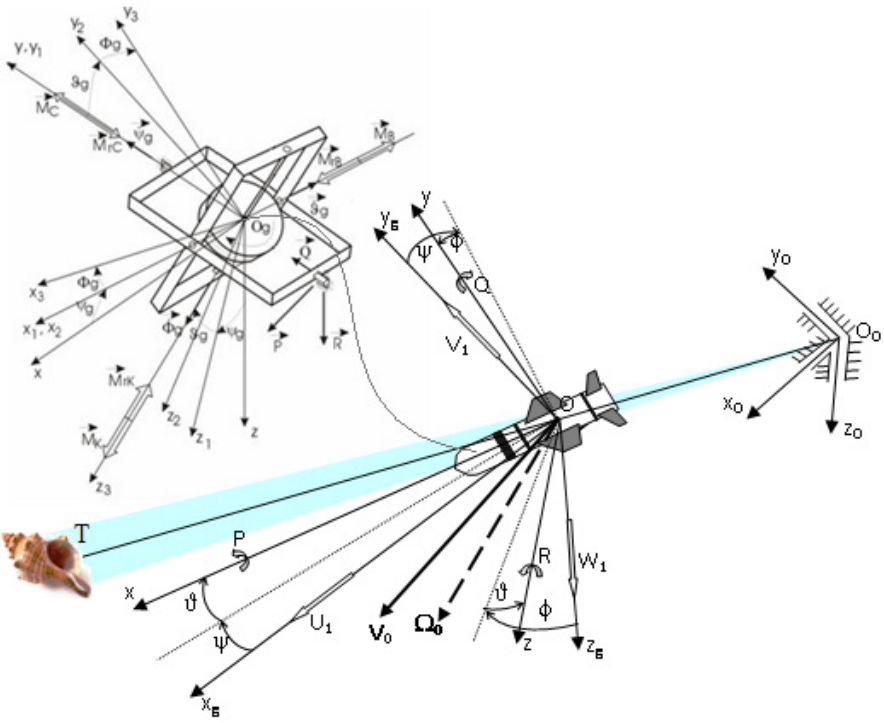

Fig. 1 General scheme of underwater vehicle together with installed gyroscope

In order to describe in space the position of a underwater vehicle and axis the gyroscope, kinematic relationships which provide information about the linear and angular position of a underwater vehicle Oxyz in relation to the $O_0x_0y_0z_0$ inertial system are used. There are a number of parameters describing the location of the

object in space, mostly based on the Euler angles or quaternions [3]. This article uses the Quasi-Euler angles. The order of rotations here is as follows:

1st rotation – $0<\psi$ (deviation angle) around Oz axis with $\dot{\psi}$ angular speed,

2nd rotation – $0<\vartheta$ (pitch angle) around Oy axis with $\dot{\vartheta}$ angular speed,

3rd rotation – $0<\phi$ (bank angle) around Ox axis with $\dot{\phi}$ angular speed.

All the basic reference systems used in the mathematical description, as well as additional systems constitute rectangular dextrorotary systems.

Components of vectors of instantaneous linear $\boldsymbol{V_0}$ and angular velocity $\boldsymbol{\Omega}$ (Fig.1) in the $O_0x_0y_0z_0$ inertial system are as follows:

Vector of the instantaneous linear velocity

$$\overline{V}_0 = U_1\bar{i}_1 + V_1\bar{j}_1 + W_1\bar{k}_1 \tag{1}$$

where: U_1 – longitudinal velocity, V_1 – lateral velocity, W_1– climb rate (Fig.1).

Vector of the instantaneous angular velocity

$$\overline{\Omega} = P\bar{i} + Q\bar{j} + R\bar{k} \tag{2}$$

where: P – angular deviation velocity, Q – angular pitching velocity, R– angular banking velocity (fig.1).

P,Q,R components of the instantaneous angular velocity constitute relationships of generalized $\dot{\phi},\dot{\vartheta},\dot{\psi}$ velocities and trigonometric functions of generalized ϕ,ϑ,ψ coordinates and are expressed by the following relationships:

$$\begin{bmatrix}\dot{\phi}\\ \dot{\vartheta}\\ \dot{\psi}\end{bmatrix} = \begin{bmatrix}1 & \sin\phi\, tg\,\vartheta & \cos\phi\, tg\,\vartheta\\ 0 & \cos\phi & -\sin\phi\\ 0 & \sin\phi\sec\vartheta & \cos\phi\sec\vartheta\end{bmatrix}\begin{bmatrix}P\\ Q\\ R\end{bmatrix} = \Lambda_{\Omega}^{-1}\begin{bmatrix}P\\ Q\\ R\end{bmatrix} \tag{3}$$

The path of underwater vehicle motion in the inertial coordinate system will be described by the following equations

$$x_1 = R_{es}\cos\varepsilon_w\cos\theta_w, \qquad y_{sx_0} = R_{es}\cos\varepsilon_w\sin\theta_w, \qquad z_{sz_0} = -R_{es}\sin\varepsilon_w \tag{4}$$

where: ε_w, θ_w [3] – angles of inclination and deflection of vector R_{es} determining the position and angular velocity of target detection and observation line.

Dynamic equations of combat movement of UAV have been derived in the work [3]. In the inertial system associated with the mother-ship $O_0x_0y_0z_0$ their form is as follows:

$$\mathbf{M}\dot{\mathbf{V}} + \mathbf{K}\mathbf{V} = \mathbf{Q} \tag{5}$$

where: $\mathbf{M}$ – inertia matrix, $\mathbf{K}$ – kinematic relations matrix, $\mathbf{V}$ – velocity vector, $\mathbf{Q}$ – vector of forces and moments of external forces.

3 Control of the Axis of Gyroscope on the Board on Underwater Vehicle

Whilst locating a target from the deck of a underwater vehicle, the axis of the gyroscope shall make the desired movements and thus whilst being directed downwards encircle, with its extension, clearly defined lines on the surface of the seabed. The echolocation system installed in the axis of the gyroscope detect signal emitted by a searched object. Therefore, one shall choose kinematic parameters of the mutual movement of the deck of a underwater vehicle and axis of the gyroscope in a way which ensures that the target will be detected with the highest possible probability. After locating the target (receiving signal from the echolocation system), the gyroscope switches to the tracking mode, that is its axis, from now on, is positioned in a specific location in space, being directed towards the object.

The gyroscope may be used as a drive of the system of detecting, tracking and illuminating the searched object (SDTIO) installed on deck of underwater vehicle's.

Equations which describe the dynamics of the astatic gyroscope, without taking into account the moments of inertia of its frames, have the following forms:

$$\begin{aligned} &J_{gk}\frac{d\omega_{yg_2}}{dt}\cos\vartheta_g + J_{gk}\omega_{gx_2}\left(\omega_{gz_2}+\omega_{gy_2}\sin\vartheta_g\right)+M_k\sin\vartheta_g + \\ &-J_{go}\left(\omega_{gz_2}+\frac{d\Phi_g}{dt}\right)\omega_{gx_2}\cos\vartheta_g+\eta_c\frac{d\psi_g}{dt}=M_c \end{aligned} \tag{6}$$

$$J_{gk}\frac{d\omega_{gx_2}}{dt}-J_{gk}\omega_{gy_2}\omega_{gz_2}+J_{go}\left(\omega_{gz_2}+\frac{d\Phi_g}{dt}\right)\omega_{gy_2}+\eta_b\frac{d\vartheta_g}{dt}=M_b \tag{7}$$

$$J_{go}\frac{d}{dt}\left(\omega_{gz_2}+\frac{d\Phi_g}{dt}\right)=M_k-M_{rk} \tag{8}$$

where: $\omega_{gx_2}=P\cos\psi_g-R\sin\psi_g+\dfrac{d\vartheta_g}{dt}$

$$\omega_{gy_2}=\left(P\cos\psi_g+R\sin\psi_g\right)\sin\vartheta_g+\left(\frac{d\psi_g}{dt}+Q\right)\cos\vartheta_g$$

$$\omega_{gz_2}=\left(P\cos\psi_g+R\sin\psi_g\right)\cos\vartheta_g-\left(\frac{d\psi_g}{dt}+Q\right)\sin\vartheta_g$$

J_{go}, J_{gk} – moments of inertia of gyroscope rotor in relation to its longitudinal axis and precession axis, correspondingly,

M_k, M_{rk} – moments of forces which drive the rotor of the gyroscope and of friction in the bearing of the rotor in the frame, correspondingly,

M_b, M_c – control moments acting on a gyroscope,

ϑ_g, ψ_g – angles of rotation of internal and external frames of gyroscope, correspondingly; with regard to the state of target tracking, the values of angles determine the position of the gyroscope axis: $\vartheta_g = \varepsilon_w$, $\psi_g = \theta_w$ [3].

With regard to the program movement of the axis of the gyroscope moves along the Archimedes spiral [4] (scanning the surface of the seabed), angles are determined on the basis of the following dependences:

$$\begin{aligned} \vartheta_{gz}(\tau) &= a_g \frac{\nu_s}{\Omega} \tau \sin\left(\frac{\nu_s}{\Omega}\tau\right) \\ \psi_{gz}(\tau) &= b_g \nu_s \tau \cos\left(\frac{\nu_s}{\Omega}\tau\right) \end{aligned} \tag{9}$$

where: a_g, b_g, ν_s – predetermined parameters of Archimedes spiral.

Fig. 3 shows the diagram of gyroscope and unmanned aerial vehicle control, whilst.

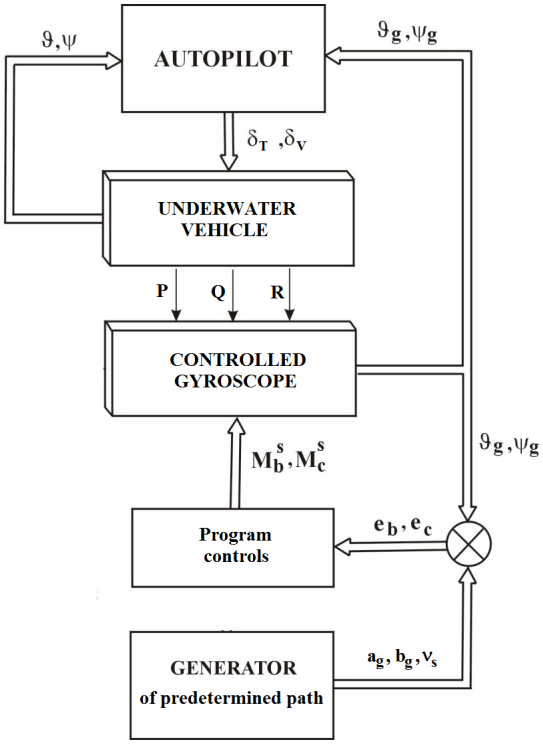

Fig. 2 Diagram of gyroscope control on the deck of underwater vehicle

Underwater vehicle, as it moves along predetermined flight path, is controlled by autopilot (Fig. 2), which develops δ_H i δ_V control signals (tail fin and tail plane) for the purposes of the actuation system of the control, on the basis of signals derived from terminally guided warhead.

Therefore the control law of autopilot, taking into account the dynamics of rudders tilt, will be described as follows:

$$T_1^H \frac{d\delta_H}{dt} + T_2^H \delta_H = K_1^H \left(\frac{d\vartheta_g}{dt} - \frac{d\vartheta_{gz}}{dt} \right) + K_2^H \left(\vartheta_g - \vartheta_{gz} \right) \tag{10}$$

$$T_1^V \frac{d\delta_V}{dt} + T_2^V \delta_V = K_1^V \left(\frac{d\psi_g}{dt} - \frac{d\psi_{gz}}{dt} \right) + K_2^V \left(\psi_g - \psi_{gz} \right) \tag{11}$$

where: T_i^j – time constants, K_i^j – amplification coefficients.

4 Conclusions

Presented mathematical method of the gyroscope control installed on the deck of a underwater vehicle allows one to carry out simulation tests of the processes of detecting, locating and tracking, with the use of a echolocation.

Theoretical considerations have shown that the high efficiency of the SDTIO is ensured by the use of selected optimal coefficients of the controller of a gyroscope system.

By adopting the proposed system, the operator's intervention in the control of a underwater vehicle may be limited only to cases when the object-lens of apparatus swerve from the predetermined path or in the event when the object-lens of the tracking system lose sight of the target.

In further studies, both theoretical and computational as well as simulation and experimental, one shall: a) determine the optimal navigation program of a underwater vehicle or b) develop such an algorithm of seabed surface scanning which would ensure the fastest target detection.

References

[1] Seong, A., Ruzzene, M., Scorcelletti, F., Bottasso, C.L.: Configuration Optimization of Supercavitating Underwater Vehicles With Maneuvering Constraints. IEEE Journal of Oceanic Engineering 35(3) (2010)

[2] Garus, J., Małecki, J.: Simulation of Plane Motion of Semiautonomous Underwater Vehicle. In: Proceedings of the European Computing Conference, pp. 126–131 (2011)

[3] Ładyżyńska-Kozdraś, E.: Application of the Maggi equations to mathematical modeling of a robotic underwater vehicle as an object with superimposed non-holonomic constraints treated as control laws. In: Solid State Phenomena, Mechatronics Systems, Mechanics and Materials, vol. 180, pp. 152–159 (2012)

[4] Ładyżyńska-Kozdraś, E., Koruba, Z.: Model of the final section of navigation of a self-guided missile steered by gyroscope. Journal of Theoretical and Applied Mechanics 50, 2 (2012)

Robotic Implementation of the Adaptive Cruise Control-Comparison of Three Control Methods

P. Shakouri, A. Ordys, and G. Collier

Faculty of Science, Engineering and Computing, Kingston University London, UK, Roehampton Vale, Friars Avenue, SW15 3DW
P.Shakouri@kingston.ac.uk

Abstract. This paper explores the practical implementation of the Adaptive Cruise Control (ACC) system on a real-time single board computer based robotic vehicle (National Instruments Robotics Starter Kit). The ACC algorithm based on three control methodologies, the fuzzy PID control, model predictive control (MPC) and conventional PID control, is deployed on a field programmable gate array (FPGA), included in the robot's architecture. The results are compared both in the simulation and using the real robot. The comparison of the performance demonstrates a good correlation between theory and real implementation, whilst highlighting problems introduced by a real system.

1 Introduction

Adaptive cruise control (ACC) system, cruise control (CC) system and emergency stop are the more common longitudinal applications, which have been studied in the field of the robotics and intelligent transportation system (ITS) [1]. The ACC system is an extension of the cruise control system, which not only controls the velocity of the vehicle but also is it capable of controlling the distance between the leader and follower vehicles to retain a safe distance. A comprehensive study on the ACC was carried out by [2]. Several model-based control approaches and architectures have been suggested and developed for designing ACC systems from the classical to the nonlinear advanced control methods, such as PID control and linear quadratic control (LQC) taking the gain scheduling approach [3-4], model predictive control (MPC) and nonlinear MPC (NMPC) [5-6], and the sliding mode controller [7] among others.

The practical implementation of the ACC system using the three control methodologies, MPC, fuzzy PID, and conventional PID control, in the application to the real-time single board computer based robotic vehicle is presented in this paper. Furthermore, the results of those controllers are compared both in the simulation and using the real robot. The paper is organized as follows: Section 2 describes the hardware and the associated system transfer function. Section 3 describes the ACC

T. Březina and R. Jabloński (eds.), *Mechatronics 2013*,
DOI: 10.1007/978-3-319-02294-9_80,

architecture, utilizing three different control methods. Section 4 presents the results of experiments and simulations. Finally, conclusions are drawn in Section 5.

2 Hardware Characteristic and System Transfer Function

This application uses two NI LabVIEW starter kit robots. The robots can be programmed either by using the high-level LabVIEW function, or by using the LabVIEW FPGA module [18]. The robot 'follower' is equipped with ultrasonic sensors for velocity and distance tracking of the 'leader'. The robot transfer function approximated through the model identification process can be presented as [8]:

$$\frac{v}{v_{sp}} = \frac{1}{0.48s^2 + s + 1} \tag{1}$$

where v and v_{sp} respectively denote the robot's velocity and velocity setpoint.

Table 1 Logical rule for switching between CC and ACC

	$v_f < v_{des}$	$v_f \geq v_{des}$
$d < d_{des}$	ACC	CC
$d \geq d_{des}$	CC	CC

3 Control Design

The system operates in two different modes - distance tracking (ACC) or velocity tracking (CC). The switching rules ([3], [5]) for transition between CC and ACC modes are illustrated in Table 1.. If the ultrasonic sensor of the follower detects a slower moving robot in front, the controller adjusts the velocity to maintain the clearance inter-distance (desired distance). If the inter-distance measured by the ultrasonic sensor is greater than the desired distance, it will switch to velocity tracking mode, known as cruise control (CC) mode.

The three control methods are investigated in this paper, model predictive control (MPC), fuzzy PID control and conventional PID control. These are explained as follows.

3.1 Conventional PID Controller

This ACC system design is based on two controllers; PID control for velocity tracking and PI control for distance tracking. Switching logic decides which of the two controllers is used to generate the input to the "follower" robot.

3.2 Model Predictive Control

In order to design an ACC system utilizing a single MPC, it is necessary to model the behaviour of the robot in front and then build a model of the overall system, including the two robots. This model is developed by augmenting the robot dynamics model of the 'follower' (equipped with an ACC system) and the dynamics due to interaction between the two robots: speed and distance tracking. The state-space equation of the robot in discrete-time form can be obtained by converting from transfer function Eq. (1):

$$x(t+1) = A_{dis}\,x(t) + B_{dis}\,v_{sp}(t) \tag{2}$$

The states of this system (follower robot) are the acceleration and velocity, $x=[a_f \; v_f]^T$. The robot velocity is also the system output.

The state-space equation of the overall system also includes the velocity of the leader robot and the distance between the robots, i.e. $x_{int\text{-}veh}=[v_l \quad d]^T$, (subscript "augd" stands for the augmented equations in discrete-time form):

$$x_{augd} = \begin{bmatrix} a_f & v_f & v_l & d \end{bmatrix}^T \tag{3}$$

$$x_{augd}(t+1) = A_{augd}\,x_{augd}(t) + B_{augd}\,v_{sp}(t) \tag{4}$$

The outputs of the augmented system are $y=[v_f \quad d \quad v_r]^T$. Here, v_r denotes the relative velocity. This output vector y is decoupled into three separate outputs y_1, y_2 and y_3. For each, the state-space equations of the system can be extended by taking the integral action into consideration to obtain the incremental model as follows [5], [9]:

$$\begin{bmatrix} \Delta x_{augd}(t+1) \\ y_i(t+1) \end{bmatrix} = \begin{bmatrix} A_{augd} & o^T \\ C_{augd\,(i)}A_{augd} & 1 \end{bmatrix} \begin{bmatrix} \Delta x_{augd}(t) \\ y_i(t) \end{bmatrix} + \begin{bmatrix} B_{augd} \\ C_{augd\,(i)}B_{augd} \end{bmatrix} \Delta v_{sp}(t) \tag{5}$$

$$y(t) = \begin{bmatrix} o & 1 \end{bmatrix} \tilde{x}_i(t) \tag{6}$$

The subscript i=1, 2, 3 indicates the sequence of elements in output vector.

Consequently, the optimal control vector $\Delta V_{sp,}$ can be obtained:

$$\Delta V_{sp} = \left(\sum_{i=1}^{q} \left[\phi_i^T \breve{R}_{yi} \phi_i \right] + \breve{R}_u \right)^{-1} \left(\sum_{i=1}^{q} \left[\breve{R}_{yi} \phi_i^T \left(R_{si} - F_i \tilde{x}_i(t) \right) \right] \right) \tag{7}$$

where q is the number of the outputs and it equals 3 for our system. Three $F_{i=1,2,3}$ and $\varphi_{i=1,2,3}$ need to be calculated to design the MPC. F and φ are general matrices in predictive control and they can be found in literature [5], [9].

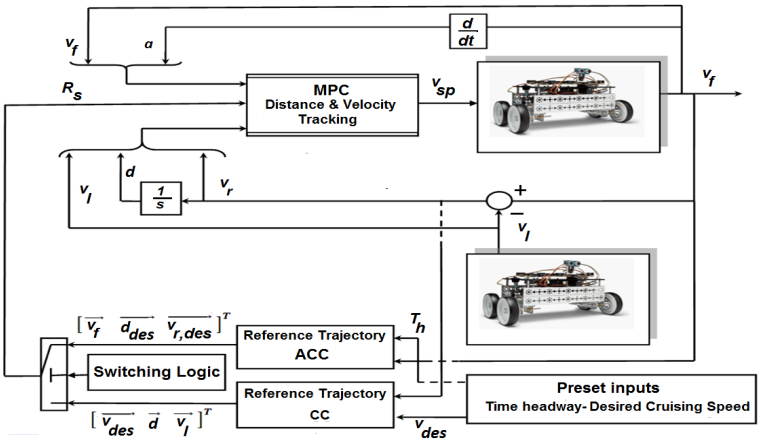

Fig. 1 Schematic diagram of the ACC system utilizing a single MPC

The schematic block diagram of the MPC is illustrated in Fig. 1. Notice that the reference trajectory (R_{s1}, R_{s2} and R_{s3}) is different depending upon whether the system operates in ACC mode or CC mode.

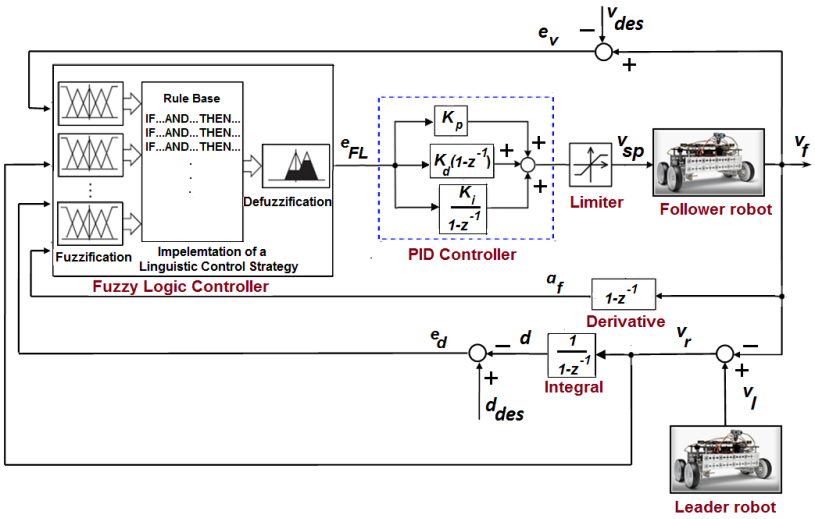

Fig. 2 Schematic diagram of the ACC system based on fuzzy PID Controller

3.3 Fuzzy PID Controller

The schematic diagram of the ACC using fuzzy PID controller is depicted in Fig. 2. The fuzzy rules calculate the consequent error value (e_{FL}) by evaluating overall dynamics of the system including the difference between the measured and reference values, i.e. the desired distance and desired cruising velocity, the velocity difference between leader and follower vehicles, and the acceleration. The fuzzy PID controller does not have a special operating point. The advantage of the fuzzy logic PID controller over the conventional PID controller is that it can implement nonlinear control strategies by using linguistic rules. The rules and membership functions for designing this fuzzy logic controller can be found in [10].

3.4 Unmeasured Parameters Estimation

The required parameters for operation of the ACC system are distance (d), follower robot velocity (v_f), acceleration (a_f) and relative velocity (v_r). The acceleration and relative velocity are unmeasured parameters and need to be estimated in the control algorithm. A discrete-time Kalman filter, which is based on the linear minimum variance (LMV) estimation of discrete-time system, is utilised to estimate the unmeasured parameters (states) of the system [11-12].

4 Simulation Results

The ACC system was first designed and tested with simulations and then deployed to the robot's LabVIEW FPGA module, for comparison purposes. Fig. 3 illustrates the results for distance tracking control (ACC) for the tests executed by using the conventional PID controller. The initial distance between the robots was set at 0.1 m. Both robots started from zero velocity and time-constant headway T_h was chosen experimentally to be 1.3 [s]. The ACC system calculates the robot velocity (Fig. 3.c) such that the distance between the follower and leader robots is retained within the desired distance (Fig.3.a-b). Since, the desired distance is a function of the velocity of the follower robot; its variation depends on the velocity. The root mean square error (RMSE) of the distance can be used as an index to assess the performance of the ACC system.

Fig. 4 and Fig. 5 show the results of the ACC operation using the MPC and fuzzy PID controller, respectively.

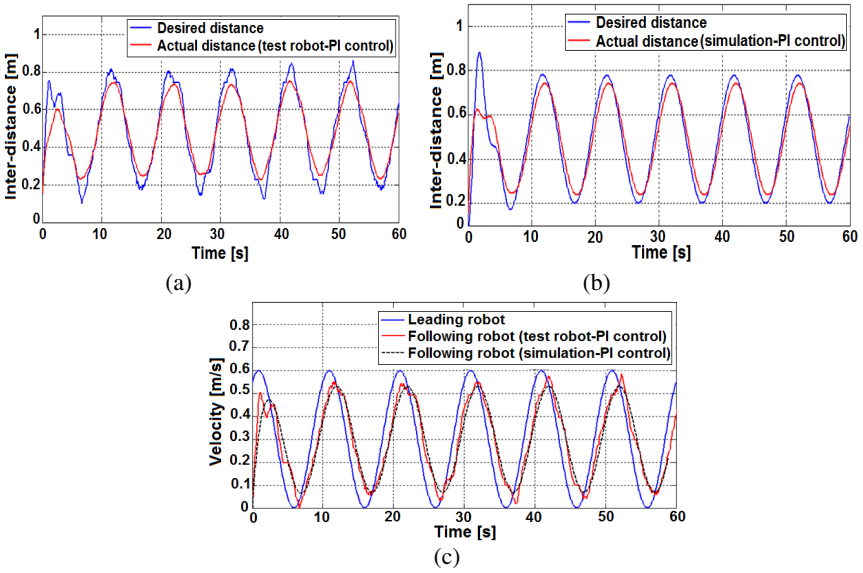

Fig. 3 Distance tracking (ACC) using PI/PID controllers: (a) inter-distance between the robots using test robot, (b) inter-distance between the robots obtained from simulation, and (c) velocities obtained during distance tracking

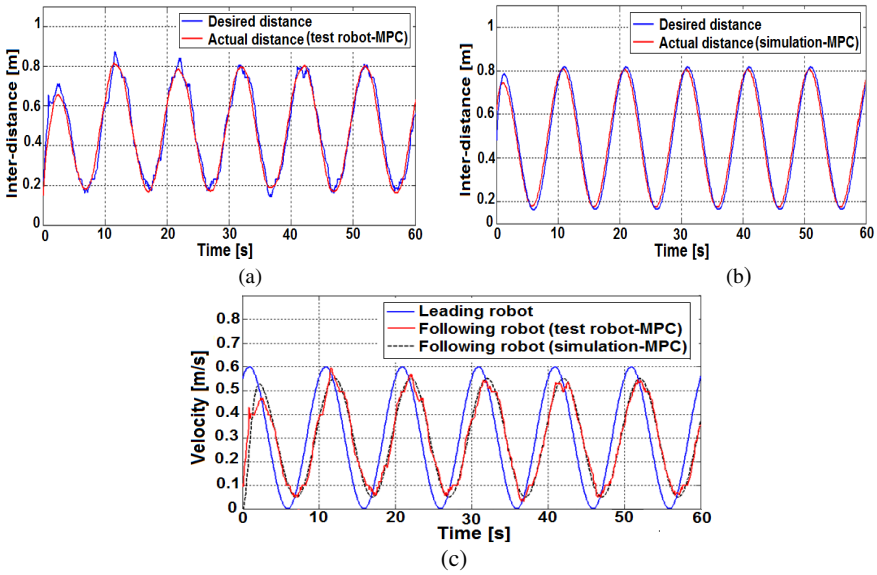

Fig. 4 Distance tracking (ACC) using MPC: (a) inter-distance between the robots using test robot, (b) inter-distance between the robots obtained from simulation, and (c) velocities obtained during distance tracking

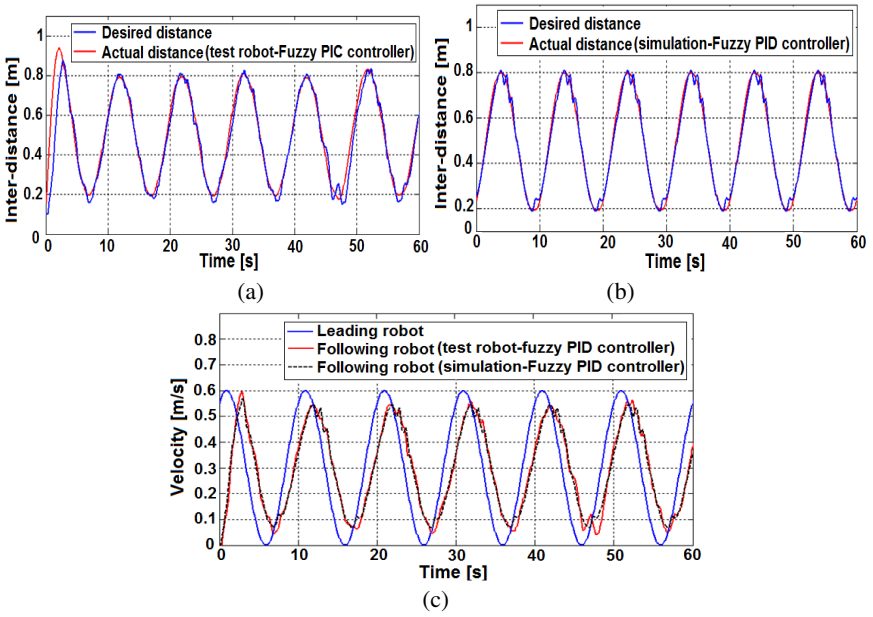

Fig. 5 Distance tracking (ACC) using Fuzzy PID controller: (a) inter-distance between the robots using test robot, (b) inter-distance between the robots obtained from simulation, and (c) velocities obtained during distance tracking

Table 2 The values of the RMSE for the distance tracking

	Simulation	Test robot
PI controller	0.0602 [m]	0.0659 [m]
MPC	0.0372 [m]	0.0391 [m]
Fuzzy PID controller	0.0211 [m]	0.0366 [m]

The values of the RSME for the distance tracking resulted from three control methodologies, both through the simulation and test robot, are given in Table. 2. The comparison between those values obtained from the real test demonstrates that fuzzy logic controller has resulted in the less distance tracking error as much as % 44 and % 6.4 compared to the conventional PID controller and MPC, respectively. While, MPC has improved the performance as much as % 41 compared to the conventional PID controller. However, the MPC proposed in this paper eliminates the need for using two separate controllers for performing the distance tracking and velocity tracking controls, which can result in more robust control performance, and it is also easier to be tuned.

5 Conclusions

Three different control methodologies for the ACC system, MPC, fuzzy PID and conventional PID controllers are proposed, designed, implemented and deployed in a real-time single board computer based robotic vehicle (National Instruments Robotics Starter Kit). A Kalman filter is also utilized for the estimation of the unmeasured parameters. Simulation and real implementation of the ACC system are compared showing a good correlation. Summarizing, for the ACC operation, both MPC and fuzzy PID controller outperform the conventional PID controller, resulting in the lower distance tracking errors. Future work may deal with the experimental test of the ACC system using the most realistic conditions, which the throttle and brake operations can be investigated. It subsequently may lead to the more advanced control solutions, e.g. nonlinear controller.

References

[1] Gerdes, J.C., Hedrick, J.K.: Vehicle Speed And Spacing Control Via Coordinated Throttle And Brake Actuation (Control Eng. Practice) 5, 1607–1614 (1997)
[2] Xiao, L., Gao, F.: A comprehensive review of the development of adaptive cruise control system. Vehicle System Dynamics 48(10), 1167–1192 (2010)
[3] Shakouri, P., Ordys, A., Laila, D.S., Askari, M.R.: Adaptive Cruise Control System: Comparing Gain-Scheduling PI and LQ Controllers. In: 18th IFAC World Congress, Milano (2011)
[4] Riis, P.: Adaptive Cruise Controller Simulation as an Embedded Distributed System. MSc thesis, Linkoping Univ. (2007)
[5] Shakouri, P., Ordys, A., Askari, M.R.: Adaptive Cruise Control with Stop & Go Function Using the State-Dependent Nonlinear Model Predictive Control Approach. ISA Transaction 51(5), 622–631 (2012)
[6] Corona, D., Lazar, M., De Schutter, B., Heemels, M.: A hybrid MPC approach to the design of a Smart adaptive cruise controller. In: Proc. of the 2006 IEEE International Conference on Control Applications, Munich, Germany, pp. 231–236 (October 2006)
[7] Zhou, J., Peng, H.: Range Policy of Adaptive Cruise Control for Improved Flow Stability and String Stability. In: Proc. of the 2004 IEEE, International Conference on Networking, Sensing & Control, Taipei, Taiwan, March 21-23 (2004)
[8] Shakouri, P., Collier, G., Ordys, A.: Teaching Control Using NI Starter Kit Robot. In: 2012 UKACC International Conference on Control, Cardiff, UK, September 3-5 (2012)
[9] Wang, L.: Model Predictive Control System Design and Implementation Using Matlab, 2nd edn. Springer (2009)
[10] Shakouri, P., Duran, O., Ordy, A., Gordana, C.: Teaching Fuzzy Logic Control Based on a Robotic Implementation. In: IFAC ACE 2013, August 28-30, Sheffield University, UK (2013)
[11] Ogata, K.: Discrete-Time Control Systems, 2nd edn. Prentice-Hall (1995)
[12] Powell, D.: Disceret Time Observers and LQG Control. Lecture note, Department of Mechanical Engineering. Massachusetts Institute of Technology (2004)

Self-learning Control for Servo Drives in Forming Technologies

M. Hoffmann[1], P. Hušek[2], H.-J. Koriath[1], V. Kučera[2], and U. Priber[1]

[1] Fraunhofer Institute for Machine Tools and Forming Technologies IWU, Reichenhainer Str. 88, 09126, Chemnitz, Germany
{michael.hoffmann,hans-joachim.koriath, Ulrich.priber}@iwu.fraunhofer.de
[2] Faculty of Electrical Engineering, Czech Technical University Prague, Technická 2, 16627 Prague 6, Czech Republic
{kucera,husek}@fel.cvut.cz

Abstract. At present, wrinkles, fissures, folds, scratches, etc. are checked visually. This may result in doubtful quality of final product, unnecessary waste, etc. This paper describes a comprehensive approach to increase the quality and efficiency of the metal forming processes by introducing a self-learning process control solution. Energy control, intelligent dies (with multiple of sensors), open architecture motion control systems, adaptronic force oscillation, are included.

1 Electromechanical and Hydraulic Servo Drive Functionalities in Press Applications

Forming is a manufacturing process for changing the geometry of a solid work piece by plastic deformation and may be divided into Pressure Forming, Tension Compression Forming, Tension Forming, Bending and Shear Forming [1].

Typical machine tools are rolling machines, tension machines, hammers, presses, knife cutting machines [2]. On the principle of energy supply press types are divided into stroke-based (linked ram and drive position), force-based (ram motion stops when ram force equal process force), energy-based (ram motion stops when drive energy is zero) and hybrid presses [3].

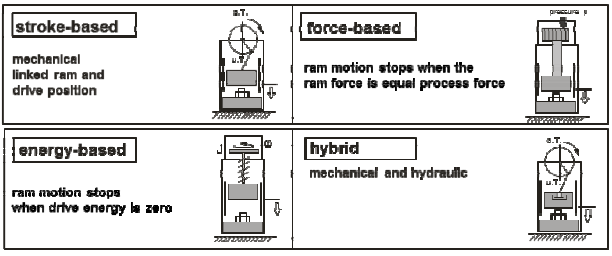

Fig. 1 Press types on the principle of force or energy supply [3]

T. Březina and R. Jabloński (eds.), *Mechatronics 2013*,
DOI: 10.1007/978-3-319-02294-9_81, © Springer International Publishing Switzerland 2014

Deep drawing is a compression-tension metal forming process in which a sheet metal blank is radially drawn into a forming die by the mechanical action of a punch. It is thus a shape transformation process with material retention. The flange region (sheet metal in the die shoulder area) experiences a radial tensile stress and a tangential compressive stress due to the material retention property. These compressive stresses (hoop stresses) often lead to flange wrinkles (wrinkles of the first order).

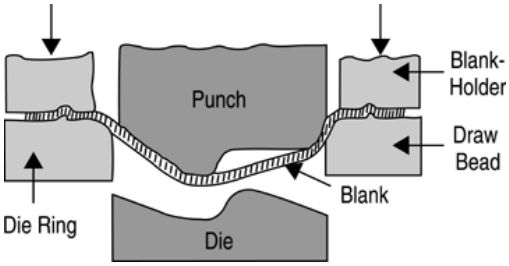

Fig. 2 A schematic section of a typical stamping die [4]

Wrinkling is not a desired result in sheet metal forming, especially when it occurs on outer skin panels where the final part appearance is a significant quality criterion. Large wrinkles can also damage the dies, reduce the functionality of the component or disrupt the subsequent assembling process. The prediction and even more the prevention of wrinkling are therefore of vital interest in sheet metal operations. The geometry and surface formed from blank sheet metal demand a very high quality of the die and process conditions in order to form the material without wrinkles, fissures, folds or scratches. Usually the work piece quality check is performed by the machine operator and is only in rare occasions robot-handled by automatic cameras.

Beside the tooling and the process parameters, the quality of the material is a decisive factor for the result of the forming process. Mild steel grades for cold forming, according to DIN EN 10130, have standard tolerances of 25% strength, 15% thickness and 20% surface in coils of steel between different suppliers. Drive functionalities in press applications are divided into main and supporting drives.

In the field of forming, for example the manufacturing of car body components, the stroke rate is often used as a criterion to describe velocity. The specification of the strain rate or of the strain velocity offers the opportunity to characterize, classify and compare these various forming processes with regard to velocity. From an economic point of view it is important to increase the stroke rate. However, if technological aspects, especially tool and machine limitations, are taken into account, the stroke rate cannot be increased indefinitely even using the most modern servo press technology [5].

The main drive moves the forming tool and provides the forming energy on the work piece. Stroke rate is defined as the velocity of the ram and measures the number of parts per minute. Examples for supporting drives in sheet metal presses are die cushion drives or ram/table inclination correcting drives, responsible for the sheet metal clamping and a constant gap between the forming tool and work piece. Electromechanical and hydraulic servo drives describe the state of the art.

1.1 Electromechanical Servo Drive Functionalities

Electromechanical servo press types are servo spindle press and servo press with a crank gear or linkage gear.

A new Fraunhofer IWU servo press uses two crank gears and torque motors controlled by Simotion controller for flexible drive structures and stroke-based or force-based forming characteristics with a stroke rate of 100 per minute.

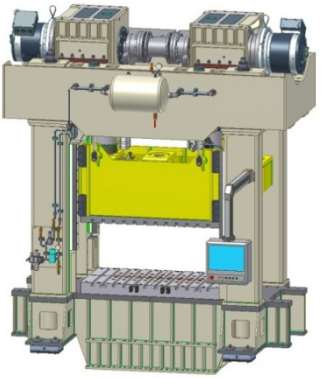

Fig. 3 Electromechanical servo press with two torque motors, planetary gears

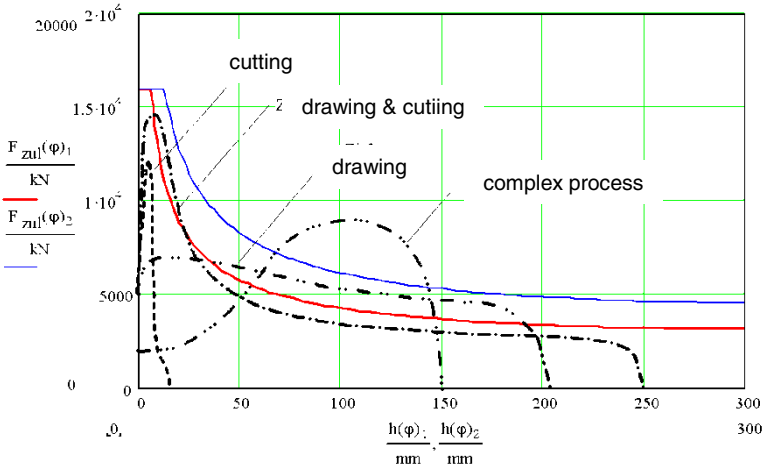

Fig. 4 Programmable force-stroke characteristic

The advantages of an electromechanical servo press are higher productivity, programmable velocity profile for several forming technologies, and motion stop during the forming process.

1.2 *Hydraulic Servo Drive Functionalities*

Hydraulic presses are force-based typically with a stroke rate of 15 per minute.

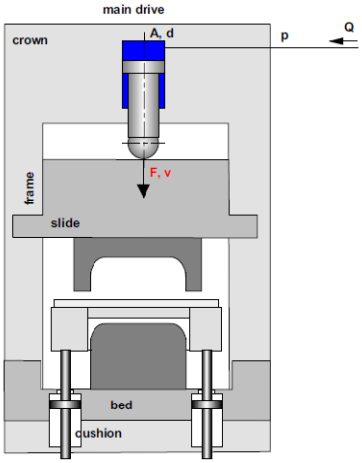

Fig. 5 Hydraulic press with cushion cylinders

The force depends on surface of the hydraulic cylinder A and the pressure p.

$$F = p * A; \tag{1}$$

The velocity of the slide is limited by the maximum of the volumetric flow Q.

$$v = Q * A; \tag{2}$$

The maximal drive force F_{max} is provided over the full stroke, but the technological force for metal forming is increasing for the bottom die position.

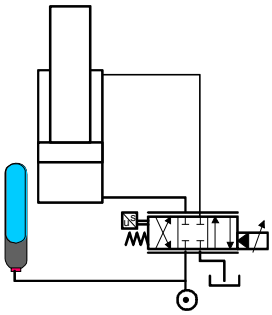

Fig. 6 Hydraulic servo drive velocity controlled by valve and pressure

In chapter 2 a new self-learning process control solution is introduced in order to increase the quality and efficiency of the metal forming processes.

2 Self-learning Control Structures for Sheet Metal Forming

The goal of the forming process is to produce good parts without wrinkling that is caused by compressive circumferential stresses and tearing that result from excessive tensile stresses.

From the control point of view this goal is reached whenever the trajectory of the process stays inside the formability window (Fig. 7) that expresses the dependence of clamping force and the depth of punch stroke [6]. The formability window is a result of the forming-limit diagram (FLD) that describes the formability limits in terms of the principal strains [7]. Unfortunately, mathematical description of the limits of the formability window is too complex depending on a huge number of parameters, many of them time-varying, that makes the task difficult. On the other hand, if suitably chosen and set, some of those parameters can be used to extend the formability window and thus make the forming process more robust.

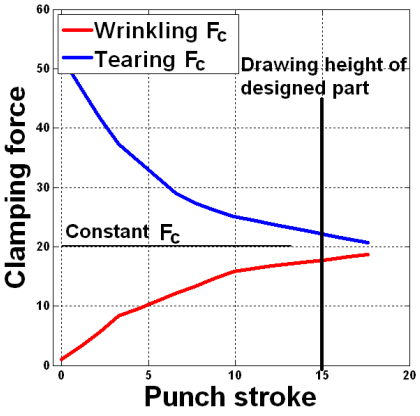

Fig. 7 Formability window

The aim of a self-learning control approach to the forming process consists in an automatic tuning of the process parameters that is applied after each stroke in such a way that the quality of the stamped part is permanently improved and achieves an acceptable level in few steps [8]. The whole tuning process is going on without any intervention of a human operator.

Using the theoretical background, experiments and new ideas the following three controlled variables were chosen: velocity of the ram, friction force, and clamping force. Based on the character of the forming process we suggest a

self-learning control strategy that uses a supervisor control scheme. The supervisory controller in the upper level will adjust the setpoints (generally time varying) of the lower level control loops. The setpoint adjustments are applied after each cycle (stroke) only whereas the low level control loops containing PID controllers operate continuously. The supervisory controller operates on data from the process (mainly sheet feed and the temperature of the sheet in different spots) as well as on linguistic information given by a human operator and adopts a fuzzy logic approach. Such a strategy is suitable especially when constant setpoints are used since, in such a case, only one parameter is tuned. For time-varying setpoints the profile is represented by some characteristic points that are subsequently tuned. Naturally, such considerations will immensely increase the number of rules for the supervisor controller and therefore will make the creation of the rule base more complicated.

The proposed strategy makes use of three independent low level control loops (Fig. 8). The first loop controls the punch velocity using the punch force hydraulic cylinder as manipulated variable. The supervisory controller sets the setpoint for punch velocity based on sheet feed information. The aim of the second loop is to control the friction force between the blank holder and the sheet by manipulating the frequency and the amplitude of the clamping force frequency oscillator. Since during the trials the correspondence between the parameters of the frequency oscillator and the quality of the stamped parts was not confirmed the frequency oscillators were not used for the final experiments. The last loop assures the control of clamping force. Since a 16 die cushion system is used, different clamping force setpoints are used for the blank holder segments placed in the corner area and the segments situated in the center of straight side area. Sheet feed information is used for accomplishing this task.

As it was mentioned earlier the supervisory controller will use IF-THEN rules that should integrate results of FEM analysis and human operator experience. The whole blank holder area was divided into four parts – left lower (LL), left upper (LU), right lower (RL) and right upper (RU). The clamping force setpoint is changed only in the part where a crack or wrinkle occurs, e.g.:

IF crack in LL THEN decrease F_{LL}
IF wrinkle in LU THEN increase F_{LU}

The value of how much the clamping force setpoint should be changed depends on the size of a crack or wrinkle. The whole rule base is then implemented by a fuzzy logic. The determination, localization, and size of tearing and wrinkling were successfully replaced by analyzing some characteristic features of sheet feed (such as the maximum sheet feed or the time instant when the maximum was reached).

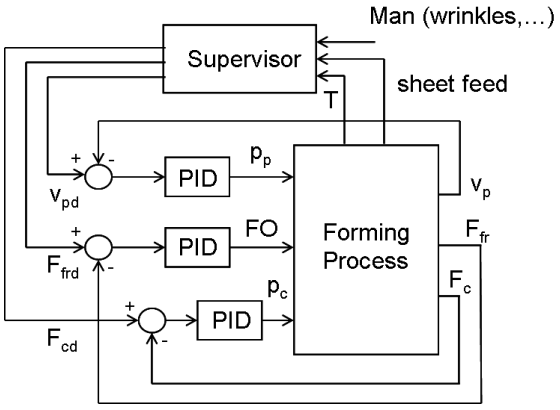

Fig. 8 Supervisor control strategy

3 Adaptive Concepts for Forming Control and Clamping Control

Deep drawing processes are highly complex in its forming aspect itself, where adaptive systems are in demand to reduce setup time, maintenance and increasing product quality by avoiding wrinkles and cracks in industrial serial production.

The primary objective is to develop, implement and verify a self-learning production system for deep drawing process that will substitute the present trial and error procedure to radically shorten the process setup times during the changing product variants and to replace a skilled operator by an automated system while preserving good quality of produced parts without cracks and wrinkles. Many determining factors influence the deep drawing process. We describe two aspects. In the components for forming control we consider the motion of the ram and his inclination. The other subsystem realizes the variable.

3.1 Adaptive Forming Control

Deep drawing processes especially identify with the fast transformation from an initial shape of the work piece to its desired finished shape. In spite of the short forming time, the process depends on a multiplicity of parameters.

Those are used to configure the process and those should ensure a high quality result of the work piece and process stability. Within forming control, deep-drawing velocity and other process variables are used to control the sheet feed, which was not able to simulate by a MATLAB model due to the high complexity of the process. The forming control supervisor strategy is built on different measurements.

In order to improve the process quality, the self-learning system can define the set-velocity by a five point ram velocity profile based to the position of the ram.

The variable ram velocity influences the clamping force control which is normally based on a constant ram velocity. The force profile definition was changed to a ram position based profile to avoid this influence.

The control concept is completed by a supervisory control that implements the self-learning algorithm. Forming control also requires sheet feed measurement, for which a sensor is exposed to rough environment conditions. It has to be robust and insensible to resist shocks and vibrations but has to provide precise measured values with high resolution and sampling rate during the deep-drawing process, which was finally running with a laser triangulation sensor tracing the sheet edge through the gap between the upper and lower tool.

The results of deep drawing tryouts results in a classification showing the dependencies between the process parameters clamping force, drawing velocity, temperature etc. and its corresponding results in deep drawing quality. Basing on this information, a supervisory control basing on fuzzy logic has been implemented into the PLC, tracing, recording and evaluating measured data with adaptive feedback to the set values of the PLC cycle by cycle. Once identified all critical values to feed the fuzzy rules, the system reacts on changing process conditions (e.g. lubrication) increasing or decreasing the set clamping force straight to a valid process window.

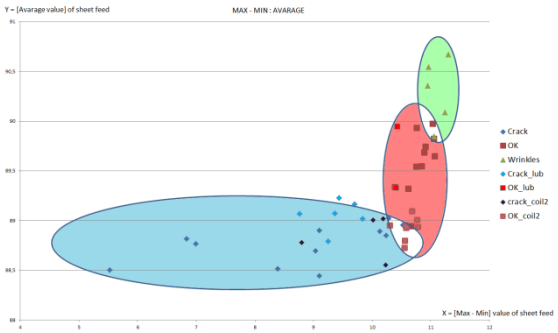

Fig. 9 Quality classification of deep drawing cycles relating on measurement data

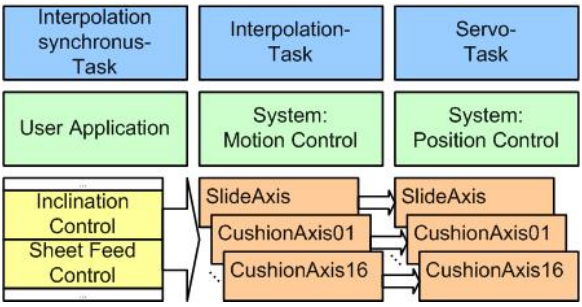

Fig. 10 Forming Control (Sheet Feed & Inclination) PLC implementation as ready to apply programs

Within the appearance of asymmetric forces, keeping good forming quality means the tool planes have to be kept parallel. Therefore a new special design of an integrated inclination control will ensure the parallelism, where four of 16 sixteen die cushion axes are used to affect compensating forces to the ram directly.

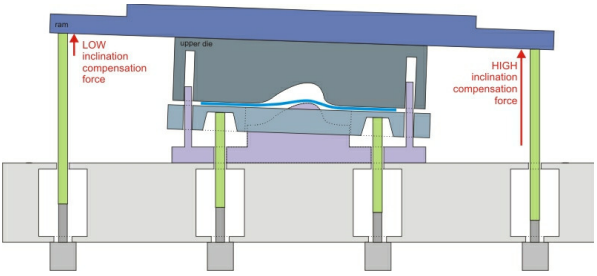

Fig. 11 Using hydraulic multiple die cushion within the blank holder clamping and the ram inclination compensation

3.2 Adaptive Clamping Control

From the knowledge of operators and engineers, the force behaviour of a close loop controlled die cushion system can be described by a set of relevant criteria.

Considering these values to be within their limits, one needs to set relating hydraulic PID controller settings. In the first instance, the modeling of the clamping control has been realized for one hydraulic axis. Therefore, the following points have been implicated for consideration of the deep drawing simulation:

- motion sequence of the ram
- process of hydraulic system
- open and closed loop control systems
- evaluation of achieved procedure (criteria calculation)

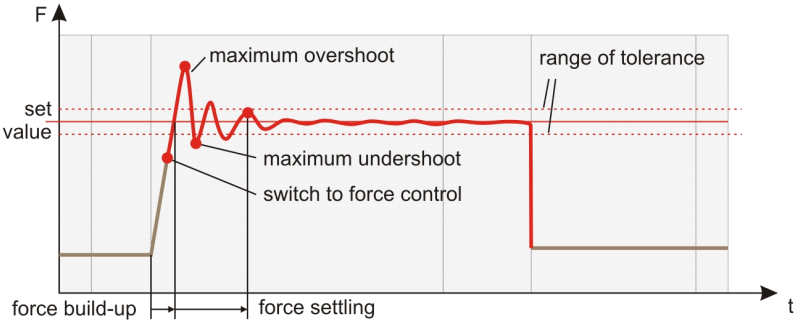

Fig. 12 Clamping force behavior with criteria to not exceed their margins

All used parameters, of which the most are not of relevance for this study, can be set or changed before a simulation cycle. After one simulation cycle, the characteristics of the process values and their derived criteria are available for evaluation in the MATLAB environment. In this way, the mode of operation of the parameters, which are of relevance for the clamping process, can be determined without experimental effort and can be clarified simulative over a wide area.

With the help of the simulation model, it was able to study the dependencies (influences) between the parameters and the criteria. Thereby some assumptions were made for the non-varying parameters, what leads to the dynamical and controlled behaviour of the demonstrator press PYZ250. By a combination of those parameters, a large number of solutions have been provided within a four dimensional domain of definition. The dependencies between the parameters and the criteria could be visualised with the help of the display format of multidimensional characteristic diagrams, resulting in a clearly-arranged consolidated result.

The idea of the clamping control system has been validated by IWU to work correctly with one axis optimising the force behaviour within its criteria. The utilisation of this system for a coupled multi axis die cushion system could not be validated due to unsteady behaviour and requires further studies on interrelating control systems.

4 Condition Monitoring Systems

4.1 Condition Monitoring for Quality

At the level of energy control, thermal sensors measure and map the work piece and die temperatures before and after the deep drawing process.

Contact measurement technologies (i.e. thermocouples) allow obtaining the temperature of the forming tool while non-contact technologies (i.e. pyrometers and IR camera) allow sheet temperature reading. Embedding of an IR camera into the forming tool is not feasible due to the dimensions of such devices. Therefore, only pre and post operation readings are possible. Non-contact technologies do not provide absolute temperature readings unless accurate material emissivity values are available.

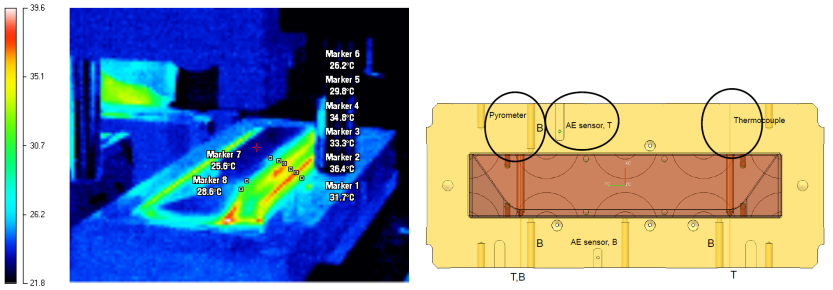

Fig. 13 Thermal picture of a drawn sheet metal work piece and thermal sensors integrated into the die

A reliable quality control has been foreseen and derived from energy maps of free-formed work pieces with pseudo-surface reflections and lubrication coatings.

Assuming that energy maps show the work piece energy

$$Wwp = Wfrict + Wform + Wclamp. \tag{3}$$

$$Wwp = f(\mu r;\ \varepsilon;\ FN;\ thickness;\ \Delta\sigma;\ die\ form;\ temperature;\ \ldots);$$
$$italic = environment \tag{4}$$

The three independent self-learning control levels of friction, forming, clamping control are subordinated to energy control and adopt their different, optimal controller parameters in changing environment conditions, changing product variants, and system training by the operator as well as by the system-inherent information. Intelligent dies and force actuators include new sensors for the measurements of process parameters such as the die gap, feed rate of the sheet, friction coefficient or clamping forces. The forming energy W_{form} depends on inner material friction caused by the deep drawing process ($\varepsilon = \sigma_{(strain)} / E_{(elastic\ modulus)}$; ε symbolizes the sheet elongation) and surface friction in the die gap, which is defined as the distance between the punch and the die and differs in the case of a die cushion inclination. The tolerance of the sheet metal thickness, strength (σ, the die form and sheet metal temperature are important environmental conditions f_{ENV} for the closed-loop control of the non-linear forming process control. The forming control level and energy control level has been realized through an indirect self-learning system in two stages: on-line estimation of the plant parameters and on-line computation of the controller parameters based on the current estimated plant model.

A Multilayer Perceptrom (MLP) Neural Network is used for a classification problem of five categories and also for classification of two categories (open-crack and No-crack).

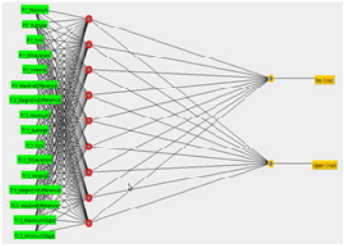

Fig. 14 Multilayer Perceptrom (MLP) Neural Network

A classifier helps us in the process of the quality of the produced part classification and its deviation for the process parameter quantification. The classification technique has been used for thermal sensors; thermocouple and pyrometers.

5 Conclusions

Mechatronics functionalities in press applications relate to electromechanical or hydraulic servo drives in combination with intelligent tools.This paper presents a comprehensive approach to increase the quality and efficiency of the metal forming processes by introducing a self-learning process control solution. The three independent self-learning control levels of friction, forming, clamping control are subordinated to energy control and adopt their different, optimal controller parameters in changing environment conditions, changing product variants, and system training by the operator as well as by the system-inherent information. The aim of a self-learning control approach to the forming process consists in an automatic tuning of the process parameters that is applied after each stroke in such a way that the quality of the stamped part is permanently improved and achieves an acceptable level in few steps.

The individual control units can be used as a stand-alone solution or in combination. The amount of the try and error tests has been successfully reduced to three. This paper summarized the results of the project LearnForm performed with the financial support from European Commission FP7.

References

[1] DIN 8582 Fertigungsverfahren Umformen DIN 8582 - Einordnung, Unterteilung, Alphabetische Übersicht, Berlin; Köln: Beuth, 6 S (2003)
[2] DIN 69651 Werkzeugmaschinen; Klassifizierung der Werkzeugmaschinen für Metallbearbeitung, Nummernschema, Kennzahlenschlüssel für Maschinengattungen. Beuth Verlag (1974)
[3] Hirsch, A.: Werkzeugmaschinen. Vieweg & Sohn Verlagsgesellschaft mbH, Braunschweig / Wiesbaden (2000)
[4] Hosford, W.F., Duncan, J.L.: Sheet Metal Forming: A Review. JOM 51(11), 39–44 (1999)
[5] Neugebauer, R., et al.: Velocity effects in metal forming and machining processes. CIRP Annals - Manufacturing Technology 60, 627–650 (2011)
[6] Doege, E., Elend, L.-E.: Design and Application of Pliable Blank Holder Systems for the Optimization of Process Conditions Sheet Metal Forming. J. of Materials Processing Tech. 111, 182–187 (2001)
[7] Obermeyer, E.J., Majlessi, S.A.: A Review of Recent Advances in the Application of Blank-Holder Force towards Improving the Forming Limits of Sheet Metal Parts. J. of Materials Processing Tech. 75, 222–234 (1997)
[8] Jang, J.-S.R.: Self-learning fuzzy controllers based on temporal back propagation. IEEE Transactions on Neural Networks 3(5), 714–723 (1992)

Automatic System for Object Recognition in Robotic Production Line for Automotive Industry

P. Božek and P. Pokorný

Slovak University of Technology, Faculty of Materials Science and Technology, Trnava, Slovakia
{pavol.bozek,peter.pokorny}@stuba.sk

Abstract. Production logistics is part of each sector. At present the automotive industry resonates in Slovakia at the first place. It is therefore necessary to deal with the quality, type, or shape deformation of each distributed piece of bodywork at the end of the production line. We compare the pair of car bodies where one is the etalon and the other is tested and compared with a reference standard model in order to detect errors or body classified to the appropriate category.

1 Introduction

Car production starts at a mill where the steel plates are cutted out to body parts. This is followed by a fully automated welding shop, where robots weld the different body parts. All models are welded on the same line. At the end of the line is automatic control of dimensions. In line samples are welded chassis all models, robots are still "see" how the car looks like. Then every car body is still checked in detail and continues to paint shop. After painting the body continues to assembly hall where about 35 % of the work carried out by robots and other activities make installers: Replacing the interior and exterior parts, engine mounting, axle, exhaust system and other mechanical components. Finally, add wheels, seats and steering wheel [10].

During the production phase, it is necessary to monitor and control the production process and detect possible errors incurred, if necessary sort by different body models and distribute them according to the type where it is needed. For these purposes, it is appropriate to use automated system that can compare the model with just the right product manufactured products and detect any inaccuracies (eg. by welding the various parts of the body, where it is compared with sample pieces produced). Another possible application is an automated system for distribution into body assembly hall – breakdown by type of bodywork.

Experiments with a fully automated system of recognizing objects met with varying levels of success. But none of them reached such a high level of accuracy that can be run completely unattended.

T. Březina and R. Jabloński (eds.), *Mechatronics 2013*,
DOI: 10.1007/978-3-319-02294-9_82,

Automatic recognition of objects dedicated work of many authors. The authors of [8] present the results of the integration of the proposed system for automatic object recognition, based on the decomposition of objects. Describe the possibility of recognizing objects independently of their position, orientation and size. The authors [11] discuss the issues and technologies for automated compilation of object models and sensors to optically recognizing strategies for detecting and determining the position of the object. The authors [12] proposed the use of advanced computational intelligence and distributed processing to mimic the human brain's thinking in recognizing objects. If it is combined with a cognitive process of detection technologies, the system can combine traditional techniques with image processing computer intelligence to determine the identity of different objects.

The contribution describes the design of the verification methods for the correct classification of the car bodies using Fourier-Mellin transformation. Consequently, the images are compared using Fourier transformation and phase correlation.

For comparison, or to determine the degree of similarity or images we used the variety of metrics, for example phase correlation and the percentage comparison.

2 Mathematical Principle

Fourier-Mellin transformation allows comparison of images which are offset, rotated and have changed scale. This method takes advantage of the fact that the shift differences are annulated because amplitude spectrum of the image and its displaced copy are identical, only their phase spectrum is different. Subsequent log-polar transformation causes that the rotation and scale will appear outwardly as a shift, so that phase correlation can be used to determine the angle of rotation and scaling between a pair of images during their registration. Phase correlation is based on the fact that two similar images in cross-spectrum create continuous sharp extreme in the place of registration and the noise is distributed randomly in discontinuous extremes [5].

2.1 Registration of Images

It is the reference image $a(x)$ and the input image $b(x)$, which has to be the identical with the reference image. The registration function of geometric transformation is to be estimated from the similarity of the characteristics of these images.

Consider that the image of $b(x)$ is the displaced copy of image $a(x)$:

$$b(\mathbf{x}) = a(\mathbf{x} - \mathbf{x}_0), \tag{1}$$

their Fourier's transformation $A(u)$ and $B(u)$ have a relationship:

$$B(\mathbf{u}) = e^{-j2\pi(\mathbf{u}^t \mathbf{x}_0)} A(\mathbf{u}). \tag{2}$$

We can construct a correlation function [4]:

$$Q_p(\mathbf{u}) = \frac{A^*(\mathbf{u})}{|A(\mathbf{u})|} \cdot \frac{B(\mathbf{u})}{|B(\mathbf{u})|} = e^{j(\theta_b(\mathbf{u}) - \theta_a(\mathbf{u}))}, \quad (3)$$

where $\theta_a(u)$ and $\theta_b(u)$ are phases of $A(u)$ and $B(u)$.

In the absence of noise, this function can be expressed in the form:

$$Q_p(\mathbf{u}) = \mathrm{e}^{-j2\pi\left(\mathbf{u}^t \mathbf{x}_0\right)}. \quad (4)$$

Its inverse Fourier transform is Dirac δ-function centered in the [4]:

$$\mathbf{u} = \mathbf{m}_0 = [x_0, y_0]^t. \quad (5)$$

Registration is accomplished by detecting the occurrence of Dirac δ-function in the inverse transformation of function Qp(u). The coordinates of the maximum culmination of δ determine the image translation.

Modification of the above method – use of the Fourier-Mellin transformation – allows registration of shifted or rotated images and with different scaling.

Fourier-Mellin transformation combines aspects of the Fourier and Mellin transformation with the transformation into a log-polar coordinates of the image.

If the amplitude spectrums |F(a)|, |F(b)| are transformed to the log-polar coordinate system (the spectrum is converted to polar coordinates and the distance from the origin of the coordinate system to the logarithmic scale), by the above described method of the phase correlation we identify not only the rotation, but also change of the scale.

Fourier-Mellin transformation converts the rotation and zooming to easy shifts in the parametric space and allows the use of the techniques of the phase correlation. Phase correlation then can be used to determine the angle of rotation and scale between the pair of images.

Picture function $f(x,y)$ may be sampled as a function $f(\theta, e^r) = f(\theta, \rho)$, where r is the distance from the center of the image see "Fig. 1".

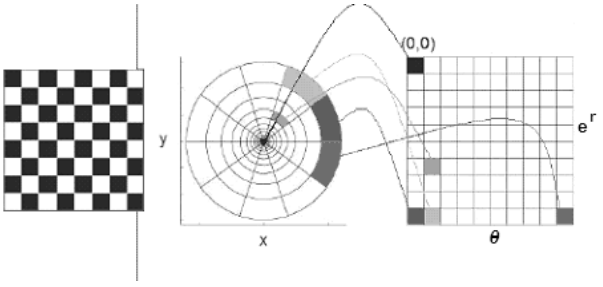

Fig. 1 Log-polar transformation [2]

Suppose that the centre of the image is the starting point for the transformation. Each pixel in the image can be represented as the distance r from the center of the image and the angle θ. If we rotate the image, only θ is changed, r remains the same.

If instead of a representation of the second pixel coordinate as the amount of r we use the exponential scale log r, we can convert the change of scale to translation.

If the image has been resized to scale according k, the Cartesian point $P(x, y)$ in the image will be in log-polar coordinates represented as P(θ, log (k . r)). Then the point P with the changed scale will be expressed as translation: P(θ, log k + log r) [6].

Used conversion from Cartesian to the log-polar coordinates:

a) Log-polar transformation of the amplitudes $|A(u,v)|$, $|B(u,v)|$ from Cartesian to the log-polar coordinate system

Fourier transformation is displayed in log-polar plane by the transformation of coordinates see: "Fig. 2".

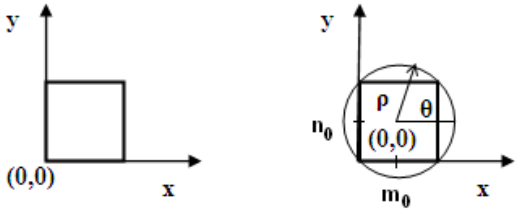

Fig. 2 Transformation of rectangular coordinates to polar by [1]

Origin (m_0, n_0) should be in the middle of the image matrix, to ensure the maximum number of pixels. If the image is formed by a square grid of $N \times N$ points, the coordinates of the center will be:

$$\begin{aligned} m_0 &= N/2; n_0 = N/2 && \text{if } N \text{ is odd}, \\ m_0 &= (N-1)/2; n_0 = (N-1)/2 && \text{if } N \text{ is even}. \end{aligned} \tag{6}$$

Maximum sampling radius for conversion will be:

$$\begin{aligned} \rho_{\max} &= \min(m_0, n_0) \ldots \text{inscribed circle}, \\ \rho_{\max} &= \text{sqrt}(m_0^2, n_0^2) \ldots \text{described circle}. \end{aligned} \tag{7}$$

If the inscribed circle is selected as the limit for conversion, some pixels, which lie outside of the circle will be ignored. If it described circle is selected, all the pixels will be included, but also defective pixels will be included (pixels inside the circle, but outside of the picture matrix). Whereas the pixels in Cartesian coordinates cannot be mapped one to one to the log-polar coordinates, the average of surrounding pixels (nearest neighbor, bilinear or bicubic downsampling) must be calculated.

Relationship between polar coordinates (ρ, θ), which is sampling the input image to the log-polar image (e^r, θ) is given by:

$$(\rho,\theta) = (e^r,\theta)\ . \tag{8}$$

For pixel mapping from the input image (x_i, y_i) to pixels of the output image (ρ_m, θ_n) applies [1]:

$$\begin{aligned} x_i &= round\left(\rho_m * \cos(\theta_n) + m_0\right), \\ y_j &= round\left(\rho_m * \sin(\theta_n) + n_0\right), \end{aligned} \tag{9}$$

where $(\rho_m,\theta_n) = (e^{rm},\theta_n)$ by (8). The input image is of dimension $i \times j$ and the output image is of $m \times n$ dimension.

b) Fourier transformation of log-polar amplitudes

$$\begin{aligned} \mathbf{A}_{lp}(\upsilon,\varpi) &= \mathcal{F}\left\{\left|A_{lp}(e^r,\theta)\right|\right\} \\ \mathbf{B}_{lp}(\upsilon,\varpi) &= \mathcal{F}\left\{\left|B_{lp}(e^r,\theta)\right|\right\} \end{aligned} \tag{10}$$

Log-polar transformation of amplitude spectrum causes the rotation and scaling to arise as the shift. It is therefore possible to use the phase correlation to detect the angle of rotation and scale between the pair of images.

Using phase correlation of the results of the Fourier-Mellin transformation A_{lp}, B_{lp}, we find the rotation size and scale of the test image *b* against a reference image *a*. By backward rotation and scaling the test image *b* we create image *b*'. Then we calculate the Fourier transformation of the image *b*' and the reference image *a*. Using phase correlation we calculate displacement of images. Backward shift of the image *b*' creates image *b*".

The detailed algorithm of registration of images using Fourier-Mellin transformation is in [9].

In „Fig. 3“ there is the amplitude and the phase spectrum of the Fourier transformation of the image of the car body and its Fourier's spectrum in log-polar coordinates.

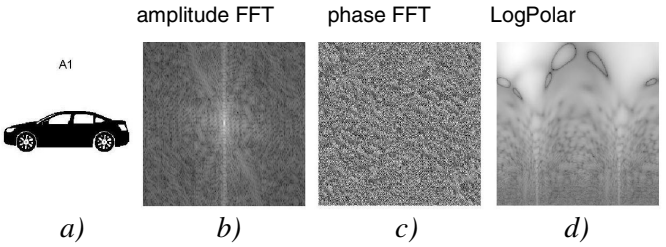

Fig. 3 a) Original image, b) Fourier spectrum amplitude in the Cartesian coordinates, c) Fourier spectrum phase in the Cartesian coordinates, d) Fourier spectrum in log-polar coordinates

2.2 Image Comparison

After registration of the images it was necessary to compare two images of bodies and determine whether they are the same model or not.

We compared the reference designs with test images in order to determine the degree of similarity or correlation between them.

To evaluate the results of the comparison of the images we used several usual or custom metrics for the calculation of comparative score that quantifies the similarities between the test and the reference image. Calculation of metrics has been verified in different combinations of the application/without application of the hamming window, application/without application of the low-pass filter.

Some of the metrics used to determine similarity between reference and test image:

MPOC, Modified Phase Only Correlation

Since the energy of the signal is lower in the high-frequency domain, phase components are not reliable in high-frequency domain. The effect of unreliable phase components in high frequencies can be limited by using filters or modifying of the POC function using spectral weighting function.

To improve the detection by removal of minor ingredients with high frequency, which have a low reliability, the function of spectral weighting $W(u, v)$ has been used [3].

$$W(u,v) = \left(\frac{u^2 + v^2}{\alpha} \right) e^{-\frac{u^2+v^2}{2\beta^2}},$$

where u, v are 2D coordinates, β is parameter, which checks width of function and α is used only to normalize.

Such modified image phase correlation function of a and b is given by [3]:

$$\tilde{q}_{a,b}(x,y) = F^{-1}\left\{ W(u,v) \frac{F_a(u,v)\ F_b{}^*(u,v)}{\left|F_a(u,v)\right|\left|F_b(u,v)\right|} \right\}.$$

The extreme value of a function $\tilde{q}_{a,b}(x,y)$ is invariable at the change of shift and brightness.

This value was used to measure the similarity of images: if two images are similar, their function MPOC gives a crisp extreme, if they are different, then the extreme decreases considerably. Graphs were displayed in the range 1–N for coordinates x, y and functional values of MPOC normalized to the range 0–1 see "Fig. 4".

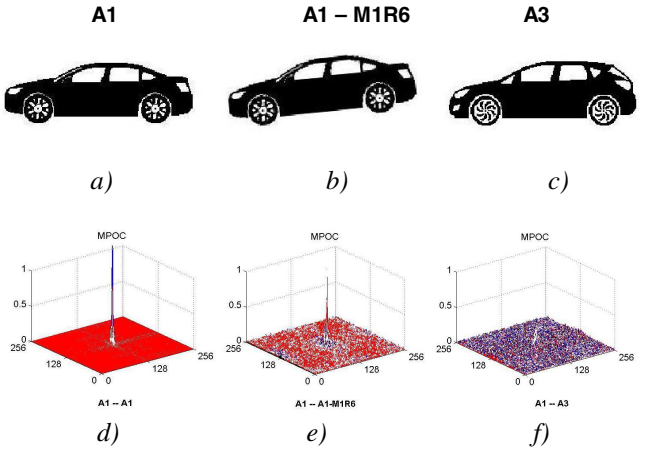

Fig. 4 Using of Modified Phase Only Correlation (MPOC): a) reference image, b–c) tested images, d) MPOC between identical images (a–a), e) MPOC between similar images (a–b), f) MPOC between various images (a–c)

PD, Percent Discrimination

Relative amount of similarity between reference and test image according to [4]:

$$PD = \frac{2[C_{ab}]_{\max}}{[C_{aa}]_{\max} + [C_{bb}]_{\max}} \times 100\ \%$$

where

$[C_{aa}]_{\max}$, $[C_{bb}]_{\max}$ a $[C_{ab}]_{\max}$ are maximal phase correlations if it is compared to a reference image $a(x, y)$ with itself, tested image $b(x, y)$ with itself and the reference image $a(x, y)$ with the image $b(x, y)$.

2.3 Decision

The calculated score is compared to the verification threshold, which will determine the degree of correlation necessary for comparison, which is to be taken as match.

On the basis of tests carried out, the threshold values of t have been set, according to which the system decision is regulated:

images generating the result greater than or equal to t are evaluated as identical (this is the same car body), images generating results lower than t are evaluated as non-compliant (these are not the same car bodies).

The decisions of system can be: match, mismatch and without result, even though there are possible changing degrees of strong matches and mismatches.

The number of properly rejected and properly accepted images depends on the preset threshold value. The value is adjustable depending on the requirements, so that the system could be more or less accurate.

3 Functionality Verification of the Algorithm

The designs of car bodies from Shutterstock [7] have been used for functional testing of the algorithm. The images were adjusted to 256 shades of gray and to the dimensions of 256 × 256 pixels due to the use of the fast Fourier transform (FFT). The test images with the parameters of the transformation were created of these images. The images have been translated in the horizontal and/or vertical direction, rotated about the different angles in both directions and the scales have been changed. The images were compared with other car bodies.

The results of the assessment are given in "Fig. 5". In the solved task it showed that the detection method used is applicable for the inclusion of the car bodies into the relevant categories.

The high success rate is achieved due to the used comparative set with rather small angle of rotation and scaling. Maximum correct recognition limit of this method has not been tested.

The images have not been properly recognized in the case of the scale too changed (0,7 and 1,3) in combination with translation and rotation.

Fig. 5 Evaluation of the identification of images

The disadvantage of the proposed method can be time computational complexity. To register the image is to be calculated: 6 × Fast Fourier Transform (FFT), 2 × log-polar resampling, 2 × phase correlation.

4 Conclusion

Monitoring process provides information about the current state of construction, which can then be compared with the original model. Comparison is used to decide on change management in implementing the project. Current methods for

retrieving and updating information on the progress of the project use digital cameras and laser-based systems.

The post describes the design of the verification method for the correct classification of the car body using a Fourier-Mellin transformation and subsequent comparison of the images using the Fourier transformation and phase correlation. Fourier-Mellin transformation offers image transformation resistant to the translation, rotation and scale. Method uses the fact that the integral transformations have their transformants in the case of translation, scaling and rotation, in the frequency area. In automatic processing it is possible to compare the images of the car bodies and find out if it is the same car body or not. It is possible to use different criteria for match, for example phase correlation, the difference correlation, the correlation coefficient, percentage comparison and comparison of calculated values with the chosen threshold for the relevant criterion. In our experiments we have set thresholds so that all the wrong couples of body works are revealed.

Acknowledgment. The article was written within the project VEGA 1/0250/11. Investigation of dynamic characteristics of the cutting process in five-axis milling in conditions of Centre of Excellence of five-axis machining and the project of European Union Structural Fonds: "Centre of Excellence of 5 - axis machining" ITMS 26220120013". and project of the Izhevsk state technological university by name M.T. Kalashnikov PSR/A2/D2.5/KAP "Development of methods for modeling and performance evaluation of manufacturing systems engineering as an information management system for automated machinery manufacturer".

References

[1] Dool, R.V.D.: Fourier-Mellin Transform. Image Processing Tools, http://www.scribd.com/doc/9480198/Tools-FourierMellin-Transform

[2] Egli, A.: Medical Image Registration 2D/3D (X-Ray/CT), http://informatik.unibas.ch/lehre/fs09/cs503/_Downloads/egli.pdf

[3] Gueham, M., Bouridane, A., Crookes, D.: Automatic recognition of partial shoeprints based on phase-only correlation. In: IEEE ICIP 2007, pp. IV–441 (2007), http://ieeexplore.ieee.org/xpl/freeabs_all.jsp?arnumber=4380049

[4] Chen, Q.S.: Image Registration and its Applications in Medical Imaging. Dissertation work, Vrije Universiteit Brussel, Deconinck (1993)

[5] Pivarčiová, E., Csongrády, T.: Fourier-transform Mellinova - tool for image registration, Aperiodikum Slovak engineers and scientists: Ideas and facts XV. 1–4/2009, 18–22 (2009) ISBN 978–80–88806–79–0

[6] Pratt, J.G.: Application of the Fourier-Mellin Transform to Translation, Rotation and Scale Invariant Plant Leaf Identification, Montreal (2000), http://digitool.library.mcgill.ca:1801/view/action/singleViewerdo?dvs=1244062994431~663&locale=sk&show_metadata=false&preferredextension=pdf&search_terms=000006662&adjacency=N&application=DIGITOOL-3&frameId=1&usePid1=true&usePid2=true

[7] Shutterstock, I.: Stock Vector Illustration: Silhouette cars on a white background (2003-2012), http://www.shutterstock.com/pic.mhtml?id=111188486
[8] Bennamoun, M., Boashash, B.: A vision system for automatic object recognitio. In: 1994 IEEE International Conference on Systems, M. and Cybernetics: Humans, Information and Technology, vol. 2, pp. 1369–1374 (1994) ISBN: 0-7803-2129-4
[9] Božek, P., Pivarčiová, E.: Registration of holographic images based on integral transformation. Computing and Informatics 31(6+), 1369–1383 (2012), http://cai.type.sk/content/2012/6+/registration-of-holographic-images-based-on-integral-transformation/
[10] Dvořák, J.: See how to produce cars Kia in Slovakia. Auto, idnes.cz, http://auto.idnes.cz/podivejte-se-jak-se-na-slovensku-vyrabeji-vozy-kia-fs9-/automoto.aspx?c=A080916_151719_automoto_fdv
[11] Ikeuchi, K., Kanade, T.: Automatic generation of object recognition programs. Proceedings of the IEEE 76(8), 1016–1035, ISSN 0018-9219, http://ieeexplore.ieee.org/xpl/login.jsp?tp=&arnumber=5972&url=http%3A%2F%2Fieeexplore.ieee.org%2Fxpls%2Fabs_all.jsp%3Farnumber%3D5972
[12] Maddox, B.G., Swadley, C.L.: An Intelligent Systems Approach to Automated Object Recognition: A Preliminary Study, Open-File Report 02-461, USGS science for a changing world, http://egsc.usgs.gov/isb/pubs/ofrs/02-461/OFR02-461.pdf

Pulse Response Identification of Inertial Model for Astatic System

J.E. Kurek

Warsaw University of Technology, Faculty of Mechatronics,
Boboli 8, 02-525 Warszawa, Poland
jkurek@mchtr.pw.edu.pl

Abstract. There is presented a method for calculation of inertial model for astatic system based on system pulse response. The method is simple and can be easily used in practice. Identified 2nd order astatic model can be applied in control algorithms more advanced than PID controller, for instance in predictive control.

1 Introduction

Simple identification method of dynamical systems based on system step response is frequently used in industrial automatic control practice, e.g. for PID controller settings [2]. There are distinguished 2 models of the control plant: (i) first order inertial model with dead-time and (ii) first order integral (astatic) model with dead-time. However, such simple models can be used also in more advanced control algorithms, e.g. for design of predictive controller.

For linear astatic system without dead-time

$$G(s) = \frac{1}{T_I s} G_s(s) \tag{1}$$

where $G_s(s)$ is asymptotically stable system without dead-time, there is commonly, as it was mentioned, calculated model in the form

$$G_{m1}(s) = \frac{1}{T_I s} e^{-T_{01} s} \tag{2}$$

for instance for calculation of PID controller settings [1].

In this note we show how to calculate more exact model for system (1) in the form

$$G_{m2}(s) = \frac{1}{T_I s} \frac{1}{Ts + 1} \tag{3}$$

based on system pulse response in very simple way. The model consists of first order integral and inertial elements, we will call this model the linear inertial astatic model.

T. Březina and R. Jabloński (eds.), *Mechatronics 2013*,
DOI: 10.1007/978-3-319-02294-9_83, © Springer International Publishing Switzerland 2014

2 Model Identification

For pulse input

$$u(t) = u_0[1(t) - 1(t - T_u)]$$

where $T_u > 0$, one obtains pulse response of astatic system (3) presented in fig. 1

$$\begin{aligned} p(t) &= \mathrm{L}^{-1}\left\{G(s)u_0\frac{1}{s}(1-e^{-T_u s})\right\} = u_0\left[\mathrm{L}^{-1}\left\{G(s)\frac{1}{s}\right\} - \mathrm{L}^{-1}\left\{G(s)\frac{1}{s}e^{-T_u s}\right\}\right] \\ &= u_0[h(t) - h(t-T_u)] \\ &= u_0\frac{1}{T_I}\left\{\left[t - T\left(1-e^{-\frac{t}{T}}\right)\right]1(t) - \left[t - T_u - T\left(1-e^{-\frac{t-T_u}{T}}\right)\right]1(t-T_u)\right\} \end{aligned} \tag{4}$$

Hence, for $t \geq T_u$ one has

$$\begin{aligned} p(t) &= u_0\frac{1}{T_I}\left\{\left[t - T\left(1-e^{-\frac{t}{T}}\right)\right] - \left[t - T_u - T\left(1-e^{-\frac{t-T_u}{T}}\right)\right]\right\} \\ &= u_0\frac{1}{T_I}\left[T_u - T\left(e^{-\frac{t-T_u}{T}} - e^{-\frac{t}{T}}\right)\right] \\ &= u_0\frac{1}{T_I}\left[T_u - Te^{-\frac{t}{T}}\left(e^{\frac{T_u}{T}} - 1\right)\right] \xrightarrow[t\to\infty]{} u_0\frac{T_u}{T_I} \end{aligned} \tag{5}$$

and, fig. 1

$$\begin{aligned} \dot{p}(t) &= -u_0\frac{1}{T_I}T\left(-\frac{1}{T}\right)e^{-\frac{t}{T}}\left(e^{\frac{T_u}{T}} - 1\right) = u_0\frac{1}{T_I}e^{-\frac{t}{T}}\left(e^{\frac{T_u}{T}} - 1\right) = \frac{1}{T_I}\frac{u_0T_u - T_I p(t)}{T} \\ &= \frac{u_0\dfrac{T_u}{T_I} - p(t)}{T} = \frac{a}{b} = \tan[\alpha(t)] \end{aligned} \tag{6}$$

Thus, based on pulse time T_u one can easily calculate integral time T_I

$$T_I = \lim_{t\to\infty}\left(u_0\frac{T_u}{p(t)}\right) = u_0\frac{T_u}{p_\infty} \tag{7}$$

and for $t_0 \geq T_u$ also inertial element time constant, fig. 1

$$T = b$$

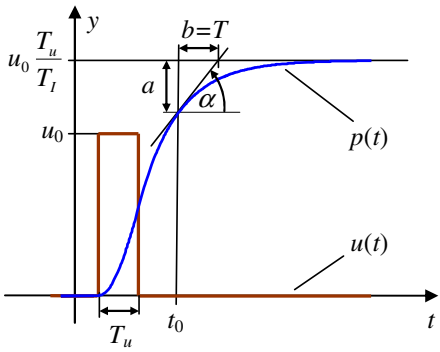

Fig. 1 Inertial astatic system pulse response, $T_u > T_I$

This is according to the fact that after the pulse is finished, $t \geq T_u$, system behaves like inertial one under step input $u(t) = u_0 \frac{T_u}{T_I} 1(t)$. It is easy to see that for $T_u = T_I$ we have $p(t) \to u_0$.

Similarly, for inertial astatic dead-time system

$$G(s) = \frac{1}{T_I s} G_s(s) e^{-T_0 s} \tag{8}$$

one can easily find the following single inertial astatic model

$$G_{m2}(s) = \frac{1}{T_I s} \frac{1}{Ts+1} e^{-T_{02} s} \tag{9}$$

Model parameters can be calculated using tangent the same way as for inertial model [1], fig. 2. Using tangent one can simple estimate dead-time T_{02} and inertial element time constant T.

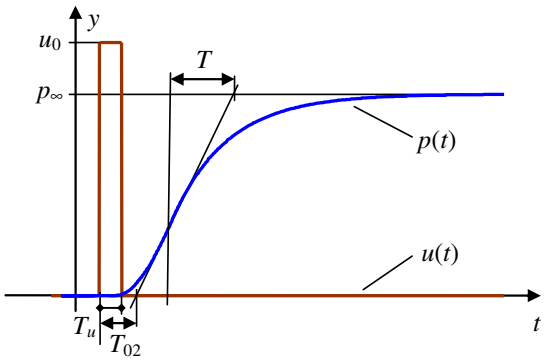

Fig. 2 Calculation of model parameters using tangent, $T_u < T_I$

It is easy to find that based on pulse response one can also calculate integral model with dead-time (2)

$$G_{m1}(s) = \frac{1}{T_I s} e^{-T_{01}s} \tag{10}$$

where

$$T_{01} = T_{02} + T > T_0$$

For the system can be also calculated model (2) similarly as for system (1).

We illustrate the approach on example.

Example 1

Pulse response of the 4th order inertial astatic system described by the transfer function

$$G(s) = \frac{1}{T_I s} G_s(s) e^{-T_0 s} = \frac{1}{2s} \frac{2.5}{10s+1} \frac{1}{8s+1} \frac{1}{5s+1} e^{-3s}$$

is presented in fig. 3.

Calculating model (9) of the system

$$G_{m2}(s) = \frac{1}{T_{Im} s} \frac{1}{T_m s + 1} e^{-T_{0m2}s}$$

one obtains, according to fig. 2, from pulse response with pulse time $T_u = 2$ and $u_0 = 0.1$, fig. 3

$$T_{0m2} = 10, \quad T_m = 16, \quad p_\infty = 0.25$$

and

$$T_{Im} = u_0 \frac{T_u}{p_\infty} = 0.1 \frac{2}{0.25} = 0.8$$

One can also calculate inertia free model for the system (10) based on pulse response

$$G_{m1}(s) = \frac{1}{T_{Im}} e^{-(T_{0m2}+T_m)s} = \frac{1}{0.8s} e^{-26s}$$

In fig. 4 there are presented step response and in fig. 5 impulse response of the system (gs) and obtained models (gm1, gm2). It is easy to see that astatic inertial model is better (more exact) than simple integral dead-time model – step response of the inertial model is almost the same as the step response of the system. Also impulse response of the inertial integral model is more similar to the response of the system than simple integral model. Thus, the inertial astatic model is better.

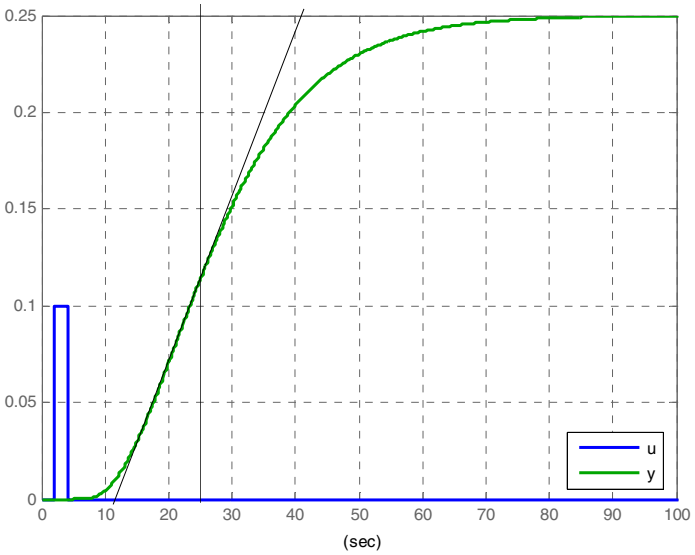

Fig. 3 Pulse response of the inertial astatic system

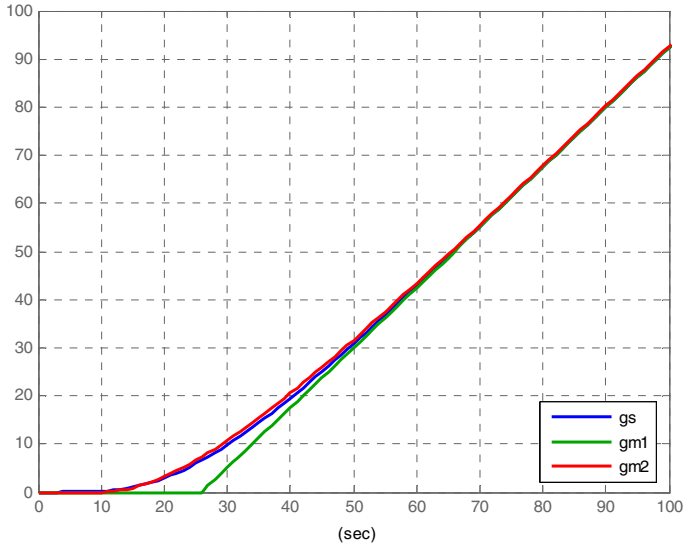

Fig. 4 Step response of the system and obtained models

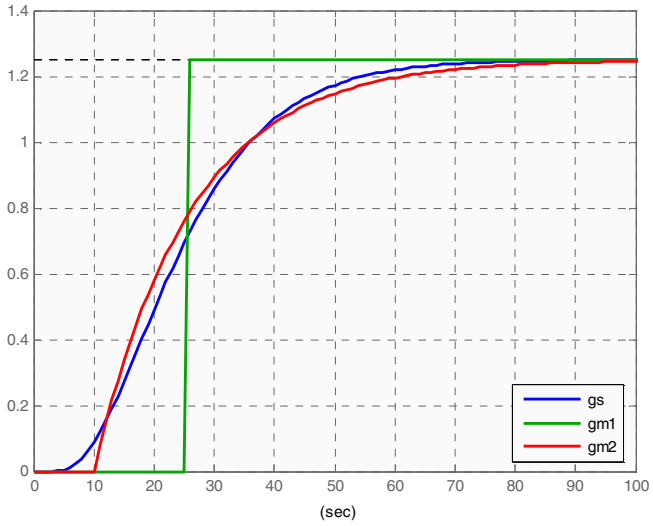

Fig. 5 Impulse response of the system and obtained models

3 Conclusions

The presented dead-time inertial model better approximates astatic system than the usually used dead-time integrator model. The proposed model can be easily calculated based on system pulse response, very similarly to the well-known dead-time integrator model based on system step response. The model should improve control in the case of astatic systems for advanced control algorithms like predictive control.

The proposed pulse response method for identification of astatic system seems better than standard method based on step response. In the proposed method magnitude of the system output is bounded whereas in step response it is unbounded. Therefore, one can say that the proposed method is more save in industrial practice. Clearly, if the pulse time would be too short and magnitude of the system response would be too small for safe model calculation one can repeat the identification with larger pulse time T_u.

References

[1] Findeisen, W. (ed.): Handbook for Control Engineer. WNT, Warsaw (1973) (in Polish)
[2] Iserman, R.: Digital Control. Springer, Bonn (1990)

Benchmarking Various Rapid Control Prototyping Targets Supported in Matlab/Simulink Development Environment

V. Lamberský and R. Grepl

Mechlab, Faculty of Mechanical Engineering, Brno University of Technology,
Technicka 2, 616 69, Brno, Czech Republic
ylambe00@stud.fme.vutbr.cz
www.mechlab.cz

Abstract. This paper presents benchmarks of various targets compatible with Simulink model based rapid control prototyping tools. The benchmarked targets are dSPACE hardware, Humusoft MF624 card, Microchip and ARM. These targets are programmed with automatically generated code from Simulink models. The benchmark models represent basic type of algorithms used in mechatronic applications (signal inverse, PID and state space controller, nonlinear inverted pendulum (2D) model and FFT algorithm). Measured computing times, provide a basic idea "how powerful" each platform is and for what applications it might be appropriate.

1 Introduction

Today, a lot of applications is developed using rapid code development methods [1, 2]. Various software products are available to support this process (e.g. Simulink, LabView [3]) together with wide range of hardware platforms which is compatible with this software. These tools for rapid code development play a significant role in many other applications, for instance Rapid Control Prototyping [4, 5].

When developing a new algorithm, usually only basics ideas of the implemented algorithm complexity and timing constraints (maximal computing time step size) are available. Based on these requirements it needs to be decided, which development platform is appropriate for given application.

Unlike the standard personal computer hardware, the embedded processors are not routinely tested by benchmarks, to evaluate their computing power. The basics information provided for each processor is its operating frequency; however the overall computing performance is affected by many factors (eg. hardware architecture, bus speeds, pipelining, compiler efficiency and optimization settings…) [6].

T. Březina and R. Jabloński (eds.), *Mechatronics 2013*,
DOI: 10.1007/978-3-319-02294-9_84,

Choosing target hardware while considering all hardware and software implementation details involves very complex computations, where some variables might be impossible to identify from requirements.

In order to identify the required computing power the virtual benchmarking method might be used [7]. However, this method is time consuming and for development purposes, the computing time does not have to be known exactly. Usually, estimating the computing period time in multiples of ten is sufficient.

Considering the previously mentioned problems the basic benchmark tests were designed to illustrate computing power of various real time targets programmed with code generated directly from Simulink model. Having results provided in this paper, the computing time of developed algorithm can be easily estimated simply by comparing with benchmarks done with similar algorithms and targets.

2 Models Used for Benchmarking

The benchmarking models were chosen to represent typical algorithms with various complexity used in system control and related mechatronic applications. Computing times were measured usin a standalone run (simple algorithms e.g. inverse of value), PIL (processor in the loop) simulation (for control algorithms e.g. PID, state space) and random values input for signal processing and simulation algorithms (e.g. FFT, IIR filter and simulating the inverted pendulum model).

All benchmarked targets were programmed with code generated from Simulink. Booth the Simulink Coder and C compiler were used with their default optimization parameters settings.

Changing the optimizations parameters used during code generation process might affect overall code efficiency. Basics information and expected performance affection by various optimization parameters is usually provided by compiler manufacturer, however this value might be different based on implemented algorithm properties. Particular values measured in real application where the code was generated directly from Simulink using various optimization parameters are presented in [6].

For most targets, the support for direct code generation from Simulink is provided either by Matworks or third party company. However, for some targets the target specific drivers and timing function need to be added manually [8].

Next sections will describe each model and its properties in more details.

Inverse of the Digital Signal

This model represents one of the simplest algorithms that can be implemented. The digital input is inverted and placed directly to output.

Since the algorithm computing complexity is minimal results from this benchmark represents time needed for simulation synchronization. This model

was implemented using logical signals (for targets which does not support this type for peripherals, the native double data type was used instead).

PID Control Algorithm

This model represents the most popular control algorithm being used.

The Simulink model consists of add and multiply operations only. Two states are maintained (one for integration and the second one for derivation). This model was implemented using 16 bit wide integers.

Inverted Pendulum Model

The 2D plant of inverted pendulum was modeled [9] using nonlinear difference equations.

This model uses double data types and implements trigonometric functions (sine, cosine).

State Space Controller with Observer

This model implements state space controller (designed for linearized inverted pendulum plant). It uses double data types and implements an observer for four states. This algorithm was implemented using double data types.

Fourier Transform

This function was implemented using Embedded Matlab function in Simulink. It uses default data type (double) and computers FT for 1024 input values using basic FFT algorithm implemented in DSP system toolbox.

The FFT algorithm is often used in signal processing applications. Results from this benchmark can help estimate computing power in signal processing applications, when using double data types.

Infinite Impulse Response Filter

This algorithm is implemented using build in Simulink block. It has 25 coefficients in nominator and 20 coefficients in denominator (45 multiply and accumulate operations). This algorithm was implemented using integer arithmetic with 32 bits precision.

3 Benchmarking the Targets

Targets for benchmarks were chosen across the wide range of available targets (with support for Simulink) to represent various solutions, from the highly powerful and expensive hardware (dSpace) to very cheap and simple units (dsPIC). Further, the computing time of simulation running on a PC (Windows in standard or accelerated mode) was added to provide additional targets for comparison.

Next sections introduce each platform and results for each benchmark models.

Windows PC (Intel E840 @ 3Ghz)

The Simulink simulation running on Windows PC is the easiest way to start the simulation. Further, measuring the time of one simulation step on a PC might help estimate performance on different platform when comparing benchmark results.

The simulation can run on PC in various modes. We have chosen the following ones for benchmarks:

- Standard simulation mode
- Accelerated simulation mode

Accelerated simulation mode requires the model to be compiled. This time was not included in measured values. As windows might interrupt the computing process this simulation were performed several times and presented times are averaged values of time that one computing step takes (Fig. 1.), measured using the build-in *tic()* and *toc()* functions.

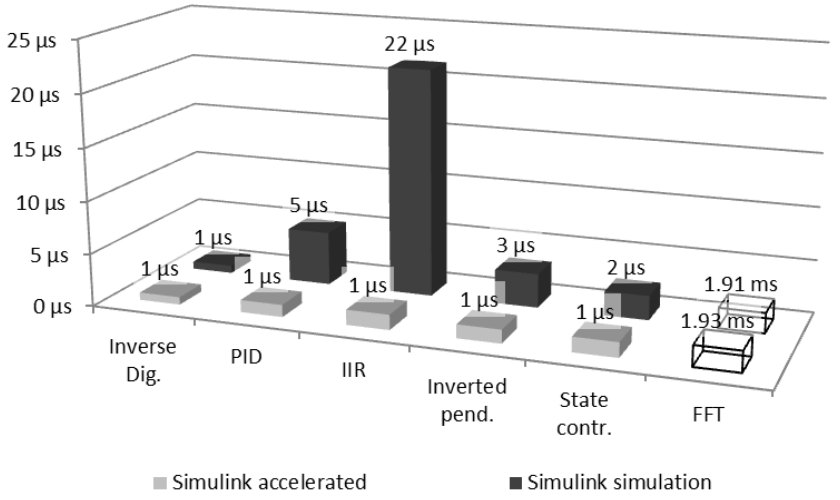

Fig. 1 Computing times for various models running standard and accelerated simulation

As can be seen from the results (Fig. 1.), the accelerated mode provides computing speed gain only for complex models. Additionally, models written in embedded functions are translated to executable code in a normal mode simulation; therefore accelerating this kind of simulation will not speed up the simulation significantly.

MF624, dSPACE

Booth the MF624 card and dSPACE hardware were designed to support development of realtime applications with Simulink product.

The MF624 card needs to be connected to a PC with Windows OS. Where signlas measured by this card can be accesed directly in simulation using Real-Time Toolbox.

The dSPACE has its own hardware on which the simulation is executed, therefore the Simulink simulation has to be compiled and downloaded to this hardware before it can be executed.

The advantage of MF624 card is that the Simulink communicates with the hardware in a real time, without a need to compile the model. But this approach limits minimum computing step as the Windows does not respond ”very quickly”.

Between targets supported by Simulink, the dSPACE hardware is one of the most powerful ones. The computing speed of MF624 card is limited even for simple models. This is caused by the need to interface with Windows drivers.

The computing times for these platforms are presented in Figure 2. The computing time of model running on a dSPACE hardware was measured using the build-in tool. Since the Windows might interrupt the simulation when using the MF624 card, the computing times were estimated, experimentally (with step resolution of 10 µs). The computing step was decreased until the simulation get “out of sync” (was not fast enough to be executed in a real time).

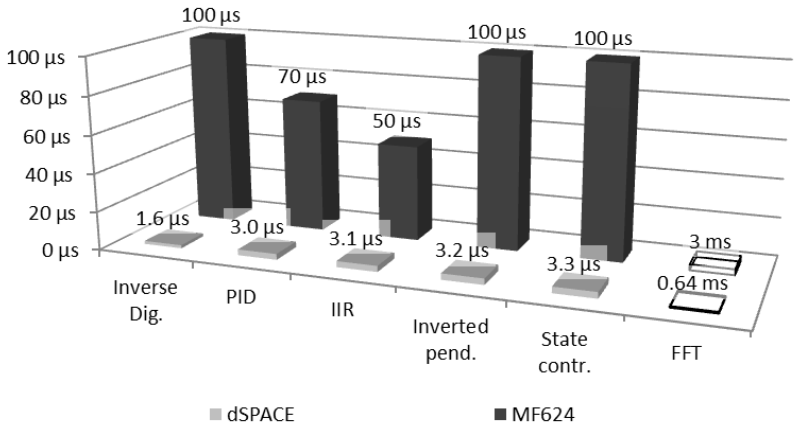

Fig. 2 Computing times for various models running on dSPACE and MF624 hardware

dsPIC, PIC32, TMS570 MCU

These microcontrollers - dsPIC (33FJ256GP710) and PIC32 (32MX795F512L) have very low computing power and they are very cheap. Code for these microcontrollers can be generated directly from Simulink using Kerhuel toolbox software and the generated executable code directly loaded to MCU.

The TMS570 MCU has an ARM Cortex ALU core, with a FPU coprocesor. The Simulink does not support direct code generation for this target, however the low level functions can be easily added to automatically generated C code from Simulink [9].

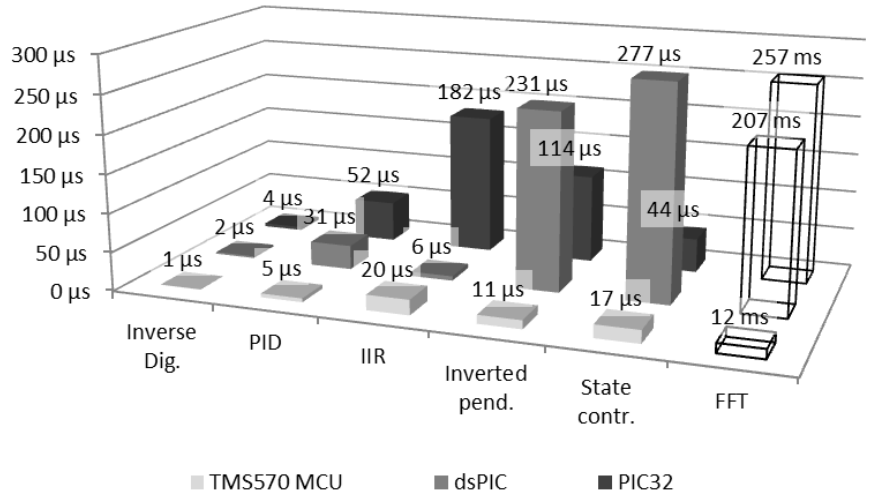

Fig. 3 Computing times for various models running on TMS570 MCU, dsPIC and PIC32 hardware

As can be seen from the results (Fig. 3.), for simulations using integer data types, the computing times between these MCUs are comparable. For simulations using double data types, the TMS570 MCU has a significantly shorter computing time. The dsPIC has twice lower computing frequency compared to the PIC32 MCU. The dsPIC has instructions optimized for digital signal filtering algorithms. This architecture optimization helped significantly shorter computing time for the IIR filter algorithm. For general algorithms (those which use various operations and functions, e.g. inverted pendulum) the computing speed is more "proportionally" related to the core frequency (TMS570MCU – 120 MHz, PIC32 – 80 MHz, dsPIC – 40 MHz).

Presented computing times were measured using scope and digital out signal synchronized with simulation (the digital out is set before one computing step starts and reset when the computation finishes).

4 Conclusions

This paper presents benchmarks designed to illustrate computing power of various targets programmed with automatically generated code to present an idea "how powerful" the benchmarked hardware is. This information is important especially

in the early stage of a new algorithm development process, when deciding, which target hardware should be used.

Results from benchmarks demonstrate the execution speed of algorithms, having various complexities. This information can be used to estimate the maximum size of computing steep, which can be achieved for particular model and hardware. Presented results should be considered as estimates. For instance, different C compiler might generate a code which is executed with a slightly different speed.

Acknowledgements. This work was supported by the European Com-mission within the FP7 project Efficient Systems and Propulsion for Small Aircraft "ESPOSA", contract No. ACP1-GA- 2011-284859-ESPOSA.

References

[1] Grepl, R., Vejlupek, J., Lambersky, V., Jasansky, M., Vadlejch, F., Coupek, P.: Development of 4WS/4WD Experimental Vehicle: platform for research and education in mechatronics. In: 2011 IEEE International Conference on Mechatronics (ICM), April 13-15, pp. 893–898 (2011)

[2] Gan, W.-S., Chong, Y.-K., Gong, W., Tan, W.-T.: Rapid prototyping system for teaching real-time digital signal processing. IEEE Trans. on Educ. 43(1), 19–24 (2000)

[3] Krejci, P., Bradac, M.: Using LabVIEW for Developing of Mechatronic System Control Unit. In: Mechatronics: Recent Technological and Scientific Advances, 9th International Conference on Mechatronics, Warsaw, Poland (2011)

[4] Grepl, R., Lee, B.: Modeling, parameter estimation and nonlinear control of automotive electronic throttle using a Rapid-Control Prototyping technique. International Journal of Automotive Technology 11(4), 601–610, doi:10.1007/s12239-010-0072-7, WOS:000279216800018

[5] Grepl, R., Lee, B.: Model Based Controller Design for Automotive Electronic Throttle. In: Recent Advances In Mechatronics: 2008-2009, 8th International Conference on Mechatronics, Luhacovice, Czech Republic (2009) WOS:000277076900036

[6] Lamberský, V., Vejlupek, J.: Benchmarking the Performance of A Dspic Controller Programed With Automatically Generated Code. In: Technical Computing Prague 2011, p. 75. ICT Prague Press, Praha (2011)

[7] The MathWorks Inc. Real-Time Workshop 7 Embedded Coder Users Guide

[8] Janka, R.S., Wills, L.M., Baumstark Jr., L.B.: Virtual Benchmarking and Model Continuity in Prototyping Embedded Multiprocessor Signal Processing Systems. IEEE Trans. Softw. Eng. 28(9), 832–846 (2002)

[9] Ljung, L., Glad, T.: Modeling of Dynamic System, 361 pages. Prentice Hall, Englewood Cliffs (1994) ISBN 0-13-597097-0

Tuning Rules Selection and Iterative Modification of PID Control System Parameters

J. Możaryn[1] and K. Malinowski[2]

[1] Warsaw University of Technology, Faculty of Mechatronics,
Institue of Automatic Control and Robotics, ul. Św. A. Boboli 8, 02-525 Warsaw, Poland
j.mozaryn@mchtr.pw.edu.pl
[2] ASKI Company, ul. Toruńska 244, 87-805, Włocławek, Poland

Abstract. There are presented theoretical aspects, and experimental results of setting a PID control system parameters. In a paper, criteria to simplify the selection of PID controller tuning rules, are given. For initially tuned controller, to improve a quality of a control system, there is proposed iterative method of PID parameters modifications that base on the analysis of quality indices in time and frequency domains.

1 Introduction

Despite all the progress in advanced control, the PID (proportional-integral-derivative) algorithm remains the most popular. The PID controller parameters are often chosen independently by an engineer, based on his experience or through some popular, simple selection methods such as Ziegler-Nichols [1] or Cohen-Coon [2]. However, regardless of the type of controlled process, there's usually requirement of exact transition response of the system. Without proper methodology, a quality of the control system may be far from desired. Therefore many scientists and engineers develop tuning rules, based on an optimization of the control system e.g. using the IMC (Internal Model Control) methodology [3], [5], [6], or minimizing chosen quality index [4], [7], [8]. Recently, manufacturers of industrial controllers equip their products with software tools that allow autotuning of PID parameters, using area or relay methods [2]. However, in many cases, it's impossible to use autotuning, or it's hard to develop one's own tuning rules, to obtain desired performance of the control system.

In this paper, preliminary parameters of the PID controller are chosen from a set of values, calculated using different tuning rules. The selection criteria of tuning rules base on the open-loop step response identification experiment. Subsequently there is proposed simple heuristic iterative modification procedure of the initially tuned parameters. It is based on the analysis of the quality indices in time and frequency domains. The aim of presented methodology is to reduce transition response time of the control system, while preserving its robustness to disturbances. Experimental results confirm a correctness of described procedure.

Presented procedure of tuning rules selection, and method of iterative improvement of the control system quality, can be easily used by a control engineers.

T. Březina and R. Jabloński (eds.), *Mechatronics 2013*,
DOI: 10.1007/978-3-319-02294-9_85,

2 Experimental Setup

Experiments were conducted on laboratory stand presented in Fig. 1.

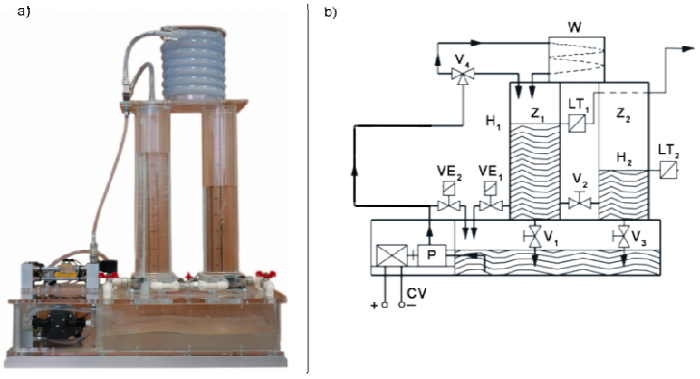

Fig. 1 Laboratory stand: (a) picture, (b) scheme

Components of the stand (Fig. 1) are: tanks Z_1 and Z_2, a pump P is controlled by standard current signal that corresponds to a change of the pump capacity 0 - 6.5 [l / min], LT_1, LT_2 are pressure transducers (measuring range 0-500 mmH20) for measuring a liquid level in each of tanks (H_1, H_2), W is elastic tube, through which the liquid can flow into the tank Z_1 (it introduces the transport delay to the object). V_1, V_2, V_3, V_4 are manually operated valves, which are used to change the way that liquid flows. There are also two electromechanical valves (VE_1, VE_2), used to introduce disturbances into the process. By ZK_1 we denote leakage from the tank Z_1 (opening the valve VE_1), and by ZK_2 we denote leakage at pump outlet (opening the valve VE_2).

During experiments, valves V_1, V_4 were opened, and valves V_2, V_3 were closed. Therefore, the controlled variable is the level of the liquid in the first tank- H_1.

3 Control System Structure

The process was controlled in closed-loop control system, presented in Fig. 2.

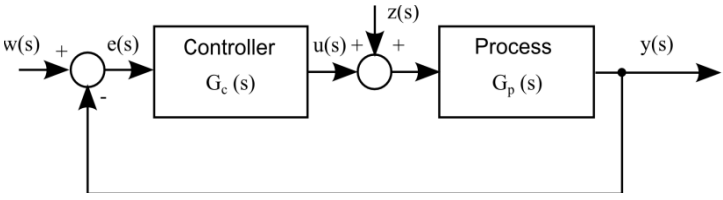

Fig. 2 Block diagram of the closed-loop control system

In the control system (Fig. 2), an output of the process y is the liquid level in the tank Z_1 (H_1). It is compared with the desired output response (setpoint) w and an output error is given as:

$$e(t) = y(t) - w(t). \tag{1}$$

The error (1) is used by the controller to adjust the control signal u which, through an actuator (pump) affects the regulated process. In the system there are disturbances z (leakage) which can be introduced, as it is described in chapter 2.

The control algorithm was implemented on a Siemens S7-1200 PLC controller.

4 Identification of Control Plant

During the identification experiment the step response method was used. The model of the process has been calculated based on response of the level H1, for change in the setpoint $w(t)$ from 50% to 60%, for the open loop system. Calculated model of the process is given in the form of first order lag plus time delay (FOLPD) model [9]:

$$G_p(s) = \frac{k}{T_z s+1} e^{-T_o s}, \tag{2}$$

where k is a model gain, T_z is a time constant and $T_0$is a time delay.

Based on the measured values the estimated model parameters are: $k = 2.1$, $T_z = 119.5\ [s]$, $T_o = 5.5\ [s]$.

5 Selection of PID Controller Parameters

For the control of the process there was used the PID controller in the parallel form with filtered derivative part, described by the following equation [9]:

$$G_c(s) = k_c\left(1 + \frac{1}{T_I s} + \frac{T_D s}{\frac{T_D}{N}s+1}\right), \tag{3}$$

where k_c is proportional gain, T_I is integral time constant, T_D is derivative time constant and T_D/N is time constant of filter (N is chosen usually as 8÷10 [4]).

The quality of the control system was analyzed in the time domain using following indexes:

Maximum error

$$e_{max} = \max\big(e(t)\big). \tag{4}$$

Overshoot

$$\gamma = \left|\frac{e_2}{e_1}\right| * 100\%, \tag{5}$$

where e_1 and e_2 are the first 2 consecutive biggest errors with opposite signs, assuming steady state value of output $y(t)$ after transient response as the zero level (baseline).

Transient response time T_R - it is the time between the moment of change of the set point $w(t)$, or introduction of disturbances $z(t)$, and the moment when the error $e(t)$ reaches a fixed value inside a boundary $|0.05e_{max}|$.

Integral Squared Error

$$ISE = \int_0^{+\infty}[e(t)^2]\,dt. \tag{6}$$

6 Preliminary Experiments – Pre-tuning of PID Controller

In [9] there are described 1731 different types of PID tuning rules, so the proper criteria should be used to choose the most suitable settings. For tuning rules selection (*pre-tuning*), used criteria were as follows:

a) Type of a process (stationary or nonstationary): the examined process is stationary process.
b) Model of the process: the equation (2) describes FOLPD model.
c) PID controller structure: the controller structure is described by (3).
d) The ratio of transport delay and the time constant of the process:

$$R = T_Z/T_o. \tag{7}$$

For the given model (2) $R \cong 0.05$.

After taking into account the criteria a) - d) there were selected 4 different PID tuning methods from [9]. First two methods developed by Morari and Zafiriou [3] (denoted M-Z), and Gong [5] base on an optimization of the control system e.g. using the Internal Model Control methodology. Another method taken for comparison was developed by *Victor Alfaro Ruiz* (denoted A-R) [7], [8], and base on a minimization of an performance index IAE (**I**ntegral of **A**bsolute value of **E**rror):

$$IAE = \int_0^{+\infty}|e(t)|\,dt. \tag{8}$$

Finally, the well-known *Zigler-Nichols* method [1] was also used.

In each case, after tuning the control system, quality indices were calculated for 3 experiments: a) step response (labeled ΔSP) of desired output value $w(t)$ between 50% and 55%, b) compensation of the disturbance ZK_1, c) compensation of the disturbance ZK_2.

Table 1 Quality indices of the examined control system with different PID settings

Quality index→	T_R [s]			γ [%]			ISE [%]		
	ΔSP	ZK_1	ZK_2	ΔSP	ZK_1	ZK_2	ΔSP	ZK_1	ZK_2
M-Z	98.5	351.0	332.0	0.0	0.0	0.0	261.4	2050.8	10 242.0
Gong	20.5	364.0	273.5	0.0	0.0	0.0	262.0	279.8	1 623.1
Z-N	30.5	32.0	35.0	26.6	7.8	13.8	121.0	11.0	70.0
A-R	10.0	235.0	235.5	0.0	0.0	0.0	147.3	126.0	1 623,.1

The results presented in Table 1 show, that the system with parameters set according to A-R method has best quality - the overshoot of the step response, or abrupt disturbances is equal to 0. Moreover, transient response time T_R =10[s] of ΔSP is relatively small. However, for disturbances ZK_1 and ZK_2 there have been very long transient response times (T_R> 200s), comparing with T_R of ΔSP, or for *Z-N* method.

Therefore, for further tuning there was chosen A-R method. This method is proposed for processes in the form (2) with the ratio R in the range $(0.04, 2.00)$. A-R tuning rules are as follows:

$$\begin{cases} k_p = \frac{1}{k}\left[0.3295 + 0.7182\left(\frac{T_z}{T_o}\right)^{0.9971}\right] \\ T_I = T_z\left[0.9781 + 0.3723\left(\frac{T_z}{T_o}\right)^{0.8456}\right] \\ T_D = 0.3416T\left(\frac{T}{T_o}\right)^{0.9414} \\ N = 10 \end{cases} \tag{9}$$

The calculated values of PID settings according to (12) are: $k_P = 7.05$, $T_I = 96.90\ [s]$, $T_D = 1.73\ [s]$, $N = 10$.

7 Iterative Modifications – Fine-Tuning of PID Controller

Desired control system, was characterized by following properties:

Property 1: Short T_R of the step response.
Property 2: Short T_R after abrupt occurrence of disturbances.
Property 3: Output signal should have no visible high-frequency oscillations.

The overall performance of the examined control system with controller parameters set according to A-R rules is good (Table 1). However, because of the long transient response to disturbances, there was proposed method of parameters modification (*fine-tuning*) to reduce it.

To specify the robustness of the system there was done analysis in the frequency domain. There were calculated gain margin ΔM and phase margin $\Delta\varphi$ of the control system [10]. Gain margin determines how much the magnitude of the control system should increase, to make it unstable. Control systems with sufficiently large gain margin and phase margin are robust to changes in the parameters of the object and external distortions. If ΔM and $\Delta\varphi$ become smaller, the control system has transient oscillatory character and the overshoot, but also has short transient response time. For further modifications there was chosen only integration time T_I. For the plant model (1) T_R, after occurrence of disturbances, decrease with reduction of T_I [11].

Proposed PID fine-tuning heuristic iterative procedure can be presented in the form of algorithm as follows:

Algorithm A1:
Step 1: Set $k = 0$. Enter the pre-tuned set of PID settings, perform the step response experiment. Calculate and save values: γ_0, ΔM_0, $\Delta\varphi_0$, and $T_{I,0} = T_I$.
Step 2: Set $= k + 1$, and $T_{I,k} = 1{,}05T_{I,k-1}$.
Step 3: Perform step response experiment, calculate values γ_k, ΔM_k, $\Delta\varphi_k$.
Step 4: If $\gamma_k < 5\%$, go to step 5, else go to step 6.
Step 5: If $\Delta M_k < (1 - 0{,}25)\Delta M_0$ and $\Delta\varphi_k < (1 - 0{,}25)\Delta\varphi_0$ go to step 2, else go to step 5.
Step 6: Set $T_I = T_{I,k-1}$.
Step 7: Stop the algorithm.

In the proposed procedure A1 integration time is reduced in order to comply with the following assumptions:

Assumption 1: Step response overshoot should be less than 5 %.
Assumption 2: The change of ΔM should be less than 25% of the original value and $\Delta\varphi$ should be less than 25% of the original value.

Results after the iterative modifications (Algroithm A1), are gathered in Table 2.

Table 2 Quality indices of the examined control system before and after modifications

	Pre-tuning (A-R)			**Fine-tuning (Algorithm A1)**		
Quality index↓	ΔSP	ZK_1	ZK_2	ΔSP	ZK_1	ZK_2
γ [%]	0.0	0.0	0.0	4.60	3.80	4.70
T_R [s]	17.5	206.0	197.5	17.50	51.00	55.00
ISE [%]	318.5	145.0	627.5	329.50	58.00	262.00
ΔM		8.2			8.2	
$\Delta\varphi$		61.9			49.3	

After analyzing results given in the Table 2, it can be seen that after the fine-tuning there were faster transient responses to the disturbances and T_R of ΔSP did not change. However, there were slight overshoot of 4-5% in all cases. After fine-tuning ISE index of ΔSP slightly increased (3.5÷4.5 %), but for both disturbances the same index significantly decreased (-60%), in comparison with the values before modifications.

It is apparent, that in the result of the fine-tuning there was significant reduction of T_R and ISE indices in case of disturbances, while maintaining quality indices of ΔSP at the similar level than before changes of PID settings.

8 Summary

In the paper describes the methodology of the improving the quality of the control system. First, there are given criteria to facilitate the selection of PID controller tuning rules. Then, for the initially tuned controller, there is also presented the heuristic iterative method (fine-tuning) to improve the quality of the control system, based on the analysis in time and frequency domains. In order to confirm the validity of proposed solution there were performed experiments of liquid level control in case of disturbances (leakages).

This paper shows importance of proper choice of the PID controller tuning rules, tailored to a particular object and controller types. Described selection criteria facilitates the work of the control engineer. Moreover, presented fine-tuning methodology for determining and modifying of the PID controller parameters can be easily applied in real control systems.

In the future we plan to develop a software for PLC controllers that allow an on-line analysis of the control system in the frequency domain.

References

[1] Ziegler, J.G., Nichols, N.B.: Optimum settings for automatic controllers. Transactions of the ASME 64, 759–768 (1942)
[2] Cohen, G.H., Coon, G.A.: Theoretical Consideration of Retarded Control. Transactions of the ASME 75, 827–834 (1953)
[3] Morari, M., Zafiriou, E.: Robust Process Control. Prentice Hall, New Jersey (1989)
[4] Åström, K.J., Hägglund, T.: PID Controllers: Theory, Design, and Tuning, 2nd edn. Instrument Society of America: Research Triangle Park, NC (1995)
[5] Gong, X., Gao, J., Zhou, C.: Extension of IMC tuning to improve controller performance. In: Proceedings of the IEEE International Conference on Systems, Man and Cybernetics, pp. 1770–1775 (1996)
[6] Skogestad, S.: Probably the best simple PID tuning rules in the world. Journal of Process Control (September 12, 2001)
[7] Alfaro Ruiz, V.M.: Optimizaciondeldesempenolosreguladoresyservomechanismos PID. Ingeniería 13(1-2), 53–62 (2003)

[8] Alfaro Ruiz, V.M.: Estimacion deldesempeno IAE optimo de losreguladores yservo-mechanismos PID. Ingeniería 15(1), 79–90 (2005)
[9] O'Dwyer, A.: Handbook of PI and PID controller tuning rules. Imperial College Press, London (2009)
[10] Bishop, R.H., Dorf, R.C.: Modern Control Systems, 12th edn. Prentice Hall (2010)
[11] Holejko, D., Kościelny, W.: Automatyka Procesów Ciągłych, OWPW (2012)

Fuzzy Approach to the Selection of Interference Fit Assembly Method

Sinitsyn A.N., Sinitsyna V.V., Abramov I.V., and Abramov A.I.

Kalashnikov Izhevsk State Technical University, Faculty of Quality Management,
Faculty Departments of Mechatronic Systems, Studencheskaya street, 7, 426069, Russia
tofkas@yandex.ru

Abstract. In this paper model of pressure couplings assembly method selection is developed using fuzzy logic technique. A systematic approach to assembly method selection problem is proposed. Example of assembly method selection problem algorithmization and solving is considered.

1 Introduction

Pressure couplings (figure 1) are widely used for torque transmission in electromechanical drives of mechatronic systems. Fierce industrial competition is spurring the search for improved quality of mechatronic product including pressure couplings. To ensure high quality of pressure couplings it is necessary to select proper assembly method. Assembly method selection is creative and quite challenge. The use of decision making systems can assist the designer in selecting the appropriate assembly method and may potentially reduce decision time, finally product cost and failure rate due to the human factor.

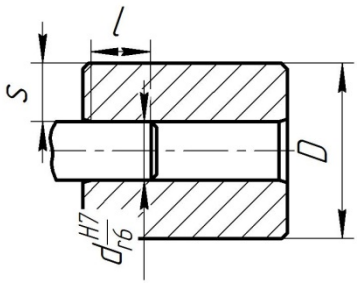

Fig. 1 Pressure coupling

2 Modelling of Decision Making System Using Fuzzy Logic

For solving not enough structured problem such as pressure coupling assembly method selection the artificial intelligence techniques are widely used. One of

T. Březina and R. Jabloński (eds.), *Mechatronics 2013*,
DOI: 10.1007/978-3-319-02294-9_86,

most effective techniques of decision-making process formalization is fuzzy set theory [10]. In this paper fuzzy logic is applied to the selection of pressure coupling assembly method.

2.1 Input Variables

A lot of factors such as geometry, physical and mechanical properties, production, economic factors impacts on the outcome of a selection. According to Pareto principle roughly 80% of the outcomes come from 20% of the influencing factors. Taking into account 80% of remaining factors that contribute 20% of the outcomes complicates decision-making without guaranteeing accuracy.

In accordance with the principle three the most valuable parameters were selected by group of experts as input variables: δ/d – relative interference; s/D – ratio of hub wall thickness to outer diameter; l/d – relative coupling length, where d – nominal coupling diameter, D – outer hub diameter, s – hub wall thickness, l – coupling length. Taking greater number of factors into consideration may improve quality of decision making.

Group of experts consisted of pressure coupling specialists, Candidates and Doctors of engineering, professors and production department specialists. Theses on pressure couplings [1, 11] and reference data of technical literature were analyzed [2, 3, 4, 5, 6, 7, 8, 12, 14, 15].

Relative interference (x_1), hub thickness ratio to outer diameter (x_2) and relative coupling length (x_3) are considered as input fuzzy variables forming fuzzy sets [9].

2.2 Output Variables

Force assembly (FA), Thermal assembly (TA), Hydro-press assembling (HPA) are considered as output fuzzy variables forming fuzzy sets.

The input and output variables membership functions of fuzzy set are presented at figures 2-5. Membership functions of output variables are the same.

2.3 Term Values

Term values are determined on the grounds of expert judgment of linguistic variable. Examination was carried out based on judgment method including following phases: experts selection, experts inquiry, quantitative evaluation forming, knowledge base creation. Linguistic variables, expert judgments of crisp variables and respective terms l are presented in table 1.

Table 1 Linguistic variables, expert judgments of crisp variables and respective terms

variables x_i, y_j	expert judgments of variables x_i, y_j	terms, l
relative interference, x_1	0,00001÷0,00019 0,00020÷0,00090 0,00100÷0,00200	light medium tight
hub thickness ratio to outer diameter, x_2	0,02500÷0,17000 0,17000÷0,35000 0,35000÷0,50000	thin-wall mean thickness havy-wall
relative coupling length, x_3	0,50000÷1,00000 1,00000÷1,50000 1,50000÷2,00000	short mean long
force assembling, y_1		not applicable rather no, then yes rather yes, then no applicable
thermal assembling, y_2		not applicable rather no, then yes rather yes, then no applicable
hydro-press assembling, y_3		not applicable rather no, then yes rather yes, then no applicable

2.4 Membership Functions

According to [10] while membership functions forming one must seek for grade of membership to extreme term being equal to one. In this case the following natural rule is obeying: the less (the great) value of variable, the greater degree of conformity to extreme term is.

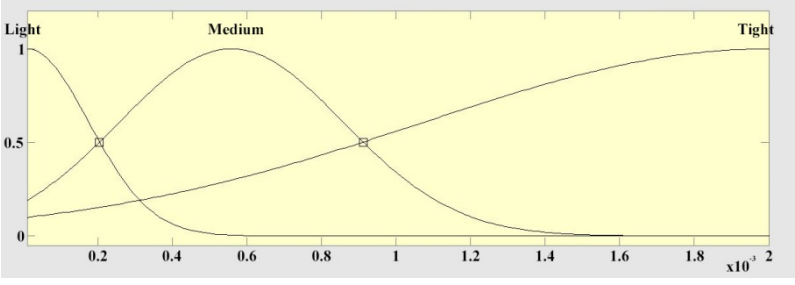

Fig. 2 Membership function of input variable "Relative interference"

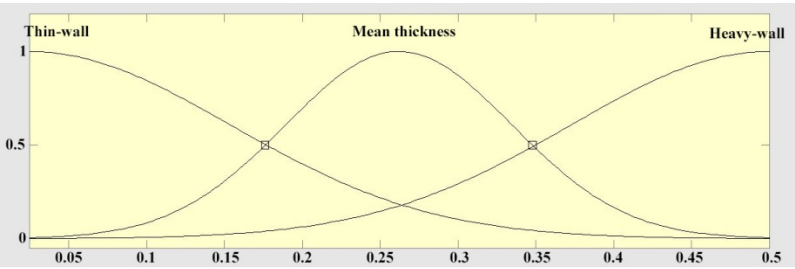

Fig. 3 Membership function of input variable "Hub thickness ratio to outer diameter"

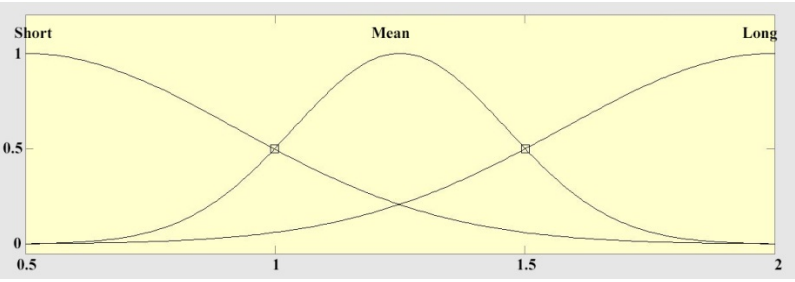

Fig. 4 Membership function of input variable "Relative coupling length"

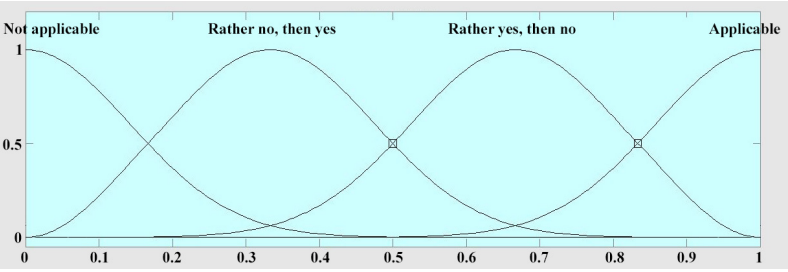

Fig. 5 Membership function of output variables "Force assembling", "Thermal assembling", "Hydro-press assembling"

2.5 Knowledge Base

Production rules were used for declaration of relationship between linguistic variables. Knowledge base designing was carried out taking into account following rules [10]:

1. For each term of output variable at least one rule must exist;
2. For any term of input variable at least one rule must exist where the term is used as antecedent.

The following set of rules and there weights are developed based on the expert judgments:

1. If “Relative coupling length” – “Short” then output for “Force assembling” is “Applicable”, for “Thermal assembling” is “Applicable”, for “Hydro-press assembling” is “Applicable” (1);
2. If “Relative coupling length” – “Mean”, then output for “Force assembling” is “Rather yes then no”, for “Thermal assembling” is “Rather no then yes”, for “Hydro-press assembling” is “Applicable” (1);
3. If “Relative coupling length” – “Long”, then output for “Force assembling” is “Not Applicable”, for “Thermal assembling” is “Not Applicable”, for “Hydro-press assembling” is “Applicable” (1);
4. If “Hub thickness ratio to outer diameter”– “Thin-wall”, then output for “Force assembling” is “Not Applicable”, for “Thermal assembling” is “Applicable”, for “Hydro-press assembling” is “Not Applicable” (0,5);
5. If “Hub thickness ratio to outer diameter”– “Mean thickness”, then output for “Force assembling” is “Rather no then yes”, for “Thermal assembling” is “Rather yes then no”, for “Hydro-press assembling” is “Rather no then yes”, (0,5);
6. If “Hub thickness ratio to outer diameter”– “Heavy-wall”, then output for “Force assembling” is “Applicable”, for “Thermal assembling” is “Applicable”, for “Hydro-press assembling” is “Applicable”, (0,5);
7. If “Relative interference” – “Light”, then output for “Force assembling” is “Applicable”, for “Thermal assembling” is “Applicable”, for “Hydro-press assembling” is “Applicable” (0,75);
8. If “Relative interference” – “Medium”, then output for “Force assembling” is “Rather no then yes”, for “Thermal assembling” is “Applicable”, for “Hydro-press assembling” is “Applicable” (0,75);
9. If “Relative interference” – “Tight”, then output for “Force assembling” is “Not Applicable”, for “Thermal assembling” is “Rather yes then no”, for “Hydro-press assembling” is “Rather yes then no”, (0,75)

where (1), (0,75), (0,5) – rule weights.

Matrix of knowledge was formed based on the formulated rules (Table 2).

Table 2 Matrix of knowledge about pressure coupling assembling method selection

	input variables			output variables			weight
	x_1	x_2	x_3	y_1	y_2	y_3	
1.	-	-	short	1,00	1,00	1,00	1,00
2.	-	-	mean	0,66	0,33	1,00	1,00
3.	-	-	long	0,00	0,00	1,00	1,00
4.	-	thin-wall	-	0,00	1,00	0,00	0,50
5.	-	mean thickness	-	0,33	0,66	0,33	0,50
6.	-	heavy-wall	-	1,00	1,00	1,00	0,50
7.	light	-	-	1,00	1,00	1,00	0,75
8.	medium	-	-	0,33	1,00	1,00	0,75
9.	tight	-	-	0,00	0,66	0,66	0,75

Crisp values of output variables are calculated by centroid defuzzification:

$$y_i = \frac{\int y_i \cdot \mu_p(y_i)dy}{\int \mu_p(y_i)dy}, \quad (1)$$

where $\mu_p(y_i)$ – resulting Membership function of output variables.

2.6 *Model of Fuzzy Logic System*

Model of fuzzy logic system for pressure coupling assembling method selection is developed in MatLab and is presented on figure 6.

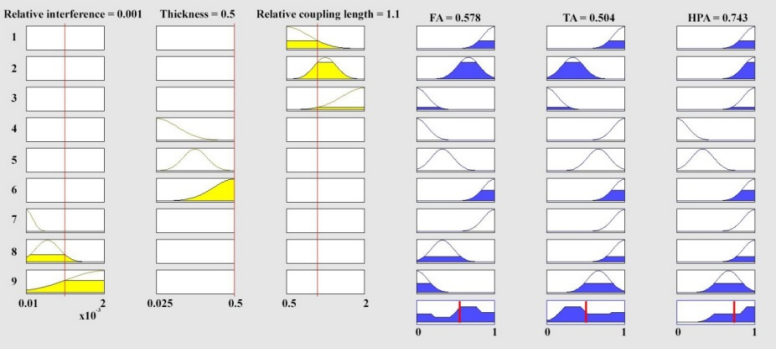

Fig. 6 Model of fuzzy logic system for pressure coupling assembling method selection

By modifying input variables values one can get science-based guidance on pressure coupling assembling method selection in form of crisp value of output variables. Input variables values are marked out by thin vertical line. Results of defuzzification are presented in right lower part of figure 6 and are marked out by thick vertical line.

After defuzzification for each output variable one can get crisp value that describes applicability level of assembling method for pressure coupling with considered input parameters. Applicability level interpretation to assembling method selection guidance is carried out in accordance with table 3.

Table 3 Results of the fuzzy logic system calculation interpretation

range of applicability level	interpretation
0,00÷0,25	not applicable
0,25÷0,50	rather no, then yes
0,50÷0,75	rather yes, then no
0,75÷1,00	applicable

3 Case Study

Fuzzy logic approach developed in this paper is tested for assembling method selection of pressure coupling - wheel pair of rolling stock. For the following values of input variables: “Relative interference” – 0,001; “Hub thickness ratio to outer diameter” – 0,5; “Relative coupling length” – 0,5; after the defuzzification output variables take the following values: “Force assembling” – 0,578; “Thermal assembling” – 0,504; “Hydro-press assembling” – 0,743 (table 4). According to the results all assembly methods are applicable, but the most suitable for considered pressure coupling parameters is “Hydro-press assembling”.

From practice and modern standards it is known that force and thermal assembling are used for wheel pairs. This divergence may indicate inadequate quality of decision making or deep-seated traditions in parts assembling that are related to human factor and run counter the goal of pressure coupling quality and reliability improvement.

Table 4 Pressure coupling parameters and values of applicability level

pressure coupling example	relative interference	hub thickness ratio to outer diameter	relative length	FA	TA	HPA
type of wheelset axle - PM3 [13]	0,001	0,500	1,100	0,578	0,504	0,743

4 Conclusions

Intelligent decision making system is developed based on fuzzy logic and judgment method. The system favours the knowledge accumulation and reuse. Improved quality of pressure couplings by proper assembly method selection may have an enormous impact on the economic viability of the final product.

The introduced system is mathematical model of corresponding unit CAD/CAM system responding in pressure coupling design.

References

[1] Abramov, I.V.: Investigation and improvement of pressure coupling hydro-press assembling: Author’s abstract of master’s thesis – Perm, – 20 p. (1970)

[2] Abramov, I.V., Fattiyev, F.F., et al.: High pressure force fit, 300 p. ISTU Publisher, Izhevsk (2002) ISBN 5-7526-0114-2

[3] Abramov, I.V., Abramov, A.I., Sinitsyn, A.N., Sinitsyna, V.V.: Stress–Strain State of Tight Joints under a Bending Moment. Russian Engineering Research 30(8), 759–762 (2010)

[4] Abramov, I.V., Abramov, A.I., Sinitsyn, A.N., Sinitsyna, V.V.: Theoretical justification of interference fit assembling and disassembling new methods. Sborka v mashinostroenii i priborostroenii (2011) №3, ISSN 0202-3350
[5] Berniker, Y.I.: Interference fit in mechanical engineering. L., Mashinostroenie, 167 p. (1966)
[6] Grechishchev, I.S. and Il'yashenko, A.A., Soedineniya s natyagom: Raschet, proektirovanie, izgotovlenie (Tight Joints: Calculation, Design, Manufacture). Mashinostroenie, Moscow (1981)
[7] Kosilov, A.G., Mesherikov, R.K.: Mechanical engineers reference book. V. 2, Mashinostroenie, 496 p. (1985)
[8] Myagkov, V.D., Paley, M.A., Romanov, A.B., Braginskiy, V.A.: Limits and fits: Reference book. L.: Mashinostroenie, – V. 1. 543 p. (1982)
[9] Shtovba, S.D.: Fuzzy system design in MATLAB. – Moscow.: Goryashaya liniya – Telekom, 288 p. (2007)
[10] Shtovba, S.D.: Introduction in fuzzy set theory and fuzzy logic, http://matlab.exponenta.ru/fuzzylogic/book1/index.php
[11] Shchenyatskii, A.V.: Stress-strain state and carrying capacity of tight multiplayer joints: Author's abstract of master's thesis. – Izhevsk, 171 p. (1993)
[12] Shchenyatskii, A.V., Abramov, I.V., Sosnovish, E.V., et al.: Theory and technology hydro-press tight joints, 496 p. ISTU publisher, Izhevsk (2012) (Monographs ISTU)
[13] GOST 4835-2006 Koleshiye pary vagonov magistralnih zhelezhih dorog kolei 1520 мм
[14] Abramov, I.V., Abramov, A.I.: Expert evaluation of the technical level of NC-Machines. University Review 5(1), 3–7 (2011) ISSN 137-6047
[15] Abramov, I.V., Abramov, A.I., Sinitsyn, A.N., Sinitsyna, V.V., Petrov, A.V.: Experimental plant for interference fit disassembling. In: 2011 14th International Symposium Mechatronika, pp. 90–92 (2011) ISBN 978-1-61284-821-1

Application of Artificial Neural Network for Speed Control of Servodrive with Variable Parameters

T. Pajchrowski

Poznan University of Technology, Faculty of Electrical Engineering, 60-965 Poznan, Poland
tomasz.pajchrowski@put.poznan.pl

Abstract. This paper presents the problem of position control with adaptive and robust speed controller for PMSM with variable moment of inertia. Both controllers use the technique of artificial neural networks. An adaptive speed control is trained on-line, and robust is trained off-line method. The position of the linear control were presented. Simulation results have been confirmed by experiment.

1 Introduction

High performance of servodrives in such applications as robots (especially arm of robot), machine tools or rolling machines has risen significantly. Control of servodrives in these systems is very sensitive to variations parameters of the drive during starting process and step change of load torque[1,2,3,6].In many of these applications the moment of inertia is variable during drive operation. Very often, the load torque depends on the angle of the motor shaft position. In all these situations robust or adaptive control is recommended, which leads to smaller sensitivity to the parameters variations [4,5,6,7,13]. In the typical cascade servodrive control three control loops are used: supervised angular position control loop with subordinate control loops of angular speed and motor torque. Such control system for servodrive with Permanent Magnet Synchronous Motor (PMSM) is presented in Fig.1. In the presented system a vector control is applied, in which stator current is controlled in two axes *d* and *q*. Current in axis *d* is kept on zero level. The speed control loop is more sensitive to variation of specified parameters than the position one because its control plant contains these variable parameters (moment of inertia, torque constant) . If the speed control loop is insensitive to parameters variations, due to a proper synthesis of its controller, the position control will be insensitive too. In the papers [4, 5 ,7] have been described two concepts of ANN adaptive controller. In [7] the neuro-fuzzy adaptive model following control (MFC) was presented. In this work the neuro-fuzzy controller is trained on-line on base of error (difference) between output signals of reference model and controlled plant. In approach described in [4, 5] an adaptive neural controller was proposed, which was trained on the base of its own control error.

T. Březina and R. Jabloński (eds.), *Mechatronics 2013*,
DOI: 10.1007/978-3-319-02294-9_87,

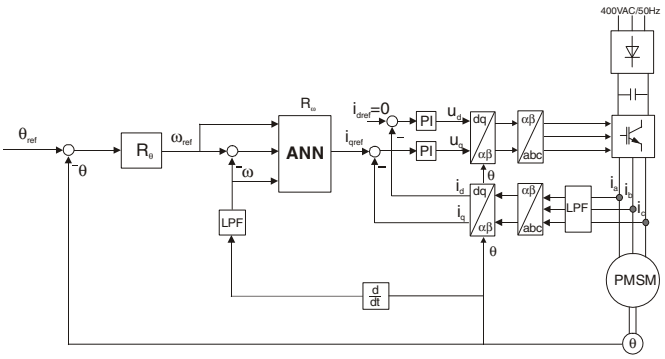

Fig. 1 Scheme of angular position and speed control system with PMSM

High requirements concerning dynamic properties of today's servodrives need proper controllers' settings adjustment. In all these situations robust or adaptive control is recommended, which leads to smaller sensitivity to the parameters variations. In such situation the key point is to design robust or adaptive speed controller. In the paper the results of adaptive control (trained on-line) with robust control [11] (trained off-line) was compared.

2 Model of the Control System

2.1 Model of the Speed Loop

A proposed structure of ANN (trained on-line), shown in Fig. 2, depends on assumed type of speed controller. The ANN structure represents nonlinear controller of PD modified type [2,3]. The modification consists in calculation a differential component only of feedback signal. The ANN network has one hidden layer with three neurons and one output neuron. Activation functions of neurons are linear. Speed and position control has been sampled with a period of 100μs, which corresponds to a sample in a real system equipped with a DSP microprocessor. The structure of robust neural controller and tuning operation shown in [11]. Properly designed robust speed controller ensures insensitivity to change the drive parameters in the loop position. It was used a linear controller P type [3,8].

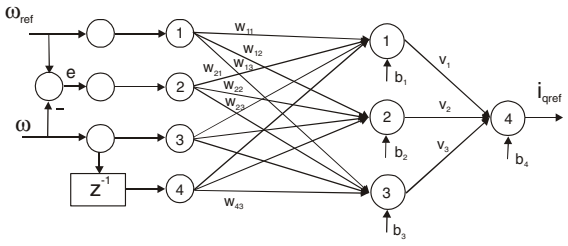

Fig. 2 Adaptive controller structure

2.2 *Model of the Variable Moment of Inertia*

The mechanical load was built (Fig. 3), whose task was to change the moment of inertia and the load as a function of change in position of the shaft, according to the equation:

$$m_d = J\frac{d\omega}{dt} + \frac{\omega^2}{2}\frac{dJ}{d\theta} \tag{1}$$

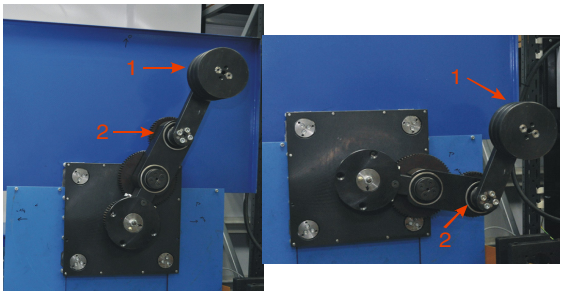

Fig. 3 Photography of the load continuously variable moment of inertia. 1 – metal rings for changing the weight; 2- arm of variable length

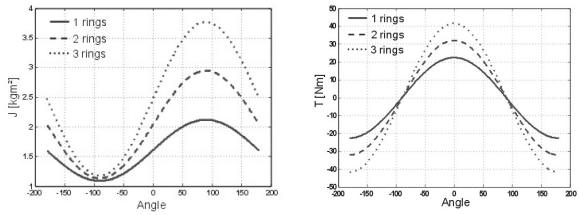

Fig. 4 Waveforms moment of inertia and load torque for the different combinations of the metal rings

Fig. 4 shows the change of the moment of inertia as a function of angle of rotation. The minimum and maximum value depends on the number of placed the metal rings and angle. For these examples, this value is 1.09kgm^2 (one metal ring is located in the lowest part of the drive), and the maximum value is 3.77kgm^2 (three metal rings) are located in the highest part of the drive). The biggest load torque is to position 0 and 180 degree, as shown in Fig. 4.

3 ANN Training Algorithm

A proposed structure of ANN, shown in Fig. 2, depends on assumed type of speed controller. The ANN structure represents nonlinear controller of PD modified type. The main difficulty in designing the adaptive neural controller is to find a

training procedure, which could be realized on-line in relatively short time. The assumed criterion for ANN training is a square of speed control error [14]:

$$E = \frac{1}{2}\left(\omega_{ref} - \omega\right)^2 \tag{2}$$

Resilient-back propagation algorithm (RPROP) was selected as an ANN training method because of its simplicity [12]. The main advantage of this method consists in calculation only a sign of error gradient instead of its value. A change of weight coefficient for j-input of i-neuron $\Delta w_{ij}(k)$ is described by equation [13]:

$$\Delta w_{ij}(k) = -\eta_{ij}(k) \cdot sign\left(\frac{\partial E(w(k))}{\partial w_{ij}}\right) \tag{3}$$

Training coefficient $\eta_{ij}(k)$ in (10) is determined individually for each weight and changed in each step of training in agreement with formulas [13]:

$$\eta_{ij} = \begin{cases} \min(a\eta_{ij}(k-1), \eta_{\max}) & \text{for } S_{ij}(k)S_{ij}(k-1) > 0 \\ \max(b\eta_{ij}(k-1), \eta_{\min}) & \text{for } S_{ij}(k)S_{ij}(k-1) < 0 \\ \eta_{ij}(k-1) & \text{for other cases} \end{cases} \tag{4}$$

where $\eta_{\min}$, $\eta_{\max}$ are minimum and maximum values of training coefficient and a, b are respectively constants coefficients of increasing (usually $a=1.2$) and decreasing (usually $b=0.5$) of training coefficient and $S_{ij}(k)$ describes equation: [13]

$$S_{ij}(k) = \frac{\partial E\left(w(k)\right)}{\partial w_{ij}} \tag{5}$$

It is worth to comment that the RPROP algorithm increases training coefficient η_{ij} according (4), when in two following training steps the sign of error function gradient is the same, decreases it when the sign is changed and keeps its constant value when the gradient is zero. The last procedure step (for other cases) means that for $S_{ij}(k)=0$ the value of training coefficient η_{ij} is without change.

4 Simulation Results

Simulation investigations of proposed control system were provided on the computer model of the system in Matlab – Simulink. In the case of the on-line system initial weights were equal to zero. In the case of off-line - the weights are determined according to the procedure shown in [11]. Robust speed control has all the parameters constant. Controller adaptive parameters presented in this paper are updated with the double sampling time, and the parameters are variable. Other interesting properties of the adaptive controller is presented in [9,10]. This study

compared the robust speed controller with adaptive speed controller for the variable moment of inertia and the load as a function of the angle (Fig. 5). In both cases, good behavior of the speed loop provides good behavior of the position loop.

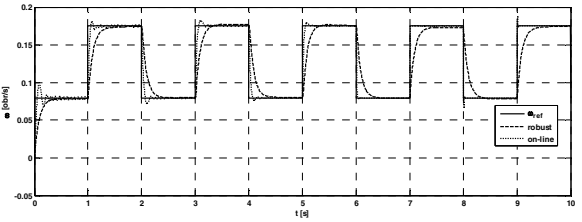

Fig. 5 Waveforms of actual speed and reference speed

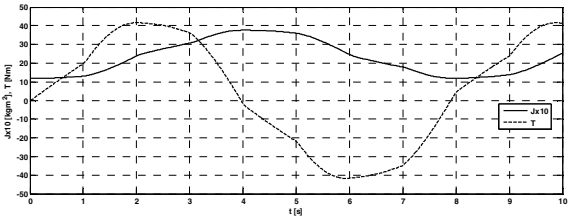

Fig. 6 Waveforms of the moment of inertia and load torque

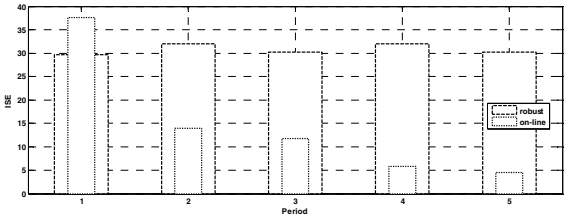

Fig. 7 ISE index value for each rate period of speed

The Fig.5-7 shows the results of simulations with adaptive speed controller ($T_a=2T_s$, T_a- adaptation time, T_s-sampling time) and robust speed controller [11]. Fig. 5 shows the reference and actual speed of the system during step change of speed. We can see at the beginning of the value of this index is a enough large for on-line process and then, this value is significantly decreased. The index value for neural robust control is similar, independent of changes of moment of inertia and load but has a higher value of the index ISE(Fig. 7). In addition, the adaptive dynamics system is faster compared to the robust system, but has a tendency to overshoot. Another major problem is step change of load torque. In Fig. 8 is shown the waveforms of speed during step change of load torque for the variable load torque. The arm has been set in two positions with minimum and maximum moment

of inertia and step change of load torque turn on. The robust controller has a higher index of ISE and settling time compared with adaptive controller (Table 1) .

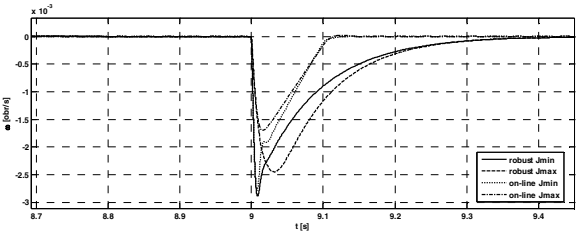

Fig. 8 Waveforms of speed on step change of load torque

Table 1 Index ISE and settling time for step change of load torque

Parameter name	Settling time [ms]	ISE
Robust J_{min}	202	0.035
Robust J_{max}	198	0.040
Adaptive J_{min}	90	0.020
Adaptive J_{max}	91	0.015

5 Experimental Results

Control algorithms were implemented on signal processor ADSP 21060. This processor allowed realizing control algorithm with sampling period equal 100 μs. The same period was assumed for PWM of inverter. The scheme of this stand was shown in previous works [9,11]. In the experimental studies was implemented a position control, shown in Fig 1. The triangular trajectory was set in the range of 0.3 to 0.7 rev. It should be noted that the used adaptive and robust neural speed controller in the system, ensures insensitive to changes on moment of inertia the position of the loop. These changes are included in the speed control loop. The adaptive speed control weight at the start were set to zero. The following figures show the results of experimental studies.

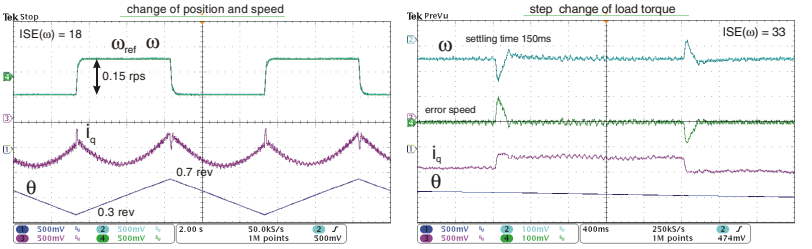

Fig. 9 Waveforms of the adaptive neural controller

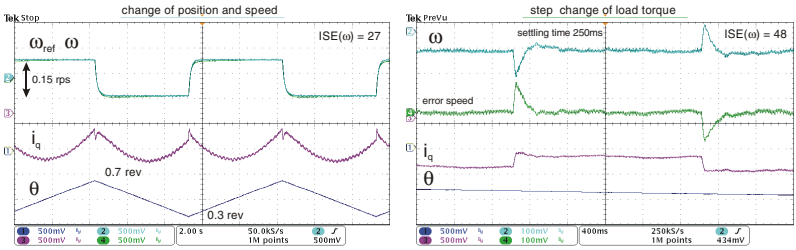

Fig. 10 Waveforms of the robust neural controller

In Fig. 9 and 10, we can see the results of the experimental response to changes in the position and speed, and step change of load torque for both controllers. Independent of the control system perfectly follows the setpoint, when the moment of inertia and the load as a function of angle is changed. In either case, the ISE index is higher for robust controller(Fig. 9,10). In addition the settling time to step change to load torque is lower for adaptive controller. The experimental results confirmed the simulation.

6 Conclusions

The concept of neural speed controller trained on-line was presented and compared with the neural robust control. The RPROP method was used to change weights on-line with fast transient processes. The results of simulation and experiments that confirm proper operation of the on-line and off-line neural speed control and the position control. The presented concept of the adaptive neural controller allows independent control dynamic properties of the speed to change servodrive parameters, especially the moment of inertia changes as a function of angle. The advantage of the adaptive controller is faster dynamics, lack of integral (no problem wind up), the smaller the speed error. The advantage of the robust controller are fixed parameters and certain behavior of the system when changing parameters.

References

[1] Akpolat, H.Z., Asher, G.M., Clare, J.C.: A practical approach to the design of robust speed controllers for machine drives. IEEE Transaction on Industrial Electronics 47(2), 315–324 (2000)

[2] Astrom, K., Hagglund, T.: PID controllers: Theory, design and tuning. ISA Research Triangle Park (1995)

[3] Ellis, G.: Control System Design Guide: Using Your Computer to Understand and Diagnose Feedback Controllers, 3rd edn. Elsevier, Academic Press (2004)

[4] Grzesiak, L., Meganek, V., Sobolewski, J.: Ufnalski B., DTC_SVM Drive with ANN-based Speed Controller. In: PELINCEC Conference. Warsaw University of Technology, CD (2005)

[5] Grzesiak, L.M., Meganek, V., Sobolewski, J., Ufnalski, B.: On-line Trained Neural Speed Controller with Variable Weight Update Period for Direct-Torque-Controller AC Drive. In: EPE-PEMC Conference, Portoroz, CD (2006)
[6] El-Sousy, F.F.M.: High-performance neural-network model-following speed controller for vector-controlled PMSM drive system. In: 2004 IEEE International Conference Industrial Technology, IEEE ICIT 2004, vol. 1, pp. 418–424 (2004)
[7] Orlowska-Kowalska, T., Szabat, K.: Control of the Drive System with Stiff and Elastic Coupling using Adaptive Neuro-Fuzzy Approach. IEEE Trans. on Industrial Electronics 51(4), 228–240 (2007)
[8] Leonard, W.: Control of electrical drives. Springer, Heiderberg (2001)
[9] Pajchrowski, T., Zawirski, K.: Adaptive Neural Speed Controller for PMSM Servodrive with Variable Parameters. In: Proceedings of EPE-PEMC 2012 ECCE Europe Conference and Exposition, Novi Sad, Serbia, September 4-6 (2012)
[10] Pajchrowski, T., Zawirski, K.: Application of artificial neural network for adaptive speed control of PMSM drive with variable parameters. In: Proceedings of XXII Symposium on Electromagnetic Phenomena in Nonlinear Circuits, EPNC 2012, Pula, Croatia, June 26-29 (2012)
[11] Pajchrowski, T., Zawirski, K.: Application of Artificial Neural Network to Robust Speed Control of Servodrive. IEEE Transaction on Industrial Electronics 54(1), 200–207 (2007)
[12] Riedmiller, M., Braun, H.: A direct adaptive method for faster backpropagation learning: The RPROP algorithm. In: IEEE International Conference on Neural Networks, March 28- April 1, vol. 1, pp. 586–591 (1993)
[13] Rahman, M.A., Hoque, M.A.: On-line adaptive artificial neural network based vector control of permanent magnet synchronous motors. IEEE Transactions on Energy Conversion 13(4), 311–318 (1988)
[14] Rutkowski, L.: Computational Intelligence Methodts and Techniques. Springer (2008)
[15] Vittek, J., Briś, P., Kakyś, P., Śtulrajter, M., Vavruś, V.: Control of Flexible Drive with PMSM emploing Forced Dynamics. In: Proc. 13th International Power Electronics and Motion (2008)

Hybrid Fuzzy – State Variable Feedback Controller of Inverted Pendulum

A. Petrovas and R. Rinkevičiene

Vilnius Gediminas Technical University, Faculty of Electronics, Naugarduko 41, LT-03227, Vilnius, Lithuania
{andrius.petrovas,roma.rinkeviciene}@vgtu.lt

Abstract. The inverted pendulum causes a lot of interest between special kind of both men made devices and found in natural world. Because the system is unstable and nonlinear it is often used for testing of new controllers. The proposed hybrid controller is composed of conventional state variable feedback controller and fuzzy controller, changing its gains. Equations of the controller are derived and presented, simulation results compared with results when single conventional state variable feedback controller is used.

1 Model of the Inverted Pendulum System

A schematic drawing of an inverted pendulum is shown in Fig. 1. System consists of a moving base (platform) *P* and the rod *S* fastened by ball joint to that. For simplification of the problem it is assumed that platform can move just in direction of *x* axis and rod can rotate with respect ball joint *0* in the drawing plane. The friction forces in the ball joint and between platform and base are neglected as well.

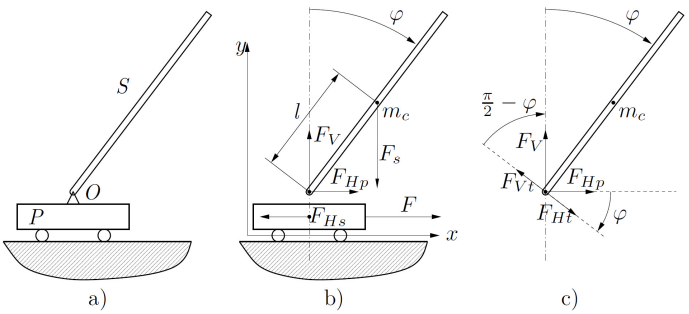

Fig. 1 A schematic drawing of inverted pendulum (a) and acting forces (b, c)

In the Fig 1.b. the forces, acting in the system are presented after replacing ball joint by corresponding reaction forces. Deflection of the pendulum from vertical line is controlled value – angle φ. The control task requires to change the platform

T. Březina and R. Jabloński (eds.), *Mechatronics 2013*,
DOI: 10.1007/978-3-319-02294-9_88, © Springer International Publishing Switzerland 2014

acting force F for keeping the rod in vertical position, which corresponds to the angle φ=0.

Set of differential equations, describing the inverted pendulum system dynamics is formed as [1]:

$$\begin{cases} F = (m+M)\ddot{x} - ml\ddot{\varphi}\cos\varphi + ml\dot{\varphi}^2\sin\varphi; \\ F_V = -ml\dot{\varphi}^2\cos\varphi - ml\ddot{\varphi}\sin\varphi + mg; \\ J\ddot{\varphi} = F_V l\sin\varphi + (F - m\ddot{x})l\cos\varphi. \end{cases} \quad (1)$$

where: m – mass of inverted pendulum rod; l – length of pendulum rod; J – inertia of pendulum rod; M – platform mass; g ≈ 9.8 m/s^2.

Our control task is to define such a function F=$f(t)$ that $\varphi \to 0$ if $t \to t_t$, where t_t – required settling time. Let us introduce the state vector $\mathbf{x}$=[v, ω, φ], where: v is speed of platform; ω is angular speed of rod and eliminate the variable F_v and make some rearrangements, then set (1) of equations can be expressed as:

$$\dot{\mathbf{x}} = \mathbf{A}(\mathbf{x})\mathbf{B}(\mathbf{x}, F); \quad (2)$$

where:

$$\mathbf{A}(\mathbf{x}) = a^{-1}\begin{bmatrix} J + ml^2\sin^2\varphi & ml\cos\varphi & 0 \\ -Ml\cos\varphi & M+m & 0 \\ 0 & 0 & a \end{bmatrix}; \quad (3)$$

$$a = (m+M)J + mMl^2 + (ml\sin\varphi)^2; \quad (4)$$

and:

$$\mathbf{B}(\mathbf{x}, F) = \begin{bmatrix} F - ml\omega^2\sin\varphi \\ -ml^2\omega^2\cos\varphi\sin\varphi + mgl\sin\varphi + Fl\cos\varphi \\ \omega \end{bmatrix}; \quad (5)$$

Using obtained expression (2), the simulation model can be carried out easy.

2 Hybrid Controller of Inverted Pendulum System

There are many methods to control inverted pendulum system. Detailed overview of those methods can be found in [2]. According [2] three main conceptions of controllers can be distinguished: controller based on PID regulator [2, 3], controller based on state feedback [4] and hybrid controller.

The main drawback of using PID regulator is related with its low robustness [2]. Another possible controller for inverted pendulum systems could be a state variable feedback controller [2, 4]. Its main advantage is robustness and accuracy. The biggest disadvantage is necessity to linearize the system; i.e control will be effective just near the point of linearization.

Modern control methods can deal with nonlinear systems. For example, fuzzy control methods are suggested for nonlinear systems or systems with uncertainties [5, 6]. Inverted pendulum is not exception - fuzzy controllers can be used for its control [7, 8, 9].

To unify the advantages of a state feedback controller and a fuzzy controller the hybrid regulator was suggested. The block diagram of such system is presented in Fig. 2.

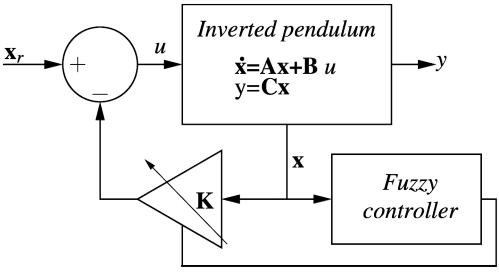

Fig. 2 The control system with hybrid fuzzy – state feedback controller

The Sugeno fuzzy controller operates together with state feedback controller. Fuzzy logic controller is used for adjusting feedback gain vector **K** according to the state variables vector **x**.

The angle φ will be measured using magnetoresistive sensors described by [10]. The ω will be calculated from φ. For the evaluation of v the MEMS accelerometer will be used.

Dynamics of inverted pendulum is described by set of equations (2). It can be noticed, that in closed loop control system the state variable **x** and system control signal F is related as:

$$F = -\mathbf{K}\mathbf{x} = -\begin{bmatrix} k_v, & k_\omega, & k_\varphi \end{bmatrix}\mathbf{x}. \tag{6}$$

Given the (6) vector (5) can be rewritten in the form:

$$\mathbf{B}(\mathbf{x},\mathbf{K}) = \begin{bmatrix} -k_v v - k_\omega \omega - k_\varphi \varphi - ml\omega^2 \sin\varphi \\ -ml^2\omega^2 \cos\varphi \sin\varphi + mgl\sin\varphi - \left(k_v v - k_\omega \omega - k_\varphi \varphi\right) l\cos\varphi \\ \omega \end{bmatrix}. \tag{7}$$

The closed loop system dynamics is described by differential equation:

$$\begin{bmatrix} \dot{v} & \dot{\omega} & \dot{\varphi} \end{bmatrix}^T = \mathbf{A}(\mathbf{x})\mathbf{B}(\mathbf{x},\mathbf{K}). \tag{8}$$

Design of controller for given operating point $\mathbf{x}=\mathbf{x}_0$ requires selecting gains k_v, k_ω and k_φ in the way to get coefficients of characteristic polynomial equal to desired one. The closed loop characteristic polynomial is:

$$d(s)\Big|_{\mathbf{x}=\mathbf{x}_0} = \Big|s\mathbf{I} - \mathbf{J}\left(k_v, k_\omega, k_\varphi\right)\Big|_{\mathbf{x}=\mathbf{x}_0}\Big| = \mathrm{s}^3 + d_2\mathrm{s}^2 + d_1\mathrm{s} + d_0. \tag{9}$$

where $\mathbf{J}$ is Jacobi matrix of (9).

If the coefficients of characteristic equation (9) will be denoted as vector $\mathbf{D}(k_v, k_\omega, k_\varphi)=[d_2\ d_1\ d_0]$ and coefficients of desired one as vector $\mathbf{E}=[e_2\ e_1\ e_0]$ the equality as:

$$\mathbf{E} = \mathbf{D}\left(k_v \quad k_\omega \quad k_\varphi\right)\Big|_{\mathbf{x}=\mathbf{x}_0} \tag{10}$$

must be valid. Design of controller requires finding variables k_v, k_ω and k_φ, i.e. vector $\mathbf{K}$, at chosen operating point $\mathbf{x}_0$.

The desired values of coefficients can be found using some kind of well-studied functions. The common solution is to use of the characteristic equation which minimize the *ITAE* integral criteria [1]. If required settling time is about 2 s, then desired coefficients vector is $\mathbf{E}$ = [5.25, 19.35, 27].

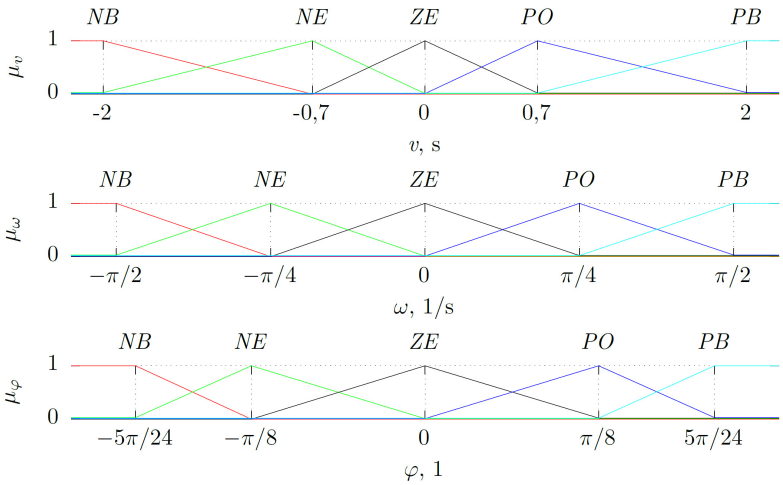

Fig. 3 Membership functions

It is quite difficult to solve equation (10) in analytic way; however the numerical solution can be obtained. For this purpose the standard function for numerical solution of nonlinear equations "fsolve", which is available in "GNU Octave", was used.

The fuzzy sets describing each controllable state variable are presented in Fig. 3. The parameters of membership functions are determined during series of numerical simulations.

According to Fig. 3 each state variable can be described by five linguistic variables, so the set of the linguistic variables is described as $\boldsymbol{L}$={*NB*, *NE*, *ZE*, *PO*, *PB*}. Let us suppose that the linguistic variables from the set $\boldsymbol{L}$ can be indexed, i.e. $\boldsymbol{L}_1$=*NB*, $\boldsymbol{L}_2$=*NE*, … , $\boldsymbol{L}_5$=*PB*. In this case the rules, on which the fuzzy controller is based, can be described in this way:

$$\boldsymbol{R}_r\text{: IF } (v \text{ is } \boldsymbol{L}_k) \text{ AND } (\omega \text{ is } \boldsymbol{L}_m) \text{ AND } (\varphi \text{ is } \boldsymbol{L}_n) \text{ THEN } \mathbf{K}_r=[k_{v\mathrm{r}}, k_{\omega\mathrm{r}}, k_{\varphi\mathrm{r}}]; \tag{11}$$

where $\boldsymbol{R}$ – rules set; $r = 25k + 5m + n - 30$ is index of the rule in the set $\boldsymbol{R}$; k, m, and n are indexes of linguistic variables and take integer values from 1 to 5; $\mathbf{K}_r$ – output vector of r-th rule; $k_{v\mathrm{r}}$, $k_{\omega\mathrm{r}}$ and $k_{\varphi\mathrm{r}}$ are numerically obtained solutions of equation (10) when $\mathbf{x}$=[core($\boldsymbol{L}_k$), core($\boldsymbol{L}_m$), core($\boldsymbol{L}_n$)].

In total with chosen system of fuzzy sets there are 5^3=125 rules therefore the output signal of fuzzy controller can be expressed as:

$$\mathbf{K} = \frac{\sum_{r=1}^{125} \mu_r \mathbf{K}_r}{\sum_{r=1}^{125} \mu_r}; \tag{11}$$

where μ_r is truth value of r-th rule.

3 Analysis of the System with Hybrid Controller

Designed hybrid fuzzy – state feedback controller is improved version of controller with state variables feedback therefore comparison of its results allows carry out advantages and shortcomings of those systems.

Investigated inverted pendulum system is characterized by parameters: m = 0.2 kg; l = 0.2 m; J = 0.01667 kg m^2; M = 1 kg.

Transients of the state variables in the system with Sugeno fuzzy controller are presented in Fig. 4. Solid lines are used for transients in the system with fuzzy controller, dash lines with state variable controller correspondingly. Initial conditions are ω_0 = 0.1 s^{-1}; .φ_0 = 0.1; v_0 = 0 and x = 0.

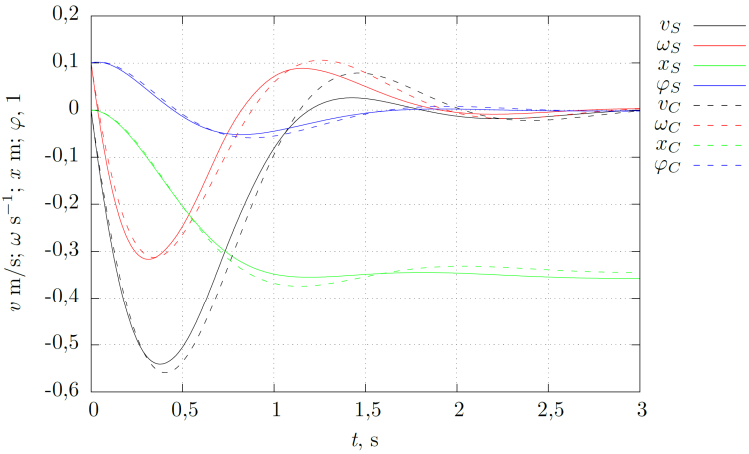

Fig. 4 Transient processes at $\omega_0 = 0.1$ s^{-1}; .$\varphi_0 = 0.1$; $v_0 = 0$ and $x = 0$

Analysis of pendulum declination angle φ with 2.5 % error of steady state value shows the settling time $t_p \approx 2$ s with hybrid controller, as with conventional feedback state variables controller it reaches 2.3 s. Overshoot using the fuzzy logic controller are also smaller.

So if the initial conditions are close to zero, there is no evident difference between conventional or fuzzy – state feedback controllers. It can be explained by linearization of nonlinear system in the operating point $\mathbf{x}_0$=[0 0 0].

The transient processes with initial conditions $\omega_0 = 0$ s^{-1}; .$\varphi_0 = 5\pi/24$; $v_0 = 0$ and $x = 0$ are shown in Fig. 5.

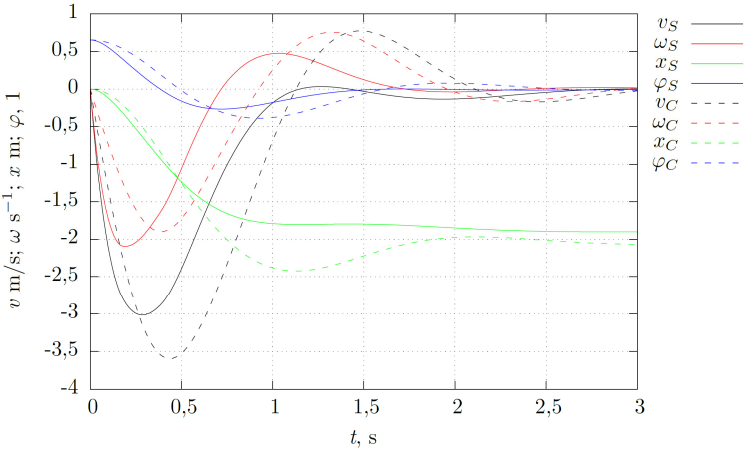

Fig. 5 Transient processes at $\omega_0 = 0$ s^{-1}; .$\varphi_0 = 5\pi/24$; $v_0 = 0$ and $x = 0$

Fig. 5 shows, that evident differences between both controllers appear at non zero initial conditions. Quantative analysis of rod declination angle, assuming the steady error of 2.5 %, in the system with fuzzy logic controller gives the output settling time $t_p \approx 1.5$ s; otherwise, in the system with conventional feedback variable controller, the settling time is $t_p \approx 3$ s.

Analysis of transients in Fig. 4 and Fig. 5 indicates that hybrid fuzzy logic – state feedback controller gives even better specifications of dynamic characteristics than were chosen in the task. Of course, the forces, acting in the system increases as well as the power, used for control, what sometimes can be undesirable.

4 Conclusions

1. The hybrid controller of inverted pendulum system is proposed, comprising state variables feedback and fuzzy logic controller.
2. The system with hybrid controller has not advantages in comparison with conventional state variables feedback controller when the initial conditions are close to linearization point.
3. The main advantages of proposed hybrid controller against conventional state variables feedback controller is ability to match dynamic specifications at moving away from linearization point.
4. The main shortcoming of proposed controller appears in more complicated its design: feedback gains should be calculated by numerical methods, there is no settled method for design of fuzzy portion of controller.
5. The system error can be reduced by increasing number of membership functions, but this way increase the overall number of rules.

Acknowledgments. This research is funded by the European Social Fund under the project "Microsensors, microactuators and controllers for mechatronic systems (Go-Smart)" (Agreement No VP1-3.1-ŠMM-08-K-01-015).

References

[1] Werner, R.: Einführung in die Mechatronik, p. 483. Teubner (2006)
[2] Akhtaruzzaman, M., Shafie, A.A.: Modeling and control of a rotary inverted pendulum using various methods, comparative assessment and result analysis. In: Proc. on International Conference on Mechatronics and Automation (ICMA), August 4-7, pp. 1342–1347 (2010)
[3] Li, W., Ding, H., Cheng, K.: An investigation on the design and performance assessment of double-PID and LQR controllers for the inverted pendulum. In: Proc. on 2012 UKACC International Conference, September 3-5, pp. 190–196 (2012)
[4] Rybovic, A., Priecinsky, M., Paskala, M.: Control of the inverted pendulum using state feedback control. In: ELEKTRO, pp. 145–148 (2012)
[5] Lilly, J.H.: Fuzzy Control and Identification, p. 231. Wiley (2011)

[6] Schröder, D.: Intelligente Verfahren: Identifikation und Regelung nichtlinearer Systeme, p. 750. Springer (2010)
[7] Poorhossein, A., Vahidian-Kamyad, A.: Design and implementation of Sugeno controller for inverted pendulum on a cart system. In: 8th International Symposium on Intelligent Systems and Informatics (SISY), September 10-11, pp. 641–646 (2010)
[8] Zhao, B., Li, S.: Design of a Fuzzy Logic Controller by Ant Colony Algorithm with Application to an Inverted Pendulum System. In: IEEE International Conference on Systems, Man, and Cybernetics, pp. 3790–3794 (October 2006)
[9] Lee, G.H., Jung, S.: Control of inverted pendulum system using a neuro-fuzzy controller for intelligent control education. In: IEEE International Conference on Mechatronics and Automation, August 5-8, pp. 965–970 (2008)
[10] Žurauskienė, N., Balevicius, S., Stankevic, V., Keršulis, S., Schneider, M., Liebfried, O., Plausinaitiene, V., Abrutis, A.: B-Scalar Sensor Using CMR Effect in Thin Polycrystalline Manganite Films. IEEE Transactions on Plasma Scienc 39(1), 411–416 (2011)

A Model Comparison Performance Index for Servo Drive Control

J. Quellmalz, M. Rehm, H. Schlegel, and W.-G. Drossel

Chemnitz University of Technology, Institute for Machine Tools and
Production Processes (IWP), Division Control and Feedback Control Systems,
Reichenhainer Strasse 70, 09126 Chemnitz, Germany
{Qjo,mreh,schho}@hrz.tu-chemnitz.de, wzm@mb.tu-chemnitz.de

Abstract. This paper describes an approach for monitoring closed loop speed control of electromechanical drives. The data of the closed loop is evaluated and concentrated to a performance index, giving a scalar value to measure setpoint change behavior. The method uses an order-reduced model as comparison basis to closed-loop signals, which is possible to implement on controller equipment. Parameterization of the comparison model is addressed even pointing out a provision without requiring a-priori knowledge. Influence of the main parameters is shown by means of simulation results. Following, experiments are carried out and compared to theoretical results. In conclusion usability and possible further improvement is discussed.

1 Introduction

In the field of process industry methods of control performance assessment (CPA) or control loop performance monitoring (CLPM) are known and widely applied. This is due to the large number of control loops and the impossibility to examine the loops operation by hand. So it is a great deal to have automatic tools to detect loops which are in bad operation to be examined further by hand [1][2]. In contrast, monitoring in cascaded position control like e.g. at machine tools, is implemented only in the sense of rough error detection Examples are switch-off limits for position error and time of maximum current flow (e.g. in case of mechanical defect/collision). Methods known cannot be easily applied in context of drive control, since there are key differences to process industry [3, pp. 66]. Some efforts have been made however [4][3]. A main problem in application is that CLPM methodology concentrates on performance in the sense of disturbance rejection - setpoint changes are rather seldom in the field of process industry. But for servo drives command action is of high interest. The paper proposes a performance index. In CLPM this is a scalar value representing the control loops behavior in some criterion. This paper offers a new approach based on comparing signals of the drive to a model calculated in parallel.

T. Březina and R. Jabloński (eds.), *Mechatronics 2013*,
DOI: 10.1007/978-3-319-02294-9_89,

2 Reduced Order Model Comparison

The model used to construct the performance index shall have only few parameters to be set up. Therefore the speed control loop is broken up in the PI-speed-controller itself and a reduced order model of the plant – which is the closed loop current control and the mechanics. In servo control theory and practice it is not unusual to use a first order lag element for the closed current control loop and a gained integrator for the mechanics representing a single mass system [5, p. 231]. So there are only four parameters for the loop as seen in figure 1. Setpoint filters can be applied but are not modelled or part of the performance measurement itself; only the filtered setpoint is used for model comparison then.

Table 1 Parameters of the modeled speed control loop

Symbol	parameter name	Unit	
		Rotary system	translational system
K_p	speed controller gain	$Nm \cdot s / rad$	$N \cdot s / m$
T_n	speed controller integral time	ms (milliseconds)	ms (milliseconds)
T_Σ	sum time constant	ms (milliseconds)	ms (milliseconds)
J	moment of inertia	$kg \cdot m^2$	kg

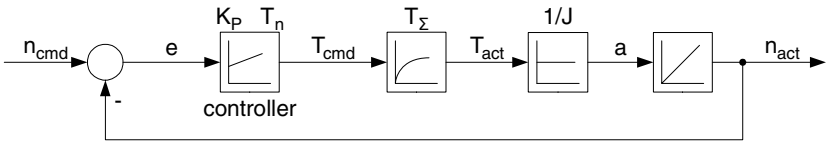

Fig. 1 Block diagram of the closed loop speed control incl. reduced order plant

2.1 Comparison Method

For comparing the model to the drive, a time-domain signal comparison is made. The concept is aligned to the integral criterion IAE (integral of absolute error, [6, p.419]), using not the control error alone but the difference between the control errors of the drive and the model.

A key feature of a performance index is the normalization, which ideally should result in independence from system excitation and a bounded interval for the performance index. The proposed scheme as seen in fig. 2 calculates IAE for the comparison model alone and lets the performance index be the ratio to this value, which can be seen as scaling. By doing this, the performance index is not right-bounded but made more excitation independent.

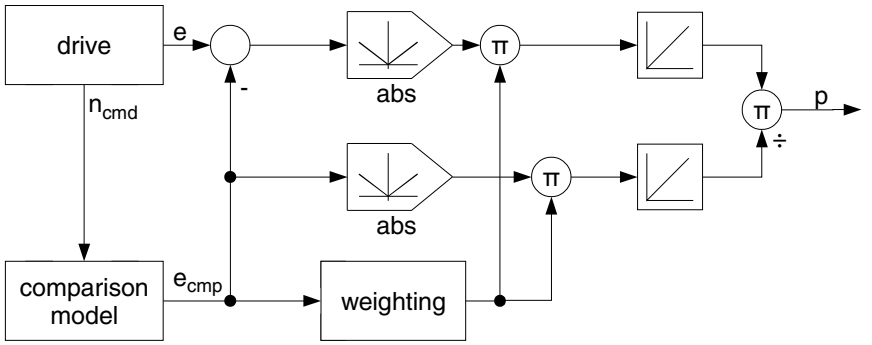

Fig. 2 Block diagram of the performance index calculation

Also, a weighting is implemented. Experiments have shown, that p is slightly growing over time although no setpoint activity is in the system, caused by signal noise or stochastic disturbance. By neglecting these time periods with signal weighting, this effect is reduced and only time periods with command activity are singled out. In contrast to fig.2 also a slower system than the comparison model could be discussed to gain more weight on control settling.

Avoiding inner loop signals of the drive as basis for scaling and weighting has the advantage, that noise and stochastic disturbance do not affect the performance index by way of these.

2.2 Parameterization

For the speed controller, an optimization rule for tuning controller parameters is the symmetrical optimum (SO) [5, p. 61]. Applied to the reduced order model used here, the controller parameters can be calculated as

$$T_n = a^2 \cdot T_\Sigma \tag{1}$$

$$K_p = \frac{J}{a \cdot T_\Sigma} \tag{2}$$

with additional parameter a for commissioning freedom [7, p. 73].

When it comes to the task of performance assessment for a given drive setup, the used controller parameter set is given, e.g. tuned at commissioning the servo drive. So, when the parameters of the comparison model used by the performance index are calculated inversely to formulas (1) and (2), it enables the performance index to measure closed-loop dynamic in terms of closeness to symmetrical optimum. Without a priori knowledge With a=2, a common setting for SO [8, p. 118], the comparison model can be parameterized as follows:

$$T_{\Sigma,cmp} = \frac{T_n}{4} \tag{3}$$

$$J_{cmp} = K_p \cdot 2 \cdot T_{\Sigma,cmp} = K_p \cdot \frac{T_n}{2} \tag{4}$$

Another approach would be the usage of model parameters identified by automatic algorithms such as proposed e.g. in [9]. So parameter or basic model deviations could possibly be monitored over time by the index. However, this is not carried out further in this paper.

For weighting, the following calculation is used throughout the paper:

$$weight = \left|e_{cmp}\right| + T_{\Sigma,cmp} \cdot \left|\frac{d\,e_{cmp}}{d\,t}\right| \tag{5}$$

2.3 Simulation

The performance index has been analyzed by simulating the drive as seen in fig. 2 similar to the comparison model as seen in fig. 1. The results are shown in fig. 3, exemplary time plots are shown in fig. 4.

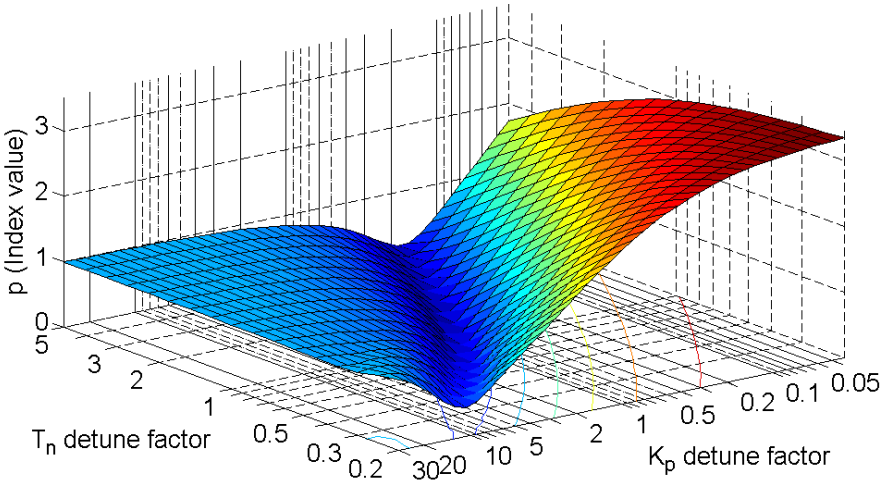

Fig. 3 Index result for logarithmic controller detuning

Of course, the index gives a value of zero for the tuned case, i.e. the controller is tuned by SO according to the reduced order model; this is measured as the best performance by this index. For both controller gain and integral time detuned upwards, the index converges to one. This is because the control loop reacts faster and the comparison model slower than a SO tuned loop (compare fig. 4

bottom-left) and therefore the integral of the difference of the control errors (comparison model to drive) approximates the control error of the comparison model itself. For the opposite area, the detuned loop acts with lower damping, tending to oscillation resulting in greater index values. Although the index has no upper bound, no order of magnitude is attained. In between, close but not exactly on the line with gain detuned inversely to integral time, is a "ditch" with relatively low index values indicating good performance while the controller is heavily detuned. So, these mistuned cases cannot be detected with high significance by this index. The reason behind is that the comparison models moment of inertia calculated by (4) is close/identical to the real moment of inertia for these cases, resulting in less difference in comparison, although absolute comparison to the SO-tuned loop shows major differences in behavior (compare fig. 4 right to top left).

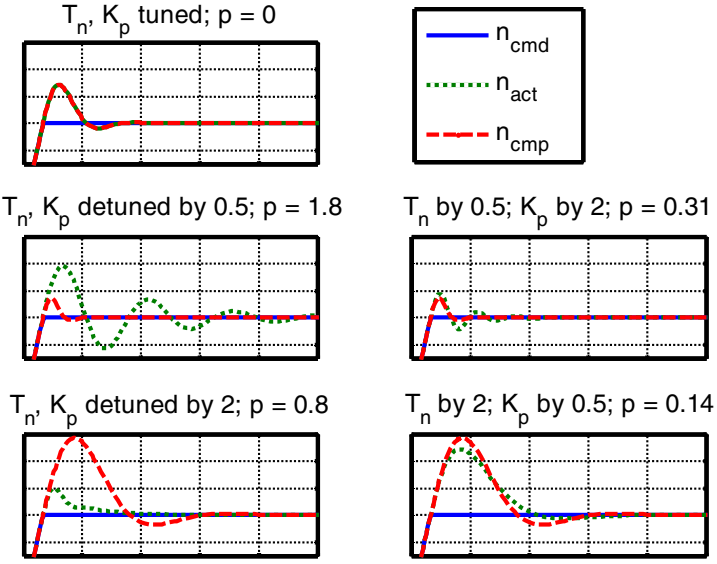

Fig. 4 Exemplary time plots of speed values, excitation by acceleration limited speed step

Simulations have been done for different excitations also, showing good independence for acceleration limited signals, e.g. ramps or trapezoidal velocity characteristics.

3 Experiments

Experiments have been carried out at a linear drives test bench, described in detail in [10]. The used z-axis is a synchronous iron core linear motor with permanent magnet excitation. Basic parameters are listed as follows.

Table 2 Basic parameters of the experimental setup

J	T_Σ	K_p tuned to SO	T_n tuned to SO
20 kg	0.625 ms	16000 Ns/m	2.5 ms

Four different controller setups and load mass variation are checked experimentally. Therefore, data is recorded via the engineering software of the drive by a sampling rate of 1.25 milliseconds, which is factor 10 to the underlying controller sample rate. The calculation of the comparison model and the performance index is done offline. In view of application, different acceleration limited excitation with closeness to practical relevance were used.

Table 3 Controller setups used for experiments

	K_p	T_n	setpoint filter time constant	
A)	16500	2.50	2.5 ms	close to tuning according to SO
B)	21000	1.90	1.9 ms	SO based on erroneous T_Σ
C)	4250	4.25	not applied	close to automatic tuning by drive system
D)	32000	5.00	0.6 ms	doubled to SO, as in [8, p. 126]

3.1 Results

As seen in table 3, the minimum value in each column is found at controller settings A or B, since they are close to the tuning tested for by the index. The slightly detuning of B cannot be detected, since it is also in the "ditch" seen in fig. 3. Trapezoidal oscillating excitation delivers closer values to the simulation results than unidirectional excitation. The cause is seen in friction at zero speed with its nonlinear characteristic. All experiments result in higher performance index values due to noise and stochastic disturbance which cannot be completely avoided.

Table 4 Experimental results comparing different excitations and controller setups

	K_p	T_n	trapezoidal (unidirectional)	trapezoidal + setpoint filter	trapezoidal, oscillating	trapez., osc. + setp. filter	simulation result
A)	16500	2.50	0.179	0.118	0.113	0.092	0.031
B)	21000	1.90	0.240	0.144	0.107	0.117	0.097
C)	4250	4.25	0.974	not applied	0.828	not applied	0.746
D)	32000	5.00	0.879	0.821	0.819	0.817	0.800

Table 5 Experimental results, moment of inertia modified (trapezoidal oscillating excitation, controller setup A)

mass	experimental result	simulation result
20 kg	0.113	0.031
28 kg	0.301	0.321
36 kg	0.499	0.596

As seen in the table above, increasing moment of inertia without changing controller parameters can be detected with good significance in the experiments, comparable to the simulation results.

4 Conclusions

The proposed performance index can be used to assess command action performance of a servo drive in terms of the parameterization of the comparison model. By reversing a tuning rule, the comparison model can be parameterized without any a priori knowledge, with the drawback of low significance for some controller detuning directions. Basic operation has been proven by using data directly from a test bench with different acceleration limited excitations Also significance for additional load mass has been shown experimentally. An online implementation, i.e. calculation of the index on drive controller equipment, is seen to be achievable straight forward; possible additional communication dead times have to be taken care of. Influence of friction can distort when calculation of the index includes a good deal of starting or settling at zero speed.

Future work has to be done by checking operation under position control and with multi-mass mechanical systems. With low significance for some cases, the performance index should not be used solely but combined with other indices to attain a substantiated picture. For practical long-term application, thoughts have to be made since the index as proposed in the paper has absolute memory. A forgetting factor similar to [11] reducing the value of the error integrators exponentially, preferably also weighted to the comparison model activity is seen most promising for this.

Acknowledgments. The Cluster of Excellence „Energy-Efficient Product and Process Innovation in Production Engineering“(eniPROD®) is funded by the European Union (European Regional Development Fund) and the Free State of Saxony.

References

[1] Jelali, M.: An overview of control performance assessment technology and industrial application. Control Engineering Practice 14, 441–466 (2006)
[2] Jelali, M.: Regelkreisüberwachung in der Metallindustrie Teil 1. 54(1), 34–46 (2006)
[3] Schönherr, R.: Regelkreisüberwachung mechatronischer Antriebssysteme, Dissertation, Verlag Wissenschaftliche Scripten, Auerbach/Germany (2012) ISBN: 978-3-942267-56-4
[4] Neugebauer, R., Schönherr, R., Schlegel, H., Quellmalz, J.:‘Überwachung und Bewertung von Antriebsregelungen. IEE Elektrische Automatisierung + Antriebstechnik, no. 11. Verlag Hüthig GmbH, Heidelberg, pp. 112 – 115 (2010), http://www.iee-online.de
[5] Schröder, D.: Elektrische Antriebe – Regelung von Antriebssystemen. Springer, Heidelberg (2009)
[6] Lutz, H., Wendt, W.: Taschenbuch der Regelungstechnik, Verlag Harri Deutsch, Frankfurt a.M (2005)
[7] Hofmann, S.: Identifikation parametrischer Modelle für geregelte elektromechanische Achsen mit modifizierter sukzessiver Polkompensation, Dissertation, Verlag Wissenschaftliche Scripten, Auerbach/Germany (2012) ISBN: 978-3-942267-64-9
[8] Groß, H., Hamann, J., Wiegärtner, G.: Elektrische Vorschubantriebe in der Automatisierungstechnik, SIEMENS. Publics Corporate Publishing, Erlangen (2006)
[9] Neugebauer, R., Hellmich, A., Hofmann, S., Schlegel, H.: Non-Invasive Parameter Identification by Using the Least Squares Method. The Archive of Mechanical Engineering LVIII, 185–194 (2011), doi:10.2478/v10180-011-0013-7
[10] Rehm, M., Quellmalz, J., Schlegel, H., Neugebauer, R.: Mechanically linked, gravity free linear drives test bench. In: Proc. LDIA 2011 - Eighth International Symposium on Linear Drives for Industrial Application, Eindhoven, pp. 219–224 (2011)
[11] Hägglund, T.: A Control loop performance monitor. Control Engineering Practice 3(11), 1543–1551 (1995)

Control Structures for Opposed Driving, Coupled Linear Drives

M. Rehm, J. Quellmalz, H. Schlegel, and W.-G. Drossel

Chemnitz University of Technology, Institute for Machine Tools and Production Processes (IWP), Division Control and Feedback Control Systems, Reichenhainer Strasse 70, 09126 Chemnitz, Germany
{mreh,qjo,schho,wzm}@hrz.tu-chemnitz.de

Abstract. In manufacturing linear motors are mainly used in the field of lightweight and highly dynamic drives. The high acceleration forces leads to vibration excitations of the machine structure that causes production inaccuracies. This can be improved by coupling two corporate acting and opposed driving linear drives in one drive train. The coupled structure can improve the static and dynamic properties by distributing the forces between both drives. In order to guarantee the requirement for high accuracy in synchronous tracking, control structures and controller tuning methods are going to be discussed based on simulation and experimental results.

1 Introduction

The conflict in the field of manufacturing consists in the reduction of cycle time by high drive dynamics while maintaining a high manufacturing accuracy. As the weakest part in the drive train, feed axes often determine the overall dynamics. These are composed of a defined number of inertias which are connected by coupling elements such as spring-damper systems or gears. The stiffness and damping of the coupling elements thereby limit the dynamics of the feed axis. An alternative to the traditional feed axes with coupling elements, such as ball screw or rack and pinion drives, are electric linear drives, short linear motors.

These consist in a first approximation of a single-mass system without any coupling elements which is the reason for higher achievable dynamics. On the other hand linear motors are limited in their maximum power and require enhanced security measures when used as vertical axes, which is why they are so far mainly used as horizontal feed axes with limited inertia. Therefore, current research focuses on advanced concepts and new solutions to extend the range of linear motors in the industrial sector. General approach in the area of the feed axes deals on the one hand with the structural modification of the mechanical part of topics such as lightweight construction, stiffness increase, drive coupling or structural integration to improve the dynamic properties of feed axes. On the other hand, closed-loop control engineering approaches exist. These are focused on

T. Březina and R. Jabloński (eds.), *Mechatronics 2013*,
DOI: 10.1007/978-3-319-02294-9_90,

suitable control structures and parameter settings for best possible tuned controllers by means of system identification procedures and control loop monitoring for a given mechanism under defined conditions. A large number of individual solutions for both approaches exist, which are always limited by the fixed parameters from the mechanical or control components.

For a holistic solution to the conflict, the system of feed axis has to be considered and optimized as a whole of mechanics and automation solution. Thus, there are approaches by coupling of linear motors to utilize their advantages in terms of dynamics by simultaneous increase of the maximum force. Typically this is realized by synchronized portal axes, so called gantry stage [1]. These have the decisive disadvantage that caused by the high dynamics and the same direction of motion of the linear motors large reaction forces into the machine frame are resulting. Similarly, the type of drive arrangement is inappropriate for vertical axes, since the weights have to be compensated and additional brake elements must be provided in case of failure. Through a novel arrangement of linear motors [2] in which both coupled drives are moving in opposite directions, the static and dynamic forces can be distributed and regulated specifically in contrast to all previous approaches. Within this paper the opposed driving coupled linear motor arrangement will be presented. Based on this, several control structures their parameterization will be introduced and discussed. Following, the effects and control precision for the different control structures will be shown by comparing the results of a simulation model and an existing test-bench.

2 Control Structures for Coupled Drives

In industrial use control structures for coupled drives are based on a cascade control of a single servo drive. Depending on the specific structure coupled drive structures only differ with respect to a single servo drive control by additional controllers, filters and feedforward paths. For this reason, the cascade control is going to be used at this point as the basis and its structure and parameterization is referred to Literature [3-7]. In the following, the different control structures for coupled drives will be presented and discussed.

The first control structure for coupled drives to be discussed is the common parallel control (PC) as shown in figure 1. In this, the contour control provides for each drive its own set point values and the drives are executing independently (parallel) from each other the given motion commands.

The set point relation between both drives can be expressed by a gear ratio, which is in case of mechanical coupled linear drives one. Caused by no tuning rules for this kind of control structure in literature, a parameterization based on the tuning rules for a single drive with cascade control is recommended. The current controllers are tuned based on the electrical part of the motor. The velocity controller shows good results when it is set, depending on stiffness and damping, according to the symmetrical optimum [3] or a two-mass system [7].

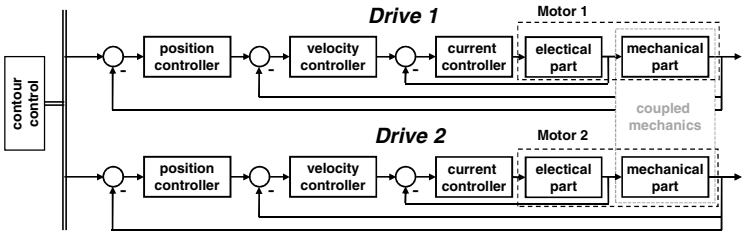

Fig. 1 Parallel Control (PC) for two mechanical coupled drives

The master-slave control (MSC) is a second control structure for coupled drives in industrial use. It is characterized by a system of one master and another slave drive. As shown in figure 2, the master drive gets the set point values from the contour control. Different to PC, the other drive (slave) gets the actual value of the master drive as its set point value. To adapt both drives, a ratio gain is in the set point path of the slave drive. A feedforward gain for the master drive to the velocity path to the slave drive (dotted line) is commonly used for faster response.

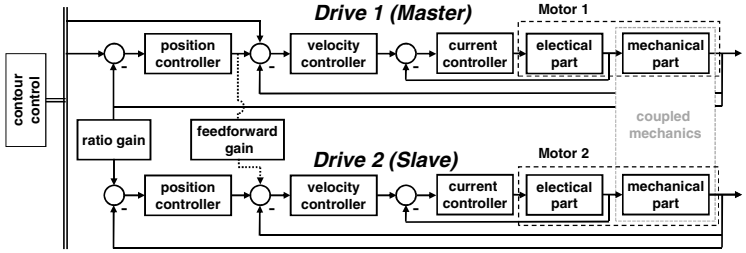

Fig. 2 Master-Slave Control (MSC) for two mechanical coupled drives

Caused by the occurring servo lag error MSC is mostly used in applications that are not so dynamically. Approved tuning rules are equal with those for the PC. Next to the industrial standard applications PC and MSC other control structures are established in the research area. First to be mentioned is the relative stiffness control (RSC) [1]. As shown in figure 3, this structure is characterized by the independent velocity loops of both drives with only one position controller on the master drive and the possibility to compensate servo lag error by an additional synchronous controller.

Typically a PI controller is used as synchronous controller, but only weak tuning rules are given. Basically the synchronous error, the difference between the actual velocities, is used for the design process. To obtain these values, the coupled mechanical system is described by using a p-canonical structure for the transfer functions. As a result, the two drive side transfer functions (influence of each drive to its own mechanics) and the two load side transfer functions (influence of each drive to the other drive mechanic) are generated [7].

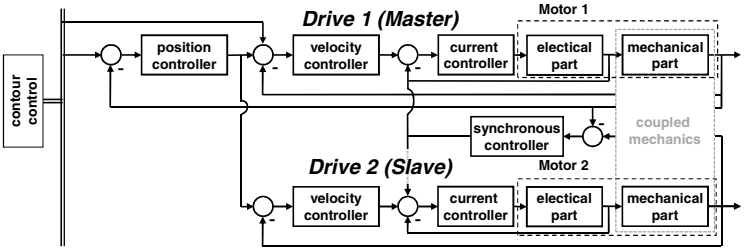

Fig. 3 Relative-Stiffness Control (RSC) for two mechanical coupled drives

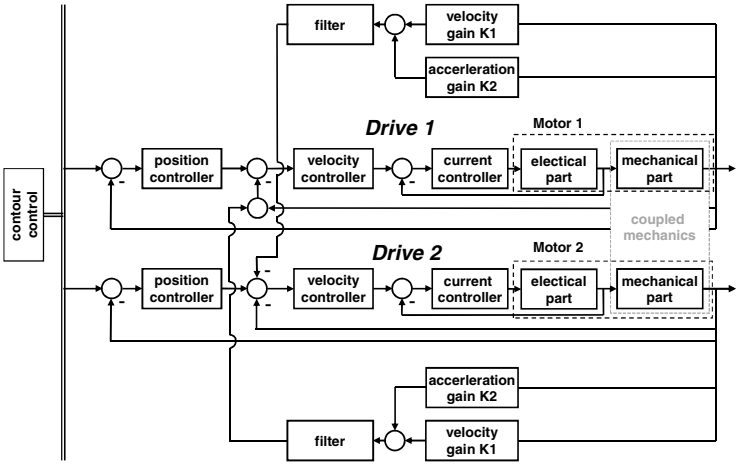

Fig. 4 Advanced Position Control (APC) for two mechanical coupled drives

By tuning the synchronous controller based on the tuning rules [3] such that the resulting bandwidth correlates with the resonance frequency of the two-mass-system of the coupled drives mechanics, a good performance of the system can be obtained.

The last control structure to be compared is the advanced position control (APC). Basically it is an extension of a single servo drive control with a two-mass system. Beside the position measurement of the drive mass, a position measurement of the load side is integrated. This new obtained signal is used as velocity and acceleration feedback. Each feedback is separately amplified and the sum is filtered. The filter is typically a PT2-filter with the resonance frequency of the two-mass system. This control structure can be adapted to a coupled drive system, as shown in figure 4. Here the measurements are additionally across linked. As described in [8], the dynamics could be improved by using simulation tools coupled with parameter optimizer. Until now, no generalities in literature [9] exist.

3 Simulation Model of Coupled Linear Drives

For comparison of simulation and experimental results a MatLab/Simulink® model of a constructed test bench [2] is developed. The simulation model, shown in figure 5, consists on the one hand of the mechanical part of coupled system (green) with friction, cogging, damping and stiffness forces. On the other hand, the controller parts (red, blue) with its cascade control structure are modeled.

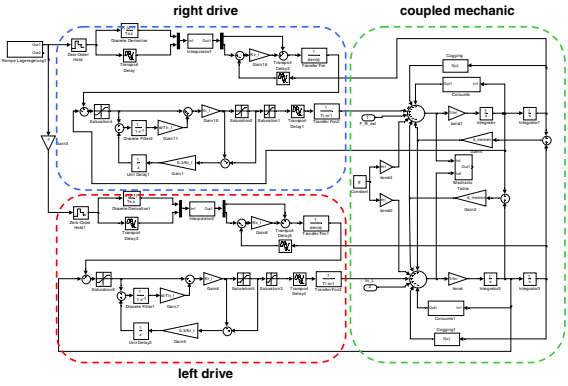

Fig. 5 Simulation model of the mechanically coupled linear motors

The model of the servo drive controller is divided into the current control loop, which is estimated as a FOPDT model, the velocity control loop with PI controller and the position control loop with a P controller, feedforward control and symmetric filter. For the adjustment of the simulation model with the test bench, several parameters (time constants, mechanical parameter) were identified [3]. Comparisons between the simulation model and experimental test-bench results show a good correlation.

4 Different Control Structures in Simulation and Experiment

The comparison of the four presented control structures is made in the time domain based on simulation and experimental results. Beside the overshoot the settling time are evaluation criteria. In addition to the command value the disturbance behavior is considered. For this a velocity test function is used with a velocity step (command value behavior) and a force step (disturbance value behavior). In a first study, PC and MSC are compared in simulation and experiment.

Basis of the study is a closed velocity loop structure (open position loop) with a velocity set point step. The parameter for simulation and experiment are identically and can be found in table 1.

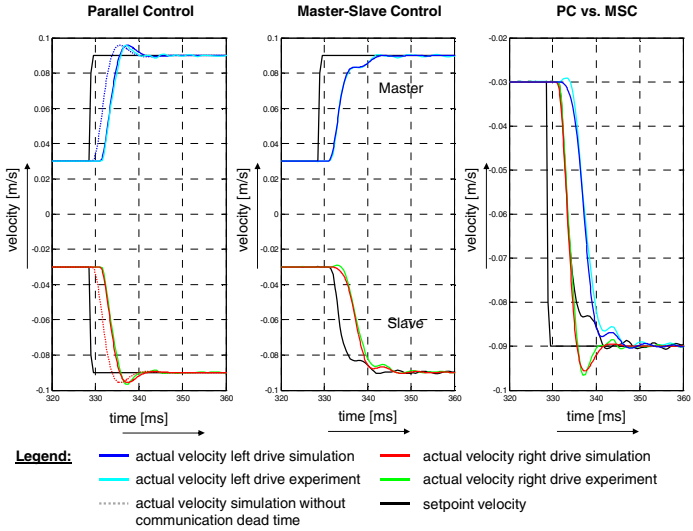

Fig. 6 Simulation and experimental results for PC and MSC

Table 1 Controller parameter for comparison of PC and MSC

parameter	parameter name	value
K_I	current loop gain	13.405 VA^{-1}
$T_{n,I}$	current loop integral time	2 ms
$f_{I,l}$	current loop set point filter	1.5 kHz
K_P	velocity loop gain	16667 Nsm^{-1}
$T_{n,P}$	velocity loop integral time	2.5 ms
$m_L = m_R$	mass left/right drive	19.6 kg

A very good correlation between simulation and experiment, as shown in figure 6, reflects the high quality of the simulation model, which is also important for further studies and comparisons based on simulation results. Caused by communication dead time the simulation model was adopted (dotted vs. solid line) to the experimental constraints. The comparison between PC and MSC shows the faster and more dynamic behavior of PC.

In a second study the set point and disturbance value behavior of PC, MSC, RSC and APC are compared based on simulation results. The left column in figure 7 shows the set point, the right column the disturbance step behavior of the velocities. Depending on the chosen structure, the upper row shows the left/master drive, the lower row the right/slave drive. Now, different form the first study, all control loops are closed and a position ramp is given as set point trajectory.

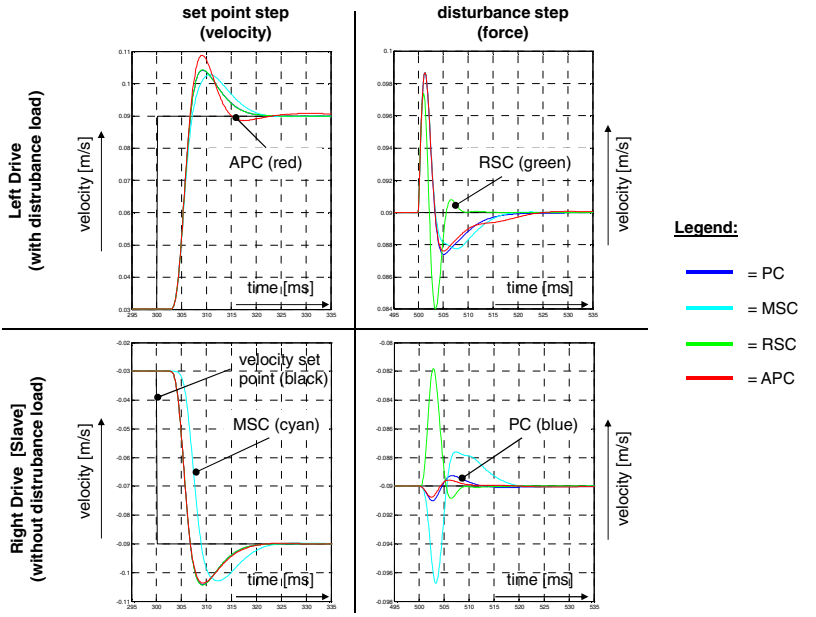

Fig. 7 Comparison of simulation results for PC, MSC, RSC and APC

The parameterization of the cascade is given in table 2, the additional controller parts are tuned as described in [3, 8]. Starting with the set point behavior PC and RSC show identical characteristics, MSC needs longer to compensate caused by the delayed slave and APC shows a higher overshot with faster compensation. Most effects can be seen in the disturbance behavior. RSC compensates markedly faster and with a shorter rise time and higher overshot. PC and APC show comparable characteristics and MSC the least dynamics.

Table 2 Controller parameter for comparison of PC, MSC, RSC and APC

parameter	parameter name	value
K_P	velocity loop gain	23000 Nsm^{-1}
$T_{n,P}$	velocity loop integral time	2.0 ms
$T_{f,n}$	velocity set point filter	2.0 ms
K_V	position loop gain	150 s^{-1}

5 Conclusions

In this paper different control structures for opposed driving coupled linear drives are presented and compared. First the control schemes PC, MSC, RSC and APC and their parameterization are discussed. Afterwards the simulation model is

introduced. Finally these control structures are compared based on simulation and experimental results. Higher control structures show best results but need more know-how for tuning and implementation.

Acknowledgments. The Cluster of Excellence „Energy-Efficient Product and Process Innovation in Production Engineering“(eniPROD®) is funded by the European Union (European Regional Development Fund) and the Free State of Saxony.

References

[1] Yao, W.-S., et al.: Modeling and control of twin parallel-axis linear servo mechanisms for high-speed machine tools. Int. J. Auto. and Smart Techn. 1(1), 77–85 (2011)
[2] Rehm, M., et al.: Mechanically linked, gravity free linear drives test bench. In: Proc. LDIA 2011 - Eighth Int. Symp. on Linear Drives for Ind. Appl., Eindhoven, pp. 219–224 (2011)
[3] Rehm, M., et al.: Control strategies for mechanically-coupled high speed linear drives. In: Proc. LDIA 2013 - Ninth Int. Symp. on Linear Drives for Ind. Appl., Hangzhou (2013)
[4] Weidauer, J., et al.: Elek. Antriebstechnik. Publics Corp. Publ, Erlangen (2011) (in german)
[5] Hofmann, S.: Ident. parametrischer Modelle für geregelte, elektromechanische Achsen mit modifizierter sukzessiver Polkompensation, Dissertation, TU Chemnitz (2012) (in german)
[6] O'Dwyer, A.: Handbook of PI and PID Controller Tuning Rules, Imp. College Press (2006)
[7] Schroeder, D., et al.: Elekt. Antriebe – Reg. von Ant. Sys., Springer, Berlin (2001) (in german)
[8] Muenster, R., et al.: Analysis of a Position Control Extension on the Model of a Servo-Screw-Press. In: Proc. SELM 2013 Intern. Symp. on Elec.Dyn. (2013)
[9] Zirn, O.: Machine Tool Analysis - Modeling, Simulation and Control of Machine Tool Manipulators, Habilitation, ETH Zurich, Suisse (2008)

The Robust Remote Control of the Manipulator

V. Ondroušek, M. Vytečka, J. Kolomazník, and M. Hammerschmiedt

Mendel University in Brno, Faculty of Business and Economics, Zemedelska 1, 613 00, Brno, Czech Republic
vit.ondrousek@mendelu.cz

Abstract. This contribution deals with the design of the remote control of the manipulator Katana, which is an industrial manipulator with five degrees of freedom. The main reason for implementing the remote control system is to maximize efficiency and speed of developing of manipulation tasks for industry. The main goal of remote control system is to switch on/off the manipulator, change the intensity of lights, detect the voltage drop, provide images of the working space, enable the supervisor to monitor the whole system and to manage establishing of connections of the wired or wireless clients.

1 Introduction

This paper deals with the issue of remote control of the manipulator Katana 6M180, which has five degrees of freedom. This robot is produced by the Swiss company Neuronics AG. The manipulators from this category KatHD300s are designed to operate in industrial applications. The main reason for implementing the remote control system is to maximize efficiency and speed of developing of manipulation tasks for industry. Another reason for introducing the remote control system is to allow access of all researchers (or PhD students) to the robot anytime, so they could work on their projects without physical presence in the laboratory. The main goal of remote control system is to switch on/off the manipulator, change the intensity of lights, detect the voltage drop, provide images of the working space, enable the supervisor to monitor the whole system and manage establishing of connections of the clients.

2 Used Approach

Choosing the suitable development environment of the whole remote control system was the first step. This environment has to allow development of the control software for Katana manipulator. The proposed solution must also enable the development of robust stable applications, which can be used in industry, especially in the production lines. The development system Control Web satisfies those restrictions and also represents an industrial standard of this field, see [6] for more

T. Březina and R. Jabloński (eds.), *Mechatronics 2013*,
DOI: 10.1007/978-3-319-02294-9_91,

details about using Control Web system for long term monitoring. Control Web system has a lot of extending modules. One of them is the Vision Lab, which offers stable and reliable methods for image processing. After the main control software was chosen, the other elements of the whole remote control system have been selected. Figure 1 shows the schema of the whole remote control system. Similar, but less general, solution of the remote control can be found in [5].

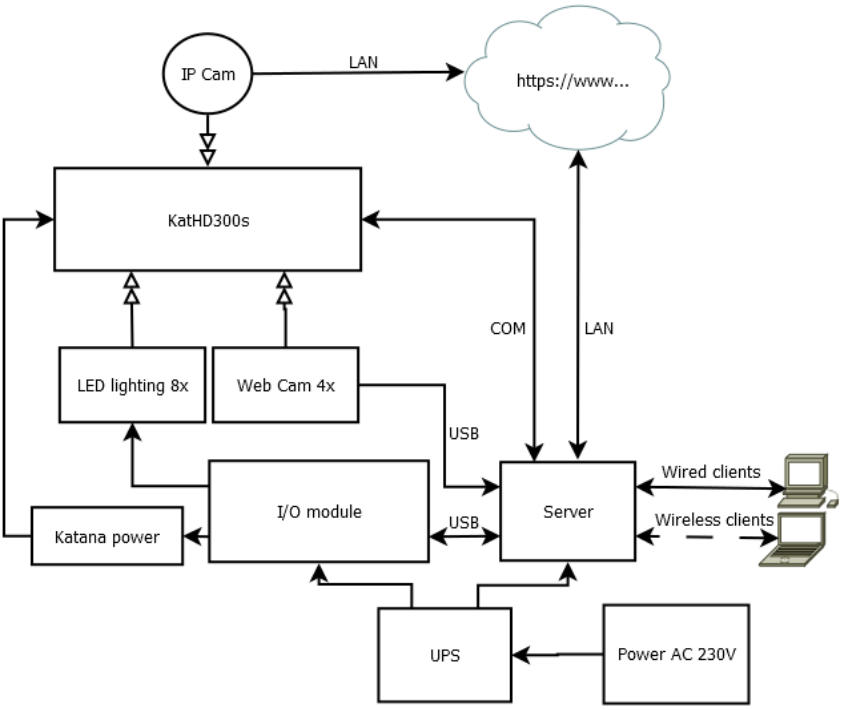

Fig. 1 Schema of the remote control system

2.1 Hardware

One of the most important things in the field of the manipulator control is following the safety standards. The protective cage of the robot was designed to meet the safety requirements, see Fig. 2. The workspace of the manipulator is defined by this cage as well. Main part of the cage is made of aluminum frame, which is connected to the manipulator. The similar design and manufacturing process, that uses the mentioned contoured profiles, was used in [3], where authors have focused on the design of the frame for the mobile robot. The circumferential planes consist of Plexiglas. The bottom surface is formed using the ABS plastic boards. There are four rails mounted in the top of the cage. These can be used to attach lights and cameras. The four cameras, each with resolution 1280x720px with 30 FPS, are currently used. These cameras are used mainly by algorithms for image processing

and objects detection. The cameras are connected into the server PC directly. An appropriate lighting of the analyzed scene is one of the critical aspects, which have the major impact on the abilities of the image processing algorithms. Therefore eight pieces of the LED straps, each consists of 75 diodes, are placed in the corners of the protective cage. Each of the straps can be switch on/off separately to allow suitable intensity of light. All of the LED straps are connected to the I/O module.

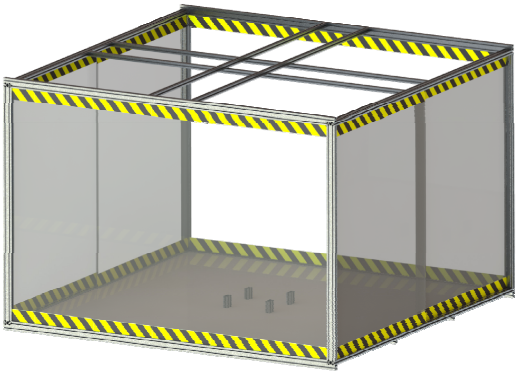

Fig. 2 Protective cage of the manipulator

There is one IP camera integrated to the proposed remote control system. This camera is not used by image processing algorithms, but it serves to the supervisor for monitoring of the whole system. This represents another safety element of the solution, which enables monitoring of each activity in the workspace.

2.2 Power Circuits and Electronics

The control electronics and power circuits, which are placed into the I/O module, serves for the control of power supply of the manipulator, detection of the voltage drop and for the lighting control as well, see Fig.1. The I/O module is based on the Datalab IO modules, which comes from the same manufacturer as the Control Web development system. This fact ensures high reliability and avoids possible problems in communication between the high level control software on the server and low level software connected to the control electronics. The first module DL-AD2 contains 4 isolated differential 16 bit analog inputs, 2 isolated 8 bit analog output, 2 isolated digital I/O. The second one DL-DO1 contains 8 relay outputs with normally open contacts with maximal limited values: voltage 230 V AC and 3A.

The power supply is also connected to the mentioned modules through the AC adapter, which enables detecting problems with the current supply. This monitoring is necessary for the disconnecting the current remote client from the manipulator and shutdown the whole device in the safe way. The UPS unit is used to

providing power during the emergency shutdown. This unit is able to provide the power to the server, manipulator and electronics for a few minutes, which is sufficient for the docking the manipulator to the safe position and shutdown all devices.

2.3 Software

All of the I/O modules and parts of the control/monitoring chain are controlled using the main control software, which runs on the server. The clients are allowed to connect to the server using the standard RDP protocol. Only one client can be connected to the server at one time, which is ensured using the reservation system. The Team Viewer is used in our solution. There are several reasons for choosing this software. First of all, it is a multiplatform application which supports Linux, MS Windows, Mac OS X, iOS, Android, etc. Secondly, the software meets high security standards, especially RSA key exchange and AES session encryption.

The main control application, which was developed using the Control Web development system, represents the main software part of the whole solution. This application starts automatically, whenever the client is authenticated and connected to the server. The server is equipped with the windows 7 operating system. The application runs for the whole time during which the client is connected to the server. The client cannot turn off the control application. On the other hand, the client is allowed to run the application in the background or use the application for its own needs, if it has assigned appropriate privileges by the reservation system.

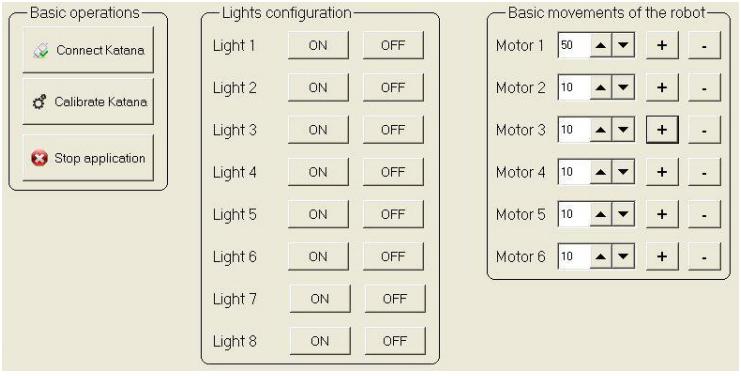

Fig. 3 Selected front panels of the main control software

The control application can be used for setting the light intensity, displaying images of the working space of the manipulator and switching off/on the manipulator. The privileges can be set separately for each action in the Control Web application. The control application also enables basic positioning of the manipulator to any configuration. Each drive (degree of freedom) can be controlled separately,

see fig. 3. The control application also handles safe shutdown of the machine and signing out the client, when the client is not active for the specified time or when the power is dropping down. Several other solutions of the basic manipulation tasks are built into the application for the educational purposes a, e.g. the students have to set up parameters of the vision control first and then the task can be solved.

The control application was developed using the Control Web system. The common panels were used for controlling the power, switching the lights, calibrating manipulator, etc. There were no special issues with completing the mentioned tasks, because all of the I/O modules originate from the same manufacturer as the development system used for the design of the application. The Vision Lab module was used to provide the images from cameras in the control application. This module enables rapid prototyping of image processing algorithms. Considering that, the system of cameras can be changed for other cameras any time in a simple manner. It was necessary to integrate the control panel based on the activeX technology to enable positioning of the manipulator. This element was developed using C++ and use the Katana Native Interface (KNI) to control the configuration of the machine. The KNI is divided into the three cooperating layers: communication interface CDL, communication protocol and the Katana Robot Model, see more in [4]. The same approach was used to create routines, which ensure the safe docking of the manipulator.

3 Achieved Results

The standalone software, that is able to identify objects in the working space of the manipulator, was created using the described solution of the remote control, as the proof of concept. This application was developed using the Control Web system and the Vision Lab module. The identification of the objects means specifying position and dimensions of the objects that are placed into to the working space. Such identification represents the first step in the most of manipulation tasks.

The resulting identification of the objects in the inappropriately lighted scene is shown on fig. 4. At first, the method for finding objects based on the colors detection (more specifically the method “detect object by threshold” from Vision Lab module) was used at the first place. This is the reliable method for such lighting conditions. This step enabled to find approximate positions of the objects in the scene. However, some objects blend together, some others are not detected at all. The shape detection method “classifier in rectangular region” was used in the second step. We assume that only the well-known shapes occur in the working space of the manipulator. The mentioned method works is the two step algorithm. The categorization of the training data is performed first. The classification of the objects, that are located in the previously found regions of the image, is performed in the second step. The analysis of the shapes enables another separation of the detected objects.

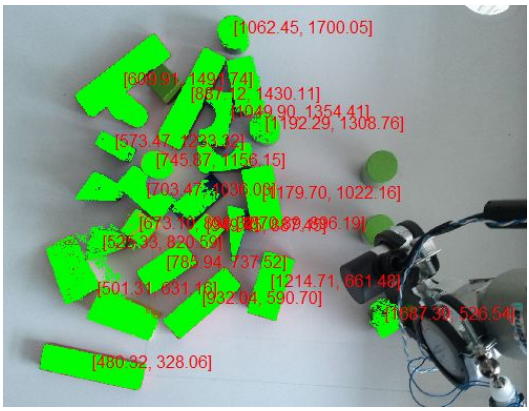

Fig. 4 Identification of the objects in the working space of the manipulator

Such separated objects can be then processed one by one to find positions and dimensions. The relative dimensions of the objects in the scene were found first, using methods "inner and outer caliper". These values were passed to the main control application and recalculated to the real coordinates of the working space of the manipulator. The dimensions recognition is sensitive to overlapping of the objects, even to the partial one. On the other hand, the object detection is resistant overlay. This problem can be solved using advanced method of image processing, see more in works of our colleagues [1] and [2], which were solved at Mendel University in Brno.

4 Conclusions

This contribution is focused on the design, realization and testing of the robust remote control system of the industrial manipulator. The main aim is to provide universal solution, which can be used for rapid prototyping of applications solving tasks of manipulation or image processing. The whole solution consists of several main parts. The hardware part is represented by the protective cage, which is the main safety element of the whole control and monitoring chain. This cage is also used for holding cameras and lights. Second part of the solution consists of I/O modules that are able to control the power supply of the manipulator, detect the voltage drop and control light intensity. The last part is represented by the software running on the server, especially the control application. This application can be used for setting the light intensity, displaying images of the working space of the manipulator, switching on/off the manipulator. The software also enables basic positioning of the manipulator to any configuration. The standalone software has been developed using Control Web system as the proof of concept. This software is able to identify objects in the working space of the manipulator. The identification of the objects is the first step in most of automated manipulation tasks in the production line. The application for the protection under utility model of the

whole proposed solution is submitted to the Industrial Property Office of the Czech Republic.

Acknowledgments. Published results were acquired using the subsidization of the Ministry of Education, Youth and Sports of the Czech Republic, research plan IGA MENDELU MP 5/2013 "Achieving effective utilization of the manipulator by introducing remote control system".

References

[1] Lýsek, J., Šťastný, J., Motyčka, A.: Object Recognition by Means of Evolved Detector and Classifier Program. In: MENDEL 2012, 18th International Conference on Soft Computing, pp. 82–87. Brno University of Technology (2012) ISBN 978-80-214-4540-6

[2] Minařík, M., Šťastný, J.: Recognition of Randomly Deformed Objects. In: MENDEL 2008, 14th International Conference on Soft Computing, pp. 275–280. Brno University of Technology (2008) ISBN 978-80-214-3675-6

[3] Ripel, T., Hrbacek, J., Krejsa, J.: Design of the Frame for Autonomous Mobile Robot with Ackerman Platform. Engineering Mechanics, 515–518 (2011) WOS:000313492700122

[4] Rouš, R.: Katana robot controlling in the Control Web system, diploma thesis, Mendel University in Brno, p. 77 (2012)

[5] Raimondi, F.M., Ciancimino, L.S., Melluso, M.: Real-time remote control of a robot manipulator using Java and client-server architecture. In: 7th WSEAS International Conference on Automatic Control, Modeling and Simulation, pp. 122–126 (2005) WOS:000231379200024

[6] Holoubek, L., Kukla, R., Kadlec, R.: Monitoring of glasshouse climatic processes with the proposal of their control. Research in Agricultural Engineering-UZPI, 48–54 (2006) ISSN 1212-9151

Control System of One-Axis Vibration-Insulation Platform with Gyroscopic-Stabilizer

R. Votrubec

Technical University of Liberec, Faculty of Mechanical Engineering,
Department of Applied Cybernetics, Studentska 2, 461 17, Liberec, Czech Republic
radek.votrubec@tul.cz

Abstract. The paper deals with stabilization of platform by means of gyroscopes. Whole platform consists of parallelogram, cardan frame and two contra-rotating gyroscopes. Whole system is described with five generalized coordinates and with two cyclic coordinates. During the first phase of the project we created a prototype platform rotating around one axis. Prototype is designed with respect to a simple way to extend the rotation about the second axis. The rotary frame is driven by the force of a gyroscope. Pneumatic motors are used to actuating gyroscopes. Pneumatic springs are used to actuating rotating frame. This paper shows control system of platform and introduces reached results of stabilization.

1 Introduction

Theme gyro stabilization platform follows the research of active ambulance stretcher. That is described in [1] and [2]. A prototype of stabilized plate consists of two rotating frames, Fig.1. The auxiliary base frame is placed on the floor. Outer upper frame can be excited by hands or put on hydraulic pistons. Upper frames are propelled by pneumatic springs. Pressures in both springs are controlled by electrical proportional valves. Two gyroscopes with vertical rotation axis are mounted to upper inner frame. Gyroscopes have the air bearing support in precession frame. Gyroscopic stabilizer mechanical system was completely described in [3]. Gyroscope with the mass about 3.5kg is driven by air turbine and has design speed over 30.000 rpm. Real speed 12000 rpm was tested with industrial compressor, which can supply air with pressure 9 bars and sufficient flow. Speed of gyroscope is measured with magnetic contact sensor. Speed is calculated from frequency of pulses. The torque motor of radial correction is mounted on precession frame axis between upper inner stabilizer and precession frame. This pneumatic torque motor is actuating device of correction and compensation system. Pneumatic springs and motors are controlled with electrical servo valves.

T. Březina and R. Jabloński (eds.), *Mechatronics 2013*,
DOI: 10.1007/978-3-319-02294-9_92,

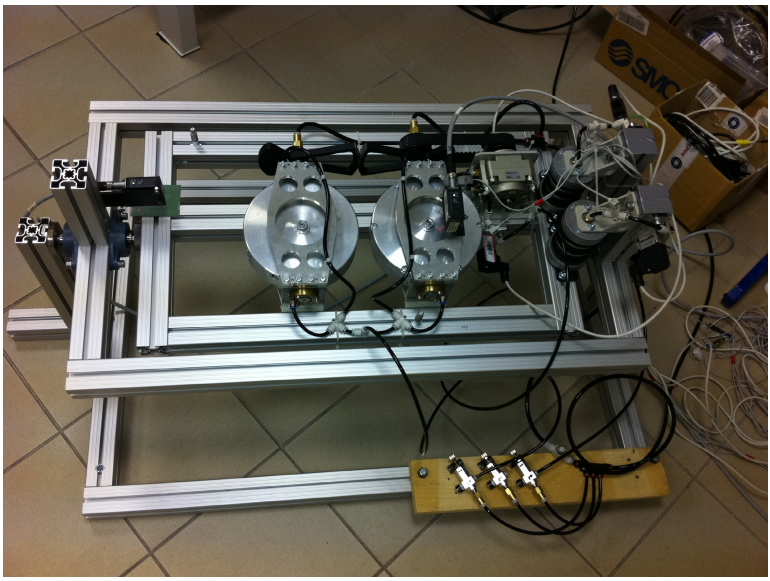

Fig. 1 The prototype of stabilized platform

2 Description of Stabilized Plate and Control Circuit

The scheme of stabilized plate is in (figure 2). Auxiliary frame, which is laid on the ground, is illustrated with red color. Base frame is green. It can be inclined. Upper inner stabilized frame is blue. This frame is propelled by pneumatic springs. Precession frames of gyroscopes are mounted on blue frame. They are driven by pneumatic motor trough the gears.

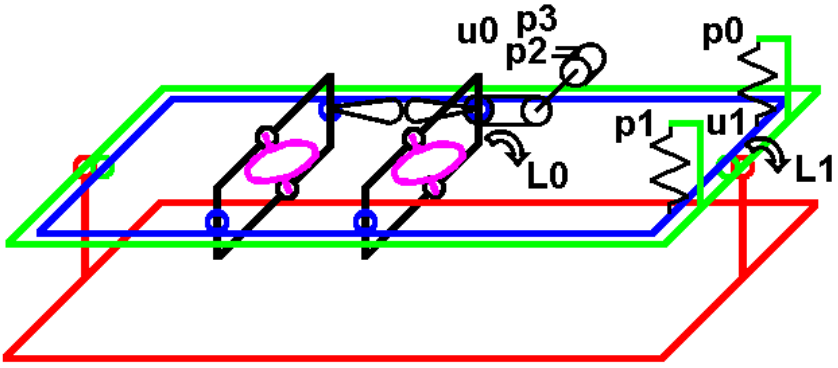

Fig. 2 The scheme of stabilized platform

The system is controlled to horizontal position of blue frame. Correction and compensation systems consist of two proportional feedbacks with PID controllers. Correction torque motor on precession frame axis is driven by feedback from sensor of stabilized frame position. It indicates direction of an apparent vertical. Compensation system has feedback, which applies the torque on stabilized frame. It is driven with respect to magnitude of precession frame angular displacement. The scheme of control circuit is in Fig. 3.

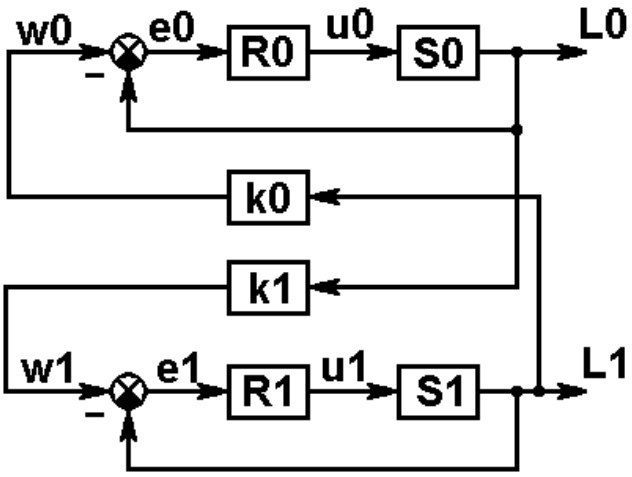

Fig. 3 Control structure

2.1 Mathematical Model

The basis of model is set of motion equations, which are derived from Lagrange equations of second kind with external torques on their right sides.

$$\frac{d}{dt}\frac{\partial T}{\partial \dot{q}_i} - \frac{\partial T}{\partial q_i} + \frac{\partial U}{\partial q_i} = M_{s_i} + M_{d_i} + M_{pas_i} + M_{cor_i} \qquad i = 1..3 \tag{1}$$

Stabilized frame has index i=1 with angle displacement q_1. Precession frame has index i=2 with angle displacement q_2. Sensor of apparent vertical has index i=3. q_3 is angle between apparent vertical and z-axis of stabilized frame. M_{Si} are torques of air springs. M_{ti} are torques of dampers, M_{pasi} are torques of passive resistances and M_{cor2} is torque of correction motor. It is only on the precession frame axis.

The whole model moreover contains air spring models and models of electric servo valves.

Torque of air springs is

$$M_{s_1} = -r_{p1}(p_1 - p_a)S_{ef}(l_1(q_1)) + r_{p2}(p_2 - p_a)S_{ef}(l_2(q_1)) \tag{2}$$

where p_1 and p_2 are pressures in springs, P_a is atmospheric pressure, S_{ef} is effective area and l_1, l_2 are lengths of springs.

For pressures inside springs we can write

$$p_i \cdot \dot{V}\left(l_i(q_1)\right) + \dot{p}_i \cdot V\left(l_i(q_1)\right) = RTG_i \tag{3}$$

where G_i is mass flow of the air.

Electric servo valves SMC VY1A01 was used. This valve has self controller of output pressure. Air mass flow through valve in direction from pressured air source to air spring can be expressed as

$$G_{PA_i} = \begin{cases} p_{in} \cdot C \cdot \rho_a \sqrt{1 - \left(\dfrac{\dfrac{p_i}{p_{in}} - b_{PA}}{1 - b_{PA}} \right)^2} & \dfrac{p_i}{p_{in}} > b_{PA} \\ p_{in} \cdot C \cdot \rho_a & \dfrac{p_i}{p_{in}} \le b_{PA} \end{cases} \tag{4}$$

Similarly mass flow in direction from air spring to the atmosphere is

$$G_{AR_i} = \begin{cases} -p_i \cdot C \cdot \rho_a \sqrt{1 - \left(\dfrac{\dfrac{p_a}{p_i} - b_{AR}}{1 - b_{AR}} \right)^2} & \dfrac{p_a}{p_i} > b_{AR} \\ -p_i \cdot C \cdot \rho_a & \dfrac{p_a}{p_i} \le b_{AR} \end{cases} \tag{5}$$

where p_{in} is pressure of air source, C is pneumatic conductivity dependent on valve opening, ϱ_a is normal air density, b_{PA} and b_{AR} are critical pressure ratios for appropriate flow direction

Parameters of used valves (including coefficients of its built-in controller) were determined experimentally.

Basis consists of two feedbacks with two PID controllers R0 and R1, Fig 3. Their parameters were optimized with integral criterion

$$J_i = \int_0^{t_{end}} \left[t^n \left(e_i\right)^2 + k\left(y_i'\right)^2 \right] dt \tag{6}$$

where e_i are control deviations., y_i are controlled values, n and k are optional weighting coefficients. Results of optimization are

$$r0_{R0} = 0{,}05 \quad r1_{R0} = 0{,}11 \quad r2_{R0} = 0{,}0023 \tag{7}$$

$$r0_{R1} = 0{,}012 \quad r1_{R1} = 0{,}54 \quad r2_{R0} = 0 \tag{8}$$

Parameters of crosslink gains K0 and K1 were adjusted as

$$K0 = 0{,}035 \quad K1 = 0{,}48 \tag{9}$$

2.2 Control Software

Control application was created in LabView. It enables to process basic measurement and setting actuating values. Control loops are integrated. All values are displayed in graphs online. Selected waveforms can be written to a file. The second application was intended for viewing and processing of measured data. Some filters and frequency analysis are implemented.

2.3 Realization of Actuating Values

Actuating value u_1 is created by means of pressures p_0 and p_1. These pressures are in pneumatic springs. Range of u_1 is from -1 till +1.

$$u1 \quad \{-1..1\} \quad [/] \tag{10}$$

$$P\max_{01} = 6 \cdot 0{,}1MPa \tag{11}$$

Each pressure is created as

$$P_0 = (u1+1)\frac{P\max_{01}}{2} \tag{12}$$

$$P_1 = P\max_{01} - P_0 \tag{13}$$

This means that

$$if \quad u1 = -1 \quad then \quad P_0 = 0 \quad and \quad P_1 = P\max_{01} \tag{14}$$

$$if \quad u1 = +1 \quad then \quad P_0 = P\max_{01} \quad and \quad P_1 = 0 \tag{15}$$

Actuating value u_0 is created similarly.

2.4 *Results of Control*

Results of control are shown in Fig.4. All pressures are displayed in upper chart. There are positions of each frame in the middle. Absolute rotation against the surrounding is in the chart below. In this case it is control of excitations of base frame by hands.

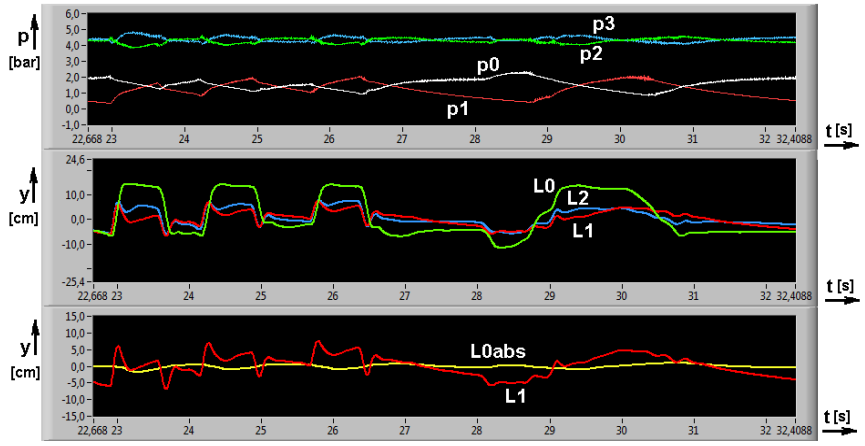

Fig. 4 Results of control, excitations of base frame by hands

3 Conclusions

The control system of stabilized plate with gyroscopes was designed and realized. Its mathematical model was created and used for optimization of controller parameters. All parameters of control circuits were adjusted and optimized. Satisfactory results of control were introduced. Simulation results were verified on real prototype of stabilized platform. Theoretical consideration of gyroscopic stabilization has been successfully verified on real system. For technical reasons it was not possible to achieve the required speed gyroscopes. Increasing speed gyroscopes would be their stabilizing effect even higher.

Acknowledgments. The research has been supported by project GAČR 101/09/1481 "The gyroscopic stabilization of the vibration-isolation system".

References

[1] Votrubec, R.: Control of active sanitary coach. In: 2141-2143, Annals of DAAAM for 2011 & Proceedings of the 22th International DAAAM Symposium, Vienna, Austria, p. 896 (2011) ISSN 1726-9679

[2] Votrubec, R.: Exhanced control of active sanitary coach with acceleration feedbacks. Journal of Applied Science in the Thermodynamics and Fluid Mechanics 2(1) (2011) ISSN 1802-9388
[3] Sivčák, M., Škoda, J.: Radial correction controllers of gyroscopic stabilizer. Journal of Vibroengineering 12(3), 300 (2010)
[4] Votrubec, R., Sivcak, M.: The Correction and Compensation Motors for the Gyroscopic Stabilizer. In: Mechatronic Systems and Materials, Diffusion and Defect Data pt.B - Solid State Phenomena, vol. 164, pp. 45–148 (2010)
[5] Škliba, J.: About a possibility of a gyroscopic stabilisation of the vibroisolation system. In: National Conference with International Participation Engineering Mechanics 2007, In Book of extended abstracts, Engineering Mechanics 2007, Svratka, pp. 275–276 (2007) ISBN 978-80-87012-06-2

Hybrid PI Sliding Mode Position and Speed Controller for Direct Drive

S. Brock

Poznan University of Technology, Institute of Control and Information Engineering
ul. Piotrowo 3A, 60-965 Poznan, Poland
Stefan.Brock@put.poznan.pl

Abstract. This paper describes a control system for a direct drive with permanent magnet synchronous motor based on a hybrid P-PI sliding mode controller and reference trajectory generator. Simulation results show that the control approach can decrease the tracking error, enhance the system's robustness and attenuate high frequency chattering in the control signal. Experimental studies confirmed the results of the simulation.

1 Introduction

In the field of robot manipulator and machine tool control, one of the important issues is robustness of the servo drive system. Robustness is the ability of a closed loop system to retain a specified dynamic performance despite plant modelling uncertainties and external disturbances. The robustness of the servo system applied to each joint of a manipulator or axis of the machine tool enables non interferences among other servo drives.

Many applications require operation under dynamically changing conditions regarding the commands position. Such changes in target position either due to the physical movement of the target or due to additional sensor information provided during the motion require on-line updating of the reference trajectory. Furthermore, in direct drive it is very important to obtain trajectory for smooth motion (i.e. no discontinuity at least in velocity and acceleration) under constraints of maximum limiting values of velocity, acceleration and jerk at the same time. This requires an on-line re-programming of the reference-trajectory based on the current position, velocity, acceleration and jerk without an abrupt change of them. In paper new concept of reference trajectory generator is used.

Sliding mode controllers are well known to be robust against bounded, unstructured modeling errors, but it is also known that they tend to cause chattering (high frequency oscillations). Of the many methods available to eliminate this phenomenon in the study on the introduction of a function of saturation and output filtering was used [1, 2, 6, 7] .

T. Březina and R. Jabloński (eds.), *Mechatronics 2013*,
DOI: 10.1007/978-3-319-02294-9_93,

The rest of this paper is organized as follows. In section 2 the proposed structure of position and speed controller is presented. Section 3 describes a structure of the direct drive system used in experiments, followed by the simulations and experimental results and discussion in section 4. Some concluding remarks are presented in section 5.

2 Hybrid PI Sliding Mode Controller

The block diagram of the proposed controller is shown in Figure 1. In the block diagram are shown the components of the hybrid controller: a P-PI position and speed controller, sliding mode controller, output integrator and references signals generator.

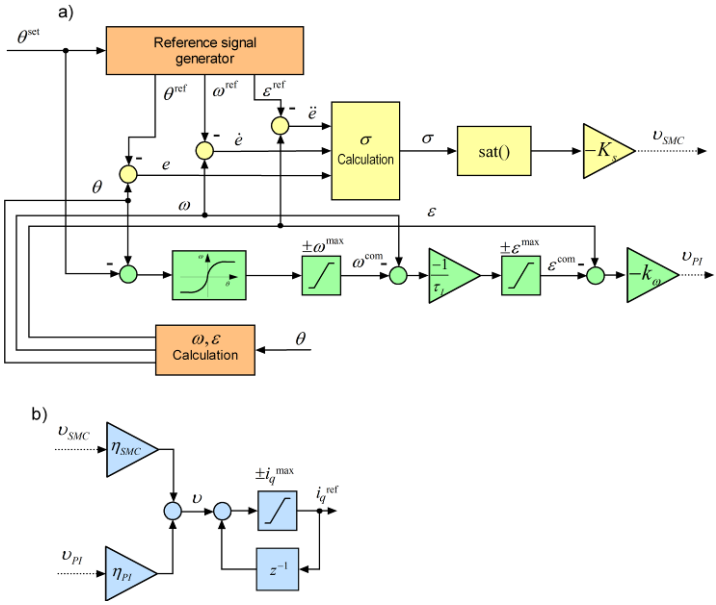

Fig. 1 Block diagram of proposed hybrid PI sliding mode controller

The output of the nonlinear position controller is the speed set point, computed according to the formula:

$$e_\theta = \theta - \theta^{\text{set}}; \quad \omega^{\text{com}} = -\min\left(\left|k_\theta \cdot e_\theta\right|, \sqrt{2 \cdot \varepsilon^{\max} \cdot e_\theta}\right) \cdot \text{sgn}(e_\theta) \tag{1}$$

Speed controller specifies the current command by the formula:

$$e_\omega = \omega - \omega^{\text{com}}; \quad i_q^{\text{ref}} = -k_\omega \cdot \left(e_\omega + \frac{1}{\tau_I} \int_0^t e_\omega \mathrm{d}\xi \right) \tag{2}$$

This controller can be represented as a serial connection of the proportional speed controller and integral acceleration controller

$$\varepsilon^{\text{com}} = -\frac{1}{\tau_I} \cdot e_\omega; \quad e_\varepsilon = \varepsilon - \varepsilon^{\text{com}}; \quad i_q^{\text{ref}} = -k_\omega \cdot \int_0^t e_\varepsilon \mathrm{d}\xi = \int_0^t \upsilon_{PI} \mathrm{d}\xi \tag{3}$$

In the above formulas (1), (3) controllers limits are omitted. The choice of control parameters is given in previous papers.

The starting point for the synthesis of the sliding controller is to define the sliding surface. The proposed solution surface is specified in the position error *e* relative to the reference value.

$$e = \theta - \theta^{\text{ref}}; \quad \dot{e} = \omega - \omega^{\text{ref}}; \quad \ddot{e} = \varepsilon - \varepsilon^{\text{ref}} \tag{4}$$

The generalized error σ on the sliding surface is equal to 0.

$$\sigma = \ddot{e} + 2 \cdot \lambda \cdot \dot{e} + \lambda^2 \cdot e \tag{5}$$

During the sliding motion generalized error σ disappears with a time constant 1/λ. The control signal υ is chosen so that the state vector to bring the switching surface, and then keep it at the surface.

$$\upsilon_{SMC} = -K_s \cdot \text{sgn}(\sigma) \qquad \text{sgn}(\sigma) = \begin{cases} -1 & \text{for} \quad \sigma < 0 \\ 0 & \text{for} \quad \sigma = 0 \\ 1 & \text{for} \quad \sigma > 1 \end{cases} \tag{6}$$

Constant K_s is chosen so as to ensure stable operation the whole range of variation of objects parameters. The output υ of the proposed sliding mode controller is not reference current signal but the first derivative of this current:

$$i_q^{\text{ref}} = \int_0^t \upsilon_{SMC} \mathrm{d}\xi \tag{7}$$

In this configuration, the sliding mode controller with the output block integrator, chattering phenomenon does not occur. Additionally, the function sgn() is replaced by a continuous function sat() of the width Φ.

$$\upsilon_{SMC} = -K_s \cdot \text{sat}(\sigma) \qquad \text{sat}(\sigma) = \begin{cases} \sigma / \Phi & \text{for} \quad |\sigma| < \Phi \\ \text{sgn}(\sigma) & \text{for} \quad |\sigma| \geq \Phi \end{cases} \tag{8}$$

Analysis of Figure 1 shows that the structure of both controllers is similar. Therefore, the signals from the both controllers can be combined before the integral block with the corresponding weights

$$i_q^{\text{ref}} = \int_0^t \left(\eta_{SMC} \cdot \upsilon_{SMC} + \eta_{PI} \cdot \upsilon_{PI}\right) \mathrm{d}\xi \tag{9}$$

In the present study assumed equal weight $\eta_{PI} = \eta_{SMC} = 0.5$, but they can be, for example, determined by the fuzzy system.

The speed is calculated by differentiation of rotor position with respect to time. It is very important to filter the speed signal adequately, to exclude the mechanical resonance amplification. The digital biquadrates multi-band filter was designed and tested. The procedure for the selection of such a filter is shown in the previous paper [4].

Reference signal generator is working in sub-optimal mode. Sample waveforms for the case of a slight step change of the desired position are shown in the figure 2. Reference waveforms consists of six phases: increase of acceleration with jerk limit (A), constant acceleration (B), continuous change of acceleration to negative value (C), constant negative acceleration (D), time-optimal braking (E) and finally exponential breaking (F) to avoid any overshoot. In case of large desired position change the additional phase with constant speed will be present.

3 Laboratory Stand

The direct drive with PMSM was tested in the presented work. Figure 3 presents the structure of the laboratory stand. The system consists of three main parts: the motor with load construction, a PWM converter and the control algorithm implemented in DSP. The data of the investigated drive are presented in the Appendix. A set of metal plates fixed to the arm mounted on the motor shaft enables us to vary the moment of inertia. The disc brake with four adjustable brake pads is fixed

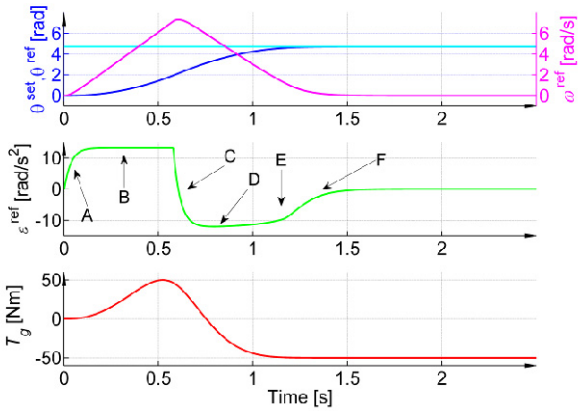

Fig. 2 References signals: top: reference position (blue), set position (cyan) and reference speed (magenta); middle: reference acceleration; bottom: gravitation torque.

to the motor shaft. This adjustable brake can be used to model dry friction, typically for many typical for many machining processes [3, 5].

The sampling time of the floating point DSP is set to 100 μs. An incremental optical encoder tests the rotor position. Field-oriented control of currents in the axes d and q is performed by applying a robust PI control algorithm. The closed current control loop is much faster than mechanical dynamics. Therefore, for the synthesis of the speed and the position controller it is assumed that references equal actual values during speed and position transients.

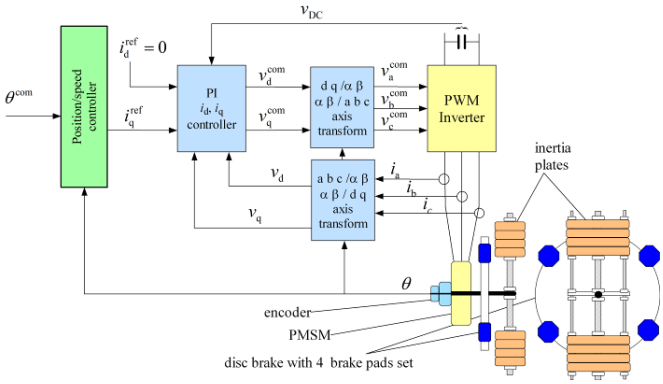

Fig. 3 Block diagram of laboratory stand with and vector controlled PMSM direct drive

4 Experiment Results

The research was carried in two phases: simulation and laboratory. During the simulation, it was examined whether the introduction of the hybrid controller improved the quality of control in relation to the P-PI controller. In Figures 4 to 6 show the trajectory tracking errors for three load configurations: low inertia,

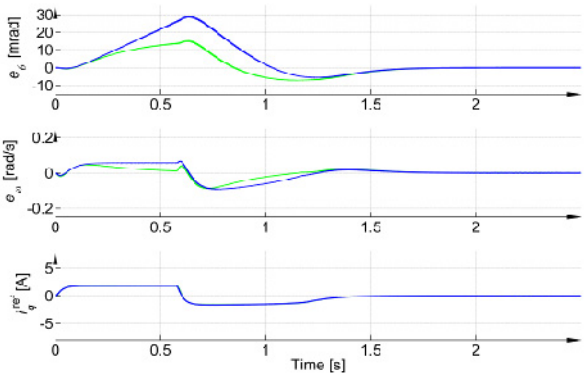

Fig. 4 Comparison of PI (blue line) and hybrid (green line) controllers. Low inertia case. Top: position error, middle: speed error, bottom: reference current. Simulations results.

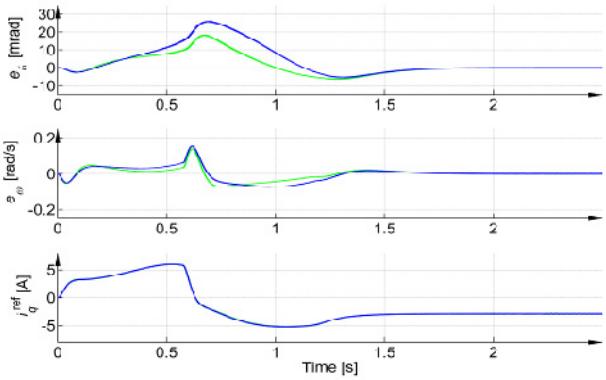

Fig. 5 Comparison of PI (blue line) and hybrid (green line) controllers. Middle inertia case, large load torque. Top: position error, middle: speed error, bottom: reference current. Simulations results.

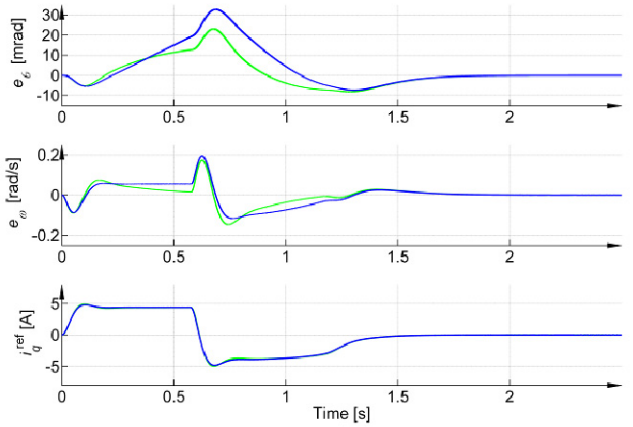

Fig. 6 Comparison of PI (blue line) and hybrid (green line) controllers. Large inertia case. Top: position error, middle: speed error, bottom: reference current. Simulations results.

medium inertia and large load torque, and high inertia. In all cases there is a reduction of the reference position tracking error. At the same time given the reference current signal is not affected by chattering. In the second phase of the study were repeated in the laboratory. Collectively the results are shown in Figure 7. For technical reasons, only position error was registered. Experimental studies confirmed the results of the simulation. The final positioning error is less than 0.1 mrad. Only if an additional test with large static friction torque the positioning error is greater than previous and is 0.2 mrad. There are small oscillations of the current (for the low inertia) due to incomplete suppression of the elastic properties of the load.

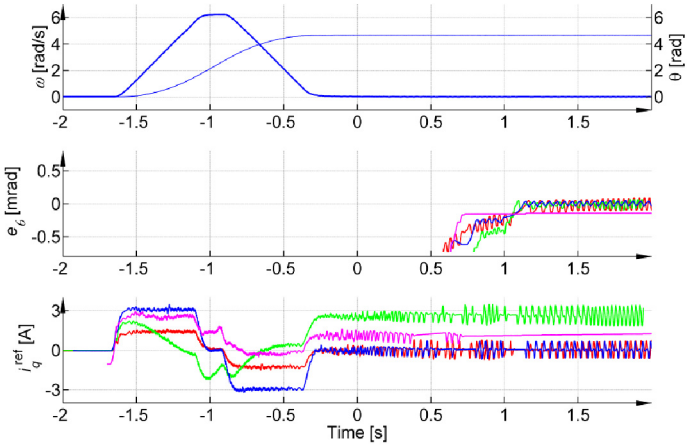

Fig. 7 Robustness of drive with proposed hybrid controller. Top: position and speed, middle: position error, bottom: reference current. Low inertia case (red line), middle inertia case with load torque (green line), large inertia case (blue line), low inertia with friction case (magenta). Experimental results.

5 Conclusion

The proposed hybrid controller combines the good dynamic properties and robustness to drive parameters change. The use of reference trajectory generator allows to define the sliding surface of the sliding mode controller. Filtering the output signal controller by integrator block eliminates chattering phenomena. Simple structure allows easy implementation in real time system.

References

[1] Arellano-Padilla, J., et al.: Robust Fuzzy-Sliding Mode Control for Motor Drives operating with Variable Loads and Pre-defined System Noise Limits. In: 9th European Conference on Power Electronics and Applications (2001)

[2] Brock, S., et al.: Modified sliding-mode speed controller for servo drives. In: IEEE International Symposium on Industrial Electronics, ISIE, pp. 635–640 (1999)

[3] Brock, S.: Sliding mode control of a permanent magnet direct drive under non-linear friction. Compel Int. J. Comput. Math. Electr. Electron. Eng. 30(3), 853–863 (2011)

[4] Brock, S., Łuczak, D.: Speed control in direct drive with non-stiff load. In: IEEE International Symposium on Industrial Electronics (ISIE), Gdańsk, Poland, pp. 1937–1942 (2011)

[5] Pajchrowski, T., et al.: Application of neuro-fuzzy techniques to robust speed control of PMSM. Compel Int. J. Comput. Math. Electr. Electron. Eng. 26(4), 1188–1203 (2007)

[6] Sabanovic, A.: Variable Structure Systems With Sliding Modes in Motion Control - A Survey. IEEE Trans. Ind. Informatics 7(2), 212–223 (2011)
[7] Young, K.D., et al.: A control engineer's guide to sliding mode control. IEEE Trans. Control Syst. Technol. 7(3), 328–342 (1999)

Data of investigated drive.

Parameters of PMSM	Unit	Value
Minimum moment of inertia	kgm^2	0.75
Maximum moment of inertia	kgm^2	5.83
Torque constant	Nm/A	17.5
Rated load torque	Nm	50
Rated value of speed	rev/s	2.41
Rated current in q axis	A	2.85
Rated voltage	V	310

Distributed Control System of Solar Domestic Hot Water Heating Using Open-Source

G. Gaspar[1], S. Pavlikova[2], and R. Masarova[1]

[1] Slovak University of Technology, Faculty of Materials Science and Technology in Trnava, Pavlinska 16, 917 24, Trnava, Slovak Republic
{gabriel.gaspar,renata.masarova}@stuba.sk
[2] Slovak University of Technology, Faculty of Chemical and Food Technology, Radlinského 9,812 37, Bratislava, Slovak Republic
sona.pavlikova@stuba.sk

Abstract. This paper deals with the use of open-source software for distributed control system of solar domestic hot water heating. It presents the hydraulic circuit of solar collectors with autonomously safe drain-back system and control components of our own design. Further are described used modules, communication protocol and the use of the control computer. Implementation of open-source software uses the Python programming language and SCADA/HMI solution pvbrowser. Using the collected operational data necessary for the improvement of the mathematical model will greatly simplify debugging similar systems in practice.

1 Introduction

Solar energy is supplied to the surface of the earth in the form of sunlight and is the basis of life on our planet. It supplies heat, which can either be used directly or can be converted into electricity [1].

Currently, there is a wide demand for utilization of free energy from environmental organizations, consumers and governments. The objectives are different from saving non-renewable energy sources through environmental protection to economic reasons. Solar water heating is due to the convenient location of our country an efficient way to achieve these goals.

Proposal of effective management of solar systems for domestic hot water (DHW) heating and visualization of operating conditions is an important parameter of evaluating the economic benefits of the ratio of energy obtained and spent. In this paper we will discuss the use of a distributed control system of our own design which allows easy adjustments in the control algorithms. The system allows measurement of operating parameters and the control of actuators, while control and data acquisition is performed using freely available open-source software pvbrowser.

T. Březina and R. Jabloński (eds.), *Mechatronics 2013*,
DOI: 10.1007/978-3-319-02294-9_94,

2 Use of Solar Energy

Solar energy is poorly predictable source of energy. Most of the energy radiated by the Sun does not reach the Earth's surface. By the measurements on the top of the Earth's atmosphere was detected level of solar radiation with an average value of 1368 W/m^2. This value is known as the solar constant.

How much solar radiation penetrates the atmosphere and is brought up to the surface depends on the solar elevation angle, which changes during the day as the sun rises and sets and also on the current state of the meteorological situation and season. Solar radiation is scattered during the passage through the atmosphere and absorbed by air molecules and water vapor impurities. The value of total solar radiation consists of three components: direct, diffuse and reflected. The thickness of the atmosphere which must the solar radiation penetrate is during the day variable. Under ideal conditions, the maximum value of the energy flow to the Earth's surface in Central Europe is around 950 W/m^2.

Drain-back connection in Fig. 1 is a non-pressure solar collector connection. Under unfavorable energy conditions (cloudy sky, night) is the collector left in stand-by mode without heat transfer fluid (water), which is at that time located in the Drain-back tank (buffer).

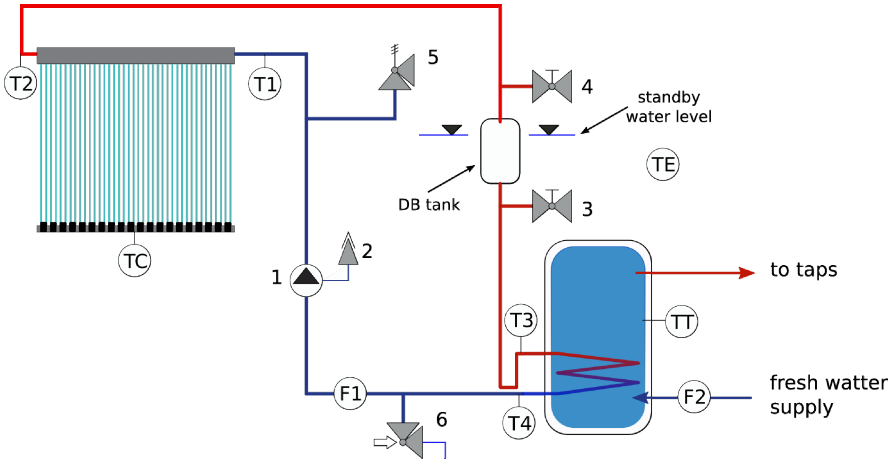

Fig. 1 Hydraulic connection of the system and sensors locations

When the pump is on, heat transfer fluid is pushed from the reservoir to flood the collector and by pumping the fluid is the thermal energy transferred from the collector to the DHW storage tank. When the pump is turned off, the fluid flows to the Drain-back tank by the gravity flow and the thermal energy transfer is interrupted. The stages of starting and stopping the system are shown on Fig. 2 Drain-back solar collector connection system is autonomously safe, i.e. the temporary shutdown of the solar system (holiday), power failure or malfunction of the pump automatically interrupts the transfer of the thermal energy from the collector to the

DHW storage tank without the risk of overheating the solar system and the uncontrolled development of the steam. When the Drain-back tank is located in a suitable location where the temperature does not drops below 0°C, as the heat transfer fluid can be used drinking water instead of possibly environmentally harmful fluids.

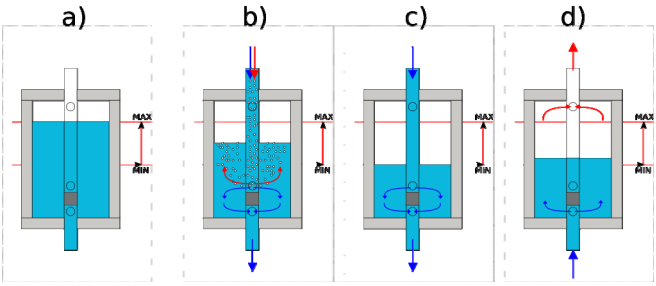

Fig. 2 The stages of starting and stopping the Drain-back system: a) stand-by, b) flooding the collector, c) system on, d) energy transfer interrupted

The objective of this work is to obtain a sufficient amount of data for use in optimization of energy harvesting and minimize heat loss and the own system energy consumption. In the system is necessary identifying its own heat losses in the piping system, loss in energy transfer, loss of radiated heat through insulations and DHW storage tank, own collector heat losses, the immediate power of the collector, the collector efficiency depending on the immediate conditions, the total energy gain of the collector, the total amount of stored energy, total energy balance of the system, the amount of energy required to operate the system.

Configuration of the experimental solar system is shown in Fig. 1. Besides technological sensors (temperature at the collector inlet T1 and outlet T2, heat transfer fluid flow F1, the temperature at the DHW storage tank inlet T3 and outlet T4, DHW storage tank temperature TT, supply water flow F2, collector temperature TC and the ambient temperature at the DHW storage tank TE) are other input data time and date for determining the maximum solar flow from astronomical tables, the position and orientation of the collector, meteorological sensors for instantaneous solar flow, the ambient temperature of the area of the collector and the speed and direction of the wind. Controlled variable is the power of the heat transfer fluid pump.

Configuration of the experimental solar system is shown in Fig. 1. Besides technological sensors (temperature at the collector inlet T1 and outlet T2, heat transfer fluid flow F1, the temperature at the DHW storage tank inlet T3 and outlet T4, DHW storage tank temperature TT, supply water flow F2, collector temperature TC and the ambient temperature at the DHW storage tank TE) are other input data time and date for determining the maximum solar flow from astronomical tables, the position and orientation of the collector, meteorological sensors for

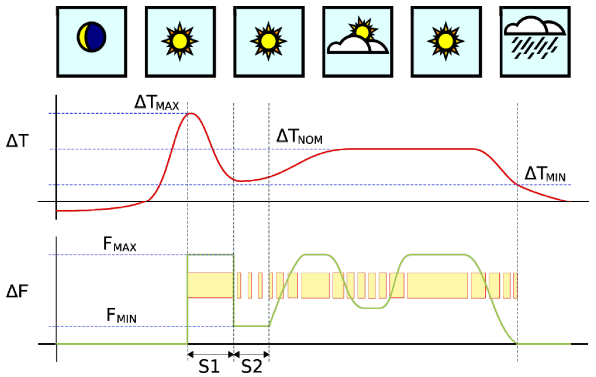

Fig. 3 Control algorithm of the system: S1 – flooding the collector, S2 – temperature conditions stabilization, T – temperature, F – flow

instantaneous solar flow, the ambient temperature of the area of the collector and the speed and direction of the wind. Controlled variable is the power of the heat transfer fluid pump.

In the proposed database [2] is stored all operational data supplemented by information on the current consumption of hot water and its temperature. Derived factors are thermal conduction losses, DHW storage tank, collector efficiency depending on the external conditions and the overall energy balance of the system. Based on the obtained data is control system algorithm shown in Fig. 3 modified with respect to the seasons and hot water consumption. The nature of the experimental system shows that the system of data collection is needed to be built flexible with the possibility of its further modification and expansion.

3 Components of the Distributed System

Standard systems for data collection are of centralized architecture, in which each individual sensor has s cable connected to the logger with a defined number of inputs and outputs. This configuration is suitable for the final device. Its main advantage is minimal need of maintenance; the disadvantage however, is in significant cost in modifications and extending of the configuration.

For the experimental system we have chosen the concept of a distributed data acquisition and control our own design which consists of separate modules. Modules process information into digital form or control actuators. The modules are interconnected into a bus with the communication cable and the whole system is controlled by a PC running GNU/Linux in Fig. 4.

Autonomous data processing, local archiving and their transformation into the digital form reduce costs and reduce demands on the power of the control processing unit. Currently are part of the system modules for weather sensors (wind direction and speed, sunlight - solar radiation), thermometers, flow meters and actuators for control of the pumps, switches and the like.

All modules are built on the STM32 ARM Cortex M3 microcontroller platform. Application part of the module for the specific interfaces to sensors and actuators intensive uses embedded peripherals of the microprocessor. Communications interface of the module is a two-wire RS485 in simplex connection with addition of the power line or RF modem in the 2.4 GHz band. As a communication protocol was chosen serial master-slave protocol uBus. The protocol is backwards compatible with MODBUS protocol and was adapted for use in microcontrollers. The communication interface is connected to the host computer via USB shown in Fig. 5.

Fig. 4 Host computer; temperature controller and USB/uBus converter based on our own design

Control algorithm for experimental measurements has been developed in Python v2.7 with support of open-source libraries such as matplotlib, pyserial, sqlite.

The basic version allows for safe system start-up, data acquisition, control, adjusting operating parameters, logging of the operational data, write to the database and simple graphical data presentation.

There are available several open-source SCADA/HMI solutions in various stages of development. For the need of remote monitoring and controlling of the system via the Internet, was chosen cross-platform open-source SCADA/HMI solution pvbrowser. This allows to monitor, control, display operational data and the overall energy balance through multiplatform client for operating systems Android, GNU/Linux, MacOS and Windows.

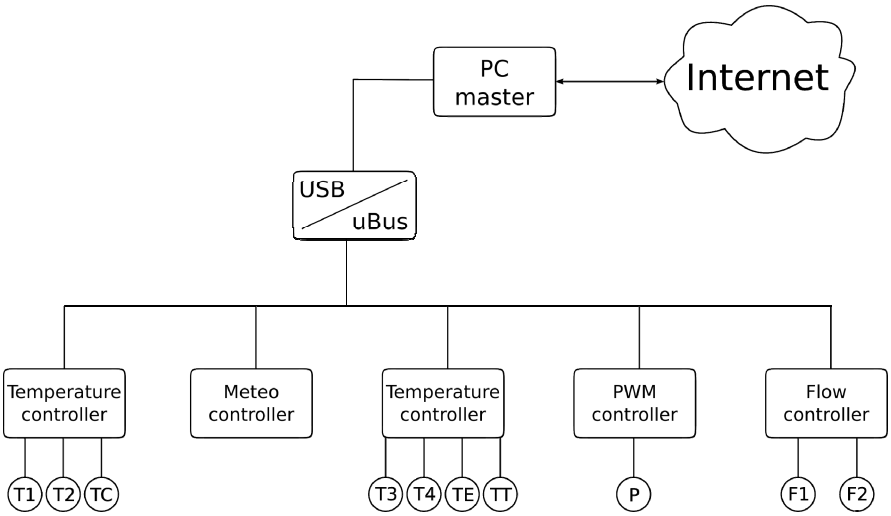

Fig. 5 Distributed control system components

4 Solution Implementation and Preliminary Results

Solar system in the configuration with three in series connected collectors with a maximum power Pmax = 2400W has been implemented in the hydraulic circuit according to Fig. 1. The collector assembly is shown in Fig. 6. 100W actuator pump was controlled with PWM module in Fig. 5, power part of the pump control optically insulated from other parts of the system. The volume of the Drain-back tank was 12 liters.

System monitoring and control over the Internet [3] has been implemented by the client application pvbrowser, sample screen in Fig. 7. Server computer of distributed control system, acted also as a pvbrowser server.

Fig. 6 Actual collector assembly

Standard control system of solar collectors is based on a simple algorithm differential thermostat, when the velocity of the heat transfer fluid flow is directly proportional to the temperature difference and the system is free from discontinuous states.

Discontinuous states occur in the Drain-back system at the system startup, system stop emergencies. Therefore, the algorithm requires detailed monitoring of temperature control with the speed of data collection 1 measurement per second and continuous evaluation with regard to the immediate amount of stored thermal energy in different parts of the system.

Fig. 7 shows the rise of temperatures in the system after emergency system stop as a result of exceeding the maximum temperature of 60 °C in the DHW storage tank. From the graph is clearly visible the rise of the collector temperature without heat transfer fluid, which was after system stop concentrated by the gravity flow in the Drain-back tank. The temperature in the rest of the system does not exceed safe levels and the solar system after the incident passed into a safe state.

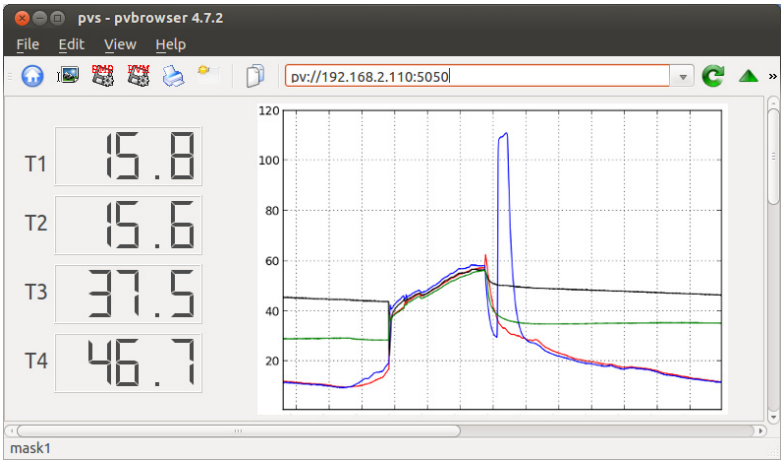

Fig. 7 Pvbrowser client application windows

5 Conclusions

Existing results demonstrated high flexibility of the proposed concept of distributed system of data collection and control, where the uBus allows easily connecting additional modules.

All obtained operating data will be used for the creation of a comprehensive mathematical model of the solar system, which will be further used for the calculation and modeling of other solar systems and their symbiosis with other sources of thermal energy.

In the future development, we expect the use of statistical and current meteorological forecasting data to support predictive control system based on local weather forecasts and publicly available meteorological models.

Acknowledgment. This paper was done within the VEGA project nr. 1/0463/13.

References

[1] Laughton, C.: Solar Domestic Water Heating. Earthscan, London & Washington (2010)

[2] Tanuska, P., Vazan, P., Kebisek, M., Moravcik, O., Schreiber, P.: Data Mining Model Building as a Support for Decision Making in Production Management. In: Wyld, D.C., Zizka, J., Nagamalai, D. (eds.) Advances in Computer Science, Engineering & Applications. AISC, vol. 166, pp. 695–701. Springer, Heidelberg (2012)

[3] Maga, D., Sitar, J., Bauer, P.: Automatic Control, Design and Results of Distance Power Electric Laboratories. In: Recent Advances In Mechatronics, pp. 978–973 (2008-2009) ISBN: 978-3-642-05021-3.

Design of Engine Control System for Small Helicopter

L. Ertl and M. Jasansky

UNIS - Mechatronics and embedded systems, Jundrovska 33, 624 00 Brno, Czech Republic
{lertl,mjasansky}@unis.cz

Abstract. This paper deals with integration of feedforward into turbo-shaft engine control algorithm and its influence on control quality. The control system provides fuel feeding, gas-generator speed control, power turbine speed control and operation limits of critical parameters. The achieved results are shown and described below.

1 Introduction

The electronic control system for small turbo-shaft engine was designed and produced. The basic control algorithm was designed according to the customer and target application requirements. The designed system shall solve significant plant nonlinearity and challenging requirements on transient state of power turbine speed caused by large disturbances. All presented results were verified on real engine.

2 Architecture of Control System

The simplified scheme of the control system is in Fig.2. The control system is made by two loops connected into a cascade structure. The loop inside controls gas-generator speed and the outside loop controls power turbine speed. Operation limiters are connected between these two loops. The limiters change the set-point value with limited authority (with only one direction - down).

2.1 Fuel Feeding System (Nfpump)

Fuel feeding system is a set of components that ensures the delivery of fuel to the engine nozzles. It is an electromechanical system equipped with two BLDC motors that drive two mechanical fuel pumps. The block diagram of feeding system is shown in Fig. 4.

T. Březina and R. Jabloński (eds.), *Mechatronics 2013*,
DOI: 10.1007/978-3-319-02294-9_95,

2.2 Gas-Generator Control

Analyses of gas generator showed significant nonlinearity, therefor the designed control system uses technique of gain scheduling from linear control theory. Main logic function switches coefficients of PI controller according to the flight mode (IDLE/FLIGHT) and according to the operation state. The transition between controller bands is without jump and with hysteresis. The controller coefficient scheduler is displayed in Fig.3. This design allows to maximize the power response of engine to changing load of power turbine in all operation conditions.

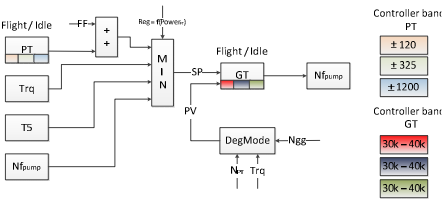

Fig. 1 Simplified scheme of control system

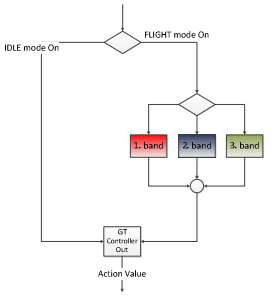

Fig. 2 PI coefficient scheduler of gas generator controller according to flight mode

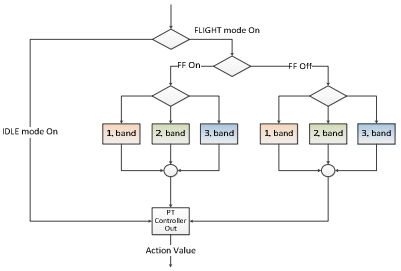

Fig. 3 PI coefficient scheduler of power turbine according to flight mode

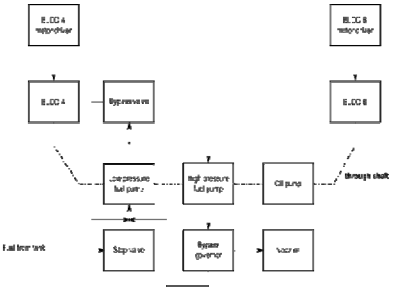

Fig. 4 Fuel feeding system

2.3 Power Turbine Control

Analyses of power turbine showed significant nonlinearity also. The design of control system using the technique of gain scheduling from linear theory was used in this case in the same way like in previous one. Only in this case were designed two three-band controllers. One of them is the very same as the previous one, but the second one has added the feedforward from collective position. The algorithm is displayed in Fig.3.

The power turbine control is divided into two controllers. There is possible to switch between both controllers during operation mode. The variant with feedforward responds better to the change of load of power turbine, therefore this variant is preferred.

The controller coefficients are split into three bands according to value of defiance between reference and actual measured value of power turbine speed. This algorithm satisfies all the requirements about reaction speed with robustness in phase and amplitude safety. The controller contains the anti-windup function because of limiters intervention.

Table 1 The example of three-band PID controller settings for power turbine

Band	Band / Gain	Kp	Ki
1	+/-1%	1	0.1
2	+/-3%	1.5	0.18
3	+/-5%	2	0.25

2.4 Power Turbine Controller Implementation – Feedforward

The feedforward was added to improve the power response. This feedforward is based on measuring the position of collective and therefore the speed of generator turbine can be increased sooner before power turbine speed starts to decrease.

The feedforward is designed as parallel table function, which output is added to the output from PID controller. The result of this operation is set as the set-point value to generator speed controller. In case of failure of feedforward, this can be disabled and the control algorithm smoothly changed to standard control without the feedforward. It is defined through eleven parameters, these can be modified according to the type of main rotor. The values of feedforward are calculated from mathematical model of rotor. In case of unknown rotor model, the dependence can be measured.

2.5 Operation Limiters

The control system has implemented operation limiters of critical parameters such as limit for maximal exhaust gas temperature or maximal torque on the power turbine shaft or maximal pump speed. These limiters are connected into the control structure, just before the inner loop, where they can change the set-point value from the outside loop.

The limiters have limited authority, they can change the set-point value only to downside. All the influences from the limiters are bounded on the bottom and simultaneously they cannot cause the decrease of gas generator speed under the defined range.

2.6 *Comparing of the Control System with or without Feedforward*

The helicopter producer expects nominal rotor speed approximately 514 rpm. Next figure compares power turbine speed in dependency to the disturbance error (collective position change). Time sequence of collective position is in fig. 6.

There was a change collective position change from an angle 4° to 9° in time 2s, this change took about 1s and then there was change of collective position from an angle 9°to 4°in time 17s, this change took also 1s.

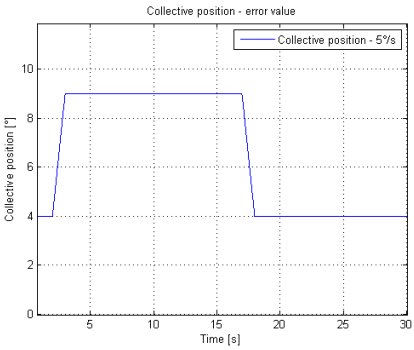

Fig. 5 The time sequence of simulated change of collective position

The simulation results are summarized in table 2. These results are shown in fig. 8-10 also and they show the difference between power turbine speed control with or without feedforward. The feedforward minimizes undershoot and overshoot of power turbine speed. There is the response of gas generator speed control to change of load in fig. 7. The responses of control algorithm with and without feedforward in upper loop are shown in these figures. Feedforward significantly improves the action value from the controller.

Table 2 The results with variable load

Test Case	Change of load	Reduced moment of inertia [kg*m^2]	PI control without feed-forward	PI control with feed-forward
1	70-280Nm/2s	0.64	485/514 - 5,6%	505/514 - 1,7%
2	70-280Nm/3s	0.64	490/514 - 4,7%	506/514 - 1,6%
3	70-280Nm/5s	0.64	497/514 - 3,3%	507/514 - 1,4%
4	70-280Nm/7s	0.64	500/514 - 2,7%	509/514 - 1,0%

It is obvious that the control algorithm with feedforward responses to power turbine load change faster than the algorithm without the feedforward. The second control algorithm is slower because of inertia of system (power turbine + redactor + rotor). The quality of regulation will be always better with the feedforward, when the inertia of a system will rise.

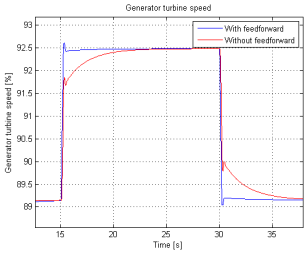

Fig. 6 Generator turbine speed – control with / without feedforward

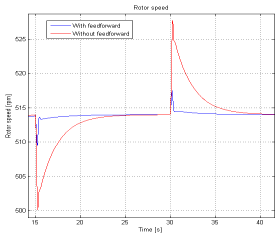

Fig. 7 System response to error value – with / without feedforward

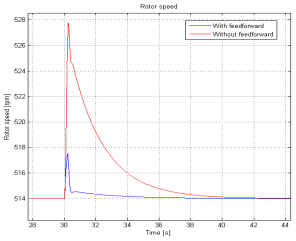

Fig. 8 Main rotor speed – The rotor load relief

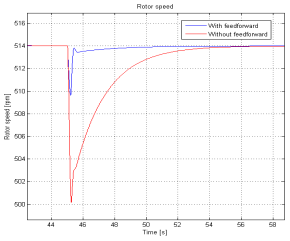

Fig. 9 Main rotor speed – The rotor load increase

3 Conclusions

Designed structure of control can be implemented on helicopter engines with feedforward or without it. The system allows to use analog and digital value of feedforward. This connection increases the quality of control during the transition states. The control can disable the feedforward during the error state or in case the superior system of helicopter does not provide the information about collective position.

The more complicated three-bands controllers have to be implemented to meet the requirements on control quality in case of the control without the feedforward. There should be more complex logic function to switch between them also. The requirements of costumer (PBS, a.s. Velká Bíteš) cannot be satisfied with only one controller.

The nonlinear dynamic model of turbo-shaft engine was created during the development process. This model was used for the simulations and tests of control algorithms. The gained experience from engine test stand in PBS proofed the correct way of design process, so it can be extended and the mathematical engine model can be improved.

Acknowledgments. The present work has been supported by the project The development of turbo-shaft engine designated for light helicopters and unmanned aircrafts "(FR-TI2/313)" under Ministry of Industry and Trade of the Czech Republic.

References

[1] Levine, W.: The control handbook, 2nd edn., p. 3526 CRC Press (2010) 978-1420073669
[2] Apkarian, P., Adams, R.J.: Advanced Gain-Scheduling Techniques for Uncertain Systems,İEEE Transactions on Control Systems Technology 6(1), 213–232 (1998)
[3] Stivers, L.S., Rice, F.J.: Aerodynamic Characteristics of Four NACA Airfoil Sections Designed for Helicopter Rotor Blades, NACA RB No. L5K02 (1946)
[4] O'Dwyer, A.: Handbook of PI and PID Controller Tuning Rules, 2nd edn. Imperial College Press, ISBN 1-86094-622-4
[5] Astroem K., Haegglund, T.: PID Controllers. Theory, Design and Tuning. Instrument Society of America, ISBN 1-55617-516-7
[6] Altmann, W.: Practical Process Control for Engineers and Technicians, IDC Technologies, ISBN 0-7506-6400-2
[7] Johnson, M.A., Moradi, M.H.: PID Control - New Identification and Design Methods. Springer, ISBN 1-85233-702-8

Application of Indices Characterizing the Shape of a Signal for Automatic Identification of Artifacts in Impedance Cardiography

P. Piskulak[1], G. Cybulski[1,2], and W. Niewiadomski[2]

[1] Warsaw University of Technology, Department of Mechatronics, Institute of Metrology and Biomedical Engineering, Św. A. Boboli 8, 02 525 Warsaw, Poland
G.Cybulski@mchtr.pw.edu.pl
[2] Mossakowski Medical Research Centre of the Polish Academy of Sciences, Department of Applied Physiology, Pawińskiego 5, 02 106 Warsaw, Poland
wiktorn@cmdik.pan.pl

Abstract. The aim of this work was to introduce five form factors describing the shape pattern of the impedance cardiography (ICG) signal during one cardiac cycle. These form factors were used for automatic classification of ICG heart evolution as either valid or artifact. For each tested cardiac cycle in a verified ICG signal, the values of the form factors were calculated and compared with the respective form factor for the pattern. We evaluated the ability of each form factor to detect artifacts based on the receiver operating characteristic (ROC) method.

1 Introduction

It is difficult (or even impossible) to analyze hemodynamic parameters during a patient's normal activity using well-established, "classical" methods [1-4]. Ambulatory impedance cardiography (AICG) monitoring is a technique allowing estimation of cardiac hemodynamics during transient events. Researchers using impedance cardiography (ICG) systems are familiar with the problem of motion artifacts during ICG signal stationary recordings. This problem is more expressed in holter-type ambulatory impedance cardiography systems due to the motion of the patient [2, 4]. The ICG signal of the first derivative is about two orders weaker than ECG, so any disturbances in electrode–skin contact resulting in a significant decrease in signal quality. The careful placement, positioning, and firm fixing of electrodes can significantly reduce the rate of artifacts [5,6]. Although the problem seems to be known, it has not so far been intensively analyzed using quantitative methods.

Willemsen et al., during the verification of their system (the VU-AMS ambulatory monitor for impedance cardiography), concluded that it is a valid device for the measurement of systolic time intervals in real-life situations, but that its applicability for absolute stroke volume and cardiac output determination remained to

T. Březina and R. Jabloński (eds.), *Mechatronics 2013*,
DOI: 10.1007/978-3-319-02294-9_96,

be established [3]. Their reservations regarded stroke volume and cardiac output values obtained only during exercise.

Since some of the AICG recordings are too noisy to analyze, it is important to automatically reject corrupted signals. This problem was considered in other papers when we evaluated the rate of artifacts for day and night recording [7] and tried to identify the artifacts' possible source [8].

Figure 1 illustrates the scale of the problem by presenting examples of noisy and relatively clean recordings obtained in the previous study when the subject walked on stairs and remained in supine position, respectively [8].

Fig. 1 The noisy (top strip) and artifact-free (bottom strip) recordings obtained in the previous study [8]

The aim of this study was to introduce five form factors (FF_i) describing the shape pattern of the impedance cardiography (ICG) signal during one cardiac cycle. We intended to use these form factors for automatic classification of ICG cardiac evolution as either a valid change or as an artifact by comparing the current cycle with the pattern.

2 Material and Methods

The computer program that automatically detects the characteristic points in the electrocardiographic (ECG) and ICG signals (dZ/dt) necessary for calculation of

hemodynamic parameters and allows the user to browse the previously recorded data was presented in another paper [13]. It also creates the pattern of the ICG signal for one cardiac cycle based on 100 evolutions. One of the form factors used in this study was defined in that paper, too [13].

In the previous studies, cardiac evolution was classified as normal basing on the wide range of the acceptable values of cardiac parameters [9-12], whereas in this study the idea was to create the pattern of the one-cycle evolution of the dz/dt signal and use it for comparison with a signal for each heart beat.

2.1 Pattern of the ICG Signal

The pattern of the first derivative ICG signal (*dz/dt*) for one heart cycle was created by averaging 100 consecutive evolutions synchronized by the R wave in a simultaneous ECG [13]. Within the averaging section the characteristic points are detected (corresponding to Q in ECG, B, C and X); these are later used to calculate the pattern shape indices. The pattern of the ICG signal, with marked characteristic points on ICG trace, is presented in Figure 2 .

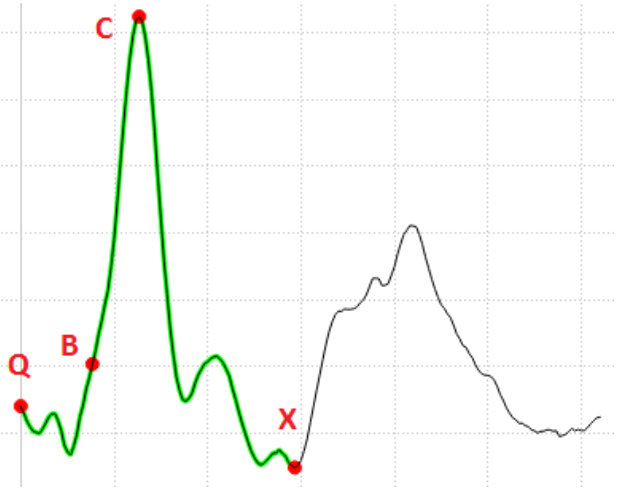

Fig. 2 The pattern of the QQ cycle with marked characteristic points on an ICG trace. B – the point where the curve crosses the base-line; C – the maximum of QQ segment; X – the minimum of QQ segment [13]

2.2 ICG Signal Form Factor Definitions

We introduced five shape descriptors (form factors) which characterize the pattern of the ICG signal. The form factors are numerical measures of specific features of

the analyzed shape – in our case, the QX period. They allow objective and easy comparison of one cycle of the ICG to the pattern. Some of the form factors were inspired by the image shape descriptors. Below, in Table 1, are the definitions of the five form factors.

Table 1 The definitions of the five form factors characterizing the shape of one cycle of ICG dz/dt signal

$FF_1 = \frac{GA}{LA}$	$FF_2 = \frac{G}{N}$	$FF_3 = \frac{L}{2\sqrt{\pi S}}$	$FF_4 = \frac{SU}{SA}$	$FF_5 = \sqrt{\frac{\sum_{i=1}^{n}(x_i - \bar{x})^2}{n-1}}$

where for

FF_1:

GA = the number of samples having values greater than the average
LA = the number of samples having values smaller than the average.

FF_2:

G = the number of samples having values greater than 2/3 amplitude of point C,
N = the total number of samples.

FF_3:

L = the length of the signal curve between the Q and X points,
S = the surface area above and below the base line within the period of QX.

FF_4:

SU= the surface area under the average value of QX segment,
SA = the surface area above the average value of QX segment.

The third form factor (FF_3) shows the relationship between the length of the curve and the sum of the area above and below the base line within the period of QX. This factor is used for automatic analysis of the ECG signal obtained in holter recordings and sometimes called Malinowska's factor. The fifth form factor (FF_5) is just the standard deviation of the cycle from the pattern, normalized according to the both length of QX and the maximum amplitude of dz/dt.

2.3 The Form Factors' Evaluation

When comparing the effectiveness of form factor in the classification of artifacts, it is important to identify the appropriate level of discrimination of a particular form factor. As a preliminary test, a 20-minute segment of ICG signal (obtained during overnight monitoring of one healthy human subject selected randomly from

a group of 12) was analyzed and each evolution was classified as normal or artifact, using both automatic and manual methods. Simultaneously, the absolute values of differences between FF_i for each detected cycle and the pattern were calculated. The value of the factor's differences and classification variable were plugged into a program plotting the receiver operating characteristic (ROC), published by Giuseppe Cardillo [14]. Thus it was possible to estimate the performance of a binary classifier system as its discrimination threshold varied. The area under the curve (AUC) is equal to the probability that a classifier will rank a randomly chosen positive instance higher than a randomly chosen negative one (assuming "positive" ranks higher than "negative") [14]. The cost effective cutoff is a point on the actual ROC curve whose distance from the upper left corner of the graph is minimal. It corresponds to the optimal cutoff value for the form factor.

3 Results

The AUC and the cost effective cutoff point for each FF are presented in Table 2. The highest AUC value was obtained for FF_5 , and the lowest, for FF_4 .

Table 2 The area under the curve (AUC) and the cost effective cutoff point for each form factor (FF_i)

	FF_1	FF_2	FF_3	FF_4	FF_5
AUC	0,6812	0,7068	0,7676	0,6489	0,8891
Cost effective cutoff point	0,7350	0,0596	0,3350	0,2940	44,40

Figures 3-5 present the ROC curves obtained for the best FF (according to the "maximum of AUC" criterion): FF_1, FF_3 , FF_5 .

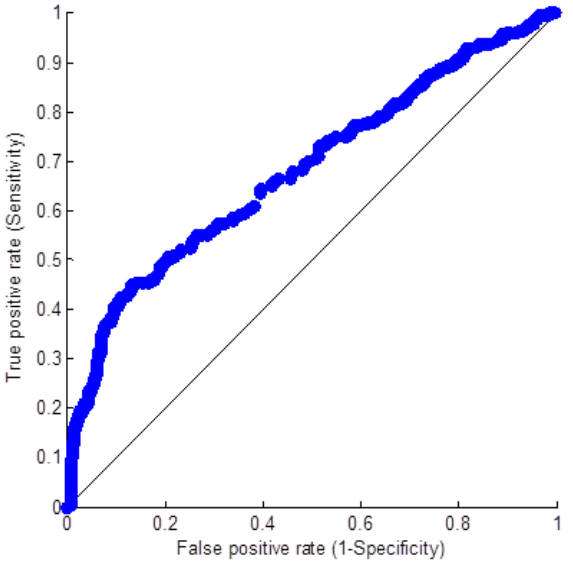

Fig. 3 The receiver operating characteristic for the first form factor (FF_1)

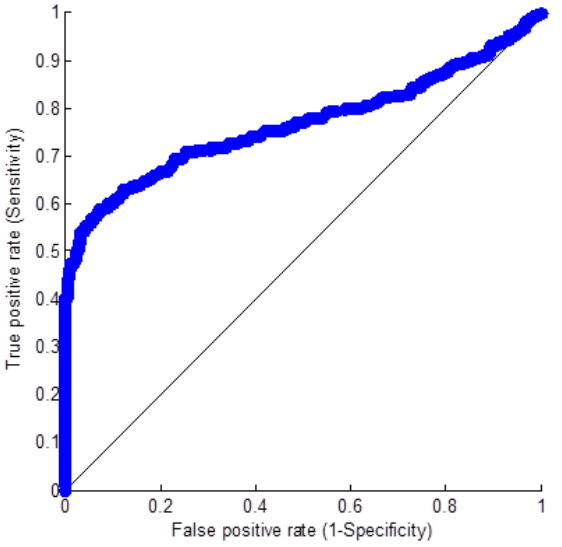

Fig. 4 The receiver operating characteristic for the third form factor (FF_3)

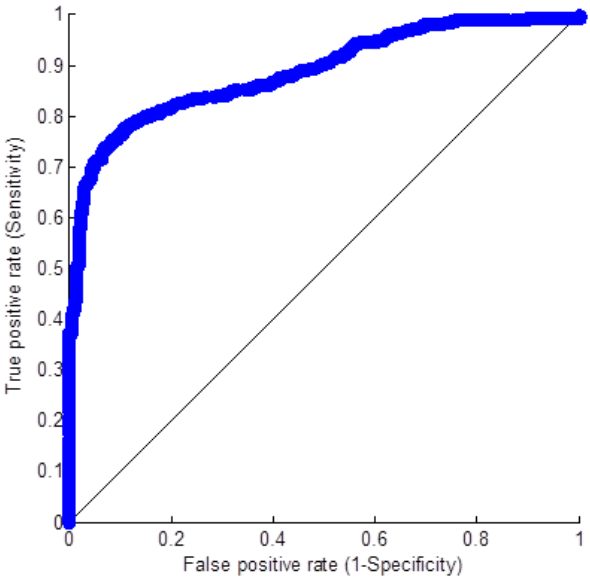

Fig. 5 The receiver operating characteristic for the fifth form factor (FF_5)

4 Conclusions

The aim of this work was to introduce five form factors describing the shape pattern of the impedance cardiography (ICG) signal during one cardiac cycle. Those form factors were used for classification of ICG heart evolution as either valid or artifact. For each tested cardiac cycle of the verified ICG signal, the values of form factors were calculated and compared with the respective form factor for the pattern.

We also sought to determine the index which could best characterize the discrepancies between the shape of the pattern and the analyzed cycle.

Acknowledgments. This study was supported by the research programs of institutions the authors are affiliated with: a) Development of the methods for noninvasive determination of control performance in cardiovascular system. b) Hemodynamic reaction to physiological stresses in humans.

References

[1] Cybulski, G., Książkiewicz, A., Łukasik, W., Niewiadomski, W., Pałko, T.: Ambulatory monitoring device for central hemodynamic and ECG signal recording on PCMCI flash memory cards. IEEE Computers in Cardiology, 505–507 (1995)

[2] Nakagawara, M., Yamakoshi, K.: A portable instrument for non-invasive monitoring of beat-by-beat cardiovascular hemodynamic parameters based on the volume-compensation and electrical-admittance method. Medical & Biological Engineering & Computing 38(1), 17–25 (2000)

[3] Willemsen, G.H., De Geus, E.J., Klaver, C.H., Van Doornen, L.J., Carroll, D.: Ambulatory monitoring of the impedance cardiogram. Psychophysiology 33(2), 184–193 (1996)

[4] Cybulski, G.: Ambulatory Impedance Cardiography. The Systems and their Applications, 1st edn. LNEE, vol. 76, p. 150. Springer, GmbH & Co. KG, Heidelberg (2011)

[5] Nakonezny, P.A., Kowalewski, R.B., Ernst, J.M., Hawkley, L.C., Lozano, D.L., Litvack, D.A., Berntson, G.G., Sollers III, J.J., Kizakevich, P., Cacioppo, J.T., Lovallo, W.R.: New ambulatory impedance cardiograph validated against the Minnesota Impedance Cardiograph. Psychophysiology 38(3), 465–473 (2001)

[6] Bogaard, H.J., Woltjer, H.H., Postmus, P.E., de Vries, P.M.: Assessment of the haemodynamic response to exercise by means of electrical impedance cardiography: method, validation and clinical applications. Physiological Measurement 18(2), 95–105 (1997)

[7] Cybulski, G., Niewiadomski, W., Gąsiorowska, A., Kwiatkowska, D.: Signal quality evaluation in Ambulatory Impedance Cardiography. In: Scharfetter, Merwa (eds.) 13th International Conference on Electrical Bioimpedance, Graz, Austria, August 29-September 2. IFMBE Proceedings, vol. 17, pp. 590–592. Springer (2007)

[8] Cybulski, G., Niewiadomski, W., Aksler, M., Strasz, A., Gąsiorowska, A., Laskowska, D., Pałko, T.: Identification of the Sources of Artefacts in the Holter-Type Impedance Cardiography Recordings. In: Jobbagy, A. (ed.) 5th European Conference of the International Federation for Medical and Biological Engineering. IFMBE Proceedings, vol. 37, pp. 1272–1274. Springer (2011) ISBN 978-3-642-23507-8

[9] Cybulski, G.: Computer method for automatic determination of stroke volume using impedance cardiography signals. Acta Physiologica Polonica 39(5-6), 494–503 (1988)

[10] Cybulski, G., Miśkiewicz, Z., Szulc, J., Torbicki, A., Pasierski, T.: A comparison between impedance cardiography and two dimensional echocardiography methods for measurements of stroke volume (SV) and systolic time intervals (STI). Journal of Physiology and Pharmacology 44(3), 251–258 (1993)

[11] Gasiorowska, A., Nazar, K., Mikulski, T., Cybulski, G.,, Niewiadomski, W., Smorawinski, J., Krzeminski, K., Porta, S., Kaciuba-Uscilko, H.: Hemodynamic and neuroendocrine predictors of lower body negative pressure (LBNP) intolerance in healthy young men. J. Physiol. Pharmacol. 2, 179–193 (2005)

[12] Cybulski, G., Michalak, E., Koźluk, E., Piątkowska, A., Niewiadomski, W.: Stroke volume and systolic time intervals: beat-to-beat comparison between echocardiography and ambulatory impedance cardiography in supine and tilted positions. Medical and Biological Engineering and Computing 42, 707–711 (2004)

[13] Piskulak, P., Cybulski, G., Niewiadomski, W., Pałko, T.: Application of the Indices characterizing the shape of signal for Automatic Identification of the Artifacts in Impedance Cardiography. In: IFMBE Proceedings (sent to the Editor)

[14] http://www.mathworks.com/matlabcentral/fileexchange/19950-roc-curve/content/roc.m

Predictive Algorithm for the Insulin Dose Selection with Continuous Glucose Monitoring System

H.J. Hawłas* and K. Lewenstein

Warsaw University of Technology, Faculty of Mechatronics, Institute of Metrology and Biomedical Engineering, 8 Sw. A. Boboli Str., 02-525 Warsaw, Poland

Abstract. Diabetes Mellitus is a disease of modern civilization affecting millions of people worldwide. On-going studies aim at developing and testing an algorithm of the automatic insulin dose calculation for systems with a personal Insulin Pump and Continuous Glucose Monitoring device (CGM), whole system would work in closed loop. Tests are carried out as in silico, or by using a computer model which is reflecting the functioning of the living organism in terms glucose-insulin metabolism. Conducted studies have shown that individually tested neural networks at the expected projections time of 30 minutes ahead are not able to unambiguously predict what the expected value of blood glucose be. However, it seems that for the correct control of glycaemia, signal of the expected BG trend is sufficient. As a evaluation tool for the designed algorithm we have used so called Control Variability Grid Analysis (CVGA) method.

1 Introduction

Entry into the twenty first century with the development of technology and the increase in the standard of living societies led to a significant increase in the incidence of so called civilization diseases. Such diseases include undoubtedly diabetes. Diabetes is a chronic disease, and if left untreated, leads to severe complications and even death. According to the World Health Organization [1], more than 220 million people worldwide suffer from it. In 2004, it is estimated that about 3.4 million people died from the effects of high blood sugar. Again according to WHO, the number of expected deaths from diabetes will double between 2010 and 2030.

Roughly speaking it can be assumed that type 1 diabetes (T1DM) is a disease in which the body is unable to independently regulate blood glucose (BG-Blood Glucose) due to lack of hormone produced by the pancreas - insulin.

As normal serum glucose levels is the value of 60 (70) - 110 (120) mg / dl, the values below 55 mg / dl is defined as a state of hypoglycaemia (hypoglycemia). The values of about 25 mg / dL severe hypoglycemia which symptoms are

* Corresponding author.

T. Březina and R. Jabloński (eds.), *Mechatronics 2013*,

DOI: 10.1007/978-3-319-02294-9_97,

convulsions and coma, and it is a life threatening condition. As the blood glucose concentration exceeds 120 mg / dl in the fasting state or 160 mg / dl postprandial state is determined as hyperglycemia. Above the 180 mg / dl is glycosuria and excrete the excess glucose into the urine.

Ongoing studies aim at developing and testing an algorithm of the automatic insulin dose calculation for systems with a personal Insulin Pump and Continuous Glucose Monitoring device (CGM), whole system would work in closed loop.

Such circuit (see Fig.1) equipped with glucose sensor and properly controlled insulin dispensing device may eventually be seen as a kind of artificial pancreas, which is a device that autonomously or with some minimal patient attention will control the level of glucose in the blood, preventing from the occurrence at both hyper-and hypoglycemia.

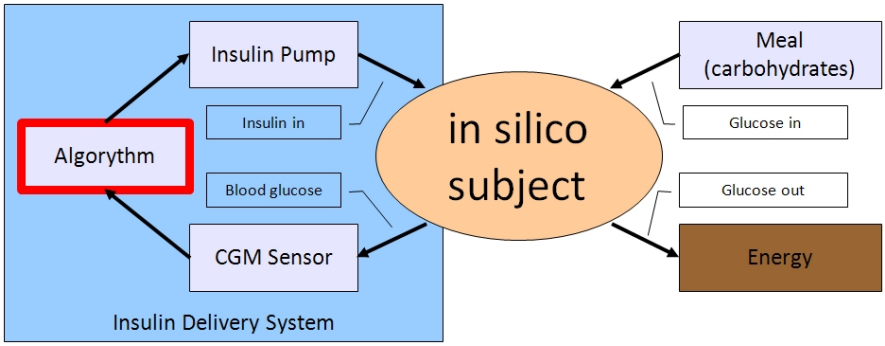

Fig. 1 Diagram of closed loop insulin delivery system

2 The Research Carried out so Far

Because commission approval is required for research on patients and there are potential risks associated with such research, we decided to focus on the "In silico" examination. Tests are carried out as in silico, or by using a computer model which is reflecting the functioning of the living organism in terms glucose-insulin metabolism.

Adopted in silico research method has many advantages and is justified by important factors, the main reason is the possibility of testing scenarios with life-threatening extreme values. An undoubted advantage of tests with the computer model is repeatable research. Patients are always in the same initial state, and during the test there are no factors distorting the result. Thanks to this study, we may notice even slight changes in the regulation, without a doubt, that they are not caused by disruptions.

Model used for our tests was developed by a team lidded by PhD. Boris Kovatchev of the University of Virginia, USA. The simulator is implemented in Matlab. [2].

The model was developed on the basis of 300 people, each of which is reflected in the simulator, locally we have 10 virtual patients at each of three age groups.

The method of in slico allows to achieve results faster and reduce costs compared to in vivo testing.

Used model was designed specifically to enable research into methods of glycemic control in combination with a closed loop feedback. The model reflects system which consists of a CGM and insulin pump and block to design the controller. Simulator due to the fact that its main purpose is testing of control systems takes into account the specificity of commercially available CGMs and insulin pumps (errors, discretization, noise) [3][4].

Mathematical glucose - insulin model is based on the work presented by Dalla Man, Cobelli [5]. Model of in-silico subject is assumes that glucose consumption and its internal secretion is controlled by insulin. Subject model is multi- compartment one. Subsystems represent important from the glucose-insulin regulation point of view organs of the relationship between them. Those subsystems include: stomach, serum, intestine, liver, kidney, brain, red blood cells or peripheral tissue glucose consuming.

It should be noted that the main drawback of the model is that it does not take into account influence of physical activity to the glucose-insulin regulation.

Our additional objective is to explore the possibility of adding to the model influ-ence of physical activity on sugar curves of patients.

An early study has been performed for insulin pumps and their parameters identi-fied and requirements for the insulin pump and the entire system of insulin deliv-ery were defined. [6] [7] [8].

We determined the most important factors affecting the control algorithm. They include: delayed action of insulin, delayed information about current BG (up to 15min) and low accuracy (even over 20% even at low concentrations), unknown demand for glucose, and only estimated value carbohydrates in the meal.

In subsequent studies we identified in silico research opportunities and possible control of BG vs. time curves shape. [9] [10] Factors which affect rate of change at rise / fall and maximum BG. (Table 1.)

The study revealed that the rate of rise in blood glucose is not affected noticeably with insulin dose.

Our studies have shown a wide variety of rate of change of BG curves depending on the subject and especially his/her age.

Our approach is that all patients be treated with a personalized algorithm.

It was established that the control algorithm will be utilize a neural network pre-dictor. Conducted studies have shown that tested neural networks at the expected projections time of 30 minutes ahead are not able to unambiguously predict what the expected value of blood glucose be. However, it seems that for the correct control of glycaemia, signal of the expected BG trend is sufficient. Tested neural network predictor generates expected trend of BG change with adequate accuracy for 30 minutes forward. (Fig. 2)

Table 1 Summary of possible influence to the BG vs. time curve shape

"+" indicates that value of observed parameter increases along with increase value of causing factor, "-" means opposite relation, „x" indicates that influence of factor was not observed, "/" denote that relation is subject specific.		Observed parameter of BG vs. time curve		
		BG max	Rise rate	Fall rate
factor	pre-meal insulin delivery time	-	x	- / x
	meal duration	-	x	x
	insulin dose	-	x	+ / x
	pre-meal insulin dose divided in to smaller doses and spread along some time (split bolus)	+	x	x
	time between split bolus doses	+	x	-

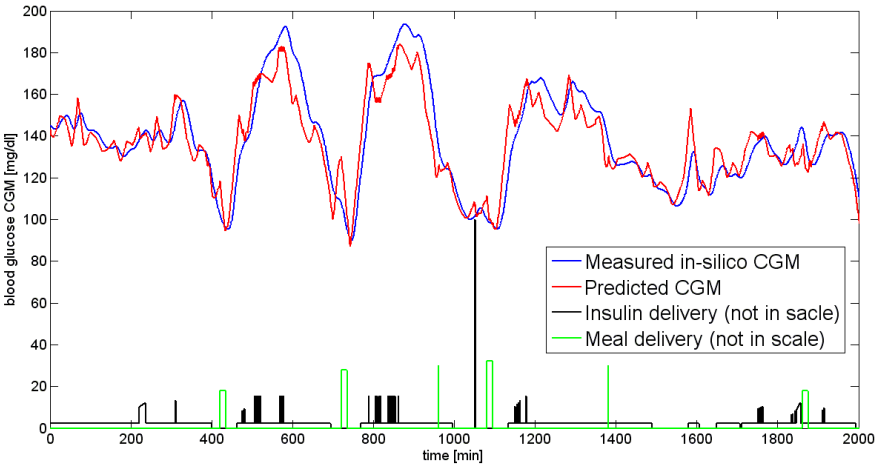

Fig. 2 Sample output of tested control algorithm

3 Evaluation of the Control Algorithm

To assess the quality control algorithm we use various statistical tools embedded in simulation environment. Mostly we use three following types of information.

1. Control Variability Grid Analysis (CVGA).

CVGA graph shows overall glycaemia control. The CVGA graph is generated as follows: for each subject a dot is plotted with (x,y) coordinates. Where x-coordinate is the minimum BG and y-coordinate is the maximum BG for an

observation period. Typically period is set to 24h. Such plot shows what is effect of treatment to the patient health. The graph is divided into 6 zones due to x and y coordinate value.

- A-zone, Accurate control.
- Lower B, Benign deviations into hypoglycemia
- Upper B, Benign deviations into hyperglycemia
- Lower C, Over-Correction of hyperglycemia
- Upper C, Over-Correction of hypoglycemia
- Lower D, Failure to Deal with hypoglycemia
- Upper D, Failure to Deal with hyperglycemia
- E-zone, Erroneous control

Points plotted in the A-zone indicates that subject BG was kept within the normal range of 90–180 mg/dL. As point is placed further form A-zone it indicates devia-tion form normoglycaemia and means greater health risk. [11] On the Figure 3 there are results for tested algorithm.

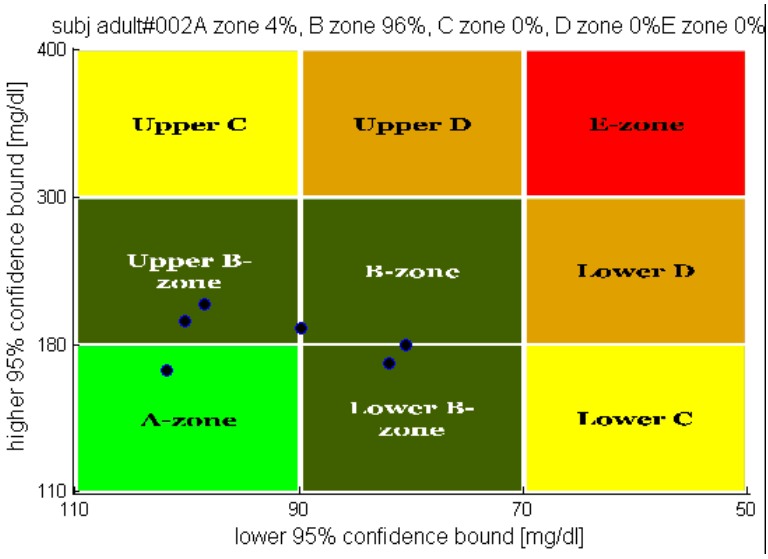

Fig. 3 Control Variability Grid Analysis for tested control algorithm

2. Blood glucose versus time curve.

Blood glucose versus time curve shows BG level or measured CGM data along the time. Graph is easiest way to observe regulation and spot characteristic points where regulator fails to control BG level.

3. Per cent time.

Percentage time of whole simulation duration at some condition for example in A-zone of CVGA (see above Figure 3 plot) or in specified BG level range. This

provides measure of regulation quality and enables to compere results between subjects, different scenarios or control algorithms.

4 Discussion of Results

At this stage of the study as a predictor of the BG trend we use a one-way neural network. Neural network is with five sigmoidal neurons in the hidden and linear output. Neural Network predicts expected BG level at maximum 30 minutes ahead. Input vector contains information about the expected meal and carbohydrate content, the current CGM reading. Network has an extra input with derivative of CGM reading.

Basing on the derivative of the neural network response (predicted BG) and the current value of CGM reading decisions are taken whether to make insulin infusion. The value of the dose is calculated on the basis of patient-specific factors available in the model.

Curves of BG vs. time during closed loop operation of described control algorithm have been shown in Figure 2. As you may notice predicted CGM curve is changing more rapidly than real CGM and differs slightly in value. That's why only derivative of predicted signal were used. On the Figure 2 you can see when meals where provided for the subject and when insulin was delivered.

So far some of subject were tested and for each subject his / her own network was trained. Training set is based on typical one-week CGM measures.

We are having more problems to tune up control algorithm for child patients then another ages groups. We expect that is due higher dynamics of young subject BG response to meal and insulin.

5 Conclusions

Presented approach to blood glucose regulation in closed loop is one many of possible methods. Presented first tests of control algorithm with neural network predictor proofs it as a quite good solution.

We are aware that presented above initial positive results is the beginning of a long journey for the success of which would be able to optimize the control algorithm together with the wording of the final requirements for the CGM sensor and pump.

Currently we are at the stage of improvement personalized neural predictor and at the same time checking the possibility of enhancing the model for the effect of the patient's physical activity. Such patient model enrichment must be made in close consultation with the medical, diabetologists doctors cooperating in the development of methodology.

We assume that in the final optimized control algorithm, we can estimate (increase) the maximum prediction interval while maintaining the correct glycaemia control.

Acknowledgments. Work was supported by Faculty of Mechatronics Dean Grant 504M 1142 0410 000. In-silicon model was founded by Institute of Metrology and Biomedical Engineering, Warsaw, Poland.

References

[1] WHO Fact sheet N°312, WHO Word Wide Web, http://www.who.int/mediacentre/factsheets/fs312/en/
[2] Kovatchev, B., Breton, M., Man, C.D., Cobelli, C.: Silico Preclinical Trials A Proof of Concept in Closed-Loop Control of Type 1 Diabetes. Journal of Diabetes Science and Technology 3(1), 44–55 (2009)
[3] Frequently Asked Questions about the UVa Type1 Metabolic Simulator
[4] Uva T1DM simulator user guide
[5] Man, C.D., Cobelli, C.: Meal Simulation Model of the Gluco se-Insulin System. IEEE Transactions on Biomedical Engineering 54(10), 1740–1749 (2007)
[6] Hawłas, H., Lewenstein, K.: The Design of an Insulin Pump – Preliminary Requirements. In: Recent Advances in Mechatronics 2008-2009, part 4, pp. 329–334 (2009)
[7] Hawłas, H., Lewenstein, K.: The design of an insulin pump - preliminary requirements (A Technical note). Polish Journal of Medical Physics and Engineering 15(1), 25–32 (2009)
[8] Hawłas, H., Lewenstein, K.: The design of an insulin pump – concept of closing the loop. Journal of Automation, Mobile Robotics & Intelligent Systems 3(4), 195–198 (2009)
[9] Hawłas, H., Lewenstein, K.: Silico Simulator as a Tool for Designing of Insulin Pump Control Algorithm. In: Mechatronics, Recent Technological and Scientific Advances, pp. 635–643 (2011)
[10] Hawłas, H., Lewenstein, K.: Analiza wpływu wymuszenia posiłek - dawka insuliny na przebieg krzywych cukrowych komputerowych modeli pacjentów. Pomiary Automatyka Kontrola 58(12), 1124–1128 (2012)
[11] Clarke, W., Kovatchev, B.: Statistical Tools to Analyze Continous Glucose Monitor Data. Diabetes Technology & Therapeutics 11(1), 45–54 (2009)

Experimental Device for Reconstructing Spinal Deviations in to a 3D Model

F. Horvát, M. Čekan, L. Šoltés, and B. Hučko

Slovak University of Technology, Department of Applied Mechanics and Mechatronics, Faculty of Mechanical Engineering, Námestie slobody 17, 812 31 Bratislava
{frantisek.horvat,michal.cekan,lukas.soltes,branislav.hucko}@stuba.sk

Abstract. The article introduces an experimental device based on optical technology for the measurement of spinal deviations in patients suffering from scoliosis or any related diseases. The electronic design of the device is explained as well as the MATLAB based control and data processing methodology. The results show that a 3D model can be reconstructed through the measurement of reflected light intensity and its subsequent interpretation. The reconstructed image shows a visible deviation in the thoracolumbar part of a patient back which can be used by medical staff to evaluate or monitor the progression of related diseases.

1 Introduction

Spinal diseases, which result in the deformation of the spine, are currently amongst the most common diseases throughout human development [1]. The early diagnoses of these diseases are crucial in stopping their further progression, and even reversing their effects. For this purpose, a wide range of diagnostic devices are used. This paper proposes a more compact experimental device which is less invasive but with comparable accuracy to already existing devices, while reducing any operational complexity.

In terms of human anatomy it is important to understand the planes *(p.)* of the human body. These planes are divided into the following:

- *medial p.* – the vertical plane which divides the human body into a mirror image of each half
- *frontal p.* – the vertical plane which is parallel with the forehead (perpendicular to the medial)
- *transverse p.* – the horizontal plane which is perpendicular to the medial and frontal planes.

To visualize the above mentioned planes on the human body we must consider a person's so called orthostatic position. This position is almost always defined as

T. Březina and R. Jabloński (eds.), *Mechatronics 2013*,
DOI: 10.1007/978-3-319-02294-9_98,

standing upright with the upper limbs freely hanging along the body with the palms facing forward. Figure 1 shows the human body planes on an orthostatic human posture [1].

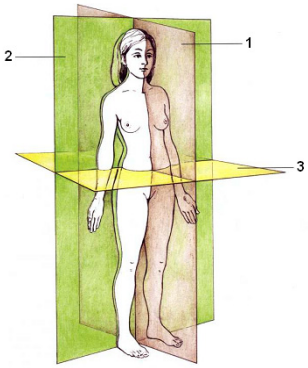

Fig. 1 Body planes: 1 - medial p. 2 - frontal p. 3 - transverse p. [1]

The scientific topic of orthopaedics deals with diseases which affect the human spine as well as diseases which effect human mobility. A disease affecting the human back often manifests themselves in the sideways deformation (along the frontal and transverse directions) of the spinal column.

Roentgen *(X-ray)* is one of the basic methods in determining a person's medical history – together with determining their current medical state. These two elements form the basis for adequate diagnosis and evaluation of the spinal column. For this purpose a wide range of devices are used such as: roentgen *(RTG)*, computed tomography *(CT)*, magnetic resonance imaging *(MRI),* and ultrasonography *(USG)* [3].

2 Experimental Device

The experimental device *(ED)* works on the principle of optical surface scanning with achromatic color – cold white [7]. The reflective properties of the scanned surface *(E)* causes changes in the intensity of light emitted *(LE).* Emitted light *(LE)* was after reflection from the scanned surface *(LR)* returned to the experimental device *(ED).* The results of these changes is an image of the scanned surface in TIFF format *(DA)* with 600 DPI. The TIFF format is then processed in the MATLAB environment to interpret its 3-D representation. The principles of the device are described in the scheme on figure 2 [4], [5], [6].

The block diagram of the device can be seen in figure 3 and its structure can be divided into four groups:

1.) frame of the device.
2.) scanning head with light energy blocks *(LB1, LB2)*. This assembly functions by moving parallel to the scanned object.
3.) motion system, which consists of a step motor *(M)*, timing belt *(TB)* and guide rod *(GR)*. The purpose of this component is to ensure the smooth and consistent motion of the scanning head.
4.) controller *(C)* and communication interface *(CI)* together with the power supply *(PS)*.

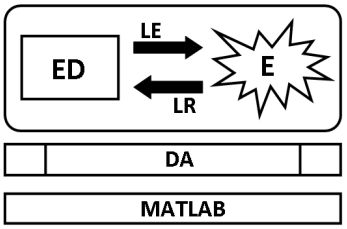

Fig. 2 Device principles: ED – experimental device, E - scanned surface, LE – light emitted, LR – light reflected, DA – data acquisition, MATLAB - processing environment

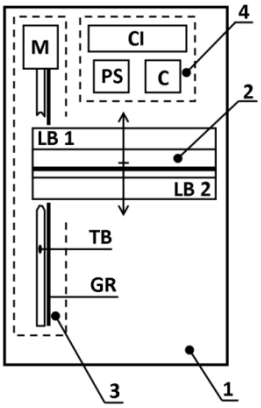

Fig. 3 Block diagram: 1) frame of the device, 2) scanning head with LB1 & LB2 – light energy blocks, 3) motion system with M – step motor, TB – timing belt, and GR – guide rod, and 4) communication and control block with C – controller , CI – communications interface, PS – power supply

From the 2D scan, the 3rd dimension is determined as the difference between the lowest and highest points of the measured object from the same base, which is expressed in formula (1). The schematic representation for determining the reference distance can be seen in figure 4.

$$D_{ref} = D_{max} - D_{min} \tag{1}$$

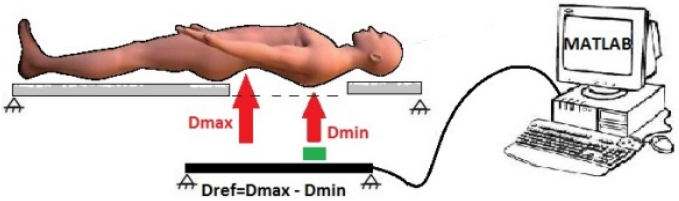

Fig. 4 Determination of the reference distance

3 Implementation

In order to quickly process and visualize measured data, the self executable application "Analysis of Spine" was created in MATLAB. The application enabled quick transformation of the scanned image and also incorporated multiple image processing filters such as: average, disk, Gaussian, Laplace and others to fulfil a wide variety of image post processing methods depending on the scanning conditions. The filters are possible to use in a default value or with the possibility to modify parameters. A secondary advantage to the processed 3-D model is the possibility to create 3-D sections of the scanned image along the transverse plane and graphically display them. Figure 5 shows the "Analysis of Spine" application interface [5], [6].

The devices function was verified on a synthetically coated polystyrene model of the human back. The difference between the lowest and highest points on the model, which according to equation (1) represent the reference distance D_{ref},

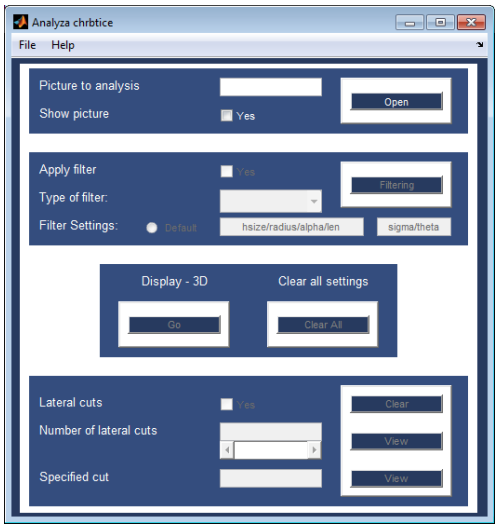

Fig. 5 "Analysis of Spine" application

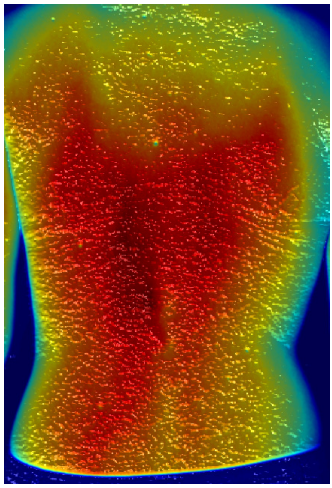

Fig. 6 Color spectrum scan of the patients back

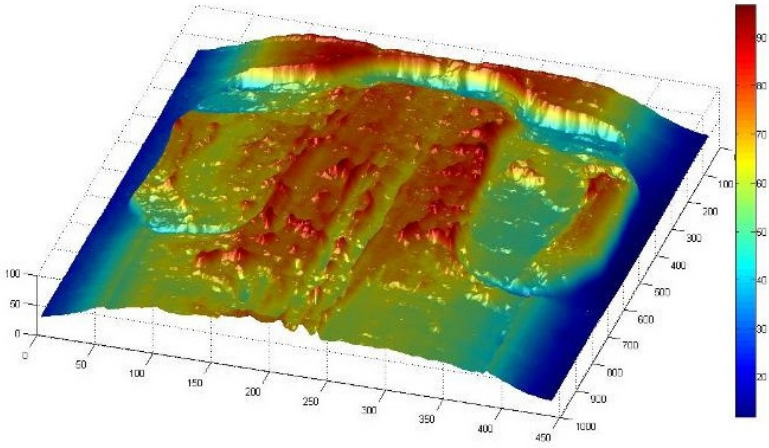

Fig. 7 3-D color spectrum from the polystyrene model of the patient back

which in the case of the polystyrene model was 0.11 m. For clarity, the 3-D model is defined in a colour spectrum, this allows for the very simple and practical determination of distance values at any point of the 3-D model. Dark blue regions of the color spectrum correspond to values equal to 0 m, whereas dark red regions correspond to the values of D_{ref}.

Once the measurements and results of the scanned polystyrene model were verified, a patient suffering from scoliosis was chosen to determine the viability of the device for clinical application. The processed colour spectrum image of the patients back and their corresponding 3-D model can be seen in figure 6 and 7 respectively, were $D_{ref} = 0.025$ m.

4 Conclusions and Discussions

The device was compact, easy to deploy and portable. Compared to conventional RTG methods in diagnosis, the experimental device offers a less invasive alternative to diagnosing the state of their illness. Provided that the proper conditions are met, the experimental scanner was capable of detailed images. Accompanying the hardware was the "Analysis of Spine" application, which proved to be very intuitive to use even for less adept PC users. The application provided basic functions that allow almost anybody to quickly perform an analysis. But the application also keeps the ability to modify or expand on key parameters for those wishing to obtain optimal results. The deviation in the patients spine is qualitatively evident from the scans in figure 6, namely in the dark red regions representing the protrusion of spinal sections which show an abnormal curvature along the left thoracolumbar region of the patients back. Above this region however, the results become less clear due to the musculoskeletal structures which may be incorrectly interpreted as the spinal column. The image depth is quantitatively assessed in figure 7 by the color spectrum and accompanied legend. The resulting device provides software which is very intuitive and easy to use, while providing enough depth for more detailed control over the data processing phase. However the actual results would benefit from a specialists qualitative opinion. Furthermore, incorporating a quantitative data processing analysis capable of determining the degree of deviation would greatly benefit the existing device and is the focus of future studies.

References

[1] Čihák, R.: Anathomy 1. Grada, Praha (2002)
[2] Huraj, E., Červeňanský, J.: Orthopedy. UK v Bratislave, Bratislava (1975)
[3] Chudáček, Z.: Radiodiagnostic. Osveta, Martin (1993)
[4] Magdolen, Ľ., Masaryk, M.: Flywheel storage energy. In: Proceedings of the eight international conference on Mechanical Engineering: Gépészet 2012. Budapest, Hungaria, May 24-25, pp. 296–300. Budapest Univeristy of Technology and Economics, Budapest (2012) ISBN 978-963-313-055-1
[5] Danko, J., Bugár, M., Staňák, V.: Energy analysis of hybrid power source during vehicle motion. In: Scientific Proceedings Faculty of Mechanical Engineering STU Bratislava, vol. 19, pp. 37–42 (2011) ISSN 1338-1954. - ISSN 1338-5011
[6] Horvat, F., Hucko, B., Cekan, M., Soltes, L.: Experimental device for determining deviations in the thoracolumbar part of the human back. In: Scientific Proceedings, Bratislava, pp. 84–92. Slovak University of Technology (2012)
[7] Bunsch, E., Sitnik, R., Michonski, J.: Tracking of aging process by multiple 3D scans analysis. In: Proceedings of SPIE (2012) ISSN: 0277-786X

Automatic Analysis of Recurrence Plot for the Needs of the Analysis of Infrasonic Signals from the Human Heart

M. Jamrozy[1], K. Lewenstein[1], and T. Leyko[2]

[1] Warsaw University of Technology, Faculty of Mechatronics, A.Boboli 8, 02-525, Warsaw, Poland
{m.jamrozy,k.lewenstein}@mchtr.pw.edu.pl, @mchtr.pw.edu.pl
[2] The Cardinal Stefan Wyszyński Institute of Cardiology, Department of Heart Failure and Transplantology, Alpejska 42, 04-628, Warsaw, Poland
leyko55@gmail.com

Abstract. The recurrence plot method, created in 1987, is included in the group of non-linear signal analysis methods. It demands embedding the signal in the phase space, where the coordinates of the point define the state of the system. In this work we try to present application of the described method in supporting the diagnosis of myocardial insufficiency. Acoustic signals from the beating heart are characteristic for the given person and depend on the chest's structure, the amount of the hypodermis and individual variability. Automatic analysis aims at replacing the subjective assessment with the algorithm, which would assume the amplitude and character of the signal for the assessed radius, for which the recurrence plots would give satisfactory image of the signal's structure. Comparing the plots from signals from healthy and sick patients allows for their easy distinguishing, thus diagnosing.

1 Introduction

The recurrence plot method was created in 1987 by Swiss physicist Jean-Pierre Eckmann. The method is included in the group of non-linear signal analysis methods, such as fractal analysis, estimation of Lapunow exponent, Poincare plots or Hurst exponent[9-12]. The method of recurrence plots allows for illustrating signals' dynamics, concentrating on the recurring phenomena occurring there. It demands embedding the signal in the phase space, where the coordinates of the point define the state of the system[13].

The analysis of signals with the use of recurrence plots requires from the person which makes calculations awareness of proceeding phenomena and characters of the signal itself. It's unacceptable to draw conclusions on the basis of signal analysis which time course is unknown or the parameters of analysis had not been

T. Březina and R. Jabloński (eds.), *Mechatronics 2013*,
DOI: 10.1007/978-3-319-02294-9_99,

properly chosen. It makes the method subjective and dependent on the performer, and also hinders the application of the whole class of signals in automatic analysis.

The method of recurrence plots enables applying RQA (Recurrence Quantification Analysis); it reduces the plot to parameters which are quantitative information on the characters of the signal being analyzed[13]. In this work we try to present application of the described method in supporting the diagnosis of myocardial insufficiency.

Chronic myocardial insufficiency is a syndrome entity, characterized by myocardiofibrosis and rebuild of myocardium, what in consequence lead to its dysfunction. The remodeling in myocardium changes the conditions of heart work into unfavorable, what results in each cardiac contraction taking place in different conditions[1]. The record of changes of pressure in the chest, collected by infrasonic microphone with auscultatory funnel at one end, has the course uncoordinated with the heart rhythm. The systems regulating heart rhythm are usually non-linear, that is why the non-linear analysis has been successfully used for this class of signals for years[5-8].

In the article there will be presented the computational procedure, allowing for performing automatic signal analysis with the use of recurrence plot method.

2 Recurrence Plot Method

We begin our work with the signal from watching time courses with the particular attention given to the amplitude, as well as character and time relation of oscillation taking place there. We ought to point out potential disturbances and artifacts and their location in time.

Preparing a recurrence plot requires embedding the signal in the phase space. This is presenting the signal in the multidimensional space, in which every another dimension is the same signal displaced in time by delta t multiplicity. The highest number of dimension is called the dimension of embedding. Such dimension and delta t value are not accidental. Time displacement can be determined with the use of autocorrelation function or the method of Average Mutual Information, which measures the dependent information between two random variables. The relation is shown by the following formula:

$$I(T) = \sum_{s(n),s(n+T)} P\big(s(n), s(n+T)\big) log_2 \left[\frac{P(s(n),s(n+T))}{P(s(n))P(s(n+T))}\right] \quad (1)$$

P(x) is the probability of occurring x value in the signal, and P(x,y) is a density of probability of occurring two random variables. The value of average mutual information is the biggest for T=0. The effect of embedding in phase space is the most favorable when delta t equals the time of time displacement for the first minimum of the function I(T). Fig. 1 presents the exemplary plot of a function I(T) [9-12].

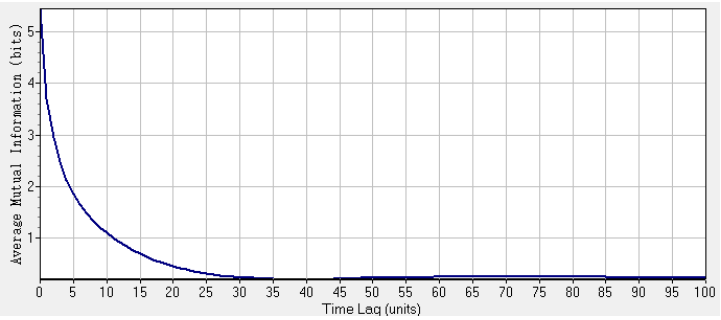

Fig. 1 The value of average mutual information in the function of the time lag

The next stage is assessing optimal dimension of embedding. Specifying this parameter lies in determining the dimension in which the similarly directed trajectories are situated close to each other and the trajectories running in different directions are separated. For this purpose the method of The Nearest False Neighbors is applied[9-12].

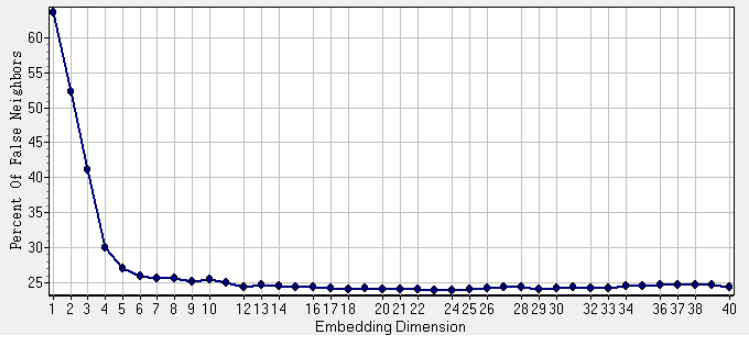

Fig. 2 The percent value of false neighbors in the function of embedding dimension

Determining the two parameters allows for reconstructing trajectory in space and drawing recurrence plot. The method of Recurrence Plot by Iwanski and Bradley is specified by the following relation:

$$R_{i,j} = \Theta\left(\varepsilon_i - \left\|x_i - x_j\right\|\right),\ x_i \epsilon \in \Re^m, i, j = 1 \ldots N \tag{2}$$

where N is the length of the analyzed time course, i, j are the coordinates on the surface, ε_i is the radius, $\|\cdot\|$ is the norm in the metric space and Θ is Heaviside's function.

Both axes of the plot represent indexes of signal samples and point's coordinates on the plot determine the numbers of the samples, the properties of which are here evaluated. The obtained plot can be then analyzed with subjective evaluation of the illustrated phenomena or we can perform RQA – Recurrence Quantification Analysis. It reduces the problem to few parameters, allowing for

the quantitative evaluation of particular phenomena appearing on the recurrence plot[13].

Summing up, in order to determine the recurrence plot of the signal the following calculations need to be done:

1. Determining Δt with the use of Average Mutual Information method
2. Determining embedding dimension with the use of The Nearest False Neighbors method
3. Embedding the signal in the phase space
4. Assessing ε_i and assigning recurrence plots for the estimated ε_i
5. Empirically selecting ε_i by assigning recurrence plots for the moment of obtaining the image of the signal's structure
6. Carrying out RQA

It has to be emphasized that points 4 and 5 make the result dependant on the experience and subjective evaluation of the performer.

3 Problems of the Automatic Application

In order to draw a plot it is essential to specify the embedding dimension of time displacement and radius. We can easily automatically designate time displacement from plot of the average mutual information by determining the first minimum of the function. We can accept the certain percent of false neighbors as optimal and automate this process. The analysis will cause finding the embedding dimension, where the percent of the nearest false neighbors is below this limit[9-12]. Both parameters are successfully estimated in many available computational programs for non-linear signal analysis (such as Visual Recurrence Analysis), that is why the problem of designating these parameters will no longer be raised here.

Determining the radius is crucial in the implementation of the algorithm, because the number of points showed on the plot is dependent on it. Empirical signals can have different amplitude and oscillation character. Acoustic signals from the beating heart are characteristic for the given person and depend on the chest's structure, the amount of the hypodermis and individual variability. Too little radius gives image of only the trajectories situated very close to each other. The choice of radius decides on which points and how many of them will be on the plot. Too big radius makes the plot illegible as it is covered by additional points, which accidentally were located nearby. These problems will be more precisely presented in the next chapter related to estimation of the radius on the example of the real measuring data.

4 Automatic Method of Recurrence Plots

The original signal from the patient registered in the data base is shown on Fig. 3.[2-4]

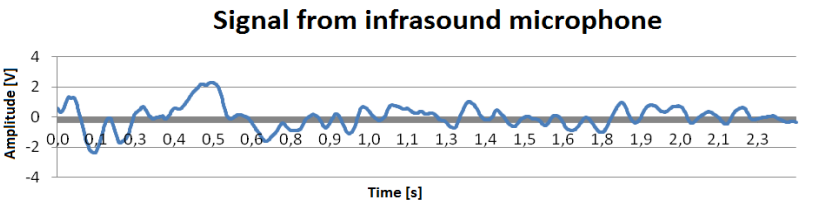

Fig. 3 The histogram of the distance between the points in the phase space

Its character makes other methods unreliable. The calculation begins with specifying the time displacement by the average mutual information method. It is carried out by very accurate determination of the first minimum of the function. Having the time displacement we then need to determine the embedding dimension by the nearest false neighbors method.

In order to assess the radius we conducted analysis of the distance between the points in the phase space. Maximal distance between the points has been divided into 100 equal sections and we counted the pairs of points in particular sections. Fig. 4 presents the described distribution.

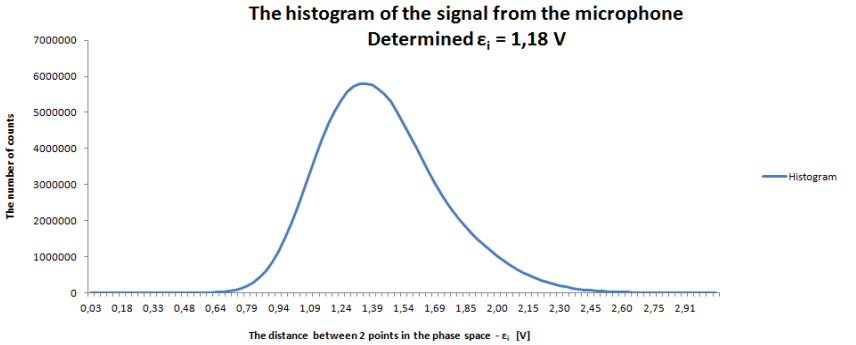

Fig. 4 The histogram of the distance between the points in the phase space

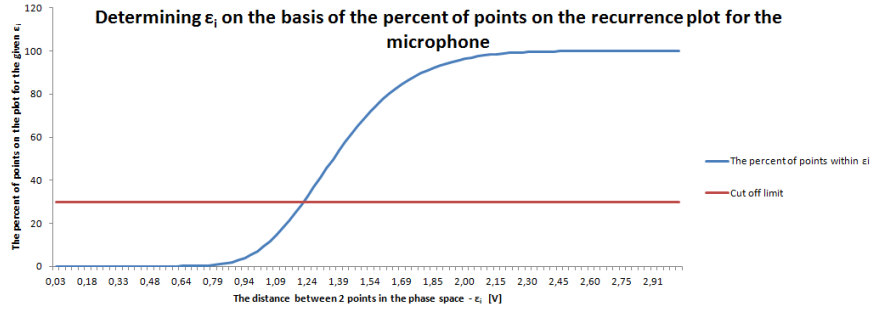

Fig. 5 The arrangement/distribution of the percent of the points presented on the recurrence plot in the radius function. The radius for the 30% of points is marked in red.

Then, we recalculated the number of counts into the percent of points shown on the plot with the given radius – Fig. 4.

From the plot we read the radii, which can allow for imaging 10%, 20%, 30%, 40% and 50% of all the points. The recurrence plots have been assigned for these values. Fig. 5 present exemplary plots for 10%, 30% and 50% of the points.

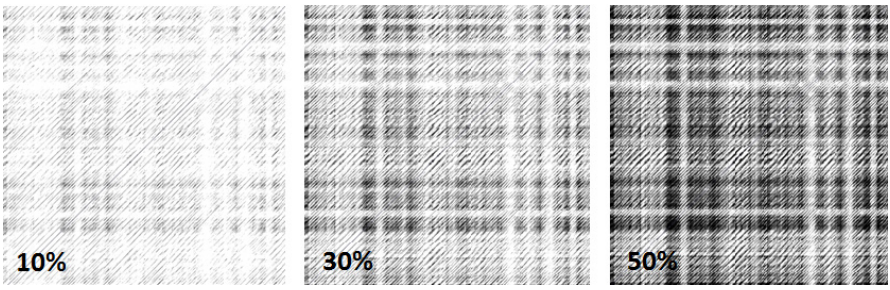

Fig. 6 Recurrence plot for 10%, 30% and 50% of the points

5 The Analysis of the Results

Points on the recurrence plot can be distributed at random, e.g. for the signal of the white noise or in lines. Such lines are analyzed in terms of being situated vertically, horizontally, or in parallel towards the main diagonal. The main diagonal is always present as the distance of each point towards itself in the signal is always smaller than the radius. The obtained line parallel to the diagonal illustrates the phenomenon of the trajectory coming back to the area where it previously performed movements with the simultaneous running nearby the movement. Vertical and horizontal lines illustrate the vicinity of one point with the trajectory. That is why increasing the radius can result in extending the parallel line towards the diagonal.

The analysis of the obtained recurrence plots consists in subjective evaluation of phenomena occurring in the signal on the basis of the obtained image. We need to be aware of the time course and select the radius in such a way so as to illustrate the phenomena in the best possible way. Automatic analysis aims at replacing the subjective assessment with the algorithm, which would assume the amplitude and character of the signal for the assessed radius, for which the recurrence plots would give satisfactory image of the signal's structure.

The presented plots best convey the rich structure of the signal when we illustrate 20 or 30% of the points. When we illustrate 10% of the points we lose the part of the points belonging to the line parallel to the diagonal, which can be noticed on the plots for 20 or 30% of the points. Increasing the number of points to 40 or 50% results in extending these lines and appearing of a lot of accidental points – the nearest false neighbors.

The presented approach causes the loss of the value of the RQA parameter called Recurrence Rate (RR) which is expressed as follows:

$$RR = \frac{1}{N^2}\sum_{i,j=1}^{N} R_{i,j} \tag{3}$$

This is a ratio between the illustrated points and the area of the plot. Thanks to using the percent of the illustrated points to the estimation of optimal radius, this factor can be defined ad hoc. Other parameters of RQA apply to the morphology of the recurrence plot, that is why they do not lose its value as the parameters of the signal.

6 Conclusions

The described method enables presenting signals in the form of recurrence plots in an automatic way at the cost of one RQA parameter – Recurrence Rate. It allows for performing the analysis of normalized signals from the patients in a mass and objective way. Such RQA of the signals can act as prognostic or diagnostic information while detecting myocardial insufficiency. Comparing the plots from signals form healthy and sick patients allows for their easy distinguishing, thus diagnosing. In the future this method could serve as the foundation for selective examination of the myocardial insufficiency.

References

[1] European Heart Journal, ESC Guidelines for the diagnosis and treatment of acute and chronic heart failure (2012), doi:10.1093/eurheartk/ehs104
[2] Jamroży, M., Lewenstein, K.: System aparaturowy do pomiaru i rejestracji cyfrowej sygnałów mechanograficznych serca oraz EKG. Miesięcznik PAK, 591–594 (2011)
[3] Jamroży, M., Lewenstein, K.: Apparatus System for Detection of Cardiac Insufficiency. In: 9th International Conference Mechatronics 2011, pp. 663–672 (2011)
[4] Jamroży, M., Lewenstein, K., Leyko, T.: Early detection of Cardiac Insufficienty. In: 8th International Conference Mechatronics 2009, pp. 407–412 (2009)
[5] Peng, Y., Sun, Z.: Characterization of QT and RR interval series during acute myocardial ischemia by means of recurrence quantification analysis. Med. Biol. Eng. Comput. 49(1), 25–31 (2011)
[6] Nguyen, C.D., Wilson, S.J., Crozier, S.: Automated quantification of the synchrogram by recurrence plot analysis. IEEE Trans. Biomed. Eng. 59(4), 946–955 (2012)
[7] Melillo, P., Bracale, M., Pecchia, L.: Nonlinear Heart Rate Variability features for real-life stress detection. Case study: students under stress due to university examination. Biomed. Eng. 10(96) (2011)
[8] Okamoto, Y., Imai, R., Yoshida, H., Taeka, K., Kuramoto, C.: Relationships among frequency domain and non-linear parameters from heart rate variability. Rinsho. Byori. 59(8), 770–773 (2011)

[9] Reich, L.E.: The transition to chaos: conservative classical systems and quantum manifestations. Springer, Berlin (1992)
[10] Sprott, J.C.: Chaos and time-series analysis. Oxford University Press (2003)
[11] Abarbanel, H.D.I.: Analysis of observed chaotic data. Institute for Nonlinear Science. Springer (1996)
[12] Kantz, H., Schreiber, T.: Nonlinear time series analysis. Cambridge University Press (1997)
[13] http://www.recurrence-plot.tk/

Evaluation of the Empirical Mode Decomposition Method as a Tool for Preprocessing Ultrasonic Cardiological Data

T. Kubik, K. Kałużyński, S. Cygan, and K. Mikołajczyk

Warsaw University of Technology, Faculty of Mechatronics, Św. Andrzeja Boboli 8, 02-525 Warsaw, Poland
t.kubik@mchtr.pw.edu.pl

Abstract. This study investigates the performance of the Empirical Mode Decomposition (EMD) method in application to the ultrasonic cardiological data. Data acquired using self-made phantom are subjected to 1D and 2D EMD algorithms. The 1D EMD yields higher signal to noise ratio improvement than the 2D EMD. In the first case upsampling only along the RF lines is necessary, whereas in the second case upsampling in both directions is required. The first IMF appears best suited for the segmentation and the 1D EMD results in IMF more suitable for segmentation that the 2D EMD.

1 Introduction

Imaging of tissue elastic properties has become an important branch of the medical diagnostic imaging [1].

Cardiac strain rate imaging using ultrasound requires accurate heart muscle indication, which requires good method of segmentation. Because of the presence of speckle noise, often unsatisfactory signal-to-noise ratio and sampling, segmentation of *myocardium* becomes a nontrivial problem. Some signal processing methods (e.g. anisotropy diffusion dedicated to speckle noise removal) have been proposed to preprocess ultrasonic radio-frequency (RF) data. Below we investigate the performance of the Empirical Mode Decomposition (EMD) as a tool for ultrasonic image preprocessing prior to segmentation.

2 Materials and Methods

The EMD method is dedicated to analysis of nonstationary and nonlinear signals with both amplitude and frequency modulations [2]. The EMD adapts to the local signal properties, using the information on the local envelopes of the signal. The EMD extracts set of signal components fulfilling particular requirements, termed Intrinsic Mode Functions (IMFs), and a residual. An IMF is a function which meets the following criteria [2]:

T. Březina and R. Jabloński (eds.), *Mechatronics 2013*,
DOI: 10.1007/978-3-319-02294-9_100,

- the number of zeros and extrema is equal or differs by no more than 1;
- the sum of envelopes of maxima and of minima of an IMF is zero.

In presence of random noise the EMD behaves as dyadic filter bank [3].

The EMD method exists in two variants – 1-dimensional and 2-dimensional. The first one may be applied to both the signal and image data, whereas the second – to image data. When applying the EMD one can therefore consider the ultrasonic image as a 2D object or, alternatively, as a collection of 1D signals. This may have significant impact on computational time, as fitting 2D surface to image extrema may be more time consuming that fitting splines to signal extrema. Another important issue is the relation of the sampling frequency to the frequency of the signal. The EMD requires significant oversampling of the signal in order to avoid creation of IMFs corresponding to non-existing signal components, thus having no physical meaning [2, 4]. In the case of ultrasonic data the situation is even more complex in that sense, that the resolution (sampling) along the wave propagation path is much higher than lateral one, which results from scan line placement. An interpolation (upsampling) of the image data may be necessary and we may apply and test two different solutions – oversampling along the lines and using the 1D EMD, or alternatively, upsampling also across the lines and using the 2D EMD, further termed BEMD.

To evaluate the effect of the EMD on the ultrasonic RF data, images of a left ventricular phantom have been processed. This phantom had a form of a truncated thick-walled ellipsoid with a fixing collar [5]. Acquisitions were carried out using a SonixTouch scanner (Ultrasonix, Canada) in the 'Research' mode. Sequences of RF data after beamforming were acquired along with B-mode data using a cardiac 2D sector probe (SA4-2/24, Ultrasonix), working at the emission frequency of 3.5 MHz. Data has been acquired at the sampling frequency of 16 MHz. Resulting images consisted of 100 lines, 3000 samples each. An image and a single RF line are presented in the Fig. 1.

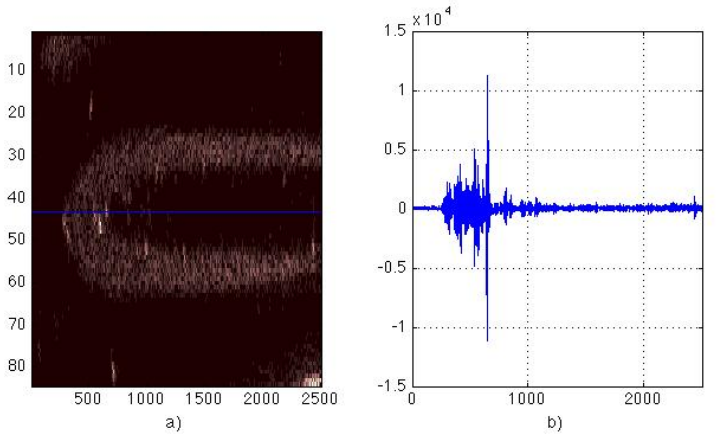

Fig. 1 a) Example input data used for the processing described in this paper. b) Single RF line signal indicated in the a) image by a blue line.

2.1 Data Preprocessing Using Empirical Mode Decomposition

Since the ratio of the sampling rate to the central frequency of the RF pulse is around 4.5, we interpolated the images along the RF lines 5, 10 and 20 times. Then the 1-dimensional EMD has been applied to reduce noise present in the image. Method parameters like algorithm stop criteria and maximum number of iterations were set to the default values suggested in [4]. We also applied BEMD to the data. The decomposition was performed with the default parameters, whereas the maximum number of the IMFs was restricted to 4. BEMD algorithm, during its sifting process, attempts to fit two surfaces per iteration [6]. Because of large differences between raw image dimensions (100 lines, 3000 samples) data interpolation across RF lines was needed to provide similar width and height of the image. Interpolation ratio was 10 times.

After decomposition we estimated noise level in the IMFs. This level is defined by the root mean square (RMS) values calculated for a part of image not containing the heart muscle:

$$RMS = \sqrt{\frac{1}{N}\sum_{n=0}^{N-1} x^2(n)} \tag{1}$$

where N is the number of considered pixels and $x(n)$ is the value of the nth pixel.

2.2 Segmentation

Because of the expected contrast improvement of the images, we decided to segment *myocardium* using methods based on thresholding, which are less computationally complex than e.g. algorithms based on active models [7].

Proposed algorithm includes following steps:

1. Thresholding separating image features from background. Assuming improvement of signal-to-noise ratio after EM decomposition, threshold was calculated automatically, using *Otsu* method. The method uses image histogram to classify pixels as the background the feature. After this step, image becomes binarized.
2. Gaussian blurring in RF lines direction.
3. Closing operation with a small kernel of size 3.
4. Cluster labelling, which labels each separate region and numbers them descending, adequately to their area [7]. After labelling the biggest cluster was left on the image.
5. Hole flooding. The processing includes enclosed area into the segments. If the whole left ventricle is visible in the image, it is important not to flood its area.

IMFs obtained using both EMD methods and not-preprocessed images have been segmented using the above procedure.

MATLAB freeware scripts performing 1-dimensional EMD [10] and BEMD were used [11]. Segmentation algorithm was implemented as a plugin in Pmod software by Pmod Technologies GmbH.

3 Results

According to preliminary results, the BEMD of the raw RF ultrasonic images brings very poor results, which we attribute to the difference between both resolutions. Therefore, further only results of BEMD after interpolation are presented and discussed. Because of BEMD is memory consuming, only parts of images have been analysed (fragments containing heart muscle edges, which are critical for the segmentation). To visualize the differences in 1D EMD and BEMD performance, the result of both decomposition methods of the same image interpolated at the same rate in both directions is shown in the Fig. 2. First three IMFs

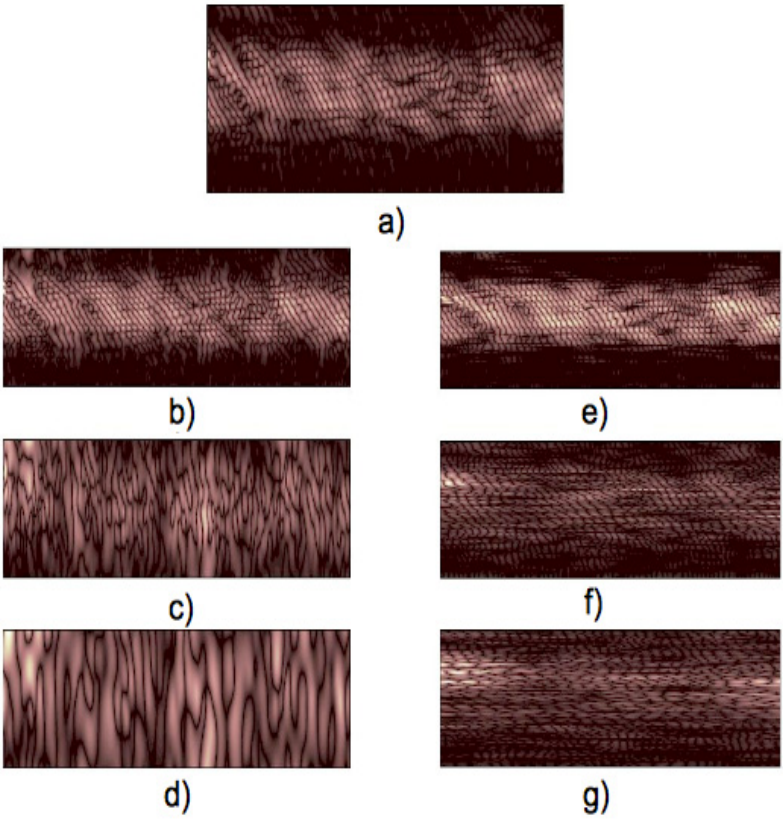

Fig. 2 Results of the 1-dimensional EMD and BEMD on the image interpolated 10 times across and 20 times along RF lines. a) Original image. b) 2D IMF no. 1. c) 2D IMF no. 2. d) 2D IMF no. 3. e) 1D IMF no. 1. f) 1D IMF no. 2. g) 1D IMF no. 3.

obtained for each type of decomposition indicate that the most important image feature is included in the first IMF. Signal to noise contrast is increasing together with the interpolation rate much faster when 1D algorithm is performed than when using BEMD (Fig.3). Because noise levels differ strongly between consecutive RF image data and IMFs, the plots show values averaged over several images (RF images or IMFs of the same order). The plot indicates clearly, that the first IMF from 1D EMD has reduced noise level with respect to the original image and therefore is more suitable input to the threshold-based segmentation process. Furthermore, the interpolation in the case of the 1D EMD beyond 5 times does not improve

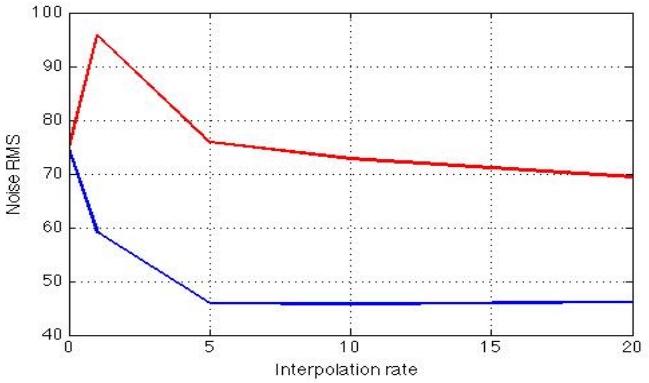

Fig. 3 Noise RMS versus the interpolation rate. Blue line shows results for 1D EMD and red line shows results for BEMD. RMS for 0 was obtained from an original image.

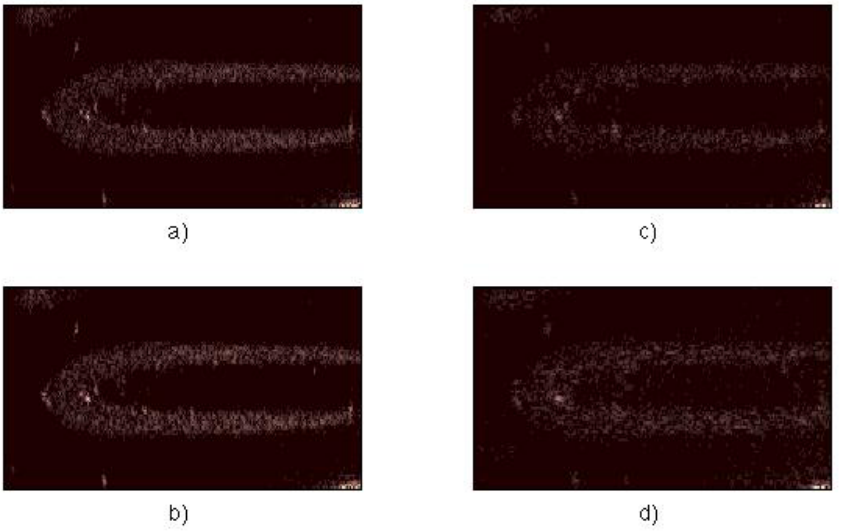

Fig. 4 Result of the 1-dimensional EMD on the image interpolated 20 times. a) Original image. b) IMF no. 1. c) IMF no. 2. d) IMF no. 3.

further signal to noise ratio, whereas in the case of BEMD further improvement is observed. The ration of noise reduction in the case of 1D EMD is of 60-75% higher for interpolations from 5 to 20 times.

On the basis of the results shown in Fig. 3. and visual assessment of the images, we decided to use 1D EMD for image preprocessing prior to segmentation. Decomposition results of the whole image are shown in Fig. 4.

Results of the segmentation using original image and first IMF are shown on Fig. 5. An improvement in segmentation accuracy can be seen. Furthermore, the segment shape obtained from the 1st IMF image has a smoother boundary than that obtained from the raw RF image.

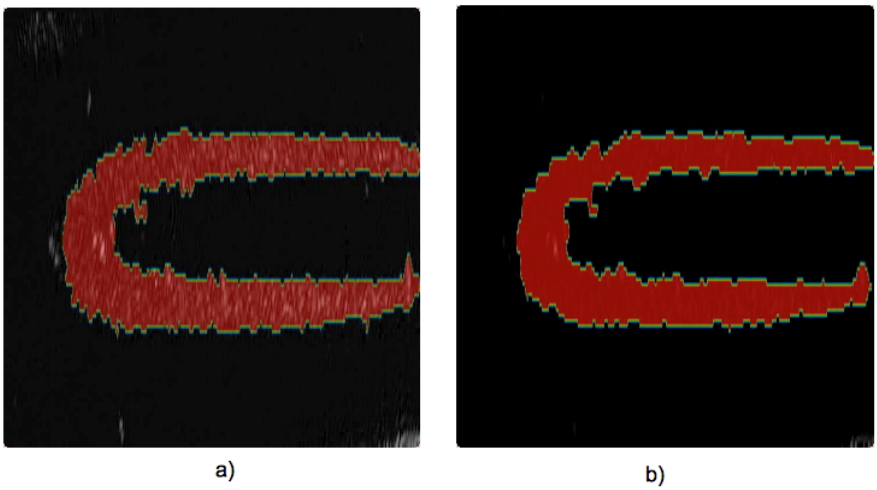

Fig. 5 a) Result of the segmentation performed on the original data. b) Result of the segmentation performed on the 1st IMF of the data.

4 Discussions and Conclusions

The IMFs resulting from EMD decomposition (1-D EMD and BEMD) show improved signal-to-noise ratio with respect to the raw image.

We have found that one-dimensional EMD shows better performance as a tool for preprocessing the RF ultrasound data. The IMFs up to order of 3 contain interpretable image data and the improvement of SNR is higher than in the case of the BEMD. In the BEMD results, regardless of interpolation applied across acquisition lines, only the first IMF contains data potentially usable for segmentation, whereas further decomposition products contain signals of residual nature [2]. Furthermore, large variations in the pixel size (width versus length) imply high interpolation across acquisition lines, when BEMD is to be applied. That interpolation and surface fitting during sifting are very time-consuming. These findings indicate, that the 1-D EMD is a more interesting tool for RF data preprocessing.

The inferior performance of the BEMD method may result from the correlation between adjacent RF lines, due to the finite dimensions of the ultrasonic beam.

Although EMD algorithms are time and memory consuming, the method could facilitate application of thresholding segmentation methods with automatic threshold setting, which are much faster than more sophisticated methods, e.g. active contours [7].

Acknowledgments. The work has been partly supported with statutory funds of the Warsaw University of Technology.

References

[1] Gao, L., Parker, K.J., Lerner, R.M., Levinson, S.F.: Imaging of the elastic properties of tissue – a review. Ultrasound Med. Biol., 959–977 (1996)
[2] Huang, N.E.: The empirical mode decomposition and the Hilbert spectrum for nonlinear and non-stationary time series analysis. Proc. Roy Soc. London A 454(4), 903–995 (1998)
[3] Flandrin, P., Rilling, G., Goncalves, P.: Empirical Mode Decomposition as a filter bank. IEEE Sig. Proc. Lett. 11, 112–114 (2004)
[4] Rilling, G., Flandrin, P., GonÁalves, P.: On Empirical Mode Decomposition and its algorithms. In: IEEE-EURASIP Workshop NSIP 2003 (2003)
[5] Heyde, B., Cygan, S., Choi, H.F., Lesniak-Plewinska, B., Barbosa, D., Elen, A., Claus, P., Loeckx, D., Kaluzynski, K., D'hooge, J.: Regional Cardiac Motion and Strain Estimation in Three-Dimensional Echocardiography: A Validation Study in Thick-Walled Univentricular Phantoms. IEEE Trans. UFFC, 668–682 (2012)
[6] Qin, X., Liu, S., Zhengqiang, W., Han, J.: Medical Image Enhancement Method Based on 2D Empirical Mode Decomposition. Bioinformatics and Biomedical Engineering, 2533–2536 (2008)
[7] Haidekker, M.A.: Advanced biomedical image analysis, pp. 173–211, 276–310 . John Wiley & Sons, Inc., New Jersey (2011)
[8] Rilling, G., Flandrin, P.: On the influence of sampling on the Empirical Mode Decomposition. In: IEEE Int. ASSP Conf. (2006)
[9] Stevenson, N., Mesbah, M., Boashash, B.: A sampling limit for the empirical mode decomposition. In: Proc. 8 Int. Symp., Signal Processing and Its Applications SPIA (2005)
[10] http://www.ens-lyon.fr/~flandrin/software.html
[11] http://www.mathworks.com/matlabcentral/fileexchange/28761

Evaluation of Bilateral Asymmetry of the Muscular Forces Using OpenSim Software and Bilateral Cyclograms

P. Kutilek[1], Z. Svoboda[2], and P. Smrcka[1]

[1] Czech Technical University in Prague, Faculty of Biomedical Engineering, nam. Sitna 3105, 272 01, Kladno, Czech Republic
kutilek@fbmi.cvut.cz
[2] Palacky University of Olomouc, Faculty of Physical Culture, Tr. Miru 115, 771 11, Olomouc, Czech Republic
zdenek.svoboda@upol.cz

Abstract. The aim of this article is to introduce a method of quantification of bilateral asymmetry of the muscular forces which can be used for rehabilitation, and also for evaluating the functionality and usability of the actuators of prosthesis. Our work focuses on quantification of asymmetry of the muscular forces using OpenSim software and bilateral cyclograms. A group of healthy children and children with cerebral palsy was measured using a Vicon MoCap system. The kinematic data were recorded and the OpenSim software system was used to identify the muscular forces, which are represented by time diagrams. The bilateral cyclograms were created to quantify the bilateral asymmetry of the muscular forces of the left and right sides of body. In order to quantify the asymmetry of the muscular forces, we have tested the application of method based on the shape of synchronized bilateral cyclograms.

1 Introduction

Nowadays, there is no appropriate widely-used application of a method for identifying bilateral asymmetry of the muscular forces during the gait cycle, or for evaluating the functionality and usability of the actuators of prosthesis or rehabilitation facilities of the future. Above all, it is difficult to identify and evaluate the muscular force curve.

Several methods are used in medical practice and research for identifying defects in muscle behaviors. Some simple methods focus on musculoskeletal geometry and enable the length of muscles to be estimated, [1]. More complex methods have been created to characterize muscular force generation, limb dynamics, and CNS control, [2-4]. Based on [2], we can take into account the two methods: kinematics and dynamics. The kinematics methods are used in conjunction with

T. Březina and R. Jabloński (eds.), *Mechatronics 2013*,
DOI: 10.1007/978-3-319-02294-9_101,

experimental measurements of movement to examine muscle lengths, [2], [5]. The dynamic methods are essential tools for understanding the motions produced by muscles. The measured kinematic data are usually processed in software to identify the muscle length, muscle force or the joint moment. The most commonly used software is LifeMOD, OpenSim, etc. Modern software and MoCap systems allow to monitor, in real time, the muscle-tendon behavior. Knowledge of muscular forces is important because a "weak" muscle that is not fully ready to create the required forces can be identified and restored. However, there is currently no method to determine the symmetry of muscular forces of the left and right sides of body during normal walking. Nowadays, clinical assessments of muscle function during movement are based especially upon the EMG activity of a muscle, [6].

Nowadays, the most widely-used technique to study the behavior of the gait characteristics in clinical practice is gait phase analysis by time and/or phase diagrams, [7], [8]. For a study of gait variables, the method based on an analysis of gait using cyclograms can also be used. The cyclograms are closed trajectories generated by simultaneously plotting two or more quantities, [9]. Usually, the creation of cyclograms is based on gait angles, [10-13]. However, cyclograms are also used in conjunction with distances, [14], forces, [15] or velocities, [16]. We focus on the potential use of the cyclogram for the evaluation of the bilateral asymmetry of the muscular forces of the left and right sides of body.

Symmetry is an important indicator of healthy gait or proper walking technique. At present, algebraic indices and statistical parameters represent two major classes of symmetry quantifiers, [17], [18]. Algebraic indices include the symmetry index and the ratio index used to compare bilateral variables such as maximum lengths. These parameters depend on discrete variables and are unable to reflect the asymmetry of variables as it evolves over a complete gait cycle. Statistical methods such as paired t-test, and parameters such as correlation coefficients, have also been used to measure asymmetry. [17], [19]. These parameters do not usually suffer from the limitations of the algebraic indices, but their computation is more complex and interpretation is less transparent. In paper [17] a technique based on the geometric properties of symmetric diagrams, also called bilateral cyclograms, was introduced. In order to quantify the symmetry, a bilateral synchronized cyclogram which represents the same gait variables and two sides of the body was obtained in the study. The approach is based on the symmetry of variable evolution and comparison of the evolution of one variable with its contralateral counterpart, [20]. The geometric parameters of the synchronized bilateral cyclogram are then used to evaluate the symmetry, [17], [21]. For the absolutely symmetrical gait the area within the curve is zero and its orientation is 45°, [17]. In the past, bilateral asymmetry of the muscular forces of the left and right sides of body of patients or healthy subjects has not been evaluated by the cyclograms. In our work, we will test the method based on the synchronized bilateral cyclogram to analyze the asymmetry of the muscular forces because applications of cyclograms to study the muscular forces can offer a wide range of applications.

2 Methods

To study the kinetic gait variables, gait analysis was performed using a motion capturing system (VICON MX; Oxford Metrics), four floor mounted force plates (AMTI, Advanced Mechanical Technology) and OpenSim (Stanford University). Marker placement followed a standard protocol, [22]. The sample frequency was 120Hz. Measurements were carried out at the Paediatric Orthopaedic Unit, Department of Paediatric Surgery, Medical University of Graz. Healthy subjects walked at a self-selected walking speed along a ten-meter walkway. Calculations of muscular forces during gait are performed using the OpenSim software. The parameter is normalized to the weight and height of the subjects. The normalization of the data is performed by using the MatLab (MathWorks, Inc.) software. The normalization of the data has been described in detail by Stansfield et al., [23].

We can choose a number of muscles for further analysis. We have chosen to use the musculus gastrocnemius medialis (m. gas. med.) that is often studied in the context of cerebral palsy, [24]. The m. gas. med. is a very powerful superficial muscle, and is involved in walking or running. Its function is plantar flexing the foot at the ankle joint and flexing the leg at the knee joint. The study of the m. gas. med. is also important for the formation of requirements for artificial muscles. The validity of assumptions could be verified by surface electromyography, [25]. Concerning the possible applications, we also chose to study the musculus soleus (m. sol.). The primary function of the m. sol. is to increase the angle between the foot and the ankle, which is also known as plantar flexion. Therefore, the m. sol. specifically plays an important role in maintaining standing posture, and thus the study of the m. sol. is important for the formation of requirements for artificial muscles. Because we deal with the symmetry of the muscular forces of the left and right sides of body, we analyzed the forces of the left (L) and right (R) muscles.

To create and study synchronized bilateral cyclograms, we used the normalized data of the muscles and a modified method based on synchronization of two plots to obtain the synchronized bilateral cyclograms, [17]. A prominent gait event such as the heel-touchdown or forefoot/foot flat-touchdown (in the case of the patients with movement disorders) was used to synchronize the two plots. The force plates were used to identify (by the MatLab) the ground foot contact. Ground foot contact is determined by the detection of the beginning of force acting on the surface of the plates. The first and last 3 gait cycles of each walking trial were excluded from the analysis to avoid acceleration/deceleration phase and three or four entire gait cycles of each walking trial are used to plot a cyclogram. The 2D synchronized bilateral cyclogram represents a set of states of normalized muscle forces. The diagrams of example of two synchronized muscle-force curves during the gait cycle and synchronized bilateral cyclogram are plotted, see Fig. 1. For a symmetric gait, i.e. muscular forces, properly synchronized twin trajectories from corresponding muscles should be identical, and cyclogram should lie on a symmetry line (SL), [17]. The SL is a straight line passing through the origin inclined at an angle 45º. We can measure cyclogram's deviation from the SL to obtain a quantification

of symmetry and use, for example, the distance of the farthest point of the synchronized bilateral cyclogram from the "ideal" SL. Obviously, the greater the distance, the greater the asymmetry.

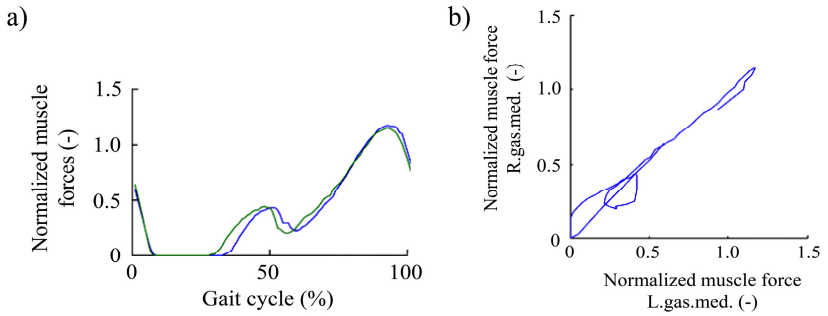

Fig. 1 Example of two synchronized muscle-force curves during the gait cycle (a) and synchronized bilateral cyclogram (b) of the musculus gastrocnemius medialis

3 Measurement and Testing

The main object of the study was to describe and verify the application of method based on the synchronized bilateral cyclogram to analyze the asymmetry of the muscular forces. The set of data to create cyclograms was measured on seven healthy subjects (children: mean height 126 cm (SD 11 cm), mean weight 30 kg (SD 5 kg)) and randomly selected children with cerebral palsy (six subjects). Healthy subjects with no clinically significant abnormality and subjects with cerebral palsy are identified by physician by evaluation of medical history and physical examination. The subjects were asked to walk properly. The human mean walking speed, i.e. selected walking speed of measured subjects, was $1.15 m.s^{-1}$. We assume that improvement or deterioration of gait symmetry is not primarily influenced by walking speed.

First, healthy subjects were asked to walk without the shoes. From each trial with variable walking speed, only one selected walking speed (same for all subjects) was used to calculate the subject's mean trial. The measured parameters of gait were performed using the OpenSim software and normalization was processed by using the MatLab software. We determined the set of states of normalized forces of the two muscles, musculus gastrocnemius medialis and musculus soleus, and then the mean values of normalized muscle forces during the gait cycle. Then we also used MatLab to create synchronized bilateral cyclograms of all measured healthy subjects, Fig. 2a and Fig. 3a, and for creating the only one synchronized bilateral cyclogram of the determined mean values of the two normalized muscle forces of all measured healthy subjects, Fig. 2b and Fig. 3b.

Second, we tested the symmetry of the muscular forces of randomly selected children with cerebral palsy. Selected subjects were asked to walk without the

shoes and any support devices. For the evaluation, we also used the same method of measurement and data processing as used for the healthy subjects. Then we used MatLab for creating synchronized bilateral cyclograms of the selected subjects with cerebral palsy, Fig. 4.

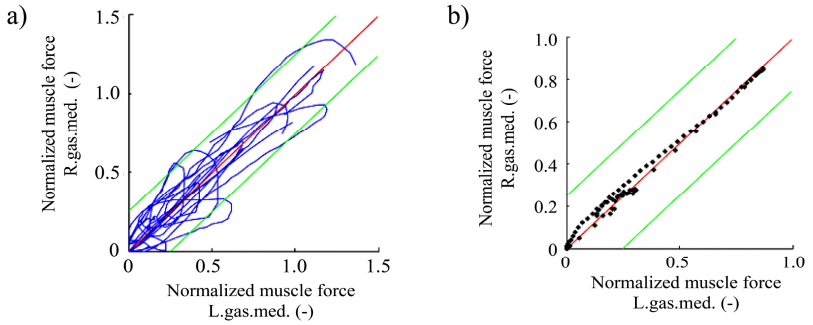

Fig. 2 The synchronized bilateral cyclograms of measured subjects (a) and the synchronized bilateral cyclogram of the determined mean values of the gas. med. forces (b).

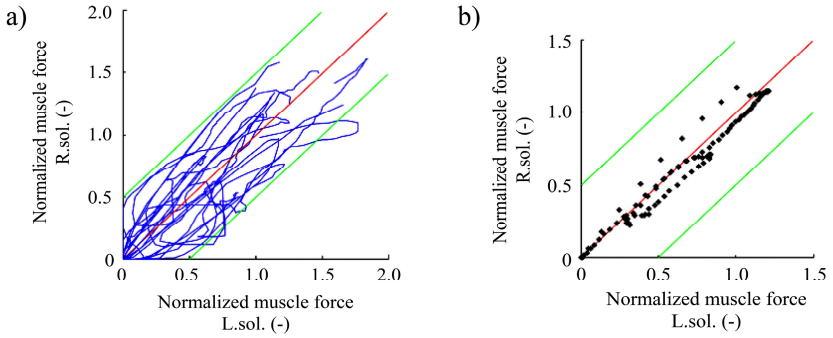

Fig. 3 The synchronized bilateral cyclograms of measured subjects (a) and the synchronized bilateral cyclogram of the determined mean values of the sol. forces (b).

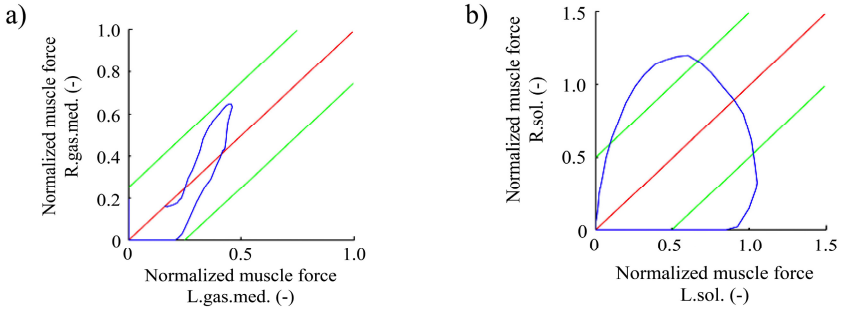

Fig. 4 Example of a synchronized bilateral cyclogram of the gas. med. forces (a) and sol. forces (b) of the subjects with cerebral palsy.

4 Results

We designed the technique to create the bilateral cyclogram of the muscular forces and tested on two muscles: m. gas. med. and m. sol. Then we used new methods for identifying the asymmetry of the muscular forces. The diagrams of the synchronized muscle-force curves during the gait cycles and synchronized bilateral cyclograms to analyze the bilateral asymmetry of the muscular forces are plotted.

For a better visual interpretation of the asymmetry, SL and two parallel lines (PLs) at the specific distance are displayed in the graphs, see Fig. 3, Fig. 4 and Fig. 5. Therefore, it is possible to directly read from the chart if the cyclogram lies between two PLs. This technique gives a measure of the distance as a relative value of the normalized force of the muscle. Suppose, if the value of the distance is greater than 0.18 (i.e. 0.25 on the x-axis or y-axis), in the case of the gas. med. forces, then the method indicates high asymmetry of the affected muscles. If the value of the distance is greater than 0.35 (i.e. 0.5 on the x-axis or y-axis) in the case of the sol. forces, then the method indicates high asymmetry of the affected muscles. The mentioned values of the distances were chosen based on previous experiments.

The Fig. 2a and Fig. 3a show the deviation of the synchronized bilateral cyclograms of all measured healthy subjects from the "ideal" SL and the one synchronized bilateral cyclogram of the determined mean values of the muscular forces, Fig. 2b and Fig. 3b. It is obvious that the cyclograms of the determined mean values of the two muscular forces do not lie on the "ideal" SL, see Fig. 2 and Fig. 3. But it is also evident that bilateral cyclograms of all measured healthy subjects lies between two PLs in almost all cases. The results are similar for the gas. med. forces and sol. forces.

We also tested the symmetry of the muscle forces of randomly selected children with cerebral palsy. Shapes of the synchronized bilateral cyclogram of the forces of m. gas. med. and m. sol. muscle of the subjects with cerebral palsy are significantly asymmetric, Fig. 4, in all cases. Six subjects with cerebral palsy were measured and the synchronized bilateral cyclogram was significantly asymmetric in all cases (i.e. cyclograms were outside the two PLs in 100% of the cases).

5 Discussion

We designed and verified new method that is derived from the commonly used cyclograms. The results indicate that the new method shows a certain asymmetry in the muscular forces of the healthy subjects but the cyclogram usually lies between the PLs at the distance (as a relative value of the normalized force of the muscle) about 0.18 from the "ideal" SL in the case of synchronized bilateral cyclogram of the gas. med. forces, and the distance about 0.35 from the "ideal" SL in the case of synchronized bilateral cyclogram of the sol. forces. And also, the bilateral cyclograms of the determined mean values of the muscular forces lie between the PLs. This means that, also in healthy subjects, there is always some asymmetry in the shape of the synchronized bilateral cyclogram, and the cyclogram does not

lie on the "ideal" SL. On the basis of the experiments, we found that the distance of 0.18 from the "ideal" SL is sufficient to identify a pathologic condition of m. gas. med., and the distance of 0.35 from the "ideal" SL is sufficient to identify a pathologic condition of m. sol. Of course, the value of the distance of the PLs from the "ideal" symmetry line may be changed in accordance with new requirements or new experimental results.

We also tested the symmetry of the muscle behavior of children with cerebral palsy. Shapes of the cyclograms are significantly asymmetric and parts of trajectories usually lie outside the interval, which is defined by the PLs at the distance of 0.18 (in the case of the m. gas. med.) or 0.35 (in the case of the m. sol.) from the "ideal" symmetry line. This asymmetry is given by the improper function of muscles, nerves or joints of the left or right side of the body.

6 Conclusions

The technique based on synchronized bilateral cyclograms is highly dependent on the quality and accuracy of the MoCap systems and used software. The shape of the synchronized bilateral cyclograms can be used to study of the complex muscle behavior and indicates the deviations of the identified muscular forces from the ideal muscle forces. This information could be important in rehabilitation medicine, and also could be used in control algorithms for lower limb prostheses or bipedal robots. The technique is also easily and intuitively understandable. New software could use the designed method in algorithms for a driven robotic gait orthosis for the purposes of locomotion therapy.

This work has not attempted to describe all potential ways of applying the synchronized bilateral cyclograms of the muscular forces. We have shown new methods that have subsequently been tested on healthy subjects and subjects with cerebral palsy. In the future study, we plan to measure more subjects with other types of disabilities and evaluate the symmetry during a longer period of therapy.

Acknowledgments. This work was done at the Joint Department of Biomedical Engineering CTU and Charles University in the framework of research program No. VG20102015002 (2010-2015, MV0/VG), sponsored by the Ministry of the Interior of the Czech Republic.

References

[1] Buford, W.L., Thompson, D.E.: A system for three-dimensional interactive simulation of hand biomechanics. IEEE Trans. Biomed. Engineer. 34(6), 444–453 (1987)

[2] Delp, S.L., Arnold, A.S., Piazza, S.J.: Graphics-based modeling and analysis of gait abnormalities. Biomed. Mater. Eng. 8(3), 227–240 (1998)

[3] Schutte, L.M., Rodgers, M.M., Zajac, F.E., Glaser, R.M.: Improving the efficacy of electrical stimulation-induced leg cycle ergometry: an analysis based on a dynamic musculoskeletal model. IEEE Trans. Rehabil. Eng. 1(1), 109–125 (1993)

[4] Yamaguchi, G.T., Zajac, F.E.: Restoring unassisted natural gait to paraplegics via functional neuromuscular simulation: a computer simulation study. IEEE Trans. Biomed. Eng. 37(9), 886–902 (1990)
[5] van der Krogt, M.M., Delp, S.L., Schwartz, M.H.: How robust is human gait to muscle weakness? Gait Posture 36(1), 113–119 (2012)
[6] Liu, M.M., Herzog, W., Savelberg, H.H.: Dynamic muscle force predictions from EMG: An artificial neural network approach. J. Electromyogr. Kinesiol. 9(1), 391–400 (1999)
[7] Gage, R.J., Hicks, R.: Gait Analysis in Prosthetics. Clin. Prosthet. Orthot. 9(3), 17–21 (1989)
[8] Janura, M., Cabell, L., Svoboda, Z., Kozakova, J., Gregorkova, A.: Kinematic analysis of gait in patients with juvenile hallux valgus deformity. J. Biomech. Sci. Eng. 3(3), 390–398 (2008)
[9] Grieve, D.W.: Gait patterns and the speed of walking. Biomed. Eng. 3(3), 119–122 (1968)
[10] Grieve, D.W.: The assessment of gait. Physiotherapy 55(11), 452–460 (1969)
[11] Kutilek, P., Viteckova, S.: Prediction of Lower Extremity Movement by Cyclograms. Acta Polytech 52(1), 51–60 (2012)
[12] Giannini, R.C., Perell, K.L.: Lower limb coordination during walking in subjects with post stroke hemiplegia vs. healthy control subjects. Clin. Kinesiol. 59(4), 63–70 (2005)
[13] Heck, A., Holleman, A.: Walk like a mathematician: an example of authentic education. In: Proc. ICTMT6, pp. 380–387 (2003)
[14] Yinga, Z., Roya, R.R., Zhonga, H., Zdunowskia, S., Edgertona, V.R., Gomez-Pinillaa, F.: BDNF–exercise interactions in the recovery of symmetrical stepping after a cervical hemisection in rats. Neuroscience 155(4), 1070–1078 (2008)
[15] Webb, A., Muir, G.: Sensorimotor behaviour following incomplete cervical spinal cord injury in the rat. Behav. Brain Res. 165(2), 147–159 (2005)
[16] Forner-Cordero, A., Koopman, H., van der Helm, F.: Describing gait as a sequence of states. J. Biomech. 39(5), 948–957 (2006)
[17] Goswami, A.: Kinematics quantification of gait symmetry based on bilateral cyclograms. In: Proc. XIXth ISB Congress, pp. 1–6 (2003)
[18] Herzog, W., Nigg, B., Read, L., Olsson, E.: Asymmetries in ground reaction force patterns in normal human gait. Med. Sci. Sport Exer. 21(1), 110–114 (1989)
[19] Pierotti, S.E., Brand, R.A., Gabel, R.H., Pedersen, D.R., Clarke, W.R.: Are leg electromyogram profiles symmetrical? J. Orthop. Res. 9(5), 720–729 (1991)
[20] Goswami, A.: New Gait Parameterization Technique by Means of Cyclogram Moments: Application to Human Slope Walking. Gait Posture 8(1), 15–26 (1998)
[21] Kutilek, P., Farkasova, B.: Prediction of Lower Extremities Movement by Angle-Angle Diagrams and Neural Networks. Acta Bioeng. Biomech. 13(2), 57–65 (2011)
[22] Ounpuu, S., Gage, J.R., Davis, R.B.: Three-dimensional lower extremity joint kinetics in normal paediatric gait. J. Pediatr. Orthop. 11(3), 341–349 (1991)
[23] Stansfield, B.W., Hillman, S.J., Hazlewood, M.E., Robb, J.E.: Regression analysis of gait parameters with speed in normal children walking at self-selected speeds. Gait Posture 23(3), 288–294 (2006)
[24] Orendurff, M.S., Aiona, M.D., Dorociak, R.D., Pierce, R.A.: Length and force of the gastrocnemius and soleus during gait following tendo Achilles lengthenings in children with equinus. Gait Posture 15(2), 130–135 (2002)
[25] Mademli, L., Arampatzis, A., Morey-Klapsing, G., Brüggemann, G.P.: Effect of ankle joint position and electrode placement on the estimation of the antagonistic moment during maximal plantarflexion. J. Electromyogr. Kinesiol. 14(5), 591–597 (2004)

Properties of Ankle-Brachial-Index (ABI) in the Light of Numerical Simulation of Pulse Wave Propagation

M. Pieniak and K. Cieślicki

Warsaw University of Technology, Institute of Automatic Control and Robotics,
ul. Św. Andrzeja Boboli 8, 02-525, Warsaw, Poland
pienio.7@wp.pl

Abstract. The aim of this study is to highlight properties of an ankle-brachial index (ABI) using a specially designed numerical simulator of pulse wave. The ABI test is used by many practitioners to detect some vascular diseases. The 19-elements, linerised 1D model was developed in order to simulate blood flow in a part of the vascular tree that includes the main arteries of the lower and upper extremities. The simulations have shown a decrease of the ABI with an increase of femoral artery stenosis. Small sensitivity of the index for the low level of femoral artery stenosis (less than 50%) was observed. Furthermore, a negative correlation between the ABI and the mean arterial pressure (MAP) in the system has been shown.

1 Introduction

It has been known that the pulse pressure waveform contains information about morphology and functions of cardiovascular system [1]. Therefore, a good understanding of mechanisms underlying pressure wave's propagation can provide valuable diagnostic and therapeutic information. Pulse pressure waves are introduced into the arterial tree due to the cyclic heart action. These waves are partially reflected when they congregate a change in the characteristic impedance. A composition of the forward-traveling wave and the reflected wave determines a form of the pulse pressure wave. Along vascular tree of large circulation the mean value of pressure diminishes. However, in its first part, i.e. along the central distributing arteries, a value of systolic blood pressure, which is the largest value of blood pressure, grows (fig 1) [2,3], producing enlargement of the pulse wave amplitude. Interference of the forward traveling waves and these, reflected from microcirculation is just responsible for that effect [2] (see Fig. 1) and is put-upon in the ankle-brachial index [2].

The ankle-brachial index (ABI) is determined as the ratio of systolic blood pressure at the ankle (pressure at posterior tibial artery or the dorsal artery) to the

T. Březina and R. Jabloński (eds.), *Mechatronics 2013*,
DOI: 10.1007/978-3-319-02294-9_102,

systolic pressure at the arm (in the brachial artery). Measurement is made at a horizontal body position, after about 10 minutes rest. It is necessary time for auto-regulation processes to fit the cardiovascular system to a new condition. The ABI is one of the simplest tools for detection of the Peripheral Artery Disease (PAD) [4]. Decreased value of blood pressure in arteries at the ankle, relative to the central blood pressure, suggests stenosis in the arterial conduits between the aorta and the ankle [5].

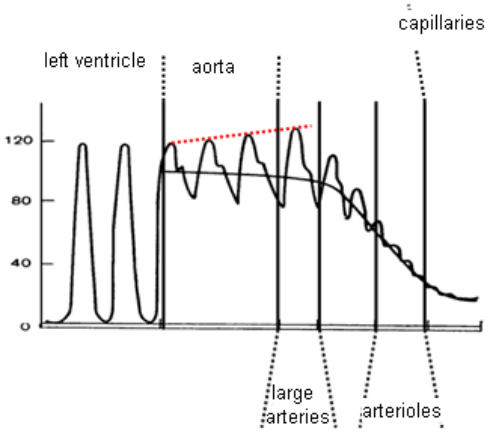

Fig. 1 Blood pressure in different parts of cardiovascular system at lying in a horizontal position men [1]

PAD concerns 12 to 14% of population and in majority of cases does not possess visible symptoms. Hence, most of the patients are not conscious about the disease and the therapy is not undertaken [5].

The physiological range of the ABI value is not clearly stated. According to the American Diabetes Association the correct value of ABI ranges from 0.91 to 1.3. The mild PAD falls into the range from 0.7 to 0.9, and the moderate ischemic disease is quoted for ratios of 0.41-0.69. Ratios of less than or equal to 0.4 are quoted as critical PAD [5]. On the other hand, the Society for Vascular Technology suggests that correct value of the ABI ranges from 1.0 to 1.4. A light cardiovascular disease falls into the range from 0.81 to 1.0, and a medium disease is quoted for ratios of 0.5-0.8. Ratios of less than 0.5 are quoted in hard, and less that 0.3 are quoted in critical cardiovascular diseases [5].

Although the ABI test is used by many practitioners to detect some vascular diseases, its advantages and limitations are not well understood. Therefore, the main purpose of this study is to analyze the ankle-brachial index using the worked out simulator of pulse wave. To the authors' best knowledge, previous studies have not investigated this research issue before.

2 Materials and Method

To accomplish the goal of this study, we built the 19 element model of vascular tree. It includes the main arteries of the lower and upper extremities, treated as a set of compliant, cylindrical tubes. It was also assumed that the length of each tube is long compared to its diameter. This assumption surely holds for the central arteries and implies that the flow is one dimensional. Our model is thus a part of much more complex 55 elements 1D model of large circulation, known from the previous studies [6,7,8,9]. On global circulation scheme shown in Fig 2a, part investigated in this study was highlighted in red.

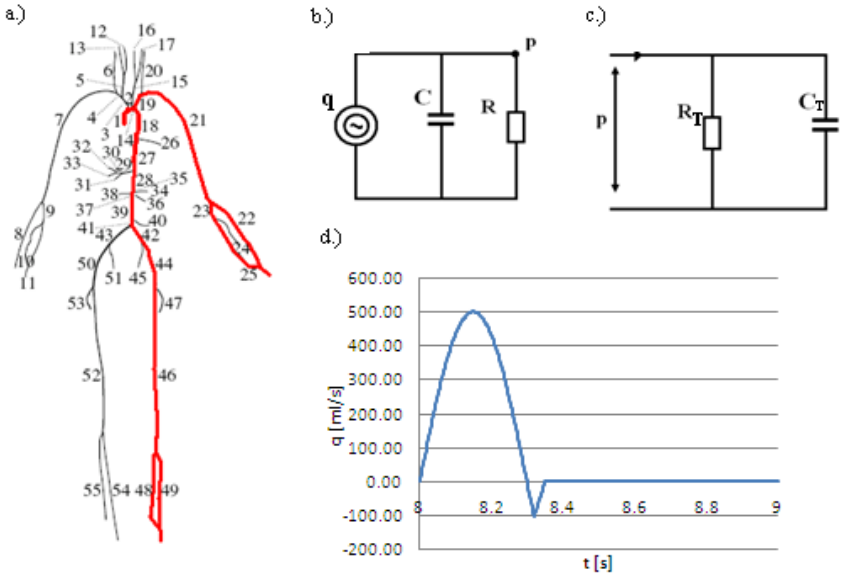

Fig. 2 a) 55-element model of arterial tree taken from [7]. The studied 19-elements structure is highlighted; b) Electric scheme of the remaining part of the arterial tree; c) Electric scheme of the peripheral resistance and compliance of microcirculation; d) Periodic inflow rate imposed at the inlet of ascending aorta (segment 1) remade from [7].

Following the assumptions, blood flow in a single arterial segment was described by two first order partial differential equations, complemented by the wall state equation, expressing the relation of the vessel's cross section and the pressure (1)[7]:

$$\begin{cases} C_H \dfrac{\partial p}{\partial t} + \dfrac{\partial q}{\partial x} = 0 \\ L_H \dfrac{\partial q}{\partial t} + \dfrac{\partial p}{\partial x} = -R_H q \\ p = \dfrac{a}{C_H} \end{cases} \tag{1}$$

where: a, p and q denote the cross section of artery, the pressure and the flow rate, respectively, t is time and x is the axial coordinate along the artery. In turn, R_H, L_H and C_H, are the viscous resistance to flow, blood inertia and wall compliance per unit length of vessel, respectively, calculated from the following formula:

$$R_H = \frac{2(\gamma+2)\mu\pi}{A_0^{\,2}}, \quad L_H = \frac{\rho}{A_0}, \quad C_H = \frac{A_0}{\rho c_0^{\,2}} \tag{2}$$

where ρ=1050Kgm^{-3} and μ=4mPas is the density and viscosity of blood, while γ=9 is a non-dimensional correction factor, which depends on the assumed velocity profile [7], A_0 is the lumen area at the reference state (p,q)=(0,0) and c_0 is a speed of pulse wave propagation:

$$c_0 = \frac{1}{\sqrt{L_H C_H}} \tag{3}$$

Table 1 Physiological data of the arterial tree (*-number from 55 elements model [7])

No.*	Arterial segment	l [cm]	d [cm]	c_0 [ms^{-1}]	R [mmHg s ml^{-1}]	C [ml mmHg^{-1}]
-	Inlet	-	-	-	0.98	1.8
1	Ascending aorta	29	4	4.3	-	-
2	Aortic arch I	22.4	2	4.3	-	-
18	Thoracic aorta I	20	5.2	4.3	-	-
19	L. subclavian	8.4	3.4	5.1	-	-
21	L. brachial	6.4	42.2	5.9	-	-
22	L. radial	3.2	23.5	9.5	-	-
23	L. ulnar I	4.4	6.7	8.4	-	-
25	L. ulnar II	3.8	17.1	8.9	-	-
27	Thoracic aorta II	13.2	10.4	5	-	-
28	Abdominal aorta I	12.2	5.3	5	-	-
35	Abdominal aorta II	12	1	4.7	-	-
37	Abdominal aorta III	11.8	1	4.7	-	-
39	Abdominal aorta IV	11.2	10.6	4.7	-	-
41	Abdominal aorta V	10.4	1	4.5	-	-
42	R. common iliac	7.2	5.8	5.3	-	-
44	R. external iliac	6	14.4	7.7	-	-
46	R. femoral	4.4	44.3	8.6	-	-
48	R. posterior tibial	3.8	32.1	12.4	-	-
49	R. anterior tibial	2.6	34.3	14.1	-	-
-	Palmar arch	4.4	2	8.4	600	0.0188
-	Plantar arch	4.2	2	8.7	900	0.0025

The remaining part of the cardiovascular system, as well as a peripheral microcirculations vessels were treated globally, as a total resistance and a total compliance of the relevant arterial system [10]. They are shown in Fig. 2b,c in a form of the electric analogy.

The geometrical and elastic parameters of the 19 arteries were extracted from the 55 elements' model reported in [6,7,8,9] (tab. 1). The remaining part of the model had a small influence on a value of the studied ankle-brachial index. It was involved in modeling to study the influence of the entrance value of pressure.

The value of flow impedance of the rest part of arterial tree (R,C) were experimentally well-chosen.

The heart activity was simulated by a pump producing volume flow rate, Q(t), displayed in Fig.2d [7]. This is good representation of heart work, which in resting conditions and stable pulse periodically shoots the same volume of blood.

Flow conditions at the bifurcation and coalescence of arteries were consequences of mass conservation and continuity of total (i.e. static and dynamic) pressure and have the form:

$$\begin{cases} q_1 - q_2 - q_3 = 0 \\ p_1 + \dfrac{\rho}{2}\left(\dfrac{q_1}{a_1}\right)^2 = p_2 + \dfrac{\rho}{2}\left(\dfrac{q_2}{a_2}\right)^2 = p_3 + \dfrac{\rho}{2}\left(\dfrac{q_3}{a_3}\right)^2 \end{cases} \tag{4}$$

where the subscripts 1,2,3 denotes mother and two daughter vessels, respectively.

For implementation of the featured model, a program in Java language has been written. To solve the set of the above equations, a numerical characteristics method has been used [1,11]. It involves finding a relation between pressure, p(x,t), and flow rate, q(x,t), on two families of characteristics. The correctness of numerical model for a single segment has been verified by comparing the results with an analytical solution of a loss-free long line.

3 Results and Discussion

The pressure value in outlet of brachial artery and in inlet to plantar arch (outlet of confluencing of anterior and posterior tibial) was taken to study the Ankle-Brachial Index (ABI). One period of pressure in these arteries in physiological state was shown in Fig. 3. The systolic and the diastolic pressure at ankle and brachial equal to 135.9/68.9 and 117.9/71.4, respectively, confirming the average value of these parameters obtained from a representative group of healthy students of the Scientific Circle of Biocybernetics and Biomedical Engineering. The ABI value equaled to 1.15 and remained within the norm.

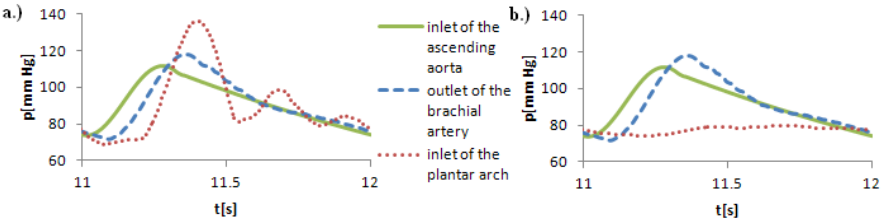

Fig. 3 Comparison of pressures in correct state (ABI=1.15) and b) in case of PAD (85% femoral artery stenosis, ABI=0.68)

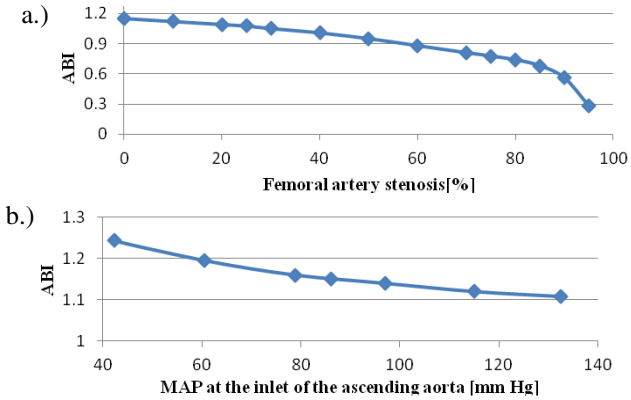

Fig. 4 Changes in ABI value in pathological states with change of a.) femoral artery stenosis and b.) mean arterial pressure at the inlet of the ascending aorta

Additionally, a delay of the peak of pressure at the level of ankle in comparison to the peak at the level of brachial was observed (Fig. 3). This result is evident concerning different distance of ankle and brachial from the heart.

One of the most frequent places where embolisms are the cause of PAD forms is the femoral artery. In case of simulation of PAD, the caliber of femoral artery was reduced gradually. Results are displayed in Fig. 4 and show a decrease of the ABI index with the severity of femoral artery's stenosis. Small sensitivity of the index for the low level of femoral artery stenosis (less than 50%) can be clearly seen. For 50% of stenosis, the ABI value was 0.95. Therefore, the acceptance of the lower limit of the normal ABI value of 0.9 in clinical practice seems to be too low.

In publication of Doroszko et al. [12] a negative correlation between the ABI and the mean arterial pressure at the inlet of the ascending aorta was observed. With the aim of checking this correlation, additional simulations were conducted. Increasing the value of mean arterial pressure from 45 to 130 mmHg we observed slight, but systematic decrease of ABI. Results are plotted in Fig 4b.

4 Conclusion

A model of the cardiovascular system has been used and applied to the study of properties of the Ankle Brachial Index. The results have shown a decrease of the ABI with an increase of femoral artery stenosis. Small sensitivity of the index for the low level of femoral artery stenosis has also been shown. Our findings suggest an increase in the accepted lower limit of the normal ABI to 1, as in recommendations of the Society for Vascular Technology. Furthermore, a negative correlation between the ABI index and the mean pressure value in the system was observed.

Although the described model is very simple, it correctly simulates the features of the ABI. Future models are recommended to take into account flow nonlinearities as well as change in the heart rate's frequency.

References

[1] Pieniak, M.: Dekompozycja ksztaltu krzywej tetna w zastosowaniu do analizy wskaznika kostka-ramie ABI(Ankle-Brachial Index) (Engineer thesis)
[2] Cieślicki, K., Przybylski, J.: Wprowadzenie do hemodynamiki krążenia. In: Tafil-Klawe, M., Klawe(red.), J.J. (eds.) Wykłady z fizjologii człowieka, pp. 438–473 (2009)
[3] Guyton, A.C., Hall, J.E.: Textbook of Medical Physiology, 11th edn., p. 163 (2006)
[4] Neubauer-Geryk, J., Bieniaszewski, L.: Wskaźnik kostka–ramię w ocenie pacjentów z ryzykiem miażdżycy. Choroby Serca i Naczyń 4(1), 1–5 (2007)
[5] Mo Al-Qaisi, D.M., Nott, D.H., King, D.H., Kaddoura, S.: Ankle Brachial Pressure Index (ABPI): An update for practitioners. Vascular Health and Risk Management 5, 833–841 (2009)
[6] Sherwin, S.J., Franke, V., Peiró, J., Parker, K.: One-dimensional modeling of a vascular network in space-time variables. J. Eng. Math. 47, 217–250 (2003)
[7] Alastruey, J., Parker, K.H., Peiró, J., Sherwin, S.J.: Analysing the pattern of pulse waves in arterial networks: a time-domain study. J. Eng. Math. 64, 331–351 (2009)
[8] Alastruey, J., Parker, K.H., Peir´o, J., Sherwin, S.J.: Lumped Parameter Outflow Models for 1-D Blood Flow Simulations: Effect on Pulse Waves and Parameter Estimation. Commun. Comput. Phys. 4, 317–336 (2008)
[9] Liang, F., Takagi, S., Himeno, R., Liu, H.: Multi-scale modeling of the human cardiovascular system with applications to aortic vascular and arterial stenoses. Med. Biol. Eng. Comput. 47, 743–755 (2009)
[10] Cieślicki, K.: Hydrodynamic conditions of cerebral circulation. AOW EXIT, Warszawa (2001) (in polish)
[11] Jungowski, W.: Jednowymiarowy nieustalony przepływ cieczy. WPW, Warszawa (1976)
[12] Doroszko, A., Drożdż, K., Gaweł, W., Gać, P., Łukasik, M., Seniuta, J., Kolman, E., Cedzyński, Ł., Roemer, R., Chachaj, A., Poręba, R., Derkacz, A., Andrzejak, R., Szuba, A.: Wskaźnik kostka–ramię, nadciśnienie tętnicze i inne czynniki wpływające na występowanie dysfunkcji rozkurczowej lewej komory. Nadciśnienie Tętnicze 12(6), 439–443 (2008)

Patient Activity Measurement in Active Elbow Orthosis

T. Ripel, J. Krejsa, and J. Hrbáček

Brno University of Technology, Faculty of Mechanical Engineering, Technická 2,
616 69, Brno, Czech Republic
{yripel00,yhrbac03}@stud.fme.vutbr.cz, krejsa@fme.vutbr.cz

Abstract. The paper is focused on problem of determining the activity of patient's forearm during the process of rehabilitation of elbow joint using the active device - motorized orthosis, equipped with the sensor to measure such activity. The measurement is the key feature for the active device to fulfill its purpose: move the actuated part of orthosis based on patient's activity thus improving the rehabilitation process. Paper gives details on used hardware, preliminary measurements and introduces the method of extracting the patient's zero activity as it is the zero activity the subsequent control system must be related to.

1 Introduction

Rehabilitation process is essential for inner joint fractures post traumatic treatment. Currently the process is realized using either trained personnel or passive motorized devices. In both cases the patient has to visit the medical facility, in latter case no feedback degrades the quality of rehabilitation process. Active orthosis is a smart device that uses sensor system to measure the activity of the patient, actuator to perform desired motion of actuated part of the orthosis and control system that controls the actuator based on the patient's activity, current position of the system, type of exercise and other variables, as denoted on Fig. 1.

Regardless the joint the active orthosis is addressed to, the measuring of patient's activity is the key input for the control system. A number of methods exist based on various principles. Electromyography (EMG) detects the the electrical potential generated by muscle cells when these cells are activated [1, 2], while mechanomyography (MMG) detects low frequency vibration that appears when a muscle is contracted using an accelerometer or microphone placed on the skin [3, 4]. MMG offers higher signal to noise ratio compared with EMG, however both methods suffer from necessity to install and calibrate expensive measuring devices.

Rehabilitation process using active orthosis is similar to usual assisted exercising, where the physiotherapist is replaced by the device.

T. Březina and R. Jabloński (eds.), *Mechatronics 2013*,
DOI: 10.1007/978-3-319-02294-9_103,

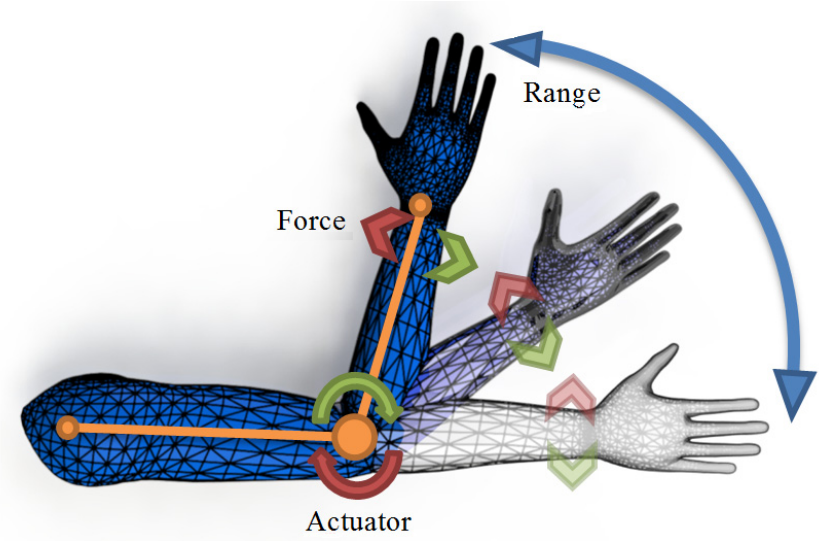

Fig. 1 Active orthosis scheme. Output axis of the actuator is collinear with the axis of elbow joint. Actuator control is based on the feedback from load gauge measuring the force effecting the forearm. The range of the device complies with human elbow range.

This paper presents the measurement system of active elbow orthosis using strain gauge in the actuated part, shows how the measurement is calibrated and how the zero activity of the patient is determined from the measured value.

2 Active Elbow Orthosis

2.1 Orthosis Mechanics

Aluminum frame of the orthosis consists of arm and forearm parts. These are connected through the worm gear providing reciprocal rotary movement invoked by the direct current drive. The self-locking character of the worm gear provides the stiffness of the orthosis, which is essential for proper function especially in static regime. The strain gauge creates link between forearm frame and the wheel of worm gear allowing to measure the tension generated by patient's effort to move the arm. The device is fixed to the arm by series of adjustable holders with Velcro straps, providing rigid and comfortable fitment. The mechanical design of the orthosis is depicted on the exploded diagram below.

Active orthosis overview diagram is shown in Fig. 2.. The orthosis is composed of the drive (1), firmly connected to the arm holder (5). The drive uses gear (3) to actuate forearm part, consisting of the strain gauge (2) being the integral part of the design and subsequent forearm holder (4).

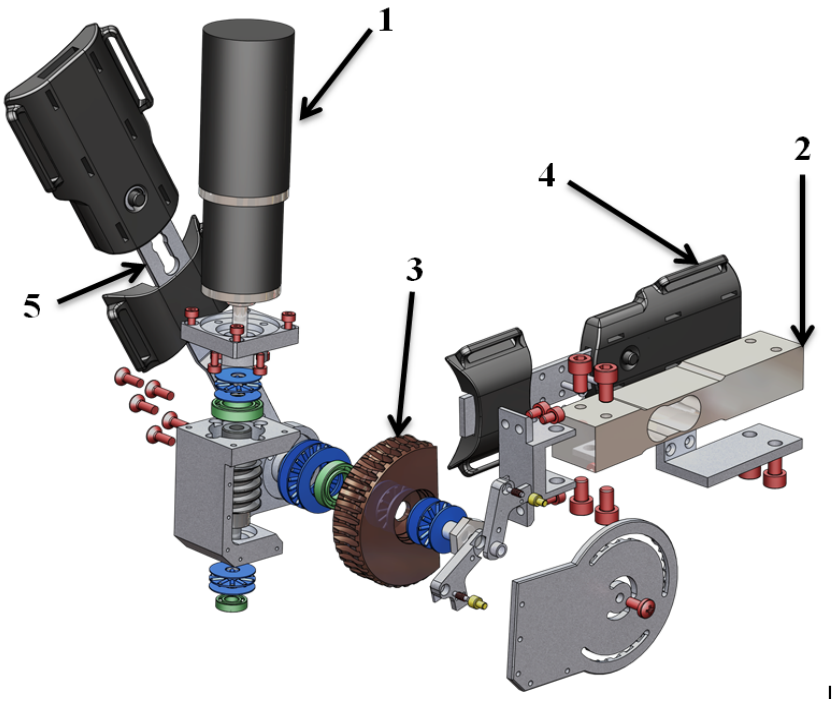

Fig. 2 Orthosis exploded diagram

2.2 Measuring Chain

The strain gauge PWKRC3 with maximum load of 400N produced by HBM is used as the primary sensor of the patient's activity. The sensor is in a bridge connection; the low-amplitude signal is conditioned by a bridge amplifier integrated to the A/D converter. This measurement unit is connected to the main low-level control unit over an I^2C bus and uploads the conversion results with frequency of 66 Hz. The control unit contains a quadrature input for the orthosis actuator feedback and logical inputs for the stop button and limit switches. The power output enables to directly drive the actuator; the unit provides closed-loop position control with speed and acceleration limiting. There is also a USB interface for communication with the high-level control layer (HL).

The position of the orthosis is determined by summing the quadrature signal increments and multiplying them by a constant given by the total gear ratio. This position is however relative to the orthosis power-on position; there is a homing procedure that allows to set the position zero using a limit switch.

The High Level is implemented as an independent application running on PC under Windows OS. It receives the strain gauge measurements together with

orthosis position, drive voltage and current and provides the control unit with motion commands.

3 Zero Activity Determination

Control system in the orthosis high level control layer determines the motion of the orthosis based on activity of the patient. Thus it is crucial to determine the zero activity of the patient, the control system can refer to. In order to find the method of such zero activity determination, preliminary measurement of raw data was performed, resulting in finding the variables that effect the zero activity. The orthosis was attached to the patient, patient was briefed to leave the forearm free and orthosis was actuated in full angle range using the constant motion velocity while data were recorded. As illustrated in Fig. 3. below, the patient individual characteristics, the direction of motion and the position of the forearm are the most influential. Furthermore the experiments proved that the way the patient is attached to the orthosis influences the measurement, even for the same patient with no mechanical changes in the orthosis variable elements.

Patient zero activity thus has to be find using the calibration prior to the exercise. The calibration process was proposed as follows:

1. Free arm motion with constant velocity for both directions in the whole range of mobility
2. Storing measured data in force/angle form
3. Calculating the parametric curve for both directions, representing the zero activity

The parameters of the curve below are then stored and provided to the control system, enabling to determine the zero activity for both directions and arbitrary angle of the orthosis.

Polynomial curve fitting was selected to extract the trends in zero activity data. In particular the two sets of couples angle/force for both directions are used. Common least squares fitting is used to calculate the coefficients of polynomial. Due to the limited resolution in angle and fast data acquisition frequency the multiple values of force for the same angle appeared in the data. Fast implementation of curve fitting using Vandermonde matrix was used in the application. The order of the curve can be set by the operator, lower orders (2-4) are usually sufficient. Figure 4. shows the calibration curves for measured data.

Example of relative activity of the patient - measured data corrected by the calibration curve - is shown on Fig. 5. up. Relative activity (or calibration error in other words) is shown for two different calibration curves, producing similar magnitude of error. Higher values at the high angle are caused by discomfort of patient with the orthosis in limit position.

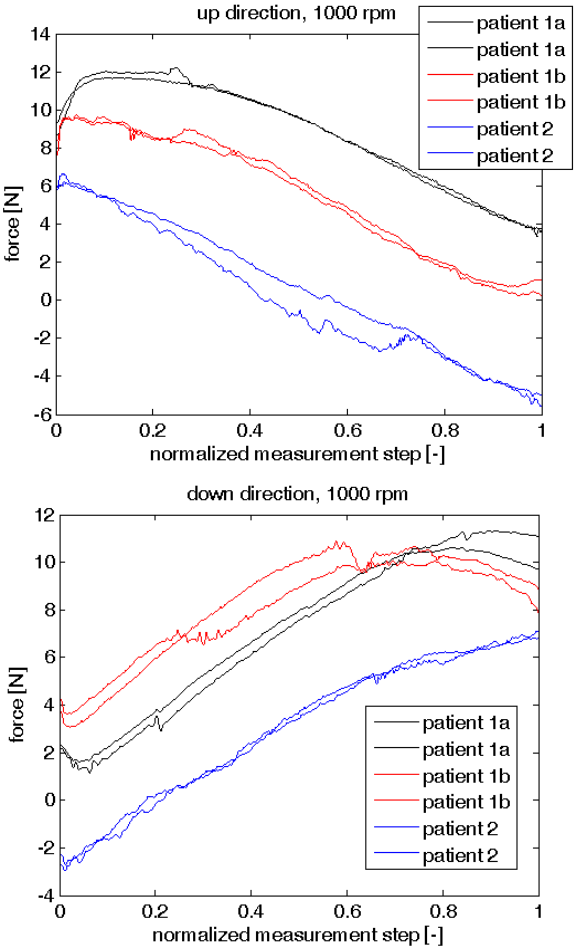

Fig. 3 Raw data of measured force values with patient free arm for both direction of motion and constant velocity of 1000 rpm on the actuator drive. Two subsequent measurements are shown for patient 2, Repeated measures are shown for patient 1, where a/b denotes different days of the measurement.

The stability of the calibration over longer period of time was tested by repeated free arm full range measurement procedure, where the difference between the measured and calibration data was recorded. In order to reduce the noise in measurement, simple circular buffer implementation of triangular kernel convolution was used for the raw data prior to the calibration curve comparison. The resulting zero activity error is shown in Fig. 5. down, where root mean square error (RMSE) is shown evolving with time for both raw data and filtered data.

Linear trend of RMSE is also shown, in both cases increasing, with the slope enabling to run the orthosis without recalibration for times exceeding the expected requirements.

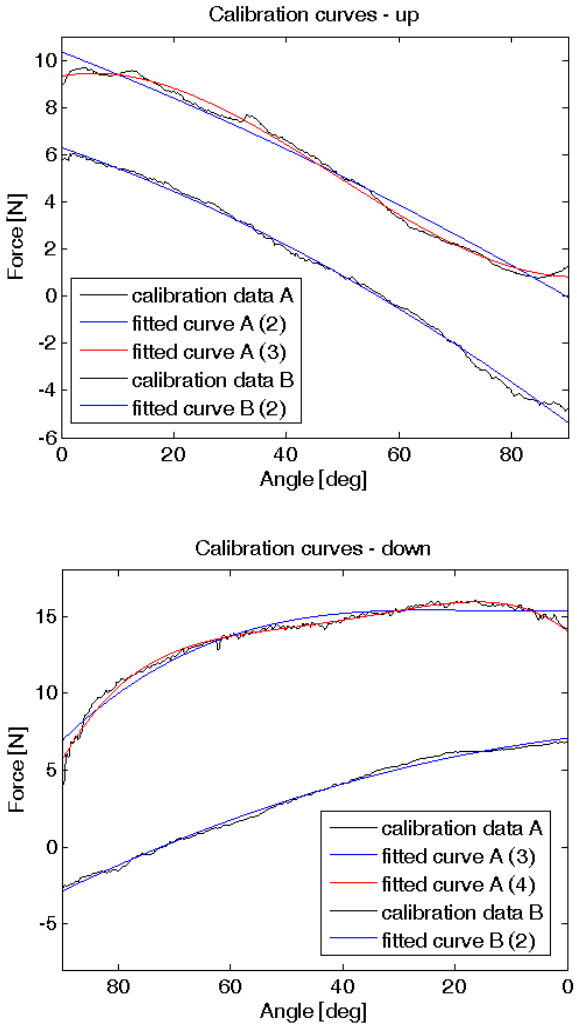

Fig. 4 Calibration data and corresponding calibration curves for both directions of motion

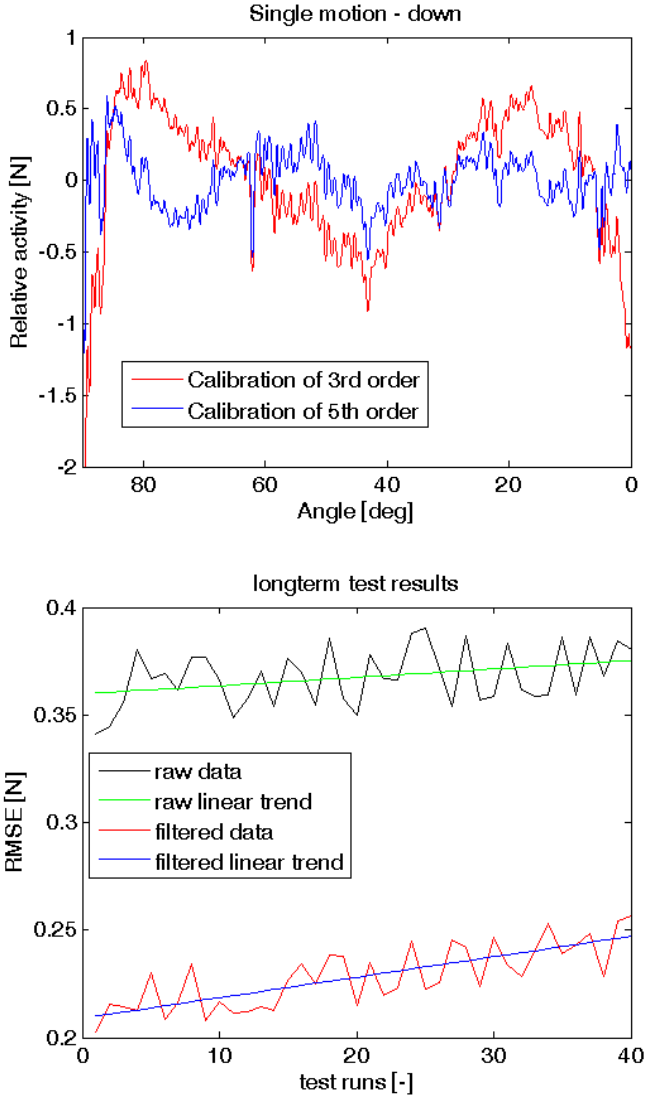

Fig. 5 Zero activity tests. Relative activity of the patient (up), long-term test results (down)

4 Conclusions

Used method of calibration and patients zero activity determination proved to be sufficient for the control system to be placed on the higher level of active orthosis control. According to our experiences, the necessity of the calibration prior to the exercise can not be avoided, while keeping the system sensitive enough. The way the patient is attached to the orthosis unfortunately plays its role. In order to

reduce the need for recalibration prior to the exercise a different mechanism of orthosis attachment would probably have to be used, however, the calibration itself as proposed takes less than minute and leads to stable and sensitive determination of patients inactivity.

Acknowledgement. Published results were acquired with the support of project FSI-S-11-15 "Design, testing and implementation of control algorithms with use of nonlinear models of mechatronics systems".

References

[1] Merlo, A., Farina, D., Merletti, R.A.: Fast and reliable technique for muscle activity detection from surface EMG signals. IEEE Trans. Biomed. Eng. 50, 316–323 (2003)
[2] Edwards, R.G., Lippold, O.: The relation between force and integrated electrical activity in fatigued muscle. J. Physiol. 132, 677–681 (1956)
[3] MA, M.Y.E.: MMG Sensor for Muscle Activity Detection: Low Cost Design, Implementation and Experimentation: a Thesis Submitted in Partial Fulfilment of the Requirements for the Degree of Masters of Engineering in Mechatronics, Massey University, Auckland, New Zealand, p. 258 (2010)
[4] Mohamed Irfan, M.R., Sudharsan, N., Santhanakrishnan, S., Geethanjali, B.: A Comparative Study of EMG and MMG Signals for Practical Applications. In: 2011 International Conference on Signal, Image Processing Applications, With workshop of ICEEA 2011 IPCSIT, vol. 21. IACSIT Press, Singapore (2011)

A Physical Model of the Human Circulatory System for the Modeling, Control and Diagnostic of Cardiac Support Processes

A. Siewnicka[1], K. Janiszowski[1], and M. Gawlikowski[2]

[1] Warsaw University of Technology, Faculty of Mechatronics, Boboli 8, 02-525, Warsaw, Poland
{a.siewnicka, kjanisz}@mchtr.pw.edu.pl
[2] Foundation of Cardiac Surgery Development, Wolności 345A, 41-800, Zabrze, Poland
mgawlik@frk.pl

Abstract. This study discusses the concept of building and capabilities of the physical model of the cardiovascular system, which will be used for research of the heart support processes. The paper describes the functionality of the system and the data acquisition configuration necessary for the purposes of assist devices modeling, control algorithms development and testing, as well as for implementation of support processes diagnostics. Exemplary hardware for elements representing the selected components of the circulatory system, is presented. Selected measurement devices and methods of pathological conditions modeling are described.

1 Introduction

In recent years extensive works were carried out in Poland to develop the heart assist device. In 1997 the POLCAS support system was introduced in to clinical use. It consisted of POLVAD-MEV extracorporeal, pulsatile cardiovascular support pump with the dedicated POLPDU-401power supply and control device. Since then further research has focused on several aspects. Works were carried out to reduce the dimensions and weight of power supply equipment and to improve the pump structure and materials in order to reduce the risk of blood clots formation. In the meantime additional problems occurred connected with withdrawing valves and previously used material from production. For this reason the development of a completely new valve type and procedures for the use of new materials were required. At the same time the works were continued to improve the control system of the prosthesis. Pulsatile pump is composed of two chambers separated by flexible membrane. The generated air pressure change in the pneumatic chamber causes the diaphragm movement and filling and emptying of the blood chamber. Work is also aimed at the development of the control algorithm providing the best medical conditions of the chamber action. This means developing methods of control that ensure full filling and emptying of the ventricle in each

T. Březina and R. Jabloński (eds.), *Mechatronics 2013*,
DOI: 10.1007/978-3-319-02294-9_104, © Springer International Publishing Switzerland 2014

cycle, which will reduce the risk of thrombosis formation. At the same time the system should allow for the setting of cardiac output value which is the amount of blood pumped by the assist device in the time interval of one minute. This implies the need to ensure adaptation of control signal to the current state of patient condition. It is a difficult task due to the reduced possibility of blood flow measurement in the device supply cannulas and therefore the unknown value of pump output. Flow measurement is possible to obtain in the laboratory conditions by ultrasonic methods, however it is not suitable for use in a clinical application because of the high cost and large size of measurement device. In order to develop and test the control systems it is necessary to perform identification measurements and examination tests of investigated algorithms. For this reason it was necessary to carry out research equipment which will allow for: approximate recreation of the conditions prevailing in the circulatory system, attaching different types of assist pumps and testing their performance under changing load conditions and different control systems. This paper presents the idea of the physical model of the cardiovascular system which is a part of the laboratory of modeling, process control and diagnostic of cardiac support processes. The project will result in advanced measurement and research system which will consist of a physical model of the circulatory system and different types of support pumps equipped with additional measuring devices enabling for testing of the control algorithms also in the case of failure or damage.

2 Materials and Methods

The research system will consist of physical hydraulic elements (Fig. 1), which will allow for the reconstruction and measurement of the hemodynamic conditions in the human circulatory system and for attaching assist devices in atrium – main artery and apex of the heart – main artery configurations. The system will operate on a blood alike liquid which will be a mixture of water and glycerin with the addition of disinfectant. Construction of the simulator will be based on a lumped parameter model of the arterial system based on three-element Windkessel[1] and ventricle models will fulfill the Frank-Starling law [2].

The system will contain left and right atriums models in the form of tanks with adequate capacity and input and output connectors. In the most of hydraulic models of the heart, atrial contraction is not simulated [3, 4]. Due to the small medical significance of this phenomenon and the high cost of its representation in proposed system, this contraction will not be realized.

Components representing the function of the left and right ventricle must provide the reproduction of the pressure wave occurring in the chamber with adequate flow value and the passive blood flow from atrium to the ventricle. Activity of ventricular model should represent the Frank-Starling law stating that stroke volume is dependent on the end systolic volume. One of the previously adapted solution is the use of pneumatically driven heart simulators [4, 5, 6]. They are

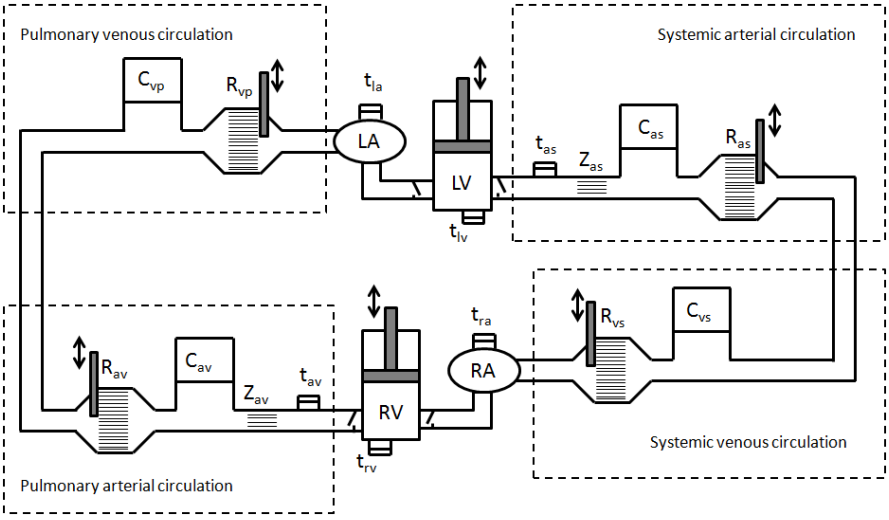

Fig. 1 Structure of the physical model of the human circulatory system. LV, RV – models of left and right ventricle, LA, RA – models of left and right atrium, C_{as}, C_{av} – systemic and pulmonary arterial compliance, C_{vs}, C_{vp} - and pulmonary venous compliance, R_{as}, R_{av} – systemic and pulmonary arterial resistance, R_{vs}, R_{vp} - and pulmonary venous resistance, Z_{as}, Z_{av} – systemic and pulmonary arterial inertance, t – support pumps connectors.

easy to make, it is possible to use pneumatic heart assist devices as the ventricle model and the control system is limited to 3-way solenoid valve. They also allow for easy reproduction of passive ventricular filling, but there is not an easy way to reproduce Frank-Starling law because the air pressure that drives the chamber must be changed adaptively to the volatility of the input and output load. This can be achieved by using the proportional controller, which generates air pressure based on end-systolic volume value [7]. However, the system is then strongly dependent on the reproducibility and sensitivity of the pressure regulator. Another option is to use an electrically driven hydraulic system which works very well as a generator of pulsatile flow. An example of this kind of pump is a commercial solution - *SuperPump* by *ViVitro Labs*. Most of these devices, however, do not represent the Frank-Starling low, but are widely used in heart valves study [8, 9]. One of the improvements applied in this solution, which enables representation of Frank-Starling low, is the usage of a mathematical model, which allows for determination of ventricular pressure value based on time-dependent elastance function. The determined pressure is a control value for the model of ventricle [10, 11] and the resulting deviation between calculated and measured pressure is given to the controller of electric motor with drives a hydraulic piston. That's why displacement pumps will be applied for the modeling of cardiac systolic function. They will be driven by actuators with force-controlled linear motors working in closed-loop. Design concept is illustrated in Fig. 2. The displacement pump will be built on the basis of POLVAD prosthetic heart but with greater maximum

capacity of blood chamber to provide conditions which are more similar to the physiological ones. The pneumatic chamber will be replaced by hydraulic structure which will carry out the function of the actuator cylinder. This space will be filled with the working fluid (silicone oil) which will be moved by linear motor-driven piston. A moving fluid will displace the diaphragm which is responsible for the movement of fluid in the blood chamber. The use of linear motor allows for precise control of the displaced volume which is necessary for realization of the Frank-Starling low. In the cylinder area a certain space with small air volume will be left to reduce the pressure rise rate. As an actuator linear motor *STA25 (Dunkenmotoren)* will be used.

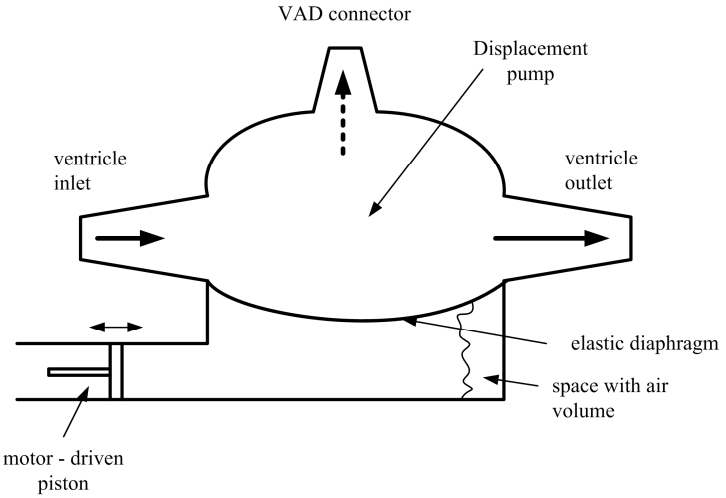

Fig. 2 Diagram of the heart ventricle model

Another elements of the physical circulatory system are the models of systemic and pulmonary circulation which should consist of elements representing resistances and compliances in systems according to three-element (systemic and pulmonary arterial circulation) or two-element (systemic and pulmonary venous circulation) Windkessel model. Compliances will be simulated by air capacitors closed to the atmosphere by moving pistons. Changes of the susceptibility value will be realized by change of the air capacitor volume realized by displacement of the piston in the cylinder by an electrical motor. In this way the flexibility of arterial system will be reproduced. The air capacitors will also be equipped with a valve that allow for connection with the atmosphere. Resistances should be modeled by adjustable elements for representation of different resistance values. In some solutions they were realized with the use of proportional hydraulic valves driven by linear motors [4]. It is possible to use any valve of this type, having ½ inch connectors and permitting operation starting from a zero pressure drop. For example *EPC-357B (Hass Manufacturing)* or *6024 valve (Burkert)* can be used. From our point of view, a better solution is to use an element constructed of

parallel elastic pipes of a small diameter placed in a tank filled with liquid (Fig. 3). The pressure of the liquid can be variously changed, so pipes will be compressed, which will increase the flow resistance. In this way, we should get a better reproduction of the circulatory system resistance for dynamic flow.

Due to the intended use of the model of the circulatory system for the study of cardiac assist devices, hydraulic system must be equipped with appropriate connectors in each ventricle, each atrium and in the elements representing the main arteries.

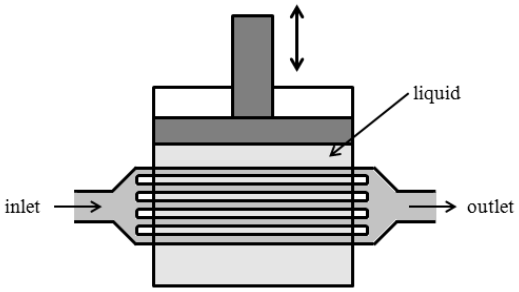

Fig. 3 Concept of vessels resistance realization

The measurement system will include pressure transducers located in the atriums (2 measurements), the left and right ventricle (2 measurements), the points representing main arteries - before and after the point of support connection (4 measurements), tanks representing arterial systems compliances (2 measurements) and tanks representing venous systems compliances (2 measurements). The measurement should be carried out by the transmitters with the range not less than ±750 mmHg and ensuring low noise value (no more than 0.5% of range). Therefore the *A-10 (WIKA)* sensors were selected. The sensors are suitable for the measuring range (-1÷1.5 bar which corresponds with -750 ÷ 1125 mmHg), has low non-linearity (0.25%), short response time (4 ms) and can work with liquid. An important feature of these sensors is the low noise level which is less than 0.3% of range. The flow measurement should be performed on inlet and outlet of the blood chamber (2 measurements) by flow meter adapted for measurement of turbulent and fast-changing flows. This is a difficult task, especially because the measuring device must not interfere with the flow or cause a pressure loss. For this reason the constriction types of flow meters and others invasive methods such as e.g. thermodilution method [12] were rejected. The possibility of using electromagnetic and ultrasonic flow meters was considered. For the electromagnetic measurement it is possible to use an *FEP300 (ABB)* or *FSM4000 (ABB)* flow meter. These devices offer high accuracy, but the frequency of measurement is too low (5 Hz - 17 Hz). Another method is the ultrasonic measurement. A well-known and frequently used solution is the *TS402 flow meter (Transonic)* with *ME11PXL* probes (to drain ½ inches). The frequency of measurements carried out by this device is a 120 Hz with 5%measurement accuracy. Clamp-on probes allows for

easy change of the measurement point and can be calibrated for various liquids. Range of measured flow is ±20 l/min. However, the cost of such measure is high (about 20 000 €).

In order to ensure full usability and flexibility of built research stand, the model of the circulatory system should provide the ability to reproduce the pathological conditions such as ventricular failure, valvular pathology or pulmonary hypertension. Simulation of the reduced performance of the ventricle will be implemented through appropriate control of the ventricle model and will reproduce the physical phenomena associated with the reduced elastance value. Vavular insufficiency will be reproduced through the use of a bypass with proportional hydraulic valve. There will also be a second valve placed behind the heart valve to simulate the state of valve blockade or occlusion in the arterial system. Control of atrium pressure value change will be implemented by connection of atriums chambers with piston system (Fig. 4). Control of the actuator will be realized by using the electric motor.

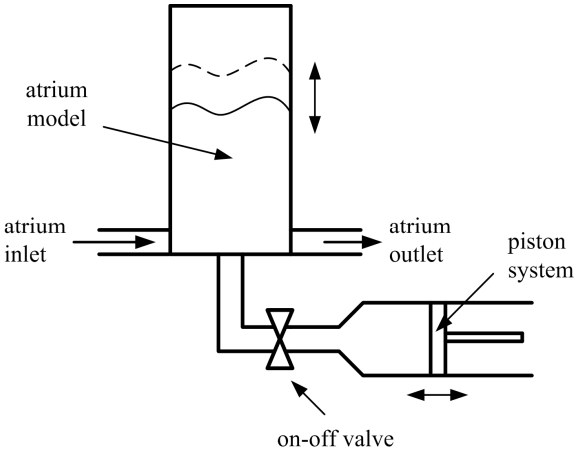

Fig. 4 Concept realization of atrium hypertension

The computer system, which will be responsible for control and data acquisition, was decided to be based on National Instruments solutions, and more specifically, on a modular real-time, high performance computing system - PXI. The system will include computer NI-PXI, fast multi-function data acquisition board, the card for motor control, analog output cards, accessories and PC computer for programming purposes.

3 Conclusions

The described physical model will allow for the simulation of cardiovascular hemodynamic conditions prevailing in the human circulatory system. Its implementation allows for developing and ongoing testing of control algorithms for heart

support pumps, both pulsatile and continuous-flow type. It will enable research for ventricular assist devices connected in a parallel way to the circulatory system in both configurations: the atrium - artery and the apex of the heart - artery. It also gives the ability to simulate a two-ventricle support. Until now those types of testing were possible to conduct using the simulation environment based on data from the in-vivo experiments carried out on pigs or on other models of human circulatory system. In Poland the only available type of that device is a hybrid cardiovascular simulator developed as a result of collaboration of research teams lead by prof. Darowski (Nałęcz Institute of Biocybernetics and Biomedical Engineering, Polish Academy of Sciences in Warsaw) and prof. Ferrari (Institute of Biocybernetics Physiology, CNR, Italy). It is based on a numerical model of the cardiovascular system implemented in real-time computer with physical part of device limited to two impedance transformers, which are mechanical devices allowing for the reconstruction of hydraulic conditions in the atrium and arterial points [13]. However, it does not allow for testing of assistive devices in the apex of the heart - artery configuration. What is more, the closed software prevents referring to the numerical model of the cardiovascular system, making the support process difficult to understand. The proposed physical model will reproduce the cardiovascular processes. The accuracy of the simulation probably won't be as good as in hybrid simulator, but the completely physical representation of the system will ensure the possibility of its adaptation for different types of support devices included in any point of the system. Furthermore, numerous diseases will be possible to simulate what is problematic in the case of the hybrid system with closed software. Therefore, the physical model is much more flexible and useful.

Acknowledgments. This work was partially supported by the Warsaw University of Technology under Dean of the Faculty of Mechatronics grant "Execution of experimental research and modification of human circulatory system model for studying the dynamics of cardiac assist devices", no. 504M-1141-0109-000.

References

[1] Westerhof, N., Lankhaar, J.W., Westerhof, B.E.: The arterial Windkessel. Medical & Biological Engineering & Computing 47(2), 131–141 (2009)

[2] Frank, O.: On the dynamics of cardiac muscle. American Heart Journal 58(2), 282–317 (1959)

[3] Pantalos, G.M., Koenig, S.C., Gillars, K.J., Giridharan, G.A., Ewert, D.L.: Characterization of an adult mock circulation for testing cardiac support devices. ASAIO Journal 50(1), 37–46 (2004)

[4] Timms, D.L., Gregory, S.D., Greatrex, N.A., Pearcy, M.J., Fraser, J.F., Steinseifer, U.: A compact mock circulation loop for the in vitro testing of cardiovascular devices. Artificial Organs 35(4), 384–391 (2011)

[5] Legendre, D., Fonseca, J., Andrade, A., Biscegli, J.F., Manrique, R., Guerrino, D., Lucchi, J.C.: Mock circulatory system for the evaluation of left ventricular assist devices, endoluminal prostheses, and vascular diseases. Artificial Organs 32(6), 461–467 (2008)

[6] Liu, Y., Allaire, P., Wu, Y., Wood, H., Olsen, D.: Construction of an artificial heart pump performance test system. Cardiovascular Engineering 6(4), 151–158 (2006)
[7] Gregory, S.D., Stevens, M., Timms, D., Pearcy, M.: Replication of the Frank-Starling response in a mock circulation loop. In: Proc. Engineering in Medicine and Biology Society, pp. 6825–6828 (2011)
[8] Labrosse, M.R., Lobo, K., Beller, C.J.: Structural analysis of the natural aortic valve in dynamics: from unpressurized to physiologically loaded. Journal of Biomechanics 43(10), 1916–1922 (2010)
[9] Claiborne, T.E., Bluestein, D., Schoephoerster, R.T.: Development and evaluation of a novel artificial catheter-deliverable prosthetic heart valve and method for in vitro testing. The International Journal of Artificial Organs 32(5), 262–271 (2009)
[10] Gwak, K.W., Paden, B.E., Noh, M.D., Antaki, J.F.: Fluidic operational amplifier for mock circulatory systems. Control Systems Technology 14(4), 602–612 (2006)
[11] Yu, Y.C., Gopalakrishnan, S.: Elastance control of a mock circulatory system for ventricular assist device test. In: Proc. American Control Conference, pp. 1009–1014 (2009)
[12] Komorowski, D., Gawlikowski, M.: Preliminary investigations regarding the blood volume estimation in pneumatically controlled ventricular assist device by pattern recognition. Advances in Soft. Computing 45, 558–565 (2007)
[13] Ferrari, G., Kozarski, M., De Lazzari, C., Gorczynska, K., Mimmo, R., Guaragno, M., Darowski, M.: Modelling of cardiovascular system: development of a hybrid (numerical-physical) model. International Journal of Artificial Organs 26(12), 1104–1114 (2003)

A New Method for Tissue Impedance Spectrometry and Its Initial Application *in vivo*

M.Władziński[1], K. Wildner[1], S. Cygan[1], B. Grobelski[2], D. Pawełczak[3], and T. Pałko[1]

[1] Warsaw University of Technology, Faculty of Mechatronics, Św. Andrzeja Boboli 8, 02-525, Warsaw, Poland
m.wladzinski@mchtr.pw.edu.pl
[2] Medical University of Lodz, Faculty of pharmacy, 90-215 Łódź, ul. Muszyńskiego 1
bartlomiej.grobelski@umed.lodz.pl
[3] Medical University of Lodz, Department of Experimental Surgery, 90-419 Łódź Al. Kościuszki 4
darekpawelczak@o2.pl

Abstract. A new method for fast tissue impedance spectrometry is proposed. This method uses an extortion with continuous, wide frequency range. Constructed hardware enabled initial application of proposed method for electrode-tissue impedance measurements on animal models. Obtained results proved to be consistent with traditional measurements methods for higher frequencies, but showed some imperfections for lower frequencies. It provided on the other hand a very significant improvement in measurement time – from several minutes to under one second.

1 Introduction

Passive electric properties of tissues, especially electric impedance can reflect their well-being. Measurements of the impedance of electrode-tissue connection or of the tissue are useful in the process of designing stimulators or biological amplifiers. In most cases measurements are carried out for a chosen set of frequencies, that allow plotting of an impedance characteristic plot.

If an examination is carried out during a surgery with limited time available, precise measurements of tissue impedance are usually impossible. Another limitation especially important at low frequencies is the excitation of tissues, which enforces limitations of amplitudes of currents applied.

Study described in this paper uses a new method for impedance measurements which is fast and requires low power extortion signals.

2 Materials and Methods

2.1 Measurement Method

Estimated impedance characteristic consists of the modulus and the phase shift angle. Typically this characteristics were measured by subsequent, independent

T. Březina and R. Jabloński (eds.), *Mechatronics 2013*,
DOI: 10.1007/978-3-319-02294-9_105,

measurements for a chosen set of frequencies. Collection of results obtained for a large number of evenly spaced frequencies enabled construction of a precise impedance characteristic. This procedure requires lengthy measurements.

Proposed method of measurements and characteristic estimation uses an extortion with a wide frequency range [1]. In described work an extortion was applied consisting of a time-limited *sinc(t)* function. Two signals – applied current extortion and the resulting voltage response measured on the electrodes are sampled and registered. Both are necessary for electric impedance characteristics estimation. Registration parameters – window length and sampling frequency are the only parameters that directly influence the precision of obtained impedance spectra [2]. Registration parameters are strongly dependent on the bandwidth of the extortion signal which should be at least four times lower than the sampling frequency. Higher sampling frequency improves the quality of the impedance phase shift characteristic estimation.

Impedance module estimation is carried out based on Fourier transforms of the applied currents and voltages registered on the object, whose impedance is being examined. Impedance spectra in form of complex numbers vectors are obtained using the FFT function. Values of voltage and current transforms for each frequency are paired and then the impedance modulus is calculated using the equation 1.

$$M_Z(f) = \frac{|U_Z(f)|}{|I_Z(f)|} \tag{1}$$

Impedance modules calculated for all available frequencies constitute a frequency domain characteristic of measured impedance module.

Frequency domain characteristic of the impedance phase shift is also obtained for each frequency point of the spectrum. Phase shift angle for each pair of complex values is calculated as an angle between two vectors on the complex plane, using the equation 2.

$$\begin{gathered} \varphi_Z(f) = s \cdot \arccos\left(\frac{\overrightarrow{U_Z(f)} \circ \overrightarrow{I_Z(f)}}{\left|\overrightarrow{U_Z(f)}\right| \cdot \left|\overrightarrow{I_Z(f)}\right|}\right) \\ s = 1 \; where \; U_Z(f) \times I_Z(f) \geq 0 \\ s = -1 \; where \; U_Z(f) \times I_Z(f) < 0 \end{gathered} \tag{2}$$

In order to preserve the continuity of the phase shift characteristic an additional condition was applied. It enforces consistent direction of vector angle calculation. Impedance phase shifts calculated for all available frequencies comprise a phase characteristic of the measured impedance.

Impedance module and phase shift characteristics provide the impedance spectrum for the whole frequency range of the extortion signal.

2.2 Measurement Hardware

For the purpose of measurements a dedicated hardware setup was made consisting of: arbitrary generator DDS-3X25, Tektronix MSO2012B oscilloscope and a set of designed for this purpose amplifiers and a current source.

Constructed circuit (fig.1.) included two channels of amplifiers receiving signals from electrodes and a precise non-inductive resistor for instantaneous current measurements. Amplifiers provided a 20dB gain and bandwidth up to 20MHz. A voltage-current converter was used as a source of application current. It was built using an operational amplifier and a Hofland circuit. Internal resistance of the current source was 15kOhm and maximum current was set to 1mA.

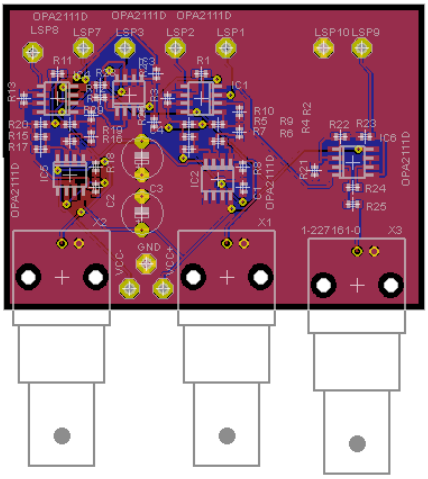

Fig. 1 The measurement circuit of impedance spectrometer

Application of commercially available devices provided ability to freely adjust registration parameters and also to modify extortion functions.

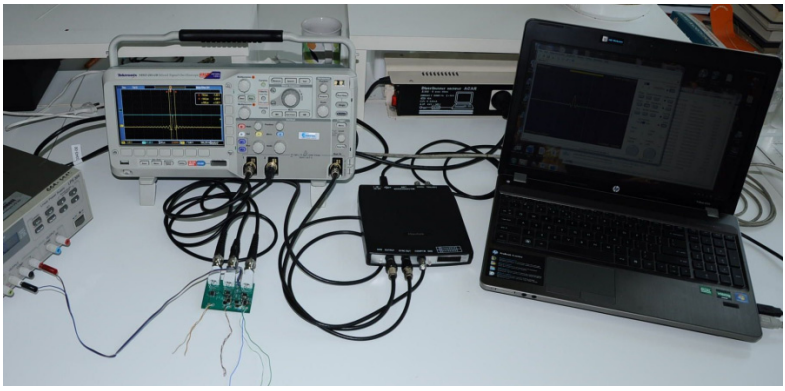

Fig. 2 The measurement setup

2.3 Experiments

Constructed setup for tissue impedance spectrometry was applied to measurements of electrode-tissue impedance as part of a project financed by National Center for Research and Development (NCBiR) "Neuroprothesis for restoring the function of upper limb in cases of brachial plexus palsy". Research was carried out on animal models in cooperation with the Medical University in Łódź under appropriate ethics committee permissions.

This project involves electrode-tissue impedance measurements during surgery and for this reason it is essential that the method is quick. Measurements were carried out as a part of examination of the influence of innervation on stimulation conditions.

Experiments were carried out on the flexor muscle of the front leg of the New Zealand White Rabbit. Steal electrodes with silver chloride coating were used (fig.3.).

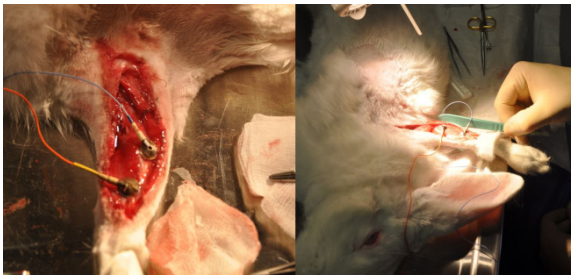

Fig. 3 Electrode placement during measurements of the electrode-tissue impedance

3 Results

For the purpose of validation of the proposed method, two impedance measurement methods were applied. As a ground truth a method with basic sinusoidal extortion for 15 different frequencies was repeated 3 times and then averaged. This procedure enabled estimation of impedance modulus and phase shift.

Frequency responses obtained using the large bandwidth extortion based on the sinc(t) function were registered for a single measurement. Results have not been averaged either in time nor in frequency domain.

Results obtained for both methods are shown in fig. 4 – modulus of impedance, and fig.5 – phase shift.

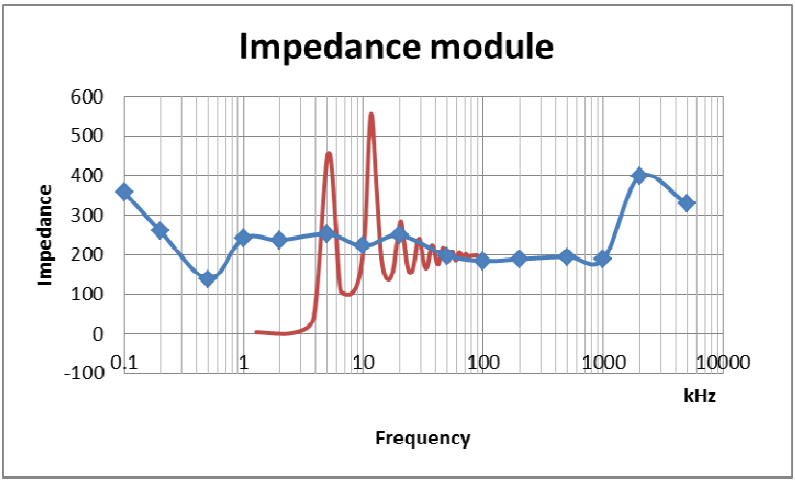

Fig. 4 Impedance module measurements results. For selected frequencies (blue), measurements conducted using the proposed method (red).

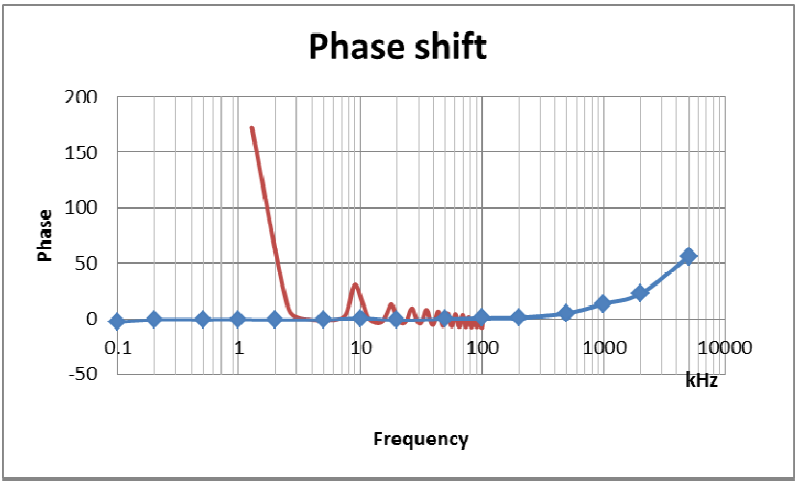

Fig. 5 Impedance phase shift measurements results. For selected frequencies (blue), measurements conducted using the proposed method (red).

4 Discussion

Both applied methods returned similar results, but the method with large bandwidth extortion showed visible fluctuations at low frequencies. This is probably caused by application of different lengths of extortion limiting window and different times of extortion and response acquisition.

Another expected advantage of the proposed method was a much shorter measurement time. This proved to be significant since for the *sinc(t)* extortion one acquisition was taken in under 1 second, and in case of the traditional method – approx. 10 minutes.

References

[1] Władziński, M., Pałko, T.: Impedance spectroscopy of tissue with extortion in a constant limited frequency band, Przegląd Elektrotechniczny R. 89 NR 1a/2013.
[2] Bracewell, R.: The Fourier Transform and Its Applications. McGraw-Hill (1965)
[3] Thielecke, H., Fleckenstein, J., Bartholomä, P., Rübe, C.: Evaluation of Impedance Spectroscopy for the Characterization of Small Biological Samples in Tissue-based Test System, September 1-5. IEEE EMBS, San Francisco (2073)

Active Artificial Lower Limb

M. Zawiski and R. Paśniczek

Warsaw University of Technology, Faculty of Mechatronics,
Św. Andrzeja Boboli 8, 02-525 Warsaw, Poland
michal_zawiski@o2.pl, roman.pasniczek@mchtr.pw.edu.pl

Abstract. From the perspective of human mobility, a loss of lower limb create a barrier that restricts normal functionality in society. In such situation, man must learn how to live with this disability. The main target of this research was to design and create an artificial lower limb with active movement support in a knee joint. The authors of the article had made an attempt to work out a simple construction of an active artificial lower limb for the people with amputated lower limb above the knee joint. The most crucial part of this paper was the design and model of an active artificial limb which would allow people with amputated lower limb above the knee joint to move.

1 Introduction

The two-footed posture makes the human gait, which have been developed through the centuries, is the most complex and highly specialised method of movement in nature. The extremely complex action, which forces groups of multiple muscles to simultaneously operate as a motor for skeletal system [4]. Lower limbs act as the support and drive and their alternating, synchronised rhythmic movements which allow for the displacement of the centre of gravity in the direction of the movement, which is define as the gait. From another point of view, gait is also a rhythmic losing and regaining balance in alternately changing stages of supporting and moving [2].

The loss of the lower limb is associated with the loss of particular components of the motor, nervous and autonomic nervous systems. The replacement reconstruction of these systems with the use of non-biological components was currently not possible due to the number of degrees of freedom and the expanded musculoskeletal control systems [1]. However, attempts are being made to partially restore the locomotive functions of lower limbs through different kinds of devices and supporting systems.

The amputation of a limb, despite its destructive nature, has from a time perspective, a preventative method for further deterioration of the state of health. The result of the amputation is persistent physiological disability, nonetheless the negative sentiments are also of great importance. In the initial period after the amputation, the stump is formed; its proper structure is the most important factor in rehabilitation and prosthesis implantation.

T. Březina and R. Jabloński (eds.), *Mechatronics 2013*,
DOI: 10.1007/978-3-319-02294-9_106,

After the appropriate treatment of the stump on the operating table, the patient immediately receives a temporary prosthesis and the forming component constitutes of the plaster prosthesis socket. The typical equipment in the case of amputation is a passive prosthesis. For many years research has been conducted in the field of active prostheses, which contain independent drives to replace the lost musculoskeletal systems [5].

At the moment, prostheses irrespectively of the applied structural solutions consist of four basic components. The first as it turns out is the most important, the prosthesis socket, and thus connecting in a mechanical way preserving the existing musculoskeletal system with non-biological performing system of the prosthesis [3]. The second component is a system that enables the bending of the knee joint and the third component is the system of a foot. The fourth component, which is usually the less technically complicated, provides a link between a knee and a foot and its main task is to provide adequate distance between the prosthesis socket and the foot.

In the case of passive prostheses, only the drive of the implanted limb is the stump and the hip joints are responsible for the movement of a stump-prosthesis system. In the case of active prostheses, the independent drives replace some musculoskeletal systems, usually in the knee joint [6]. For example, of all the most technically advanced prosthesis with inbuilt drives and electronic control is Ossur's "Power Knee". The installed drive ensures ideal smoothness of gait and comfort for those who wear the prosthesis by regulating the automation of bending and straightening, which frees a person after amputation from constant concentration in the process of moving. This type of prosthesis gives a possibility of alternate ascending the stairs and climbing even steep hills. However, the cost of "Power Knee" is very high, what in most cases makes it unattainable for the disabled person.

This paper presents a prototype of an artificial lower limb with active-assisted motion of the knee joint. It was developed at the Institute of Metrology and Biomedical Engineering of the Warsaw University of Technology for a Master Thesis.

2 Construction Assumptions and Implemented Prosthesis Project

The main assumption of the project was the ability of bending and straightening the knee joint in the range of angles of the limb while in physiological conditions present in walking and going up the stairs. It was assumed that the energy expenditure in connection with walking of the person after amputation would be as low as possible. The prosthesis foot system constitutes a swinging mechanism enabling easy transfer of the body mass during the stages of movement. The control system allows to read the current, relevant parameters of movement and to assign the speed of bending and straightening of the knee joint. The cooperation of the

knee and tarsal joints are necessary for the purpose of achieving satisfactory smoothness of walking.

The mechanical construction of the prosthesis prototype reconstructs two essential systems which performs the function of a limb: tarsal and knee joints. The tarsal joint constitutes a swinging mechanism which enables moving the body mass during the support stage. The rotary movement is limited (Fig. 1).

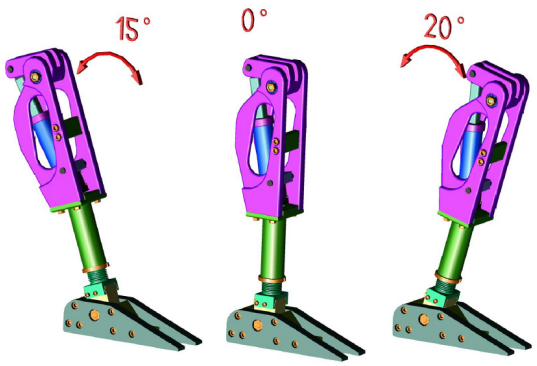

Fig. 1 The range of changes in the angles of deflection – forward 20°, backwards 15°

The bending of the knee joint was performed by the actuator driven by a stepping motor (Fig. 2). This motor was coupled with the power screw, the rotation of which causes linear movement of the retractable lever of the actuator connected with the swinging component of the knee. The extension of the lever results in turning of the swinging component, thus changes the angle of bending in the knee joint of the prosthesis.

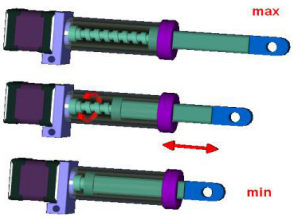

Fig. 2 Actuator's structure

The range of angles was limited by the length of pulling out the lever of the actuator and is included in the range of 5° to 50°. It was restricted by the limit switches to the range of 0° to 45°, which protects it against exceeding permissible values of the angles of bending (Fig. 3). The model is made of metal.

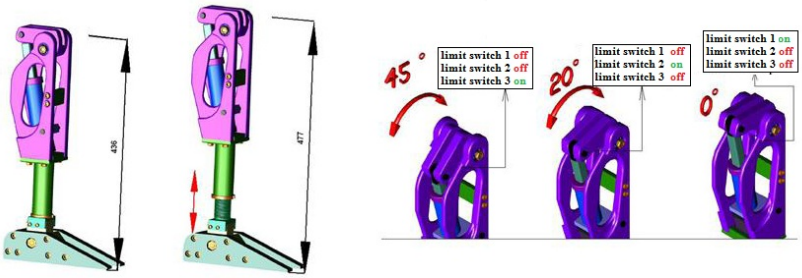

Fig. 3 The model of the prosthesis. The range of permissible angles of bending in the knee joint.

In order to control the bending of the knee joint and assign appropriate parameters of movement, a control system have been made composed of analogue-to-digital converter, generator of rectangular pulse, drive in the form of a stepping motor and limit switches. The graphic interface enables reading the essential parameters as well as the assigned speed and angle of bending in the knee joint. The manual is in VISUAL BASIC EXPRESS EDITION 2005.

The main control element in this system is a PC computer, which controls the operation of 8 bit analogue-to-digital converter via the LPT port. Depending on the values provided in the input of the converter, we received proportional voltage in the output, which is then delivered to the input of rectangular pulse generator. Depending on the values of the voltage on the generator's output we get the course of rectangular pulse with the period of filling of 50% and the frequency proportional to the given voltage, while the U/f relation is linear within the entire range. The signal from the generator is then directed to the input of the controller of the stepping motor. The output of the controller supplies directly to the coils of the stepping motor, which rotates at the speed proportional to the frequency of signal on the input of the controller. The work of the motor causes the rotation of a swinging component of the knee, which the ranges were controlled by the limit switches. Signals from the switches were delivered to the LPT port and on this basis there are generated signals controlling the analogue-to-digital converter (Fig. 4).

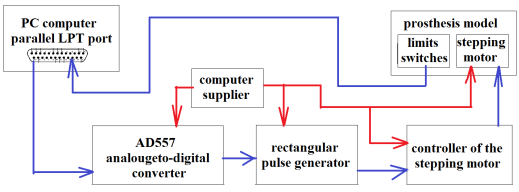

Fig. 4 Block diagram of the prosthesis prototype controller. Casing of the controller with the built-up communication ports.

In order to form the characteristics of the angle and the speed of bending in the knee joint, a program had been developed in which it was possible to set, with the use of sliders, the speed of movement and the period of stopping of the swinging component of the knee joint in the appropriate moments in the cycle of walking (Fig. 5). Characteristics of the course are shown in the form of a diagram shortly after one completed cycle of walking. The diagram field "1" from figure 5 is empty because the program was waiting for the end of the cycle. After the end of the cycle in the field "1", current characteristics and field "2" are shown and becomes a measurement field (marked by red numbers 1,2 and 3 on fig. 5). Similarly, following another cycle, field "3" becomes the active field and so on. Such form of graphic representation makes it possible for convenient observation of changes in the angle and speed in the knee joint, as well as rapid modification of characteristics.

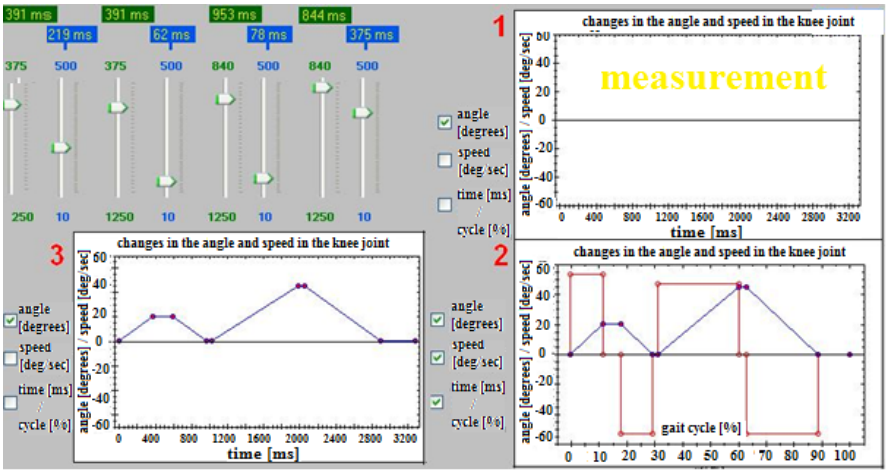

Fig. 5 Forming the characteristics of changes in the angle and speed in the knee joint of the prosthesis model, Exemplary characteristics obtained during conducted examination of the produced prosthesis model

In the designed model it was not possible to set up and run the formation of the course of acceleration and of the movement of the swinging element. The study was limited to examining the linear speeds. The stepping motor had the ability to accelerate to the desired speed in a very short period of time, which was a few ms and was short enough to produce the escalating and falling edges of the speed in the form of vertical courses.

3 Test of Prototype

Fig. 6 shows a comparison between the general characteristics of the dependency of angle and the speed of bending in the physiological knee joint during a completed gait cycle with the characteristics of the parameters for the developed prototype of the prosthesis.

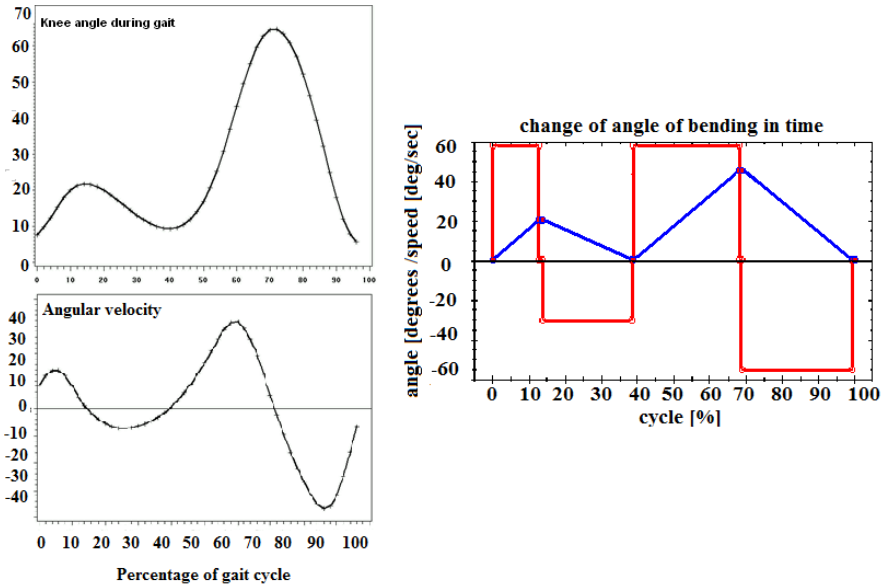

Fig. 6 Comparison of relation of the angle and the speed of bending the knee in the function of time during walking with the obtained characteristics of these parameters for the developed model of the prosthesis [7], [8]

Despite of the fact of using only constant speed, the fidelity of reconstructing the course was quite high, although the feedback information in the completed control loop comes only from the limit switches. It seems that the application of additional sensor would significantly improve the controlling process, which together with regulation of acceleration would faithfully reconstruct the general characteristics of walking. The developed prototype of the prosthesis provides such possibility, however it was limited to the application of 3 sensors for purpose of research examination. When a solution with active support of movement is concerned, a serious problem was the way of the power supply. In the case of the presented prototype the average current necessary for supplying the system (except the PC computer) equals 2,9 A. Despite the fact of using increasingly smaller and more efficient links and accumulators, the operating time of the system is several hours.

4 Conclusions

On the basis of the currently existing knowledge it is possible to prepare such system of the artificial lower limb which would possess movement functions similar to the functions of a real limb as regards kinematics. However, the feedback loop does not give a possibility to fully use the performing system due to the insufficient information from the artificial receptors. With the use of up-to-date types of prostheses

it is possible to practice sport, drive a car and even take part in competitive mountain climbing. However, their main drawback was the narrow specialization functions, as well as limited movement possibilities to the very narrow and predetermined purpose. It seems that the lack of movement universalism lies in the fact that even the best movement program was still a closed algorithm and performs only movements which had been previously programmed. So there was no possibility of learning. In the case of prostheses with mechanical control, the receptors constitute different kinds of sensors (angle, displacement etc.). As it turns out, the number of information gathered by these sensors were too small in comparison with the information gathered by the human body through the senses. It appears that this large amount of information that were coming from the external environment and powerful calculating system of the human brain was connected to the extended musculoskeletal system constitutes universalism of movement of the healthy limbs.

References

[1] Bober, T., Zawadzki, J.: Biomechanika układu ruchu człowieka, Katedra Biomechaniki AWF we Wrocławiu, wydanie II poprawione Wrocław (2003) ISBN: 83-910251-3-6
[2] Tejszerska, D., Świtoński, E.: Biomechanika inżynierska. Zagadnienia wybrane. Laboratorium. In: Wydawnictwo Politechniki Śląskiej, Wyd. I, Gliwice (2004)
[3] Jarząba, S., Pozowskiego, A.: Praca zbiorowa p.r., Rehabilitacja interdyscyplinarna, Wrocław (2009) ISBN:978-83-7055-560-3, ISBN: 83-7335-271-6
[4] The natural history of human gait and posture. Part 1. Spine and pelvis. C. Owen Lovejoy Department of Anthropology, Division of Biomedical Sciences, Matthew Ferrini Institute of Human Evolutionary Research, Kent State University, Kent, OH 44242, USA
[5] Kirkup, J.: A History of Limb Amputation, ISBN-13: 978-1-84628-443-4
[6] Vucina, A., Hudec, M.: Kinematic and Forces in the Above-Knee Prothesis During The Stairs Climbing, ISSN 1726-4529.
[7] http://moon.ouhsc.edu/dthompso/gait/knmatics/gait.htm
[8] http://www.ossur.com

Evaluation and Testing of Novel Ocular Tactile Tonometry Device

E.T. Enikov[1], P.P. Polyvás[1], R. Jančo[2], and M. Madarász[2]

[1] University of Arizona, Aerospace and Mechanical Engineering Department, 1130 N Mountain Ave, 85719, Tucson, Arizona
{enikov,polyvasp}@email.arizona.edu
[2] Slovak University of Technology in Bratislava, Faculty of Mechanical Engineering, Námestie slobody 17, 81231, Bratislava, Slovakia
roland.janco@stuba.sk, marcel.madarasz@gmail.com

Abstract. This article describes the experimental analysis of a novel trans-scleral tonometer based on the use of multiple force sensors forming a mechanical stiffness sensor. This approach is similar to an instrumented form of digital palpation tonometry in which manual palpation is used to conclude the stiffness, and hence, the intraocular pressure of the eye. Force data obtained from these probes correlate with the intraocular pressure (IOP) of the eye. Enucleated porcine eyes were used to validate the approach. A noticeable amount of hysteresis has been observed during indentations. Analysis of the experimental data indicates that stress relaxation in the visco-elastic corneo-scleral shell is the primary factor of the observed hysteresis. Further tests under different indentation rates show that the novel tonometer is expected to have an accuracy of ± 1mmHg when the indentation rate is kept below 0.5 mm/sec for pressure range of 10-35 mmHg.

1 Introduction

Tonometry is an eye pressure measurement that is most commonly performed on the cornea. Its objective is to determine the intraocular pressure of the eye and diagnose diseases such as glaucoma. The golden standard of tonometry is the Goldman applanation technique (GAT), where the cornea is flattened to a predetermined area. The applied force then is correlated with the intraocular pressure under the assumption that the cornea thickness and properties are known [1]. When applied to thicker corneas, the method can lead to pressure overestimation, while on thinner corneas or on corneas corrected with LASIK, the method can lead to underestimation [2, 3]. Further limitation of GAT is the fact that it cannot be self-administered at home, thus limiting the frequency at which GAT can be performed economically. Not surprisingly, a large number of alternative techniques and devices have been reported. These include portable versions of the GAT tonometers such as the Perkins and Draeger tonometers [4, 5], the MacKay-Marg tonometer (Tonopen) [6], a non-contact air-puff tonometer [7], and

T. Březina and R. Jabloński (eds.), *Mechatronics 2013*,
DOI: 10.1007/978-3-319-02294-9_107,

a rebound tonometer (I-Care) [8]. More recently, two trans-scleral tonometers have also been reported a rebound tonometer (Diaton), which uses a plunger rebounding from the sclera [9], and a trans-scleral indentation tonometer (Pro-View), which is based on measuring the force resulting in a pressure phosphene reaction [10].

The motivation behind this work is the evaluation of a novel trans-scleral tonometry concept akin to an old technique known as digital palpation tonometry (DPT) [11]. DPT is based on human tactile sensing and is performed by lightly pressing the fingertips of both index fingers onto the upper part of the eye through the eyelid. Typically, the two fingers are pressed in an alternating sequence, allowing the examiner to feel the flexibility of the sclera and gauge its tension. While very convenient, this method is subjective and, therefore, inaccurate. This paper reports on an experimental and numerical analysis of sensorized tactile tonometry applied through the sclera of enucleated porcine eyes.

1.1 Pressure Relaxation Analysis

To examine the cause of the pressure drop, static pressurization experiments were made. The eyeball was first pressurized to 10 mmHg, the perfusion system was closed to keep constant volume inside the eyeball. The initial pressure was adjusted by setting the height of the saline column to the appropriate level, while recording the pressure electronically with a pressure sensor connected to the saline column and placed at the level of the eye. The eye-pressure sensor branch was then closed to isolate the water column from the eye. Approximately 1-2 seconds later, the data collection was initiated.

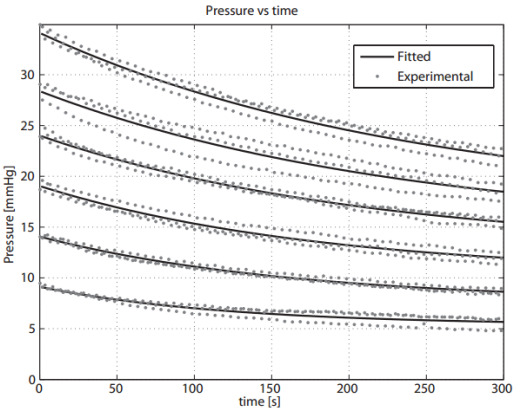

Fig. 1 IOP relaxation for different pressure levels

During this period, the eye started to relax leading to a small difference in the initial pressure level of each experiment.

After closing the system, its internal pressure was recorded for 300 seconds. The procedure was repeated three times at each pressure level from 10 to 35 mmHg in 5 mmHg increments. As is the case with other tissues, the relaxation rate depends on the stress level [11]. The results are shown on Figure 1. No significant difference between the relaxation functions of the three relaxation cycles was observed, which is uncommon for excised tissues. Making difference between leakage-induced pressure relaxation and structural relaxation is difficult without the ability to measure the leakage directly or prevent structural relaxation. To circumvent this problem, Brubaker encased enucleated eyes in a gypsum cast, allowing measurements of outflow under constant-volume conditions [5]. The results showed that when the sclera is prevented from stretching, only 3 μL of fluid are necessary to raise the pressure from 10 to 50 mmHg, compared to 21 μL required for similar pressurization of a freely expanding eye. The seven-fold increase in the required fluid volume is a clear indication that visco-elasticity of the corneo-scleral shell can be a significant contributing factor to the pressure relaxation. The data from Fig. 1 was analyzed with a first-order relaxation model

$$p(t) = p_{\infty} + (p_0 - p_{\infty})\exp(-t/\tau_e), \tag{1}$$

which allowed extraction of the parameters p_{∞}, p_0, τ_e for different starting pressures as shown in Table 1. An analytical model of the pressure relaxation due to fluid leakage only was also developed in order to interpret the experimental data. The model assumes slow deformation, i.e. the deformation due to visco-elastic relaxation of the sclera has already taken place. The elasticity of the corneo-scleral shell can be obtained from steady-state pressure-volume curves that exist for both human [12] and porcine eyes [13]. As is customarily done, a quadratic polynomial is fitted to the steady state p-V curve, which after differentiation produces the following relationship between the slope of the curve and the pressure

$$\frac{dp}{dV} = a + bp\,, \tag{2}$$

where a and b are positive constants. For enucleated porcine eyes without chemical post-treatment, this procedure yields a = 0:04 mmHg/μL and b = 0:0003μ L^{-1}.

Table 1 Relaxation parameters

p_0 ,*mmHg*	p_{∞} , *mmHg*	τ_e ,sec	$\bar{\tau}$,*sec*
9.1	5.3	122	5677
14.1	7.6	164	5808
19.1	10.3	181	5934
24.0	12.8	213	6052
28.4	14.6	235	6147
34.1	17.0	244	6264

During pressurization, some of the fluid escaped through the epi-scleral veins according to a flow rate law

$$Q = -\frac{p}{R_0(1+\eta p)}, \tag{3}$$

where R is the hydraulic resistance of the drainage system and η is the outflow obstruction coefficient [15]. For porcine eyes, R = 3.60 mmHg min/μL and η = .015 mmHg^{-1} [5]. Combining (2) and (3) into a fluid conservation law, one obtains

$$\dot{V} = \frac{dV}{dp}\dot{p} = \frac{\dot{p}}{a+bp} = -Q = -\frac{p}{R_0(1+\eta p)}, \tag{4}$$

Equation (4) can be re-written in a standard form as a non-linear ordinary differential equation for the intraocular pressure with a pressure dependent time constant, $\tau(p) = R_0(1+\eta p)/(a+bp)$

$$\frac{R_0(1+\eta p)}{a+bp}\dot{p} + p = 0, \tag{5}$$

It is easy to show that the solution of (5) is given by

$$\frac{p}{(a+bp)x} = \frac{p_0}{(a+bp_0)x}\exp\left(-\frac{a}{R_0}t\right) \tag{6}$$

where X = (b - $a\eta$)/b is a constant. Based on this solution, one can derive an expression for the average time constant of the response based on integration of $\tau(p)$ over the test pressure range

$$\bar{\tau} = \frac{1}{p_0 - p_\infty}\int_{p_0}^{p_\infty}\tau(p)dp = \frac{R_0\eta}{b}\left[1 - \frac{a\eta - b}{b\eta(p_0 - p_\infty)}\ln\frac{a+bp_0}{a+bp_\infty}\right] \tag{7}$$

Since $p_0 > p_\infty$, the time constant, $\bar{\tau}$ is monotonically increasing with increasing eye pressure when $\eta > b/a$ and monotonically decreasing when $\eta < b/a$. For the parameters used here, $\eta > b/a$, which agrees with the increasing trend observed in the experimental data for τ_e in Table 1.The large difference between the experimentally observed pressure relaxation time constants and the ones predicted on the basis of outflow indicates that leakage is not the likely cause of the observed pressure relaxation. Recent pull-tests on scleral strips obtained from monkey [9] and porcine [14] eyes yielded average relaxation time constants of 183

sec and 200 sec, respectively. Since no outflow is present in these studies, the relaxation time-constant is solely due to stress relaxation. The average time-constant over the pressure range used in the present study is 193 sec, which compares favorably with the aforementioned studies. It is therefore concluded, that the dominant relaxation process over the first 200-300 sec of the palpation experiment is primarily visco-elastic relaxation of the corneo-scleral shell.

1.2 Tonometer Concept

As illustrated in Fig. 2, four probes are attached rigidly to a single carrier. There is a probe in the center surrounded by three probes forming an equilateral triangle. During the measurement, all four probes move together and the reaction forces are recorded.

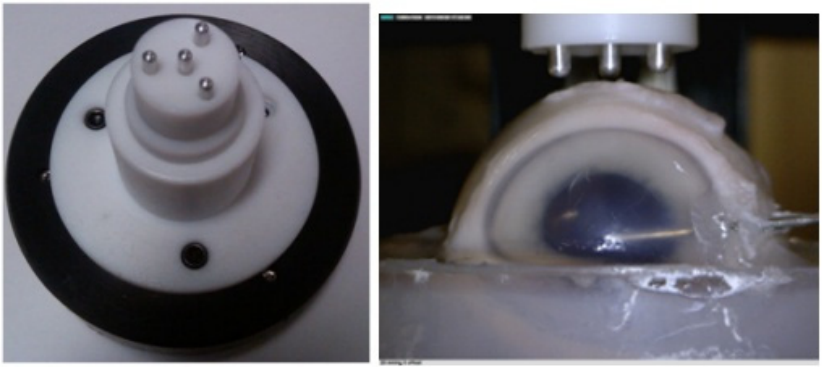

Fig. 2 Tactile tonometer prototype (left) applied on pressurized porcine eye (right)

1.3 Experimental Results of Testing Porcine Eyes

Enucleated porcine eyes (First Vision Tech, Mesquite, TX) were used in this study. The sacrificed pigs were of age 2-5 years old. After enucleation, the eyes were placed in a sealed plastic bag filled with saline solution and were shipped overnight on the day of slaughter in an ice filled box. The eyeballs were kept in laboratory refrigerator at 4 C and tested within 3-4 days postmortem. The experiments were performed at 22C ambient laboratory temperature. Agarose solution in water (30 g/l) was used to form the artificial eye socket. The globe was placed in a petri dish (55mm diameter, 15 mm depth) and the agarose solution was poured around the eye up to the brim of the dish. Depending on the size of the eye, approximately half of it was embedded in the socket. To align the eye with respect the probes, the embedded eye-dish assembly was mounted on a horizontal x-y translation stage. Multiple indentation sites were tested while comparing the initial non-zero readings of the three outer probes. The position resulting in the best agreement between these values (within 5 mN) was considered as the reference position for all subsequent measurements on that eye.

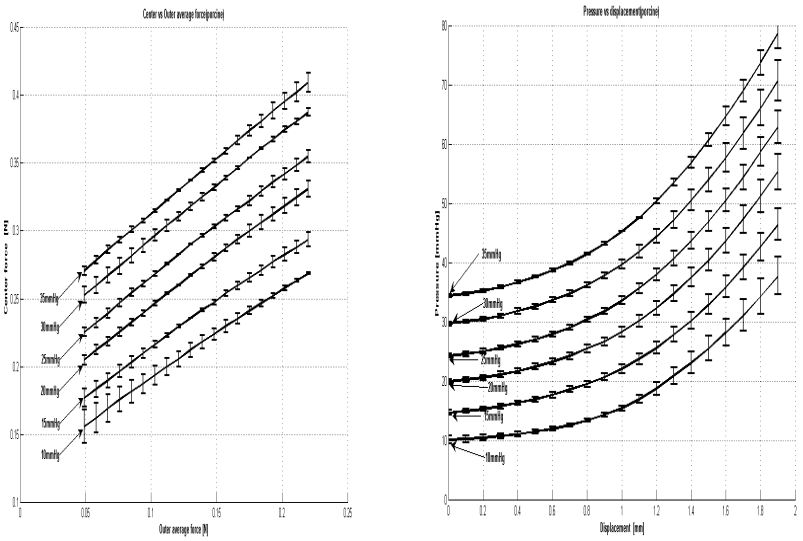

Fig. 3 Measured average force vs center force (left) pressure vs time (right)

The data shown in Fig.3. represents tests from 9 different eyes with the error bars representing the maxi-mum and minimum values from these measurements.

The horizontal axis of the figure represents the average force on the outer probes, while the vertical axis measures the force on the center probe. Because of the spherical shape of the eyeball, the central probe reaches the globe first and the outer probes touch the eye with a slight delay. This is the reason why, initially, only the force on the center probe increases, followed by contact and non-zero force measured by the second probe. The variation of IOP can be best seen by the location of the "knee" of the curves recorded by the central probe when the outer ring contacts the eye. The sensitivity can be adjusted by adjusting the offset between the central and outer probes. Based on these tests, it can be inferred that on average a force change of 10 mN corresponds to a change of 1 mmHg of IOP. To achieve an accuracy of ± 1 mmHg pressure, the force error measured by the central probe needs to be less than 20 mN.

2 Conclusions

A four-probe tonometer concept based on a concentric arrangement of the four force probes has been introduced. Applying the sensors to porcine eye pressurized at different levels showed that the force data alone can be used to infer the intraocular pressure in the eyes. Analysis of the pressure relaxation data showed that the measurement should be performed with indentation velocities below 0.5 mm/sec. The primary cause of the pressure relaxation has been attributed to the stress relaxation of the corneo-scleral shell.

The effects of lateral misalignment by approximately 1 mm in x- and z direction, and the effect of a 3-degree tilt were examined in previous studies. [16]

These effects resulted in approximately 20 mN of force error. Given that this force variation is equivalent to about 1 mmHg, to obtain this accuracy, the tonometer need to be positioned within ±1 mm of linear and ±3 degrees of the desired application position.

Fig. 4 Application mask

A further alternative could be an application through the eye lid, leading to the possibility of a trans-palpebral tonometery. One possible solution of such control is through the use of an anatomically contoured adapter mask that can provide control of the position and orientation of the sensor with respect to the face as illustrated in Fig. 4. The development and evaluation of such mask is beyond the scope of the present work.

Acknowledgement. This work was supported by a bilateral grant from the U.S.Dept. of Education (#P116J080016), the Atlantis program of the European Commission (2008-1767/001-001 CPT USMOBI), by NSF Grant# 1311851, by Grant Agency of APVV no. SK-CZ-0028-11and Grant Agency of VEGA no. 1/0627/13.

References

[1] Stodtmeister, R.: Applanation tonometry and cor-rection according to corneal thickness. Acta Ophthalmo-logica Scandinavica 76(3), 319–324 (1998)

[2] Bhan, A., Browning, A., Shah, S., Hamilton, R., Dave, D., Dua, H.: Effect of corneal thickness in intraocular pressure measurements with the pneumotonometer, goldmann applanation tonometer, and tono-pen. Investigative Ophthalmology & Visual Science 43, 1389–1392 (2002)

[3] Faucher, A., Gregoire, J., Blondeau, P.: Accuracy of goldmann tonometry after refractive surgery. Journal of Cataract and Refractive Surgery 23, 832–838 (1997)

[4] Wallace, J., Lowell, H.G.: Perkins hand-held applanation tonometer. a clinical evaluation. British Journal of Ophthalmology 52(7), 568–572 (1968)

[5] Pohjola, S., Niiranen, M.: Clinical evaluation of the draeger applanation tonometer. Acta Ophthalmologica 46(6), 1159–1164 (1968)
[6] Moses, R.A., Grodzki, W.J.: The macakymarg tonometer. Acta Ophthalmologica 49(5), 800–804 (1971)
[7] Evans, K., Wishart, P.K.: Intraocular pressure measurement in children using the keeler pulsair tonometer. Ophthalmic and Physiological Optics 12(3), 287–290 (1992)
[8] Fernandes, P., Daz-Rey, J.A., Queirs, A., Gonzalez-Meijome, J.M., Jorge, J.: Comparison of the i-care rebound tonometer with the goldmann tonometer in a normal population. Ophthalmic and Physiological Optics 25(5), 436–440 (2005)
[9] Doherty, M.D., Carrim, Z.I., O'Neill, D.P.: Diaton tonometry: an assessment of validity and prefer-ence against goldmann tonometry. Clinical & Experimen-tal Ophthalmology (2011)
[10] Herse, P., Hans, A., Hall, J., Langejans, J., Markoulli, M.: The proview eye pressure monitor: influence of clinical factors on accuracy and agreement with the goldmann tonometer. Ophthalmic and Physiological Optics 25(5), 416–420 (2005)
[11] Institution Acta Ophthalmologica Scandinavica: Chapter 1: Historical Review. Acta Ophthalmologica 40(S69), 7–15 (1962)
[12] Liu, J., He, X.: Mathematical model of the conreo-scleral shell as applied to intraocular pressure-volume relations and applanation tonometery. Annals of Biomedical Engineering 1, 87–98 (1972)
[13] Liu, J., He, X.: Corneal stiffness affects iop elevation during rapid volume change in the eye. Investigative Ophthalmology & Visual Science 50(5), 2224–2229 (2009)
[14] Mortazavi, A.M., Simon, B.R., Stamer, W.D., Geest, J.P.V.: Drained secant modulus for himan and porcine peripapillary sclera using uncon ned compression testing. Experimental Eye Research 89, 892–897 (2009)
[15] Nihard, P.: Influence de la pression oculaire sur la resistance a l'ecoulement de l'humeur aquese. Acta Ophthalmologica 40, 12–27 (1962)
[16] Polyvas, P., Madarasz, M., Enikov, E.: Development of Tactile Eye Stiffness Sensor. Journal of Experimental Mechanics 53(5), 819–828 (2013), doi:10.1007/s11340-012-9682-5
[17] Polyvás, P.P., Peyman, G., Enikov, E.: Trans-scleral tactile tonometry: An instrumented approach. Medical Engineering and Physics 35, 937–943 (2013)
[18] Magdolen, Ľ., Masaryk, M.: Flywheel storage energy. In: Proceedings of the Eight International Conference on Mechanical Engineering: Gépészet, Budapest, Hungaria, May 24-25, pp. 296–300. Budapest Univeristy of Technology and Economics, Budapest (2012) ISBN 978-963-313-055-1
[19] Danko, J., Bugár, M., Staňák, V.: Energy analysis of hybrid power source during vehicle motion. In: Scientific Proceedings Faculty of Mechanical Engineering STU Bratislava, vol. 19, pp. 37–42 (2011) ISSN 1338-1954. - ISSN 1338-5011 (ONLINE)

Calculation of the Bio-ceramic Material Parameters

V. Fuis and P. Janicek

Centre of Mechatronics – Institute of Thermomechanics AS CR and
Brno University of Technology, Faculty of Mechanical Engineering, Technicka 2,
616 69, Brno, Czech Republic
{fuis,janicek}@fme.vutbr.cz

Abstract. The paper deals with calculation of the parameters of bio-ceramic material from a set of destruction tests of whole ceramic heads of total hip joint endoprosthesis. This approach is suitable in the case if it not possible to cut out the specimens from the ceramic heads, because the heads are too small. From the measured values of circumferential strains of the head's external spherical surface under destruction, the state of stress in the head under destruction was established using the FEM. From the values obtained, the sought for parameters of the ceramic material were calculated using Weibull's weakest-link theory.

1 Introduction

Centre of Mechatronics solves the clinical biomechanical problems for a long time [17 - 19]. A problem that is being solved now is the destruction of the ceramic heads of total hip joint endoprostheses in vivo, that had occurred in a series of Czech hospitals [2], [4] (Fig. 1). The ceramic heads [15, 16] are made of Al_2O_3 and put on conical stem made of austenitic steel [9]. The reliability of the ceramic component is based on Weibull weakest-link theory [1] and the failure probability depends on three Weibull's parameters [3]. These parameters are obtained from the statistical analysis of the set of the destructed specimens which are subjected to 3- or 4- point bending [7].

For computational modelling of failure probability, two computation models are used which differ from each other in that which stresses are included into the computation. The first more simple model includes into the computation only the first principal stress - σ_1 (see relation (1)), whereas the second model includes into the computation all three principal stresses [10]. This model is suitable for cases where the second and the third principal stress take marked tensile values nearing to the values of the first principal stress [4], [14]. In case of a ceramic head of total hip joint endoprosthesis, the probability of its failure can be computed using a more simple model, since the maximum values of the second principal stress take at most 30 % of the value of the first principal stress in the head [8], [11], [13].

T. Březina and R. Jabloński (eds.), *Mechatronics 2013*,
DOI: 10.1007/978-3-319-02294-9_108,

For computation of the ceramic head failure probability, the following relation is used, that is based on Weibull's weakest-link theory [3]:

$$P_f = 1 - e^{-\sum_{i=1}^{n}\left(\frac{\sigma_i - \sigma_u}{\sigma_o}\right)^m \Delta V_i}, \qquad \sigma_i \geq \sigma_u, \tag{1}$$

where : n – number of elements into which the analysed head is divided, using the finite elements method, ΔV_i – volume of the i-th element, σ_i – first principal stress (σ_1) acting in volume ΔV_i, σ_u- stress, beneath the value of which material failure does not occur, σ_o – normalised material strength of a volume unit of material, *m* - Weibull modulus (connected with the scatter of measured values). These parameters are derived from processing the destruction forces obtained from a set of 3- or 4- point bending tests [5]. This way of assessing material parameters is universally applicable to any ceramic product, from which specimens are made for the mentioned bending test. The number of specimens must exceed 35, if the Weibull statistical method of the weakest link is at all to be applied. Small components present another problem which applies also to ceramic heads, namely that the cut out specimens are too small. Small specimens can be subjected only to 3-point bending, at which maximum tensile stress is concentrated only in a small area in the middle of the specimen, in contrast to 4-point bending at which maximum tensile stresses concentrate in two areas between two supports. The material characteristics obtained from 4-point bending tests show a greater plausibility than those from 3-point bending tests; therefore 4-point bending test is to be preferred.

Fig. 1 In vivo destructed ceramic heads

2 Experimental Destructions

For carrying out the destruction of a set of ceramic heads a special testing jig has been made in which the heads are subjected to compressive load that acts only on the surface of the head's opening, as shown in Fig. 2. In the course of the test, circumferential strains are measured on the head's external surface.

The compression load acting on the head was developed by the testing device ZWICK Z 020-TND whose head loaded the jig's piston which, in turn, acted on rubber NBR 90 inside the jig, which, subsequently, acted on the ceramic head.

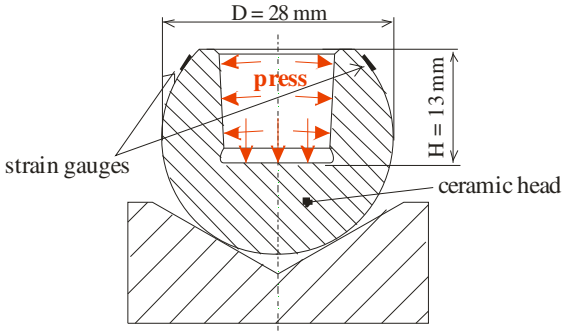

Fig. 2 Scheme of the head's loading

The result of experiments was a set of the strain values established under the destruction of the individual heads – Fig. 3.

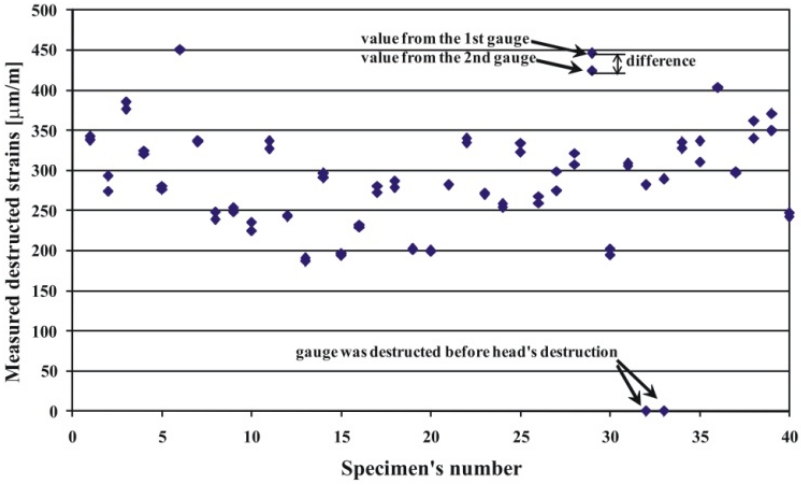

Fig. 3 Circumferential strain values under the heads' destructions

3 Calculation of the Bio-material Parameters

In the first phase, from the strains established under the heads' destruction, the stress field produced by the destruction had to be defined. To this purpose, computational modelling (FEM method) was used and the Table 1 shows the maximum tensile stress in each head under the destruction. Each j-th destructed head is assigned the probability of its failure, e.g. from the relation $P_f(j) = j/(r+1)$, where j is the serial number of the arranged head and r is the total number of destructed heads, in our case r = 40.

Table 1 Maximum destruction stress in the heads arranged in descending order

j	$\sigma_{1max\text{-}dest}$ [MPa]	P_f	*j*	$\sigma_{1max\text{-}dest}$ [MPa]	P_f
1	208.4	0.024	21	314.8	0.512
2	216.4	0.049	22	322.8	0.537
3	217.1	0.073	23	324.5	0.561
4	221.8	0.098	24	330.5	0.585
5	224.5	0.122	25	340.8	0.610
6	250.8	0.146	26	343.0	0.634
7	255.6	0.171	27	346.2	0.659
8	266.6	0.195	28	357.2	0.683
9	270.4	0.220	29	360.1	0.707
10	270.6	0.244	30	364.7	0.732
11	277.2	0.268	31	365.2	0.756
12	283.6	0.293	32	371.2	0.780
13	289.1	0.317	33	374.5	0.805
14	301.3	0.341	34	377.1	0.829
15	303.9	0.366	35	379.3	0.854
16	305.5	0.390	36	390.2	0.878
17	306.4	0.415	37	420.1	0.902
18	307.7	0.439	38	449.3	0.927
19	311.1	0.463	39	473.4	0.951
20	314.4	0.488	40	501.7	0.976

The first of Weibull parameters is stress σ_u, which must be lower than the minimum value $\sigma_{1max\text{-}dest}$. In this paper the conservative approach is considered and $\sigma_u = 0$ MPa, then all tensile stresses influence the body's destruction.

The second parameter (Weibull modulus m) is connected with the dispersion of experimentally established values and it is determined as gradient of a line interlaid with experimentally established data from the Table 1. Weibull modulus for $\sigma_u = 0$ MPa is shown in the Fig. 4 and its value is ***m = 5.3058***.

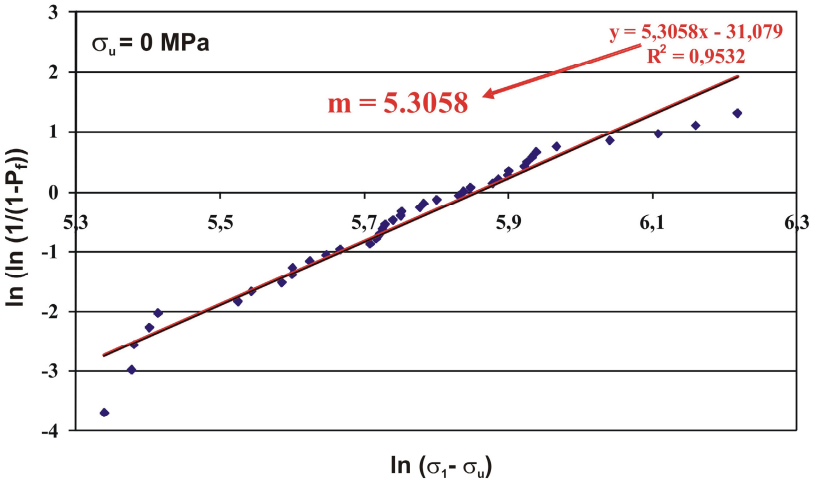

Fig. 4 Weibull plot of the normalized modulus of rupture data

The last of the parameters (normalised volume strength σ_o) is calculated from the following equation:

$$\sigma_o = \sqrt[m]{\sum_{i=1}^{n}(\sigma_i - \sigma_u)^m \Delta V_i}\,,\ \sigma_i \geq \sigma_u \tag{2}$$

which was derived by modification of the equation (1) for $P_f = 1\text{-}1/e = 0.63212$ (failure probability for the experimental data and for the material parameters will be the same – 0.63212 – see fitted point in Fig. 5). The value of the last material parameter σ_o is 583.7 MPa m $^{3/5.3058}$.

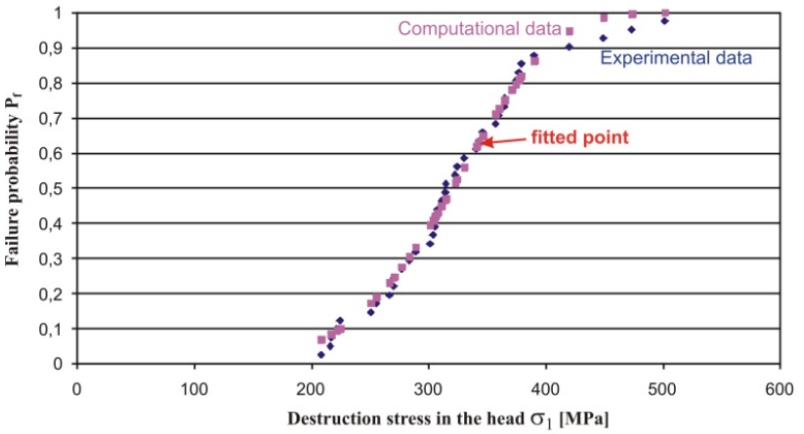

Fig. 5 Comparison of the experimental and computational data for 2-parameter Weibull material model

From the comparison of the experimental and computational data in Fig. 5 implies the following result: 2-parameter Weibull material parameters well fit the experimental data in the region P_f between 10% and 90%. For the low values of the failure probability ($P_f < 10\%$) difference the difference between experimental and computational data is large (the bioimplants have to reach the very low failure probability so this model have to be improved – for example fitting point will be moved from $P_f = 0.63212$ to value 0.024 (the first sample in the Table 1)).

4 Conclusion

The material parameters of ceramic material used for manufacture of heads of total hip joint endoprosthesis have been determined on the basis of a set of head destruction tests. The analysis of the calculated material parameters shows the possibility to use this approach to calculation of the material parameters of the bio-ceramic with the Weibull distribution of the strength.

The reliability of the parameters thus obtained is higher than those obtained from specimens cut out from the heads, because their dimensions are markedly smaller than those required by the standard. The presented approach is general and applicable to any brittle material whose strength characteristics exhibit Weibull probability distribution.

Acknowledgments. The research has been supported by the project of the Czech Science Foundation GA CR nr. 13-34632S – Increasing the level of computational modeling of the behavior of the ceramic head for total hip joint endoprosthesis.

References

[1] Basu, B., Tiwari, D., Kundu, D., Prasad, R.: Is distribution the most appropriate statistical strength distribution for brittle materials? Ceramics International 35(1), 237–246 (2009)

[2] Fuis, V., Janicek, P.: Stress and reliability analyses of damaged ceramic femoral heads. In: Proc. Conference on Damage and Fracture Mechanics, Structures and Materials, vol. 12, pp. 475–485 (2002)

[3] Bush, D.: Designing Ceramic Components for Structural Applications. J. Mater. Eng. Perf. ASM Int. 2, 851–862 (1993)

[4] Fuis, V., Koukal, M., Florian, Z.: Shape Deviations of the Contact Areas of the Total Hip Replacement. In: Proc. 9th International Conference on Mechatronics, Mechatronics: Recent Technological and Scientific Advances, pp. 203–212 (2011)

[5] McLean, A.F., Hartsock, D.L.: Engineered materials handbook, Ceramics and Glasses, vol. 4, pp. 676–689. ASM International (1991)

[6] Fuis, V., Malek, M., Janicek, P.: Probability of destruction of Ceramics using Weibull's Theory. In: Proc. 17th International Conference on Engineering Mechanics, pp. 155–158 (2011)

[7] Fok, S.L., Smart, J.: The Accuracy of Failure Predictions Based on Weibull Statistics. Journal of the European Ceramic Society 15, 905–908 (1995)

[8] Fuis, V., Janicek, P., Houfek, L.: Stress and Reliability Analyses of the Hip Joint Endoprosthesis Ceramic Head with Macro and Micro Shape Deviations. In: IFMBE Proceedings of 13th International Conf. on Biomedical Engineering, vol. 23(1-3), pp. 1580–1583 (2008)
[9] Fuis, V.: Tensile Stress Analysis of the Ceramic Head with Micro and Macro Shape Deviations of the Contact Areas, Recent Advances in Mechatronics: 2008-2009. In: Proc. International Conference on Mechatronics, pp. 425–430 (2009)
[10] Fetta, T., Ernsta, E., Munza, et al.: Weibull analysis of ceramics under high stress gradients. Journal of the European Ceramic Society 23, 2031–2037 (2003)
[11] Fuis, V.: Stress and reliability analyses of ceramic femoral heads with 3D manufacturing inaccuracies. In: Proc. 11th World Congress in Mechanism and Machine Science, pp. 2197–2201 (2004)
[12] Jiang, R., Murthy, D.N.P.: A study of Weibull shape parameter: Properties and significance. Reliability Engineering and System Safety 96, 1619–1626 (2011)
[13] Fuis, V., Navrat, T., Hlavon, P., et al.: Reliability of the Ceramic Head of the Total Hip Joint Endoprosthesis Using Weibull's Weakest-link Theory. In: IFMBE Proc. World Congress on Medical Physics and Biomedical Engineering, vol. 14, pp. 2941–2944 (2006)
[14] Hudak, D., Tiryakioglu, M.: On comparing the shape parameters of two Weibull distributions. Materials Science and Engineering A 528, 8028–8030 (2011)
[15] Vrbka, M., Navrat, T., Krupka, I., et al.: Study of film formation in bovine serum lubricated contacts under rolling/sliding conditions. Proc. of the Institution of Mechanical Engineers Part J-Journal of Engineering Tribology 228, 1–17 (2013)
[16] Vrbka, M., Krupka, I., Svoboda, P., et al.: Effect of shot peening on rolling contact fatigue and lubricant film thickness within mixed lubricated non-conformal rolling/sliding contacts. Tribology International 44(12), 1726–1735 (2011)
[17] Cizmar, I., Florian, Z., Navrat, T., et al.: A Biomechanical Study of a Suture between the Deltoid Muscle and a Free Tendon Graft for Reconstruction of the Elbow Extension. Biomedical Papers-Olomouc 155, 79–83 (2011)
[18] Fuis, V., Varga, J.: Stress Analyses of the Hip Joint Endoprosthesis Ceramic Head with Different Shapes of the Cone Opening. In: Proc. 13th International Conf. on Biomedical Engineering, IFMBE Proceedings, vol. 23(1-3), pp. 2012–2015 (2008)
[19] Janu, I., Kocis, J., Navrat, T., et al.: A Comparative Analysis of Socon CS and Socon Pedicle Screws in View of their Use for Treatment of Osteoporotic Fractures of the Thora-columbal Spine. A Biomechanical Study. Acta Chirurgiae Orthopaedicae et Traumatologiae Cechoslovaca 78(4), 334–338 (2011)

Effect of Contact Condition on Film Thickness Formation in Artificial Joints

T. Návrat[1], M. Vrbka[1,3], J. Laštůvka[1], I. Křupka[1,3], M. Hartl[1], and J. Gallo[2]

[1] Brno University of Technology, Faculty of Mechanical Engineering, Technická 2896/2, 616 69, Brno, Czech Republic
{navrat,vrbka.m,krupka,hartl}@fme.vutbr.cz
[2] University Hospital Olomouc, I.P. Pavlova 6, 775 20 Olomouc, Czech Republic
jiri.gallo@fnol.cz
[3] CEITEC - Central European Institute of Technology, Brno University of Technology, Komenského nám. 2, 602 00 Brno, Czech Republic

Abstract. Total hip replacement is the most effective method for treating severe degenerative, post-traumatic and other diseases of the hip joint. Nevertheless wear of artificial implants remains a serious health issue especially for metal-on-metal hip components where the formation of metallic wear debris has been linked to adverse tissue necrosis and increased of metal ions in the blood. Wear in MOM joints is essentially dependent on interfacial lubrication processes, which are subjected to the complex research work at the present time. The aim of this study is to analyze formation of lubrication film and experimental mapping of the lubricating film thickness of bovine serum within the contact between an artificial metal or ceramic femoral head and a glass disc and analyze effect of proteins on the film formation under rolling/sliding conditions. The film thickness was studied experimentally using film colorimetric interferometry. This study showed that protein formation plays an important role in the lubrication processes of artificial joints of the human. Due to challenging of this study the more complex research work is carried out at the present time.

1 Introduction

Total hip arthoplasty (THA) is the most effective method for treating severe degenerative, post-traumatic and other diseases of the hip joint. It is estimated that more than 1,000,000 THAs are performed each year globally. More importantly, modelled future projections expect further increase in the need for THAs [1]. The main reason for late failure of THA is aseptic loosening [2] followed by instability of the THA that compromises predominantly the early postoperative period [3].

Wear is influenced by the articulating surfaces and not only the biomaterials [4, 5], hence the wear rate could be reduced by the tribological parameters modification. Among these the key one is the lubrication regime having direct influence on

T. Březina and R. Jabloński (eds.), *Mechatronics 2013*,
DOI: 10.1007/978-3-319-02294-9_109,

the friction coefficient. Bovine serum (BS) is used nowadays as a model synovial fluid lubricant for modelling the wear and friction properties of artificial joints. The artificial joint articulation is simulated using simple ball-on-disc configuration of the artificial (metal or ceramic) femoral head [6] and a glass disc.

This paper should contribute to amend of research findings presented in the current studies that are mainly focused on experimental analyses of central film thickness in the contact zone. That is why the aim of this study is to perform detail experimental mapping of lubricating film thickness of BS within a whole contact zone between artificial metal or ceramic femoral head and glass disc and analyzed effect of proteins on film formation.

2 Methods

Mapping of lubricating film of several BS concentrations was observed using an optical test rig in which a circular contact is formed between a glass disc and a metal or ceramic head of total hip joint replacement. BS (Sigma-Aldrich B9433, protein concentration 75.3 mg/ml) and sterile water were used for preparing samples with appropriate w/w concentrations.

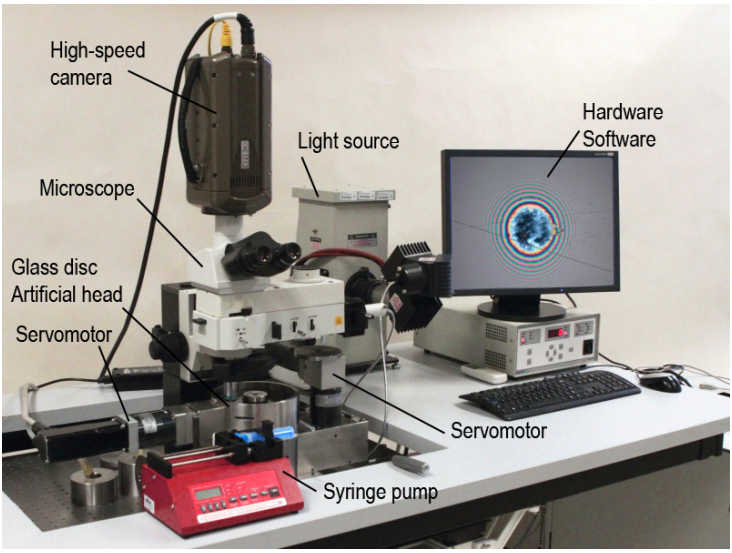

Fig. 1 Optical test rig for lubricant film thickness measurements

Mapping of lubricating film of BS solution was observed using an optical test rig (Fig. 1) in which a circular contact is formed between a glass disc and a metal head of total hip joint replacement (Fig. 2). The artificial heads were rotated by servomotor against the disc to provide pure rolling and sliding conditions.

The tests were performed under a steady state load of 5 N, which corresponds to mean Hertzian pressure of 180 MPa. All components in contact with BS were cleaned carefully before each test. The duration of the one test was 300 seconds, while for the first 180 seconds the BS was supplied using a syringe attached to a linear motor to maintain constant volume rate and a needle clamp. Experiments were realized at room temperature of 24 °C under steady state load of 5 N corresponding to mean Hertzian pressure of 180 MPa for metal head. The contact formed between the glass disc and the artificial heads was illuminated by xenon or halogen lamp. Obtained chromatic interferograms were recorded with a high-speed digital camera (CMOS or 3CCD) and evaluated with thin film colorimetric interferometry. Detailed description of this technique is given in [8, 9]. The chromatic interferograms were taken at 24 Hz sample rate and 800x600 pixels resolution.

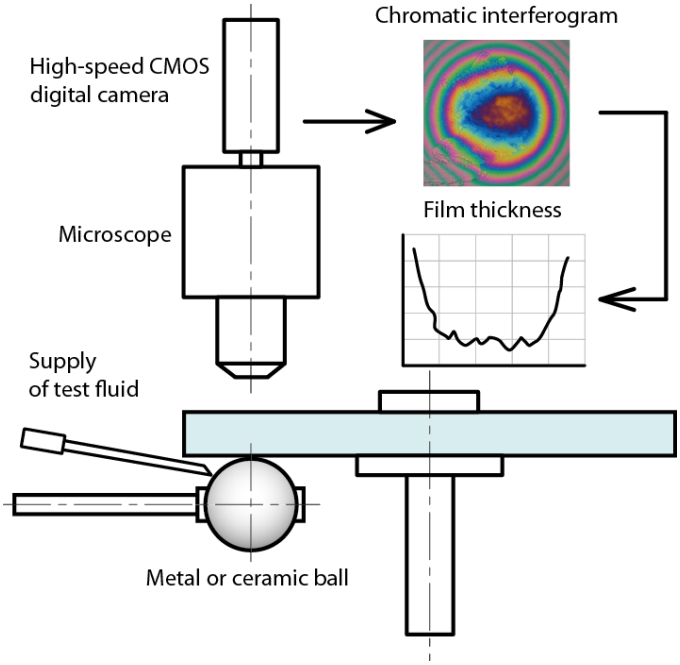

Fig. 2 Schematic diagram of film thickness mapping

3 Results and Discussion

The film thickness was studied as a function of time for the three different kinematic conditions. During the tests, the BS was passing through the contact zone, and 21 interferograms were selected and evaluated. For every interferogram, the

average film thickness value in the central area was plotted in a graph to show the time progress. The graphs describing the development of the film for the tests are shown in Figs. 3 and 4. The time-thickness diagrams show the formation of lubricating film over a period of 300 seconds for different slide-to-roll ratio conditions.

The first case of pure rolling (Fig. 3) shows a steadily increasing lubricating film which reaches a thickness of 23 nm at the end of the measurement. The thickness distribution in the contact zone is uniform and does not show any noticeable signs of protein aggregations. This shows that only the base film contributes to the total film thickness.

The second case of (slide-to-roll ratio is -1.5, the head is faster than the disc) shows formation of thin lubricating film, with thickness about 2 to 4 nm during the whole measurement, only seldom increased by small protein aggregations of thickness about 10 nm.

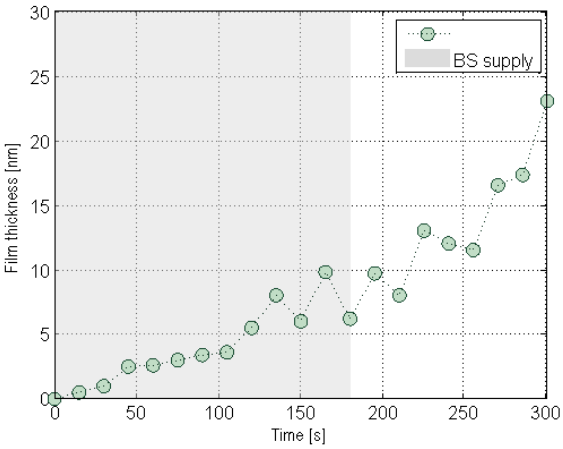

Fig. 3 Central film thicknesses plotted as a function of time for slide-to-roll ratio 0

The last case of (slide-to-roll ratio is 1.5, the disc is faster than the ball, Fig. 4) shows different behavior, as we can see a formation of thicker aggregated protein regions passing through the thinner base film. The thicker protein film reaches thickness of 60 to 120 nm, whereas the base film varies slightly with thickness of 4 to 20 nm. The interferograms show large areas of aggregated proteins over the thin base film running through the contact zone without any significant time dependence. The results obtained from this test are in agreement with those of Myant et al. [7], who presented that BS film thickness increases for the test and also supported the idea of inlet protein aggregation and forming of a much thicker lubricating film than expected.

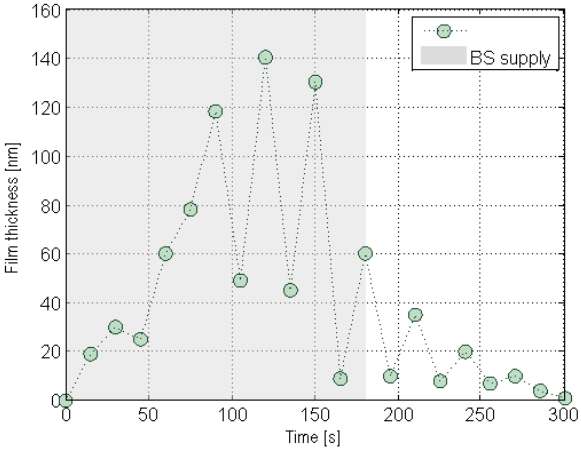

Fig. 4 Central film thicknesses plotted as a function of time for slide-to-roll ratio 1.5

4 Conclusions

Film formation between the artificial metal femoral head and the glass disc was observed using BS as a lubricant. Film thickness measurements were performed as a function of time under pure rolling and rolling/sliding conditions. It is obvious from performed experiments that formation of lubricant film thickness is markedly dependent on the kinematic conditions acting in the contact. Due to this fact, a more complex program of experiments is to be carried out in the near future, to describe the film formation in ceramic head contact for the same slide-to-roll conditions and also to study the effect of temperature and different slide-to-roll conditions.

Acknowledgments. The present work has been supported by European Regional Development Fund in the framework of the research project NETME Centre under the Operational Programme Research and Development for Innovation. Reg. Nr. CZ.1.05/2.1.00/01.0002, id code: ED0002/01/01, project name: NETME Centre –New Technologies for Mechanical Engineering.

References

[1] Kurtz, S.M., Ong, K.L., Schmier, J., Mowat, F., Saleh, K., Dybvik, E., et al.: Future Clinical and Economic Impact of Revision Total Hip and Knee Arthroplasty. The Journal of Bone & Joint Surgery 89, 144–151 (2007)

[2] Fuis, V., Koukal, M., Florian, Z.: Shape Deviations of the Contact Areas of the Total Hip Replacement. In: Proc. 9th International Conference on Mechatronics, pp. 203–212 (2011)

[3] Corbett, K.L., Losina, E., Nti, A.A., Prokopetz, J.J.Z., Katz, J.N.: Population-Based Rates of Revision of Primary Total Hip Arthroplasty: A Systematic Review. PLoS ONE 5(1-8), e13520 (2010)

[4] Fuis, V., Malek, M., Janicek, P.: Probability of destruction of Ceramics using Weibull's Theory. In: Proc. 17th International Conference on Engineering Mechanics, pp. 155–158 (2011)
[5] Fuis, V.: Stress and reliability analyses of ceramic femoral heads with 3D manufacturing inaccuracies. In: Proc. 11th World Congress in Mechanism and Machine Science, pp. 2197–2201 (2004)
[6] Fuis, V., Navrat, T., Hlavon, P., et al.: Reliability of the Ceramic Head of the Total Hip Joint Endoprosthesis Using Weibull's Weakest-link Theory. In: IFMBE Proc. of World Congress on Medical Physics and Biomedical Engineering, vol. 14, pp. 2941–2944 (2006)
[7] Myant, C., Underwood, R., Fan, J., Cann, P.M.: The effect of protein content and load on film formation and wear. Journal of the Mechanical Behavior of Biomedical Materials 6, 30–40 (2002)
[8] Hartl, M., Křupka, I., Poliščuk, R., Liška, M.: An automatic system for real-time evaluation of EHD film thickness and shape based on the colorimetric interferometry. Tribol. T. 42, 303–309 (1999)
[9] Hartl, M., Krupka, I., Poliscuk, R., Liska, M., Molimard, J., Querry, M., Vergne, P.: Thin film colorimetric interferometry. Tribol. T. 44, 270–276 (2001)

Model Based Design of a Self-balancing Vehicle: A Mechatronic System Design Case Study

R. Grepl

MechLab, Brno University of Technology, Faculty of Mechanical Engineering,
Technicka 2, 616 69, Brno, Czech Republic
grepl@fme.vutbr.cz
www.mechlab.cz

Abstract. The design and control of a self-balancing vehicle is an ideal case study for the teaching of mechatronics. It is a challenging topic that attracts the students' attention and increases their motivation. It includes several topics of highly practical importance such as modelling, system identification, filtering of the measured signal, implementing the embedded system or tuning of the PID or the LQR/LQG controller. After the theoretical introduction and simulation students can easily build the robot and program it with the automatically generated code, literally in a few hours, using widely available LEGO NXT Mindstorms. Model based design (MBD) offers an interesting framework for such a complex project. This paper focuses on the parameter estimation of a nonlinear analytical model and on the implementation of fault management. The published results are based on our experiences with the designing and use of our own laboratory experimental vehicle.

1 Introduction

The design and control of an unstable balancing vehicle or robot is very popular among researchers and educators [1,2,9] due to the following reasons: a) It is considered as an interesting and attractive problem which significantly increases the motivation of the students; b) It is a naturally unstable system thus control is a challenge and it can also be used as a good example of enabling technology; c) There are several usable approaches leading to functioning control: from hand tuned PID to the LQG; d) Several signal processing techniques can be used for the tilt angle estimation, from the gyro integration through the Complementary filter to the Kalman filter.

This paper deals with our own experiences with the design and operation of balancing vehicle at the MechLab (Mechatronics Laboratory), FME, BUT. The focus is set on the Model Based Design (MBD) approach and the educational significance of its application. Also, the contribution of this paper includes the description of the step-by-step procedure for the plant parameter estimation based on several simplifications of the complete nonlinear model and the corresponding experimental setups. Furthermore, the implementation of Fault Management in the Simulink environment is shown.

T. Březina and R. Jabloński (eds.), *Mechatronics 2013*,
DOI: 10.1007/978-3-319-02294-9_110,

Two educational platforms are used for the demonstration of the aspects mentioned above: 1) LEGO Mindstorms NXT 2 based robot; 2) The Keywatko III. experimental balancing vehicle, aka Hummer, developed at MechLab [5,6,13,14] shown in Fig. 1.

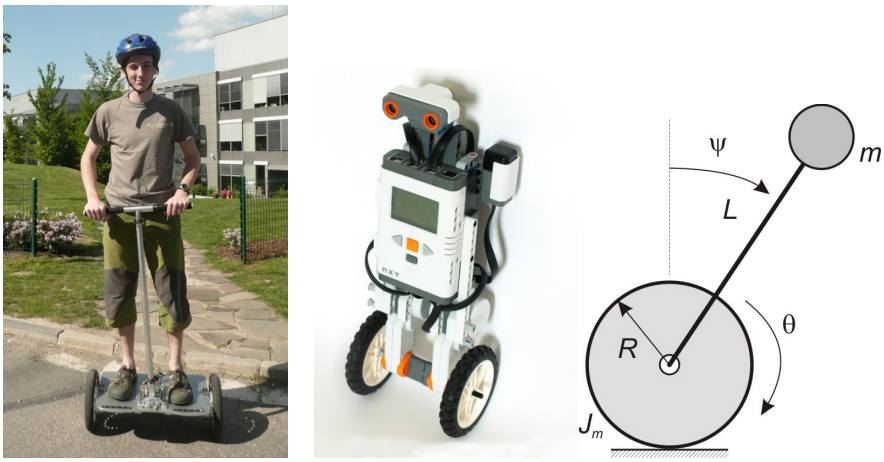

Fig. 1 The balancing vehicle developed at MechLab, Brno University of Technology (left); Educational balancing robot built using LEGO Mindstorms NXT 2.0 (middle); Schematics of balancing vehicle/robot (right)

The MBD is the methodology applied in designing the embedded software. Usually, the following main phases are distinguished: 1) Plant modelling, 2) Controller design, 3) Offline simulations, 4) Real-time simulations (RCP,SIL,PIL,HIL) and 5) Deployment. For more information about MBD in mechatronics, see e.g. [7].

2 Modelling and Parameter Estimation

The model of the vehicle dynamics can be found in many references such as [2,9]. However, the description of the identification experiment is usually omitted despite the fact that it is very important from the practical point of view and also very interesting from the pedagogical perspective.

Because the plant is naturally unstable, special attention should be paid to the arrangement of the experiment. What is shown further in this paper is how one can estimate individual parameters step by step using different (stable and open loop) data measurements before approaching the estimation of the whole eq.(1).

Firstly the complete nonlinear model is presented, which allows preparing experiments with the operating point far from the linearization used later for the control.

Due to the fact that control is usually designed separately for the balancing and the turning of the vehicle, the equations for balancing are presented only. Assuming the ψ is the absolute tilt angle, the θ is the rolling of the wheel, the other parameters according to Fig. 1 and the DC motor modelled as static system, one can obtain the following motion equations of the system:

$$\mathbf{M}\begin{bmatrix}\ddot{\psi}\\ \ddot{\theta}\end{bmatrix}+\begin{bmatrix}-mgL\sin\psi\\ -mLR\dot{\psi}^2\sin\psi\end{bmatrix}+\mathbf{B}\begin{bmatrix}\dot{\psi}\\ \dot{\theta}\end{bmatrix}+\begin{bmatrix}-T\text{sign}(\dot{\theta}-\dot{\psi})\\ T\text{sign}(\dot{\theta}-\dot{\psi})+T_{ROL}\text{sign}(\dot{\theta})\end{bmatrix}=c_{MOT}\begin{bmatrix}-1\\ 1\end{bmatrix}u$$
$$\mathbf{M}=\begin{bmatrix}mL^2 & mLR\cos\psi\\ mLR\cos\psi & mR^2+J_m\end{bmatrix},\quad \mathbf{B}=\begin{bmatrix}b^* & -b^*\\ -b^* & b^*+b_{ROL}\end{bmatrix} \tag{1}$$

where b is the viscous damping, T is dry friction and c_{MOT} is the constant derived from the static model of the DC motor.

Most of the parameters above are difficult to measure or calculate. The m and L could be inaccurate due to model simplification, b and T are impossible to measure at all. Therefore, the data measured on a real system must be used to fit the assumed model (1). In this section, the sequence of experiments is described which allows a step by step estimate of some parameters.

Experiment nr. 1: Free Wheel Rotation and Drive on Flat Ground

Assuming $\psi = const.;\dot{\psi},\ddot{\psi}=0$ and no load is applied to the wheels, the following equation describes the system motion:

$$J_m\ddot{\theta}+b^*\dot{\theta}+T\text{sign}(\dot{\theta})=c_{MOT}u \tag{2}$$

Similarly, if the vehicle is driven on a flat surface (using the supporting wheel shown in Fig. 2), one can get the equation of this form:

$$(mR^2+J_m)\ddot{\theta}+(b^*+b_{ROL})\dot{\theta}+(T+T_{ROL})\text{sign}(\dot{\theta})=c_{MOT}u \tag{3}$$

Formally, these two experimental setups lead to the same equation with three parameters to be obtained:

$$p_1\ddot{\theta}+p_2\dot{\theta}+p_3\text{sign}(\dot{\theta})=u \tag{4}$$

It is understandable that only e.g. the ratio $p_1=(mR^2+J_m)/c_{MOT}$ can be estimated from the data.

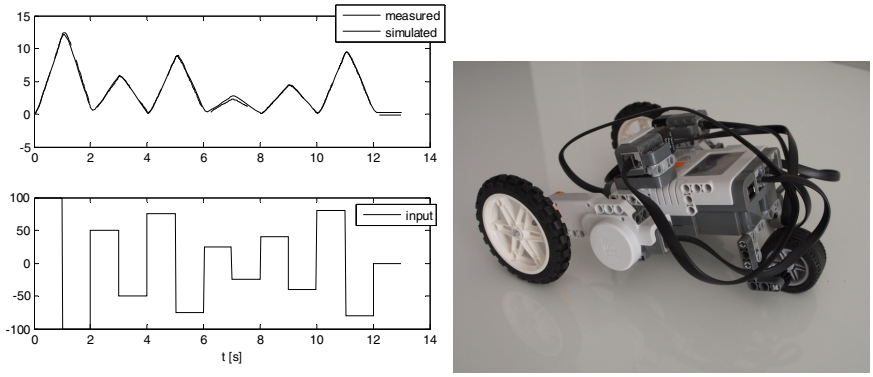

Fig. 2 Experiment "Ride on the flat ground": Comparison of measured position and simulation with estimated parameters (left); photo of the real system (right)

Experiment nr. 2: Drive on an Inclined Surface

Assuming $\psi = const.; \dot{\psi}, \ddot{\psi} = 0$ and driving up the hill is shown in Fig. 3, the equation of motion changes into the form of

$$p_1\ddot{\theta} + p_2\dot{\theta} + p_3 \text{sign}(\dot{\theta}) = u - \frac{mgR\sin(\alpha)}{c_{MOT}} \tag{5}$$

Due to the fact that the parameters p_1, p_2, p_3 are identical to the previous experiment, the fourth parameter c_{MOT} can be estimated.

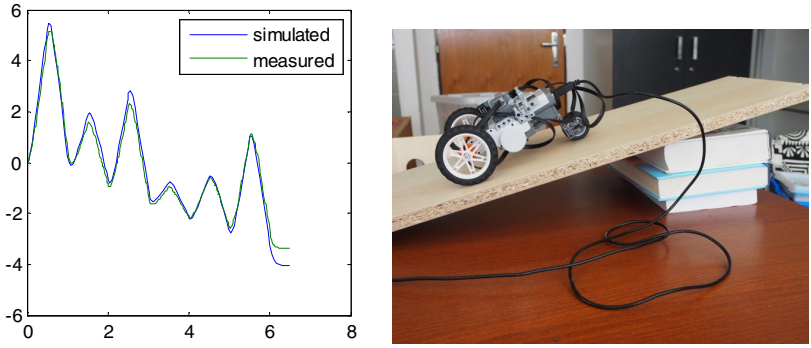

Fig. 3 Experiment "Drive on an inclined surface": Comparison of measured position and simulation with estimated parameters (left); photo of the real system (right)

Experiment nr. 3: Swinging with Fixed Wheels

Assuming $\theta, \dot{\theta}, \ddot{\theta} = 0$, the equation is of the form:

$$mL^2\ddot{\psi} - mgL\sin\psi + b^*\dot{\psi} + T\text{sign}(\dot{\psi}) = -c_{MOT}u \tag{6}$$

The c_{MOT} is already known, therefore the parameters $s_1 = mL^2$, $s_2 = -mgL$, $s_3 = b^*$ and $w_4 = T$ can be directly estimated.

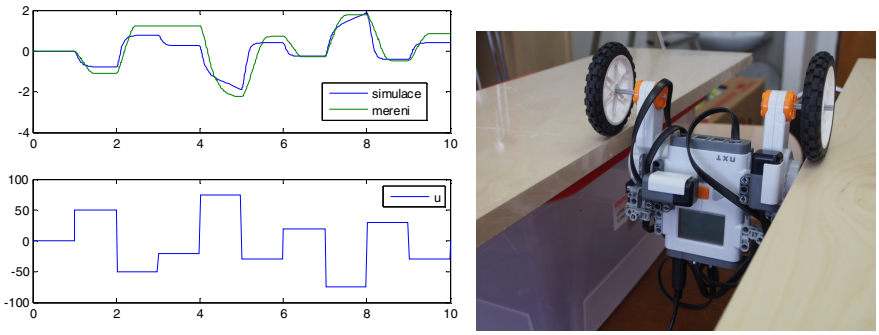

Fig. 4 Experiment "Swinging with fixed wheels": Comparison of measured position and simulation with estimated parameters (left); photo of the real system (right)

Experiment nr. 4: Full Dynamics (stable)

The experiment with full dynamics of eq. (1) can be realized for the stable arrangement of the system shown in Fig. 4. Fig. 5 shows the measured and simulated responses of the system upon the input voltage step.

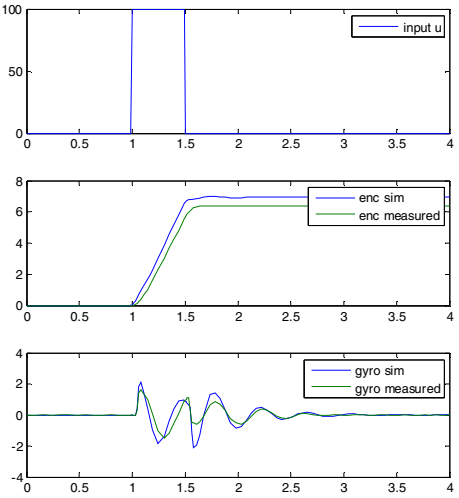

Fig. 5 Experiment "Full dynamics (stable)": Comparison of measured position and simulation with estimated parameters

3 Signal Processing and Controller Design

Considering the practical control of the balancing vehicle, the signal processing is of the highest importance. The controller can be tuned using a trial and error method (thus the model and its parameter estimation are not necessary) but the measured signals from the sensor must always be somehow filtered and processed.

Typically, the encoders, gyro and accelerometer [10,11,12] are available on the vehicle. Some other sensors can be used for better precision or for redundancy.

The most important task is to calculate the tilt angle which cannot be directly measured. Besides e.g. the Kalman filter which needs a good system model, the following two simple approaches are used: a) numerical integration of the gyro signal (the gyro drift must be precisely estimated and removed); b) Complementary filter, which combines the gyro $\dot{\varphi}_{GYRO}$ (with high pass filter) and accelerometer φ_{ACC} (with low pass filter). The resulting algorithm is very simple and intuitive and requires only one constant c to be tuned [1,3]:

$$\varphi_k = (1-c)(\varphi_{k-1} + \dot{\varphi}_{GYRO} T_S) + c\varphi_{ACC} \tag{7}$$

The control algorithm running on our vehicle Keywatko III., aka Hummer, uses c=0.02 with the Ts = 10ms.

4 Real-Time Prototyping and Production Code Deployment

Real-time control prototyping (RCP) is a very important part of MBD and can significantly reduce time to market and development costs.

The RCP, as well as production code generation, is based on the Simulink code generation technology available through a Simulink Coder and an Embedded Coder. For some educational platforms such as Arduino, Beagleboard or NXT Mindstorms the embedded code generation is allowed just with the Simulink licence alone (since R2012b). Real-time data logging and parameters tuning are available through the External mode via a wireless Bluetooth serial line. This tool chain was used for the data measurement and control of the Lego Balancing vehicle shown in Section 2.2.

The RCP of the Keywatko III., aka Hummer, shown in Fig. 1, was performed using an I/O card MF624 and RealTime Toolbox. This tool chain is very advantageous for educational use (and popular among the students) because no compilation to C is needed and the full features of Simulink can be used, including variable step solvers [4].

Next, the dsPIC33f 16bit microcontroller was used as the final controller, together with the Kerhuel blockset, allowing code generation from the Simulink including I/O drivers.

5 Fault Diagnosis and Management

One of the key features of mechatronics is the possibility to include additional functions into the system due to the available computation capacity of the embedded microprocessor. The typical functionality is fault detection, diagnosis and management [7,8].

In the case of practical implementation of the control algorithm for a balancing vehicle, at least the following issues must be considered: a) sensor functionality check; b) battery level tracking; c) safe transition to degraded mode (e.g. control with less sensor functionality). For that reason usually some sensor redundancy is required.

The common framework consists of the controller and supervisor part of software [8]. The supervisor watched the inputs and outputs of the system and switches between operation modes (Fig. 6). The easiest way to implement these algorithms is to use state diagrams using StateFlow. The switching between different controller subsystems related to the operating modes can be done using a Switch – Case structure.

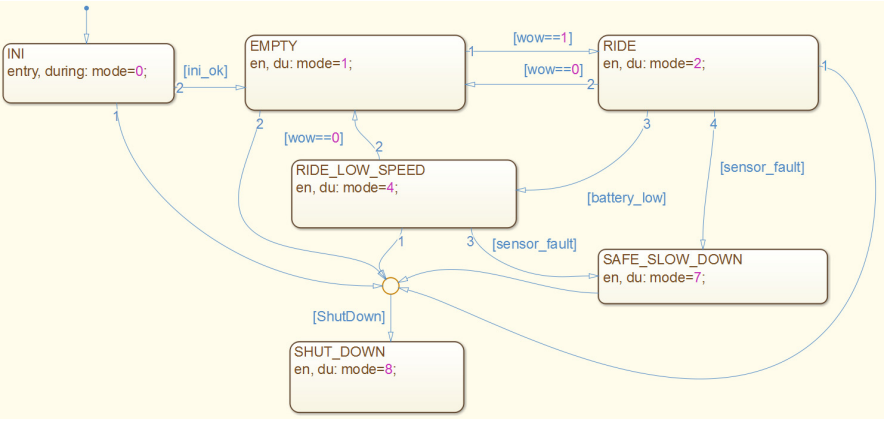

Fig. 6 Implementation of the operating mode switching in the StateFlow

6 Conclusions

The MBD of the self-balancing vehicle can be very successfully used in education for the demonstration of several aspects of a complex mechatronic system. Freshmen can gain satisfactory results just with a hand tuned PID and a complementary filter while graduates can apply modern control theory and a Kalman filter.

The use of the automatically generated code from the Simulink can significantly accelerate the design and test procedures, and often in educational environments can in fact enable the successful completion of the project.

This paper presents several aspects of the MBD of a balancing vehicle with the focus on parameter estimation, which significantly motivates the analytical modelling of the plant and also fault management which is an important part of virtually all real embedded systems. However it is often neglected in classrooms.

Acknowledgments. The present work has been supported by European Regional Development Fund in the framework of the research project NETME Centre under the Operational Programme Research and Development for Innovation. Reg. Nr. CZ.1.05/2.1.00/01.0002, id code: ED0002/01/01, project name: NETME Centre –New Technologies for Mechanical Engineering).

References

[1] Colton, S.: The balance filter – A simple solution for Integrating Accelerometer and Gyroscope Measurements for a Balancing problem, report, http://web.mit.edu/scolton/www/filter.pdf
[2] Grasser, F., D'Arrigo, A., Colombi, S., Rufer, A.C.: JOE: a mobile, inverted pendulum. IEEE Transactions on Industrial Electronics 49(1), 107–114 (2002)
[3] Grepl, R., Zouhar, F., Štěpánek, J., Horák, P.: The Development of Self-balancing Vehicle: A Platform for Education in Mechatronics. Technical Computing Prague 2011 (2011)
[4] Grepl, R.: Real-Time Control Prototyping in MATLAB/Simulink: Review of tools for research and education in mechatronics. In: 2011 IEEE International Conference on Mechatronics, Mechatronics (ICM), April 13-15, pp. 881–886 (2011)
[5] Grepl, R., Zouhar, F., Štěpánek, J., Horák, P.: The Development of Self-balancing Vehicle: A Platform for Education in Mechatronics. Technical Computing Prague 2011 (2011)
[6] Horák, P.: Control of laboratory model of unstable balancing vehicle, master thesis, MechLab, BUT (2011)
[7] Isermann, R.: Mechatronic systems - Innovative products with embedded control. In: Control Engineering Practice, vol. 16, pp. 14–29 (2008)
[8] Isermann, R.: Fault-Diagnosis Systems: An Introduction from Fault Detection to Fault Tolerance. Springer (2006)
[9] Lin, S., Tsai, C.: Development of a Self-Balancing Human Transportation Vehicle for the Teaching of Feedback Control. IEEE Transaction on Education 52(1) (2009)
[10] Łuczak, S., Oleksiuk, W., Bodnicki, M.: Sensing Tilt with MEMS Accelerometers. IEEE Sensors J. 6(6), 1669–1675 (2006)
[11] Łuczak, S.: Advanced Algorithm for Measuring Tilt with MEMS Accelerometers. Recent Advances in Mechatronics, 511–515 (2007), doi:10.1007/978-3-540-73956-2_100, WOS:000251017700100
[12] Łuczak, S.: Specific Measurements of Tilt with MEMS Accelerometers, Mechatronics. Recent Technological and Scientific Advances, 705–711 (2011), doi:10.1007/978-3-642-23244-2_85, WOS:000309670600085
[13] Štěpánek, J.: System identification, sensory system and implementation of control algorithm for unstable balancing vehicle, master thesis, MechLab, BUT (2011)
[14] Zouhar, F.: Design of construction, control and electronics for unstable balancing vehicle, master thesis, MechLab, BUT (2011)

The Design and Use of 3DOF Manipulator as a Platform for Education in Mechatronics

D. Klimes, T. Ripel, M. Suransky, and J. Vejlupek

Mechlab, Faculty of Mechanical Engineering, Technicka 2,
Brno University of Technology, 616 69, Brno, Czech Republic
y115682@stud.fme.vutbr.cz
www.mechlab.cz

Abstract. This article deals with the manipulator applied as an educational platform in mechatronics. All important parts of the design procedure are presented, including mechanical construction, electronics, control and safety management, with the use of additional sensors. The visual tracking of the end effector as an example of the practical task is also described.

1 Introduction

Currently, the use of different kinds of manipulators has expanded to various industries, where they have increasingly replaced humans. For education in mechatronics it is therefore desirable to have an educational platform which could show problems of the design and use of such manipulators [1], [2], [3].

This educational platform should be composed of commercially available components (COTS), should ensure modularity and total openness with the possibility of placing additional sensors. Such a teaching tool would be suitable for teaching the kinematics and dynamics of manipulators as well as for the classical and advanced control algorithms [4] which use the identified model of the plant. The educational platform should be capable of high dynamics movements, in order to show the influence of dynamic motion and gravitational forces.

Today the most widespread educational tool is Lego Mindstorm [5]. Due to the large clearances of Lego parts, it was not possible to achieve very precise and dynamic movements at the same time. Often used as an actuator for small educational manipulators, servo drives are commercially available [6]. Their use simplifies the design itself and consequently control of the manipulator. The disadvantage is, however, relatively little dynamic movement. Large and self-locking these actuators also present a simple way to demonstrate the influence of gravity.

For the design of an educational model it was used enough to use dimensioned DC motors geared to be sluggish. The design should be based on the kinematic and dynamic model of the manipulator in Simmechanics [7], [8].

T. Březina and R. Jabloński (eds.), *Mechatronics 2013*,
DOI: 10.1007/978-3-319-02294-9_111,

2 Mechanical Design

The three DOF (degrees of freedom) device of the RRR type has been chosen as a representative of a manipulator commonly used in the robotic industry. The body consists of four parts, connected by rotary joints into an open chain mechanism finished by an end effector. The aluminum frame provides both a rigid and sufficiently light construction. All three rotary joints are driven by direct current motors with worm gearboxes. Figure 1 shows a CAD model of the device.

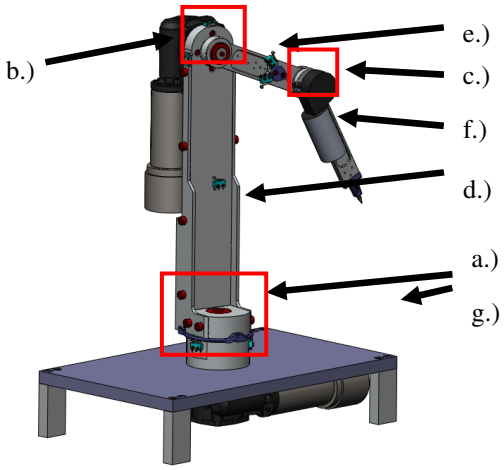

Fig. 1 The manipulator CAD model

The joint a.) controls rotation of the whole device in 320° range around its axis perpendicular to the base g.). The joint b.) moves arms e.) and f.) in a range of 270° and the last joint c.) ensures rotary movement of arm f.) in a range of 290°. The mechanical design of joints a.) and b.) is shown in the figures below in detail.

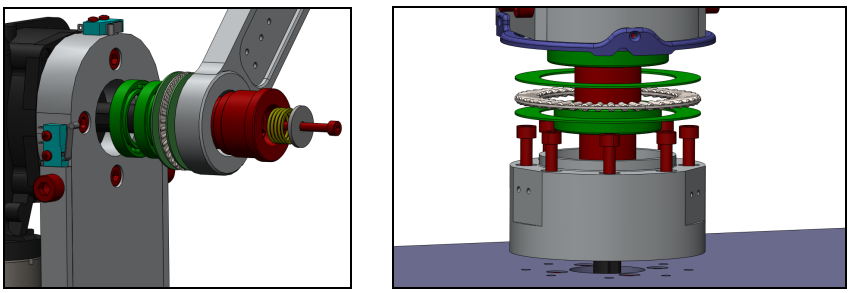

Fig. 2 Left – detail of the joint b.), right – detail of the joint a.)

3 Electronics

The basic control hardware is the MF624 input/output card which is commonly used for education in mechatronics. This card generates and processes the signals used to control the manipulator. Because the designed manipulator can achieve very dynamic movements, it is necessary for educational purposes to ensure safe operation. For movement of the manipulator in the area of the work it has protective electronics that evaluate the current state of the manipulator together with limit switches, all on a hardware level. No overrun of allowable torque is provided by sensing the current (LEM), where the current value is evaluated in the software. Everything is integrated into the library usable in Simulink.

The power electronics consist of three full H-bridges, which are connected to DC motors. The complete diagram is shown in Fig. 3.

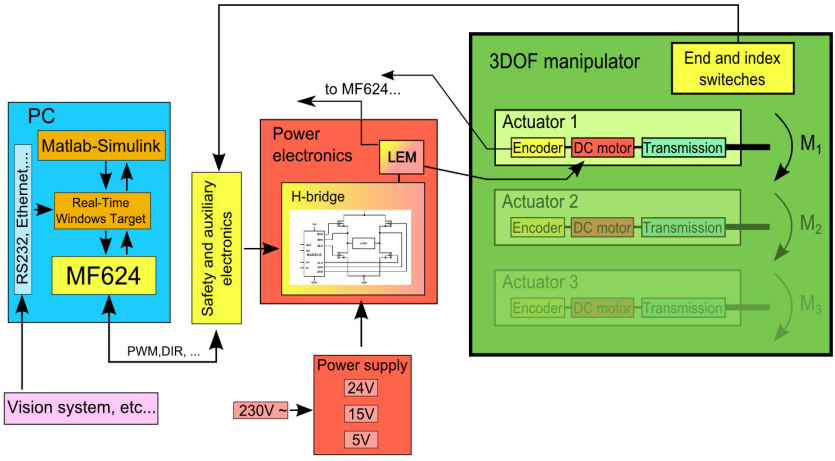

Fig. 3 The complete diagram of electronics

4 Control Methods

The first and simplest method for manipulator control was to design a separate PID regulator for each drive. Tuning of these PID regulators was quite easy due to the powerful drives used.

Second method was feedforward control. For this type of regulator an inverse dynamic model of the manipulator was required [9]. Some parameters of the dynamic model, for example dimensions, masses and inertia matrices of parts, were found out from constructing a model in SolidWorks software. Other parameters, like for example friction coefficients, were found out experimentally.

In Fig.4 it is obvious, that the manipulator control is based on feedforward, and reaches excellent results comparable with a well tuned PID regulator.

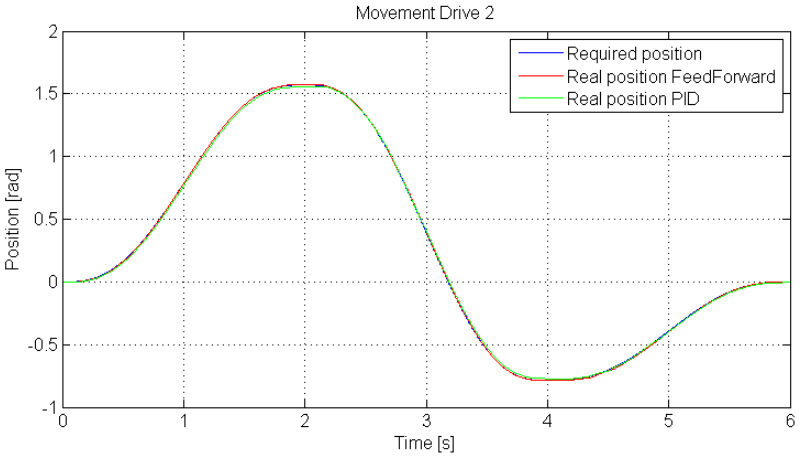

Fig. 4 Time progress of swing using PID reg. a feedforward reg.

5 Practical Use of Manipulator with Redundant Sensors

For educational use the platform is supplemented by further sensors, such as accelerometers. The manipulator platform is also complemented by a vision system (a product of National Instruments) which is commonly used in the industry as well as in education [10].

5.1 Use of Redundant Accelerometer for Sensing Rotation

An important task is finding the absolute rotary position of the actuator (output from transmission). If the reducing gear ratio is too large, it is simply not possible to use an index signal from the encoder (which is located on the motor shaft).

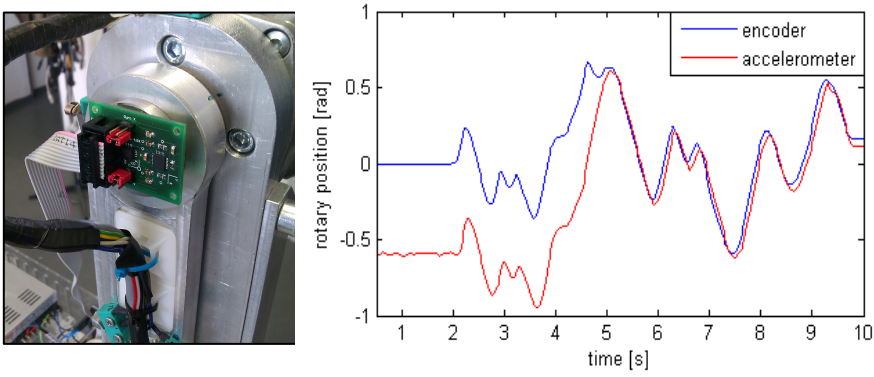

Fig. 5 Location of the accelerometer, which is used for sensing rotation (on the left). Time progress rotary position of second actuator, which is obtained from the encoder or the accelerometer (on the right).

When the manipulator is starting, there must be an initialization sequence executed using signals from the index switches (for finding the absolute rotary pos. of the actuator).

An alternative method is to use a signal from the accelerometer at the time when the manipulator is not moving (at the start of using the manipulator).

A comparison of the rotary position of the actuator obtained from an "absolute" accelerometer and a "relative" encoder (which uses an index switch) is shown in fig. 5. The accelerometer was placed on the axes of the second actuator, so that it only sensed the acceleration of gravity.

5.2 Use of Vision System for Tracking

Using smart cameras NI1742 created a complex mechatronic system that performs the monitoring and controlling of the position of the end effector in the *y* and *z* axes. Inspection for image processing and evaluation is created in Vision Builder AI (from National Instruments), which is easy to use and suitable for demonstrating the commonly used methods of image processing.

A simple algorithm evaluates the position defined by the marks, which is located near the end effector. Due to relatively slow imaging, use is restricted to rather slower movements of the manipulator (for educational purposes it is sufficient).

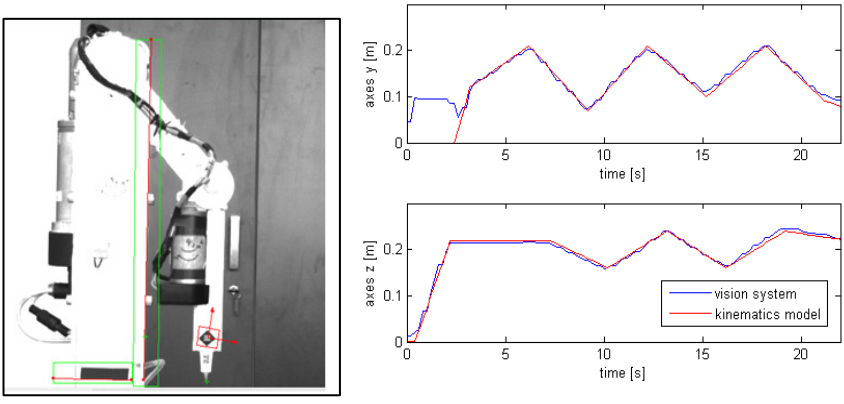

Fig. 6 Output of inspection in VBAI (on the left). Time progress of position of the end effector in axes y, z (on the right).

6 Conclusions

This article deals with the design and use of a typical mechatronic system, which is a 3DOF manipulator. The final educational platform is easy to use for the different control methods [11], [12].

The platform is designed so that it is possible to make highly dynamic movements. It can be further extended and modified according to the requirements of the target application. For application control and processing of the signal a Matlab-Simulink was used, communicating with the vision system from National Instruments.

Acknowledgments. This work was supported by the BUT project FSI-J-12-1808 "Modelling and control of high speed and precision manipulators".

References

[1] Zezula, P., Vlachy, D., Grepl, R.: Simulation modeling, optimalization and stabilisation of biped robot, In: Recent Advances in Mechatronics, Int. Conf. on Mechatronics, Warsaw, POLAND (2007), doi 10.1007/978-3-540-73956-2_25, WOS:000251017700025

[2] Bodnicki, M., Sęklewski, M.: Design of Small-Outline Robot – Simulator of Gait of an Amphibian. In: Recent Advances in Mechatronics, pp. 77–81 (2007)

[3] Wierciak, J., Jasińska-Choromańska, D., Szykiedans, K.: Orthotic Robot as a Mechatronic System. In: Mechatronics. Recent Technological and Scientific Advances, pp. 579–588 (2011)

[4] Krejsa, J., Vechet, S., Hrbacek, J., Schreiber, P.: High Level Software Architecture for Autonomous Mobile Robot. In: Recent Advances in Mechatronics, pp. 185–190 (2008-2009), WOS: 000277076900032

[5] Galvan, S., Botturi, D., Castellani, A., Fiorini, P.: Innovative Robotics Teaching Using Lego Sets. In: IEEE Int. Conf. Robotics and Automation (2006)

[6] Cocota Jr., J.A.N., Fujita, H.S., da Silva, I.J.: A Low-cost Robot Manipulator for Education. In: Technologies Applied to Electronics Teaching (TAEE), pp. 164–169 (2012)

[7] Grepl, R.: Simulation of unilateral constraint in MBS software SimMechanics. In: Recent Advances in Mechatronics, International Conference on Mechatronics, Warsaw, POLAND (2007), doi 10.1007/978-3-540-73956-2_63, WOS:000251017700063

[8] Grepl, R., Vlach, R., Krejci, P.: Modelling of unilateral constraints for virtual prototyping in SimMechanics. In: IEEE International Conference on Mechatronics, Kumamoto, Japan (2007), WOS: 000254288200023

[9] Grepl, R.: Extended kinematics for control of quadruped robot. In: Recent Advances in Mechatronics, International Conference on Mechatronics, Warsaw, Poland (2007), doi 10.1007/978-3-540-73956-2_26, WOS:000251017700026

[10] Krejci, P.: Bradac,M., Using LabVIEW for Developing of Mechatronic System Control Unit. In: Mechatronics: Recent Technological and Scientific advances, 9th Int. Conference on Mechatronics, Warsaw, Poland (2011), WOS:000309670600038

[11] Krejsa, J., Vechet, S.: Mobile Robot Motion Planner Via Neural Network. In: Engineering Mechanics 2011, 327-330 (2011), WOS: 000313492700075

[12] Vechet, S.: The Rule Based Path Planner for Autonomous Mobile Robot. In: Mendel 2011-17th Int. Conference on Soft Computing, pp. 546-551(2011), WOS:000302647900084

Jasper – A Platform for Teaching Mechatronics

G. Gaspar[1], S. Pavlikova[2], P. Fabo[3], and P. Pavlík[4]

[1] Slovak University of Technology, Faculty of Materials Science and Technology in Trnava, Pavlinska 16, 917 24, Trnava, Slovak Republic
gabriel.gaspar@stuba.sk
[2] Slovak University of Technology, Faculty of Chemical and Food Technology, Radlinského 9,812 37, Bratislava, Slovak Republic
sona.pavlikova@stuba.sk
[3] Comenius University in Bratislava, Faculty of Mathematics Physics and Informatics, Department of Experimental Physics, Mlynská dolina 842 48 Bratislava 4, Slovak republic
[4] University of Žilina, Faculty of electrical engineering, Univerzitná 1, 010 26 Žilina, Slovak republic

Abstract. The paper deals with the concept of the graphical open-source programming environment to support education in mechatronics. Proposed multiplatform environment was created in Java and allows the creation of control programs for mechatronic systems without detailed knowledge of the syntax of a particular programming language. Part of the development environment is the hardware platform for connecting sensors and actuators for the creation of stationary mechatronic systems, mobile robots and laboratory experiments that can be controlled from an interactive development environment.

1 Introduction

At present time is apparent the onset of visual programming tools for programmers, to hide internal solution of technological procedures, often considerably large, allowing them concentrating on the core solution of the problem. The use of such tools in practice requires a different style of work, in which detailed knowledge of the syntax of a particular programming language is replaced with a capability of comprehensive view of the problem and finding its solution algorithm.

For teaching of such work style, there are several platforms available. Their attractiveness in the learning process is enhanced by support of specific hardware manufacturer. A typical representative of such a programming environment is Lego Mindstorms [1]. A fundamental lack of standard commercial environments is their closed character. These programming environments have limited options for adding custom modules that address the specific requirements of the user. Hardware is restricted to a particular set of components created by the manufacturer without any possibility of extending the functionality with products of other vendors or custom user solutions.

T. Březina and R. Jabloński (eds.), *Mechatronics 2013*,
DOI: 10.1007/978-3-319-02294-9_112,

2 General Requirements

For teaching robotics, mechatronics, experiment control and data collection [4, 5, 7], we proposed a platform based on on-line system management (e.g. robot, experiment) divided into two basic parts:

- control part (control algorithm, data processing, visualization parameters) is implemented in the control computer (desktop, Windows , Linux), and the control algorithm, data collection and data evaluation is made in a specialized graphical environment. Where appropriate there can also be used standard programming languages (Java, Python, C / C + + with the help of pre-built libraries) and common programming environment used with these languages (Eclipse, Netbeans, etc.).
- sensors for data collection and actuators are operated in a separate section (process-board) controlled by a microcontroller. The process-board is connected to the control computer using a standard USB interface. In the case of stationary systems, the communication with the host computer is performed via cable and for simple applications can be powered directly from the computer. For mobile robotic applications is used RF line and the robot also includes an autonomous power supply. In terms of teaching, this concept brings the advantage of simple incremental tuning of the system, because all process parameters are available in real time and the system can be step through and debugged using the standard program tools that are a part of the chosen programming language.

Based on the above, we have defined platform requirements described in detail in the following chapters.

3 Hardware Requirements

- process-board based on 32-bit ARM Cortex M3 platform with the implementation of the basic functional blocks for mechatronic and robotic systems (A/D, D/A converters, timers for measuring time intervals and generating time sequences - PWM, digital input and output ports)
- predefined and configured interfaces for connecting sensors and actuators - ultrasonic and optical sensors, servos, DC motors, IRC, stepper motors
- extensibility for specialized versions for controlling physical laboratory experiments (LabBoard), robotic applications (RobotBoard), stationary mechatronic systems (ControlBoard)
- modular concept from simple USB port powered versions to galvanically isolated power supply with built-in overload protection with power monitoring

Block diagram of the proposed platform for robot control RobotBoard is shown in Fig. 1. The platform is implemented on the STM32F100 microprocessor and allows you to connect 2 DC motors (field distribution eg. in [6]), 4 standard analog servos, has 8 digital inputs and 8 outputs and 4 12-bit analog inputs. All inputs and outputs are protected against short circuit and overload.

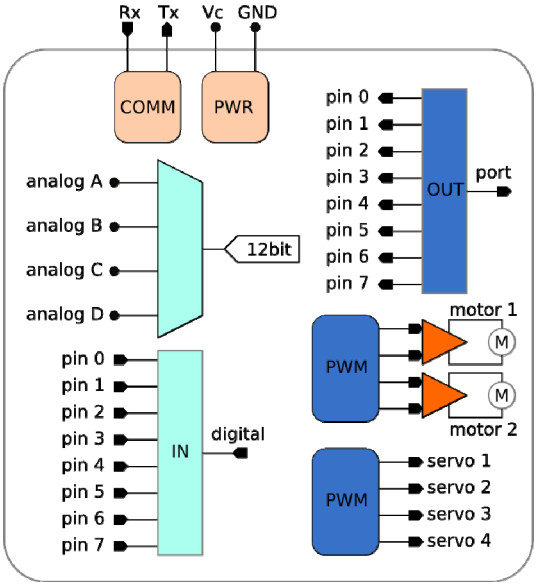

Fig. 1 Block diagram of the RobotBoard platform implemented on the STM32 microprocessor

4 System Requirements

- control of mechatronic systems in real time
- number of complete information exchange between the control program and process-board (including processing in process-board) at least 100 times per second
- packet-oriented communication protocol with detection of error conditions
- multiplatform and modular system with the possibility of further expansion
- connection between the computer and process-board via standard USB without the need to install special drivers into the operating system, communication with process-board by cable or RF modem (2.4GHz, range 80m) in Fig. 2.

To meet the requirements above, we primary chose system using a standard USB communication interface. As a communication protocol was chosen modified master-slave MODBUS protocol. Protocol modifications were aimed to

reduce complexity for implementation on small microcontrollers and the modified protocol is known as uBUS. Complete implementation of the uBUS protocol state diagram on 8-bit CY8C29466 processor occupies about 700 bytes.

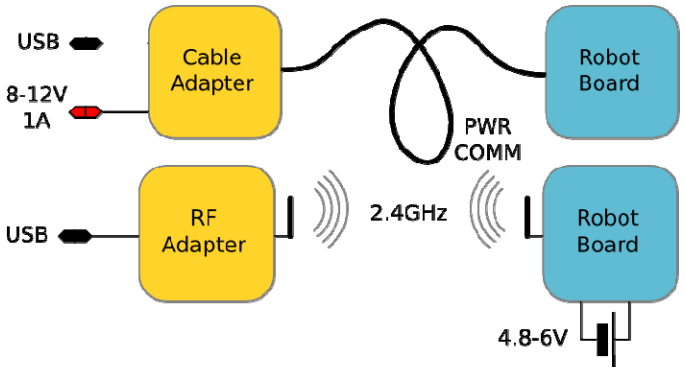

Fig. 2 Communication for stationary and mobile applications

5 Program Requirements

- beginner friendly compact graphical environment that eliminates the risk of syntax errors in programming
- libraries for advanced users to interact with a process-board for standard programming languages and operating systems using the standard compilers or interpreters
- all program interfaces are defined as open formats

6 Jasper – Graphical Programming Environment

Block-oriented graphical programming environment is important for beginners, because at the appropriate elemental design it eliminates programming errors (syntax, brackets, etc.) and allows focusing on the semantic part of the work.

For implementing a functional prototype of the graphical programming environment we used a basic idea of Scratch programming environment [2], which involves the use of block of defined shape, while the shape of the blocks defines their mutual use. Scratch is developed by MIT and is primarily focused on teaching programming for children (at primary level) and has only limited support of selected hardware. Further development of this environment is heading to cross-platform web application, which simplifies deployment of this program in the teaching environment (does not require installation, etc.). On the other hand, it complicates possible integration of the hardware into the environment.

In Jasper was the idea of blocks from Scratch environment re-implemented in Java language with respect to the maximum process-board integration directly into the programming environment.

The basic block corresponds to one command in a standard programming language. Block has a defined input and output terminal, using terminals blocks are classified to the program structures. Whenever moving block, the corresponding closest target terminal of another block is activated. When the block is released and the target terminal is activated, blocks are automatically arranged and/or regrouped. An example of a simple program and its output is shown in Fig. 3.

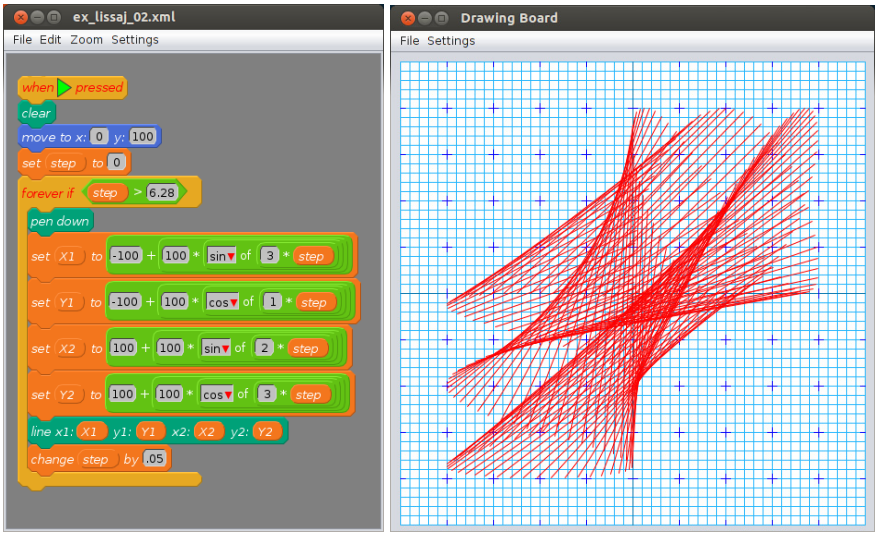

Fig. 3 A simple program and its graphical output

Basic blocks are depending on their function color coded, which enhances the clarity of the resulting program. In addition to basic blocks are in an environment defined shape different block for variables, numeric and relational operators. These blocks can be nested, and compatibility rules are determined by their shape. Blocks are arranged in library groups according to their meaning. On the desktop of the editor program are moved using drag-and-drop. Library of RobotBoard control blocks is shown in Fig. 4.

In terms of expression means, Jasper environment corresponds to the level of BASIC programming language, but without using jump instruction. From a programming standpoint is the area of the visibility of variables bounded to use in a single editor space program, but the program may consist of multiple edit windows. Each block structure is interpreted at runtime as a separate thread. Jasper environment therefore enables parallel operation of several programs simultaneously. Programs can share system resources, therefore locks are implemented in the environment that allow access to shared resources (e.g. communication interface) always only for one thread.

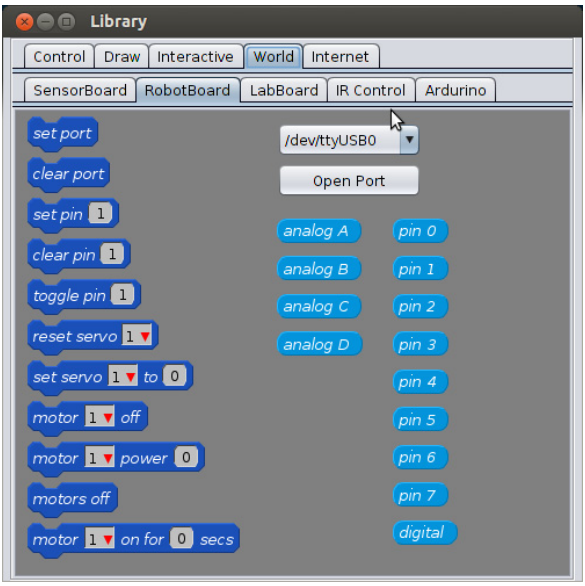

Fig. 4 Component library for RobotBoard

Library of blocks contains a set of basic blocks to control run-time, operators and variables, blocks for drawing on the graphics board, blocks representing virtual devices and a set of blocks for control of process-board.

Jasper programming environment in the current stage of development is in the state of functional prototype to validate used technology. Current project status is given in [3].

7 Conclusion

This paper describes the features of the proposed open-source platform for teaching robotics, mechatronics, control experiments and data collection. Platform allows wide use in teaching robotics and mechatronics in high schools.

It can also be applied in designing of physical experiments and teaching programming in elementary schools. The limited extent of the contribution does not allow a detailed description of all features, readers will recommend to the source [3].

References

[1] The Lego Group. Lego.com MINDSTORMS (2013), `http://mindstorms.lego.com/en-us/default.aspx` (cit. May 12, 2013)

[2] MIT Media Lab. Scratch (2013), http://scratch.mit.edu/ (cit. May 12, 2013)
[3] TNTECH. Jasper-EN (2012), http://wiki.tntech.eu/index.php?title=Jasper_-_EN (cit. June 12, 2013)
[4] Svoboda, J., Simak, B., Zeman, T., Hrad, J.: Educational activities of the CTU Prague team in EMC and support of the EMC development problems in the Czech Republic. In: Electromagnetic Compatibility 1996 – 13th International Wroclaw Symposium, pp. 208–211. Institute of Telecommunications, Wroclaw (1996) ISBN 83-901999-4-7
[5] Dudak, J., Gaspar, G., Maga, D., Pavlikova, S.: Kiwiki: Open-Source Portal for Education in Mechatronics. In: MECHATRONICS: Recent Technological and Scientific Advances, pp. 499–505 (2011) ISBN 978-3-642-23243-5
[6] Maga, D., Hartansky, R.: Numericke metody riesenia elektromechanickych uloh, 113 p. Trencianska univerzita Alexandra Dubceka v Trencíne, Trencin (2001) ISBN 80-88914-29-9
[7] Hrad, J., Zeman, T., Hajek, J.: Multilanguage e-learning course for industrial automation. In: Learning to Live in the Knowledge Society, pp. 371–372. Springer, New York (2008) ISBN 978-0-387-09728-2

Model-Based Design of Mobile Platform with Integrated Actuator – Design with Respect to Mechatronic Education

O. Andrs, Z. Hadas, J. Kovar, J. Vetiška, and V. Singule

Faculty of Mechanical Engineering, Brno University of Technology, Technicka 2896/2, 616 69, Brno, Czech Republic
{andrs,hadas,kovar,vetiska,singule}@fme.vutbr.cz

Abstract. This paper deals with a model-based design of an actuator for a mobile platform. This paper presents way how to use model-based design of this mechatronic system with respect to mechatronic education. The presented mobile platform is used for shifting of a load in defined linear trajectory. Platform speed, maximal weight of the load and capacity of battery are used for the optimal actuator design. The actuator has to be integrated inside platform housing and it is limiting factor for design of this system. Several steps of model-based design are presented with respect of mechatronic approach and these steps are well known for our mechatronic students. The presented approach provides way how to develop such mechatronic system based on the model.

1 Introduction

This paper deals with a model-based design of an integrated actuator for a mobile platform. The presented mobile platform is used for shifting of a load in defined linear trajectory. Platform speed, maximal weight of load and capacity of batteries are used for the optimal actuator design. The actuator has to be integrated inside platform housing and it is limiting factor for design of this system.

These requirements of presented mechatronic system provides very interesting task for mechatronic students at Brno University of Technology. The main aim of our paper is presentation of mechatronic approach and using of model-based design in development cycle of this mechatronic system.

2 Model-Based Design in Mechatronic Education

Model-based design is a method of systems development associated with design of complex mechatronic systems [1]. This method is used in many applications like motion control, industrial equipment, aerospace and automotive applications.

T. Březina and R. Jabloński (eds.), *Mechatronics 2013*,
DOI: 10.1007/978-3-319-02294-9_113,

Therefore the using of model-based design is very important in education process of mechatronic students in our University. The model-based design here described is based on a simulation modeling of mechatronic systems due to very high flexibility in education process. The students have to describe inputs and outputs and establishing a common framework inside the development process. Students design simulation model and they improve it during this development process. The schematic diagram of the model-based design is shown in Fig. 1.

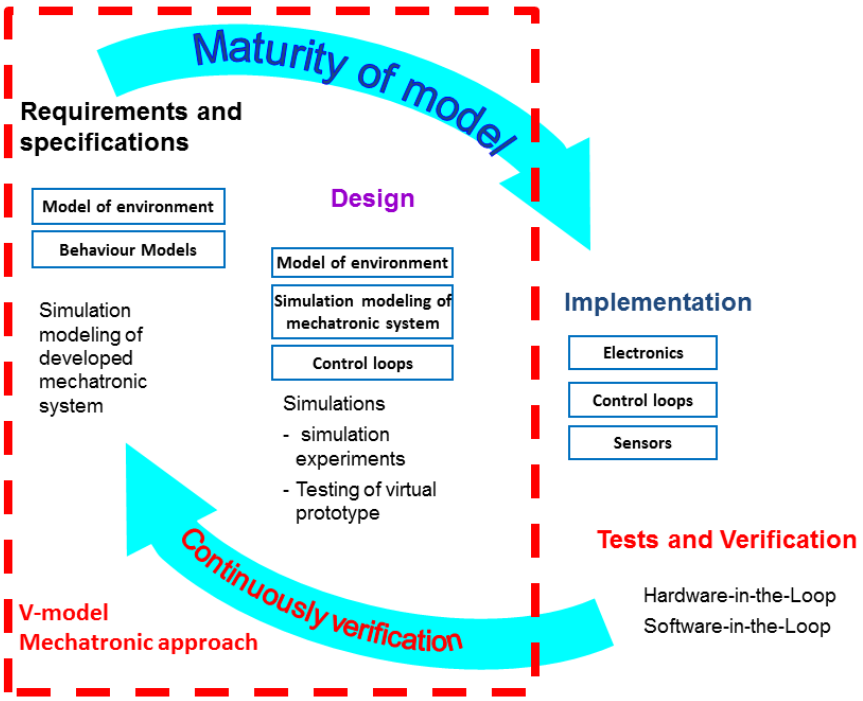

Fig. 1 Model-based Design of Mechatronic System Development

Model based design is usually substituted for a model-based control design method which provides an efficient approach for establishing a common framework for communication inside the design process of hardware and software implementation. Here considered method describes the whole development process of mechatronic system design. The design of new mechatronic systems starts with supporting of a development cycle which can be described as V-model with frameworks of mechatronic approach [2]. The used V-model in our development cycle is shown in Fig. 2. This model fits in with model-based design and it provides very useful tool for mechatronic education [3].

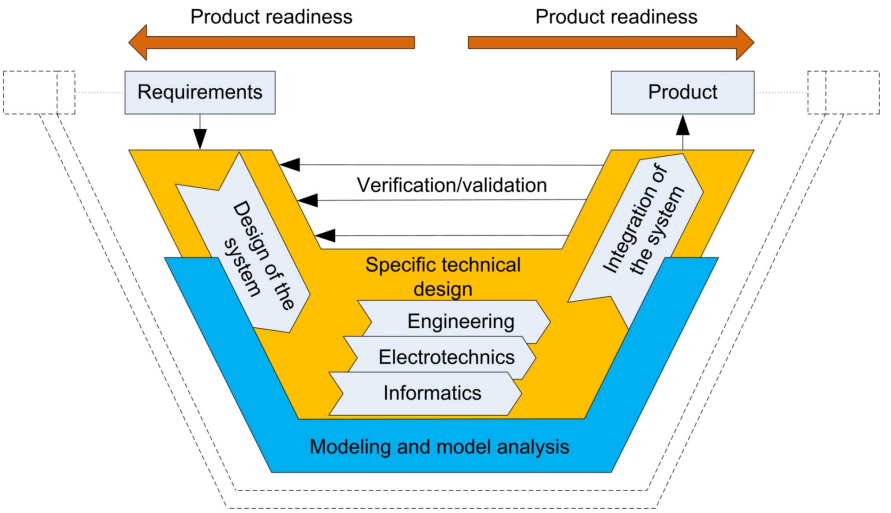

Fig. 2 V-model - Mechatronic Approach of System Development

3 Mobile Platform with Integrated Actuator

The aim of this paper is presenting of model-based design method, which is used for education of mechatronic students in our University. This method is presented on the development of a mobile platform with integrated actuator. The requirements for this task is using of integrated actuator inside platform housing. A power supply for actuator is batteries, which can be charged from solar panel. These batteries and electronics have to be integrated in platform housing too.

3.1 Model of Mobile Platform

The mobile platform consists of a platform, actuated and supported wheels, actuators, control, power electronics and batteries. The mobile platform is actuated by

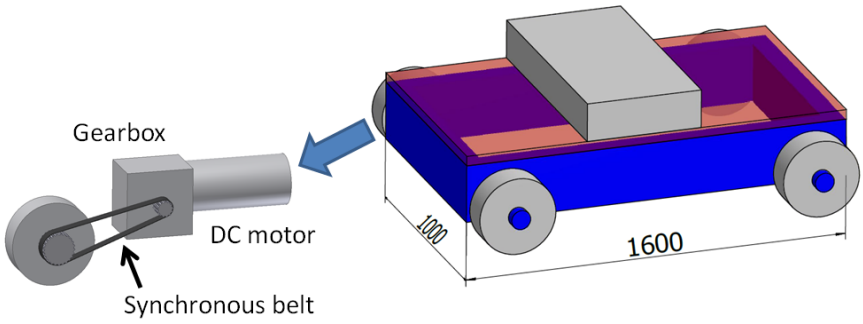

Fig. 3 Schematic diagram of mobile platform and proposal of integrated wheel actuator

pair of wheels and assumed weight is around 200 kg. The wheel actuator has to be integrated inside platform housing. The wheel motion is provided by 24 Volts DC motor with gearbox (planar or worm) and transmit of torque from DC motor to wheel is provided by a synchronous belt. The schematic diagram is shown in Fig. 3.

3.2 *Multi-body Model of Platform Actuator*

The mechanical design is very important for development of actuator [4]. The simulation model was designed in multi body system ADAMS, which can be used for dynamic analyses of electro-mechanical systems. This model consists of DC motor, gearbox, belt, wheel and platform and the model was realized with simple geometry at the first step of V-model iteration and final mechanical design is shown in Fig. 4. This model contains electromechanical equation of DC motor and the system behavior is observed [5]. The results of ideal DC motor start were analyzed and a current of DC motor are presented in Fig. 5. This model can be analyzed in co-simulation strategy together with model of electronics in Simulink and electrical parts is simulated and controlled in Simulink model and mechanical part is solved in multi-body system ADAMS as was presented in paper [6].

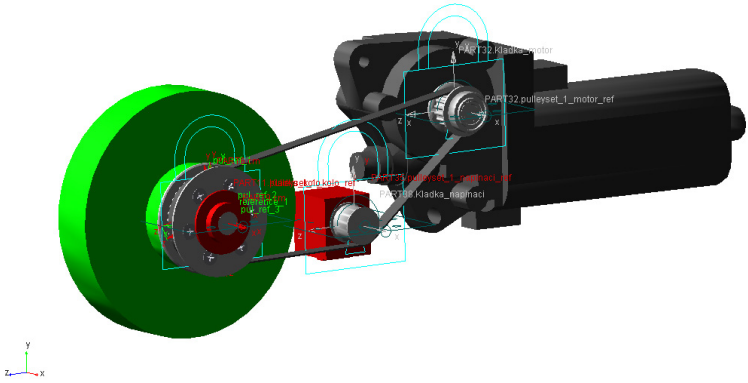

Fig. 4 Multi-body Model of DC Motor of Mobile Platform

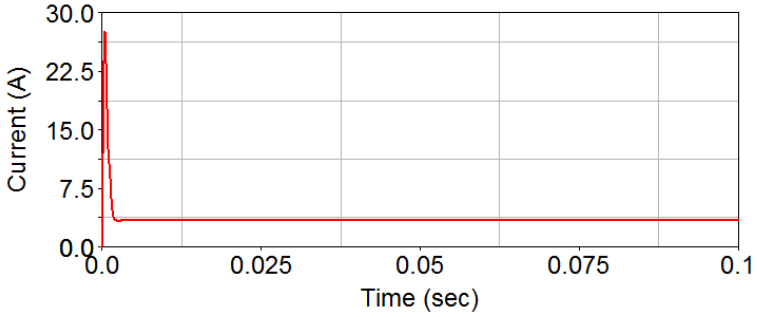

Fig. 5 Results of Dynamic Analyses - Current of DC motor – Weight of Platform 120 kg

3.3 CAD Model

The simulation results are a good starting point for virtual design finishing. Completion of the main actuator functional units including integration into the machine frame was resolved. During the creation of a virtual model was also considered and integrated the possibility of placing the sensors and the control electronics with batteries. The used sensors are placed outside the machine frame due to the requirement of easy accessibility. Virtual design assumes a couple of sensors pair with optical and inductive sensors. The electric control unit with batteries and charger are integrated together in one box inside the machine frame. Details of virtual design are presented in Fig. 6.

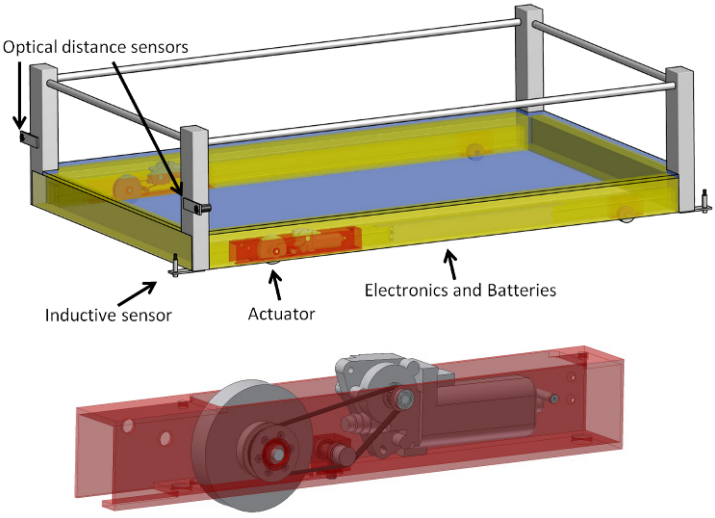

Fig. 6 CAD Model of Platform and Detail of CAD model of Actuator with DC motor

3.4 Control and Sensors

The proposed platform is remotely operated by wireless remote controller. The direction of platform movement (forward and backward) can be selected by wireless controller and also the stop of platform can be indicated. A switching of the motor direction is carried out by an implemented relay. Starting and braking of platform is realized by variable duty cycle of power signal with PWM modulation, which controls the electromotor [7]. Switching frequency of power signal is 20 kHz. Resolution of PWM is about 8 bits (it is sufficient for this type of task).

For purpose of detecting end of moving track as well of detecting a foreign object in workspace the movable platform is equipped by suitable sensors. The first type of sensors are inductive sensors E2A-M12KN08-WP-B1 2M, whose are able to detecting end of a moving track. For purpose of detection of foreign objects (obstacles) the optical distance sensors S15-PA-2-C00-PK are implemented. The

control unit is equipped with a measurement of over-current, supply voltage and temperature for protective purposes.

3.5 *Electronics and Batteries*

The operational and technical requirements implied the need to design control and power electronics which generates output signals for controlling of the actuators [8]. Designed electronics is powered by LiPo Battery Pack 3300 mAh 4S 16.8V which supplies enough energy for maximal 20 minutes of continuous operation. The battery pack is then continuously fed from a solar panel U_{eff} = 18.5 V, P_{max} 35W through four channels Li-Po charger. The schematic diagram of electronic system is shown in Fig. 7.

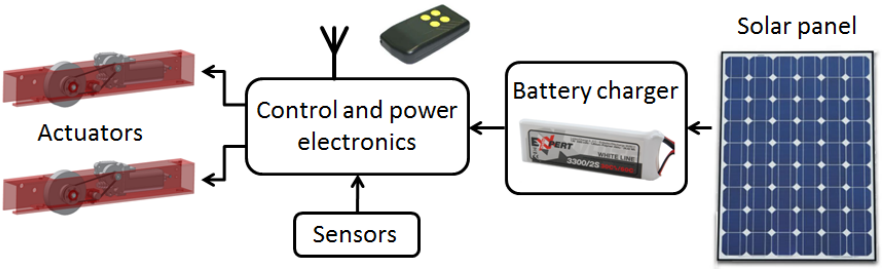

Fig. 7 Diagram of Electronics System

The main part of the control unit represents microcontroller PIC16F887 which processes signals from the sensors and generates control signals for controlling the power components (transistors and relays). An integrated AD converter is used to measure supply voltage and current of driven actuators. The developed control unit is shown in Fig. 8.

Fig. 8 Control and Power Electronics Board

3.6 *Test*

The final development phase included developing a testing device that had undergone series of tests. It is shown in Fig. 9. This process was accompanied by

controlling of the integration and interaction between the different systems. A series of tests was carried out consisting of two way movement to the selected track. These tests verified the correct operation of the control system and actuators themselves. Gradually, there were simulated all combinations of states corresponding to different information from the sensors. Average power supply current drawn by actuators during the experiments was approximately 4 A (8 A peaks) with platform load about 80 kg. The load is lower than was simulated in the first development cycle of simulation modeling. The real movement speed was affected by surface undulations to range 5 mm per meter.

Fig. 9 Mobile Platform under Test Load

4 Conclusions

The aim of this paper is presenting of model-based design and mechatronics approach, which was used for development of the mobile platform with integrated actuator. This task was prepared by our graduated Ph.D. students and it will be used for education of mechatronic students in our University.

This task is based on multi-body model of this mechatronic system which consists of mechanical assembly, actuator with gearbox, power supply, electronics and sensors. The appropriate model of this system is created and simulated and the optimal parameters are designed.

This mechatronic system was realized on the base of simulation results. Electronics and power supply was created and this mechatronic system was tested. The whole presented concept of the mobile platform with integrated actuator presents simple interdisciplinary task and it is very useful for mechatronic education.

Acknowledgments. The present work has been supported by European Regional Development Fund in the framework of the research project NETME Centre under the Operational Programme Research and Development for Innovation. Reg. Nr. CZ.1.05/2.1.00/01.0002, id code: ED0002/01/01, project name: NETME Centre – New Technologies for Mechanical Engineering.

References

[1] HUMUSOFT s.r.o., http://www.humusoft.cz/produkty/matlab/mbd
[2] VDI 2206. Design methodology for mechatronic systems (2002)
[3] Kovar, J., Andrs, O., Brezina, L., Singule, V.: Laboratory Delta Robot For Mechatronic Education Purposes. In: Proceedings of International Symposium on Power Electronics, Electrical Drives, Automation and Motion, SPEEDAM 2012, pp. 1209–1212 (2012)
[4] Brezina, T., Andrs, O., Brezina, L., Hadas, Z., Houska, P., Kovar, J., Vetiska, J.: Virtual Design of Industrial Manipulator Using Mechatronic Approach. In: Proceedings of the International Conference on Advances in Mechatronics 2011 (AIM 2011), pp. 105–110 (2011)
[5] Hadas, Z., Brezina, T., Andrs, O., Vetiska, J., Brezina, L.: Simulation Modeling of Mechatronic System with Flexible Parts. In: 15th International Power Electronics and Motion Control Conference and Exposition, EPE- PEMC 2012 ECCE Europe, LS2e.1/1-7 (2012)
[6] Brezina, T., Vetiska, J., Hadas, Z., Brezina, L.: Simulation, Modelling and Control of Mechatronic Systems with Flexible Parts. In: Jablonski, R., Brezina, T. (eds.) Proc. 9th Int. Conf. Mechatronics 2011, pp. 569–578. Springer, Berlin (2011)
[7] Andrs, O., Brezina, T., Kovar, J.: Design of fuzzy logic controller for DC motor. In: Mechatronics Recent Technological and Scientific Advances pp. 9–18 (2011)
[8] Andrs, O., Kovar, J.: Forward Kinematics Modelling of a Parallel Device for Cord Implants Tuning. In: Proceedings of 19th International Conference on Soft Computing. Mendel Journal series, pp. 283–288 (2013)

Author Index